Polymer 52 (2011) v–xvi

Contents lists available at ScienceDirect

Polymer

journal homepage: www.elsevier.com/locate/polymer

Polymer Vol. 52, No. 4, 17 February 2011

Contents

POLYMER COMMUNICATIONS

DNA-functionalized thermoresponsive bioconjugates synthesized via ATRP and click chemistry pp 895–900

Pengju Pan[a], Masahiro Fujita[a,*], Wei-Yang Ooi[a,b], Kumar Sudesh[b], Tohru Takarada[a], Atsushi Goto[c], Mizuo Maeda[a,*]

[a] *Bioengineering Laboratory, RIKEN, Hirosawa 2-1, Wako, Saitama 351-0198, Japan*
[b] *Ecobiomaterial Research Laboratory, School of Biological Sciences, Universiti Sains Malaysia, Minden, 11800 Penang, Malaysia*
[c] *Institute for Chemical Research, Kyoto University, Uji, Kyoto 611-0011, Japan*

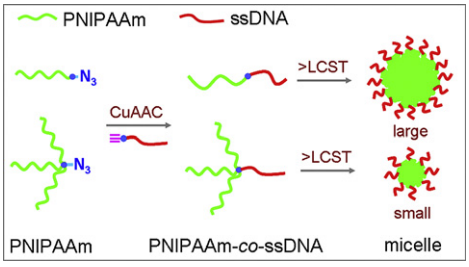

Poly(vinyl chloride) (PVC) hollow fibre membranes for gas separation pp 901–903

C.A. Jones[a], S.A. Gordeyev[b], S.J. Shilton[a,*]

[a] *Department of Chemical and Process Engineering, University of Strathclyde, James Weir Building, 75 Montrose Street, Glasgow G11XJ, Scotland, United Kingdom*
[b] *Institute of Nanotechnology, Lord Hope Building, 141 St. James Road, Glasgow G40LT, Scotland, United Kingdom*

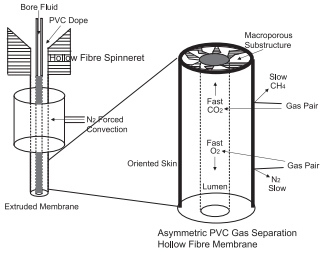

POLYMER PAPERS

Poly(butylene terephthalate) modified with ethoxylated bisphenol S with increased glass transition temperature and improved thermal stability pp 904–911

N. Lotti, M. Colonna*, M. Fiorini, L. Finelli, C. Berti

Dipartimento di Ingegneria Civile, Ambientale e dei Materiali, Via Terracini 28 40131 Bologna, Italy

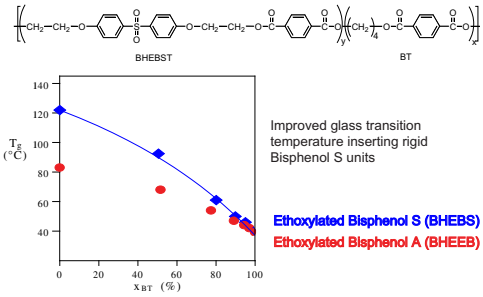

Polymer grafted silver and copper nanoparticles with exceptional stability against aggregation by a high yield one-pot synthesis pp 912–920

Stefan Bokern, Julia Getze, Seema Agarwal, Andreas Greiner*

Philipps-Universität Marburg, Department of Chemistry and Scientific Center of Materials Science, Hans-Meerwein-Strasse, Marburg D-35032, Germany

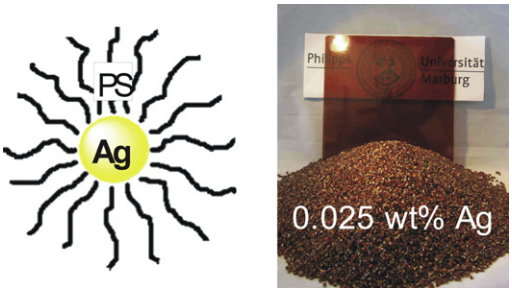

Synthesis and characterization of new poly(ortho ester amidine) copolymers for non-viral gene delivery pp 921–932

Rupei Tang[a,*], Weihang Ji[b], Chun Wang[b,*]

[a] *School of Medicine and Pharmaceutics, Jiangnan University, 1800 Lihu Road, Wuxi 214122, PR China*
[b] *Department of Biomedical Engineering, University of Minnesota, 7-105 Hasselmo Hall, 312 Church Street S. E., Minneapolis, MN 55455, USA*

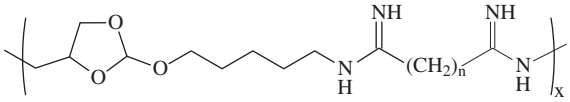

Degradable micelles based on hydrolytically degradable amphiphilic graft copolymers for doxorubicin delivery pp 933–941

Jun Chen[a,e], Malcolm M.Q. Xing[c,d,e,**], Wen Zhong[a,b,*]

[a] *Department of Textile Sciences, Faculty of Human Ecology, University of Manitoba, Winnipeg, MB R3T 2N2, Canada*
[b] *Department of Medical Microbiology, Faculty of Medicine, University of Manitoba, Canada*
[c] *Department of Mechanical Engineering, University of Manitoba, Canada*
[d] *Department of Biochemistry and Medical Genetics, University of Manitoba, Canada*
[e] *Manitoba Institute of Child Health, Canada*

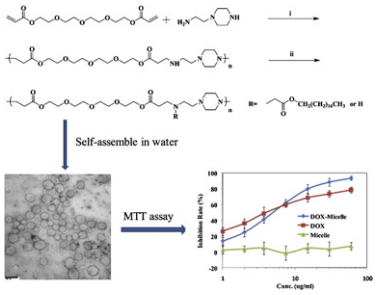

Polymer particles with a pomegranate-like internal structure via micro-dispersive polymerization in a geometrically confined reaction space I. Experimental study **pp 942–948**

Carla V. Luciani, Kyu Yong Choi*, Joong Jin Han, Yunju Jung

Department of Chemical and Biomolecular Engineering, University of Maryland, College Park, MD 20742, USA

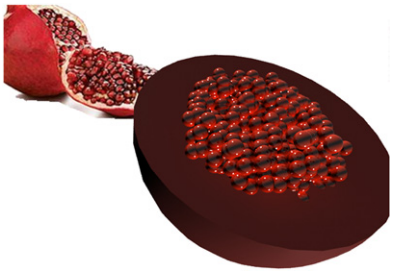

Synthesis and characterization of trifluoromethyl substituted styrene polymers and copolymers with methacrylates: Effects of trifluoromethyl substituent on styrene **pp 949–953**

Hongxiang Teng[a,c], Liping Lou[a,c], Kotaro Koike[a,b], Yasuhiro Koike[b,c], Yoshi Okamoto[a,c,*]

[a] *Polymer Research Institute, Polytechnic Institute of New York University, 6 Metrotech Center, Brooklyn, NY 11201, United States*
[b] *Faculty of Science and Technology, Keio University, Yokohama 223-8522, Japan*
[c] *Koike Photonics Polymer Project, ERATO-SORST, Japan Science and Technology Agency, Kawasaki 212-0032, Japan*

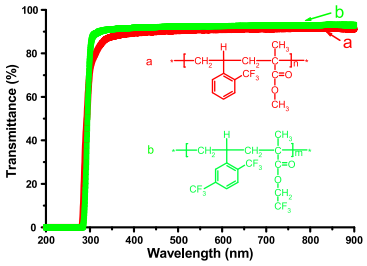

Synthesis, characterization and hydrolysis of aromatic polyazomethines containing non-coplanar biphenyl structures **pp 954–964**

Jyh-Chien Chen[a,*], Yen-Chun Liu[a], Jyh-Jong Ju[a], Chi-Jui Chiang[a], Yaw-Tern Chern[b]

[a] *Department of Polymer Engineering, National Taiwan University of Science and Technology, No. 43, Sec. 4, Keelung Rd., Taipei 10607, Taiwan*
[b] *Department of Chemical Engineering, National Taiwan University of Science and Technology, No. 43, Sec. 4, Keelung Rd., Taipei 10607, Taiwan*

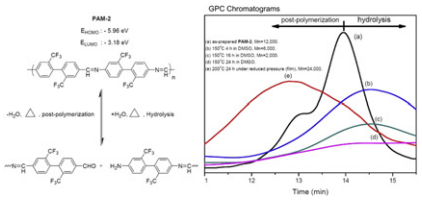

Effects of TS-1 zeolite structures on physical properties and enzymatic degradation of Poly (butylene succinate) (PBS)/TS-1 zeolite hybrid composites **pp 965–975**

Sung Yeon Hwang[a], Eui Sang Yoo[b], Seung Soon Im[a,*]

[a] *Department of Fiber and Polymer Engineering, College of Engineering, Hanyang University, 17 Haengdang-dong, Seongdong-gu, Seoul 133-791, Republic of Korea*
[b] *KITECH Textile Ecology Laboratory, 1271-18 Sa 1 Dong, Sangrokgu, Ansan City, Gyungido, Republic of Korea*

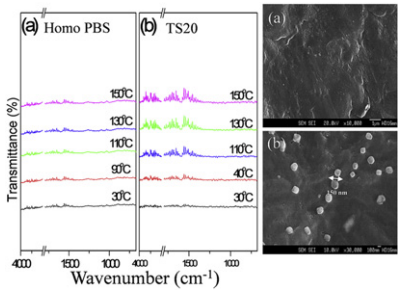

Carbazole/fluorene copolymers with dimesitylboron pendants for blue light-emitting diodes **pp 976–986**

Ying-Hsiao Chen[a], Yu-Ying Lin[a], Yung-Chung Chen[b], Jiann T. Lin[b], Rong-Ho Lee[a,*], Wen-Jang Kuo[c], Ru-Jong Jeng[a,*]

[a] *Department of Chemical Engineering, National Chung Hsing University, Taichung 402, Taiwan*
[b] *Institute of Chemistry, Academia Sinica, Taipei 115, Taiwan*
[c] *Department of Applied Chemistry, National University of Kaohsiung, Kaohsiung 811, Taiwan*

A series of random and alternating carbazole/fluorene copolymers with various dimesitylboron-containing carbazole contents were synthesized by Suzuki polymerization for use as a light-emitting layer in blue light-emitting diodes.

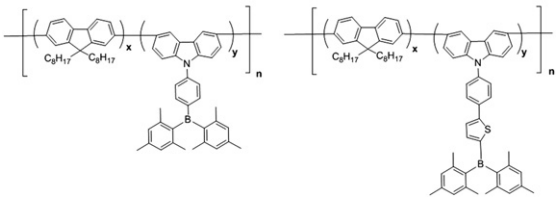

Poly(acrylic acid)-grafted magnetic nanoparticle for conjugation with folic acid **pp 987–995**

Metha Rutnakornpituk*, Nipaporn Puangsin, Pawinee Theamdee, Boonjira Rutnakornpituk, Uthai Wichai

Department of Chemistry and Center of Excellence for Innovation in Chemistry, Faculty of Science, Naresuan University, Phitsanulok 65000, Thailand

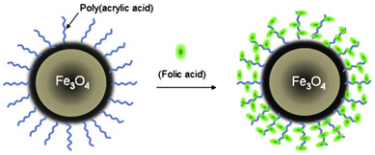

A novel cell support membrane for skin tissue engineering: Gelatin film cross-linked with 2-chloro-1-methylpyridinium iodide **pp 996–1003**

Ming-kung Yeh[a], Yan-ming Liang[b], Kuang-ming Cheng[a], Niann-Tzyy Dai[c], Cheng-che Liu[a], Jenn-jong Young[a,*]

[a] *Institute of Preventive Medicine, National Defense Medical Center, PO Box 90048-700, Sanhsia, Taipei 237, Taiwan, ROC*
[b] *Graduate Institute of Biomedical Engineering, National Taiwan University of Science and Technology, Taipei, Taiwan, ROC*
[c] *Division of Plastic and Reconstructive Surgery, Tri-Service General Hospital; National Defense Medical Center, Taipei, Taiwan, ROC*

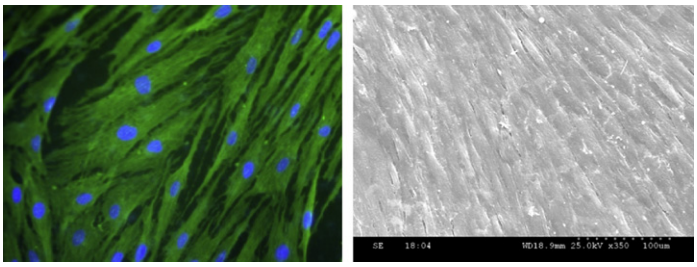

Highly branched benzoxazine monomer based on cyclotriphosphazene: Synthesis and properties of the monomer and polybenzoxazines **pp 1004–1012**

Xiong Wu[a], Yun Zhou[b], Shu-Zheng Liu[a], Ya-Ni Guo[a], Jin-Jun Qiu[a], Cheng-Mei Liu[a,*]

[a] *School of Chemistry and Chemical Engineering, Huazhong University of Science and Technology, Wuhan 430074, PR China*
[b] *Institute of Marine Materials Science and Engineering, Shanghai Maritime University, Shanghai 200135, PR China*

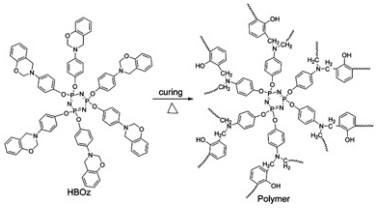

Thermal cross-link behavior of an amorphous poly (para-arylene sulfide sulfone amide) **pp 1013–1018**

Yaqi Yang[a], Gang Zhang[b], Jing Liu[c], Shengru Long[b], Xiaojun Wang[b], Jie Yang[a,b,*]

[a] *College of Polymer Science and Engineering, State Key Laboratory of Polymer Materials Engineering of China, Sichuan University, Chengdu 610065, PR China*
[b] *Institute of Materials Science and Technology, Sichuan University, Chengdu 610064, PR China*
[c] *College of Chemistry, Sichuan University, Chengdu 610064, PR China*

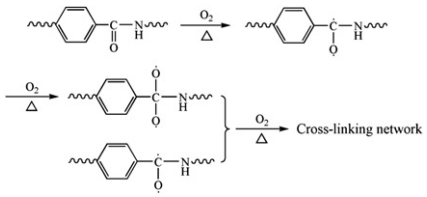

Comparison of two cationic polymeric flocculant architectures on the destabilization of negatively charged latex suspensions **pp 1019–1026**

Daniel Palomino[a], David Hunkeler[b], Serge Stoll[a,*]

[a] *University of Geneva, F.-A. Forel Institute, Group of Environmental Physical Chemistry, 10 Route de Suisse, 1290 Versoix, Switzerland*
[b] *Aqua+TECH Specialties, chemin du Chalet-du-Bac 4, CH-1283 La Plaine, Switzerland*

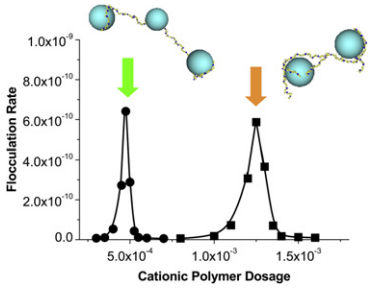

Influences of polymer matrix melt viscosity and molecular weight on MWCNT agglomerate dispersion **pp 1027–1036**

Gaurav R. Kasaliwal, Andreas Göldel, Petra Pötschke[*], Gert Heinrich

Leibniz Institute of Polymer Research Dresden, Hohe Str. 6, 01069 Dresden, Germany

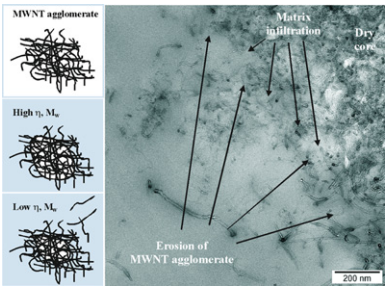

Uniaxial compression and stretching deformation of an i-PP/EPDM/organoclay nanocomposite **pp 1037–1044**

Arthur Thompson[a], Otávio Bianchi[b], Cintia L.G. Amorim[a], Cristóvão Lemos[c], Sérgio R. Teixeira[d], Dimitrios Samios[b], Cristiano Giacomelli[e], Janaina S. Crespo[a], Giovanna Machado[d,f,*]

[a] *Programa de Pós Graduação em Materiais, Universidade de Caxias do Sul, Caxias do Sul, Brazil*
[b] *Instituto de Química, Universidade Federal do Rio Grande do Sul, Porto Alegre, Brazil*
[c] *Centro de Tecnologia e Inovação, Braskem S/A, Triunfo, Brazil*
[d] *Instituto de Física, Universidade Federal do Rio Grande do Sul, Porto Alegre, Brazil*
[e] *Departamento de Química, Universidade Federal de Santa Maria, Santa Maria, Brazil*
[f] *Centro de Tecnologias Estratégicas do Nordeste, Cetene, Recife, Brazil*

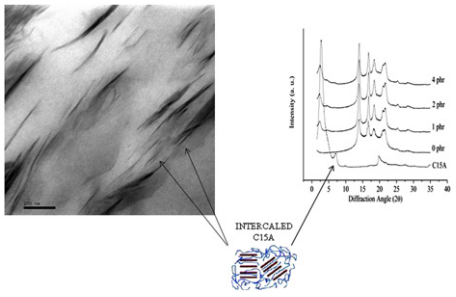

Synthesis and characterization of CdS quantum dots with carboxylic-functionalized poly (vinyl alcohol) for bioconjugation pp 1045–1054

Herman S. Mansur[a,*], Alexandra A.P. Mansur[a], J.C. González[b]

[a] *Department of Metallurgical and Materials Engineering, Federal University of Minas Gerais, School of Engineering, Av. Antonio Carlos, 662731270-901 Belo Horizonte, MG, Brazil*
[b] *Department of Physics, Federal University of Minas Gerais, Brazil*

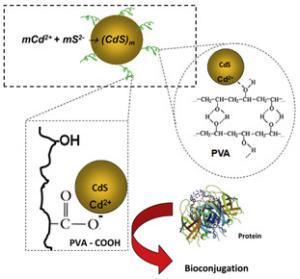

Melt-crystallized nylon-6 nucleated by the constrained chains of its non-stoichiometric cyclodextrin inclusion compounds and the nylon-6 coalesced from them pp 1055–1062

A. Mohan, A. Gurarslan, X. Joyner, R. Child, A.E. Tonelli[*]

Fiber & Polymer Science Program, North Carolina State University, Campus Box 8301, Raleigh, NC 27695-8301, USA

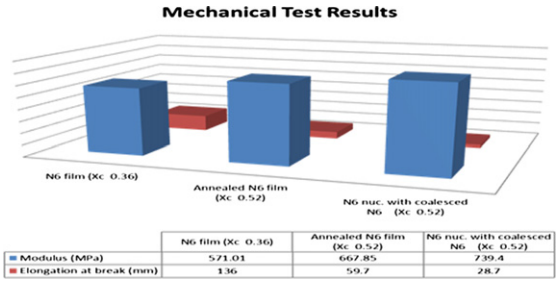

	N6 film (Xc 0.36)	Annealed N6 film (Xc 0.52)	N6 nuc. with coalesced N6 (Xc 0.52)
Modulus (MPa)	571.01	667.85	739.4
Elongation at break (mm)	136	59.7	28.7

Shape memory polymer system of semi-interpenetrating network structure composed of crosslinked poly (methyl methacrylate) and poly (ethylene oxide) pp 1063–1070

Debdatta Ratna[a,*], J. Karger-Kocsis[b]

[a] *Naval Materials Research Laboratory, Shil Badlapur Road, Addl. Ambernath, Maharastra 421506, India*
[b] *Department of Polymer Engineering, Faculty of Mechanical Engineering, Budapest University of Technology and Economics, H-1111 Budapest, Hungary*

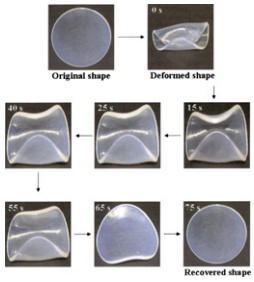

Effect of tethering on the structure-property relationship of TPU-dual modified Laponite clay nanocomposites prepared by *ex-situ* and *in-situ* techniques pp 1071–1083

Ananta K. Mishra[a], Santanu Chattopadhyay[a,*], P.R. Rajamohanan[b], Golok B. Nando[a,**]

[a] *Rubber Technology Center, Indian Institute of Technology Kharagpur, Kharagpur 721 302, India*
[b] *Central NMR Facility, National Chemical Laboratory, Pune 411008, India*

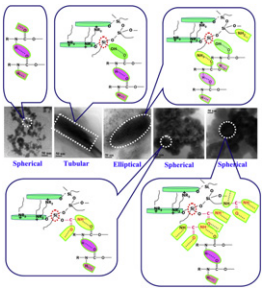

Investigation of the complexation of proteins with neutral water soluble polymers through model analysis method **pp 1084–1091**

Zhiqiang Su[a], Liang Zhang[b], Jiaohong Zhao[a], Xiaonong Chen[a,b,*]

[a] *Key Laboratory of Beijing City on Preparation and Processing of Novel Polymer Materials, Beijing University of Chemical Technology, Beijing 100029, China*
[b] *Key Laboratory of carbon fiber and functional polymers, Ministry of Education, Beijing University of Chemical Technology, Beijing 100029, China*

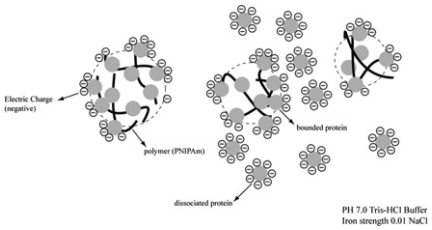

Effect of N-substituents on the surface characteristics and hydrogen bonding network of polybenzoxazines **pp 1092–1101**

Huijie Dong, Zhong Xin[*], Xin Lu, Yuhao Lv

State Key Laboratory of Chemical Engineering, East China University of Science and Technology, Shanghai 200237, China

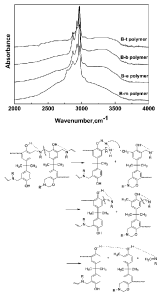

Nucleation effect on polymorphism of melt-crystallized syndiotactic polystyrene **pp 1102–1106**

Ming Lu[a], Xiang Zhao[b], Lan Chen[c], Xiaomin Xiong[c], Jingxiu Zhang[c], Kancheng Mai[b,*], Chuanbin Wu[a,**]

[a] *School of Pharmaceutical Sciences, Sun Yat-sen University, Guangzhou 510006, China*
[b] *School of Chemistry and Chemical Engineering, Sun Yat-sen University, Guangzhou 510275, China*
[c] *School of Physics and Engineering, Sun Yat-sen University, Guangzhou 510275, China*

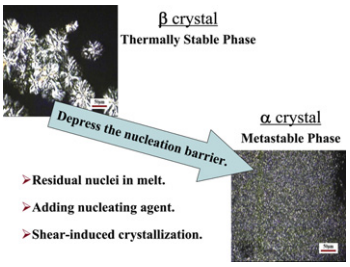

Formation and reorganization of the mesophase of random copolymers of propylene and 1-butene **pp 1107–1115**

Daniela Mileva[a], René Androsch[a,*], Evgeny Zhuravlev[b], Christoph Schick[b], Bernhard Wunderlich[c]

[a] *Martin-Luther-University Halle-Wittenberg, Center of Engineering Sciences, D-06099 Halle/Saale, Germany*
[b] *University of Rostock, Institute of Physics, D-18051 Rostock, Germany*
[c] *200 Baltusrol Rd., Knoxville, TN 379234-37-7, USA*

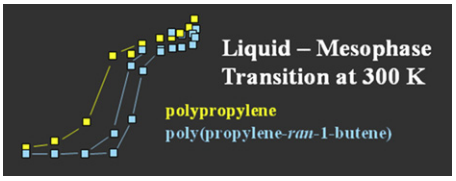

Morphology of syndiotactic polypropylene/alumina nanocomposites pp 1116–1123

Le Thuy Truong[a,b], Åge Larsen[a,*], Børge Holme[a], Finn Knut Hansen[b], Jaan Roots[b]

[a] *SINTEF Materials and Chemistry, P.O. Box 124 Blindern, NO-0314 Oslo, Norway*
[b] *University of Oslo, Department of Chemistry, P.O. Box 1033 Blindern, NO-0315 Oslo, Norway*

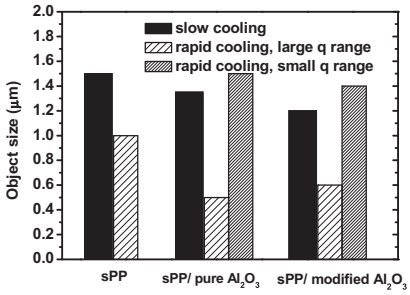

Structure–property relationships on uniaxially oriented carbon nanotube/polyethylene composites pp 1124–1132

Giuliana Gorrasi[a,*], Roberta Di Lieto[a], Giovanni Patimo[b], Salvatore De Pasquale[b], Andrea Sorrentino[a,*]

[a] *Department of Chemical and Food Engineering, University of Salerno, via Ponte don Melillo, 84084 Fisciano, Salerno, Italy*
[b] *Department of Physics E.R. Caianiello, University of Salerno, via Ponte don Melillo, 84084 Fisciano, Salerno, Italy*

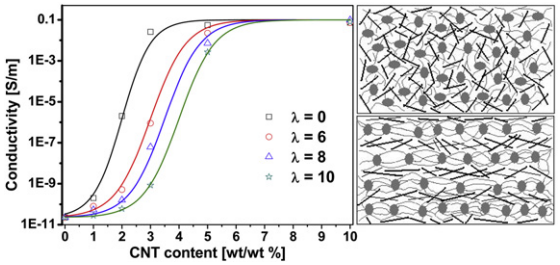

Crystal growth pattern changes in low molecular weight poly(ethylene oxide) ultrathin films pp 1133–1140

Guoliang Zhang[a], Yan Cao[b], Liuxin Jin[a], Ping Zheng[a], Ryan M. Van Horn[b], Bernard Lotz[c,**], Stephen Z.D. Cheng[b,*], Wei Wang[a,**]

[a] *The Key Laboratory of Functional Polymer Materials of Ministry of Education and Institute of Polymer Chemistry, College of Chemistry, Nankai University, Tianjin 300071, China*
[b] *Department of Polymer Science, College of Polymer Science and Polymer Engineering, The University of Akron, Akron, OH 44325-3909, USA*
[c] *Institut Charles Sadron, 23 Rue du Loess, BP 84047, Strasbourg 67034, France*

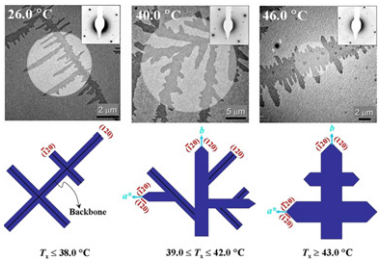

Effect of organoclay on the morphology, phase stability and mechanical properties of polypropylene/polystyrene blends pp 1141–1154

Rajkiran R. Tiwari, D.R. Paul[*]

Department of Chemical Engineering and Texas Materials Institute, The University of Texas at Austin, Austin, Texas 78712, USA

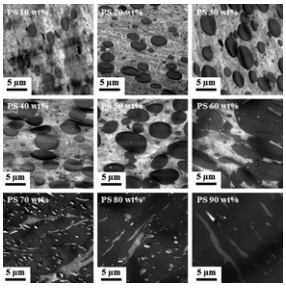

Wear resistant UHMWPE with high toughness by high temperature melting and subsequent radiation cross-linking **pp 1155–1162**

Jun Fu[a,b], Bassem W. Ghali[a], Andrew J. Lozynsky[a], Ebru Oral[a,b,*], Orhun K. Muratoglu[a,b]

[a] *Harris Orthopaedic Laboratory, Massachusetts General Hospital, 55 Fruit Street, Boston, MA 02114, USA*
[b] *Department of Orthopedic Surgery, Harvard Medical School, Boston, MA, USA*

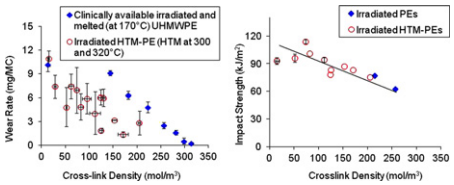

Structure and dynamic mechanical properties of highly oriented PS/clay nanolaminates over the entire composition range **pp 1163–1171**

Erik Dunkerley[a], Hilmar Koerner[b,c], Richard A. Vaia[b], Daniel Schmidt[a,*]

[a] *Department of Plastics Engineering/Nanomanufacturing Center, University of Massachusetts Lowell, Lowell, MA 01854, USA*
[b] *Nanostructured and Biological Materials Branch, United States Air Force Research Laboratory, WPAFB, OH, USA*
[c] *UES Inc., Dayton, OH, USA*

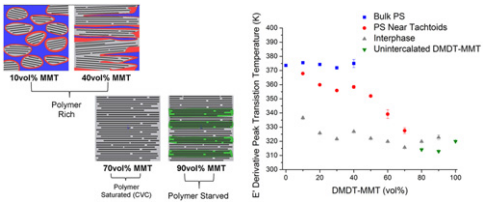

Structural and property changes during uniaxial drawing of ethylene–tetrafluoroethylene copolymer films as analyzed by *in-situ* X-ray measurements **pp 1172–1179**

Yasunori Ono[a], Masaki Kakiage[a], Takeshi Yamanobe[a], Yasumasa Yukawa[b], Yoshiaki Higuchi[b], Hiroki Kamiya[b], Kiyotaka Arai[c], Hiroki Uehara[a,*]

[a] *Department of Chemistry and Chemical Biology, Gunma University, Kiryu, Gunma 376-8515, Japan*
[b] *R & D Division, Asahi Glass Co., Ltd., Ichihara, Chiba 290-8566, Japan*
[c] *Central Laboratory, Asahi Glass Co., Ltd., Yokohama, Kanagawa 221-8755, Japan*

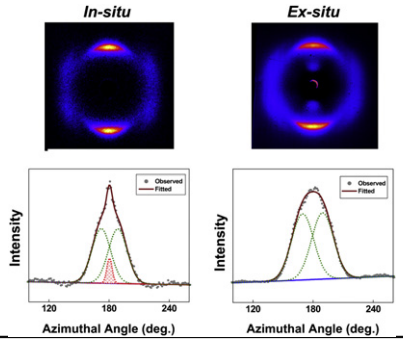

Film instability induced evolution of hierarchical structures in annealed ultrathin films of an asymmetric block copolymer on polar substrates **pp 1180–1190**

Ya-Sen Sun[a,*], Shih-Wei Chien[a], Jiun-You Liou[a], Chiu Hun Su[b], Kuei-Fen Liao[b]

[a] *Department of Chemical and Materials Engineering, National Central University, Taoyuan 32001, Taiwan*
[b] *National Synchrotron Radiation Research Center, Hsinchu 30077, Taiwan*

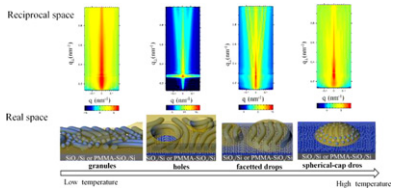

Hierarchical self-assembly of fluorine-containing diblock copolymer: From onion-like nanospheres to superstructured microspheres **pp 1191–1196**

Shan Qin, Hong Li, Wangzhang Yuan, Yongming Zhang*

School of Chemistry and Chemical Technology, Shanghai Jiao Tong University, Shanghai 200240, People's Republic of China

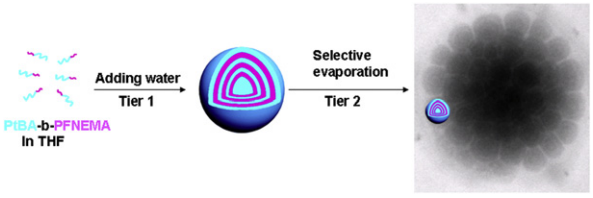

Structure of polyamide 6 and poly (*p*-benzamide) in their rod-coil-rod triblock copolymers investigated with in situ wide angle X-ray diffraction **pp 1197–1205**

Lu Xu[a], Junjun Li[a], Daoliang Wang[a], Youju Huang[a], Mingming Chen[b], Liangbin Li[a,b,*], Guoqiang Pan[a]

[a] *National Synchrotron Radiation Laboratory and College of Nuclear Science and Technology, University of Science and Technology of China, Hefei, China*
[b] *Department of Polymer Science and Engineering, CAS Key Lab of Soft Matter Chemistry, University of Science and Technology of China, Hefei, China*

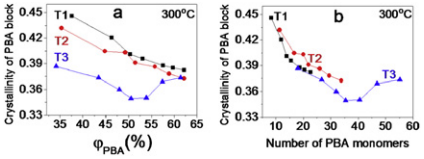

Theoretical study of molecular interactions of TNT, acrylic acid, and ethylene glycol dimethacrylate – Elements of molecularly imprinted polymer modeling process **pp 1206–1216**

Julia Saloni[a], Pawel Lipkowski[b], Samuel S.R. Dasary[a], Yerramilli Anjaneyulu[a], Hongtao Yu[a], Glake Hill, Jr.[a,*]

[a] *Department of Chemistry and Biochemistry, Jackson State University, Jackson, MS 3921, USA*
[b] *Department of Chemistry, Wroclaw University of Technology, Wroclaw, Poland*

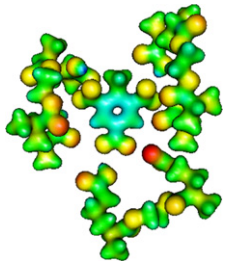

*Corresponding author

Abstracted/indexed in: AGRICOLA, Beilstein, BIOSIS Previews, CAB Abstracts, Chemical Abstracts. Current Contents: Life Sciences, Current Contents: Physical, Chemical and Earth Sciences, Current Contents Search, Derwent Drug File, Ei compendex, EMBASE/Excerpta Medica, Medline, PASCAL, Research Alert, Science Citation Index, SciSearch. Also covered in the abstract and citation database SCOPUS®. Full text available on ScienceDirect®

ELSEVIER

ISSN 0032-3861

Author Index

Agarwal, S. 912
Amorim, C. L. G. 1037
Androsch, R. 1107
Anjaneyulu, Y. 1206
Arai, K. 1172

Berti, C. 904
Bianchi, O. 1037
Bokern, S. 912

Cao, Y. 1133
Chattopadhyay, S. 1071
Chen, J. 933
Chen, J.-C. 954
Chen, L. 1102
Chen, M. 1197
Chen, X. 1084
Chen, Y.-C. 976
Chen, Y.-H. 976
Cheng, K.-m. 996
Cheng, S. Z. D. 1133
Chern, Y.-T. 954
Chiang, C.-J. 954
Chien, S.-W. 1180
Child, R. 1055
Choi, K. Y. 942
Colonna, M. 904
Crespo, J. S. 1037

Dai, N.-T. 996
Dasary, S. S. R. 1206
De Pasquale, S. 1124
Di Lieto, R. 1124
Dong, H. 1092
Dunkerley, E. 1163

Finelli, L. 904
Fiorini, M. 904
Fu, J. 1155
Fujita, M. 895

Getze, J. 912
Ghali, B. W. 1155
Giacomelli, C. 1037
Göldel, A. 1027
González, J. C. 1045
Gordeyev, S. A. 901
Gorrasi, G. 1124
Goto, A. 895
Greiner, A. 912
Guo, Y.-N. 1004
Gurarslan, A. 1055

Han, J. J. 942
Hansen, F. K. 1116
Heinrich, G. 1027
Higuchi, Y. 1172
Hill, G., Jr. 1206
Holme, B. 1116
Huang, Y. 1197
Hunkeler, D. 1019
Hwang, S. Y. 965

Im, S. S. 965

Jeng, R.-J. 976
Ji, W. 921
Jin, L. 1133
Jones, C. A. 901
Joyner, X. 1055
Ju, J.-J. 954
Jung, Y. 942

Kakiage, M. 1172
Kamiya, H. 1172
Karger-Kocsis, J. 1063
Kasaliwal, G. R. 1027
Koerner, H. 1163
Koike, K. 949
Koike, Y. 949
Kuo, W.-J. 976

Larsen, Å. 1116
Lee, R.-H. 976
Lemos, C. 1037
Li, H. 1191
Li, J. 1197
Li, L. 1197
Liang, Y.-m. 996
Liao, K.-F. 1180
Lin, J. T. 976
Lin, Y.-Y. 976
Liou, J.-Y. 1180
Lipkowski, P. 1206
Liu, C.-c. 996
Liu, C.-M. 1004
Liu, J. 1013
Liu, S.-Z. 1004
Liu, Y.-C. 954
Long, S. 1013
Lotti, N. 904
Lotz, B. 1133
Lou, L. 949
Lozynsky, A. J. 1155
Lu, M. 1102
Lu, X. 1092
Luciani, C. V. 942
Lv, Y. 1092

Machado, G. 1037
Maeda, M. 895
Mai, K. 1102
Mansur, A. A. P. 1045
Mansur, H. S. 1045
Mileva, D. 1107
Mishra, A. K. 1071
Mohan, A. 1055
Muratoglu, O. K. 1155

Nando, G. B. 1071

Okamoto, Y. 949
Ono, Y. 1172
Ooi, W.-Y. 895
Oral, E. 1155

Palomino, D. 1019
Pan, G. 1197
Pan, P. 895
Patimo, G. 1124
Paul, D. R. 1141
Pötschke, P. 1027
Puangsin, N. 987

Qin, S. 1191
Qiu, J.-J. 1004

Rajamohanan, P. R. 1071
Ratna, D. 1063
Roots, J. 1116
Rutnakornpituk, B. 987
Rutnakornpituk, M. 987

Saloni, J. 1206
Samios, D. 1037
Schick, C. 1107
Schmidt, D. 1163
Shilton, S. J. 901
Sorrentino, A. 1124
Stoll, S. 1019
Su, C. H. 1180
Su, Z. 1084
Sudesh, K. 895
Sun, Y.-S. 1180

Takarada, T. 895
Tang, R. 921
Teixeira, S. R. 1037
Teng, H. 949
Theamdee, P. 987
Thompson, A. 1037
Tiwari, R. R. 1141
Tonelli, A. E. 1055
Truong, L. T. 1116

Uehara, H. 1172

Vaia, R. A. 1163
Van Horn, R. M. 1133

Wang, C. 921
Wang, D. 1197
Wang, W. 1133
Wang, X. 1013
Wichai, U. 987
Wu, C. 1102
Wu, X. 1004
Wunderlich, B. 1107

Xin, Z. 1092
Xing, M. M. Q. 933
Xiong, X. 1102
Xu, L. 1197

Yamanobe, T. 1172
Yang, J. 1013
Yang, Y. 1013
Yeh, M.-k. 996
Yoo, E. S. 965
Young, J.-j. 996
Yu, H. 1206
Yuan, W. 1191
Yukawa, Y. 1172

Zhang, G. 1013,
Zhang Guoliang 1133
Zhang, J. 1102
Zhang, L. 1084
Zhang, Y. 1191
Zhao, J. 1084
Zhao, X. 1102
Zheng, P. 1133
Zhong, W. 933
Zhou, Y. 1004
Zhuravlev, E. 1107

Polymer 52 (2011) 895–900

Contents lists available at ScienceDirect

Polymer

journal homepage: www.elsevier.com/locate/polymer

Polymer Communication

DNA-functionalized thermoresponsive bioconjugates synthesized via ATRP and click chemistry

Pengju Pan [a], Masahiro Fujita [a,*], Wei-Yang Ooi [a,b], Kumar Sudesh [b], Tohru Takarada [a], Atsushi Goto [c], Mizuo Maeda [a,*]

[a] Bioengineering Laboratory, RIKEN, Hirosawa 2-1, Wako, Saitama 351-0198, Japan
[b] Ecobiomaterial Research Laboratory, School of Biological Sciences, Universiti Sains Malaysia, Minden, 11800 Penang, Malaysia
[c] Institute for Chemical Research, Kyoto University, Uji, Kyoto 611-0011, Japan

ARTICLE INFO

Article history:
Received 29 October 2010
Received in revised form
7 January 2011
Accepted 9 January 2011
Available online 15 January 2011

Keywords:
DNA
ATRP
Click chemistry

ABSTRACT

Diblock and miktoarm star-shaped thermoresponsive copolymers composed of single-stranded DNA (ssDNA) and poly(*N*-isopropylacrylamide) were successfully synthesized with combination of atom transfer radical polymerization (ATRP) and click chemistry. This approach should be generalizable to other DNA-functionalized copolymers. Such copolymers self-assemble into spherical micelles with ssDNA corona in aqueous solution above the lower critical solution temperature. The micellar size can be tuned from the macromolecular architecture. These DNA-encoded micellar particles are able to encapsulate and release hydrophobic guest molecules upon changing temperature.

1. Introduction

The unique structures and self-recognition property of DNA make it a versatile building block for molecular self-assembly. The programmable assembly of DNA-encoded nanoparticles has been extensively studied for a number of inorganic nanoparticles such as gold colloids [1–3], which has shown many promising biodiagnostic applications. However, the studies on DNA-controlled assembly of soft nanoparticles and their applications are scarce [4–7]. A reason for this may be the lack of straightforward and efficient methods to prepare the DNA-decorated soft nanoparticles. Amphiphilic copolymers can form versatile molecular assemblies in an aqueous media, for instance, spherical, cylindrical micelles, and vesicles [8]. Therefore, the self-assembly of amphiphilic copolymers with hydrophilic DNA blocks would be a promising method to create the DNA-encoded soft nanoparticles. Because DNA is an informational molecule, the DNA chains decorated within the micellar coronas would afford the soft nanoparticles novel biofunctions such as targeted drug/gene deliveries and biodiagnostics, as compared to the traditional copolymer micelles.

We have previously prepared the poly(*N*-isopropylacrylamide) (PNIPAAm)/ssDNA graft copolymers via free radical polymerization [9,10]. PNIPAAm is a typical thermoresponsive polymer showing a lower critical solution temperature (LCST) around ~32 °C. Therefore, the graft copolymer forms micelles above its LCST. The micelles can recognize the sequence of target DNA, suggesting that the DNA-encoded micelle is a new class of functional material for turbidimetric detection of single nucleotide polymorphism (SNP) [9,10]. Due to the low controllability of conventional radical polymerization, the as-prepared graft copolymers have less-defined structure and broad molecular weight distribution, and thus the resulting micelles are probably less-defined. Because the copolymer composition and architecture are the crucial factors in self-assembly [8], well-defined copolymers with respect to compositions, architectures, and functionalities are essential for the fabrication of DNA-encoded micelles with controllable morphology. This could also optimize the functions of such micelles in biodiagnostics and molecular assemblies.

Controlled radical polymerization is often used to synthesize well-defined polymers for conjugation to biomacromolecules (e.g., proteins and peptides) [11–13]. The most employed techniques have included atom transfer radical polymerization (ATRP) and reversible addition-fragmentation chain transfer (RAFT) polymerization. Recently, RAFT polymerization has proven successful for

* Corresponding authors. Tel.: +81 48 467 9312; fax: +81 48 462 4658.
E-mail addresses: mfujita@riken.jp (M. Fujita), mizuo@riken.jp (M. Maeda).

0032-3861/$ – see front matter © 2011 Elsevier Ltd. All rights reserved.
doi:10.1016/j.polymer.2011.01.016

the synthesis of linear polymer-DNA conjugates [14–16]. In addition, the copper-catalyzed azide-alkyne cycloaddition (CuAAC) [17], a prototypical example of click reaction, has been recognized as a facile and versatile chemistry for bioconjugation [11–13] and DNA modification [18].

Due to the unique structures, the star-shaped copolymers usually assemble into the micellar particles with very different structures and morphologies from their linear analogues [19–21]. So far, the synthesis of bioconjugates of nucleic acid and synthetic polymer were mainly focused on the linear diblock [4,5,22–26] or graft architectures [9,10,27]. The star-shaped conjugates of nucleic acid and synthetic polymer remain unexplored. Both ATRP and RAFT polymerization have been widely employed to prepare the star-shaped polymers [28]. However, the RAFT star polymerization, especially the R-RAFT star approach, usually leads to the multimodal and broad molecular weight distribution with dramatically decreased structural homogeneity due to the formation of linear living chains [29,30]. Therefore, ATRP, a typical core-first method, is considered to possess better control over the star polymer architecture [28].

Herein, we report a novel method to prepare the DNA-functionalized diblock and miktoarm star-shaped copolymers. To our knowledge, this represents the first example that ATRP and click chemistry are employed to prepare the nucleic acid/polymer bioconjugates. Moreover, the thermo-triggered micellation of these bioconjugates was investigated. The ability of such micelles for uptake and release of hydrophobic guest molecules was also evaluated.

2. Experimental part

2.1. Materials

The reagents were purchased from Wako Pure Chemical Industries Ltd. (Osaka, Japan) or Tokyo Chemical Industry Co., Ltd (Tokyo, Japan) and used without further purification, unless specified otherwise. *N*-isopropylacrylamide (NIPAAm) was purified by recrystallization from toluene/hexane (1/1, *v*/*v*). Tris[2-(dimethylamino)-ethyl]amine (Me_6TREN) was prepared according to the literatures [31,32]. Copper(I) bromide (CuBr) was stirred in glacial acetic acid overnight, filtered, and rinsed with ethanol and diethyl ether under argon, followed by drying under vacuum at room temperature for 24 h. Tris(benzyltriazolylmethyl)amine (TBTA) was purchased from Sigma–Aldrich (St Louis, MO, USA). 5′-Aminohexyl terminated oligonucleotide, NH_2–$(CH_2)_6$–5′GCCACCAGC3′ [9,10], was purchased from Operon Biotechnologies (Tokyo, Japan).

The synthetic routes of diblock and miktoarm star-shaped PNIPAAm-*co*-ssDNA copolymers are illustrated in Scheme 1. Detailed experimental procedures for the syntheses of 5′-alkyne modified oligonucleotide (**3**) and azide-functionalized initiators (**6a** and **6b**) are described in Supporting Information. Briefly, the azide-terminated linear initiator (**6a**) was prepared according to a published method [33]. The azido-alcohol intermediate (**5a**) was attained by treatment of bromo-alcohol (**4a**) with NaN_3. Subsequent esterification of (**5a**) with 2-bromoisobutyryl bromide afforded the desired azide-ester initiator (**6a**). Star-shaped initiator (**6b**) bearing one azide and three bromo-groups was synthesized from monobromo pentaerythritol (**4b**) using a similar route.

2.2. ATRP of PNIPAAm homopolymers (*7a*, *7b*)

Azide-functionalized linear and 3-arm star-shaped PNIPAAm homopolymers (**7a** and **7b**) were prepared via ATRP. A typical polymerization procedure for the azide-terminated linear PNIPAAm with a target degree of polymerization (DP) of 400 is described as follows. NIPAAm (2.0 g, 17.7 mmol), **6a** (10.43 mg, 0.0442 mmol), Me_6TREN (12.22 mg, 0.0530 mmol), and *i*-propanol (4.0 g) were mixed in a Schlenk flask and degassed using three

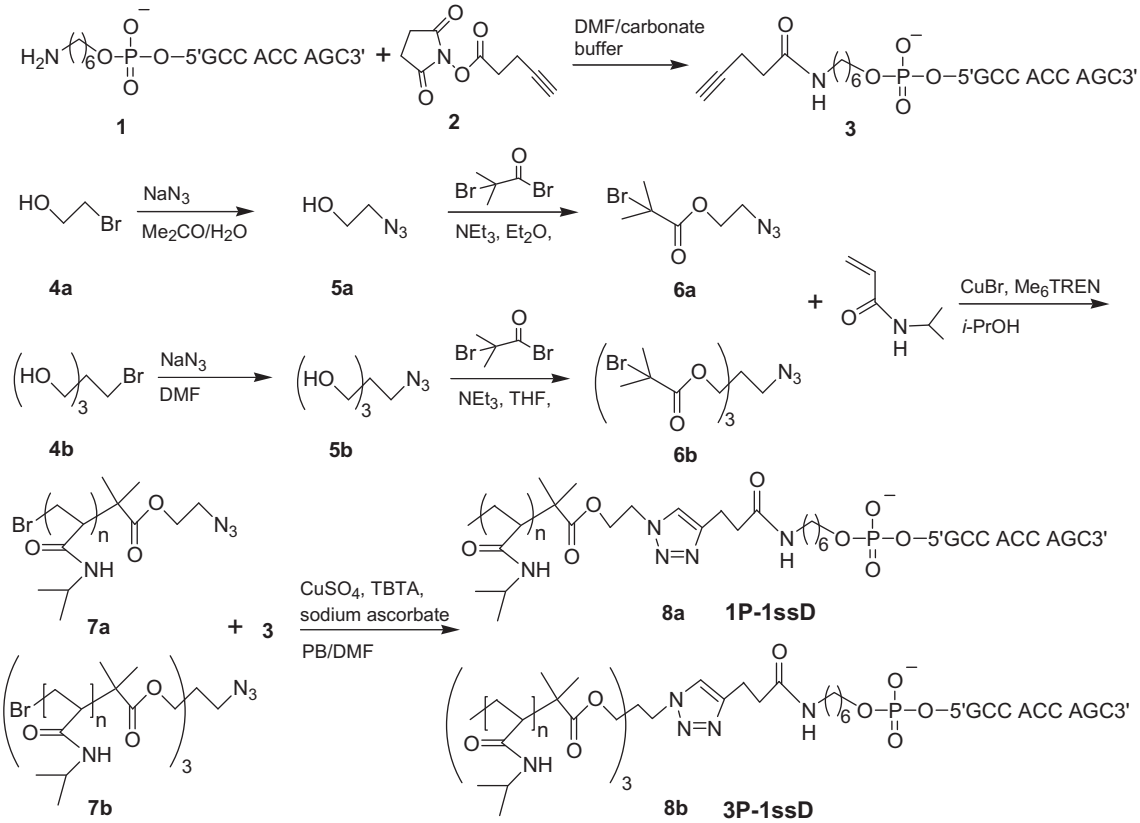

Scheme 1. Synthetic route of diblock and miktoarm star-shaped PNIPAAm-*co*-ssDNA copolymers.

freeze-pump-thaw cycles. While the mixture was frozen, CuBr (6.34 g, 0.0442 mmol) was added. The flask was then filled with argon and the mixture was left to melt at room temperature. The reaction mixture was stirred for 5 h at 25 °C. After polymerization, the mixture was passed through an alumina column with THF as the eluent. The polymer was purified by precipitation from THF into hexane four times and then dried under vacuum to yield **7a** (1.06 g, yield: 53%) as white solid. For the azide-functionalized 3-arm star-shaped PNIPAAm homopolymer (**7b**), **6b** was utilized as initiator, and its synthetic procedure is the same to that of **7a**. The feed ratios of initiator (**6b**), catalyst, and ligand were 1/3/3.6. The linear and 3-arm star-shaped PNIPAAm homopolymers are marked as $1P_m$ and $3P_m$, respectively, where *m* represents the overall DP including all arms.

2.3. Preparation of PNIPAAm-co-ssDNA copolymers (*8a*, *8b*)

A solution of **3** (100 nmol) in 2.5 mL phosphate buffer (PB) (pH 7.2, 20 mM) and 1.0 μmol of **7a** or **7b** (in 2.5 mL DMF) were added to a 10 mL plastic culture tube. A stock solution (0.1 mL) of catalyst/ligand (1.0 μmol of $CuSO_4$, 1.1 μmol of TBTA) in dimethyl sulfoxide (DMSO)/water (*v*/*v*, 1/1) and 4.0 μmol (0.79 mg) of sodium ascorbate were then added. The reaction mixture was shaken at 15 °C for 20 h. The crude mixture was then purified via a high-performance liquid chromatography (HPLC) equipped with a preparative anionic exchange column (SP Sepharose Fast Flow, GE healthcare) using tris–HCl buffer (pH 7.4, 10 mM) as the starting buffer and tris–HCl buffer (pH 7.4, 10 mM) with 0.5 M NaCl as the elution buffer (Fig. S1). Appropriate fractions were collected, dialyzed against water (MWCO = 3500), and lyophilized. This crude product was further purified via gel permeation chromatography (Sephadex G-50, GE healthcare) using tris–HCl buffer (pH 7.4, 10 mM) as the mobile phase (Fig. S2). The fractions corresponding to copolymers were collected, dialyzed against water (MWCO = 3500), and lyophilized to afford **8a** (yield: 84%) or **8b** (yield: 71%) as white solid. The diblock and miktoarm star-shaped (consisting of 3 PNIPAAm arms and 1 ssDNA arm) PNIPAAm-*co*-ssDNA copolymers are denoted as $1P_m$-$1ssD_n$ and $3P_m$-$1ssD_n$, respectively, where *m* is DP of PNIPAAm and *n* is DP of ssDNA.

2.4. Measurements

Fourier transform infrared (FTIR) spectra were recorded on a JASCO FTIR-615 spectrometer (Tokyo, Japan). MALDI-TOF mass spectrometric analysis of 5′-alkyne modified oligonucleotide was conducted on a Bruker Daltonics Ultraflex Mass Spectrometer (Billerica, MA, USA) in the negative-ion reflector mode. The molecular weights of PNIPAAm homopolymers and their copolymers were determined by a gel permeation chromatography (Shimadzu, Kyoto, Japan) equipped with a multi-angle laser light scattering detector (DAWN8$^+$, Wyatt Technologies, Santa Barbara, CA, USA) (GPC-MALLS). A Shodex OHpak SB-803 HQ column (Showa Denko, Tokyo, Japan) was used. High-sensitivity differential scanning calorimetry (DSC) measurements were performed on a VP-DSC microcalorimeter (MicroCal Inc., Northampton, MA, USA). The temperature-dependent transmittances of PNIPAAm homopolymers and their copolymers were measured on a UV-2550 UV–Vis spectrophotometer (Shimadzu, Kyoto, Japan) equipped with a temperature-controlled sample holder. Fluorescence spectra were measured by an FP-6500 Spectrofluorometer (JASCO, Tokyo, Japan) equipped with a JASCO ETC-273T temperature controller. The dynamic light scattering (DLS) analysis was conducted on a Zetasizer Nano-ZS instrument (Malvern Instruments, Malvern, UK) with a scattering angle of 173°. Synchrotron radiation small-angle X-ray scattering (SAXS) measurements were carried out at the BL45XU RIKEN Structural Biology Beamline I of SPring-8, Harima, Japan. The detailed characterization procedures are described in Supporting Information.

3. Results and discussion

As seen in Table 1, the polymerizations gave the products **7a** and **7b** in relatively high yields. A 3-arm star-shaped initiator (**6b**) bears 3 initiation sites (i.e., bromo-groups) and the molar ratio of initiation site to monomer for $3P_{252}$ (1/100) is much higher than that for $1P_{280}$ (1/400). Therefore, the former showed higher yield in ATRP. GPC-MALLS chromatograms of as-prepared homopolymers demonstrated sharp peaks with $M_w/M_n < 1.1$ (Fig. S3). The measured molecular weights of the homopolymers obtained are similar to those calculated theoretically (Table 1). FTIR spectra of the homopolymers showed the stretching vibration band of azide at 2108 cm^{-1} (Fig. 1a) [34], indicative of the high tolerance of ATRP to azide functional group [35]. Consequently, ATRP is an efficient method to prepare the azide-functionalized PNIPAAm with controllable molecular weights and architectures.

For the CuAAC click reaction, we converted the terminal of 5′-amino modified oligonucleotide (**1**) to alkyne by the coupling reaction with an NHS-activated alkyne modifier (**2**) [36]. The reverse-phase HPLC (RP-HPLC) analysis (Fig. S4) indicated the nearly quantitative conversion. MALDI-TOF mass spectrometry also confirmed the successful preparation of 5′-alkyne modified oligonucleotide (**3**) (exact mass calcd: 2926.59; Found: 2926.48). Diblock and miktoarm star-shaped PNIPAAm-*co*-ssDNA copolymers (**8a** and **8b**) were synthesized by coupling **3** with **7a** or **7b** via the CuAAC click chemistry. TBTA is a necessary ligand to this reaction to avoid the degradation of oligonucleotide by copper ion

Table 1
Molecular weights, thermal and structural parameters of PNIPAAm homopolymers and PNIPAAm-*co*-ssDNA copolymers.

Code	$[M]_0/[I]_0$[a]	Yield (%)	$M_{n,th}$[b] (kDa)	M_n[c] (kDa)	M_w/M_n[c]	T_p[d] (°C)	T_{cp}[e] (°C)	R_h[f] (nm)	R_g[g] (nm)	R_g/R_h	N_{ass}[g]
$1P_{280}$	400/1	53	24.2	31.7	1.08	35.1	35.5	–	–	–	–
$3P_{252}$	300/1	69	24.0	28.6	1.07	34.8	34.3	–	–	–	–
$1P_{280}$–$1ssD_9$	–	–	27.1	29.2	1.07	38.7	–	24.3	17.2	0.71	137
$3P_{252}$–$1ssD_9$	–	–	26.9	26.0	1.02	43.0	–	15.2	11.1	0.73	67

[a] Feed ratio (mol/mol) of NIPAAm ($[M]_0$) to initiator ($[I]_0$) in ATRP.
[b] Calculated molecular weight. For PNIPAAm homopolymer, $M_{n,th} = M_{n,initiator} + ([M]_0/[I]_0) \times$ yield $\times$ 113.16. For copolymer, $M_{n,th} = M_{n,th}$ (PNIPAAm) + $M_{n,DNA}$, $M_{n,DNA} = 2.928$ kDa.
[c] M_n and M_w of PNIPAAm homopolymers were measured by GPC-MALLS using DMF with 0.1 M LiBr as eluent; M_n and M_w of copolymers were measured by GPC-MALLS using tris–HCl buffer (pH 7.4, 10 mM) with 0.1 M NaCl as eluent.
[d] Peak temperature in DSC heating curve.
[e] Cloud point, corresponding to the temperature with 50% transmittance for solution of PNIPAAm homopolymer.
[f] R_h was attained from DLS measurements for copolymer micelles (2 mg/mL) in PB (pH 7.4, 10 mM) at 60 °C.
[g] R_g and N_{ass} were attained from SAXS measurements for copolymer micelles (2 mg/mL) in PB (pH 7.4, 10 mM) at 60 °C.

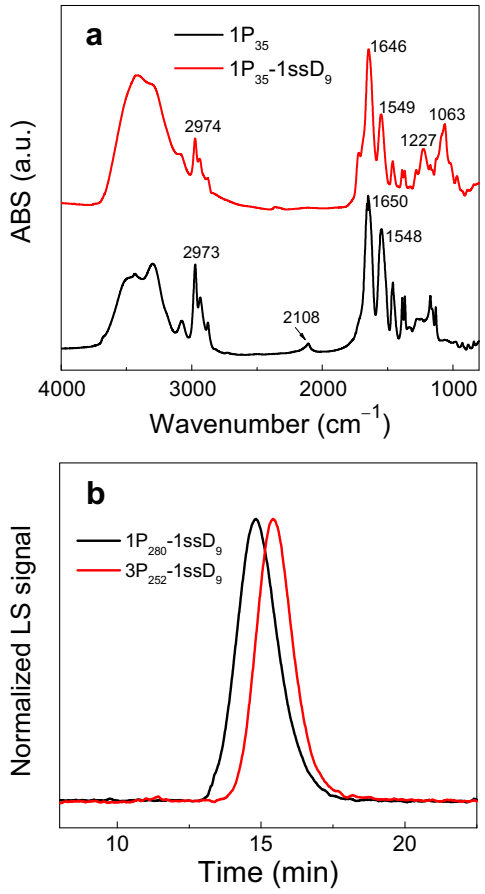

Fig. 1. (a) FTIR spectra of PNIPAAm homopolymer and PNIPAAm-*co*-ssDNA copolymer. (b) GPC-MALLS chromatograms of PNIPAAm-*co*-ssDNA copolymers.

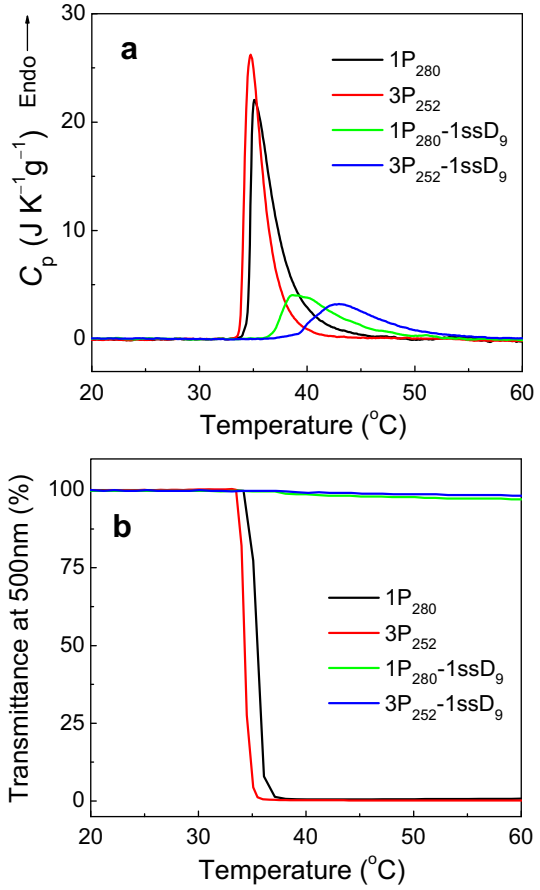

Fig. 2. (a) DSC thermograms and (b) transmittance at a wavelength of 500 nm recorded upon heating (1 °C/min) of $1P_{280}$–$1ssD_9$, $3P_{252}$–$1ssD_9$, and their corresponding PNIPAAm homopolymers in PB (pH 7.4, 10 mM). The polymer concentration is 0.5 mg/mL.

[18]. The unreacted homopolymer and 5′-alkyne modified oligonucleotide were separated from the copolymer using anionic exchange chromatography (Fig. S1) and gel permeation chromatography (Fig. S2).

The copolymers obtained were characterized by UV–Vis, FTIR spectroscopy, and GPC-MALLS. The UV–Vis spectra of copolymers showed the characteristic absorption of DNA at ~260 nm (Fig. S5). As shown in Fig. 1a, instead of the absorption band of azide at 2108 cm^{-1}, the characteristic absorptions of DNA nucleotide, for instance, the bands at 1063 and 1227 cm^{-1} (the symmetric and asymmetric stretching vibrations of DNA phosphodiester bond) [37], were detected. In addition, the absorptions of PNIPAAm such as the bands at 2974 cm^{-1} (CH_3 asymmetric stretching), 1646 cm^{-1} (C=O stretching, amide I), and 1549 cm^{-1} (N–H bending, amide II) were observed [35]. As seen in Fig. 1b, GPC-MALLS chromatograms of the obtained copolymers exhibited sharp peaks with the narrow molecular weight distributions ($M_w/M_n < 1.1$).

Furthermore, the thermoresponsive phase transition of PNIPAAm homopolymers and their copolymers was examined by high-sensitivity DSC and UV–Vis spectroscopy. Fig. 2 shows the DSC heating curves and temperature-dependent transmittance for PNIPAAm homopolymers and their copolymers in 10 mM PB (pH 7.4). The peak temperature (T_p) and cloud point (T_{cp}), both of which are the typical indicators of LCST, are listed in Table 1. As shown in Fig. 2a, the copolymers exhibited higher LCSTs than their original homopolymers, ascribing to the hydrophilic nature of DNA. It was also found that the phase transition depends on the macromolecular architecture. The 3-arm homopolymer ($3P_{252}$) showed a slightly lower LCST than the linear one ($1P_{280}$), which is possibly due to the fact that the former bears a larger hydrophobic initiator in macromolecular center and more hydrophobic bromo-groups in the end of each arm [34,38]. As shown in Fig. 2a and Table 1, the miktoarm star-shaped copolymer ($3P_{252}$–$1ssD_9$) showed a higher LCST than its linear counterpart ($1P_{280}$–$1ssD_9$). Although the exact reason for this phenomenon is unclear at present, this could be ascribed to the effects of ssDNA chain position. The ssDNA chain connects to the macromolecular center in the star-shaped copolymer, and thus it might affect the collapse and aggregation of PNIPAAm segments more pronouncedly than that in the diblock copolymer where ssDNA links to the terminal of PNIPAAm. As shown in Fig. 2b, the solutions of PNIPAAm homopolymers became turbid and their transmittances dropped to nearly zero above LCST. Nevertheless, no remarkable decrease in transmittance was detected in the copolymer solutions around LCST, indicative of the formation of nanoscale colloidal particles above LCST [10].

Therefore, the thermo-triggered micellation of PNIPAAm-*co*-ssDNA was investigated by DLS. Parts a and b of Fig. 3 depict the temperature dependence of hydrodynamic radius (R_h) and its distribution at 60 °C for the copolymer solutions in 10 mM PB (pH 7.4). The R_h increased dramatically upon heating to LCST (35–40 °C). The copolymers were found to form the assemblies with R_h of ~25 nm for $1P_{280}$–$1ssD_9$ and ~15 nm for $3P_{252}$–$1ssD_9$, ascribed to the micellation of PNIPAAm-*co*-ssDNA above LCST. Both the diblock and miktoarm star-shaped copolymers gave the very narrow distribution in micellar size (Fig. 3b), which is probably

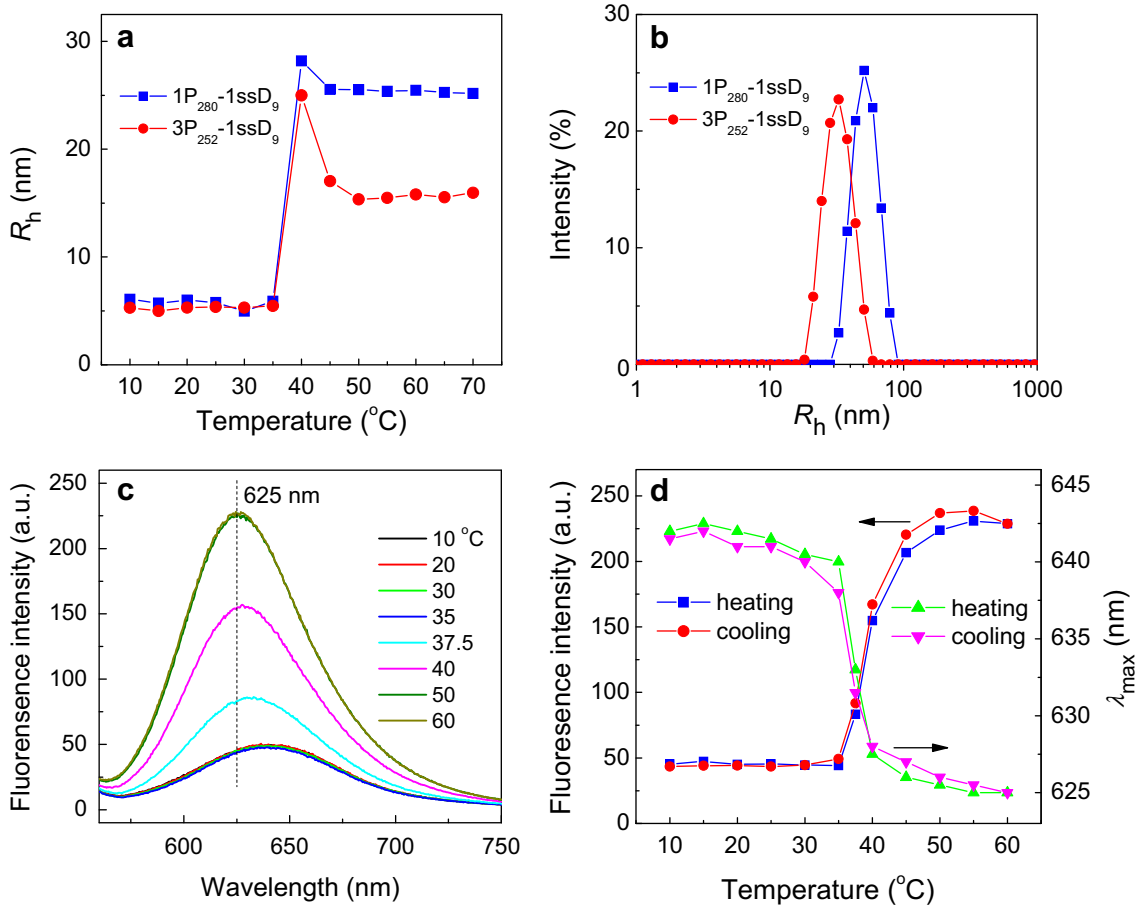

Fig. 3. (a) Temperature dependence of R_h and (b) size distribution at 60 °C of $1P_{280}$–$1ssD_9$ and $3P_{252}$–$1ssD_9$ in PB (pH 7.4, 10 mM) with a copolymer concentration of 0.5 mg/mL. (c) Fluorescence emission spectra collected upon heating from 10 to 60 °C and (d) temperature dependences of emission intensity at 625 nm and maximum emission wavelength for Nile Red (λ_{exc} = 550 nm) in the solution (0.5 mg/mL) of $1P_{280}$–$1ssD_9$ in PB (pH 7.4, 10 mM).

attributable to the well-defined, uniform structure and narrow molecular weight distribution of as-prepared copolymers. The critical micelle concentration (CMC) of PNIPAAm-*co*-ssDNA above LCST was estimated via DLS [39]. It was found that the CMC values of the copolymers of $1P_{280}$–$1ssD_9$ and $3P_{252}$–$1ssD_9$ are around 15 mg/L at 60 °C and they show no discernible dependence on temperature within the temperature range investigated (50–70 °C).

The micellation of copolymer was also studied using synchrotron radiation SAXS. The radius of gyration (R_g) and the association number of molecules per micelle (N_{ass}) were estimated according to Guinier law [40], which is a shape- and size-independent model (see Supporting Information). Because the individual macromolecule contains only one ssDNA, the number of ssDNA within a micellar corona is considered to be the same as N_{ass}. Interestingly, the micellar size of PNIPAAm-*co*-ssDNA significantly depended on its macromolecular architecture. N_{ass} of star-shaped copolymer was much smaller than its diblock counterpart (Table 1), even though these two copolymers have the similar molecular weight and composition. This may account for the dramatically smaller R_h and R_g of star-shaped copolymer than its diblock counterpart. Therefore, controlling the copolymer topologies would be an efficient way to tune the micellar size and morphology of PNIPAAm-*co*-ssDNA. Further details of the copolymer architectural dependence of micellar morphology will be reported in our forthcoming paper. Moreover, the R_g/R_h ratios of both copolymers are in the range of 0.71–0.73 (Table 1), which are very close to the theoretical value of a spherical particle (0.775) [40].

The thermoresponsive micellation of copolymer was further examined using fluorescence spectroscopy, with Nile Red as a hydrophobic probe. Fig. 3c shows the fluorescence emission spectra of Nile Red in the solution of $1P_{280}$–$1ssD_9$ upon heating. Under the excitation at λ_{exc} = 550 nm, the fluorescence emission maximum of Nile Red in the copolymer solution below LCST located at 643 nm. With the increase in temperature to above LCST, the emission peak shifted to a shorter wavelength (625 nm) and its intensity increased remarkably. This indicated that the fluorescent dye is incorporated into the hydrophobic environment [41], namely, the copolymer assembles into the micellar particles consisting of PNIPAAm core surrounded by ssDNA corona.

The changes of the emission intensity at 625 nm and the maximum emission wavelength (λ_{max}) upon heating and cooling are shown as a function of temperature in Fig. 3d. The encapsulation/release of hydrophobic probe was entirely reversible, where was observed a remarkable increase in fluorescence intensity and a blue-shift from 643 ± 2 to 625 nm upon heating and vice versa (Fig. S7). These observations suggest the potentials of such copolymer micelles in the controlled encapsulation, release, and delivery of functionally hydrophobic substances.

4. Conclusion

This study reports a new method to prepare the DNA-functionalized copolymeric bioconjugates with the tunable and well-defined architectures, as well as a facile method to fabricate the DNA-

encoded soft nanoparticles. The thermal-triggered micellation of these copolymers solution was verified. These PNIPAAm-*co*-ssDNA copolymers assembled into spherical micelles above LCST and their micellar sizes could be tuned from the macromolecular architectures. Moreover, the potential of such DNA-encoded micelles in delivery of functional hydrophobic molecules was shown by reversible uptake and release of an organic dye in aqueous solution.

Acknowledgements

This work was financially supported by a Grant-in-Aid for Scientific Research on Innovative Areas "Molecular Soft-Interface Science" from the Ministry of Education, Culture, Sports, Science and Technology of Japan. W. Y. Ooi thanks USM Fellowship for financial support.

Appendix. Supplementary data

Supplementary data associated with this article can be found in the on-line version, at doi:10.1016/j.polymer.2011.01.016.

References

[1] Rosi NL, Mirkin CA. Chem Rev 2005;105:1547–62.
[2] Nykypanchuk D, Maye MM, van der Lelie D, Gang O. Nature 2008;451:549–52.
[3] Park SY, Lytton-Jean AKR, Lee B, Weigand S, Schatz GC, Mirkin CA. Nature 2008;451:553–6.
[4] Li Z, Zhang Y, Fullhart P, Mirkin CA. Nano Lett 2004;4:1055–8.
[5] Ding K, Alemdaroglu FE, Borsch M, Berger R, Herrmann A. Angew Chem Int Ed 2007;46:1172–5.
[6] Jakobsen U, Simonsen AC, Vogel S. J Am Chem Soc 2008;130:10462–3.
[7] Chien MP, Rush AM, Thompson MP, Gianneschi NC. Angew Chem Int Ed 2010;49:5076–80.
[8] Blanazs A, Armes SP, Ryan AJ. Macromol Rapid Commun 2009;30:267–77.
[9] Mori T, Maeda M. Polym J 2002;34:624–8.
[10] Mori T, Maeda M. Langmuir 2004;20:313–9.
[11] Nicolas J, Mantovani G, Haddleton DM. Macromol Rapid Commun 2007;28:1083–111.
[12] Heredia KL, Maynard HD. Org Biomol Chem 2007;5:45–53.
[13] Klok HA. Macromolecules 2009;42:7990–8000.
[14] Heredia KL, Nguyen TH, Chang CW, Bulmus V, Davis TP, Maynard HD. Chem Commun; 2008:3245–7.
[15] Boyer C, Bulmus V, Davis TP. Macromol Rapid Commun 2009;30:493–7.
[16] Kanayama N, Shibata H, Kimura A, Miyamoto D, Takarada T, Maeda M. Biomacromolecules 2009;10:805–13.
[17] Rostovtsev VV, Green LG, Fokin VV, Sharpless KB. Angew Chem Int Ed 2002;41:2596–9.
[18] Gramlich PME, Wirges CT, Manetto A, Carell T. Angew Chem Int Ed 2008;47:8350–8.
[19] Li Z, Kesselman E, Talmon Y, Hillmyer MA, Lodge TP. Science 2004;306:98–101.
[20] Yun J, Faust R, Szilágyi LS, Kéki S, Zsuga M. Macromolecules 2003;36:1717–23.
[21] Yin H, Kang SW, Bae YH. Macromolecules 2009;42:7456–64.
[22] Jeong JH, Park TG. Bioconjug Chem 2001;12:917–23.
[23] Oishi M, Nagasaki Y, Itaka K, Nishiyama N, Kataoka K. J Am Chem Soc 2005;127:1624–5.
[24] Alemdaroglu FE, Herrmann A. Org Biomol Chem 2007;5:1311–20.
[25] Safak M, Alemdaroglu FE, Li Y, Ergen E, Herrmann A. Adv Mater 2007;19:1499–505.
[26] Teixeira Jr F, Rigler P, Vebert-Nardin C. Chem Commun; 2007:1130–2.
[27] Fluegel S, Maskos M. Biomacromolecules 2007;8:700–2.
[28] Braunecker WA, Matyjaszewski K. Prog Polym Sci 2007;32:93–146.
[29] Stenzel-Rosenbaum M, Davis TP, Chen V, Fane AG. J Polym Sci A Polym Chem 2001;39:2777–83.
[30] Hart-Smith G, Chaffey-Millar H, Barner-Kowollik C. Macromolecules 2008;41:3023–41.
[31] Britovsek GJP, England J, White AJP. Inorg Chem 2005;44:8125–34.
[32] Xia JH, Zhang X, Matyjaszewski K. Macromolecules 1999;32:3531–3.
[33] Mantovani G, Ladmiral V, Tao L, Haddleton DM. Chem Commun; 2005:2089–91.
[34] Narumi A, Fuchise K, Kakuchi R, Toda A, Satoh T, Kawaguchi S, et al. Macromol Rapid Commun 2008;29:1126–33.
[35] To clearly see the bands of azide and oligonucleotide, a shorter homopolymer ($1P_{35}$) and its copolymer ($1P_{35}$-$1ssD_9$) were synthesized and used for FTIR measurement.
[36] Humenik M, Huang Y, Wang Y, Sprinzl M. Chembiochem 2007;8:1103–6.
[37] Falk M, Hartman KA, Lord RC. J Am Chem Soc 1963;85:391–4.
[38] Duan Q, Narumi A, Miura Y, Shen X, Sato S, Satoh T, et al. Polym J 2006;38:306–10.
[39] Giri N, James SL. Chem Commun 2011;47:245–7.
[40] Roe RJ. Methods of X-ray and neutron scattering in polymer science. New York: Oxford University Press; 2000. pp.167–70.
[41] Goodwin AP, Mynar JL, Ma Y, Fleming GR, Fréchet JMJ. J Am Chem Soc 2005;127:9952–3.

Polymer 52 (2011) 901–903

Contents lists available at ScienceDirect

Polymer

journal homepage: www.elsevier.com/locate/polymer

Polymer Communication

Poly(vinyl chloride) (PVC) hollow fibre membranes for gas separation

C.A. Jones [a], S.A. Gordeyev [b], S.J. Shilton [a,*]

[a] Department of Chemical and Process Engineering, University of Strathclyde, James Weir Building, 75 Montrose Street, Glasgow G11XJ, Scotland, United Kingdom
[b] Institute of Nanotechnology, Lord Hope Building, 141 St. James Road, Glasgow G40LT, Scotland, United Kingdom

ARTICLE INFO

Article history:
Received 6 October 2010
Accepted 6 January 2011
Available online 13 January 2011

Keywords:
PVC
Hollow fibre spinning
Gas separation

ABSTRACT

Poly(vinyl chloride) (PVC) gas separation hollow fibre membranes were produced from multicomponent dopes using dry/wet forced convection spinning. Membranes spun from a low polymer content solution exhibited disappointing gas separation properties. Their low selectivities were indicative of thick skins and high surface porosities. In contrast, high polymer content spun fibres showed good gas separation properties. Selectivities were high, active layers relatively thin and surface porosities moderate. Coating with poly(dimethylsiloxane) nullified the surface pores. The favourable performance of the high polymer content spun fibres was also related to shear rate and forced convection residence time during spinning. To the knowledge of the authors, this work represents the first reported success in producing PVC hollow fibre membranes with morphologies suitable for gas separation. The development of PVC hollow fibres relates to the ultimate quest to produce membranes capable of reliably separating oxygen and ozone gas mixtures.

1. Introduction

Little work has been carried out involving polyvinylchloride (PVC) as a gas separation membrane forming polymer. The reports that are published tend to relate to dense homogeneous flat sheet membranes [1–3] and films [4].

PVC is a low permeability, slightly crystalline, glassy polymer and, as such, presents a challenge to the gas separation membranologist. The low permeability coefficients of gases in PVC demand ultra-thin essentially defect free membrane active layers if the intrinsic selectivity of the polymer is to be realised at reasonable pressure-normalised fluxes in a working membrane. The spinning of PVC hollow fibre membranes is largely limited to ultrafiltration technology [5,6]. Low permeation glassy semi-crystalline polymers, problematic for gas separation, can be used to fabricate porous media such as microfiltration and ultrafiltration membranes [7].

In the case of using PVC in gas separation hollow fibre membrane technology, viscosity limits the polymer concentration in the spinning solution. Higher dope concentrations can achieve defect free skins but the dopes are often unspinnable due to their high viscosities. PVC ultrafiltration hollow fibre membranes can be produced from lower concentration dopes since porous structures are desirable.

The selection of PVC as a membrane forming polymer in this work relates to the ultimate desire to develop hollow fibres for oxygen/ozone separation. Such membranes would have a huge impact on industrial applications involving ozone such as water purification, bleaching and sterilisation. The economics of ozone production would be greatly improved if oxygen could be separated from generated ozone and then recycled back to the ozone generator.PVC and the coating material, polydimethylsiloxane both exhibit good resistance to ozone.

To our knowledge, this work seeks, for the first time, to produce PVC hollow fibre membranes with morphologies suitable for gas separation. Historical lab standard spinning conditions are employed [8] with two multicomponent PVC dopes: one at lower polymer concentration and one at higher. The rationale behind muticomponent spinning solutions has been explained elsewhere [9]. The higher concentration PVC system studied here pushes the boundary of spinnability and as such requires the dope reservoir to be kept at elevated temperature during spinning. The lower concentration solution represents more conventional ambient temperature spinning conditions.

The permeation performance of the PVC hollow fibre membranes was tested with four gases: oxygen, nitrogen, carbon dioxide and methane.

2. Experimental

2.1. Membrane spinning

Asymmetric PVC hollow fibre membranes intended for gas separation were fabricated using a dry/wet spinning process with

* Corresponding author. Tel.: +44 141 548 2380.
E-mail address: simon.shilton@strath.ac.uk (S.J. Shilton).

0032-3861/$ – see front matter © 2011 Elsevier Ltd. All rights reserved.
doi:10.1016/j.polymer.2011.01.013

Table 1
General spinning conditions.

Spinneret dimensions	OD 635 μm, ID 229 μm aspect ratio (length to gap) 1.4
Internal coagulant composition	20% (w/w) potassium acetate in water (water activity 0.9)/water
Internal coagulant temperature	20 ± 2 °C
Dope extrusion rate	2.0–2.5 cm^3/min
Dope extrusion rate:internal coagulant injection rate	3:1
Forced convection gas	Nitrogen
Forced convection flowrate	4 L/min 3 impingement jets
Forced convection chamber height	5–6 cm
Forced convection temperature	20 ± 2 °C
External bath composition	Water
External bath temperature	14 ± 0.5 °C
Jet stretch ratio (wind-up speed: extrusion speed)	1:1

forced convection in the dry gap. The spinning dope consisted of four components: PVC (Aldritch, Mwt 43,000), N,N dimethylacetamide (DMac), tetrahydrofuran (THF) and ethanol. THF is a highly volatile solvent and evaporates quickly during forced convection. Non-solvent, ethanol is present in the dope to speed up precipitation. Both effects are thought to assist skin formation. The forced convection chamber was positioned immediately underneath the spinneret from which the filament was extruded vertically downwards. The chamber, a cylinder (diameter 5 cm and various heights), was flushed with nitrogen gas. The nitrogen was introduced through three ¼" tubes 120° apart that each abutted upon the chamber normal to the surface at mid-height. Full details of the hollow fibre membrane spinning and preparation procedures can be found in a previous paper [8]. General spinning conditions are found in Table 1.

2.2. Gas permeation

The membranes were potted into modules and tested before and after coating with polydimethylsiloxane (Sylgard 184, Dow Corning). Coating is a standard technique that repairs any small defects or pores that exist in the membrane active layer [10]. The pressure-normalised fluxes of the fibres were measured for O_2, N_2, CO_2 and CH_4 at 25 °C and at a pressure drop of 5 bar. Membrane selectivities were determined by taking the ratio of pressure-normalised fluxes. Values were the average of at least six modules tested.

3. Results and discussion

Table 2 shows the gas permeation performance of PVC hollow fibres spun at high and low polymer concentration. The low concentration spun membranes exhibit disappointing selectivities characteristic of Knudsen diffusion for both uncoated and coated fibres. Pressure-normalised flux is greatly reduced on coating for these samples indicating that pores have been plugged. However, the low coated selectivities for the low concentration spun fibres suggest a morphology of thick skins and high surface porosity where Knudsen diffusion through the open pore length beneath the PDMS plugs, is the dominant flow mechanism.

Table 3
Intrinsic permeation properties of PVC to a number of gases (various sources).

Source [ref.]	Permeabilty coefficient × 10^{10} (cm^3(STP)cm/s cm^2 cmHg)				Intrinsic selectivity	
	P_{O2}	P_{N2}	P_{CO2}	P_{CH4}	P_{O2}/P_{N2}	P_{CO2}/P_{CH4}
[1]	0.07	0.01	0.25	–	7.0	–
[2]	0.124	0.022	0.540	0.024	5.6	22.5
[3]	–	–	–	–	5.0	20.0
[4]	–	0.00945	0.243	0.0108	–	22.5
[4]	–	0.00668	0.184	0.00850	–	21.6
[11]	0.12	0.04	1.0	–	3.0	–
[12]	–	0.028	0.32	0.06	–	5.33
[13]	0.05	0.01	0.15	0.025	5.0	6.0
[14]	–	–	0.16	0.0106	–	15.1

The coated data for the high concentration spun hollow fibres show much higher selectivities indicative of low-defect solution diffusion driven membranes. Literature based permeability coefficients and intrinsic selectivities of gases in PVC are given in Table 3. The data is diverse but the O_2/N_2 intrinsic selectivity is reasonably consistent with an average value of 5.12. The O_2/N_2 selectivity of the high concentration spun membranes given in Table 2 has a value of 4.2 which is greater than 80% of the intrinsic selectivity value of 5.12. Pesek and Koros proposed that if the selectivity of a membrane is greater than 80% of the intrinsic value, then a sensible estimation of active layer thickness can be made through the permeability coefficient as solution diffusion will be the predominant mode of transmission [15]. Adopting this '80% rule', taking the oxygen pressure-normalised flux from Table 2 and using the average permeability coefficient for oxygen from Table 3, gives an estimated active layer thickness of 532Å. This, coupled with low surface porosities (negated through coating), indicates a much more favourable membrane structure for the high concentration spun material. Information regarding fine structural details is included in Table 4. A more complete resistance modelling analysis could have been carried out to determine more detailed structural details [16] but given the disappointing performance of the low concentration spun material, this would have been overkill for this work.

The contrasting structures of the two membrane types studied here may relate to rheological and phase inversion effects during spinning. Table 4 gives the dope extrusion rates, hence the levels of shear rate experienced by the polymer solutions during extrusion, and the residence times of the filaments in the forced convection chamber during spinning. A higher dope extrusion rate imparts a greater shear rate in the polymer solution at the wall of the spinneret during extrusion. This has been shown to cause thinner more oriented and hence more selective active layers to be produced [17,18]. Also, within the range studied here, a reduced residence time in the forced convection chamber may prevent the active layer from overgrowing [18]. Both effects are consistent with the superior structure and performance of the high concentration PVC spun membranes reported here. In addition, the polymer

Table 2
PVC hollow fibre membrane gas permeation properties.

Fibre type	Dope composition % w/w PVC/THF/DMac/ethanol	Uncoated pressure-normalised flux			Coated pressure-normalised flux					
		$P_{O2} \times 10^6$ (cm^3(STP)/s cm^2 cmHg)	P_{N2}	P_{O2}/P_{N2} selectivity	$P_{O2} \times 10^6$ (cm^3(STP)/s cm^2 cmHg)	P_{N2}	P_{CO2}	P_{CH4}	P_{O2}/P_{N2} selectivity	P_{CO2}/P_{CH4} selectivity
PVC-L	24/7/53/16	3754	4227	0.888	17	16	24	26	1.057	0.937
PVC-H	28/6/50/16	–	–	–	1.71	0.41	6.64	0.74	4.2	9.0

Table 4
PVC hollow fibre spinning conditions and membrane structure.

Fibre type	Dope composition % w/w PVC/THF/DMac/ethanol	Dope extrusion rate (cm3/min)	Jet stretch ratio (−)	Forced convection residence time (s)	Membrane fine structural details	
					Active layer thickness (Å)	Surface porosity $\times 10^6$ (m^2/m^2)
PVC-L	24/7/53/16	2	1	0.5	Thick	Prohibitively high
PVC-H	28/6/50/16[a]	2.5	1	0.33	532Å	Moderate

[a] dope reservoir kept warm to maintain spinnable dope viscosity.

content in the low concentration spun fibres may insufficient for proper skin coalescence to occur [19]. This would be consistent with greater surface porosities in these samples.

4. Conclusions and recommendations

The PVC hollow fibres spun from the high concentration dope exhibit properties suitable for the separation of gases with healthy selectivities being achieved for both the O_2/N_2 and CO_2/CH_4 systems. This work represents a 'sighting shot' in the development of PVC hollow fibres for gas separation and relates to the ultimate desire to develop membranes for oxygen/ozone separation. Whilst preliminary tests have indicated that the high concentration spun membranes produced in this work are capable of achieving a degree of separation for the O_2/O_3 system [20], further research is underway to improve PVC membrane quality and oxygen/ozone gas testing protocols.

Acknowledgements

The authors wish to acknowledge the financial support of Filtration Ltd and the EPSRC (Doctoral Training Grant).

References

[1] Bierbrauer K, Lopez-Gonzalez M, Riande E, Mijangos C. Gas transport in fluorothiophenyl modified PVC membranes. Journal of Membrane Science 2010;362:164–71.
[2] Tiemblo P, Guzman J, Riande E, Mijangos C, Reinecke H. The gas transport properties of PVC functionalized with mercapto pyridine groups. Macromolecules 2002;35:420–4.
[3] Tiemblo P, Guzman J, Riande E, Mijangos C, Reinecke H. Effect of physical aging on the gas transport properties of PVC and PVC modified with pyridine groups. Polymer 2001;42:4817–23.
[4] El-Hibri MJ, Paul DR. Effects of uniaxial drawing and heat-treatment on gas sorption and transport in PVC. Journal of Applied Polymer Science 1985;30:3649–78.
[5] Khayet M, Garcia-Payo MC, Qusay FA, Zubaidy MA. Structural and performance studies of poly(vinyl chloride) hollow fiber membranes prepared at different air gap lengths. Journal of Membrane Science 2009;330:30–9.
[6] Xu J, Z- Xu L. Poly(vinyl chloride) (PVC) hollow fiber ultrafiltration membranes prepared from PVC/additives/solvent. Journal of Membrane Science 2002;208:203–12.
[7] Yang M-C, Tong J-H. Loose ultrafiltration of proteins using hydrolized polyacrylonitrile hollow fiber. Journal of Membrane Science 1997;132:63–71.
[8] Ismail AF, Dunkin IR, Gallivan SL, Shilton SJ. Production of super selective polysulfone hollow fibre membranes for gas separation. Polymer 1999;40:6499–506.
[9] Gordeyev SA, Shilton SJ. Forced convection spinning of gas separation hollow fibre membranes: some underlying factors, mechanisms and effects. Journal of Membrane Science 2004;229:225–33.
[10] Ward RR, Chang RC, Danos JC, Carden Jr JA, Monsanto Co.. Process for coating bundles of hollow fiber membranes, US Patent 4214020; 1980.
[11] Li NN. Recent developments in separation science. CRC Press; 1987.
[12] Tikhomirov BP, Hopfenberg HB, Stannett V, Williams JL. Permeation, solution and diffusion of gases and water vapor in unplasticized poly(vinyl chloride). Die Makromolekulare Chemie 1968;118:177–88.
[13] Baker RW, Blume I. Permselective membranes to separate gases. Chemtech 1986;16:232–8.
[14] Mulder M. Basic principles of membrane technology. Kluwer Academic Publishers; 1996.
[15] Pesek SC, Koros WJ. Aqueous quenched asymmetric polysulfone membranes prepared by dry/wet phase separation. Journal of Membrane Science 1993;81:71–88.
[16] Shilton SJ, Bell G, Ferguson J. The deduction of fine structural details of gas separation hollow fibre membranes using resistance modelling of gas permeation. Polymer 1996;37:485–92.
[17] Ismail AF, Shilton SJ, Dunkin IR, Gallivan SL. Direct measurement of rheologically induced molecular orientation in gas separation hollow fibre membranes and effects on selectivity. Journal of Membrane Science 1997;126:133–7.
[18] Sharpe ID, Ismail AF, Shilton SJ. A study of extrusion shear and forced convection residence time in the spinning of polysulfone hollow fiber membranes for gas separation. Separation and Purification Technology 1999;17:101–9.
[19] Pinnau I, Koros WJ. A qualitative skin layer formation mechanism for membranes made by dry/wet phase inversion. Journal of Polymer Science, Part B: Polymer Physics 1993;31:419–27.
[20] Neilson G, Styler B. private communication.

Polymer 52 (2011) 904–911

Contents lists available at ScienceDirect

Polymer

journal homepage: www.elsevier.com/locate/polymer

Poly(butylene terephthalate) modified with ethoxylated bisphenol S with increased glass transition temperature and improved thermal stability

N. Lotti, M. Colonna*, M. Fiorini, L. Finelli, C. Berti

Dipartimento di Ingegneria Civile, Ambientale e dei Materiali, Via Terracini 28 40131 Bologna, Italy

ARTICLE INFO

Article history:
Received 11 November 2010
Received in revised form
4 January 2011
Accepted 9 January 2011
Available online 15 January 2011

Keywords:
Terephthalate polyester
Bisphenol S
Thermal properties

ABSTRACT

Novel copolyesters have been prepared by polycondensation and by melt mixing of poly(butylene terephthalate) with an ethoxylated bisphenol S. No side reactions occur during the synthesis of the samples, as proved by NMR analysis. The polyesters were examined by TGA and DSC. The insertion of the bisphenol S (sulfonyldiphenol) group significantly improved the thermal stability of the polymer. The thermal analysis carried out using DSC technique showed that the T_m of the copolymers decreased with increasing co-unit content, differently from T_g, which on the contrary increased, exceeding in some cases 100 °C, and crystallization rate decreased. A polymer containing only terephthalate moieties and ethoxylated bisphenol S has been prepared for the first time.

1. Introduction

Terephthalate polyesters are widely used as engineering thermoplastic materials due to their good chemical resistance, high thermal and dimensional stability, high strength and rigidity coupled with good surface hardness and gloss [1]. These polymers have found the main applications in precision moulding for electrical and electronic devices, domestic and office appliances and automotive parts. Poly(butylene terephthalate) (PBT) is the most widely used terephthalate polyester as engineering thermoplastic due to its high crystallization rate and high crystallinity which imparts good solvent and hydrolysis resistance. The main drawback of terephthalate polyesters lies in their low impact resistance especially at low temperatures. On the contrary, one of the most important features of bisphenol A polycarbonate (PC) is its high impact resistance, even at low temperatures. It is reported in the literature [2,3] that the high impact resistance of PC can be ascribed to its capability to absorb high impact energy which, in turns, has been correlated with secondary transitions involving cooperative motions of bisphenol A (BPA) units that take place at very low temperature ($T\gamma = -105$ °C from dynamic mechanical analysis [2]). However, PC presents poor solvent resistance. For these reasons blends of PC with PBT are industrially used for applications where low temperature impact resistance and solvent resistance are both required, as for example, in car bumpers.

Bisphenol A cannot be directly incorporated in the polyester main chain since aromatic diols are not active in esterification reactions with terephthalic acid or dimethyl terephthalate and therefore has to be modified in order to be inserted in the polyester backbone during a normal polycondensation process [1].

We have reported [4,5] that the insertion of bisphenol A (BPA) units inside a terephthalate polyester leads to an increase in glass transition temperature and in thermal stability of PBT, PET and PPT. Similar results have been reported by Koning et al. [6] on block copolymers obtained by solid state polymerisation. The approach we have followed consists in the derivatization of BPA *via* ethoxylation and the functionalized BPA was used directly in melt mixing with terephthalate polyesters. We studied bis(hydroxyethyl ether) of bisphenol A (BHEEB), since several easy and low-cost routes for the synthesis of BHEEB are reported in the literature [7–11], for example by reaction between ethylene carbonate (ETC) and BPA [7] and by reaction of PC, ethylene glycol and ETC in presence of sodium hydroxide. The reaction of BPA with ETC permits the preparation of ethoxylated bisphenol A without the formation of aliphatic–aliphatic ether linkages as usually observed when ethylene oxide is used. The insertion of ethoxylated BPA units in the polyester backbone has been performed during the polymerisation or by melt mixing, which in our opinion is the most interesting method when a low amount of diol has to be incorporated in order to obtain semicrystalline materials. Melt mixing allows recycled terephthalate polyesters to be used and can be performed in shorter reaction times compared to the full polymerisation procedure.

It has been reported [12] that the insertion of sulfonyldiphenol units (bisphenol S, BPS) leads to a more consistent improvement in

* Corresponding author. Tel.: +390512090331; fax: +390512090322.
E-mail address: martino.colonna@unibo.it (M. Colonna).

0032-3861/$ – see front matter © 2011 Elsevier Ltd. All rights reserved.
doi:10.1016/j.polymer.2011.01.018

T_g of terephthalate copolyesters with respect to the use of BPA derivatives. This behavior has been attributed to the higher rigidity of the BPS unit since in this molecule it is not possible to bend the C–S–C bonds due to the presence of S–O double bonds. Recently, the synthesis of copolyesters based on terephthalic acid, ethylene glycol, cyclohexane dimethanol and bis(hydroxyethyl ether) of bisphenol S (BHEBS) has been patented by Turner and Sublett from Eastman Kodak [13]. They reported that the PETG copolymers with BHEBS present higher T_g and improvements in environmental stress cracking resistance after lipid exposure. They also claim the use of butanediol as monomer but always in combination with another aliphatic glycol. Therefore, it is of interest for the industrial and scientific community the study of the effect of these units on other polyesters and the properties of a polymer containing only terephthalate-BHEBS (BHEBST) units.

The aim of our work was to prepare semicrystalline copolymers containing bisphenol S moieties. To the best of our knowledge, the literature does not report a complete and systematic study of the synthesis and of the properties of terephthalate polyesters containing BHEBS units.

In this paper we report the synthesis of poly(butylene terephthalate) containing BHEBST units and the chemical and thermal characterization of the copolymers synthesised. The synthesis of the polyesters have been performed both by melt mixing of PBT with BHEBS and subsequent polycondensation under vacuum, and by melt polycondensation starting from monomers. It has to be emphasized that the synthesis of a polyester containing only terephthalate and ethoxylated bisphenol S units (PBHEBST) has been never carried out before.

2. Experimental

2.1. Materials

Poly(butylene terephthalate) (PBT, Valox 315, M_w 125000) was a gift of SABIC Innovative Plastics. PBT was dried overnight at 120 °C under vacuum before use. ETC, BPS, DMT, butanediol (BD) and Titanium butoxide (TBT) (all from Aldrich Chemicals) were high purity products and were not purified before use.

2.2. Gel-permeation chromatography

Molecular weight data were obtained by gel permeation chromatography at 30 °C using a 1100 Agilent Series system with a UV spectrophotometer (at 254 nm wavelength) as detector, equipped with Agilent PLgel 5μ MiniMIX-C column (250/4.6 length/i.d., in mm). A mixture of chloroform/1,1,1,3,3,3-hexafluoro-2-propanol ($CHCl_3$/HFIP) (95/5 v/v) was used as eluent with a 0.3 mL/min flow, and sample concentrations of about 2 mg/mL were applied. A molecular weight calibration curve was obtained with several monodisperse polystyrene standards in the range of molecular weight 2000–200,000 g/mol.

2.3. NMR spectroscopy

^{1}H NMR *and* ^{13}C NMR spectra were recorded with a Varian XL-300 spectrometer (chemical shifts are downfield from tetramethylsilane (TMS)). The solvent was $CDCl_3$ for monomers and a mixture of $CF_3COOD/CDCl_3$ (20/80, wt.-%) for the polymers.

2.4. Thermal analysis

2.4.1. TGA measurements

Thermogravimetric curves were obtained both in air and under nitrogen atmosphere using a Perkin Elmer TGA7 apparatus (gas flow: 50 mL/min) at 10 °C/min heating rate up to 900 °C.

2.4.2. DSC measurements

Calorimetric measurements were carried out by means of a Perkin Elmer DSC7 instrument equipped with a liquid sub ambient accessory and calibrated with high purity standards (indium and cyclohexane). With the aim of measuring the glass transition and the melting temperatures of the polymers under investigation, the external block temperature control was set at −60 °C and weighed samples of c.a. 10 mg were encapsulated in aluminum pans and heated to about 40 °C above fusion temperature at a rate of 20 °C/min (first scan), held there for 3 min, and then rapidly quenched to −10 °C. Finally, they were reheated from −10 °C to a temperature well above the fusion temperature of the sample at a heating rate of 20 °C/min (second scan). The glass-transition temperature T_g was taken as the midpoint of the heat capacity increment Δc_p associated with the glass-to-rubber transition. The melting temperature (T_m) and the crystallization temperature (T_c) were determined as the peak value of the endothermal and the exothermal phenomena in the DSC curve, respectively. The specific heat increment Δc_p, associated with the glass transition of the amorphous phase, was calculated from the vertical distance between the two extrapolated baselines at the glass transition temperature. The heat of fusion (ΔH_m) and the heat of crystallization (ΔH_c) of the crystal phase were calculated from the areas of the DSC endotherm and exotherm, respectively. In order to determine the crystallization rate under non-isothermal conditions, the samples were heated at 20 °C/min to about 40 °C above fusion temperature, kept there for 3 min and then cooled at 10 °C/min. The temperature corresponding to the maximum of the exothermic peak in the DSC cooling-curve (T_{cc}) can be correlated to the crystallization rate.

2.5. Syntheses

2.5.1. BHEBS synthesis from BPS and ETC

The reaction was carried out in a 500 mL three-neck round-bottom flask equipped with a nitrogen inlet and a reflux condenser. BPS (125 g; 0.50 mol), ETC (90.0 g; 1.02 mol) and K_2CO_3 (0.30 g; 2.83 mmol) were mixed under a stream of nitrogen. The mixture was heated at 220 °C for 2 h following the progress of the reaction by thin layer chromatography. The crude product was crushed into powder and washed three times with a 2M solution of KOH in water and twice with water (yield 95%).

^{1}H NMR analysis (solvent $CDCl_3$): δ (ppm downfield from TMS) 7.8 (4H, d), 6.90 (4H, d), 4.10 (4H, t).

2.5.2. Synthesis of copolyesters by melt mixing of PBT with BHEBS

The melt mixing of PBT and BHEBS was performed in a Brabender Plasticorder PL2000/W50. 50.0 g of PBT were charged in the Brabender mixer heated at 245 °C. After the complete melting of the polymer, BHEBS and 100 ppm of TBT catalyst (as titanium with respect to the final terephthalate polyester) were added and the mixing chamber closed with a cover to seal the mixer.

The reactions were performed in two stages; in the first one, carried out at atmospheric pressure for 15 min, the alcoholysis of the polyester by BHEBS took place. In the second stage, the pressure was carefully reduced down to 2 mbar in 30 min and butanediol was distilled off from the mixing chamber and recovered in a condenser. The reaction was stopped when no further increase in the torque signal was observed. The second stage time varied from 30 min to 2 h depending on the BHEEB amount added. The copolyesters obtained and analyzed in this work will be indicated as PBT/BHEBSTX, where X is the amount of BHEBST co-units expressed as mol %.

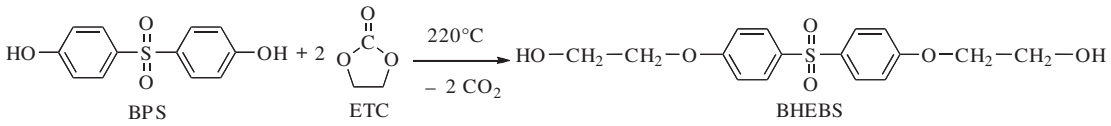

Fig. 1. Ethoxylated bisphenol S (BHEBS) synthesis.

2.5.3. Polyester syntheses from BHEBS, dimethyl terephthalate and butanediol

The synthesis of the copolymers was also performed starting from the monomers according to the standard two-step procedure for polyester synthesis [14].

DMT (50.0 g; 257 mmol), BD (29.6 g; 329 mmol), and BHEBS were introduced in a 250 mL three-neck round-bottom flask provided with mechanical stirring, a torque meter, a Dean Stark condenser and a 20 cm reflux column heated at 60 °C. TBT (100 ppm as titanium with respect to the final polymer) was added to the reagents and the flask was placed in an oil bath at 150 °C. The temperature was then increased to 230 °C over 30 min and kept at that temperature until no significant increase in distillate volume was observed (120 min from the catalyst addition). By ^{1}H NMR analysis, no BHEBS was found in the distillate. The Dean Stark condenser was removed and the reactor was connected with a liquid nitrogen cooled trap. The reaction temperature was then increased to 245 °C and dynamic vacuum was slowly applied. The reaction was conducted at 1 mbar until no increase in torque signal was observed (150 min from vacuum application). The chemical structure (by ^{1}H NMR), molecular weight (by GPC), and colour of the final polymer do not significantly differ from that of the polymer obtained by reactive blending.

A polymer from DMT and BHEBS was synthesised using the same procedure described above. In this case a 5 mol% excess of BHEBS with respect to DMT was used. The reaction was conducted for 2 h at 215 °C at atmospheric pressure and for 170 min at 245 °C under dynamic vacuum (1 mbar).

3. Results and discussion

BPS can be easily ethoxylated in very high yields by reaction with ethylene carbonate (Fig. 1).

The insertion of ethoxylated BPS inside the polyester can be performed either by melt mixing with the polyester (and subsequent polycondensation to reach high M_w) (Fig. 2) or starting from monomers. We have performed mainly the first route but we have also successfully tested the second method. ^{1}H NMR and ^{13}C NMR analysis showed no significant differences (end-groups, side reactions and degree of randomness) in the chemical composition of the polymers obtained with the two methods Table 1.

The BHEBS insertion by reactive blending is quantitative and no side reactions have been observed. For example, the ^{1}H NMR spectrum of PBT/BHEBST20 is reported in Fig. 3. The NMR spectrum shows only the expected peaks of the PBT and of the BHEBST units according to the assignment of the peaks reported on top of Fig. 3. No peak due to side reactions (for example vinyl end-groups) has been found in the NMR spectrum. The amount of BHEBS inserted has been calculated comparing the peak of the bisphenol S units at

Table 1
PBT/BHEBST copolymers prepared by reactive blending at 245 °C.

BHEBS Feed (mol%)	BHEBS inserted (mol %)	Second stage time (h)	M_w GPC (g/mol)	M_n GPC (g/mol)
5	4.9	2	52660	30350
10	10.1	2	63740	37500
20	19.9	2	41370	18960
50	49.5	3	33590	14570

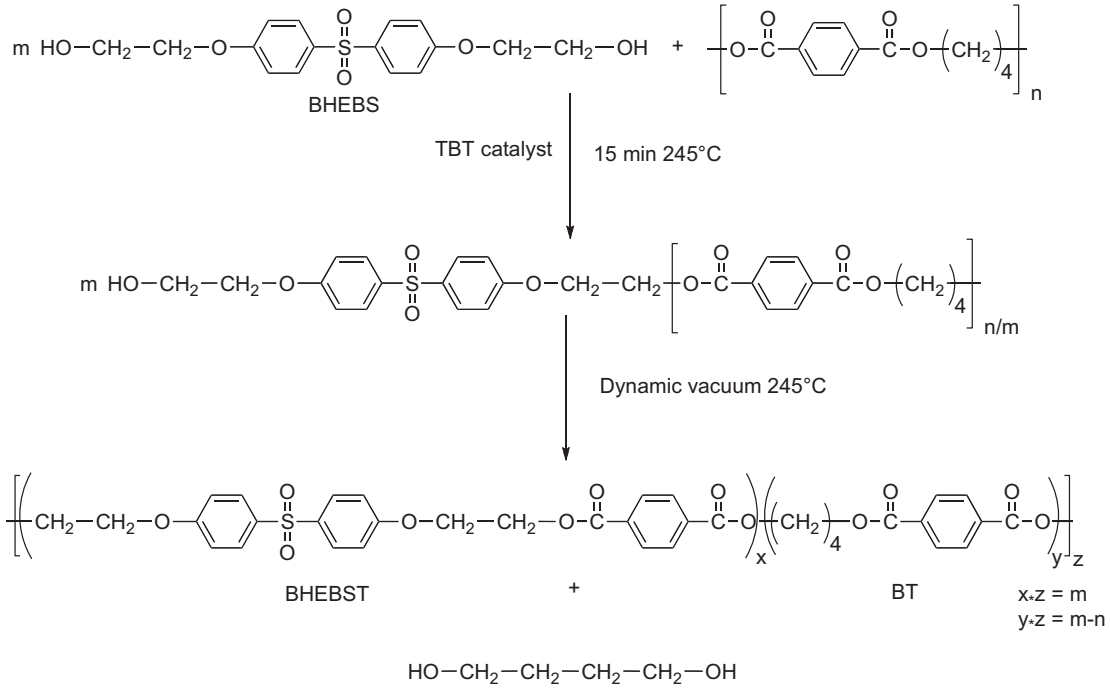

Fig. 2. Insertion of ethoxylated BPS units inside the polyester chain by reactive blending with PBT.

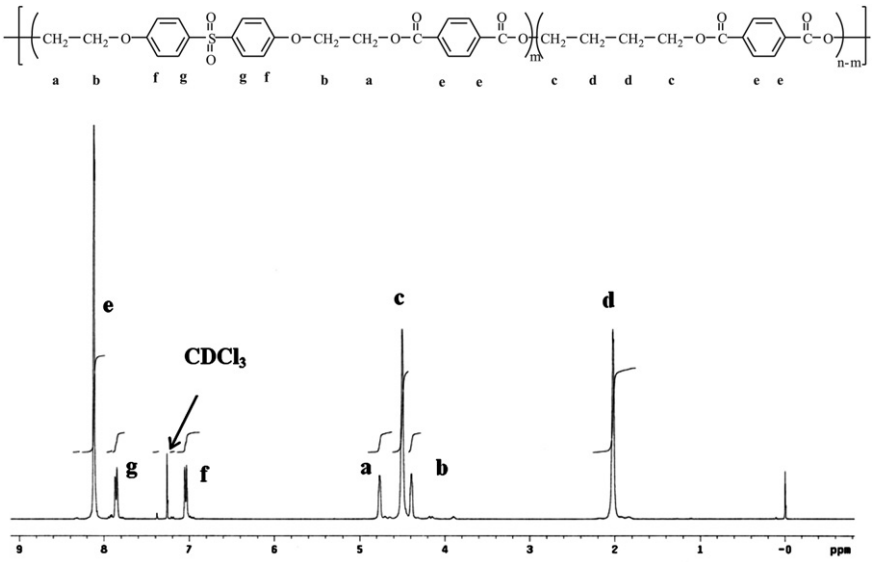

Fig. 3. ^{1}H NMR of PBT/BHEBST20.

δ = 7.0 ppm (4H) with that of the terephthalate group at δ = 8.1 ppm (4H) after dissolution of the polymer in a mixture of $CHCl_3/CF_3COOH$ 80/20 (v/v) and precipitation in methanol.

The distribution of BHEBST units along the polyester chain is random as verified by ^{13}C NMR (see as an example PBT/BHEBST50 copolymer in Fig. 5). In this case four different triads can be formed by reaction between the two diols (butanediol labeled B and BHEBS labeled S) and the terephthalate unit (T) (Fig. 4). According to Fig. 5, in ^{13}C NMR spectrum the triad S–T–S should give rise to a single signal of the carboxyl groups (a in Fig. 5) and of the aromatic carbon bonded to the carboxyl groups (b in Fig. 5). Also the triad B–T–B should give rise to a single signal. On the contrary, both the triad S–T–B and B–T–S should give rise to two different signals in ^{13}C NMR analysis. Taking into account that in PBT/BHEBST50 polymer the unit B and S are present in equal amounts and that the two signals of the triads S–T–B and B–T–S are equivalent, if the co-monomers are randomly distributed along the polymer chain, four signals of equal intensity should be present, since the four triads are equally probable. Indeed, the two expansions in Fig. 5 show that four signals of the same intensity are present, indicating that the expected random distribution of co-monomeric units have been achieved.

The polyester from DMT and BHEBS has been prepared by a standard two steps melt process using TBT catalyst. The final M_w of the polymer was 30 000 g/mol (measured by GPC). The ^{1}H NMR spectrum in Fig. 6 shows only the expected peaks. Again, no side reaction was detected by ^{1}H NMR analysis. End groups are mainly methyl ester while a small amount of BHEBS end-groups has been found. As mentioned in the Introduction, this is the first synthesis reported in the literature of BHEBS terephthalate polyester.

The copolyesters and the two parent homopolymers were preliminarily examined using thermogravimetric analysis. Investigation of the thermal stability was carried out both in air and under nitrogen atmosphere. Typical weight-loss curves as a function of temperature under nitrogen atmosphere are shown in Fig. 7a. As it can be seen, PBT/BHEBST5 sample shows a thermal stability similar to that of pure PBT, whereas in the case of the copolymers containing from 10 to 50 mol % of BHEBST co-units, the thermal stability appears to depend on composition, being higher as BHEBST unit content is increased. Furthermore, it can be noted that for all the samples in Fig. 7a, the weight-loss takes place almost completely in one-step, except for pure PBHEBST whose TGA curve shows two weight-loss steps.

Lastly, the thermogravimetric curve of PBT is characterized by a very low char residue (5%), whereas that of pure PBHEEBT shows the highest char residue among all the samples under investigation (25%). As far as the copolymers are concerned, the char residue appears to depend on composition, increasing as the amount of BHEBST co-units is increased. An analogous dependence on composition of the thermal stability was observed in air (see Fig. 7b), even though all the samples are characterized by a weight-loss of 100% and the thermal degradation process takes place always in two separate steps, the latter one being more evident as higher is the amount of BHEBST unit in the polymeric chain. The improved thermal stability of PBT by introduction of BHEBST units along the polymeric chain may be explained as due to the steric hindrance and high stiffness of the co-units, which prevent thermal degradation reactions, which usually occur in polyesters when heated [15,16]. An analogous result was obtained previously by us investigating the effect of the introduction of the 2,2-bis[4-(ethyl-enoxy)-1,4-phenylene]propane terephthalate co-monomeric units on the thermal stability of PBT [5].

The polyesters were afterwards examined by differential scanning calorimetry: the influence of molecular weight (M_w) on the glass transition and melting phenomena of the samples under investigation can be excluded, having PBT, PBHEBST and PBT/BHEBST polyesters of high and similar M_w values. It is well established that the melting behavior of a polymer is affected by its previous thermal history and therefore, in order to provide the

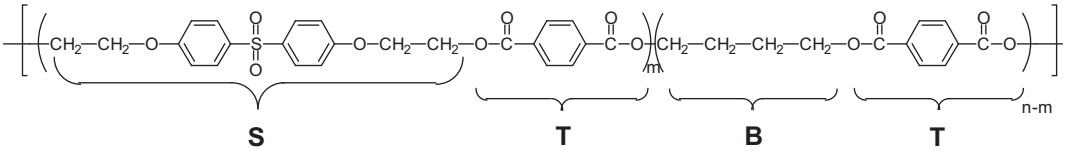

Fig. 4. Repeating units in PBT/BHEBST polymers.

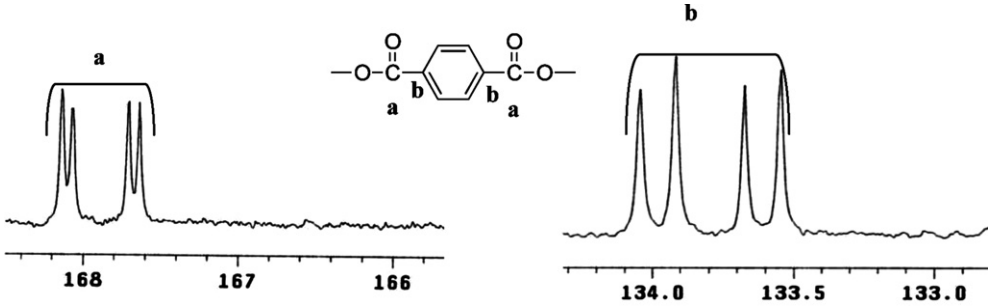

Fig. 5. Expansion of ^{13}C NMR of PBT/BHEBST50.

same heat treatment to all the samples investigated, prior to thermal analysis each sample was kept at room temperature for about 4 weeks. The DSC traces of the so-treated samples are reported in Fig. 8 and the results obtained in Table 2.

In all cases, a glass transition and a melting endotherm are evident, with exception of PBHEBST, whose DSC trace is characterized only by an endothermal baseline deviation associated with the glass transition phenomenon. First of all, it has to be emphasized that the phase behavior of the two parent homopolymers is opposite: PBT is semicrystalline, whereas PBHEBST is completely amorphous. As it is well known, the crystallization capacity of a polymer is correlated with several factors, such as the symmetry and the flexibility of the polymeric chain. In PBHEBST the presence of the very rigid bisphenol S group causes a drastic reduction of flexibility, hindering completely the ability of crystallizing of this polymer.

As far as the melting phenomenon is concerned, the calorimetric results indicate that an increase in the amount of the co-monomer BHEBST leads to a reduction in both of the melting temperature and the heat of fusion (see Fig. 9a), as usually found in random copolymers with only one co-unit taking part in the crystallization process. Furthermore, in the copolymers the endotherm region is broader, suggesting the presence of a larger distribution of crystallites with different degree of perfection.

The melting point reduction can be examined in order to estimate the equilibrium melting temperature T_m° and the equilibrium heat of fusion ΔH_m° of crystallizable unit. The Flory's treatment [17], commonly used in the past and derived assuming that the fusion concerns the disappearance of long sequences of crystallizable units, underestimates the melting point depression of random copolymers. As a matter of fact, the concentration of long sequences decreases with increasing co-unit content, and the experimental T_m values are consequently lower than those postulated by the theory. On the contrary, the equation proposed by Baur [18] takes into account the effect of sequence length of crystallizable units which can crystallize only when their length corresponds to the crystal thickness. Baur's equation is given by [18]:

$$1/T_m = 1/T_m^o - (R/\Delta H_m^o)(\ln x_C - 2x_C(1 - x_C)) \quad (1)$$

where T_m is the melting temperature of a random copolymer with molar fraction x_C of crystallizable co-monomer C, T_m° is the equilibrium melting temperature of the homopolymer (in this case PBT) and R is the gas constant. On the basis of equation (1), the T_ms were

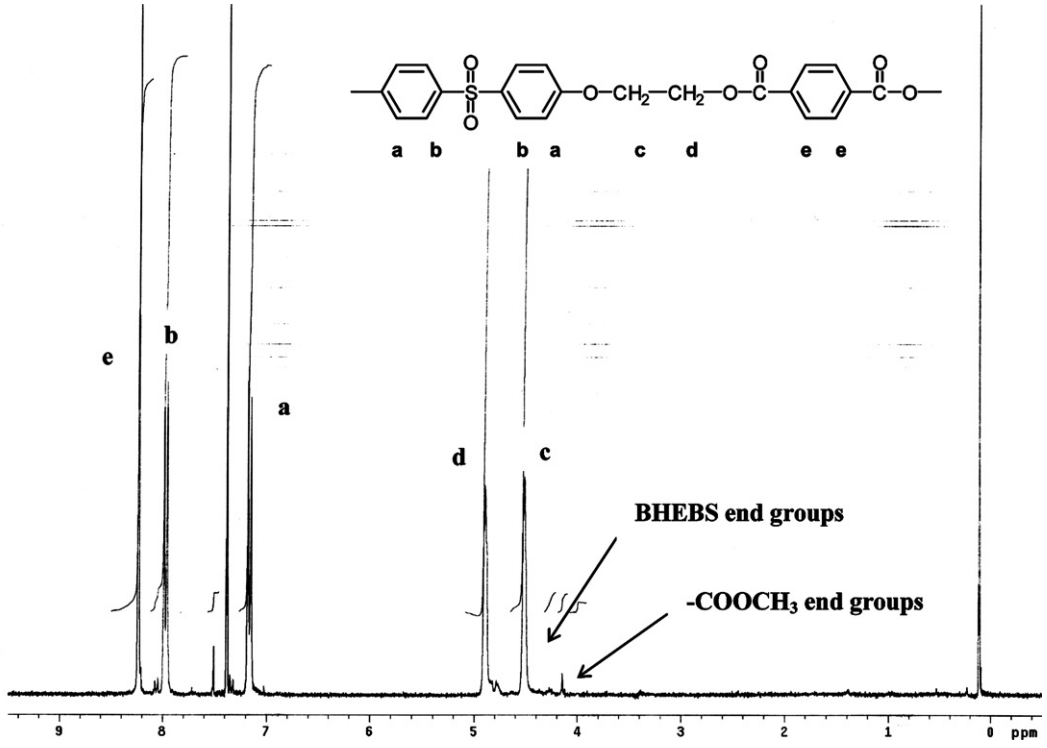

Fig. 6. ^1H NMR of PBHEBST polymer.

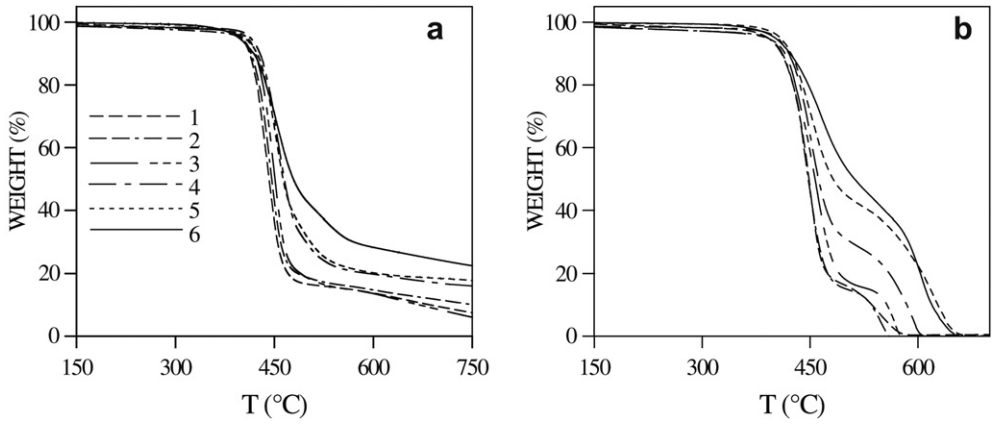

Fig. 7. TGA curves of (1) PBT, (2) PBT/BHEBST5, (3) PBT/BHEBST10, (4) PBT/BHEBST20, (5) PBT/BHEBST50, (6) PBHEBST at 10 °C/min in: (a) nitrogen; (b) air.

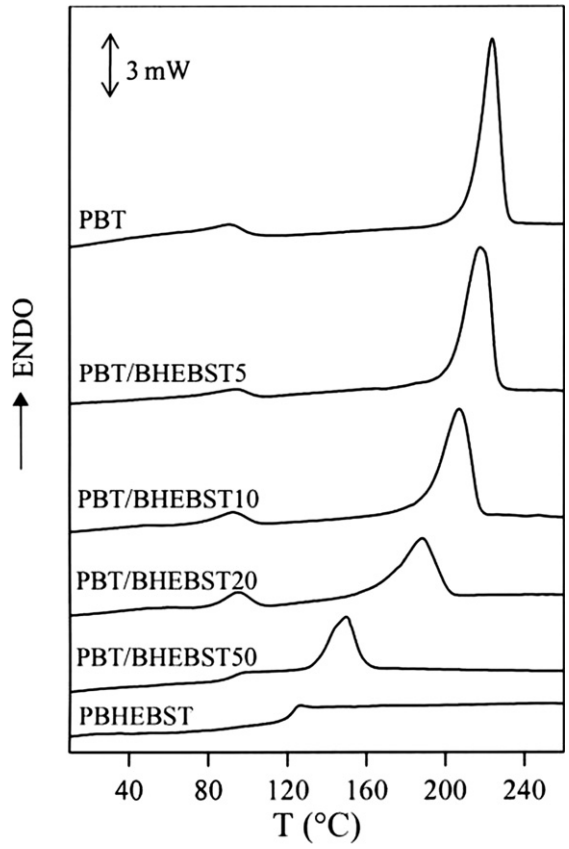

Fig. 8. Calorimetric curves of PBT, PBHEBST and their random copolymers (1st scan).

reciprocally plotted against $-[lnx_C - 2x_C(1-x_C)]$ in Fig. 9b and the equilibrium melting temperature and the heat of fusion for the completely crystalline PBT were extrapolated. As can be noted, the plot shows a good linearity and this result can be considered a further proof of the random nature of the copolymers investigated as well as of the exclusion of the co-units from the crystalline lattice of PBT.The T_m° and the ΔH_m° values estimated on the basis of Baur's equation were found to be 228 °C and 122 J/g, in good agreement with the ones reported in the literature for PBT homopolymer [19–21].

It is known that a partially crystalline material usually exhibits a different glass transition behavior than the analogous completely amorphous material. In fact, although some conflicting results are reported in the literature [22], crystallinity usually acts like cross-linking and raises T_g through its restrictive effect on segmental motion of amorphous polymer chains. Therefore, in order to study the influence of the chemical structure on the glass transition of random copolymers, the phenomenon should be examined in the total absence of crystallinity. Rapid cooling (quenching) from the melt is the method commonly used to prevent crystallization and to obtain polymers in a completely amorphous condition. In this view, all the samples under investigation were subjected to such thermal treatment (see the Experimental section for the details). The calorimetric curves of the polymers so treated are reported in Fig. 10. In all cases, except for PBHEBST and PBT/BHEBST50, the calorimetric traces show a glass transition followed by an exothermal "cold crystallization" peak and a melting endotherm at higher temperature. As far as PBT and the PBT/BHEBST copolymers poor in BHEBST units (up to 5 mol %) are concerned, the enthalpy associated with the crystallization phenomenon is lower than that of the fusion endotherm, indicating that these samples cannot be frozen into a completely amorphous state by quenching. Nevertheless, a portion of amorphous material, once T_g is exceeded, acquires enough mobility to rearrange and crystallize. The DSC curves of such samples are therefore typical of partially crystalline

Table 2
Thermal characterization data of PBT/BHEBST random copolymers (enthalpy has not been normalized by composition).

Sample	$T_{10\%}$[a] (°C)	$T_{50\%}$[b] (°C)	1st scan		2nd scan						T_{cc}[c] (°C)
			T_m (°C)	ΔH_m (J/g)	T_g (°C)	Δc_p (J/g°C)	T_c (°C)	ΔH_c (J/g)	T_m (°C)	ΔH_m (J/g)	
PBT	378	403	224	57	41	0.085	47	4	223	56	196
PBT/BHEBST5	381	406	216	54	46	0.226	59	27	213	52	183
PBT/BHEBST10	384	410	207	45	50	0.313	80	34	204	35	167
PBT/BHEBST20	389	424	188	34	61	0.327	119	26	186	26	144
PBT/BHEBST50	394	449	150	19	94	0.331	–	–	–	–	–
PBHEBST	411	470	–	–	122	0.325	–	–	–	–	–

[a] $T_{10\%}$ temperature at which the sample loose 10% of its weight.
[b] $T_{50\%}$ temperature at which the sample loose 50% of its weight.
[c] T_{cc} temperature corresponding to the maximum of the exothermic peak in the DSC cooling-curve.

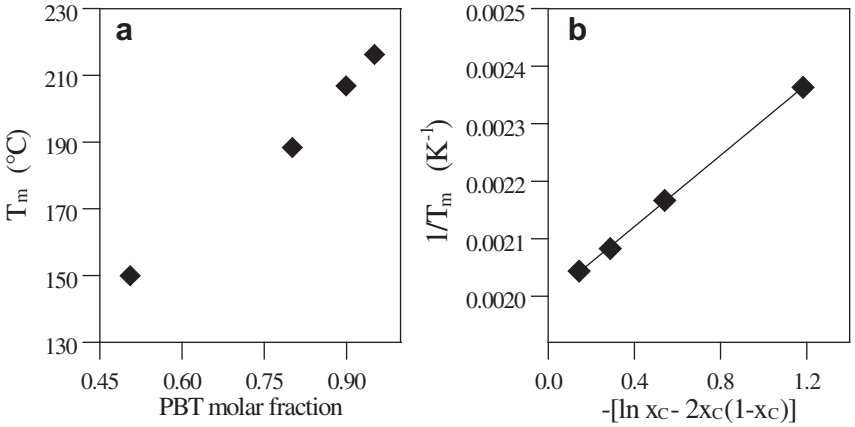

Fig. 9. (a) Melting temperatures (T_m) as a function of composition; (b) $1/T_m$-composition plot according to Baur's equation.

polymers. As a matter of fact, it is well known that PBT cannot be frozen in a completely amorphous glassy state, due to its high crystallization rate [23].

In the case of PBT/BHEBST10 and PBT/BHEBST20, the enthalpy of crystallization very well compares with the corresponding heat of fusion, indicating that the polymers were completely amorphous. As regards the calorimetric curves of pure PBHEBST and copolymer containing 50 mol % of BHEBST units, only an intense endothermal baseline deviation associated with the glass transition is observed. The phase behavior of copolymers was found to depend on composition: in fact, samples able to crystallize during the scan are obtained exclusively at high PBT content.

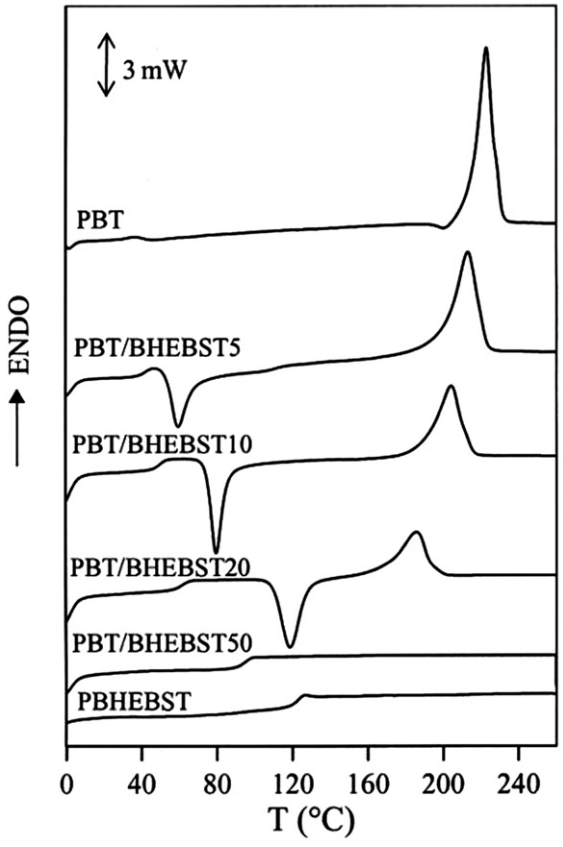

Fig. 10. Calorimetric curves of PBT, PBHEBST and PBT/BHEBST random copolymers after melt quenching.

As can be seen in Fig. 11 and from the data collected in Table 2, the glass transition temperature is influenced by the amount of BHEBST units in the polymer chains. The T_g values associated with the glass transition are plotted in Fig. 11 as a function of BT unit content together with those of random PBT/BHEEBT copolymers previously investigated [5]. As far as the trend of the glass transition temperature with the composition of PBT/BHEBST copolymers is concerned, one can observe that T_g values increase as BHEBST unit content is increased, due to the stiffening effect of the moieties deriving from bisphenol S in the polymeric chain. Comparing the data of the two copolymeric systems, it can be evicted that the increment of T_g is more consistent for PBT/BHEBST copolymers, due to the higher rigidity of bisphenol S compared to bisphenol A.

In amorphous random copolymers, T_g is usually a monotonic function of composition [24] and the commonest relationship used to predict T_g as a function of comonomer content is the Fox equation [25]:

$$1/T_g = w_I/T_{gI} + w_{II}/T_{gII} \quad (2)$$

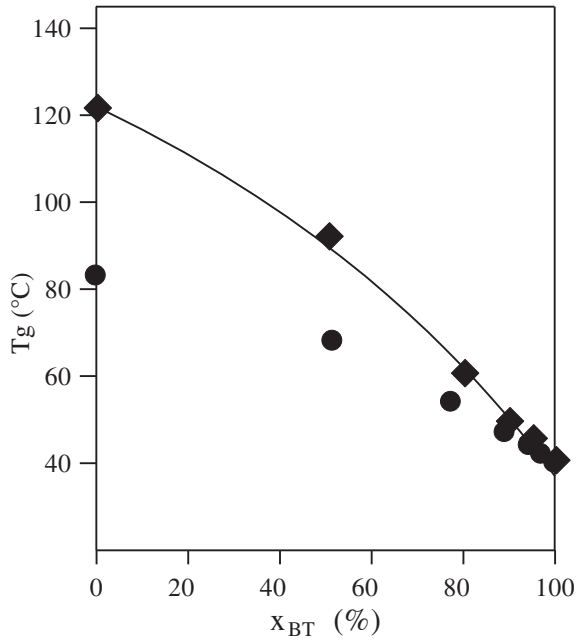

Fig. 11. Composition dependence of T_g for (◆) PBT/BHEBST and (●) PBT/BHEEBT (from ref. 5) random copolymers; theoretical curve of T_g *vs.* composition calculated on the basis of Fox equation.

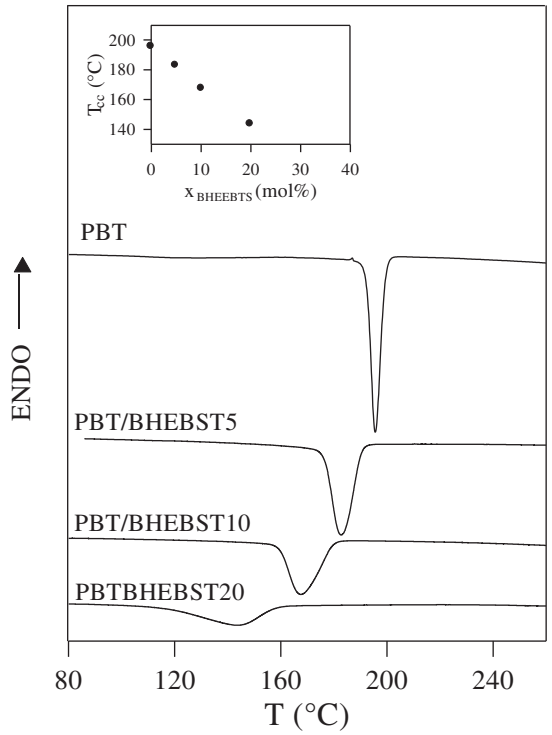

Fig. 12. DSC crystallization exotherms of PBT and PBT/BHEBST random copolymers cooled from the melt at 10 °C/min. In the inset: T_{cc} as a function BHEBST unit content.

where T_{gI} and T_{gII} are the glass transition temperatures of the pure homopolymers and w_I and w_{II} the respective weight fractions. As shown in Fig. 11, the Fox equation accurately fits the experimental data, using for PBHEBST the glass transition temperature experimentally measured by us, and fixing for PBT the value of 37 °C reported in the literature [23]. Its applicability can be considered an evidence of the random nature of the copolymers under investigation.

Lastly, in order to get preliminary results on the effect of composition on the crystallization rate of PBT, non-isothermal experiments were carried out, subjecting the samples to the thermal treatment described in the Experimental Section. It is worth remembering that the half-time of primary crystallization in isothermal experiments correlates with the temperature corresponding to the maximum of the crystallization peak in non-isothermal experiments (T_{cc}) [26], being this latter more easily obtainable. The exothermic crystallization peaks of the samples under investigation are reported in Fig. 12, with the exception of pure PBHEBST and PBT/BHEBST50 copolymer, these samples being not able to crystallize even though cooled from the melt at very low rate (1 °C/min). From the inset, where the T_{cc} values are reported as a function of composition, it can be observed that the temperature corresponding to the maximum of the exothermal crystallization peak regularly decrease as the BHEBST unit content is increased.

This trend indicates a decrement of the overall crystallization rate of PBT, due to the presence of the co-units (BHEBST), which act as obstacles in the regular packing of polymer chains. This behavior can be explained taking into account that the presence of bisphenol S groups increases the difficulty of close packing to form a crystalline array.

4. Conclusions

Our research showed that the insertion of bisphenol S units inside terephthalate polyesters backbone provides an efficient route to vary in a proper way the thermal properties. Copolymer composition turns out to be an important parameter in determining the characteristics of the samples under investigation.

In particular, such a chemical modification induces:

- a significant increase of the thermal stability, which widens the processability window;
- a decrease of the melting temperature, due to a limit to the lamellar thickness as a result of the presence of BHEBST chain segments. In fact, in the presence of these ones, the envisaged mode of chain attachment does affect the driving force term as well as the barrier, preventing the formation of very thick crystallites;
- a significant increase of the glass transition temperature, which in some copolymers exceeds 100 °C value;
- a decrease of the crystallization rate, due to the rejection of the stiff BHEBST co-units in the amorphous phase.

References

[1] Pilati F. Polyesters. In: Allen G, editor. Comprehensive polymer science, vol. 5. Oxford: Pergamon Press; 1989. Chapter 17.
[2] Freitag D, Fengler G, Morbitzer L. Angew Chem 1991;30:1598–610.
[3] Xiao C, Yee AF. Macromolecules 1992;25:6800–9.
[4] Berti C, Colonna M, Fiorini M, Lorenzetti C, Marchese P. Macromol Mat Eng 2004;289(1):49–55.
[5] Munari A, Finelli L, Lotti N, Berti C, Colonna M, Lorenzetti C. Polymer 2003;44 (5):1409–20.
[6] Jansen MAG, Goossens JGP, De Wit G, Bailly C, Koning CE. Macromolecules 2005;38(7):2659–64.
[7] Hait SB, Sivaram S. Polym Intl 1998;47:439–44.
[8] Oku A, Tanaka S, Hata S. Polymer 2000;41:6749–53.
[9] Hu LC, Oku A, Yamada E. J Appl Polym Sci 1997;63:595–601.
[10] Hu LC, Oku A, Yamada E. Polym J 1997;29:708–12.
[11] Hu LC, Oku A, Yamada E. Polymer 1998;39:3841–5.
[12] Turner RS. J Polym Sci 2004;42:5847–52.
[13] Turner RS, Sublett BJ. USPatent 6120889 2000.
[14] Banach TE, Berti C, Colonna M, Fiorini M, Marianucci E, Messori M, et al. Polymer 2001;42(18):7511–6.
[15] Montaudo G, Pugliesi C. In: Grassie N, editor. Developments in polymer degradation, vol. 7. London: Applied Science; 1987. p. 35.
[16] Garozzo D, Giuffrida M, Montaudo G. Macromolecules 1986;19:1643–9.
[17] Flory PJ. Trans Faraday Soc 1955;51:848–57.
[18] Baur H, Baltorowicz M. Makromol Chem 1966;98:297–301.
[19] Runt J, Miley DM, Zhang X, Kallagher KP, McFeaters K. Fishbum J Macromolecules 1992;25(7):1929–34.
[20] Huo PP, Cebe P. Macromolecules 1993;26(12):3127–30.
[21] Righetti MC. Munari A Macromol Chem Phys 1997;198(2):363–78.
[22] Boyer RF. Rub Chem Tech 1963;36(5):1303–421.
[23] Bicerano J. Prediction of polymer properties. New York: Marcel Dekker; 1996.
[24] Eisenberg A. Physical properties of polymers. Washington: ACS; 1984.
[25] Fox G. Bull Am Phys Soc 1956;1:123.
[26] Legras R, Dekoninck JM, Vanzieleghem A, Mercier JP, Nield E. Polymer 1986;27(1):109–17.

Polymer 52 (2011) 912–920

Contents lists available at ScienceDirect

Polymer

journal homepage: www.elsevier.com/locate/polymer

Polymer grafted silver and copper nanoparticles with exceptional stability against aggregation by a high yield one-pot synthesis

Stefan Bokern, Julia Getze, Seema Agarwal, Andreas Greiner*

Philipps-Universität Marburg, Department of Chemistry and Scientific Center of Materials Science, Hans-Meerwein-Strasse, Marburg D-35032, Germany

ARTICLE INFO

Article history:
Received 21 October 2010
Received in revised form
12 December 2010
Accepted 13 December 2010
Available online 5 January 2011

Keywords:
Nanoparticles
Functionalization
Polystyrene

ABSTRACT

A straightforward synthesis of silver nanoparticles (mean diameters well below 4 nm) with a "graft-to" polystyrene shell (PS@Ag) is described and different synthesis routes are compared. In addition to standard methods like TEM, XRD, UV/Vis and DSC the hybrid material has also been characterized by gel permeation chromatography (GPC).

Long-term stable hybrid materials with silver contents up to 18 wt-% have been realized. The exceptional stability allows industrial-scale processing by melt extrusion. No aggregation or agglomeration of silver nanoparticles is observed after melt co-extrusion with conventional polystyrene at 190 °C. The co-extruded blends with silver nanoparticle contents up to 1 wt-% show a homogenous dispersion of nanoparticles in the polystyrene matrix. The synthesis route has also been applied to PS-block-PMMA stabilized silver nanoparticles and to copper to yield polystyrene-stabilized copper nanoparticles with diameters well below 3 nm.

1. Introduction

Nanoparticles have gained significant interest in fundamental research as well as in technical applications. One important class of nanoparticles is metal nanoparticles, which have been utilized for numerous applications, eg. in the field of catalysis [1–5], for optical modulations [6–9] and for antibacterial coatings [10,11]. Due to their immense surface energy, metal nanoparticles have a strong inherent tendency to aggregate and agglomerate. This limits most industrial applications of nanoparticles especially in catalysis, due to the surface dependency of chemisorption [12].

Most strategies of aggregation prevention are based on fixation on surfaces [13], in a matrix [14] or by functionalization with a surfactant. A wide array of surfactants has been realized, e.g. small organic molecules like citrates [15], mercaptanes [16] and phosphines [17] or large surfactants like polymers [18–21].

Grafting of metal nanoparticles with a polymer can be realized by "grafting from" or "grafting to" methods. "Grafting from" methods can be accomplished by functionalizing a metal nanoparticle with polymerization initiators, e.g. to coat gold nanoparticles with a PMMA shell by surface-initiated ATRP [22]. "Grafting to" can be accomplished by end group or chain functionalization of polymers with a group which tends to bind to the nanoparticles surface, e.g. a thiol end group [20] or poly-4-vinylpyridine-blocks to stabilize gold nanoparticles [21]. A particular grafting of gold nanoparticles was accomplished recently by immobilization of thiol-functionalized vinyl monomers on a gold nanoparticle surface followed by radical polymerization of immobilized vinyl monomers. This results in polymer-coated gold nanoparticles carrying a single chemical functionality introduced with the initiator [23]. However, scaling up of this approach is still a challenge.

We wondered whether polymer-compatible metal nanoparticles like silver nanoparticles could be prepared by a straightforward approach in large scale for standard polymer processing techniques like melt extrusion. As a result consideration of theses we present a highly versatile approach to polymer-coated silver and copper nanoparticles by synthesizing thiolate-terminated polymers by anionic polymerization (eg. polystyrene) followed by in situ reduction of the corresponding metal salts. The resulting materials show exceptional stability of the contained metal nanoparticles in dispersion as well as in polymer melt. This allows processing of polymer/metal nanoparticle hybrid materials by industrial-scale methods like melt extrusion or solvent casting and thereby novel applications of metal nanoparticles.

2. Experimental section

2.1. Materials

Tetrahydrofuran (THF, BASF) has been purified by distillation over sodium/molecular sieve (Solvona®) and benzophenone and

* Corresponding author. Tel.: +49 6421 28 25573; fax: +49 6421 28 25785.
E-mail address: greiner@staff.uni-marburg.de (A. Greiner).

0032-3861/$ – see front matter © 2011 Elsevier Ltd. All rights reserved.
doi:10.1016/j.polymer.2010.12.031

stored under argon. Other solvents have been purified by distillation. Styrene (BASF) and methyl methacrylate (MMA, BASF) have been purified by distillation over calcium hydride and stored at −20 °C under argon. Argon (99.999%, AIR LIQUIDE), ethylene sulfide (98%, ALDRICH), silver trifluoroacetate (98%, ACROS), copper(II) acetylacetonate (98%, ACROS), *sec*-butyllithium (*sec*-BuLi, 1.4 mol/l in cyclohexane, ALDRICH), 1,1-diphenylethylene (DPE, 99%, ACROS), hydrazine (1 mol/l in THF, ALDRICH), Superhydride® (triethylboron hydride, 1 mol/l in THF, ALDRICH), trifluoroacetic acid (99%, ACROS) and polystyrene (type 144 C, $M_n = 10^5$ g/mol, BASF) have been used as received.

2.2. Instrumentation

The number–average molecular weights (M_n) and the weight–average molecular weights (M_w) of pure polymers were determined by gel permeation chromatography (GPC) using a Knauer system equipped with a PSS–SDV (10 μm) 50 × 8 mm² column and two columns 600 × 8 mm² at 25 °C, a differential refractive index detector, and a UV photometer using THF as eluent at a flow rate of 0.8 ml/min and linear polystyrene (PSS) as standard. The number–average molecular weights (M_n) and the weight–average molecular weights (M_w) of the nanoparticles/polymer hybrid materials were determined by gel permeation chromatography (GPC) using a Knauer system equipped with a 50 × 8 mm² precolumn, three linear 10 μm SDV columns 300 × 8 mm² at 25 °C, a differential refractive index detector, and a UV photometer measuring at 400 nm (selective for plasmon resonance absorption of silver) using DMF as eluent at a flow rate of 0.6 ml/min and linear polystyrene (PSS) as standard. For the diode array detector measurements, this system was extended with an HP Diode Array Detector model 1040 measuring between 261 and 600 nm between the UV and RI detector with a flow rate of 1 ml/min ^{1}H (300.13 MHz) and ^{13}C (75.47 MHz) NMR spectra were recorded on Bruker Avance 300 A and Avance 300 B spectrometers, respectively, using $CDCl_3$ as solvent.

Mettler thermal analyzers having 851 TG and 821 DSC modules were utilized for the thermal characterization of the polymers. Indium and zinc standards were used for temperature and enthalpy calibration of the 821 DSC module. Differential scanning calorimetric (DSC) scans were recorded in nitrogen atmosphere (flowrate 80 ml/min) at a heating rate of 10 °C/min between 25 and 150 °C. The glass transition temperature (T_g) was taken as the inflection point of the observed shift in the baseline of the second heating cycle of a DSC scan. Thermal stability was determined by recording thermogravimetric (TG) traces in nitrogen atmosphere (flow rate 50 mL/min) using powdered samples. A heating rate of 10 °C/min and a sample size of 8 ± 2 mg were used in each experiment.

The TEM measurements have been done on a JEM 3010 by JEOL. A LaB_6-crystal has been used as a cathode at a voltage of 300 kV. Pictures have been taken with a 4 megapixel CCD camera at magnifications of 200 000–250 000 for normal measurements and 1.2–1.5 mio for high-resolution TEM (HR–TEM) measurements. Samples have been prepared from very dilute chloroform dispersion by dip-coating a Quantifoil 300 mesh copper grid with graphite coating. For size calculation the software ImageJ (version 1.40 g) of the National Institute of Health, USA, has been used. The mean particle diameter was calculated from at least 120 particles/sample.

A Perkin–Elmer Lambda 9 UV/Vis/NIR spectrophotometer was used for UV/Vis absorption spectroscopy. The concentration of the samples was between 0.5 and 1.5 g/l, the cuvette length was 0.5 cm.

For XRD a Siemens Diffractometer D50 has been used. Polymer films have been fixated on a silicon carrier and a step length of $2\theta = 0.05°$ has been used. The radiation source was Cu–K_α radiation with a wavelength of 154 pm.

FT–IR spectra have been done with the Digilab Excalibur Series. The samples in powder form were put on an ATR unit MIRacle of the company Pike Technology. As software WinIRPro Version 3.3 from Digilab has been used.

2.3. Synthesis of macroinitiator

A dry Schlenk tube equipped with a magnetic stir bar was charged with 6.1 ml of *sec*-BuLi (1.4 mol/l in cyclohexane, 8.5 mmol) and 10 ml cyclohexane. The mixture was heated to 40 °C. Styrene (2.0 ml, 17 mmol) was added slowly. After 20 min the deep-red viscous solution has been cooled to room temperature and stored at −20 °C.

2.3.1. Synthesis of thiolate/thiol-functionalized polystyrene (PS–SH)

As a general procedure the synthesis and characterization of the sample PS_{4400} (M_n = 4400) is described. A dry Schlenk flask equipped with a magnetic stir bar was charged with 250 ml of dry THF and warmed to 25 °C. The macroinitiator solution was added dropwise to remove traces of water until a stable deep-red colour developed. Another 27.2 ml of macroinitiator solution (3.6 mmol) was added. After 5 min styrene (14.2 g, 136 mmol) has been added. After 10 min ethylene sulfide has been added dropwise to the deep-red solution until the colour of the solution changed to a pale yellow. The solution has been stored at 4 °C.

When using *sec*-BuLi instead of the macroinitiator, THF is cooled to −78 °C before and during the reaction. After quenching of water traces a stable yellow colour developed and the desired amount of initiator was added. Otherwise the procedure was not changed.

For characterization, part of the solution has been precipitated as thiol-functionalized polystyrene in hydrochloric acid/methanol (1:10), washed with methanol and water and dried in vacuum at 60 °C overnight. Yield: 13.5 g (95%), M_n = 4400, M_w = 5830, M_w/M_n = 1.33, T_g = 73 °C, TGA: $T_{5\%}$ = 348 °C, ^{1}H NMR (300 MHz, $CDCl_3$), δ/ppm = 7.40–7.08 (m, 3H, br, PS, C_6H_5), 6.95–6.60 (m, 2H, br, PS, C_6H_5), 2.64 (0.05H, br, EtS) 2.50–1.32 (m, 3.1H, br, polymer backbone), 0.95–0.73 (m, 0.22H, br, *sec*-Butyl initiator fragment) ^{13}C NMR (75 MHz, $CDCl_3$), δ/ppm = 145.7 (br), 145.3 (br), 128.0 (br), 125.6 (br), 44.22 (br), 40.4, 31.5, 26.9, 11.2, 11.0, IR (υ/cm^{-1}): 3059 (m), 3025 (m), 2922, (s), 2368 (w), 2338 (w), 1943 (w), 1871 (w), 1802 (w), 1739 (w), 1655 (w), 1601 (s), 1543 (w), 1493 (s), 1447 (s), 1369 (m), 1323 (ww), 1181 (w), 1154 (w), 1069 (w), 1027 (m), 964 (w), 906 (m), 841 (w), 756 (s), 698 (ss), 622 (w), UV/Vis: λ_{max} = 260 nm.

2.3.2. Synthesis of polystyrene-stabilized silver nanoparticles (PS@Ag)

As a general procedure the synthesis and characterization of the sample $PS_{4400}Ag_{3.5}$ is described. A solution of thiolate-functionalized polystyrene in THF (sample PS_{4400}, 10 ml, M_n = 4400, M_w = 5830, 17.9 mmol/l, 179 μmol, 1 eq.) has been synthesized by the macroinitiator route as described above. A solution of silver trifluoroacetate in THF (20 ml, 31.1 mmol/l, 627 μmol, 3.5 eq.) has been added over 20 s under vigorous stirring. Immediately a deep-brown colour developed. After 30 min the product has been precipitated in 300 ml of methanol, washed with water and methanol and dried overnight at 60 °C in vacuum. The product was isolated as a deep-brown fine powder in quantitative yields in respect to the polymer.

GPC: UV/Vis-Detector (400 nm): M_n = 53600, M_w = 55200, M_w/M_n = 1.03, bimodal, (PS@Ag); RI–Detector: M_n = 55470, M_w = 57100, M_w/M_n = 1.03, bimodal (PS@Ag); M_n = 4400, M_w = 5830 M_w/M_n = 1.3, monomodal (PS–SH). T_g = 87 °C, TGA: $T_{5\%}$ = 369 °C, $m_{residue}$ = 12%. ^{1}H NMR (300 MHz, $CDCl_3$), δ/ppm = 7.40–7.08 (m, 3.0H, br, PS), 6.95–6.60 (m, 2.0H, br, PS), 2.46–0.79 (m, 3.3H, br, EtS, PS) 0.73 (m, 0.3H, br, *s*-Bu) ^{13}C NMR (75 MHz, $CDCl_3$): δ/ppm = 145.7

(br), 145.3 (br), 128.0 (br), 125.6 (br), 44.22 (br), 40.4, 31.5, 30.9, 11.2, 11.1 IR: 3060 (m), 3026 (m), 2923 (s), 2849 (m), 2364 (w), 2338 (w), 1943 (w), 1870 (w), 1802 (w), 1735 (w), 1655 (w), 1601 (s), 1542 (ww), 1493 (s), 1450 (s), 1374 (m), 1312 (ww), 1191 (w), 1181 (w), 1154 (w), 1069 (w), 1028 (m), 964 (w), 906 (m), 841 (w), 756 (s), 698 (ss), 621 (w), UV/Vis: λ_{max} = 260 nm (PS), 431 nm (Ag plasmon resonance absorption), TEM: spherical silver nanoparticles, mean diameter 2.3 ± 0.7 nm.

2.3.3. Synthesis of polystyrene-stabilized silver nanoparticles by superhydride reduction

The synthesis of the sample $rPS_{4900}Ag_8$ is described. A solution of thiolate-functionalized polystyrene in THF (sample PS_{4900}, 20 ml, M_n = 4900, M_w = 6220, 13.0 mmol/l, 260 μmol, 1 eq.) was synthesized as described previously. Trifluoroacetic acid (50 μl, 0.7 mmol, 2.7 eq.) was added, followed by addition of a solution of silver trifluoroacetate in THF (8 ml, 0.25 mol/l, 2 mmol, 8 eq.) over 20 s. Superhydride (1 mol/l in THF, 3 ml, 3 mmol, 11 eq.) was added dropwise over 20 s under vigorous stirring, immediately a deep-brown colour developed. After 30 min the product has been precipitated in 300 ml of methanol, washed with water and methanol and dried overnight at 60 °C in vacuum. The product was isolated as a deep-brown fine powder in quantitative yield.

GPC: UV/Vis-Detector (400 nm): M_n = 175900, M_w = 176300, M_w/M_n = 1.00, monomodal, (PS@Ag); RI-Detector:M_n = 175900, M_w = 176300, M_w/M_n = 1.00, monomodal (PS@Ag); M_n = 4900, M_w = 6220 M_w/M_n = 1.27, monomodal (PS–SH), UV/Vis: $\lambda_{max\ absorption}$ = 259 nm, 446 nm. TEM: spherical silver nanoparticles, mean diameter 1.7 ± 0.5 nm.

2.3.4. Synthesis of thiolate-terminated PMMA-PS-blockcopolymer (PS-PMMA-SH)

A dry Schlenk flask equipped with a magnetic stir bar was charged with 20 ml of dry THF and warmed to 25 °C. The macroinitiator solution was added dropwise to remove traces of water until a stable deep-red colour developed. Another 0.65 ml of macroinitiator (0.10 mmol) solution was added. After 5 min styrene (3.4 ml, 29 mmol, 290 eq.) has been added quickly. After further 5 min 1,1-diphenylethelene (90 mg, 0.5 mmol, 5 eq.) has been added dropwise. After further 5 min methyl methacrylate (0.49 ml, 4.6 mmol, 46 eq.) has been added quickly. After 10 min ethylene sulfide (12 mg, 0.2 mmol, 2 eq.) has been added dropwise to the solution.

For analysis, part of the solution has been precipitated as thiol-functionalized polymer in hydrochloric acid/methanol (1:10), washed with methanol and water and dried in vacuum at 60 °C overnight. Yield: 3.2 g (93%), GPC: M_n = 35940, M_w = 52170, M_w/M_n = 1.45, ^{1}H NMR (300 MHz, $CDCl_3$), δ/ppm = 7.26–6.89 (m, 3H, br, PS), 6.89–6.22 (m, 2H, br, PS), 3.65 (s, 0.34H, br, PMMA), 2.58–0.59 (m, 3.7H, br, PS, PMMA) ^{13}C NMR (75 MHz, $CDCl_3$), δ/ppm = 145.3 (br), 145.2 (br), 128.3, 128.0, 127.9, 127.6 (br), 127.4, 127.3, 125.6 (br), 125.5, 51.8, 44.5 (br), 43.9 (br), 40.6, 40.4, 40.3

Block length calculated from ^{1}H NMR and GPC, Polymerization degrees P_n: P_n(Styrene) = 306, P_n(MMA) = 41.

2.3.5. Synthesis of silver nanoparticles stabilized by thiolate-terminated PS-block-PMMA (PS-PMMA@Ag)

To the synthesized solution of the PS-block-PMMA-thiolate described previously, a solution of silver trifluoroacetate in THF (c = 35 mmol/l, 10 ml, 350 μmol 1.1 eq.) has been added. Immediately a deep-brown colour developed. The product has been precipitated in 300 ml methanol, washed with water and methanol and dried overnight at 60 °C in vacuum. The product was isolated as a deep-brown fine powder.

Yield: 3.03 g (85%), UV/Vis: λ_{max} = 260 nm, 426 nm. TEM: spherical silver nanoparticles, mean diameter = 4.3 nm ± 1.5 nm.

2.3.6. Synthesis of polystyrene-stabilized copper nanoparticles (PS@Cu)

A solution of thiolate-functionalized polystyrene PS_{4400} in THF (10 ml, M_n = 4400, M_w = 5830, 11.1 mmol/l, 111 μmol, 1 eq.) has been synthesized as described above. Copper(II)-acetylacetonate in THF (10 ml, 27.0 mmol/l, 270 μmol, 2.47 eq) has been added. A solution of hydrazine in THF (1 ml, 1 mol/l, 1 mmol, 9.4 eq) has been added dropwise over 10 min. The precipitating white side product has been removed by filtration. The clear greenish solution has been added to a tenfold excess of methanol, the product PS@Cu precipitated as colourless flakes and has been filtered off, washed with water and methanol and dried overnight in vacuum at 60 °C. Yield: 263 mg (52%), UV/Vis: λ_{max} = 252 nm, 310 nm. TEM: Spherical copper nanoparticles mean diameter 2.2 nm ± 0.7 nm.

3. Results and discussion

Anionic polymerization of styrene in THF has been initiated by a macroinitiator at room temperature, followed by quenching with ethylene sulfide to yield a thiolate-terminated polystyrene. Unlike the direct initiation with *sec*-BuLi, the macroinitiator route allowed anionic polymerization of styrene at room temperature without initiator decay, which is convenient for bigger batches or online synthesis. Using the macroinitiator route, thiol-terminated polystyrene has been isolated in near-quantitative yields with molecular weights between 4.000 and 12.000 and polydispersities generally below 1.4. Using *sec*-BuLi as initiator at −78 °C, functionalized polymers with molecular weights between 530 and 91.000 with polydispersities generally below 1.3 have been isolated in quantitative yields. A 1:1 ratio between *sec*-BuLi and ethylene sulfide end groups [24] has been found in all cases in the ^{1}H NMR spectra, as shown in Fig. 1. In the shown example PS_{4400}, a molecular weight of 4500 has been calculated by end group determination. This is a close match to the GPC measurement of M_n = 4400. This shows that every polymer chain contains exactly one thiol end group and no poly(ethylene sulfide) block has been synthesized.

Immediately upon addition of a solution of silver trifluoroacetate in THF, a deep-brown colour developed, characteristic for silver nanoparticles. Due to the low initiator efficiency of the macroinitiator of about 35%, it can be concluded that unreacted *sec*-BuLi decomposes quickly in the macroinitiator synthesis step to lithium hydride, which is able to reduce silver cations to silver after the polymerization step [25]. The formed silver nanoparticles are stabilized by the thiolate-terminated polystyrene via coordination of the thiolate group to the silver nanoparticle surface (Fig. 2). Direct initiation with *sec*-BuLi does not lead to this spontaneous

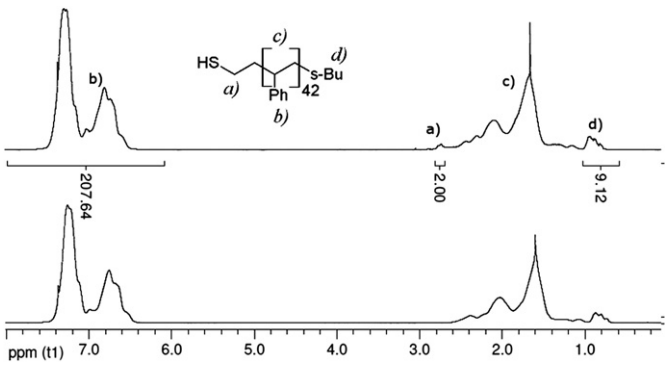

Fig. 1. ^{1}H-NMR spectra of polystyrene with methanol quenching (lower spectrum) and with ethylene sulfide quenching (upper spectrum, sample PS4400). The spectra are identical except for the signal at d = 2.8 ppm marked with a) [24].

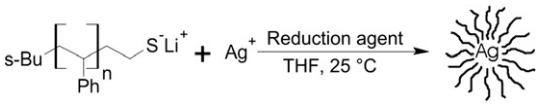

Fig. 2. Synthesis of polystyrene-stabilized silver nanoparticles PS@Ag via in situ reduction of silver trifluoroacetate in THF.

formation of nanoparticles. Unfunctionalized polystyrene leads to bulk silver formation.

The polystyrene-stabilized silver nanoparticles (PS@Ag) can undergo common polymer workup by precipitation. The resulting deep-brown material is fully redispersible in organic solvents and reprecipitable without apparent limit. Aggregation or agglomeration of particles was not observed in chloroform, dichlormethane, pyridine, acetone, toluene, DMF, MTBE or peroxide-free THF.

In XRD, a broadened Ag(111) reflex at $2\theta = 38°$ was observable in addition to the amorphous halo of polystyrene (Fig. 3). The nanoparticle diameter calculated by the Scherrer equation in this sample $PS_{4400}Ag_{3.5}$ is 2.5 nm [26]. In TEM (Fig. 4), the same sample showed particles with a mean diameter of 2.3 nm, in close agreement with the XRD measurement. The HR–TEM picture showed lattice distances of around 240 pm, close to the literature value of 233 pm for Ag(111) [27]. A significant dependency of the mean particle diameter on mixing speed, reaction time, repeating redispersion/reprecipitation cycles or polystyrene chain length has not been observed in any sample.

The UV/Vis spectrum of PS@Ag (Fig. 5) showed absorptions of both polystyrene and silver nanoparticles [8].

A sample run with different amounts of silver salt in the synthesis is shown in Table 1. The absorption strength of a single nanoparticle does not change significantly in the observed size region, so the maximum absorption of PS@Ag is nearly proportional to the number of silver nanoparticles. Using this method, it has been found that a molar ratio of silver salt to polymer between 2 and 3 in the feed is ideal for a maximal amount of unaggregated nanoparticles. Less silver, e.g. exactly one equivalent, does not lead to the formation of nanoparticles. This is caused by the concentration dependency of the redox reaction between the reduction agent and silver cations. More silver salt than 4 equivalents generally lead to formation of deformed particles and aggregates. The example $PS_{4900}Ag_8$ with an eightfold molar excess of silver is shown in Fig. 6. At higher amounts of silver salt, more thiolates are bound as silver(I) complexes, leaving less to stabilize forming

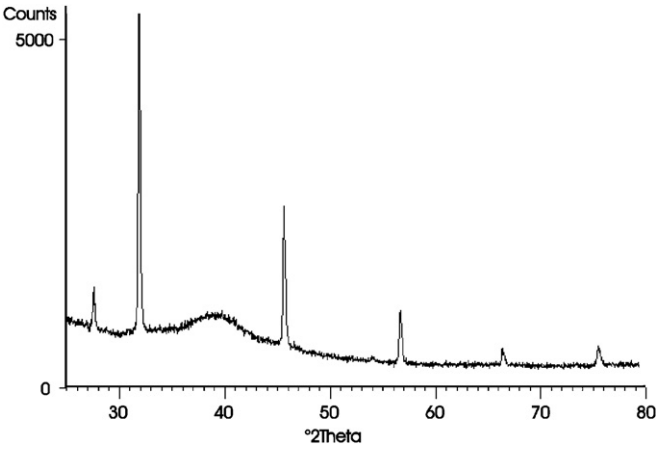

Fig. 3. XRD of PS@Ag, sample $PS_{4400}Ag_{3.5}$. Sharp signals are due to the NaCl standard needed for Scherrer calculation. The PS halo is visible on the left side, the Ag nanoparticle reflex is shown between $2\theta = 37°$ and 42°.

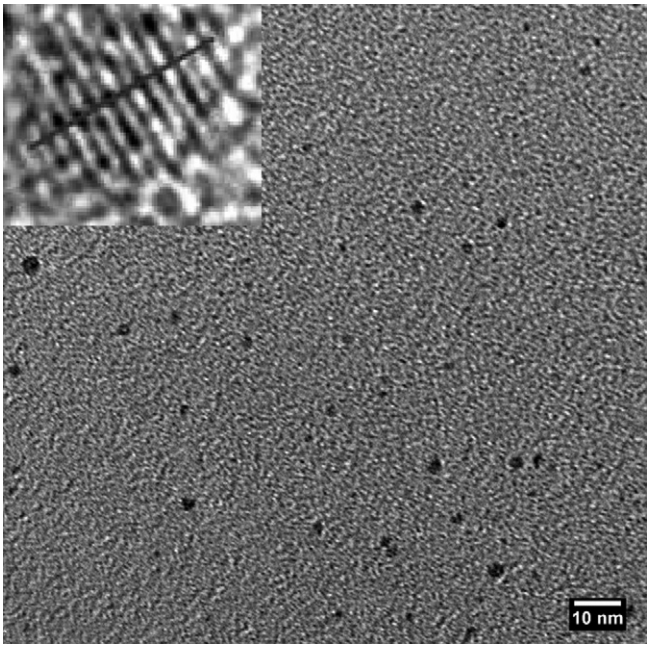

Fig. 4. TEM and HR-TEM of PS@Ag, sample $PS_{4400}Ag_{3.5}$, from chloroform dispersion. HR-TEM (left corner) shows lattices of a single silver nanoparticle. The line marks 2.70 nm, the lattice distance here is roughly 240 pm.

nanoparticles against aggregation. The aggregation of nanoparticles is known to quench the plasmon resonance absorption, [28] this is also seen here. Generally, higher silver ratios also lead to formation of bigger particles and with much higher dispersities, but in all cases a mean particle diameter well below 4 nm has been realized. Still, even under optimized conditions a complete reduction of the silver salt is not possible using the macroinitiator route due to the limited amount of reduction agent in this system, leading to a molar ratio of about 55(Ag):45(Polymer) at best in the composite material, determined by EDX measurements.

With an additional homogenous reducing agent like Superhydride, higher concentrations of silver nanoparticles can be

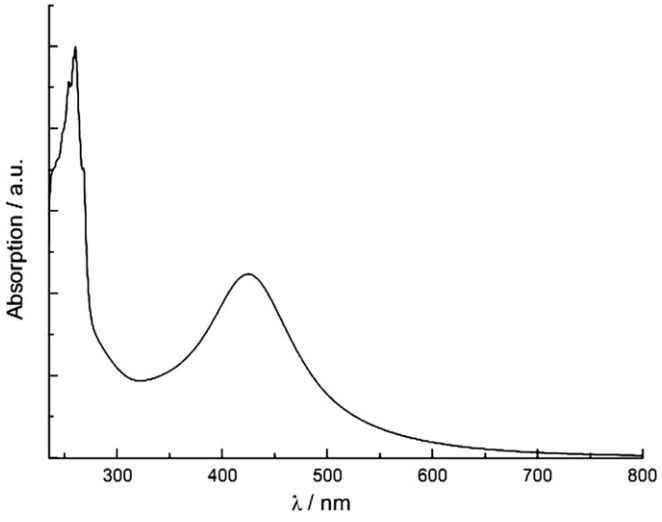

Fig. 5. UV/Vis spectrum of PS@Ag, sample $PS_{4400}Ag_{3.5}$, redispersed in chloroform. The absorption maximum at 265 nm is characteristic for polystyrene, the absorption maximum at 430 nm is characteristic for the plasmon resonance absorption of silver nanoparticles.

Table 1
Samples of PS@Ag synthesized without additional reduction agent. Ag:PS describes the molar ratio of silver salt to thiolate-functionalized polystyrene during particle synthesis. The same thiolate-functionalized polymer with M_n = 4900 and M_w = 6220 (PS_{4900}) has been used for all samples. ϵ_{max} describes the maximum absorption of the plasmon resonance between 410 and 430 nm relative to sample $PS_{4900}Ag_{1.5}$.

Sample	Ag:PS ratio	d_{Ag}/nm	ϵ_{max}
$PS_{4900}Ag_1$	1.0	–	0
$PS_{4900}Ag_{1.5}$	1.5	2.9 ± 1.6	1
$PS_{4900}Ag_2$	2	2.3 ± 1.6	3.2
$PS_{4900}Ag_{2.6}$	2.6	3.1 ± 2.5	7.8
$PS_{4900}Ag_4$	4	3.4 ± 2.8	15.2
$PS_{4900}Ag_6$	6	3.1 ± 2.0[a]	13.2
$PS_{4900}Ag_8$	8	3.8 ± 2.2[a]	10.2

[a] Heavy aggregation and deformation of nanoparticles observable in TEM.

realized. A similar route has been used to yield octadecanethiol-stabilized platinum nanoparticles and polymer-stabilized gold nanoparticles [29,30].

It was found that even with an eightfold excess of silver salt, stable and well dispersed silver nanoparticles were formed, except in samples with very small polystyrene chains ($rPS_{530}Ag_8$) due to their limited ability to stabilize nanoparticles sterically. The mean particle diameter was generally slightly lower than in the samples synthesized without Superhydride, between 1.7 and 2.5 nm, with low dispersities (Table 2). The small size is explained by the very fast nanoparticle nucleation caused by Superhydride due to its very high reduction strength [31]. When comparing two samples with identical PS chain length and identical amount of silver salt synthesized by the macroinitiator route (sample $PS_{4900}Ag_8$) and by the Superhydride route (sample $rPS_{4900}Ag_8$) a tenfold increase in the strength of the plasmon resonance absorption has been observed. This indicates a drastic increase in the concentration of nonaggregated silver nanoparticles. This is also seen in the TEM pictures, although because of the low particle size and the electron-scattering polymer matrix the nanoparticles are hard to distinguish from the background noise (Fig. 7). No residue silver salts were found after the reaction, ensuring complete conversion of the used silver salt to silver nanoparticles, in agreement with the silver content determined by TGA measurement.

Table 2
Samples of PS@Ag synthesized by Superhydride reduction. Ag:PS describes the molar ratio between silver salt and thiolate. M_{Ag} describes the molecular weight of the silver-containing GPC signal. Free PS describes the GPC RI signal of unbound PS-SH vs. total RI signal.

Sample	M_n PS	Ag:PS	d_{Ag}/nm	M_{Ag}	Free PS/%	T_g/°C
$rPS_{530}Ag_0$	530	0	–	–	100	59
$rPS_{530}Ag_8$	530	8	2[a]	9.8e4	46	66
$rPS_{4900}Ag_0$	4900	0	–	–	100	83
$rPS_{4900}Ag_1$	4900	1	1.6 ± 1.1	–	–	89
$rPS_{4900}Ag_8$	4900	8	1.7 ± 0.5	1.8e5	53	92
$rPS_{5350}Ag_0$–1[b]	5350	0	–	–	100	87
$rPS_{5350}Ag_0$–2[c]	5350	0	–	–	100	86
$rPS_{5350}Ag_1$	5350	1	2.5 ± 0.8	1.7e6	73	91
$rPS_{5350}Ag_{2.6}$	5350	2.6	2.3 ± 0.6	2.0e6	69	94
$rPS_{5350}Ag_{3.5}$	5350	3.5	2.5 ± 0.7	1.9e6	55	96
$rPS_{5350}Ag_5$	5350	5	2.4 ± 0.9	7.5e5	40	94
$rPS_{5350}Ag_8$	5350	8	1.8 ± 0.8	9.8e5	62	94
$rPS_{5350}Ag_{12}$	5350	12	2.2 ± 0.7[d]	1.4e6	93	96
$rPS_{44190}Ag_0$	44190	0	–	–	100	101
$rPS_{44190}Ag_8$	44190	8	2.4 ± 0.6	3.0e6	80	102
$rPS_{91110}Ag_0$	91110	0	–	–	100	103
$rPS_{91110}Ag_8$	91110	8	2.1 ± 0.6	>4.0e6[e]	77	103

[a] 20% of particles with diameter > 30 nm.
[b] Acidic workup (PS-SH).
[c] Alkaline workup (PS-SLi).
[d] Heavy aggregation.
[e] Excess volume.

In addition to the standard characterization methods for nanoparticles we also employed methods which are normally used for polymers only, like GPC. Only few literature examples are known for GPC with metal nanoparticles, nearly exclusively in aqueous systems [32–34]. To the best of our knowledge there is only one example of GPC characterization of metal nanoparticles coated with a hydrophobic polymer in literature, but without selective detection of nanoparticles [35].

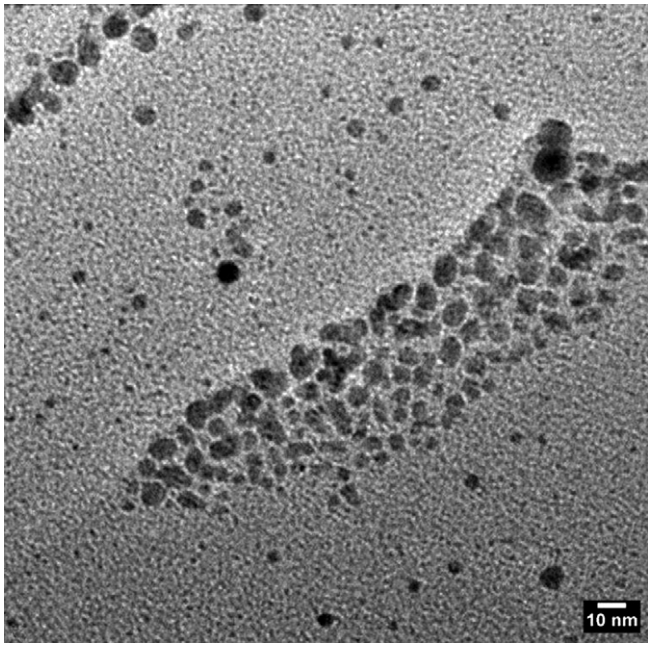

Fig. 6. Aggregation of strongly deformed silver nanoparticles due to a high amount of silver salt, molar r atio of Ag:PS = 8:1 (sample $PS_{4900}Ag_8$).

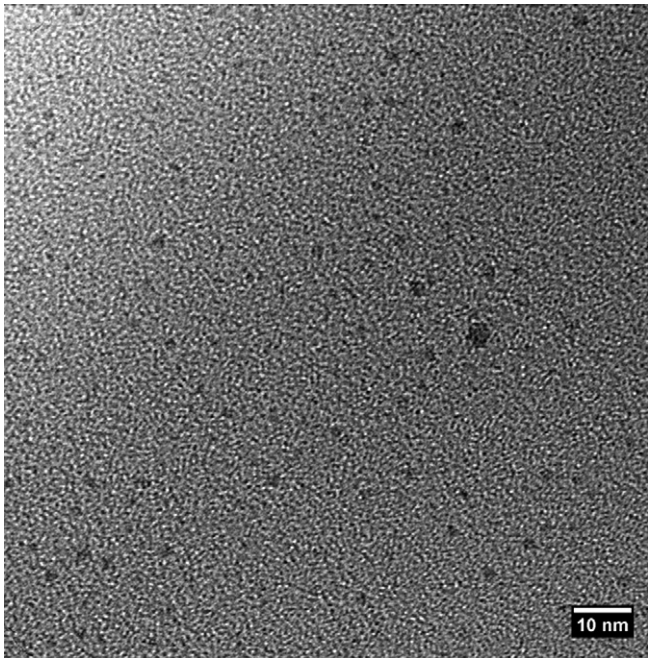

Fig. 7. TEM of PS@Ag, sample $rPS_{4900}Ag_8$ (Superhydride reduction), the particles are low-size, spherical and do not form aggregates.

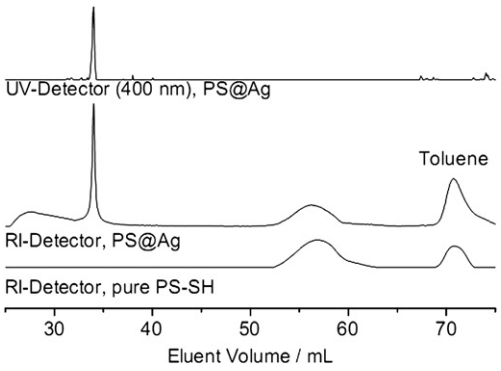

Fig. 8. GPC of sample $rPS_{5350}Ag_5$ in DMF (upper two elugrams) in comparison to the pure thiol-terminated PS_{5350} (lowest elugram). The signal at 56 ml belongs to end-functionalized PS_{5350} while the signal at 34 ml belongs to PS@Ag (M_p = 750.000), showing both an RI and a UV signal.

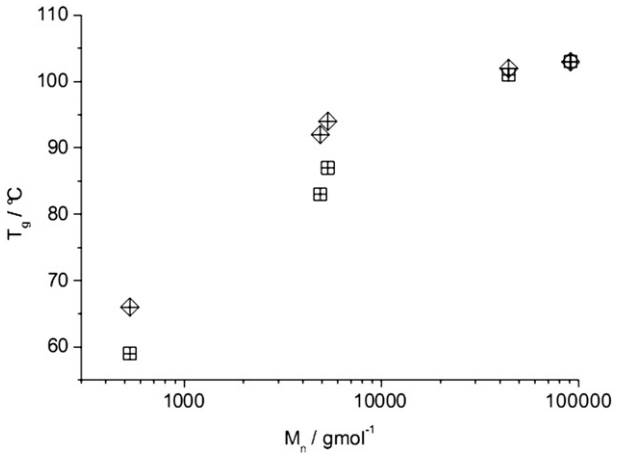

Fig. 10. Glass transition temperatures before (○) and after (○) addition of silver nanoparticles to thiolate-terminated polystyrene with different molecular weights (data from Table 2, Ag:PS = 8:1).

In Fig. 8 the results of a GPC measurement of the sample $rPS_{5350}Ag_5$ is shown. Using a UV-detector measuring at 400 nm, silver nanoparticles have been detected in a signal with a molecular weight of 750.000 relative to linear polystyrene.

The polydispersity of this nanoparticle-containing signal is surprisingly low in all samples, between 1.00 and 1.01. This can be explained by the coordination of multiple polydisperse polymer chains on a single silver nanoparticle, averaging the dispersity of the bound polymer chains. The molecular weight of this signal increases with the molecular weight of the polymer used (Table 2). This indicates that polystyrene is bound directly to the silver nanoparticles. There also appears to be a great amount of free polystyrene in all samples, which may result from the desorption of polystyrene, followed by coordination of DMF to the nanoparticles surface, which is known to be able to coordinate to silver nanoparticle surfaces [36]. This behaviour would also benefit from the low sample concentrations used in GPC due to the very large excess of DMF. It has also been found when increasing the PS chain length and keeping the excess of silver identical, the amount of free PS increases. This behaviour is in accordance with the assumption that larger PS chains are more readily able to protect silver nanoparticles sterically, so less PS chains are coordinated to silver nanoparticles. It has been found when increasing the amount of silver, the amount of free PS decreases (from 46% in $rPS_{530}Ag_8$ to 77% in $rPS_{91110}Ag_8$). It increases drastically again with very high amounts of silver when there are aggregates observable in TEM. The aggregates cannot elute due to their size, so they are not detected, shifting the observed amount of PS towards unbound PS.

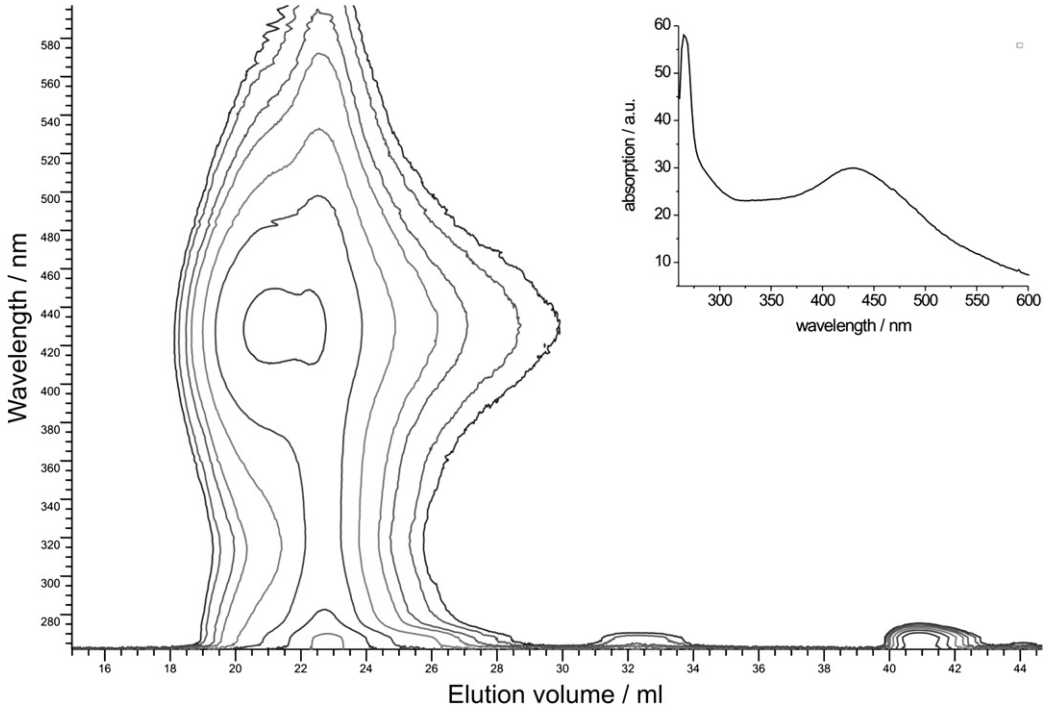

Fig. 9. GPC of sample $rPS_{5350}Ag_5$, DAD isoabsorbance plot. The *x*-axis shows the elution volume, the *y*-axis shows the wavelength. Identifiable compounds are toluene (42 ml), polystyrene (32 ml) and PS@Ag (27 ml). Upper right corner: Absorption spectrum of PS@Ag at an elution of 27 ml, showing a polystyrene absorption maximum at 265 nm and a silver nanoparticles absorption maximum at 440 nm. Due to a changed setup the signals are broader than in the setup used in Fig. 8.

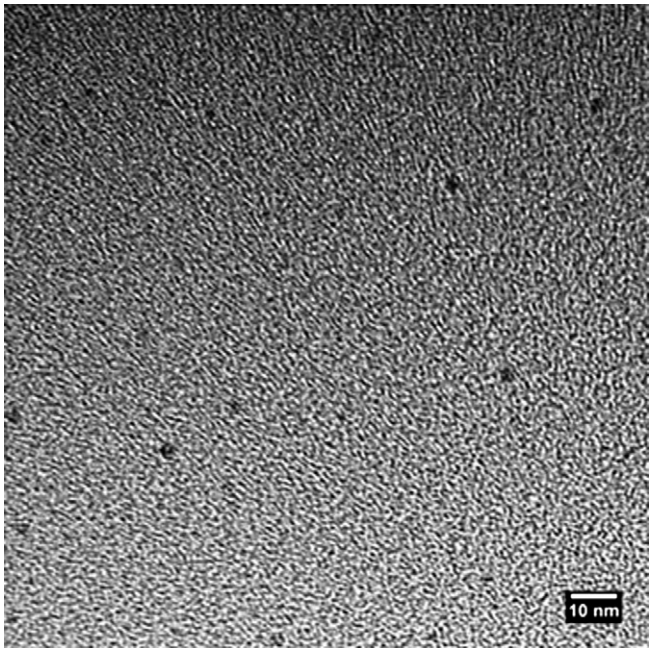

Fig. 11. TEM picture of a PS@Ag/PS blend after processing. This blend contains 0.1 wt.-% silver nanoparticles. The sample has been co-extruded with polystyrene at 190 °C and heat-pressed at 190 °C into a 25 × 25 × 0.3 cm plate. Part of this plate has been redispersed in chloroform for this TEM measurement.

Additional proof for the postulated structure is generated by using a diode array detector which can measure online UV/Vis spectra in combination with GPC. As expected, the sharp signal thought to be PS@Ag shows to have absorption of both polystyrene and silver nanoparticles (Fig. 9).

The measured molecular weight of PS@Ag is surprisingly high compared to the theoretically expected value, which can be estimated by taking graft densities of 0.6 chains/nm^2 from a comparable system of PS_{2000}@Au with a nanoparticles diameter of 4.4 nm [20]. This leads to an expected upper molecular weight of 23 200 for the shown example of $rPS_{5350}Ag_5$, far lower than the measured MW of 750 000. This shows that the measured molecular weight should not be taken as an absolute value due to effects not considered here. The PS@Ag should not behave like linear polystyrene standard but rather like hyperbranched or star-shaped polymers, falsifying the measured molecular weight. Interaction with the solvents may also be an explanation of the unexpected elution of the PS@Ag-nanoparticles. Without further research of the behaviour of polymer-stabilized nanoparticles in GPC, the measured molecular weights of PS@Ag can only be compared relative to each other, the absolute molecular weight differs too much from the theoretically expected value. Despite this, nanoparticles-selective size exclusion chromatography appears to be a powerful analysis method for polymer-stabilized nanoparticles, allowing the separate detection of free and bound polymer chains.

The dependency of the glass transition temperature on the amount of silver nanoparticles is also shown in Table 2. The glass transition temperature increases with the amount of silver nanoparticles, from 86 °C to 94–96 °C, but does not rise above this value. In Fig. 10 it is shown that the increase of T_g is stronger with low molecular weight polystyrene and not noticeable anymore at $M_n = 91110$ g/mol. This behaviour is in agreement with the theory that the glass transition temperature of a polymer-nanoparticle composite increases in comparison to the bulk material when there are attractive forces between nanoparticles and polymer matrix due to confinement effects [37]. For high molecular weight polystyrene this effect can be neglected.

The stability of PS@Ag against aggregation and agglomeration is very high in dispersion as well as melt state. In order to investigate this further we have studied blends of PS@Ag and PS. PS@Ag has been blended with conventional polystyrene by co-precipitation or co-extrusion in different ratios. Nanoparticle weight contents between 9 wt.-% and 0.01 wt.-% in the blends have been realized, but above 1 wt-% the blends become too brittle for processing. In all cases the resulting blend is completely homogenous, has a yellow to black colour (depending on silver content) and high transparency above 600 nm independent of silver content. No phase separation has been observed via TEM, digital microscope or scanning electron microscope (supporting information). In addition, all samples show mutual glass transition temperatures in all ratios, so the blend can be expected to be completely compatible. This shows that the grafted polystyrene chains act as very efficient mediators between the hydrophilic nanoparticles and the hydrophobic polymer.

It is notable that during co-extrusion, no aggregation or agglomeration has been observed after processing, even at 190 °C

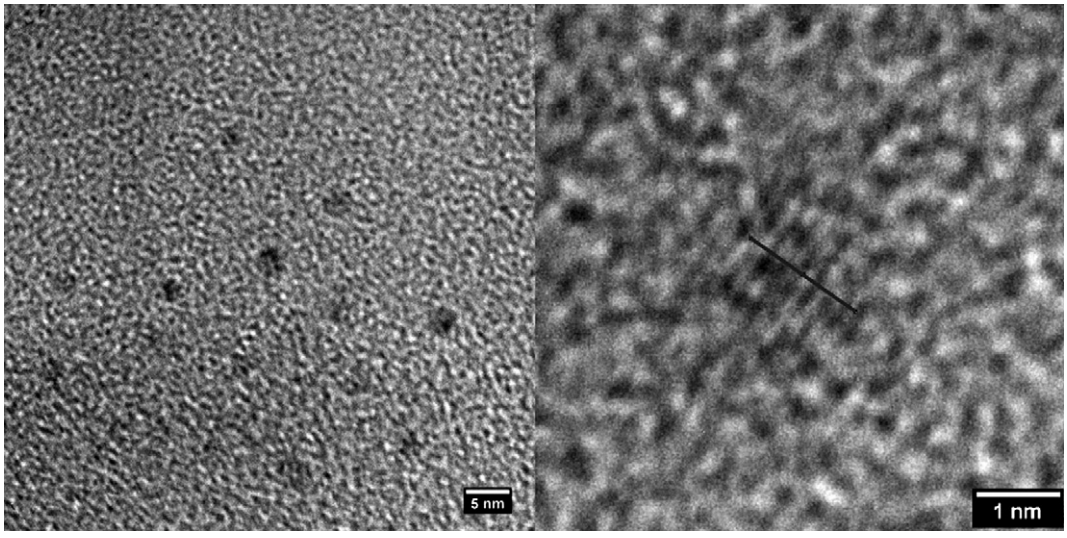

Fig. 12. TEM and HR-TEM pictures of synthesized polystyrene-stabilized copper nanoparticles. The line marks 1.49 nm.

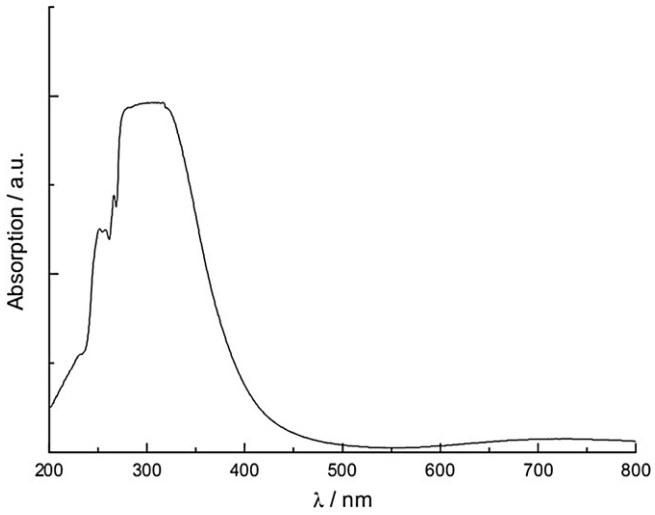

Fig. 13. UV/Vis spectrum of PS@Cu. The absorption maximum around 260 nm is due to polystyrene while the broad absorption with a maximum around 310 nm is due to copper nanoparticles.

as seen by TEM (Fig. 11). All silver nanoparticles show to be isolated from each other, no size or change in the absorption behaviour (UV/Vis) was observed. This ensures that PS@Ag can be processed without changes in chemistry or structure with industrial methods. The resulting material is completely redispersible. Silver nanoparticles are known to be sensitive to oxidation, so a granulated blend (0.025 wt.-%, as shown in the Table of Contents graphic) was put into HNO_3 (32.5%) under vigorous stirring. After a week a slight colour loss was observed, but no silver ions could be detected in the solution, indicating a slight surface etching of the nanoparticles, which reduces the plasmon resonance absorption [38]. Sodium chloride or hydrochloric acid had no effect on the material. This shows that the polystyrene matrix efficiently protects the silver nanoparticles.

The synthesis strategy has also been applied to other metals. Copper nanoparticles stabilized by thiol-terminated polystyrene have been synthesized by a similar approach we presented for silver nanoparticles. The desired product could be synthesized by dissolving copper(II)acetylacetonate in a solution of thiolate-functionalized polystyrene and adding an excess of hydrazine as reduction agent [39]. Although copper nanoparticles are known to be very sensitive to oxidation (Indicated by a developing greenish colour), no significant decay has been observed here. The synthesized PS@Cu has been analyzed via TEM and UV/VIS. In TEM (Fig. 12), copper nanoparticles with diameter around 2.2 nm are clearly visible, with lattice distances characteristic for copper [40].

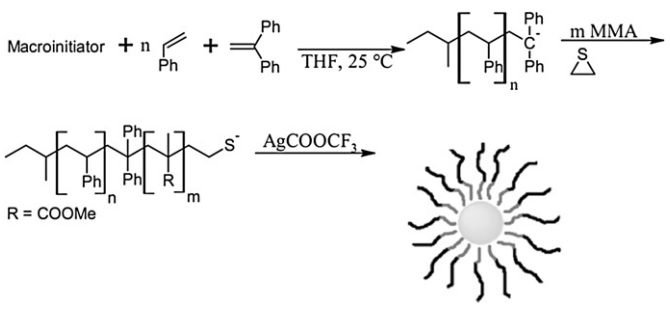

Fig. 14. One-pot synthesis of PS-PMMA-blockcopolymer-stabilized silver nanoparticles.

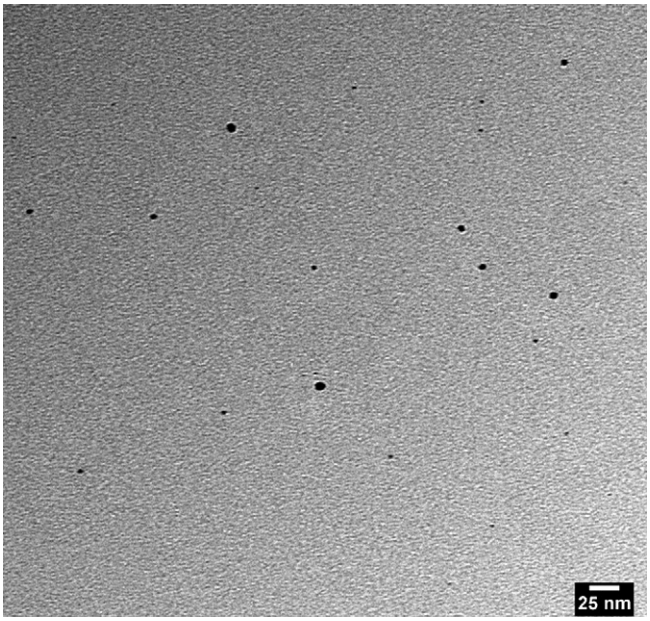

Fig. 15. TEM picture of PS-block-PMMA-stabilized silver nanoparticles prepared from the chloroform dispersion. No aggregation is observed.

The UV/Vis spectrum of PS@Cu seen in Fig. 13 is characteristic for the scattering of copper nanoparticles in this size region [41].

Further we synthesized silver nanoparticles stabilized by a PS-PMMA-blockcopolymer hull in a one-pot synthesis to show the versatility of the route. PS-block-PMMA has been synthesized by anionic polymerization with 1,1-diphenylethylene as linker to lower chain end reactivity [42] and terminated with ethylene sulfide to yield thiolate-terminated PS-block-PMMA. Silver trifluoroacetate was added, resulting in PS-block-PMMA@Ag (Fig. 14). The material is completely redispersible, with a nanoparticle diameter of 4.3 ± 1.5 nm (Fig. 15).

4. Conclusion

We have shown a convenient route to synthesize polymer-stabilized metal nanoparticles in near-quantitative yields in a one-pot system with polystyrene-stabilized silver nanoparticles as main example. The material (PS@Ag) is exceptionally stable against thermal and chemical degradation, thus allowing processing by melt-co-extrusion with polystyrene. The resulting blend has a high transparency, shows no phase separation and a single glass transition temperature. During co-extrusion and co-precipitation no aggregation or agglomeration of nanoparticles has been observed. Although not shown here in detail, it should not remain unmentioned that dispersions of polystyrene-stabilized nanoparticles as prepared here show exceptional stability against aggregation in organic solvents like toluene etc. and this for a period of several month.

This one-pot concept reported here has been also successfully transferred to other systems like polystyrene-stabilized copper nanoparticles and PS-PMMA-blockcopolymer-stabilized silver nanoparticles. Lithium hydride, formed due to the use of a macroinitiator with limited initiation efficiency, has been used as reduction agent. The formed silver nanoparticles are stabilized by thiolate-terminated polystyrene, but this simple concept is limited to a certain amount of silver. This inconvenience has been eliminated by adding an additional homogenous reduction agent like triethylboron hydride (Superhydride), allowing silver contents up to at least 18 wt.-% in the final composite without loss of particle stability. The addition of

nanoparticles to the end-functionalized polymer led to a rise in glass transition temperature, but this effect less significant with higher molecular weight polystyrene chains. GPC has been demonstrated as a powerful method for the analysis of polymer-silver nanoparticles conjugates eg. for the detection of unbound polymer chains and the polymer-stabilized silver nanoparticles. The GPC/DAD measurements allowed proof of the coordination of polystyrene chains to the silver nanoparticles surface. However, interactions between sample and GPC solvent make quantitative measurements by GPC impossible without further studies.

The stability of PS@Ag allowed industrial-scale processing by co-extrusion with conventional polystyrene at 190 °C without any degrading effect on the silver nanoparticles. Blends with silver contents up to 1 wt-% have shown homogenously dispersed nanoparticles in the polystyrene matrix.

The resulting composite material may be interesting as anti-bacterial coatings or for optical applications, for example as a medium for a random laser [7]. Future work will also concentrate on the influence of polymer-stabilized metal nanoparticles on the mechanical properties of blends with conventional polymers.

Acknowledgments

We thank Dr. A. Schaper and M. Hellwig of the Scientific Center for Materials Science Marburg for help with TEM pictures and the work group of Prof. B. Harbrecht for help with XRD measurements.

Appendix. Supplementary material

Supplementary data related to this article can be found online at doi:10.1016/j.polymer.2010.12.031.

References

[1] Daniel M-C, Astruc D. Chem Rev 2004;104(1):293–346 [and references therein].
[2] Schubert MM, Hackenberg S, van Veen AC, Muhler M, Plzak V, Behm RJ. J Catal 2001;192:113–22.
[3] Raffa P, Evangelisti C, Vitelli G, Salvatori P. Tetrahed Lett 2008;49:3221–4.
[4] Arcadi A. Chem Rev 2008;108:3266–325 [and references therein].
[5] Li Z, Brouwver C, He C. Chem Rev 2008;108:3239–65 [and references therein].
[6] Caseri W. Macromol Rapid Comm 2000;21:705–22 [and references therein].
[7] Meng X, Fujita K, Zong Y, Murai S, Tanaka K. Appl Phys Lett 2008;92:201112. Meng X, Fujita K, Murai S, Zong Y, Akasaka S, Hasegawa H, Tanaka K, physica status solidi 2009;6:S102–S105.
[8] Evanoff DD, Chumanov G. Chem Phys Chem 2005;6:1221–31.
[9] Carotenuto G, La Peruta G, Nicolais L. Sensors Actuators B Chem 2006;114:1092–5.
[10] Wong KYK. In: Kumar C, editor. Metallic nanomaterials. 1st ed. Weinheim: Wiley-VCH; 2009. p. 149–72 [and references therein].
[11] Jain P, Pradeep T. Biotechnol Bioeng 2004;90:59–63.
[12] Zhong C-J, Maye MM, Luo J, Han L, Kariuki N. Nanoparticles: building blocks for Nanotechnology. 1st ed. New York: Rotello VM, Ed.; Kluwer Academic/Plenium Publishers; 2004. 113–142.
[13] Pol VG, Gedanken A, Calderón-Moreno J, Palchik V, Slifkin MA, Weiss AM. Chem Mater 2003;15:3402.
[14] Möller M, Spatz JP, Roescher A. Adv Mater 1996;8:337–40.
[15] Turkevitch J, Stevenson PC, Hillier J. A study of the nucleation and growth process in the synthesis of colloidal gold. Discuss Faraday Soc 1951;11:55–75.
[16] Brust M, Walker M, Bethell D, Schiffrin DJ, Whyman R. J Chem Soc Chem Commun; 1994:801–2.
[17] Weare WW, Reed SM, Warner MG, Hutchison JE. J Am Chem Soc 2000;122:12890–1.
[18] Sarkar A, Mukherjee T, Kapoor S. J Phys Chem C 2008;112:3334–40.
[19] Gindy ME, Panagiotopoulos AZ, Prud'homme RK. Langmuir 2008;24:83–90.
[20] Corbierre MK, Cameron NS, Lennox RB. Langmuir 2004;20:2867–73.
[21] Fahmi A, Pietsch T, Mendoza C, Cheval N. Mater Today 2009;12:44–50.
[22] Ohno K, Oh K, Tsujii Y, Fukuda T. Macromolecules 2002;35:8989–93.
[23] Krüger C, Agarwal S, Greiner A. J Am Chem Soc 2008;130:2710–1.
[24] Kim J, Kim SS, Kim KH, Jin YH, Hong SM, Hwang SS, et al. Polymer 2004;45:3527–33.
[25] Glaze WH, Lin J, Felton EG. J Org Chem 1966;31:2643–5.
[26] Cavicchioli M, Varanda LC, Massabni AC, Melnikov P. Mat Lett 2005;59:3585–9.
[27] Torigoe K, Nakajima Y, Esumi K. J Phys Chem 1993;97:8304–9.
[28] Xie Y, Ye R, Liu H. Colloids Surf A 2006;279:175–8.
[29] Yee C, Scotti M, Ulman A, White H, Rafailovich M, Sokolov J. Langmuir 1999;15:4314–6.
[30] Shan J, Nuopponen M, Jiang H, Viitala T, Kauppinen E, Kontturi K, et al. Macromolecules 2005;38:2918–26.
[31] Polte J, Ahner TT, Delissen F, Sokolov S, Emmerling F, Thünemann AF, et al. J Am Chem Soc 2010;132:1296–301.
[32] Liu F-K, Wei G-T. Chromatographia 2004;59:115–9.
[33] Wei G-T, Liu F-K. J Chromatogr A 1999;836:253–60.
[34] Wei G-T, Liu F-K, Wang CRC. Anal Chem 1999;71:2085–91.
[35] Watson KJ, Zhu J, Nguyen ST, Mirkin CA. Pure Appl Chem 2000;72:67–72.
[36] Pastoriza-Santos I, Liz-Marzan LM. Langmuir 1999;15:948–51.
[37] Rittigstein P, Torkelson JM. J Poly Sci B 2006;44:2935–43.
[38] Quadroni L, Chumanov G. J Am Chem Soc 1999;121:10642–3.
[39] Chou CC, Chang JL, Zen JM. In: Kumar C, editor. Metallic nanomaterials. 1st ed. Weinheim: Wiley-VCH; 2009. p. 71–89 [and references therein].
[40] Lisiecki I, Filankembo A, Sack-Kongehl H, Weiss K, Pileni M-P, Urban J. Phys Rev B 2000;61:4968–74.
[41] Chen S, Sommers JM. J Phys Chem B 2001;105:8816–20.
[42] Auschra C, Stadler R. Polym Bull 1993;30:257–64.

Polymer 52 (2011) 921–932

Contents lists available at ScienceDirect

Polymer

journal homepage: www.elsevier.com/locate/polymer

Synthesis and characterization of new poly(ortho ester amidine) copolymers for non-viral gene delivery

Rupei Tang [a,*], Weihang Ji [b], Chun Wang [b,*]

[a] School of Medicine and Pharmaceutics, Jiangnan University, 1800 Lihu Road, Wuxi 214122, PR China
[b] Department of Biomedical Engineering, University of Minnesota, 7-105 Hasselmo Hall, 312 Church Street S. E., Minneapolis, MN 55455, USA

ARTICLE INFO

Article history:
Received 8 October 2010
Received in revised form
20 December 2010
Accepted 28 December 2010
Available online 9 January 2011

Keywords:
Copolymer
Ortho ester
Gene delivery

ABSTRACT

A new type of pH-labile cationic polymers, poly(ortho ester amidine) (POEAmd) copolymers, has been synthesized and characterized with potential future application as gene delivery carriers. The acid-labile POEAmd copolymer was synthesized by polycondensation of a new ortho ester diamine monomer with dimethylaliphatimidates, and a non-acid-labile polyamidine (PAmd) copolymer was also synthesized for comparison using a triethylene glycol diamine monomer. Both copolymers were easily dissolved in water, and can efficiently bind and condense plasmid DNA at neutral pH, forming nano-scale polyplexes. The physicochemical properties of the polyplexes have been studied using dynamic light scattering, gel electrophoresis, ethidium bromide exclusion, and heparin competition. The average size of the polyplexes was dependent on the amidine:phosphate (N:P) ratio of the polymers to DNA. Polyplexes containing the acid-labile POEAmd or the non-acid-labile PAmd showed similar average particle size, comparable strength of condensing DNA, and resistance to electrostatic destabilization. They also share similar metabolic toxicity to cells as measured by MTT assay. Importantly, the acid-labile polyplexes undergo accelerated polymer degradation at mildly acid-pHs, resulting in increasing particle size and the release of intact DNA plasmid. Polyplexes from both types of polyamidines caused distinct changes in the scattering properties of Baby Hamster Kidney (BHK-21) cells, showing swelling and increasing intracellular granularity. These cellular responses are uniquely different from other cationic polymers such as polyethylenimine and point to stress-related mechanisms specific to the polyamidines. Gene transfection of BHK-21 cells was evaluated by flow cytometry. The positive yet modest transfection efficiency by the polyamidines (acid-labile and non-acid-labile alike) underscores the importance of balancing polymer degradation and DNA release with endosomal escape. Insights gained from studying such acid-labile polyamidine-based DNA carriers and their interaction with cells may contribute to improved design of practically useful gene delivery systems.

1. Introduction

Non-viral vectors based on cationic polymers have gained significant attention over the past decades for the delivery of nucleic acids in gene therapy due to many potential advantages, such as large DNA loading capacity, ease of large-scale production, and reduced immunogenicity which has been a key issue associated with the use of viral vectors [1]. A wide variety of cationic polymers have been developed for gene delivery, such as poly(L-lysine) (PLL), poly(ethylenimine) (PEI), poly(amidoamine) dendrimer, etc [2]. These cationic polymers can condense DNA and form stable polymer/DNA complexes via electrostatic interaction and protect nucleic acids from enzymatic digestion, providing unlimited DNA packaging capacity, well-defined physicochemical properties, and a high degree of molecular diversity that allows extensive modifications to overcome extracellular and intracellular obstacles of gene delivery [3]. Research efforts are currently focused on development of safe and efficient polymeric carriers that can form complex with DNA and can avoid biological barriers for gene delivery [4]. Among the main barriers for non-viral gene delivery, endosomal escape and release of nucleic acids from the carriers once arrived at target sites are crucial efficiency-determining steps [5,6].

Hydrolysis of adenosine triphosphate (ATP) energizes the ion-transport processes across the cell membrane, and in turn makes

* Corresponding authors. Tel.: +86 612 626 3990; fax: +86 612 626 6583.
E-mail addresses: tangrp99@iccas.ac.cn (R. Tang), wangx504@umn.edu (C. Wang).

0032-3861/$ – see front matter © 2011 Elsevier Ltd. All rights reserved.
doi:10.1016/j.polymer.2010.12.057

the endosomal and lysosomal compartments of cells significantly more acidic (pH 5.0–6.2) than the cytosol or intracellular space (~pH 7.4) [7]. Remarkably, some viruses have evolved to use pH-sensitive peptides to facilitate their escape from the endosomes, resulting in high gene transfection [8]. Non-viral DNA vectors that utilize this significant drop in pH of endosomes and lysosomes often show improved gene transfection, and several designing strategies of "smart" cationic polymers have been successfully developed. The most used method is to create polymer blocks with amine groups with low pK_a values around 5 that have been shown to exhibit "proton sponge" potential, and these compounds are able to buffer the endosome and results in endosomal swelling and lysis, thus in turn releasing the DNA into the cytoplasm [9–13]. Similarly, incorporation of chloroquine into the DNA/vector complex often exhibit efficient gene transfection, because chloroquine is a well-known lysosomotropic agent that raises the pH of lysosomal environment, in turn hampering the enzymes involved in lysosomal degradation [14–16]. Another strategy developed recently is the incorporation of amine groups with acid-labile linkages, such as β-amino esters [17,18], acetal [19,20], ketal [21,22] and vinyl ether [23,24] into the polymer main-chains, where the endosomal acidic environment can hydrolyze the linker group to yield fragmentation products that raise the osmotic pressure within the vesicles, causing leakage and release. There is considerable flexibility in the design of pH-responsive cationic polymer vectors, where different linkage configurations can be implemented to generate desired physico-chemical properties, and different hydrolysis kinetics and hydrolyzed products can be designed with different membrane-destabilizing capacities.

Poly(ortho esters) (POEs) are an important type of acid-labile polymers with excellent biocompatibility [25–28]. Compared to vinyl ether and acetal and ketal, the ortho ester bond hydrolyzes more quickly in response to mildly acid condition [25,26,29]. We are interested in designing non-viral polymeric gene delivery vectors through the incorporation of ortho ester linker with functional groups containing positive charges. Recently, Davis *et al.* reported the synthesis of sugar-containing cationic polyamidine-based copolymers and their application in gene delivery with relatively high transfection efficiency and high cytotoxicity [30,31]. These polyamidines are not known to degrade readily and they are insensitive to endosomal acidic pH. In this study, we focus on a new type of acid-labile polyamidine-based copolymer system with the introduction of ortho ester into the copolymer main-chains, which may potentially serve as a molecular platform for the elucidation of the relationship between endosomal escape of polymer–DNA complex and DNA release triggered by pH-sensitive polymer degradation in the context of gene delivery. We hypothesized that incorporation of ortho esters to the polymer main-chains would facilitate efficient gene delivery via enhanced endosomal escape of complex and release of DNA. Hydrolysis of ortho esters in the mildly acidic endosomes would increase osmotic pressure and swelling of the carriers, which is expected to help to supplement the poor buffering capacity of polyamidines due to their pKa values as high as about 11 [32] and to efficiently unpack nucleic acids due to the dissociation of copolymer vectors. Here we report the synthesis of the new polyamidine-based copolymers, poly(ortho ester amidines) (POEAmd), and the results of physicochemical characterization of copolymer/DNA plasmid polyplexes, including pH-triggered DNA release. We also characterized *in vitro* interactions of the polyplexes with Baby Hamster Kidney (BHK-21) cells (including cytotoxicity, cell morphology, and gene transfection), aiming to illustrate how the structure of pH-sensitive acid-labile polymeric vectors may influence the function of delivering DNA to cells.

2. Experimental section

2.1. General methods of characterization

The ^1H and ^{13}C NMR spectra were recorded on a Varian Unity spectrometer (300 MHz), and chemical shifts were recorded in ppm. High-resolution mass spectra in electrospray-ionization (ESI) experiments were obtained on a Bruker MicrOTOF-Q mass spectrometer. Elemental analysis was conducted on a Carlo Erba 1108 automatic analyzer. The molecular weight and polydispersity of copolymers were determined by aqueous GPC analysis relative to PEG standard calibration (Waters 1525 binary HPLC pump, a Waters 2414 differential refractometer, and a Waters YMC HPLC column) using a mixture of 0.5 M $NaNO_3$ and 0.1 M Tris buffer (pH 7.2) as eluent at a flow rate of 1.0 mL/min at 35 °C. All sample solutions were filtered through a 0.45 μm filter before analysis.

2.2. Materials

Tetrahydrofuran (THF) was distilled over sodium and benzophenone, and acetonitrile was dried by distillation over CaH_2. 5-Trifluoroacetylaminopentanol was synthesized as described previously [27]. All other solvents and reagents were analytical-grade, purchased commercially, and used without further purification.

2.3. Synthesis

2.3.1. 2,2,2-Trifluoro-N-(2,3-dihydroxypropyl) acetamide (**1**)

To a stirred mixture of 3-amino-1,2-propanediol (18.80 g, 0.21 mol) in acetonitrile (120 mL) under argon was added dropwise ethyl trifluoroacetate (34.30 g, 0.24 mol). After 4 h, the solvent was evaporated, and the residue was dissolved in ethyl acetate (200 mL), washed with aqueous $KHSO_4$ and brine, then dried over $MgSO_4$, and concentrated to yield 34.90 g (91%) of 2,2,2-trifluoro-*N*-(2,3-dihydroxypropyl)-acetamide as colorless oil. ^1H NMR (300 MHz, CD_3OD): δ (ppm) 3.27–3.29 (m, 2H, NH–CH_2), 3.47–3.49 (m, 2H, CH_2–OH), 3.70–3.78 (m, 1H, C*H*–OH), 7.60 (b, 1H, N*H*).

2.3.2. 2,2,2-Trifluoro-N-(2-methoxy-[1,3]-dioxolan-4-ylmethyl) acetamide (**2**)

To a stirred mixture of **1** (13.50 g, 72.15 mmol), trimethyl orthoformate (34.89 g, 0.33 mol), and acetonitrile (110 mL) was added *p*-toluene sulfonic acid (*p*-TSA; a trace amount). The mixture was reacted for 6 h at room temperature, followed by evaporation of most of volatile components. The residue was dissolved in ethyl acetate (250 mL), washed successively with saturated aqueous sodium hydrogen carbonate and brine, dried over $MgSO_4$, and concentrated to yield 14.55 g (88%) of 2,2,2-trifluoro-*N*-(2-methoxy-[1,3] dioxolan-4-ylmethyl) acetamide as oil. ^1H NMR (300 MHz, $CDCl_3$): δ (ppm) 3.34–3.40 (d, 3H, O–CH_3), 3.45–3.71 (m, 2H, NH–CH_2), 4.15–4.25 (m, 2H, O–CH_2), 4.46–4.53 (m, 1H, O–C*H*), 5.74–5.79 (d, 1H, C*H*OCH$_3$), 6.70–7.64 (b, 1H, N*H*).

2.3.3. 2,2,2-Trifluoro-N-(2-(5′-trifluoroacetylaminopentyloxy)-[1,3]-dioxolan-4-ylmethyl) acetamide (**3**)

A mixture of **2** (9.90 g, 43.20 mmol), 5-trifluoroacetylaminopentanol (8.60 g, 43.20 mmol), and pyridinium *p*-toluene sulfonate (110.00 mg, 0.44 mmol) was heated at 130 °C until no volatile component was distilled. After cooling to room temperature, the residue was purified with column chromatography (silica gel, ethyl acetate/hexane (1/1) as eluent) to yield 15.41 g (90%) of 2,2,2-trifluoro-*N*-(2-(5′-trifluoroacetylaminopentyloxy)-[1,3]dioxolan-4-ylmethyl) acetamide as oil. ^1H NMR (300 MHz, $CDCl_3$): δ (ppm) 1.39–1.44 (t, 2H, CH_2), 1.51–1.62 (m, 4H, CH_2), 3.35–3.38 (m, 2H, NH–CH_2), 3.62–3.65 (m, 2H, NH–CH_2), 4.05–4.17 (m, 2H, O–CH_2),

4.31–4.37 (m, 1H, O–C*H*), 5.71–5.78 (d, 1H, C*H*OCH$_3$), 6.73–6.95 (b, 1H, N*H*), 7.25–7.51 (b, 1H, N*H*).

2.3.4. 4-Aminomethyl-2-aminopentyloxy-[1,3]-dioxolan (*monomer*)

The trifluoroacetamide **3** (13.35 g, 33.70 mmol) was dissolved in THF (90 mL), and sodium hydroxide (2.0 M, 75 mL) was added. The mixture was vigorously stirred overnight, extracted with diethyl ether, dried over $MgSO_4$, and evaporated. The residue was purified with column chromatography (silica gel, methanol/dichloromethane (1/10) as eluent) to yield 6.08 g (88%) of 4-aminomethyl-2-aminopentyloxy-[1,3]-dioxolan as oil. ^{1}H NMR (300 MHz, $CDCl_3$): δ (ppm) 1.35–1.61 (m, 6H, CH_2), 2.70–2.90 (m, 4H, CH_2–NH_2), 3.48–3.79 (m, 4H, O–CH_2), 4.02–4.09 (m, 1H, O–C*H*). 5.80–5.86 (d, 1H, C*H*OCH$_3$); ^{13}C NMR ($CDCl_3$, δ ppm): 23.12, 29.39, 33.30, 33.51, 42.08, 44.42, 62.28, 67.14, 70.95, 78.33, 115.45, 115.79; Calcd: ($C_9H_{20}N_2O_3$) 204.3, found *m*/*z* 205.2 (M + H$^+$), Anal. Calcd for ($C_9H_{20}N_2O_3$): C, 52.92; H, 9.87; N, 13.71. Found: C, 52.84; H, 9.80; N, 13.65.

2.3.5. Synthesis of acid-labile poly(ortho ester amidines) (*POEAmd 1–3*)

The copolymers (**POEAmd 1–3**) were synthesized using the same procedure of polycondensation, and the synthesis of **POEAmd 1** is described here as an example: dimethyladipimidate dihydrochloride (0.60 g, 2.45 mmol) was added to a stirred mixture of the monomer (0.50 g, 2.45 mmol) and 0.5 M Na_2CO_3 aqueous solution (0.90 mL, 4.50 mmol) under argon, reacted for 24 h at room temperature, and placed in a semi-permeable dialysis membrane (MW cut-off: 3500), and dialyzed against distilled water with a trace amount of triethylamine for 24 h. The obtained **POEAmd 1** was lyophilized, and the molecular weight and polydispersity of the product was determined by aqueous GPC.

2.3.6. Synthesis of non-acid-labile polyamidines (*PAmd 1–3*)

The copolymers (**PAmd 1–3**) were synthesized using the same procedure of polycondensation, and the synthesis of **PAmd 1** is described here as an example: dimethyladipimidate dihydrochloride (0.56 g, 2.27 mmol) was added to a stirred mixture of the 4,7,10-trioxa-1,13-tridecanediamine (0.50 g, 2.27 mmol) and 0.5 M $NaCO_3$ aqueous solution (0.90 mL, 4.50 mmol) under argon, reacted for 24 h at room temperature, and placed in a semi-permeable dialysis membrane (MW cut-off: 3500), and dialyzed against distilled water for 24 h. The obtained **PAmd 1** was lyophilized, and the molecular weight and polydispersity of the product was determined by aqueous GPC.

2.4. Determination of the mechanism and rate of hydrolysis of the poly(ortho ester amidine)

POEAmd 1 copolymer was dissolved in 150 mM *d*-phosphate buffer (pH 7.4) and *d*-acetate buffers (150 mM, pH 6, 5, and 4) at 5 mg/mL, and the ^{1}H NMR spectra were recorded on a Varian Unity spectrometer (300 MHz) at different time points. The rate of hydrolysis of the ortho ester in the polymer main-chain was calculated as the ratio (percentage) of the integrated area of the NMR peak at 8.01 ppm to the sum of the areas of peaks at 8.01 and 5.79 ppm.

2.5. Preparation of polyplexes and gel retardation assay

Polymer/DNA complexes (polyplexes) of N:P ratios ranging from 1:8 to 24:1 were prepared by adding 25 μL of polymer solution in 20 mM HEPES (pH 7.4) to 25 μL of DNA plasmid solution (0.2 μg/μL in 20 mM HEPES, pH 7.4), vortexed for 10 s, and the dispersions were incubated for 30 min at room temperature. To ascertain DNA binding, the polyplexes were analyzed by gel electrophoresis on a 1.0% agarose gel containing 0.5 μg/mL ethidium bromide. To determine the strength of DNA binding by copolymers, polyplexes at N:P ratio of 8:1 were incubated with increasing concentrations of heparin (0.1–1.5 IU per μg of DNA) for 10 min at room temperature and analyzed by agarose gel electrophoresis. To determine the stability of polyplex under acidic pH condition, polyplexes at N:P ratio of 8:1 were incubated overnight in pH 7.4 and 5 (50 mM phosphate and acetate buffers, respectively) at room temperature, and visualized by agarose gel electrophoresis.

2.6. Dynamic light scattering (DLS) and zeta-potential measurements

The average hydrodynamic diameter and polydispersity index of polyplexes in HEPES buffer (20 mM, pH 7.4) at 25 °C were determined using a ZetaPlus Particle Analyzer (Brookhaven Instruments Corporation, Holtsville, NY; 27 mW lasers; 658 nm incident beams, 90° scattering angle). Polyplexes with N:P ratios ranging from 1:4 to 24:1 were prepared as described above and diluted 20 times to a final volume of 2 mL in HEPES buffer before measurement. Simultaneously the zeta-potential of the polyplexes was determined using the ZetaPal module of the Particle Analyzer. To determine colloidal stability of polyplexes against different pH values, polyplexes of N:P ratio of 8:1 was incubated in 20 mM phosphate buffer (pH 7.4) and 20 mM acetate buffers (pH 6, 5, and 4), and the change in average hydrodynamic diameter of the polyplexes was monitored continuously for up to 40 min.

2.7. Ethidium bromide exclusion assay

The effect of the N:P ratio on the degree of plasmid DNA condensation in polyplex was estimated from the reduction in fluorescence intensity of ethidium bromide (EtBr) due to the exclusion from condensed DNA. EtBr solutions (1%, 8 μL) were added into the polymer/DNA complex solution (10 μg of plasmid DNA, 100 μL) prepared at various N:P ratios. After 15 min, 200 μL of the polyplexes were added to a 96-well plate, and the decrease in EtBr fluorescence intensity was measured in triplicates as described previously [33] using a Bio-Tek Synergy HT plate reader with excitation wavelength at 518 nm and an emission wavelength of 605 nm. Results were expressed as relative fluorescence intensity. The fluorescence intensity of uncondensed plasmid DNA solution with EtBr was set at 100%, after correction of the background of EtBr without plasmid DNA.

2.8. Cytotoxicity assay

The cytotoxicity of the polyplexes was evaluated by an MTT (3-(4,5-dimethyl-thiazol-2-yl)-2,5-diphenyl tetrazolium bromide) assay [34]. Baby hamster kidney (BHK-21) cells (ATCC) were seeded into 96-well plates at 10000 cells/well and cultured with polyplexes of various concentrations for 24 h in Dulbecco's Modified Eagle Medium supplemented with 10% FBS, 10 mM HEPES, 100 U/mL penicillin/streptomycin at 5% CO_2 and 37 °C. MTT in PBS (5 mg/mL, 20 μL) was added to each well reaching a final concentration of 0.5 mg/mL. After 4 h unreacted MTT was removed by aspiration. The formazan crystals were dissolved in 100 μL of DMSO and the absorbance was measured at 570 nm using a Bio-Tek Synergy HT plate reader. Cell viability was calculated by [Absorbance of cells exposed to polyplexes]/[Absorbance of cells cultured without polyplexes] in percentage.

2.9. In vitro transfection and the effect on cell morphology

To prepare polyplexes for *in vitro* transfection, polymers were mixed with plasmid DNA containing a CMV promoter and a green

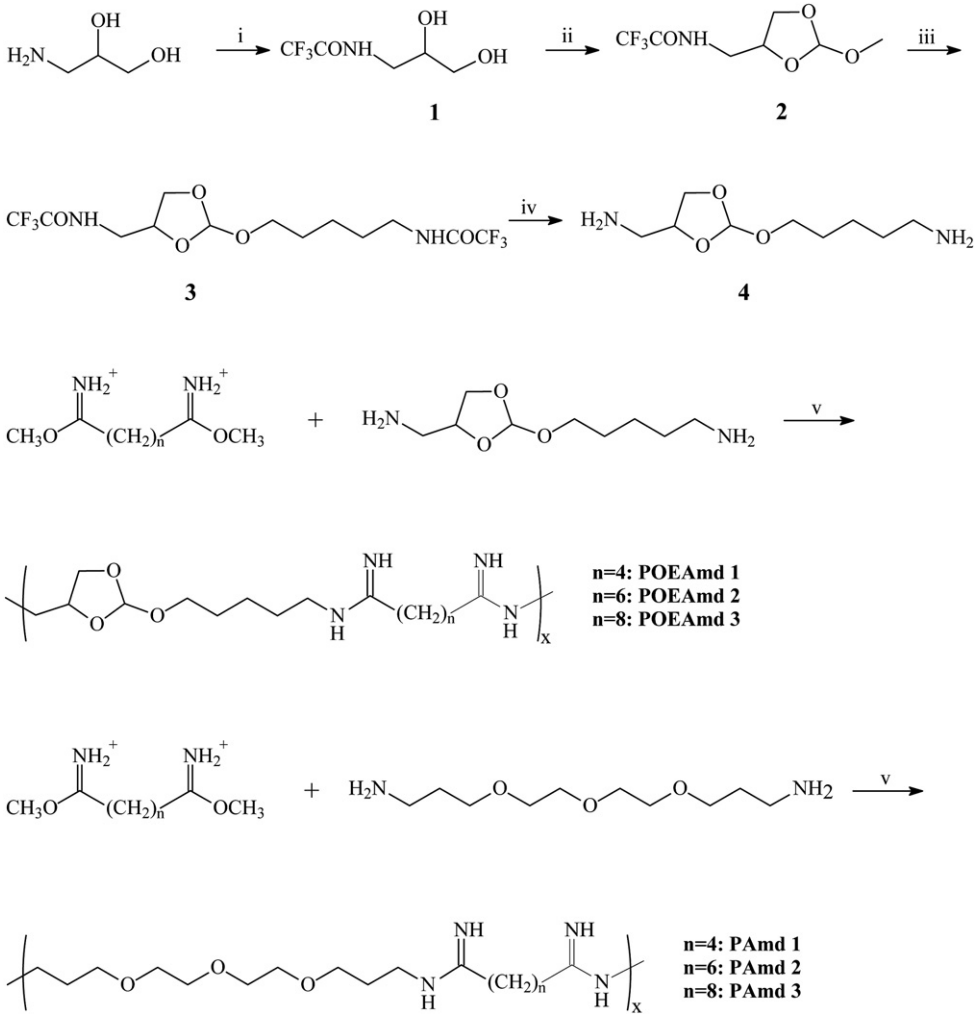

Scheme 1. Reagents and conditions: (i) Ethyl trifluoroacetate, acetonitrile; ii) Trimethyl orthoformate, *p*-toluene sulfonic acid (*p*-TSA), acetonitrile; (iii) 5-trifluoroacetylamino-1-pentanol, pyridinium *p*-TSA; (iv) NaOH/H_2O/THF; (v) 0.5 M Na_2CO_3.

fluorescence protein reporter gene (pCMV-EGFP, purchased from Elim Biopharmaceuticals) at N:P ratios of 4:1, 8:1, and 16:1. BHK-21 cells were seeded in 6-well plates with a density of 100,000 cells per well and cultured for 24 h before polyplexes were added. Afterward polyplexes were added at 4 μg DNA per well in 2 mL of serum-free media, and incubated for 4 h. The polyplex containing media was then discarded and the cells were washed by DPBS and cultured in fresh media with 10% serum for 20 h. The cells were then trypsinized and harvested in FACS buffer (DPBS with 1% BSA, 0.1% NaN_3). The percentage of transfected cells was determined by measuring GFP expression in the cell population using a FACSCalibur 501 flow cytometer (Beckman Coulter). The GFP positive gate was set based on the cell population treated with polyplexes containing firefly luciferase plasmid, which does not produce GFP, to compensate for potential change in cell autofluorescence due to exposure to cationic polymers. The front and side scattering of light by the cells exposed to polyplexes with different N:P ratios were also determined.

3. Results and discussion

3.1. Synthesis and characterization of POEAmd copolymers

The key acid-labile ortho ester diamine monomer was synthesized in four steps (Scheme 1): 2,2,2-trifluoro-*N*-(2,3-dihydroxypropyl) acetamide (**1**) was obtained by using 3-amino-1,2-propanediol as the starting material, which then reacted with trimethyl orthoformate in the presence of catalytic *p*-toluene sulfonic acid to give the ortho ester **2**. The compound **3** was easily obtained by transesterification between compound **2** and trifluoroacetylaminopentanol. The TFA-protecting groups of compound **3** were removed by aqueous sodium hydroxide in THF, and the acid-labile bifunctional monomer was easily obtained with the total yield of approximately 63%. The ^1H and ^{13}C NMR spectra confirmed that the monomer was pure and structurally correct (Fig. 1). The highly hydrolytically labile ortho ester is built into the monomer, and is stabilized by the neighboring primary amines, allowing for easy handling and long-term storage. The diamine monomer can be copolymerized readily with any multifunctional amine-reactive monomers to produce a range of structurally and functionally diverse, biodegradable copolymers, for examples, poly(ortho ester amides) [27] and poly(ortho ester amidines) as reported here.

We synthesized poly(ortho ester amidines) (POEAmd) via polycondensation of the acid-labile ortho ester diamine monomer with dimethylaliphatimidate dihydrochloride with different alkyl groups (Scheme 1). Similarly, we also synthesized a series of non-acid-labile polyamidines (PAmd) by polycondensation of 4,7,10-trioxa-1,13-tridecanediamine with various dimethylaliphatimidates. **POEAmd 1** and **PAmd 1** copolymers were easily dissolved in water, and their

chemical structures were confirmed by ^{1}H NMR (Fig. 2). However, other POEAmd and PAmd copolymers were not soluble in water, probably due to the increased hydrophobicity resulted from increased length of alkyl groups. The average number molecular weight and distribution of **POEAmd 1** and **PAmd 1** were determined by GPC, and calculated to be 6500 and 6800 with polydispersity index of 1.81 and 1.95, relatively, as shown in Table 1.

3.2. Kinetics of polymer hydrolysis and pH-dependence

Ortho ester structures are highly hydrolytically labile and acid-sensitive [35]. There are two possible pathways of hydrolysis for cyclic ortho esters that involve exocyclic and endocyclic breakage of the ortho ester bond [25,26]. In a recent report, *trans*-*N*-(2-ethyoxy-1,3-dioxan-5-yl)methacrylamide, a monomer containing a six-membered cyclic ortho ester, was incorporated in block copolymer micelles [36]. This ortho ester hydrolyzed through both exocyclic and endocyclic pathways, giving rise to a mixture of two chemically distinct products with different solubility in water [37]. Our group have recently developed novel micelle-like nanoparticles based on pH-responsive copolymers, poly(ethylene glycol)-*block*-poly(*N*-(2-methoxy-[1,3]dioxolan-4-ylmethyl) methacrylamides) (PEG-*b*-PMYM), whose hydrolysis of the ortho ester side-chains follows a distinct exocyclic mechanism and shows pH-dependent kinetics confirmed by ^{1}H NMR spectra [29]. Here the five-membered ortho ester group from the side-chains of the PMYM block [29] has been built into the main-chain of the poly(ortho ester amidine) copolymer, **POEAmd 1**.

To understand the hydrolytic mechanism of **POEAmd 1**, NMR studies were carried out to follow the time-course of hydrolysis for up to 48 h in aqueous buffers of physiological (pH 7.4) and mildly acidic pHs (6, 5, and 4), and the results are shown in Fig. 3. The peak at 5.79 ppm (denoted as "a") is characteristic of the ortho ester proton before hydrolysis (Scheme 2). At pH 7.4 over the course of 48 h, the area of peak "a" decreased only slightly, suggesting that only a small amount of the ortho ester hydrolyzed and that most of

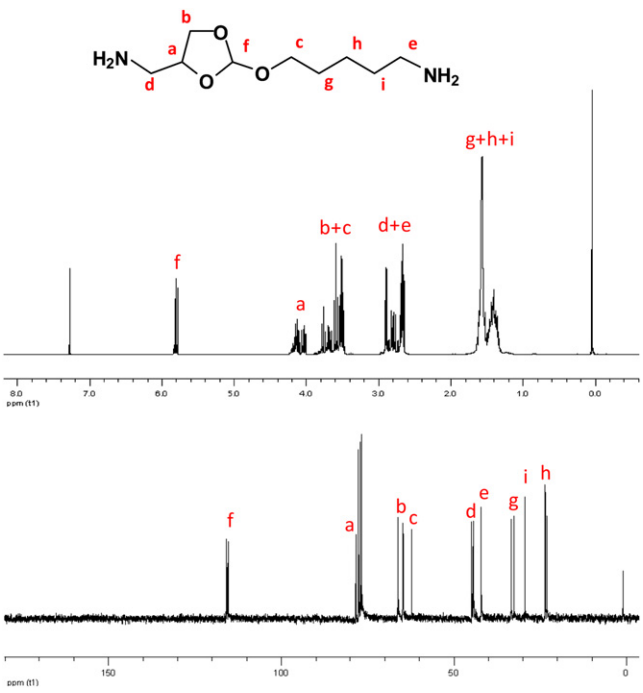

Fig. 1. ^{1}H and ^{13}C NMR spectra of the ortho ester diamine monomer.

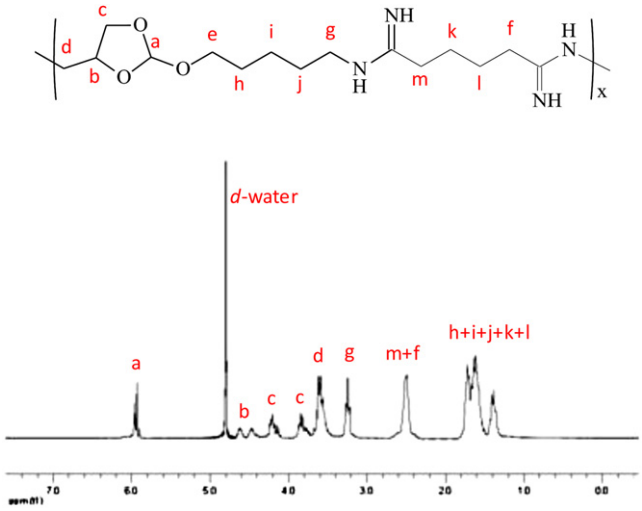

Fig. 2. ^{1}H NMR spectrum of **POEAmd 1**.

the ortho ester groups remained intact. Concurrently, a new peak at 8.01 ppm (denoted as "b") appeared after approximately 24 h (Fig. 3), which corresponds to the proton of formate. The endocyclic pathway of hydrolysis would produce two different kinds of formate, one appended to the copolymer and a small molecule, methyl formate, whereas the exocyclic pathway should yield only the polymeric formate (Scheme 2). Here we observed a single formate peak between 8 and 8.2 ppm even after extensive hydrolysis at pH 4 for 48 h (Fig. 3), demonstrating that the hydrolysis of **POEAmd 1** follows the exocyclic pathway exclusively, unlike the six-membered ortho ester ring structure reported before [37]. This finding agrees with previous studies on other related cyclic ortho esters and may be attributed to the unique stereoelectronic and steric effects of the ring structure [25,29,38].

Furthermore, we found that at all time points and all pHs, the increase in the integral area of peak "b" was equal to the decrease of peak "a", and that the sum of the two peaks remained constant (Fig. 3). Taken together, the NMR data confirm that the ortho ester structure of **POEAmd 1** copolymer undergo exocyclic cleavage, and are converted quantitatively to a pair of stereo-isomers containing a hydroxyl and a formate (Scheme 2). The progression of ortho ester hydrolysis is revealed by the NMR analysis (Fig. 3) and can be quantified based on the changing integral area of peak "a" (representing the ortho ester proton before hydrolysis) and peak "b" (representing the formate proton as a result of hydrolysis). We define the degree of hydrolysis to be the percentage of peak "b" relative to the sum of the peaks "a" and "b". The time/pH-dependence of hydrolysis is shown spectroscopically in Fig. 3 and quantitatively in Fig. 4. As expected, hydrolysis of the ortho ester structure is highly sensitive to pH and is much accelerated at more acidic pHs. At pH 7.4 and 6, 5% and 81% of the ortho esters were hydrolyzed within 48 h, whereas the hydrolysis was essentially complete in 48 and 8 h when pH was lowered to 5 and 4, respectively (Fig. 3). The ability of achieving markedly different hydrolysis kinetics from days to hours over a fairly narrow pH range (from 7.4

Table 1
Polymerization results of POEAmd and PAmd copolymers.

Polymer	Yield (%)	M_n ($\times 10^{-4}$)	M_w ($\times 10^{-4}$)	PDI
POEAmd 1	55	0.65	1.18	1.81
PAmd 1	51	0.68	1.33	1.95

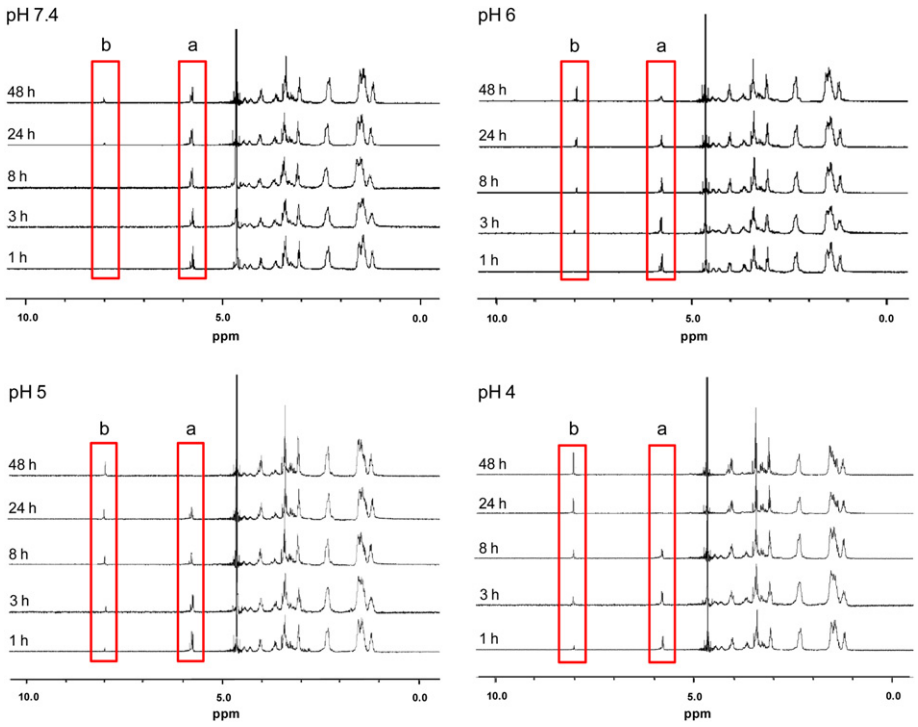

Fig. 3. ^{1}H NMR spectra of **POEAmd 1** (5 mg/mL) in *d*-buffers of pH 7.4, 6, 5, and 4, at different time points up to 48 h. Peaks labeled with "a" and "b" are protons characteristic to the cyclic ortho ester and formate groups, respectively (Scheme 2).

to 4), as we have demonstrated here, bodes well for the potential of using such polymer systems for pH-triggered gene delivery.

3.3. DNA binding and condensation

Gel retardation assay shows that **POEAmd 1** and **PAmd 1** copolymers were both able to bind to and completely neutralize the negative charges of a DNA plasmid at the N:P ratio of 1:1 and beyond, as shown in Fig. 5a. The polymer–DNA condensation can be characterized by the quenching of the fluorescence of ethidium bromide (EtBr) due to the formation of complexes, where charge neutralization and subsequent condensation of DNA prevents EtBr from intercalating into DNA double-helix. As shown in Fig. 5b, the fluorescence intensity of EtBr decreased with an increase in the N:P ratio and reached a minimum at about N:P of 2, which was consistent with the progressive complexation of copolymer with plasmid DNA, inhibiting the intercalation of EtBr into plasmid DNA. DLS reveals that the average particle size of polyplexes in aqueous buffer spanned almost the same range of 75–210 nm with much dependence on the N:P ratio (Fig. 5c). The size distribution of each type of polyplex was also quite narrow with PDI ranging from 0.05 to 0.25. At N:P ratio of 1:1, average particle size stabilizes around 160–210 nm for these two polyplexes (Fig. 5c), and greatly decrease to be about 80 nm when the N:P ratio is above 1:1. Polyplexes formed by **POEAmd 1** and **PAmd 1** had similar zeta-potential values (49.95 ± 6.68 mV and 47.04 ± 4.48 mV, respectively). Discrete, compact polyplexes formed at N:P ratio of 8:1 (Fig. 5c) were selected for further characterization to understand the polyplex stability in physiological conditions. The polyplexes were further analyzed by agarose gel electrophoresis after incubation with increasing amount of heparin, a polyanion that can compete with DNA for the binding to the polycation. As shown in Fig. 5d, the threshold concentration of heparin at which polyplex disruption occurred was 0.4 IU for polyplexes of both **POEAmd 1** and **PAmd 1**. Taken together, these results illustrate the ability of using polyamidine-based copolymers to control the formation of defined and narrowly dispersed polyplexes, which is highly important in light of the notion that cell-specific targeting and internalization can be much affected by the size of the particulates [39,40].

3.4. Stability of polyplexes and acid-triggered DNA release

The stability of polyplexes at N:P ratio of 8:1 was studied in phosphate and acetate buffers (20 mM, pH 7.4, 6, 5 and 4), and in the presence of increasing amount of heparin at physiological ionic strength (150 mM NaCl, pH 7.4). First, the average size dependence of

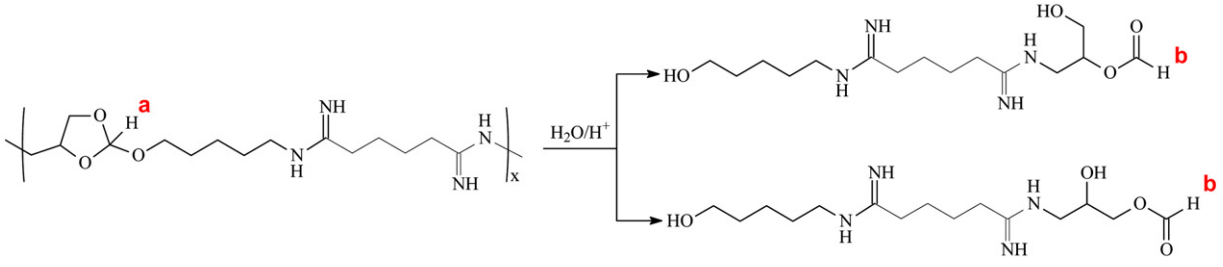

Scheme 2.

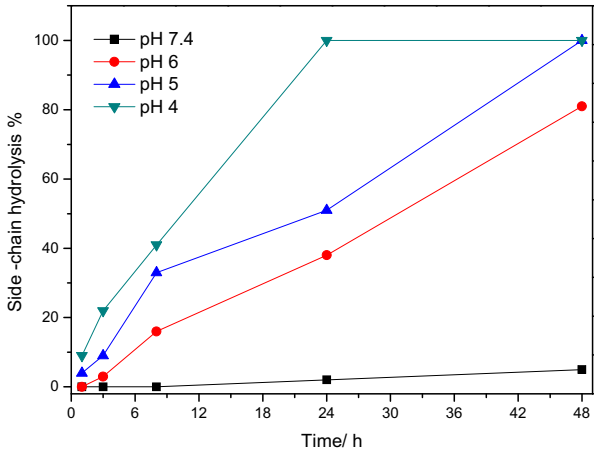

Fig. 4. Time and pH-dependence of ortho ester hydrolysis in **POEAmd 1** based on the NMR spectra shown in Fig. 3.

polyplexes on incubation time was determined by DLS measurements in different pH conditions. Due to the hydrolysis of **POEAmd 1** in mildly acidic conditions, polyplexes formed by **POEAmd 1** rapidly dissociate, and the size greatly increased to be 700–800 nm in 36 min at pH 5 and 4 (Fig. 6a). On the contrary, polyplexes formed by non-acid-labile **PAmd 1** only enlarged slightly even at pH 4 over the same period of time (Fig. 6b). To determine if polymer hydrolysis at acidic pH does trigger the release of DNA, the polyplexes were exposed to pH 7.4 and 5 and then analyzed by agarose gel electrophoresis. DNA remained bound to the non-acid-labile **PAmd 1** regardless of pH (Fig. 6c). However, the acid-labile **POEAmd 1** bound to DNA stably at pH 7.4 and released free DNA at pH 5, presumably due to the polymer degradation and the subsequent loss of DNA condensation. Both DLS and gel electrophoresis experiments demonstrated that acid-labile ortho ester linkages in the polymer main-chain has a profound impact on the colloidal stability of polyplexes and that acid-pH-triggered DNA release can be achieved by the acid-labile poly(ortho ester amidine).

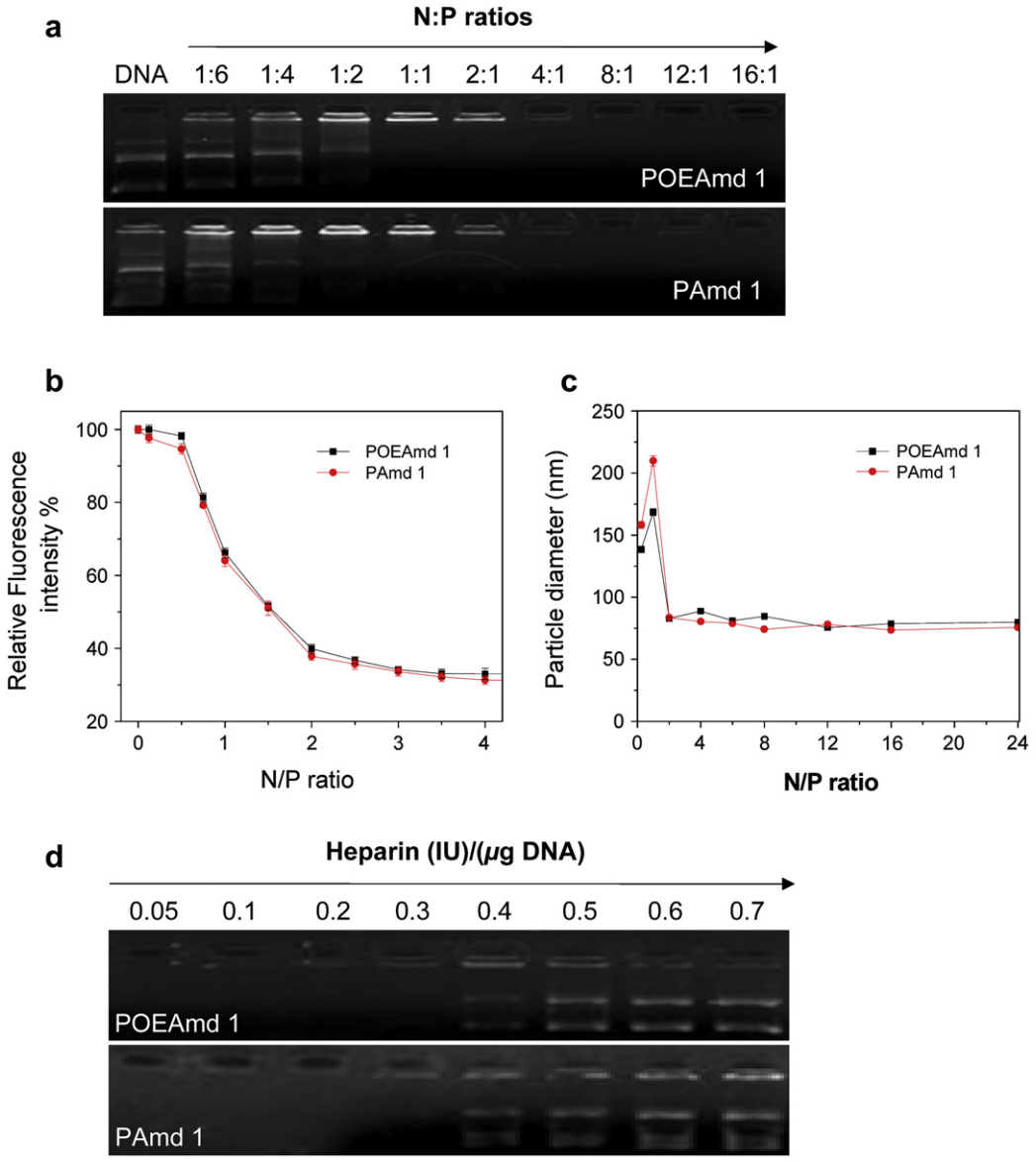

Fig. 5. Characterization of plasmid DNA binding and condensation by **POEAmd 1** and **PAmd 1**. (a) Gel retardation assay of polyplexes prepared at various N:P ratios; (b) Estimation of plasmid DNA condensation by ethidium bromide exclusion assay; (c) DLS determination of the average particle size of polyplexes in aqueous buffer (20 mM HEPES, pH 7.4) as a function of N:P ratio; (d) Dissociation of DNA from polymers induced by increasing amount of heparin.

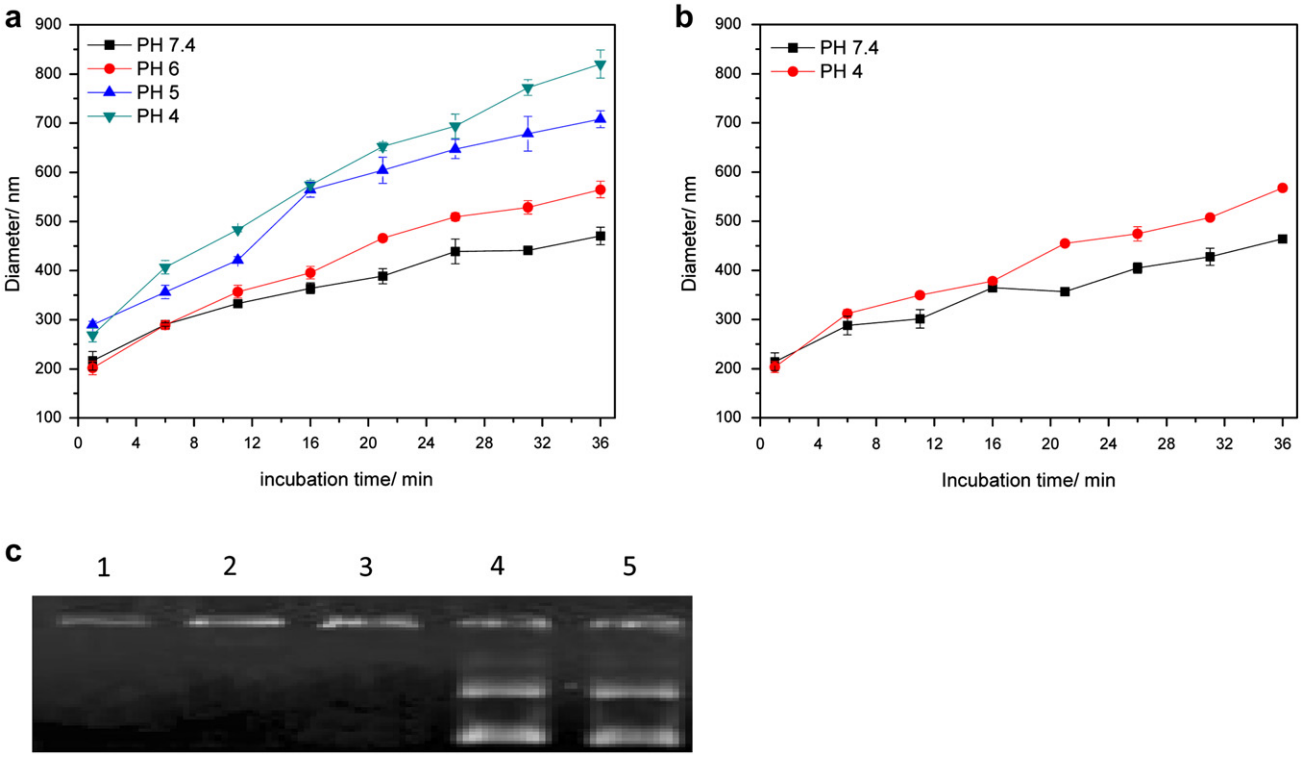

Fig. 6. Stability of polyplexes at N:P ratio of 8:1. (a) Time-dependent stability of polyplexes formed from the acid-labile **POEAmd 1** in different pHs; (b) Stability of DNA from the non-acid-labile **PAmd 1** in different pHs; (c) Gel retardation assay of stability of polyplexes; lane 1: **PAmd 1**/DNA, pH 7.4; lane 2: **POEAmd 1**/DNA, pH 7.4; lane 3: **PAmd 1**/DNA, pH 5; lane 4: **POEAmd 1**/DNA, pH 5; line 5: Plasmid DNA only, pH 7.4.

3.5. *In vitro* cytotoxicity and gene transfection

BHK-21 cells were used for the evaluation of *in vitro* toxicity and transfection of the polyplexes formed from **POEAmd 1** and **PAmd 1**, and branched polyethylenimine (PEI) (M_w: 25 kDa) as a control. At N:P ratio of 16:1 or less, the polyplexes formed from **POEAmd 1** and **PAmd 1** were not toxic to BHK-21 cells (Fig. 7a). In contrast, polyplexes formed by branched PEI was more toxic, killing much of BHK-21 cells at N:P ratio of 16:1 (Fig. 7a). When N:P ratio exceeded 16:1, all polyplexes formed from polymers including **POEAmd 1** and **PAmd 1** showed some toxicity, which is consistent with that of polyamidine-based copolymers [30,31]. The difference in cytotoxicity between the polyamidines and PEI was more pronounced when comparing these polymers at equivalent mass. For example, mass concentration of 20 μg/mL of PEI reduced cell viability to 65%, yet at the same mass concentration of the polyamidines, cell viability was higher than 95% (Fig. 7b). These results suggest that compared to branched PEI, the polyamidines appear much less toxic to cells and that both the acid-labile and non-acid-labile polymers share similar cytotoxicity.

The effect on the BHK-21 cells by polyplex formed from **POEAmd 1** and **PAmd 1** were further assessed by examining the light scattering properties of the cells under transfection conditions, as shown in Fig. 8. Generally, front scattering intensity correlates with the size of cells, and side-scattering intensity correlates with the granularity or internal structure of cells. Untreated normal cell population within the "live" gate shows a single population with certain scattering properties: the majority

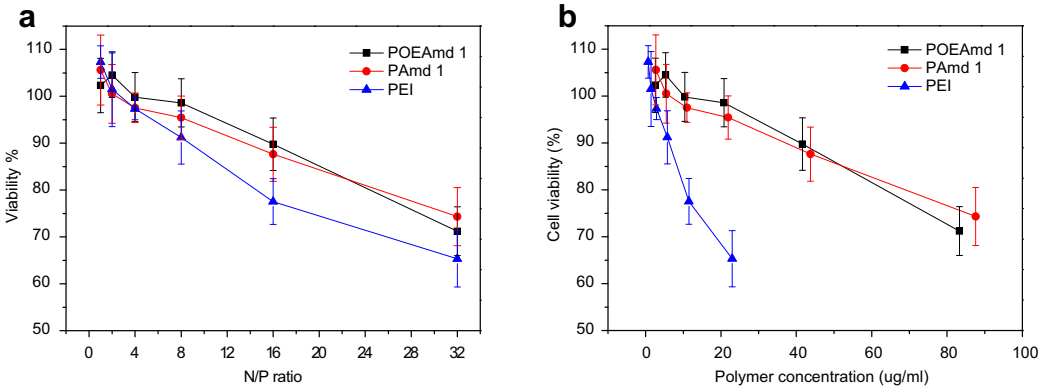

Fig. 7. Cytotoxicity of polyplexes in BHK-21 cells determined using an MTT assay. (a) Polyplexes at various N:P ratios; (b) Polyplexes by mass concentration. Cells treated with culture media only were taken as the 100% viability.

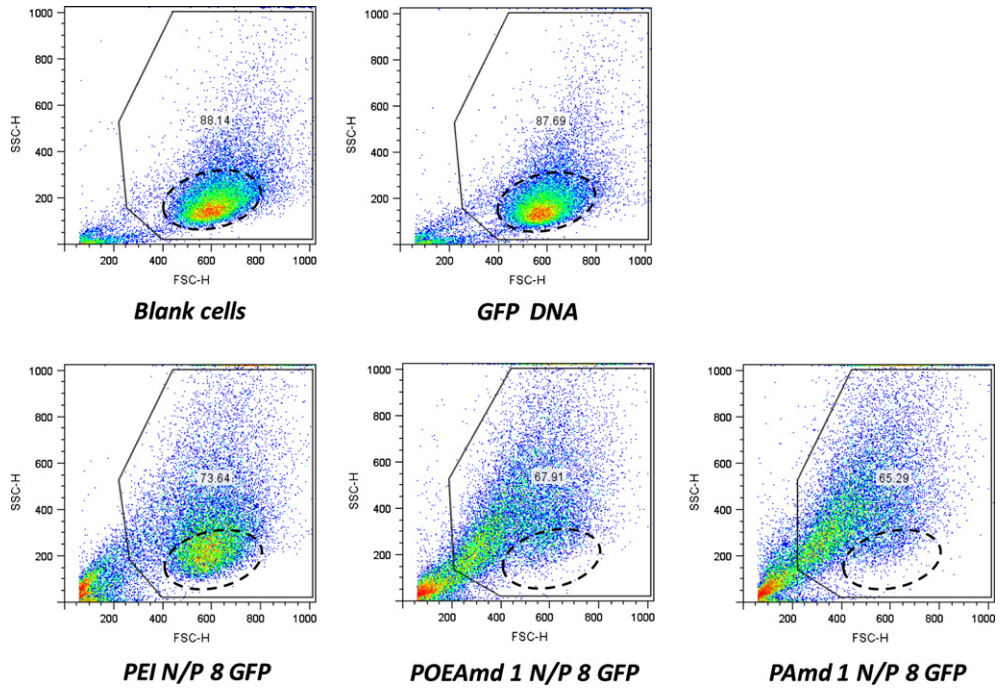

Fig. 8. Scattering properties of BHK-21 cells exposed to polyplexes transfection for 4 h in serum-free medium, followed by post-transfection incubation for 20 h in 10% serum-containing medium. Dotted circle points to the normal cell population.

of cells have front scatter from 400 to 800, side scatter from 100 to 300 (Fig. 8). At least 88% of the cells are gated as "live". Plasmid DNA treated cells are almost identical to untreated cells with the same percentage of cells gated as "live". PEI/DNA treated cells have slightly lower viable cells (73%) due to toxicity of the PEI. Compared with untreated cells or cells treated with plasmid DNA only, these cells have similar front scattering intensity but slightly larger side-scattering intensity. This suggests that after PEI/DNA incubation, the cells maintain their original size but become more granular. After being treated with DNA complexed to **POEAmd 1** and **PAmd 1**, there is a slight decrease in cell viability than PEI, suggesting that the polyamidines are slightly more toxic than PEI under serum-free condition, which differs from the MTT data that were acquired in complete media. The scattering properties of these cells are markedly different than the PEI-treated cells. Here many cells appeared to have shrunk with lower front scattering intensity in the range of 300–500. Even more cells have high side-scattering intensity and high granularity. There is no apparent difference between the acid-degradable **POEAmd 1** and the non-degradable **PAmd 1**.

The observations on cell morphology based on light scattering properties were further confirmed by direct visualization of cells using light microscopy. Blank cells cultured on tissue culture plates spread well on the substrate and proliferated (Fig. 9a), whereas cells exposed to PEI polyplexes had a lower cell number and some of the cells appeared rounded and shrunken with more granularity (Fig. 9b). After treatment with **POEAmd 1** polyplexes, even more cells had rounded shapes and internal granularity was more pronounced (Fig. 9c). There was no significant difference between cells treated with the acid-labile **POEAmd 1** and the non-acid-labile **PAmd 1**. At higher magnification the untreated blank cells appeared rather smooth (Fig. 9d), yet polyplex-treated cells contained numerous, large vesicular structures in the cytoplasm (Fig. 9e and f).

These studies show that the polyamidine-based copolymers are able to trigger distinct cellular changes, resulting in smaller overall size and higher granularity. Cationic polymers are known to cause cellular stress and even death via primarily the apoptotic pathway [41,42]. Some cationic polymers are also reported to alter the morphology and light scattering properties of macrophages [43,44]. In the case of the polyamidines and the BHK-21 cells, both acid-labile and non-acid-labile polymer/DNA complexes had similar effects on cell morphology and scattering properties, probably due to their similar positive surface charges with zeta-potential values of 49.95 ± 6.68 mV and 47.04 ± 4.48 mV, respectively. It is possible that these cellular changes are related to cellular stress responses toward highly positively charged colloidal polymer/DNA particles and the initiation of cell death pathways, such as early apoptosis and autophagy, or "self-eating", a survival mechanism by cells under stress [45]. Autophagy is known to cause shrinkage of cells and the formation of autophagosomes, the large vesicular subcellular organelle and the hallmark of autophagy, which may account for the increase in subcellular granularity. It is also possible that some cells, while still being alive, may have begun the early phase of apoptosis, in response to the polyamidines, which may contribute to changes in decreasing cell size and increasing granularity. While PEI/DNA complexes at the same N:P ratio were also positively charged with a slightly lower zeta-potential (34.45 ± 7.54 mV), the effect on cell viability, size and morphology was not as pronounced as that of the polyamidines (Figs. 9 and 10). Although the cationic nature of all these polymers may play an important role, the exact mechanism appears to be unique to the polyamidines and is not entirely clear at this point. Further clarification and exploitation of these mechanisms may lead to refined polymer carriers that trigger specific responses in target cells.

Transfection efficiency of BHK-21 cells was assessed using GFP as the reporter gene. In a typical experiment, transfection by naked GFP plasmid was, as expected, extremely low ($\sim$0.02%), similar to blank cells and cells treated with polyplexes of luciferase plasmid (Fig. 10). On the other hand, transfection with polyplexes composed of 25-kDa branched PEI and GFP plasmid at N:P ratio of 8 resulted in GFP positive cells of almost 16% (Fig. 10). Compared to PEI, the transfection efficiency by the polyamidine/DNA complexes was real yet surprisingly low, ranging from $\sim$0.1 to 0.2% (Fig. 10). Polyplexes

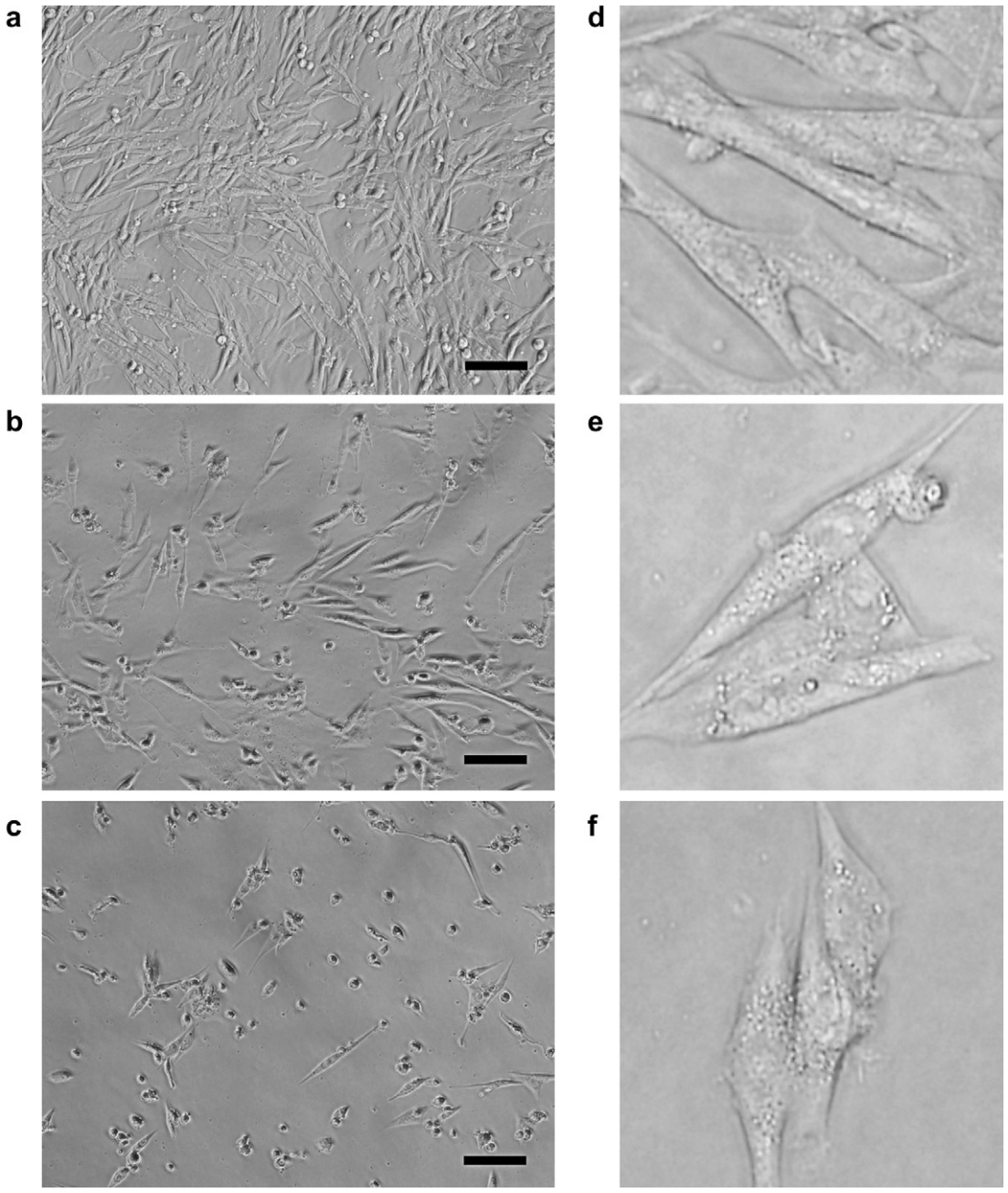

Fig. 9. Morphology of BHK-21 cells exposed to polyplex transfection for 4 h in serum-free medium, followed by post-transfection incubation for 20 h in 10% serum-containing medium. Shown are representative bright-field light microscopy images of blank cells (a) and cells treated with PEI polyplexes (b) or **POEAmd 1** polyplexes (c). Further magnified images of blank cells (d) and polyplex-treated cells (e) and (f) with higher internal granularity. Scale bar: 100 μm.

of N:P ratio of 4 and 8 were generally more efficient than N:P ratio of 16.

Key obstacles to non-viral gene transfer have been identified to be cellular uptake, endosomal escape, nuclear translocation, and DNA release from carrier [46]. We have shown that both types of polyamidine described here are capable of binding to and condensing plasmid DNA into nanoparticles of similar size and stability. Therefore, it is reasonable to predict that the polyplexes will be internalized in similar degrees by cells via endocytosis. We have also shown that only the acid-labile poly(ortho ester amidine) but not the non-acid-labile polyamidine is capable of degrading at endosomal pH ($\sim$5) and releasing DNA. Interestingly, however, we did not observe significant difference in gene transfection between the acid-labile and the non-labile polyamidines. There are several possible reasons for this observation. One possibility is that the rate of acid-triggered hydrolysis may not be optimally tuned to cause endosome disruption, and the DNA might have been released too quickly and too early. Another possibility is that unlike the PEI, the chemical structures of the polyamidine and its hydrolytic products might not facilitate direct endosomal escape through the "proton sponge" mechanism. In either case, the consequence would be that the DNA is trapped in the endosome, digested, and deactivated. The results reported here illustrate the importance of optimizing the timing of acid-triggered DNA release and endosomal escape by proper design of the acid-labile chemistry of the polymer carrier. The poly(ortho ester amidine) chemistry is highly versatile, which

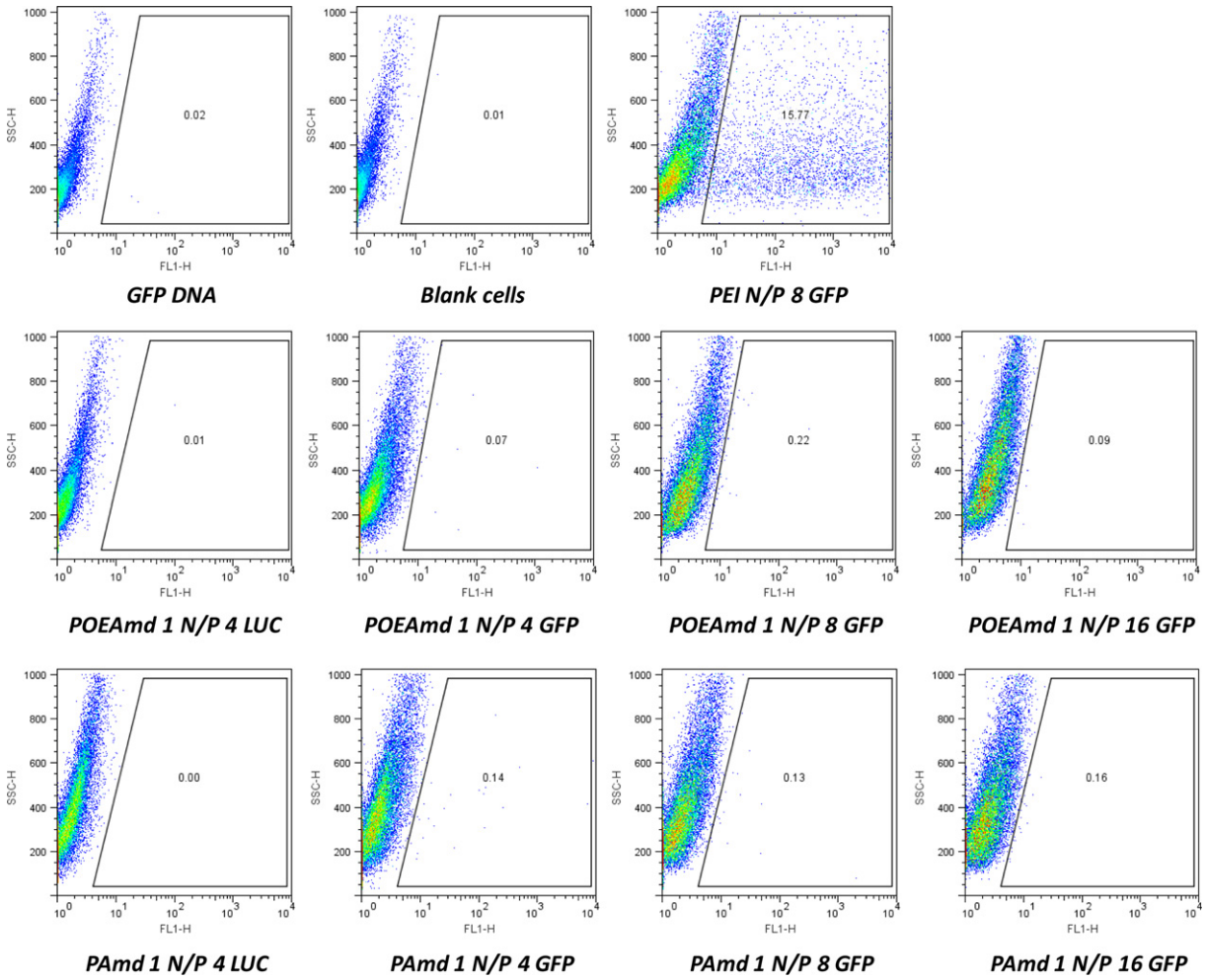

Fig. 10. Representative gene transfection of BHK-21 cells. The cells were incubated with the polyplexes of various N:P ratio for 4 h in the absence of serum, and GFP expression was quantified by FACS 20 h later. The GFP positive gate was set based on the transfection results of polyplexes using a luciferase (LUC) plasmid to exclude the influence of cell autofluorescence. The numbers in each panel are the fractions of GFP positive cells in percentage of the total live cells.

should allow for further tuning of the acid-labile degradation rate and for incorporating chemical functionalities to promote endosomal escape. The validation of such material designs by subcellular trafficking studies will be the focus of future research.

4. Conclusions

We have demonstrated the synthesis and characterization of a new type of acid-labile poly(ortho ester amidine) copolymers, POEAmd. We showed that structures of POEAmd had a profound impact on the physicochemical properties of the polyplexes, including nanoparticle size and stability, as well as biological properties such as DNA release, cytotoxicity, and gene transfection. Furthermore, the POEAmd triggered intracellular stress responses that are unique and distinguished from other cationic polymers. Further understanding of the polymer/cell interaction and refining the pH-triggered polymer degradation should lead to more efficient polyamidine-based gene delivery carriers.

Acknowledgments

The financial support to this work is in part by the NIH (Grant R01CA129189, to C. Wang), the NSF CAREER Award (BES 0547613, to C. Wang), the Program for New Century Excellent Talents in University (No. NCET-10-0435, to R. Tang), the National Natural Science Foundation of China (No. 21004030, 50873080, to R. Tang), the Natural Science Foundation of Jiangsu Province of China (No. BK2010145, to R. Tang), and the Fundamental Research Funds for the Central Universities of China (JUSRP21013, to R. Tang).

References

[1] Mintzer MV, Simanek EE. Chem Rev 2009;109:259–302.
[2] O'Rorke S, Keeney M, Pandit A. Prog Polym Sci 2010;35:441–58.
[3] Jeong J, Kim S, Park T. Prog Polym Sci 2007;32:1239–74.
[4] Niven R, Pearlman R, Wedeking T, Mackeigan J, Noker P, Simpson-Herren L, et al. J Pharm Sci 1998;87:1292–9.
[5] Medina-Kauwe LK, Xie J, Hamm-Alvarez S. Gene Ther 2005;12:1734–51.
[6] Schaffer DV, Fidelman NA, Dan N, Lauffenburger DA. Biotechnol Bioeng 2000;67:598–606.
[7] Ohkuma S, Poole B. Proc Natl Acad Sci U S A 1978;75:3327–31.
[8] Kielian MC, Marsh M, Helenius A. EMBO J 1986;5:3103–9.
[9] Wagner E. Adv Drug Deliv Rev 1999;38:279–89.
[10] Honig D, DeRouchey J, Jungmann R, Koch C, Plank C, Radler JO. Biomacromolecules 2010;11:1802–9.
[11] Liu Y, Nguyen J, Steele T, Merkel O, Kissel T. Polymer 2009;50:3895–904.
[12] van de Wetering P, Cherng JY, Talsma H, Hennink WE. J Control Release 1997;49:59–69.
[13] Layman JM, Ramirez SM, Green MD, Long TE. Biomacromolecules 2009;10:1244–52.
[14] De Duve C, De Barsy T, Poole B, Trouet A, Tulkens P, Van Hoof F. Biochem Pharmacol 1974;23:2495–531.
[15] Cho YW, Kim JD, Park K. J Pharm Pharmacol 2003;55:721–34.
[16] Tang RP, Palumbo RN, Nagarajan L, Krogstad E, Wang C. J Control Release 2010;142:229–37.

[17] Brito L, Little S, Langer R, Amiji M. Biomacromolecules 2008;9:1179–87.
[18] Green JJ, Zugates GT, Tedford NC, Huang YH, Griffith LG, Lauffenburger DA, et al. Adv Mater 2007;19:2836–42.
[19] Lu JS, Li NJ, Xu QF, Ge JF, Lu JM, Xia XW. Polymer 2010;51:1709–15.
[20] Knorr V, Russ V, Allmendinger L, Ogris M, Wagner E. Bioconjug Chem 2008;19:1625–34.
[21] Shim MS, Kwon YJ. J Control Release 2009;133:206–13.
[22] Shim MS, Kwon YJ. Biomaterials 2010;31:3404–13.
[23] Boomer JA, Qualls MM, Inerowicz HD, Haynes RH, Patri VS, Kim JM, et al. Bioconjug Chem 2009;20:47–59.
[24] Xu ZH, Gu WW, Chen LL, Gao Y, Zhang ZW, Li YP. Biomacromolecules 2008;9:3119–26.
[25] Heller J, Barr J, Ng SY, Abdellauoi KS, Gurny R. Adv Drug Deliv Rev 2002;54:1015–39.
[26] Heller J, Barr J. Biomacromolecules 2004;5:1625–32.
[27] Tang RP, Palumbo RN, Ji WH, Wang C. Biomacromolecules 2009;10:722–7.
[28] Wang C, Ge Q, Ting D, Nguyen D, Shen HR, Chen JZ, et al. Nat Mater 2004;3:190–6.
[29] Tang RP, Ji WH, Wang C. Macromol Biosci 2010;10:192–201.
[30] Hwang SJ, Bellocq NC, Davis ME. Bioconjug Chem 2001;12:280–90.
[31] Gonzalez H, Hwang SJ, Davis ME. Bioconjug Chem 1999;10:1068–74.
[32] Savitsky AO, Gasilova ER, Ten'kovtsev AV. Polym Sci Ser A 2009;51:259–68.
[33] Petersen H, Kunath K, Martin AL, Stolnik S, Roberts CJ, Davises MC, et al. Biomacromolecules 2002;3:926–36.
[34] Mosmann T. J Immunol Methods 1983;65:55–63.
[35] Heller J. Adv Polym Sci 1993;107:41–92.
[36] Huang X, Du F, Cheng J, Dong Y, Liang D, Ji S, et al. Macromolecules 2009;42:783–90.
[37] Huang X, Du F, Liang D, Lin SS, Li Z. Macromolecules 2008;41:5433–40.
[38] Oikawa M, Wada A, Okazaki F, Kusumoto S. J Org Chem 1996;61:4469–71.
[39] Jilek S, Merkle HP, Walter E. Adv Drug Deliv Rev 2005;57:377–90.
[40] Manolova V, Flace A, Bauer M, Schwarz K, Saudan P, Bachmann MF. J Immunol 2008;38:1404–13.
[41] Hunter AC. Adv Drug Deliv Rev 2006;58:1523–31.
[42] Hunter AC, Moghimi SM. Biochim Biophys Acta 2010;1797:1203–9.
[43] Kuo JH, Jan MS, Lin YL. J Control Release 2007;120:51–9.
[44] Kuo JH, Chang CH, Lin YL, Wu CJ. Colloids Surf B 2008;64:307–13.
[45] Klionsky DJ. Nat Rev Mol Cell Biol 2007;8:931–7.
[46] Pack D, Hoffman AS, Pun S, Stayton PS. Nat Rev Drug Discov 2005;4:581–93.

Polymer 52 (2011) 933–941

Contents lists available at ScienceDirect

Polymer

journal homepage: www.elsevier.com/locate/polymer

Degradable micelles based on hydrolytically degradable amphiphilic graft copolymers for doxorubicin delivery

Jun Chen [a,e], Malcolm M.Q. Xing [c,d,e,**], Wen Zhong [a,b,*]

[a] Department of Textile Sciences, Faculty of Human Ecology, University of Manitoba, Winnipeg, MB R3T 2N2, Canada
[b] Department of Medical Microbiology, Faculty of Medicine, University of Manitoba, Canada
[c] Department of Mechanical Engineering, University of Manitoba, Canada
[d] Department of Biochemistry and Medical Genetics, University of Manitoba, Canada
[e] Manitoba Institute of Child Health, Canada

ARTICLE INFO

Article history:
Received 21 September 2010
Received in revised form
22 December 2010
Accepted 28 December 2010
Available online 9 January 2011

Keywords:
Degradable micelle
Graft copolymer
Anticancer nanomedicine

ABSTRACT

Micelles based on a low-toxic and hydrolytically degradable poly(β-amino ester)-*g*-octadecyl acrylate (PAE-*g*-ODA) amphiphilic copolymer were developed for doxorubicin (DOX) delivery. A two-step reaction pathway was used to synthesize PAE-*g*-ODA copolymers with poly(ethylene glycol) segments in the backbone via Michael-type addition reaction. Copolymers with various grafting degrees were obtained by tuning the feeding molar ratios of acrylate/formed secondary amine and the grafting reaction time. Among this series of copolymers, PAE-g-ODA-2 (PAE-*g*-ODA with 45% ODA side chains) were found to form spherical micelles with an average size of 72.5 nm, as determined by dynamic light scattering (DLS) and transmission electron microscope (TEM), whereas the other PAE-*g*-ODA copolymers fail to form stable micelles with a narrow size distribution in an aqueous solution. The titration curve illustrated that PAE-g-ODA-2 has a high buffer capacity in the pH range of 7.5–5. The hydrolytic degradation of PAE-g-ODA-2 copolymer in PBS buffer (pH 7.4, 37 °C) was monitored by ^{1}H NMR. It was found that up to 70% ester groups in the backbones were hydrolyzed in 48 h. The DOX-loaded micelles release about 70% trapped DOX within 48 h in physiological condition. Cytotoxicity assay showed a low cytotoxicity of PAE-g-ODA-2 micelles as well as a higher inhibition against HepG2 tumor cells of DOX-loaded micelles than free DOX.

1. Introduction

Polymeric micelles self-assembled from amphiphilic block or graft copolymers have been extensively explored as one of the most promising nanosized drug carriers for the controlled release of various hydrophobic anticancer drugs including doxorubicin (DOX) and paclitaxel [1–3]. Drugs incorporated in polymeric micelles exhibit such therapeutic advantages over free drugs as prolonged circulation time by avoiding rapid clearance by the renal and reticuloendothelial system (RES), enhanced drug solubility in water, passive targeting to the tumor tissues via the enhanced permeability and retention (EPR) effect, decreased side effects, and improved drug bioavailability [4–7]. The core-shell structure of the polymer micelles is essential in their pharmaceutical applications. The hydrophobic core of the micelles is usually loaded with a variety of therapeutic or diagnostic agents, while the hydrophilic shell, like a corona, stabilizes the micelles in an aqueous solution. Poly(ethylene glycol), or PEG, is one of the most widely used hydrophilic moieties, because it is highly hydrated, readily water soluble, non-toxic and non-immunogenic [8,9]. In particular, PEG chains can efficiently prevent the interactions of the micelles with serum proteins and cells, avoid particle opsonization, and render them "unrecognizable" by the reticuloendothelial system (RES) in the liver and spleen [10–12].

The kinetics of a drug being released from its carriers may affect their cell-killing efficacy. DOX is an anticancer drug that has been widely used in the treatment of different types of tumors [13,14]. DOX is known to interact with DNA by intercalation and to inhibit the biosynthesis of macromolecules [15,16]. It is crucial, therefore, to deliver DOX into the cytoplasm and/or the cell nucleus.

Poly(β-amino ester)s (PAE), a group of cationic polymers containing amino groups, were originally developed for gene delivery [17–19]. They have been used to condense DNA to form polycation/DNA complexes by electrostatic interaction, and their high buffer capacity facilitates endosomal escape of the polycation/DNA

* Corresponding author. Department of Textile Sciences, Faculty of Human Ecology, University of Manitoba, Canada. Fax: +1 204 4747592.
** Corresponding author. Department of Mechanical Engineering, Faculty of Engineering, University of Manitoba, Canada.
E-mail addresses: xing@cc.umanitoba.ca (M.M.Q. Xing), zhong@cc.umanitoba.ca (W. Zhong).

0032-3861/$ – see front matter © 2011 Elsevier Ltd. All rights reserved.
doi:10.1016/j.polymer.2010.12.056

complexes via the "proton sponge" effect. Recently, PAE-based nanoparticles with positive charges on their surface were reported to promote nanoparticle endocytosis and intracellular delivery of DOX [20–22]. With ester groups in the backbones, the poly(β-amino ester)s were designed to degrade under physiological condition.

Generally, linear poly(β-amino ester) can be prepared by Michael addition polymerizations of diacrylate with secondary bis (amine)s [18]. However, the reactivity of amine groups typically fits the following order: secondary amine (original) > primary amine >> secondary amine (formed) [23,24]. As a result, a reaction between triamine monomers and bisacrylates monomers that are equal in molar masses produces linear polymers. The topology of these polymers can also be controlled by adjusting polymerization temperature. Hong et al. [25] reported that the reactivity of the formed secondary amines can be significantly enhanced by elevating the reacting temperature to 48 °C, when hyperbranched polymers formed.

We herein report a novel approach to synthesize amphiphilic graft copolymers with PEG-based poly(β-amino ester)s in the backbones and octadecyl groups (ODA) in the side chains. The linear poly(β-amino ester)s were synthesized via Michael addition polymerization of *N*-aminoethyl piperazine (AEPZ) and poly (ethylene glycol) diacrylate (PEGDA) at 40 °C. Another Michael addition reaction was then allowed to take place between the ODA and the formed secondary amines in the backbones of the linear poly(PEGDA–AEPZ) (PAE) at a higher temperature (60 °C) to yield ODA-grafted PAE. The degradation behavior of the PAE-*g*-ODA was investigated by a ^{1}H NMR spectrometry. *In vitro* DOX release from DOX-loaded PAE-*g*-ODA micelles were evaluated. MTT assay was used to evaluate the cytotoxicity of PAE-*g*-ODA copolymer.

2. Materials and methods

2.1. Materials

All chemicals were purchased from Sigma–Aldrich Canada Ltd. (Oakville, Ontario, Canada) and used without further purification unless otherwise noted. The 3- (4, 5-dimethyl thiazolyl-2)-2, 5-diphenyl tetrazolium bromide (MTT) cell proliferation assay kits were from Biotium Inc. (Hayward, CA). Dialysis membrane (3.5 kDa MWCO), 0.45 μm Millipore Millex Syringe Filters were purchased from Fisher Scientific (Ottawa, ON, CANADA). Carbon Coated Copper Grids were purchased from Canemco Inc. (Core, Quebec, Canada).

2.2. Instruments

^{1}H NMR spectra were recorded on a Bruker Avance 300 NMR spectrometer (300 MHz) with $CDCl_3$ as the solvent. The UV absorbance was recorded with a Varian Cary-50 UV–vis spectrophotometer. The fluorescence intensity of pyrene was recorded with a Varian Cary Eclipse fluorescence spectrophotometer.

The number average (Mn) and weight average (Mw) molecular weights and polydispersity index (PDI = Mw/Mn) were determined by a Tetrahydrofuran (THF) based gel permeation chromatography (THF GPC), which was conducted on a Waters Chromatography, Inc. (Milford, MA) system equipped with an Waters Alliance HPLC System (Waters 2695 Separation Module), a Waters 2414 Differential Refractometer with temperature control, a Waters 2996 Photodiode Array Detector and a set of four columns (separation range 100–20 K and 1000–10 M). The system was equilibrated at 25 °C in pre-filtered THF, which served as polymer solvent and eluent (flow rate set to 1.00 ml/min). Polymer solutions were prepared at concentrations of 3 mg/ml and an injection volume of 100 μL was used. Data collection and analysis were performed with Empower Pro software. The system was calibrated with polystyrene standards (Polymer Laboratories, Amherst, MA).

Images of the micelles were taken by a Joel 1010 TEM (Transmission Electron Microscope) at 60 kV using a LaB6 filament and recorded using an AMT digital camera. Micrographs were collected at 60,000× magnifications. Hydrodynamic diameters (D_h) and size distributions were determined by a Malvern Zetasizer Nano-S dynamic light scattering (DLS) system (Malvern Instruments Ltd. Worcestershire, UK). Measurements were conducted at room temperature.

2.3. Synthesis and characterization of PAE-g-ODA copolymers

The graft copolymer PAE-*g*-ODA was typically synthesized as follows: PEG diacrylate (PEGDA) (302 mg, 1.0 mmol) and AEPZ (129 mg, 1 mmol) were added into a 20 ml borosilicate vial containing a magnetic stirrer bar, and 5 ml DMSO was added to dissolve the mixture into a clear solution. The reaction lasted for 3 days at 40 °C to yield poly(β-amino ester) (PAE) precursor (310 mg, yield: 72%). ^{1}H NMR (ppm): δ 2.40–2.60 (−C**H$_2$**COO−), 2.60–2.80 (−C**H$_2$**N(CH$_2$)$_2$−) 2.90–3.00 (−C**H$_2$**NHCH$_2$−), 3.60–3.8 (−C**H$_2$**OC**H$_2$**−), 4.2–4.3 (4H, −COOC**H$_2$**CH$_2$O−). Mn = 10.8 × 10^3 g/mol, Mw = 14.1 × 10^3 g/mol, PDI = 1.30.

ODA (649 mg, 2.0 mmol) was then added and 5 ml chloroform was also added to increase the solubility of ODA in the reaction solution. The graft reaction was performed at 60 °C for predetermined time. The mixture was precipitated in a large excess amount of cold diethyl ether, then in cold hexane and finally dried in vacuum for 2 days. The typical yielding of the copolymer was about 60%. ^{1}H NMR (ppm): δ 0.80–0.90 (−CH$_2$(CH$_2$)$_{15}$C**H$_3$**), 1.20–1.40 (−CH$_2$(C**H$_2$**)$_{15}$CH$_3$), 1.60–1.70 (−C**H$_2$**(CH$_2$)$_{15}$CH$_3$), 2.40–2.60 (−C**H$_2$**COO−), 2.60–2.80 (−C**H$_2$**N(CH$_2$)$_2$−) 2.90–3.00 (−C**H$_2$**NHCH$_2$−), 3.60–3.8 (−C**H$_2$**OC**H$_2$**−), 4.0–4.1 (−COOC**H$_2$**(CH$_2$)$_{16}$CH$_3$), 4.2–4.3 (4H, −COOC**H$_2$**CH$_2$O−).

2.4. Titration of PAE-g-ODA copolymers

The buffer capacity of copolymer was monitored by means of titrations as follows: the PAE-*g*-ODA-2 or branched PEI (Mw = 25 KDa) was dissolved in distilled water at a concentration of 2 mg/ml. The solution was titrated with a 0.1 M HCl aqueous solution at an increment of 10 μl. The pH decreases of the solution were monitored with a pH meter at room temperature. The buffer capacity of the polymers can be defined as the percentage of the amine groups which were protonated in the pH range of 7.5–5. The equation (Equation (1)) to calculate the buffer capacity of the polymers was [26,27]:

$$\text{Buffer Capacity}\ (\%) = V(\text{HCl}) \times 0.1\text{M}/N\ \text{mol} \times 100\% \quad (1)$$

here, V is volume of the 0.1 M HCl added into the polymer solution; N is the total molar amount of amine groups in the polymer solution.

2.5. In vitro hydrolysis of PAE-g-ODA copolymer

The hydrolytic degradation of PAE-*g*-ODA-2 copolymer in physiological conditions was monitored by ^{1}H NMR. In brief, PAE-*g*-ODA-2 was dispersed in a PBS (pH 7.4, 0.1 M) at a concentration of 25 mg/ml. A vial containing such a degradation solution was placed in a shaking bath at 37 °C, 80 rpm. At predeterminated time, 200 μl buffer was taken out and freeze-dried. The percentage of residual ester groups in the backbones of the degraded copolymer to that of the original copolymers can be calculated from the Equation:

$$x(\%) = I4.20/(I4.20 + I3.6) \times 4 \times 100$$

where x represents the percentage of residual ester groups in reference to the original polymers, $I_{4.20}$ and $I_{3.6}$ represent the integrals at δ4.20 and δ3.60 respectively.

2.6. Preparation and characterization of PAE-g-ODA micelles

The PAE-g-ODA micelles were prepared using the dialysis method. PAE-g-ODA copolymer (20 mg) was dissolved in 2 ml of THF while being stirred. 10 ml distilled water was added dropwise, and constantly stirred. The solution was then dialyzed against water for 24 h (molecular weight cutoff = 3500) to form the micelles.

The critical micelle concentration (CMC) of the graft copolymer in water was monitored by fluorescence spectroscopy using pyrene as a probe. 20 μl of pyrene acetone solution (20 μg/ml) were added to 4 ml vials, and acetone was then allowed to evaporate to dry. 4 ml of aqueous solution containing 0.1–128 mg/l of PAE-g-ODA copolymers were added to the vials, respectively. The final concentration of pyrene in each sample solution was 0.1 μg/ml. The excitation spectra (300–360 nm) of the solutions were recorded as emission wavelength of 395 nm with the excitation and emission bandwidths set at 5 nm. The ratios of the peak intensities at 338 nm over 334 nm ($I338/I334$) of the excitation spectra were recorded and plotted versus polymer concentration. The CMC value was taken from the intersection points of the tangent to the curve at the high concentrations with the horizontal line through the point at the low concentrations.

Hydrodynamic diameter and size distribution of the micelles were determined by dynamic light scattering (DLS). Measurements were carried out at 20 °C using Zetasizer Nano-S from Malvern Instruments. Solution of the micelles (250 mg/l) was passed through a 0.45 μm pore size filter prior to measurement. The morphology of micelles was examined by transmission electron microscope (TEM). The digital images were taken by Joel 1010 TEM at 60 kV using a LaB6 filament and recorded using an AMT digital camera. The TEM samples were prepared as follows: a drop of the isolated micelle solution was dropcast on a carbon coated copper grid (400-mesh) and dried in air. Then 2% (w/v) of uranyl acetate solution was dropped on the grid and was allowed to be in contact with the micelles for 1 min before excess liquid was removed using a filter paper. The grid is dried in air for 1 h before microscope observation. The average diameters of the particles were averaged from the measurements of 10 different particles in the TEM micrographs.

2.7. Preparation of DOX-loaded PAE-g-ODA-2 copolymer micelles

DOX-loaded micelles of PAE-g-ODA-2 graft copolymer were prepared as follows: Briefly, 1 mg of DOX was dissolved in 5 ml THF and mixed with 1.5 equiv of triethylamine. Then 10 mg of PAE-g-ODA-2 graft copolymer was added into the solution, which was stirred for 60 min. 5 ml distilled water was added dropwise with vigorous stirring. The dispersed DOX-loaded polymeric micelles were dialyzed against distilled water (molecular weight cutoff = 3500) for 24 h to remove free DOX and byproducts. Finally, the DOX-loaded micelles were lyophilized into a red solid. The drug loading efficiency of the DOX-loaded polymeric micelles was determined by dissolving them in THF and quantifying the amount of loaded DOX using a UV–vis spectroscopy, referring to its absorbance at 480 nm. To determine the drug loading content, DOX-loaded micelles were dissolved in THF and analyzed using a fluorescence spectroscopy.

Drug loading content and drug loading efficiency were calculated according to the following equations (Equation (3):

$$\text{Drug loading content} = (\text{weight of loaded drug/weight of copolymer}) \times 100\%$$

$$\text{Drug loading efficiency} = (\text{weight of loaded drug/weight of feeding drug}) \times 100\%$$

2.8. In vitro DOX release of PAE-g-ODA-2 copolymeric micelles

Dispersed DOX-loaded polymeric micelles were added to a dialysis membrane tube (molecular weight cutoff = 3500), which was then incubated in 30 ml phosphate buffer saline at pH 7.4 at 37 °C in a water bath with a shaking rate at 80 rpm. At predetermined frequencies, 6 ml incubated solution was taken out and 6 ml fresh PBS was added to refill the incubation solution to 30 ml. DOX release profiles were determined by measuring the UV–vis absorbance of the solutions at 480 nm.

2.9. Cytotoxicity of DOX-loaded PAE-g-ODA-2 micelles

Hepatoma cells (HepG2) were used to investigate cell inhibition of DOX-loaded nanoparticles. HepG2 cells were obtained from the American Type Culture Collection and cultured with Dulbecco's modified Eagle's medium (DMEM, GIBCO) supplemented with 10% fetal bovine serum (FBS, GIBCO), 1.0×10^5 U/l penicillin (Sigma) and 100 mg/l streptomycin (Sigma) at 37 °C in 5% CO_2.

The cytotoxicity of the PAE-g-ODA-2 micelles loaded with DOX was determined using an MTT assay. HepG2 cells were seeded into a 96-well tissue culture plate at a density of 8000 cells/well and were incubated at 37 °C in 5% CO_2. The growth medium was replaced with fresh DMEM after 24 h. Then the DOX-loaded PAE-g-ODA-2 polymeric micelle solution and controls (free DOX and blank micelle solutions) were added into wells (six wells per sample). After 48 h of incubation, 10 μL MTT solution was added to each well and incubation was continued for another 4 h. The medium was removed and 200 μL DMSO was added into each well to dissolve the formazan by pipetting up and down for several times. The absorbance of each well was measured using an ELISA plate reader at a test wavelength of 570 nm and a reference wavelength of 630 nm. The cell inhibition of the samples was calculated as Equation (4):

$$\text{Cell inhibition}(\%) = \frac{I_{control} - I_{\text{sample}}}{I_{\text{control}}} \times 100\%$$

where I_{sample} and I_{control} represent the intensity determined for cells treated with different samples and for control cells (untreated), respectively.

3. Results and discussion

3.1. Synthesis and characterization of PAE-g-ODA graft copolymers

The Michael addition polymerization of triamines (AEPZ) and acrylate (PEGDA) in equimolar quantities was performed in DMSO. In Michael-type polymerization, the reactivity of amine groups to acrylate groups was known to follow the sequence of secondary amine (original) > primary amine >> secondary amine (formed) [24]. For example, AEPZ contains one secondary amine (original) and one primary amine, in which the secondary amines (original) have a higher reactivity than the primary amines. This is due to the

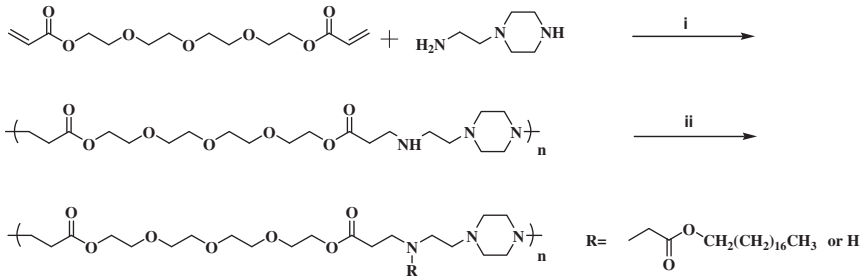

Scheme 1. Synthetic pathway for PAE-g-ODA series polymers. (i) DMSO, 40 °C, 3 days; (ii) Chloroform, Octadecyl acrylate, 60 °C, predeterminated time.

Table 1
The grafting reaction conditions and results of graft copolymers.

Sample	Temperature[a] (°C)	Time[a] (h)	Feed ratio[b]	Yield	Graft degree[c]
PAE-g-ODA-1	60	24	2/1	74%	24%
PAE-g-ODA-2	60	72	2/1	66%	45%
PAE-g-ODA-3	60	168	2/1	32%	85%
PAE-g-ODA-4	60	72	1/1	71%	27%

[a] The temperature and time for grafting reaction.
[b] The molar ratio between ODA and AEPZ.
[c] GD = *I*4.08 × 2/*I*4.2 × 100%.

steric hindrance of cyclic aliphatic rings on the secondary amines (original) of AEPZ is much lower than both the primary amine and formed secondary amine, and the inductive effect of aliphatic substituent on the nitrogen atoms increases their electron density. Meanwhile, the high steric hindrance of polymer chains leads to the lowest reactivity of the secondary amine (formed). As a result, for the formed secondary amines, there is little opportunity to participate in the reaction at equal feed molar ratio of diacrylate/AEPZ. In addition, the topology of these polymers can be also controlled by adjusting the polymerization temperature as shown by Hong et al. [25], who reported that the relative reactivity of the formed secondary amines is significantly enhanced by elevating reaction temperature to above 48 °C, when hyperbranched polymers are formed. Therefore, linear poly(β-amino ester)s containing secondary and tertiary amines in the backbones can be obtained from a Michael addition polymerizations of AEPZ and PEGDA in equimolar quantities in a relatively low temperature (Scheme 1).

To our knowledge, there has been little reported work on graft polymers formed via a synthesis by Michael addition of acrylate to secondary amine (formed). Such reaction is therefore studied in our work for the preparation of graft copolymers. A typical grafting reaction of poly(PEGDA–AEPZ) proceeds according to Scheme 1. The reaction between linear poly(PEGDA–AEPZ) and ODA were carried out in DMSO/chloroform ($v/v = 1$), in which chloroform was added to increase the solubility of ODA in the reaction mixtures. The reaction conditions and results are listed in Table 1. To determine the grafting degree of the copolymers, the reaction was followed by ^{1}H NMR measurements. The ^{1}H NMR spectra of four

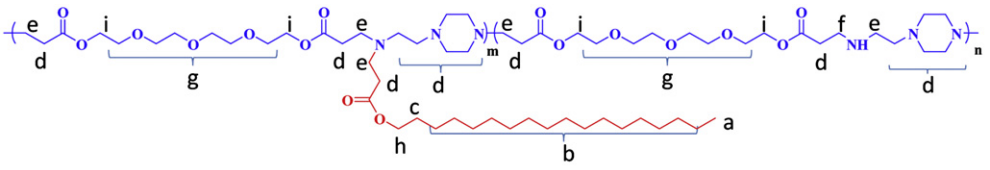

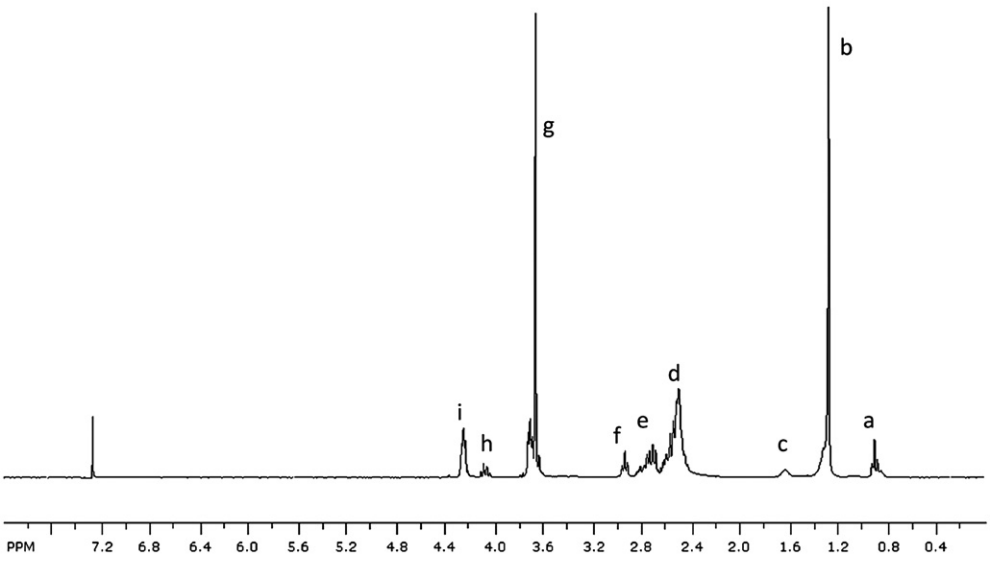

Fig. 1. Typical ^{1}H NMR spectrum (300 MHz, CDCl3) of PAE-g-ODA-2.

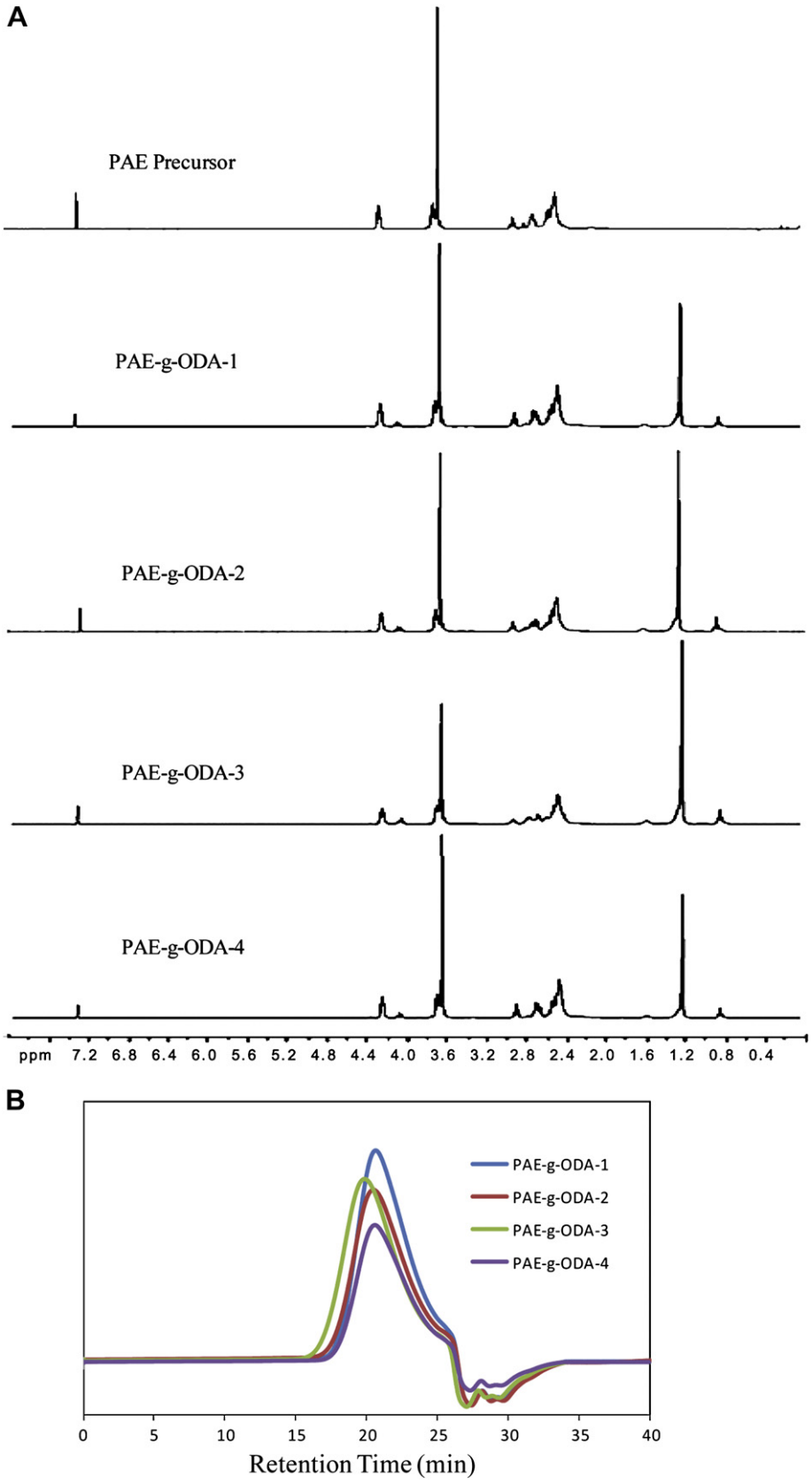

Fig. 2. (A) The ^{1}H NMR spectra of PAE precursor and PAE-*g*-ODA series copolymers series polymers. (B) The GPC traces of PAE-*g*-ODA series copolymers.

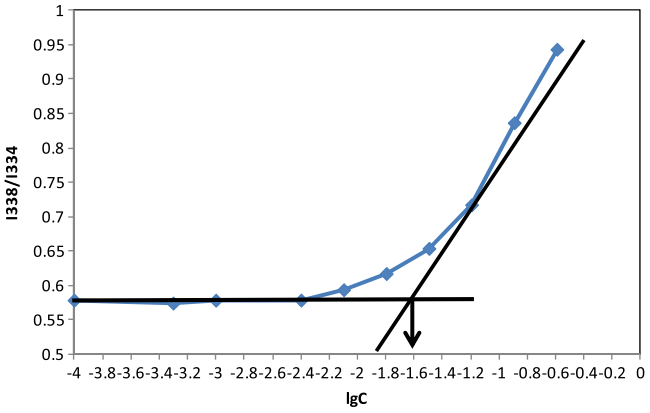

Fig. 3. The critical micelle concentration as a function of PAE-g-ODA-2 concentration in PBS buffer (pH = 7.4, 0.1 M).

Table 2
Characterization of PAE-*g*-ODA series copolymers and micelles.

Sample	Mna ($\times 10^3$)	PDI[a]	Theoretical Mn[b] ($\times 10^3$)	CMC[c] (mg/l)	Size[d] (nm)	PI[d]
PAE-g-ODA-1	12.6	2.2	12.8	45	516.0	0.280
PAE-g-ODA-2	13.8	2.6	14.7	25	72.5	0.146
PAE-g-ODA-3	25.9	2.9	18.0	25	19.5	0.675
PAE-g-ODA-4	13.6	2.1	13.1	32	326.4	0.359

[a] Determined by GPC (THF as the eluent, 1.0 mL/min, 30 °C, polystyrene standards).
[b] Calculated from the Mn of PAE precursor and grafting degree data via ^{1}H NMR determination.
[c] Determined using pyrene as a fluorescence probe.
[d] Size and PI (size polydispersity index) of micelles and DOX-loaded micelles were determined by DLS.

grafting copolymers, poly(PEGDA–AEPZ)-*g*-ODA with different ODA contents, are shown in Figs. 1 and 2. The two typical peaks of δ4.08 and δ4.20 in the spectra were attributed to the protons of methylene groups adjacent to the ester groups in the ODA chains and that of methylene groups adjacent to the ester groups in the backbones, respectively. Accordingly, the grafting degrees (GD) of the copolymers can be calculated based on ^{1}H NMR data according to Equation. (5):

$$GD = I4.08\times 2/I4.2\times 100\% \quad (5)$$

Different reaction times and feeding ratios of poly(PEGDA–AEPZ) to ODA were used in the preparation of the graft copolymers. As shown in Table 1, the grafting degree of copolymer was found to increase with the increase of reaction time; the degree of grafting was 24% in 24 h, while it reached 85% in 72 h. In addition, the higher molar ratio of ODA to poly(PEGDA–AEPZ) results in the higher graft degree in the same reaction time. However, it was found that the yield of the graft copolymer decreases as the graft degree of copolymers increases. A possible reason could be that copolymers with a higher percentage of ODA are more difficult to be precipitated out in the excess of diethyl ether as compared to the copolymers with a lower percentage of ODA.

The CMC of the PAE-*g*-ODA copolymers was monitored by a fluorescence spectrometry using pyrene as a probe. Pyrene has been widely used as a hydrophobic fluorescence probe for micelle formation, in which, the ratio *I*338/*I*334, defined as the intensity of the first vibrational band relative to the third vibrational band, can be used as an index of micelle hydrophobicity [28]. As shown in Fig. 3, the CMC value was defined as the concentration corresponding to crossing point of the tangent to the curve with the horizontal tangent through the point at the low concentrations. The CMC values of the four copolymers were listed in Table 2. The CMC of PAE-*g*-ODA-2 was about 25 mg/l, indicating that a stable core-shell structure remains in such a low concentration.

According to the "proton sponge hypothesis" suggested by Behr et al. [29], the buffer capacity of a polycation at a low pH may play an important role in facilitating endosomal escape of polycation/DNA complexes. This feature can be also used to facilitate drug-loaded nanoparticles breaking through the endosomal membrane to release the drug into cytosol. The inhibition of DOX against tumor cells is known to be realized by interacting with DNA by intercalation and prohibiting macromolecules biosynthesis [16]. It is crucial, therefore, to deliver DOX into the cytoplasm and/or nucleus of the cells. The precise pH value of a polymer solution was monitored for adding different concentrations of H^+ to determine the buffer capacity of this kind of polycations. After titration by adding 0.1 M HCl, the titration curve of copolymers was shown in the range of pH 4–8 (Fig. 4A). In Fig. 4B, the titration curves of copolymer and branched bPEI 25 KDa were compared in the range of pH 5–7.5. Calculating from the Equation (1), the results showed that PAE-*g*-ODA-2 had 40% protonation compared with 24% protonation of bPEI 25 KDa, which indicated the higher buffer capacity of PAE-*g*-ODA-2 copolymer in the pH range of 5–7.5. According to the 'proton sponge' hypothesis, the high buffer capacity between pH = 5–7.5 may play an important role in endosomal escape and consequently contribute to the high delivery efficacy of loaded cargos.

The hydrolytic degradation kinetics of PAE-*g*-ODA-2 at 37 °C was monitored using ^{1}H NMR. As shown in Fig. 5A, when the hydrolytic degradation of ester groups in the backbone of poly(β-amino ester) occurred, the integral at δ4.20 attributed to the methylene protons adjacent to the ester groups, gradually decreased and the integral at δ3.60 gradually increased. And the content of residual ester groups in reference to the original copolymer can be calculated by comparing the integrals of signal at δ4.20 attributed to the methylene protons

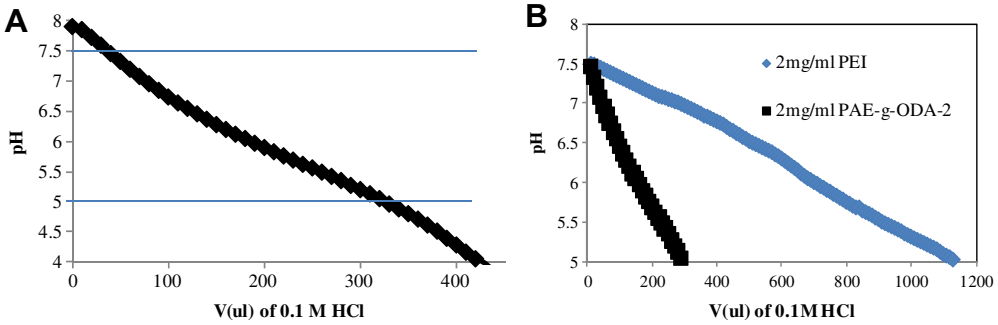

Fig. 4. (A) The titration curve of PAE-g-ODA-2. A solution of copolymer (2 mg/mL) in water titrated with 0.1 mol/l HCl. (B) The titration curve of PAE-g-ODA-2 (2 mg/ml) and branched PEI (Mw 25 KDa, 2 mg/ml) in the pH of 7.5–5.

adjacent to ester groups with the integrals of signal at δ3.60 attributed to the methylene protons adjacent to the oxygen group (−O-**CH_2**−) and the hydroxyl group (HO**CH_2**−) derived from the hydrolysis of ester groups, which was shown in Equation (2):

$$x(\%) = I4.20/(I4.20 + I3.6)\times 4\times 100 \quad (2)$$

where x represented the percentage of residual ester groups in reference to the original polymers, $I_{4.20}$ and $I_{3.6}$ represented the integrals at δ4.20 and δ3.60 respectively.

The degradation curve of PAE-g-ODA-2 in PBS at pH 7.4 was shown in Fig. 5B. The degradation was fast in the first 6 h with a 50% loss of ester groups, while it slowed down during the following 42 h with another 15% loss of ester groups. The fast degradation of the ester groups in the backbones may result from the good hydrophilicity of the PEG-based poly(β-amino ester)s [18]. Based on this result, it can be predicted that the micelles would undergo a fast degradation and thereby release the loading cargos when copolymeric micelles were utilized in physiological condition.

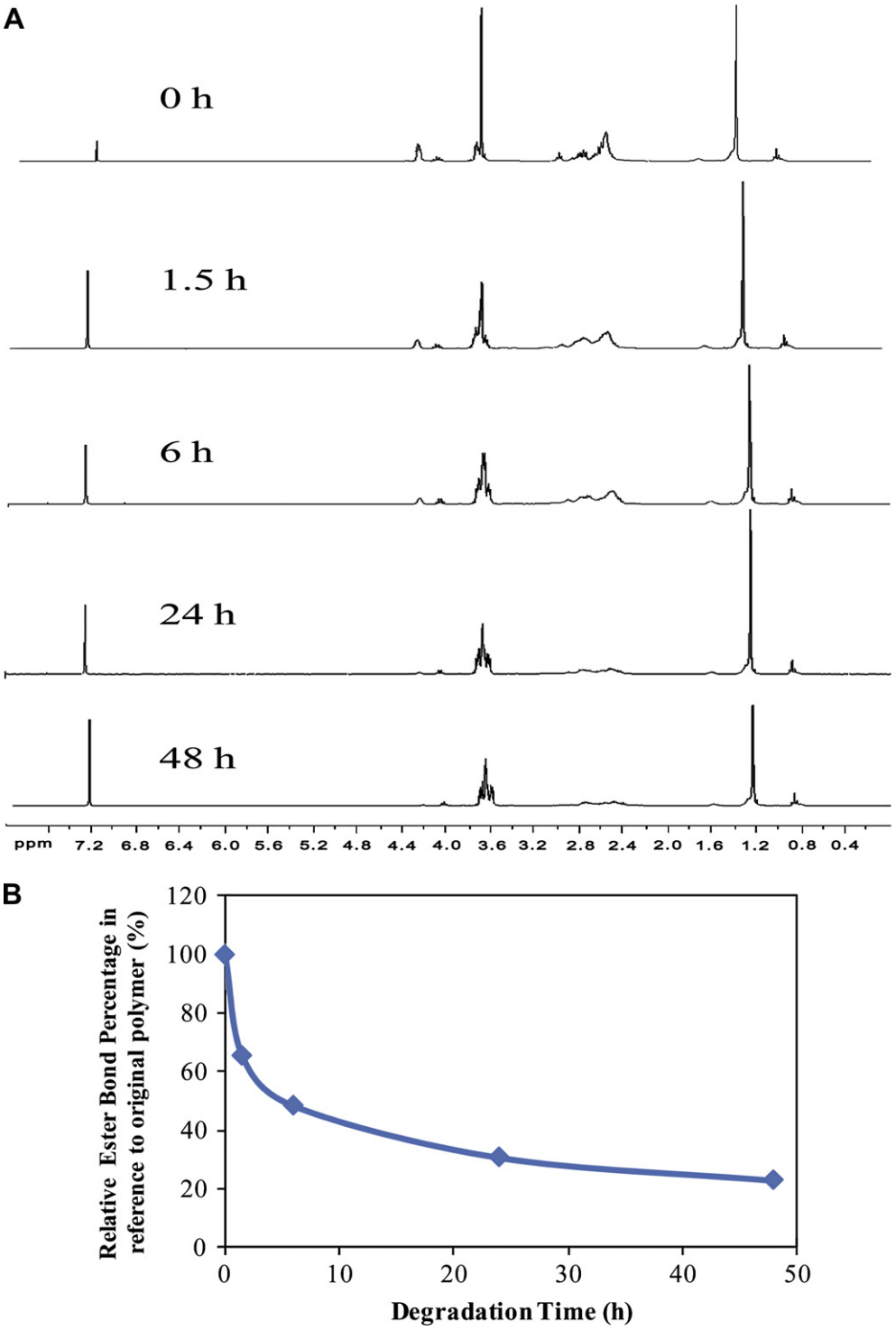

Fig. 5. A) The ^{1}H NMR spectra of PAE-g-ODA-2 degraded in phosphate buffer (0.1 M, pH 7.4) in different degradation time. (B) The residual ester groups percentage of PAE-g-ODA-2 at 37 °C in PBS buffer at pH 7.4.

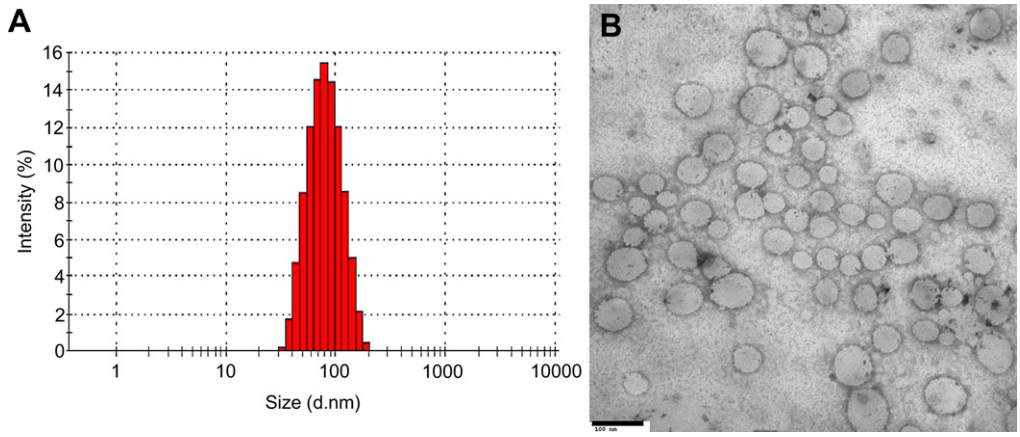

Fig. 6. (A) The micelles size and size distribution determined by DLS. (B) The TEM micrograph of PAE-g-ODA-2 in water solution.

3.2. Characterization of blank and DOX-loaded PAE-g-ODA copolymeric micelles

According to dynamic light scattering (DLS) measurement, the average diameter of the blank PAE-g-ODA-2 copolymeric micelles in an aqueous solution was about 72.5 nm with a polydispersity index of 0.146 (Fig. 6A). The DLS graph showed a monodial distribution of PAE-g-ODA-2 copolymeric micelles in aqueous solution. TEM micrograph revealed that the blank micelles had spherical morphology (Fig. 6B) with an average size of about 64 nm. TEM micrograph gives a smaller size of the micelles as compared to DLS, probably due to the shrinkage of the PEG shell when being dried. These results indicate that the copolymeric micelles were well dispersed in aqueous medium and were given homogeneous nanosized micelle structures. The PEG segments in the PAE-g-ODA-2 backbones can efficiently shield the positive charges of the backbones and stabilize the micelles in the dispersion solutions. As to the other PAE-g-ODA copolymers with different densities of ODA chains, however, their micelles sizes were larger or more widely distributed, indicating defected or unstable core-shell structures of the nanoparticles in aqueous media. The structure of the micelles may be affected by the ratio between the length of the hydrophilicity moiety to that of the hydrophobicity moiety [30]. It can be concluded that when the molecular weight ratio of the hydrophobic moiety is around 40% of the copolymer, stable micelles could form in an aqueous medium.

Dialysis method was used to prepare DOX-loaded PAE-g-ODA copolymeric micelles. The designated drug loading content was set at 10 wt%. The results showed that the drug loading efficiencies were approximately 35% for the polymeric micelles. The size of DOX-loaded micelles was about 126 nm as determined by DLS. The increased average size of the DOX-loaded copolymeric micelles, as compared to blank micelles, may be caused by the drug molecules that have got entrapped in the hydrophobic cores.

3.3. In vitro DOX release from the PAE-g-ODA-2 copolymeric micelles

The profiles of DOX release from the PAE-g-ODA-2 copolymeric micelles were investigated using the dialysis method. In predetermined interval, 6 ml incubated solution was taken out from 30 ml incubation solution and 6 ml fresh buffer solution was added to refill the incubation volume to 30 ml. The solutions taken out at different time intervals were examined under a UV–vis spectrometer at 480 nm, which is the characteristic absorbance of DOX. As shown in Fig. 7, in PBS at pH 7.4, there was a release of about 30% of the incorporated DOX within the first 6 h, followed by a very slow release of DOX from the micelles in the next 42 h. This result was in accordance with the degradation profile of the polymer backbones, which underwent a fast degradation in the first 6 h and a relatively slower degradation in the following 42 h. DOX diffused out of the core quickly in the first 6 h probably due to the collapse of the micelles via quick degradation of the hydrophilic shell. Then the degradation rate of the hydrophilic backbones decreased, the drug

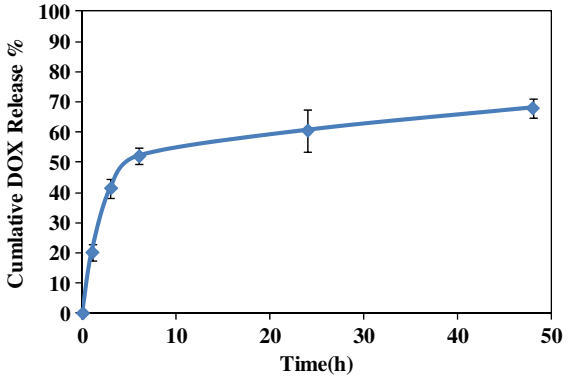

Fig. 7. The DOX release from PAE-g-ODA-2-Dox micelles in PBS (pH = 7.4, 0.1 M).

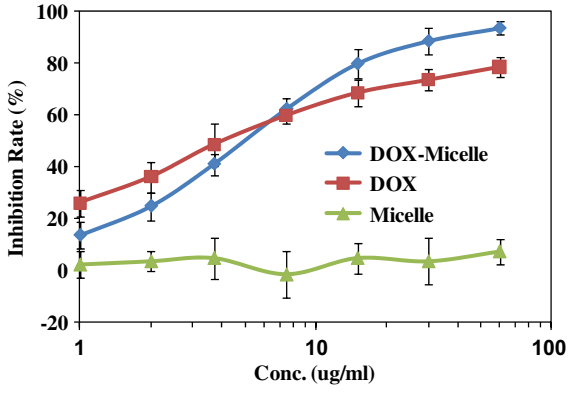

Fig. 8. The cytotoxicity of free DOX, PAE-g-ODA-2 copolymeric micelles and DOX-loaded PAE-g-ODA-2 copolymeric micelles as a function of DOX concentration.

release also slowed down. After 48 h, about 65% DOX were released from the micelles, while the rest 35% DOX may be entrapped in the aggregations formed by the degradation products of the copolymers, and therefore are released in a much lower rate. Compared with degradation data in Fig. 5, up to 80% ester groups in the backbones were hydrolyzed in 48 h in PBS. However, in Fig. 7, the release rate was only 65% after 48 h. One possibility is that after degradation of ester groups in the copolymer up to 80%, the 20% residual oligomers and even the hydrolyzed fragments still have the amphiphilic structure which leads to the possibility of forming some kind of loose core-shell structure. Thus a small amount of hydrophobic drug will stay in the hydrophobic part and exhibit a very slow diffusion.

3.4. Cytotoxicity of DOX-loaded PAE-g-ODA-2 micelles

Cytotoxicity of the DOX-loaded micelles to HepG2 cells as a function of the drug dose was determined using an MTT assay. As shown in Fig. 8, PAE-*g*-ODA-2 showed low cytotoxicity to HepG2 cells, probably due to the PEG-based poly(β-amino ester) backbones. The PEG repeat units in the backbones are non-toxic and can dramatically shield the positive charges of the amine groups in the backbones. Furthermore, their quick degradations into small molecules can result in a lower cytotoxicity as well. DOX-loaded micelles were found to have higher cytotoxicity against the tumor cells than free DOX in high doses.

4. Conclusion

PEG-based poly(β-amino ester)-graft-octadecyl acrylate (PAE-*g*-ODA) co-polymers were successfully synthesized in this study. Two-step reaction pathway was used to synthesize the graft copolymer. The grafting degree in graft copolymers can be easily controlled by tuning the feeding molar ratios of acrylate/formed secondary amine and the reaction time. PAE-*g*-ODA-2 can efficiently form spherical micelles with an average diameter of 72.5 nm in water. This micelle showed a high buffer capacity in the pH range from 7.5 to 5 and illustrated a fast degradation in the physiological condition. The cell inhibition of the DOX-loaded micelles was higher than that of free DOX in high doses while the micelles itself showed very low cytotoxicity. All these data suggested that these degradable micelles self-assembled by PAE-*g*-ODA graft copolymer could be a potential anticancer drug nanocarrier.

Acknowledgment

Our work is supported by the NSERC (Natural Sciences and Engineering Research Council of Canada) Discovery Grant and NSERC RTI (Research Tools and Instrument) Grant. We thank Dr. J. Stetefeld for DLS measurement performed at the Department of Chemistry of UM.

References

[1] Rosler A, Vandermeulen GWM, Klok H-A. Adv Drug Delivery Rev 2001;53(1):95–108.
[2] Kataoka K, Harada A, Nagasaki Y. Adv Drug Delivery Rev 2001;47(1):113–31.
[3] Kwon GS, Forrest ML. Drug Dev Res 2006;67(1):15–22.
[4] Maeda H, Wu J, Sawa T, Matsumura Y, Hori K. J Control Release 2000;65(1–2):271–84.
[5] Nayak S, Lyon LA. Angew Chem Int Ed 2005;44(47):7686–708.
[6] Torchilin VP. Pharm Res 2007;24(1):1–16.
[7] Maeda H. Adv Enzyme Regul 2001;41(1):189–207.
[8] Kwon GS, Kataoka K. Adv Drug Delivery Rev 1995;16(2–3):295–309.
[9] Tobío M, Gref R, Sánchez A, Langer R, Alonso MJ. Pharm Res 1998;15(2):270–5.
[10] Jeon SI, Lee JH, Andrade JD, Degennes PG. J Colloid Interface Sci 1991;142(1):149–58.
[11] Jeon SI, Andrade JD. J Colloid Interface Sci 1991;142(1):159–66.
[12] Otsuka H, Nagasaki Y, Kataoka K. Curr Opin Colloid Interface Sci 2001;6(1):3–10.
[13] Matsumura Y, Hamaguchi T, Ura T, Muro K, Yamada Y, Shimada Y, et al. Br J Cancer 2004;91(10):1775–81.
[14] Lee ES, Na K, Bae YH. J Control Release 2005;103(2):405–18.
[15] Gewirtz DA. Biochem Pharmacol 1999;57(7):727–41.
[16] Momparler RL, Karon M, Siegel SE, Avila F. Cancer Res 1976;36(8):2891–5.
[17] Lynn DM, Amiji MM, Langer R. Angew Chem Int Ed 2001;40(9):1707–10.
[18] Lynn DM, Langer R. J Am Chem Soc 2000;122(44):10761–8.
[19] Chen J, Huang SW, Liu M, Zhuo RX. Polymer 2007;48(3):675–81.
[20] Shen Y, Tang H, Zhan Y, Van Kirk EA, Murdoch WJ. Nanomedicine NBM 2009;5(2):192–201.
[21] Kim MS, Hwang SJ, Han JK, Choi EK, Park HJ, Kim JS, et al. Macromol Rapid Commun 2006;27(6):447–51.
[22] Ko J, Park K, Kim Y-S, Kim MS, Han JK, Kim K, et al. J Control Release 2007;123(2):109–15.
[23] Wang D, Liu Y, Hong CY, Pan CY. J Polym Sci A Polym Chem 2005;43(21):5127–37.
[24] Wu DC, Liu Y, Chen L, He CB, Chung TS, Goh SH. Macromolecules 2005;38(13):5519–25.
[25] Hong CY, You YZ, Wu DC, Liu Y, Pan CY. J Am Chem Soc 2007;129(17):5354–5.
[26] Lin C, Zhong ZY, Lok MC, Jiang XL, Hennink WE, Feijen J, et al. Bioconjug Chem 2007;18(1):138–45.
[27] Ou M, Wang XL, Xu RZ, Chang CW, Bull DA, Kim SW. Bioconjug Chem 2008;19(3):626–33.
[28] Astafieva I, Zhong XF, Eisenberg A. Macromolecules 1993;26(26):7339–52.
[29] Boussif O, Lezoualch F, Zanta MA, Mergny MD, Scherman D, Demeneix B, et al. Proc Natl Acad Sci U S A 1995;92(16):7297–301.
[30] Allen C, Maysinger D, Eisenberg A. Colloids Surf B Biointerfaces 1999;16(1–4):3–27.

Polymer 52 (2011) 942–948

Contents lists available at ScienceDirect

Polymer

journal homepage: www.elsevier.com/locate/polymer

Polymer particles with a pomegranate-like internal structure via micro-dispersive polymerization in a geometrically confined reaction space I. Experimental study

Carla V. Luciani, Kyu Yong Choi*, Joong Jin Han, Yunju Jung

Department of Chemical and Biomolecular Engineering, University of Maryland, College Park, MD 20742, USA

ARTICLE INFO

Article history:
Received 8 November 2010
Received in revised form
16 December 2010
Accepted 23 December 2010
Available online 4 January 2011

Keywords:
Suspension polymerization
Dispersion polymerization
Poly(methyl methacrylate)

ABSTRACT

The synthesis of micron-sized polymer particles with a core-shell pomegranate-like morphology is presented. The proposed polymerization technique takes advantage of a reaction-induced micro-phase separation within a suspended organic liquid droplet containing monomer, a chemical initiator, a steric stabilizer, and a poor solvent for the polymer. With an increase in monomer conversion, the monomer droplet suspended in a continuous aqueous medium is transformed first into a micro-capsule with a thick pericellular membrane, and eventually into a polymer particle packed with 300–500 nm polymer sub-particles. The experimentally observed evolution of particle morphology indicates that the reaction pathway is strongly influenced by micro-phase separation and transport phenomena. In the first stage of polymerization, a pseudo-homogeneous polymerization takes place at the droplet surface, followed by a starved macro-dispersive polymerization in the inner region where polymer precipitates out from the solvent phase as nano-sized sub-particles.

1. Introduction

The preparation of polymer particles with complex internal morphologies such as core-shell, single-hollow, and multi-hollow has been the subject of active research in recent years because of the broad impact of such particles in both scientific and industrial fields. Some notable applications of these particles include micro-encapsulation, protection of biologically active materials, thermal insulation, hiding agents for coatings, sensors, floating materials, and temperature-responsive materials [1–10]. Currently, most of these polymer particles or precursors with complex internal structures are synthesized by emulsion polymerization or one of its variations (*i.e.*, dynamic swelling method, interfacial polymerization, colloidosome method, polymerization with functionalized silica-template and post-reaction etching, layer-by-layer assembly, etc.) [11–16].

Emulsion polymerization is a facile method to synthesize sub-micron sized particles of various morphologies. However, there are also growing interests in producing polymer particles with complex internal morphologies in the supra-micron size range. For instance, poly(methyl methacrylate) (PMMA) particles of 5–50 μm with multiple internal cavities can be used in light diffusing films for high luminance in the backlight unit (BLU) of a liquid crystal display (LCD) device. In a conventional BLU, a light diffusing film is made of polyester coated with layers of solid PMMA particles [17]. Micron-sized polymer particles with multiple internal cavities are more effective than conventional solid particles because they offer an increased light diffraction path length for the same or even smaller particle layer thickness. For the encapsulation of voluminous pathogens such as *salmonella*, polymer particles that can provide a sufficiently large space (*e.g.*, tens of microns) are also needed [18]. To prepare such micron-sized polymer particles of complex internal morphologies, synthetic methods other than emulsion polymerization are needed.

Suspension polymerization is generally used to produce solid polymer particles of 10–100 μm or even larger. In suspension polymerization, the size of monomer droplets is essentially determined by the mechanical agitation and the type and concentration of suspension stabilizers. However, suspension polymerization of certain monomers that accompanies the precipitation of polymer particles yields some interesting particle morphologies. For instance, the suspension polymerization of vinyl chloride in presence of a primary steric stabilizer and a moderate agitation produces unicellular PVC grains [19]. Due to the insolubility of poly (vinyl chloride) (PVC) in its monomer, polymer chains precipitate inside the suspended micro-droplets when reaching a chain length of about 20 repeating units. These precipitating chains form unstable nano-domains that eventually aggregate to produce primary particle nuclei of about 100 nm [20]. In the last stages of the polymerization, nuclei also aggregate to produce a complex multi-porous structure inside the suspended droplets. A primary stabilizer is used to prevent the agglomeration of droplets, whereas

* Corresponding author. Tel.: +1 301 405 1907; fax: +1 301 405 0523.
E-mail address: choi@umd.edu (K.Y. Choi).

0032-3861/$ – see front matter © 2010 Elsevier Ltd. All rights reserved.
doi:10.1016/j.polymer.2010.12.055

a secondary stabilizer is used to prevent sub-particles agglomeration. Interestingly, PVC grains are usually surrounded by an external pericellular membrane or skin. Several mechanisms have been proposed to explain the skin formation including grafting reactions onto the primary suspension stabilizer, aggregation of sub-particles at the droplet/water interface, and polymerization of the monomer present in the water phase [19–22].

Recently, our research group has investigated the inverse suspension terpolymerizations of acrylamide, neutralized methacrylic acid, and a crosslinker in a nonpolar hydrocarbon medium to produce polymer particles with complex internal morphologies such as single- and multi-hollow structures [18]. Monomers and crosslinker were dissolved in water prior to prepare the suspension. Since the crosslinking reactions rendered the polymer insoluble in water as the polymerization proceeded, an intra-droplet phase separation was induced at early stages of the polymerization. At the end of the reaction, water was removed from the polymer particles by evaporation, and micron-sized polymer micro-capsules were left behind. Such micro-capsules can be readily used for bio-encapsulation of voluminous virulent pathogens [18].

In this article, we report a modified suspension polymerization of methyl methacrylate (MMA) in the presence of a nonpolar hydrocarbon solvent such as *n*-hexane to produce a novel core-shell pomegranate-like structure. Since the method involves a dispersion polymerization in a confined reaction space (*i.e.*, micron-sized monomer droplet), we call it Micro-Dispersive Polymerization in a Confined Reaction Space (MDPCRS). Unlike PVC, PMMA is completely soluble in its monomer and the intra-droplet phase separation is induced by the addition of the nonpolar hydrocarbon solvent that provides a thermodynamic environment favorable for the sub-particle precipitation. Moreover, the insolubility of polymer chains inside the droplets increases as the polymerization proceeds due to the continuous depletion of the monomer.

2. Experimental work

Methyl methacrylate (MMA) (Aldrich) and lauroyl peroxide (LPO) (Across Organics) were used as monomer and oil-soluble initiator, respectively; *n*-hexane (Fisher Scientifics) was used as nonpolar nonsolvent and methacryloxypropyl-terminated poly(dimethylsiloxane) (PDMS) (MW = 4000–6000 Da) (Gelest) was used as oil-soluble steric stabilizer. Polyvinyl alcohol (PVA) (89% hydrolyzed, MW = 85,000–124,000 Da) (Sigma) was used as water-soluble suspension stabilizer. The MDPCRSs were carried out as follows. The oil-phase components (*i.e.*, monomer, initiator, solvent, PDMS, and LPO) were mixed together at room temperature until complete dissolution of LPO. The initial monomer content was 75 wt.%, and the initial concentrations of LPO and PDMS were 3 and 1.5 wt.% (monomer-based), respectively. The oil phase was added to an aqueous solution containing dissolved PVA (10 g/L-water). The suspension was first homogenized using a high-shear rotor–stator mixer, and then loaded in a 500 mL jacketed-reactor. The reaction mixture was purged with nitrogen for 30 min, and the reaction was carried out at 70 °C for 90 min under mechanical agitation (~500 rpm). Samples were taken from the reactor at different times, and the produced polymer particles were washed with methanol, filtered, and dried under vacuum overnight. For comparison, regular macro-dispersive polymerizations were also carried out. To this purpose, the oil-phase components were mixed together in 20-mL glass vials until complete dissolution of LPO, purged with nitrogen gas, sealed, and quenched in an oil bath at 70 °C. No agitation was applied.

Monomer conversion (x) was measured by a standard gravimetric technique that consists of precipitating the particle with methanol, filtering, and drying the powder until constant weight is reached. Polymer molecular weights were determined by gel permeation chromatography (GPC), using a UV detector and PLgel 10 μm MIXED-B columns (Polymer Laboratories). Chloroform was used as the mobile phase and PMMA standards of narrow molecular weight distribution were used to calibrate the column. The internal morphologies of the polymer particles were examined by scanning electron microscopy (SEM). To analyze their cross-section, cured epoxy embedded particles were either microtomed using a Leica RM2235 microtome or mechanically fractured. In conjunction with SEM, element mappings were carried out by Energy Dispersion X-ray (EDX) spectroscopy (Hitachi SU-70 Analytical UHR FEG-SEM).

3. Results and discussion

3.1. General interpretation of the core-shell pomegranate-like structure

The evolutions of monomer conversion, polymer average molecular weights, and polymer molecular weight distribution are presented in Figs. 1 and 2, respectively. In Fig. 1, the symbols represent the experimentally measured monomer conversion data in the proposed MDPCRS and the solid lines represent model-simulated homogeneous polymerization results shown for comparison. More details about the simulations are presented in Section 3.2. As expected, the monomer conversion in the MDPCRS increases almost linearly with time at the early stages of the polymerization (up to about 20% conversion). Evidenced by the considerable increase of the polymer weight-average molecular weight and polydispersity (see Fig. 2a,b), diffusion-controlled termination reactions strongly affect the polymerization. In fact, the auto-acceleration os clearly seen to start at a fractional monomer conversion of about 0.2 (see Fig. 1). The monomer conversion is almost complete in less than 90 min. Initially, at $x > 0.3$, a slight reduction of the polymer average molecular weights is observed (see Fig. 2a). This may be caused by the decomposition kinetics of LPO which forces the total concentration of radicals to reach a maximum at intermediate monomer conversions, thus inducing an initial reduction of the polymer molecular weights [23]. However, it is important to notice that such slight reduction can be simply generated by the experimental error from GPC measurement. The experimental conversion data also indicates that glass effect is not affecting the reaction significantly. Interestingly, a high molecular weight shoulder in the MWD curve appears at low monomer conversions (see MWD at $x = 0.22$ in Fig. 2b). Thereafter, this population becomes the most significant one, while the initial low molecular weight chains appear as a shoulder at the left hand side of the MWD (see $x = 0.90–0.99$ in Fig. 2b). This is a clear evidence

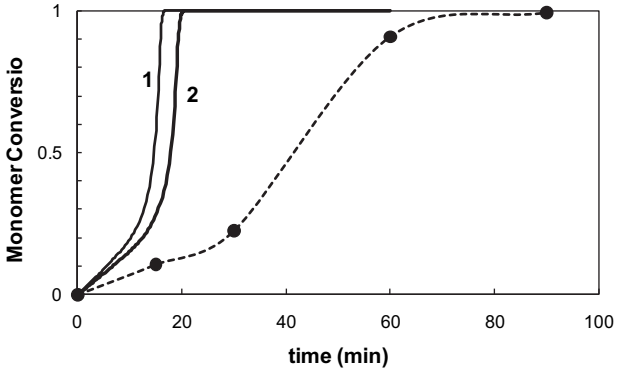

Fig. 1. Evolution of the monomer conversion with the reaction time. Dashed trace is included to guide the eye only. Continuous traces (curves 1 and 2) indicate the simulations for a comparable strictly bulk polymerization (1) and a homogeneous polymerization using the same monomer/solvent concentrations as that used for MDPCRS (2).

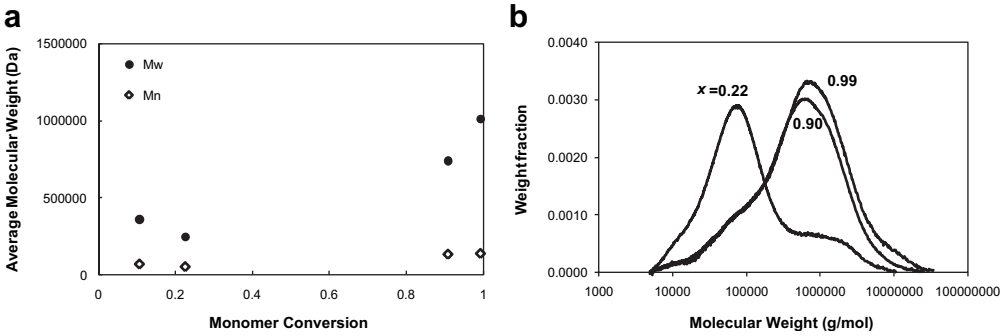

Fig. 2. Evolution with the monomer conversion of (a) polymer average molecular weights; and (b) polymer molecular weight distributions.

of the simultaneous generation of polymer of different molecular weights caused by the presence of different phases, and hence polymerization environments, in the system.

For the MDPCRS experiment, the evolution of the internal particle morphology is shown in Fig. 3. It can be seen that a pericellular membrane of about 2 μm-thickness is developed at early stages of the polymerization (Fig. 3a), when internal structure is not observed yet. After 60 min of polymerization, the nascent precipitation of nano-sized polymer sub-particles is observed inside almost empty polymer micro-capsules (Fig. 3b). Interestingly, such nascent sub-particles that precipitate within the core of the droplets are eventually located at the internal surface of the skin. This is because sub-particles are pushed from the core toward the internal surface of the skin as the solvent is removed to dry the particles for analysis. At the end of the MDPCRS, polymer particles with 2-μm thick shell are packed with nearly monodisperse sub-particles of about 300–400 nm (Fig. 3c). The morphology of this particle resembles a pomegranate, and hence we call it a core-shell pomegranate-like structure. It is also interesting to observe in Fig. 3 that the shell or pericellular membrane is a fairly solid structure rather than an agglomeration of polymer sub-particles, suggesting that the mechanisms for the formation of the shell and the sub-particles can be different.

To understand the morphological evolution throughout the polymerization, we shall first consider the thermodynamic characteristics of the system as represented by the ternary phase diagram shown in Fig. 4. Details about experimental determination of the cloud points and the calculation of binodal and spinodal curves can be found elsewhere [24]. In Fig. 4, point A denotes the initial composition of the reaction mixture used in our experiment. Since no polymerization takes place in the aqueous phase because PVA does not form micelles in the water phase and because LPO initiator is only soluble in the suspended oil phase, the suspended monomer droplets can be adopted as isolated micro-batch reactors. Therefore, as a first approximation, the reaction path inside the suspended monomer micro-droplets can be represented by a straight line parallel to the monomer/polymer axis, as indicated by reaction path ABC in Fig. 4. It can be seen that the investigated MMA/PMMA/*n*-hexane ternary system phase separates at relatively low monomer conversions, when the reaction path intercepts the binodal curve (at $x \approx 0.03$ as indicated in the inset of Fig. 4). However, as we will show later in this article, the actual reaction path does not stay on that straight line because of complex physical and chemical phenomena coexisting in the monomer micro-droplet.

As soon as the reaction path intersects the binodal curve, polymer chains start precipitating in a continuous solvent-rich medium in the form of primary sub-particles. These sub-particles should undergo agglomeration until the amount of PDMS (*i.e.*, secondary steric stabilizer) is able to prevent it. Interestingly, the binodal and spinodal curves are overlapped in the region where the reaction path intersects the binodal curve, suggesting that the morphology evolution is ruled by spinodal decomposition rather than nucleation and growth mechanism [25].

So far, the suggested polymerization mechanism is equivalent to that observed in a regular macro-dispersive polymerization of MMA in the presence of a nonpolar hydrocarbon solvent without mechanical agitation. However, this mainly thermodynamic approach does not fully explain the formation of the pericellular membrane observed in Fig. 3. For that reason, a more complete interpretation is required to describe the unusual morphology formation observed in our experimental study.

According to the foregoing experimental results shown in Fig. 3, polymerization mechanisms with different time constants seem to compete inside the suspended monomer droplets. Here, we note the significant differences in the water solubility of the MMA (~1.5 g/L of water) and the *n*-hexane (~0.013 g/L of water). When an organic droplet containing MMA and *n*-hexane is suspended in water, the droplet-water interface becomes the region where MMA, primary suspension stabilizer, and water coexist. However, this

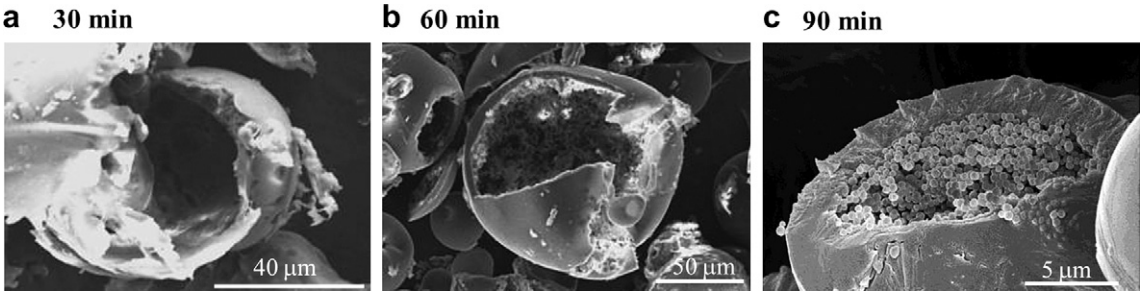

Fig. 3. Evolution of the internal particle morphology throughout the micro-dispersive suspension polymerization of MMA in the presence of *n*-hexane.

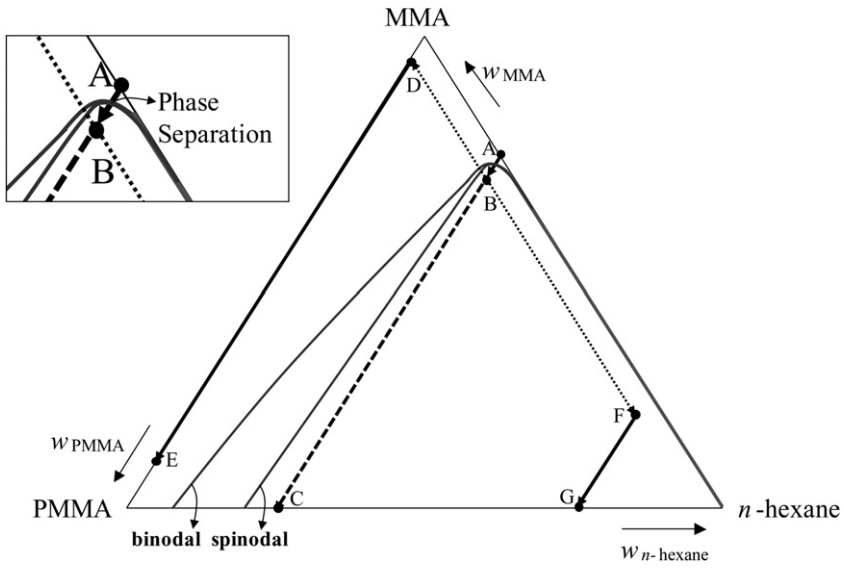

Fig. 4. Ternary phase diagram of MMA/PMMA/*n*-hexane system at 70 °C [24]. Gray lines indicate the binodal and spinodal curves. Possible reaction paths corresponding to the investigated MDPCRS are also depicted (arrows). Inset magnifies the region where system phase separation takes place.

region should be very unfavorable for *n*-hexane because it is strongly hydrophobic. Hence, the formation of an intra-droplet compositional profile should be promoted. Since the outer region of the suspended monomer droplets is a better host for the monomer rather than for the hydrophobic solvent, a faster pseudo-homogeneous polymerization should be induced, leading to the early formation of a dense polymeric structure at the particle surface. Conversely, the inner region of the droplet should be an excellent host for the hydrophobic solvent, thus promoting the precipitation of polymer sub-particles. The rate of this second mechanism should be much slower due to the dilution effect caused by the high concentration of the nonpolar solvent. Moreover, due to the low concentration of monomer at the inner region of the droplet, the dispersion polymerization can be considered to take place under "starved" conditions. A schematic representation of the suggested morphological interpretation is presented in Fig. 5. Indirect confirmations of the validity of the proposed phenomenological interpretation are presented in Sections 3.2 and 3.3.

Let us consider again Fig. 4 with the foregoing core-shell formation mechanism. From points A to B, the intra-droplet concentration profile may still not be completely developed and the reaction path should certainly follow that of a conventional macro-dispersive polymerization as explained before (*i.e.*, precipitation of primary sub-particles take place after the system phase separation point). As the concentration profile is fully developed in point B, the reaction path splits into two different reaction paths: one that describes the polymerization at the outer region of the micro-droplet (points D and E), and the other that describes the polymerization at the micro-droplet core (points F and G). The segment between points D and E in Fig. 4 represents the homogeneous polymerization that is taking place at the micro-droplet surface. For simplicity, the reaction was assumed to occur in a quasi-bulk fashion (*i.e.*, no solvent was allowed to be dissolved in the outer region and the reaction path is on the MMA/PMMA axis). However, Fig. 4 shows that polymerization containing up to 8.5% still proceed homogeneously, and points D and E can be located anywhere in that region. On the other hand, segment between points F and G represents the *starved macro-dispersive polymerization* at the micro-droplet core which contains a very high concentration of solvent. Although the actual positions of points B, D, E, F, G in Fig. 4 are unknown, this qualitative description allows us to schematically describe the coexisting kinetic and thermodynamic phenomena according to our phenomenological interpretation.

3.2. Study of the pericellular membrane formation

Although we have suggested that a homogeneous polymerization of monomer is mainly responsible for the early formation of particle shells, the parallelism between PVC process and the

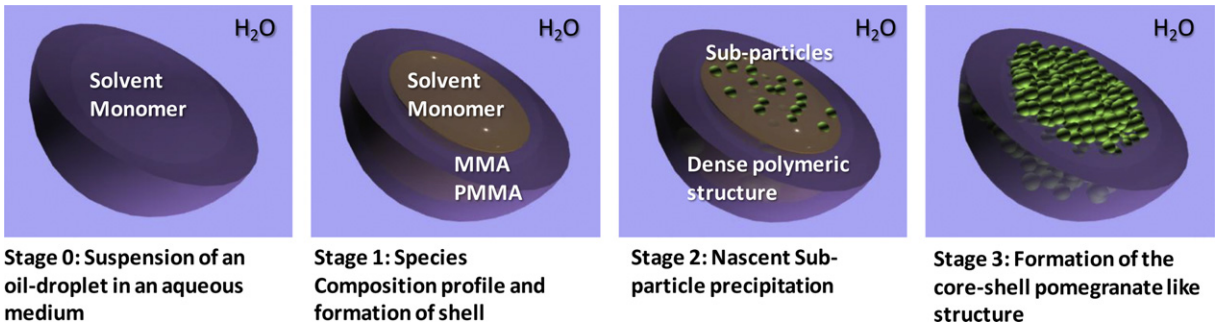

Fig. 5. Morphological interpretation of the evolution of the core-shell pomegranate-like structure.

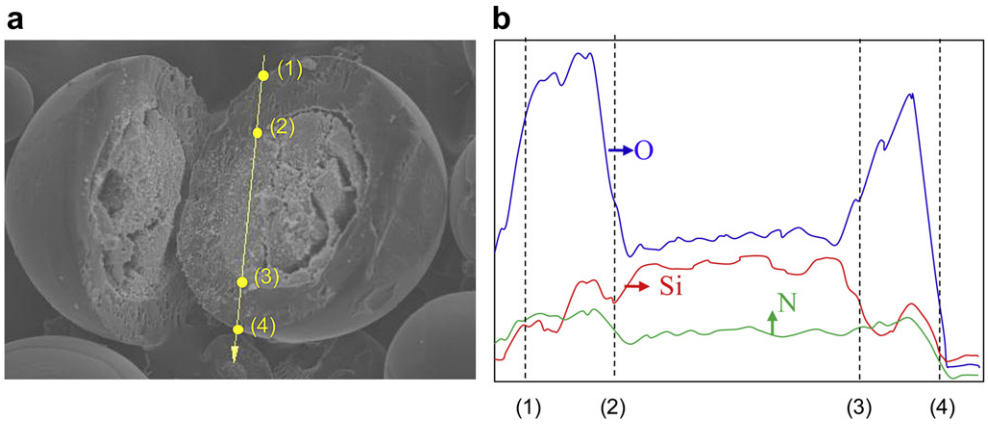

Fig. 6. EDX analysis of a core-shell pomegranate-like particle.

proposed polymerization technique indicates that other mechanisms such as agglomeration of nano-sized polymer sub-particles or grafting of PVA at the droplet surface could also be responsible for the formation of this unusual structure. Due to the relatively small fraction of PVA that is adsorbed onto the monomer suspended droplets [26], it was hard to believe for these authors that grafting reaction of PVA could be the only responsible for the skin formation. However, the agglomeration of sub-particles at the droplet surface needed to be tested. In order to validate the proposed interpretation, the cross-section of core-shell pomegranate-like particle was analyzed by EDX spectroscopy (see Fig. 6). Interestingly, a high concentration of Si was observed at the particle core (where nano-sized sub-particles are located), but Si concentration was significantly reduced at the particle shell. Si is one of the main components of PDMS which is used as steric stabilizer of nano-sized sub-particles. The result allowed us to conclude that the particle pericellular membrane is not (mainly) produced via agglomeration of polymer sub-particles, but by different polymerization mechanism. It is interesting to notice however that some agglomeration between particle and the pericellular membrane does happen, since the reduction of Si concentration at the particle shell is gradual rather than abrupt close to the internal surface of the skin (Fig. 6).

A detailed quantitative justification of the particle morphology evolution will be presented in our forthcoming paper. However, some simple calculations can provide the readers some indirect validation regarding how realistic it is to consider that a homogenous polymerization mechanism is actually driving the pericellular membrane formation. Fig. 3a shows that the particle skin is formed in less than 30 min. If our hypothesis is correct, a standard model for a homogeneous and strictly bulk polymerization should show that most of the monomer is consumed in less than 30 min.

Table 1 shows the basic reactions that may take place during a bulk homogeneous polymerization of MMA: thermal decomposition of the initiator (I) to generate initiator radicals (I•), propagation of radicals with the monomer (M) to produce growing radicals of length n (R_n•), and termination by disproportionation to produce polymer dead chains of length n (P_n). Assuming that chain transfers reactions do not affect the reactivity of generated radicals, the following well-known set of ordinary differential equation can be written to describe the bulk polymerization kinetics:

$$\frac{d[\mathrm{I}]}{dt} = -k_d[\mathrm{I}] \tag{1}$$

$$\frac{d[\mathrm{I}^{\cdot}]}{dt} = 2fk_d[\mathrm{I}] - k_p[\mathrm{I}^{\cdot}][\mathrm{M}] \tag{2}$$

$$\frac{d[\mathrm{M}]}{dt} = -k_p[\mathrm{R}^{\cdot}][\mathrm{M}] \tag{3}$$

$$\frac{d[\mathrm{R}^{\cdot}]}{dt} = k_p[\mathrm{I}^{\cdot}][\mathrm{M}] - k_{td}[\mathrm{R}^{\cdot}]^2 \tag{4}$$

where [R•] accounts for the total concentration of radicals ($[\mathrm{R}^{\cdot}] = \sum_{n=1}^{\infty}[\mathrm{R}_n^{\cdot}]$), k_d, k_p, and k_{td} are the kinetic constants for the initiator decomposition, propagation, and termination by disproportionation, respectively; and f is the initiator efficiency factor. Using the kinetic parameters listed in Table 2, the evolution of the monomer conversion was simulated (see continuous trace "1" in Fig. 1). To this purpose, the set of ordinary differential Eqs. (1)–(4) was solved using a modified Rosenbrock method for stiff systems. The initial conditions were obtained from a bulk recipe containing monomer and initiator only. Table 2 also shows how the "apparent" termination rate constant was estimated when the gel effect is taking into account in terms of the free-volume [27]. Interestingly, during a strictly bulk polymerization most of the monomer is

Table 1
Kinetic mechanism for a bulk polymerization of MMA (n, m = 1,2,…,∞).

Initiation
$\mathrm{I} \xrightarrow{k_d} 2\mathrm{I}^{\cdot}$
Propagation
$\mathrm{I}^{\cdot} + \mathrm{M} \xrightarrow{k_p} \mathrm{R}_1^{\cdot}$
$\mathrm{R}_n^{\cdot} + \mathrm{M} \xrightarrow{k_p} \mathrm{R}_{n+1}^{\cdot}$
Termination
$\mathrm{R}_n^{\cdot} + \mathrm{R}_m^{\cdot} \xrightarrow{k_{td}} \mathrm{P}_n + \mathrm{P}_m$

Table 2
Kinetic Parameters for model simulations.

Parameter	Value	Ref.
f	0.5	This work
k_d (s^{-1})	$1.28 \times 10^{16}\exp(-16{,}158/T)$	Manufacturer
k_p (L mol^{-1} s^{-1})	$7.0 \times 10^{6}\exp(-3171/T)$	[27]
k_{td} (L mol^{-1} s^{-1})	$g_t \times k_{td,0}$	[27]
$k_{td,0}$	$1.76 \times 10^{9}\exp(-1409/T)$	[27]
g_t ($\nu_f \geq \nu_{fcr}$)	$0.10575\exp\{17.15\,[\nu_f - 0.01715\,(T-273.15)]\}$	[27]
g_t ($\nu_f < \nu_{fcr}$)	$2.3\times10^{-6}\exp(75\nu_f)$	[27]
ν_f[a]	$0.025 + 0.001\sum_{i=M,S,P}(T - T_{g,i})\phi_i$	[27]
ν_{fcr}	$0.186 - 2.96\times10^{-4}\,(T-273.15)$	[27]

[a] M, S, P represent monomer, solvent, and polymer, respectively. $T_{g,i}$ is the glass transition temperature of the species, with $T_{g,M}$ = 167 K, $T_{g,S}$ = 178 K, $T_{g,P}$ = 387 K; and ϕ_i is the volume fraction of species i in the reaction mixture.

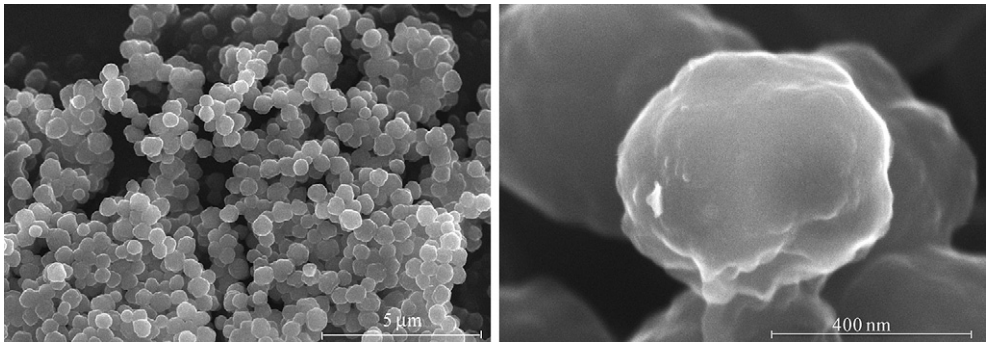

Fig. 7. SEM images of particles obtained after 90 min of a regular macro-dispersive polymerization of MMA in *n*-hexane under "starved" conditions (*i.e.*, 72.6 wt.% *n*-hexane).

consumed in less than 20 min. Another simulation was also performed considering a homogeneous polymerization that follows points A–C in Fig. 4 (see continuous trace "2" in Fig. 1). In this last case, the dilution effect caused by the presence of solvent was adopted to set the initial condition but the system phase separation was neglected. It can be observed a quite fast consumption of monomer. Recall that the suggested kinetics neglects the system heterogeneity. Hence, any preferential accumulation of species in the coexisting phases is also neglected.

Our observations of the early formation of the pericellular membrane and the very low concentration of Si in it support the morphological interpretation regarding the significant effect on the formation of the particle pericellular membrane of the homogeneous polymerization at the droplet surface.

3.3. Study of the pomegranate-like core formation

The formation of sub-particles of 300–500 nm in a core-shell pomegranate-like structure as shown in Fig. 3c is interesting because macro-dispersive polymerizations of MMA in nonpolar hydrocarbon solvents usually produce uniform polymer particles of a few microns [28–39]. According to our foregoing interpretation of the morphological development, the inner region of the droplets contains just a small fraction of the monomer but most of the solvent after a shell is formed. As a result, the mechanism in the inner region can be adopted as a dispersion polymerization under starved conditions. To test this hypothesis, we performed a regular dispersion polymerization that emulates the conditions which may be regulating the inner region of the suspended monomer micro-droplets.

Using the density of the polymer and the shell thickness shown in Fig. 3c, we estimated the mass of polymer contained at the particle pericellular membrane (*i.e.*, 88.7 wt.% of the initial monomer mass contained in a suspended monomer micro-droplet). Since at the end of the polymerization the monomer conversion is close to 100% (see Fig. 1), we could also estimate the remaining fraction of monomer that was eventually polymerized (heterogeneously) at the droplet core. Assuming that all the solvent and PDMS were preferentially located at the inner region of the droplets, the recipe of the starved dispersion polymerization was determined as follows: 72.6 wt.% of *n*-hexane and 3.52 wt.% of PDMS. (Recall that the original recipe used for the MDPCRS contained only 25 wt.% of *n*-hexane.) We assumed that the initiator was evenly distributed between the inner and outer regions of the suspended droplets. Therefore, the global molar concentration of initiator used in our experiment was the same as that used in MDPCRS. Using this crude estimation, a starved dispersion polymerization was carried out at 70 °C. Interestingly, quite uniform polymer particles of about 400–500 nm were obtained after 90 min of reaction (see Fig. 7). Moreover, these polymer particles were fairly similar in size to those in Fig. 3c.

For comparison, we also used the same recipe as that used for MDPCRS to perform a regular macro-dispersive polymerization. The recipe contained 75 wt.% of MMA, and 3 and 1.5 wt.% (monomer-based) of LPO and PDMS, respectively. As indicated in Fig. 8, it yielded a quasi-bulk structure where agglomerated particles cannot preserve their identity during the course of the polymerization. The generated nano-domains are not stabilized to produce uniform polymer particles. Instead, they are massively agglomerated. This result indicates that the polymerization inside a droplet did not follow the reaction path for a regular macro-dispersive polymerization.

In the case of starved macro-dispersion polymerization described before, we assumed that just 11.3 wt.% of the initial monomer mass is heterogeneously polymerized to produce sub-particles. For comparison, we also calculated the mass of monodisperse sub-particles of 400 nm closely packed in a spherical container with the

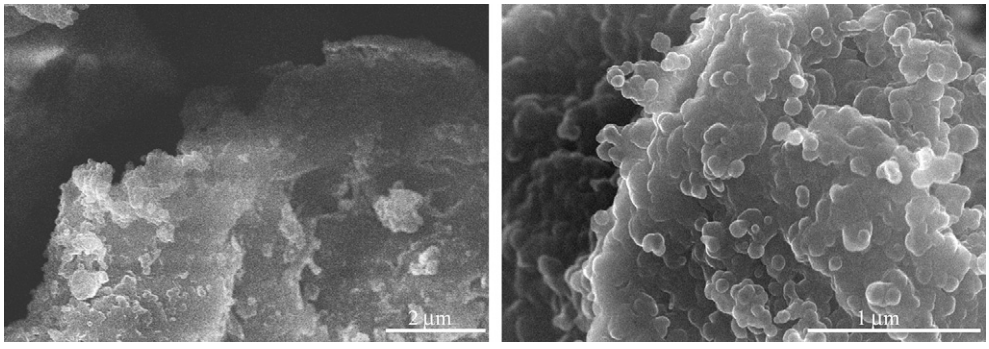

Fig. 8. SEM images of particles obtained after 90 min of a regular macro-dispersive polymerization of MMA in *n*-hexane under MDPCRS conditions (*i.e.*, 25 wt.% *n*-hexane).

same internal diameter of the pericellular membrane shown in Fig. 3. Assuming that the coordination number of sub-particles (*i.e.*, number of nearest neighbors) can vary from 6 to 12, the conversion of monomer heterogeneously polymerized should vary between 37 and 60 wt.%. Even the lower limit of that range is 3.3 times higher than that calculated from the thickness of the shell. This significant discrepancy may be caused by an overestimation of the monomer homogeneously polymerized. This also indicates that some fraction of the pericellular membrane might have been indeed formed by agglomeration of polymer sub-particles, as discussed in Section 3.2.

4. Concluding remarks

This article presents a new synthetic method to produce polymer particles with a core-shell pomegranate-like morphology in a suspended monomer micro-droplet. A micro-phase separation is induced during the course of the polymerization. Due to the different solubilities of monomer and a hydrophobic solvent in the continuous aqueous medium, a pseudo-homogeneous polymerization seems to regulate the reaction at the droplet surface until a stable pericellular membrane is formed. Thereafter, a micro-dispersion polymerization in the core portion of the particle proceeds under starved conditions. As a result, nano-sized sub-particles precipitate out from the liquid phase and the particle is eventually packed with these sub-particles into a pomegranate-like structure. A mathematical model is currently being developed to quantify the morphological development in a suspended monomer/solvent droplet.

References

[1] Emmerich O, Hugenberg N, Schmidt M, Sheiko SS, Baumann F, Deubzer B, et al. Adv Mater 1999;11(15):1299–303.
[2] O'Donnell PB, McGinity JW. Adv Drug Deliv Rev 1997;28(1):25–42.
[3] Zhu KJ, Jiang HL, Du XY, Wang J, Xu WX, Liu SF. J Microencapsul 2001;18(2):247–60.
[4] Im SH, Jeong UY, Xia YN. Nat Mater 2005;4:671–5.
[5] Wu HS, Sun F, Dimonie VL, Klein. A. U.S. Patent 5,834,526, 1998.
[6] Itou N, Masukawa T, Ozaki I, Hattori M, Kasai K. Colloids Surf A 1999;153(1–3):311–6.
[7] Gross JR, U.S. Patent 5,403,870, 1995.
[8] Okubo M, Minami H, Komura T. J Appl Polym Sci 2003;88(2):428–33.
[9] Li GL, Yang XY, Wang B, Wang JY, Yang XL. Polymer 2008;49(16):3436–43.
[10] Soane DS, Houston MR, U.S. Patent 6,617,364 B2, 2003.
[11] Okubo M, Konishi Y, Inohara T, Minami HJ. Appl Polym Sci 2002;86(5):1087–91.
[12] Jiang BB, Gao CY, Shen JC. Colloid Polym Sci 2006;284(5):513–9.
[13] Dinsmore AD, Hsu MF, Nikolaides MG, Marquez M, Bausch AR, Weitz DA. Science 2002;298:1006–9.
[14] Xu XL, Asher SA. J Am Chem Soc 2004;126(25):7940–5.
[15] He XD, Ge XW, Wang MZ, Zhang ZC. J Colloid Interface Sci 2006;299(2):791–6.
[16] McDonald CJ, Devon MJ. Adv Colloid Interface Sci 2002;99(3):181–213.
[17] Kuo HP, Chuang MY, Lin CC. Powder Technol 2009;192(1):116–21.
[18] Luciani CV, Choi KY, Xiao Z. Chem Eng Technol 2010;33(11):1833–40.
[19] Allsopp MW. Manufacture and processing of PVC. New York: MacMillan Publishing Co; 1982.
[20] Alexopoulos AH, Kiparissides C. Chem Eng Sci 2007;62(15):3970–83.
[21] Davidson JA, Witenhafer DE. J Polym Sci B 1980;18(1):51–69.
[22] Smallwood PV. Polymer 1986;27(10):1609–18.
[23] Emdadi L, Luciani CV, Lee SY, Baick IH, Choi KY. Polym Eng Sci; 2010 [in press].
[24] Jung Y, Luciani CV, Han JJ, Choi KY. J Appl Polym Sci 2010;116(6):3648–58.
[25] Saxena R, Caneba GT. Polym Eng Sci 2002;42(5):1019–31.
[26] Lazrak N, Le Bolay N, Ricard A. Eur Polym J 1998;34(11):1637–47.
[27] Crowley TJ, Choi KY. Ind Eng Chem Res 1997;36(5):3676–84.
[28] Barrett KE, Thomas HR. J Polym Sci A 1969;7:2621–50.
[29] Barrett KE. Dispersion polymerization in organic media. London: J. Wiley & Sons; 1975.
[30] Dawkins JV, Taylor G. Polymer 1979;20:599–604.
[31] Antl L, Goodwin JW, Hill RD, Ottewill RH, Owens SM, Papworth S. Colloids Surf 1986;17:67–78.
[32] Winnik MA, Lukas R, Chen WF, Furlong P, Croucher MD. Makromol Chem Macromol Symp 1987;10–11:483–501.
[33] Williamson B, Lukas R, Winnik MA, Croucher MD. J Colloid Interface Sci 1987;119(2):559–64.
[34] Pathmamanoharan C, Slob C, Lekkerkerker HNW. Colloid Polym Sci 1989;267:448–50.
[35] Pelton RH, Osterroth A, Brook MA. J Colloid Int Sci 1990;137(1):120–7.
[36] Stejskal J, Kratochvíl P, Koňák Č. Polymer 1991;32(13):2435–42.
[37] Kargupta K, Rai P, Kumar A. J Appl Polym Sci 1993;49:1309–29.
[38] Srinivasan SA, Hedrick JL, McKean DR, Miller RD, Hilbom JG. Polymer 1998;39(6–7):1497–501.
[39] Klein SM, Manoharan VN, Pine DJ, Lange FF. Colloid Polym Sci 2003;282(1):7–13.

Polymer 52 (2011) 949–953

Contents lists available at ScienceDirect

Polymer

journal homepage: www.elsevier.com/locate/polymer

Synthesis and characterization of trifluoromethyl substituted styrene polymers and copolymers with methacrylates: Effects of trifluoromethyl substituent on styrene

Hongxiang Teng [a,c], Liping Lou [a,c], Kotaro Koike [a,b], Yasuhiro Koike [b,c], Yoshi Okamoto [a,c,*]

[a] Polymer Research Institute, Polytechnic Institute of New York University, 6 Metrotech Center, Brooklyn, NY 11201, United States
[b] Faculty of Science and Technology, Keio University, Yokohama 223-8522, Japan
[c] Koike Photonics Polymer Project, ERATO-SORST, Japan Science and Technology Agency, Kawasaki 212-0032, Japan

ARTICLE INFO

Article history:
Received 12 October 2010
Received in revised form
10 December 2010
Accepted 20 December 2010
Available online 30 December 2010

Keywords:
Trifluoromethyl styrenes
Homopolymer
Copolymer

ABSTRACT

2-Trifluoromethyl styrene (2TFMS), 2,5-bis(trifluoromethyl) styrene (25BTFMS), and 3,5-bis(trifluoromethyl) styrene (35BTFMS) were synthesized. These styrenes were readily polymerized in bulk and also in solution using AIBN as a free radical initiator. The polymerization rate of these trifluoromethyl substituted styrenes and other monomers such as styrene (St), pentafluorostyrene (PFS) and 4-trifluoromethyl-tetrafluorostyrene (TFMTFS) were measured in benzene and dioxane by monitoring the ^{1}H NMR spectra of the double bond hydrogen. The order of polymerization rates was TFMTFS > 35BTFMS > 25BTFMS > PFS > 2TFMS > St. T_gs of styrene polymers with CF_3 substituted on the ortho position of the phenyl ring were much higher than those of the meta and para substituted styrenes due to the steric hindrance of the bulky CF_3 group close to the polymer main chain, which resulted in a decrease in the segment mobility of the polymer chains and an increasing T_g of the polymers. The copolymers of 2TFMS with methyl methacrylate (MMA) and also 25BTFMS with trifluoroethyl methacrylate (TFEMA) were prepared. T_gs of the copolymers were in the range of 120–145 °C and the copolymers were transparent and thermally stable. The copolymer films were flexible and exhibited high transmittance as the homopolymers of MMA and TFEMA. Thus, these copolymers may be utilized as novel optical materials.

1. Introduction

Polystyrene (PS) is a commercially important polymer with good light transmittance. The favorable physical properties of PS coupled with ease of processing make it useful as optical device materials [1]. However, high losses in the visible and near infrared region are dominated by the combinations of stretch and deformation vibrations of C–H bonds [2,3]. When heavier atoms such as deuterium or fluorine replace the hydrogen atoms in C–H bond, the band vibration energy is decreased and thus the absorption band is minimized. Thus, we have previously synthesized fluorine containing polystyrene such as poly(2,3,4,5,6-pentafluorostyrene) and poly(4-trifluoromethyl 2,3,5,6-tetrafluorostyrene) [4]. They are thermally stable and transparent, but their glass transition temperatures (T_g) were about 110 °C. However, some applications such as in automobile and airplane require optical polymers with higher T_g (>120 °C) [5–8].

Bomer and Hagemann have synthesized various CF_3 substituted styrenes and their homopolymers. They reported that when CF_3 group substituted on the ortho position of polystyrene, the T_g was considerably higher (175 °C) than those of CF_3 on the meta and para positions whose T_gs were 63 and 101 °C, respectively [9]. This is due to the steric hindrance of the bulky CF_3 group (the Van der Waals volume of CF_3 is 42.6 Å^3 compared to CH_3 with 16.8 Å^3) [10] at the ortho position, which results in a decrease in the segmental mobility of the polymer chains and greatly increases the T_g of the polystyrene. Thus, we have further investigated the CF_3 substituted polystyrenes for possible optical polymer materials with higher T_g. Various fluorine containing styrene monomers (Fig. 1) were synthesized and the polymerization rates of these styrene monomers in benzene and dioxane solutions were measured. Also reported here are the thermal and optical properties of the trifluoromethyl substituted styrenes homopolymers as well as their copolymers with methyl methacrylate and 2,2,2-trifluoroethyl methacrylate.

* Corresponding author. Polymer Research Institute, Polytechnic Institute of New York University, 6 Metrotech Center, Brooklyn, NY 11201, United States.
E-mail address: yokamoto@poly.edu (Y. Okamoto).

0032-3861/$ – see front matter © 2011 Elsevier Ltd. All rights reserved.
doi:10.1016/j.polymer.2010.12.045

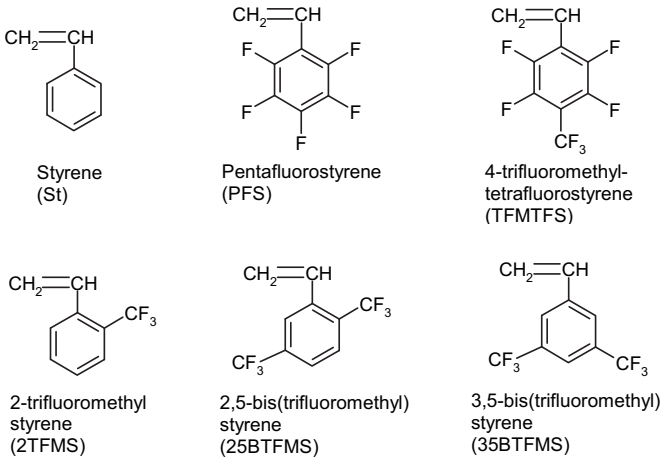

Fig. 1. Chemical structures of styrene monomers investigated.

2. Experimental

2.1. Materials

All solvents, methyl methacrylate (MMA), styrene (St) and 2,2′-azobisisobutyronitrile (AIBN) were purchased from Aldrich. 2,3,4,5,6-Pentafluorostyrene (PFS), 2-trifluoromethyl-bromobenzene, 2,5-bis (trifluoromethyl)-bromobenzene, 3,5-bis(trifluoromethyl)-bromobenzene and 4-trifluoromethyl-2,3,5,6-tetrafluoro-bromobenzene were purchased from SynQuest Co. AIBN was purified through the recrystallization from methanol. All monomers were distilled before use.

2.2. Characterization

^{1}H NMR and ^{19}F NMR spectra were recorded by a Bruker AC 300 spectrometer at 300 and 282 MHz, respectively. Chemical shifts are reported in ppm from internal TMS or $CFCl_3$. The differential scanning calorimetry (DSC) measurement was performed on a DSC 2920 module in conjunction with the TA Instruments 5100 system at a scan rate of 10 °C/min under a nitrogen atmosphere. The instrument was calibrated using indium and zinc as calibration standards for the temperature and enthalpy changes. The midpoint of the heat capacity transition was taken as T_g. Thermogravimetric analysis (TGA) was performed on Hi-Res Modulated TGA 2950 thermogravimetric analyzer under nitrogen at a heating rate of 20 °C/min. The extrapolation of break in the TGA curve was taken as the decomposition temperature (T_d). The molecular weights of polymer samples were determined by gel permeation chromatography (GPC) (Waters 510) using THF as the eluent at a flow rate of 1.0 mL/min. The molecular calibration curves were obtained using polystyrene standards. The refractive indices were measured using a Metricon model 2010 prism coupler, and the measurement accuracy is ±0.0005. The transmittance of polymer films was measured with a UV/VIS spectrometer (Lambda 800, Perkin Elmer, Inc.) at a scanning rate of 100 nm/min. The film thickness was in the range of 110–200 μm.

2.3. Synthesis of styrene monomers

Except for those purchased, styrene monomers were prepared via the dehydration of the related alcohols, which were synthesized by the reaction of corresponding Grignard reagents with acetaldehyde (Scheme 1). In a typical procedure, the Grignard agent was prepared from the related bromide compound and magnesium in anhydrous THF. After slowly adding acetaldehyde, the reaction mixture was treated with diluted hydrochloric acid solution. The resulted alcohol was subjected to distillation under vacuum. The styrene monomers were obtained as a colorless liquid by the elimination of water from alcohols with phosphorous pentoxide, followed by the distillation under vacuum.

2-trifluoromethyl styrene (2TFMS): b.p. 65–66 °C/30 mmHg with a yield of 57%. ^{1}H NMR ($CDCl_3$): 5.30 (dd, *J1 = 1.1 Hz*, *J2* = 11.0 Hz, 1H), 5.66 (d, *J* = 17.2 Hz, 1H), 7.00 (m, 1H), 7.30–7.70 (m, 4H). ^{19}F NMR ($CDCl_3$): −59.5 (s, 3F).

2,5-bis(trifluoromethyl) styrene (25BTFMS): b.p. 70–71 °C/30 mmHg with a yield of 60%. ^{1}H NMR ($CDCl_3$): 5.43 (dd, *J1 = 0.6 Hz*, *J2* = 11.1 Hz, 1H), 5.80 (d, *J* = 17.2 Hz, 1H), 7.00 (m, 1H), 7.60–7.90 (m, 3H). ^{19}F NMR ($CDCl_3$): −60.2 (s, 3F), −63.3 (s, 3F).

3,5-bis(trifluoromethyl) styrene (35BTFMS): b.p. 72–73 °C/30 mmHg with a yield of 55%. ^{1}H NMR ($CDCl_3$): 5.49 (d, *J = 11.0 Hz*, 1H), 5.90 (d, *J* = 17.6 Hz, 1H), 6.77 (dd, *J*1 = 11.0 Hz, *J*2 = 17.6 Hz, 1H), 7.70–7.90 (m, 3H). ^{19}F NMR ($CDCl_3$): −63.2 (s, 6F).

4-trifluoromethyl-2,3,5,6-tetrafluorostyrene (TFMTFS): b.p. 36–37 °C/20 mmHg with a yield of 58%. ^{1}H NMR ($CDCl_3$): 5.87 (d, *J* = 11.8 Hz, 1 H), 6.24 (d, *J* = 17.9 Hz, 1H), 6.71 (dd, *J* = 11.8 Hz, *J* = 17.9 Hz, 1H). ^{19}F NMR ($CDCl_3$): −56.37 (m, 3 F), −141.86 (m, 4F).

2.4. Polymerization

Polymerizations were carried out in bulk for the general characterization purpose, or in benzene and dioxane solutions for kinetics study. AIBN was used as the free radical initiator in all the polymerizations. Monomers and initiator were transferred into a glass tube, which was subject to three times of the freeze–pump–thaw cycles and followed by sealing with flame under vacuum. After polymerizing in a water bath at 60–80 °C for 20–30 h, the tube was opened carefully, and the content was purified by the precipitation from THF solution to a large amount of methanol or hexane. The polymer collected was dried in vacuum oven at 60 °C for 48 h.

2.5. Kinetics

The polymerization rate can be expressed as following equations [11]:

$$R_p = k_p\left(\frac{fk_d}{k_t}\right)^{1/2}[I]^{1/2}[M] \quad (1)$$

$$\ln\frac{[M]_0}{[M]} = k[I]^{1/2}t \quad (2)$$

where R_p is the polymerization rate, k_p is the propagation rate coefficient, f is the initiator decomposition efficiency, k_d is the

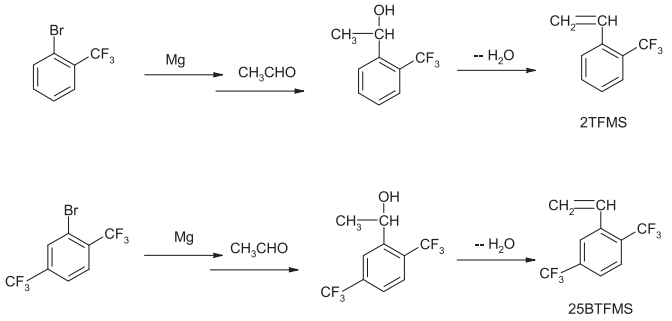

Scheme 1. Synthesis routes for the preparation of substituted styrene monomers.

initiator decomposition rate coefficient, k_t is the termination rate coefficient, [I] is the initiator concentration, [M] is the monomer concentration, k is the observed polymerization rate coefficient, and t is the polymerization time. The change of the monomer concentration could be monitored by ^{1}H NMR measurements of the double bond protons (Fig. 2).

2.6. Reactivity ratio

The reactivity ratios of each pair of comonomers in a copolymerization were calculated according to the Mayo–Lewis method [12].

3. Results and discussion

The CF_3 substituted styrenes were readily polymerized in bulk and also in solutions using AIBN as a free radical initiator. To study the effect of the F and CF_3 substitution on the activity of related styrene monomers, the polymerization kinetics was carried out in nonpolar solvent benzene and polar solvent dioxane. To obtain accurate results, the solvents used in kinetics study were purified carefully with the traditional methods. The polymerization rate was monitored by measuring the double bond protons in monomers (Fig. 2). The observed polymerization rate coefficient k was calculated according to Eqn. (2) (Table 1). It was found that the polymerization is faster in a polar solvent such as dioxane than in a less polar solvent such as benzene, which is agreeing to the literature results [13].

The free radical initiated polymerization of styrene has been widely investigated [14–17]. The head to tail placement would be expected to be overwhelmingly predominant, since successive propagating radicals formed by the attachment of a radical at the β carbon of the double bond is more stable due to the resonance effects of the phenyl group and less steric hindrance. The situation with substitution on the benzene ring of substituted styrene monomers should be the same.

As shown in Fig. 2, when X has a more electron-withdrawing property, such as Cl and CN, the polymerization rate of the monomer was found to be faster than those of X having an electron donating property, such as CH_3 and OCH_3 [18]. The polymerization rates of para substituted styrenes were following a Hammett σ–ρ relationship [19].

The protons in nonfluorinated styrene appeared in the upper field in NMR spectrum as comparing to those in fluorosubstituted styrenes due to the electron-withdrawing property of F and CF_3 (Fig. 3). The protons in TFMTFS appeared at a lower field than those of PFS because the CF_3 group is a more electron-withdrawing group than the F atom. To reveal the structure and activity relationship, the chemical shifts of the proton H^2 were plotted against the polymerization rate coefficients of these styrene monomers, and a linear relationship was found as shown in Fig. 4. Besides the solvent effect as mentioned above, the polymerization rates of these styrene monomers were in the decreasing order of TFMTFS > 35BTFMS > 25BTFMS > PFS > 2TFMS > St.

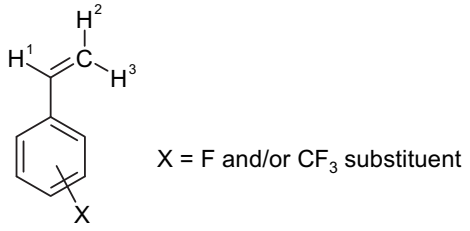

Fig. 2. Proton identification of the substituted styrene monomers.

Table 1
Polymerization rate constants of styrene monomers at 50 °C.

	k (benzene) ($\times 10^{-5}$ L$^{1/2}$/mol$^{1/2}$ S)	k (dioxane) ($\times 10^{-5}$ L$^{1/2}$/mol$^{1/2}$ S)	T_g(°C)
St	2.4	4.0	105
PFS	4.8	9.8	108
TFMTFS	8.7	16	112
2TFMS	3.1	6.1	165
25BTFMS	7.7	10	160
35BTFMS	6.1	15	116

It can be seen that the more the electron-drawing substitution, the more active the monomer is. The polymerization rates of fluorinated styrene are faster than that of regular styrene because of this polarity effect [20]. The CF_3 substitution at the para position of TFMTFS has much stronger polarity effect when comparing with the F substitution at the same position in PFS. When X is CF_3 group, the Hammett constant σ_p is 0.54, where ρ was calculated as 0.6. While X is F atom only, the Hammett constant σ_p is 0.062 [21]. It can be seen that there is a big difference between CF_3 and F substitutions at the para position of the benzene ring, which could explain the big difference between the polymerization activities of PFS and TFMTFS. The polymerization rate of 25BTFMS is much slower than that of 35BTFMS due to the steric effect of the CF_3 group at the ortho position of 25BTFMS.

T_gs of 2TFMS, 25BTFMS and 35BTFMS homopolymers were 165, 160 and 116 °C [22], respectively, and T_gs of PFS and TFMTFS homopolymers were 108 and 112 °C, respectively (Table 1). As can be seen, T_gs of polymers with CF_3 substituted at the ortho position of the phenyl ring are much higher in comparison with P35BTFMS. This is due to the steric hindrance of the bulky CF_3 group near the polymer main chain, which resulted in a decreased segmental mobility of the polymer chains and the increased T_g of the polymers.

Comparing with homopolymers, copolymer systems produce more variable properties. Generally, the copolymerization can decrease the crystallinity and increase the flexibility of the polymer materials. Styrene polymers have higher thermal and chemical stabilities. While they exhibit poor mechanical properties and are difficult to prepare thin fibers due to the rigid polymer structure. Comparatively, acrylate polymers showed excellent processing properties, while they can be only utilized at a low temperature environment due to the low T_g. The combination of the positive properties from styrene polymers and acrylate polymers would be an ideal result. However, as optical materials, copolymers tend to have extremely high light scattering loss due to the large heterogeneous macromolecular structure and the corresponding

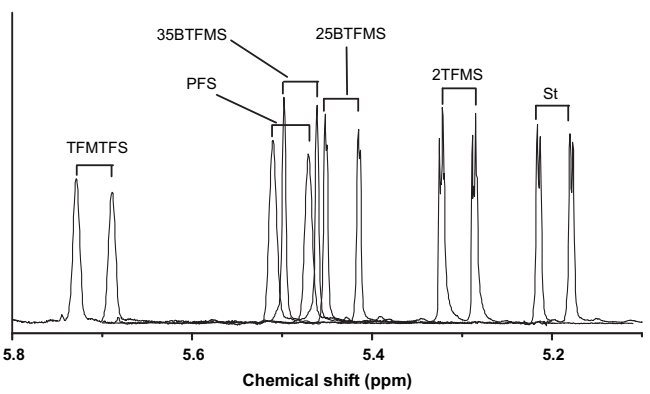

Fig. 3. ^{1}H NMR spectra for the H^2 protons of the double bonds in styrene monomers.

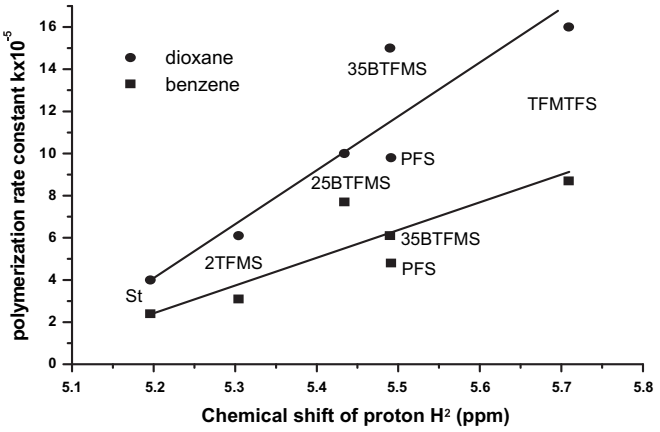

Fig. 4. Relationship of the polymerization rate constants and the chemical shifts of H^2 protons.

heterogeneity of the refractive index distribution. Consequently, copolymers have not been the leading candidate for photonic materials.

The copolymerization reactivity ratios r_1 and r_2 were found to be 0.84 and 1.55 for MMA and 2TFMS, respectively (Table 2), which indicate that these two monomers produce copolymers with the random composition. The refractive indices of poly(2TFMS) and PMMA are 1.51 and 1.50 at 532 nm, respectively. The very close refractive indices of the different polymeric units could minimize the light scattering. Combining the random copolymer chain structure characteristics, the transparent copolymer could be produced from the two monomers. The same situation is in the case of the trifluoroethyl methacrylate (TFEMA) and 25BTFMS system. The copolymerization reactivity ratios r_1 and r_2 are 0.64 and 1.18 for TFEMA and 25BTFMS, respectively. The refractive indices of poly (25BTFMS and PTFEMA) are 1.45 and 1.44 at 532 nm, which are also very close to each other. Therefore, these copolymers may exhibit no light scattering [23]. Thus, the copolymers of MMA with 2TFMS and also the copolymers of TFEMA with 25BTFMS were prepared for possible novel optical applications (Table 3).

These copolymers exhibit a single glass transition temperature, which indicates that they have a random homogeneous macromolecular structure (Table 3). T_gs of the copolymers are dependent on their composition and follow a linear relationship as shown in Fig. 5. This makes it possible to design the copolymers with different refractive indices for different applications. In comparison to the low T_g of methacrylate polymers and the poor mechanical properties of the styrene polymers, these copolymers offer the higher T_g (>130 °C) required for special applications of optical polymers in high temperature environment [5–8], while maintaining the excellent processability.

The copolymers were found to degrade at above 310 °C in TGA measurements, which means these copolymers are thermally stable in comparison with MMA and TFEMA homopolymers and are capable to the general fiber preparation procedure at 200–300 °C. The data in Table 3 also showed that copolymers have higher molecular weight in comparison to the homopolymers. This high molecular weight is precious for the special preparation method for

Table 2
The monomer reactivity ratios of comonomer pair.

M_1/M_2	r_1	r_2	r_1r_2
MMA/2TFMS	0.84 ± 0.04	1.55 ± 0.08	1.30
TFEMA/25BTFMS	0.64 ± 0.03	1.18 ± 0.06	0.76

Table 3
Thermal analysis and molecular weight results.

Sample	Composition (wt%)	T_g (°C)	T_d (°C)	M_w	M_n
1	MMA	108	338	101.000	39.500
2	MMA/2TFMS = 74/26	127	312	–	–
3	MMA/2TFMS = 50/50	136	341	337.700	99.200
4	MMA/2TFMS = 26/74	146	338	–	–
5	2TFMS	165	382	193.100	59.700
6	TFEMA	75	280	241.600	86.200
7	TFEMA/25BTFMS = 76/24	86	311	–	–
8	TFEMA/25BTFMS = 51/49	103	322	344.400	89.300
9	TFEMA/25BTFMS = 25/75	129	332	–	–
10	25BTFMS	160	366	266.300	88.800

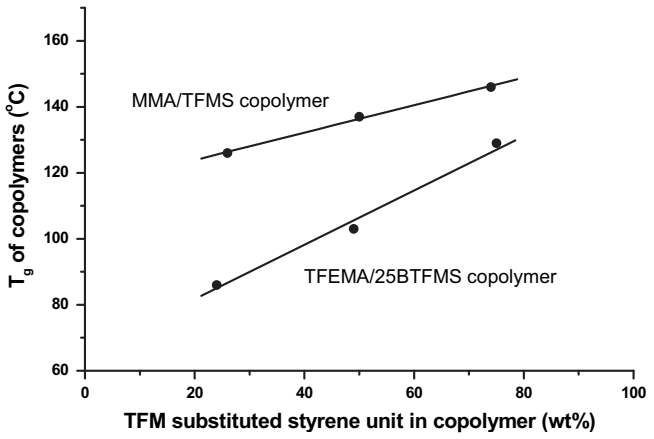

Fig. 5. Composition dependence of T_gs for MMA/2TFMS and TFEMA/25BTFMS copolymers.

the gradient index plastic optical fiber (GI-POF), since it is necessary to add dopants and chain transfer agents in the system during the preparation, while keeping the good mechanical properties of the polymer material [24,25].

The refractive indices of the copolymers from methacrylates and CF_3 substituted styrenes were studied at different wavelengths (532 nm, 633 nm, 839 nm), and the composition dependence of the refractive index was plotted in Fig. 6. The results show that there is a linear relationship between the refractive indices of the copolymers and their compositions. It suggests that there is no macrophysical property change such as density, which may occur during the

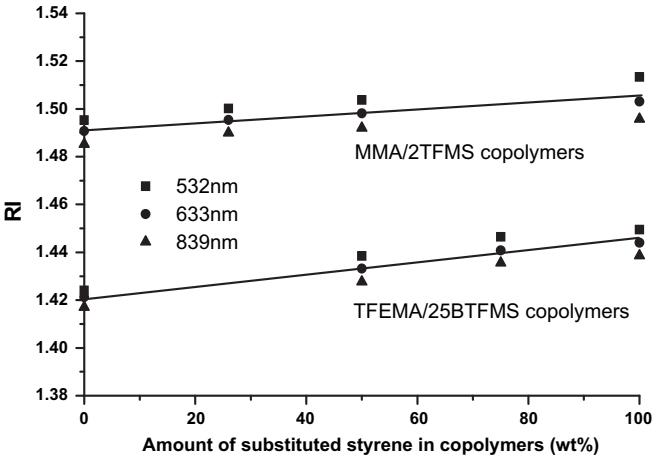

Fig. 6. Composition dependence of the refractive index for copolymer systems.

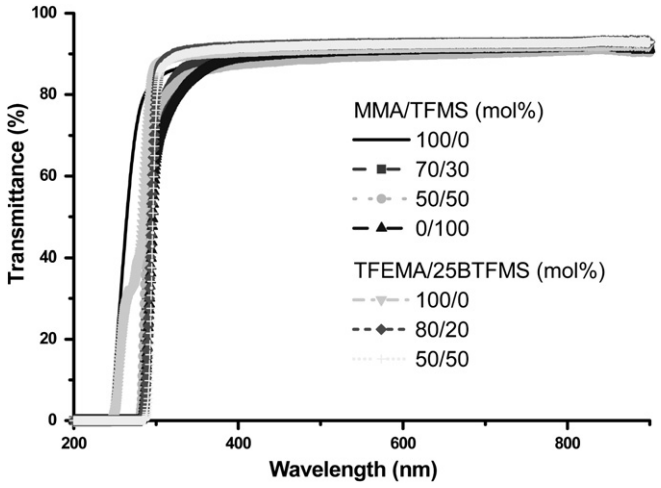

Fig. 7. Transmittance spectra of MMA/2TFMS and TFEMA/25BTFMS copolymer systems.

formation of the copolymers. This is agreeing with the conclusion of the homogeneous macromolecular structure from the T_g results.

Fig. 7 showed that these copolymer films (110–200 μm) exhibit similar transmittance (~90%) as the homopolymers of MMA and TFEMA in the 300–900 nm wavelength range. This high transmittance should result from the random copolymer composition due to the similar reactivity ratio of the two monomers and the negligible light scattering due to the similar refractive indices of the two monomeric units in the polymer chains. Since most copolymers have high light scattering due to the heterogeneous macromolecular structure, these transparent copolymers are combining the excellent mechanical properties of acrylate polymers, high thermal stability of styrene polymers and the desired optical properties similar to amorphous homopolymers.

4. Conclusion

Homopolymers of 2TFMS and 25BTFMS, as well as their copolymers with MMA and TFEMA, exhibited relatively high T_gs, high thermal stability and high transmittance. These polymers may be utilized as novel optical materials.

References

[1] Ziemann O, Krauser J, Zamgow PE, Daum W. POF Handbook. 2nd ed. Berlin: Springer; 2008. 166–168.
[2] Groh W. Makromol Chem 1988;189:2861–70.
[3] Groh W. Macromolecules 1991;24:6660–8.
[4] Lou L, Koike Y, Okamoto Y. J Polym Sci Part A Polym Chem 2010;48:4938–42.
[5] Truong TK. Commercial airplane fiber optics needs, opportunities, challenges, the 19th International Conference on Plastic Optical Fibers, Japan, October 2010.
[6] Ziemann O, Krauser J, Zamgow PE, Daum W. POF Handbook. 2nd ed. Berlin: Springer; 2008. 157–158.
[7] Koike K, Koike Y. J Lightw Technol 2009;27:41–6.
[8] Sato M, Hirai M, Ishigure T, Koike Y. J Lightw Technol 2000;18:2139–45.
[9] Boner B, Hagemann H. Angew Makro Chem 1982;109:285–93.
[10] Chambers RD. Fluorine in Organic Chemistry. CRC Press; 2000. p 92.
[11] Odian G. Principles of polymerization. 2nd ed. John Wiley and Sons; 1981. pp. 197–199.
[12] Mayo FR, Lewis FM. J Am Chem Soc 1944;66:1594–601.
[13] Beuermann S, Buback M. Progr Polym Sci 2002;27:191–254.
[14] Coote ML, Davis TP. Macromolecules 1999;32:4290–8.
[15] Buback M, Garcia-Rubio L, Gilbert R, Napper D, Guillot J, Hamielec A, et al. J Polym Sci Part C Polym Lett 1988;26:293–7.
[16] Mahabadi HK. Macromolecules 1985;18:1319–24.
[17] Walling C, Briggs ER, Wolfstirn BK, Mayo FR. J Am Chem Soc 1948;70: 1537–42.
[18] Imoto M, Kinoshita M, Nishigaki M. Makro Chem; 1965:217–30.
[19] Pryor W, Huang TL. Macromolecules 1962;2:70–7.
[20] Hammett Louis P. Chem Rev 1935;17:125–36.
[21] Hansch C, Leo A, Taft RW. Chem Rev 1991;91:165–95.
[22] The T_g of 35BTFMS homopolymer was reported as 60 °C in reference [6].
[23] Koike K, Kado T, Satoh Z, Okamoto Y, Koike Y. Polymer 2010;51:1377–85.
[24] Koike K, Teng H, Okamoto Y, Koike Y. Proc ICPOF; 2007:318–9.
[25] Koike Y, Koike K. J Polym Sci Part B Polym Phys 2011;49:2–17.

Polymer 52 (2011) 954–964

Contents lists available at ScienceDirect

Polymer

journal homepage: www.elsevier.com/locate/polymer

Synthesis, characterization and hydrolysis of aromatic polyazomethines containing non-coplanar biphenyl structures

Jyh-Chien Chen [a,*], Yen-Chun Liu [a], Jyh-Jong Ju [a], Chi-Jui Chiang [a], Yaw-Tern Chern [b]

[a] Department of Polymer Engineering, National Taiwan University of Science and Technology, No. 43, Sec. 4, Keelung Rd., Taipei 10607, Taiwan
[b] Department of Chemical Engineering, National Taiwan University of Science and Technology, No. 43, Sec. 4, Keelung Rd., Taipei 10607, Taiwan

ARTICLE INFO

Article history:
Received 15 October 2010
Received in revised form
24 December 2010
Accepted 6 January 2011
Available online 12 January 2011

Keywords:
Polyazomethines
Conjugated polymers
Hydrolysis

ABSTRACT

New polyazomethines containing electron-withdrawing trifluoromethyl group and non-coplanar biphenyl structures were prepared at room temperature under reduced pressure. It was found that these polyazomethines would undergo hydrolysis in DMSO solution at temperature higher than 50 °C. The hydrolysis, evidenced by ^{1}H NMR spectra and GPC chromatograms, was resulted from the reverse reaction of azomethine formation and was facilitated at higher temperature. The GPC results also suggested that post-polymerization would be possible if polyazomethine films were heated at elevated temperature (200 °C) under reduced pressure (0.27 torr). The HOMO (−5.69 to −5.96 eV) and LUMO (−3.04 to −3.18 eV) energy levels of the new polyazomethines are much lower than those of other polyazomethines. Combined with the excellent solubility and good thermal stability, non-coplanar biphenyl structure containing electron-withdrawing trifluoromethyl group could be a new candidate as electron acceptor for the structure design of new conjugated polymers.

1. Introduction

Aromatic polyazomethines, containing C═N linkage, exhibit excellent thermal stability, good mechanical properties and, in some cases, liquid crystalline morphology [1]. In addition to high performance fiber and metal-chelating ability [2,3], they have been also investigated for the opto-electrical applications such as hole-transport layer for OLED, semiconductor, non-linear optics (NLO) and photovoltaic cell [4–7]. However, these applications have been limited by their poor solubility in common organic solvents and low molecular weights. Besides, the relatively rare availability of new dialdehyde monomers also hindered the chemical structure modifications of polyazomethines. Many strategies have been reported to improve the solubility of polyazomethines. The introduction of flexible alkyl and alkoxy groups as the substituents has been proved to be effective, although at the expense of their thermal stability [8–10]. The incorporations of bulky substituents such as triphenylamine, tetraphenylethylene and diphenylfluorene, have been investigated [11–13]. The copolymerization of electron-rich, solubility-enhancing aromatic or heterocyclic units such as thiophene, carbazole and fluorene [14–17], has also been explored. The C═N linkages of polyazomethines are electron-withdrawing group and therefore can be used to tune the HOMO and LOMO energy levels of the electron-rich conjugated polymers to fit the best combination of energy levels and charge mobility in a multilayer device. However, in most cases, the enhancements in solubility of these conjugated polymers are resulted from the long alkyl or alkoxy side chains attached on the electron-rich units, leading to lower thermal stability.

The chemical modifications of polyazomethines are mainly achieved by synthesizing new diamines and then polymerizing them with commercially available dialdehydes. These attempts targeting at either solubility enhancement or investigating their optical and electrical properties are limited by the rare availability of new dialdehyde monomers. Most dialdehyde monomers are prepared by electrophilic substitution (Vilsmeier reaction) on an electron-rich aromatic or heterocyclic ring [18]. The preparation of new dialdehydes by the reduction of cyano group has rarely been reported [19].

Conventionally, polyazomethines are prepared by solution polymerization from diamines and dialdehydes either at room temperature or at higher temperature [20]. The premature precipitation during polymerization, as a result of poor solubility, often leads to low molecular weight products. Even for soluble polyazomethines, it is often difficult to achieve high molecular weight. Several polymerization conditions have been applied. In some cases, LiCl was used as the water absorption agents [21]. It has also been demonstrated that polymerization at room temperature

* Corresponding author. Fax: +886 2 27376544.
E-mail address: jcchen@mail.ntust.edu.tw (J.-C. Chen).

0032-3861/$ – see front matter © 2011 Elsevier Ltd. All rights reserved.
doi:10.1016/j.polymer.2011.01.011

under vacuum in weakly acidic *m*-cresol is the best method to obtain the highest molecular weight [13]. However, the reason has not been fully explained. In addition, the formation of azomethine linkage is, like esterification, actually reversible. In the presence of water, hydrolysis might predominate under suitable conditions [22]. However, this issue has never been addressed in polyazomethine study.

In this study, a new aromatic dialdehyde containing electron-withdrawing trifluoromethyl groups at the 2 and 2′ positions of biphenyl was synthesized. The aldehyde functionality was achieved by the reduction of cyano groups. Organosoluble polyazomethines were prepared from this dialdehyde with 2,2′-disubstituted-4,4′-benzidines, 4,4′-oxydianiline and *p*-phenylenediamine by solution polycondensation at room temperature under reduced pressure. The hydrolysis of azomethine linkages at the presence of trace water was investigated by ^{1}H NMR spectroscopy and GPC chromatography. The thermal, optical and electrochemical properties of these new polyazomethines were also investigated. The effects of strong electron-withdrawing trifluoromethyl groups and non-coplanar biphenyl structures on the HOMO and LUMO energy levels were also discussed.

2. Experimental

2.1. Materials

Tetrabutylammonium perchlorate (TBAP) used in cyclic voltammetric measurements was recrystallized twice with ethyl acetate and dried at 120 °C under reduced pressure overnight. All of other reagents were purchased from commercial companies and used as received. All of the solvents used in this study were purified according to standard methods prior to use. 2,2′-Dimethyl-4,4′-benzidine (**DMB 6**) and 2,2′-bis(trifluoromethyl)-4,4′-benzidine (**TFMB 7**) were synthesized according to reported procedures with some modifications [23,24].

2.2. Measurements

All melting points were determined on a Mel-Temp capillary melting point apparatus. Proton (^{1}H NMR) and carbon (^{13}C NMR) nuclear magnetic resonance spectra were measured at 500 and 125 MHz on a Bruker Avance-500 spectrometer, respectively. Infrared spectra were obtained with a Digilab-FTS1000 FTIR. Mass spectroscopy was conducted on a Finnigan TSQ 700 mass spectrometer. Elemental analyses were performed on a Heraeus Vario analyzer. High performance liquid chromatography was performed on a JASCO HPLC system equipped with a UV (254 nm) detector using a Thermo Hypersil column (250 mm × 4.6 mm, particle size 5 μm) with an 80/20 (v/v) acetonitrile/water mixture as the solvent. Inherent viscosities were determined with a Cannon–Ubbelohde No. 100 viscometer at 30.0 ± 0.1 °C in *N*-methyl-2-pyrrolidinone (NMP). Molecular weights were measured on a JASCO GPC system (PU-980) equipped with an RI detector (RI-930), a Jordi Gel DVB Mixed Bed column (250 mm × 10 mm) column, using dimethylacetamide (DMAc) as the eluent and calibrated with polystyrene standards. Thermal gravimetric analyses (TGA) were performed in nitrogen with a TA TGA Q500 thermogravimetric analyzer using a heating rate of 10 °C min^{-1}. Differential scanning calorimeter (DSC Pyris 1) was used to measure the glass transition temperatures under nitrogen at a heating rate of 10 °C min^{-1}. UV-visible measurements were carried out on a Cary-100 UV-Visible spectrometer at room temperature. Photoluminescence (PL) measurements were carried out on a Perkin–Elmer F4500 photoluminescence spectrometer. Fluorescence quantum yield (Φ_{PL}) of the polymer in chloroform was measured by 10^{-5} M quinine sulfate in 1 N H_2SO_4 as reference standard ($\Phi_{PL} = 0.546$). Cyclic voltammetric (CV) measurements were carried out on a CH Instrument 611C electrochemical analyzer at room temperature in a three-electrode electrochemical cell with a working electrode (polymer film coated on ITO glass), a reference electrode (Ag/Ag$^+$, referenced against ferrocene/ferrocium (Fc/Fc$^+$), 0.09 V), and a counter electrode (Pt gauze) at a scan rate of 100 mV s^{-1}. CV measurements for polymer films were performed in an electrolyte solution of 0.1 M tetrabutylammonium perchlorate (TBAP) in acetonitrile. The potential window at oxidative scan was 0–2.5 V and reductive scan was 0 to −2.5 V, respectively. The wide-angle X-ray diffraction (WXRD) data were collected on a PANalytical X'Pert PRO X-ray powder diffraction.

2.3. Synthesis of monomers

Monomers (**1**)–(**4**) were synthesized by procedures in our previous work [33].

2.3.1. 2,2-Bis(trifluoromethyl)-4,4-biphenyldicarbaldehyde (*5*)

To a 100 mL, three-neck, round-bottom flask equipped with condenser and mechanical stirrer were added 0.30 g (0.88 mmol) of 2,2′-bis(trifluoromethyl)-4,4′-biphenyldicarbonitrile (**4**) and 10 mL of toluene. After 9 mL (10.09 mmol) of diisobutylaluminium hydride (DIBAL-H) (20% in hexane) was slowly added with a syringe under nitrogen atmosphere, the reaction mixture was further stirred at 16 °C for 18 h under nitrogen atmosphere. The reaction mixture was then poured into a vigorously stirred solution of methanol/water (1:1, v/v) and kept at 0 °C with ice bath for 3 h. After 200 mL of 2M HCl solution was added, the mixture was extracted with 200 mL of ether twice. The combined organic phase was collected and washed many times with water and dried with anhydrous magnesium sulfate. The organic phase was evaporated and dried under reduced pressure at 60 °C overnight. The crude product was then sublimated under reduced pressure at 70 °C to afford 0.18 g (59.0% yield) of white crystals: mp 118–120 °C; FTIR (KBr) : 2757 cm^{-1} (aldehyde C–H stretching), 1705 cm^{-1} (aldehyde C=O stretching). ^{1}H NMR (500 MHz, DMSO-d_6, δ, ppm): 10.17 (s, 2H, aldehyde-H_d), 8.41 (d, J = 0.8 Hz, 2H, Ar–H_a), 8.26 (dd, J = 0.8 and 8.0 Hz, 2H, Ar–H_b) and 7.70 (d, J = 8.0 Hz, 2H, Ar–H_c). ^{13}C NMR (125 MHz, DMSO-d_6, δ, ppm): CF_3 (q) (C7) 119.99, 122.17, 124.35, 126.54, C–CF_3 (q) (C6) 127.63, 127.87, 128.12, 128.37, 127.24 (C5), 131.80 (C2), 132.36 (C3), 136.41 (C4), 141.00 (C1), 191.87 (C8). EIMS (*m*/*z*): Calcd. for $C_{16}H_8F_6O_2$: 346.0428; Found: 346.0 [M] $^+$; 344.9 [M − 1]$^+$. Anal. Calcd for $C_{16}H_8F_6O_2$: C: 55.50, H: 2.33%; Found : C: 55.51%, H: 2.45%.

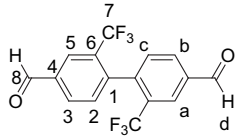

(**5**)

2.3.2. 3,3′-Dibromoazoxybenzene

To a 250 mL, three-neck, round-bottom flask equipped with a mechanical stirrer, a condenser, and a stopper were added 60 mL of ethanol and 21.20 g (530.00 mmol) of sodium hydroxide. The reaction mixture was heated at 70 °C until most of sodium hydroxide was dissolved. After 66.4 mL of ethylene glycol and 10.00 g (49.50 mmol) of 1-bromo-3nitrobenzene were added, the reaction mixture was heated at reflux for 2 h. The warm mixture was poured into 300 mL of ice water and stirred for 30 min. The brown solid that formed was collected by filtration and washed

several times with water. After drying under reduced pressure at 90 °C overnight, 7.71 g (80.0% yield) of crude product was obtained. The crude product was used in the next procedure without further purification. A small portion of crude product was decolorized with charcoal and recrystallized from acetone to afford a yellow powder: mp 114–115 °C; ^{1}H NMR (500 MHz, DMSO-d_6, δ, ppm): 8.42–7.25 (m, 8H, Ar–H_{a-d}).

2.3.3. 2,2′-Dibromo-4,4′-diaminobiphenyl (**8**)

To a 250 mL, three-neck, round-bottom flask equipped with a mechanical stirrer, a condenser, and a thermometer were added 18.50 g (12.45 mmol) of 3,3′-dibromoazoxybenzene, 115 mL of tetrahydrofuran and 161 mL of glacial acetic acid. Zinc dust (12.90 g) was added slowly so the temperature of the reaction mixture was maintained below 40 °C. After the addition of zinc dust, 23 mL of 85% phosphoric acid was added slowly so the temperature of the reaction mixture was maintained below 55 °C. After stirring for 30 min, the reaction mixture was filtered to remove zinc dust. The filtrate was poured into 300 mL of water. The aqueous phase was extracted twice with 100 mL of methylene chloride. The combined organic phase was added dropwise to 60 mL of conc. hydrochloric acid at 0 °C and stirred for 30 min. The precipitate that formed was collected by filtration and washed with methylene chloride and then dissolved in 1 L of hot water. After the solution was filtered, the clear filtrate was neutralized with ammonium hydroxide. The precipitate that formed was collected and recrystallized from toluene to afford 9.02 g (56.0% yield) of white crystal: mp 151–153 °C (lit [25]. mp 152–156 °C); ^{1}H NMR (500 MHz, DMSO-d_6, δ, ppm): 6.85–6.81 (m, 4H, Ar–$H_{a,c}$), 6.54 (dd, J = 2.0 and 8.2 Hz, 2H, Ar–H_b) and 5.35 (s, 4H, NH_2–H_d).

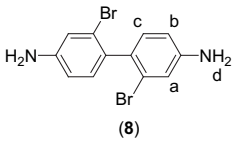

(**8**)

2.3.4. 2,2′-Diphenyl-4,4′-diaminobiphenyl (**9**)

To a 250 mL, three-neck, round-bottom flask equipped with a mechanical stirrer, a condenser, and a nitrogen inlet were added 3.00 g (8.76 mmol) of 2,2′-dibromo-4,4′-diaminobiphenyl (**8**) and 54 mL of toluene. After the solution was heated at 50 °C under nitrogen and became clear, 4.26 g (40.00 mmol) of sodium carbonate in 18 mL of water and 0.66 g (0.57 mmol) of Pd(P(Ph_3))$_4$ were added. After the solution was vigorously stirred for 30 min, a solution of 2.70 g (22.14 mmol) of phenylboronic acid in 18 mL of ethanol was added. The reaction solution was heated at reflux for 24 h under nitrogen. After the reaction mixture was allowed to cool to room temperature, it was filtered to remove insoluble components. The filtrate was collected and washed several times with a saturated NaCl aqueous solution. After dried with anhydrous magnesium sulfate, the combined organic phase was evaporated to dryness under reduced pressure. The crude product was recrystallized from a mixture of water and methanol to afford 2.10 g (71.0% yield) of light-brown crystals. mp 152–153 °C (lit [26]. mp 151–152 °C); ^{1}H NMR (500 MHz, DMSO-d_6, δ, ppm): 7.07–7.03 (m, 6H, Ar–$H_{f,g}$), 6.83 (d, J = 7.7 Hz, 2H, Ar–H_c), 6.47 (d, J = 6.9 Hz, 4H, Ar–H_e), 6.66 (d, J = 7.7 Hz, 2H, Ar–H_b), 6.34 (s, 2H, Ar–H_a) and 5.00 (s, 4H, NH_2–H_d).

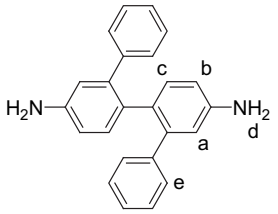

(**9**)

2.4. Synthesis of polyazomethines

Polyazomethines **PAM-1**–**7** were prepared by solution polymerization using equimolar dialdehyde and diamine at room temperature under reduced pressure (0.27 torr). The synthesis of **PAM-2** was used as an example to illustrate the general synthetic procedure. To a 100 mL, three-neck, round-bottom flask were added 0.50 g (1.40 mmol) of 2,2′-bis(trifluoromethyl)-4,4′-biphenyldicarbaldehyde (**5**), 0.45 g (1.40 mmol) of diamine (**7**) and 10 mL of *m*-cresol. After the reaction mixture was stirred at room temperature for 48 h under reduced pressure, it was poured into a mixture of methanol and water (1:1, v/v). The precipitate that formed was collected by filtration and washed with hot ethanol (Soxhlet apparatus) for 12 h and dried at 100 °C overnight under reduced pressure to afford 0.85 g (96.0% yield) of powder. IR (KBr): 3402 cm^{-1} (NH_2 end group), 3057 cm^{-1} (aromatic), 2735 cm^{-1} (aldehyde end group O=C–H stretching), 1702 cm^{-1} (aldehyde end group O=C stretching), and 1625 cm^{-1} (azomethine C=N stretching). ^{1}H NMR (500 MHz, DMSO-d_6, δ, ppm): 10.19 (d, J = 7.0 Hz, 1H, aldehyde end group), 9.02 (d, J = 4.5 Hz, 2H, azomethine HC=N), 8.51 (d, J = 6.0 Hz, 2H, Ar–H), 8.36–8.34 (m, 2H, Ar–H), 7.84 (d, J = 6.0 Hz, 2H, Ar–H), 7.72–7.63 (m, 4H, Ar–H) and

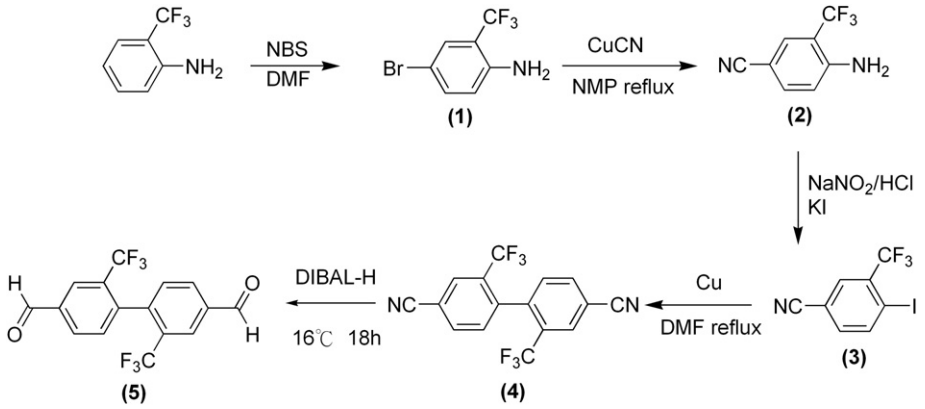

Scheme 1. Synthesis of 2,2′-bis(trifluoromethyl)-4,4′-biphenyldicarbaldehyde (**5**).

7.54 (d, $J = 7.5$ Hz, 2H, Ar—H) and 5.74 (br, 2H, NH_2 end group). The inherent viscosity of the obtained **PAM-2** was 0.50 dL/g (measured at a concentration of 0.5 g/dL in NMP at 30 °C). The other polyazomethines were prepared by the same procedure.

3. Results and discussion

3.1. Synthesis of monomers

The new dialdehyde, 2,2′-bis(trifluoromethyl)-4,4′-biphenyldicarbaldehyde (**5**), containing electron-withdrawing trifluoromethyl groups at the 2 and 2′ positions of biphenyl, was synthesized by a five-step synthetic route as shown in Scheme 1. 2-Aminobenzotrifluoride was first brominated at the *para* position by *N*-bromosuccinimide (NBS) in DMF. The aromatic bromide (**1**) that formed was converted to cyanide compound (**2**) by copper cyanide in NMP. The amino group of compound (**2**) was then transformed to aromatic iodide (**3**) by diazotization then Sandmeyer reaction. The iodide compound (**3**) was coupled by Ullmann coupling reaction in the presence of activated copper powder in DMF to form 2,2′-bis (trifluoromethyl)-4,4′-biphenyldicarbonitrile (**4**). The new dialdehyde (**5**) was then obtained by the reduction of cyano compound (**4**) using diisobutylaluminium hydride (DIBAL-H) as reducing agent. The as-prepared dialdehyde was purified by sublimation at 70 °C under reduced pressure before polymerization. ^{1}H NMR spectrum of dialdehyde (**5**) is shown in Fig. 1(a). The singlet peak at 10.17 ppm was attributed to the aldehyde hydrogen. The other absorption peaks in the aromatic region (7–9 ppm) were assigned to the corresponding hydrogen as shown in Fig. 1(a). IR spectrum of dialdehyde (**5**) is shown in Fig. 2. The absorption peaks at 2757 cm^{-1} (aldehyde C—H stretching) and 1705 cm^{-1} (aldehyde C═O stretching) also showed the formation of aldehyde group. The spectra of ^{1}H NMR, ^{13}C NMR and IR, together with the result of elemental analysis, confirmed the structure of the new dialdehyde (**5**). Several approaches to simplify the synthetic route have been carried out without success. For example, the attempt to direct formylation (electrophilic reaction) of 2,2′-bis(trifluoromethyl)biphenyl by $POCl_3$ and DMF was unsuccessful. It might be resulted from the electron deficiency of the biphenyl moiety due to the presence of strong electron-withdrawing trifluoromethyl group.

Diamines, 2,2′-dibromo-4,4′-benzidine (**8**) and 2,2′-diphenyl-4,4′-benzidine (**9**) were prepared according to the synthetic route shown in Scheme 2. First, 1-bromo-3-nitrobezene was reduced to azoxy compound, which then underwent benzidine rearrangement in the presence of zinc dust to form 2,2′-dibromo-4,4′-benzidine (**8**). 2,2′-Diphenyl-4,4′-benzidine (**9**) was then obtained by Suzuki coupling reaction between phenylboronic acid and diamine (**8**).

3.2. Synthesis of polyazomethines

Polyazomethines **PAM-1**–**7** were prepared in quantitative yields by reacting equimolar diamines and dialdehydes in *m*-cresol at

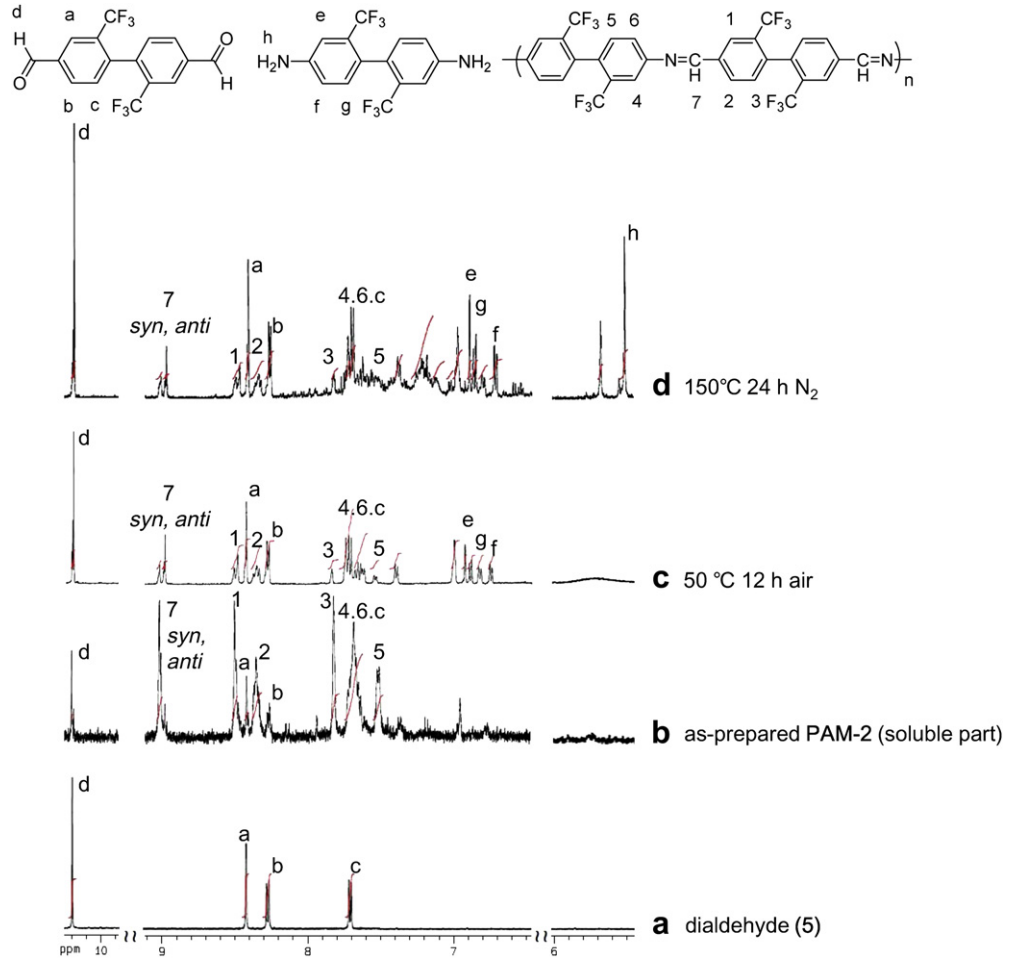

Fig. 1. ^{1}H NMR spectra in DMSO-d_6 of (a) monomer (**5**), (b) as-prepared **PAM-2** (soluble part) and hydrolysis of **PAM-2** with various condition, (c) 50 °C for 12 h in air, (d) 150 °C for 24 h in nitrogen.

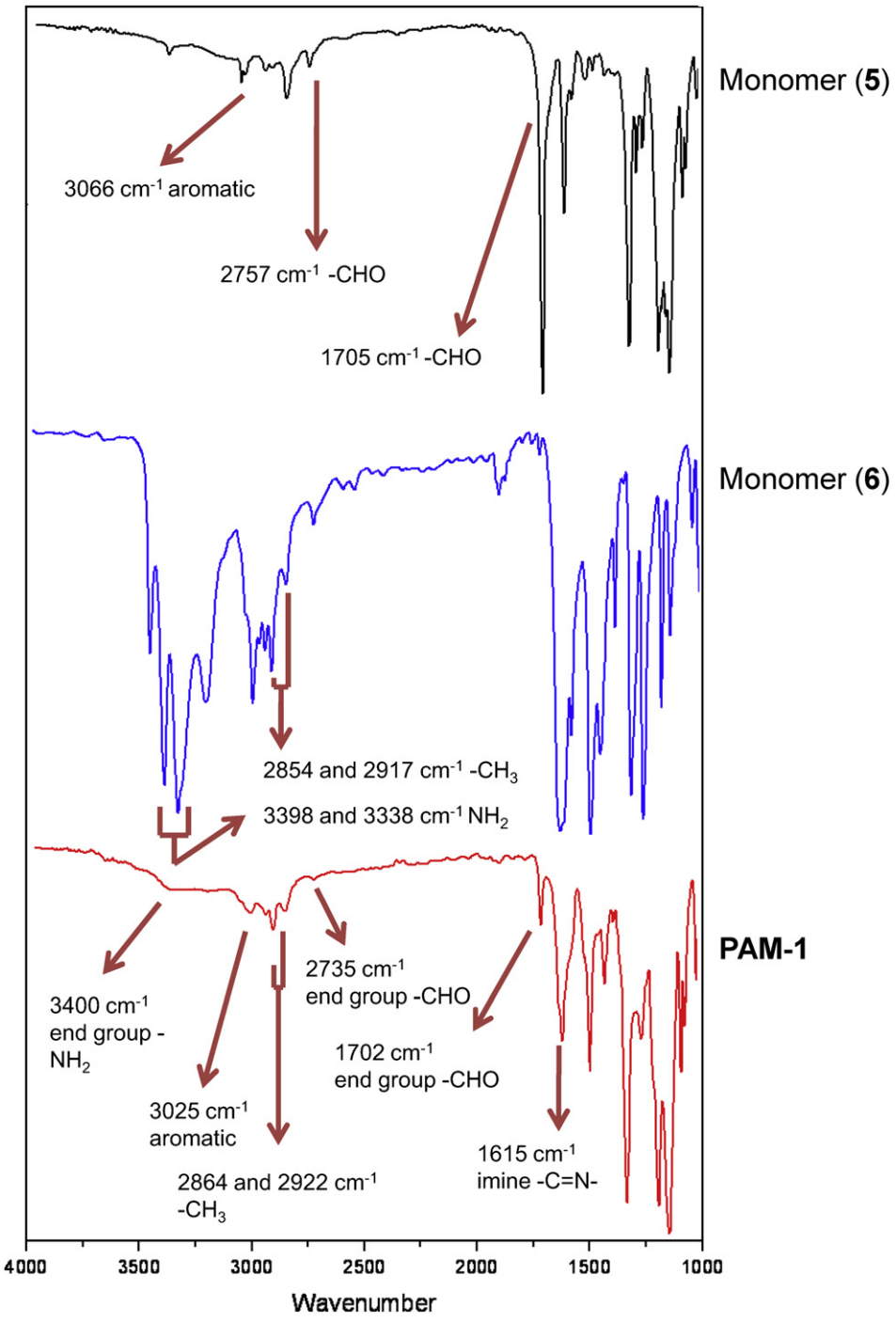

Fig. 2. IR spectra of monomers (**5**), (**6**) and **PAM-1** (KBr).

room temperature under reduced pressure as shown in Scheme 3. Polyazomethines **PAM-1**–**4** were prepared by using the new trifluoromethyl-containing dialdehyde (**5**) and four substituted benzidines (**6**–**9**). The substituents of these benzidines included methyl (**PAM-1**), trifluoromethyl (**PAM-2**), bromide (**PAM-3**) and phenyl (**PAM-4**). 4,4′-Oxydianiline (**ODA**) and *p*-phenylenediamine (**PDA**) were also used to prepare polyazomethines **PAM-5** and **PAM-6**, respectively. In comparison to **PAM-6**, **PAM-7** was prepared by reacting terephthalic dicarbaldehyde (**TPDCA**) with 2,2′-bis(trifluoromethyl)-4,4′-benzidine (**TFMB 7**). All the polyazomethines **PAM-1**–**7** remained in solution without any premature precipitation throughout the polymerization and were prepared in quantitative yields (Table 1). A representative IR spectrum of **PAM-1** is shown in Fig. 2. The characteristic peak appearing at 1615 cm^{-1} (C═N stretching) confirmed the formation of azomethine linkage. A representative ^1H NMR spectrum of as-prepared **PAM-2** (soluble part in DMSO-d_6) is shown in Fig. 1(b). Because of the limited solubility of **PAM-2** in DMSO-d_6, ^1H NMR sample was prepared by dissolving 0.1% (w/v) as-prepared **PAM-2** in DMSO-d_6 at room temperature and then removing the insoluble part by filtration. The peaks appearing at 9.02 ppm were assigned to the hydrogen of the azomethine linkage. These peaks suggested the existence of *syn* and *anti* configurations in the polymer backbone as reported earlier [27,28]. It was also found from the ^1H NMR spectrum of **PAM-2**

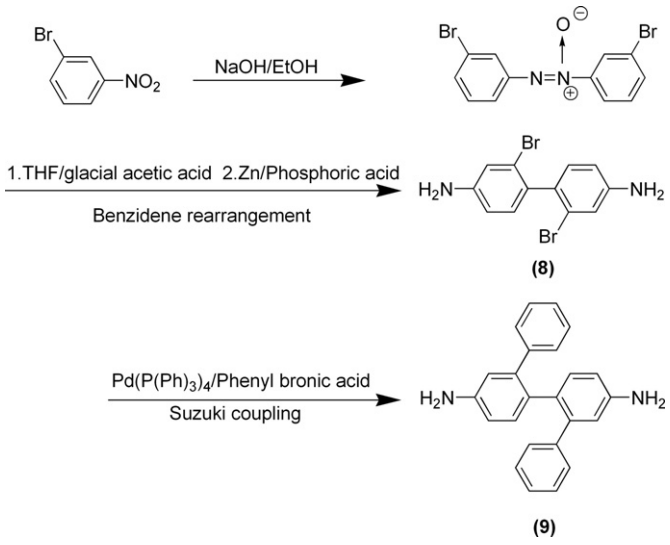

Scheme 2. Synthesis of 2,2′-diphenyl-4,4′-diaminobiphenyl (**9**).

soluble part that an appreciated amount of chain-end aldehyde (10.19 ppm) remained. However, it was surprising that the absorption peak of amine end groups (5.74 ppm) was almost invisible. It might be resulted from the slow exchange rate of protons on nitrogen and the electrical quadrupole moment of ^{14}N nucleus. The protons on the nitrogen might respond by giving a broad peak that disappears in the baseline.

Table 1
Inherent viscosity, M_n, M_w and yield of polyazomethines.

	η_{inh}[a] (dL/g)	M_n[b] (10^4 g/mol)	M_w[b] (10^4 g/mol)	Yield (%)
PAM-1	0.79	2.4	7.5	96
PAM-2	0.50	1.2	2.5	96
PAM-3	0.38	1.3	3.0	98
PAM-4	0.32	1.3	3.0	97
PAM-5	0.33	1.4	3.5	96
PAM-6	0.79	2.0	5.1	96
PAM-7	0.44	1.6	3.7	96

[a] Measured at a polymer concentration of 0.5 g/dL in NMP at 30 °C.
[b] By GPC in DMAc (relative to polystyrene standards).

3.3. Characterizations of polyazomethines

The inherent viscosity and molecular weights (determined by GPC in DMAc and calibrated by polystyrene standards) are reported in Table 1. The as-prepared polyazomethines had inherent viscosity in the range of 0.32–0.79 dL/g (measured at a polymer concentration of 0.5 g/dL in NMP at 30 °C). The number-averaged molecular weights ranged from 12,000 to 24,000 g/mole. These values are high when compared with those of conventional aromatic polyazomethines. The molecular weights estimated from the intensity

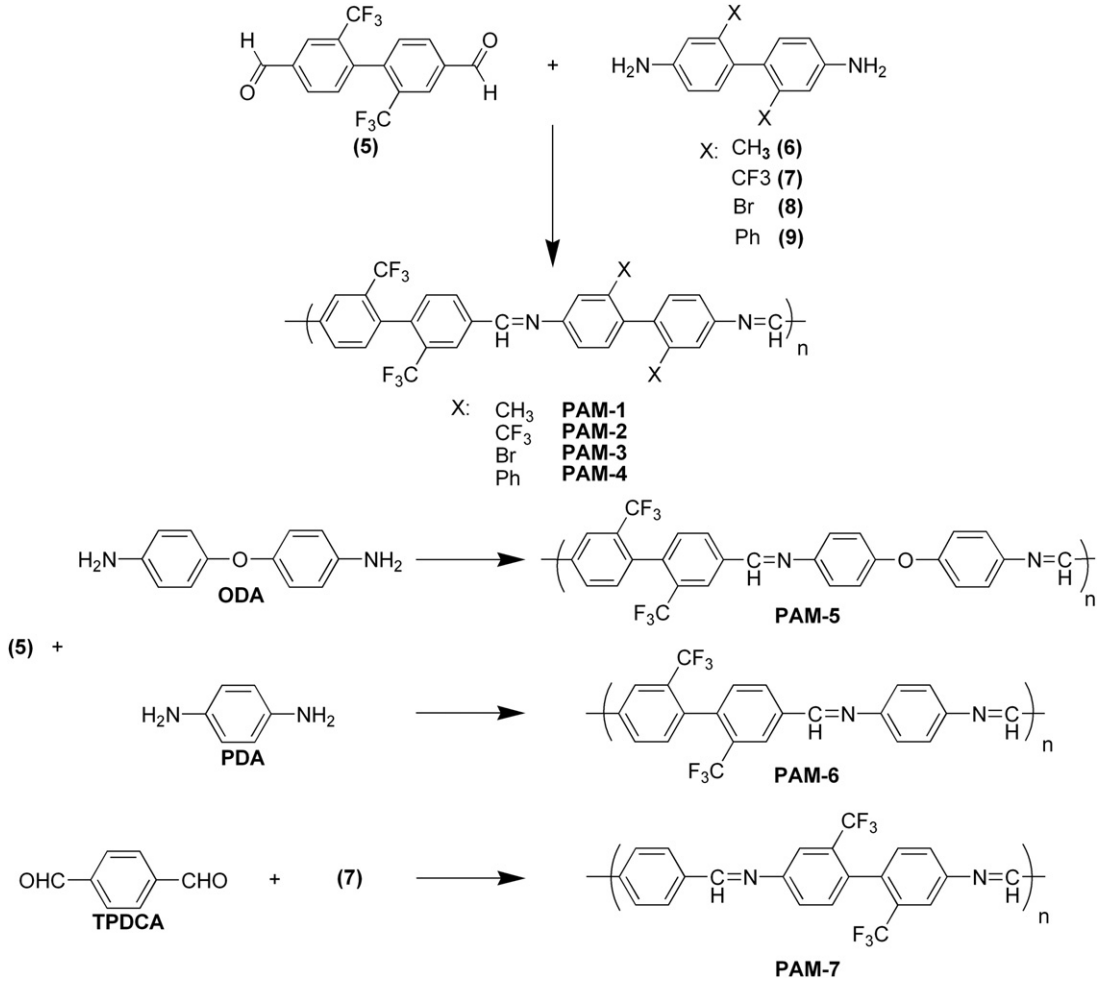

Scheme 3. Synthesis of polyazomethines.

of chain-end aldehyde peak (10.19 ppm) and that of azomethine hydrogen (9.02 ppm) from the ^{1}H NMR spectra were much smaller than those measured by GPC. It was attributed to the limited solubility of these polyazomethines in DMSO-d_6 solvent. The molecular weights estimated by ^{1}H NMR spectra represented only the soluble part of polyazomethines in DMSO-d_6. These polyazomethines were, however, totally soluble in DMAc, the solvent for GPC. Among these polyazomethines, **PAM-1** and **PAM-6**, prepared from the new dialdehyde (**5**) and 2,2′-dimethyl-4,4′-benzidine (**6**) and *p*-phenylenediamine (PDA), respectively, had the highest molecular weights. It might be attributed to the high reactivity of the new aldehyde (**5**) and these two diamines.

Different methods have been reported for the preparation of polyazomethines. These methods involved polymerization at different temperatures, including at toluene-water azeotropic temperature [29], at 160 °C in *m*-cresol [16] or NMP/HMPA [30], and at room temperature with or without reduced pressure [12,13]. In order to find out the best condition to achieve the highest molecular weights, **PAM-1** and **PAM-2** were prepared for 48 h in *m*-cresol at room temperature under reduced pressure (condition A), in *m*-cresol at reflux temperature under nitrogen atmosphere (condition B) and in NMP/HMPA (1:1, v/v) at room temperature condition C. Table 2 shows the inherent viscosity and molecular weights of **PAM-1** and **PAM-2** prepared in different conditions. **PAM-1** prepared in *m*-cresol at room temperature under reduced pressure (condition A) had the highest M_n of 24,000 g/mole. When the temperature was raised to reflux temperature (condition B), **PAM-1** had the lowest M_n of 3000 g/mole. When **PAM-1** was prepared in NMP/HMPA (1:1, v/v) at room temperature for 48 h (condition C), the M_n was 12,000 g/mole. **PAM-2** experienced the same effect, highest M_n was obtained by condition A, the lowest M_n by condition B. From these data, it can be concluded that polyazomethines with the highest M_n can be obtained by room temperature solution polymerization in *m*-cresol under reduced pressure. It was pointed out that weakly acidic *m*-cresol had an activating effect on the azomethine formation [13]. The dialdehyde was activated by acidic solvents and deactivated by basic solvents. However, too strongly acidic solvent might deactivate diamine. Therefore, weakly acidic solvent such as *m*-cresol might be the best polymerization medium. Table 2 also shows that polyazomethines prepared at room temperature had higher M_n than at reflux temperature. This phenomenon was to be discussed in the next section (Hydrolysis and Post-Polymerization).

The solubility behavior of these new polyazomethines in different organic solvents is reported in Table 3. All of these polyazomethines can be dissolved (20 mg in 1 mL of solvent) at room temperature in DMF, DMAc, NMP and *m*-cresol and were partially soluble in DMSO and THF. Especially, **PAM-6** and **PAM-7**, containing the most rigid *p*-phenylene structure, were still soluble in polar organic solvents. Conventional aromatic polyazomethines are insoluble in organic solvents. For example, polyazomethine **PAM-8**, containing similar structures with **PAM-6** and **PAM-7**, can be prepared from 4,4′-benzidine with terephthalic dicarbaldehyde (**TPDCA**). It was only soluble in concentrated sulfuric acid [9].

Table 2
Inherent viscosity, M_n, M_w and yield of **PAM-1** and **PAM-2** prepared in different conditions.

	Condition[a]	η_{inh}[b] (dL/g)	M_n[c] (10^4 g/mol)	M_w[c] (10^4 g/mol)	Yield (%)
PAM-1	(A)	0.79	2.4	7.5	96
	(B)	0.20	0.3	0.5	98
	(C)	0.53	1.2	2.2	96
PAM-2	(A)	0.50	1.2	2.5	96
	(B)	0.12	0.2	0.3	95
	(C)	0.32	0.4	0.6	96

[a] (A) *m*-cresol, at room temperature under reduced pressure for 48 h; (B) *m*-cresol, at reflux for 48 h; (C) NMP/HMPA (1:1, v/v), at room temperature for 48 h.
[b] Measured at a polymer concentration of 0.5 g/dL in NMP at 30 °C.
[c] By GPC in DMAc (relative to polystyrene standards).

Table 3
Solubility of polyazomethines.

	Solubility[a]							
	m-cresol	NMP	DMF	DMAc	DMSO	THF	Chloroform	Acetone
PAM-1	++	++	++	++	+−	+−	+−	−
PAM-2	++	++	++	++	+−	+−	+−	+−
PAM-3	++	++	++	++	+−	+−	+−	+−
PAM-4	++	++	++	++	+−	+−	+−	+−
PAM-5	++	++	++	++	+−	+−	+−	+−
PAM-6	++	++	++	++	+−	+−	−	−
PAM-7	++	++	++	++	+−	+−	−	−

Abbreviations: THF, tetrahydrofuran; DMF, dimethylformamide; DMAc, dimethylacetamide; NMP, *N*-methyl-2-pyrrolidinone; DMSO, dimethyl sulfoxide.
[a] The solubility was determined by using 20 mg sample in 1 mL of stirred solvent. ++: soluble at room temperature; +−: partially soluble at room temperature; −: insoluble at room temperature.

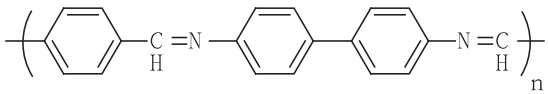

PAM-8

It has been reported that the C═N linkage of polyazomethine is not in the same plane with the adjacent *N*-phenyl ring due to the repulsion force between the hydrogen atom of the C═N linkage and the adjacent *N*-phenylene ring [31]. The torsional angle has been calculated to be 30.4°. However, this non-coplanar conformation resulted from C═N linkage alone is not sufficient to provide good solubility for polyazomethines. The excellent solubility of these new polyazomethines **PAM-1**–**7** was resulted from the combined effects of trifluoromethyl groups of the new dialdehyde (**5**) moiety and the non-coplanar biphenyl structures. The biphenyl structures are forced to adapt a non-coplanar conformation by the bulky substituents at the 2 and 2′ positions of biphenyls. Both of trifluoromethyl groups and non-coplanar biphenyls have been incorporated into polyimides [32], polyamides [25] and poly(*p*-biphenylene-1,3,4-oxidiazole) [33] to enhance the solubility with great success. This enhanced solubility is attributed to the loose interchain packing resulted from the bulkiness of trifluoromethyl groups and non-coplanar biphenyl structures. Furthermore, the same enhancements in solubility of these new polyazomethines were also observed regardless various diamines were used.

Fig. 3 shows the wide-angle X-ray diffraction patterns of polyazomethines **PAM-1**–**7**. There were no crystalline peaks can be observed, indicating that these new polyazomethines were amorphous in nature. This can be also attributed to their non-coplanar biphenyl structures which might hinder polymer chain packing.

3.4. Hydrolysis and post-polymerization

Because of the limited solubility of these polyazomethines in DMSO-d_6, we attempted to heat the NMR sample tubes to obtain a homogeneous solution. It was found that the aldehyde peaks became more prominent and azomethine hydrogen peaks diminished when the NMR sample tubes were heated, indicating the decrease in molecular weight. The azomethine linkage of small organic molecules has ever been reported for its hydrolysis phenomenon at the presence of water [22]. In some cases, the formation of azomethine (imine) linkage was exploited to protect aldehyde and ketone groups, which were then reclaimed by the following hydrolysis in refluxing organic solvents [34]. However, the hydrolysis of polyazomethines has never been mentioned

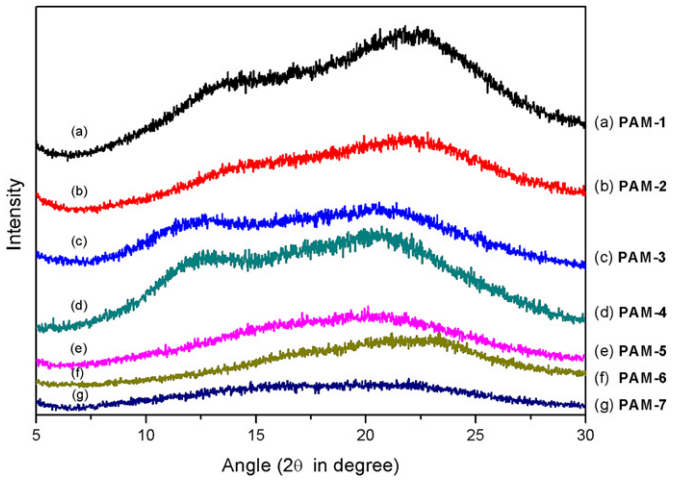

Fig. 3. Wide-angle X-ray diffraction patterns of polyazomethines **PAM-1**–**7**.

before. In order to study the hydrolysis of these polyazomethines in solution state, **PAM-2** was used as the example. Fig. 1(b) is the ^{1}H NMR spectrum of as-prepared **PAM-2** soluble part in DMSO-d_6 at room temperature. Fig. 1(c) shows the ^{1}H NMR spectrum of as-prepared **PAM-2** heated at 50 °C for 12 h in air to form a homogeneous DMSO-d_6 solution. It was found that the intensity of the aldehyde peaks (10.19 ppm) increased and that of azomethine hydrogen peaks (9.02 ppm) diminished as temperature increased. From the increased intensity of aldehyde peak, it is obvious that polyazomethines could undergo hydrolysis in DMSO-d_6 solvent even only trace of water (inherently exists in DMSO-d_6) is present as depicted in Scheme 4. The amine peak at 5.74 ppm in Fig. 1(c) was broad and not prominent. This might be attributed to the slow exchange rate of protons on nitrogen and the electrical quadrupole moment of ^{14}N nucleus. Fig. 1(d) shows the ^{1}H NMR spectrum of the same as-prepared **PAM-2** heated at 150 °C for 24 h in DMSO-d_6 under nitrogen atmosphere to form a homogeneous solution. The intensity of the aldehyde and amine peaks was more intense and that of the azomethine hydrogen peaks was decreased. Under nitrogen atmosphere, the amine peaks can be observed at 5.53 and 5.74 ppm. These peaks were attributed to the hydrolyzed diamine monomers and the amino groups of polyazomethine chain-ends, respectively. From these ^{1}H NMR spectra (Fig. 1), it indicates that the hydrolysis of polyazomethine **PAM-2** is more pronounced at elevated temperature. It also implies that the reversed reaction of

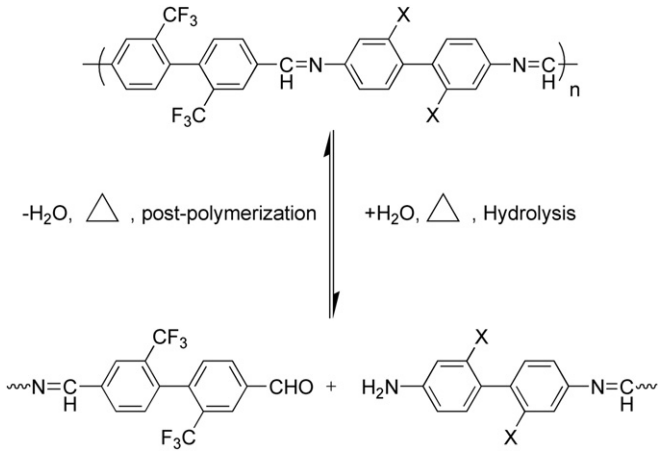

Scheme 4. Hydrolysis of polyazomethines in solution state.

azomethine formation is favored at elevated temperature in the presence of even trace amount of water. This is consistent with the results from Table 2. In the same solvent (*m*-cresol), polymerization at room temperature gave higher molecular weights than at reflux temperature.

The hydrolysis of these new polyazomethines was further evidenced by the GPC measurements. Fig. 4 shows the GPC chromatograms of as-prepared **PAM-2** after different levels of hydrolysis and post-polymerization. The hydrolysis was carried out by dissolving as-prepared **PAM-2** in DMSO (0.1%, w/v) at 150 °C for different periods of time. **PAM-2** can be totally dissolved in DMSO at 150 °C. The GPC chromatogram (Fig. 4(a)) of as-prepared **PAM**-2 was bimodal with number average molecular weight (M_n) of 12,000 g/mole. When the 0.1% (w/v) of **PAM-2** solution in DMSO was heated at 150 °C for 4 h in air, the GPC chromatogram (Fig. 4(b)) became monomodal and indicated a lower molecular weight (M_n) of 6000 g/mole. As the hydrolysis lasted to 16 h, M_n decreased to 2000 g/mole Fig. 4(c). After **PAM-2** solution was heated at 150 °C for 24 h, it became difficult to determine the molecular weight from its GPC chromatogram due to the low signal intensity (Fig. 4(d)). It indicated that **PAM-2** was mostly hydrolyzed to oligomers whose molecular weights were beyond the lower limit of the GPC measurement. Even though water was not added, the trace amount of water in DMSO solvent is enough for the hydrolysis of polyazomethines at 150 °C. Aromatic polyazomethines have been known for their high thermal stability. This is true only for polyazomethines in their solid states. From the ^{1}H NMR spectra (Fig. 1) and GPC chromatograms (Fig. 4), it suggests that in solution state the polyazomethine could be easily hydrolyzed in the presence of a trace amount of water at temperature even as low as 50 °C.

It has been well know that the molecular weights of polyazomethines are generally lower than those of aromatic condensation polymers such as polyamides and polyimides. In addition to the effects of the chemical structures and the reactivity of monomers, this phenomenon might possibly be resulted from the hydrolysis during sample preparation for GPC measurement. In some cases, heating might be necessary to obtain a homogeneous solution, leading to hydrolysis and thus lower molecular weights.

It has also been reported that polyazomethine can undergo post-polymerization at high temperature [12]. A thin film (ca. 2 μm)

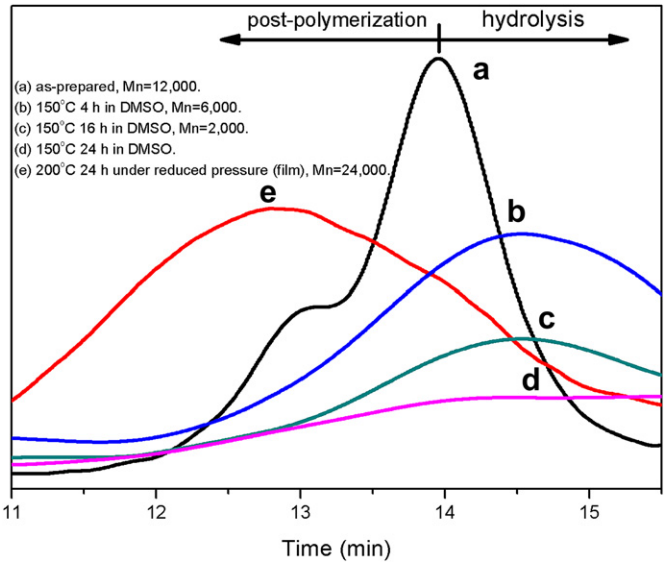

Fig. 4. GPC chromatograms of **PAM-2** (a) as-prepared, (b) heated at 150 °C for 4 h in DMSO, (c) for 16 h in DMSO, (d) for 24 h in DMSO, and (e) thin film heated at 200 °C under reduced pressure for 24 h.

was prepared by spin-coating 2% (w/v) of **PAM-2** in DMF solution on glass and heating at 50 °C for 1 h then 200 °C for 24 h under reduced pressure. The GPC chromatogram of this post-polymerized **PAM-2** thin film is shown in Fig. 4(d). The M_n increased from 12,000 to 24,000 g/mole. It was attributed to the post-polymerization from amine and aldehyde groups of as-prepared **PAM-2** chain-ends. It suggests that in solid state polyazomethines can undergo post-polymerization at elevated temperature. The GPC results combined with ^{1}H NMR spectra suggested that even though hydrolysis can occur in DMSO solution, leading to low molecular weight, polyazomethine films with high molecular weights can be still obtained if the films were prepared at elevated temperature under reduced pressure. In summary, polyazomethines prepared in *m*-cresol at room temperature under reduced pressure had the highest molecular weights. Post-polymerization at elevated temperature (200 °C) in solid film can further increase their molecular weights.

3.5. Thermal properties

The thermal properties of polyazomethines were evaluated by DSC and TGA. The results, including glass transition temperatures (Tg), decomposition temperatures at 5% ($T_{5\%}$), 10% ($T_{10\%}$) weight loss, and residual weight percent (R_{w800}) at 800 °C in nitrogen atmosphere, are summarized in Table 4. The new polyazomethines **PAM-1**–**7** exhibited high glass transition temperatures ranging from 265 to 324 °C. **PAM-5** derived from the new dialdehyde (**5**) and 4,4′-ODA had the lowest glass transition temperature at 265 °C. It might be due to the flexibility of ether linkage on **PAM-5** backbone. On the other hand, **PAM-4** derived from the new dialdehyde (**5**) and diamine (**9**) containing bulky phenyl substituents had the highest Tg (324 °C). This might be resulted from the fact that **PAM-4** containing phenyl substituents had higher chain rigidity than other polyazomethines. **PAM-2** containing bulky trifluoromethyl groups on both dialdehyde and diamine moieties also exhibited high glass transition temperature at 287 °C. **PAM-6** and **PAM-7**, which had the same chemical structures except the azomethine arrangements, showed similar glass transition temperatures at 272 and 271 °C, respectively. It suggested that the azomethine arrangements of polyazomethines might have little effect on their glass transition temperatures.

Fig. 5 shows the TGA thermograms of **PAM-2** as-prepared (Fig. 5(a)) and after isothermal treatment at 200 °C for 90 min before heating scan (Fig. 5(b)). The as-prepared **PAM-2** experienced an initial weight loss starting at around 190 °C. This initial weight loss was attributed to water released from the post-polymerization between chain-end amine and aldehyde groups. When **PAM-2** was heated under nitrogen at 200 °C for 90 min, the thermogram (Fig. 5(b)) shows no trace of post-polymerization and exhibited $T_{5\%}$ at 482 °C. All the decomposition temperatures of polyazomethines **PAM-1**–**7** were determined after the isothermal treatment (200 °C in nitrogen for 90 min) to exclude the effect of post-polymerization. The decomposition temperatures in nitrogen atmosphere at 5% and 10% weight loss of **PAM-1**–**7** were in the range of 416–487 °C and 463–506 °C, respectively. Their residual weights at 800 °C in nitrogen ranged from 40 to 63%. These polyazomethines exhibited high thermal stability without any significant weight loss up to 400 °C. This further confirmed that the enhancement in solubility by non-coplanar biphenyl structures can be achieved without sacrificing the thermal stability.

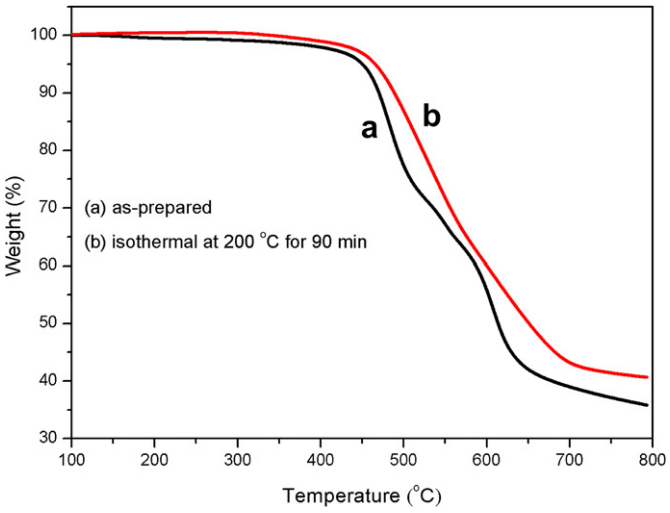

Fig. 5. TGA thermograms of **PAM-2** (a) as-prepared and (b) isothermal at 200 °C for 90 min.

3.6. Optical properties

The optical properties of **PAM-1**–**7** were investigated by UV–vis and photoluminescence (PL) spectroscopy by using their 10^{-5} M chloroform solution. The results are summarized in Table 5. All the polyazomethines showed azomethine characteristic absorption at 326–360 nm (Fig. 6). Among these polyazomethines, **PAM-2** containing electron-withdrawing trifluoromethyl substituents on both diamine and dialdehyde moieties showed the most hypsochromic shift with maximum absorption wavelength at 326 nm. On the contrary, **PAM-4** containing electron-rich phenyl substituents on its diamine moiety showed the most bathochromic shift with maximum absorption wavelength at 360 nm. **PAM-5** containing ether linkage on its backbone had maximum absorption wavelength at 344 nm. This value is close to those of other polyazomethines in this study if electronic effect is excluded (i.e. **PAM-2** and **PAM-4**). It indicates that the ether linkage and the non-coplanar biphenyl structures might have the similar effect on interrupting the conjugation along the polymer backbones. Compared with polyazomethine **PAM-8** prepared from 4,4′-benzidine with terephthalic dicarbaldehyde (**TPDCA**) (maximum

Table 4
Thermal properties of polyazomethines.

	Tg[a] (°C)	$T_{5\%}$[b] (°C)	$T_{10\%}$[b] (°C)	Char yield[c] (wt.%)
PAM-1	273	416	470	62
PAM-2	287	482	502	40
PAM-3	270	475	506	63
PAM-4	324	432	468	48
PAM-5	265	438	463	47
PAM-6	272	487	501	42
PAM-7	271	484	498	40

[a] Measured by DSC at a heating rate of 10 °C/min in nitrogen.
[b] Measured by TGA at a heating rate of 10 °C/min in nitrogen.
[c] Residual weight percentage at 800 °C in nitrogen.

Table 5
Optical properties of polyazomethines.

	λ_{abs}[a] (nm)	λ_{onset} (nm)	λ_{emi}[b] (nm)	Φ_{PL}[c] (%)
PAM-1	348	398	433	0.13
PAM-2	326	391	425	0.05
PAM-3	357	408	434	0.05
PAM-4	360	410	491	1.45
PAM-5	344	397	431	0.61
PAM-6	345	400	468	1.10
PAM-7	344	401	442	0.05

[a] Measured by UV–vis spectroscopy in chloroform (10^{-5} M).
[b] Measured by photoluminescence spectroscopy in chloroform (10^{-5} M).
[c] Quantum efficiency relative to quinine sulfate (10^{-5} M quinine sulfate in 1 N H_2SO_4).

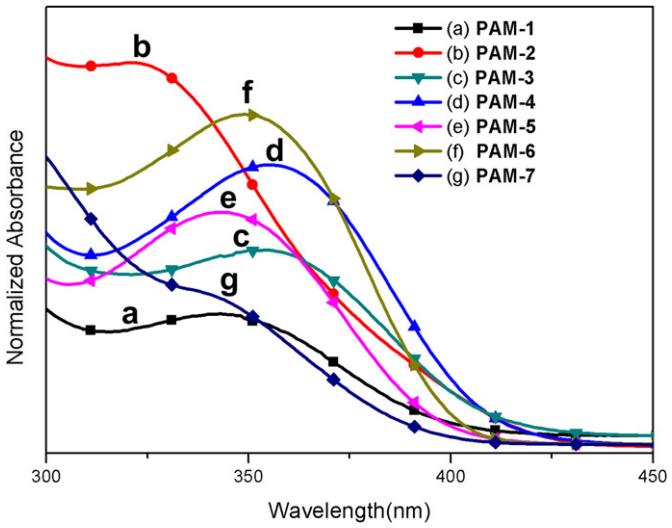

Fig. 6. UV–vis spectra of **PAM-1**–**7** in chloroform solution (10^{-5} M).

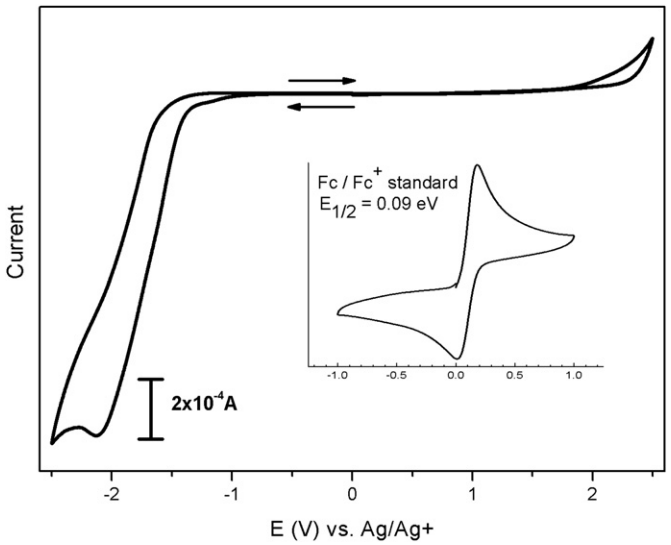

Fig. 8. Cyclic voltammogram (CV) of **PAM-6**.

absorption wavelength at 491 nm in concentrated sulfuric acid) [9], **PAM-1**–**7** exhibited significant hypsochromic shift due to the interruption of conjugation along the polymer backbones.

Photoluminescence (PL) spectra were recorded by using the maximum absorption wavelength as the excited wavelength in chloroform solution (10^{-5} M). The representative PL spectra of **PAM-4**, **PAM-5** and **PAM-6** are shown in Fig. 7. All the polyazomethines **PAM-1**–**7** showed a broad emission peak with emission wavelengths ranging from 425 to 491 nm. PL quantum efficiency of polyazomethines was calculated by using quinine sulfate (10^{-5} M) in 1 N H_2SO_4 as standard ($\Phi = 0.546$) [15]. These new polyazomethines had PL quantum efficiency ranging from 0.05 to 1.45%. It was reported that polyazomethines had PL quantum efficiency less than 0.03%, which is much lower than those of the analogous poly(arylenevinylene)s and polyfluorenes [15]. The low PL quantum efficiency limits their applications as the luminescent layers.

3.7. Electrochemical properties

The electrochemical properties of these polyazomethines were investigated by cyclic voltammetry (CV). A representative cyclic voltammogram of **PAM-6** in 0.1 M n-Bu_4NClO_4/acetonitrile solution with a scan rate of 100 mV s^{-1} is shown in Fig. 8. The values of HOMO, LUMO and energy gap were calculated by similar equations from previous publication [35]. The electrochemical properties are summarized in Table 6. All of the polyazomethines showed an irreversible peak both at oxidation and reduction region. However, the polymer films remained stable during repeating scans and showed essentially the same cyclic voltammograms. The irreversibility, indicating the short lifetime of the formed radical anions and radical cations during electrochemical processes, might be resulted from the short conjugation length of the non-coplanar biphenyls and the electron-withdrawing nature of trifluoromethyl group.

The HOMO and LUMO energy levels were determined to be −5.69 to −5.96 and −3.04 to −3.18 eV, respectively. These values are much lower when compared with those (E_{HOMO} = −5.19 eV, E_{LUMO} = −2.46 eV) of polyazomethine **PAM-8** prepared from 4,4′-benzidine and terephthalic dicarbaldehyde (**TPDCA**) [9]. The LUMO energy level is related to the conjugation length and the electron-accepting ability of polymers. The higher the delocalization of π electrons, the easier the acceptance of an additional electron during reduction process. Although these new polyazomethines had shorter conjugation length due to the interruption of conjugation along the polymer backbones, the presence of strong electron-withdrawing trifluoromethyl group outweighed the effect of short conjugation length, leading to low E_{LUMO} [33]. The low E_{HOMO} was

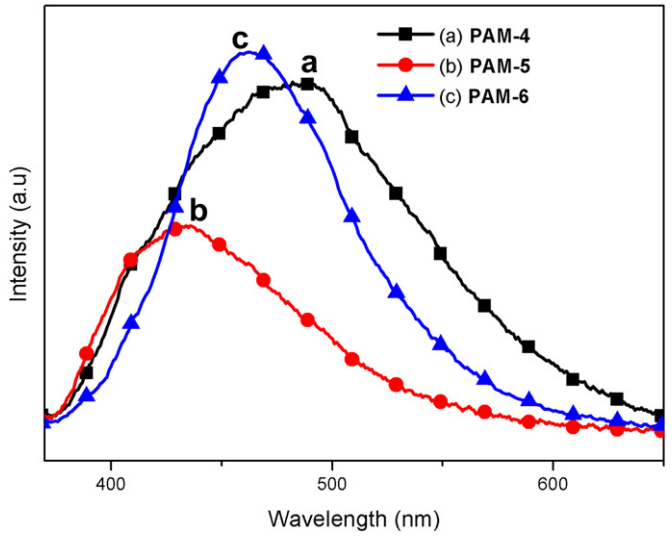

Fig. 7. PL spectra of **PAM-4**, **5** and **6** in chloroform solution (10^{-5} M).

Table 6
Electrochemical properties of polyazomethines.

	Reduction[a] (V)	Oxidation[a] (V)	E_{HOMO}[b] (eV)	E_{LUMO}[c] (eV)	Eg[d] (eV)
	E^{Re}_{onset}	E^{Oxi}_{onset}			
PAM-1	−1.66	1.10	−5.81	−3.05	2.76
PAM-2	−1.53	1.27	−5.96	−3.18	2.80
PAM-3	−1.65	1.05	−5.76	−3.06	2.70
PAM-4	−1.67	0.98	−5.69	−3.04	2.65
PAM-5	−1.62	1.09	−5.80	−3.09	2.71
PAM-6	−1.57	1.22	−5.93	−3.14	2.79
PAM-7	−1.55	1.21	−5.92	−3.16	2.76

[a] Measured by cyclic voltammetry.
[b] $E_{HOMO} = -(E^{Oxi}_{onset} + 4.80 - 0.09$ eV) [35].
[c] $E_{LUMO} = -(E^{Re}_{onset} + 4.80 - 0.09$ eV) [35].
[d] Calculated by the equation : $Eg = E_{LUMO} - E_{HOMO}$ [35].

also resulted from the electron-withdrawing trifluoromethyl group. For example, **PAM-2** containing electron-withdrawing trifluoromethyl group on both diamine and dialdehyde moieties exhibited exceptionally low E_{HOMO} of −5.96 eV. It can be concluded that trifluoromethyl-containing non-coplanar biphenyls could be regarded as a new electron acceptor when designing a donor-acceptor system for different applications. This electron acceptor can be used to tune the HOMO, LUMO energy levels and charge mobility for electron-rich conjugated polymers.

The electrochemical energy gaps of these new polyazomethines were in the range of 2.65–2.80 eV. It was reported that the energy gap is resulted from the combined effects of the conjugated length of the polymer backbone and the electronic nature of the substituents (electron-rich or electron-withdrawing) [9]. The energy gaps of **PAM-6** (2.79 eV) and **PAM-7** (2.76 eV) were larger than that of **PAM-8** (2.73 eV). **PAM-6** and **PAM-7** with bulky trifluoromethyl group give larger twisted angles than **PAM-8** along the biphenyl structure. The larger twisted angle combined with the electron-withdrawing nature of trifluoromethyl group gives larger energy gaps of **PAM-6** and **PAM-7** compared with that of **PAM-8**. However, for **PAM-1**–**5**, their energy gaps are difficult to rationalize when compared with that of **PAM-8**. It is probably due to this combined effect of planarity and electronic nature of the substituents on the energy gap.

4. Conclusions

A new dialdehyde containing electron-withdrawing trifluoromethyl groups at the 2 and 2′ positions of biphenyl was prepared via a five-step synthetic route. The formed polyazomethines exhibited excellent solubility in polar organic solvents such as DMF, DMAc, NMP and *m*-cresol while maintained their high thermal stability. It was found that these polyazomethines would undergo hydrolysis in solution. The hydrolysis, evidenced by ^{1}H NMR spectra and GPC chromatograms, was resulted from the reverse reaction of azomethine formation and was favored at higher temperature. It was concluded that polyazomethines prepared in *m*-cresol at room temperature under reduced pressure had the highest molecular weights. Post-polymerization of polyazomethine thin films at elevated temperature can further increased their molecular weights. These polyazomethines also had low electrochemical E_{HOMO}s and E_{LUMO}s. This is resulted from the combined effects of electron-withdrawing trifluoromethyl group and non-coplanar biphenyls. Combined with the excellent solubility and high thermal stability, 2,2′-bis(trifluoromethyl)-4,4′-biphenyl structure could be a new choice as the electron acceptor for the structure design of new conjugated polymers.

References

[1] Iwan A, Sek D. Prog Polym Sci 2008;33(2):289–345.
[2] Morgan PW, Kwolek SL, Pletcher TC. Macromolecules 1987;20(4):729–39.
[3] Higuchi M, Tsuruta M, Chiba H, Shiki S, Yamamoto K. J Am Chem Soc 2003;125(33):9988–97.
[4] Niu H, Huang Y, Bai X, Li X, Zhang G. Mater Chem Phys 2004;86(1):33–7.
[5] Bourgeaux M, Skene WG. Macromolecules 2007;40(6):1792–5.
[6] Dutta PK, Jain P, Sen P, Trivedi R, Sen PK, Dutta J. Eur Polym J 2003;39(5):1007–11.
[7] Hindson JC, Ulgut B, Friend RH, Greenham NC, Norder B, Kotlewski A, et al. J Mater Chem 2010;20(5):937–44.
[8] Park SB, Kim H, Zin WC, Jung JC. Macromolecules 1993;26(7):1627–32.
[9] Yang CJ, Jenekhe SA. Macromolecules 1995;28(4):1180–96.
[10] Thomas O, Inganas O, Andersson MR. Macromolecules 1998;31(8):2676–8.
[11] Liou GS, Lin HY, Hsieh YL, Yang YL. J Polym Sci Part A Polym Chem 2007;45(21):4921–32.
[12] Matsumoto T, Yamada F, Kurosaki T. Macromolecules 1997;30(12):3547–52.
[13] Park KH, Tani T, Kakimoto M, Imai Y. Macromol Chem Phys 1998;199(6):1029–33.
[14] Wang C, Shieh S, Legoff E, Kanatzidis MG. Macromolecules 1996;29(9):3147–56.
[15] Tsai FC, Chang CC, Liu CL, Chen WC, Jenekhe SA. Macromolecules 2005;38(5):1958–66.
[16] Kim HC, Kim JS, Kim KS, Park HK, Baek S, Ree M. J Polym Sci Part A Polym Chem 2004;42(4):825–34.
[17] Grigoras M, Antonoaia NC. Polym Int 2005;54(12):1641–6.
[18] Mallegol T, Gmouh S, Meziane MAA, Blanchard-Desce M, Mongin O. Synthesis 2005;2005(11):1771–4.
[19] Anuragudom P, Newaz SS, Phanichphant S, Lee TR. Macromolecules 2006;39(10):3494–9.
[20] Morgan PW, Pletcher TC, Kwolek SL. Polym Prepr 1983;24:470.
[21] Yang CJ, Jenekhe SA. Chem Mater 1991;3(5):878–87.
[22] Zhao D, Moore JS. J Org Chem 2002;67(11):3548–54.
[23] Everitt PM, Loh SM, Turner EE. J Chem Soc; 1960:4587.
[24] Shiang WR, Woo EP. J Polym Sci Polym Chem Ed 1993;31(8):2081–91.
[25] Rogers HG, Gaudiana RA, Hollinsed WC, Kalyanaraman PS, Manello JS, McGowan C, et al. Macromolecules 1985;18(6):1058–68.
[26] Sako S. Bull Chem Soc Jpn 1935;10(12):593–4.
[27] Olinga TE, Destri S, Botta C, Porzio W, Consonni R. Macromolecules 1998;31(4):1070–8.
[28] Destri S, Khotinal A, Porzio W. Macromolecules 1998;31(4):1079–86.
[29] Beam CF, Brown J, Hall RW, Bernhardt FC, Sides KL, Mack MH, et al. J Polym Sci Polym Chem Ed 1978;16(10):2679–81.
[30] Sek D, Iwan A, Jarzabek B, Kaczmarczyk B, Kasperczyk J, Mazurak Z, et al. Macromolecules 2008;41(18):6653–63.
[31] Liu CL, Tsai FC, Chang CC, Hsieh KH, Lin JL, Chen WC. Polymer 2005;46(13):4950–7.
[32] Li F, Fang S, Ge JJ, Honigfort PS, Chen JC, Harris FW, et al. Polymer 1999;40(16):4571–83.
[33] Chen JC, Chiang CJ, Liu YC. Synth Met 2010;160(18):1953–61.
[34] Greene TW, Wuts PGM. In protective groups in organic synthesis [Chapter 4]. New York: Wiley; 1999. 359–360.
[35] Yasuda T, Imase T, Yamamoto T. Macromolecules 2005;38(17):7378–85.

Polymer 52 (2011) 965–975

Contents lists available at ScienceDirect

Polymer

journal homepage: www.elsevier.com/locate/polymer

Effects of TS-1 zeolite structures on physical properties and enzymatic degradation of Poly (butylene succinate) (PBS)/TS-1 zeolite hybrid composites

Sung Yeon Hwang [a], Eui Sang Yoo [b], Seung Soon Im [a,*]

[a] Department of Fiber and Polymer Engineering, College of Engineering, Hanyang University, 17 Haengdang-dong, Seongdong-gu, Seoul 133-791, Republic of Korea
[b] KITECH Textile Ecology Laboratory, 1271-18 Sa 1 Dong, Sangrokgu, Ansan City, Gyungido, Republic of Korea

ARTICLE INFO

Article history:
Received 9 November 2010
Received in revised form
28 December 2010
Accepted 6 January 2011
Available online 13 January 2011

Keywords:
TS-1 zeolite
Biodegradable polymer
Enzymatic hydrolysis

ABSTRACT

The objective of this study was to investigate how the water uptake features and carrier characteristics of the TS-1 zeolite affected the physical and rheological properties, morphological parameters, and enzymatic hydrolysis of Poly (butylene succinate) (PBS). The introduction of TS-1 zeolite as catalyst was developed for the preparation of PBS/TS-1 zeolite hybrid composites (PTHC) without heavy metal toxic substance in the context on clean technology. The TS-1 zeolite can act as a catalyst as well as a reinforcement filler with the result that PTHC can show marked increases in tensile properties and elongation at breakage in the solid state. The rheological properties of PTHC with high zeolite contents showed low values of complex viscosity, as compared with PTHC with low TS-1 zeolite contents, due to the volatilization of water released from the zeolite pores during esterification. The introduction of the TS-1 zeolite in the PBS matrix was not significantly affected by changes in the size of the long period, lamella thickness, or the amorphous region, indicating that PBS chains do not penetrate into zeolite pores, as confirmed by SAXS profiles. In enzymatic hydrolysis over 90 days, the enzymatic hydrolysis rates of PTHC significantly accelerated with increasing TS-1 zeolite contents, compared with Homo PBS. This result indicated that TS-1 zeolite can act as a carrier for enzyme activation, resulting in enzymatic hydrolysis, occurring from the amorphous area on the surface into the inside of the film.

1. Introduction

Zeolites, generally defined as high-ordered microporous materials, have been used as heterogeneous catalysts in many reactions, such as aromatization, cracking, esterification, alkylation, and methanol conversions. They have also been used in petroleum refining as drying agents, ion exchangers, animal food additives, nuclear effluent treatment, and membranes in numerous industrial fields [1–7]. Zeolite activity in these applications depends on the active sites, high surface area, and pore volumes. Thus, many researchers have studied the synthesis of new ordered microporous materials for various applications [8–16].

Among the many zeolite types, titanium silicate-1 (TS-1) zeolite has been found to have strong catalytic activity [17–23]. The titanium in TS-1 replaces silicon in a tetrahedral site of the MFI silicate lattice. TS-1 combines the advantages of having the high coordination ability of Ti^{4+} ions with the hydrophobicity of the silicate framework. In particular, the adsorption of water molecules in the pores is closely associated with the surface structure, stability, and activity of Ti sites in TS-1[18–21].

The pores in zeolite have cationic ions for charge balance, and some pores are filled with zeolitic water, resulting in cationic ions that can readily be transported in pores. Thus, TS-1 zeolite is an inorganic ion exchanger with high ion exchange capabilities. High thermal energy readily allows zeolitic water to be desorbed from the zeolite pore. The desorbed zeolite has a strong inclination to quickly fill up pores with water molecules and small polar molecules because this is a natural phenomenon to decrease lattice energy.

Considering the unique characteristics of TS-1 zeolite, it is likely that TS-1 zeolite would have a great effect on biodegradable polymer products with superior properties on the following basis. Firstly, the use of TS-1 zeolite as a catalyst in the synthesis of biodegradable polymer is important in terms of clean technology. The catalytic activity of TS-1 zeolite is closely related to the presence of isolated framework titanium species, strong acid sites on the well-defined microporous structures that are responsible for the shape selectivity, microporous size, the distribution of Ti, and the stability of structures. Despite the limited premises of TS-1 zeolite as efficient heterogeneous catalysts, it is widely recognized that TS-1 zeolite is a highly efficiently heterogeneous catalyst as well as being appropriate for heavy metal-free catalysts. Secondly,

* Corresponding author. Tel.: +82 2 2220 0495; fax:+82 2 2297 5859.
E-mail address: imss007@hanyang.ac.kr (S.S. Im).

0032-3861/$ – see front matter © 2011 Elsevier Ltd. All rights reserved.
doi:10.1016/j.polymer.2011.01.010

it should not rule out the possibility that TS-1 zeolite can act as a reinforcement filler. TS-1 zeolite consists of a silicate framework with a bulk particle size (100 nm ~ 1μm). Thus, the introduction of TS-1 zeolite should facilitate the preparation of hybrid materials as alternatives to enhance the physical properties of biodegradable polymers by the introduction of organic/inorganic particles, such as clay [24,25], silica [26], polyhedral oligosilsesquioxane (POSS) [27], and chitosan [28]. Thirdly, the selective adsorption features of TS-1 zeolite by high ion exchange capabilities would be expected to utilize TS-1 zeolite as trap functional carrier. Using these unique characteristics, a study on zeolites is being carried out for application to the immobilization of enzymes for biosencing as a carrier [29,30].

This makes possible the synthesis of multifunctional biodegradable hybrid materials by considering the unique feature of TS-1 zeolite such as shape selective catalyst, silicate framework and molecular adsorption.

Studies on polymer–zeolite hybrid materials have been reported over recent decades [31–36]. Graeser and Spange [31] investigated the cationic polymerization of various substituted vinyl ethers with HY zeolite and the combined properties of novel hybrid materials. Several papers [35–37] have shown that zeolite can act as reinforcement filler and nucleation agent in polymer matrices to increase thermal and mechanical properties. However, to date no study has been reported regarding biodegradable polymer hybrid materials using zeolite.

We expected that the unique characteristics of TS-1 zeolite would lead to enhanced physical properties and biodegradability of biodegradable polymers. In this study, TS-1 zeolite can act as catalyst, a reinforcement filler and affect the biodegradation rate at the same time. We prepared composite materials composed of Poly (butylene succinate) (PBS) and TS-1 zeolite by *in situ* polymerization with no conventional catalyst. This study described the consequences of the water uptake features and carrier characteristic of TS-1 zeolite on physical properties during melt processing and biodegradability.

We anticipate that PBS/TS-1 zeolite hybrid materials may have advantages in applications in the agriculture sector, packaging technologies, coatings, and drug delivery vesicles because of the unique characteristic of TS-1 zeolite.

2. Experimental

2.1. Materials

The TS-1 zeolite was kindly provided by the Korea Institute of Ceramic Eng. & Tech (KICET). The amount of Ti(IV) incorporated in the used TS-1 zeolite framework is consistent with a Si:Ti ratio of 62 based on X-ray fluorescence spectrometry. We also purchased 1,4 butanediol (99%) and succinic acid (99%) from Sigma–Aldrich (St. Louis, MO, USA). Reagents were used without further purification.

2.2. Preparation of the PBS/TS-1 zeolite hybrid composite

The PBS/TS-1 zeolite hybrid composite (PTHC) was prepared with TS-1 zeolite (~ 2.0 wt% of succinic acid weight) by a two-step *in situ* polymerization processing. First, TS-1 zeolite (0.5–2 wt%) was dispersed in 1,4 butanediol (0.6 mol) using an ultrasonic processor (VCX500, 500 W, 20 kHz; Sonic, Danbury, CT, USA) for 30 min before the ester interchange reaction. While the slurry was stirred vigorously, succinic acid (0.5 mol) was added without a heterogeneous catalyst. The mixture was then heated to 190 °C in an oil bath and subjected to mechanical stirring at 250 rpm under a nitrogen atmosphere. The temperature was increased to 240 °C at 10 °C/min with gradually reduced pressure to ensure that water and low-molecular-weight condensates were removed continuously, and the mixture was maintained at 240 °C for 3 h. The resulting samples were repeatedly washed with water and dried in a vacuum for 24 h at 50 °C. Sample codes were denoted by zeolite name and content. For example, "TS20" represents a PTHC with 2.0 wt% zeolite content.

2.3. Characterizations

The N_2 adsorption–desorption isotherm of TS-1 zeolite were performed using a Quantachrom Autosorb-1 after the sample had been degassed at 200 °C. Thermogravimetric analysis coupled with infrared spectroscopy [TG-IR, TG 209 °C Iris® (Netzsch, Exton, PA, USA) coupled with a Tensor 27 FTIR (Bruker Optics, Billerica, MA, USA)] was used to determine the qualitative and quantitative identification of the adsorbed water gases released directly from the sample during the thermal melting behavior as a function of temperature and time. The TGA was performed at a heating rate of 10 °C/min from 20 °C to 150 °C under a nitrogen atmosphere at a flow rate of 20 mL/min. IR spectra were collected at a 4 cm^{-1} resolution over the range of 600–4000 cm^{-1} on a continuous basis.

Mechanical tests were conducted using a tensile strength evaluator (Instron 4465; Instron Corp., Norwood, MA, USA) with a crosshead speed of 10 mm/min at room temperature. The rheological behaviors of all samples were measured using a dynamic oscillatory viscometer (ARES; Rheometric Scientific Inc., Piscataway, NJ, USA) with parallel plate geometry, 120 mm diameter, and a 1.0-mm gap distance between the parallel plates.

The experiment was performed with a frequency sweep ranging from 0.5 to 500 rad/s at a 10% strain level at 150 °C. SAXS experiments were conducted at the 4C1 SAXS Beamline of the Pohang Accelerator Laboratory (Korea). The storage ring was operated at 2.5 GeV and a ring current of 150–200 mA. The X-ray wavelength was 0.1608 nm and the beam size at the focal point was less than 1 mm^2, focused by a platinum-coated silicon premirror through a double-crystal monochromator. The scattering intensity was detected with a two-dimensional CCD camera. The scattering angle was calculated with a Bragg spacing of 32.78 nm for a SEBS crystal at $q = 0.19165\ nm^{-1}$ as a reference peak for SAXS. The samples were melted at 150 °C in the melting chamber to eliminate their thermal histories, quickly heated to the designated isothermal crystallization temperature (80 °C and 92 °C), and maintained for 30 min to allow for complete crystallization. The scattering profiles were monitored with exposure times of 27.7 s.

The static contact angles of the PTHC were measured using the sessile drop method with a contact shape analyzer (DSA 100; Krüss, Hamburg, Germany) to study the effect of the zeolite on hydrophilicity. Distilled water was used to measure the evolution of the contact angle with time. Water droplets (2 μL) were dropped onto the surface of the 0.3-mm-thick amorphous film. Before testing, the film samples were dried in desiccators at a normal state (20 °C) for 48 h to achieve conditioning. Each reported value is the average of at least five time replicates.

The enzymatic hydrolysis test of samples was carried out at 37 ± 0.5 °C in reciprocating shaking water bath for 90 days. Each of the films (20 mm × 30 mm, 0.3 ± 0.02 mm) was placed in a glass bottle with 30 mL of 0.2 M phosphate-buffered saline solution with 1.7 mg of lipase (Sigma–Aldrich; *Pseudomonas* sp.). Samples were removed from the solution every week, washed with distilled water several times, dried for 24 h under reduced pressure, and weighed for 90 days.

Wide-angle XRD (WAXD) experiments were conducted with Cu K_α radiation ($\lambda = 1.54$ Å) on an X-ray generator (Rigaku Corp., Tokyo, Japan) operating at 40 kV and 100 mA to investigate structural changes in the PTHC after enzymatic hydrolysis. Samples were scanned at a rate of 5°/min from 3° to 50° in 2θ.

Ultra-thin sections (~50 nm) of the pressed film were prepared for the TEM analysis on a microtome equipped with a diamond knife. The sections were collected from a distilled water trough and floated directly onto Cu grids. The enzymatically hydrolyzed film surfaces were observed by field emission scanning electron microscopy (FE-SEM) (JSM-633F; JEOL Ltd., Tokyo, Japan). Intrinsic viscosity (IV) was determined using a Cannon-Ubbelohde micro-viscometer (Cannon Instrument Co., State College, PA, USA) at 30 °C. The samples were dissolved at a concentration of 0.2 g/dL in chloroform. IV was calculated by the Solomon–Ciuta equation for a one-point measurement. The IV values obtained were used to obtain average molecular mass by the Mark–Houwink equation. The change in heat-flow curves of the PTHC before and after enzymatic hydrolysis were measured on a Perkin–Elmer DSC 7 (Perkin–Elmer, Wellesley, MA, USA) under a dry nitrogen atmosphere with heating and cooling rates of 10 °C/min between 30 °C and 150 °C. To eliminate previous thermal history, all samples were maintained at 150 °C for 5 min. Cooling and the second heat scan were then performed at a rate of 10 °C/min.

3. Results and discussion

3.1. Morphological and pore textural properties of TS-1 zeolite

Although TS-1 zeolite are widely used in chemical synthesis as catalyst, the analysis of morphological and pore textural properties of TS-1 zeolite need to be confirmed. Because the catalytic activity was affected such as pore size, uniformity and structure of micropores [3]. Fig. 1 shows the N_2 adsorption-desorption isotherm (Fig. 1 (a)) and electron microscopic investigation on TS-1 zeolite (Fig. 1 (b) and (c)). The N_2 adsorption-desorption isotherm of TS-1 zeolite showed typical characteristic for mesoporous MFI zeolite. TS-1 zeolite has a Brunauer-Emmett-Teller (BET) surface area of 334 $m^2 g^{-1}$ and pore volume of 0.53 mL/g, similar to the case of reference mesoporous MFI zeolite [3,9]. The pore size distributions of TS-1 zeolite was obtained by applying the Barrett-Joyner-Halenda (BJH) model. A maximum peak is observed around 1.6–2.6 nm. Fig. 1 (b) shows SEM image of TS-1 zeolite particles. The particle size is in the range of 80–100 nm with uniformly globular morphologies. TEM image is very helpful to confirm the dispersion state of TS-1 zeolite in PBS matrix. As shown Fig. 1 (c), TS-1 zeolite is well dispersed in PBS matrix with uniform size of 100 nm.

3.1.1. Water uptake properties of TS-1 zeolite observed by TG-IR

The water absorbilities of the TS-1 zeolite were directly demonstrated by quantitative analyses to clarify the effect of the TS-1 zeolite during melt processing with increasing temperature. The TG-IR technique can contribute to investigating water volatilization formed during melt processing (Fig. 2). The TG-IR peaks of Homo PBS and TS20 during phase change from 20 °C to 150 °C are shown in Fig. 2(a) and (b). Normally, the intensity of TG-IR for volatized water formed is visible in the ranges 3600–3900 cm^{-1} and 1400–1800 cm^{-1} [38–40]. In the case of Homo PBS, the intensity of TG-IR in Fig. 2(a) shows that volatilized water was dimly visible in the ranges 3600–3900 cm^{-1} and 1400–1800 cm^{-1} due to the initial moisture content of the PBS matrix. However, the intensity of the characteristic peak for initial volatilized water showed no change up to the melt state at 150 °C. In the case of TS20 (Fig. 2(b)), the initial intensity of volatilized water in the solid state (20 °C) for TS20 was similar to that of Homo PBS. The intensity of the characteristic water peak gradually increased with increasing temperature up to the melting state (150 °C). This result was attributable to the release of zeolitic water from TS-1 zeolite pores as a result of the external force (thermal energy). A mass loss of volatilized water in each phase for TS20 can be recorded in the TG curve (Fig. 2(c)). The mass change in volatilized water, even in small quantities, occurred at around 40–80 °C

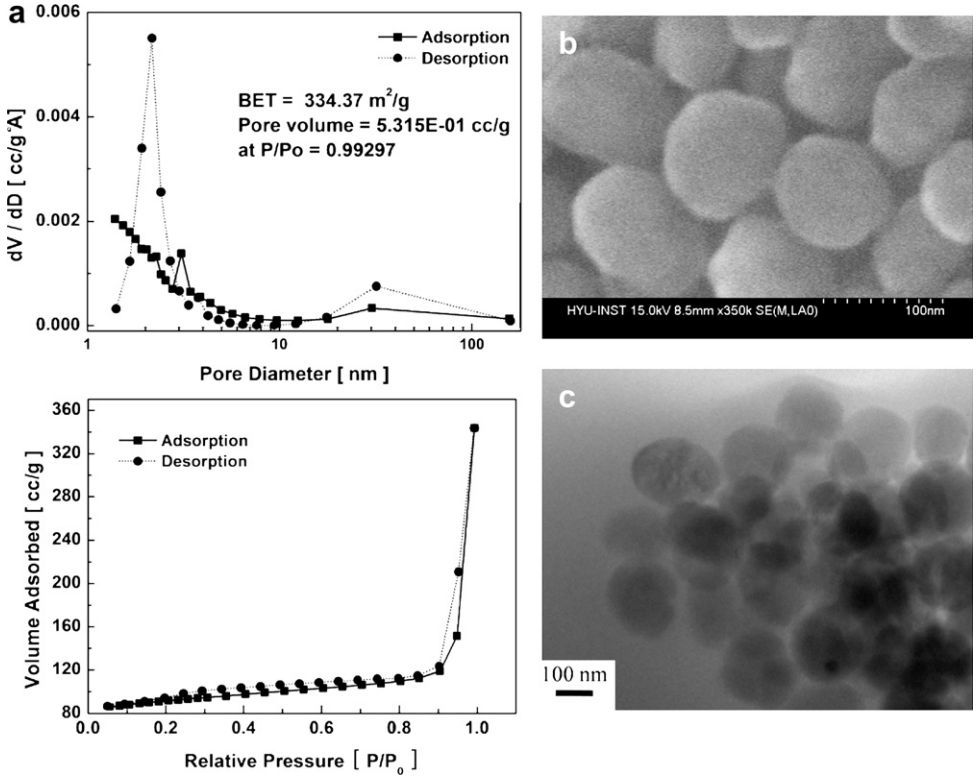

Fig. 1. (a) The pore size distribution curves and N_2 adsorption/desorption isotherms of TS-1 zeolite (b) SEM image of TS-1 zeolite at high magnification (×350k) (c) TEM image of TS20.

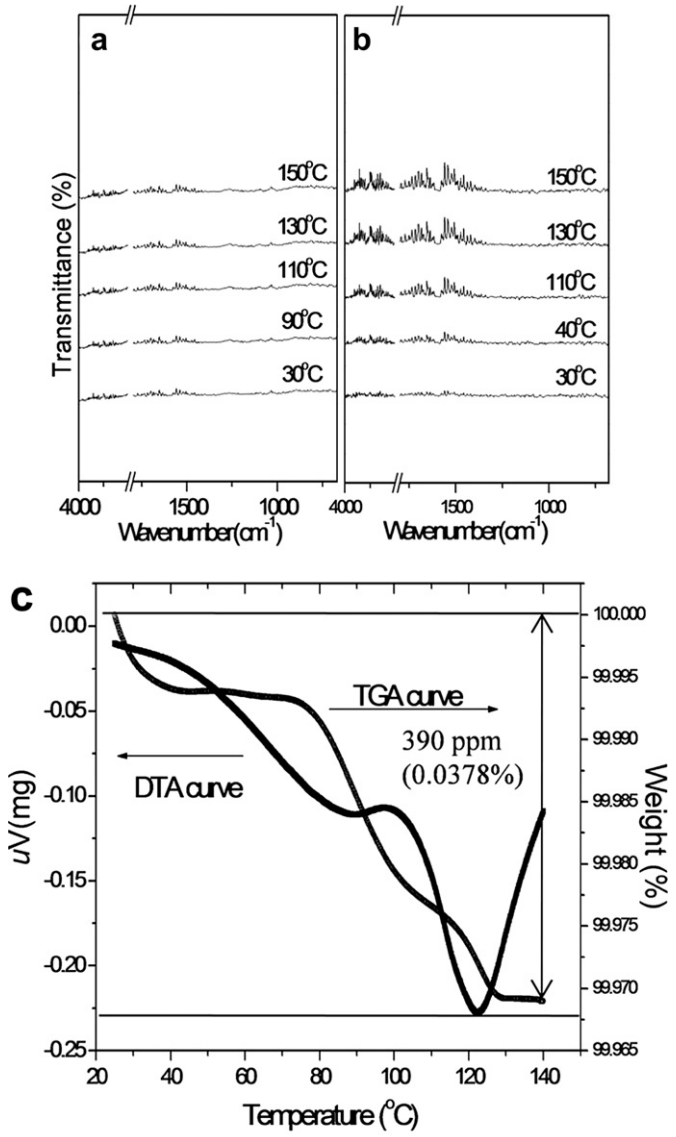

Fig. 2. TG-IR spectra of volatilized water in (a) Homo PBS and (b) TS20 and (c) the rate of weight loss for TS20 during the phase transition from 20 °C to 150 °C.

(rubbery state) and gradually increased to the melt state. This result is consistent with the results shown in Fig. 2(b). The three-dimensional plot supported the change in the adsorption peak for volatilized water as a function of temperature and/or time (Fig. 3). In the case of Homo PBS (Fig. 3(a)), the average intensity of the IR adsorption is even, regardless of temperature and/or time, whereas the average intensity of the IR adsorption for TS20 (Fig. 3(b)) gradually increased with increasing temperature and/or time at 180 s.

3.1.2. Mechanical properties of films (solid state)

Table 1 shows the mechanical properties of PTHC films with various zeolite contents in the solid state. As shown in Table 1, the tensile strength of TS05 and TS10 increased by 6% and 19%, respectively, compared with Homo PBS. This increase was anticipated because it was affected by the interfacial interaction between the TS-1 zeolite and PBS due to the high surface energy of the zeolite and the increased dispersibility of TS-1 zeolite particles [35,41]. At 2.0 wt% of TS-1 zeolite, the tensile strength began to decrease, likely due to spontaneous agglomeration of zeolite particles. Elongation at breakage showed the same trend as the tensile strength values in Table 1. Young's modulus increased continuously with increasing TS-1 zeolite contents for the PTHC due to the rigidity of the TS-1 zeolite. These results are in good agreement with other reported studies on polymer/inorganic filler nanocomposites [42,43].

3.1.3. Rheological properties (melt state)

To investigate the influence of water molecule adsorption/desorption characteristics of the TS-1 zeolite on PBS matrix flow in the melt state, the rheological behavior of the PTHC was assessed by ARES. Fig. 4(a) and (b) show the shear viscosity and storage modulus as function of shear rate for Homo PBS and PTHC at 150 °C. Homo PBS showed a Newtonian plateau at low shear rate regions (Fig. 4(a)) that gradually disappeared with increasing shear rate [25,44]. Compared with Homo PBS, the shear viscosity of the PTHC increased relatively over the shear rate ranges and exhibited high decreases in shear thinning [25,45]. From this result, we anticipated that TS-1 zeolite content can lead to acceleration of the chain orientation of the PBS under shear. Note that the shear viscosity of TS10 and TS20 decreased slightly, in comparison with TS05, at low shear rates. This is because of the presence of released zeolitic water from TS-1 zeolite cages [46,47]. Generally, when the zeolite was heated, the zeolite was dehydrated and became empty cages. However, the TS-1 zeolite quickly absorbs small molecules with polar groups into the empty cages. This situation has been attributed to decreasing the lattice energy in the cages. Thus, the TS-1 zeolite absorbed polar molecules, such as water molecules, during the synthetic process and the dynamic viscosity was decreased by released water molecules in the melt states. The storage modulus of the PTHC (Fig. 4(b)) showed higher values than that of Homo PBS over the total range of shear rates. The Cole–Cole plot of the Homo PBS and the TS-1 zeolite composite are shown in Fig. 4(c). The slope of the TS-1 zeolite hybrid composite (1.40) was shallower than that of Homo PBS (1.53) with no zeolite contents, indicating that the TS-1 zeolite composite is a heterogeneous system and much energy are dissipated in disrupting the network structures. In view of the observation above, one can enhance the mechanical properties with TS-1 zeolite in the solid states without disturbing zeolitic water. On the other hand, water volatilization can exert an influence on physical properties, such as complex viscosity and storage modulus, in the melt state when an external force is applied to the PTHC.

3.1.4. Change of microstructural parameters during isothermal crystallization

The TS-1 zeolite consists of the zeolitic mesoporous three-dimensional channel system with straight channels, interconnected by zigzag channels [5,8]. The presence of large pore sizes in the TS-1 zeolite allows easy transfer of polar molecules through the pores during bulk polymerization. Considering the unique characteristics of the TS-1 zeolite, we could not exclude the possibility that the TS-1 zeolite may have an effect on changes in microstructural parameters and crystallization behavior of the PTHC. Changes in the microstructural parameters of Homo PBS and PTHC at the isothermal crystallization temperatures of 80 °C and 92 °C were analyzed using synchrotron X-ray radiation to investigate any TS-1 zeolite effect. Morphological parameters, including the long period (L), the average lamellar thickness (l_c), and the amorphous layer thickness (l_a), were obtained from the linear correlation function curve (Fig. 5(a) and (b)). The L and l_a for all samples decreased slightly with crystallization time, indicating the formation of additional lamella layers between the two existing dominant lamella during isothermal crystallization [48]. In particular, the values of the long period and the amorphous layer thickness for all samples at 92 °C (Fig. 5(b)) decreased steeply compared with those at 80 °C (Fig. 5(a)). The average l_c (37 Å) and L (98 Å) at 92 °C were higher than the values (28 Å and 90 Å,

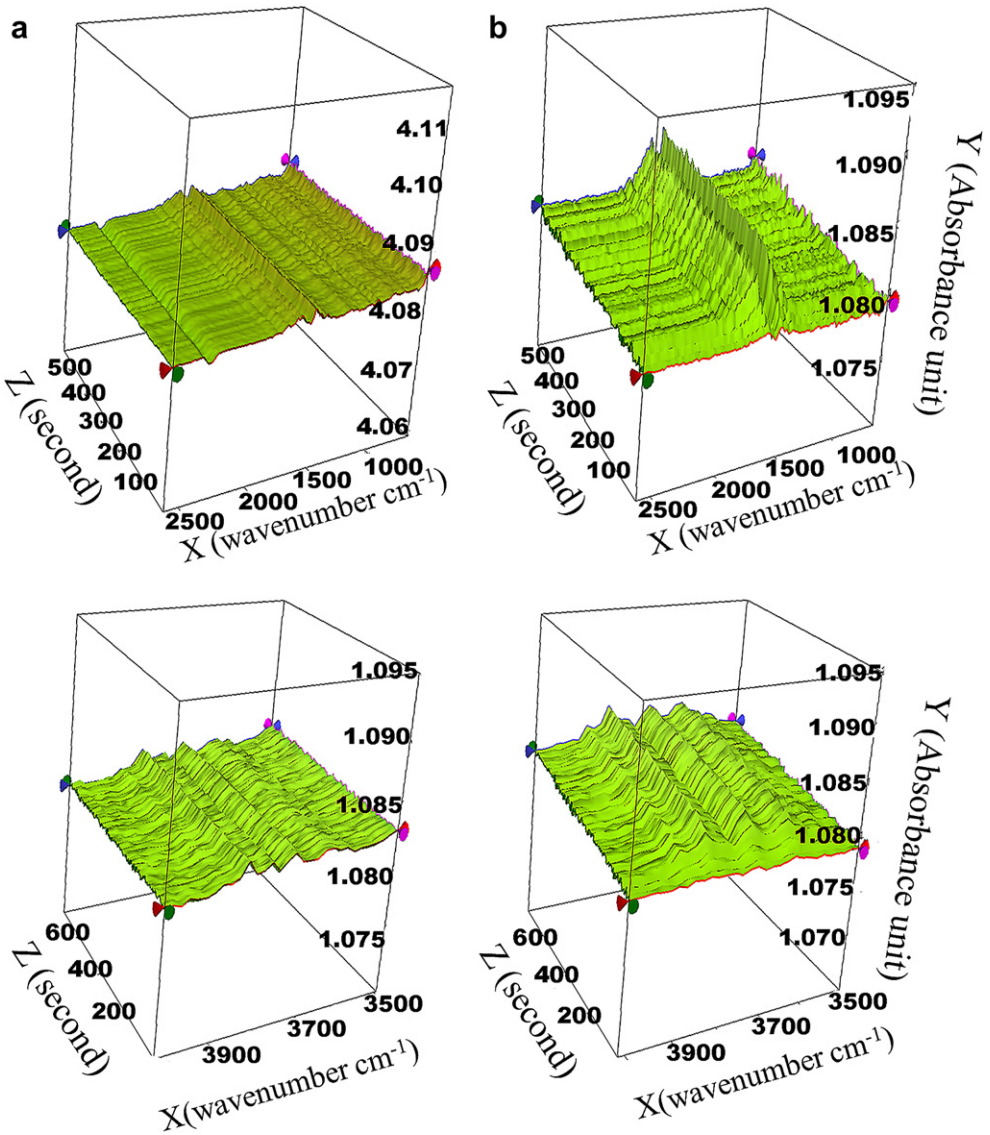

Fig. 3. Three-dimensional TG-IR spectra of (a) Homo PBS and (b) TS20 during the phase transition ranged from 20 °C to 150 °C.

respectively) at 80 °C. To explain these results, one must consider the crystallization phenomenon in two steps, nucleation and crystal growth. In the case of a low crystallization temperature (80 °C), the crystallization was predominantly affected by nucleation because critical-sized nuclei with low surface energy were readily formed at low temperature. Thus, observing the changes in the amorphous layer thickness at 80 °C compared with those at 92 °C is not easy. However, the critical nucleus was difficult to form at the higher crystallization temperature (92 °C) and the crystallization process has a tendency to depend on molecular diffusion at higher temperatures. Thus, crystals grow bigger at higher temperature as shown in Fig. 5(a) and (b). Also, the variations in the l_c and L with crystallization time are more significant in the case of higher crystallization temperature. Note that the introduction of the TS-1 zeolite had almost no effect on changes in morphological features. Before testing, we could not exclude the possibility that PBS molecules go through the TS-1 zeolite pores because the pores are big enough to let the polymer molecules percolate to some degree. In the TS-1 zeolite hybrid system, however, no evidence for the molecular percolation through the TS-1 zeolite pores was observed. The lamella thickness of the PTHCs was similar to that of Homo PBS at any TS-1 zeolite content. The TS-1 zeolite may merely act as a catalyst due to the strong acid sites on the frameworks and not allow PBS molecules to penetrate into the pores. This result is inconsistent with that of previous paper about Polymer/A-zeolite composite [48]. As seen in the SAXS two-dimensional pattern in Fig. 5(c) and (d), the initially isothermal crystallization regions of the PBS/TS-1 zeolite hybrid composite quickly shows a circle diffraction pattern, indicating that the TS-1 zeolite can be effective in crystallization behavior, acting as nucleation agents. The morphological changes caused by the nucleation effect of TS-1 zeolite were observed every minute. These results, expressed in a one–dimensional correlation function, will be discussed in another paper with the isothermal crystallization behavior of the PTHC in detail.

Table 1
Mechanical properties of Homo PBS and PTHC film.

Sample	Tensile strength (MPa)	Elongation at break (%)	Young's modulus (MPa)
PBS	32.8 ± 0.7	180.8 ± 4.9	384.7 ± 8.3
TS05	34.7 ± 1.2	182.8 ± 2.6	425.2 ± 14.2
TS10	38.1 ± 1.5	250.6 ± 10.3	432.6 ± 6.2
TS20	35.2 ± 1.8	140.9 ± 12.3	471.1 ± 9.7

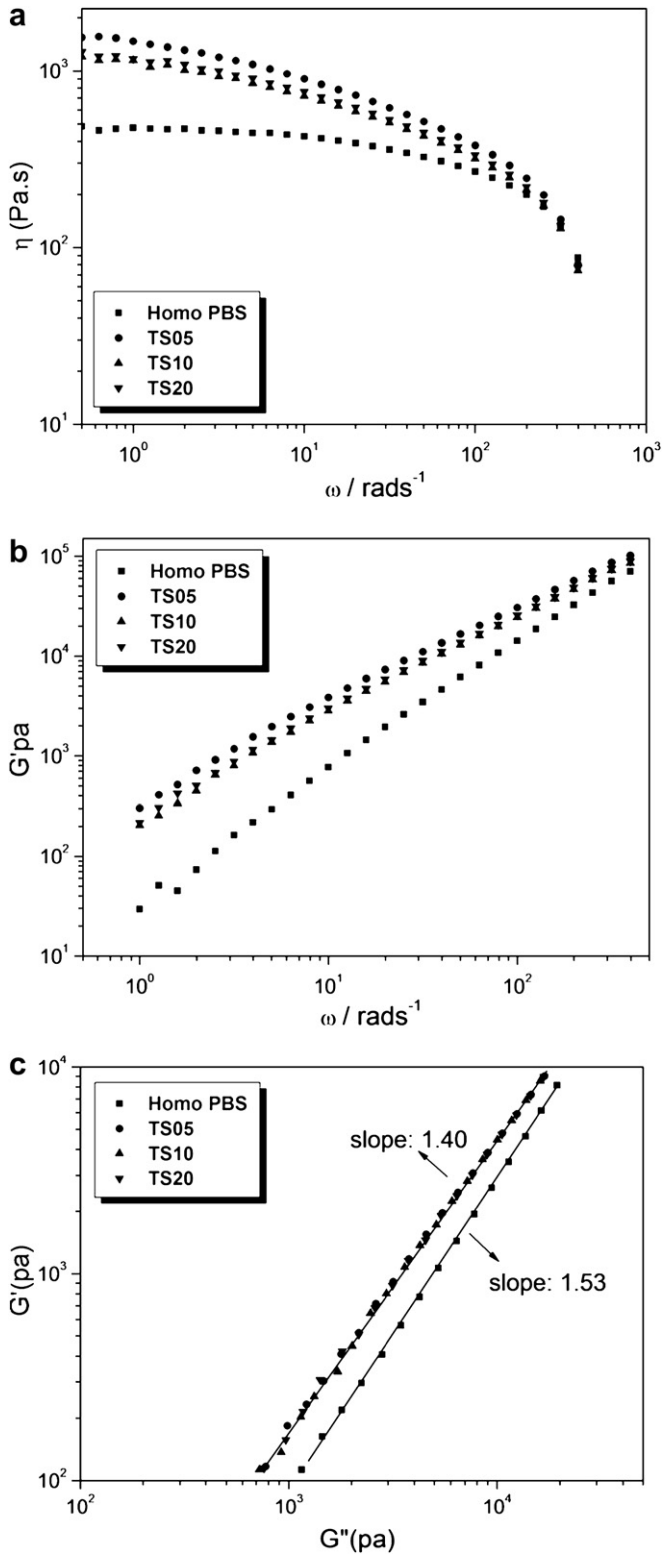

Fig. 4. (a) Shear viscosity versus shear rate, (b) storage modulus, and (c) Cole–Cole plots for Homo PBS and TS-1 zeolite nanocomposite at 150 °C.

3.1.5. Enzymatic hydrolysis tests

To determine the enzymatic hydrolysis of aliphatic biodegradable polymers, several factors must be considered, such as the molecular weight, chemical structure, the specific bond type(s) (e.g., ester, ether, amide, urethanes), and the degree of hydrophilicity and crystallinity [49–54]. As seen Table 2, the IV before the enzymatic hydrolysis test was similar for all samples, ranging from 0.97 to 1.02. This indicates that the molecular weight of each PTHC was comparable to that of Homo PBS. The chemical structure of each PTHC was unchanged in comparison with Homo PBS either (see below). Thus, molecular weight and chemical structure were not important considerations in this case because these parameters were controlled by the same conditions. The contact angle of PTHC films was evaluated to determine the hydrophilicity for samples because the amount of absorbed water on the surface has a decisive effect on enzymatic hydrolysis behavior [49]. The water contact angle of the PTHC gradually decreases with increasing TS-1 zeolite content (Table 2), indicating that the introduction of TS-1 zeolite can effectively enhance the hydrophilicity of the PBS/TS-1 hybrid composite. After the enzymatic hydrolysis test for 90 days, the water contact angles of all hydrolyzed samples greatly decreased as compared to those of initial films. This result was attributable to ester groups being hydrolyzed, resulting in an increase in hydrophilic terminal groups.

Fig. 6 shows the weight loss of enzymatic hydrolysis for all samples in buffer solutions at pH 7.4 and 37 ± 0.5 °C. The degree of enzymatic hydrolysis increased with the introduced content of TS-1 zeolite, although a big difference does not exist between TS10 and TS20. Generally, enzymatic hydrolysis shows saturation in weight loss with the amount and kinds of enzyme used. In this experiment using TS-1 zeolite and *Pseudomonas* lipase, the TS-1 zeolite acts as an accelerator of enzymatic hydrolysis under 1 wt% content of zeolite, resulting in higher hydrolysis rates with higher zeolite contents. However, the enzyme's hydrolytic effect seemed to reach a maximum when the TS-1 zeolite content was above 1 wt%, resulting in no major difference between the TS10 and TS20 samples. The enzymatic hydrolysis rates closely depend on optimum pH and temperature, as well as optimum enzyme concentration. Thus, the enzymatic hydrolysis rate increases steeply with increases in enzyme content, to an optimum value, and then decreases gradually [51]. In particular, the effect of the TS-1 zeolite on the hydrolysis rate was absolute under 1 wt% enzyme content. In the case of TS10 or TS20, the quantitative loss of weight of the films was nearly double in comparison with those of Homo PBS, which indicates that the TS-1 zeolite significantly influenced the enzymatic hydrolysis rate.

Weight loss in enzymatic hydrolysis provides a general trend about the effect of TS-1 zeolite content on the rate of enzymatic hydrolysis. However, these results are inadequate to determine how enzymatic hydrolysis proceeds during the period of a biodegradation test. Indeed, morphological examinations are also necessary. SEM micrographs of surface morphologies for Homo PBS, TS10, and TS20 before and after enzymatic hydrolysis tests are shown in Fig. 7. The film surface before the hydrolysis test for Homo PBS showed a smooth appearance (Fig. 7(a)), whereas TS-1 zeolite stuck out into the surface and was evenly dispersed in proportion to the TS-1 zeolite contents (Fig. 7(b) and (c)). In the case of the enzymatically hydrolyzed samples (see Fig. 7(e)–(g)), surface erosion and small cracks were observed in all samples for Homo PBS and the TS-1 zeolite hybrid composite. However, the morphological images in the SEM micrographs apparently showed no difference between Homo PBS and PTHC, except for the projecting TS-1 zeolite on the surface. This result is seemingly inconsistent with Fig. 6, whereby the weight loss for TS20 was higher than that of Homo PBS. This may have been due to the enzymatic hydrolysis mechanism for the PTHC being different from that of Homo PBS.

To investigate the enzymatic hydrolysis process in detail, changes in crystallinity before and after enzymatic hydrolysis were characterized by WAXD (Fig. 8). Before the enzymatic hydrolysis test, several factors must be considered, such as the tested

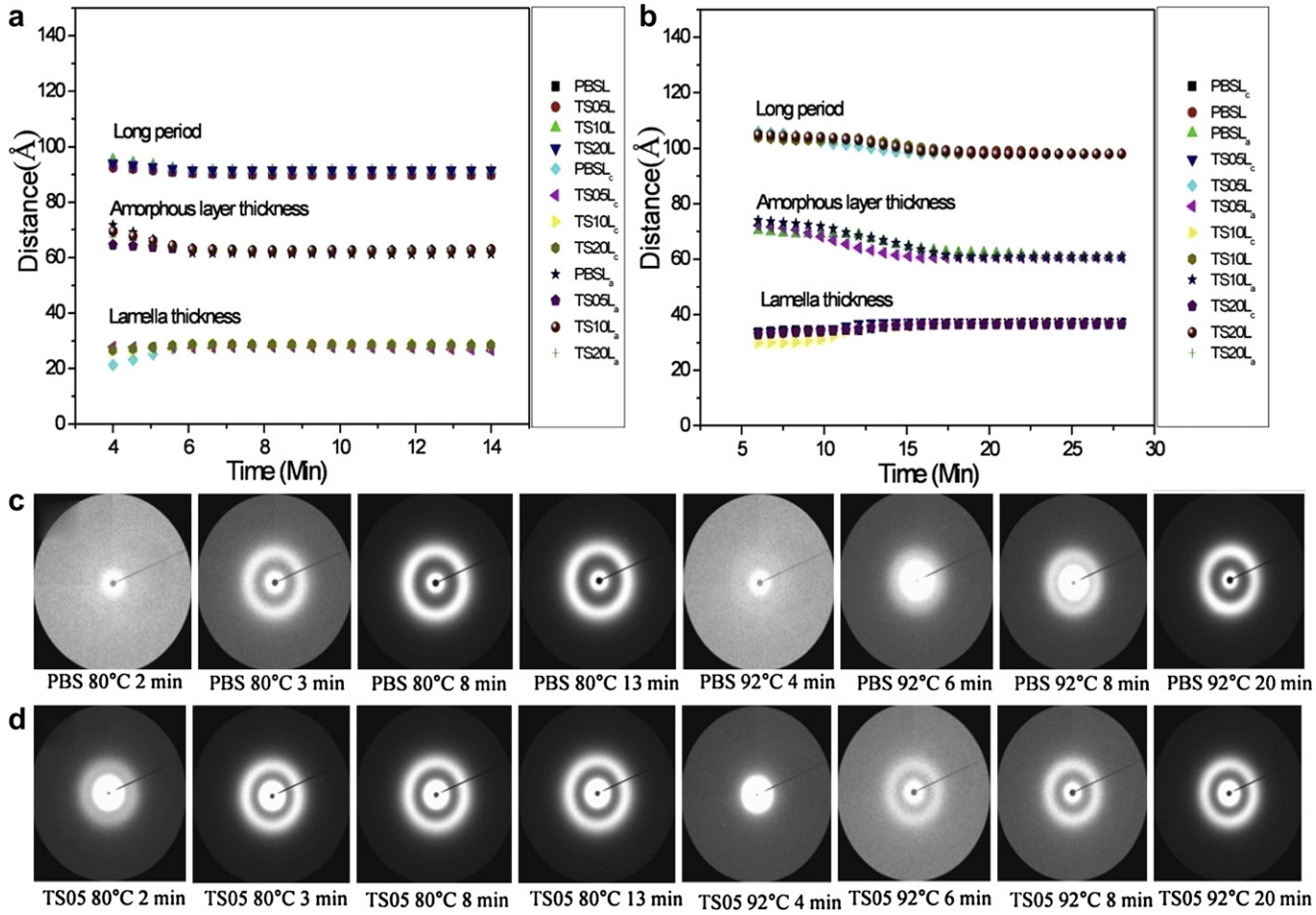

Fig. 5. Change in the microstructure parameters of various samples at the designated isothermal crystallization temperatures of (a) 80 °C and (b) 92 °C; two-dimensional SAXS pattern of (c) Homo PBS and (d) TS05 during isothermal crystallization at 80 °C and 92 °C.

temperature, pH conditions, the kind of enzyme used, and the crystallinity of the samples [50–52]. In particular, the degree of crystallinity is a most important factor. Yoshie et al. [51] reported that the degree of crystallinity and lamellar crystal size had significant effects on the degradation process. Generally, the lower the degree of crystallinity and the thinner the lamella crystals are, the faster the enzymatic hydrolysis is. As previously shown in Fig. 5, the thickness of the lamella crystals was similar for both Homo PBS and PTHC. The crystallinities of the initial film for all samples had similar values (47%; Fig. 8), indicating that the TS-1 zeolite did not have an effect on or change the chemical structure or crystallinity. Thus, we could investigate how the TS-1 zeolite affected the enzymatic hydrolysis under the control of other variables. Fig. 8 shows the change in crystallinity values for all samples before and after the enzymatic hydrolyzed test. In the case of Homo PBS, no apparent change was seen in the values of crystallinity

Table 2
. The intrinsic viscosity and water contact angles on the PTHCs before and after the enzymatic hydrolysis test.

Sample	Intrinsic viscosity (IV)		Water contact angles (°)	
	Before enzymatic hydrolysis test	After enzymatic hydrolysis test	Before enzymatic hydrolysis test	After enzymatic hydrolysis test
PBS	1.00	0.98	85.6 (1.0)	77.8 (0.7)
TS05	1.02	0.86	78.8 (0.6)	73.4 (1.5)
TS10	0.98	0.74	76.9 (1.2)	70.3 (2.1)
TS20	0.97	0.71	75.4 (1.8)	68.1 (2.3)

Values in parentheses are standard deviations ($n = 5$).

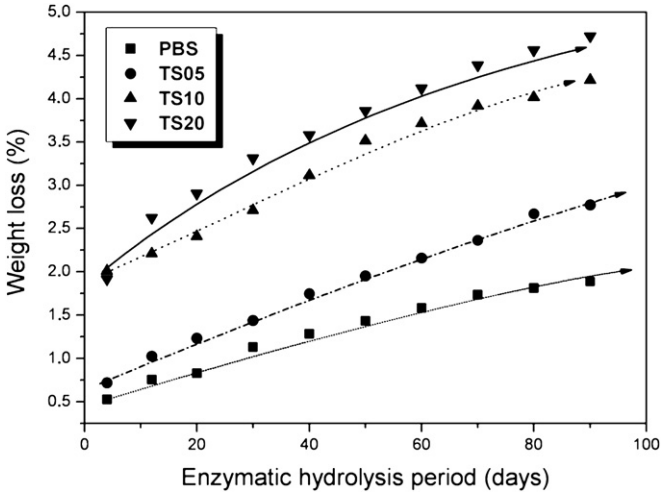

Fig. 6. Weight loss versus hydrolysis time for Homo PBS and PTHC samples during enzymatic hydrolysis at pH 7.4 and 37.5 °C.

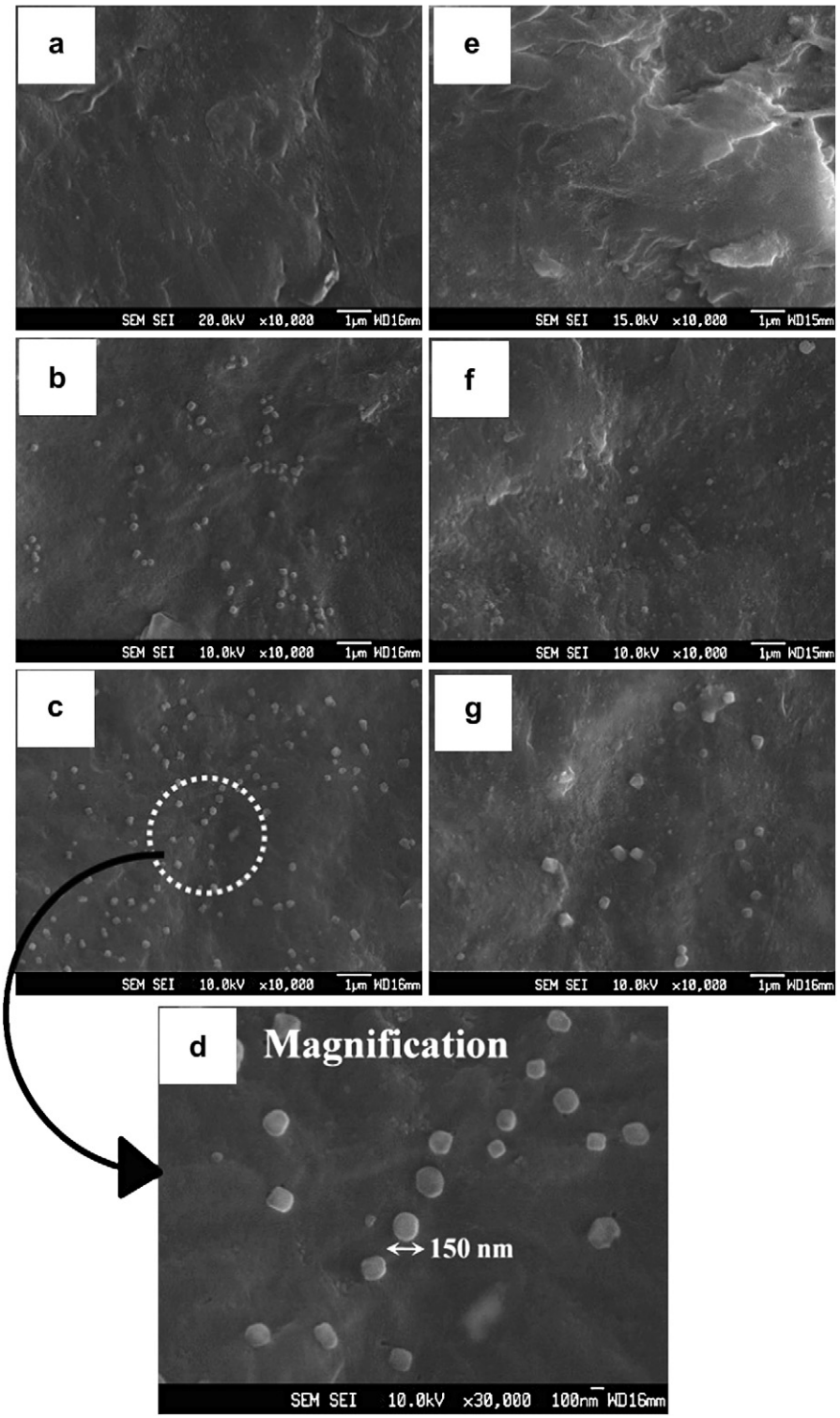

Fig. 7. SEM micrographs of surfaces for (a) Homo PBS, (b) TS10, (c) TS20, and (d) TS20 (magnification) before the enzymatic hydrolysis test and (e) Homo PBS, (f) TS10, and (g) TS20 after the enzymatic hydrolysis test.

before and after enzymatic hydrolysis, with the enzyme primarily attacking the amorphous surface area [51,52]. On the other hand, before the hydrolysis test, the degree of crystallinity of TS10 and TS20 was the same (47%) as that of Homo PBS. After enzymatic hydrolysis, the degree of crystallinity gradually increased with the increase in TS-1 zeolite content (Fig. 8(b) and (c); 51.2% and 53.5%, respectively). Thus, TS20 showed the greatest weight loss in enzymatic hydrolysis among the samples. In general, studies have reported that enzymes attach to the surface of films and preferentially hydrolyze amorphous areas of the surface [49–52]. Because the surface morphological images in SEM micrographs showed no apparent difference between Homo PBS and TS20,

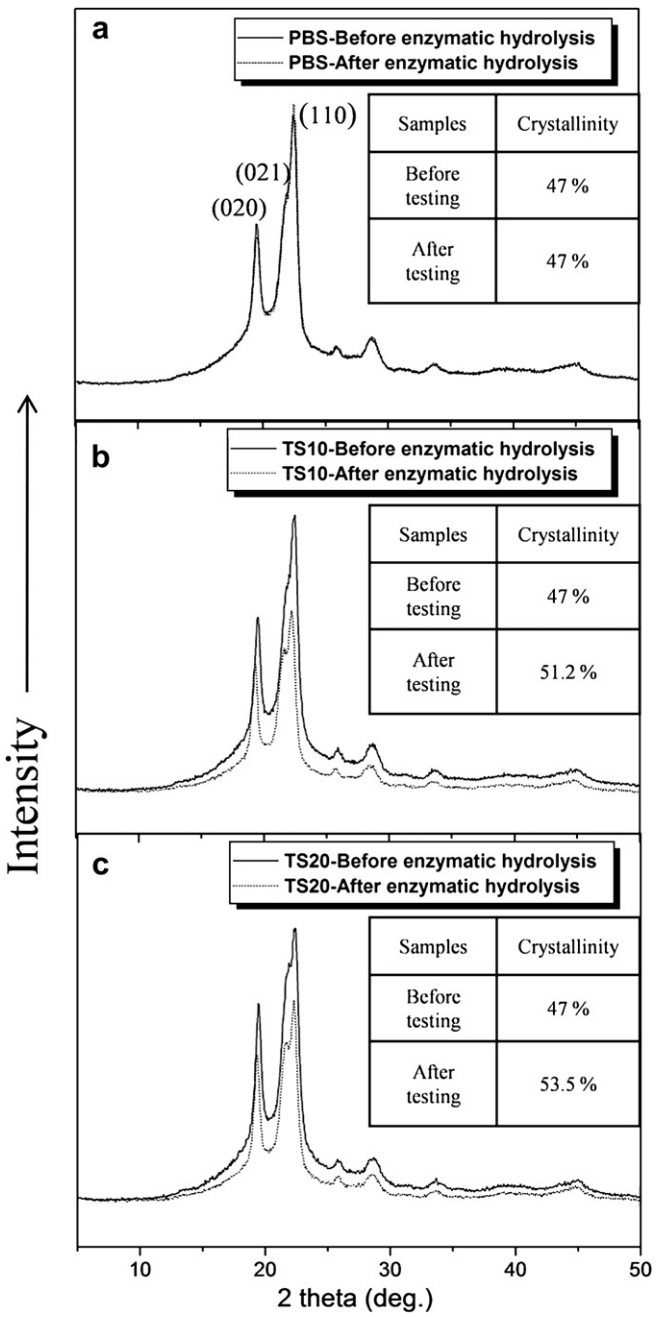

Fig. 8. WAXD pattern of (a) Homo PBS, (b) TS10, and (c) TS20 before and after the enzymatic hydrolysis test.

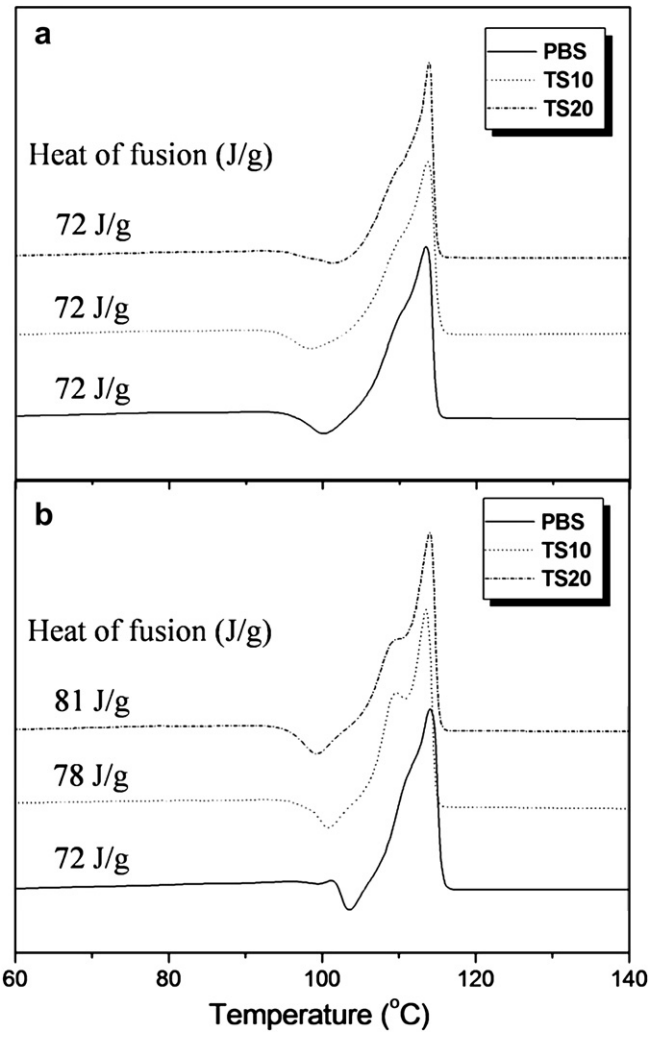

Fig. 9. DSC curves and heat of fusion for Homo PBS, TS10, and TS20 before (a) and after (b) the enzymatic hydrolysis test.

surface erosion alone apparently does not explain the reason for the significantly decreased amorphous regions in the TS20. This result may be reasonably interpreted if we consider that TS-1 zeolite can act as a substrate for enzyme loadings, resulting in increased activity in enzymatic degradability to the amorphous phase of the film inside [29].

The IV measurement and DSC experiment were performed to investigate the change in molecular weight before and after the enzymatic hydrolysis test (Table 2; Fig. 9). The IV of Homo PBS before enzymatic hydrolysis was similar to that after enzymatic hydrolysis, showing that the molecular weights did not greatly change because it was hydrolyzed on the amorphous surface only. However, as shown in Table 2, the IV of PTHC decreased significantly as the TS-1 zeolite content increased, indicating that molecular weights were significantly reduced by enzymatic hydrolysis. The DSC thermogram also supports the above IV explanation (Fig. 9). Fig. 9 shows the second heating thermogram of Homo PBS, TS10, and TS20 before and after the enzymatic hydrolysis test. In the case before the enzymatic hydrolysis in Fig. 9(a), the melting point and heat of fusion for all samples showed similar values. However, after the enzymatic hydrolysis (Fig. 9(a)), Homo PBS showed a largely unchanged heat of fusion (72 J/g) and thermogram curve as compared to before the enzymatic hydrolysis. On the other hand, the thermogram curve for TS10 and TS20 shows a hollow curve and increased heat of fusion with increased TS-1 zeolite content (78 J/g and 81 J/g, respectively). This result demonstrates that the TS-1 zeolite has a great effect in decreasing molecular weight caused by an increase in the activity of enzymatic degradability into the amorphous phase of the film's interior. After considering all factors of the enzymatic hydrolysis test, SEM morphology, IV value test, and DSC thermograms, we conclude that the TS-1 zeolite can be used as a carrier for enzyme loading due to its high desorption capacity and that high enzyme activities significantly affected enzymatic hydrolysis, resulting in a decrease in molecular weight. The typical enzymatic hydrolysis process for PTHC that TS-1 zeolite functions as enzyme carrier is schematically illustrated in Fig. 10.

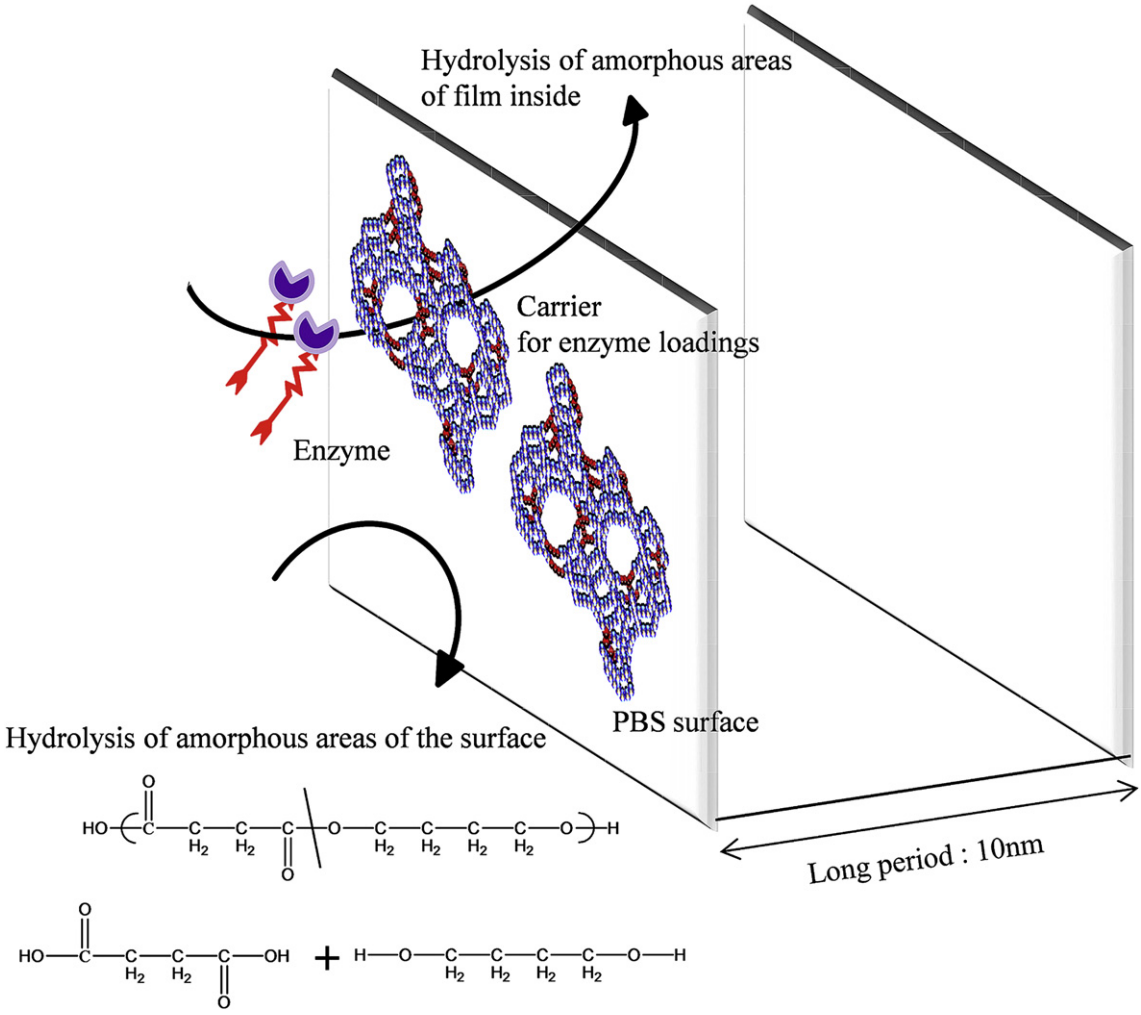

Fig. 10. Schematic representation of enzymatic hydrolysis process for PTHC.

4. Conclusions

Multifunctional biodegradable hybrid material was synthesized by TS-1 zeolite as heavy metal-free catalyst. This study investigated how water uptake features and carrier characteristics of TS-1 zeolite have effects on the physical and rheological properties, morphological parameters, and the enzymatic hydrolysis of PTHCs. The physical properties of PTHC films were significantly increased by the TS-1 zeolite frame acting as a reinforcement filler in the solid state. On the other hand, the water volatilization, released from TS-1 zeolite pores, induced a decrease in the complex viscosity for PTHCs in the melt state. The enzymatic hydrolysis rates of PTHCs were gradually accelerated with increasing TS-1 zeolite contents, which can act as substrate for enzyme loading; the resulting enzymatic hydrolysis occurs from amorphous areas on the surface to those in the interior of the film. Due to the unique characteristics of PTHC, we conclude that PTHC holds potential promise as a material for environmentally sensitive applications, such as packaging materials, and in the agricultural and biomedical fields, which require high physical properties, a high biodegradation rate, and easy processing.

References

[1] van Bekkum H, Flanigen EM, Jansen JC, editors. Introduction to Zeolite Science and Practice. Amsterdam: Elsevier; 1991.
[2] Pérez-Ramírez J, Verboekend D, Bonilla A, Abelló S. Adv Funct Mater 2009;19(24):3972–9.
[3] Srivastava R, Choi MK, Ryoo R. Chem Commun 2006;43:4489–91.
[4] Shan W, Yu T, Wang B, Hu J, Zhang Y, Wang X, et al. Chem Mater 2006;18(14):3169–72.
[5] Li S, Tuan VA, Falconer JL, Nobel RD. Chem Mater 2001;13(5):1865–73.
[6] Johnson SA, Brigham ES, Ollivier PJ, Mallouk TE. Chem Mater 1997;9(11):2448–58.
[7] Valtchev VE. Chem Mater 2007;14(3):956–8.
[8] Kortunov P, Vasenkow S, Chmelik C, Kärger J, Ruthven DM, Wloch J. Chem Mater 2004;16(18):3552–8.
[9] Pan DH, Yuan P, Zhao LZ, Liu N, Zhou L, Wei GF, et al. Chem Mater 2009;21(22):5413–25.
[10] Lee YJ, Kim SJ, Ahn DC, Shin NS. Chem Mater 2007;19(9):2277–82.
[11] Choi MK, Cho HS, Srivastava R, Venkatesan C, Choi DH, Ryoo R. Nat Mater 2006;5(9):718–23.
[12] Devriese LI, Colls L, Aerts A, Martens JA, Baron GV, Denayer JFM. Adv Funct Mater 2007;17(18):3911–7.
[13] Tsotsalas M, Busby M, Gianolio E, Aime S, Cola LD. Chem Mater 2008;20(18):5888–93.
[14] Tuan VA, Li SG, Falconer JL, Noble RD. Chem Mater 2002;14(2):489–92.
[15] Dong J, Xu ZH, Kuznicki SM. Adv Funct Mater 2009;19(8):1268–75.
[16] Choi KH, Cho HS, de Ménorval LC, Ryoo R. Chem Mater 2009;21(23):5664–73.
[17] Jung TK, Shul YG. Chem Mater 1997;9(2):420–2.
[18] Grieneisen JL, Kessler H, Fache E, Le Govic AM. Micropor Mesopor Mat 2000;37(3):379–86.
[19] Phonthammachai N, Krissanasaeranee E, Gulari E, Jamieson AM, Wongkasemjit S. Mater Chem Phys 2006;97(2–3):458–67.
[20] Li YG, Lee YM, Porter JF. J Mater Sci 2002;37(10):1959–65.
[21] Sebastián V, Lin Z, Rocha J, Téllez C, Santamaría J, Coronas J. Chem Mater 2006;18(10):2472–9.
[22] Qiu FR, Wang XB, Zhang XF, Liu H, Liu SQ, Yeung KL. Chem Eng J Phys 2009;147(2–3):316–22.

[23] Taramasso M, Perego G, Notari B. US Patent 1983; 4,410,501.
[24] Ray SS, Okamoto K, Okamoto M. Macromolecules 2003;36(7):2355–67.
[25] Lim ST, Hyun YH, Choi HJ, Jhon MS. Chem Mater 2002;14(4):1839–44.
[26] Rhee SH, Lee YK, Lim BS. Biomacromolecules 2004;5(4):1575–9.
[27] Knight PT, Lee KM, Qin HU, Mather PT. Biomacromolecules 2008;9(9):2458–67.
[28] de Mesquita JP, Donnici CL, Pereira FV. Biomacromolecules 2010;11(2):473–80.
[29] Wang Y, Caruso F. Adv Funct Mater 2004;14(10):1012–8.
[30] Hua J, Han Y. Chem Mater 2009;21(12):2344–8.
[31] Graeser A, Spange S. Chem Mater 1998;10(7):1814–9.
[32] Jeong HK, Krych W, Ramanan H, Nair S, Marand E, Tsapatsis M. Chem Mater 2004;16(20):3838–45.
[33] Suárez S, Devaux A, Banuelos J, Bossart O, Kunzmann A, Calzaferri G. Adv Funct Mater 2007;17(14):2298–306.
[34] Sen S, Bardakci B, Yavuz AG, Gök AU. Eur Polym J 2008;44(8):2708–17.
[35] Pehlivan H, Balköse D, Tihminlioğlu F. Compos Sci Technol 2005;65(13):2049–58.
[36] Özmichi F, Balköse D, Ülkü S. J Polym Sci Part B Polym Phys 2001;82(12):2913–21.
[37] Shin YH, Lee WD, Im SS. Macromol Res 2007;15(7):662–70.
[38] Karimi B, Biglari A, Clark JH, Budarin V. Angew Chem Int Ed 2007;46(38):7210–3.
[39] Chen X, Jiao C. Polym Degrad Stabil 2008;93(12):2222–5.
[40] Gallas JP, Goupil JM, Vimont A, Lavalley JC, Gil B, Gilson JP, et al. Langmuir 2009;25(10):5825–34.
[41] Frisch HL, Mark JE. Chem Mater 1996;8(8):1735–8.
[42] Hwang SY, Yoo ES, Im SS. Polym Degrad Stabil 2009;94(12):2163–9.
[43] Rong MZ, Zhang MQ, Zheng YX, Zeng HM, Walter R, Friedrich K. Polymer 2001;42(1):167–83.
[44] Gupta RK, Kennel E, Kim KJ. Polymer Nanocomposite Handbook. London: Taylor and Francis; 2010.
[45] Chae DW, Kim BC. Compos Sci Technol 2007;42(1):167–83.
[46] Mondal P, Ch Deka R. Bull Catal Soc India 2007;6:151–9.
[47] Jentys A, Catlow CRA. Catal Lett 1993;22(3):251–7.
[48] Lee WD, Im SS. J Polym Sci Part B Polym Phys 2007;45(1):28–40.
[49] Tsuji H, Miyauchi S. Biomacromolecules 2001;2(2):597–604.
[50] Parageorgiou GZ, Bikiaris DN. Biomacromolecules 2007;8(8):2437–49.
[51] Yoshie N, Oike Y, Kasuya K, Doi Y, Inoue Y. Biomacromolecules 2002;3(6):1320–6.
[52] Bikiaris DN, Papageorgiou GZ, Achilias DS, Pavlidou E, Stergiou A. Eur Polym J 2007;43(6):2491–503.
[53] Kurokawa K, Yamashita K, Doi Y, Abe H. Biomacromolecules 2008;9(3):1071–8.
[54] Numata K, Finne-Wistrand A, Albertsson AC, Doi Y, Abe H. Biomacromolecules 2008;9(8):2180–5.

Polymer 52 (2011) 976–986

Contents lists available at ScienceDirect

Polymer

journal homepage: www.elsevier.com/locate/polymer

Carbazole/fluorene copolymers with dimesitylboron pendants for blue light-emitting diodes

Ying-Hsiao Chen [a], Yu-Ying Lin [a], Yung-Chung Chen [b], Jiann T. Lin [b], Rong-Ho Lee [a,*], Wen-Jang Kuo [c], Ru-Jong Jeng [a,*]

[a] Department of Chemical Engineering, National Chung Hsing University, Taichung 402, Taiwan
[b] Institute of Chemistry, Academia Sinica, Taipei 115, Taiwan
[c] Department of Applied Chemistry, National University of Kaohsiung, Kaohsiung 811, Taiwan

ARTICLE INFO

Article history:
Received 25 September 2010
Received in revised form
16 December 2010
Accepted 24 December 2010
Available online 9 January 2011

Keywords:
Light-emitting polymer
Carbazole derivative
Dimesitylboron group

ABSTRACT

A series of random and alternating carbazole/fluorene copolymers with various dimesitylboron-containing carbazole derivative contents were synthesized by Suzuki polymerization for use as a light-emitting layer in blue light-emitting diodes. Two carbazole derivatives, CzPhB and CzPhThB consisted of a carbazoyl group as the donor and a dimesitylboron group as the acceptor group, separated by phenyl and phenylthiophene groups π-conjugated systems, respectively. The copolymers exhibited good thermal stability and blue emission in both solution and the solid state. Moreover, the CzPhB/fluorene and CzPhThB/fluorene copolymers exhibited a higher PL quantum efficiency than the fluorene-based homopolymer (POF). Higher brightness and larger current efficiency were observed for the CzPhB/fluorene and CzPhThB/fluorene copolymer-based devices compared to the POF-based device. Additionally, the CzPhThB/fluorene copolymer-based devices had better EL performances than the CzPhB/fluorene copolymer-based devices. The turn-on voltage, maximal brightness, and highest luminescence efficiency of the carbazole/fluorene copolymer-based devices were found to be 4.5–8.5 V, 436 cd/m^2, and 0.51 cd/A, respectively.

1. Introduction

In the past decades, polymer light-emitting diodes (PLEDs) have received attention because of their applications in full-color flat panel displays and solid state lighting sources [1,2]. PLEDs have a number of advantages over inorganic or organic small molecule-based light-emitting diodes, including easy processing, low operating voltages, low cost fabrication, and high flexibility [3]. For a full-color display, the need to develop more stable and highly efficient three primary color (red, green, and blue) emitters is important for allowing PLEDs to become commercial products [4]. Of particular interest are blue light-emitting materials, which can serve as either blue light sources in a full-color display or as host materials for lower energy fluorescent or phosphorescent dyes [5–8]. Therefore, developing stable blue EL materials with high efficiency and excellent Commission Internationale de L'Enclairage (CIE) coordinates (y-coordinate value < 0.15) is essential to realizing such applications.

Conjugated polyfluorenes (PFs) have evolved to be the most promising candidates for blue-emitting materials for PLEDs because of their highly efficient blue emission in photoluminescence (PL) and electroluminescence (EL), excellent thermal and chemical stability, and good solubility in common organic solvents [9–13]. However, an undesired emission appearing in the long-wavelength division (from 500 to 600 nm) of the emission spectra of PF homopolymers not only hampers the EL efficiency, but impairs the color purity. Either the formation of aggregates/excimers or degradation of the polymers during operation of the PF-based PLEDs has been proposed as the source of this problem [14–16]. The long-wavelength emission could be curtailed by introducing bulky substituents or long alkyl chains at the C-9 position of the fluorene unit through copolymerization with appropriate co-monomers or the attachment of bulky end-capping groups, among others [17–24]. Additionally, most PF-type polymers with low highest occupied molecular orbital (HOMO) levels have a high energy barrier to hole-injection from the anode, resulting in imbalanced charge mobility and subsequent low quantum efficiency [25,26]. Chemical structure modification of PFs by incorporating electron-donor moieties, such as triarylamine, carbazole, and thiophene groups, seems to improve the deficiency in hole-injection properties [20,27,28]. It is well-known that

* Corresponding authors. Tel.: +886 4 22854724; fax: +886 4 22854734.
E-mail addresses: rhl@dragon.nchu.edu.tw (R.-H. Lee), rjjeng@dragon.nchu.edu.tw (R.-J. Jeng).

0032-3861/$ – see front matter © 2011 Elsevier Ltd. All rights reserved.
doi:10.1016/j.polymer.2010.12.060

attaching a carbazole moiety to the molecular scaffold can significantly enhance the thermal stability and HOMO energy level of light-emitting polymers (LEPs). Moreover, the 3-, 6- or 9-position of the carbazole moiety can be easily functionalized, and thus the photo-physical properties of the polymers can be tuned [29–32]. N-arylated carbazoles, in which a phenyl or napthyl group is attached at the 9-position of the carbazole, have shown excellent thermal stability and good electro-optical properties in small-molecule OLEDs [33]. As far as the conjugated polymer is concerned, the imbalanced transport properties between the holes and electrons are another crucial factor deciding the efficiency of PLEDs. Due the poor electron-mobility of LEPs, the attachment of electron-deficient groups (such as pyridine, benzothiadiazole, quinoxalines, and oxadiazole, etc.) onto a polymer chain has proven to be an effective methodology to promote its electron transport capabilities [34–37]. Several studies have also demonstrated that borane-derivatives are potential luminescent and electron-transporting materials [38–40]. The air and moisture stabilities of electron-deficient arylboranes can be improved by incorporating the non-coplanar dimesityl group into the molecules [41–43]. Moreover, the non-coplanar structure of dimesitylborane could hinder the molecular close packing in the solid state. A stable amorphous film was formed for a dimesitylborane moiety containing carbazole derivative [40]. Although arylborane-containing fluorophores have been successfully developed as light emitters, only a few arylborane moieties containing LEPs have been proposed for PLED applications [44–47]. Chujo et al. synthesized a series of alternating copolymers by the hydroboration polymerization of aromatic diynes and mesitylborane [44]. Blue emission was observed for the copolymers in dilute solution state. The copolymers containing boron atoms in the main-chains are expected to act as electron-deficient π-conjugated systems, where π-conjugation length is extended via the vacant *p*-orbital of the boron atom [44]. However, the EL properties of the main chain organoboron polymer-based emitting layers have not been investigated. In addition, Yamaguchi and coworkers reported a series of highly emissive diborylphenylene containing poly(arylenethyynylene)s [45,46]. The presence of bulky diarylboryl substituents not only acts as a good electron-accepting unit, but also prevents the interaction and aggregation between the polymer backbones. However, these poly(arylenethyynylene)s exhibited sky-blue to green emission as thin films due to the strongly intramolecular charge transfer (ICT) transition from the π-conjugated backbone to the diborylphenylene unit. EL properties of the poly(arylenethyynylene)s were not discussed even through the fact that highly absolute quantum yields were observed for these polymer-based thin films [46]. More recently, two *N*-*p*-(diarylboryl)phenyl-substituted polycarbazoles were reported by Lambert et al. [47]. Although the authors demonstrated a light-emitting device based on N-*p*-(diarylboryl)phenyl-substituted 3,6-linked polycarbazoles, but only the EL spectrum was shown in the literature.

Base on the above, highly blue emissive conjugated polymers could be obtained by the incorporation of the electron-deficient arylborane unit into the conjugated polymers [44–47]. It is important to note that EL properties have never been discussed for these arylborane unit containing conjugated polymers. In addition to the bipolar structure in the polymer, the conjugation length in both side-chain moiety and polymer backbone should be taken into account for pursuing a polymer-based device with excellent EL performances. In this study, a series of random and alternating carbazole/fluorene copolymers with various contents of dimesitylboron-containing carbazole derivatives were designed and synthesized for use as blue emitters in PLEDs because the bipolar carbazole-π-dimesitylboron unit exhibits a high PL quantum efficiency in both solution and the solid state [40]. Two carbazole derivatives, CzPhB and CzPhThB consisted of a carbazoyl group as the donor and a dimesitylboron group as the acceptor group, separated by phenyl and phenyl-thiophene groups π-conjugated systems, respectively. Incorporating the bipolar carbazole derivative as the pendant of the conjugated polymer was favorable for improvement of the charge-injection/transporting characteristics of the PF. Excellent EL properties were expected for these carbazole/fluorene copolymer-based PLEDs. The thermal stability, electrochemical properties, photo-physical behavior, and EL performances of the carbazole/fluorene copolymer-based devices are discussed in detail as the chemical structures and carbazole derivative content of the copolymers are taken into account.

2. Experimental

2.1. Materials

All reactions and manipulations were performed in a nitrogen atmosphere using standard Schlenk techniques. All chromatographic separations were carried out on silica gel. 9H-carbazole, 1,4-dibromobenzene, N-bromosuccinimide (NBS), copper powder and 18-crown-6 were purchased from Acros Co. Potassium carbonate (K_2CO_3) was bought from Fisher Scientific. Tetrakis-triphenylphosphine palladium(0) [$Pd(PPh_3)_4$] was purchased from Strem Chemicals. 2.7-Dibromo-9,9-dioctylfluorene (compound **3**), n-butyl lithium and dimesitylboron fluoride were obtained from Aldrich Co. *o*-Dichlorobenzene (DCB) was bought from TEDIA. Tetrahydrofuran (THF) and toluene were purified by distillation from sodium in the presence of benzophenone. Detailed synthetic procedures for the carbazole derivatives (CzPhB and CzPhThB) and carbazole/fluorene copolymers are report hereafter and are shown in Schemes 1 and 2.

2.2. Synthesis of monomers

2.2.1. Synthesis of 9-(4-bromophenyl)-9H-carbazole (compound 1) [48]

A stirred mixture of 9*H*-carbazole (5.02 g, 30 mmol), 1,4-dibromobenzene (14.13 g, 60 mmol), K_2CO_3 (16.56 g, 120 mmol), Cu powder (1.94 g, 30 mmol) and 18-crown-6 (3.71 g, 15 mmol) in DCB (120 ml) was degassed with nitrogen for 1 h. The reaction mixture was then refluxed under a nitrogen atmosphere for 16 h. The crude mixture was filtered, and the residue was washed with dichloromethane. The combined filtrates were then evaporated to dryness. The product was purified by flash column chromatography (silica gel, hexane) to give compound 1 (7.0 g, yield = 73%) as a white solid. ^{1}H NMR (600 MHz, $CDCl_3$): δ [ppm]: 7.26–7.31 (m, 2H), 7.35–7.38 (m, 3H), 7.40–7.45 (m, 3H), 7.72 (d, J = 8.7 Hz, 2H), 8.13 (d, J = 7.8 Hz, 2H). ^{13}C NMR (75 MHz, $CDCl_3$): δ [ppm]: 109.53, 120.20, 120.37, 120.87, 123.47, 126.07, 128.71, 133.10, 136.79, 140.60. HRMS (*m*/*z*): calcd for $C_{18}H_{12}BrN$: 321.0153. Found: 321.0162. Anal. calcd for $C_{18}H_{12}BrN$: C, 67.10; H, 3.75; N, 4.35. Found: C, 67.45; H, 3.73; N, 4.21.

2.2.2. Synthesis of 9-(4-(thiophen-2-yl)phenyl)-9H-carbazole (compound 2)

50 mL of anhydrous toluene was added to a mixture of compound 1 (3.22 g, 10 mmol) and 2-thiopheneboronic acid (2.77 g, 10 mmol). After 10 mL of 2 M aqueous K_2CO_3 was added to the stirred mixture, the reaction mixture was degassed with nitrogen for 1 h. Then Pd $(PPh_3)_4$ (0.03 g, 0.05 mmol) was added to the mixture. The solution was further refluxed under a nitrogen atmosphere for 48 h. After the reaction solution was cooled to room temperature, the whole mixture was poured into water, and the organic layer was separated and washed with water. The organic extracts were dried over $MgSO_4$ and concentrated by rotary evaporation. After the solvent was

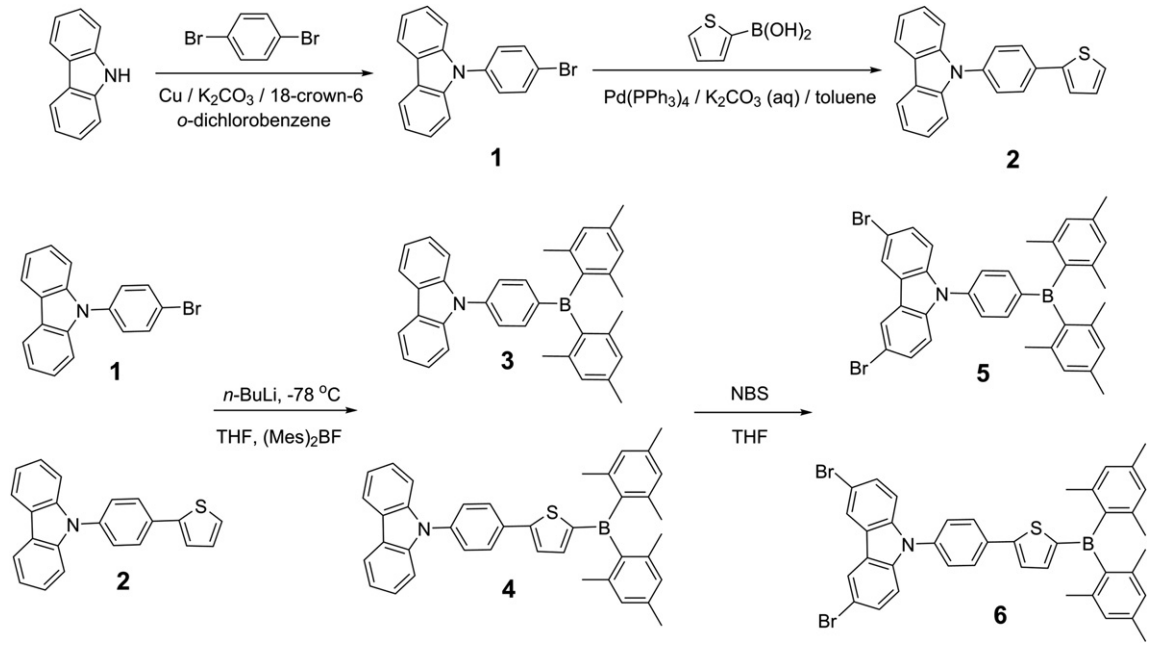

Scheme 1. Synthetic routes of monomers.

evaporated, the crude product was further purified by column chromatography on silica gel using hexane as the eluent to yield compound 2 (2.34 g, yield = 72%) as a white solid. ^{1}H NMR (600 MHz, $CDCl_3$): δ [ppm]: 7.12 (t, J = 3.9 Hz, 1H), 7.28–7.35 (m, 3H), 7.39–7.44 (m, 5H), 7.56 (d, J = 8.4 Hz, 2H), 7.70 (d, J = 8.7 Hz, 2H), 8.14 (d, J = 7.8 Hz, 2H). ^{13}C NMR (75 MHz, $CDCl_3$): δ [ppm]: 109.76, 120.01, 120.31, 123.42, 123.57, 125.30, 125.97, 127.22, 127.41, 128.22, 133.51, 136.77, 140.74, 143.39. HRMS (m/z): calcd for $C_{22}H_{15}NS$: 325.0925. Found: 325.0923. Anal. calcd for $C_{22}H_{15}NS$: C, 81.20; H, 4.65; N, 4.30. Found: C, 81.25; H, 4.30; N, 4.28.

2.2.3. Synthesis of 9-(4-(dimesitylboryl)phenyl)-9H-carbazole (compound 3)

Under a nitrogen atmosphere, n-butyl lithium (4.4 ml, 11 mmol, 2.5 M in hexane) was added to a solution of compound 1 (3.2 g, 10 mmol) in dry THF (50 mL) at −78 °C. After 1 h of stirring,

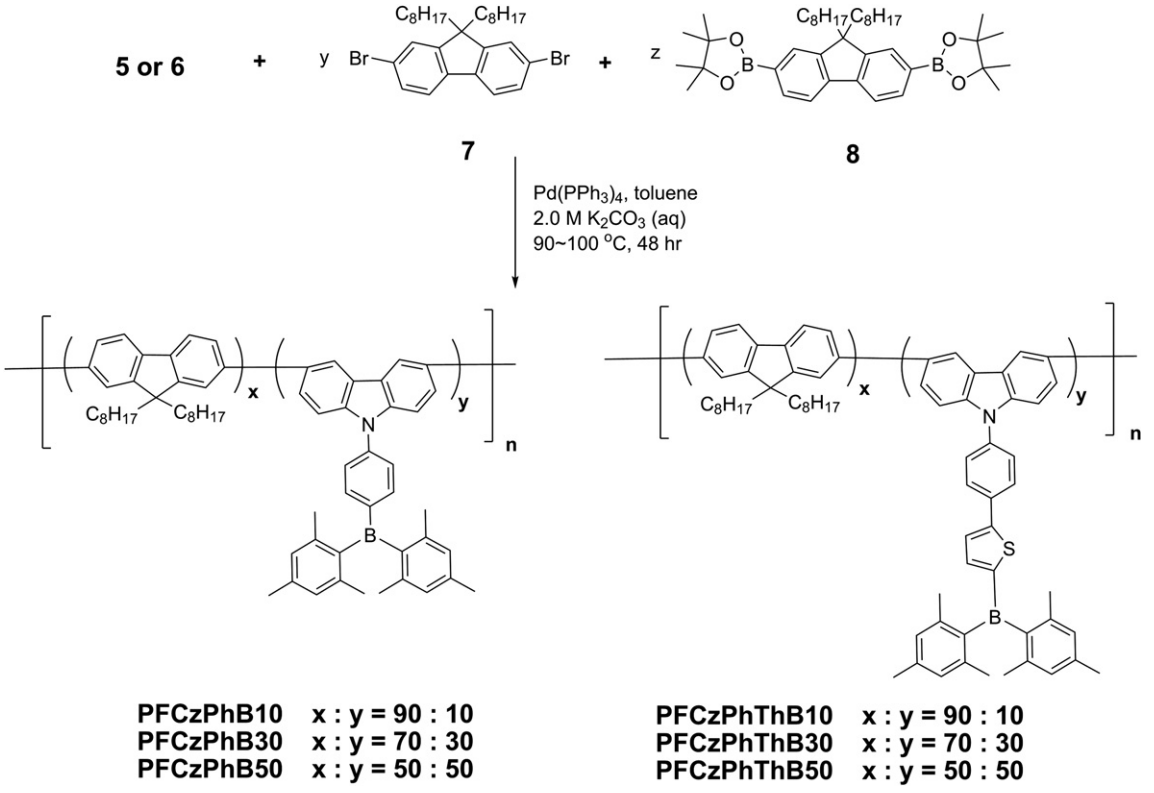

Scheme 2. Synthetic routes of the carbazole/fluorene copolymers.

dimesitylboron fluoride (3.0 g, 11 mmol) in 15 mL of THF was added slowly to the reaction mixture, which was stirred for a further 12 h. The reaction mixture was then cooled to room temperature and quenched with 2 N HCl. The solution was extracted with ethyl acetate and the organic layer was dried over $MgSO_4$, filtered, and evaporated to yield a crude solid. The crude product was purified by column chromatography to afford a white solid of compound 3 (3.42 g, yield = 70%). ^{1}H NMR (600 MHz, $CDCl_3$): δ [ppm]: 2.08 (s, 12H), 2.31 (s, 6H), 6.85 (s, 4H), 7.28 (t, J = 8.1 Hz, 2H), 7.40 (t, J = 8.1 Hz, 2H), 7.49 (d, J = 7.8 Hz, 2H), 7.56 (d, J = 8.4 Hz, 2H), 7.73 (d, J = 8.1 Hz, 2H), 8.12 (d, J = 7.2 Hz, 2H). ^{13}C NMR (75 MHz, $CDCl_3$): δ [ppm]: 21.24, 23.51, 109.94, 120.22, 120.34, 123.66, 125.89, 125.98, 126.89, 127.2, 128.309, 137.95, 138.89, 140.37, 140.83. FABMS (m/z): calcd for $C_{36}H_{34}BN$: 491.2784. Found: 491.2786. Anal. calcd for $C_{36}H_{34}BN$: C, 87.98; H, 6.97; N, 2.85. Found: C, 87.57; H, 7.11; N, 2.38.

2.2.4. Synthesis of 9-(4-(5-(dimesitylboryl)thiophen-2-yl)phenyl)-9H-carbazole (compound 4)

Compound 2 (3.25 g, 10 mmol), n-butyl lithium (4.4 mL, 11 mmol, 2.5 M in hexane) and dimesitylboron fluoride (3.0 g, 11 mmol) were allowed to react according to the procedure for compound 3. A pale yellow solid of compound 4 was obtained (3.44 g, Yield = 60%). ^{1}H NMR (600 MHz, $CDCl_3$): δ [ppm]: 8.15 (d, J = 7.8 Hz, 2H), 7.90 (d, J = 8.7 Hz, 2H), 7.54–7.59 (m, 3H), 7.47–7.49 (m, 5H), 7.41–7.45 (m, 2H), 6.86 (s, 4H), 2.32 (s, 6H), 2.18 (s, 12H). ^{13}C NMR (75 MHz, $CDCl_3$): δ [ppm]: 21.23, 23.48, 109.73, 120.12, 120.34, 123.49, 125.75, 126.01, 127.32, 127.52, 128.20, 133.11, 137.66, 138.61, 140.62, 140.86, 141.70, 155.73. HRMS (m/z): calcd for $C_{40}H_{36}BNS$: 573.2662. Found: 573.2658. Anal. calcd for $C_{40}H_{36}BNS$: C, 83.76; H, 6.33; N, 2.44. Found: C, 83.59; H, 6.77; N, 2.07.

2.2.5. Synthesis of 3,6-dibromo-9-(4-(dimesitylboryl)phenyl)-9H-carbazole (compound 5, CzPhB)

N-Bromosuccinimide (3.92 g, 22 mmol) was added portion wise to a solution of compound 3 (4.91 g, 10.00 mmol) in THF (80 mL). The mixture was stirred at room temperature under a nitrogen atmosphere for 16 h. The whole mixture was then poured into water, and the organic layer was separated and washed with water. The organic extracts were dried over anhydrous Na_2SO_4, filtered, and evaporated to yield a crude solid. The crude product was further purified by column chromatography using silica gel and eluting with hexane to afford a white solid, compound 5 (4.01 g, yield = 62%). ^{1}H NMR (600 MHz, $CDCl_3$): δ [ppm]: 2.08 (s, 12H), 2.32 (s, 6H), 6.86 (s, 4H), 7.32 (d, J = 9.0 Hz, 2H), 7.31–7.48 (m, 4H), 7.74 (d, J = 8.4 Hz, 2H), 8.15 (s, 2H). ^{13}C NMR (75 MHz, $CDCl_3$): δ [ppm]: 21.26, 23.53, 111.65, 113.32, 123.24, 124.18, 125.70, 128.34, 129.42, 138.02, 139.04, 139.33, 140.78.FABMS (m/z): calcd for $C_{36}H_{32}BBr_2N$: 647.0995. Found: 647.1002. Anal. calcd for $C_{36}H_{32}BBr_2N$: C, 66.60; H, 4.97; N, 2.16. Found: C, 66.48; H, 5.17; N, 1.92.

2.2.6. Synthesis of 3,6-dibromo-9-(4-(5-(dimesitylboryl)thiophen-2-yl)phenyl)-9H-carbazole (compound 6, CzPhThB)

N-Bromosuccinimide (3.92 g, 22.0 mmol) and compound 4 (5.73 g, 10.0 mmol) were allowed to react according to the procedure for compound 5. A pale yellow solid, compound 6 (CzPhThB) was obtained (4.08 g, Yield = 56%). ^{1}H NMR (600 MHz, $CDCl_3$): δ [ppm]: 2.17 (s, 12H), 2.32 (s, 6H), 6.86 (s, 4H), 7.24 (d, J = 8.7 Hz, 2H), 7.44–7.48 (m, 4H), 7.50–7.54 (m, 3H), 7.86 (d, J = 8.4 Hz, 2H), 8.16 (d, J = 1.8 Hz, 2H). ^{13}C NMR (75 MHz, $CDCl_3$): δ [ppm]: 21.24, 23.48, 111.42, 113.25, 123.24, 124.01, 125.95, 127.16, 127.68, 128.22, 129.47, 133.79, 136.55, 138.67, 139.57, 140.83, 141.05, 141.64, 150.29, 155.18. FABMS (m/z): calcd for $C_{40}H_{34}BBr_2NS$: 729.0872. Found: 729.0887. Anal. calcd for $C_{40}H_{34}BBr_2NS$: C, 65.69; H, 4.69; N, 1.92. Found: C, 65.63; H, 5.08; N, 1.39.

2.3. Synthesis of carbazole/fluorene copolymers

2.3.1. Synthesis of PFCzPhB10

As shown in Scheme 2, the carbazole/fluorene copolymers were prepared via the standard Suzuki polycondensation reaction, as previously reported [49]. A stirred mixture of compound 5 (0.13 g, 0.2 mmol), compound 7 (0.44, 0.8 mmol), compound 8 (0.64 g, 1 mmol), $Pd(PPh_3)_4$ (0.035 g, 3 mol %), an aqueous solution of K_2CO_3 (2 M, 12 mL), and anhydrous toluene (30 mL) was degassed with nitrogen for 1 h. The mixture was heated to 90 °C and stirred under a nitrogen atmosphere for 48 h. After cooling to room temperature, the whole mixture was poured into methanol, and the precipitated polymer was filtered out. The crude product was then dissolved in a small amount of THF and precipitated several times with methanol. The polymer was further purified by a Soxhlet extraction in acetone for 24 h. A pale yellow solid product PFCzPhB10 was obtained in 61% yield (0.49 g). ^{1}H NMR (600 MHz, $CDCl_3$): δ [ppm]: 0.78–0.86 (br, 54H), 0.90–1.35 (br, 216H), 2.06–2.18 (br, 48H), 2.34 (s, 6H), 6.88 (s, 4H), 7.58–7.90 (m, 62H), 8.35–8.52 (br, 2H). Anal. Found (%) for PFCzPhB10 [$(C_{36}H_{32}NB)_{0.1}(C_{29}H_{40})_{0.9}$]: C, 89.55; H, 9.85; N, 0.35. Found: C, 88.99; H, 10.84; N, 0.38.

2.3.2. Synthesis of PFCzPhB30

With the same procedure as that described for the synthesis of copolymer PFCzPhB10, compound 5 (0.39 g, 0.6 mmol), compound 7 (0.22 g, 0.4 mmol) and compound 8 (0.64 g, 1 mmol) were used to prepare copolymer PFCzPhB30. A pale yellow solid was obtained in 63% yield (0.53 g). ^{1}H NMR (600 MHz, $CDCl_3$): δ [ppm]: 0.60–0.86 (br, 14H), 0.90–1.30 (br, 56H), 2.05–2.15 (br, 21H), 2.34 (s, 6H), 6.86 (s, 4H), 7.47–7.98 (br, 22H), 8.35–8.52 (br, 2H). Anal. Found (%) for PFCzPhB30 [$(C_{36}H_{32}NB)_{0.3}(C_{29}H_{40})_{0.7}$]: C, 89.3; H, 9.0; N, 1.0. Found: C, 88.5; H, 9.56; N, 0.12.

2.3.3. Synthesis of PFCzPhB50

With the same procedure as that described for the synthesis of copolymer PFCzPhB10, compound 5 (0.65 g, 1 mmol) and compound 8 (0.64 g, 1 mmol) were used to prepare copolymer PFCzPhB50. The PFCzPhB50 polymer was obtained as a pale yellow solid after drying under vacuum at 60 °C overnight (0.45 g, yield = 51%). ^{1}H NMR (600 MHz, $CDCl_3$): δ [ppm]: 0.74–0.88 (br, 6H), 1.0–1.2 (br, 24H), 1.80–2.10 (br, 16H), 2.31–2.40 (d, 6H), 6.86 (s, 4H), 7.50–8.10 (m, 14H), 8.50–8.62 (br, 2H). Anal. Found (%) for PFCzPhB50 [$C_{65}H_{72}NB$]: C, 88.96; H, 8.2; N, 1.6. Found: C, 88.12; H, 9.52; N, 1.48.

2.3.4. Synthesis of PFCzPhThB10

With the same procedure as that described for the synthesis of copolymer PFCzPhB10, compound 6 (0.15 g, 0.2 mmol), compound 7 (0.44 g, 0.8 mmol) and compound 8 (0.64 g, 1 mmol) were used to prepare copolymer PFCzPhThB10. A pale yellow solid was obtained in 66% yield (0.54 g). ^{1}H NMR (600 MHz, $CDCl_3$): δ [ppm]: 0.77–0.88 (br, 54H), 0.95–1.27 (br, 216H), 2.05–2.18 (br, 48H), 2.38 (s, 6H), 6.83 (s, 4H), 7.31–7.48 (m, 2H), 7.57–7.88 (m, 62H), 8.30–8.60 (d, 2H). Anal. Found (%) for PFCzPhThB10 [$(C_{40}H_{34}NBS)_{0.1}(C_{29}H_{40})_{0.9}$]: C, 88.92; H, 9.70; N, 0.34; S, 0.79. Found: C, 88.17; H, 9.69; N, 0.30; S, 0.74.

2.3.5. Synthesis of PFCzPhThB30

With the same procedure as that described for the synthesis of copolymer PFCzPhB10, compound 6 (0.44 g, 0.6 mmol), compound 7 (0.22 g, 0.4 mmol) and compound 8 (0.64 g, 1 mmol) were used to prepare copolymer PFCzPhThB30. A pale yellow solid was obtained in 65% yield (0.58 g). ^{1}H NMR (600 MHz, $CDCl_3$): δ [ppm]: 0.60–0.92 (br, 14H), 0.95–1.20 (br, 56H), 1.80–2.18 (br, 21H), 2.36 (s, 6H), 6.82 (s, 4H), 7.34–7.50 (m, 2H), 7.55–7.97 (m, 22H), 8.30–8.60 (br, 2H). Anal. Found (%) for PFCzPhThB30 [$(C_{40}H_{34}NBS)_{0.3}(C_{29}H_{40})_{0.7}$]:

C, 87.53; H, 8.63; N, 0.95; S, 0.72. Found: C, 87.45; H, 8.60; N, 0.89; S, 0.68.

2.3.6. Synthesis of PFCzPhThB50

With the same procedure as that described for the synthesis of copolymer PFCzPhB10, compound 6 (0.73 g, 1 mmol) and compound 8 (0.64 g, 1 mmol) were used to prepare copolymer PFCzPhThB50. A pale yellow solid was obtained in 44% yield (0.42 g). ^{1}H NMR (600 MHz, $CDCl_3$): δ [ppm]: 0.60–0.92 (br, 6H), 0.92–1.25 (br, 24H), 1.80–2.10 (br, 16H), 2.25–2.38 (br, 6H), 6.82 (s, 4H), 7.34–7.50 (br, 2H), 7.50–7.98 (m, 14H), 8.30–8.60 (br, 2H). Anal. Found (%) for PFCzPhThB50 [$C_{69}H_{74}NBS$]: C, 86.36; H, 7.72; N, 1.46; S, 0.34. Found: C, 86.31; H, 7.94; N, 1.36; S, 0.32.

2.4. Instruments

^{1}H NMR spectra were recorded on a Bruker AMX-600 MHz spectrometer, and elemental analysis was carried out on an elemental analyzer (Elementar Vario EL III). Mass spectra were carried out on a Finnigan/Thermo Quest MAT mass spectrometer. Gel permeation chromatography (GPC) measurements were performed on a Waters chromatograph (Waters 1515 plus Autosampler) using two Waters Styragel linear columns with polystyrene as a standard and THF as the eluent. Glass transition temperatures (T_gs) were measured by differential scanning calorimetry (TechMax Instruments DSC 6220) in a nitrogen atmosphere at a heating rate of 10 °C/min. Thermogravimetric analysis (TGA) of the polymers was measured under a nitrogen atmosphere at a heating rate of 20 °C/min by using a Thermo-gravimetric analyzer (VersaTherm thermo-gravimetric analyzer). The UV–vis absorption and PL spectra were recorded on a Shimadzu UV-1240 spectrophotometer and an Acton Research Spectra Pro-150 spectrometer, respectively. Cyclic voltammetric (CV) measurements were conducted on a CHI model611D with the use of a three-electrode cell, in which an ITO sheet, a platinum wire and silver/silver nitrate (Ag/Ag^+) were used as the working electrode, counter electrode and reference electrode, respectively. All electrochemical experiments were performed in deoxygenated acetonitrile (CH_3CN) solution with 0.1 M tetrabutylammonium perchlorate (Bu_4NCl_6) as the electrolyte.

2.5. EL device fabrication and electro-optical characterization

The PLED structure in this study was ITO glass/hole-transporting material (HTM)/copolymer/TPBI/LiF/Al. The ITO-coated glass, with a sheet resistance of 8 Ω/sq, was purchased from Applied Film Corp. Glass substrates with patterned ITO electrodes were washed well and cleaned with an O_2 plasma treatment. A thin film (60 nm) of HTM poly(3,4-ethylenedioxythiophene) doped with poly(styrenesulfonate) (PEDOT:PSS, CH8000, Bayer) was formed on the ITO layer of a glass substrate by the spin-casting method and dried at 130 °C for 1 h. Light-emitting layers were then spin-coated (1500 rpm) from the LEP solutions (10 mg/mL) onto the HTM layer and dried at 80 °C for 1 h in a glove box. LEP solutions were prepared with 1,2-dichloroethane (DCE). The hole-blocking and electron-transporting material, TPBI, was evaporated to a thickness of 30 nm in a vacuum chamber. Finally, a thin LiF (1 nm) cathode was thermally deposited onto the light-emitting layer, followed by the deposition of Al (120 nm) metal as the top layer, in a high-vacuum chamber. After the electrode deposition, the PLED was transferred from the evaporation chamber to a glove box purged with high-purity nitrogen gas to keep oxygen and moisture levels below 1 ppm. The device was then encapsulated with glass covers sealed with UV-cured epoxy glue in the glove box. The deposition rate of the cathode was operated with a quartz thickness monitor (FU-12CR). The EL spectra, luminescence, and current-voltage characteristics of the devices were measured on a programmable electrometer with current and voltage sources (Keithley 2400) and a Newport Optics 1835C luminance spectrophotometer.

3. Results and discussion

3.1. Synthesis and Characterization

Scheme 1 illustrates the synthetic routes of the monomer and carbazole/fluorene copolymers. Compound 1 was synthesized from carbazole and 1,4-dibromobenzene through an Ullmann coupling reaction [48] and then further reacted with thiophen-2-ylboronic acid via Suzuki coupling to obtain compound 2. Compound 1 and compound 2 were then further reacted with *n*-BuLi in THF at −78 °C, followed by the addition of dimesitylboron fluoride to give compounds 3 and 4, respectively. Compounds 5 (CzPhB) and 6 (CzPhThB) were obtained through bromination at the 3- and 6-positions of carbazole compounds 3 and 4 with NBS in THF at room temperature, respectively. A series of CzPhB/fluorene and CzPhThB/fluorene copolymers (PFCzPhB and PFCzPhThB) were synthesized via Suzuki coupling reaction of the appropriate diboronates and dibromo compounds in toluene at 90 °C for 48 h in the presence of $Pd(PPh_3)_4$ and 2 M K_2CO_3. The chemical structures of the conjugated polymers were verified by ^{1}H NMR spectroscopy, and the spectra of PFCzPhB50 and PFCzPhThB50 are shown in Fig. 1. The signals in the ranges of 0.79–2.27 ppm were assigned to the dihexyl chains, whereas the peaks at 6.38–8.52 ppm were attributed to the protons of the fluorene and carbazole rings. The absorption peak of proton *i* was observed at 2.2–2.4 ppm, which corresponds to the protons of methyl groups in the dimesitylboryl moiety. The characteristic peak at around 0.6–0.9 ppm was assigned to the protons of the methyl group in dihexyl chains of the fluorene unit. According to the ^{1}H NMR spectrum of PFCzPhB50, the integral values of protons *i* and *a* are about 8.13 and 8.43, respectively. This demonstrates that the molar percentage of the CzPhB unit was about 50% for PFCzPhB50. In the case of PFCzPhThB50, the integration values of peaks *i* and *a* are about 7.82 and 7.53, respectively, meaning the amount of the CzPhThB unit was about 50% for PFCzPhThB50. The molar ratio of the carbazole derivative and 9,9-dioctylfluorene in the copolymers according to ^{1}H NMR are summarized in Table 1. The chemical shifts and relative intensities of the signals are in agreement with the proposed structures for the carbazole/fluorene copolymers. The molar ratio of the carbazole derivative and 9,9-dioctylfluorene in the copolymers according to ^{1}H NMR are summarized in Table 1. The chemical shifts and relative intensities of the signals are in agreement with the proposed structures for the carbazole/fluorene copolymers.

The number- and weight-average molecular weights (M_n and M_w) of the carbazole/fluorene copolymers are summarized in Table 2. The M_n and M_w of copolymers PFCzPhB10-PFCzPhB50 were in the range of 11.7–16.3 and 26.3–38.5 kg/mol, respectively, while the M_n of the poly(9,9-dioctylfluorene) (POF) was 19.2 kg/mol and the M_w for POF was 38.1 kg/mol. For copolymers PFCzPhThB10-PFCzPhThB50, the M_n and M_w were in the range of 8.4–14.6 and 18.2–36.5 kg/mol, respectively. Generally, the thermal stability of conjugated polymers plays an important role in the operating stability of a PLED. Operational lifetime of a PLED is directly related to the thermal stability of the LEP. Therefore, high T_g and T_d are important requisites for application of an LEP in outdoor displays. TGA and DSC thermograms of the copolymers are shown in Fig. 2. The temperatures at which five percent weight loss occurred for the copolymers are summarized in Table 1. The T_ds of PFCzPhB10-PFCzPhB50 were found to be approximately 408–412 °C, while the copolymers PFCzPhThB10-PFCzPhThB50 had a T_ds in the range of 340–425 °C. Thermal stability is affected by the molecular weight

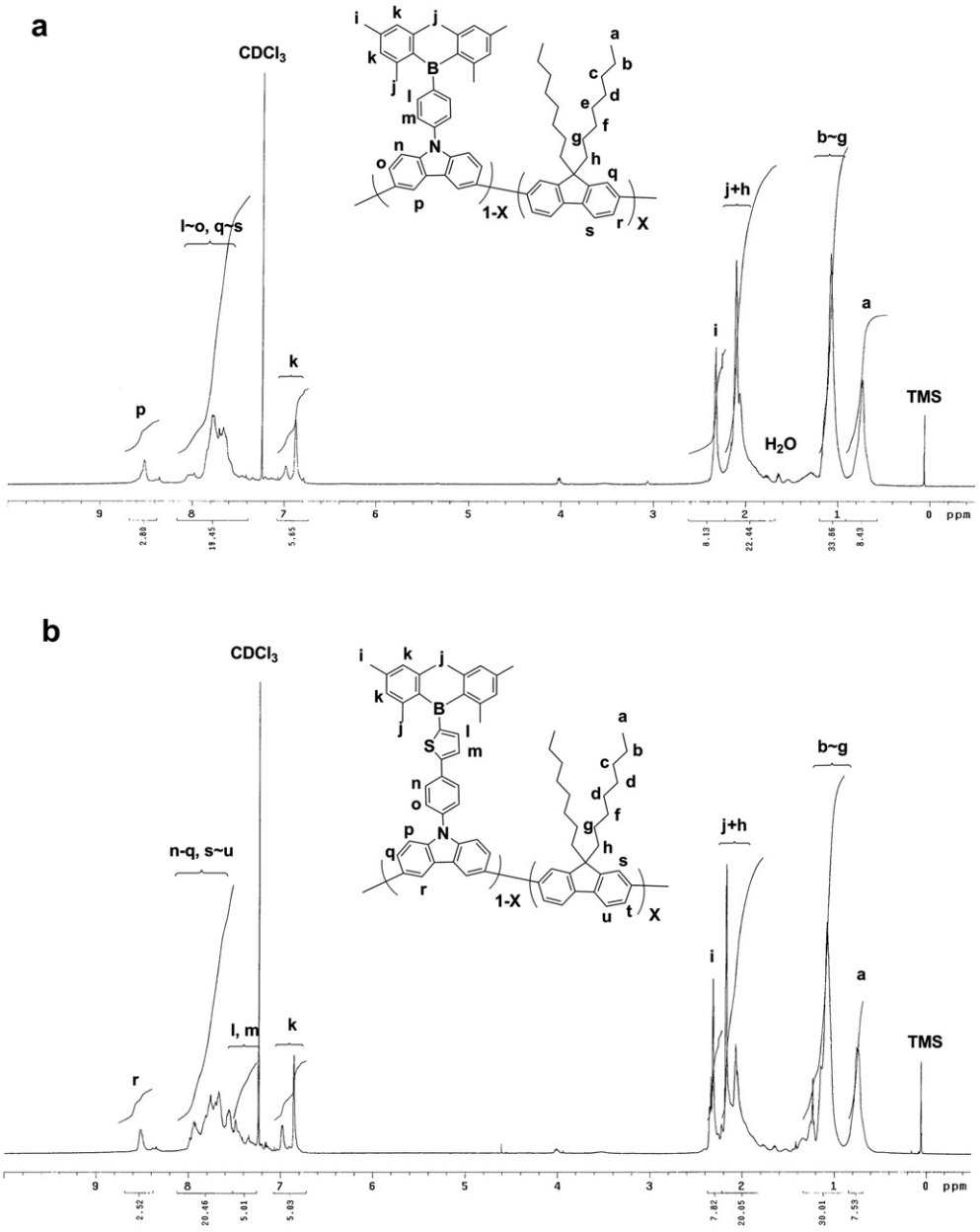

Fig. 1. ^{1}H NMR spectra of (a) PFCzPhB50 and (b) PFCzPhThB50.

and the chemical structure of the conjugated polymer backbone. The conjugated polymers with low molecular weight possess low thermal stability. For example, PFCzPhThB50 has the lowest molecular weight and showed the lowest T_d of all of the polymers. The T_g of the POF was about 100 °C, while the T_gs values of CzPhB/fluorene copolymers were around 83–92 °C. For the CzPhThB/fluorene copolymers, the T_gs values were in the range of 105–117 °C. The results indicated that the CzPhThB/fluorene copolymers showed a slightly higher T_g than the CzPhB/fluorene copolymers. This can presumably be attributed to the more rigid molecular segment of the CzPhThB/fluorene copolymers compared to those of the CzPhB/fluorene copolymers. In addition, the solubilities of the conjugated polymers in organic solvents are summarized in Table 2. The carbazole/fluorene copolymers were completely soluble in most organic solvent at room temperature, including toluene, THF, DCE, chloroform ($CHCl_3$), and chlorobenzene (CB). However, the copolymers were only partially soluble in 1,4-dioxane and dimethylacetamide at room temperature, but completely soluble after a mild heating procedure.

3.2. Photo-physical properties

UV–vis absorption and PL spectra of the carbazole/fluorene copolymers in DCE (1×10^{-5} M) solution and thin films are shown in Fig. 3. The photo-physical properties of the copolymers are itemized in Table 3. All polymers exhibited only a distinct absorption band, which was attributed to the π–π^* electronic transition of the conjugated polymer backbones. In dilute DCE solution, the absorption maximum wavelengths (λ_{max}) of the PFCzPhB10, PFCzPhB30, and PFCzPhB50 were 376, 365 and 344 nm, respectively, while PFCzPhThB10, PFCzPhThB30, and PFCzPhThB50 were located at 378, 366, and 356 nm, respectively. Notably, with an increase of carbazole-π-boron units in the polymer main chain, the absorbance spectra of CzPhB/fluorene and the CzPhThB/fluorene

Table 1
Compositions, molecular weights, and thermal properties of the carbazole/fluorene copolymers.

Copolymers	Cz-π-B unit (%)[a]	Cz-π-B unit (%)[b]	M_n ($\times 10^3$)	M_w ($\times 10^3$)	PDI (M_n/M_w)	T_d (°C)	T_g (°C)
POF	–	–	19.2	38.1	1.98	432	100
PFCzPhB10	10	12	16.3	38.5	2.36	408	92
PFCzPhB30	30	29	12.0	26.3	2.19	412	83
PFCzPhB50	50	50	11.7	29.3	2.51	409	86
PFCzPhThB10	10	11	14.6	36.5	2.49	425	105
PFCzPhThB30	30	31	9.3	21.1	2.28	420	108
PFCzPhThB50	50	50	8.4	18.2	2.16	340	117

[a] Molar ratio of carbazole unit in feed monomer mixture.
[b] Molar ratio of carbazole unit calculated from ^{1}H NMR spectra.

Table 2
Solubility of the carbazole/fluorene copolymers in the organic solvents.

Copolymers	Toluene	THF[a]	DCE[a]	$CHCl_3$[a]	CB[a]	1,4-dioxane	DMAc[a]
POF	++[b]	++	++	++	++	+–[b]	+–
PFCzPhB10	++	++	++	++	++	+–	+–
PFCzPhB30	++	++	++	++	++	++	+–
PFCzPhB50	++	++	++	++	++	++	+–
PFCzPhThB10	++	++	++	++	++	+–	+–
PFCzPhThB30	++	++	++	++	++	++	+–
PFCzPhThB50	++	++	++	++	++	++	+–

[a] Organic solvents: Tetrahydrofuran (THF), 1,2-dichloroethane (DCE), chloroform ($CHCl_3$), chlorobenzene (CB), and dimethylacetamide (DMAc).
[b] The solubility was measured in the concentration of 1 mg/mL; ++: soluble at room temperature; +–: partially soluble at room temperature.

copolymers exhibited a blue-shift, which was also found in previous reports on the analogous fluorene-carbazole copolymers [32]. Such a hypsochromic shift is probably attributable to interruption of the π-conjugation along the polymer backbone caused by the meta-linkage between the fluorene unit and the carbazole-π-boron unit. This would result in the conjugation length of the polymer being shortened [20]. Additionally, the absorption spectra of PFCzPhB10 and PFCzPhThB10 were similar to that of POF due to the minimal content of carbazole-π-boron units in the backbone. However, as the content of the carbazole-π-boron units increased to 50%, the spectral characteristics of PFCzPhB50 ($\lambda_{max} = 344$ nm) and PFCzPhThB50 ($\lambda_{max} = 356$ nm) were assigned to the combined electronic contribution from the carbazole and fluorene segments, which indicated that the electronic configurations of both units in the copolymers were almost mixed. Similar absorption results were previously reported for a 3,6-linked carbazole-fluorene/spirofluorene alternating copolymer [32]. Therefore, the absorption results of the copolymers confirmed that changing the content of the 3,6-linked carbazole units could effectively manipulate the maximal absorption wavelength of the copolymer. In addition, the maximum absorption values of the copolymers in a thin film were red-shifted slightly compared to those of the copolymers in DCE solution. These results were attributed to the interactions and π–π stacking between the polymer chains.

When irradiated with UV light at 350 nm, the PL emission colors of the copolymers in solution and as thin films ranged from blue to green. In dilute DCE solution, the main emission peaks of copolymers PFCzPhB10, PFCzPhB30, and PFCzPhB50 were 417, 470, and 474 nm, respectively. As shown in Fig. 3, the PL spectrum of the PFCzPhB10 showed maximum correspondence to the 0–0 transition at around 420 nm, with a well defined vibronic feature (0–1 transition) at around 436 nm, which is almost identical to that of POF [11]. On the other hand, PFCzPhB30 showed a sky-blue emission peak at 470 nm, with a shoulder emission peak at 418 nm, while PFCzPhB50 demonstrated a featureless vibronic PL spectrum,

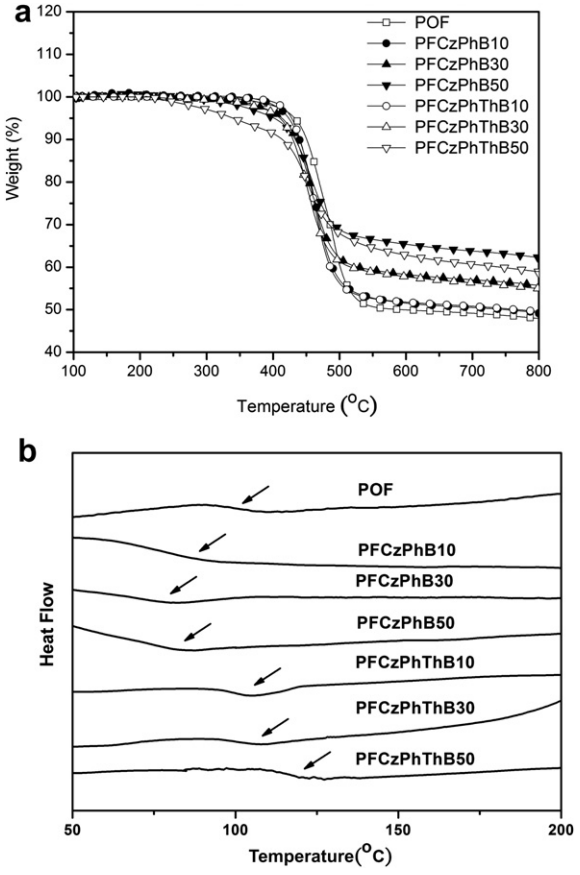

Fig. 2. TGA (a) and DSC (b) thermograms of the copolymers.

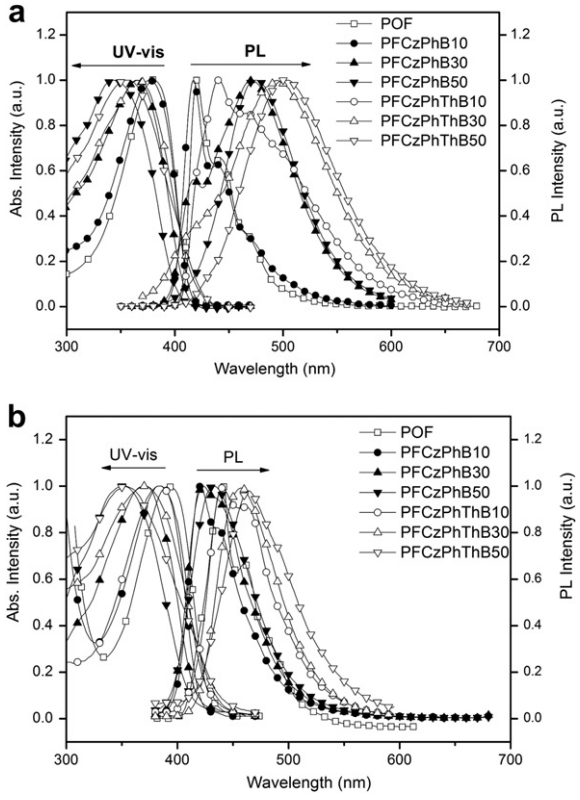

Fig. 3. UV–vis and PL spectra of the carbazole/fluorene copolymers in (a) DCE solution and (b) thin films.

reflecting their different electronic features. Accordingly, upon increasing the content of the CzPhB moiety, the PL spectra of the CzPhB/fluorene copolymers revealed a relatively intensive emission peak at around 470 nm in dilute DCE solutions. This result can be explained as follows: partial ICT from fluorene segments to the carbazole-π-boron units occurred with an increasing content of 3,6-linked carbazole-π-boron units in the polymer main chain [50]. As a result, the relative intensity of the emission peak at 470 nm was strikingly enhanced. Such ICT behavior had been observed in other conjugated polymers with donor–acceptor segments [51]. In DCE solution, the main emission peaks of copolymers PFCzPhThB10, PFCzPhThB30, and PFCzPhThB50 were at 440, 495, and 503 nm, respectively. The PL emission maximum values of the CzPhThB/fluorene copolymers exhibited a large red-shift compared to those of the CzPhB/fluorene copolymers. This PL trend was also observed for the copolymers in the thin film state. Such differences in PL spectra between CzPhB/fluorene and the CzPhThB/fluorene copolymers may be attributed to incorporation of the thiophene moiety at the 9-position of carbazole, which not only enhances the strength of the ICT effect via its high delocalization properties, but also extend the side-chain conjugation length at the 9-position of the carbazole [52]. On the other hand, thin films of CzPhB/fluorene and CzPhThB/fluorene copolymers showed small red-shifts in their PL maxima upon increasing the carbazole-π-boron unit content. This could be due to less π-stacking aggregation in the polymer backbone because of the meta-linkage of the carbazole and/or the non-planar structures of the dimesitylboryl groups. Furthermore, with increasing carbazole-π-boron unit content, PL maxima of the copolymers in DCE solution exhibited a largely red-shifted as compared to those of the copolymers as thin films. This is due to the solvatochromic effect of the copolymers in polar organic solvent [47]. Lambert et al. reported that the PL spectra of N-*p*-(diarylboryl) phenyl-substituted 3,6-linked polycarbazoles show significant solvatochromic shifts in polar organic solvents with respect to the PL spectra of the copolymers as thin films [47]. Therefore, the large red-shift was possibly caused by the dipole–dipole interaction between the polar solvent (DCE) and bipolar side chains of CzPhB/fluorene and CzPhThB/fluorene copolymers.

The PL quantum efficiencies (Φ_{fl}) of the carbazole/fluorene copolymers in DCE are summarized in Table 4. The Φ_{fl} values of these copolymers were measured in dilute DCE solution by comparing their emission with that of a standard solution of 9,10-diphenylanthracene in cyclohexane ($\Phi_{fl} = 0.90$) at room temperature. Accordingly, the Φ_{fl} values of POF, PFCzPhB10, PFCzPhB30, and PFCzPhB50 were 58, 60, 63, and 53%, respectively, while the Φ_{fl} values of PFCzPhThB10, PFCzPhThB30, and PFCzPhThB50 were 72, 69, and 65%, respectively. The CzPhB/fluorene and CzPhThB/fluorene copolymers show higher Φ_{fl} values than the POF. This was attributed to the dual fluorescence arising from a fluorescent delocalized state of the POF backbone and from a fluorescent ICT between the dimesitylboron and carbazole groups. However, the Φ_{fl} values of the copolymers decreased upon increasing the carbazole derivative content (CzPhB or CzPhThB) in the polymer main chain. Increasing the high meta-linkage carbazole moiety content results in interruption of the π-conjugation along the polymer backbone, and thus, the effective conjugation length of the polymer is shortened. Therefore, the Φ_{fl} values of the copolymers decreased slightly with increasing carbazole derivative content

The PL stability of the CzPhB/fluorene and CzPhThB/fluorene copolymers as solid films was further investigated by thermal annealing at 200 °C for 1 h. As shown in Fig. 4, the annealed polymer film exhibited a new broad green emission peak at about 528 nm, which was attributed the formation of low-energy excimer aggregates at high temperature [53,54]. High thermal energy causes the chain conformation to be altered to a higher inter-chain order or packing density. An aggregation or excimer was likely formed among the polymer chains, which led to the occurrence of an inter-chain exciton emission at longer wavelengths. However, a relatively lower intensity of green emission peak was observed for the CzPhB/fluorene and CzPhThB/fluorene copolymers with higher carbazole moiety contents. A greater PL stability was observed for both the CzPhB/fluorene and CzPhThB/fluorene copolymers compared to that of the POF homopolymer. This was attributed to suppression of the polymer chain packing and aggregation due to the presence of kink linkages between the fluorene unit and carbazole-π-boron unit and/or the presence of non-coplanar dimesitylboryl groups as pendants [41,42]. Therefore, better PL stability was obtained for the carbazole/fluorene copolymer with higher carbazole units.

Table 3
Optical properties of the carbazole/fluorene copolymers.

Copolymers	λ_{max}^{UV} (nm)[a]	λ_{max}^{UV} (nm)[b]	λ_{max}^{PL} (nm)[c]	λ_{max}^{PL} (nm)[d]	Φ_{fl} (%)[e]
POF	382	391	420, 442, 470	440, 460, 484	58
PFCzPhB10	376	384	417, 439, 468	420, 436	60
PFCzPhB30	365	372	418, 470	422, 435	63
PFCzPhB50	344	351	474	431	53
PFCzPhThB10	378	384	441, 466, 498	439, 462	72
PFCzPhThB30	366	370	419, 495	456	69
PFCzPhThB50	356	352	501	464	65

[a] Maximal absorption wavelength of the copolymers in DCE.
[b] Maximal absorption wavelength of the copolymers as solid film.
[c] Maximal PL wavelength of the copolymers in DCE.
[d] Maximal PL wavelength of the copolymers as solid film.
[e] PL quantum efficiency (Φ_{fl}) of the copolymers in DCE.

3.3. Electrochemical properties

CV was employed to investigate the electrochemical behavior and to estimate the HOMO and LUMO energy levels of the copolymers. The HOMO levels of the copolymers were calculated from the onset potential of oxidation (E_{onset}^{ox}) by assuming the absolute energy level of ferrocene at −4.8 eV below the vacuum level. The LUMO levels were calculated from the HOMO energy level and the absorption edge [55,56]. The oxidation and reduction behaviors of the copolymers are shown in Fig. 5. The CV curves of all copolymers showed broad spectra with single quasi-reversible oxidation and reduction waves. The electrochemical properties of the copolymers are summarized in Table 4. The E_{onset}^{ox} values were observed at about 1.01, 0.84, and 0.78 V for PFCzPhB10, PFCzPhB30, and PFCzPhB50, respectively. Moreover, the optical band gaps (E_gs) of copolymers PFCzPhB10, PFCzPhB30, and PFCzPhB50, determined from the absorption edge, were 2.89, 2.91, and 2.96 eV, respectively. Therefore, the LUMO levels of PFCzPhB10, PFCzPhB30, and PFCzPhB50 were 2.82, 2.63, and 2.53 eV, respectively, while the HOMO levels were 5.72, 5.55 and 5.49 eV. In addition, the values of E_{onset}^{ox} for PFCzPhThB10, PFCzPhThB30, and PFCzPhThB50 were about 1.04, 0.87 and 0.85 V, respectively. Moreover, E_gs of copolymers PFCzPhThB10, PFCzPhThB30, and PFCzPhThB50 were

Table 4
Electrochemical properties of the carbazole/fluorene copolymers.

Copolymers	E_{ox} (V)[a]	LUMO (eV)	HOMO (eV)	E_g^{opt} (eV)[b]
POF	1.08	−2.96	−5.78	2.82
PFCzPhB10	1.01	−2.82	−5.72	2.89
PFCzPhB30	0.84	−2.63	−5.55	2.91
PFCzPhB50	0.78	−2.53	−5.49	2.96
PFCzPhThB10	1.04	−2.93	−5.75	2.82
PFCzPhThB30	0.87	−2.78	−5.58	2.80
PFCzPhThB50	0.85	−2.19	−5.56	2.77

[a] Onset oxidation potential versus $Ag/AgNO_3$.
[b] Estimated from the UV–vis absorption edge.

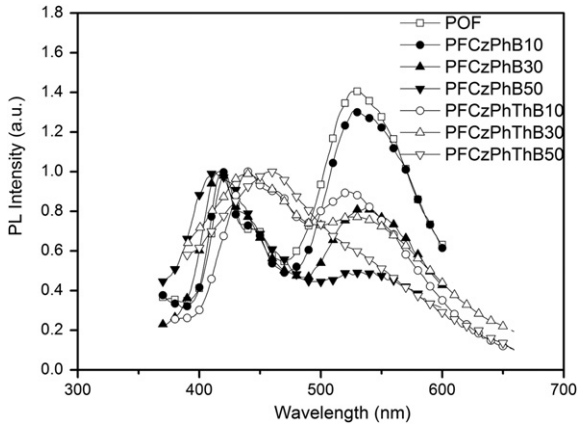

Fig. 4. PL spectra of the carbazole/fluorene copolymers as thin films after being treated at 200 °C for 1 h.

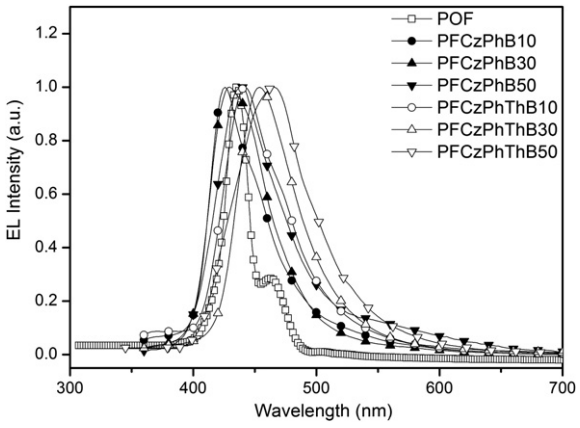

Fig. 6. EL spectra of the carbazole/fluorene copolymer-based devices.

2.89, 2.91, and 2.96 eV, respectively. Hence, the LUMO levels of PFCzPhThB10, PFCzPhThB30, and PFCzPhThB50 were 2.93, 2.78, and 2.79 eV, respectively, while the HOMO levels were 5.75, 5.78, and 5.56 eV. Using the same approach, the LUMO and HOMO levels of POF were about 2.90 and 5.76 eV, respectively. The CV results indicated that the E_{onset}^{ox} values of the copolymers decreased upon increasing the content of the electron-rich carbazole derivative. Moreover, with the same carbazole unit content, higher E_{onset}^{ox} values were observed for the CzPhThB/fluorene copolymers compared to those of the CzPhB/fluorene copolymers. When compared to the phenyl-linked CzPhB moiety, better conjugation of the phenyl/thiophene linkage results in a poor electro-donating capacity of the CzPhThB moiety. Therefore, higher E_{onset}^{ox} values were observed for the CzPhThB/fluorene copolymers. In addition, the E_gs of CzPhB/fluorene copolymers were increased by increasing the CzPhB unit content, while the E_gs of the CzPhThB/fluorene copolymers were decreased upon increasing CzPhThB content. For the CzPhB/fluorene-based copolymers, the meta/kink-linkage between the fluorene unit and carbazole-π-boron units resists π-conjugation along the polymer backbone [20]. Moreover, the presence of the dimesitylboryl group reduced the coplanarity of the carbazole-based pendant and polymer backbone. Therefore, the E_gs of the copolymers were increased with increasing CzPhB unit content. Nevertheless, the coplanarity between the pendant and backbone would increase because of the enhancement of the effective conjugation length and rigidity of the pendants. A decrease of the E_gs of CzPhThB/fluorene copolymers with increasing pendant content was attributed to improved coplanarity between the phenyl/thiophene-linked carbazole moiety and polymer backbone. Apart from that, higher LUMO and HOMO levels were observed for the carbazole/fluorene copolymers compared to the POF homopolymer due to incorporation of the electron-rich unit into the polymer backbone. A higher HOMO level is favorable for hole-injection to the light-emitting layer from an ITO transparent anode [20].

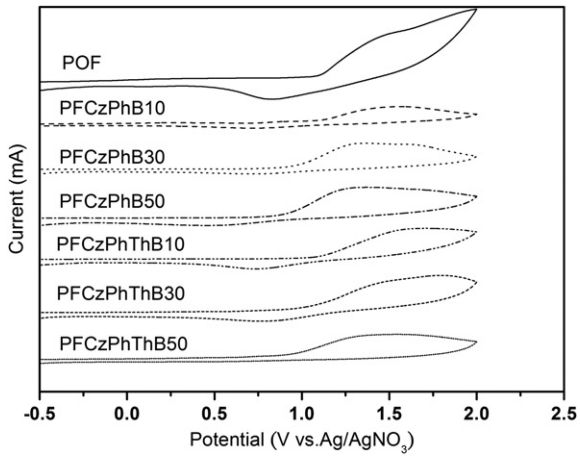

Fig. 5. CV spectra of the carbazole/fluorene copolymers in the thin film state.

3.4. EL properties of carbazole/fluorene copolymers-based devices

For the carbazole/fluorene copolymers, the HOMO levels increased with increasing carbazole-π-boron unit content, and thus facilitated hole-injection into the copolymer-based light-emitting layer from the indium tin oxide anode. However, the LUMO energy levels were also enhanced upon increasing the carbazole-π-boron unit content. A higher LUMO level will result in the poor electron injection to the light-emitting layer from the cathode. Therefore, multilayer devices were fabricated with the configuration of ITO/PEDOT/copolymer/TPBI (30 nm)/LiF(1 nm)/Al (120 nm) in this work. An electron injection/transporting layer of TPBI was inserted into the light-emitting layer and cathode interface for better electron and hole charge balance. The EL spectra of the CzPhB/fluorene and CzPhThB/fluorene copolymer-based devices are shown in Fig. 6. The EL emission maximum wavelength, full width at half-maximum (fwhm) of EL, and CIE coordinates of the carbazole/fluorene copolymer-based devices are summarized in Table 5. The EL spectra showed a main emission peak at around 426–438 and 442–466 nm, respectively, for the CzPhB/fluorene and CzPhThB/fluorene copolymer-based devices, without any shoulder emission of an excimer or exciplex at around 500 nm. Not much difference was observed for the maximal EL emission wavelengths of the PLEDs in comparison with the maximal PL emission wavelengths of

Table 5
Electroluminescence properties of the carbazole/fluorene copolymers-based devices.

Copolymers	λ_{max}^{EL} (nm)	fwhm (nm)	V_{on} (V)[a]	Max luminance (cd/m^2)	Max efficiency (cd/A)	CIE (x, y)[b]
POF	436	22	6.5	130	0.23	(0.17, 0.08)
PFCzPhB10	426	48	6.0	101	0.18	(0.17, 0.09)
PFCzPhB30	430	52	8.0	92	0.26	(0.16, 0.07)
PFCzPhB50	438	60	8.5	94	0.22	(0.18, 0.13)
PFCzPhThB10	442	58	6.5	445	0.51	(0.16, 0.11)
PFCzPhThB30	454	56	5.5	414	0.34	(0.16, 0.13)
PFCzPhThB50	466	70	6.5	288	0.19	(0.21, 0.21)

[a] Turn-on voltage at 1 cd/m^2.
[b] CIE (x, y): Commission Internationale de L'Eclairage coordinates.

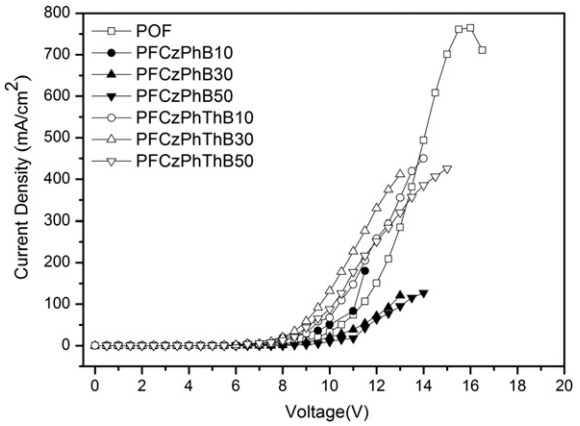

Fig. 7. Current density versus voltage of the carbazole/fluorene copolymer-based devices.

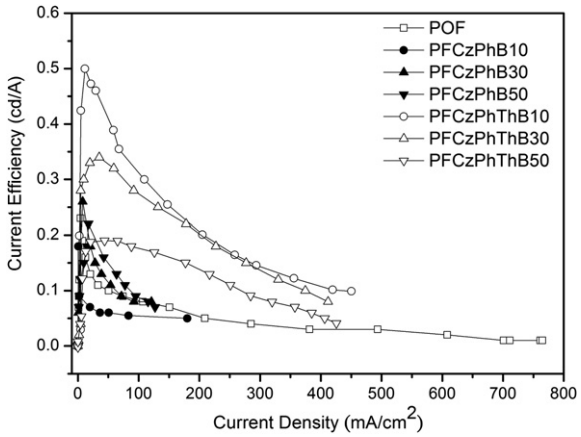

Fig. 9. Current efficiency versus current density of the carbazole/fluorene copolymer-based devices.

the copolymers in the solid state. Nevertheless, the fwhm values of the EL emission peaks were increased upon increasing the carbazole-π-dimesitylborane content in the CzPhB/fluorene and CzPhThB/fluorene copolymer-based devices. This is because partial emission was contributed from the light-emitting side-chain conjugated pendants. The CIE coordinates of the PFCzPhB10-, PFCzPhB30- and PFCzPhB50-based devices were (0.17, 0.09), (0.16, 0.07), and (0.18, 0.13), respectively, while the CIE coordinates of PFCzPhThB10, PFCzPhThB30 and PFCzPhThB50 were (0.16, 0.11), (0.16, 0.13), and (0.21, 0.21), respectively. High color purities of the PLEDs indicated that these carbazole/fluorene copolymers are good candidates for use as blue-emitting layers in PLEDs.

The EL properties of the CzPhB/fluorene and CzPhThB/fluorene copolymer-based devices are shown in Figs. 7–9. The turn-on voltages of the CzPhB/fluorene and CzPhThB/fluorene copolymer-based devices were about 6.0–8.5 V and 5.5–6.5 V, respectively. The maximum brightness of the CzPhB/fluorene and CzPhThB/fluorene copolymer-based devices were about 92–101 cd/m^2 and 288–445 cd/m^2, while the current efficiencies were about 0.18–0.26 cd/A and 0.19–0.51 cd/A, respectively. Moreover, the POF-based device showed a maximum brightness of 130 cd/m^2 and current efficiency of 0.23 cd/A. The EL performances of POF-based device were poorer than those reported in the literature [11,25]. This is attributed to the low molecular weight of POF. Low molecular weight led to the poor thin film quality and low brightness and small current efficiency of the POF-based device [54]. Clearly, the carbazole/fluorene copolymer-based devices showed the better EL performances than the POF-based devices, especially for the CzPhThB/fluorene copolymer-based devices. The better EL performance of the carbazole/fluorene copolymer-based devices was attributed to dual fluorescence arising from the polymer backbone and the carbazole-π-boron unit. The reduction of polymer chain aggregation via incorporation of the carbazole-π-boron unit into the polymer backbone is another reason for the better EL performance of the devices. In addition, higher brightness and larger current efficiency were observed for the CzPhThB/fluorene copolymer-based devices compared to those of the CzPhB/fluorene copolymer-based devices. This is because the phenyl/thiophene-linked CzPhThB unit possesses a longer effective conjugation length than the phenyl-linked CzPhB unit, and thus better EL performances were observed with the CzPhThB/fluorene copolymer-based devices. Apart from that, lower values of brightness and current efficiency were observed for the devices fabricated from the CzPhThB/fluorene copolymers with higher CzPhThB contents. Interruption of the π-conjugation along the polymer backbone via the incorporation of a high meta-linkage carbazole moiety content occurs in these cases, and thus the EL performances of the PLEDs are reduced.

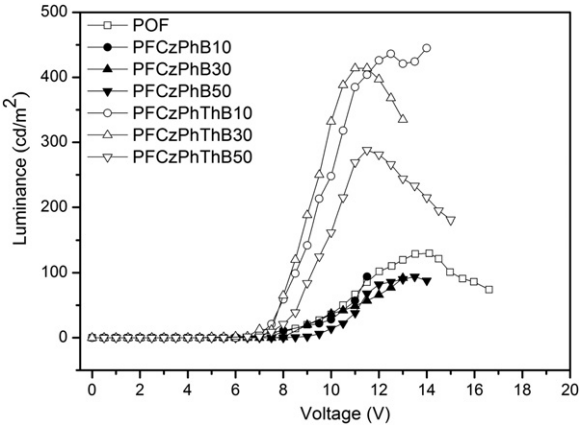

Fig. 8. Luminescence versus voltage of the carbazole/fluorene copolymer-based devices (applied voltage: 11 V).

4. Conclusion

A series of novel carbazole/fluorene copolymers with dimesitylboron pendants were synthesized by Suzuki coupling. Excellent thermal stability was observed for the copolymers due to incorporation of the rigid carbazole-π-boron (CzPhB and CzPhThB) pendants in the fluorene-based backbone. The CzPhB/fluorene and CzPhThB/fluorene copolymers showed a higher PL quantum efficiency than the POF. Moreover, higher brightness and larger current efficiency were observed for the CzPhB/fluorene and CzPhThB/fluorene copolymer-based devices compared to the POF-based devices, which was attributed to the dual fluorescence arising from the polymer backbone and the carbazole-π-boron pendants. The reduction of polymer chain aggregation via incorporation of the rigid pendants into the polymer backbone is another reason for the better EL performance of the carbazole/fluorene copolymer-based devices. In addition, the phenyl/thiophene-linked CzPhThB unit possesses a longer effective conjugation length than the phenyl-linked CzPhB unit, and thus the CzPhThB/fluorene copolymer-based devices had better EL performance than the CzPhB/fluorene copolymer-based devices. It was concluded that the EL properties of the copolymer-based devices were strongly dependant on the effective conjugation length and content of the carbazole-π-boron pendant.

Acknowledgements

Financial support from National Science Council (NSC) and Ministry of Education, Taiwan under ATU plan are gratefully acknowledged.

References

[1] Burroughes JH, Bradley DDC, Brown AR, Marks RN, Mackay K, Friend RH, et al. Nature 1990;347:539–41.
[2] Friend RH, Gymer RW, Holmes AB, Burroughes JH, Marks RN, Taliani C, et al. Nature 1999;397:121–8.
[3] Kobayashi H, Kanbe S, Seki S, Kigchi H, Kimura M, Yudasaka I, et al. Synth Met 2000;111–112:125–8.
[4] Lee RH, Lin KT, Huang CY. J Polym Sci Part B Polym Phys 2007;45:330–41.
[5] Kido J, Hongawa K, Okuyama K, Nagai K. Appl Phys Lett 1994;64:815–7.
[6] McGehee MD, Bergstedt T, Zhang C, Saab AP, O'Regan MB, Bazan GC, et al. Adv Mater 1999;11:1349–54.
[7] Chen FC, Yang Y, Thompson ME, Kido J. Appl Phys Lett 2002;80:2308–10.
[8] Zhang K, Tao Y, Yang C, You H, Zou Y, Qin J, et al. Chem Mater 2008;20:7324–31.
[9] Kido J, Shionoya H, Nagai K. Appl Phys Lett 1995;67:2281–3.
[10] Larmat FJ, Reynolds R, Reinhardt BA, Brott LL, Clarson SJ. J Polym Sci Part A Polym Chem 1997;35:3627–36.
[11] Neher D. Macromol Rapid Commun 2001;22:1365–85.
[12] Gong X, Robinson MR, Ostrowski JC, Moses D, Bazan GC, Heeger AJ. Adv Mater 2002;14:581–5.
[13] Babel A, Jenekhe SA. Macromolecules 2003;36:7759–64.
[14] List EJW, Guentner R, Freitas PS, Scherf U. Adv Mater 2002;14:374–8.
[15] Moses D, Gong X, Iyer PK, Bazan GC, Heeger AJ, Xiao SS. Adv Funct Mater 2003;13:325–30.
[16] Gaal M, List EJW, Scherf U. Macromolecules 2003;36:4236–7.
[17] Klärner G, Davey MH, Chen WD, Scott JC, Miller RD. Adv Mater 1998;10:993–7.
[18] Kulkarni AP, Zhu Y, Jenekhe SA. Macromolecules 2005;38:1553–63.
[19] Wong KT, Chien YY, Chen RT, Wang CF, Lin YT, Chiang HH, et al. J Am Chem Soc 2002;124:11576–7.
[20] Xia C, Advincula RC. Macromolecules 2001;34:5854–9.
[21] Ho MH, Wu YS, Wen SW, Chen TM, Chen CH. Appl Phys Lett 2007;91:083515–7.
[22] Huang B, Li J, Jiang Z, Qin J, Yu G, Liu Y. Macromolecules 2005;38:6915–22.
[23] Vak D, Jo J, Ghim J, Chun C, Lim B, Heeger AJ, Kim DY. Macromolecules 2006;39:6433–9.
[24] Yan JC, Cheng X, Zhou QL, Pei J. Macromolecules 2007;40:832–9.
[25] Graice AW, Bradley DDC, Bernius MT, Inbasekaran M, Wu WW, Woo EP. Appl Phys Lett 1998;73:629–31.
[26] Yan H, Huang QL, Cui J, Veinot JGC, Kern MM, Marks T. Adv Mater 2003;15:835–8.
[27] Pu YJ, Soma M, Kido J, Nishide H. Chem Mater 2001;13:3817–9.
[28] Donat-Bouillud A, Lévesque I, Tao Y, D'Iorio M. Chem Mater 2000;12:1931–6.
[29] Koene BE, Loy DE, Thompson ME. Chem Mater 1998;10:2235–50.
[30] Kundu P, Thomas KRJ, Lin JT, Tao YT, Chien CH. Adv Funct Mater 2003;13:445–52.
[31] Kuo WJ, Lin SL, Chen SD, Chang CP, Lee RH, Jeng RJ. Thin Solid Films 2008;516:4145–52.
[32] Li Y, Ding J, Day M, Tao Y, Lu J, D'iorio M. Chem Mater 2004;16:2165–73.
[33] Thomas KRJ, Lin JT, Tao YT, Ko CW. J Am Chem Soc 2001;123:9404–11.
[34] Lui SP, Chan HSO, Ng SC. J Polym Sci Part A Polym Chem 2004;42:4792–801.
[35] Herguth P, Jiang X, Liu MS, Jen AKY. Macromolecules 2002;35:6094–100.
[36] Tsami A, Yang XH, Galbrecht F, Farrell T, Li H, Adamczyk S, et al. J Polym Sci Part A Polym Chem 2007;45:4773–85.
[37] Lee RH, Hsu HF, Chan LH, Chen CT. Polymer 2006;47:7001–12.
[38] Noda T, Ogawa H, Shirota Y. Adv Mater 1999;11:283–5.
[39] Doi H, Kinoshita M, Okumoto K, Shirota Y. Chem Mater 2003;15:1080–9.
[40] Lin SL, Chan LH, Lee RH, Yen MY, Kuo WJ, Chen CT, et al. Adv Mater 2008;20:3947–52.
[41] Entwistle CD, Marder TB. Angew Chem Int Ed 2002;41:2927–31.
[42] Entwistle CD, Marder TB. Chem Mater 2004;16:4574–85.
[43] Jia WL, Feng XD, Bai DR, Lu ZH, Wang S, Vamvounis G. Chem Mater 2005;17:164–70.
[44] Matsumi N, Naka K, Chujo Y. J Am Chem Soc 1998;120:5112–3.
[45] Zhao CH, Wakamiya A, Inukai Y, Yamaguchi S. J Am Chem Soc 2006;128:15934–5.
[46] Zhao CH, Wakamiya A, Yamaguchi S. Macromolecules 2007;40:3898–900.
[47] Reitzenstein D, Lambert C. Macromolecules 2009;42:773–82.
[48] Liu Y, Nishiura M, Wang Y, Hou ZM. J Am Chem Soc 2006;128:5592–3.
[49] Miyaura N, Suzuki A. Chem Rev 1995;95:2457–83.
[50] Chen RT, Chen SH, Hsieh BY, Chen Y. J Polym Sci Part A Polym Chem 2009;47:2821–34.
[51] Wu WC, Liu CL, Chen WC. Polymer 2006;47:527–38.
[52] Jen AKY, Rao VP, Wong KY, Drost KJ. Chem Commun; 1993:90–3.
[53] Lee RH, Wang YY. J Appl Polym Sci 2008;107:459–3468.
[54] Lee RH, Chen WS, Wang YY. Thin Solid Films 2009;517:5747–56.
[55] Miller LL, Nordblom GD, Mayeda EA. J Org Chem 1972;37:916–8.
[56] Yang CJ, Jenekhe SA. Macromolecules 1995;28:1180–96.

Polymer 52 (2011) 987–995

Contents lists available at ScienceDirect

Polymer

journal homepage: www.elsevier.com/locate/polymer

Poly(acrylic acid)-grafted magnetic nanoparticle for conjugation with folic acid

Metha Rutnakornpituk*, Nipaporn Puangsin, Pawinee Theamdee, Boonjira Rutnakornpituk, Uthai Wichai

Department of Chemistry and Center of Excellence for Innovation in Chemistry, Faculty of Science, Naresuan University, Phitsanulok 65000, Thailand

ARTICLE INFO

Article history:
Received 7 October 2010
Received in revised form
22 December 2010
Accepted 24 December 2010
Available online 9 January 2011

Keywords:
Nanoparticle
poly(acrylic acid)
ATRP

ABSTRACT

Poly(acrylic acid) (poly(AA))-grafted magnetite nanoparticles (MNPs) prepared *via* surface-initiated atom transfer radical polymerization (ATRP) of *t*-butyl acrylate, followed by acid-catalyzed deprotection of *t*–butyl groups, is herein presented. In addition to serve as both steric and electrostatic stabilizers, poly(AA) grafted on MNP surface also served as a platform for conjugating folic acid, a cancer cell targeting agent. Fourier transform infrared spectroscopy (FTIR) was used to monitor the reaction progress in each step of the syntheses. The particle size was 8 nm in diameter without significant aggregation during the preparation process. Photocorrelation spectroscopy (PCS) indicated that, as increasing pH of the dispersions, their hydrodynamic diameter was decreased and negatively charge surface was obtained. According to thermogravimetric analysis (TGA), up to 14 wt% of folic acid (about 400 molecules of folic acid per particle) was bound to the surface-modified MNPs. This novel nanocomplex is hypothetically viable to efficiently graft other affinity molecules on their surfaces and thus might be suitable for use as an efficient drug delivery vehicle particularly for cancer treatment.

1. Introduction

Synthesis of magnetite nanoparticles (MNPs) coated with a thin film of organic polymer has recently attracted much attention due to their potential biomedical applications such as magnetic resonance imaging [1–6], magnetic separation, controlled drug release [7] and hyperthermia treatment of tumor cells [8]. A thin shell of polymeric coating on the particle surface is necessary to prevent nanometer-sized particle aggregation due to their inherent anisotropic dipolar interaction, resulting in losing the specific properties associated with their nanometer dimensions [9,10]. In addition, the polymers on their surface can provide a platform for incorporating biological functional molecules, such as amino acid [11], protein [12,13] and DNA [14–16], for particle labeling with fluorescent molecules [10,17] and for attaching folic acid [18,19], a receptor for tumor cells.

Recently, atom transfer radical polymerization (ATRP) has been reported as a potential "grafting-from" method for surface modification [20,21,27]. ATRP is a living/controlled radical polymerization method, which does not require stringent experimental conditions [22,23]. ATRP enables for the polymerization and block copolymerization of a wide range of functional monomers such as styrene [24–26], methacrylate [27], acrylate [28,29] and methacrylamide [30], yielding polymers with narrowly dispersed molecular weights. Surface modification of nanoparticles *via* ATRP has attracted a great attention in recent years. As compared to a conventional radical polymerization, surface-initiated ATRP from nanoparticles produced polymers with narrow polydispersity index (PDI) and proceeded in a controlled fashion [31]. In addition, the advantage of ATRP technique as compared to other controlled radical polymerization (CRP) techniques is that the polymerization can be initiated at low reaction temperature, while other CRP techniques such as reversible addition-fragmentation chain transfer (RAFT) and nitroxide-mediated polymerizations require relatively high reaction temperature to generate radicals from azo or peroxide initiators. Moreover, functionalization of the particle surface with alkyl halide, the ATRP initiating species, can be easily carried out either by physical absorption of acid-containing halides [36] or covalent bonding of ATRP initiating halides *via* silanization [32]. The "grafting from" strategy *via* ATRP has thus been mostly adopted for MNP surface modification with a variety of polymeric surfactants such as polystyrene [27], poly(methyl methacrylate) [33], poly(ethylene glycol) methacylate [34,35] and poly(acrylamide) [36].

The aim of the current work is to adopt a "grafting from" method to modify MNP surfaces with poly(*t*-butyl acrylate) (poly(*t*-BA)) *via* ATRP, followed by acid-catalyzed deprotection of *t*-butyl groups to obtain poly(AA)-grafted MNP. It is thought that ATRP can offer well-defined water dispersible poly(AA) stabilizers with low molecular weight distribution on the particle surface. The carboxylic acid groups overexpressed on its surface are readily reactive toward molecules containing functional groups such as amine and alcohol. It has thus gained our attention because, not only serving as steric and electrostatic surfactants [37], poly(AA) can also be used as a key intermediate

* Corresponding author. Tel.: +66 5596 3464; fax: +66 5596 1025.
E-mail address: methar@nu.ac.th (M. Rutnakornpituk).

0032-3861/$ – see front matter © 2011 Elsevier Ltd. All rights reserved.
doi:10.1016/j.polymer.2010.12.059

for grafting a large range of functional molecules [38,39]. Folic acid (FA) is of particular interest in this work because it can specifically conjugate with folate receptors overexpressed on cancer cell membranes [40]. Precedents have reported the immobilization of FA on the outermost surface of MNPs coated with other polymeric surfactants [41–44]. Therefore, it is expected that the multifunctional FA-grafted MNPs prepared in this work should bind to cancer cell membranes specifically and consequently improve uptake efficiency of the MNP to the cells. The detail studies on the efficiency on treating cancer cells of this complex are warranted for a future investigation.

In the present work, poly(AA)-coated MNPs were thus prepared *via* surface-initiated ATRP of *t*-BA, followed by acid-catalyzed hydrolysis of *t*-butyl groups. FTIR was used to monitor the reaction progress in each step. Thermogravimetric analysis (TGA) was used to investigate percent of each composition in the polymer-MNP complex. Transmission electron microscopy (TEM) technique was also used to monitor the particle size and the presence of the polymer in the complex. Vibrating sample magnetometry (VSM) was performed to reveal their magnetic properties. In combination with UV–visible spectrophotometry and FTIR, TGA technique was conducted to evidence the existence of FA in the complexes.

2. Experimental section

2.1. Materials

Unless otherwise stated, all reagents were used without further purification: iron (III) acetylacetonate ($Fe(acac)_3$), 99% (Acros), benzyl alcohol (Unilab), 3-aminopropyl triethoxysilane (APS), 99% (Acros), triethylamine (TEA) (Carto Erba), 2-bromoisobutyryl bromide (BIBB), 98% (Acros), copper (I) bromide (CuBr), 98% (Acros), *N,N,N′,N″,N″*-pentamethyldiethylenetriamine (PMDETA), ethyl-α-bromoisobutyrate (Aldrich), 99% (Acros), folic acid, 97% (Fluka), N-hydroxyl succinamide (NHS), 98% (Acros), dicyclohexyl carbodiimide (DCC), 99% (Acros), di-*t*-butyl dicarbonate (Boc_2O), 99% (Aldrich), ethylene diamine (EDA), 99.5% (Fluka), trifluoroacetic acid (TFA), 99.5% (Fluka). *t*-Butyl acrylate (*t*-BA), 99% (Fluka), was distilled under vacuum prior to use.

2.2. Synthesis

2.2.1. Synthesis of oleic acid-coated magnetite nanoparticles (MNPs)

MNPs were prepared *via* thermal decomposition following the method previously described [45]. In a typical procedure, $Fe(acac)_3$ (1.0 g, 2.81 mmol) and benzyl alcohol (20 ml) were mixed by magnetic stirring in a three-neck flask with nitrogen flow. The mixture was heated to 200 °C for 48 h. The precipitant was then removed from the dispersion using an external magnet and washed with ethanol and CH_2Cl_2 repeatedly to remove benzyl alcohol. The particles were then dried at room temperature under reduced pressure. To prepare oleic acid-coated MNPs, the dried MNPs (0.6 g) were introduced into an oleic acid solution in dried toluene (4 ml oleic acid in 30 ml THF) and ultrasonicated for 3 h.

2.2.2. Synthesis of 2-bromo-2-methyl-N-(3-(triethoxysilyl) propanamide (BTPAm))

To a stirred solution of 3-aminopropyl triethoxysilane (APS) (0.18 ml, 0.8 mmol) and triethylamine (TEA) (0.12 ml, 0.8 mmol) in dried toluene (10 ml), 2-bromoisobutyryl bromide (BIBB) (0.1 ml, 0.8 mmol) in dried toluene (10 ml) was added dropwise at 0 °C for 2 h under nitrogen. The reaction mixture was warmed to room temperature and stirred for 24 h. The mixture was passed through a filter paper to remove salts and the filtrate was evaporated to remove the unreacted TEA under reduced pressure. The resulting product, BTPAm, was yellowish thick liquid (78% yield). ^{1}H NMR (400 MHz, $CDCl_3$) δ_H: 0.60 [m, 2H, Si–C<u>H</u>$_2$, 1.20 [t, 9H, O–CH$_2$–C<u>H</u>$_3$], 1.65 [m, 2H, Si–CH$_2$–C<u>H</u>$_2$], 1.95, [s, 6H, C<u>H</u>$_3$–C–Br], 3.25 [m, 2H, C<u>H</u>$_2$–NH], 3.80 [m, 6H, CH$_3$–C<u>H</u>$_2$–O]. FT-IR (KBr disc) υ_{max}: 3345 cm^{-1} (NH stretching), 2975–2889 cm^{-1} (C–H stretching), 1738 cm^{-1} (C=O of acid bromide stretching), 1658 cm^{-1} (C=O of amide stretching), 1532 cm^{-1} (NH bending), 1442 cm^{-1} (C–N stretching), 1286 cm^{-1} (C–Br stretching), 1112–1026 (Si–O stretching).

2.2.3. Immobilization of 2-bromo-2-methyl-N-(3-(triethoxysilyl) propanamide (BTPAm)) onto MNP surface (BTPAm-coated MNPs) (Fig. 1)

To immobilize BTPAm on the oleic acid-coated MNP surface, the MNP-toluene dispersion (0.1 g of oleic acid-coated MNPs in 5 ml toluene) (30 ml), BTPAm (0.90 ml) and 2 M TEA in toluene (6 ml) were added into a round bottom flask. The mixture was stirred for 24 h at room temperature under nitrogen. The particles were subsequently precipitated in methanol, following by magnet separation to obtain the BTPAm-modified MNPs. Then, the MNPs were re-dispersed in toluene and re-precipitated in methanol. This procedure was repeated several times to completely remove unreacted BTPAm. The particles were finally dried *in vacuo*.

2.2.4. Synthesis of poly(t-butyl acrylate)-coated MNPs (poly(t-BA)-coated MNPs) via ATRP reaction

To a schlenk tube containing dioxane (1 ml), CuBr (0.3 g, 0.0021 mol), and PMDETA (0.42 ml, 0.0021 mol) were added under nitrogen blanket. The mixture was stirred until homogenous blue color was observed. Then, *t*-butyl acrylate (*t*-BA) (3 ml, 0.021 mol) monomer and BTPAm-immobilized MNPs (0.3 g) were added *via* a syringe. The mixture was degassed and nitrogen-purged by three freeze-thaw cycles. The solution was then heated to 90 °C for 24 h to commence ATRP reaction. At a given time, the reactions were ceased and poly(*t*-BA)-grafted MNPs were magnetically separated and washed thoroughly with methanol and dried *in vacuo*.

2.2.5. Synthesis of poly(acrylic acid)-coated MNPs (poly(AA)-coated MNPs) via hydrolysis of poly(t-butyl acrylate)-coated MNPs

Poly(*t*-BA)-coated MNPs were hydrolyzed to obtain acrylic acid functional groups on MNP surfaces. Briefly, poly(*t*-BA)-coated MNPs (0.05 g) were hydrolyzed in a 20-ml TFA solution (0.1 M of TFA in THF) at room temperature for 24 h. The solution was concentrated under reduced pressure, diluted with CH_2Cl_2, and repeatedly precipitated in cold hexane. The precipitate was separated by a permanent magnet and dried *in vacuo*. The possible reactions between TFA and polymers coated on MNP surface are illustrated in supplementary data.

2.2.6. Synthesis of N-(2-aminoethyl) folic acid (EDA-FA) (Fig. 2)

2.2.6.1. Protection of an amino group of ethylene diamine (EDA) with t-butyl carbamate (Boc). A solution of di-*t*-butyl dicarbonate (Boc_2O) (0.23 ml, 1 mmol) in anhydrous CH_2Cl_2 (10 ml) was added dropwise to a cold solution of ethylene diamine (EDA) (0.67 ml, 10 mmol) in anhydrous CH_2Cl_2 (10 ml) at 0 °C under nitrogen atmosphere. The mixture was magnetically stirred at 0 °C for 2 h and at room temperature for 24 h. Then, distilled water (5 ml) was added into the mixture to dissolve the precipitate. The organic layer was washed with brine (15 ml) 5 times, dried over anhydrous Na_2SO_4, and then concentrated under reduced pressure to give *t*-butyl *N*-(2-aminoethyl) carbamate (EDA-Boc), appearing as thick oil (82% yield). ^{1}H NMR (400 MHz, $CDCl_3$) δ_H: 1.40 [s, 9H, C<u>H</u>$_3$ Boc], 2.80 [m, 2H, C<u>H</u>$_2$–NH$_2$], 3.20[m, 2H, CH$_2$–C<u>H</u>$_2$–NH-Boc]. FTIR (KBr disc) υ_{max}: 3360 cm^{-1} (NH stretching), 2955–2923 cm^{-1} (C–H stretching), 1693 cm^{-1} (C=O of amide stretching), 1525 cm^{-1} (NH bending), 1366-1277 cm^{-1} (C–N bending), 1172 cm^{-1} (C–O stretching).

2.2.6.2. Coupling folic acid with the amino-protected EDA. To a stirred solution of FA (0.275 g, 6.25 10^{-4} mol) in anhydrous DMSO (5 ml) and pyridine (4 ml), the solution of EDA-Boc (0.10 g, 6.25 10^{-4} mol) and DCC (0.21 g, 7.5 10^{-4} mol) in anhydrous DMSO (5 ml) were added. The mixture was stirred at room temperature for 18 h under nitrogen blanket. After the reaction completed, the mixture was gradually poured into a vigorously stirred diethyl ether (20 ml) at 0 °C. The yellow precipitate was collected and washed with cold diethyl ether several times and dried under high vacuum to obtain {*t*-butyl N-(2-aminoethyl) carbamate} folic acid (Boc-EDA-FA), appearing as a yellow solid (85% yield). ^{1}H NMR (400 MHz, DMSO-d_6) δ_H: 1.40 [s, 9H, C$\underline{H}_3$ Boc], 2.0 [m, 2H, C$\underline{H}_2$–CH$_2$–CO–NH], 2.40 [m, 2H, C$\underline{H}_2$–CO–NH], 2.90 [m, 2H, C$\underline{H}_2$–NH–CO], 3.10 [m, 2H, C$\underline{H}_2$–NH–Boc], 4.30 [m, 1H, HOOC–C$\underline{H}$–NH], 4.50 [d, 2H, phenyl-NH-C$\underline{H}_2$ folic acid], 6.60 [d, J = 8 Hz, 2H, 2CH=C$\underline{H}$ phenyl folic acid], 6.90 [t, 1H, phenyl-N$\underline{H}$-CH$_2$], 7.60 [d, J = 8 Hz, 2H, 2C$\underline{H}$=CH phenyl folic acid], 8.60 [s, 1$\underline{H}$, N=C$\underline{H}$ Ar folic acid]. FTIR (KBr disc) υ_{max}: 3360–2600 cm^{-1} (OH and $\underline{N}$H stretching), 1700 cm^{-1} (C=O of amide stretching), 1605 cm^{-1} (C–O of acid stretching), 1168 cm^{-1} (C–O stretching).

TFA (2 ml) was then added to Boc-EDA-FA and stirred at room temperature. After 2 h stirring, TFA was removed under reduced pressure and the resulting residue was dissolved in anhydrous DMF. Pyridine was added until a formation of yellow precipitate and it was subsequently washed with diethyl ether and dried to give *N*-(2-aminoethyl) folic acid (EDA-FA) (80% yield, T_m 290 °C). ^{1}H NMR (400 MHz, DMSO-d_6) δ_H: 2.0 [m, 2H, C$\underline{H}_2$–CH$_2$–CO–NH], 2.40 [m, 2H, C$\underline{H}_2$–CO–NH], 2.60 [m, 2H, C$\underline{H}_2$–NH–CO], 3.30 [m, 2H, C$\underline{H}_2$–N$\underline{H}_2$], 4.20 [m, 1H, HOOC-C$\underline{H}$-NH], 4.40 [d, 2H, phenyl-NH-C$\underline{H}_2$ folic acid], 6.60 [d, J = 8 Hz, 2H, 2CH=C$\underline{H}$ phenyl folic acid], 6.90 [t, 1H, Phenyl-N$\underline{H}$-CH$_2$], 7.70 [d, J = 8 Hz, 2H, 2C$\underline{H}$=CH phenyl folic acid], 8.60 [s, 1H, N=C$\underline{H}$ Ar folic acid]. FTIR (KBr disc) υ_{max}: 3600–2800 cm^{-1} (OH and $\underline{N}$H stretching), 1684 cm^{-1} (C=O of amide stretching), 1605 cm^{-1} (C–O of acid stretching), 1532–1335 cm^{-1} (C–N bending), 1202–1132 cm^{-1} (C–O stretching).

2.2.7. Immobilization of folic acid on the surfaces of poly(AA)-coated MNPs

Poly(AA)-coated MNPs were dispersed in a 10 ml aqueous solution containing NHS (40 mg) and EDC·HCl (20 mg) and the mixture was kept in a dark place for 2 h. The particles were recovered, washed with water and dried *in vacuo*. Then, the particles were added in a solution of 200 mg of EDA-FA and 50 mg of EDC in 10 ml anhydrous DMSO. The suspension was agitated overnight at 37 °C in dark. The particles were then recovered, washed with DMSO and methanol several times and dried *in vacuo*.

2.3. Characterization

FTIR was performed on a Perkin–Elmer Model 1600 Series FTIR Spectrophotometer. The solid samples were mixed with KBr to form pellets. Nuclear magnetic resonance spectroscopy (NMR) was performed on a 400 MHz Bruker NMR spectrometer using $CDCl_3$ as a solvent. Gel permeation chromatography (GPC) data was conducted on PLgel 10 μm mixed B2 columns and a refractive index detector. Tetrahydrofuran (THF) was used as a solvent with a flow rate of 1 ml/min at 30 °C. TEM were performed using a Philips Tecnai 12 operated at 120 kV equipped with Gatan model 782 CCD camera. TGA was performed on SDTA 851 Mettler-Toledo at the temperature ranging between 25 and 600 °C at a heating rate of 20 °C/min under oxygen atmosphere. VSM was performed at room temperature using a Standard 7403 Series, Lakeshore vibrating sample magnetometer. The magnetic moment was investigated over a range of applied magnetic fields from −10,000 to +10,000 G using 30 min sweep time. Hydrodynamic diameter of the particles was measured *via* PCS using NanoZS4700 nanoseries Malvern

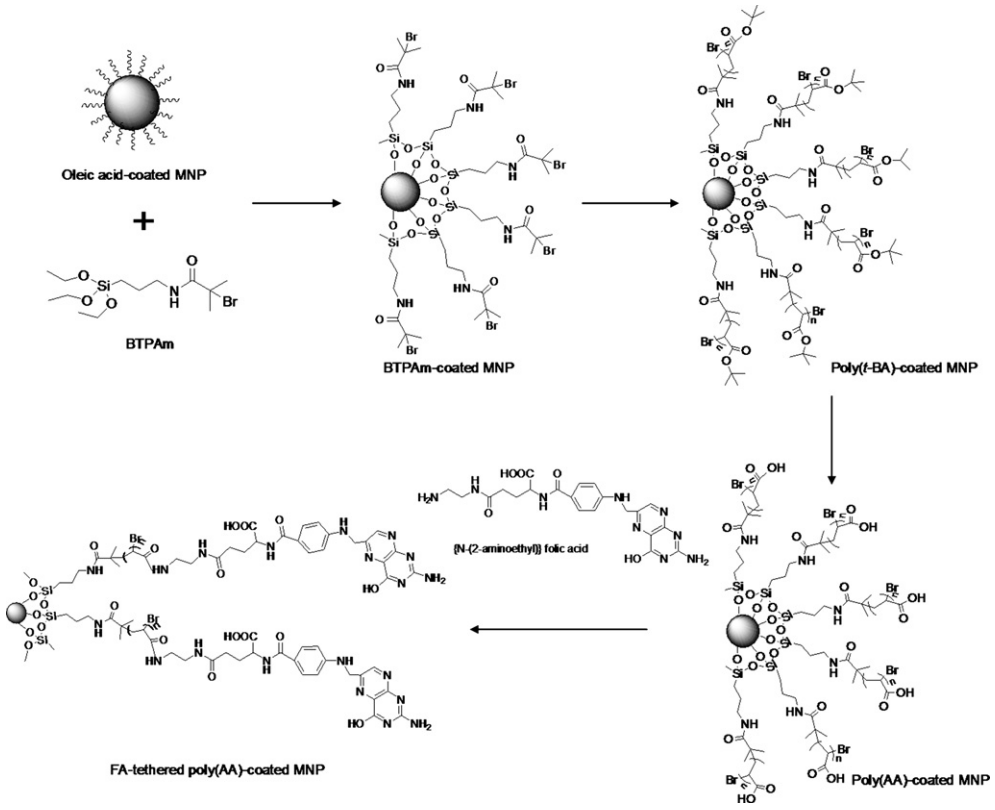

Fig. 1. Synthesis of poly(AA)-coated MNPs *via* ATRP reaction and immobilization of folic acid.

instrument. The sample dispersions were sonicated for 10 min before the measurement at 25 °C. The presence of FA was investigated using SPECORD S100 UV–Visible spectrophotometer (Analytikjena AG) coupled with a photo diode array detector at $\lambda_{max} = 371$ nm.

3. Results and discussion

The aim of this work is to modify MNP surfaces with poly(AA) and immobilize folic acid on their surfaces. Poly(AA) grafted on the particle surfaces is thought to provide steric and electrostatic stabilizations and dispersibility of the particles in aqueous media. Another major advantage of this system was that the carboxylic acid-enriched surfaces of poly(AA)-grafted MNPs provided a platform for efficient surface immobilization of any functional molecules such as DNA, drugs, protein and fluorescent molecules. Hence, the novelty of this current work is that this is the first report on synthesizing multifunctional poly(AA)-coated MNPs for attaching folic acid (FA), a model molecule in this work. Precedents have reported the immobilization of biomolecules on the distal ends of MNPs coated with other polymeric surfactant [41–44]. This novel system is hypothesized to increase the loading efficiency of FA on the MNP surfaces.

To perform surface-initiated ATRP from MNPs, BTPAm, a molecule containing an ATRP initiating site was first synthesized through amidization between APS and BIBB, followed by silanization of triethoxysilane of BTPAm on MNP surface. The results of the synthesis of BTPAm including FTIR and ^{1}H NMR are illustrated in supplementary data. To immobilize BTPAm on MNP surfaces, bare MNPs were first coated with oleic acid to form well dispersed MNPs in toluene. The advantage of this procedure was that the MNPs were well dispersible in the media before reacting with BTPAm, allowing BTPAm to effectively silanize to their surfaces due to its greater surface approaching ability in the dispersed MNPs.

Fig. 3 displays FTIR spectra of poly(*t*-BA)-coated MNPs withdrawn from the dispersions at 1, 6, 12 and 24 h of ATRP reaction. Because ATRP is known as a controlled radical polymerization, the time period for the ATRP reaction is thus crucial for tuning the molecular weight of the polymers. A progressive growth of ester linkage signals (–O(C=O)- stretching, ~1724 cm^{-1} and C–O stretching, ~1147 cm^{-1}) of *t*-BA repeating units in relative to those of a Si–O signal of the linker (~1100–1020 cm^{-1} and ~800 cm^{-1}) indicated that the molecular weights of poly(*t*-BA) on MNP surfaces increased as increasing ATRP reaction time. It should be noted that the signal corresponding to Fe-O bonds from MNP core (~589 cm^{-1}) were observed throughout the reactions without significant change in its intensity.

Weight loss from TGA technique of poly(*t*-BA)-coated MNPs at various ATRP reaction times was investigated to determine the relative amount of poly(*t*-BA) that can be grafted on the particle surface. It should be noted that the particles were separated from the uncoordinated species using an external magnet. Using an assumption that % char yield was the weight of magnetite remaining at 600 °C, the weight loss of the surface-modified MNPs was thus attributed to the decomposition of organic components including BTPAm and poly(*t*-BA) that complexed to the particle surface. Hence, percent char yield of bare MNP and MNP coated with BTPAm were determined to obtain percent of BTPAm in the complexes in each sample. According to TGA results, percent of BTPAm in the complexes was about 2 wt%, while percents of poly(*t*-BA) were 3 wt%, 15 wt%, 26 wt% and 43 wt% of the complexes at 1, 6, 12 and 24 h ATRP reaction times, respectively (Fig. 4). This was a supportive result to FTIR that poly(*t*-BA) chain length was prolonged when ATRP reaction time was extended.

To investigate the molecular weight and the molecular weight distribution of poly(*t*-BA), small amount of ethyl bromoisobutylate (EBiB) was added in the dispersion as a "sacrificial initiator" to form free poly(*t*-BA) along with poly(*t*-BA) grafted on MNP. After 24 h of

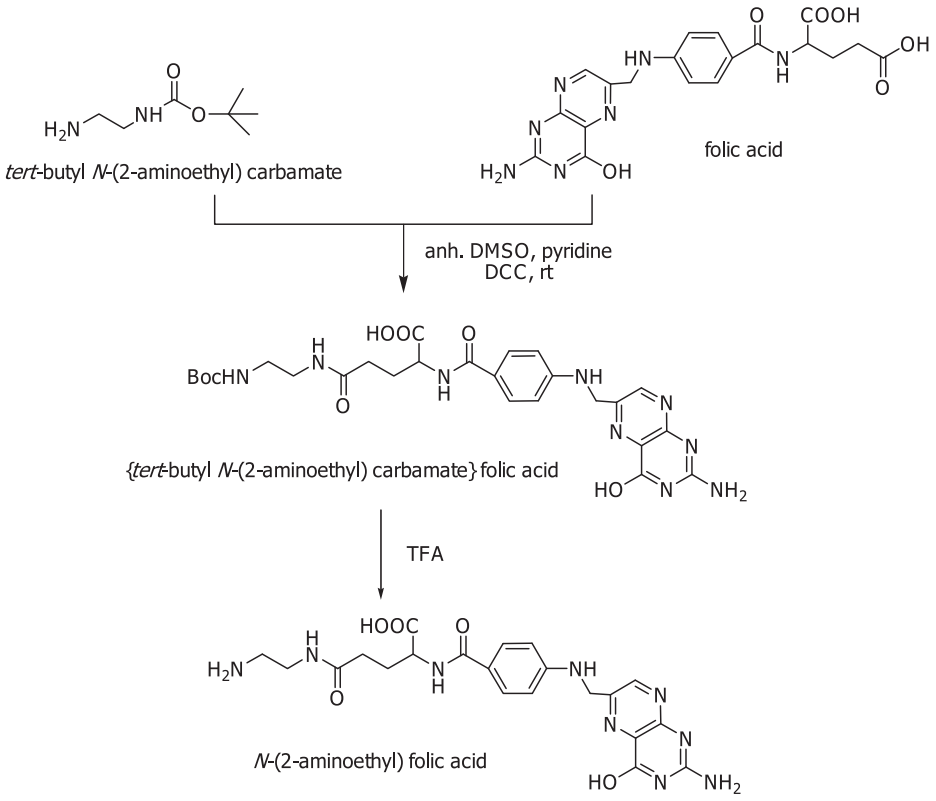

Fig. 2. Synthesis of *N*-(2-aminoethyl) folic acid (EDA-FA).

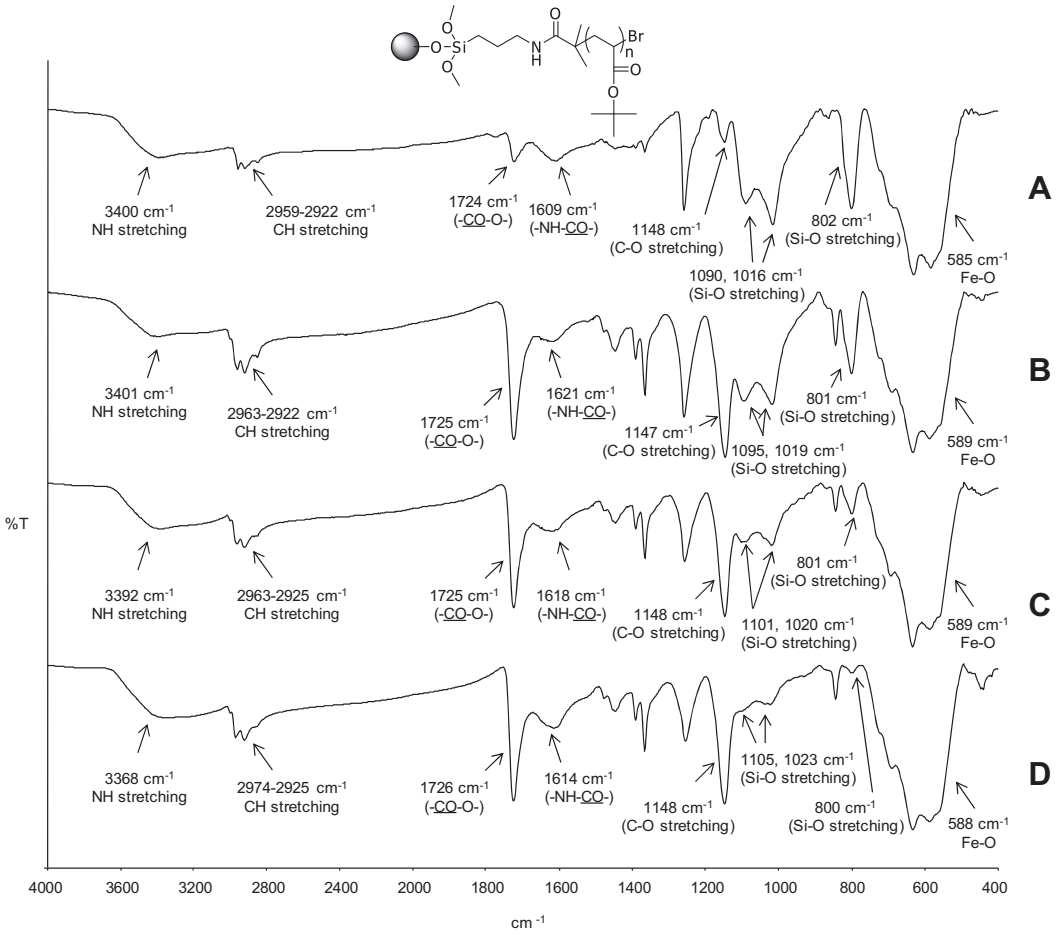

Fig. 3. FTIR spectra of poly(*t*-BA)-coated MNP at various ATRP reaction times, A) 1 h, B) 6 h, C) 12 h and D) 24 h.

the reaction, the free poly(*t*-BA) was removed from the MNP complex using an external magnet. According to GPC results, molecular weight of poly(*t*-BA) was about 18,600 g/mol and its molecular weight distribution was about 1.22. This narrow molecular weight distribution indicated the living mechanism of controlled radical polymerization. ^{1}H NMR spectrum of free poly(*t*-BA) is shown in supplementary data.

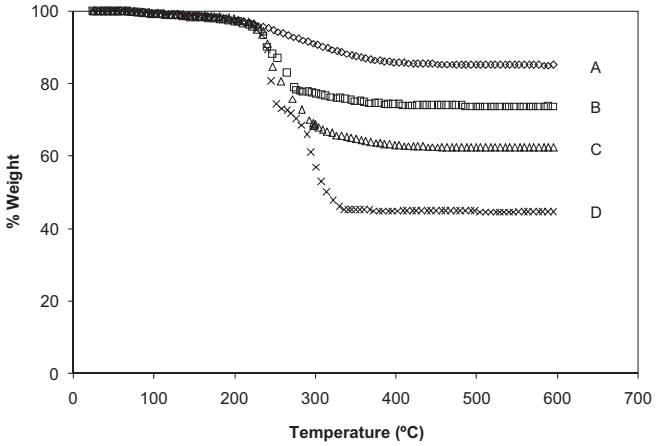

Fig. 4. TGA thermograms of poly(*t*-BA)-coated MNPs at various ATRP reaction times, A) 1 h, B) 6 h, C) 12 h and D) 24 h.

TEM images of MNP complexes at each step of the reaction are illustrated in Fig. 5. Bare MNPs observed in Fig. 5A were well organized because they were somewhat uniformed in size, which was in the range of 6–10 nm in diameter with the average of about 8 nm. Surface modification of the MNPs resulted in a slightly broader size distribution due to the presence of organic compounds coated on their surface (Fig. 5B–D). However, the average particle size was not significant difference from those of bare MNPs. It should be noted that poly(*t*-BA)-coated MNPs were well dispersed in toluene due to the existence of hydrophobic poly(*t*-BA) on their surface (Fig. 5C), while poly(AA)-coated MNPs were well dispersed in water because of the presence of hydrophilic and charge surfactants of poly(AA) (Fig. 5D).

The *M-H* curves of bare MNP, BTPAm-coated MNP, poly(*t*-BA)-coated MNPs and poly(AA)-coated MNP were illustrated in Fig. 6. They showed superparamagnetic behavior at room temperature as indicated by the absence of reminance and coercivity upon removing an external applied magnetic field. According to the results in Table 1, the decrease of saturation magnetization (M_s) from 59 emu/g of bare MNPs to 27 emu/g of poly(*t*-BA)-coated MNPs was attributed to the presence of the organic surfactant on their surface, resulting in the decrease of percent of magnetite in the complexes. After the hydrolysis of poly(*t*-BA) to form poly(AA)-coated MNP, its M_s value increased from 27 to 39 emu/g sample due to the removal of *t*-BA groups in poly(*t*-BA), which subsequently increased percent of magnetite in the complexes. Interestingly, when taking percent of magnetite in the complex into account, the M_s values in emu/g magnetite basis of these complexes were not

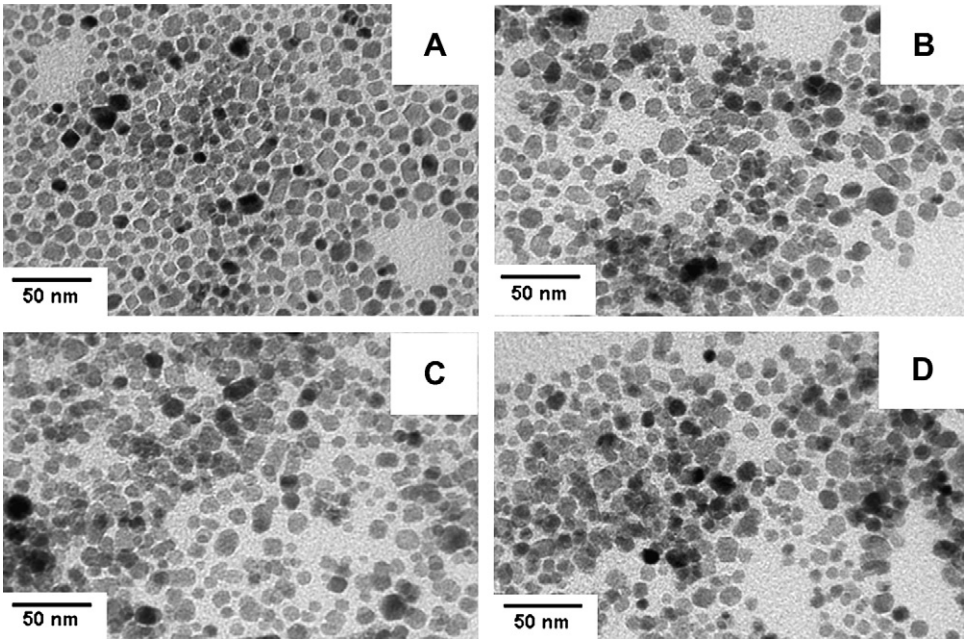

Fig. 5. TEM images of A) bare MNPs, B) BTPAm-coated MNPs, C) poly(*t*-BA)-coated MNPs, D) poly(AA)-coated MNPs. In the TEM sample preparation, MNPs in Figure A–C were dispersed in toluene and those in Figure D were dispersed in water.

significantly different from each other, indicating that magnetic properties of the particles were not considerably affected upon ATRP of poly(*t*-BA) and hydrolysis to form poly(AA)-coated MNPs.

After the hydrolysis reaction, it was conceived that MNPs having carboxylic acid-enriched surfaces were obtained. These carboxylic acid functional groups are readily reactive toward coupling reactions with other molecules having affinity functional groups such as amine and alcohol. In the current work, folic acid (FA) was chemically immobilized on the surface-modified MNPs. FA has two carboxylic acid groups at the α and γ positions, which can covalently react with amino functional groups of EDA. However, it has already been verified that γ-COOH is more accessible to covalently react with amino groups due to its high reactivity [46,47]. FA needs to be first activated with ethylene diamine (EDA) to obtain primary amine-terminated FA (*N*-(2-aminoethyl) folic acid or EDA-FA). This logical strategy enhanced the reactivity of FA to efficiently react with carboxylic acid overexpressed on the surface of poly(AA)-coated MNPs through amidization reaction. Results of the synthesis of EDA-FA including FTIR and ^{1}H NMR spectra were detailed in supplementary data.

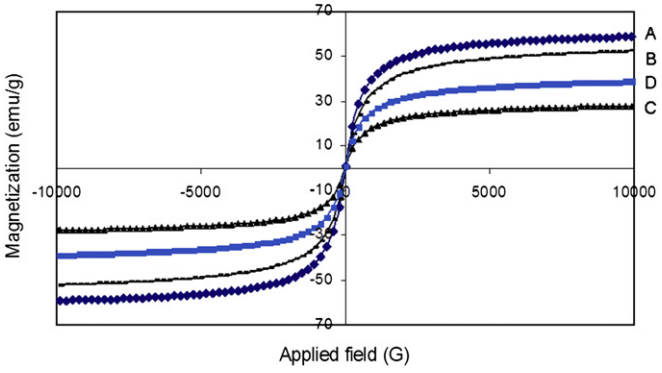

Fig. 6. *M-H* curves of A) bare MNP, B) BTPAm-coated MNP, C) poly(*t*-BA)-coated MNP and D) poly(AA)-coated MNP.

In the grafting reaction between poly(AA)-coated MNPs and EDA-FA, *N*-hydroxyl succinimide (NHS) was used to activate the dangling carboxylic acid groups. FTIR spectra of the products in each step were thus illustrated in comparison with the starting compounds (Fig. 7). Fig. 7A showed the FTIR spectrum of poly(AA)-coated MNPs and those of NHS was depicted in Fig. 7B. In Fig. 7C, the sharp and strong characteristic signal of ester linkages appeared at 1723 cm^{-1}, indicating the coupling reaction between carboxylic acid of poly(AA)-coated MNPs and NHS. In addition, Fe-O linkages of magnetite core were also observed at 586 cm^{-1}. After the coupling reaction with EDA-FA (Fig. 7D), the characteristic signals of FA, such as 1700–1500 cm^{-1} and 1153–1069 cm^{-1}, appeared in the FA-bound MNPs (Fig. 7E), indicating the successful conjugation of FA on the MNP surfaces.

UV–visible spectrophotometry was also applied to confirm the presence of FA in the conjugated MNP complex. FA showed a λ_{max} value at 371 nm (Fig. 8A), whilst those of FA-conjugated MNPs also exhibited a weak absorbance signal at the same wavelength (Fig. 8B). It is worth to mention that poly(AA)-coated MNPs before FA loading did not show any absorbance signal at the same wavelength (Fig. 8C). This result implied that FA was, to some extent, covalently conjugated to the MNP surfaces.

To determine percentage of magnetite core and organic shell in the complexes in each step of the reactions, the complexes were characterized *via* TGA to investigate their mass loss. Bare MNPs manifested a drastic weight loss between 200 and 350 °C with 90%

Table 1
Percentage of magnetite in the complex and their magnetic properties.

Sample	emu/g sample[a]	% Fe_3O_4[b]	emu/g Fe_3O_4
Bare MNP	59	90	65
BTPAm-coated MNP	53	88	60
Poly(*t*-BA)-coated MNP	27	45	61
Poly(AA)-coated MNP	39	63	62

[a] Estimated from the saturation magnetization (M_s) at 10,000 G from VSM technique.
[b] Estimated from % char yield at 600 °C from TGA technique.

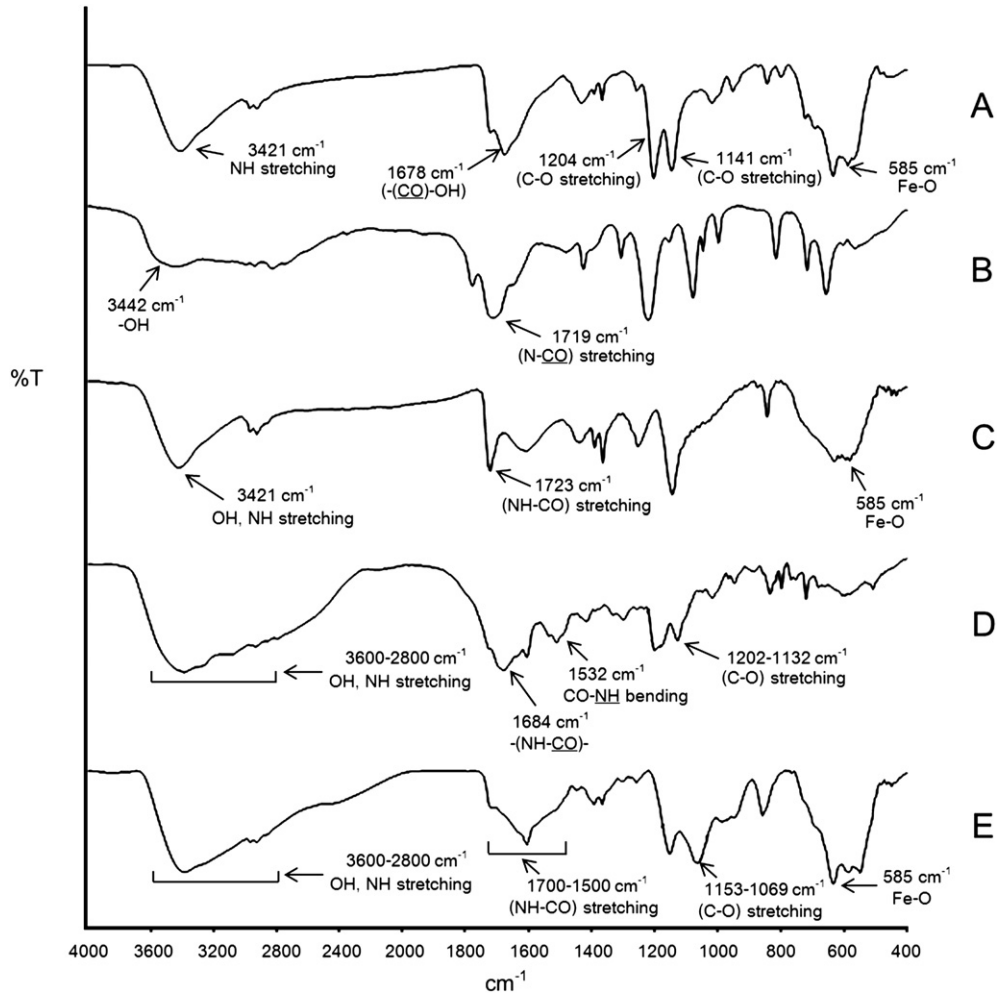

Fig. 7. FTIR spectra of (A) poly(AA)-coated MNP, (B) NHS, (C) NHS-poly(AA)-coated MNP, (D) EDA-FA and (E) FA-poly(AA)-coated MNP.

char yield (Fig. 9A). This was attributable to the decomposition or desorption of the absorbed ammonium salt at elevated temperature and eventually loss some weight [48,49]. The weight loss of MNPs coated with BTPAm, poly(*t*-BA) and poly(AA) were attributed to the decomposition of organic components complexing to the particle surface and % char yields were the weight of magnetite core. From TGA thermograms in Fig. 9B,C, there was about 2 wt% of BTPAm and 49 wt% of poly(*t*-BA) in poly(*t*-BA)-coated MNPs. The

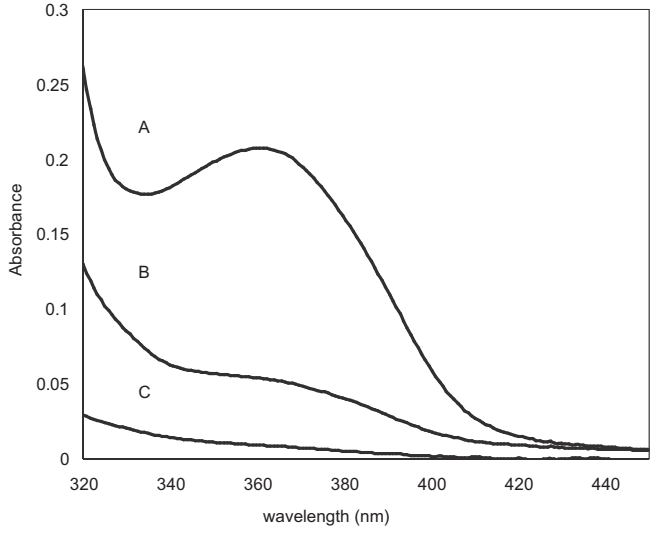

Fig. 8. UV–visible spectra of (A) folic acid (FA), (B) FA-conjugated MNP and (C) poly (AA)-coated MNP without FA.

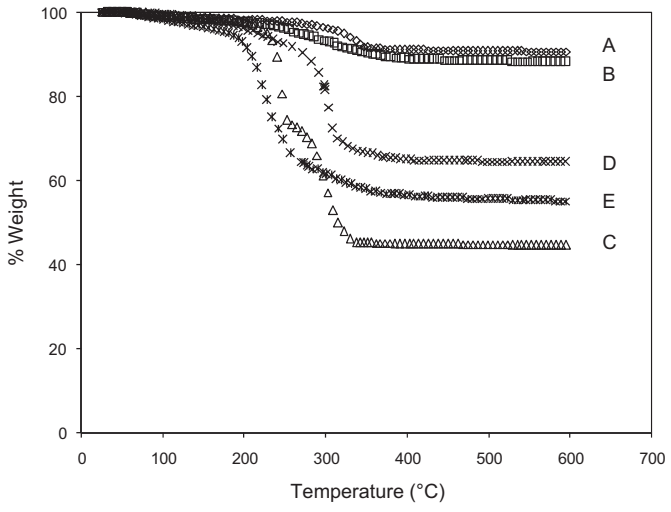

Fig. 9. TGA thermograms of (A) bare MNP, (B) BTPAm-coated MNP, (C) poly(*t*-BA) coated MNP, (D) poly(AA)-coated MNP and (E) FA-poly(AA)-coated MNP.

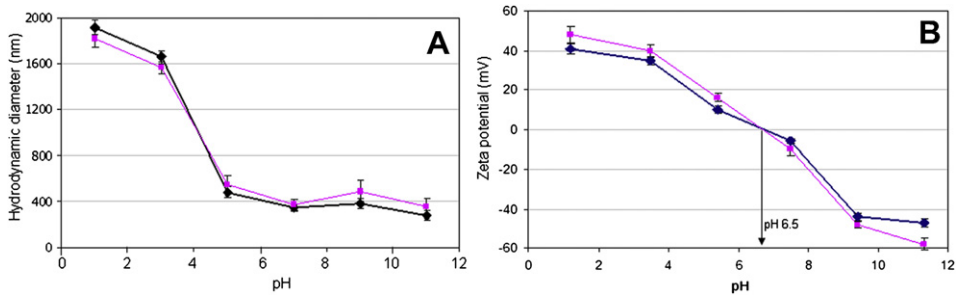

Fig. 10. The effect of pH of the aqueous dispersions containing poly(AA)-coated MNP (◆) and FA-poly(AA)-coated MNP (■) on their hydrodynamic diameter and zeta potential. The experiments were performed at 25 °C.

grafting density of BTPAm, the initiating site for ATRP on the particle, can be calculated and it was found that there was about 0.8 molecule/nm^2 (150 molecules/particle). Examples of the calculation are illustrated in supplementary data. The grafting density of poly(*t*-BA) were comparable to that of BTPAm on the surface.

After the hydrolysis of poly(*t*-BA), percent of organic components in the case of poly(AA)-coated MNPs significantly dropped (from 49 to 27 wt%) due to the removal of *t*-BA groups from the polymeric layer of the particles (Fig. 9D). The 27 wt% of poly(AA) corresponded to 23 carboxylic acid/nm^2 (4600 acid/particle). From Fig. 9E, there was about 14 wt% of FA in the complex, corresponding to about 2 FA molecules/nm^2 (400 FA molecules/particle). Therefore, percent conversion of carboxylic acid to FA was about 8%. The lowering temperature of TGA curve in Fig. 9E (FA-poly (AA)-coated MNP) as compared to that in Fig. 9D (poly (AA)-coated MNP) was attributed to the weight loss of FA component in the complex. The decomposed TGA thermogram of free FA has been investigated and shown in supplementary data. In addition, it was also found that there was about 2.7 FA molecules/site of the ATRP initiator (400 FA molecule/150 sites of BTPAm in a single particle). The limited number of the % conversion and grafting density of FA on the particle surface was attributed to limited accessibility of bulky FA to react with steric poly (AA). However, the grafting density of FA might be improved by copolymerization of poly(AA) with other polymers to lessen steric hindrance of the compact poly(AA), so that FA con be more effectively conjugated. Also, utilization of spacer from the particle surface is another approach that can diminish steric hindrance on the dense surface.

Because carboxylic acid functional groups can be easily ionized in an aqueous solution, it is thus interesting to understand how pH of the dispersions affect hydrodynamic diameter and surface charge of poly(AA)-coated MNPs and FA-poly(AA)-coated MNP. pH of the aqueous dispersions containing the complexes (0.2 mg/ml) were varied from approximately 1–11 and their hydrodynamic diameters were determined *via* PCS technique. In both samples, as pH of the dispersions increased, their hydrodynamic diameters rapidly decreased at acidic pH (ranging between pH 1.2–5.4) and gradually decreased at pH ranging between 5.4 and 11.3 (Fig. 10). It was hypothesized that as increasing pH of the dispersions, ionization of carboxylic acid on the surface of poly(AA)-coated MNPs took place, resulting in the formation of carboxylate ions on their surfaces. The negative charges of carboxylate ions led to additional electrostatic repulsion toward neighboring particles and thus prevented massive flocculation.

The results from zeta potential measurements also supported this assumption. The surface charges of poly(AA)-coated MNPs were positive at the pH ranging between 1.2 and 6.5 and negative at the pH range of 6.5–11.3, implying that point of zero charge (PZC) of this complex was pH 6.5 (Fig. 10). It was also found that FA-containing complex showed a slightly higher zeta potential than the other at pH ranging between 1.2 and 6.5. This was attributed to the presence of amines in FA structure, resulting in protonated amino groups. Similarly, the enriched amines in the complex might also influence the lower zeta potential in FA-containing complex at basic pH.

The large size of the particles in DLS as compared to those from TEM measurements (8 nm in diameter) might come from the fact that there were some nano-clusters of particles in the dispersions. These nano-clusters of the particles can be observed in TEM measurements from the first step of the particle synthesis (shown in supplementary data). When poly(AA) was chemically grafted on their surface, these clusters still presented. Although these nano-clusters existed in the dispersions, the particles were well dispersible in aqueous dispersions without macroscopic aggregation visibly observed because there were poly(AA) coated on their surface.

Cytotoxicity testings of poly(AA)-coated MNP and FA-poly(AA)-coated MNP were also performed. According to our preliminary results, it was found that the dispersions were not toxic against Vero cell line up to 50 μg/ml concentration of the sample (sulforhodamine B (SRB) assay method). Detail studies regarding the toxicity of the magnetite complexes are warranted for future studies.

4. Conclusions

This work presented a “grafting from” strategy to modify MNP surfaces with poly(*t*-BA) *via* ATRP, followed by a hydrolysis of *t*-BA groups to obtain poly(AA) and finally immobilization of folic acid on their surfaces. The originality of this work is that this is the first report on modifying MNP surface with poly(AA) which serves as a platform for folic acid immobilization. Because the folate receptor is overexpressed on the surface of cancer cells, it is for this reason that folic acid is of particular interest in the current work in an attempt to facilitate the intracellular uptake by specific cancer cells for cancer therapy. Folic acid was successfully activated with ethylene diamine (EDA) to obtain primary amine-terminated folic acid derivative. This logical strategy enhanced the reactivity of folic acid to be efficiently immobilized on MNP surfaces through amidization reaction.

In addition to the use of binding affinity of carboxylic acid functional groups, poly(AA) on their surface can also provide stabilization mechanisms through both steric repulsion due to the long chain polymers and electrostatic repulsion owing to the formation of negative charges in basic pH dispersions. Furthermore, poly(AA) on their surfaces also promoted particle dispersibility in water, which is a minimum requirement for biomedical uses. This novel magnetically guidable nanocomplex might be suitable for use as an efficient drug delivery vehicle particularly for cancer treatment.

Acknowledgement

The authors thank the Thailand Research Fund (TRF) and Naresuan University (DBG5380001) for financial funding. The Center of Excellence for Innovation in Chemistry (PERCH-CIC), Commission on Higher Education, Ministry of Education is also gratefully acknowledged for financial support.

Appendix. Supplementary data

Proposed reaction mechanisms of trifluoroacetic acid (TFA) with the polymers on MNP surface. FTIR and ^{1}H NMR spectra of 2-bromo-2-methyl-*N*-(3-(triethoxysilyl) propanamide (BTPAm)) and *N*-(2-aminoethyl) folic acid (EDA-FA). ^{1}H NMR spectrum of poly(t-BA), TEM images showing some nano-aggregation. Examples of calculation of grafting density. TGA thermogram of folic acid.

Appendix. Supplementary data

Supplementary data associated with this article can be found in the online version, at doi:10.1016/j.polymer.2010.12.059.

References

[1] Pei W, Kumadaa H, Natusmea T, Saitoa H, Ishio S. J Magn Magn Mater 2007;310:2375–7.
[2] Sun S, Murray CB, Weller D, Folks L, Moser A. Science 2000;287:1989–92.
[3] Teng X, Yang H. J Am Chem Soc 2003;125:14559–63.
[4] Casula MF, Floris P, Innocenti C, Lascialfari A, Marinone M, Corti M, et al. Chem Mater 2010;22:1739–48.
[5] Anders S, Sun S, Murray CB, Rettner CT, Best ME, Thomson T, et al. Microelectron Eng 2002;61-62:569–75.
[6] Woo K, Hong J, Choi S, Lee HW, Ahn JP, Kim CS, et al. Chem Mater 2004;16:2814–8.
[7] Zhang J, Misra RDK. Acta Biomater 2007;3:838–50.
[8] Laurent S, Forge D, Port M, Roch A, Robic C, Elst LV, et al. Chem Rev 2008;108:2064–110.
[9] Veiseh O, Gunn JW, Zhang M. Adv Drug Deliv Rev 2010;62:284–304.
[10] Sahoo Y, Goodarzi A, Swihart MT, Ohulchanskyy TY, Kaur N, Furlani EP. J Phys Chem 2005;109:3879–85.
[11] Hayashi K, Ono K, Suzuki H, Sawada M, Moriya M, Sakamoto W, et al. Chem Mater 2010;22:3768–72.
[12] Feng PB, Gao F, Gu HC. J Colloid Interface Sci 2005;284:1–6.
[13] Liu X, Xing J, Guan Y, Shan G, Liu H. Colloids Surf A Physicochem Eng 2004;238:127–31.
[14] Mornet S, Vekris A, Bonnet J, Duguet E, Grasset F, Choy JH, et al. Mater Lett 2000;42:183–8.
[15] Cheng G, Zhao J, Tu Y, He P, Fang Y. Anal Chem Acta 2005;533:11–6.
[16] Lellouche J, Senthil G, Joseph A, Buzhansky L, Bruce I, Bauminger ER, et al. J Am Chem Soc 2005;127:11998–2006.
[17] Corr SA, Rakovich YP, Gun'ko YK. Nanoscale Res Lett 2008;3:87–104.
[18] Zhang Y, Kohler N, Zhang M. Biomaterials 2002;23:1553–61.
[19] Sonvico F, Mornet S, Vasseur S, Dubernet C, Jaillard D, Degrouard J, et al. Bioconjug Chem 2005;16:1181–8.
[20] Zhoua Y, Wang S, Ding B, Yang Z. Chem Eng J 2008;138:578–85.
[21] Fischer H. Chem Rev 2001;101:3581–610.
[22] Pyun J, Jia S, Kowalewski T, Patterson GD, Matyjaszewski K. Macromolecules 2003;36:5094–104.
[23] Hu B, Fuchs A, Huseyin S, Gordaninejad F, Evrensel C. Polymer 2006;47:7653–63.
[24] Zhao H, Shipp DA. Chem Mater 2003;15:2693–5.
[25] Liu G, Yan X, Lu Z, Curda SA, Lal J. Chem Mater 2005;17:4985–91.
[26] Sun Y, Ding X, Zheng Z, Cheng X, Hu X, Peng Y. Euro Polym J 2007;43:762–72.
[27] Hermann High LR, Holder SJ, Penfold HV. Macromolecules 2007;40:7157–65.
[28] Shipp DA, Wang JL, Matyjaszewski K. Macromolecules 1998;31:8005–8.
[29] Xia J, Gaynor SG, Matyjaszewski K. Macromolecules 1998;31:5958–9.
[30] Teodorescu M, Matyjaszewski K. Macromolecules 1999;32:4826–31.
[31] Raghuraman GK, Rühe J, Dhamodharan R. Nanopart Res 2008;10:415–27.
[32] Czaun M, Hevesi L, Takafuji M, Ihara H. Chem Commun; 2008:2124–6.
[33] Marutanil E, Yamamoto S, Ninjbadgar T, Tsujii Y, Fukuda T, Takano M. Polymer 2004;45:2231–5.
[34] Zhou Y, Wang S, Ding B, Yang Z. Chem Eng J 2007;40:6217–23.
[35] Fan QL, Neoh KG, Kang ET, Shuter B, Wang SC. Biomaterials 2007;28:5426–36.
[36] Frimpong RA, Hilt JZ. Nanotechnology 2008;19:1–7.
[37] Si S, Kotal A, Mandal TK, Giri S, Nakamura H, Kohara T. Chem Mater 2004;16:3489–96.
[38] Zhang M, Breiner T, Mori H, Muller AHE. Polymer 2003;44:1449–58.
[39] Wan S, Zheng Y, Liu Y, Yan H, Liu KJ. Mater Chem 2005;15:3424–30.
[40] Sauzedde F, Elaïssari A, Pichot C. Colloid Polym Sci 1999;277:846–55.
[41] Ng V, Lee YV, Chen BT, Adeyeye AO. Nanotechnology 2002;13:554–8.
[42] Hayashi K, Moriya M, Sakamoto W, Yogo T. Chem Mater 2009;21:1318–25.
[43] Kohler N, Fryxell GE, Zhang M. J Am Chem Soc 2004;126:7206–11.
[44] Landmark KJ, DiMaggio S, Ward J, Kelly C, Vogt S, Hong S, et al. ACS Nano 2008;2:773–83.
[45] Pinna N, Grancharov S, Beato P, Bonville P, Antonietti M, Niederberger M. Chem Mater 2005;17:3044–9.
[46] Mohapatra S, Mallick SK, Maiti TK, Ghosh SK, Pramanik P. Nanotechnology 2007;18:385102.
[47] Park EK, Lee SB, Lee YM. Biomaterials 2005;26:1053–61.
[48] Rutnakornpituk M, Meerod S, Boontha B, Wichai U. Polymer 2009;50:3508–15.
[49] Tao K, Dou H, Sun K. Chem Mater 2006;18:5273–8.

Polymer 52 (2011) 996–1003

Contents lists available at ScienceDirect

Polymer

journal homepage: www.elsevier.com/locate/polymer

A novel cell support membrane for skin tissue engineering: Gelatin film cross-linked with 2-chloro-1-methylpyridinium iodide

Ming-kung Yeh [a], Yan-ming Liang [b], Kuang-ming Cheng [a], Niann-Tzyy Dai [c], Cheng-che Liu [a], Jenn-jong Young [a,*]

[a] Institute of Preventive Medicine, National Defense Medical Center, PO Box 90048-700, Sanhsia, Taipei 237, Taiwan, ROC
[b] Graduate Institute of Biomedical Engineering, National Taiwan University of Science and Technology, Taipei, Taiwan, ROC
[c] Division of Plastic and Reconstructive Surgery, Tri-Service General Hospital; National Defense Medical Center, Taipei, Taiwan, ROC

ARTICLE INFO

Article history:
Received 25 August 2010
Received in revised form
28 October 2010
Accepted 31 October 2010
Available online 4 November 2010

Keywords:
Gelatin membrane
2-Chloro-1-methylpyridinium iodide
Heterogeneous cross-linking

ABSTRACT

A novel method for preparing cell support membrane which employs heterogeneously cross-linking (CR) process to prepare water-insoluble gelatin (GEL) films was suggested, and compared with 1-ethyl-(3,3-dimethylaminopropyl)carbodiimide. In this study, we found that 2-chloro-1-methylpyridinium iodide (CMPI) is an effective zero-length cross-linker of gelatin, and showed a superior activation ability of carboxylic acid sodium salt under heterogeneous reaction. The CMPI-CR-GEL films showed high water uptake ability, reasonable biodegradability, and excellent cytocompatibility. In vitro studies with 3T3 fibroblasts demonstrated an increased cell viability for those cells grown on CMPI-CR-GEL membranes, and significantly increased cell numbers from Day 1–12. Furthermore, under heterogeneous process, the gelatin film can fabricate in advance, and maintained the original dimension, thickness, and shape after cross-link. Meanwhile, the reaction residues can be easy removed by rinsing and washing processes. These characteristics make the process easily transfer to industrial manufacturing in the future.

1. Introduction

Tissue engineering has been applied to various tissues, and particularly significant progress has been made in the areas of skin, cartilage, and bone regeneration. Skin tissue engineering provides a prospective source of advanced therapies for treatment of acute and chronic skin wounds [1–3]. Scaffolds of natural and synthetic polymers have been used to facilitate tissue regeneration. The design concept of skin equivalent is based on existing models comprising a stratified squamous epithelium grown on a collagen-containing matrix populated with dermal fibroblasts. It is envisaged that the tissue-like character of this construct would generate a three-dimensional and organotypic culture, demonstrating correct epithelial differentiation, morphology, and proliferation rates similar to that found in skin [4]. Certain key factors require consideration for optimizing the performance of tissue engineering system [3]. These are biomaterial selection, additional solvent required for processing, the formulation conditions, and cell type. The most important key factor in the design of a tissue engineering delivery system is the choice of an appropriate polymeric excipient [5,6], which must meet several requirements, including suitable mechanical properties, biodegradation kinetics, tissue compatibility, cell compatibility, cell and nutrition permeability, and ease of processing. Theoretically, engineering of skin substitutes can allow deliberate fabrication of biomaterials with properties that address specific patho-biologic conditions (e.g., burns, scar, cutaneous ulcers, and congenital anomalies). Collagen is currently one of the most popular materials for scaffold production in soft tissue repair and reconstruction such as Apligraf® tissue engineered human skin equivalent [7]. The disadvantages of collagen are however offset by possible toxicity caused by residual catalysts, initiators and unreacted or partially reacted chemical cross-linking agents that are generally employed to improve stability and mechanical properties. In here, we developed a cost down material combined with easy industrial prepared that have the potential to become useful biomaterials. By design and incorporation of specific therapeutic factors in skin substitutes, promotion of wound healing and reduction of morbidity and mortality from large wounds may be achieved.

Gelatin (GEL) is obtained by a controlled hydrolysis of the fibrous insoluble protein, collagen, which is widely found in nature and is the major component of cartilage, skin, bones and connective tissue, and constitutes the major part of the extracellular matrices (ECM). However, gelatin has a relatively low antigenicity because it

* Corresponding author. Tel.: +886 2 81777038x19917; fax: +886 2 26736954.
E-mail address: jjyoung@ms49.hinet.net (J.-j. Young).

0032-3861/$ – see front matter © 2010 Elsevier Ltd. All rights reserved.
doi:10.1016/j.polymer.2010.10.060

is denatured, which is in contrast to the high antigenicity of collagen due to its direct animal origin. In addition, the biocompatible, biodegradable, nontoxic and noncarcinogenic properties of gelatin has seen wide-ranging applications in the pharmaceutical and medical fields; for example, in sealants for vascular prostheses, bone-repairing matrices, wound healing agents and scaffolds for tissue engineering. Furthermore, gelatin is significantly less expensive than collagen.

Gelatin hydrogel, film, and sponge quickly hydrate in aqueous media and rapidly degrade *in vivo*. Cross-linking gelatin can improve its mechanical properties, increase stability, and make gelatin scaffolds insoluble in water. A number of cross-linking methods have been achieved by adding enzyme such as transglutaminase [8,9] or chemical agents such as fructose [10], dextran dialdehyde [11], diepoxy [12], formaldehyde [13], glutaraldehyde [10,13,14], genipin [12,15,16], diisocyanates [17], or carbodiimides [18]. However, these cross-linking agents may themselves be toxic chemicals and/or bind to biopolymers during the cross-linking reaction and subsequently be released into the host as a result of biodegradation.

Water-soluble 1-ethyl-(3,3-dimethylaminopropyl)carbodiimide (EDC) has been used as a zero-length cross-linker of biomaterials, such as gelatin [10,12,19], collagen [20], hyaluronic acid (HA) [21], heparin [22], collagen-HA [23], collagen-chitosan (CS) [24], collagen-chondroitin sulfate (ChS) [25], GEL-CS [26], GEL-HA [27], GEL-alginate [28], GEL-ChS [29], GEL-ChS-HA [30], GEL-CS-HA [31], and tissues [32]. Theoretically, EDC is a zero-length cross-linker that will not chemically bind to biopolymers during cross-linking reactions. However, in our previous report, we found that N-acylurea substitutions were introduced into the HA molecules by means of an O→N migration mechanism during the EDC cross-linking procedure [33]. Furthermore, EDC is an expensive and hygroscopic coupling reagent that must be store at −20 °C, it rapidly loses its activity in low pH aqueous media and only reacts with carboxyl groups at a relatively narrow low pH range (3.5–4.5) [34]. Therefore, it would be helpful to identify other cross-linking reagents that could be used in place of EDC for bioconjugation in aqueous media.

The Mukaiyama reagent [35], 2-chloro-1-methylpyridinium iodide (CMPI), is a room-temperature stable coupling reagent used for the synthesis of peptides of biological interest, and it has the following advantages: low toxicity, water soluble, simple reaction conditions, short reaction time, high yields and is less expensive than EDC. CMPI was used as the activating reagent of carboxyl group in the cross-linking reaction of polysaccharide such as HA [36], alginate [37] or carboxymethylcellulose [38]. However, in those reports, the reaction only performed on carboxylic acid quaternary ammonium salt and carried out in organic solvent such as DMF or DMSO under homogeneous reaction condition. The quaternary ammonium salt was obtained from carboxylic acid sodium salt via an ion displacement technique by ionic exchange resin [39], and it has to transfer back to the sodium salt after reaction; the procedure is long-winded and inconvenient, and the reaction residues were hardly removed after cross-link. In our laboratory, we found that the CMPI cross-linking reaction of HA film can perform on carboxylic acid sodium salt and carried out in aqueous solution under heterogeneous reaction condition [33]. However, there have not been any reports regarding the use of CMPI in the cross-linking of gelatin films. The HA (polysaccharide) and gelatin (polypeptide) have quite different properties, and the cross-linking bonds formed within the HA and gelatin molecules were ester and amide bonds, respectively. Thus, it is worthy to investigate the effect of CMPI in the heterogeneously cross-linking reaction of gelatin film. Furthermore, it is unlike homogeneous process, as the biomaterials can be fabricated to different dimensions, thicknesses, shapes and physical forms (such as films and sponges) in advance, and then cross-linked using the heterogeneous process without loss of these attributes. Meanwhile, the reaction residues can be easy removed by rinsing and washing processes. These characteristics make this process easily transfer to industrial manufacturing in the future.

In this study, the gelatin membranes were prepared by impregnation of gelatin film with a cross-linking solution of CMPI or EDC. The cross-linking characteristics, in vitro biodegradation rate, 3T3 fibroblasts cell proliferation ability and cytocompatibility of both CR-GEL films were investigated and compared.

2. Experimental section

2.1. Materials

Gelatin (from porcine skin) was purchased from Fluka (Buchs, Switzerland). 1-Ethyl-(3, 3-dimethylaminopropyl)carbodiimide hydrochloride (EDC), hydrindantin, triethylamine, glutaraldehyde, hexamethyl-disilazane (HMDS), fetal bovine serum, collagenase type I, collagenase type IV (from *Clostridium histolyticum*), and 2-Chloro-1-methylpyridinium iodide (CMPI) were obtained from Sigma–Aldrich (St. Louis, MO, USA). Ninhydrin, acetone, ethanol, and dimethylsulfoxide (DMSO) were commercially available from Merck (Darmstadt, Germany). Dulbecco's Modified Eagle Medium (DMEM), antibiotics solution (100 IU/ml penicillin and 100 μg/ml streptomycin), trypsin-EDTA solution, and phosphate-buffer saline (PBS, pH 7.4) were purchased from Gibco BRL (Grand Island, NY, USA). Monoclonal mouse anti-human beta-actin antibody (1:1000) and fluorescein (FITC)-conjugated goat anti-mouse IgG (1:200) were purchased from Novus Biologicals (Littleton, CO, USA) and Jackson Immuno Research Laboratories (West Grove, PA, USA), respectively.

2.2. Heterogeneous cross-linking of gelatin films with CMPI or EDC

A total of 2 wt% of gelatin solution was prepared from the gelatin powder using milli-Q water at 45–50 °C. Then, 30 g of gelatin solution was poured into a polystyrene Petri dish (inner diameter of 8.6 cm). The cast solution was allowed to air dry within Laminar flow hood at room temperature for 2 days; then the film was peeled off (0.1 mm thick) carefully and dried *in vacuo* (<0.1 mmHg) over 8 h, and stored in electric desiccators before further use.

Gelatin films were weighed and directly immersed in an 80% aqueous acetone solution containing 10 mM CMPI (presence of Et_3N; molar ratio of Et_3N/CMPI = 1:1) or EDC (absence of Et_3N) at a range of 0.133–2 mmol cross-linking reagent per gram of gelatin. The films were then shaken at room temperature for 24 h. The CR-GEL films were washed with 80% aqueous acetone solution (3 × 50 ml) and acetone (20 ml), and then placed between two pieces of filter paper to flatten them out. The films were dried for 24 h at room temperature under reduced pressure (<0.1 mmHg) and stored in electric desiccators before further use.

2.3. Measurement of the water content

CR-GEL films with a known weight were immersed in PBS (pH 7.4) at room temperature for 4 h and then placed between two pieces of filter paper to wipe off the excess water. The swollen films were weighed, followed by drying under reduced pressure (<0.1 mmHg) at room temperature for 24 h, and then weighed again to calculate their water content by the following equation (1):

$$\text{Water content}\ (\%) = [(Ws - Wd)/Ws] \times 100 \quad (1)$$

where *Ws* is the weight of swollen films and *Wd* is the weight of dried films.

2.4. Determination of the degree of cross-linking by ninhydrin assay

The ninhydrin solution was prepared as described by Moore [40]. Briefly, ninhydrin (2 g) and hydrindantin (0.3 g) were dissolved in 75 ml DMSO under a stream of nitrogen gas. After adding 25 ml lithium acetate buffer (4 N, pH 5.2), the resulting dark red solution was further bubbled with nitrogen for at least 2 min, sealed and stored in a refrigerator (4 °C). Fresh ninhydrin solution was prepared each day. Subsequently, about 1 mg of CR-GEL film in 1 ml of water and ninhydrin solution (1 ml) was put in a screw-capped sample vial and then heated in a boiling water bath for 30 min. After heating, the vials were immediately cooled to room temperature in a cold water bath. Then, 5 ml of 50% aqueous ethanol was added to each vial and thoroughly mixed with a Vortex mixer for 20 s. The optical absorbance of the solution was recorded on a spectrophotometer (CT-8200; ChromTech, Singapore) at 570 nm. Gelatin at various known concentrations (2, 1, 0.5, 0.25, 0.125 and 0 mg/ml) served as the standard. Linear regression was performed with commercial statistical software on a personal computer. The amount of free ε-amino groups in the residual gelatin was proportional to the optical absorbance of the solution. The extent of cross-linking was defined as:

$$\text{Cross} - \text{linking degree}\ (\%) = (1 - NH_t/NH_0) \times 100 \quad (2)$$

where NH_0 is the amount of free amino groups in the gelatin before cross-linking and NH_t is the amount of free amino groups after cross-linking.

2.5. In vitro degradation of CR-GEL films

Pieces of CR-GEL film with known dry weights were immersed in PBS Collagenase (type IV, 60 μg/ml) solution at a sample concentration of 2 mg of CR-GEL film per milliliter of medium, and then the percentage of weight remaining was determined at 37 °C. The enzyme medium was changed every 7 days. At the predetermined intervals, the swollen films were taken out and washed twice with excess milli-Q water. The swollen films were dried under vacuum (<0.1 mmHg) at room temperature for 24 h and then weighed again to determine the percentage of weight remaining based on equation (3).

$$\text{Weight remaining}\ (\%) = Wr/Wo \times 100 \quad (3)$$

where *Wo* is the weight before degradation and *Wr* is the remaining weight after degradation.

2.6. Cell culture

Fibroblasts used in this study were isolated from human dermis by collagenase (type I) digestion [41,42]. Briefly, the epidermis and subcutaneous tissue of human skin were removed using a scalpel. The residual dermis was diced into 0.5–1 mm sized tissues and washed three times with PBS (pH 7.4) supplemented with 1% antibiotic solution (100 IU/ml penicillin and 100 μg/ml streptomycin). These dermis pieces were then placed in a spinner flask containing 10 ml of 1 mg/ml collagenase (type I) in Dulbecco's modified Eagle medium (DMEM) supplemented with 1% antibiotic solution. After digestion in an incubator (37 °C, 5% CO_2) for 5 h, the digestion was discontinued by addition of commercial DMEM supplemented with 10% fetal bovine serum and 1% antibiotic solution (complete medium). The digested solution was filtered through a copper mesh (cell strainer, 200 mesh) and then centrifuged at 1000 rpm for 10 min. The cell suspensions were cultured at 37 °C with 5% CO_2, and 95% humidity in complete medium. The culture medium was changed every 3 days. Cells were passaged at confluence, and the 4–8th passage fibroblasts were used for the seeding.

2.7. Cell adhesion

For cell adhesion studies, human fibroblasts were seeded in 4 ml glass shell vials containing square sheets (1 cm [w] × 1 cm [l]) of CR-GEL membranes at a density of 4.0×10^4 cells/vial. Cells were cultured in complete medium, which was changed every 12 h, for 12 days. Cells were also seeded in 24-well plastic tissue culture plates as controls. All the materials used were sterilized in advance by immersion in 70% ethanol for 4 h.

At Day 4 and 10, cells were labeled with a monoclonal mouse anti-human beta-actin antibody (1:1000) and fluorescein (FITC)-conjugated goat anti-mouse IgG secondary antibody (1:200) to visualize cell nuclei and F-actin filaments, respectively. Then, samples were then prepared on glass slides. GFP fluorescence was visualized using an inverted fluorescence microscope (TE 2000-U; Nikon, Tokyo, Japan) equipped with a GFP filter cube. GFP images were used to quantify the total cell area using NIH ImageJ software.

Total cell numbers were quantified at Day 1, 4, 7, 10, and 12 (mean ± SE) to enable construction of cell growth curves. Each substrate with its attached cells was washed in sterile PBS, and the CR-GEL membrane samples were transferred to 24-well plates. Cell detachment was performed by adding 0.25% trypsin in EDTA solution (0.5 ml) to each sample well and incubating at 37 °C for 3 min. Trypsin was inactivated by adding fibroblast culture medium. Cell detachment from the CR-GEL film was assisted by aspiration, and cells were counted using a Weber's haemocytometer. Samples of each substrate type were seeded in triplicate to obtain each time point measurement.

2.8. Cell encapsulation

3T3 fibroblasts were trypsinized and resuspended in a CR-GEL membrane containing 0.5% (w/v) photoinitiator at a concentration of 4.0×10^4 cells/vial. The glass slides containing membranes were washed with PBS and incubated for 8 h in 3T3 medium under standard culture conditions. A LIVE/DEAD Viability/Cytotoxicity Kit (Invitrogen, Carlsbad, CA, USA) was used to quantify cell viability on the membranes according to the manufacturer's instructions.

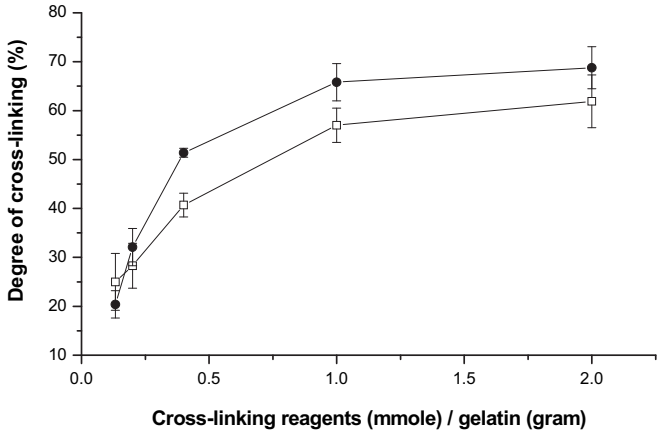

Fig. 1. Effect of molar ratio of CMPI and EDC on the cross-linking degree of CR-GEL films. (□) CMPI-CR-GEL; (●) EDC-CR-GEL. Cross-linking: 10 mM cross-linking reagents and Et_3N (Et_3N/CMPI = 1, Et_3N/EDC = 0) in 80% acetone aqueous solution at room temperature for 24 h.

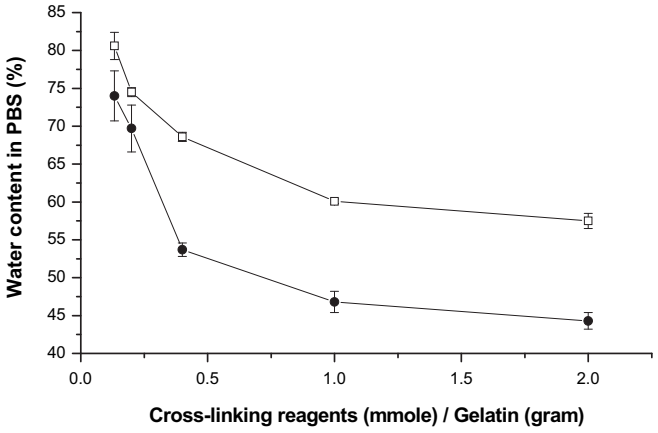

Fig. 2. Water content of CR-GEL films in PBS solution (pH 7.4) at room temperature for 4 h (□) CMPI-CR-GEL; (●) EDC-CR-GEL. Cross-linking: 10 mM cross-linking reagents and Et_3N (Et_3N/CMPI = 1, Et_3N/EDC = 0) in 80% acetone aqueous solution at room temperature for 24 h.

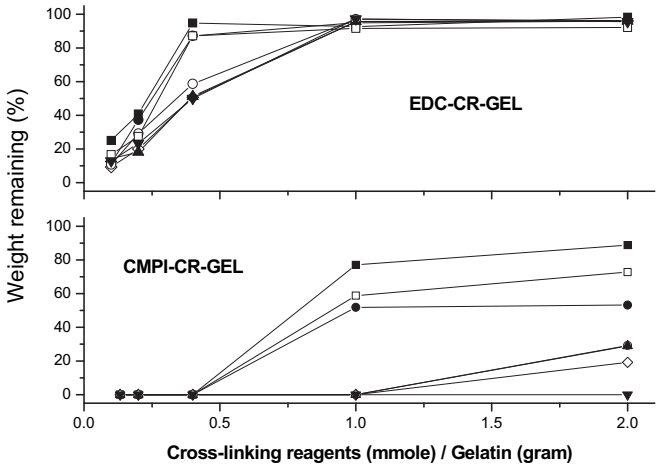

Fig. 4. *In vitro* degradation of cross-linked gelatin films in PBS collagenase solution (60 μg/ml, pH 7.4) at 37 °C. (■) 1 days; (□) 4 days; (●) 7 days; (○) 14 days; (▲) 21days; (◇) 28 days; (▼) 35 days. Cross-linking: 10 mM cross-linking reagents and Et_3N (Et_3N/CMPI = 1, Et_3N/EDC = 0) in 80% acetone aqueous solution at room temperature for 24 h.

2.9. Morphology

The morphology of fibroblasts attached on membranes after 4 and 7 days in cell culture was examined via scanning electron microscopy (SEM) using a Hitachi S-3000N microscope (Hitachi, Tokyo, Japan). The culture media was removed, and the samples were rinsed briefly with PBS before fixing the cells by addition of 2.5% glutaraldehyde in PBS for 30 min. The cells were then washed with 0.1 M sodium cacodylate buffer and dehydrated in a series of ethanol dilutions (20–100%) for 10 min per dilution. The membrane samples with attached cells were dried overnight in hexamethyldisilazane (HMDS), attached to aluminum SEM stubs using carbon tabs, and sputter coated with gold prior to examination.

2.10. Statistical analysis

Data were analyzed using the ANOVA two-factor with replication test and variances were further investigated using the Student Newman–Keuls test. Data are shown as mean ± SE (standard error) where sample numbers (n) were not less than three. Statistical significance was accepted when the p value was less than 0.05 ($p < 0.05$).

3. Results and discussion

3.1. Cross-linking of gelatin films under heterogeneous reaction condition

In the present study, the gelatin films were cross-linked with different volumes of either CMPI or EDC solution at room temperature using the film immersion method. It is known that both CMPI and EDC easily lose their activity in aqueous solution. In order to prevent CMPI and EDC deactivation and to prevent the gelatin films from dissolving during the overnight reaction period, this heterogeneous reaction must be carried out in an aqueous organic solution. Results showed that just 10 mM of CMPI or EDC in an 80% (v/v) aqueous acetone or an 80% (v/v) aqueous ethanol solution was enough to obtain water-insoluble CR-GEL membranes. According to a previous report [27], in the case of a homogeneous reaction in which the EDC solution is directly added to the reaction solution, at least 20 wt% of EDC is required to obtain an insoluble GEL-HA sponge. Furthermore, the cross-linking reaction carried out in aqueous acetone demonstrated a better efficiency than that in aqueous ethanol (data not shown).

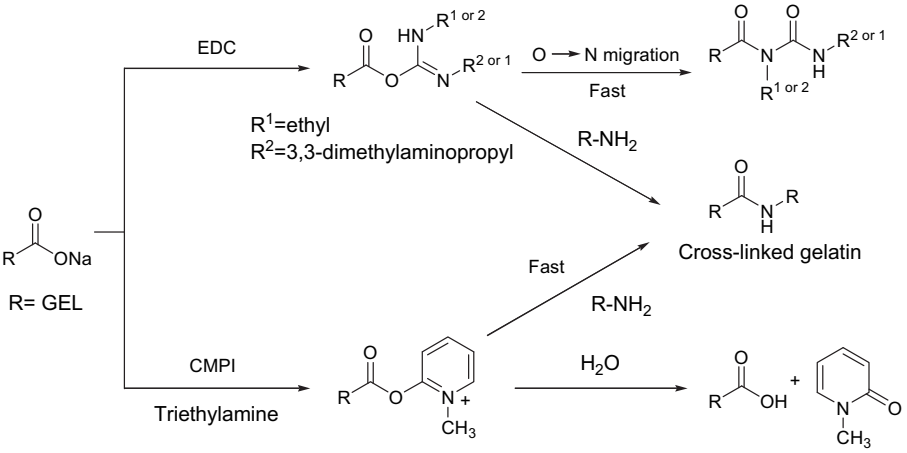

Fig. 3. The mechanism of cross-linking of gelatin films reacted with EDC and CMPI.

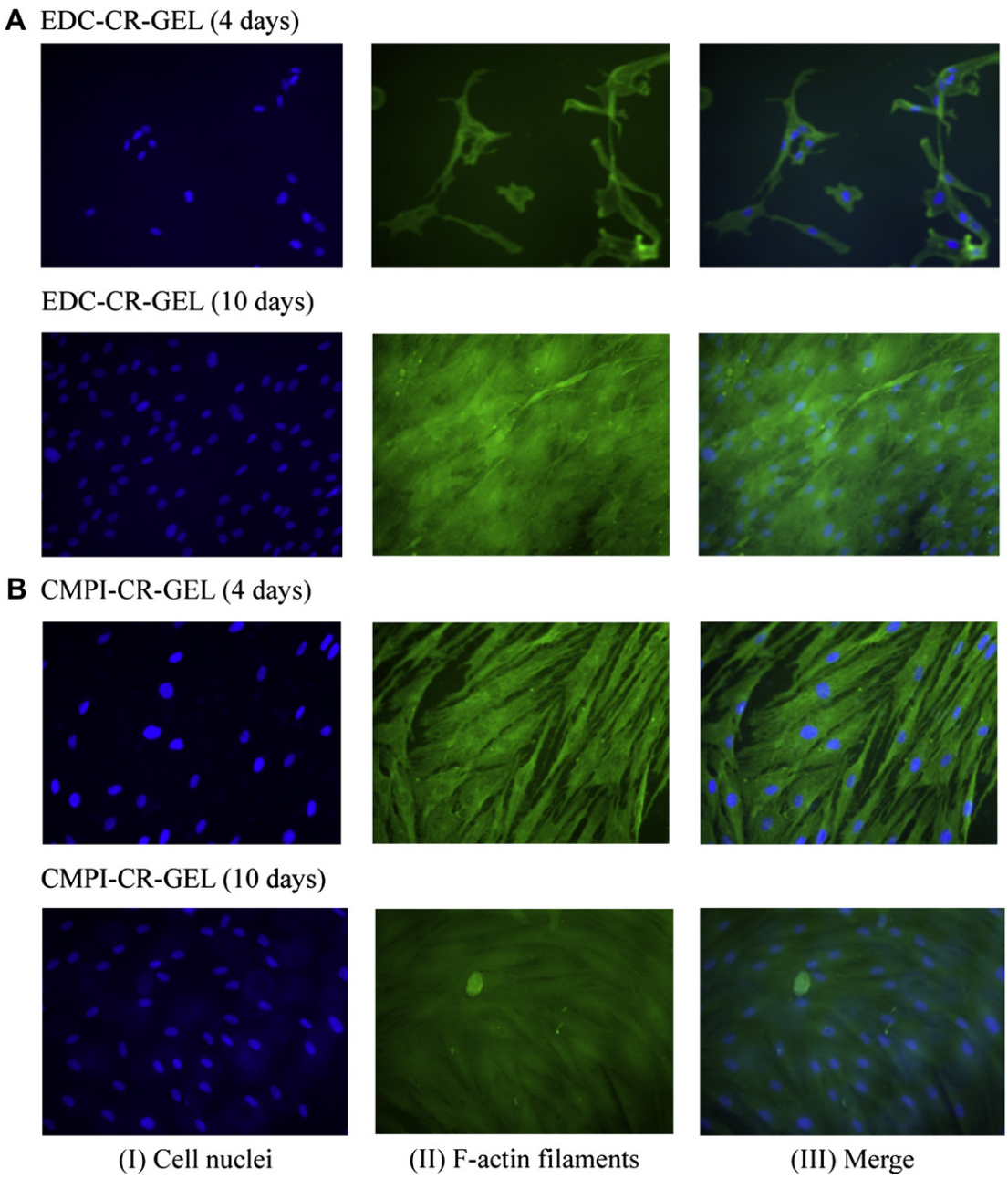

Fig. 5. Photomicrographs of cell adhesion, proliferation and migration on EDC-CR-GEL (A), and CMPI-CR-GEL (B) membrane surfaces cultured in vitro at 37 °C for 4 and 10 days.

Both CMPI and EDC are useful reagents for carboxyl group activation. The intra- or intermolecular cross-linking reaction via amide bond formation occurred between the carboxyl group of glutamic acid or aspartic acid residues and the ε-amino group of lysine residues within the same or different gelatin molecules, respectively. The quantity of amide bonds formation after cross-linking is difficult to observe directly using spectrometry methods. Thus, the extent of cross-linking of the gelatin film must be evaluated using indirect measurements, such as the content of free amino groups, the ability to take up water, and the in vitro enzymatic degradation rate. Furthermore, it is hard to estimate the percentage of glutamic acid and aspartic acid residues in gelatin, thus we used molar ratios of cross-linking reagents based on the weight of the gelatin film rather than equivalents based on the carboxyl functional groups in the following quantitative determination.

3.2. Degree of cross-linking of gelatin films

The extent of cross-linking was determined by monitoring of change in the free ε-amino group content in the test CR-GEL film using the ninhydrin assay. Ninhydrin (2,2-dihydroxy-1,3-indandione) is a well-know, widely used chemical for the colorimetric determination of amino acids. Ninhydrin is reduced in the presence of free amino groups to produce an aldehyde and carbon dioxide via a three-step reaction. The used of ninhydrin depends on the formation of a purple color (Ruhemann's purple) with amine functionality.

Fig. 1 shows the relationships between the degrees of cross-linking of the CR-GEL films with different molar ratios of zero-length cross-linkers. The result indicated that the extent of cross-linking of the films was affected by the amount of CMPI or EDC. The degree of

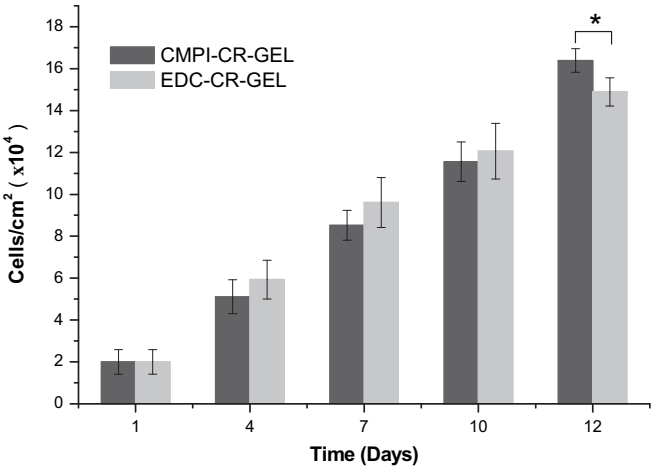

Fig. 6. Cell proliferation assay. The histogram indicates the viable cell number per 0.6 mm^2 area from both EDC-CR-GEL and CMPI-CR-GEL membranes at various time points. Differences were significant at $^*p < 0.05$.

cross-linking increased with the molar ratio of CMPI and EDC up to a maximum value of about 61.9% and 68.8%, respectively. This tendency reflected the fact that the remnants of free amino groups in the CR-GEL film reached a plateau. According to the cross-linking mechanism, carboxyl group activation reagents have different cross-linking types compared to bi-functional cross-linkers. In the case of carboxyl group activation reagents, the cross-linking bridge occurs between the carboxyl group and the amino group, with each cross-linking bridge consuming only one free amino group. However, in the case of bi-functional cross-linkers, each cross-linking bridge consumes two free amino groups. Thus, when using the ninhydrin assay as a measurement method, the gelatin film cross-linked with CMPI or EDC would have twice the cross-linking bridge density compared to those cross-linked with bi-functional cross-linkers with the same degree of cross-linking. Since, no spacer is introduced for amide-bond-type cross-linking, zero-length cross-linkers may form intramolecular cross-links within a gelatin molecule or short-range intermolecular cross-links between two adjacent gelatin molecules. The consumption of the free amino groups in the gelatin molecules is limited, thus the maximum degree of cross-linking of the CR-GEL film is constant and independent of the type of zero-length cross-linkers used. In fact, the degree of cross-linking of the insoluble CR-GEL films measured by the ninhydrin assay was higher than the actual degree of cross-linking; this is because only the free amino groups on the surface of the gelatin film could reduce ninhydrin. The different maximum degrees of cross-linking between the CMPI-CR-GEL (61.9%) and EDC-CR-GEL (68.8%) films might have been influenced by difference in the surface area of the gelatin films, as the gelatin films had different thickness and were shrunk at different ratios during the cross-linking process depending on the type and the amount of the cross-linkers used.

3.3. Water uptake ability of CR-GEL films

The water uptake ability of the gelatin film is a function of the percentage of theoretical cross-linking. Highly cross-linked film tends to show lower water uptake since the highly cross-linked structure could not sustain much water within their network structure. All the CR-GEL films were saturated within 4 h (data not shown). After immersed in PBS (pH 7.4) for 4 h, the dependence of water contents of CR-GEL films on the molar ratio of CR-GEL films is shown in Fig. 2. Apparently, it showed the tendency toward the decreasing water uptake ability with the increase in molar ratios of cross-linking reagents. EDC-CR-GEL films had much more water content decreasing (29.7%) than CMPI (23.1%) at the range of 0.133 and 2 mmol. As our previous mentioned, the cross-linking degree of gelatin reached the maximum value at 2 mmol of molar ratio of CMPI and EDC. However, the lowest water content of the EDC-CR-GEL film (44.3%) was much lower than the CMPI-CR-GEL film (57.5%). This phenomenon can be explained by the different cross-linking reaction mechanisms of CMPI and EDC (Fig. 3). EDC reacts with a carboxyl group to form an unstable intermediate O-acylurea under acidic conditions, after which the nearby free amino group acts as a nucleophile undergoing a substitution reaction and generating an amide bond. However, because of a steric effect, not all O-acylurea can react with an amino group to form an amide bond, thus it rearranges to form a stable N-acylurea by means of an O→N migration mechanism. In contrast, the intermediate obtained from the reaction between a carboxyl group and CMPI shows a relatively high reactivity and stability. It reacts with a nearby free amino group of the same or different molecule of gelatin to form an inter- or intramolecular cross-link, and the unreacted intermediate can hydrolyze back to the carboxylic acid without introducing any hydrophobic substituent during the cross-linking process. The introduced of a hydrophobic N-acylurea substituent certainly reduced the water uptake ability of the EDC-CR-GEL film. This is the reason why the lowest water content of EDC-CR-GEL film (44.3%) was much lower than CMPI-CR-GEL film (57.5%) at cross-linking saturation. This is also evidence indicating that an N-acylurea substituent was introduced to the gelatin molecule during the EDC cross-linking process.

The water-soluble EDC was also used in the fixation of bioprosthetic tissue, such as heart valve [43]. Since gelatin is the primary structure of collagen, thus using EDC as cross-linking reagent may also introduce large quantities of hydrophobic N-acylurea substituent to the collagen molecules within the tissue. This phenomenon may change the molecular structure and distorted the conformation of the collagen molecules, and causing the EDC fixed tissue to lose its water uptake ability, biodegradability and cytocompatibility. Furthermore, there is some possibility that this hydrophobic N-acylurea substituent may themselves be cytotoxic chemicals and subsequently be released into the host as a result of biodegradation. Apparently, using CMPI in place of EDC in the fixation of bioprosthetic tissue may avoid the disadvantage and the risk caused by EDC.

3.4. In vitro enzymatic stability of CR-GEL films

Bacterial collagenase from *C. histolyticum* was selected as the enzyme for our in vitro degradation studies. It is reported that bacterial collagenase, a specific protease, splits gelatin and collagen molecules into small water-soluble fragments between X and Gly in the Pro-X-Gly-Pro-X sequence. The in vitro degradation profiles of the CR-GEL films in PBS collagenase solution (60 μg/ml, pH 7.4) at 37 °C are shown in Fig. 4. The degradation behavior of the CR-GEL film is quite different with the CR-HA film as our previous report [33]. It can be seen that the CMPI-CR-GEL films had much higher degradation rates in the PBS collagenase solution than the EDC-CR-GEL films. The gelatin films cross-linked with less than 0.4 mmol of CMPI were fully digested within 4 days, and remained only 19% of its initial weight at day 28 in the case of 2 mmol of CMPI used. However, the gelatin films cross-linked with more than 1 mmol of EDC remained over 90% of their initial weight from day 1 to day 35. Furthermore, additional degradation of all EDC-CR-GEL films was mostly absent after 14 days of incubation. The enzymatic degradation rate of CR-GEL films may be influence by two factors: the degree of cross-linking and the bioavailability of the enzyme. Fig. 1 shows that there were similar degrees of cross-linking of the CR-GEL films formed using the same molar ratios of CMPI and EDC.

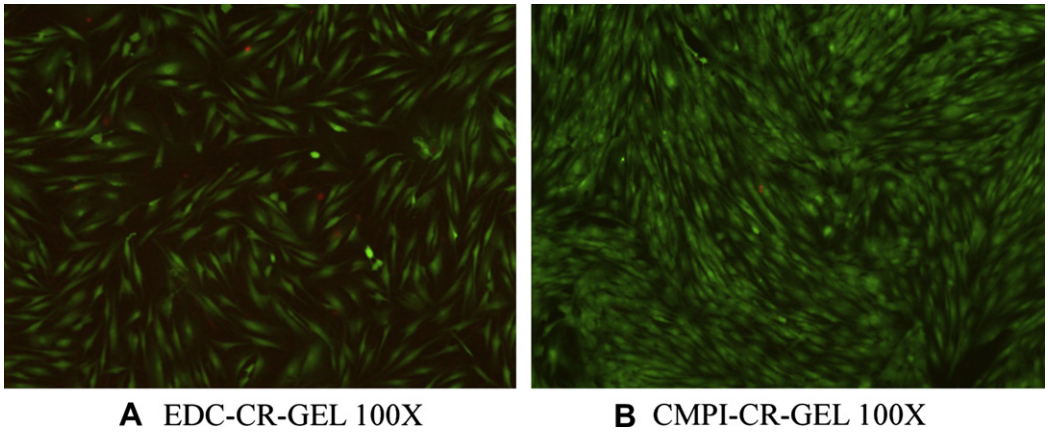

Fig. 7. Characterization of embedded 3T3 fibroblasts behavior in EDC-CR-GEL (A) or CMPI-CR-GEL (B) film. Macroscopic images of cell morphology were stained with calcein-AM (live: green)/ethidium homodimer (death: red) LIVE/DEAD assay 24 h after encapsulation.

Thus, the different degradation behaviors between CMPI- and EDC-CR-GEL films were not affected by their degree of cross-linking. Therefore, the limited degradation of EDC-CR-GEL films was likely due to the introduction of the hydrophobic N-acylurea substituent, which changed the conformation of the cleavage site and prohibited its availability to collagenase.

3.5. Interaction of 3T3 fibroblasts with CR-GEL films

The ability to bind to scaffold materials is essential for cell survival and function in engineered tissues. Cell infiltration and proliferation are crucial for a scaffold to support and guide tissue regeneration. Therefore, the 3T3 fibroblasts adhesion on CMPI- and EDC-CR-GEL membrane surfaces are shown in Fig. 5, and the proliferation rates are shown in Fig. 6. Fig. 5 presents the images of human fibroblasts cultured for 4 and 10 days in the EDC-CR-GEL (A) and CMPI-CR-GEL (B) membranes. Exploiting the photomicrographs sequential scanning mode, a large number of fibroblasts were easily distinguished from the membranes (Fig. 5-I). The merged image (Fig. 5-III) revealed that the fibroblasts tightly adhered to the surface of membrane with a typical shuttle-like morphology. Cells on the EDC- or CMPI-CR-GEL surfaces elongated, migrated, and aggregated with surrounding cells forming branched and interconnected multicellular networks by Day 4. After 7 days in culture, cells readily

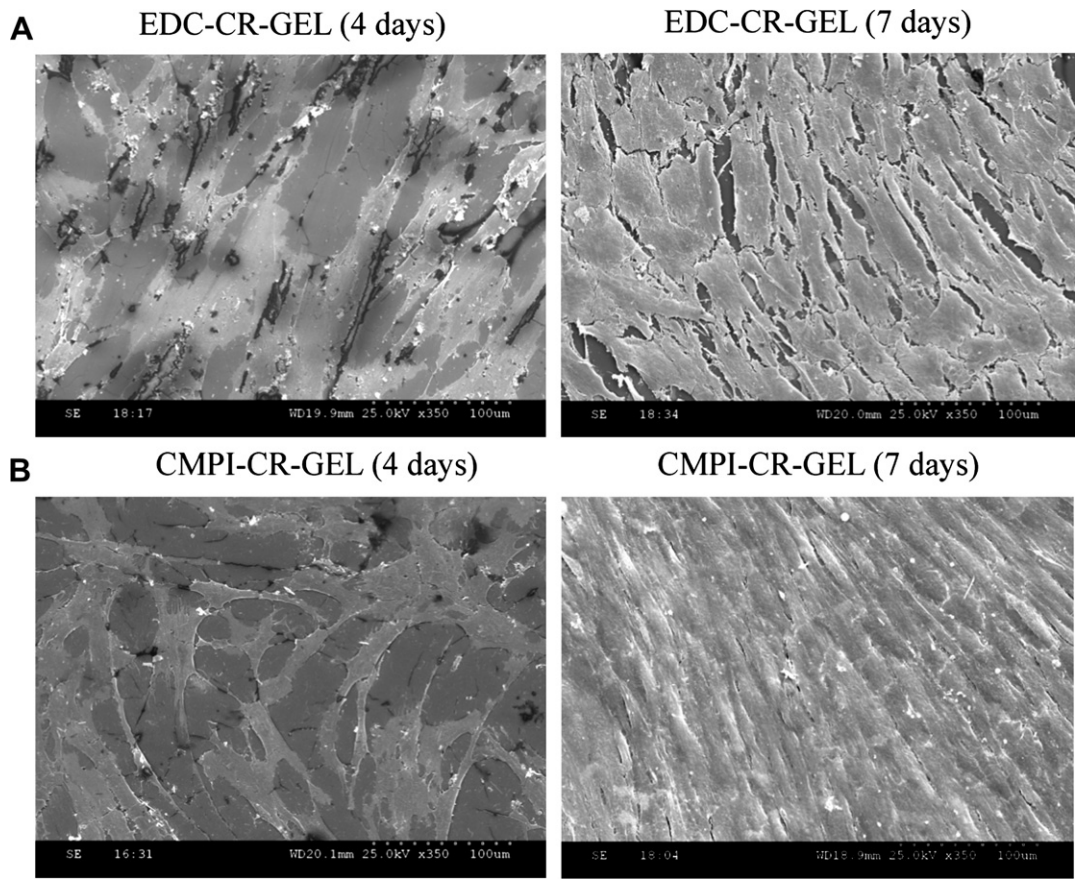

Fig. 8. SEM images for spread of 3T3 fibroblasts of the EDC-CR-GEL membrane (A), and the CMPI-CR-GEL membrane (B), after 4 and 7 days culture in vitro.

elongated and migrated in all CR-GEL membranes. Moreover, in CMPI-CR-GEL membranes, more cells elongated, migrated and formed interconnected networks with neighboring cells compared to the EDC-CR-GEL membranes. Cell proliferation was determined over time as an additional measure of cell compatibility (Fig. 6). Both EDC- and CMPI-CR-GEL membranes demonstrated significantly increased cell numbers over 4 days, increasing at least 2- or 3-fold over this time period, and cell numbers steadily rose from Day 1–12. As determined within the first 10 days, there were no significant differences in the cell number, the measurements being within the range of standard error. However, significant differences ($p < 0.05$) in overall cell numbers between EDC- and CMPI-CR-GEL membranes were seen by Day 12.

Viability of 3T3 cells after encapsulation in CMPI-CR-GEL membranes for 24 h was clearly higher than that in the EDC-CR-GEL membranes (Fig. 7). General losses in viability may occur due to encapsulation stress, nutrient limitations, drying during processing or stress due to transient swelling after placement in media. However, potential cytotoxicity of the EDC-CR-GEL and CMPI-CR-GEL membranes was not evident.

Adhesion of 3T3 fibroblasts on the CR-GEL membranes was observed by SEM at Day 4 and 7 after cell seeding (Fig. 8). The EDC- and CMPI-CR-GEL scaffolds exhibited smoothly surface microstructure and no obviously pores were observed. The 3T3 fibroblasts adhered on the membrane surface, and exhibited flattened and uniformly morphology. The overall cellular morphology appeared to be largely single cell-width networks on the CR-GEL membranes, with an overall width of 20 μm and length of 100 μm. The CMPI-CR-GEL membrane was apparent indicating effective cell–substrate binding. SEM images revealed rounded fibroblasts in contact with CMPI-CR-GEL membrane surfaces at Day 4 and spread cells at Day 7(Fig. 8B).

Many of the currently available tissue engineering membranes suffer from poor mechanical properties, cell binding and viability, or the inability to control the microarchitecture. Native ECM molecules, such as gelatin, can be used to create cell-laden microgels, however, the ability to create lasting micropatterns is limited, typically due to insufficient mechanical robustness. CMPI-CR-GEL membranes had strong mechanical and degradation properties demonstrated significant cell adhesion, and had excellent encapsulated cell viability. These features greatly enhanced the ability of the cells to proliferate, elongate, migrate, and organize into higher-order structures. These results indicated that the CMPI-CR-GEL scaffold retained the original cytocompatibility of gelatin. Potential cytotoxicity of CMPI was not evidenced in these experiments, as all the in vitro results indicated that the CMPI-CR-GEL membranes had good biocompatibility. Further study of the tissue response to these membranes *in vivo* is thus warranted.

4. Conclusions

The water-soluble EDC was used plentifully as a zero-length cross-linker of biomaterials such as proteins and polysaccharides. Theoretically, residue from the reagent is not introduced during the EDC cross-linking reaction; in fact, large quantities of hydrophobic N-acylurea substituents were introduced into carboxyl groups of the biomaterial. This phenomenon may have changed the molecular structure and distorted the conformation of biomaterial, thus, causing the EDC cross-linked biomaterials to lose its water uptake ability, biodegradability and biocompatibility.

In this study, we using CMPI in placed of EDC as a zero-length cross-linker of gelatin film. The obtained results indicated that CMPI showed comparable cross-linking ability with EDC and without introduction of any hydrophobic substituent. Moreover, the CMPI-CR-GEL films showed an increased water uptake ability, cell support ability and cytocompatability compared with the EDC-CR-GEL films. The study of the thermal and mechanical properties of CMPI-CR-GEL films and the use of CMPI as a cross-linking reagent in other biomaterials and composites are currently in progress in our laboratory.

Acknowledgment

Financial support for this work was provided by the National Science Council (NSC 98-2320-B-016-003-MY3) and National Defense Medical Center (99P4-3) of the Republic of China.

References

[1] Scuderi N, Anniboletti T, Carlesimo B, Onesti MG. In Vivo 2009;23:991–1003.
[2] Metcalfe AD, Ferguson MW. Biomaterials 2007;28:5100–13.
[3] Hrabchak C, Flynn L. Expert Rev Med Devices 2006;3:373–85.
[4] Mano JF, Silva GA, Azevedo HS, Malafaya PB, Sousa RA, Silva SS, et al. J R Soc Interface 2007;4:999–1030.
[5] Malafaya PB, Silva GA, Reis RL. Adv Drug Deliv Rev 2007;59:207–33.
[6] Yannas IV. Wound Repair Regen 1998;6:518–23.
[7] Yannas IV. In vivo synthesis of tissues and organs. In: Lanza RP, langer R, Vacanti J, editors. Principles of tissue engineering. 2nd ed. , San Diego: Academic Press; 2000. p. 167–78.
[8] Broderick EP, O'Halloran DM, Rochev YA, Griffin M, Collighan RJ, Pandit AS. J Biomed Mater Res Appl Biomater 2005;72B:37–42.
[9] Yung CW, Wu LQ, Tullman JA, Payne GF, Bentley WE, Barbari TA. J Biomed Mater Res 2007;83A:1039–46.
[10] Ulubayram K, Aksu E, Gurham SID, Serbetci K, Hasirci N. J Biomater Sci Polym Edn 2002;13:1203–19.
[11] Draye JP, Delaey B, Van de Voorde A, Van Den Bulcke A, De Reu B, Schacht E. Biomaterials 1998;19:1677–87.
[12] Sung HW, Huang DM, Chang WH, Huang RN, Hsu JC. J Biomed Mater Res 1999;46:520–30.
[13] Ray RR, Jana SC, Nanda G. J Appl Bacteriol 1995;79:157–62.
[14] Matsuda S, Iwata H, Se N, Ikada Y. J Biomed Mater Res 1999;45:20–7.
[15] Lien SM, Li WT, Huang TJ. Mater Sci Eng C 2008;28:36–43.
[16] Yao CH, Liu BS, Chang CJ, Hsu SH, Chen YS. Mater Chem Phys 2004;83:204–8.
[17] Apostolov AA, Boneva D, Vassileva E, Mark JE, Fakirov S. J Appl Polym Sci 2000;76:2041–8.
[18] Sheehan JC, Hlavka JJ. J Am Chem Soc 1957;79:4528–9.
[19] Lai JY, Li YT. Mater Sci Eng C 2010;30:677–85.
[20] Olde Damink LHH, Dijkstra PJ, van Luyn MJA, van Wachem PB, Nieuwenhuis P, Feijen J. Biomaterials 1996;17:765–73.
[21] Tomihata K, Ikada Y. J Biomed Mater Res 1997;37:243–51.
[22] Oliveira GB, Carvalho Jr LB, Silva MPC. Biomaterials 2003;24:4777–83.
[23] Taguchi T, Ikoma T, Tanaka J. J Biomed Mater Res 2002;61:330–6.
[24] Wang XH, Li DP, Wang WJ, Feng QL, Cui FZ, Xu YX, et al. Biomaterials 2003;24:3213–20.
[25] Pieper JS, van der Kraan PM, Hafmans T, Kamp J, Buma P, van Susante JLC, et al. Biomaterials 2002;23:3183–92.
[26] Kolodziejska I, Piotrowska B, Bulge M, Tylingo R. Carbohydr Polym 2006;65:404–9.
[27] Choi YS, Hong SR, Lee YM, Song KW, Park MH, Nam YS. J Biomed Mater Res B Appl Biomater 1999;48:631–9.
[28] Choi YS, Hong SR, Lee YM, Song KW, Park MH, Nam YS. Biomaterials 1999;20:409–17.
[29] Kuijpers AJ, van Wachem PB, van Luyn MJA, Brouwer LA, Engbers GHM, Krijgsveld J, et al. Biomaterials 2000;21:1763–72.
[30] Wang TW, Sun JS, Wu HC, Tsuang YH, Wang WH, Lin FH. Biomaterials 2006;27:5689–97.
[31] Liu H, Yin Y, Yao K, Ma D, Cui L, Cao Y. Biomaterials 2004;25:3523–30.
[32] Sung HW, Chang WH, Ma CY, Lee MH. J Biomed Mater Res 2003;64A:427–38.
[33] Young JJ, Cheng KM, Tsou TL, Liu HW, Wang HJ. J Biomater Sci Polym Edn 2004;15:767–80.
[34] Nakajima N, Ikada Y. Bioconjug Chem 1995;6:123–30.
[35] Mukaiyama T, Usui M, Saigo K. Chem Lett; 1976:49–50.
[36] Gamini A, Paoletti S, Toffanin R, Micali F, Michielin L, Bevilacqua C. Biomaterials 2002;23:1161–7.
[37] Leone G, Torricelli P, Chiumiento A, Facchini A, Barbucci R. J Biomed Mater Res 2008;84A:391–401.
[38] Leone G, Fini M, Torricelli P, Giardino R, Barbucci R. J Mater Sci Mater Med 2008;19:2873–80.
[39] Della Valle F, Romeo A. EP No. 341745B1, 1994.
[40] Moore SJ. Biol Chem 1968;243:6281–3.
[41] Dai NT, Yeh MK, Liu DD, Adams EF, Chiang CH, Yen CY, et al. Biochem Biophys Res Commun 2005;329:905–8.
[42] Dai NT, Williamson MR, Khammo N, Adams EF, Coombes AG. Biomaterials 2004;25:4263–71.
[43] Everaerts F, Torrianni M, van Luyn M, van Wachem P, Feijen J, Hendriks M. Biomaterials 2004;25:5523–30.

Polymer 52 (2011) 1004–1012

Contents lists available at ScienceDirect

Polymer

journal homepage: www.elsevier.com/locate/polymer

Highly branched benzoxazine monomer based on cyclotriphosphazene: Synthesis and properties of the monomer and polybenzoxazines

Xiong Wu [a], Yun Zhou [b], Shu-Zheng Liu [a], Ya-Ni Guo [a], Jin-Jun Qiu [a], Cheng-Mei Liu [a,*]

[a] School of Chemistry and Chemical Engineering, Huazhong University of Science and Technology, Wuhan 430074, PR China
[b] Institute of Marine Materials Science and Engineering, Shanghai Maritime University, Shanghai 200135, PR China

ARTICLE INFO

Article history:
Received 9 September 2010
Received in revised form
22 November 2010
Accepted 1 January 2011
Available online 9 January 2011

Keywords:
Cyclotriphosphazene
Benzoxazine
Ring-opening polymerization

ABSTRACT

A hyperbranched organic–inorganic hybrid benzoxazine monomer based on cyclotriphosphazene (CP) has been synthesized, which possesses six organic benzoxazine moieties distributed on the inorganic ring of CP. The high molecular weight (1491 g/mol) monomer showed excellent solubility in common organic solvents. Fourier transform infrared spectroscopy (FT-IR) and differential scanning calorimetry (DSC) were used to study the thermal ring-opening polymerization reaction of the novel benzoxazine monomer. FT-IR spectrum implied that the characteristic absorption peaks of the benzoxazine ring disappeared completely after curing at 240 °C for 1 h, which illustrated that the completion of polymerization reaction. DSC plots indicated that the melting point of the new monomer was 77 °C and an exothermic peak was 225 °C owing to the ring-opening polymerization of the monomer. Due to its highly steric crosslinking structure with rigid and thermal stable inorganic CP as the core, the polybenzoxazine based on the new monomer showed excellent thermal stability and mechanic properties. The char yield of the polymer at 850 °C was 66.9% in nitrogen, and the T_g of the polybenzoxazine was 152 °C.

1. Introduction

Recently, there has been an increasing interest in design and preparation of polybenzoxazine because the materials are developed class of high-performance thermosetting resins instead of common phenolic–formaldehyde resin in high-tech field. These thermosetting resins not only possess all the advantages of traditional phenolic resins such as excellent mechanical and thermal properties, but also have unique advantages of near-zero shrinkage upon curing, thermal and flame retardant, low water absorption and remarkable molecular design flexibility [1]. Furthermore, the polybenzoxazine resins can be easily gained from corresponding monomers under heat polymerization with or without catalyst, and the corresponding monomers can be conveniently generated by the Mannich condensation reaction of phenol, formaldehyde, and primary amine [2].

However, there are also several shortcomings that limit the application of common polybenzoxazine resins, such as high polymerization temperature, difficulty in processing and poor mechanic strength (low toughness) [3] and low-level flame retardant. To properly solve these problems and overcome the encountering disadvantages, lots of researchers have attempted many methods. Generally, the methodologies can be summarized in three approaches:

(i) Blending with other high-performance polymers or filling with inorganic materials. Rubber [4], polycarbonate [5], poly (ε-caprolactone) [6], polyurethane [7], epoxy [8] and other polymers were blended with the benzoxazine resins to improve the mechanic and thermal properties. Phosphorus-containing resin [9,10], clay [11] and magnetic Fe_3O_4 [12] were added to polybenzoxazine to modify flame retardant and thermal stability, or to prepare functional materials.

(ii) Synthesis of new polymeric precursors. There were three modes: (a) Main-chain precursors: Liu [13] and Ishida reported the concept of oligomeric benzoxazine resins where oxazine rings were in the main chain. Pedro and his copartners [14] synthesized a series of highly fluorinated main chain polybenzoxazines. Commonly, high molecular weight polybenzoxazine precursors were mostly synthesized from aromatic or aliphatic diamine and bisphenol with paraformaldehyde; (b) Side-chain precursors: Side-chain polymer strategy was a way to incorporate benzoxazine moieties into a polymer backbone to achieve a highly dense network, “click reaction” was the most popular routine to achieve this aim [15–17]. Using this method, benzoxazine groups were grafted to PVC, polystyrene, polybutadiene; (c) Cross-linkable telechelic polymers with benzoxazine moieties at the chain

* Corresponding author. Tel.: +86 27 87544831; fax: +86 27 87543632.
E-mail address: liukui@mail.hust.edu.cn (C.-M. Liu).

0032-3861/$ – see front matter © 2011 Elsevier Ltd. All rights reserved.
doi:10.1016/j.polymer.2011.01.003

end [18,19]. These three kinds of polymeric precursors with benzoxazine moieties were allowed later crosslinking for dimensional stability, chemical resistance, and high-temperature stability.

(iii) Design and synthesis of new benzoxazine monomers with additional functionality. One strategy was introducing additional polymerizable groups into benzoxazine, such as nitrile [20], acetylene [21], propargyl [22], allyl [23], maleimide [24] or epoxy [25] functionalities. This approach allowed increasing crosslinking density and minimizing dangling side groups, thus leading to improving toughness and thermal properties. Another strategy was introducing self-catalyst groups into benzoxazine. Carboxylic acid [26], oxyalcohol [27] and primary amine [28] functional groups were connected to benzoxazine to lower the polymerization temperature. Furthermore, the effect of different substituted groups on polymerization temperature and thermal stability of polybenzoxazine were also investigated in-depth [29].

Among the mentioned above the three methods to improve the performance of polybenzoxazine, designing new benzoxazine monomer is a more attractive approach to overcome the shortcomings of traditional polybenzoxazine. By now, although most of benzoxazine monomers consisted of organic element only, more and more attention has been paid to design and synthesis of inorganic heteroatom-containing benzoxazine monomer [30–35]. Cyclotriphosphazene (CP) derivatives are typical classes of organic–inorganic compounds with a planar non-delocalized cyclic ring consisting of alternating N and P atoms. Six functional groups can be attached onto a CP ring and the groups are normally projected above and below the CP plane due to steric hindrance [36–38]. Because of the versatility of cyclotriphosphazene chemistry, the CP ring of high stability and biocompatibility allows a wide range of functional groups to be attached onto CP. Highly branched conductive polyaniline with high electrochromic contrast based on CP [39], star-branched polymers with CP cores [40], catalysts of transition metal ionic compounds based on CP [41], CP conjugates with varied properties in vitro [42] and flame-retardant CP-containing polyurethanes [43] were prepared through different methods. By introducing the CP units into the polymers or compounds, the corresponding hybrid materials were endowed with thermal stability and environment-friendly flame-retardant properties or other functionalities.

In current study, a star-like benzoxazine monomer based on CP has been synthesized, and the new benzoxazine monomer possesses six benzoxazine moieties substituted onto CP ring. The new hyperbranched benzoxazine monomer underwent ring-opening polymerization with or without catalysts to produce highly dimensional crosslinking structure with rigidly inorganic CP as the core. The structure of the new monomer was confirmed by ^{1}H NMR, ^{13}C NMR, ^{31}P NMR and elemental analysis. Fourier transform infrared spectroscopy (FT-IR) and differential scanning calorimetry (DSC) were used to study the thermal ring-opening polymerization reaction of the monomer; the thermal property and mechanic performance of the thermoset polymer were also evaluated by thermal gravimetric analyzer and dynamic mechanical thermal analysis (DMA), respectively.

2. Experimental

2.1. Materials

4-acetamidophenol (98%) was purchased from Alfa Aesar Reagent Co., Ltd., USA. Salicylaldehyde (≥98%), sodium borohydride (96%), paraformaldehyde (95%), phenol, p-hydroxylbenzoic acid (≥99%), p-aminobenzoic acid (≥99%), sodium hydroxide (≥96%), and potassium carbonate were all gained from Sinopharm Chemical Reagent Co., Ltd., China. Hexachlorocyclotriphosphazene (synthesized as described in the literature [44]) was recrystallized from dry hexane followed by sublimation (60 °C, 0.05 mmHg) twice before use (mp 112.5–113.0 °C). Hexaphenoxycyclotriphosphazene (HPP) was prepared according to the report [45]. All solvents were purified by standard procedures.

2.2. Measurements

The structure of the compound was verified by proton (^{1}H), carbon (^{13}C) and phosphorus (^{31}P) nuclear magnetic resonance spectroscopy (NMR) using Bruker AV400 NMR spectrometer at proton frequency of 400 MHz as well as the corresponding carbon and phosphorus frequencies at room temperature using deuterated solvents as the solvent. Signals were averaged from 256 transients for ^{1}H NMR and ^{31}P NMR, and 1024 transients for ^{13}C NMR to yield spectra with sufficient signal-to-noise ratio. Thermal transitions were monitored with a differential scanning calorimeter (DSC), Model 204F1 from NETZSCH Instruments, and scan rate of 10 °C/min over a temperature range of 30–300 °C and nitrogen flow rate of 20 mL/min were used in DSC experiments. Thermogravimetric analysis (TGA) was performed with a NETZSCH Instruments' High Resolution STA 409PC thermogravimetric analyzer that was purged with nitrogen at a flow rate of 70 mL/min. A heating rate of 20 °C/min was used and scanning range was from 40 °C to 850 °C. Infrared spectra were recorded using a Bruker VERTEX 70 Fourier transform infrared spectrometer (FT-IR) with a heating device. Elemental analysis was carried out on a German Vario Micro cube microanalyzer. Mechanical properties were measured using a dynamic mechanical thermal analysis (DMA) apparatus (PerkinElmer, Diamond DMA). Specimens (50 × 10 × 1.0 mm) were tested in 3 point bending mode. The thermal transitions were studied in the scope of 20–200 °C at a heating rate of 4 °C/min and at a fixed frequency of 1 Hz.

2.3. Synthesis of $[N_3P_3(OC_6H_4\{NHC(O)CH_3\}\text{-}4)_6]$ (**I**)

This compound was synthesized as reported [46]. White crystal, Yield: 91%, MP. 252–255 °C ^{1}H NMR (DMSO-d_6, TMS, ppm): 9.92 (1H, –NH), 6.79–7.45(4H, dd, Ar–H), 2.04(3H, $-CH_3$). ^{13}C NMR (DMSO-d_6, TMS, ppm): 168.0(C=O), 144.9(C–O), 136.4(C–N), 120.5 (CH), 119.9(CH), 23.8(CH_3). ^{31}P NMR (DMSO-d_6, ppm): 9.18.

2.4. Synthesis of $[N_3P_3(OC_6H_4\{NH_2\}\text{-}4)_6]$ (**II**)

The compound was synthesized as reported [46]. White powder, yield: 80%, MP. 172–174 °C ^{1}H NMR (DMSO-d_6, TMS, ppm):

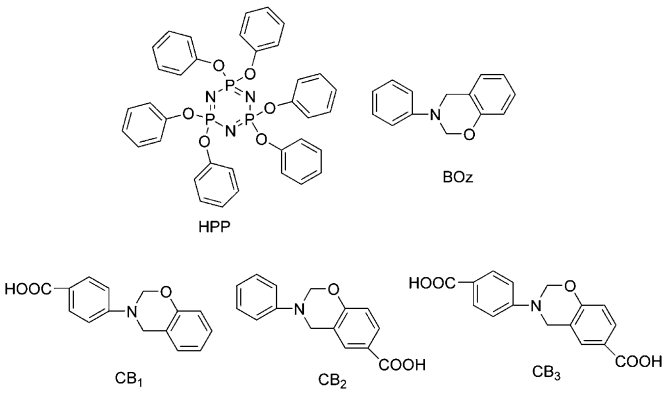

Fig. 1. The structures of HPP, BOz, CB_1, CB_2 and CB_3.

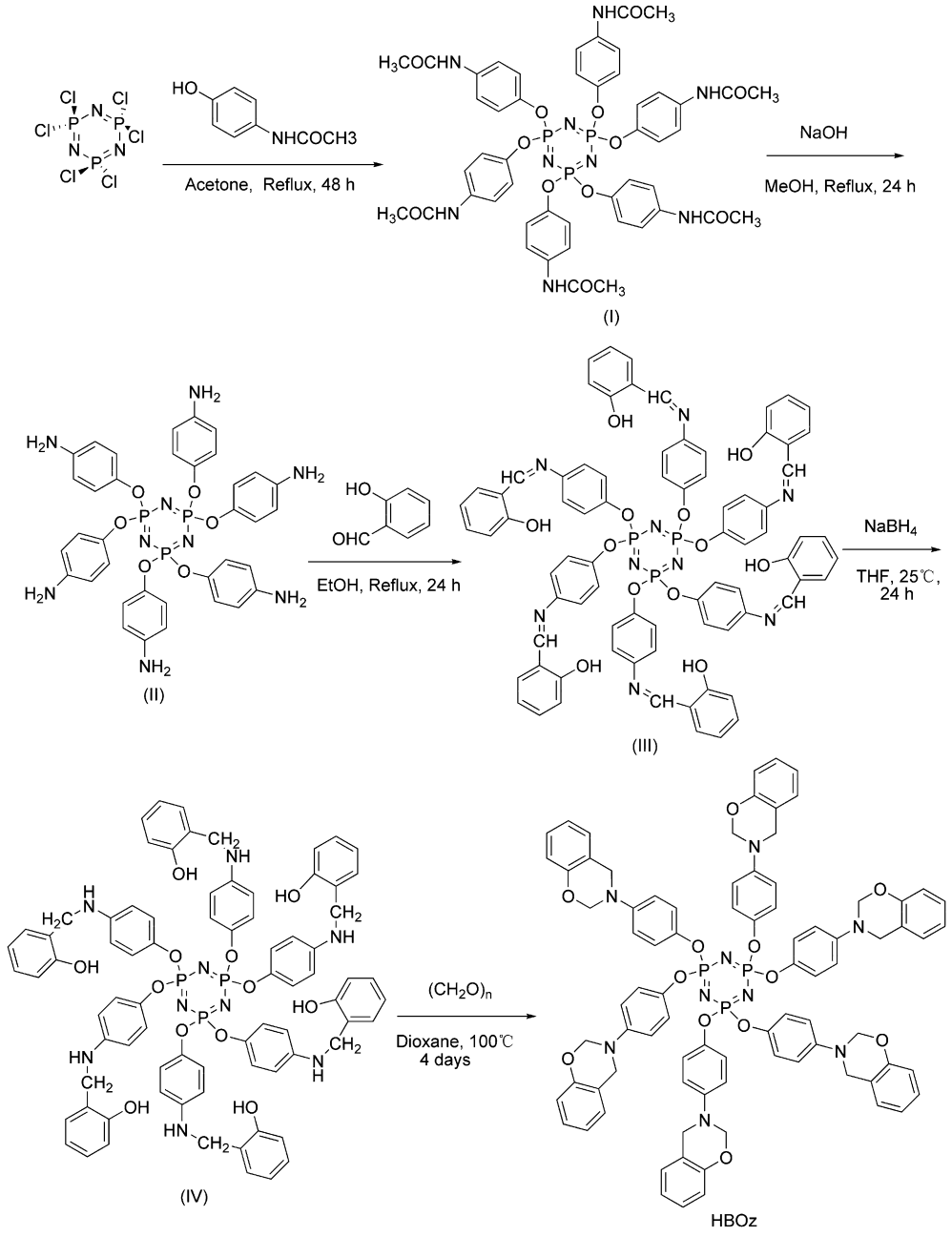

Scheme 1. Synthesis of highly branched benzoxazine HBOz.

6.41–6.52(4H, dd, Ar–H), 4.91(2H, Ar–NH_2). ^{13}C NMR (DMSO-d_6, TMS, ppm): 145.3(C–N), 140.5(C–O), 120.6(CH), 113.9(CH). ^{31}P NMR (DMSO-d_6, ppm): 10.67.

2.5. Synthesis of $[N_3P_3(OC_6H_4\{NHCC_6H_4(2\text{-}OH)\}\text{-}4)_6]$ (**III**)

A solution of salicylaldehyde (18.3 g, 149.9 mmol) in ethanol (50 mL) was added to a solution of **II** (16.3 g, 20.8 mmol) in ethanol (200 mL) under argon atmosphere, and the mixture was refluxed under vigorous stirring for 24 h. The resulting yellow solid (compound **III**) was filtered off and washed with a large excess of water, ethanol (3 × 5 mL), and hexane (3 × 5 mL) and dried in vacuum at 40 °C for 48 h. Yield: 27.5 g (96%), MP. 152–154 °C ^{1}H NMR (DMSO-d_6, TMS, ppm): 12.88(1H, CH=N), 8.84(1H, HO–Ar), 6.86–7.49(8H, Ar–H). ^{13}C NMR (DMSO-d_6, TMS, ppm): 164.5(C–OH), 161.3(C=N), 149.6(C–O), 146.5(C–N), 134.4(CH), 133.7(CH), 123.8(CH), 122.6(CH), 120.3(C), 120.2(CH), 117.7(CH). ^{31}P NMR (DMSO-d_6, ppm): 9.12. Elemental analysis Calcd. (%) for $C_{78}H_{60}N_9O_{12}P_3$: C, 66.52; H, 4.29; N, 8.95. Found: C, 65.46; H, 4.33; N, 9.00.

2.6. Synthesis of $[N_3P_3(OC_6H_4\{NHCH_2C_6H_4(2\text{-}OH)\}\text{-}4)_6]$ (**IV**)

Sodium borohydride (1.8 g, 46.1 mmol) was added to a solution of **III** (18 g, 12.8 mmol) in 150 mL tetrahydrofuran (THF) in small portion while stirring. After reaction at 25 °C for 12 h, 100 mL water was added to the solution, and the mixture was stirred at 25 °C for another 12 h. Then the solution was evaporated under reduced pressure to remove the organic solvent, the resulting solid was extracted with CH_2Cl_2, washed with water, dried over anhydrous Na_2SO_4, concentrated and precipitated in petroleum ether. Pale

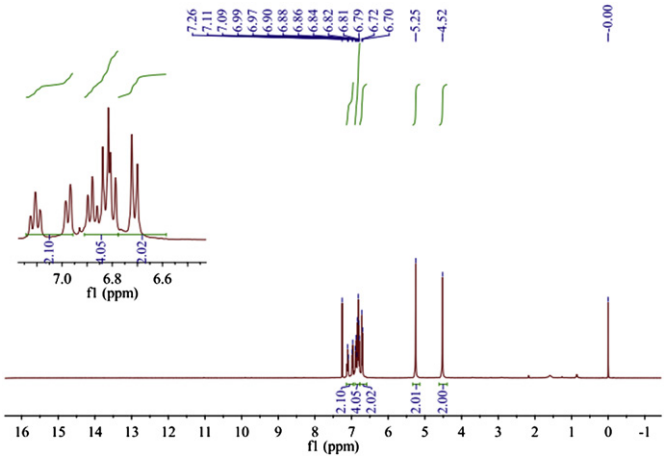

Fig. 2. ^{1}H NMR spectrum of HBOz (solvent: $CDCl_3$).

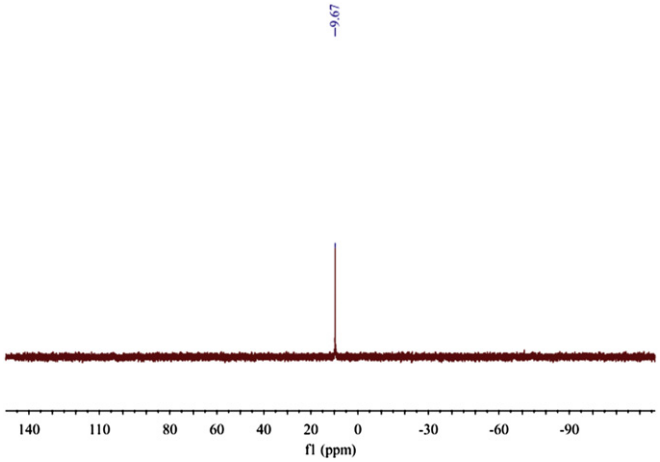

Fig. 4. ^{31}P NMR spectrum of HBOz (solvent: $CDCl_3$).

powder was gained, and dried in vacuum at 40 °C for 48 h. Yield: 16.3 g (90%), MP. 154–156 °C ^{1}H NMR (Acetone-d_6, TMS, ppm): 9.50 (1H, HO–Ar), 6.41–7.17(8H, Ar–H), 5.78(1H, NH), 4.14–4.16(2H, CH_2). ^{13}C NMR (Acetone-d_6, TMS, ppm): 155.9(C–OH), 146.8(C–N), 134.9(C–O), 129.2(C–CH_2), 128.3(CH), 126.4(CH), 121.8(CH), 119.6 (CH), 115.7(CH), 113.2(CH), 42.8(CH_2). ^{31}P NMR (Acetone-d_6, ppm): 10.62. Elemental analysis Calcd. (%) for $C_{78}H_{72}N_9O_{12}P_3$: C, 65.96; H, 5.11; N, 8.88. Found: C, 65.78; H, 5.06; N, 8.88.

2.7. Synthesis of $[N_3P_3(OC_6H_4\{NCH_2CH_2C_6H_4(2\text{-}O)\}\text{-}4)_6]$ (HBOz)

A solution of **IV** (10.0 g, 7.0 mmol) and paraformaldehyde (1.9 g, 63.4 mmol) in 150 mL 1,4-dioxane was stirred at 100 °C for 4 days under an argon atmosphere. Then the solution was evaporated under reduced pressure to remove the organic solvent, the resulting solid was dissolved in CH_2Cl_2, and washed with diluted solution of sodium hydroxide. The organic layer was collected, dried over anhydrous Na_2SO_4, concentrated and then precipitated in petroleum ether. A light yellow powder was collected, dried in vacuum at 40 °C for 48 h. Yield: 9.9 g (95%), MP. 75–77 °C.

2.8. Synthesis of $C_6H_4NCH_2CH_2C_6H_4(2\text{-}O)$ (BOz), (4-COOH) $C_6H_4NCH_2CH_2C_6H_4(2\text{-}O)$ (CB_1), $C_6H_4NCH_2CH_2C_6H_3(2\text{-}O)(4\text{-}COOH)$ (CB_2), and (4-COOH)$C_6H_4NCH_2CH_2C_6H_3(2\text{-}O)(4\text{-}COOH)$ (CB_3)

The structures of BOz, CB_1, CB_2 and CB_3 were showed in Fig. 1 and synthesized as reported methods [26].

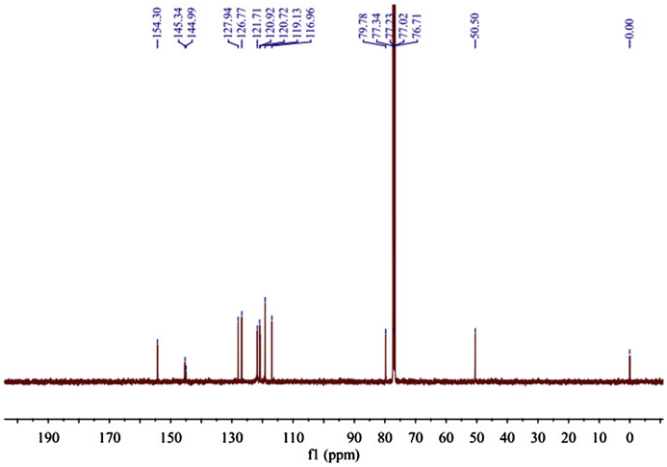

Fig. 3. ^{13}C NMR spectrum of HBOz (solvent: $CDCl_3$).

3. Results and discussion

3.1. Synthesis and characterization

The HBOz monomer was synthesized according to Scheme 1. The overall yield after five steps was about 60%. The purified sample was satisfactory for further analysis. Herein, the structure of the novel HBOz monomer was confirmed with ^{1}H, ^{13}C, ^{31}P NMR and element analysis.

Fig. 2 shows the ^{1}H NMR spectrum of HBOz. Resonances appearing at 4.52 ppm and 5.25 ppm are assigned to the methylene protons of Ar–CH_2–N and O–CH_2–N of the oxazine ring, respectively. The multiplets at 6.70–6.72, 6.79–6.88, and 6.90–7.11 ppm are assigned to the aromatic protons.

In the corresponding ^{13}C NMR spectrum in Fig. 3, resonances appearing at 50.5 ppm and 79.7 ppm are assigned to the methylene carbons of Ar–CH_2–N and O–CH_2–N of the oxazine ring, respectively. Other chemical shifts (ppm) are assigned to the aromatic carbon resonances: 154.3(C–O), 145.3(C–N), 144.9(C–O), 127.9 (CH), 126.8(CH), 121.7(C), 120.9(CH), 120.7(CH), 119.1(CH), 116.9 (CH).

The ^{31}P NMR is shown in Fig. 4, and there is a single peak at 9.67 ppm, which indicates that the substituted reaction onto CP ring was complete.

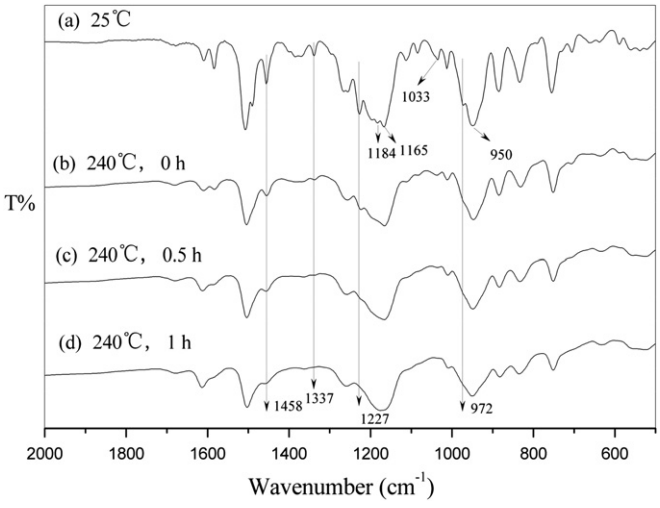

Fig. 5. The FT-IR spectra of HBOz and HBOz curing at 240 °C for different time in the region between 2000 and 500 cm^{-1}.

Elemental analysis for HBOz is following: Calcd. (%): C, 67.60; H, 4.86; N, 8.45. Found: C, 66.86; H, 4.91; N, 8.57. All analysis results indicate that the desired hyperbranched benzoxazine monomer has been prepared successfully.

3.2. Curing behavior of HBOz monomer monitored by FT-IR

The ring-opening polymerization characteristic was monitored by FT-IR spectrometer, the results were shown in Fig. 5. The KBr pill containing HBOz powder was heated at 240 °C for different time and the FT-IR spectra were recorded. The characteristic absorption bands due to benzoxazine structure are situated at 972 cm^{-1} (out of plane-bending vibrations of C–H), 1227 cm^{-1} (asymmetric stretching of C–O–C), 1184 cm^{-1} (asymmetric stretching of C–N–C), 1033 cm^{-1} (symmetric stretching of C–O–C), and 1337 cm^{-1} (CH_2 wagging), respectively [47]. The wave-numbers from 700 cm^{-1} to 900 cm^{-1} and at 1458 cm^{-1} are assigned to disubstituted benzene ring; two very strong absorption peaks located at 950 cm^{-1} and 1165 cm^{-1} are corresponding to stretching of P–O–Ar and N=P, respectively. The spectrum of Fig. 5(b) was recorded immediately after the sample pill was quickly heated to 240 °C. It was found that the intensity of characteristic absorption of benzoxazine structure and disubstituted benzene ring obviously decreased, the characteristic peaks located at 972 cm^{-1} and 1337 cm^{-1} were nearly to disappear. When the curing time was prolonged to 0.5 h and 1 h at 240 °C, the intensity of benzoxazine characteristic peaks continued to decrease, then disappeared after 1 h. These results indicate that the HBOz monomer has been polymerized completely. At the same time, the intensity of disubstituted benzene ring's characteristic peaks located in the range of 700 cm^{-1}–900 cm^{-1} and 1458 cm^{-1} also began to decrease gradually, this indicated a high substitution pattern of the aromatic rings as a consequence of the crosslinking reactions, and the ring-opening reaction model of HBOz was displayed in Scheme 2. Besides, comparing the absorption peaks located at 950 cm^{-1} and 1165 cm^{-1} from Fig. 5(a–d), there were no significant changes even under high temperature for 1 h, which illustrated that the inorganic CP ring was thermally stable at such condition.

3.3. Curing behavior of HBOz monomer scanned by DSC

It is known that the high polymerization temperature is one important factor that limits the application of polybenzoxazine. The curing behavior of the new monomer HBOz was examined by DSC. Herein, several catalysts were used to estimate the possibility of decreasing the polymerization temperature of HBOz monomer by mixing the catalysts with HBOz powder. Three compounds whose boiling point temperatures are higher than 180 °C were utilized as the catalyst because of the high polymerization temperature of benzoxazines. These catalysts were imidazole (C_i), N, N-dimethylbenzylamine (C_{ii}) and a neutral salt [48] obtained from the reaction of diethanolamine and p-toluenesulfonic acid with the molar ratio 1:1 (C_{iii}). The results of the heat curing behaviors using the catalysts to reduce the polymerization temperatures of the monomer were shown in Fig. 6, a sharp exothermic peak corresponding to the ring-opening polymerization was observed for HBOz, the onset and maximum temperatures of the exotherm were 177 °C and 225 °C, respectively. The amount of exotherm for HBOz was 215.5 J/g. In addition, there was a small endothermic peak corresponding to melting point at 77 °C for HBOz. By adding curing catalysts with the content of 3 wt% to HBOz monomer, the exothermic peaks changed obviously from the DSC results. For HBOz/C_i-3 wt%, the onset and maximum temperatures of the exotherm were reduced to 132 °C and 215 °C, respectively. The corresponding amount of exotherm was lowered to 202.4 J/g; for HBOz/C_{ii}-3 wt% and HBOz/C_{iii}-3 wt%, the onset temperatures of the exotherm were both reduced to 135 °C, the maximum temperatures of the exotherm were separately lowered to 222 °C and 212 °C. And the corresponding amounts of exotherm were correspondingly diminished to 204.5 J/g and 70.8 J/g, respectively. Comparing to HBOz, the polymerization temperatures and enthalpies were obviously reduced. Besides, the HBOz/catalysts mixtures with catalysts' contents of 1 wt% and 5 wt% were also investigated and the results were summarized in Table 1. It was found that the onset exothermic temperatures, maximum exothermic temperatures and exothermic enthalpies were all decreased with the increase of the catalysts' content.

On the other hand, carboxylic acid-containing benzoxazines (Fig. 1) used as the functional catalysts were also studied. Andreu [26] reported that CB_1, CB_2 and CB_3 produced significant decrease in the polymerization temperature of BOz monomer. Herein, the carboxylic acid-containing benzoxazines were also added to HBOz monomer as curing catalysts. To carry out this study, several samples of HBOz/CB_1, HBOz/CB_2 and HBOz/CB_3 were prepared, and scanned by DSC. The results obtained from heating DSC plots were collected in Fig. 7. When small amount (3 wt%) of carboxylic acid-

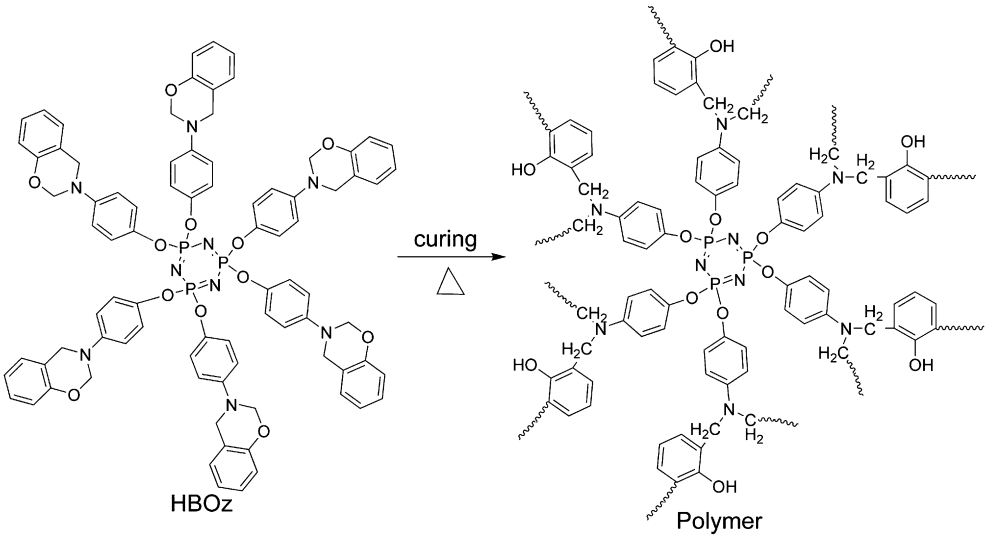

Scheme 2. Polymerization of HBOz monomer under heating.

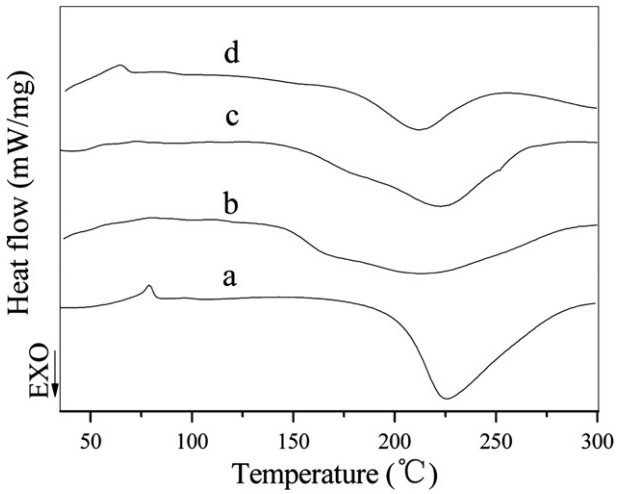

Fig. 6. DSC plots of HBOz monomer using common catalysts with the content of 3 wt%. a. HBOz, b. HBOz/C_i-3 wt%, c. HBOz/C_{ii}-3 wt%, d. HBOz/C_{iii}-3 wt%.

containing benzoxazines were added, the maximum exothermic peaks had little change, the onset temperatures of the exothermic peaks (T_o) just reduced a little comparing with that of pure HBOz: the T_o of HBOz/CB_1-3 wt%, HBOz/CB_2-3 wt% and HBOz/CB_3-3 wt% were lowered to 172 °C, 168 °C and 172 °C, respectively; and it was 177 °C for HBOz. However, the exothermic enthalpies had significant decrease: the enthalpies of HBOz/CB_1-3 wt%, HBOz/CB_2-3 wt% and HBOz/CB_3-3 wt% were reduced to 191.6 J/g, 197.7 J/g and 191.3 J/g, respectively; while it was 215.5 J/g for HBOz. Changing the amounts of carboxylic acid-containing benzoxazines at 1 wt% and 5 wt% level resulted in similar effect and the results were also summarized in Table 1. We can conclude that carboxylic acid-containing benzoxazines show little effect on decrease polymerization temperature, but the exothermic enthalpies are diminished obviously with increasing the catalysts' content and it will let the monomer mixture polymerize more mildly than that of pure monomer.

Table 1
Thermal property of HBOz/Catalysts series samples.

Samples	T_m[a] (°C)	T_o[b] (°C)	T_{max}[c] (°C)	ΔH[d] (J/g)	$T_{5\%}$[e] (°C)	$T_{10\%}$[f] (°C)	T_{max}[g] (°C)	Y_c[h] (%)
HBOz	77	177	225	215.5	403	449	453	66.9
HBOz/C_i-1 wt%	80	140	224	213.6	374	431	445	60.4
HBOz/C_i-3 wt%	–	132	215	202.4	378	419	441	59.4
HBOz/C_i-5 wt%	88	115	208	193.5	373	405	459	57.8
HBOz/C_{ii}-1 wt%	70	167	228	207.2	341	401	440	56.7
HBOz/C_{ii}-3 wt%	–	135	222	204.5	379	422	435	57.2
HBOz/C_{ii}-5 wt%	78	130	225	202.7	301	402	471	30.3
HBOz/C_{iii}-1 wt%	78	138	220	135.2	363	401	420	60.5
HBOz/C_{iii}-3 wt%	68	135	212	70.88	329	374	434	51.2
HBOz/C_{iii}-5 wt%	–	130	203	60.1	331	384	423	43.5
HBOz/CB_1-1 wt%	78	176	225	199.6	395	435	492	61.4
HBOz/CB_1-3 wt%	79	172	225	191.6	409	450	478	62.4
HBOz/CB_1-5 wt%	76	168	222	153.1	415	457	461	59.0
HBOz/CB_2-1 wt%	78	170	225	203.7	398	436	450	58.7
HBOz/CB_2-3 wt%	78	168	225	197.7	400	441	474	60.3
HBOz/CB_2-5 wt%	78	160	225	189.0	393	436	470	60.1
HBOz/CB_3-1 wt%	77	175	225	202.1	390	429	445	57.7
HBOz/CB_3-3 wt%	79	172	225	191.3	395	437	468	59.3
HBOz/CB_3-5 wt%	75	168	221	187.5	387	429	462	58.5

[a] Melt point temperature determined by DSC (10 °C/min).
[b] Onset temperature of exothermic peak.
[c] Maximum of the polymerization exotherm.
[d] Polymerization enthalpy by DSC.
[e] $T_{5\%}$: The temperature for which the weight loss is 5% by TGA scan (20 °C/min) under nitrogen.
[f] $T_{10\%}$: The temperature for which the weight loss is 10%.
[g] T_{max}: Maximum weight loss temperature.
[h] Y_c: Char yields at 850 °C.

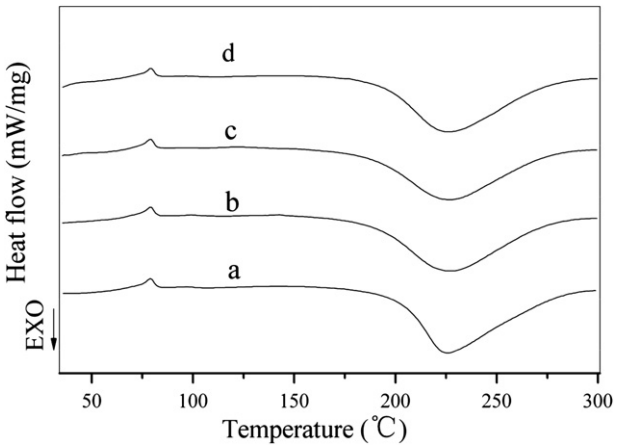

Fig. 7. DSC plots of HBOz monomer using functional catalysts with the content of 3 wt %. a. HBOz, b. HBOz/CB_1-3 wt%, c. HBOz/CB_2-3 wt%, d. HBOz/CB_3-3 wt%.

Comparing the two series of catalysts, it is clear to find that the common curing catalysts (C_i, C_{ii} and C_{iii}) are more suitable for the curing of HBOz than the carboxylic acid-containing benzoxazines, they effectively decrease the polymerization temperature. The carboxylic acid-containing benzoxazines reduced the polymerization temperature of BOz effectively in report [47], but not obviously in HBOz system. Possible reason is that the common curing catalysts can dilute the reaction mixture, low viscosity is a benefit to the polymerization rate; but functional carboxylic acid-containing catalysts can copolymerize with the monomer, the high viscosity system owing to the highly crosslinking polymerization reaction between HBOz and functional catalysts restrains the catalytic activity of the carboxylic acid groups located on the carboxylic acid-containing benzoxazines (Fig. 7).

3.4. Thermal properties of the new polybenzoxazines

A series of samples forming by HBOz powder with different curing catalysts (see in Table 1) were added to test tubes, and the

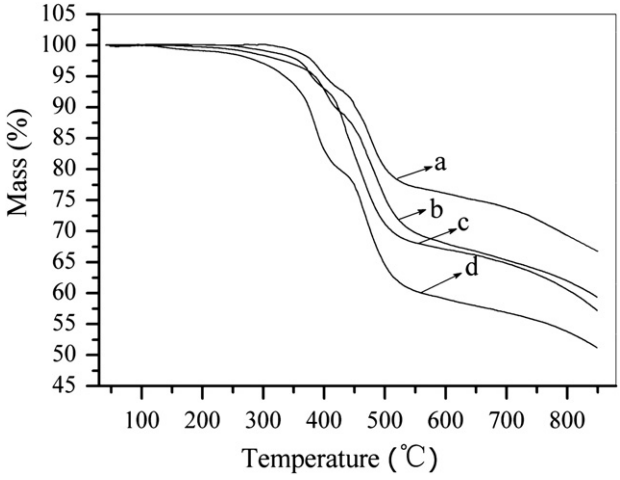

Fig. 8. TG curves of PHBOz by curing HBOz monomer using common curing catalysts with the content of 3 wt%. a. PHBOz, b. PHBOz/C_i-3 wt%, c. PHBOz/C_{ii}-3 wt%, d. PHBOz/C_{iii}-3 wt%.

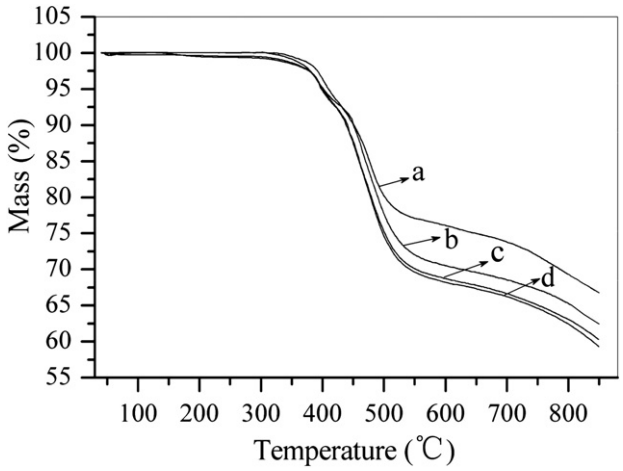

Fig. 9. TG curves of PHBOz by curing HBOz monomer using functional curing catalysts with the content of 3 wt%. a. PHBOz, b. PHBOz/CB_1-3 wt%, c. PHBOz/CB_2-3 wt%, d. PHBOz/CB_3-3 wt%.

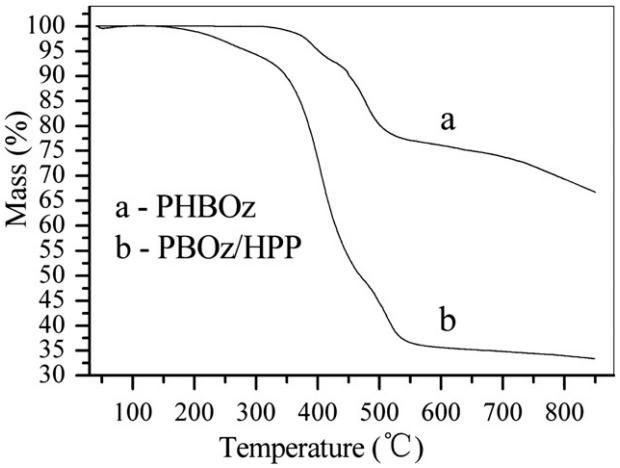

Fig. 11. TG curves of PHBOz and PBOz/HPP.

sample tubes were cured stepwise at 120 °C for 1 h and 200 °C for 2 h, and then post-cured at 220 and 240 °C for 1 h each in salt-bath under an argon atmosphere. All the cured samples were dark red color. Thermal stability of the novel polybenzoxazines was investigated by TGA. The TGA profiles of polybenzoxazines from the polymerization of HBOz monomer, HBOz/C_i-3 wt%, HBOz/C_{ii}-3 wt%, and HBOz/C_{iii}-3 wt% were shown in Fig. 8. The 5% and 10% weight loss temperatures ($T_{5\%}$ and $T_{10\%}$) for PHBOz were 403 and 449 °C, respectively. While with 3 wt% catalysts, the $T_{5\%}$ and $T_{10\%}$ were all lower than that of PHBOz: for PHBOz/C_i-3 wt%, they were 378 and 419 °C, respectively; for PHBOz/C_{ii}-3 wt%, they were 379 and 422 °C; meanwhile they were 329 and 374 °C for PHBOz/C_{iii}-3 wt%. Similarly, the maximum weight loss temperature (T_m) of PHBOz was also higher than those of the others with catalysts, and the details were shown in Table 1. The Char yields at 850 °C (Y_c) of polybenzoxazines were also recorded in Table 1. The Y_c of PHBOz was as high as 66.9%, and the others with 3 wt% these common catalysts were much lower than that of PHBOz, PHBOz/C_{iii}-3 wt% sample held the lowest yield, only 51.2%. It is well known that the common catalysts do not copolymerize with the monomer for lack of reactive groups; they remain in the polybenzoxazine systems after polymerization and act as unstable impurities. The remaining catalyst will accelerate the degradation of polybenzoxazine under high temperature and result in reducing the heat resistance (Fig. 9).

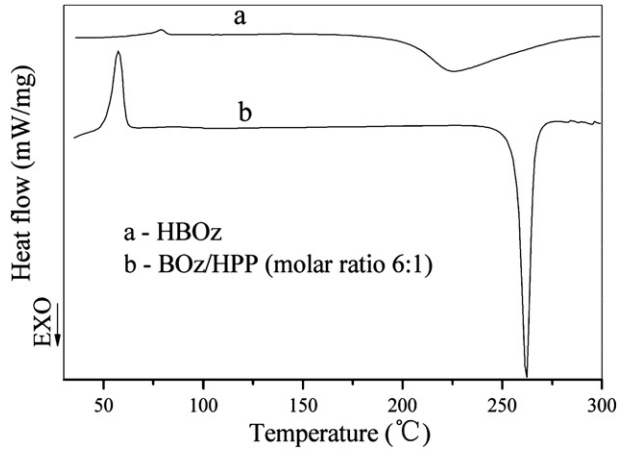

Fig. 10. DSC curves of HBOz and BOz/HPP (molar ratio 6:1).

The thermal stability of the novel polybenzoxazines using functional curing catalysts (CB_1, CB_2 and CB_3) was also investigated by TGA, the results were shown in Fig. 9 and Table 1. It was excited to find that the thermal stability of the polybenzoxazines with acid-containing benzoxazines was as good as that of PHBOz, some of them were even higher than that of PHBOz. For example, the 5% and T_m for PHBOz/CB_1 were higher than that of PHBOz, they were 409 and 478 °C, respectively (PHBOz were separately 401 and 451 °C). The $T_{5\%}$ and $T_{10\%}$ of PHBOz with different contents of functional catalysts were separately located in the range of 390–410 °C and 430–460 °C. And the T_m and Y_c were mainly distributed in the range of 460–490 °C and 58%–62%, respectively. These factors reflecting to the thermal stability were better than that of PHBOz with common curing catalysts (C_i, C_{ii} and C_{iii}). The reasons maybe result from the reactive benzoxazines groups on the acid-containing benzoxazines, which can copolymerize with HBOz monomers and get into the skeleton of crosslinking system.

3.5. Thermal properties of HBOz and PHBOz comparing to monofunctional benzoxazine and its polymers

To compare the thermal properties with common polybenzoxazines, another benzoxazine sample was introduced, which was prepared from the mixtures of BOz monomer and HPP at molar ratio of 6:1 (Its theoretical elemental composition is similar to HBOz). BOz/HPP was polymerized under the same curing condition of PHBOz to obtain PBOz/HPP polymer. The DSC curves of HBOz monomer and BOz/HPP are shown in Fig. 10. A sharp exothermic

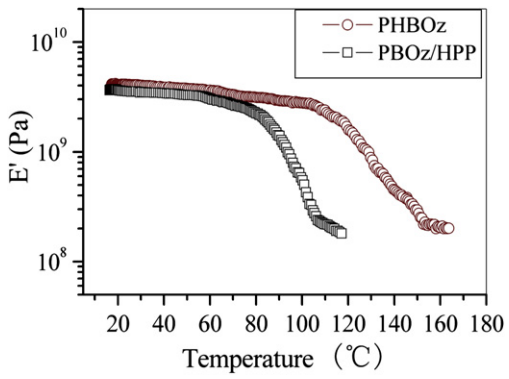

Fig. 12. Storage moduli of PHBOz and PBOz/HPP polybenzoxazines.

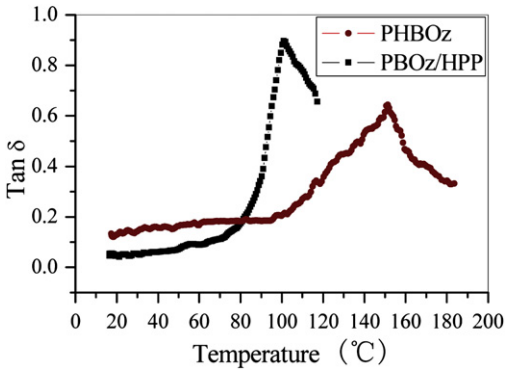

Fig. 13. Tanδ of PHBOz and PBOz/HPP polybenzoxazines.

peak is observed for BOz/HPP, and the maximum temperature of the exotherm is 262 °C, which is nearly 40 °C higher than that of HBOz monomer. An endothermic peak at 58 °C is assigned to the melting point of BOz/HPP mixture, which is a little lower than that of HBOz. The enthalpy of BOz/HPP is 211.2 J/g, which is near to 215.5 J/g of HBOz.

The thermal stability of PBOz/HPP and PHBOz was also carried out on TGA, the results were shown in Fig. 11. As expected, the thermal stability of PHBOz was much higher than that of PBOz/HPP, $T_{5\%}$ of them were 403 and 285 °C, respectively; and Y_c at 850 °C of them were 66.9% and 33.4%, respectively. The results illustrate that PHBOz polymer shows much higher thermal stability than that of common monofunctional polybenzoxazine composite. The reason is deemed that the inorganic cyclotriphosphazene ring possesses high thermal stability for its unique structure and can act as an ideal core to prepare high-performance organic–inorganic hybrid materials. At the same time the branched benzoxazine moieties are spatially distributed above and below the CP ring, and bring the new polybenzoxazine a highly spatial crosslinking structure which minimizes dangling side groups and improves dimensionally thermal stability.

3.6. Mechanic property of the new polybenzoxazine

The dynamic mechanical behavior of the cured benzoxazine resins was obtained as a function of the temperature beginning in the glassy state of each sample to the rubbery plateau of each material. As seen in Fig. 12, the storage modulus (E′) of PHBOz at room temperature is 4.14 GPa, which is a little higher than that of PBOz/HPP (3.64 GPa). The E′ value of PHBOz starts to decrease at about 120 °C, while the E′ value of PBOz/HPP begins to decrease at about 80 °C. Comparing the decreasing slope of the E′ value from glassy state to rubbery plateau for PHBOz and PBOz/HPP, it is found that the decreasing slope of PHBOz is obviously lower than that of PBOz/HPP. The glass transition temperatures (T_g) of the polybenzoxazines can be deduced in Fig. 13 from the corresponding temperature of peak of tanδ value. T_g of PHBOz and PBOz/HPP are 152 °C and 101 °C, respectively. The tanδ value of PHBOz is much lower than that of PBOz/HPP after 80 °C because of higher dimensional crosslinking structures of PHBOz. It is known to us that PBOz/HPP is low crosslinking structure, while it is highly steric crosslinking structure for PHBOz curing from the star-branched organic–inorganic hybrid benzoxazine. Besides, there are lots of rigid and stable CP in the PHBOz as crosslinking cores, which also contribute to improving the mechanic properties of PHBOz to some extent. For these reasons mentioned above, PHBOz shows higher mechanic performance than that of PBOz/HPP under heat.

4. Conclusions

We have synthesized a novel star-branched benzoxazine monomer based on CP ring, the new organic–inorganic hybrid benzoxazine monomer possesses low melting point (77 °C) and good solubility in common solvents though with high molecular weight. The new benzoxazine monomer could be ring-opening polymerized completely at 240 °C for 1 h, according to the disappearance of benzoxazine characteristic peaks located at 1227 cm^{-1} and 972 cm^{-1}. A sharp exothermic peak at 225 °C for ring-opening polymerization of the benzoxazine monomer was observed at DSC plots, and the onset polymerized temperature was about 180 °C. Two species of curing catalysts were used to reduce the polymerization temperature, the common catalysts (C_i, C_{ii} and C_{iii}) could effectively decrease the onset polymerization temperature and exothermic enthalpy with small amount of them ($\leq$5 wt%), but they led to reduction in corresponding polymers' thermal stability; while using the functional catalysts (carboxylic acid-containing benzoxazines: CB_1, CB_2 and CB_3), the onset polymerization temperatures had little decrease, but final polymers held excellent thermal stability from TGA results, some of them were even higher than that of the pure polybenzoxazine. Comparing to the blending resin of BOz/HPP, the polymerization temperature of the benzoxazine monomer was about 40 °C lower than that of BOz/HPP mixture. Besides, the hyperbranched polybenzoxazine also showed outstanding thermal stability and good mechanic performance resulting from the highly dimensional crosslinking structure with the core of rigid and stable inorganic CP ring. It had higher thermal stability ($T_{5\%}$ at 403 °C) and higher char yield (66.9% char yield at 850 °C) than that of PBOz/HPP blend. And the T_g of PHBOz was as high as 152 °C, which was about 50 °C higher than that of PBOz/HPP resin. The new polybenzoxazine may be an applicable material in the application of high technology for its excellent thermal stability and mechanic properties.

Acknowledgment

This work was supported by the National Natural Science Foundation of China (No. 50703013) and Independent Innovative Position of Hubei Province. All authors give sincerely thanks to Analysis and Testing Center of HUST for NMR and E.A. test.

Appendix. Supplementary material

Figures showing ^1H, ^{13}C, ^{31}P NMR, DSC plots and TGA curves can be found online at doi:10.1016/j.polymer.2011.01.003.

References

[1] (a) Chernykh A, Agag T, Ishida H. Polymer 2009;50:3153–7;
(b) Ning X, Ishida H. J Polym Sci Part A Polym Chem 1994;32:1121–9;
(c) Ishida H, Allen DJ. J Polym Sci Part B Polym Phys 1996;34:1019–130;
(d) Ghosh NN, Kiskan B, Yagci Y. Prog Polym Sci 2007;32:1344–91;
(e) Shen SB, Ishida H. J Polym Sci Part B Polym Phys 1999;37:3257–68;
(f) Kim HD, Ishida H. J Appl Polym Sci 2001;79:1207–19;
(g) Liu X, Gu Y. J Appl Polym Sci 2002;84:1107–13;
(h) Takeichi T, Agag T. High Perform Polym 2006;18:777–97.
[2] (a) Riess G, Schwob JM, Guth G, Roche M, Lande B. In: Culbertson BM, McGrath JE, editors. Advances in polymer synthesis. New York: Plenum; 1985. p. 27–40;
(b) Burke W. J Org Chem 1949;71:109–14.
[3] Yagci Y, Kiskan B, Ghosh N. J Polym Sci Part A Polym Chem 2009;47:5565–76.
[4] Jang J, Seo D. J Appl Polym Sci 1998;67:1–10.
[5] Ishida H, Lee YH. J Appl Polym Sci 2001;81:1021–34.
[6] Zheng SX, Lu H, Guo QP. Macromol Chem Phys 2004;205:1547–58.
[7] Takeichi T, Guo Y, Agag T. J Polym Sci Part A Polym Chem 2000;38:4165–76.
[8] Ishida H, Allen DJ. Polymer 1996;37:4487–95.
[9] Espinosa MA, Cádiz V, Galià M. J Polym Sci Part A Polym Chem 2004;42:279–89.
[10] Espinosa MA, Galià M, Cádiz V. Polymer 2004;45:6103–9.

[11] Agag T, Takeichi T. Polymer 2000;41:7083–90.
[12] Kiskan B, Demirel AL, Kamer O, Yagci Y. J Polym Sci Part A Polym Chem 2008;46:6780–8.
[13] Liu J. Synthesis, Characterization, Reaction Mechanism and Kinetics of 3,4-Dihydro-2H-1,3- benzoxazine and its Polymers. Ph.D. Thesis. Cleveland, OH: Case Western Reserve University; May 1995.
[14] Velez-Herrera P, Doyama K, Abe H. Macromolecules 2008;41:9704–14.
[15] Kiskan B, Demiray G, Yagci Y. J Polym Sci Part A Polym Chem 2008;46:3512–8.
[16] Ergin M, Kiskan B, Gacal B, Yagci Y. Macromolecules 2007;40:4724–7.
[17] Kukut M, Kiskan B, Yagci Y. Des Monomers Polym 2009;12:167–76.
[18] Kiskan B, Colak D, Muftuoglu AE, Cianga I, Yagci Y. Macromol Rapid Commun 2005;26:819–24.
[19] Tasdelen MA, Kiskan B, Yagci Y. Macromol Rapid Commun 2006;27:1539–44.
[20] Brunovska Z, Ishida H. J Appl Polym Sci 1999;73:2937–49.
[21] Kim HJ, Brunovska Z, Ishida H. Polymer 1999;40:6565–73.
[22] Agag T, Takeichi T. Macromolecules 2001;34:7257–63.
[23] Agag T, Takeichi T. Macromolecules 2003;36:6010–7.
[24] Ishida H, Ohba S. Polymer 2005;46:5588–95.
[25] Andreu R, Espinosa MA, Galià M, Cádiz V, Ronda JC, Reina JA. J Polym Sci Part A Polym Chem 2006;44:1529–40.
[26] Andreu R, Reina JA, Ronda JC. J Polym Sci Part A Polym Chem 2008;46:3353–66.
[27] Kiskan B, Koz B, Yagci Y. J Polym Sci Part A Polym Chem 2009;47:6955–61.
[28] Agag T, Arza CR, Maurer FHJ, Ishida H. Macromolecules 2010;43:2748–58.
[29] Sudo A, Hirayama S, Endo T. J Polym Sci Part A Polym Chem 2010;48:2777–82.
[30] Lin CH, Cai SX, Leu TS. J Polym Sci Part A Polym Chem 2006;44:3454–68.
[31] Liu Y, Hsu C, Chou C. J Polym Sci Part A Polym Chem 2007;45:1007–15.
[32] Huang J, Kuo S, Huang H. J Appl Polym Sci 2009;111:628–34.
[33] Spontón M, Ligadas G, Ronda JC, Galià M, Cádiz V. Polym Degrad Stab 2009;94:1693–9.
[34] Ye YS, Yen YC, Chang FC. Polymer 2009;50:3196–203.
[35] Liu YF, Yue ZQ, Gao JG. Polymer 2010;51:3722–9.
[36] Wisian-Neilson P. In: Glerià M, Jaeger RD, editors. Phosphazenes: a worldwide insight. New York: Nova Science; 2004. p. 109–25.
[37] Allcock HR. Chemistry and applications of polyphosphazenes. Hoboken: Wiley-Interscience; 2003 [part II].
[38] Sudhakar S, Sellinger A. Macromol Rapid Commun 2006;27:247–54.
[39] Jia P, Xu J, Ma J. Eur Polym J 2009;45:772–8.
[40] Chang JY, Ji HJ, Han MJ. Macromolecules 1994;27:1376–80.
[41] Harmjanz M, Scoot BL, Burns CJ. Chem Commun; 2002:1386–7.
[42] Cho YW, Lee J, Song S. Bioconjugate Chem 2005;16:1529–35.
[43] Yuan CY, Chen SY, Tsai CH. Polym Adv Technol 2005;16:393–9.
[44] Jaeger RD, Glerià M. Prog Polym Sci 1998;23:179–276.
[45] Ye C, Zhang Z, Liu W. Synth Commun 2002;32:203–9.
[46] Barberá J, Jiménez J, Laguna A. Chem Mater 2006;18:5437–45.
[47] Andreu R, Reina JA, Ronda JC. J Polym Sci Part A Polym Chem 2008;46:6091–101.
[48] Kimura H, Matsumoto A, Ohtsuka K. J Appl Polym Sci 2008;107:710–8.

Polymer 52 (2011) 1013–1018

Contents lists available at ScienceDirect

Polymer

journal homepage: www.elsevier.com/locate/polymer

Thermal cross-link behavior of an amorphous poly (para-arylene sulfide sulfone amide)

Yaqi Yang [a], Gang Zhang [b], Jing Liu [c], Shengru Long [b], Xiaojun Wang [b], Jie Yang [a,b,*]

[a] College of Polymer Science and Engineering, State Key Laboratory of Polymer Materials Engineering of China, Sichuan University, Chengdu 610065, PR China
[b] Institute of Materials Science and Technology, Sichuan University, Chengdu 610064, PR China
[c] College of Chemistry, Sichuan University, Chengdu 610064, PR China

ARTICLE INFO

Article history:
Received 13 September 2010
Received in revised form
10 December 2010
Accepted 1 January 2011
Available online 9 January 2011

Keywords:
Poly (para-arylene sulfide sulfone amide)
Thermal curing
Cross-link behavior

ABSTRACT

Cross-link behavior of an amorphous poly (para-arylene sulfide sulfone amide) synthesized via low temperature solution polycondensation was observed for the first time, when the polymer was subject to a series of thermal curing at 260 °C in air condition. The formation of cross-link network was demonstrated by the DSC and TGA results that T_g of the polymer enhanced from 259.17 °C to 268.89 °C, and the 1% weight loss temperature increased remarkably from 243.75 °C to 345.87 °C. EPR analysis further suggested that two kinds of free radicals, CO• and C•, induced by thermal curing were responsible for this cross-link behavior. According to FT-IR spectrum, the origin of these free radicals was confirmed as amide C=O group in the polymer backbone. The cross-linking type was attributed to conventional radical cross-link reaction and the cross-link mechanism was discussed in detail subsequently.

1. Introduction

Poly (phenylene sulfide) (PPS) is a semi-crystalline thermoplastic engineering polymer, which has attracted much attention from researchers due to its excellent mechanical properties, good solvent resistance, high temperature resistance and so on [1–10]. As a structurally modified material of PPS, an amorphous poly (arylene sulfide sulfone amide) (PASSA) was synthesized via low temperature solution polycondensation in our laboratory [11]. It possesses the desirable dimensional stability and chemical resistance of PPS as well as the high strength of polyamide (PA); in addition, it has higher glass-transition temperature than PPS which makes up for the disadvantage of PPS. PASSA is soluble in some polar solvents due to its improved solubility compared to PPS, such as *N*-methyl-2-pyrrolidone (NMP) and *N*,*N*-dimethylformamide (DMF), but it still has much higher chemical resistance than PA. The superior characteristics of PASSA make it valuable and potentially applicable in polymer electrolyte membranes, composite bipolar plates, conductive materials, surface mounted devices, vehicle sensors and so on [12–15].

Thermal behavior is one of the most significant characteristics of polymers due to its crucial influence in application. So it is of great importance to understand the changes in chemical structures and physical properties, which may occur during thermal histories. In recent years, a large number of experimental data have established the thermal properties of PPS [16–19]. Gies et al. [20] reported that PPS thermal curing in the presence of oxygen leaded to oxygen uptake in the form of sulfoxides in the PPS backbone. Perng [21] researched the mechanism and kinetic model for thermal decomposition behavior of PPS by stepwise pyrolysis/gas chromatography/mass spectrometry and thermogravimetry analysis/mass spectrometry techniques. However, there were few literatures that discussed the thermal properties of amorphous structurally modified materials of PPS. Wang [22] studied the thermal degradation of poly (phenylene sulfide sulfone) (PPSS) by thermogravimetric analysis, and suggested the reaction mechanism was a Dn deceleration type. It is not yet clear about the thermal behavior before degradation of these amorphous polymers. For the purpose of theoretical research and application, it is necessary to study the thermal properties of this PASSA resin.

In our previous work, the effect of annealing treatment on meta-PASSA in nitrogen atmosphere was studied [23]. The result showed that decarboxylation of the terminal carboxylic acid group occurred during the annealing treatment, and annealed *m*-PASSA exhibited different thermal properties compared to the untreated one. However, no cross-link behavior of the polymer was discovered in this work.

In the recent study, we present experimental results on thermal curing of para-PASSA in air condition. Our aim is to learn the thermal property of this polymer and the changes of chain

* Corresponding author. Institute of Materials Science and Technology, Sichuan University, Chengdu 610064, PR China. Tel./fax: +86 28 85412866.
E-mail address: ppsf@scu.edu.cn (J. Yang).

0032-3861/$ – see front matter © 2011 Elsevier Ltd. All rights reserved.
doi:10.1016/j.polymer.2011.01.001

structure in different thermal histories. Thermal cross-link behavior of the polymer is demonstrated for the first time via the enhancement of glass-transition temperature and 1% weight loss temperature. Amide C=O group in the polymer backbone produces two kinds of free radicals which are responsible for this cross-link behavior, and the reaction mechanism is discussed.

2. Experimental

2.1. Materials

4,4′-Dichloro diphenyl sulfone (DCDPS) was supplied by Jinsheng Chemical Reagents Company (Huaian, China). 4-Aminothiophenol was acquired from Shouerfu Chemical Reagent Corporation (Jinyun, China). 1,4-Benzenedicarbonyl chloride was purchased from Lianda Chemical Reagent Corporation (Nanchang, China). Sodium hydroxide (NaOH) and potassium carbonate (K_2CO_3) were gained from Changlian Chemical Reagent Corporation (Chengdu, China). *N*,*N*-dimethylformamide (DMF) and anhydrous alcohol were obtained from Kelong Chemical Reagent Corporation (Chengdu, China). *N*-methyl-2-pyrrolidone (NMP) was provided by Jinlong Chemical Industry Company (Nanjing, China). All the above chemicals were commercial products and used as received.

2.2. Synthesis of p-PASSA

The monomer, 4,4′-bis(4-aminophenylthio) diphenyl sulfone, was synthesized using DCDPS via an aromatic nucleophilic substitution reaction. The typical reaction condition was at 150 °C in nitrogen atmosphere.

The synthesis of para-PASSA was performed following the polycondensation method in a glass batch reactor. The proper amounts of 4,4′-bis(4-aminophenylthio) diphenyl sulfone and appropriate 1,4-benzenedicarbonyl chloride with a molar ratio of 1.01/1.00 were charged into the reaction tube of the polycondensation apparatus. The reaction mixture was dissolved in NMP at freezing temperature remaining for hours [11]. The product was washed repeatedly with hot water and then dried at 120 °C for 48 h. The synthesis route is shown in Fig. 1.

2.3. Preparation of the p-PASSA membranes

The *p*-PASSA membranes were prepared by dissolving the polymer powders in NMP, and then casting the solution on microscopy slides directly. The films were subsequently dried in an oven at 80 °C for 24 h to remove the residual solvent.

2.4. Thermal curing

The prepared polymer (powder or membrane) was subject to a series of thermal histories by being heated at 260 °C for 2 h, 6 h and 10 h, respectively, in air, oxygen and nitrogen environment, followed by the cooling in air until the temperature drops to the indoor one. The samples for ESR measurement should be quenched into ice water after the treatment to freeze the unreacted free radicals.

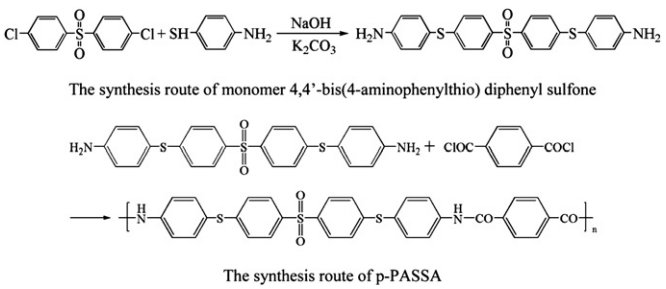

Fig. 1. Schematic illustrations of synthesis route of *p*-PASSA.

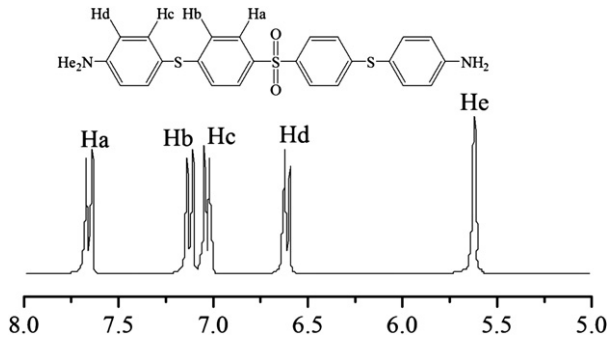

Fig. 2. ^{1}H NMR spectrum of BAPS.

2.5. Thermal property measurements

Differential scanning calorimetry (DSC) was performed using the NETZSCH DSC 200 PC thermal analysis equipment with polymer powders, fitted with a cooler system using liquid nitrogen. It was operated at a gas rate of 10 ml/min in nitrogen atmosphere. The heating rate of DSC measurement was 10 °C/min.

Thermogravimetric analysis (TGA) measurements were conducted using the TGA Q500 V6.4 Build 193 thermal analysis equipment with a heating rate of 10 °C/min in nitrogen atmosphere.

2.6. Characterization of the polymer structure and molecular weight

Fourier-transform infrared (FT-IR) spectroscopic measurements were characterized by examining thin, homogeneous membranes in the NEXUS670 FT-IR instrument.

Nuclear magnetic resonance (^{1}H NMR) instrument was used to provide the chain structure with a BRUKER-400 NMR Spectrometer. The samples were dissolved in deuterated dimethyl sulfoxide.

X-ray diffraction (XRD) analyses were carried out with a Philips electronic instrument (X'pert Pro MPD) using Cu–Ka radiation at 40 kV and 150 mA with scanning from 0° to 50°.

Molecular weight distributions were measured by conventional gel permeation chromatography (GPC) system equipped with a Waters 515 Isocratic HPLC pump, a Waters 2414 refractive index detector, GPC measurements were carried out at 60 °C using DMF as eluent with a flow rate of 1.0 mL/min. The system was calibrated with linear polystyrene standards.

2.7. Characterization of free radicals

Electron Paramagnetic Resonance (EPR) measurements were conducted at 15 °C on an X-band JEOL JES-FA200 EPR spectrometer, and operated at a 9.4 GHz modulation field with microwave power of 1 mW. When the microwave power saturation method was used, the microwave power was changed from 0.04 mW to 49 mW. The radical concentration was characterized by the ESR spectrum intensity compared to a standard sample of weak pitch. The sample powders or membranes (18.5 ± 0.2 mg) were examined in a quartz cell.

Table 1
Chemical shifts (δ) of the monomer.

Chemical shifts δ (ppm)	Ha	Hb	Hc	Hd	He
BAPS	7.661	7.134	7.038	6.615	5.620

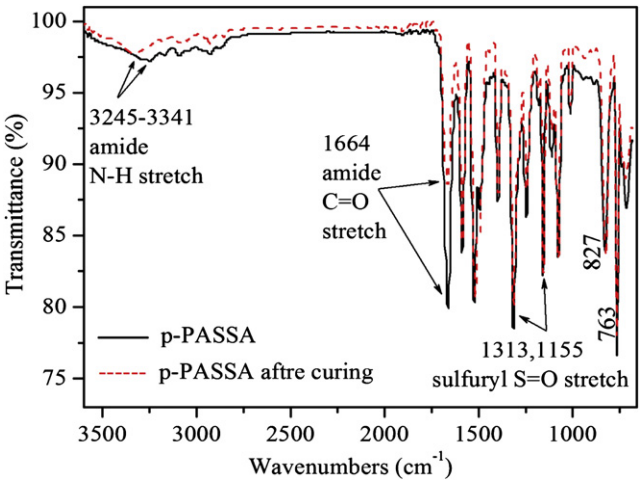

Fig. 3. FT-IR spectrum of *p*-PASSA before curing (black line), and after curing in air at 260 °C for 10 h (dash line).

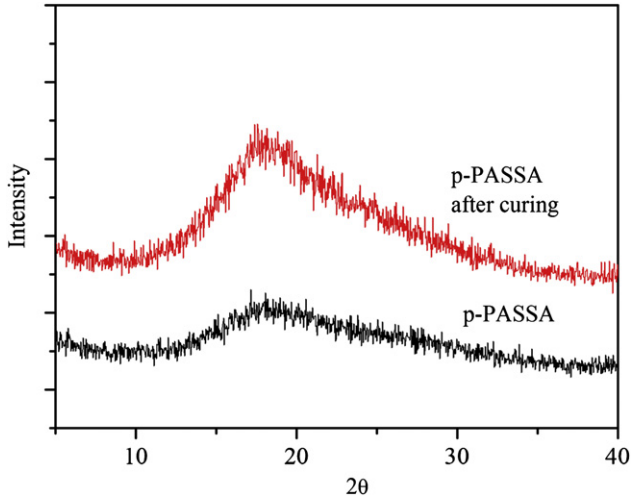

Fig. 4. Wide-angle X-ray diffraction of *p*-PASSA before curing (black line), and after curing in air at 260 °C for 10 h (red line). (For interpretation of the references to colour in this figure legend, the reader is referred to the web version of this article).

3. Results and discussion

3.1. Structure and molecular weight characterization

The chemical structures of monomer and polymer were characterized with ^{1}H NMR and FT-IR spectrometer. ^{1}H NMR spectra for 4,4′-bis(4-aminophenylthio) diphenyl sulfone (BAPS) is shown in Fig. 2 and details are tabulated in Table 1. Five groups of peaks appear in the NMR spectrum, and the ratio of corresponding integral curves is 1:1:1:1:1, which implies the symmetric disubstitution of the benzene ring. This structure can also be verified by the representative FT-IR spectrum of the polymer (Fig. 3).

The presence of sulfuryl S═O stretch in the backbone of the polymer is indicated by absorption at 1313 cm^{-1} and 1155 cm^{-1} [24], and the broad band in the 3245–3341 cm^{-1} region corresponds to the N–H stretch [25,26]. The absorption peaks around 763 cm^{-1} and 827 cm^{-1} are attributed to the C–H out of plane stretch of 1,4-disubstituted benzene, which indicate a linear or 1,4-conjugated phenyl structure. This fact is in agreement with Wang's work on synthesis of poly (phenylenesulfidephenylenamine) by self-polycondensation of methyl-(4-anilinophenyl) sulfide [27].

The aggregative structure of *p*-PASSA was determined by the XRD analysis. The presence of strong polar O═S═O bonds in a repeated unit of the polymer backbone imparts a highly amorphous character to the polymer as is evident from the presence of a broad amorphous diffraction peak (Fig. 4) [28]. The position of a quite wide peak in the range of 15–25° is taken as a measure of the most probable intersegmental spacing [29], and the narrow peak of *p*-PASSA after curing compared to the untreated one results from the reduction of distances among molecules.

Molecular weight of the polymer was determined by GPC analysis with M_n value of 59,565, and M_w value of 215,930.

3.2. TGA measurements

TG and DTG curves of the polymer, measured in nitrogen, are presented in Fig. 5 and details are listed in Table 2. The onset degradation temperature is as high as 456.37 °C, which is a good indication of the polymer thermal stability.

The comparison in Table 2 indicates that thermal stability of the polymer is improved after curing. The 1% weight loss temperature rises remarkably from 243.75 °C to 345.87 °C, and weight loss at 800 °C decreases by about 2%. The mass loss is due to the elimination of volatile species from the polymer. The low 1% weight loss temperature of *p*-PASSA before treatment implies that some volatiles and low molecular weight oligomers are contained in the samples [30]. The enhanced temperature of 1% weight loss and reduced weight loss at 800 °C after curing suggest that thermal cross-link behavior of the polymer could exist and the oligomers are efficiently incorporated into the cross-linked structure during the treatment process. To identify the existence of cross-link behavior, DSC measurements were employed as described below.

3.3. DSC measurements

Fig. 6 represents the DSC curves of *p*-PASSA samples which were subject to different thermal histories. The endothermic peaks

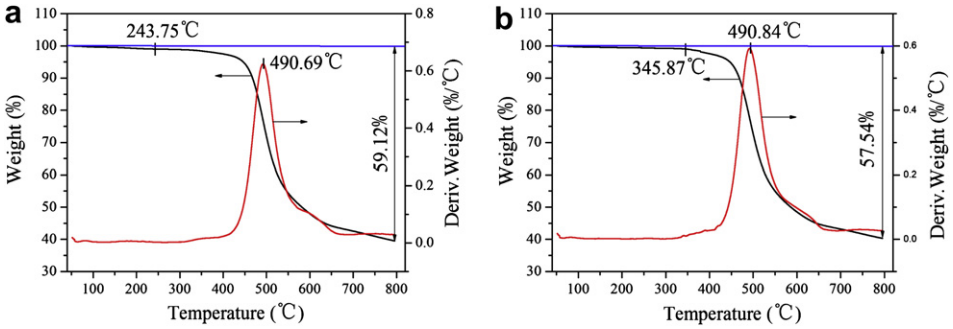

Fig. 5. TG and DTG curves of *p*-PASSA before curing (a), and after curing in air at 260 °C for 10 h (b) heated at 10 °C/min in nitrogen.

Table 2
Thermal properties of *p*-PASSA: results of TGA measurements.

Samples	1% weight loss temperature (°C)	Onset degradation temperature (°C)	Maximal degradation temperature (°C)	Weight loss at 800 °C (%)
p-PASSA before curing	243.75	456.37	490.69	59.12
p-PASSA after curing	345.87	457.84	490.84	57.54

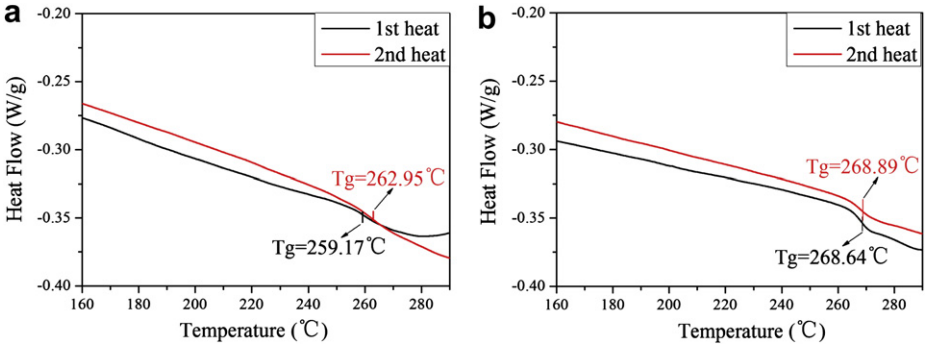

Fig. 6. DSC thermograms of *p*-PASSA before curing (a), and after curing in air at 260 °C for 10 h (b) measured with a 10 °C/min heat–cool–heat cycle in nitrogen.

revealed in the scans are attributed to the glass transition of the polymer [23]. In Fig. 6a, the T_g value increases by nearly 4 °C in the second heating curve. This is indicative of curing and indicating the presence of cross-link structure [31]. After thermal curing at 260 °C for 10 h in air, the T_g value increases from 259.17 °C to 268.64 °C (Fig. 6b), and the T_g values in the first and second heating curves are almost the same. This fact implies that the cross-link structure has already formed. Furthermore, the second sample was put in a vial with ~3 mL of NMP. After 1 week, the sample was not dissolved in the solvent. This also illustrates that thermal curing has occurred to a sufficient extent to form the cross-link material.

3.4. EPR measurements

EPR analysis is used to identify the generation of free radicals [32], and confirm the cross-link reaction type. The effect of thermal curing on *p*-PASSA powders in a time span of 0–10 h was studied by using the EPR spectrum. As it can be seen from Fig. 7, a typical single line shape ($g = 2.0023$) is exhibited in the spectrum. R_1 is used hereinafter to represent this kind of free radicals. A comparison of the line feature clearly shows an enhancement of the peaks with the increase of curing time, which indicates a rise of R_1 free radical concentration.

The variation of radical concentration with time is shown in Fig. 8. The curve of concentration versus treatment time can be divided into three stages. The first 3-h is a stage of activating free radicals. In this stage, free radicals have little chance to impact each other, which is caused by their few existences, so the concentration rises with time linearly from 0.007×10^{13} spins mg^{-1} to 4.36×10^{13} spins mg^{-1}. The radicals increase slightly in the next stage from 3 to 6 h, only from 4.36×10^{13} spins mg^{-1} to 6.62×10^{13} spins mg^{-1}. It is considered that the free radicals are initiated and consumed via the cross-linking reaction in this stage [33]. The rate of radical generation is only a little above the rate of consumption, which results in the mildly rise of concentration. When the treatment time is above 6 h, the concentration enhances linearly again. It is inferred that a network structure has already formed in this stage, and the free radicals produced are not consumed anymore. This fact corresponds to the DSC result at the same curing temperature.

From the line shape in Fig. 7 one can see that the left side of the peak is a little wider than the right one, which is highlighted by an

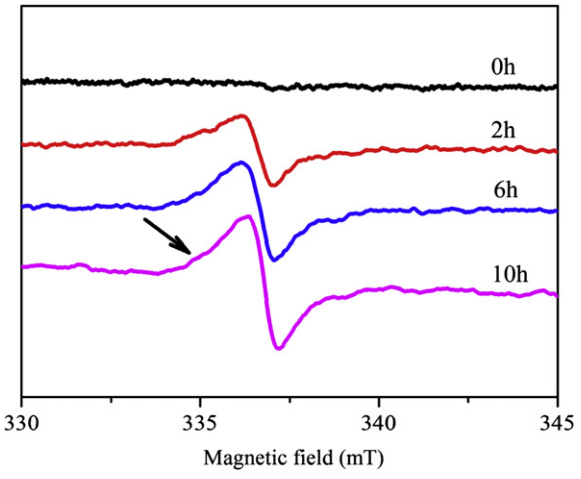

Fig. 7. EPR spectrum of *p*-PASSA samples for different thermal curing times at 260 °C in air.

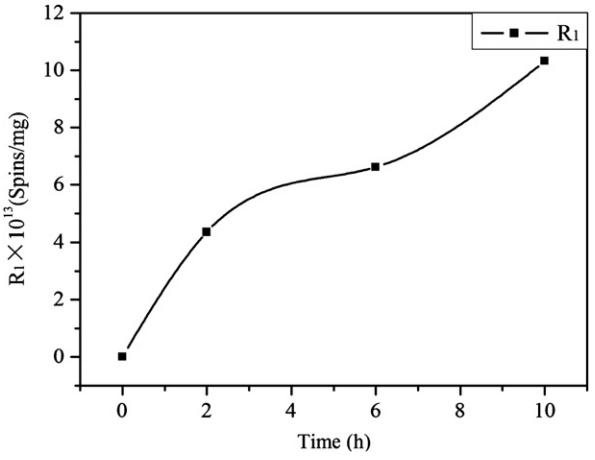

Fig. 8. Concentration of R_1 free radicals vs. time of thermal curing.

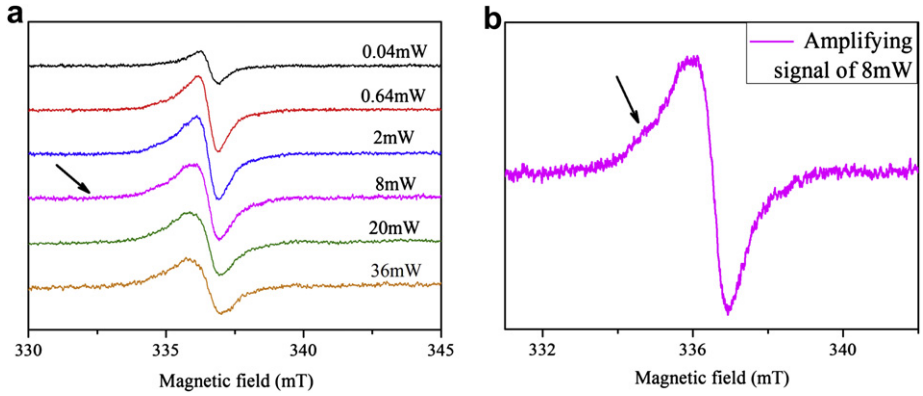

Fig. 9. EPR spectrum of *p*-PASSA samples cured in air at 260 °C for 10 h with different power.

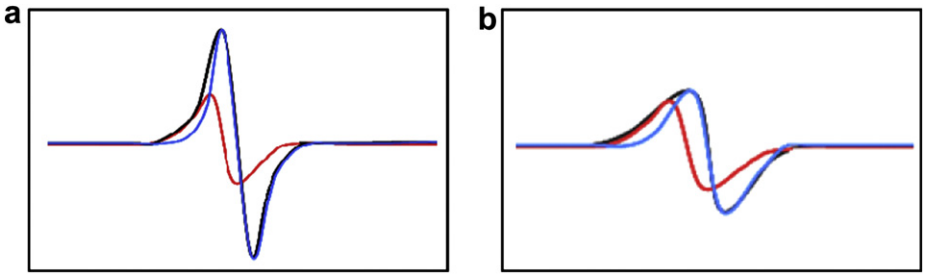

Fig. 10. Schematic illustrations of EPR signals at different microwave power: (a) 2 mW; (b) 36 mW.

arrow. It is possible that another weak peak (R_2) covered by R_1 exists, so the microwave power saturation method is employed to confirm and differentiate them [34].

With the increase of microwave power in Fig. 9a, R_2 signal appeared gradually, which could be observed in the amplifying signal of 8 mW (Fig. 9b). Due to the few number of R_2 free radicals, the R_2 signal is so weak that covered the R_1 signal. Meanwhile, the EPR signal enhanced to maximum at 2 mW, and then weakened gradually. The variations of signal intensities are attributed to the saturated characteristic of R_1 radicals [33], which is easily saturated by microwave power at a level around 2 mW. The phenomenon that left side of the peak widened with the increase of power could be explained by the existence of R_2 free radicals. As shown in Fig. 10, the EPR signal is the superposition of R_1 (blue line) and R_2 (red line). When microwave power grows above 2 mW, R_1 signal is saturated and weakens gradually. However, R_2 signal does not saturate with power easily, which increases slightly in the power range (Fig. 10b). In conclusion, the different saturated characteristics of R_1 and R_2 are the reason for broadened left side of the peak in EPR signals.

The phenomenon that EPR signal enhanced with the increase of thermal curing time suggested that R_1 may be oxygen free radicals because of the treatment environment in air. In order to analyze the origin of these free radicals, a group of contrast experiments were carried out in N_2, air and O_2 atmosphere, respectively, with a thermal curing at 260 °C for 10 h.

A comparison of the three signals in EPR spectrum (Fig. 11a) clearly shows that the radical concentration produced in N_2 is much lower than that in air, and close to the untreated one, meanwhile O_2 environment induces the highest radical concentration. Fig. 11b is the amplifying signal of the sample cured in N_2, from which one can see that the R_1 signal decreased sharply due to the curing environment, and R_2 signal is clearer in this picture (highlighted by an arrow). So it is considered that the production of R_1 and R_2 is closely related to O_2, and R_1 could be RO• free radicals.

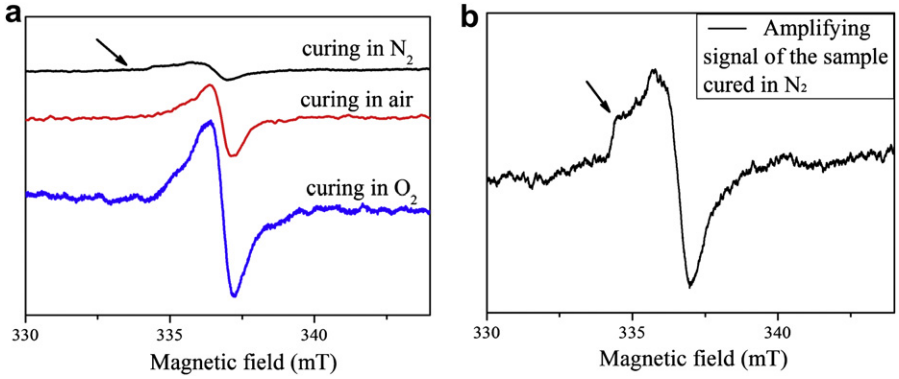

Fig. 11. EPR spectrum of *p*-PASSA samples cured in different atmosphere at 260 °C for 10 h.

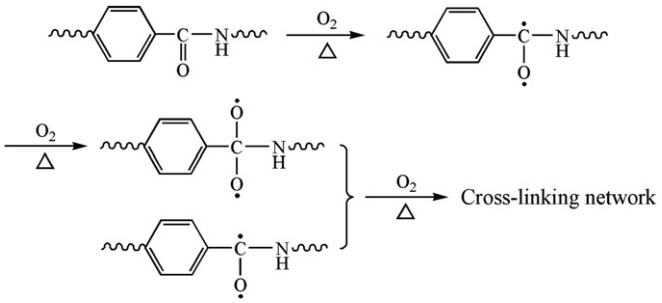

Fig. 12. Schematic illustrations of the cross-link reaction process.

According to the FT-IR spectrum of the polymer (Fig. 3), an obvious decrease in the amide C═O peak at 1644 cm^{-1} after curing is observed, which coincides with our inference. Therefore it can be concluded that the origin of R_1 and R_2 is the amide C═O group. Combined with EPR analysis it is reasonable that R_1 are CO• free radicals, and R_2 are C• free radicals. The cross-linking reaction mechanism is suggested as below.

3.5. Possible reaction mechanism of cross-link

Based on the research hereinbefore, the thermal cross-link behavior of *p*-PASSA could be explained by the following mechanism.

The double bonds of amide C═O are opened when they are subject to thermal curing in air, and two kinds of free radicals, C• and CO•, are produced consequently. With the effect of O_2, most C• are transformed into CO• free radicals, which causes the higher concentration of R_1 than R_2. The cross-linking network was formed afterward which was induced by these two kinds of free radicals. The cross-linking reaction type belongs to conventional radical cross-link reaction, and the reaction process is shown in Fig. 12.

4. Conclusions

An amorphous *p*-PASSA was synthesized via low temperature solution polycondensation. The polymer with high glass-transition temperature (259 °C) and thermal stability suggests a potential use in heat-resistant materials.

We have demonstrated, for the first time, the thermal cross-link behavior of the polymer at 260 °C in air condition. The results showed that the formation of cross-link network enhanced the T_g from 259.17 °C to 268.89 °C, and the 1% weight loss temperature of the polymer increased remarkably from 243.75 °C to 345.87 °C. Two kinds of free radicals, CO• and C•, existed in the polymer, and concentration of the former was much higher than that of the latter. These two kinds of free radicals were responsible for the intermolecular cross-linking behavior. The cross-linking type was attributed to conventional radical cross-link reaction, and the reaction mechanism was also suggested.

This cross-linkable polymer represents a new class of super engineering plastic with great thermal stability. Further investigations regarding the processing and mechanical properties of this material are in active progress and the results will be presented in our future articles.

Acknowledgements

This work is financially supported by the National High Technology Research and Development Programme of China (863 program) with the project No. 2007AA03Z561. We would like to express our sincere thanks to Dr. Guodong Li of Jilin University for his kind assistance in Electron Paramagnetic Resonance (EPR) measurement.

References

[1] Schuster M, de Araujo CC, Atanasov V, Andersen HT, Kreuer KD, Maier J. Macromolecules 2009;42:3129–37.
[2] Naffakh M, Marco C, Gomez MA, Gomez-Herrero J, Jimenez I. J Phys Chem B 2009;113:10104–11.
[3] Jeon IY, Lee HJ, Choi YS, Tan LS, Baek JB. Macromolecules 2008;41:7423–32.
[4] Naffakh M, Marco C, Gomez MA, Gomez-Herrero J, Jimenez I. J Phys Chem B 2009;113:7107–15.
[5] Zou H, Wang K, Zhang Q, Fu Q. Polymer 2006;47:7821–6.
[6] Naffakh M, Marco C, Gomez MA, Gomez-Herrero J, Jimenez I. J Phys Chem B 2008;112:14819–28.
[7] Sasanuma Y, Hayashi Y, Matoba H, Touma I, Ohta H, Sawanobori M, et al. Macromolecules 2002;35:8216–26.
[8] Guo YL, Bradshaw RD. Polymer 2009;50:4048–55.
[9] Zhang RC, Xu Y, Lu A, Cheng KM, Huang YG, Li ZM. Polymer 2008;49:2604–13.
[10] Feller LM, Cerritelli S, Textor M, Hubbell JA, Tosatti SGP. Macromolecules 2005;38:10503–10.
[11] Yang J. CN1935874.
[12] Barique MA, Wu LB, Takimoto N, Kidena K, Ohira A. J Phys Chem B 2009;113:15921–7.
[13] Xia LG, Li AJ, Wang WQ, Yin Q, Lin H, Zhao YB. J Power Sources 2008;178:363–7.
[14] Huang J, Baird DG, McGrath JE. J Power Sources 2005;150:110–9.
[15] Mighri F, Huneault MA, Champagne MF. Polym Eng Sci 2004;44(9):1755–65.
[16] Tanthapanichakoon W, Furuuchi M, Nitta KH, Hata M, Endoh S, Otani Y. Polym Degrad Stab 2006;91:1637–44.
[17] Hawkins RT. Macromolecules 1976;9(2):189–94.
[18] Scobbo JJ, Hwang CR. Polym Eng Sci 1994;34(23):1744–9.
[19] Gies AP, Geibel JF, Hercules DM. Macromolecules 2010;43:952–67.
[20] Gies AP, Geibel JF, Hercules DM. Macromolecules 2010;43:943–51.
[21] Perng LH. Polym Degrad Stab 2000;69:323–32.
[22] Wang HD, Yang J, Long SR, Wang XJ, Yang Z, Li GX. Polym Degrad Stab 2004;83:1637–44.
[23] Liu J, Zhang G, Long SR, Wang XJ, Yang J. J Macromol Sci Part B Physics 2010;49(2):229–35.
[24] Lakshmi RTSM, Vyas MK, Brar AS, Varma IK. Eur Polym J 2006;42:1423–32.
[25] Song Z, Baker WE. J Polym Sci Part A Polym Chem 1992;30:1589–600.
[26] Semsarzadeh MA, Poursorkhabi V. Polym Degrad Stab 2009;94:1860–6.
[27] Wang LX, Wang FS, Zhang JP, Wang RS, Soczka-Guth T, Mullen K. Synthetic Met 1999;101:320.
[28] Poojari Y, Clarson SJ. Macromolecules 2010;43:4616–22.
[29] Niemela S, Leppanen J, Sundholm F. Polymer 1996;37(18):4155–65.
[30] Iseki T, Narisawa M, Katase Y, Oka K, Dohmaru T, Okamura K. Chem Mater 2001;13:4163–9.
[31] Mukherjee I, Drake K, Berke-Schlessel D, Lelkes PI, Yeh JM, Wei Y. Macromolecules 2010;43:3277–85.
[32] Bhadra S, Khastgir D. Polym Degrad Stab 2007;92:1824–32.
[33] Niu YM, Wang GB, Zhang SX, Na Y, Jiang ZH. Polym Int 2005;54:180–4.
[34] Hill DJ, Choi B- K. Polym Int 1999;48:956.

Polymer 52 (2011) 1019–1026

Contents lists available at ScienceDirect

Polymer

journal homepage: www.elsevier.com/locate/polymer

Comparison of two cationic polymeric flocculant architectures on the destabilization of negatively charged latex suspensions

Daniel Palomino [a], David Hunkeler [b], Serge Stoll [a,*]

[a] University of Geneva, F.-A. Forel Institute, Group of Environmental Physical Chemistry, 10 Route de Suisse, 1290 Versoix, Switzerland
[b] Aqua+TECH Specialties, chemin du Chalet-du-Bac 4, CH-1283 La Plaine, Switzerland

ARTICLE INFO

Article history:
Received 27 March 2009
Received in revised form
6 May 2010
Accepted 15 December 2010
Available online 22 December 2010

Keywords:
Linear and branched polyelectrolytes
Kinetics flocculation rate constants
Floc fractal dimensions

ABSTRACT

Flocculation studies between cationic polymers and oppositely charged colloidal particles are reported in which both flocculation kinetics and floc structures are systematically investigated. The flocculation rate constant, stability ratio and kinetics laws are experimentally determined using particle counting for two polymer architectures; a cationic linear polymer and a two-branched polymer. Comparisons are also made using NaCl at different ionic concentrations for the destabilization of the colloidal particles. Detailed measurements of electrophoretic mobility and kinetics rate constants on varying the polymer dosage are reported. Results suggest that the polymer architecture plays important roles on the polymer dosage for the rapid destabilization of the colloidal suspension. The branched polymer at optimal dosage exhibits the highest flocculation rate constant, whereas on the other hand, the linear polymer concentration range of flocculation is larger. In both cases, polymer flocculation is more efficient by a factor of 5–6 than charge screening effects due to the presence of salt. Analysis of the stability ratio indicates that tele-bridging flocculation and electrostatic forces dictate the stability of the charged latex particle suspension. It is shown that the fractal concepts which are valid for aggregation processes are also applicable here and branched polymers as well as linear polymers yield to the formation of compact flocs in comparison to those obtained with salt.

1. Introduction

In the aquatic systems, flocculation processes are playing essential roles in removing pollutants [1,2]. Trace metals and organic pollutants are mainly adsorbed at the surface of mineral particles like silicates, alumino-silicates or iron oxyhydroxides [3,4] owing to their high specific surface area, diffusivity and reactivity. In these systems algal and bacterial exudates composed of polysaccharide chains promote the flocculation of these mineral particles and the subsequent removal of pollutants. Flocculation is also used in numerous industrial processes such as water purification and wastewater treatment where flocculation is usually induced by positively charged synthetic polymers (polyelectrolytes) [5,6]. Considering wastewater treatment, the liquid phase needs to be rapidly separated with the highest efficiency from the solid one in order to obtain a clear filtrate, avoid to reject pollutants into natural aquatic systems, and maintain the maximum of pollutants in the minimum dry matter volume to minimize the waste quantity to treat, recycle or simply stock. Unfortunately, and for several reasons, polymeric flocculants are not always used in a rational way for optimal flocculation with regards to the natural fluctuations of the suspended material concentration, composition or, optimal dosage determination. Therefore, an improved understanding of the interaction mechanisms between cationic flocculants and colloidal particles is important for the rational use of polymeric flocculants. Furthermore, the synthesis of new polymer structures to accelerate coagulation rates beyond diffusion control and improve the efficiency of the flocculation processes by enlarging for example the polymer flocculation concentration range in which polymers are efficient is another important aspect [7,8].

From a fundamental point of view, there are two principal forces to consider in colloidal particle aggregation processes. The first concerns the long distance electrostatic repulsions between colloids which prevent coagulation while the second is related to the short distance van der Waals attractions which promote coagulation [9,10]. Simple electrolytes such as iron chloride ($FeCl_3$) or aluminium sulphate ($Al_2(SO_4)_3$), polysalts, including aluminium polychlorosulfates ($Al_xCl_y(SO_4)_z$), modify the nature of the electrostatic repulsions between particles by promoting electrostatic attractions [11–13]. As a result, the probability of forming permanent bonds between particles increases and screening effects, charge neutralization and charge

* Corresponding author. Tel.: +41 22 379 0333; fax: +41 22 379 0302.
E-mail address: serge.stoll@unige.ch (S. Stoll).

0032-3861/$ – see front matter © 2010 Elsevier Ltd. All rights reserved.
doi:10.1016/j.polymer.2010.12.033

inversion mechanisms are involved. The use of charged synthetic or biopolymers involves different mechanisms [7]. When the polymer radius of gyration is small in comparison to the particle size, aggregation is mainly promoted by local polymer adsorption and local inversion of the particle surface charges. Oppositely charged patches are then created which can interact with bare surfaces. Depending of the polymer concentration, complete surface charge neutralization can also be achieved at the colloid surface so that van der Waals forces, which are always attractive, can induce particle aggregation. However, if polymer dosage is not controlled, an excess of polymers will disperse the colloidal suspension by charge inversion or steric stabilization [14]. Polymer dosage is hence an important parameter for optimal destabilization of colloidal suspensions but also for economic reasons since excess of polymer represent extra costs. Three significant regimes have to be considered when i) polymer concentration is too low to induce rapid flocculation, ii) polymer concentration has an optimal value for rapid destabilization and iii) polymer concentration is too high and results in colloids restabilization [15]. It should be noted that, other than polymer dosage, there are several parameters to consider in order to achieve optimal flocculation conditions. They concern polymer geometry, polymer linear charge density and sign (oppositely charged polymer are usually used), and polymer intrinsic flexibility which are expected to control not only the aggregate structure but also the kinetics of flocculation. These parameters have to be considered for the rational synthesis of new flocculant structures. To show how little differences in some parameters can influence aggregation processes, Zhou and Franks [16] measured zeta potential and floc sizes of particle–polymer mixtures using Dynamic Light Scattering. They demonstrated that the flocculation mechanism of 90 nm silica particles, by addition of charged cationic polymers, was variable in accordance with polymer dosage, solid concentration, background electrolyte concentration and shear rate. Some parameters were correlated such as the increase of the polymer charge with the aggregate mass fractal dimension, reflecting the mechanisms involved. It was also observed that weakly charged polymers promote bridging whereas highly charged polymers induce electrostatic patch flocculation or full charge neutralization. Furthermore, it was shown that the polymer dosage influences both the aggregation mechanisms and the aggregate geometry. On the other hand, Yang [17] studied the flocculation of kaolin suspensions using small-angle laser light scattering. It was shown that the low molecular weight and highly charged polydiallyldimethylammonium chloride polymers induce aggregation by charge neutralization. The observed flocculation rate values were small and the resulting flocs compact. High molecular weight and relatively low charge density polymers were shown to promote bridging aggregation, high flocculation rates and less compact flocs. Rasteiro and Garcia [18] applied light diffraction spectroscopy to monitor the flocculation, deflocculation and reflocculation processes of cationic, linear and branched polyelectrolyte/precipitated calcium carbonate mixtures when different types of shear forces were applied. Floc resistance was correlated with floc structures, based on mass fractal dimension data. They also investigated the effect of the presence of inorganic salts on the polyelectrolyte performance and required flocculant dosage [19] showing that the presence of inorganic salts affects significantly the overall performance of the polyelectrolytes. Such studies also demonstrate that polymer molecular weight and charge are important parameters to consider in the understanding of flocculation mechanisms and floc geometry.

In this study, positively charged linear chains and positively charged branched polymers having two branches are used, and the influence of the polyelectrolyte microscale architecture on the kinetics of flocculation, polymer dosage, change of the electric properties of the colloidal particles, floc structures are addressed in an quantitative way. The polymers are evaluated on the destabilization of a solution containing well defined negatively charged particles. Optimal flocculation conditions and kinetics constants are determined by adjusting the polymer concentration. Stability ratio and collision efficiency parameters are calculated to get an insight into the parameters governing the flocculation processes. Floc structures are then examined to obtain the fractal dimension of the resulting structures. In all cases, flocculation rates, optimal polymer dosage and stability ratio are compared with salt induced particle destabilization (homocoagulation). Based on a detailed analysis of electrophoretic measurements and variations of the stability ratio, flocculation mechanisms are discussed, comparison is made with the salt situation and the validity of the DLVO theory to describe salt induced aggregation is verified.

2. Experimental

2.1. Flocculant composition and properties

Sodium chloride 99.5% from Acros Organics was used to adjust the solution electrolyte concentration and promote salt induced aggregation. Positively charged linear (AF BHMW) and the two-branched (AF B1^{++}) polyacrylamide polymers synthesized by Aqua + Tech Specialties S.A (Switzerland) [20,21] were used to induce the flocculation of well characterized and monodisperse latex particles. The polymer charge, molar mass and intrinsic viscosity are given in Table 1.

2.1.1. Materials

White crystals of acrylamide monomer *(AAM)* were supplied by Kemira water (formerly Cytec, Botlek, Netherlands) and used as received. Dimethylaminomethyl methacrylate (DMAEA) quaternized with methyl chloride was obtained from Ciba Specialty Chemicals (Bradford, England) as an aqueous solution (80%). For the polymerization in inverse-emulsion, the aqueous phase was emulsified in Exxsol D-100, a narrow cut of an isoparaffinic mixture without any VOCs (supplied by Exxon Chemical, Koln, Germany). Sorbitan monoisostearate (Montane 70) as well as polyethoxylated sorbitan monooleate (Montanox 80) purchased from Seppic (Paris, France) were also used as nonionic stabilizing agents. Type I reagent grade water with a resistance of 18.2 mΩ/cm was obtained through a series of deionization. 2,2′-azobis(2,4 dimethylvaleronitrile) (V-65, Wako Chemical, Germany) was used as received as oil soluble initiator. Certified ACS EDTA (ethylene diamine tetra-acetic acid, disodium salt dihydrate) (Fluka, Switzerland) was used as a chelating agent in the copolymerization with unpurified monomers. Adipic acid purchased from Riedel-de Haen (Seelze, Germany) was further used to prevent polymer hydrolysis. Rolfor TR/8 Cisalpina (Italy) was employed as wetting agent to invert the polymer-emulsions with excess water to yield a highly viscous dilute polymer solution.

2.1.2. Polymer synthesis

The polymerization reaction of acrylamide with dimethylaminoethyl acrylate quaternized methyl chloride, was performed in a 1-L stainless glass reactor cooled with a jacket and a water bath. The water-to-organic phase ratio was 2.7:1 by weight. The monomer concentration was nominally 40 wt% of the total mass of emulsion and the emulsifier blend was dissolved in the organic phase at

Table 1
Polymer properties (cationic flocculants). η represents the intrinsic viscosity, R_h the hydrodynamic radius and ζ the zeta potential.

Name	Charge [Wt %]	Number of branches	η [mL/g]	Molar mass [10^6 g/mol]	R_h [nm]	ζ [mV]
AF BHMW	80	0	1720	7.2	311 ± 11	+72 ± 3
AF B1^{++}	80	2	2636	12	252 ± 21	+78 ± 3

a concentration of 2.3 wt% of the total reaction mass. The HLB value was approximately 5.8. The chemical initiator 2,2′-azobis(2,4-dimethyvaleronitrile) (V-65, Wako Chemicals. Neuss, Germany) dissolved into xylene was added into the reactor at 40 °C. The reaction time was 6 h and following an isothermal period of 1–2 h the reaction was allowed to exotherm to a temperature between 70 and 80 °C.

2.1.3. Inversion and viscometric characterization of the inverse-emulsion

The inversion of polymerized inverse-emulsions was carried out as follows. In a large and baffled beaker (l-L capacity), 500 g of deionized water was stirred at 400 rpm (Rushton type of impeller). A precalculated amount of emulsion (containing the inverting surfactant) was added to yield 0.1 wt% active weight of polymer in solution was added within a short time (less than 1 s) directly to the center of the vortex. The agitation speed was further increased to 600 rpm and maintained for an additional 5 min. A rapid increase in solution viscosity and the absence of agglomerates in the aqueous phase usually indicated a good inversion. The resulting polymer diluted solution was then characterized by viscosity measurements. The polymer viscosity was measured with a model L VDVII + viscometer (Brookfield, Stoughton, MA, USA) at 50 rpm and room temperature [22].

2.2. Latex particle properties

Monodisperse spheres of latex polystyrene from IDC (Interfacials Dynamics Corporation) were used. Their mean diameter was determined by TEM and found equal to 0.99 ± 0.03 μm. The spheres were provided in an aqueous suspension containing 81 g/L of latex particles. The particle number, per milliliter of solution, equalled to 1.5×10^{11} and the specific surface area to 5.7×10^4 [cm^2/g]. The latex particles exhibit negatively charged surfaces due to the presence of sulphate groups (7.6×10^5 per particle) and the charge density has a constant value equal to 3.9 [μC/cm^2] for pH values above 4. The charge content, equal to 2.3 [μEq/g], was determined using conductimetric titrations. The Zeta potential of the latex particles was measured with a Malvern Zetasizer Nano and found equal to -100 ± 3 mV for a NaCl concentration equal to $1.5 \cdot 10^{-4}$ M.

2.3. Size distribution determination and zeta potential measurements

A Coulter® Counter Multisizer II™ was used to measure the decay of the number of colloidal monomers (free particles) with time. This device determines through 256 channels the equivalent size (from 1 to 30 μm) and number of particles or aggregates passing through an aperture orifice of 50 μm. Each measurement is performed during 30 s corresponding to 287 μl of solution. Isoton™ IIA was used as a support electrolyte. It was pre-filtered with a 0.22 μm Millipore® ISOPORE™ GTTP filter to reduce the background noise. It should be noted here that the diameter given by Coulter® Counter corresponds to the diameter of the sphere equivalent to the aggregate as if all the latex monomers were collapsed in one compact volume. In order to determine experimental kinetics aggregation rates K_S, the decrease with time of the free latex particles number has been followed in the 1 μm channel in order to take into consideration only non aggregated particles (free monomers).

The Malvern Zetasizer Nano instrument was used to measure the zeta potential of the latex particles in solution as a function of flocculation time and polymer concentration. Each sample was measured 5 times with 15 sub-runs for each measure. Between runs a pause of 10 s was imposed to allow the system to relax and stabilize before the next measurement.

2.4. Determination of the aggregate fractal dimension D_f

Mandelbrot [23] introduced fractal dimension concepts to various objects such as colloidal aggregates to quantitatively describe their structural properties. To gain insight into the aggregate structures, by considering mass distribution in space, flocs were magnified 40 times with a Laborlux S microscope from Leitz. Images were taken with a Nikon D90 then treated with the SigmaScan Pro 4 software to enhance the contrast between the background and the aggregates. The total number of aggregates, relative masses (in term of total number of pixels) and aggregate dimensions (here the major axis lengths) were calculated to determine D_f according to the scaling law relationship [24]:

$$m \sim l^{D_f} \tag{1}$$

where m represents the aggregate mass (number of pixels) and l the aggregate major axis length in reduced coordinates. D_f was calculated by considering a log/log plot of m versus l. In order to validate this method we applied this procedure to solid spheres and lines and D_f values equal to 2.00 ± 0.01 and 1.05 ± 0.03 respectively were found in good agreement with the theoretical expected values [24].

3. Results and discussions

3.1. Aggregation in presence of salt

The influence of the concentration of simple electrolyte on the aggregation kinetics of latex suspensions was investigated first. Salt is expected to screen the electrostatic repulsive forces between latex particles. Increasing the salt concentration C_i is thus expected to result in an increase of the aggregation rate constant. Suspension containing 0.5 g/L suspensions of latex particles have been destabilized at 25 °C by adjusting the final salt concentrations to 0.15, 0.18, 0.2, 0.25, 0.5 and 1 M in orthokinetic conditions at a mixing speed of 100 ± 2 RPM.

From the monomer number evolution with time the aggregation rate constants K_S were calculated and compared to 1st and 2nd order kinetic laws. Aggregation rate constants K_S were found to follow a 2nd order process according to:

$$\frac{dN_1}{dt} = -K_S |N_1|^2 \tag{2}$$

A linear proportionality between time and the inverse of the number of free particles N_1 was found (Fig. 1).

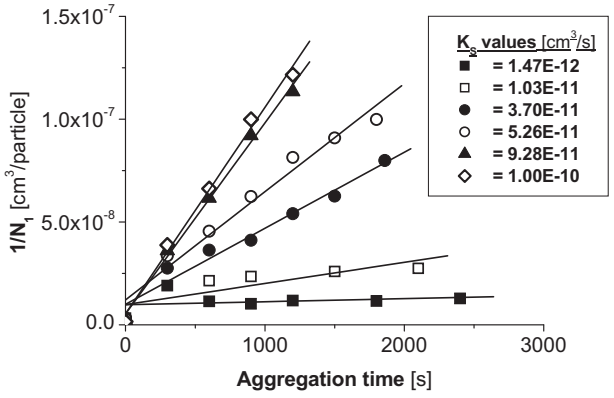

Fig. 1. Experimental kinetic aggregation rates K_S [cm^3/s] values obtained from the evolution of the inverse number of free particles versus time during the destabilization of 0.5 g/L solutions of negatively charged latex particles using different NaCl salt concentrations : ■ = 0.15, □ = 0.18, ● = 0.2, ○ = 0.25, ▲ = 0.5, ◇ = 1M.

K_S was directly obtained from the slope value for each salt concentration and was found to increase continuously with increasing C_i. The initial number of particles at t_0 was determined by the Coulter Counter in order to get more accurate linear regressions [25]. To get an insight into the aggregation rate constant variation with salt concentration, K_S values are summarized in Fig. 2. A rapid increase of K_S is observed at $C_i = 0.15$M followed by a plateau for salt concentrations greater than 0.5M.

Using the DLVO theory [9,10], the experimental K_S evolution with C_i was compared with theoretical calculations of the total interaction potentials between two latex particles (Fig. 3). The total interaction potential $V_T(H)$ was expressed as the sum of the van der Waals attractive forces $V_{vdW}(H)$ and electrostatic repulsive forces $V_{el}(H)$. The van-der-Waals-Hamaker and the Linear Superposition Approximation [25,26] were used to evaluate $V_{vdW}(H)$ and $V_{el}(H)$:

$$V_{vdW}(H) = -\frac{A_{1,3,1}}{6}\cdot\left\{\frac{2a^2}{H(H+4a)}+\frac{2a^2}{(H+2a)^2}+\ln\left(\frac{H(H+4a)}{(H+2a)^2}\right)\right\} \quad (3)$$

$$V_{el}(H) = 2\pi\varepsilon_0\varepsilon_r a\Psi_0^2 e^{-\kappa H} \quad (4)$$

where $A_{1,3,1}$ represents the Hamaker constant which corresponds to 1.40×10^{-20} [J] and represents an average value for latex particles [27–29], a the radius of the latex particle (0.5 μm) and H the distance between the two particle surfaces. ε_0 and ε_r are respectively the vacuum permittivity and the water relative permittivity whereas Ψ_0 represents the latex surface potential which was calculated for each ionic strength [15]. Finally, the Debye-Hückel parameter [15,28] was calculated according to :

$$\kappa = \sqrt{\frac{2n_0e_0^2}{\varepsilon_r\varepsilon_0 k_B T}} \quad (5)$$

By comparing Figs. 2 and 3, good agreement is found between the experimental values and the theoretical predictions. Fig. 3 shows that within the range 0.25–1M NaCl the interaction curves are fully attractive; particles can aggregate rapidly and this situation corresponds to the maximum aggregation rate plateau value observed in Fig. 2 when NaCl concentration $C_i \geq 0.4$. When $C_i < 0.25$M, due to the presence of an energetic barrier, particles repel significantly hence reducing the aggregation rate. In such cases, the effect of colloid interactions is often expressed as a collision efficiency factor α (with $0 \leq \alpha \leq 1$). A collision efficiency of unity implies that every collision leads to permanent attachment. Repulsion forces reduce the collision efficiency such that practically no aggregation occurs. Because of the key role played by this parameter, the sticking probability α was determined by considering the ratio between the rate constant determined in the fast aggregation regime at high salt concentration, and assuming a value $\alpha = 1$ for the highest aggregation rate constant value obtained experimentally [14]. For example, the sticking probability was assumed to be equal to 0.10 at 0.18M NaCl indicating that 10% of the collisions between elementary particles result in the formation of a permanent bond.

The reciprocal value of α, $w = 1/\alpha$, known as the stability ratio w was calculated and presented in Fig. 4 as a function of the salt concentration. Fig. 4 shows that log w decreases linearly when log [NaCl] increases. When [NaCl] > 0.2M, log w becomes constant and equal to 1. This value of [NaCl] corresponds to the Critical Coagulation Concentration (CCC = 0.2M). For [NaCl] < CCC, the energy barrier disappears and particle aggregation can occur at a maximum

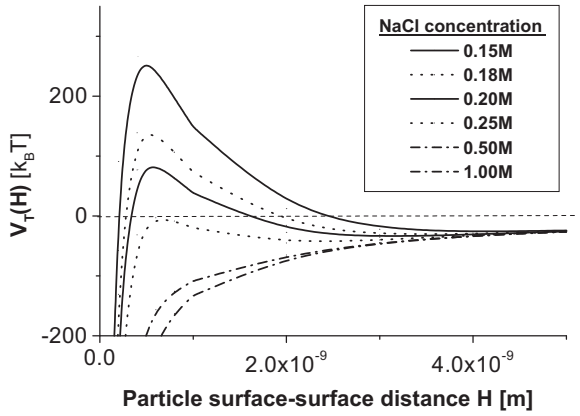

Fig. 3. DLVO interaction potentials between two latex particles as function of : i) the distance H between their surfaces by considering the contribution of the van der Waals attractive forces and the repulsive electrostatic forces and ii) by adjusting the salt concentration C_i. It should be noted that the repulsive energetic barrier disappears when $C_i \geq 0.25$M.

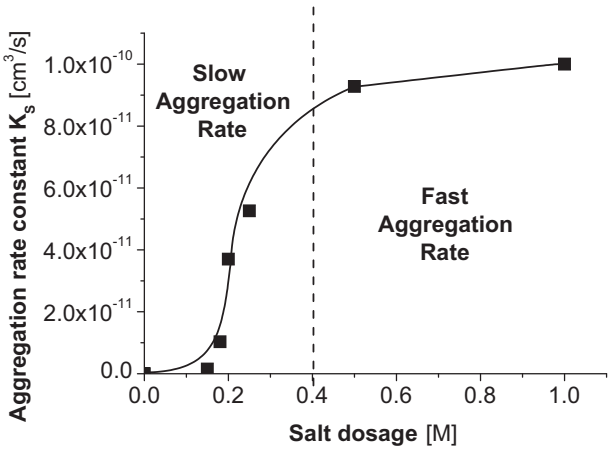

Fig. 2. Evolution of K_S with NaCl salt dosage concentration. The vertical dotted line corresponds to the salt concentration at which the interaction potential between the surfaces of two latex particles results in fast aggregation rate.

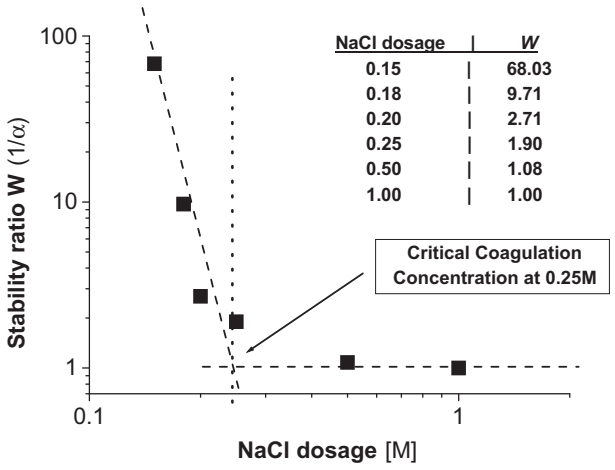

Fig. 4. The Critical Coagulation Concentration (CCC) is determined by plotting the inverse of the sticking probability (stability ratio w) as a function of the salt concentration. The α (sticking probability) values for the different NaCl concentrations are presented in the insert. The CCC value corresponds to a salt concentration equal to 0.25M.

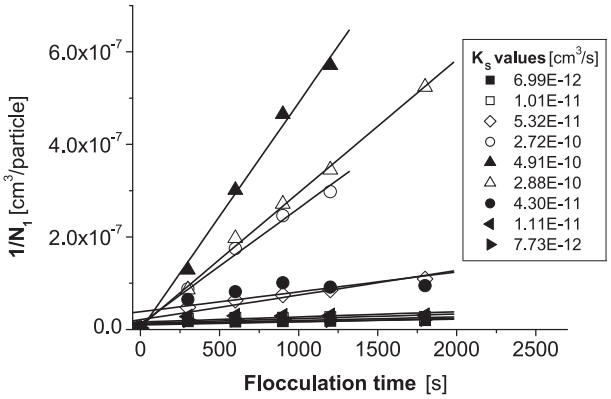

Fig. 5. Variation of the inverse of the number of free latex particles as a function of the flocculation time. Experimental K_S values in the inset are obtained from the different slopes and for the destabilization of 0.5 g/L solutions of latex particles at different linear polymer AF BHMW concentrations: ■ = 3, □ = 3.5, ◇ = 4, ○ = 4.5, ▲ = 4.75, Δ = 5, ● = 5.25, ◄ = 5.5, ► = $6 \cdot 10^{-4}$ g/L.

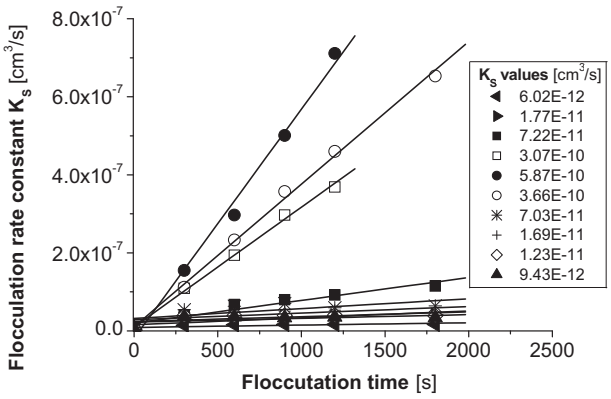

Fig. 7. Experimental K_S values obtained during the destabilization of 1 g/L solutions of latex particles at different branched polymer AF B1^{++} concentrations: ◄ = 8, ► = 10, ■ = 11, □ = 12, ● = 12.5, ○ = 13, * = 13.5, + = 14, ◇ = 15, ▲ = $16 \cdot 10^{-4}$ g/L.

rate, determined by the transport rate and the collision frequency between latex particles.

3.2. Flocculation in presence of linear cationic polymer chains

The destabilization of the latex suspension is now investigated by using oppositely charged linear polymers (AF BHMW). 1 g/L suspensions of latex particles have been considered at 25 °C by adjusting the final AF BHMW concentrations to 3, 3.5, 4, 4.5, 4.75, 5, 5.25, 5.5, 6, 7 [10^{-4} g/L] and at a constant mixing speed equal to 100 ± 2 RPM. The kinetic law is also found to follow a 2nd order process, since a linear proportionality between time and the inverse of the number of free particles N_1 is only obtained in such conditions (Fig. 5).

K_S values are directly obtained from the slope values in Fig. 5. As shown in Fig. 6, representing the K_s variations as a function of the polymer dosage, and in contrast to the salt effect which promotes aggregation until a maximum plateau value, the increase of polymer concentration is first promoting the flocculation of latex suspensions until a maximum value which represents the optimal flocculant dosage. After this point, the increase of polymer concentration stabilizes the latex suspension. It is important to note here that the highest K_S value is about 5 times higher than the one obtained previously using salt. The adsorbed polymer here significantly decreases the suspension stability and accelerates the aggregation rate beyond diffusion control. One complementary information can also be extracted from Fig. 6: the polymer effective flocculation dosage window. The width of the polymer dosage window gives information about the polymer efficiency concentration domain. The larger is the window, the more efficient will be the flocculant in different situations resulting for example from initial particle concentration variations. Another important parameter is the zeta potential of the free latex particles which is also presented in Fig. 6. The zeta potential variations show that the free latex particles are still negatively charged within the range of the effective window of flocculation. This parameter gives important information about the polymer flocculation mechanism which is discussed more in detail in Section 3.4.

3.3. Flocculation in presence of branched cationic polymer chains

The behaviour of the latex suspension is then investigated by using the oppositely charged two-branched polymers (AF B1^{++}). In order to compare from a kinetic point of view the linear and branched polymer behaviour we used strictly the same procedure and parameters for both experiments, varying only the polymer geometry. The calculated K_S values as a function of the AF B1^{++} polymer concentration are presented in Fig. 7.

The highest K_S value obtained at optimal polymer dosage is equal to 5.87×10^{-10} [cm^3/s]. Such a value is about 6 times higher than the maximum value obtained with the salt experiment and significantly higher than the highest K_S value obtained with the linear polymer at optimal dosage. As for AF BHMW, Fig. 8 shows

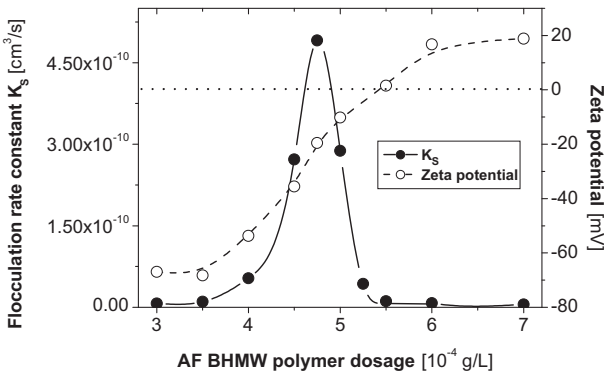

Fig. 6. K_S and zeta potential evolutions as a function of the concentration of AF BHMW polymer. The K_S maximum value is obtained at $4.75 \cdot 10^{-4}$ g/L of linear polymer and for a zeta potential value equal to −19 mV. The effective flocculation window corresponds to a polymer concentration range from 3.5 to 5.5 [10^{-4} g/L] and zeta potential range from −60 to −10 mV.

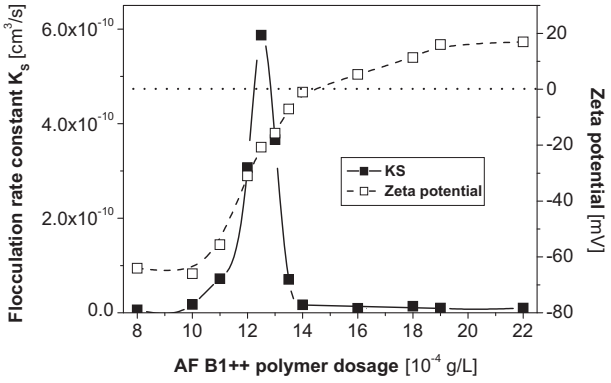

Fig. 8. K_S and zeta potential evolution as a function of AF B1^{++} polymer concentrations. The K_S maximum value is obtained at $12.5 \cdot 10^{-4}$ g/L of branched polymer and for a zeta potential value of −21 mV. The effective flocculation window corresponds to a polymer concentration range from 10.5 to 13.5 [10^{-4} g/L] and zeta potential range from −50 to −10 mV.

that using AF B1^{++} the free latex particles are still negatively charged within the range of the effective window of flocculation.

For comparison, the corresponding stability ratio evolution of the two polymers with dosage is presented in Fig. 9. Two main differences between the linear and branched polymers are found: i) branched polymers destabilize the latex suspensions significantly faster than the linear polymers ii) the width of the linear polymer dosage window is substantially larger than the branched one. Such observations reveal a better efficiency at the optimal dosage for the AF B1^{++} despite the fact that more important quantities are needed. The Critical Flocculation Concentration* (CFC*) and CFC** [30,31] are also calculated and presented in Fig. 9. The evolution of w can be described into three different regimes: i) one region where flocculation is increased (decrease of the stability ratio w) by increasing the polymer dosage. The maximum value obtained in this region is represented by the CFC*, ii) a second region where the stability ratio w has its maximum value and the polymer its maximum efficiency, iii) a third region where w increases again indicating the stabilization of the colloid suspension.

3.4. Flocculation mechanisms

To get an insight into the flocculation mechanisms, IDC latex spheres, linear and branched polymer hydrodynamic radius R_h were measured by DLS with a Malvern Zetasizer Nano ZS. The results below show that polymer R_h, respectively 311 ± 11 nm for linear polymers and 252 ± 20 nm for two-branched polymers, are slightly lower than the IDC particle R_h which is equal to 508 ± 37 nm. Experiments clearly demonstrate that the latex particle zeta potential is increasing with the polymer dosage from −100 mV up to charge reversal and stabilization at +20 mV. Here polymer adsorption leads to the characteristic charge reversal (or overcharging) of the latex particles after one isoelectric point (IEP). When adding polymer at the optimal flocculation dosage, the zeta potential is found close to −20 mV for both linear and branched polymer denoting that, in the two cases, the main flocculation mechanism is not related to a charge neutralization process. Also owing to the hydrodynamic radius and molar masses of the two polymers, the patch neutralization process is not expected, at optimal dosage, to play an important role. These findings suggest that “tele-bridging” flocculation and electrostatic forces dictate the stability of our oppositely charged latex particle suspension. The stability ratio w versus the polymer dose which is shown in Fig. 9 reveals the important finding of this paper. One observes the characteristic “U” shaped plots with the minimum situated at optimal dosage and before the IEP. After the IEP, by

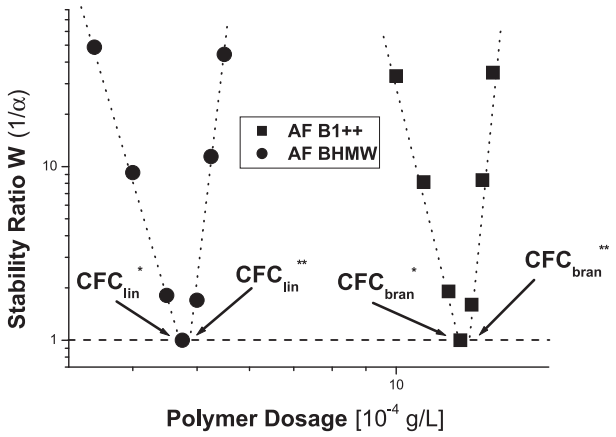

Fig. 9. Log–log plot of the stability ratio w versus the AF BHMW and AF B1^{++} polymer concentrations. The Critical Flocculation Concentrations$^{*/**}$ (CFC* and CFC**) were determined for both polymers respectively $CFC^{*/**}_{lin}$ for AF BHMW and $CFC^{*/**}_{bran}$ for AF B1^{++}.

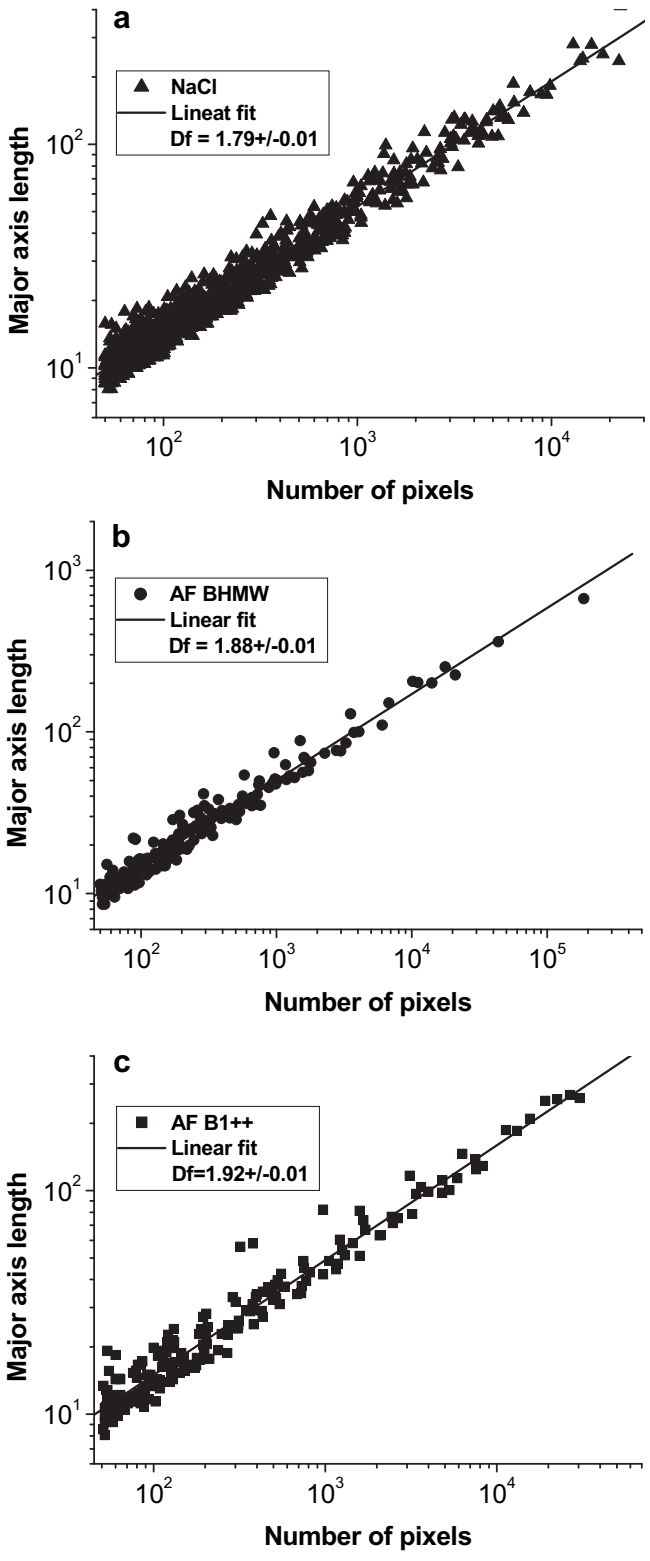

Fig. 10. Log–log plot of the major axis length as a function of number of pixels for the aggregates obtained by destabilization of latex suspensions after 2400 s and at optimal dosage of: (a) NaCl, (b) linear polymer, (c) branched polymer. Average D_f values obtained by analyzing 10 pictures of each solution, and by considering three decades in number of pixels, correspond to 1.80 ± 0.02 with NaCl, 1.88 ± 0.04 with the linear polymer and 1.91 ± 0.03 with the branched polymer.

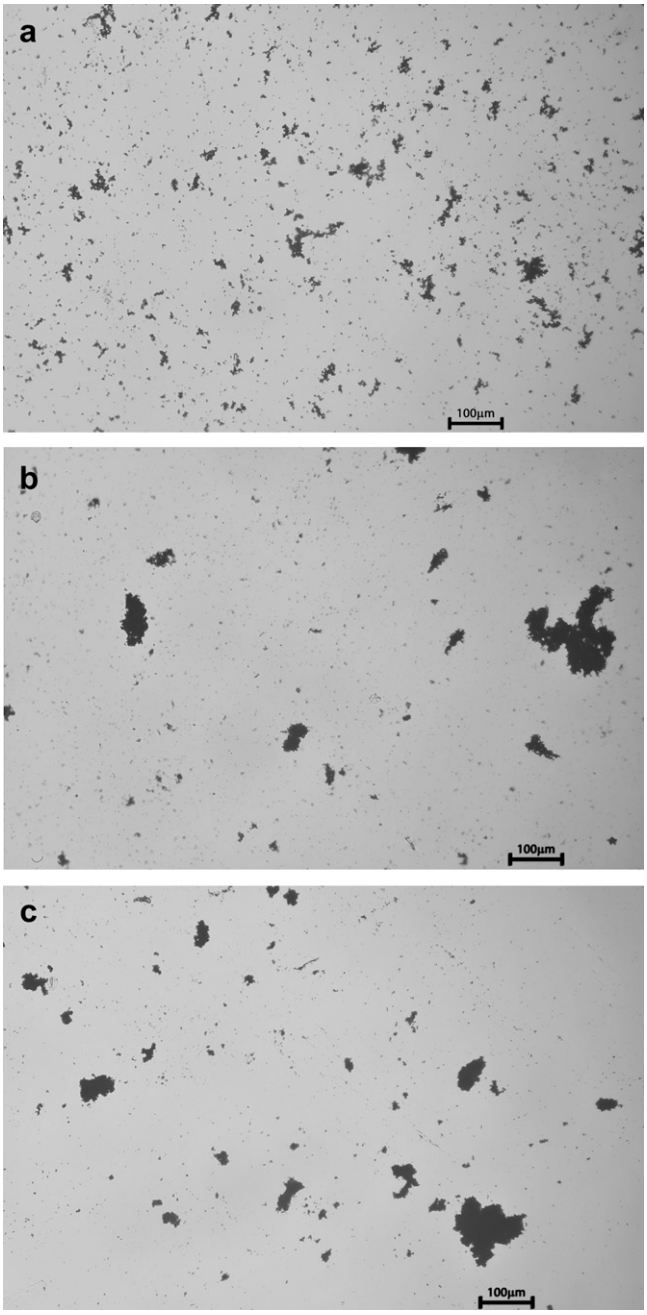

Fig. 11. Aggregate and floc pictures obtained by destabilization of latex suspensions at optimal dosage using : (a) NaCl, (b) linear polymer, (c) branched polymer. Large structures are observed for both polymers in agreement with the high kinetics aggregation rates. Aggregates obtained with salt are smaller and exhibit open structures.

increasing the polymer dose, a steric stabilization, due to bound polymer layers at the latex particles is achieved hence preventing them from coagulation via attractive van der Waals forces. One also observes in Fig. 9 that the stability ratio is rapidly increasing after the CFC** (asymmetric "U" shaped). Indeed, after the CFC**, steric and electrostatic stabilization of the polymer is rapidly achieved owing to the relative large dimensions of the two polymers in comparison to the latex particle sizes.

3.5. Determination of the floc structures

In order to evaluate the fractal character and calculate the floc fractal dimensions in presence of salt, linear and branched polymers, flocs were collected after 2400 s at optimal salt and polymer dosage (respectively: 0.5M, $4.75 \cdot 10^{-4}$ g/L and $1.25 \cdot 10^{-3}$ g/L). For each situation, 10 samples representing at least 1000 aggregates were analysed. In Fig. 10 is presented on log–log plots the variation of the flocs major axis lengths as a function of their masses (number of pixels). Pictures corresponding to the resulting flocs are given in Fig. 11 for the salt, linear and branched polymers. The fractal dimension D_f (1.80 ± 0.02) of aggregates induced by NaCl charge screening is in good agreement with the common values found for the cluster–cluster aggregation model [32,33] for the diffusion limited aggregation process (DLCA) which results in the formation of open structures.

Flocs induced by linear and branched polymers exhibit significant higher D_f values, respectively 1.88 ± 0.04 and 1.91 ± 0.03, denoting that theses flocs are more compact and larger in good agreement with the respective kinetics rate constants. There is a noteworthy difference between flocs induced by the presence of linear polymers and those by branched polymers which are more dense.

4. Conclusions

A Coulter Counter was used to investigate in a systematic way the floc formation between negatively charged particles and oppositely charged polymeric flocculants. Kinetics aspects as well as structural parameters (fractal dimensions) with special focus on the effects of polymer dosage were investigated. The role of polymer dosage on the flocculation rate constants, stability ratio w variations and the determination of the CCC were also investigated and a systematic comparison was made with salt induced particles aggregation for a better estimation of polymer efficiency and optimal dosage concentration range.

Our study points out the differences between the flocculation and the salt induced destabilization mechanisms. At optimal polymer dosage, the flocculation rate constants are significantly larger than the aggregation rate constant obtained with salt i.e. when charge screening has reached its optimal effect. The structure of the polymer is shown to play a significant role on the kinetics of flocculation, floc characteristics, and the range of concentration over which flocculation occurs. Optimal polymer dosage concentration is higher for the branched polymer which exhibits a greater flocculation rate constant, whereas the linear polymer is shown to have a larger concentration domain of use.

Overall, our findings suggest that bridging flocculation and electrostatic forces dictate here the stability of the charged latex particle suspension, in comparison to charge neutralization and patch formation flocculation mechanisms. Another interesting result of this study is the fact that the analysis of the resulting structures clearly demonstrates the fractal character of the flocs and exhibits a significant difference between the two polymers denoting the importance of the polymer architecture not only in the kinetics rate constant and concentration range, but also in the fractal floc structure which is expected to control important floc properties such as floc settling velocity and cohesion. Mixtures of polymers and salt will be investigated in a future paper to gain insight into the effect of charge screening on the polymeric flocculant efficiency.

Acknowledgments

The authors are grateful to E. Pefferkorn, J. Buffle, J.L. Loizeau, S. Ulrich, M. Seijo, F. Carnal for useful discussions and comments. The authors also acknowledge the Aqua + Tech Specialties SA (La Plaine, Geneva, Switzerland) for supplying the flocculant samples.

References

[1] Buffle J, Vitre RRD. Chemical and biological regulation of aquatic systems. CRC Press; 1994.
[2] Santschi P. Particle flux and trace metal residence time in natural waters. Limnol Oceanogr 1984;29:1100–8.
[3] Buffle J, Wilkinson K, Stoll S, Filella M, Zhang J. A generalized description of aquatic colloidal interactions: the three-colloidal component approach. Environ Sci Technol 1998;32:2887–99.
[4] Wilkinson KJ, Balnois E, Leppard GG, Buffle J. Characteristic features of the major components of freshwater colloidal organic matter revealed by transmission electron and atomic force microscopy. Colloids and Surfaces A: Physicochemical and Engineering Aspects 1999;155:287–310.
[5] Schwoyer W, editor. Polyelectrolytes for water and wastewater treatment; 1981.
[6] Gregory J. Particles in water properties and processes; 2005.
[7] Stoll S, Buffle J. Computer simulation of bridging flocculation processes: the role of colloid to polymer concentration ratio on aggregation kinetics. Journal of Colloid and Interface Science 1996;180:548–63.
[8] Agarwal M, Srinivasan R, Mishra A. Synthesis of *Plantago Psyllium* mucilage grafted polyacrylamide and its flocculation efficiency in tannery and domestic wastewater. Journal of Polymer Research 2002;9:69–73.
[9] Verwey E, Overbeek J. Theory of the stability of lyophobic colloids. Dover Publications; 1948.
[10] Deryagin B, Landau L. Theory of the stability of strongly charged lyophobic sols and of the adhesion of strongly charged particles in solutions of electrolytes. Acta Physicochim. URSS 1941;14:633–62.
[11] Van Benschoten JE, Edzwald JK. Chemical aspects of coagulation using aluminum salts-I. Hydrolytic reactions of alum and polyaluminum chloride. Water Research 1990;24:1519–26.
[12] Van Benschoten JE, Edzwald JK. Chemical aspects of coagulation using aluminum salts-II. coagulation of fulvic acid using alum and polyaluminum chloride. Water Research 1990;24:1527–35.
[13] Duan J, Gregory J. Coagulation by hydrolysing metal salts. Advances in Colloid and Interface Science 2003;100–102:475–502.
[14] Ferretti R, Stoll S, Zhang J, Buffle J. Flocculation of hematite particles by a comparatively large rigid polysaccharide: schizophyllan. Journal of Colloid and Interface Science 2003;266:328–38.
[15] Elimelech M, Williams R, Jia X, Gregory J. Particle deposition and aggregation: measurement, modeling and simulation. Butterworth-Heinemann; 1997.
[16] Zhou Y, Franks G. Flocculation mechanism induced by cationic polymers investigated by light scattering. Langmuir 2006;22:6775–86.
[17] Yu J, Wang D, Ge X, Yan M, Yang M. Flocculation of kaolin particles by two typical polyelectrolytes: a comparative study on the kinetics and floc structures. Colloids Surf., A 2006;290:288–94.
[18] Rasteiro M, Garcia F, Ferreira P, Blanco A, Negro C, Antunes E. Evaluation of flocs resistance and reflocculation capacity using the LDS technique. Powder Technology 2008;183:231–8.
[19] Antunes E, Garcia FAP, Ferreira P, Blanco A, Negro C, Rasteiro MG. Effect of water cationic content on flocculation, flocs resistance and reflocculation capacity of PCC induced by polyelectrolytes. Industrial & Engineering Chemistry Research 2008;47:6006–13.
[20] Barajas J, Hunkeler D, Wandrey C. Polyacrylamide copolymeric flocculants with homogeneous branching: hetereophase synthesis and characterization. Polym News 2004;29:239–46.
[21] Hunkeler D, Wandrey C. Polyelectrolytes: research, development, and applications. International Journal for Chemistry 2001;55:223–7. Chimia.
[22] Stoll S, Wandrey C, Hünkeler D. Rational Formulation of Water Based Flocculants: Interactions, local Nanostructure and Dimensions. in Preparation. (sans date).
[23] Mandelbrot B. The fractal geometry of nature. San Francisco: W.H. Freeman; 1982.
[24] Senesi N, Wilkinson KJ. Biophysical chemistry of fractal structures and processes in environmental systems. Wiley; 2008.
[25] Lopez J. Electrostatic heteroaggregation process arising in two-component colloidal dispersion; 1996.
[26] Plaza RC, Quirantes A, Delgado AV. Stability of dispersions of colloidal hematite/yttrium oxide core-shell particles. Journal of Colloid and Interface Science 2002;252:102–8.
[27] Rubio-Hernandez FJ. On the Hamaker function of polystyrene model colloids. Colloids and Surfaces A: Physicochemical and Engineering Aspects 1994;88:141–5.
[28] Hunter RJ. Foundations of colloid science. 2nd ed. USA: Oxford University Press; 2001.
[29] Puertas AM, de las Nieves FJ. Colloidal stability of polymer colloids with variable surface charge. Journal of Colloid and Interface Science 1999;216:221–9.
[30] Liang W, Bognolo G, Tadros TF. Stability of dispersions in the presence of graft copolymer. 1. Adsorption of graft copolymers on latex dispersions and the stability and rheology of the resulting dispersions. Langmuir 1995;11:2899–904.
[31] Sharma A, Tan SN, Walz JY. Measurement of colloidal stability in solutions of simple, nonadsorbing polyelectrolytes. Journal of Colloid and Interface Science 1997;190:392–407.
[32] Weitz DA, Oliveria M. Fractal structures formed by kinetic aggregation of aqueous gold colloids. Phys. Rev. Lett. 1984;52:1433.
[33] Waite TD. Measurement and implications of floc structure in water and wastewater treatment. Colloids and Surfaces A: Physicochemical and Engineering Aspects 1999;151:27–41.

Polymer 52 (2011) 1027–1036

Contents lists available at ScienceDirect

Polymer

journal homepage: www.elsevier.com/locate/polymer

Influences of polymer matrix melt viscosity and molecular weight on MWCNT agglomerate dispersion

Gaurav R. Kasaliwal, Andreas Göldel, Petra Pötschke*, Gert Heinrich

Leibniz Institute of Polymer Research Dresden, Hohe Str. 6, 01069 Dresden, Germany

ARTICLE INFO

Article history:
Received 10 September 2010
Received in revised form
28 December 2010
Accepted 5 January 2011
Available online 11 January 2011

Keywords:
Multiwalled carbon nanotubes
Polymer composites
Dispersion

ABSTRACT

In order to study the influence of melt viscosity and molecular weight on nanotube dispersion and electrical volume resistivity, three different polycarbonates (PCs) varying in molecular weight were melt compounded with 1 wt% multiwalled carbon nanotubes (MWCNTs, Baytubes® 150 HP) using a small-scale compounder. The experiments were performed at constant melt temperature but at varying mixing speeds, thereby applying different magnitudes of shear stress. Light transmission microscopy was used to access the state of agglomerate dispersion, and electrical resistivities of the composites were measured on pressed plates. The results indicate that with increasing matrix viscosity the agglomerate dispersion gets better when using constant mixing conditions but worse considering comparable shear stress values. To study the effect of molecular weight, in a second set of experiments melt temperatures were adjusted so that all PCs had similar viscosity and mixing was performed at constant mixing speed. As investigated on two viscosity levels, the composites based on the low molecular weight matrix showed smaller sized un-dispersed primary agglomerates as compared to composites with higher molecular weight matrices, highlighting the role of matrix infiltration into primary nanotube agglomerates as the first step of dispersion. The resistivity values of composites prepared using low viscosity matrices were lower than those of composites from high viscosity matrix.

1. Introduction

The production of composites based on polymer and multiwalled carbon nanotubes (MWCNT) by melt processing has acquired great interest for research, as it is a fast and economic method for industrial scale manufacturing. For the commercial success of these composites and, especially to get suitable mechanical properties, it is necessary to produce these composites free of un-dispersed primary agglomerates. However, it has been discussed in literature [1–7] that it is difficult to get rid of un-dispersed primary MWCNT agglomerates during melt compounding, particularly if the agglomerate density of the used nanotube materials is relatively high. In the process of dispersive mixing operation during melt compounding of polymer-filler systems, the applied shear stresses acting on the nanotube agglomerates cause their size reduction. If the filler agglomerates are infiltrated by the polymer melt, the infiltration can affect the packing structure and the agglomerate strength of the agglomerates or alter the cohesive forces binding small agglomerates within bigger ones [7]. This might weaken the agglomerates which then require relatively lower shear stresses for their size reduction. For this reason, the applied shear stresses and the melt infiltration into the nanotube agglomerate structure play a decisive role in controlling and accelerating the size reduction of filler agglomerates during melt processing. In this context the polymer matrix properties like melt viscosity and molecular weight are important factors that might affect these processes. In literature, some investigations concerning the influence of matrix melt viscosity on the dispersion of fillers like carbon black (CB), calcium carbonate ($CaCO_3$), nanoclay etc., and also on nanotubes (CNTs) have been reported and some of them are summarised below.

Yamada et al. [8] reported the influence of polydimethylsiloxane (PDMS) infiltration on the dispersion kinetics of carbon black (CB) agglomerates. They found that the viscosity of the matrix and the porosity of the agglomerates are important factors that affect infiltration and therefore the process of filler dispersion. The authors stated that the matrix with the higher melt viscosity would infiltrate slower into agglomerates than the low melt viscosity matrix [9]. Similar observations have been reported by Levresse et al. for $CaCO_3$ agglomerates [10]. The authors modelled the infiltration kinetics into $CaCO_3$ agglomerates and found that decreasing agglomerate radius, agglomerate density, and polymer viscosity result in higher infiltration rates. Roland et al. reported on the

* Corresponding author. Tel.: +49 351 4658 395; fax: +49 351 4858 565.
E-mail address: poe@ipfdd.de (P. Pötschke).

0032-3861/$ – see front matter © 2011 Elsevier Ltd. All rights reserved.
doi:10.1016/j.polymer.2011.01.007

dispersion of CB in linear and branched polyisobutylene (PIB) by performing dynamic mechanical analysis and electrical resistivity measurements [11]. The measured values reflected that the dispersion of CB was worse in branched PIB as compared to that observed in linear PIB even though high shear stresses were applied. It can be interpreted that the branching of PIB restricted its infiltration into CB agglomerates. In a study dealing with the intercalation of nanoclay in polystyrene (PS) during annealing, Vaia et al. found that faster intercalation of nanoclay was achieved in a matrix with lower melt viscosity and molecular weight as investigated using X-ray diffraction [12].

The shear stress present in the compounder during melt compounding is crucial for the agglomerate size reduction. A high melt viscosity of the matrix would help to apply higher shear stresses on agglomerates leading to their faster dispersion. In fillers like nanoclay, several such studies are reported like in [13–15] where better dispersion is claimed to be achieved by using high melt viscosity matrices thereby applying high shear stresses. However, these studies observed tendencies based on experiments where only a single/fixed mixing speed was employed.

In case of polymer-MWCNT systems few studies have been reported where the influence of matrix viscosity on MWCNT dispersion or composite properties is investigated systematically. For example, Le et al. [16] reported the state of dispersion of MWCNT in natural rubbers varying in melt viscosity by using online measured electrical conductance. Lowering the viscosity of the starting rubber until an optimum level resulted in faster MWCNT agglomerate dispersion at a certain mixing speed. This was related to the optimal balance between infiltration speed of rubber chains into MWCNT agglomerates and the shear stress transferred by the mechanical forces in the mixer. Mičušík et al. diluted an industrial polypropylene (PP) masterbatch with other PPs of varying viscosity [3]. Lower resistivity values or lower electrical and rheological percolation thresholds were obtained for composites based on low melt viscosity or low molecular weight matrices. Hermant et al. produced polymethylmethacrylate (PMMA) and PS latex based composites and observed lower percolation thresholds in composites which had higher fractions of lower molecular weight polymer [17]. In a recent study, Socher et al. produced composites using different molecular weights and end group functionalities of polyamide 12 (PA12, acid and amine excess) [18]. Composites of low molecular weight PA12 with acid excess showed lower percolation thresholds than those based on high molecular weight and amino terminated materials. However, at a fixed mixing speed, the best MWCNT dispersion was obtained in high viscous PA12 composites.

The influence of variation in melt viscosity, induced by different compounding temperatures, on MWCNT dispersion during melt compounding of polycarbonate (PC) with 1 wt% MWCNT was reported in Ref. [4]. At low mixing speeds, MWCNT dispersion was better in high viscosity matrix as the applied shear stresses were also high. At high mixing speeds similar states of dispersion were observed irrespective of the set melt temperature or viscosity. The results are in agreement with Le et al. [16] and indicated that high shear stresses are not the only requirement to achieve good dispersion of MWCNT agglomerates.

However, the common view in melt mixing of polymers with agglomerated nanotubes is that high applied shear stresses give best dispersion, even if there are some opposite results already reported in literature. In order to clarify that, a systematic study varying the polymer viscosity and thus the applied shear stresses was done on a model system, namely amorphous polycarbonate with MWCNTs Baytubes, representing an agglomerated CNT material with relatively high agglomerate density. The special focus was on the role of melt viscosity on matrix infiltration into primary nanotube agglomerates and its influence on the dispersion process.

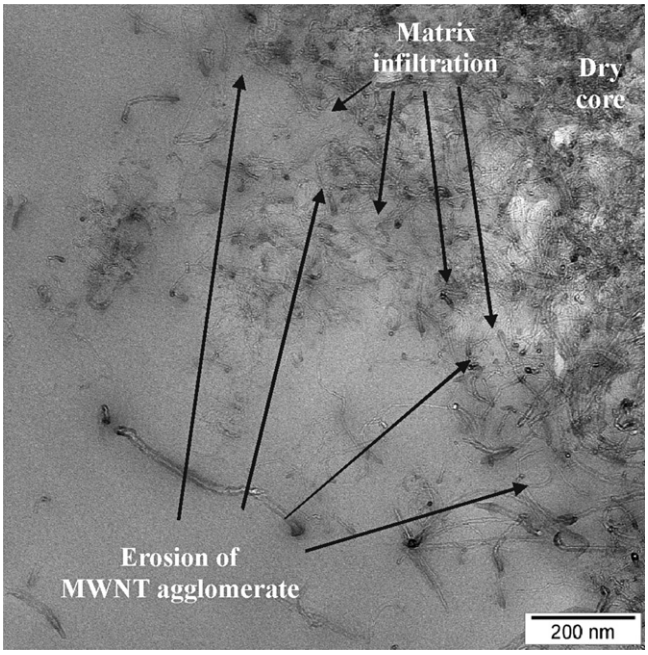

Fig. 1. TEM micrograph illustrating matrix infiltration and subsequent separation of MWCNT due to erosion from the agglomerate surface.

To illustrate the process of matrix infiltration, in Fig. 1 a TEM image of one MWCNT agglomerate undergoing dispersion in a polycarbonate melt is shown. The melt infiltrates the agglomerate and tubes from the surface of the agglomerate are being separated and dispersed in the melt.

In order to investigate the distinct influences of applied shear stresses and melt infiltration on MWCNT agglomerate dispersion, three PCs differing in molecular weight were melt mixed with 1 wt % Baytubes C150HP using a DACA microcompounder by varying the applied mixing speed. To investigate the influence of melt viscosity on agglomerate dispersion, in a first set of experiments compounding was done at a constant temperature leading to different shear stresses for the different PCs. In a second set of experiments, the compounding temperatures were adjusted in a way that the PC has similar melt viscosity and thereby solely the influence of matrix molecular weight on agglomerate dispersion could be observed. The state of macrodispersion at different levels of applied shear stress was analysed using optical micrographs and the electrical properties of the composites produced under the different conditions are discussed.

2. Experimental

2.1. Materials

As polycarbonates, a low viscosity grade Makrolon® 2205, a medium viscosity grade Makrolon® 2600, and a high viscosity grade Makrolon® 3108 (from Bayer MaterialScience AG, Germany) with a density of 1.2 g/cm^3 were selected. In Table 1, molecular weights, melt viscosities at 280 °C, and melt temperatures to reach a certain viscosity level of these polycarbonates are given.

The MWCNTs used in this work (Baytubes® C150HP, Bayer MaterialScience AG, Germany) are produced by a catalytic chemical vapour deposition process and were supplied as agglomerates. The carbon purity of this highly purified material is >99%, the outer mean nanotube diameter is reported to be in the range of 13–16 nm, the length of the tubes is in the range of 1to >10 μm, and their bulk

Table 1
Melt volume flow rates MVR, molecular weights (M_w, M_n, PD), zero shear melt viscosities, and melt temperature to reach desired viscosity levels of different polycarbonates.

Polycarbonate	MVR[c] (cm^3/10 min @ 300 °C/1.2 kg)	M_w[a] (g/mol)	M_n[a] (g/mol)	Polydispersity (DP)[a]	Complex viscosity[b] at 280 °C (Pa s)	Melt temperature (°C) to reach viscosity level[b] of	
						~500 Pa s [d]	~1200 Pa s [d]
Makrolon 2205	36	20,100	7700	2.62	240	260	240
Makrolon 2600	12.5	26,200	9500	2.76	720	290	265
Makrolon 3108	6	29,800	11,400	2.62	1240	310	280

[a] Molecular weights determined by GPC using THF as solvent.
[b] Zero shear melt viscosities determined using an ARES oscillatory rheometer in frequency sweeps (strain 5%).
[c] MVR from material data sheets.
[d] Determined using an ARES oscillatory rheometer using dynamic temperature ramp. 0.1 rad/sec, strain 5%.

density is 140–230 kg/m^3 [19]. The porosity of these MWCNT agglomerates is found to be 0.18 [7].

These MWCNT agglomerates have a broad particle size distribution (4.5 μm–600 μm) [7]. For a part of the investigations, the primary MWCNT agglomerates were sieved and separated into certain size classes (using a Fritsch sieving equipment, sieving amplitude 2, time 20 min). The separated size fractions were: over 500 microns (top cut), 355–400 microns, 100–125 microns, and below 63 microns (bottom cut).

Before melt mixing, PC and MWCNTs were dried overnight at 100 °C in vacuum.

2.2. Composite preparation

2.2.1. Melt compounding

A DACA microcompounder (DACA Instruments, Goleta, CA) representing a small-scale, co-rotating twin-screw microcompounder with a bypass and a filling volume of 4.5 cm^3 was used for melt mixing. In this compounder, mixing parameters such as mixing temperature, speed, and time can be easily controlled and the torque values can be monitored. The material was added step wise in the running microcompounder and a charge of 4.2 g material was processed during each experiment. The mixing duration was set to the short time of 5 min considering the maximal residence time in a twin-screw extrusion process. The material was taken out as a strand (diameter ~ 2 mm) using the set screw speeds through the heated cylindrical die into air without additional cooling or drawing. As reported in a previous study [4], Baytubes C150HP show electrical percolation in PC at 1 wt% and so this concentration was used for the present study. The experiments were performed in two sets.

Set 1: To investigate the influence of melt viscosity on CNT dispersion, melt-compounding temperature (barrel temperature) was set at 280 °C. To apply different shear stresses, mixing speeds of 10, 30, 50, 75, 100, 150, 200, 250, and 300 rpm were employed, thereby using the complete mixing speed range of the equipment.

The applied shear stress was calculated using equation (1):

$$\tau_{applied} = K' \cdot \eta \cdot \dot{\gamma} \quad (1)$$

The shear rate $\dot{\gamma}$ was evaluated following Ref. [20]:

$$\dot{\gamma} = \frac{\pi \cdot (D - 2\delta) \cdot N}{\delta} \quad (2)$$

Here, K' (for spherical particles) was set to 2.5 [21], D is the screw diameter (9.725 mm) and δ is the screw clearance with barrel (100 μm), N is the mixing speed in rps. The viscosity values η at the applied shear rates $\dot{\gamma}$ were taken from Ref. [22].

Set 2: To investigate the distinct influence of the matrix molecular weight in a second set of experiments two melt viscosity levels, namely viscosity level 1 of 500 Pa s and viscosity level 2 of 1200 Pa s, were applied. The viscosity levels were controlled by adjusting the melt temperatures (barrel temperature) for the different PCs as indicated in Table 1. The compounding was carried out at a mixing speed of 100 rpm. For the sieved fractions of MWCNT, melt compounding was performed on viscosity level 1 only.

2.2.2. Compression moulding

The extruded strands were compression moulded into circular plates (diameter 60 mm, thickness 0.5 mm) using a Weber hot press (Model PW 40EH, Paul Otto Weber GmbH, Remshalden, Germany). Compression moulding was carried out following the detailed procedure described in Ref. [4]. For composites prepared by set-1, the moulding was carried out at 265 °C using a pressing time of 1 min and pressing speed of 6 mm/s. For composites prepared in set 2, only those samples prepared with un-sieved MWCNT were compression moulded and the temperatures were adjusted (as indicated in Table 1) to maintain the viscosity level 1 and 2 also during the pressing procedure whereas other pressing conditions remained same.

2.3. Composite characterisation

2.3.1. Optical microscopy

For light transmission optical microscopy, thin sections of 20 microns thickness were prepared from extruded strands (perpendicular to extrusion direction) using an RM 2055 microtome (Leica, Germany) at room temperature. A glass knife with a cut angle of 35° was used. The thin sections were imaged with a BH2 microscope equipped with a camera DP71 (both Olympus) considering the entire cross-sectional area.

From the micrographs the area ratio of un-dispersed agglomerates to the micrograph area (A, in %) was analysed using digital image processing (software ImageJ). Further, un-dispersed agglomerates are classified as per the size classes based on their circle equivalent diameters (size class with 10 μm width). Agglomerates smaller than 1 μm were excluded for further data evaluation and interpretation.

To have a sufficient statistics of measured values, at least eight images from four different positions along the length of the strand were used for analysis leading to an investigated area of at least 4.8 mm^2.

2.3.2. Electrical measurements

Electrical volume resistivity measurements were performed either on compression-moulded circular plates (diameter: 60 mm, thickness 0.5 mm) or on strips depending upon their resistivity values. For high resistivity samples (resistivity $> 10^7$ Ω cm), a Keithley Electrometer 6517A with a 8009 Resistivity test fixture equipped with ring electrodes was used. For samples having lower volume resistivity, the measurements were performed on strips (~20 mm × ~7 mm) cut from the compression-moulded plates using a four-point test fixture combined with a Keithley Multimeter DMM 2000. The four-point test fixture has gold contact wires with

a distance of 16 mm between the source electrodes and 10 mm between the measuring electrodes. The volume resistivity was measured at 24 °C and 40% relative humidity. Before measurements, the surfaces of the samples were cleaned with ethanol. For each specimen at least two measurements were made for high resistivity and four for low resistivity samples.

3. Results and discussion

3.1. Influence of PC melt viscosity

3.1.1. Investigation of MWCNT dispersion

Optical micrographs of composites with 1 wt% Baytubes® C150HP prepared using the PCs with different viscosity at selected mixing speeds are shown in Fig. 2.

In Fig. 3, the area ratio of un-dispersed agglomerates, A, is plotted versus the mixing speed. At lower mixing speeds, relatively larger sizes of agglomerates resulting in higher A values were observed in the matrix with the low viscosity as compared to medium and high viscosity matrices. However, as higher mixing speeds were employed, the difference in the state of MWCNT agglomerate dispersion between the PC narrows. Interestingly, above a certain mixing speed, here on and above 200 rpm, the difference in the state of dispersion becomes marginal. Thus, the use of high mixing speeds results in similar states of dispersion of CNT agglomerates in all matrices.

To analyse the rate of morphology development in different PC matrices with increasing mixing speed, the relative change in the area ratio $(1-(A_x/A_0)$ i.e. the relative decrease in the area of un-dispersed agglomerates A_x at any mixing speed x in correlation to the area A_0 at a mixing speed of 10 rpm) was evaluated. These relative changes in area ratio are plotted versus the mixing speed for all three PC matrices in Fig. 4 illustrating a common curve.

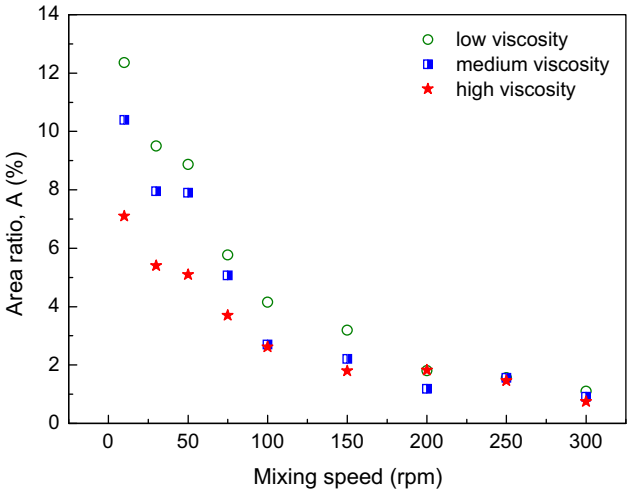

Fig. 3. Area ratio *A* versus mixing speed of PCs with different matrix viscosity and 1 wt% MWCNT.

Irrespective of matrix viscosity and the initial state of dispersion, approximately 90% change in the area ratio was realised by increasing the mixing speed from 10 rpm to 300 rpm.

In Fig. 5, the shear stress applied from the PC matrices varying in melt viscosity onto the primary agglomerates is plotted versus the mixing speed. Obviously, higher shear stresses are exerted by the high viscosity matrix as compared to the lower viscosity ones. The difference in the applied shear stress becomes more evident as the mixing speed increases.

The applied shear stress is responsible for the evolution of the MWCNT agglomerate dispersion in the composites. The shear stress

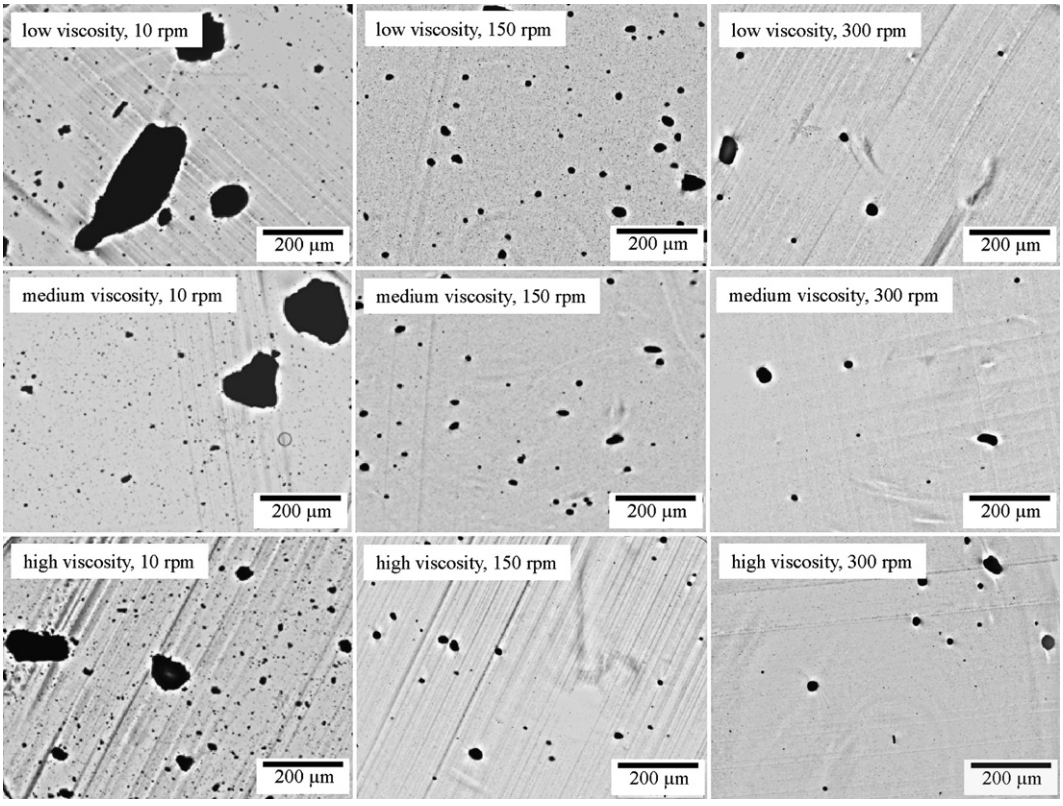

Fig. 2. Optical micrographs illustrating the state of agglomerate dispersion of 1 wt% MWCNT in PCs with different melt viscosity at selected mixing speeds.

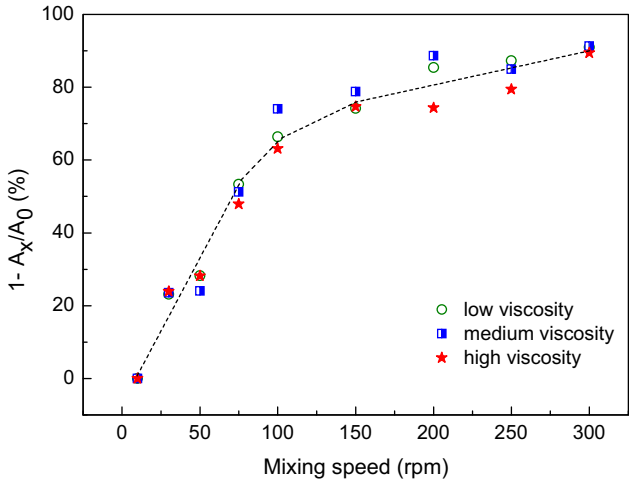

Fig. 4. Relative change in area ratio $(1-(A_x/A_0))$ versus mixing speed.

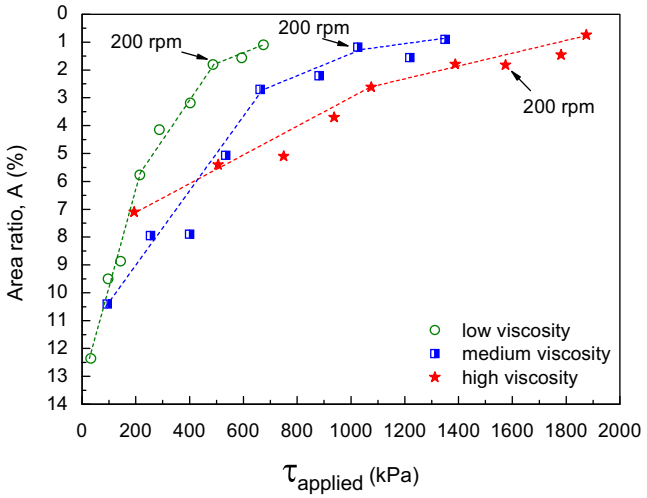

Fig. 6. Area ratio A versus applied shear stress $\tau_{applied}$ for different matrix melt viscosities.

causes break up and dispersion of the agglomerates. To observe the difference in MWCNT agglomerate dispersion in correlation to the applied shear stress, the area ratio A was plotted versus applied shear stress in Fig. 6. As the mixing speed and the shear stress increase, the dispersion improves in all matrices. Interestingly, as the applied shear stress increases, the change in area ratio is faster in low viscosity matrix followed by medium and high viscosity matrix. At shear stresses corresponding to 200 rpm and higher mixing speeds, surprisingly only a marginal difference is observed in the area ratio of un-dispersed agglomerates among composites made by the different PC. In Fig. 7, the relative change in the area ratio with mixing speed is plotted versus applied shear stress. Much higher applied shear stress was required for high viscosity matrix as compared to medium and low viscosity matrix to achieve comparable relative area changes $(1-(A_x/A_0))$. This result of faster development in area ratio with applied shear stress at lower matrix viscosity is on the first view unexpected. However, it illustrates the role of the infiltration process as first step of the dispersion process.

The filler agglomerates usually have a certain porosity, which facilitates melt infiltration into them. Further, the pores present in the agglomerates allow flow within them, which is driven by the shearing motions present within the external fluids. This internal flow affects the manner in which the hydrodynamic stress is distributed within the agglomerate [8]. In the process of filler dispersion during melt compounding, mainly the applied shear stresses acting on the agglomerates are responsible for their size reduction. The molecular weight of the polymers and the melt viscosity (which is temperature dependent) influence in different ways the final state of filler dispersion. If melt viscosity is high then the applied shear stresses on the agglomerates are high; on the other hand, if the melt viscosity is low melt infiltration into the agglomerates is pronounced so that their strength can be significantly weakened. Further, peripheral erosion of agglomerates is also enhanced by infiltrated surfaces. High melt viscosity of matrix slows the infiltration speed but produces high shear stress and vice versa for low viscosity matrix.

The agglomerates in the low viscosity matrix can be assumed to be more complete infiltrated than the agglomerates in medium and high viscosity matrices. At lower mixing speeds, poor dispersion was observed in the low viscosity matrix because the applied shear stress was also quite low. Thus, at low speeds better dispersion was observed in high viscosity matrix as applied shear stresses are high. However, at high mixing speeds, in low viscosity matrix the shear stresses are high enough to disperse the infiltrated MWCNT

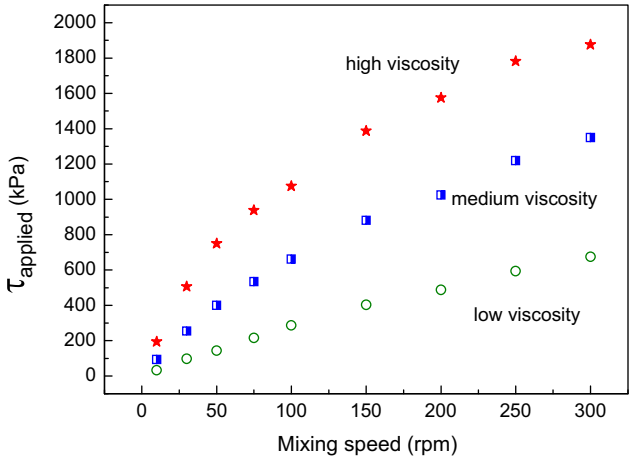

Fig. 5. Applied shear stress $\tau_{applied}$ versus mixing speed for polycarbonates varying in melt viscosity.

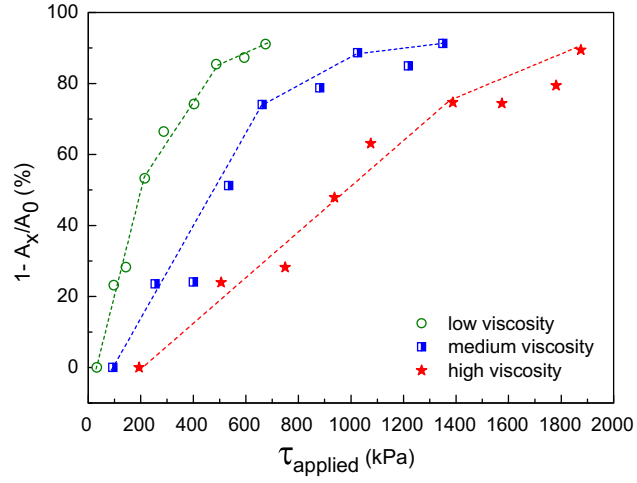

Fig. 7. Relative change in area ratio $(1-(A_x/A_0))$ versus applied shear stress $\tau_{applied}$ for different matrix melt viscosities.

agglomerates having lower agglomerate strength. Thus, although much higher shear stress is applied using a high viscosity matrix, a similar level of dispersion is achieved as in low viscosity matrix. At higher mixing speeds a counteracting balance is observed between melt infiltration and applied shear stress. Considering the applied shear stress, MWCNT agglomerates offer relatively less resistance for dispersion in low viscosity matrix than in a high viscosity matrix. The resistance for dispersion is generally the cohesive strength of agglomerates. In order to estimate this resistance for dispersion of agglomerates or the cohesive strength of the agglomerates in the following paragraph a model is proposed.

For a given matrix, at the lowest mixing speed considered, in our case at 10 rpm, a certain state of dispersion was achieved which was further improved as higher shear stresses were applied at higher mixing speeds. A schematic description of this improvement in dispersion due to the applied shear stress is shown in Fig. 8.

Assuming that the change in the area ratio with applied shear stress is proportional to the initial area ratio, equation (3) can be derived:

$$\frac{d\,A'}{d\,\tau_{\text{applied}}} \propto A' \tag{3}$$

Integrating equation (3) for $A' = A_0$ (at 10 rpm) to $A' = A_x$ at x rpm results in

$$\ln\frac{A_x}{A_0} = -k\cdot\Delta\tau_{\text{applied}} \rightarrow k = \frac{1}{\tau_{\text{cohesive}}} \tag{4}$$

where the constant of proportionality k is the inverse of the cohesive strength of the agglomerates.

In Fig. 9, $\ln(A_x/A_0)$ is plotted versus the applied shear stress. The dotted lines represent the fits of equation (4).

From the slope k of the dotted lines the resistance of the agglomerates against dispersion, i.e. the average cohesive strength of (partially infiltrated) agglomerates in a given polymer melt, is estimated. For low viscosity matrix it is 0.26 MPa, for medium viscosity it is 0.5 MPa, and for high viscosity it is 0.82 MPa. The lower value of τ_{cohesive} obtained for MWCNT agglomerates in a low viscosity matrix indicates that using low viscosity matrices is favourable for manufacturing composites. Further, applying high shear stress on agglomerates might cause breakage of tubes and this might be undesirable. Applying high shear stress is also undesirable for polymers as they can degrade by polymer chain breakage. It has been stated previously that it is difficult to get rid of the agglomerates of certain low size classes, as such agglomerates have very high agglomerate strengths [7]. However, the values calculated here indicate average τ_{cohesive} over all agglomerate size classes. The values are helpful to estimate and understand that agglomerates can be dispersed in low melt viscosity matrix at relatively low expense of energy as compared to medium or high viscosity matrix.

3.1.2. Electrical resistivity

To investigate the state of electrical network formation in these composites, volume resistivity measurements were carried out and

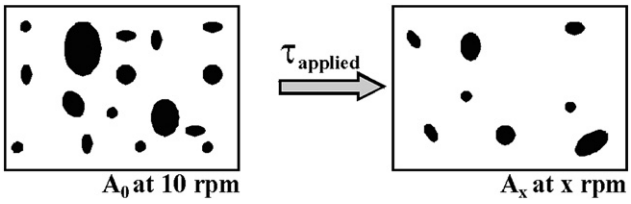

Fig. 8. Schematic showing the improvement in dispersion by increasing rotation speed and thus applied shear stress.

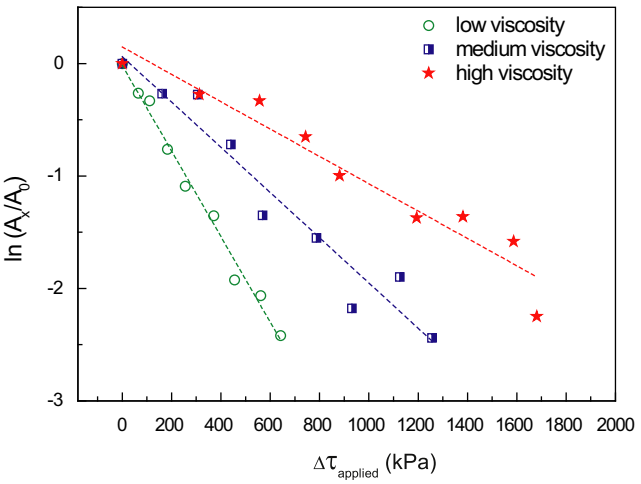

Fig. 9. $\ln(A_x/A_0)$ versus $\Delta\tau_{\text{applied}}$ (dotted lines indicate the fits of equation (4)).

are plotted in Fig. 10 versus the mixing speed employed during melt mixing.

All composite produced at low mixing speeds (50 rpm and below) are non-conductive. As higher mixing speeds were employed, the resistivity of all composites decreases. However, the decrease in the resistivity of composites is not similar. On one hand, the decrease in the resistivity of composites based on low and medium viscosity PC is strong and starting from 75 rpm, these composites are electrically percolated. Nevertheless, further increase in the mixing speed does not help in further decreasing the resistivity. On the other hand, the resistivities of the composites produced using PC with high melt viscosity decrease slowly with increasing mixing speed and reach a semi-conductive state. However, at the highest mixing speed employed the resistivity of the composite increases. This anomaly of increase in resistivity might be due to breakage of tubes during compounding, but this is only a hypothesis, as the breakage in tube length was not investigated in this study.

It has to be taken into account that pressing of the plates used for resistivity measurements was done at a constant temperature of 265 °C leading possibly to different states of secondary agglomeration. Higher re-agglomeration at lower viscosity may lead to lower resistivity values as compared to lower re-agglomeration at higher matrix viscosity ([4] and the references therein).

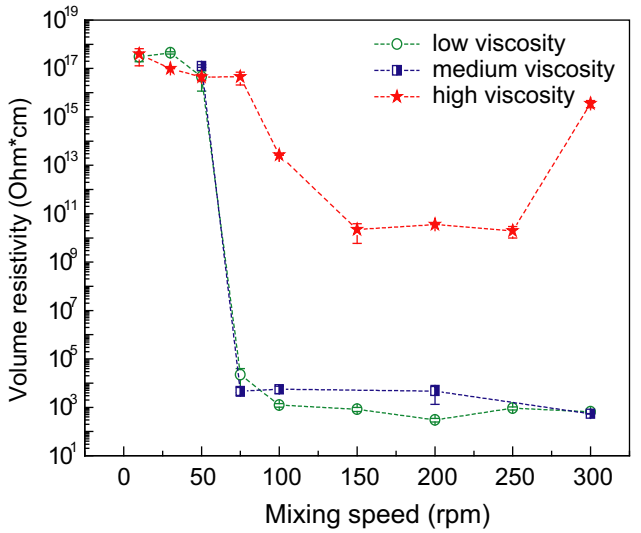

Fig. 10. Electrical resistivity of composites with 1 wt% MWCNT vs. mixing speed.

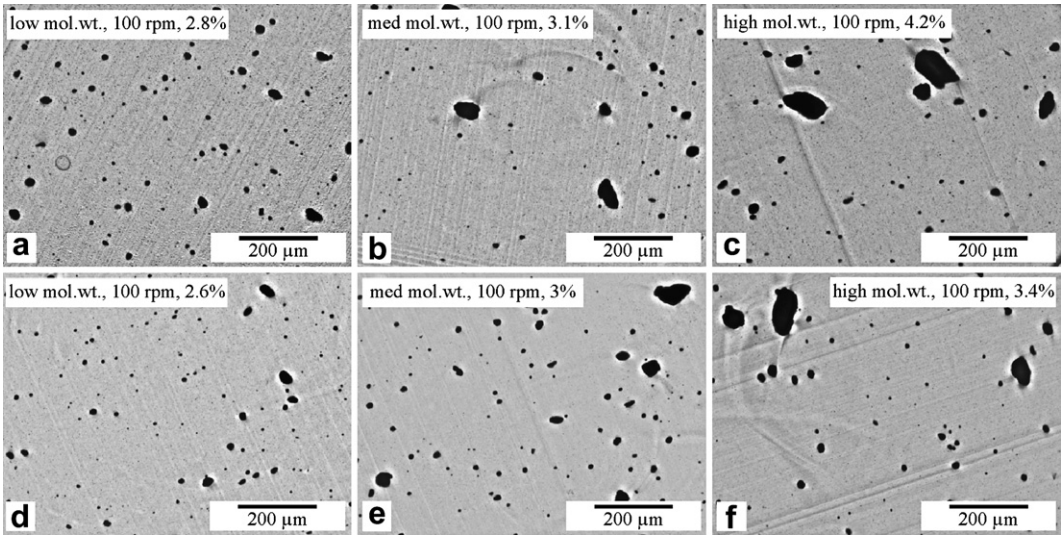

Fig. 11. Optical micrographs of PC with 1 wt% MWCNT prepared at two viscosity level: (a–c) low melt viscosity level (ca. 500 Pa s) (d–f) high melt viscosity level (ca. 1200 Pa s). As matrix molecular weight increases (from left to right), the size of un-dispersed MWCNT agglomerate increases. The area ratio *A* is indicated in %.

3.2. Influence of PC molecular weight

3.2.1. Investigation of MWCNT dispersion

Polymers vary in melt viscosity due to the difference in their molecular weight. To investigate if the polycarbonate matrix molecular weight has an additional influence (next to the viscosity effect) on CNT dispersion, melt mixing was performed by adjusting temperatures in a way that the polycarbonates with different molecular weights had similar viscosities. Thus, at a given mixing speed the applied shear stresses are comparable. In Fig. 11, optical micrographs are shown illustrating the state of dispersion of MWCNT agglomerates for composites produced at low viscosity level (500 Pa s, Fig. 11(a–c)) and for composites produced at high viscosity level (1200 Pa s, Fig. 11(d–f)). The number of agglomerates is plotted versus the equivalent diameter of un-dispersed agglomerates in Fig. 12. From these experiments it was found that at higher molecular weight of the matrix, the size of the largest un-dispersed agglomerates was higher. A considerable difference in the area ratio was also observed with increasing values at higher molecular weights. This tendency was observed at both viscosity levels. Nevertheless, the possibility of finding relative large sized agglomerates is not completely ruled out in low or medium molecular weight matrices even though they were not detected.

3.2.2. MWCNT dispersion of different agglomerate size fractions

In order to verify the effect of molecular weight on the size of un-dispersed agglomerates from different size classes, four sieved fractions of Baytubes® C150HP were used in melt compounding with the different polycarbonates. In Fig. 13, the size distribution i.e. the number of agglomerates is plotted versus the equivalent diameter of un-dispersed agglomerates observed in these composites. The results verify the earlier mentioned observation that the size of the largest un-dispersed agglomerate increases with the matrix molecular weight. It was also found that the sieved agglomerates from the highest size classes undergo the maximum size change. In those composites where initial MWCNT agglomerate size fractions of

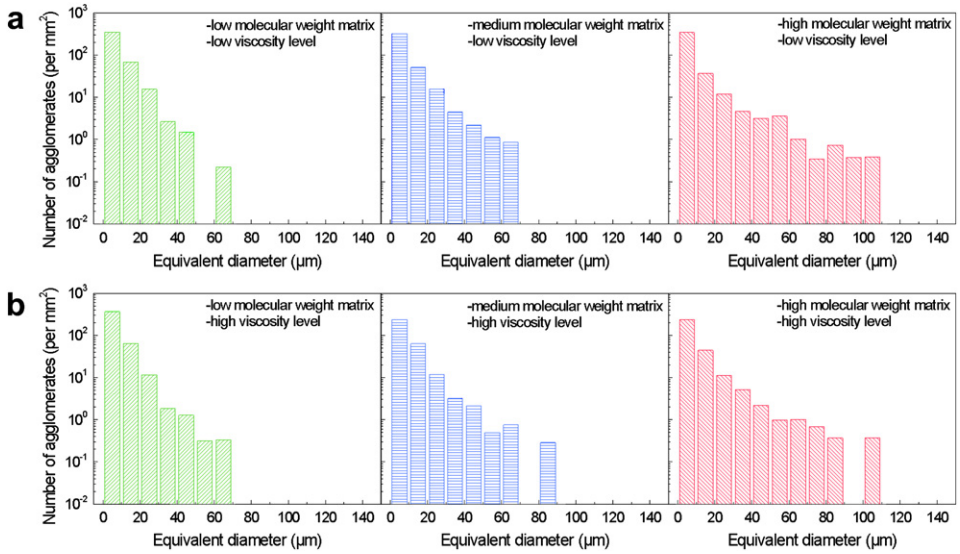

Fig. 12. Size distribution of un-dispersed agglomerates observed in PC with 1 wt% MWCNT (a) composites produced at low viscosity level (500 Pa s) and (b) composites produced at high viscosity level (1200 Pa s).

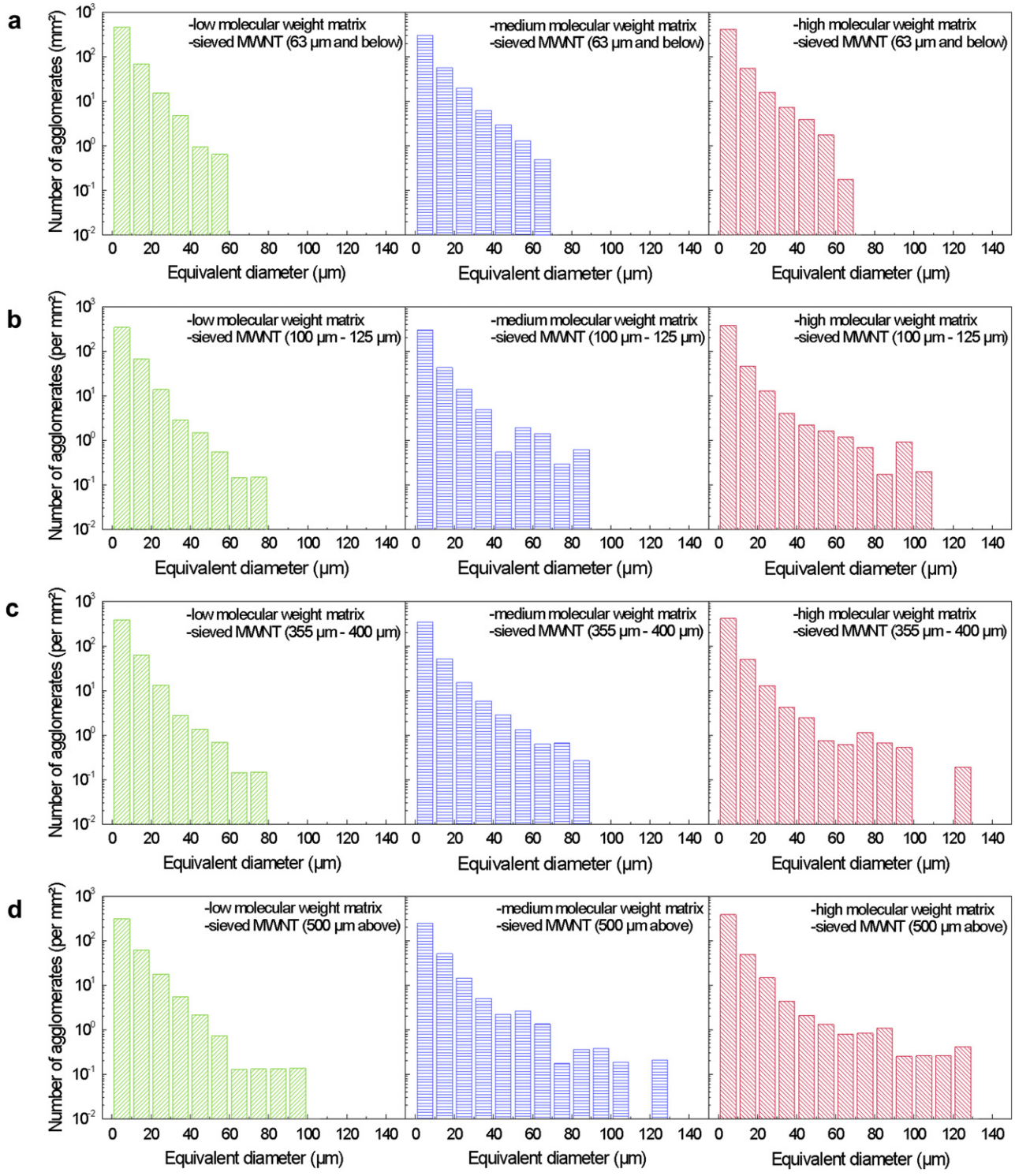

Fig. 13. Size distribution of un-dispersed agglomerate observed in 1 wt% MWCNT composites produced using different PC at melt viscosity level 1 (500 Pa s). MWCNT from different size fractions were used (a) below 63 μm, (b) 100–125 μm, (c) 355–400 μm, (d) 500 μm and above.

500 μm and above and 355–400 μm were used, the maximum size of un-dispersed agglomerate was found to be below 130 μm. Large sized agglomerates were broken down to small sized agglomerates and the decrease in agglomerate size was significant. In composites where smaller MWCNT agglomerate size fractions of 100–125 μm and below 63 μm are used, the observed size of largest un-dispersed agglomerates was 110 μm and 62 μm, respectively. Scurati et al. [23] observed during dispersing silica in PDMS that fractional reduction in large sized agglomerates occurs faster than for small sized agglomerates, when dispersion occurs under identical hydrodynamic conditions.

3.2.3. *Electrical resistivity*

The electrical volume resistivity of the composites prepared using un-sieved MWCNT and by adjusting the melt viscosity during melt processing (compounding and moulding) is plotted in Fig. 14 versus

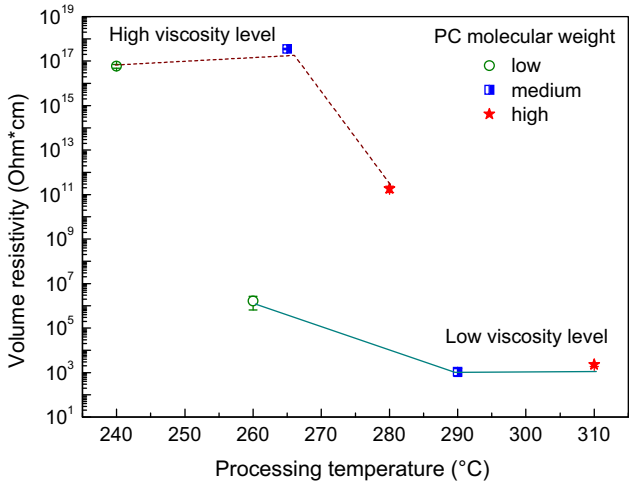

Fig. 14. Volume resistivity versus processing temperature of composites prepared using different molecular weight matrices.

the processing temperature. As expected, the composites processed at low viscosity level had lower resistivity values as compared to those prepared at high viscosity level. In literature, such observations were reported quite often and the lower level in resistivity at lower matrix viscosity was attributed to more pronounced secondary agglomeration of MWCNT ([4] and the references therein). During compression moulding, the movement of tubes for such secondary agglomeration intensifies at lower melt viscosity or longer annealing time at higher melt viscosity.

It was expected that the resistivity values of the composites produced at a given viscosity level should be in a similar range. However, an additional influence of temperature apart from viscosity on electrical volume resistivity is observed.

At the high viscosity level, only the highest molecular weight PC processed at the highest temperature of 280 °C results in composites with resistivities deviating from the insulating range. At the low viscosity level, the composites based on medium and high molecular weight, processed at the higher temperatures of 290 °C and 310 °C, respectively, showed lower resistivity values than the composite based on PC with low molecular weight. The lower resistivity values were achieved despite higher agglomerate area ratios at higher molecular weights. The experiments were repeated to confirm the tendencies. The results indicate that the melt temperature plays an additional role in lowering resistivities although the melt viscosities during mixing and compression moulding were same. Possibly, next to viscosity effects on the remaining primary agglomerates, the formation of a network consisting of separated nanotubes and agglomerates is more pronounced at higher temperatures. Higher melt temperature also leaves more time for structuration during cooling at similar rates, possibly thereby contributing to the observed reduction in electrical resistivity.

4. Summary and conclusion

The influence of polymer matrix melt viscosity and molecular weight on the dispersion of MWCNT agglomerates was investigated on the model system of polycarbonate and Baytubes® C150HP.

In studies concerning the effect of melt viscosity on MWCNT agglomerate dispersion it was observed that at low mixing speed better dispersion was obtained in the matrix with high melt viscosity, indicating that high shear stresses are necessary for good dispersion. Interestingly, above a certain mixing speed, independent of viscosity, similar states of dispersion were achieved in all composites although significantly different levels of shear stress were applied. This illustrates a balance between the counteracting effects of matrix viscosity on agglomerate infiltration and agglomerate dispersion. The faster improvement in dispersion with shear stress clearly reflects that MWCNT agglomerates have lower resistance to disperse or disperse relatively easier when incorporated into low viscosity matrices as compared to high viscosity matrices.

The electrical resistivity values of these composites indicate that high melt viscosity of the matrix can hamper the nanotube network formation which is in agreement with other results reported in literature (e.g. Ref. [18]).

In studies concerning the effect of molecular weight on MWCNT agglomerate dispersion it was observed that increasing the matrix molecular weight, despite constant melt viscosities achieved by adapting melt temperatures, results in larger un-dispersed agglomerates. This finding illustrates the very important role of matrix infiltration into the primary agglomerates as the first step of dispersion which is much faster and more complete in case of low molecular matrices. This is also reflected in lower values of the resistance of the agglomerates against dispersion, i.e. the average cohesive strength of (partially infiltrated) agglomerates in case of the low molecular PC as it was estimated from the slope of the relative agglomerate area ratio versus the change in applied shear stress.

Further, sieved MWCNT agglomerates from four different size classes were used to confirm this observation. These results show that sieved agglomerates from larger size classes undergo higher changes in size than agglomerates from smaller size classes.

The electrical resistivity values of the composites produced at constant melt viscosity level of the matrices indicate that increasing melt temperature has an additional influence on lowering the resistivity.

The results clearly indicate that the step of melt infiltration into primary agglomerates, which at a given nanotube agglomerate structure is faster at low melt viscosities and molecular weights of the matrix, plays an important role in lowering the agglomerate strength. Thus, the infiltration has, next to the applied shear stresses, a big influence on the agglomerate dispersion by rupture and erosion mechanisms.

In order to optimise agglomerate dispersion, attention has to be paid on that infiltration step despite just only to apply high shear stresses.

The tendencies found can be assumed to be also applicable to other polymer matrices and nanotube types, even if those may have different agglomerate properties and specific infiltration conditions and kinetics.

Acknowledgement

The authors thank Bayer MaterialScience AG, Germany, for supplying Baytubes® C150HP and polycarbonates, Dr. Albena Lederer for GPC measurements, and Dr. Michaela Gedan-Smolka for help with sieving of MWCNT agglomerates (both IPF Dresden). This research and development project was funded by the German Federal Ministry of Education and Research (BMBF) within the Framework Concept “Research for Tomorrow’s Production” (funding number 02PU2392) and managed by the Project Management Agency Karlsruhe (PTKA).

References

[1] Takase H. Evaluation and applications of dispersing carbon nanotube in the polymers. In: Hosokawa M, Nogi K, Naito M, Yokoyama T, editors. Nanoparticle technology handbook. Elsevier; 2007. p. 644.
[2] Prashantha K, Soulestin J, Lacrampe MF, Krawczak P, Dupin G, Claes M. Composites Science and Technology 2009;69:1756–63.

[3] Mičušík M, Omastová M, Krupa I, Prokes J, Pissis P, Logakis E, et al. Journal of Applied Polymer Science 2009;113(4):2536–51.
[4] Kasaliwal G, Göldel A, Pötschke P. Journal of Applied Polymer Science 2009;112(6):3494–509.
[5] Du FM, Scogna RC, Zhou W, Brand S, Fischer JE, Winey KI. Macromolecules 2004;37(24):9048–55.
[6] Ganss M, Satapathy BK, Thunga M, Weidisch R, Pötschke P, Jehnichen D. Acta Materialia 2008;56(10):2247–61.
[7] Kasaliwal G, Göldel A, Pegel S, Pötschke P, Heinrich G. Polymer 2010;51 (12):2708–20.
[8] Yamada H, Manas-Zloczower I, Feke DL. Powder Technology 1997;92(2):163–9.
[9] Yamada H, Manas-Zloczower I, Feke DL. Rubber Chemistry and Technology 1998;71(1):1–16.
[10] Levresse P, Manas-Zloczower I, Feke DL, Bomal Y, Bortzmeyer D. Powder Technology 1999;106(1–2):62–70.
[11] Roland CM, Robertson CG, Nikiel L, Puskas JE. Rubber Chemistry and Technology 2004;77(2):372–9.
[12] Vaia RA, Jandt KD, Kramer EJ, Giannelis EP. Macromolecules 1995;28 (24):8080–5.
[13] Chu D, Nguyen Q, Baird DG. Polymer Composites 2007;28(4):499–511.
[14] Fornes TD, Yoon PJ, Keskkula H, Paul DR. Polymer 2001;42(25):9929–40.
[15] Gianelli W, Ferrara G, Camino G, Pellegatti G, Rosenthal J, Trombini RC. Polymer 2005;46(18):7037–46.
[16] Le HH, Kasaliwal G, Ilisch S, Radusch HJ. KGK-Kautschuk Gummi Kunststoffe 2009;62(6):326–33.
[17] Hermant MC, Smeets NMB, van Hal RCF, Meuldijk J, Heuts HPA, Klumperman B, et al. E-Polymers; 2009:022.
[18] Socher R, Krause B, Boldt R, Hermasch S, Wursche R, Pötschke P. Composites Science and Technology 2011;71(3):306–14.
[19] Baytubes C150HP datasheet. Bayer MaterialScience AG, Germany, Edition; 2007-05-14.
[20] Rauwendaal C. Polymer extrusion. Munich: Hanser Publishers; 1986. 181.
[21] Elmendorp JJ. Dispersive mixing in liquid systems. In: Rauwendaal C, editor. Mixing in polymer processing. New York: Dekker; 1991.
[22] Makrolons–viscosity shear rate. Bayer MaterialScience AG, Global Innovations - Polycarbonates, D-51368 Leverkusen, Germany, www.bayermaterialscience.com.
[23] Scurati A, Feke DL, Manas-Zloczower I. Chemical Engineering Science 2005;60 (23):6564–73.

Polymer 52 (2011) 1037–1044

Contents lists available at ScienceDirect

Polymer

journal homepage: www.elsevier.com/locate/polymer

Uniaxial compression and stretching deformation of an i-PP/EPDM/organoclay nanocomposite

Arthur Thompson [a], Otávio Bianchi [b], Cintia L.G. Amorim [a], Cristóvão Lemos [c], Sérgio R. Teixeira [d], Dimitrios Samios [b], Cristiano Giacomelli [e], Janaina S. Crespo [a], Giovanna Machado [d,f,*]

[a] Programa de Pós Graduação em Materiais, Universidade de Caxias do Sul, Caxias do Sul, Brazil
[b] Instituto de Química, Universidade Federal do Rio Grande do Sul, Porto Alegre, Brazil
[c] Centro de Tecnologia e Inovação, Braskem S/A, Triunfo, Brazil
[d] Instituto de Física, Universidade Federal do Rio Grande do Sul, Porto Alegre, Brazil
[e] Departamento de Química, Universidade Federal de Santa Maria, Santa Maria, Brazil
[f] Centro de Tecnologias Estratégicas do Nordeste, Cetene, Recife, Brazil

ARTICLE INFO

Article history:
Received 1 October 2010
Received in revised form
22 December 2010
Accepted 1 January 2011
Available online 13 January 2011

Keywords:
Nanocomposites
EPDM
Polypropylene

ABSTRACT

In this study, the morphology and rheological properties of nanocomposites prepared by melt mixing of isotactic polypropylene (i-PP), ethylene-propylene-diene terpolymer rubber (EPDM), and Cloisite 15A organoclay, were investigated at rest and under of uniaxial compression and stretching deformations at room temperature. Transmission electron microscopy (TEM) and wide-angle X-ray diffraction (WAXD) experiments revealed that intercalation took place between the clay and the blend. The lamellar long period (L) of the polymeric structure determined by small-angle X-ray scattering (SAXS) was found to increase upon the addition of nanoclay, which also resulted in variations in the angle of rotation (ϕ) between the polymer and clay lamellae. The intercalated nanoclay improved the storage and loss modulus of the resulting materials in the melt state significantly, as determined from oscillatory rheology analyses. Finally, we verified that the uniaxial plane deformation caused by compression of the nanocomposites contributed to the reduction of crystalline domains in the blend, while the crystallinity remained almost constant in the case of uniaxial stretching deformation.

Published by Elsevier Ltd.

1. Introduction

Polymeric blends consisting of polypropylene (PP) and ethylene-propylene-diene terpolymer (EPDM) rubber have widespread applications in the industry due to their excellent chemical and thermal properties. In some cases, however, these materials exhibit poor mechanical resistance. Nonetheless, the mechanical resistance can be conveniently reinforced by a number of approaches, including the addition of fillers such as nanoclays. Recently, nanometer-sized clay particles have garnered increasing interest as a means to tune the properties of polymeric materials [1–4] with cost-effective and naturally occurring materials. The studies reported to date in the literature show that the mechanical properties of specimens are improved by intercalation of the polymer and the clay [3,5–14].

There have been considerable efforts toward the discovery and subsequent characterization of novel clay systems. Montmorillonites are been the most studied class of clays and have attracted much attention due to their physical chemical versatility and low cost. The interaction between montmorillonite-like surfaces with a number of chemical functions, such as quaternary ammonium salts, allows for the modification and control of the mechanisms of interaction between nanoclays and their surroundings. For instance, Cloisite®15A (C15A) is a montmorillonite with a negatively charged surface that has been modified with antagonists comprising positively charged quaternary ammonium salts containing an alkyl chain [2,15–17]. This clay has proved to be an interesting alternative as an inorganic filler in polymeric materials for the purpose of tuning selected properties of materials such as mechanical resistance and gas barrier [9–13,18].

Nevertheless, the effect of the organoclay is strongly related to the extent of its dispersion within the polymer matrix. In general, three types of nanocomposites, namely immiscible or agglomerated, intercalated and exfoliated nanocomposite, can be produced by mixing an organic polymer and an inorganic nanoclay. In an agglomerated composite, interactions between polymer chains

* Corresponding author. Programa de Pós Graduação em Materiais, CCET, Universidade de Caxias do Sul, Caxias do Sul, Brazil. Tel./fax: +55 81 3334 7231.
E-mail address: giovannamachado@uol.com.br (G. Machado).

0032-3861/$ – see front matter Published by Elsevier Ltd.
doi:10.1016/j.polymer.2011.01.005

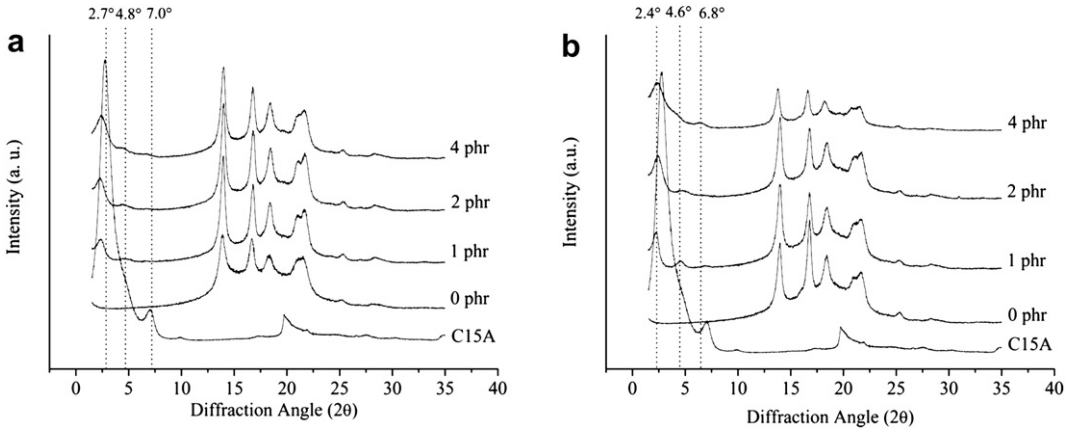

Fig. 1. WAXD diffraction patterns recorded at rest for (a) 75/25 and (b) 60/40 wt% i-PP/EPDM blends containing different amounts of C15A, as indicated.

remain practically the same because of the limited clay-polymer interfacial area that is generated in the new material. Consequently, the properties will resemble those of a conventional micro-composite. On the other hand, the lamellar structure usually swells upon intercalation of polymer chains in the clay galleries, creating novel polymer–clay interaction mechanisms that impart significant improvements to the materials properties. Such improvements can be made far more effective with much less inorganic content by producing exfoliated nanocomposites in which the clay platelets are fully separated from one another and are dispersed individually in the polymer matrix. Therefore, it can be rationalized that the higher the degree of exfoliation, the greater the effect of organoclay on the properties of the resulting hybrid materials. It should be noted, however, that the effect of organoclays can be explained by the theory of nanocomposites in most cases without invoking any special "nano-effect" [19].

Within this context, the development of novel isotatic polypropylene (i-PP)/ethylene-propylene-diene terpolymer (EPDM) rubber nanocomposite systems containing naturally occurring montmorillonites have been already investigated by many groups [3–13,19] because of their great potential for applications in the automotive industry where they can contribute to weight reduction, and consequently, more fuel-efficient vehicles. Recently, Mehta et al. [9] reported an increase of nearly 100% in the tensile strength of a 70/30 (wt%) i-PP/EPDM blend in the presence of 3 phr C15A. This improvement is very sensitive to the concentration of the nanoclay, as demonstrated by Mishra et al [18]. These authors studied the incorporation of up to 10 phr of C20A (of similar polarity to C15A) in a 75/25 (wt%) i-PP/EPDM blend. They verified that the presence of the C20A nanoclay promoted a 60% increase in the tensile strength, a 40% augmentation in the elongation at break, and an increase of up to 100% in the storage modulus. However, such effects on the mechanical properties were much more accentuated with lower concentrations of clay. In particular, it was observed that the characteristics of the nanocomposites had a tendency to either stabilize or decline with concentrations above 3 phr.

At the molecular level, the incorporation of clay into a polymer blend results in novel interfacial interactions between the components of the resulting material. Not surprisingly, these interactions are the origin of most changes in the polymer chain conformation and crystallinity. The latter, in particular, is normally subjected to appreciable changes during the mechanical deformation of the material by compression or stretching. If consistently applied in a uniaxial direction, such mechanical work may induce anisotropic responses due to orientation effects [20–31]. A study by Pluta et al. [27], for example, revealed that the stretching of i-PP at 110 °C led to well-defined chain orientation in the sample. Aboulfaraj et al. [20] observed different spherulite deformations under stretching depending on the crystal structure of the i-PP, with spherulites of the β phase having a tendency to suffer plastic deformation at lower loads than spherulites of the γ phase.

Some studies have been conducted with stretching deformations in elastomers and composites. Obviously, these materials tend to elongate more than polyolefins before suffering permanent deformation. For example, Asami et al. [22] observed that stretching deformation imparts a better orientation of crosslinkings in blends of i-PP and dynamically vulcanized EPDM. The uniaxial stretching deformation also changes the structure of thermoplastic polyurethane (TPU) due to the formation of tactoids [25,32]. In contrast to the considerable efforts devoted to the effect of

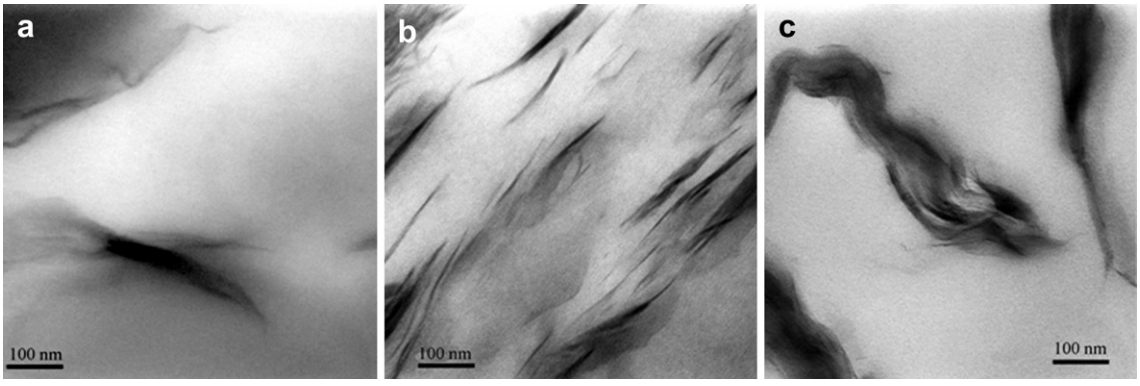

Fig. 2. TEM images of 75/25 wt% i-PP/EPDM blends containing (a) 1 phr, (b) 2 phr, and (c) 4 phr of C15A organoclay.

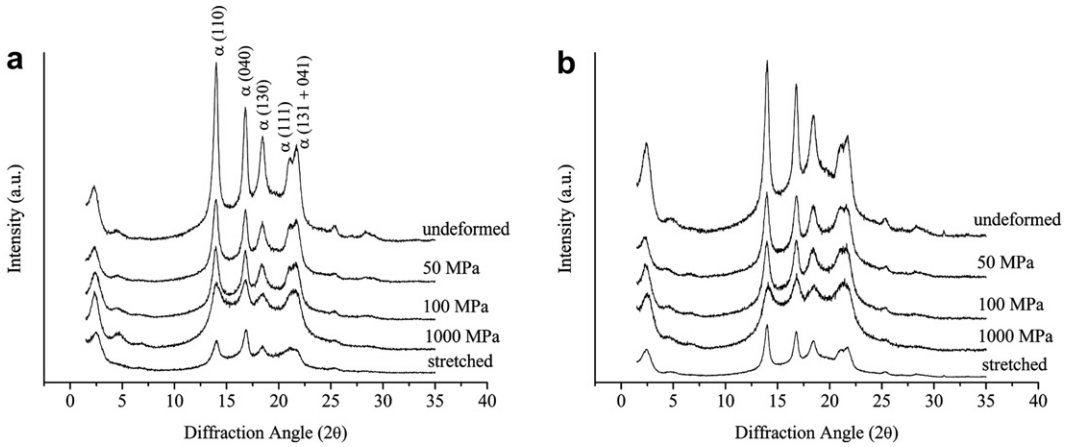

Fig. 3. WAXD diffraction patterns for (a) 75/25 and (b) 60/40 wt% i-PP/EPDM blends containing 2 phr C15A recorded under uniaxial compression at pressures indicated and stretching.

stretching deformation on the characteristics of polymer materials, there are only a few studies addressing the influence of uniaxial compression deformation [33–37].

In this study, we investigated the morphology and rheological properties of nanocomposites prepared by melt mixing of i-PP, EPDM rubber and Cloisite 15A nanoclay at rest and under uniaxial compression and stretching deformations at room temperature.

2. Experimental

2.1. Preparation of nanocomposites

Nanocomposites were prepared by melt mixing isotatic polypropylene (i-PP, Braskem H-606), ethylene-propylene-diene terpolymer rubber (EPDM, DSM Keltan-27) and Cloisite® 15A (C15A,

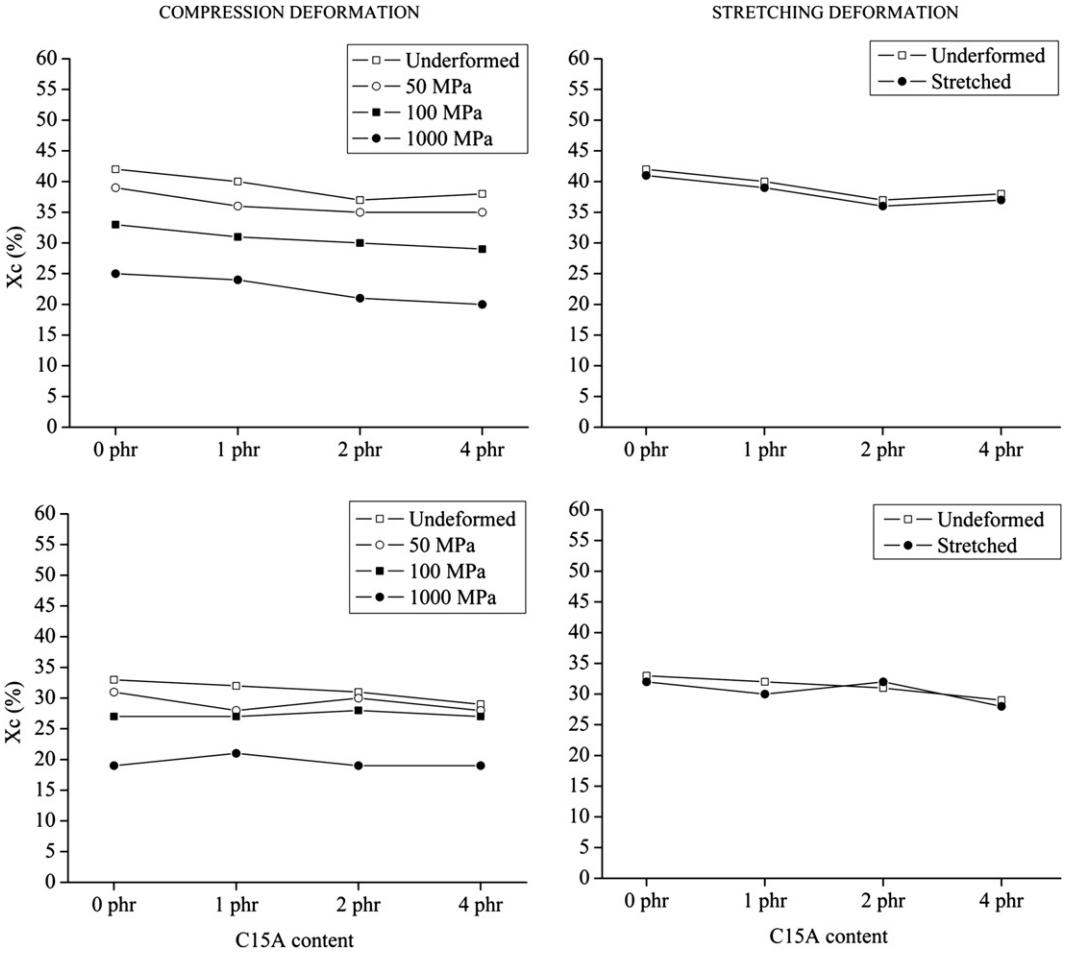

Fig. 4. Degree of crystallinity (X_c) determined by WAXD as a function of the C15A concentration for 75/25 (top) and 60/40 (botton) wt% i-PP/EPDM blends under uniaxial compression (left) and stretching (right).

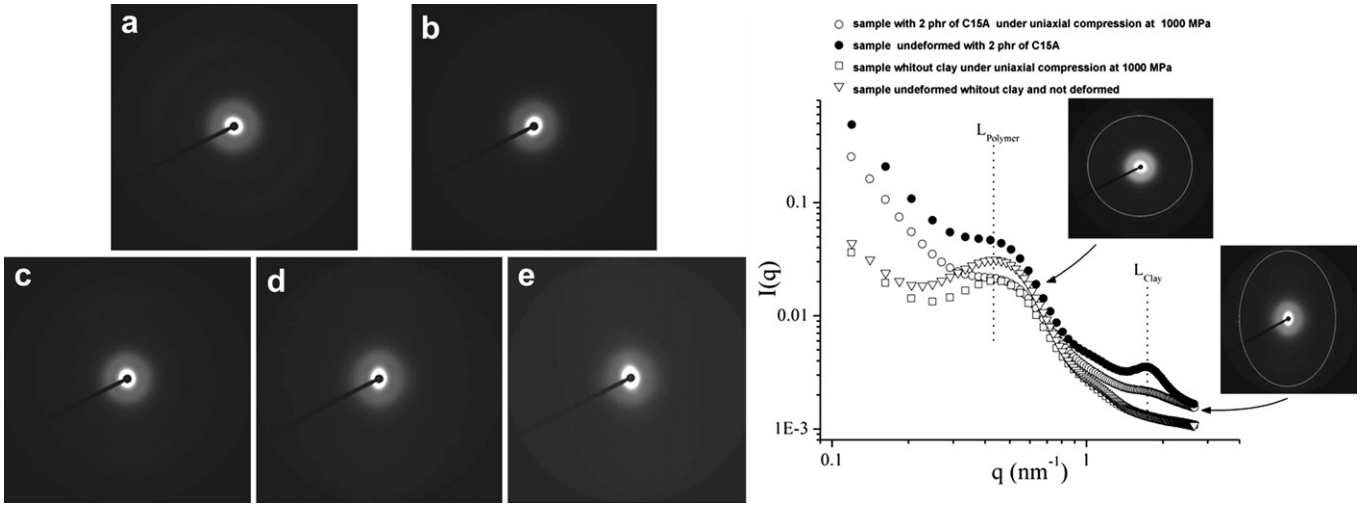

Fig. 5. 2D-SAXS patterns of 75/25 wt% i-PP/EPDM blends with 2 phr of C15A recorded (a) undeformed, and under uniaxial compression at (b) 50 MPa, (c) 100 MPa, (d) 1000 MPa, and (e) deformed by stretching to 100% of their initial length.

Southern Clay) in a Haake Rheocorder operating at 190 °C and a 100 rpm rotor speed for a total mixing time of 15 min. The blend composition was 75/25 or 60/40 wt% i-PP/EPDM, while the concentrations of C15A investigated in this work were 0, 1, 2 and 4 phr. The resulting materials were hot-pressed at 190 °C for 5 min using a Schulz PHS press operating at 10 MPa and 7.5 MPa to obtain samples with an average thickness of 1.0 and 2.0 mm, respectively.

2.2. Uniaxial deformation

The samples were subjected to compression and stretching deformation. The uniaxial compression was carried out using 2.0 mm thick samples, which were placed in a channel die [38], and deformed at room temperature using a Carver Monarch G30-H hydraulic press at 50, 100 and 1000 MPa. The duration of compression was 30 s, and the pressure was applied in the *z*-axis direction of the samples. The uniaxial compression ratio, E, is defined by equation (1), where l_o and l_f are the initial and final sample dimensions along the compression axis, respectively. Uniaxial compression ratios of 20, 40 and 100% were achieved for deformations at 50, 100 and 1000 MPa, respectively. The advantage of applying plane strain compression in a channel die was that the deformation was homogeneous, thus avoiding spurious cavitation phenomena, such as the "microneckings" observed by Peterlin [39], during uniaxial stretching deformation. For uniaxial stretching tests, plates of 1.0 mm thick samples were cut with 30 mm in length and 10 mm neck and deformed by streching to 100% of their initial length (equation (1)) in room temperature.

$$E = \frac{l_f - l_0}{l_0} \times 100 \tag{1}$$

2.3. Wide angle X-Ray diffraction (WAXD)

WAXD measurements were performed using a Shimadzu XRD-6000 apparatus operating at 40 kV and 30 mA. Diffraction data were collected at room temperature in the Bragg–Brentano θ-2θ geometry with CuKα radiation ($\lambda = 1.5405$ Å). The scanning covered the 1.5–35° range at a rate of 0.5°/min. The thickness of the samples oscillated between 1.0 and 2.0 mm because of the deformation. The diffraction patterns were normalized, and then the degree of crystallinity (X_c) was calculated according to equation (2) below:

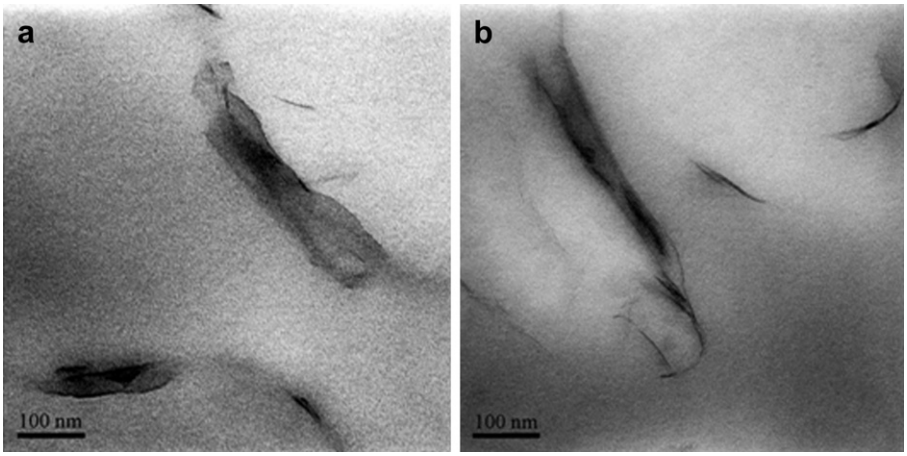

Fig. 6. TEM images of nanocomposites consisting of 75/25 wt% i-PP/EPDM and 2.0 phr C15A after (a) compression at 1000 MPa and (b) stretching deformations.

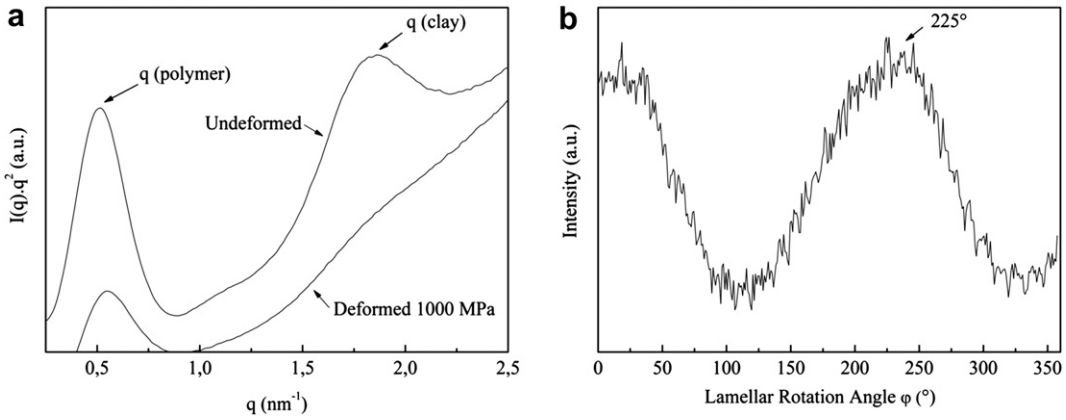

Fig. 7. Representative (a) SAXS curves for 75/25 wt% i-PP/EPDM blends containing 2.0 phr of C15A, and (b) lamellar rotation angle φ related to $q_{polymer}$.

$$X_c = \frac{A_c}{A_c + A_a} \tag{2}$$

where A_c is the crystalline area, and A_a is the amorphous area in the diffraction pattern [40].

2.4. Small angle X-ray scattering (SAXS)

The SAXS technique was employed in this study to identify the lamellar long period (L) and lamellar rotation angle (ϕ) of the nanocomposites. The experiments were conducted at the D11A SAXS1 beamline of the Brazilian Synchrotron Light Laboratory (LNLS, Campinas). The collimated beam crossed the samples and was scattered to a 2D CCD detector with an active area of 16 cm^2. The 2D scattering patterns were collected using slightly different experimental parameters depending on the nature of the deformation. For uniaxial compression, the exposure time was 60 s, the sample-to-detector distance was 1244 mm, and $\lambda = 1.488$ Å. For uniaxial stretching, the exposure time was 300 s, the sample-to-detector distance was 1446 mm, and $\lambda = 1.530$ Å. Silver behanate was used for sample-to-detector distance calibration. SAXS data were analyzed using the FIT2D software developed by A. Hammersley [41] and the SASfit software package developed by J. Kohlbrecher [42]. The lamellar long period (L) was calculated from the equation

$$L = \frac{2\pi}{q\mathrm{max}} \tag{3}$$

where $q$max is the wavevector corresponding to peak scattering intensity.

2.5. Transmission electron microscopy (TEM)

The samples for TEM analysis were microtomed into 70 nm thick slices with a cryogenic diamond knife in a Leica Ultracut at −120 °C. The specimens were imaged using a JEOL JEM 1200 EX II microscope operating at an accelerating voltage of 80 kV.

2.6. Oscillatory rheology

The viscoelastic behaviors of the nanocomposites were analyzed in a melt state using an Anton Parr MCR 101 dynamic oscillatory rheometer equipped with 25 mm diameter parallel plate geometry at 190 °C under nitrogen atmosphere. The gap between the plates was maintained at 2 mm. The linear viscoelastic region was determined using an amplitude sweep experiment. The frequency sweep tests were performed using stress control, as determined in the amplitude sweep experiment. The storage modulus (G′) and loss modulus (G″) were measured as a function of angular frequency (ω) from 100 to 0.1 rad/s.

3. Results and discussion

3.1. Characterization of nanocomposites

The typical WAXD diffractograms of 75/25 and 60/40 wt% i-PP/EPDM blends with different concentrations of C15A are shown in Fig. 1. The diffraction profile of C15A exhibited several characteristic crystalline reflections defined by Bragg's law, with three well-defined peaks at 2.7°, 4.8° and 7.0° (see dotted lines in Fig. 1a). The latter, in particular, was indicative of the platelet separation or d-spacing, thus being very sensitive to intercalations of the species in the clay galleries. Indeed, these three clay-related peaks were displaced toward lower angles for all nanocomposites (see dotted lines in Fig. 1b) in comparison to the pristine clay, suggesting the intercalation of polymer chains in the clay structure with a consequent increase in the spacing between galleries. However, agglomeration of clay particles occurred as their concentration increased, as revealed by TEM imaging analysis of the blends having the highest amount of clay and EPDM. The TEM micrographs shown in Fig. 2 correspond to 75/25 wt% i-PP/EPDM blends containing (a) 1.0 phr, (b) 2.0 phr, and (c) 4.0 phr of C15A organoclay. Fig. 2a and b, which has similar characteristics to those in previous works [6–11], show evidence of the intercalation of polymer chains into the confined regions within the layered silicate structure. The presence of domains consisting of clay agglomerates (tactoids) [32] for nanocomposites having the highest amount of clay is also clear in Fig. 2c.

The characteristic diffraction peaks associated with the crystalline phase of the i-PP polymer appeared in the $2\theta = 13°–25°$ range. Direct comparison of their absolute intensities can be used as an indication of variations in the crystalline fraction for a series of analog nanocomposites. Using such an approach, the degree of crystallinity of the nanocomposites was found to remain within the experimental error, thus suggesting that the presence of C15A clay did not affect the conformation or mobility of i-PP chains.

3.2. Effect of uniaxial compression and stretching deformations

Uniaxial compression caused a significant decrease in the degree of crystallinity due to the shear stress applied to the

Table 1
Values of lamellar long period (L) and rotation angle (ϕ) for i-PP/EPDM blends containing different amounts of organoclay at rest (undeformed) and under uniaxial deformation (compression and stretching).

Parameters	Uniaxial deformation											
	Undeformed				Compression (1000 MPa)				Stretching (100%)			
	0[a]	1[a]	2[a]	4[a]	0[a]	1[a]	2[a]	4[a]	0[a]	1[a]	2[a]	4[a]
Blend composition - 75/25 wt.%												
L polymer (nm) ± 0.02	11.85	12.08	12.31	12.08	11.85	11.42	11.63	11.21	11.95	11.30	11.33	11.08
L clay (nm) ± 0.02	–	3.31	3.39	3.32	–	0	0	0	–	3.23	3.17	3.03
ϕ (polymer) (°) ± 5	240	180	225	220	255	255	260	270	255	290	300	315
ϕ (clay) (°) ± 5	–	145	160	190	–	260	280	305	–	260	270	310
Blend composition - 60/40 wt.%												
L polymer (nm) ± 0.02	12.08	11.63	11.42	11.42	11.02	10.83	11.42	11.02	10.98	10.85	11.32	10.94
L clay (nm) ± 0.02	–	3.67	3.29	3.24	–	0	0	0	–	3.57	3.53	3.09
ϕ (polymer) (°) ± 5	240	245	210	210	265	260	280	280	280	300	295	300
ϕ (clay) (°) ± 5	–	165	180	185	–	240	260	270	–	270	285	305

[a] Nanoclay content in phr.

material. The WAXD diffraction patterns given in Fig. 3 are for (a) 75/25 and (b) 60/40 wt% i-PP/EPDM blends containing 2 phr C15A and recorded under uniaxial compression at different pressures. The intensity of the i-PP-related peaks decreased with the increase in shear stress due to the amorphization of the nanocomposite. The same observation also applies for specimens subjected to stretching deformation, as can deduced from their diffraction profiles provided in Fig. 3. In the latter case, however, the intensity reduction was more accentuated, and the amorphous region seemed to have shortened, suggesting that the crystallinity did not change much. This behavior can be attributed to the micronecking phenomenon [39], as well as to the deformation (especially by stretching), which induced preferential orientation in the (040) plane.

The effect of the organoclay and stretching and compression deformations on the crystallinity of nanocomposites is summarized in Fig. 4. The results show that the crystallinity decreased upon compression but remained practically constant when samples were deformed by stretching. Such observation can be explained on the basis of the formation of microneckings during the stretching deformation. In fact, microneckings can lead to the development of domains with small crystallites, which ultimately contribute to the existence of highly oriented microcrystalline regions in the deformed material. The authors believe that the crystallinity decreased upon compression and stretching, but to samples deformed by stretching this is not evident due to the development of domains with small crystallites caused by microneckings which conceal important information in relation to the decrease of crystallinity. Furthemore, the degree of crystallinity decreased with the augmentation of the EPDM content in the nanocomposites.

It is also worth noting that the direction of the shear stress generated a preferential orientation of the crystalline domains and polymer chains, which scattered the x-ray beam anisotropically as a result. Representative 2D-SAXS patterns for 75/25 wt% of i-PP/EPDM blends containing 2.0 phr C15A under different load ratios of uniaxial compressions and under stretching are depicted in Fig. 5. In this figure, the scattering behavior was clearly isotropic under uniaxial compression at 50 and 100 MPa, but became anisotropic under compression at 1000 MPa or under stretching (see Fig. 5d and e, respectively). The Fig. 5 inhighlights shows 1D x-ray sacttering and and 2D diffractin pattern to better clarify the effects of addition of clay during the deformation.

When applied to the nanocomposites investigated in this work, the deformations also contributed to the improvement of the dispersion of the organoclay particles, as judged from TEM and SAXS experiments. First, the TEM micrographs given in Fig. 6 confirmed the reduced amount of tactoids for samples subjected to either compression (Fig. 6a) or stretching (Fig. 6b), compared to the undeformed material (Fig. 2b). Then SAXS experiments showed very clear changes in the lamellar periods of both polymer and nanoclay. The characteristic scattering peaks ($q_{polymer}$ and q_{clay} respectively) of these periods are defined in Fig. 7 for a representative sample. Upon deformation, q_{clay} almost disappear (see Fig. 7a). In fact, in the 2D diffraction pattern can be observed anisotropic behavior (Fig. 5) with the deformation and we believe in the possibility that the compression deformation acts as a reasonable cause for the disappearance of the clay lamellae structure, due to the probable flow of clay galleries under such deformation conditions, that consequently contribute to the loss of scattering signal.

The lamellar long period (L) and the lamellar rotation angle (ϕ) were obtained from the $q_{polymer}$ and q_{clay} values defined in Fig. 7a. Table 1 shows the variation of these parameters as a function of the clay content and the nature of the deformation. The results indicate that the L for the polymer increased sligh upon the addition of clay

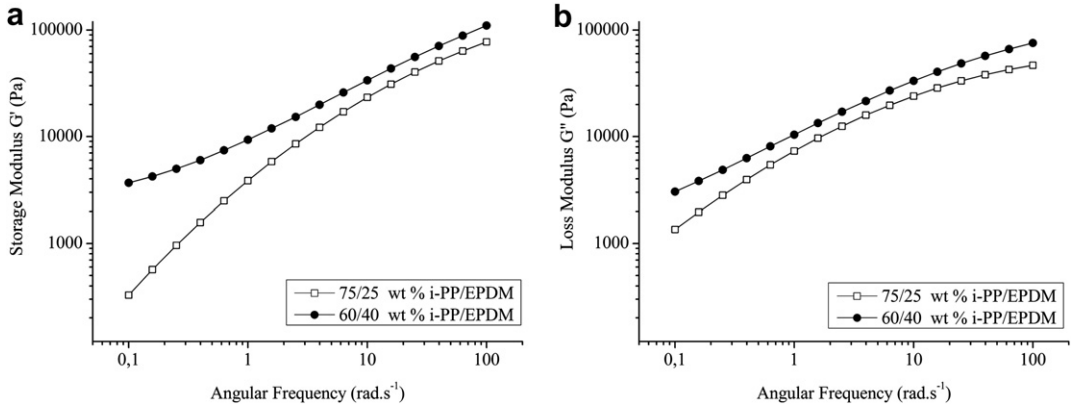

Fig. 8. (a) Storage G′ and (b) Loss G″ moduli *vs.* angular frequency for 75/25 and 60/40 wt% i-PP/EPDM blends.

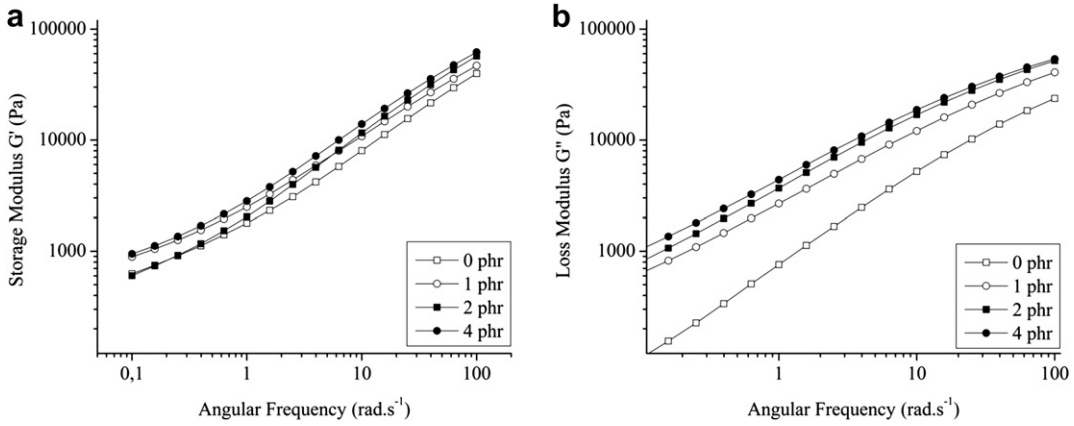

Fig. 9. (a) Storage G′ and (b) Loss G″ moduli *vs.* angular frequency for 75/25 wt% i-PP/EPDM blends with different contents of clay, as indicated.

for 75/25 wt% of i-PP/EPDM blends, whereas the opposite trend was observed for 60/40 wt% of i-PP/EPDM blends. The uniaxial deformation by compression and stretching of the blends result in a slight reduction of this spacing that may be related to experimental errors.

The values of the ϕ increased considerably with the deformation, especially for the peak of q related to the clay in the blends. The addition of clay also increased the lamellar movement in the blend, which was revealed by the increase in ϕ. However, this effect had a tendency to stabilize as more clay was added to the system. The lamellar movement of the clay followed the polymer, and the ϕ of the lamellaes of clay also increased. L also decreased with the deformation, which made the lamellar spacing smaller, explaining the fact that ϕ was practically constant in the deformed samples, even with the addition of clay. In the case of clay galleries, the angle ϕ of deformed samples followed the tendency of the undeformed samples.

3.3. Rheological properties

The rheological behavior of polymer nanocomposites in a melt state is very critical to the understanding of processability and structure–property relationships for these materials. Melt rheology measurements can also probe the behavior of the relatively large material that is crucial from the macroscopic point of view. The storage modulus (G′) and loss modulus (G″) for i-PP/EPDM 75/25 and 60/40 wt% without the addition of clay are shown in Fig. 8a and b, respectively. The addition of a higher content of EPDM into i-PP resulted in an increase in the storage modulus. These increases in the elastic component were caused by the presence of the entanglements in the amorphous EPDM rubber [43]. Fig. 9a and b show the isothermal curves of both dynamic moduli, G′ and G″, respectively for the 75/25 wt% i-PP/EPDM blend with 0, 1, 2 and 4 phr of clay. Generally, the use of nanoparticles leads to a greater gain in the viscous elastic component due to the formation of a physical network caused by the dispersion of clay in the polymeric matrix [44]. The enhancement in rheological properties is generally attributed to percolated networks formed by the physical interactions of the clay platelets. However, there is a reduction of percolation threshold compared to the case of isotropic spheres due to the anisotropy of the tactoids and the individual layers that prevent the free rotation of these elements [45].

Krishnamoorti and Giannelis [46] proposed that the presence of the silicate layers alone is not sufficient to produce the non-terminal flow behavior of delaminated hybrids. The domains structure of silicate layers oriented in some preferable direction and the lack of complete relaxation of the chains, caused by end-tethered polymer molecules, contribute to the pseudo-solid-like response of nanocomposites at low frequencies.

The addition of clay in an i-PP/EPDM blend resulted in a small increase in the elastic component. Meanwhile, we observed an increase in the viscous component with a large addition of clay. This observation may be related to the lower energy storage per cycle sinusoidal deformation caused by the low compatibility between the clay and the polymer phases. The reduction in energy storage was due to the fact that the tactoids of the clay had an intercalated morphology, as show in WAXD and TEM analysis.

Another factor that can contribute to an increase in energy loss is the cluster formation in clay particles. Similar results were

observed in blends of the PP/EVA and PP/EVOH. The addition of clay into the polymer matrix resulted in an alternative mechanism of dissipation energy [47].

This behavior was also observed in the 60/40 wt% i-PP/EPDM blend and has been reported in previous studies. We believe that this is another indication of the intercalation between the blend and the clay [43, 48–51].

4. Conclusions

A nanocomposite was obtained by the addition of the organoclay C15A to a blend of i-PP and EPDM. WAXD patterns demonstrated that the clay was intercalated in the polymers chains, which was corroborated by the techniques of TEM and oscillatory rheology. The SAXS analysis demonstrated that the lamellar long period L increased with the introduction of clay into the blends and decreased with the deformation, either under compression or stretching. Additionally, there was a variation in the angle of rotation ϕ of the polymer and clay's lamellaes with the addition of the C15A, and this variation had a tendency to stabilize when it took place with the amount of clay introduced due to the consequent restriction of molecular movement. We also demonstrated that the uniaxial compression and stretching of the nanocomposites produced a reduction of intensity in the peaks. Under the compression deformations, the crystallinity of the nanocomposites decreased significantly, while under the stretching deformation, the crystallinity remained virtually constant due to the phenomenon of microneckings. Furthermore, the addition of clay into the blend resulted in an increase in energy dissipation by sinusoidal deformation because of the formation of the intercalated morphology during melt processing.

Acknowledgements

The authors are grateful to Ciaflex Indústria de Borrachas Ltda and Braskem for supplying the EPDM and i-PP polymers, respectively. CAPES and CNPq are acknowledged for financial support, and the LNLS for SAXS. The authors are indebted to C. Lopes and M. Queiroz for TEM experiments.

References

[1] Wang Z, Pinnavaia T. Chem Mater 1998;10:3769.
[2] Xiong J, Zheng Z, Jiag H, Ye S, Wang X. Compos Part A - Appl S 2006;38:132.
[3] Kurokaya Y, Yasuda H, Kashiwagi M, Oya A. J Mater Sci Lett 1997;16:1970.
[4] Kato M, Usuki A, Okada A, Kurauchi T. J Appl Polym Sci 1997;63:137.
[5] Hesegawa N, Okamoto H, Kato M, Usuki A. J Appl Polym Sci 2000;78:1918.
[6] Lee W, Lim YT, Park OO. Polym Bull 2000;45:191.
[7] Zhang Q, Fu Q, Jiang L, Lei Y. Polym Int 2000;49:1561.
[8] Zheng H, Peng Z, Zhang Y. Polym Test 2004;23:217.
[9] Mehta S, Mirabella F, Ruefner K, Bafna A. J Appl Polym Sci 2004;92:928.
[10] Lee H, Fasulo P, Rodgers W, Paul D. Polymer 2005;46:11673.
[11] Lee H, Fasulo P, Rodgers W, Paul D. Polymer 2006;47:3528.
[12] Thompson M, Yeung K. Polym Degrad Stab 2006;91:2396.
[13] Liu Y, Kontopoulou M. Polymer 2006;47:7731.
[14] Zanetti M, Camino G, Reichert P, Mullhaupt R. Macromol Rapid Comm 2001;22:176.
[15] Hussain F, Hojjati M, Okamoto M, Gorga R. J Compos Mater 2006;40:1511.
[16] Ray S, Bousmina M. Polymer 2005;46:12430.
[17] González J, Retsos H, Verdejo R, Toki S. Macromolecules 2008;41:6763.
[18] Mishra J, Hwang K, Ha C. Polymer 1995;46:2995.
[19] Paul D, Robeson L. Polymer 2008;49:3187.
[20] Aboulfaraj M, G'Sell C, Ulrich B, Dahoun A. Polymer 1995;36:731.
[21] Abraham F, Alshuth T, Jerrams S. Mater Design 2005;26:239.
[22] Asami T, Nitta K. Polymer 2004;45:5301.
[23] Bartczak Z, Galeski A. Polymer 1996;37:2113.
[24] Boger A, Heise B, Troll C, Marti O, Rieger B. Eur Polym J 2007;43:3573.
[25] Finnigan B, Jack K, Campbell K, Halley P. Macromolecules 2005;38:7386.
[26] Koike Y, Cakmak M. Polymer 2003;44:4249.
[27] Pluta M, Bartczak Z, Galeski A. Polymer 2000;41:2271.
[28] Prasath G, Maiti S. Polym Test 2008;27:752.
[29] Schoene A, Ziabicki A, Jarecki K. Polymer 2005;46:3927.
[30] Sen T, Sharaf M, Mark J, Kloczkowski A. Polymer 2005;46:7301.
[31] Shinoda M, Bathurst R. Geotext Geomembranes 2004;22:205.
[32] Gefu J, Guiqiang L. Mater Sci Eng A 2008;498:327.
[33] Argon A, Cohen R, Bartczak Z. Macromolecules 1992;25:5036.
[34] Argon A, Cohen R, Bartczak Z. Polymer 1994;35:3427.
[35] Galeski A, Argon A, Cohen R. Macromolecules 1991;24:3953.
[36] Galeski A, Argon A, Cohen R, Bartczak Z. Macromolecules 1992;25:5705.
[37] Lin L, Argon A. Macromolecules 1992;25:4011.
[38] Samios D, Tokumoto S, Denardin E. Int J Plasticity 2006;22:1924.
[39] Peterlin A. J Mater Sci 1971;6:490.
[40] Machado G, Denardin E, Kinast E, Gonçalves M, De Luca M, Teixeira S, et al. Eur Polym J 2005;41:129.
[41] Hammersley AP Scientific software FIT2 http://www.esrf.eu/computing/scientific/FIT2D/. [accessed 28.07.09]
[42] Kohlbrecher J. Software package SASfit for fitting small-angle scattering curves, http://kur.web.psi.ch/sans1/SANSSoft/sasfit.html; 2009.
[43] Mishra J, Hwang K, Ha C. Polymer 1995;46:1995.
[44] Kotsilkova R. Mech Time-Depend Mater 2002;6:283.
[45] Kim D, Fasulo P, Rodgers W, Paul D. Polymer 2007;48:5960.
[46] Krishnamoorti R, Giannelis E. Macromolecules 1997;30:4097.
[47] Dal Castel C, Bianchi O, Oviedo M, Liberman S, Mauler R, Oliveira R. Mater Sci Eng C 2009;29:602.
[48] Bandyopadhyay J, Ray S. Polymer 2010;51:1437.
[49] Dan C, Lee M, Kim Y, Min B, Kim J. Polymer 2006;47:6718.
[50] Pattanayak A, Jana S. Polymer 2005;46:3394.
[51] Veja-Baudrit J, Sibaja-Ballestero M, Vásquez P, Terregrosa-Maciá S, Martín-Martínez J. Int J Adhes Adhes 2007;27:469.

Polymer 52 (2011) 1045–1054

Contents lists available at ScienceDirect

Polymer

journal homepage: www.elsevier.com/locate/polymer

Synthesis and characterization of CdS quantum dots with carboxylic-functionalized poly (vinyl alcohol) for bioconjugation

Herman S. Mansur [a,*], Alexandra A.P. Mansur [a], J.C. González [b]

[a] Department of Metallurgical and Materials Engineering, Federal University of Minas Gerais, School of Engineering, Av. Antonio Carlos, 662731270-901 Belo Horizonte, MG, Brazil
[b] Department of Physics, Federal University of Minas Gerais, Brazil

ARTICLE INFO

Article history:
Received 14 October 2010
Received in revised form
22 December 2010
Accepted 1 January 2011
Available online 11 January 2011

Keywords:
Poly(vinyl alcohol)
Nanoparticles
UV–vis spectroscopy

ABSTRACT

In the present research it is reported the synthesis and characterization of CdS nanoparticles (NPs) prepared using carboxylic-functionalized poly (vinyl alcohol) (PVA) as the ligand via aqueous route at room temperature and ambient pressure. Different molar concentrations of carboxylic-PVA and PVA were investigated aiming at producing stable colloidal systems. Carboxylic-PVA was conjugated with BSA (bovine serum albumin) and used as capping ligand in the preparation of CdS nanocrystals. UV–visible spectroscopy, photoluminescence spectroscopy, and transmission electron microscopy were used to characterize the kinetics and the relative stability of polymer-capped CdS nanocrystals. The results have clearly indicated that the carboxylic-functionalized PVA was much more effective on nucleating and stabilizing colloidal CdS nanoparticles in aqueous suspensions compared to PVA. In addition, the CdS nanocrystals were obtained in the so-called "quantum-size confinement regime", with the calculated average size below 4.0 nm and fluorescent activity. Thus, a novel simple route was successfully developed for synthesizing nanohybrids based on quantum dots and water-soluble chemically functionalized polymers with incorporated carboxylic moiety with the possibility of direct bioconjugation.

1. Introduction

Since the early studies pioneered by Brus and co-workers [1] quantum confinements of semiconductors have drawn the attention of the research community. Physical, chemical, and electronic properties of these zero-dimensional entities change dramatically because of quantum effects. The semiconductor nanocrystals, often referred as "quantum dots" (QDs), are one of the most popular terms in nano-science of the 21st century, essentially because of the alterations in the material as a result of the direct influence of the ultra-small length scale on the energy band distribution in the material [2]. These are promising nanomaterials concerning to the exploitation of their properties in all areas of science, mainly those associated with biomedical applications such as nanobiotechnology and nanomedicine [2,3]. The synthesis of QDs was first described in 1982 by Efros [4] and Ekimov [5] who grew nanocrystals of semiconductors in glass matrices. Since then, several publications have reported the preparation of semiconductor nanoparticles in all sorts of systems, LB films [6,7], SAM [8], zeolites [9], organic [10], biomolecules [11,12] and conductive polymers [13]. Nevertheless, despite the relative success on developing QDs, most of the methods are in hydrophobic medium using organic solvents at high temperatures. Usually, these nanocrystals have surfaces that readily oxidize when exposed to water. Moreover, they have to be synthesized in organic solvents under an inert atmosphere and then transferred into aqueous media through a capping ligand exchange. Despite reasonably effective, ligand exchange typically produces less than ideal surface stabilization and product luminescence yield may be limited due to particle agglomeration and growth during the exchange process [3]. More recently, few studies of water-soluble nanoparticles have been published, but frequently with complex routes and/or using expensive precursors [14]. In addition, to be used in biological environments they must exhibit compatibility to the physiological medium where water is abundant and with the large number of molecules such as peptides, enzymes, proteins, among others. Regardless the route one may choose, the final system size should be maintained within a very restricted range as the "hydrodynamic diameter" will determine its behavior in most biological applications [3,10]. As a consequence, the development of novel methods for producing water soluble QDs, with long-time stability, narrow size distributions and biocompatibility, associated with the least possible "hydrodynamic diameter" is still a challenge

* Corresponding author. Tel.:+55 31 3409 1843; fax:+55 31 3409 1815.
E-mail address: hmansur@demet.ufmg.br (H.S. Mansur).

0032-3861/$ – see front matter © 2011 Elsevier Ltd. All rights reserved.
doi:10.1016/j.polymer.2011.01.004

to be overcome. Amongst several choices, polymeric materials come as an interesting possibility of synthesizing semiconductor nanocrystals, as they share some of the major requirements for that purpose. Polymers are commercially available, many are water soluble, biocompatible, and have been widely used in the chemistry of colloids as dispersants, chelates, surfactants, food industry, ligands and so forth. In the realm of water compatible polymers reported in literature, poly (vinyl alcohol) (PVA) and its related products appear as one very interesting choice for preparing colloidal suspensions, due to their biocompatibility and biodegradability aiming at medicine, biology and pharmaceutics applications [15,16]. PVA is a hydrophilic semi-crystalline polymer produced by polymerization of vinyl acetate to poly (vinyl acetate) (PVAc), and successive hydrolysis to PVA. This reaction is incomplete resulting in polymer with different degrees of hydrolysis (DH) [17]. So, it is a copolymer of poly(vinyl alcohol) and poly(vinyl acetate) referred as poly(vinyl alcohol-co-vinyl acetate). PVA is commercially available in highly hydrolyzed grades (DH > 98.5%) and partially hydrolyzed ones (DH from 80.0 to 98.5%) [18]. The degree of hydrolysis or the molar content of acetate groups in PVA affects its physical–chemical properties, such as solubility, hydrophilic/hydrophobic interactions, pH-sensitivity and viscosity [19]. The pH-sensitive systems have experienced increasing interest as novel polymeric materials [18]. Stimuli-responsive structures based on PVA may be achieved during the synthesis (monomers and precursors) or by posterior chemical grafting, for instance, with carboxylic groups [20]. Despite of being a very dynamic area of research, the use of chemically modified PVA as stabilizer for the production of quantum dots colloidal suspensions is relatively unexplored. In fact, several studies have been published using PVA or poly (vinyl-pyrrolidone) (PVP) as stabilizers for semiconductor nanoparticles, but none of them have actually reached biological application [21–23]. Actually, the relatively low reactivity of alcohol groups has significantly narrowed its direct bioconjugation with biomolecules such as proteins, antibodies and carbohydrates. The usual alternative has been the incorporation of amine and carboxylic groups to enhance such possibility of molecule coupling but at the cost of increasing the "hydrodynamic size" of the entire bioconjugated system [14]. So, direct aqueous-phase synthesis of semiconductor nanocrystals in a single step with suitable quantum yield would provide a convenient and plausible alternative to the labor-intensive method of organic-phase synthesis followed by ligand exchange concerning to biomedical applications.

Thus, in the present study, it is reported the synthesis and characterization of CdS quantum dots obtained in PVA and carboxylic-PVA aqueous solutions using colloidal chemistry. To the best of our knowledge, this is the first report to investigate CdS nanoparticles successfully produced in the quantum size range using carboxylic-functionalized PVA as "capping" ligand. Also, these results were compared with conventional PVA, regarding to the polymer concentration and colloidal stability. Moreover, CdS quantum dots were successfully produced and stabilized using PVA-carboxylic bioconjugated to bovine serum albumin. Hence, the synthesis of such nanohybrid system with incorporated carboxylic moiety in the polymer chain has brought the possibility of direct bioconjugation.

2. Materials and methods

All reagents and precursors, thioacetamide (Sigma–Aldrich, Cat#163678, >99%), cadmium perchlorate hydrate (Aldrich, Cat#401374, $CdClO_4.6.H_2O$), sodium hydroxide (Merck, Cat# 1.06498.1000, ≥99%) were used as-received, without any further purification. Poly(vinyl alcohol) with degree of hydrolysis >99.3% and average molecular weight (M_w) = 85 000–124 000 g/mol was supplied by Aldrich (Cat#363146). PVA chemically functionalized (PVA–COOH) containing 1.0 mol% carboxylic acid units was kindly donated by Kuraray Corporation (Poval KM-118, Viscosity 26.0–34.0 [mPa.s], Mw = 85 000–124 000 g/mol, degree of hydrolysis = 95.5–98.5%). Strictly, the polymer can be referred as a terpolymer Poly(vinyl alcohol-vinyl acetate-itaconic acid). Bovine serum albumin (BSA) lyophilized powder was supplied by Sigma (Cat#A9418). EDC (1-Ethyl-3-[3-dimethylaminopropyl] carbodiimide hydrochloride, Sigma–Aldrich) in the presence N-Hydroxysulfosuccinimide sodium salt (NHS-sulfo, Sigma–Aldrich) was used as cross linker. De-ionized water (DI-water, Millipore Simplicity™) with resistivity of 18 MΩ cm was used in the preparation all solutions.

2.1. Preparation methods of precursor solutions

2.1.1. Preparation of a solution of thioacetamide 8.0×10^{-3} mol l^{-1} (8.0 mM)

Approximately 0.0601 g CH_3CSNH_2 was added to 75 ml of DI-water in a 100 ml flask and homogenized under moderate manual stirring for 10–15 min. Then, the volume was completed to 100 ml with DI-water. This sulfur precursor stock solution was referred as "SOL-A".

2.1.2. Preparation of a cadmium perchlorate solution 1.0×10^{-2} mol l^{-1} (10 mM)

Approximately 0.4193 g of $Cd(ClO_4)_2.6H_2O$ was added to 75 ml of DI-water in a 100 ml flask and homogenized under moderate manual stirring for 10–15 min. Then, the volume was completed to 100 ml with DI-water. This cadmium precursor stock solution was referred as "SOL-B".

2.1.3. Preparation of poly(vinyl alcohol) solution: 1.0 mol l^{-1} (1.0 M)

Approximately 4.4 g of PVA (PVA molar unity of 44.0 g/mol) was added to 80 ml of DI-water in a 100 ml flask. Then, the mixture was heated to (85 ± 5)° under vigorous magnetic stirring and kept for 4 h when a clear solution was reached. This PVA stock solution was referred as "SOL-C". This PVA solution was diluted by 10, 100 and 1000 for preparing the 1.0×10^{-1} mol l^{-1}, 1.0×10^{-2} mol l^{-1} and 1.0×10^{-3} mol l^{-1} solutions, respectively. For clarity, Poly(vinyl alcohol) will be referred as PVA–OH.

2.1.4. Preparation of PVA-carboxylic (PVA-COOH) solution: 1.0 mol l^{-1} (1.0 M)

Approximately 4.4 g of Poly(vinyl alcohol-vinyl acetate-itaconic acid) (molar unity of ~44.6 g/mol) was added to 80 ml of DI-water in a 100 ml flask. Then, the mixture was heated to (85 ± 5)° under vigorous magnetic stirring and kept for 4 h when a clear solution was reached. This PVA-COOH stock solution was referred as "SOL-D". This PVA-COOH solution was diluted by 10, 100 and 1000 for preparing the 1.0×10^{-1} mol l^{-1}, 1.0×10^{-2} mol l^{-1} and 1.0×10^{-3} mol l^{-1} solutions, respectively.

In Fig. 1 it is shown the schematic representation of the experimental procedure performed for the synthesis of CdS-PVA-OH and CdS-PVA-COOH capped systems.

2.1.5. Bioconjugation of BSA to PVA-COOH

PVA-COOH solution (1.0 mol l^{-1}) was prepared according to previously described procedure in Section 2.1.4 ("SOL-D"). EDC (10 mg, 1.0 wt%), NHS-sulfo (23 mg, 2.3 wt%) and BSA (5 mg, 0.5 wt %) were dissolved in phosphate saline buffer pH 7.4 (1.0 ml). Bioconjugation process was carried out as follows: 500 μl of 1.0 wt% EDC solution and 500 μl of 2.3 wt% NHS-sulfo solution were dissolved in 10 ml of PVA-COOH aqueous solution (1.0 mol l^{-1}) and magnetically stirred for 15 min at (23 ± 2)C°. Under stirring, 200 μl of 0.5 wt% of BSA solution was added. After 10 min of mixing, the system was incubated at (23 ± 2)°C for 2–3 h. The reaction has led

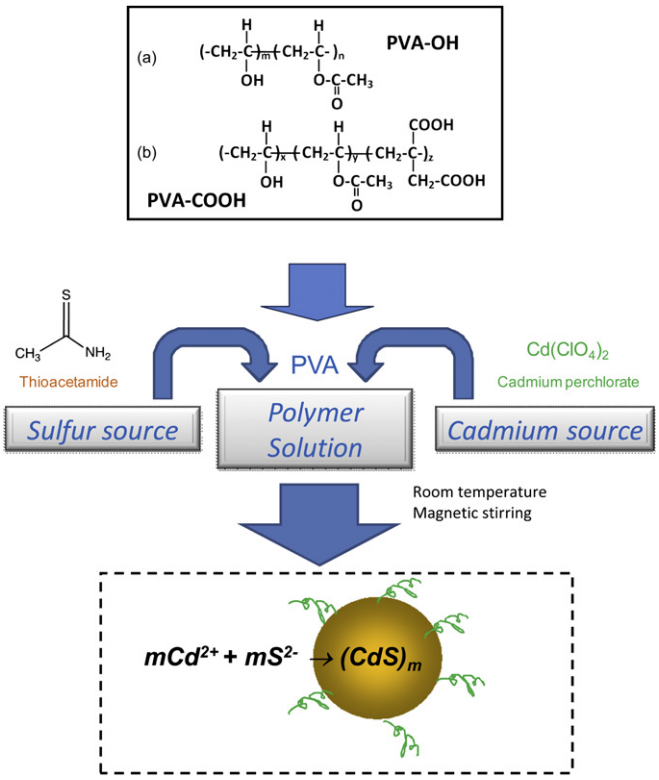

Fig. 1. Representation of the designed experimental procedure for the CdS-PVA colloidal system; Molecular structures of (a) poly(vinyl alcohol) PVA-OH, and (b) PVA-COOH.

to the formation of amide bonds between carboxylic groups from PVA-COOH and amines from BSA (protein-NH_2). This bioconjugated complex was referred as "PVA-C(O)NH-BSA" ("SOL-E"). The bioconjugated system "PVA-C(O)NH-BSA" was purified and concentrated using ultra-centrifugal device with 100 000 M_W cutoff cellulose membrane (Amicon filter, Millipore). Centrifugation was conducted for 30 min (6 cycles × 5 min per cycle, @ 12 000 rpm, 4 °C) using a Hettich Mikro 200R centrifuge. After the first cycle, it was washed 5 times with 300 μl DI-water. Centrifugal force removes the excess of reagents (EDC Mw = 191.7 g/mol; NHS-sulfo = 217.1 g/mol) or unreacted BSA (~67 kDa) and PVA-COOH through the membrane into the filtrate vial. The resulting conjugate (PVA-C(O)NH-BSA) was resuspended in 500 μl of DI-water and stored at 4 °C until further use.

2.2. Synthesis of CdS nanoparticles in PVA solutions

CdS nanoparticles were synthesized via aqueous route in a reaction flask by using the stock solutions as detailed in the previous section, Cd^{2+} and sulfur precursors, and PVA-OH, PVA-COOH or PVA-C(O)NH-BSA as capping ligands. The simplified reaction is represented in Equation (1):

$$Cd^{2+} + CH_3C(S)NH_2 + H_2O \rightarrow CdS + CH_3C(O)NH_2 + 2H^+ \qquad (1)$$

A typical synthesis was carried out as follows: 2 ml of PVA solution (SOL-C for PVA-OH, SOL-D for PVA-COOH or SOL-E for PVA-C(O)NH-BSA) and 45 ml of DI-water were added to the flask reacting vessel. Under moderate magnetic stirring, the pH was adjusted to (11.5 ± 0.5) with NaOH (1.0 mol l^{-1}) slowly added in droplets for approximately 2–5 min. Then, 4.0 ml of cadmium precursor ($Cd(ClO_4)_2$, SOL-B) and 2.5 ml of sulfur source solution (CH_3CSNH_2, SOL-A) were added to the flask (S:Cd molar ratio was kept at 1:2). The solution turned yellowish and sampling aliquots of 1.0 ml were collected at different time intervals (3 h, 6 h, 8 h, 24 h, 48 h and 9 days) for UV–vis spectroscopy measurements, which were used for kinetics analysis and colloidal stability evaluation. The actual polymer concentration during the synthesis of the nanoparticles was diluted by approximately 25 times the original stock solutions (~2 ml:50 ml).

2.3. UV–visible spectroscopy characterization

UV–Vis spectroscopy measurements were conducted using Perkin–Elmer equipment (Lambda EZ-210), wavelength from 600 nm to 190 nm, in transmission mode, using quartz cuvette. The absorption spectra were used to monitor the reaction for the formation of CdS QDs and their relative colloidal stability in the medium. Moreover, based on the "absorbance onset" of the curve it was possible to calculate the average nanoparticles sizes and their optical properties. All experiments were conducted in triplicates ($n = 3$) unless specifically noted. Statistical analysis was performed assuming the mean and the standard deviation where needed.

2.4. TEM-EDS spectroscopy characterization

The nanostructural characterizations of the CdS-polymer samples based on the images and the electron diffraction patterns (ED) were conducted using a Tecnai G2-20-FEI transmission electron microscope (TEM) at an accelerating voltage of 200 kV. The Energy-dispersive X-ray spectra (EDS) were collected in the TEM for chemical analysis.

2.5. Photoluminescence spectroscopy characterization

The emission spectra of the CdS-Polymer nanohybrids were acquired by using an Ocean Optics USB4000 VIS–NIR spectrophotometer and a Helium–Cadmium (HeCd) laser at $\lambda = 442$ nm (violet–blue, 15 mW of power) as the excitation source. All the photoluminescence (PL) spectra were collected at room temperature.

3. Results and discussion

3.1. UV–Vis spectroscopy of PVA-capped CdS quantum dots

3.1.1. Effect of PVA concentration on CdS formation and stability

In order to investigate the effectiveness of PVA working as a stabilizer for preparing CdS nanocrystals in aqueous medium, three different concentrations of PVA solutions were tested. It is broadly known that semiconductor nanoparticles made from II–VI elements exhibit a very pronounced change in their optical absorption properties when their sizes were reduced below a certain diameter. Hence, in this study CdS nanoparticles colloids were extensively characterized based on the UV–visible spectroscopy results. In Fig. 2, it is shown the UV–vis spectra of the system immediately after the thioacetamide precursor was added to the cadmium perchlorate and PVA solutions. It can be observed in Fig. 2 that, at relatively high PVA concentrations, i.e. 1.0 and 10^{-1} mol l^{-1}, represented by curves (a) and (b), respectively, there were significant changes in the absorption spectra at about 500 nm. That aspect can be attributed to the formation of CdS nanoparticles shifting the relative position of the absorption onset. On the other hand, at a lower PVA content [10^{-2} mol l^{-1}, Fig. 2(c)], the spectrum did not present noticeable changes on the absorption curve in that same wavelength range. Thus, at this polymer concentration, the "as-prepared" colloidal suspensions of CdS nanoparticles were not stable. It should be mentioned that the peak at approximately

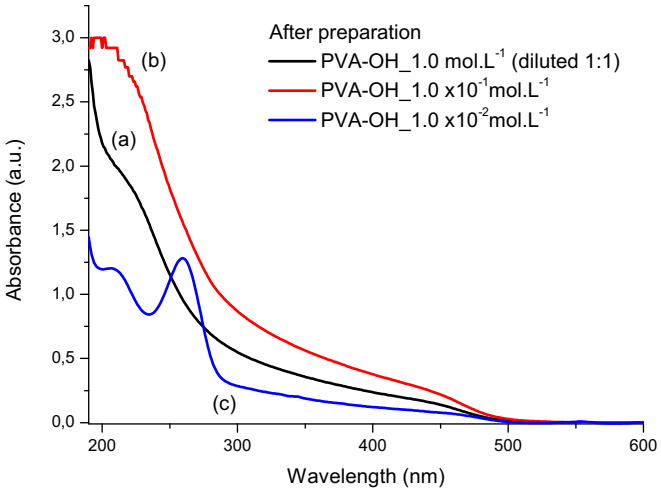

Fig. 2. UV–Vis spectra of PVA-OH solutions with different concentrations (at initial stage): (a) 1.0 mol l^{-1}, (b) 1.0 × 10^{-1} mol l^{-1}, and (c) 1.0 × 10^{-2} mol l^{-1}.

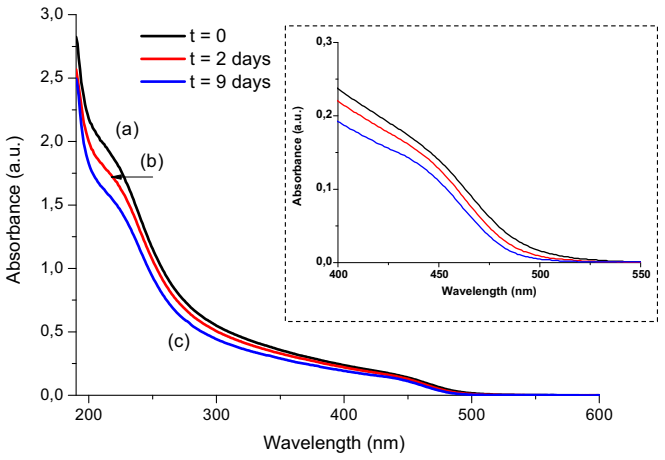

Fig. 4. UV–Vis spectra of PVA-OH at 1.0 mol l^{-1} concentration regarding to the stability of the quantum dots after the preparation (a); 2 days (b); 9 days (c). Insert: detail of the "absorbance onset" region.

~280 nm was associated with the thioacetamide precursor. At alkaline pH, the thioacetamide was practically all consumed based on the reaction (Eq. (1)), as the kinetics of thioacetamide decomposition is favored by the increase in pH. The stabilization effect was even more evident after 24 h from the initial reaction of the CdS nanocrystals formation, as it can be verified in the spectra shown in Fig. 3. The "absorbance onset" values were not apparent in both curves, Fig. 3b and Fig. 3c, at the PVA concentrations of 10^{-1} mol l^{-1} and 10^{-2} mol l^{-1}, respectively. Thus, it could be assumed that the CdS-PVA colloidal systems were not stable at these concentrations. It means the CdS nanocrystals may have flocculated or they perhaps have grown to bulk-size. In both cases, the spectra would be consistent with the curves presented in Fig. 3b and Fig. 3c. Nevertheless, the system was stable for 24 h at the PVA concentration of 1.0 mol l^{-1} [Fig. 3a]. In fact, it can be observed in Fig. 4 that the semiconductor nanocrystals of CdS formed in the PVA aqueous solution (1.0 mol l^{-1}) did not present major changes based on their visible absorption curves from the initial stage up to 9 days.

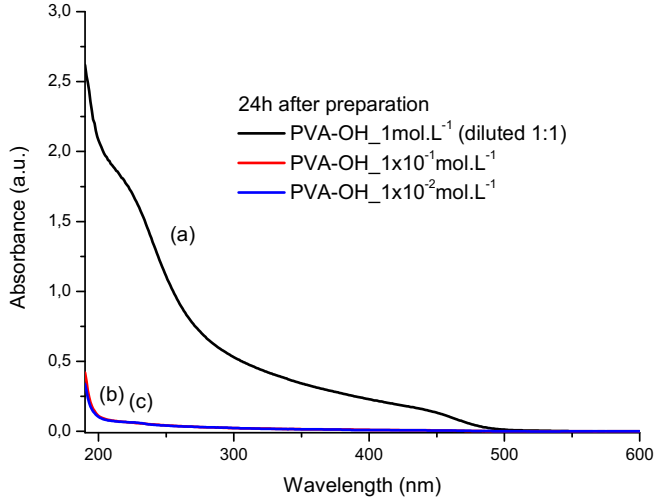

Fig. 3. UV–Vis spectra of PVA-OH solutions with different concentrations (at 24 h): (a) 1.0 mol l^{-1}, (b) 1.0 × 10^{-1} mol l^{-1}, and (c) 1.0 × 10^{-2} mol l^{-1}.

3.1.2. CdS nanoparticle size determination in colloidal media

At this point, it is assumed that a short background on physics and chemistry of semiconductor nanocrystals would be recommended. This subject is intrinsically multidisciplinary and some fundamental considerations are required to properly understand and explore the number of possibilities on conjugating QDs with polymers. Nevertheless, an in-depth analysis of this topic based on quantum theory is beyond the scope of this paper. So, optical excitation of electrons from the valence band to the conduction band produces an abrupt increase in the absorbance at the wavelength associated with the band gap energy. Due to their extreme small size, semiconductor nanoparticles with the dimensions below the so-called "bohr-radius" will present a quantum-confinement effect, related to the strong interaction between the pair "hole-electron" generated by exciting photon [1]. It means that after reaching a specific threshold in particle size (R = radius), the band gap is larger than that of the original bulk material [3]. The reported bulk value for CdS band gap is approximately 2.4 eV or wavelength $\lambda = 514$ nm. For CdS, the quantum size effect occurs as the cluster diameter becomes comparable to or smaller than the exciton diameter of about 6.0 nm (about 3000–4000 atoms) [24]. As a consequence, through UV–vis spectra data, the "absorbance onset" on the curve will be directly related to the altered band gap caused by the quantum-confinement effect.

Essentially, in this study, the average nanoparticle size was determined from Henglein's empirical model [25] which relates the CdS nanoparticle diameter ($2R$) to the optical "absorption onset" from UV–vis spectra according to Eq. (2):

$$2R_{cds}(\mathrm{nm}) = 0.1/(0.1338 - 0.0002345\lambda_{QD}) \quad (2)$$

Where: λ_{QD} is the wavelength from the spectral "absorption onset". The parameter λ_{QD} can be estimated directly from the intersection of the sharply decreasing region of the UV–vis spectrum with the baseline. However, the assessment of the optical band gap has been accepted as a more accurate method for obtaining the wavelength value (λ_{QD}) associated with the "absorbance onset".

Therefore, in the present research, the optical band gap was estimated from absorption coefficient data as a function of wavelength using the "Tauc relation" [26,27], as shown in Eq. (3):

$$\alpha h\nu = B\left(h\nu - E_{qd}\right)^n \quad (3)$$

Where: α is the absorption coefficient, $h\nu$ is the photon energy, B is the band form parameter, E_{qd} is the optical band gap of the

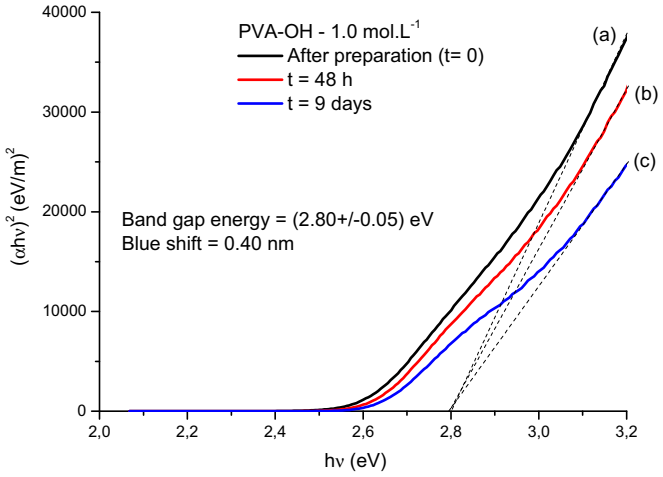

Fig. 5. Optical absorption spectra of CdS nanoparticles in PVA-OH solution at the concentration of 1.0 mol l^{-1} after preparation (a); 48 h (b); 9 days (c).

nanoparticles, and $n = 1/2$ for direct band gap and 2 for indirect band gap. It this case, $n = 1/2$ as CdS is a direct band gap semiconductor. Therefore, one can estimate the direct band gap value from the plots of $(\alpha h\nu)^2$ versus $(h\nu)$ and extrapolating the straight portion of the graph to $(h\nu)$ axis, i.e. at $\alpha = 0$ (dashed lines in Fig. 5). It should be pointed out that these are relative values extracted from the method which are usually compared to bulk values. Nevertheless, it has been widely accepted as the most accurate way of estimating average particle size from the UV–vis spectroscopy technique.

Based on these theories, it was possible to characterize the formation, stability and average sizes of cadmium sulfide nanoparticles in PVA colloidal solutions though UV–vis spectroscopy. Furthermore, the bandgaps of the samples were calculated in order to determine if there was a "size quantization" effect in the synthesized materials.

In Fig. 5, it is presented the results for the stability of the system which was monitored since the very beginning when the reaction has initiated up to 9 days. It can be observed that the synthesized CdS colloidal suspensions were rather stable, with the calculated average band gap of $E_{qd} = (2.80 \pm 0.05)$ eV, which is higher than the bulk value of 2.4 eV reported for CdS. Thus, the "blue-shift" of about 0.4 eV (i.e. 2.8–2.4 eV or from $\lambda = 514$ nm–443 nm) has proven that the CdS quantum dots were successfully synthesized under these conditions. Moreover, this fact has given strong evidence that they were chemically stable as colloidal aqueous solution for a fairly long "shelf-life" period.

Hence, a similar analysis was conducted for the whole set of colloidal systems using PVA polymer as the "capping" agent and the results for band gap energy and CdS nanocrystals sizes are summarized in Table 1. These results for PVA-OH samples are presented in Fig. 6. It can be observed the correlation between the calculated band gap energies ("blue-shift") with time of colloidal preparation for each PVA-OH concentration, considering the time immediately after the addition of the sulfur precursor up to 168 h (9 days).

From the colloidal chemistry perspective, these results can be primarily analyzed and discussed by assuming that both thermodynamics and kinetics aspects associated with the formation of cadmium sulfide are very favorable. That is, the reaction of Cd^{2+} with sulfides in water medium producing CdS crystals would certainly cause a reduction in the free-energy ($\Delta G < 0$). Regarding to kinetics, the reaction rate is determined by the extremely small value of the "solubility product constant" ($K_{sp} = 8.0 \times 10^{-27}$). However, after being formed, the nucleated nanocrystals would tend to grow or agglomerate mostly driven by the decrease in surface energy, i.e. by reducing the surface area (S) to volume (V) ratio as in Eq. (4):

$$S/V = \left(\pi R^2\right) \Big/ \left((4/3)\pi R^3\right) = 3/(4\mathrm{R}) \tag{4}$$

Thus, based on classic theories the growth of the nanoparticles may have occurred by two favored pathways [22]:

a) The growth of CdS on the nucleated seeds (Eq. (5)):

$$Cd^{2+}(aq) + S^{2-} + (CdS)_m \rightarrow (CdS)_{m+1} \tag{5}$$

b) The process of "Ostwald ripening" whereby larger seeds grew at the expense of the smaller ones (Eq. (6)):

$$(CdS)_n + (CdS)_k \rightarrow (CdS)_{k+1} \qquad (k > n) \tag{6}$$

Therefore, in order to stabilize the just formed particles in the aqueous solution, a relatively high concentration of PVA-OH capping agent has to be utilized. Apparently, the most likely mechanism acting on the system is the reduction of the surface energy by the interactions with the hydroxyl groups from PVA-OH chains, as schematically represented in Fig. 7. In order words, it could be considered that the CdS quantum dots were effectively stabilized by a polymeric-capping effect, as the diffusion of ions (Cd^{2+} or S^{-2}) was significantly restricted by the PVA surface layer limiting further particle growth. Obviously, several other interactions were present in such complex dynamic system as described in the excellent recent review from Nel and co-workers [28]. For instance, electrostatic forces, hydrophilic and hydrophobic interactions, hydrogen bonds (PVA alcohol groups), steric hindrance among polymer chains will influence the overall behavior of the colloidal system. It was not found in the literature previous reports addressing the effect of molecular weight (M_W), molecular weight distribution and degree of hydrolysis (DH) of PVA on the stability of

Table 1
Parameters of CdS nanoparticles formation in PVA-OH and PVA-COOH media at different concentrations and reaction time: band gap energy, "blue-shift", size.

PVA concentration			1.0 mol l^{-1}		1.0×10^{-1} mol l^{-1}		1.0×10^{-2} mol l^{-1}	
Time			t_o	t_∞	t_o	t_∞	t_o	t_∞
Stabilizer	PVA-OH	Band Gap (eV)	2.80	2.80	2.78	Bulk*	2.80	Bulk*
		"Blue-shift" (eV)	0.40	0.40	0.38	Bulk*	0.40	Bulk*
		Absorbance onset (λ, nm)	443	443	446	Bulk*	443	Bulk*
		Particle Size (2R,nm)	3.3	3.3	3.4	Bulk*	3.3	Bulk*
	PVA-COOH	Band Gap (eV)	2.81	2.81	2.78	2.78	2.75	Bulk*
		"Blue-shift" (eV)	0.41	0.41	0.38	0.38	0.35	Bulk*
		Absorbance onset (λ, nm)	441	441	446	446	451	Bulk*
		Particle Size (2R,nm)	3.3	3.3	3.4	3.4	3.6	Bulk*

t_∞ = after 9 days of reaction; t_o = initial time of reaction; Bulk* = bulk crystals or flocculated.

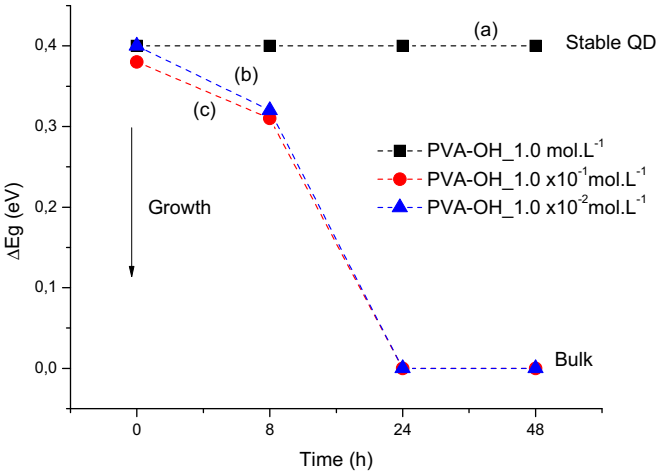

Fig. 6. Evolution of the "blue-shift" of CdS nanoparticles in PVA-OH solution at the concentration of (a) 1.0 mol l^{-1}; (b) 1.0 × 10^{-1} mol l^{-1}; (c) 1.0 × 10^{-2} mol l^{-1}. (For interpretation of the references to colour in this figure legend, the reader is referred to the web version of this article).

CdS quantum dots in biological or clinical use. However, theoretically, it can be assumed that PVA with low M_W and intermediate DH would be easier to be biodegraded by the mammals' metabolic system and later excretion by liver and kidneys. On the other hand, there is a limit on reducing the polymer M_W as it should also work as capping ligand during the QDs formation. That would certainly require a more in-depth investigation and also a large number of experiments to reach the optimum balance among all properties needed to be suitable for biomedical applications.

3.1.3. *Effect of PVA-COOH concentration on CdS formation and stability*

Aiming at moving a step forward on understanding these interactions between CdS quantum dots and polymer-capping agents, PVA chemically functionalized with carboxylic groups (PVA-COOH)

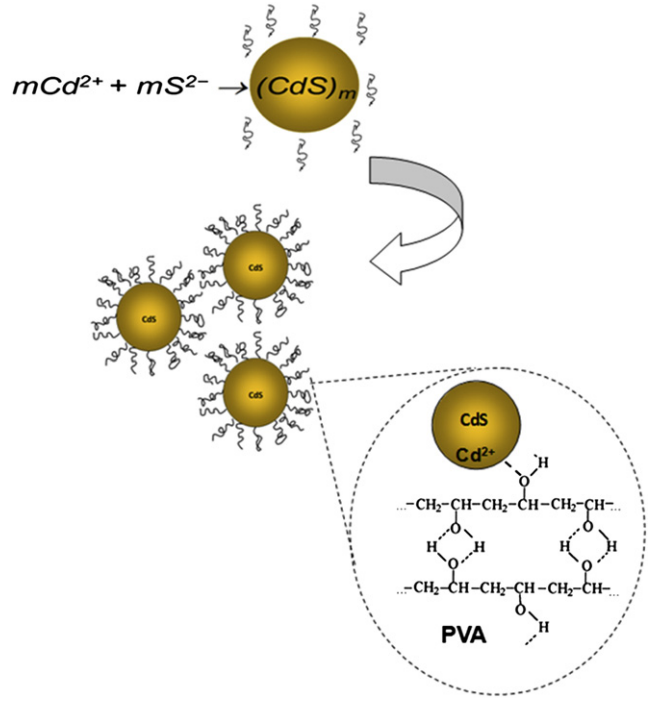

Fig. 7. Schematic representation of the mechanism acting in the system: reduction of the high surface energy by interaction with the hydroxyl groups from PVA-OH chains.

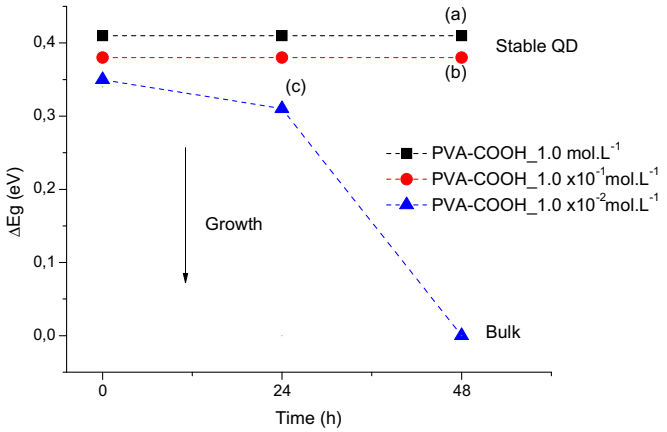

Fig. 8. Stability and band gap analysis of CdS nanoparticles in PVA-COOH solution at the concentration of (a) 1.0 mol l^{-1}; (b) 1.0 × 10^{-1} mol l^{-1}; (c) 1.0 × 10^{-2} mol l^{-1}.

was also prepared via aqueous colloidal routes using. Fig. 8 presents the results of the changes on band gap energy using PVA-COOH at 3 M concentrations, 1.0, 10^{-1}, and 10^{-2} mol l^{-1}. It can be clearly observed that for PVA-COOH with the concentrations of 1.0 mol l^{-1} and 10^{-1} mol l^{-1} (Fig. 8a and Fig. 8b, respectively) no significant alterations were detected from the initial stage of the reaction up to 48 h. On the other hand, the band gap shift was smaller at a lower PVA-COOH concentration (10^{-2} mol l^{-1}, Fig. 8c). That was directly related to the CdS nanoparticles growth and/or coalescence causing the formation of agglomerates as discussed in previous section (Eq. (5) and (6)). These results of PVA-COOH functionalized compared to those of PVA-OH without chemical modification of the polymer chain (Fig. 6) have evidenced a major contribution from the carboxylic groups on stabilizing the CdS nanoparticles in the quantum-size range. Indeed, it is worth mentioning that the capping behavior in the PVA-COOH solution was approximately 10 times more effective than the solution of PVA-OH by taking into account their respective molar concentrations, 10^{-1} mol l^{-1} and 1.0 mol l^{-1}.

Once more, by considering the mechanism of colloidal particles stabilization in solution, it may be assumed that the new carboxylic species added to the PVA-COOH polymeric chains have been attracted by the dangling bonds of Cd–S at the quantum dots surfaces. Besides that, at the used alkaline pH (pH > 11.0) the

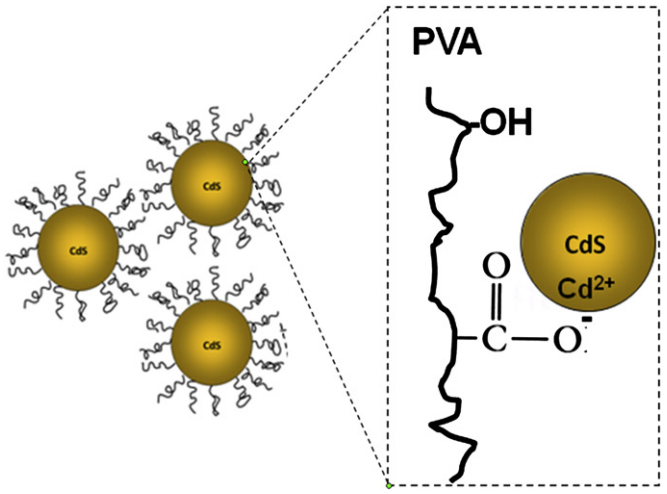

Fig. 9. Schematic representation of the mechanism acting in the system: reduction of the high surface energy by interaction with the carboxylate groups from PVA-COOH chains.

carboxylic groups from PVA-COOH should be partially ionized forming carboxylates (COO^-). As a consequence, these negatively charged regions of PVA-COOH would have driven to a much stronger attractive force with the positively charged ions (Cd^{2+}) at the nanoparticles surface. The function of the polymer in this case was to compete with sulfide (S^{2-}) for metal ion-binding sites and, presumably, to sterically hinder small nanoparticles from aggregating together and growing into larger ones. Also, Cd^{2+} at the surface would be stabilized by forming chelates with carboxylates ("electron-donor"). The schematic representation of this system is illustrated in Fig. 9. It can be assumed that, for charged polymer systems, such as PVA-COOH, mainly strong electrostatic interactions have worked and influenced the adsorption at the nanoparticles surfaces balancing their charges. On the other hand, for uncharged polymers (PVA-OH), H-bonding and solvation forces were expected to be more significant.

It should be emphasized that it is a simplified approach for the developed system. Although the adsorption behavior of PVA polymer on solid–liquid interface is well documented in the literature, the amount adsorbed and the kinetics are strongly dependent on the molecular weight and the number of acetate groups of PVA, resulting in different properties and behavior. The adsorption forces usually increase when the degree of hydrolysis of the PVA is increased mostly due to the formation of hydrogen bonds. Also, the presence of the hydrophobic acetate groups affects the conformation of polymer chains adsorbed onto the nanoparticles surfaces [29]. By adding functional groups such as carboxylic, the adsorption phenomenon is more complex as the polymer chain has to reach a 3D conformation to match the overall balance of forces involved. That effect was reported in our recent work where CdSe nanocrystals were successfully produced in carboxylic modified polymer via aqueous colloidal route [30].

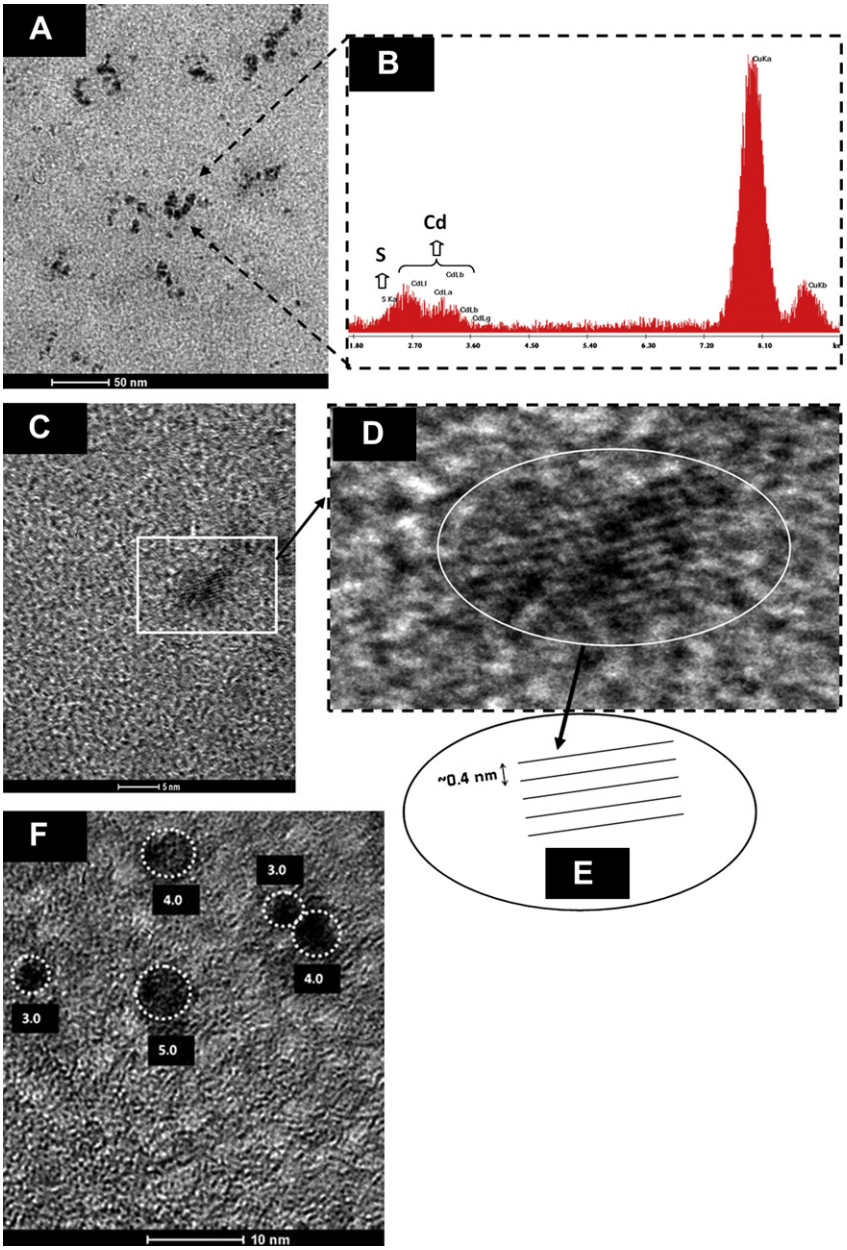

Fig. 10. (A) TEM image of produced CdS/PVA-COOH quantum dots; (B) EDS spectrum of CdS/PVA-COOH QDs; (C) Image of QDs lattice arrangements by electron diffraction; (D) detailed nanocrystal plane spacing and representative drawing (E); TEM image of CdS/PVA-COOH quantum dots with estimated nanoparticles sizes (F);

3.2. Characterization of CdS quantum dots by TEM coupled to EDS spectroscopy

UV–visible absorption spectroscopy has been widely utilized for estimating semiconductor nanoparticles sizes, as it is a straightforward technique of monitoring the nanocrystals nucleation and growth in colloidal media. Nevertheless, in this research a more in-depth and complementary evaluation of the quantum dots characterization was carried out using transmission electron microscopy (TEM). The morphological and structural analyses of the quantum dot-polymer systems were performed by electronic transmission microscopy experiments associated with the electron diffraction patterns (EDP). A representative TEM image of CdS-PVA-COOH system is shown in Fig. 10A and F. It can be observed a fairly uniform nanoparticles size distribution, typically within the range of 1–5 nm and the estimated mean size centered at 3–4 nm. Also, the Energy-dispersive X-ray spectra (EDS) have shown the chemical analysis of the nanocrystals with Cd and S as the major elements (Fig. 10B), excluding the copper and carbon peaks related to the TEM grid. These TEM results have proven that CdS quantum dots were properly stabilized by the PVA-COOH capping polymer within the quantum-confinement size range and they were also consistent with the values estimated by UV–Visible spectroscopy in the previous section. In Fig. 10C and D it can be clearly verified the electron diffraction patterns associated with the CdS quantum dots crystalline structure with plane spacing of about ~4–5 Å. These results are well-matched to the values reported in the literature for the CdS QDs with wurtzite-like crystal structures (wurtzite, a = 4.160; c = 6.756 Å) [31,32].

3.3. Photoluminescence spectroscopy of polymer-capped CdS quantum dots

Despite not being the major goal of the present study, it is known that some other properties are important to be investigated before using such colloidal system as biomarkers. For instance, the QDs photo-stability could be accessed by photoluminescence spectroscopy. In that sense, photoluminescence (PL) spectroscopy was conducted aiming at verifying the preliminary activity of the CdS nanocrystals produced via aqueous route using a relatively facile method with carboxylic-functionalized PVA as capping agent. Fig. 11A presents a typical PL emission spectrum for CdS nanocrystals synthesized with the carboxylic modified PVA as capping ligand. The PL emission peak energy was centered at approximately λ = 520 nm ("green"), for all polymer concentrations tested. A similar behavior was also observed for CdS nanocrystals stabilized by "conventional" PVA (PVA-OH, PL not shown). Also, the fluorescence images were captured by using a 12 million pixels color digital camera. Fig. 11B shows the characteristic "green" fluorescence image of CdS/PVA-COOH QDs in aqueous colloidal solution excited by laser source at λ = 442 nm (violet–blue, 15 mW of power). Fig. 11C presents the image of the synthesized CdS/PVA-COOH QDs with a bright green fluorescence when exposed to ultraviolet light radiation (compartment, light source λ = 254 nm). These results have given support for considering this novel system based on CdS-PVA-COOH to be potentially used in biolabeling applications as it has indeed shown PL behavior. Besides that, it brings an environmentally friendly alternative to the labor-intensive method of organic-phase synthesis followed by ligand exchange. The choice of PVA polymer comes as an alternative to other aqueous routes, with some advantages. PVA and PVA-COOH are biocompatible and biodegradable comparable to Polyethylene glycol (PEG). Different from PEG, which is always very hydrophilic, PVA and its derivatives can be chosen based on the polymer chain and the degree of hydrolysis (ratio of acetates/alcohol groups) which offers a unique opportunity for preparing solutions with

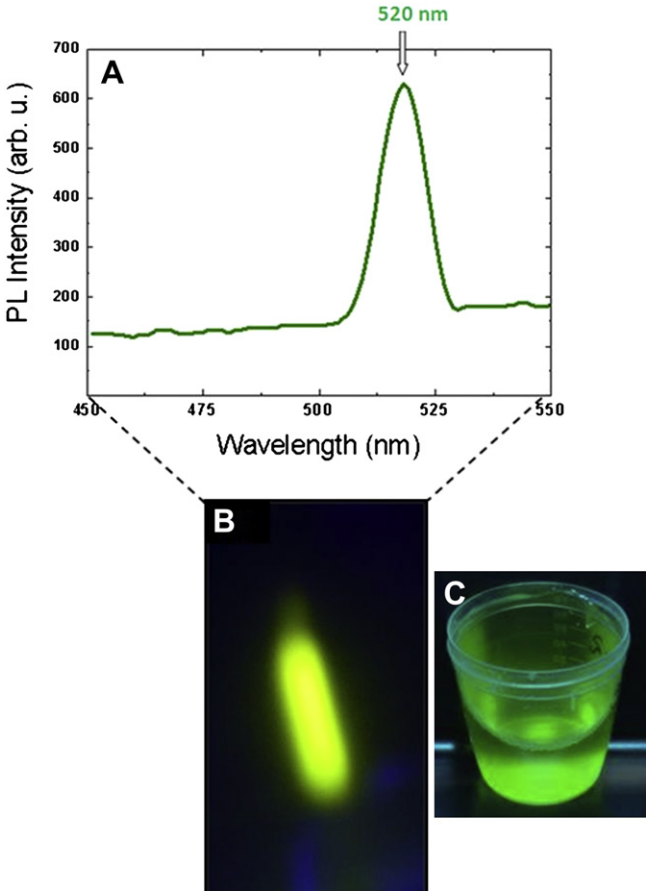

Fig. 11. (A) Fluorescence spectrum and (B) Fluorescence image of CdS/PVA-COOH QDs in aqueous colloidal solution excited by laser source at λ = 442 nm (violet–blue, 15 mW of power); (C) image of CdS/PVA-COOH QDs in ultraviolet light compartment. (For interpretation of the references to colour in this figure legend, the reader is referred to the web version of this article).

a wide range of properties (viscosity, solubility, degradability etc.) (Fig. 12).

Therefore, it can be highlighted the following aspects when comparing to other published studies:

1) PVA-derived polymer [terpolymer, Poly(vinyl alcohol-vinyl acetate-itaconic acid)] was utilized as the novel capping agent with carboxylic pendant groups (PVA-COOH) which has decreased about 10 times the concentration of ligand needed when compared to PVA(PVA-OH);
2) The precursor [Cd:S] molar ratio used was [2:1] as compared to the large majority of previously consulted publications which have used [1:1]. That has made possible some "free" Cd^{2+} cations at the quantum dots surfaces for charge balancing with carboxylate anions ($-COO^-$). As a consequence, it has resulted in more stable colloidal systems;
3) The partial substitution of alcohol by carboxylic groups increases the potential reactivity of the quantum dots-Polymer systems with biomolecules;
4) In addition, the choice of using a carboxylic functional polymer may contribute for reducing the total "hydrodynamic diameter" of the bioconjugate QD-polymer-protein, as it can be produced in a single-step process.

Thus, in order to move further aiming at biological applications of this developed work, one may consider a designed system with

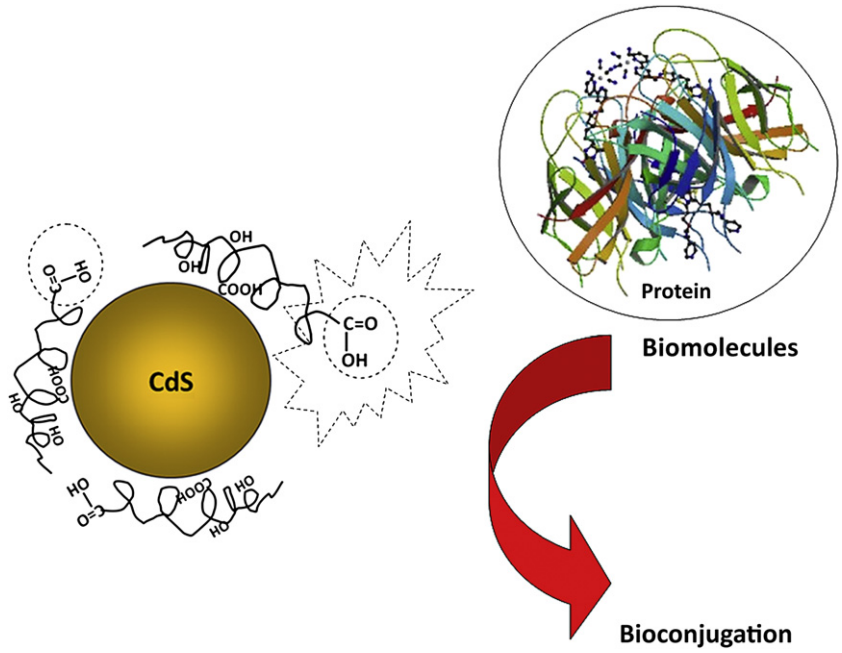

Fig. 12. Representative drawing of potential alternatives for bioconjugation with the carboxylate groups from PVA-modified chains (not in scale).

the choice of the carboxylic group as a chemical functionality in PVA to be utilized as a reactive "coupling group" for potential bioconjugation. For instance, the synthesis of quantum dot-polymer (CdS/PVA-COOH) structures conjugated with biological moieties (Fig. 12) such as proteins.

3.4. CdS quantum dots capped by PVA-C(O)NH-BSA bioconjugates

As a proof of concept, it was designed and performed a set of experiments. PVA-COOH was conjugated with BSA (bovine serum albumin) considered as a "model" biomolecule. The reaction of

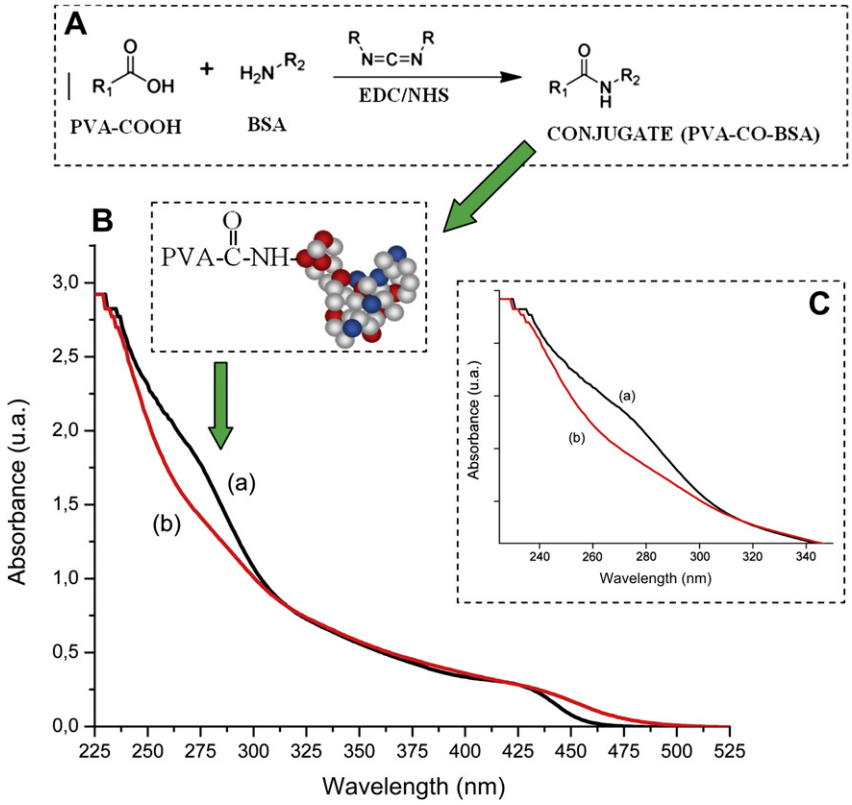

Fig. 13. (A) Schematic representation of the bioconjugation reaction between PVA-COOH and BSA with the formation of an amide using a carbodiimide linker; (B) UV–Vis spectra of CdS quantum dots with PVA-COOH (a) and with (b) PVA-C(O)NH-BSA bioconjugation; (C) Insert: detail of the UV–Vis spectra of the amide region.

the carboxyl-reactive 1-Ethyl-3-(3-dimethylaminopropyl)carbodiimide (EDC) was utilized as a "zero-length" cross linker in the presence of NHS-sulfo (catalyst) for covalently coupling the carboxylic group from PVA-COOH to the amines from BSA (protein-NH_2). The formation of an amide linkage is expected to occur straightforward ("PVA-C(O)NH-BSA"). Also, EDC has the advantages of not being incorporated into the structure of the protein and not being toxic in comparison with cross-linkers (glutaraldehyde). The results are summarized in Fig. 13. In Fig. 13A, it is shown the schematic representation of the bioconjugation reaction with the formation of an amide using carbodiimide (EDC/NHS-sulfo). It can be observed in the UV–Vis spectra (Fig. 13B and C) the increase of absorbance in the amide region (curve b) of the conjugated PVA-C(O)NH-BSA compared to the PVA-COOH not conjugated (curve a). It is important to be pointed out that no detectable differences were observed in the CdS quantum dots average sizes prepared using both capping ligands, PVA-COOH or PVA-C(O)NH-BSA. Therefore, the results have clearly proven that CdS quantum dots were successfully produced/stabilized using a novel approach based on PVA-COOH bioconjugated to BSA.

4. Conclusion

It can be summarized that in the present study an aqueous colloidal route for producing CdS quantum dots was developed using both PVA-OH and carboxylic-functionalized PVA-COOH as polymer-capping agents. Regarding to the colloidal system stability, the carboxylic groups in the polymeric chain have decreased about 10 times the amount of ligand required for obtaining water stable suspensions. They have shown relatively adequate activity and stability in PL assays, good dispersion, and the capped surfaces by alcohol and carboxylic groups. The use of carboxylic group in the functionalized PVA (PVA-COOH) potentially increases the overall interactions leading to stability of the system with other chemical species when compared to alcohol groups (PVA-OH). In fact, the designed system based on the chemically active polymer (PVA-COOH) was successfully bioconjugated to the "model protein" (BSA), via carboxylic-amine reactions, leading to the formation of amide covalent bonds (PVA-C(O)NH-BSA). The synthesized CdS/PVA-COOH and CdS/PVA-C(O)NH-BSA nanocrystals represent hybrid inorganic–organic materials that can be both fabricated and functionalized with biomolecules in a relative facile synthetic route. In that sense, this novel nanostructured system opens a wide window of possibilities in biomedical research and applications for producing water soluble inorganic fluorophores based on quantum dots.

Acknowledgments

The authors acknowledge the financial support from CAPES (Proc:5548-09-8; PNPD/2010; 433/2010), FAPEMIG (Proc:PPM-00343-09), and CNPq (Proc:305098/2007-1). Also, the authors thank the contribution from Microscopy Center/UFMG staff for TEM analysis.

References

[1] Brus LE. J Chem Phys 1984;80:4403–9.
[2] Medintz IL, Uyeda HT, Goldman ER, Mattoussi H. Nature Materials 2005;4:435–46.
[3] Mansur H. Wiley Int. Reviews: Nanomedicine and Nanobiotechnology 2010;2:113–29.
[4] Efros AL. Sov Phys Semicond 1982;16:772–5.
[5] Ekimov AI, Onushchenko AA. Sov Phys Semicond 1982;16:775–8.
[6] Mansur HS, Grieser F, Marychurch MS, Biggs S, Urquhart RS, Furlong DN. J Chem Soc, Faraday Trans 1995;91:665–72.
[7] Mandal P, Srinivasa RS, Talwar SS, Major SS. Applied Surface Science 2008;254(16):5028–33.
[8] Shin SK, Yoon HJ, Jung YJ, Park JW. Current Opinion in Chemical Biology 2006;10(5):423–9.
[9] Jeong NC, Kim HS, Yoon KB. Langmuir 2005;21(13):6038–47.
[10] Choi HS, Liu W, Misra P, Tanaka E, Zimmer JP, Ipe BI, et al. Nature Biotechnology 2007;25:1165–70.
[11] Ma N, Tikhomirov G, Kelley SO. Acc Chem Res 2010;43(2):173–80.
[12] Pinaud F, King D, Moore H-P, Weiss S. J Am Chem Soc 2004;126:6115–23.
[13] Mansur HS, Vasconcelos WL, Grieser F, Caruso F. Journal of Materials Science 1999;34(21):5285–91.
[14] Li H, Shih WY, Shih W-H. Ind Eng Chem Res 2007;46:2013–9.
[15] Peppas NA, Simmons REP. J Drug Del Sci Tech 2004;14(4):285–9.
[16] Costa-Júnior ES, Barbosa-Stancioli EF, Mansur AAP, Vasconcelos WL, Mansur HS. Carbohydrate Polymers 2009;76(3):472–81.
[17] Hassan CM, Peppas NA. Adv Polym Sci 2000;153:37–65.
[18] Mansur HS, Sadahira CM, Souza AN, Mansur AAP. Materials Science and Engineering: C 2008;28(4):539–48.
[19] Briscoe B, Luckham P, Zhu S. Polymer 2000;41:3851–60.
[20] Moritani T, Kajitani K. Polymer 1997;38(12):2933–45.
[21] Wang H, Chen Z, Fang P, Wang S. Materials Chemistry and Physics 2007;106:443–6.
[22] Ma X-D, Qian X-F, Yin J, Xi H-A, Zhu Z. Journal of Colloid and Interface Science 2002;252:77–81.
[23] Yang YJ, Xiang BJ. Journal of Crystal Growth 2005;284:453–8.
[24] Spanhel L, Haase M, Weller H, Henglein A. J Am Chem Soc 1987;109:5649–55.
[25] Weller H, Schmidt HM, Koch U, Fojtik A, Baral S, Henglein A, et al. Chemical Physics Letters 1986;124(6):557–60.
[26] Tauc J, Menth A. J Non-Cryst Solids 1972;8-10:569–85.
[27] Winter JO, Gomez N, Gatzert S, Schmidt CE, Korgel BA. Colloids and Surfaces, A: Physicochemical and Engineering Aspects 2005;254(1–3):147–57.
[28] Nel AE, Mädler L, Velegol D, Xia T, Hoek EMV, Somasundaran P, et al. Nature Materials 2009;8:543–57.
[29] Chibowski S, Paszkiewicz M. J Dispers Sci Technol 2001;22:281–9.
[30] Mansur HS, Mansur AAP. Materials Chemistry and Physics 2011;125(3):709–17.
[31] Reiss P, Protiere M, Li L. Small 2009;5(2):154–68.
[32] Li Y, Zhu Y, Yang X, Li C. Cryst Growth Des 2008;8(12):4494–8.

Polymer 52 (2011) 1055–1062

Contents lists available at ScienceDirect

Polymer

journal homepage: www.elsevier.com/locate/polymer

Melt-crystallized nylon-6 nucleated by the constrained chains of its non-stoichiometric cyclodextrin inclusion compounds and the nylon-6 coalesced from them

A. Mohan, A. Gurarslan, X. Joyner, R. Child, A.E. Tonelli*

Fiber & Polymer Science Program, North Carolina State University, Campus Box 8301, Raleigh, NC 27695-8301, USA

ARTICLE INFO

Article history:
Received 22 November 2010
Received in revised form
21 December 2010
Accepted 21 December 2010
Available online 30 December 2010

Keywords:
Constrained nylon-6
Nucleated melt crystallization
Cyclodextrin

ABSTRACT

Non-covalently bonded crystalline inclusion compounds (ICs) have been formed by threading host cyclic starches, cyclodextrins (CDs), onto guest nylon-6 (N-6) chains. When excess N-6 is employed, non-stoichiometric (n-s)-N-6-CD-ICs, with partially uncovered and "dangling" N-6 chains, result. While the host crystalline CD lattice is stable to ~300 °C, the uncovered, yet constrained, portions of the N-6 chains emanating from the CD-IC surfaces may crystallize below, or be molten above ~225 °C, and confer upon them shape-memory. When heated between the T_m of N-6 and the decomposition temperature of the (n-s)-N-6-CD-IC, they may be deformed into a new shape, which is retained following a rapid quench below T_m. When this newly-shaped sample is heated above the T_m of the un-included and crystalline portions of N-6, it reverts back to its original shape in response to the constraining CD-IC crystals.

When added at low concentrations, the non-toxic (n-s)-N-6-CD-ICs serve as effective nucleating agents for the bulk crystallization of N-6 from the melt. This is a consequence of the ability of the N-6 chains protruding from their (n-s)-CD-ICs to crystallize more rapidly and at higher temperatures than bulk N-6 chains when their molten mixture is cooled, thereby providing finely dispersed crystalline nuclei for the subsequent crystallization of the bulk N-6 chains. Melt-crystallized N-6 nucleated with (n-s)-N-6-CD-ICs have finer grained more homogeneous morphologies than un-nucleated N-6 samples. Furthermore, N-6s coalesced from their CD-ICs by appropriate removal of the host CD are also found to effectively nucleate the melt-crystallization of bulk N-6, even after long periods of annealing above the T_m of N-6. N-6 coalesced from stoichiometric CD-ICs, with full N-6 coverage, and from (n-s)-N-6-CD-ICs, with only partial N-6 coverage, show very similar crystallization behaviors and both are effective as nucleants, and this is reflected by their higher densities and improved mechanical properties.

1. Introduction

Harada and Kamachi first demonstrated in 1990 [1], using poly (ethylene oxide) oligomers, that non-covalently bonded crystalline inclusion compounds (ICs) could be formed between guest polymers and the host cyclic starches, cyclodextrins (CDs) (See Fig. 1a). This is accomplished by threading of the guest polymers through the narrow CD cavities to form polymer threaded crystalline stacks of CDs, as illustrated in Fig. 1b and c.

More recently [2–7] it has been demonstrated that crystalline non-stoichiometric (n-s)-polymer-CD-ICs can be obtained if an excess of the guest polymer is used during their formation. Note in Fig. 2 that incomplete coverage of the threaded guest polymers results in the "dangling" of un-included portions of the polymer chains from (n-s)-polymer-CD-IC crystalline surfaces. If the guest polymer is crystallizable, then those portions of the chains "dangling" from (n-s)-polymer-CD-ICs may also crystallize. As a consequence, when small amounts of (n-s)-polymer-CD-ICs are added to the same neat bulk polymer, they have been observed [2–7] to function as very effective nucleation agents during melt-crystallization. This is presumably due to the ability of the "dangling" chains to more readily crystallize at higher temperatures, thereby providing nuclei for the crystallization of the bulk polymer chains as they are cooled further from the melt.

This approach is limited to polymers with melting temperatures, T_m, that are below that of the decomposition temperature (~300 °C) of their CD-IC crystals. Because of the biodegradable/bioabsorbable and non-toxic natures of CDs, (n-s)-polymer-CD-ICs potentially provide environmentally responsible nucleants for enhancing the melt-crystallization of polymers and improving their properties [6–9].

* Corresponding author.
E-mail address: alan_tonelli@ncsu.edu (A.E. Tonelli).

0032-3861/$ – see front matter © 2010 Elsevier Ltd. All rights reserved.
doi:10.1016/j.polymer.2010.12.049

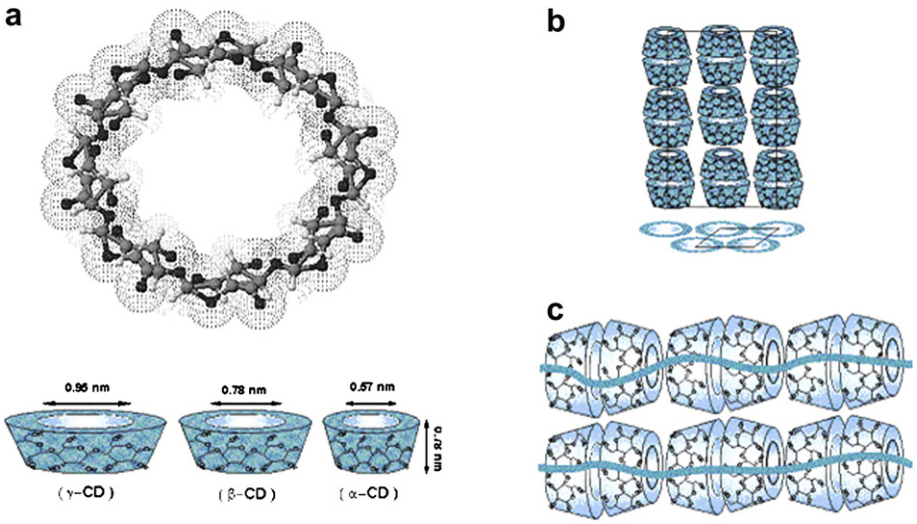

Fig. 1. CD structures and cavity dimensions (a) and the channel crystal structure of polymer-CD-ICs (b) and (c).

Recently we have reported (n-s)-CD-ICs formed between α- and γ-CD hosts and nylon-6 (N-6) guests [10]. Anionically initiated, ring-opening polymerization of ε-caprolactam produced N-6 samples with different molecular weights (MW = M_w, with $M_w/M_n \sim 2$) ranging from 100,000 to 600,000 Da. When combined with commercial N-6 samples with MWs = 30,000 and 60,000 Da, this series of N-6 samples provided an opportunity to compare the effects of MW on the melt crystallization of "free" neat bulk and "dangling" constrained (n-s)-CD-IC N-6 chains. Several different N-6:CD ratios were employed in the formation of (n-s)-N-6-CD-ICs to determine the effect of "dangling" chain length on their crystallizability. In addition, both α- and γ-CDs were selected as hosts, because single and pairs of side-by-side N-6 chains, respectively, are threaded through their ICs [11], producing different constraints on the N-6 chains that "dangle" from them, and which were demonstrated to effect their crystallization. Here we report further on the effectiveness of (n-s)-N-6-CD-ICs to act as nucleants in the melt-crystallization of bulk N-6 when added in small amounts, including the isothermal crystallization kinetics of neat and nucleated N-6 samples.

Following the careful removal of the host CDs from N-6-CD-ICs, the resulting coalesced N-6s were also examined for their abilities to nucleate the melt-crystallization of bulk N-6. The morphologies, mechanical properties, and densities of melt-crystallized as-received and coalesced N-6 films and those nucleated with (n-s)-N-6-CD-ICs and coalesced N-6s are compared. In addition, the "shape-memory" behavior of (n-s)-N-6-CD-ICs is also demonstrated.

2. Experimental

2.1. Materials and methods

Aside from coalesced N-6 and nucleated N-6 films formed by precipitation, all materials used and N-6 samples formed were described previously [10], with the exception of N-6 with a molecular weight of 60,000 (Ultramid B4001©) obtained from BASF. Coalescence of N-6 from its CD-ICs was accomplished by treatment with dilute aqueous solutions of HCL or extensive washing with warm water. In addition to the previously employed solvent-casting

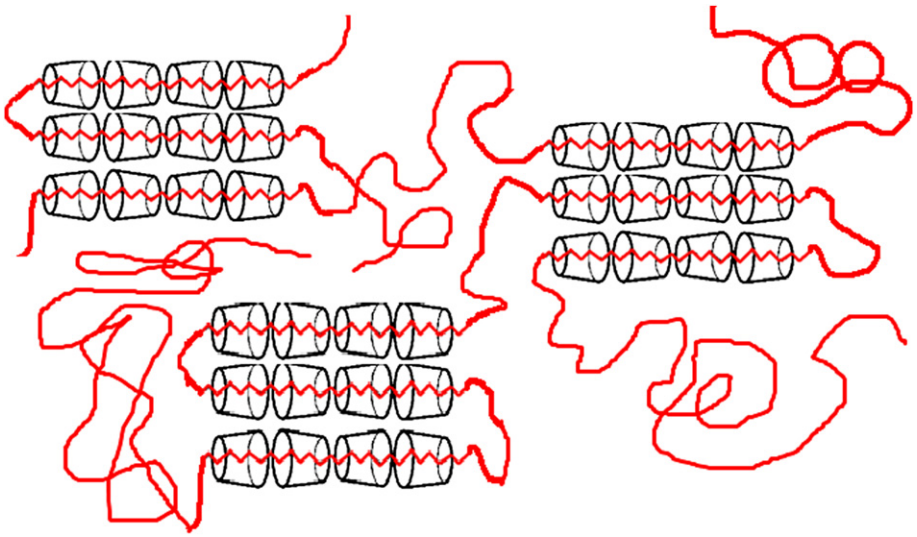

Fig. 2. Schematic representation of a (n-s)-polymer-CD-IC.

method, we also formed nucleated N-6 films by suspending the nucleants in formic acid solutions of N-6, followed by precipitation into acetone and by melt-pressing the precipitated N-6/nucleant mixtures. Similarly, the DSC and microscopy observations reported here were described previously [10], except for the isothermal melt-crystallization kinetics of neat and nucleated N-6s observed by DSC. These N-6 films were heated in the DSC, maintained in the melt at 250 °C for 5 min, and cooled at −10 °C/min to 185 or 200 °C, where the time dependent increase in their crystallization exotherms were observed.

2.2. Densities

N-6 film densities were determined by floatation in a mixed solution of carbon tetrachloride (CT) and toluene (T), whose densities are greater ($\rho_{CT} = 1.594$ g/cm^3) and less ($\rho_T = 0.8668$ g/cm^3) than N-6. Small portions of N-6 film were floated atop 25 ml of CT in a 100 ml graduated cylinder containing a magnetic stir bar that was placed on a magnetic stir plate. The tip of a 50 ml burette containing T was inserted through aluminum foil that covered the mouth of the graduated cylinder. While stirring, T was slowly dripped in (∼10 drops/ml) until the N-6 film sank below the surface of and became suspended in the CT/T solution when stirring was stopped. The volume of T, vol(T), required to achieve suspension of N-6 was then used to determine the N-6 film density, $\rho_{N\text{-}6}$, from

$$\rho_{N-6} = [\mathrm{vol(T)}\rho_T + 25\rho_{CT}]/[\mathrm{vol(T)} + 25].$$

Comparative N-6 film densities were observed for melt-crystallized as-received and coalesced N-6 samples possessing the same crystallinity, as determined by DSC. This was achieved by simultaneously placing a portion of each of the N-6 melt-crystallized films in the graduated cylinder containing CT, and adding T as just described. The film that first began to sink and became

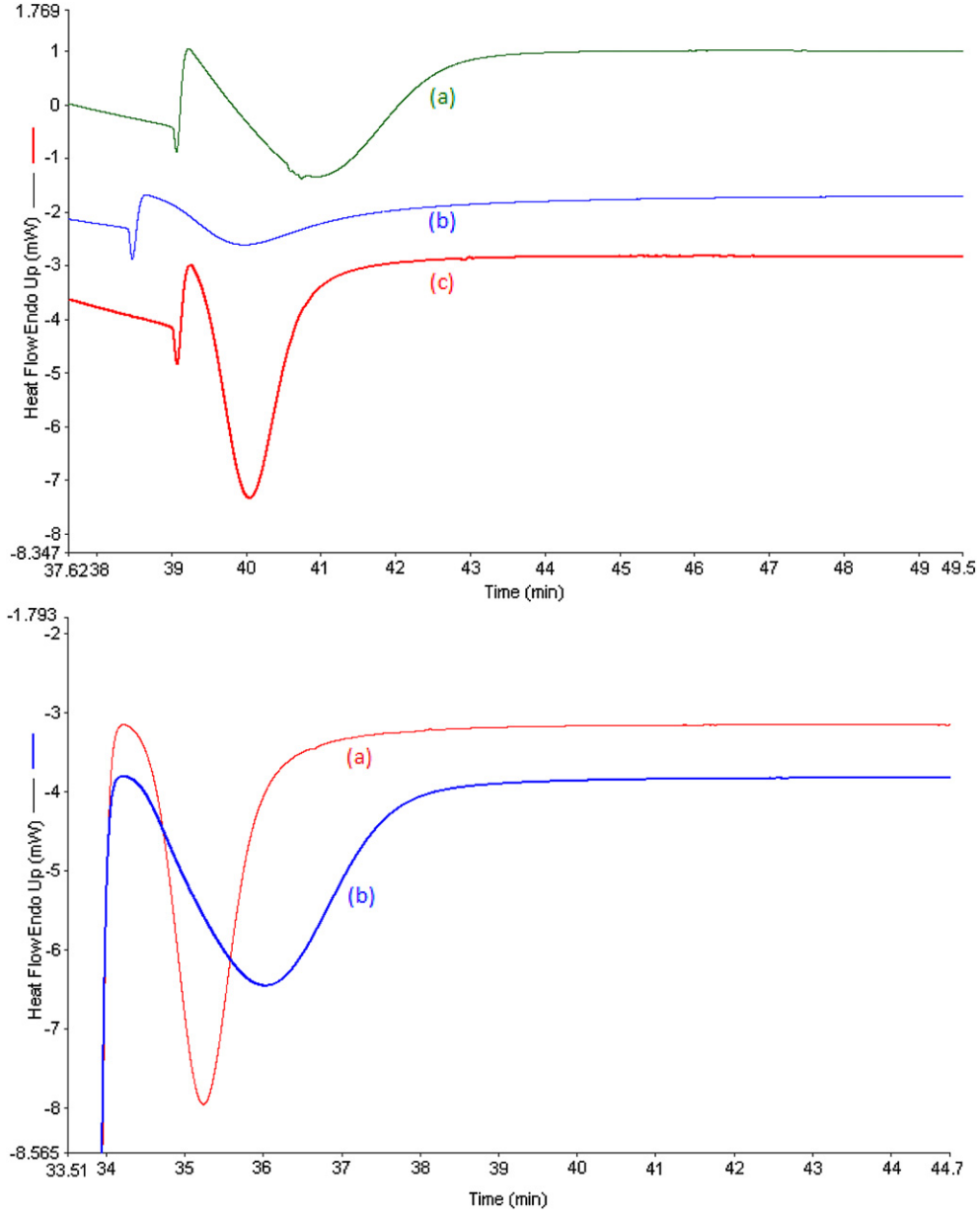

Fig. 3. After cooling from 250 °C in the melt at −10 °C/min, isothermal crystallization (upper panel) of N-6 (MW = 600,000 Da) (a), its 3:1 (n-s)-N-6-α-CD-IC (b), and N-6 nucleated with 2 wt% of the 3:1 (n-s)-N-6-α-CD-IC (c) at 185 °C and in the lower panel of neat N-6 (b) and N-6 nucleated with 2 wt% of the 3:1 (n-s)- N-6-α-CD-IC (a) at 200 °C.

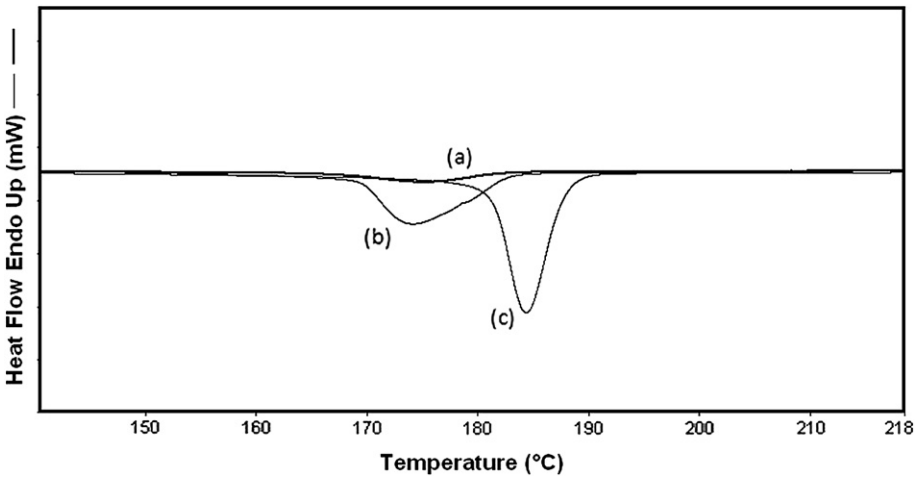

Fig. 4. DSC cooling scans (−5 °C/min) for neat (a) N6 (600,000 g/mol), (b) 6:1 (n-s)-N6-γ-CD-IC and (c) N6 with 2 wt% 6:1 (n-s)-N6-γ-CD-IC.

suspended in the CT/T column had the highest density, which must be attributed to closer packing of chains in the amorphous regions of the sample.

2.3. Tensile testing

Tensile tests were conducted according to ASTM D-882-97 using a MTS Q-Test™/5,CRE type tester. The test specimens were prepared by cutting 0.14–0.15 mm thick films into 6 mm wide and 90 mm long dog bone shapes using a template. Tensile tests were performed using a 250lb load cell, and the gauge length was 50 mm. The cross-head speed was 500 mm/min for as-received N-6 films and 50 mm/min for the other films. Load-elongation curve, modulus, peak load, and elongation at break data were acquired at the end of each test, and each value of the mechanical properties reported was an average of at least five film test specimens.

2.4. "Shape-memory" test

Melt-pressed films, 6.5 cm in length, 0.8 cm in width, and 0.15 mm thick, of neat N-6 (60,000 g/mol) and its 3:1 (n-s)-α-CD-IC (2 samples) were suspended over closely adjacent and inverted petri dishes. A 2g weight was placed on top of the suspended portion of one of the 3:1 (n-s)-α-CD-IC films, and they were placed in a vacuum oven and subsequently heated to 250 °C. Upon removal from the oven and cooling to room temperature, the small weight was removed and the films were returned to the 250 °C oven.

3. Results and discussion

3.1. "Shape-memory" of (n-s)-N-6-CD-ICs

While the neat N-6 film melted completely and flowed down the sides of both supporting petri dishes, the 3:1 (n-s)-N-6-α-CD-IC films only softened and sagged very slightly (no weight) and dramatically (2 g weight) between the supporting petri dishes, but remained integral without flowing. Upon removal of the small weight and return of the severely sagging 3:1 (n-s)-N-6-α-CD-IC film to the 250 °C oven, the sagging suspended film retracted almost completely, until it appeared closely similar to the 3:1 (n-s)-N-6-α-CD-IC film without the weight that was heated to 250 °C. While this procedure is only a qualitative test for shape-memory, it does demonstrate that (n-s)-N-6-CD-ICs are essentially networks cross-linked with and held together by the CD-IC crystalline domains containing included portions of N-6 chains. When heated above the T_m of N-6, the N-6 chains and the (n-s)-N-6-CD-IC

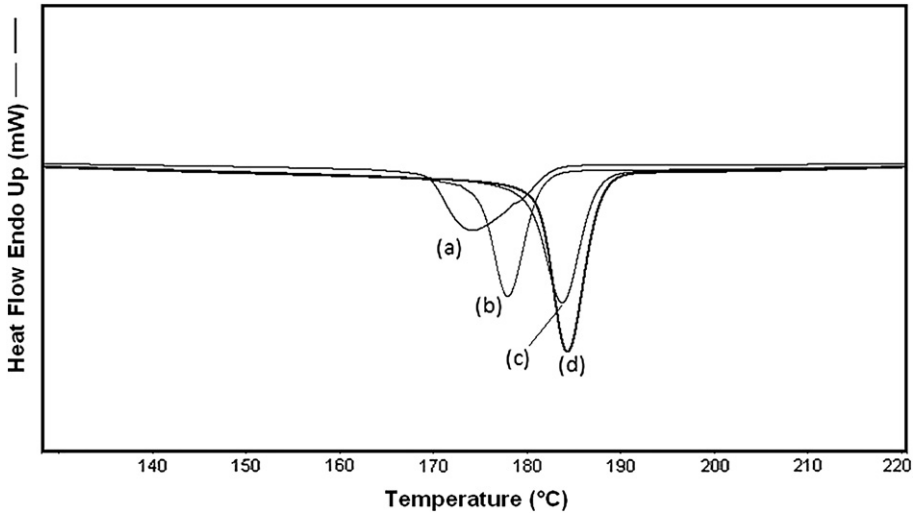

Fig. 5. DSC cooling scans (−5 °C/min) for neat (a) N6 sample (600,000 g/mol) (b) N6 with 2 wt% 3:1 (n-s)-N6-α-CD IC, (c) N-6 with 2 wt% talc, and (d) N6 with 2 wt% 6:1 (n-s)-N6-γ-CD-IC, from low to high maximum crystallization temperatures, respectively.

Table 1
Melt-Crystallization of Nylon-6 with 2 wt% of Various Nucleants.

Samples	T_m	T_c	ΔH_c	X_c[a]
60k Neat	222	175	58	37
60k + α-CD	217	184	55	35
60k + 1:1 α-CD	217	184	60	38
60k + 3:1 α-CD	220	185	62	33
60k + Talc	220	193	64	34
60k + γ-CD	217	181	53	29
600k Neat	223	174	45	24
600k + α-CD	218	179	44	23
600k + 1:1 α-CD	220	180	47	25
600k + Coal N6	220	182	51	27
600k + 3:1 α-CD	221	179	53	29
600k + Coal N6	220	182	56	30
600k + γ-CD	220	178	40	21
600k + 2:1 γ-CD	221	180	53	29
600k + 6:1 γ-CD	220	184	57	30
600k + Talc	221	183	50	26

[a] $X_c = \Delta H_c/\Delta H_m^O$, with $\Delta H_m^O = 160$ J/g [18,19].

network as a whole may be stretched. In addition, this implies that the un-included portions of at least some N-6 chains do not actually "dangle", but instead are constrained on both ends by inclusion in different CD-IC crystals.

3.2. Isothermal crystallization of (n-s)-N-6-CD-ICs

Fig. 3 presents the isothermal crystallization of neat N-6 (MW = 60,000 Da), its 3:1 (n-s)-N-6-α-CD-IC, and N-6 nucleated with 2 wt% of the 3:1 (n-s)-N-6-α-CD-IC. Each sample was heated into the melt at 250 °C, maintained there for 5 min, cooled at −10 °C/min to T_C = 185 or 200 °C, and their melt crystallization(ΔH_C) observed as a function of time. It is clear that the un-included N-6 chains in the 3:1 (n-s)-N-6-α-CD-IC and the N-6 chains in the N-6 sample nucleated by them crystallize faster than the neat bulk N-6 chains, similar to results observed, though not presented here, when cooling more rapidly than −10 °C/min from the melt to T_C (Comparison with the DSC results seen subsequently in Fig. 5 indicates why faster cooling rates were not necessary.) This provides visual and quantitative kinetic verification of the ability of (n-s)-N-6-CD-ICs to act as effective nucleants for the melt-crystallization of N-6 and is complimentary to the thermodynamic results subsequently presented (Table 1) and discussed. Though similar isothermal crystallization observations were not made for N-6 coalesced from its CD-ICs, they were found to be at least as effective as (n-s)-N-6-CD-ICs as nucleants for the melt-crystallization of bulk N-6, but without the introduction of any non-N-6 additive (See below).

3.3. (n-s)-N-6-CD-IC nucleated N-6

Even though N-6 in both neat and 6:1 (n-s)-γ-CD-IC samples seem to crystallize similarly (Fig. 4), note that the 6:1 (n-s)-n-6-γ-CD-IC nevertheless seems to effectively nucleate the melt-crystallization of bulk N-6. In fact 6:1 (n-s)-N6-γ-CD-IC appears a more effective nucleant than the 3:1(n-s)-N6-α-CD-IC judging from the DSC cooling scans in Fig. 5. Even though the un-included portions of N-6 chains in the 6–1 γ-CD-IC crystallize to a lesser extent and at a lower temperature than those in the 3:1 α-CD-IC [10], they are nevertheless more effective in nucleating the melt-crystallization of bulk N-6. This behavior may be related to the presence of side-by-side pairs of N-6 chains "dangling" from the surfaces of (n-s)-N-6-γ-CD-IC crystals, compared to the single N-6 chains emerging from(n-s)-N-6-α-CD-IC crystals. On the other hand, the morphology produced by the 3:1 N-6-α-CD-IC in Fig. 6 appears more homogeneous and of a finer grain than that seen in the N-6 sample nucleated with 6:1 (n-s)-N6-γ-CD IC. Because we have not yet determined the particle sizes of the nucleants used here, reasons offered to explain observed differences in the melt-crystallized morphologies produced by them are tentative [3,5].

3.4. N-6 nucleated with coalesced N-6

Note below in Fig. 7, that the N-6 chains coalesced from 1:1 and 3:1 (n-s)-N-6- α-CD-ICs crystallize at higher temperatures than

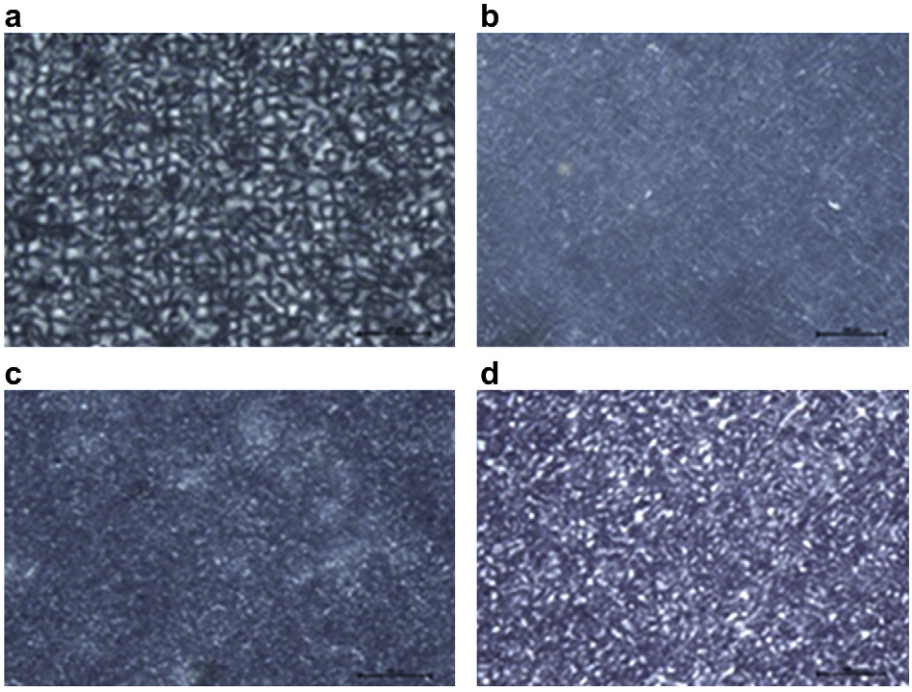

Fig. 6. Polarized micrographs of melt-crystallized N6 films. (a) neat N6 (600,000 g/mol), (b) N6 with 2 wt% 3:1 (n-s)-N6-α-CD IC, (c) N-6 with 2 wt% talc, and (d) N6 with wt% 6:1 (n-s)-N6-γ-CD IC.

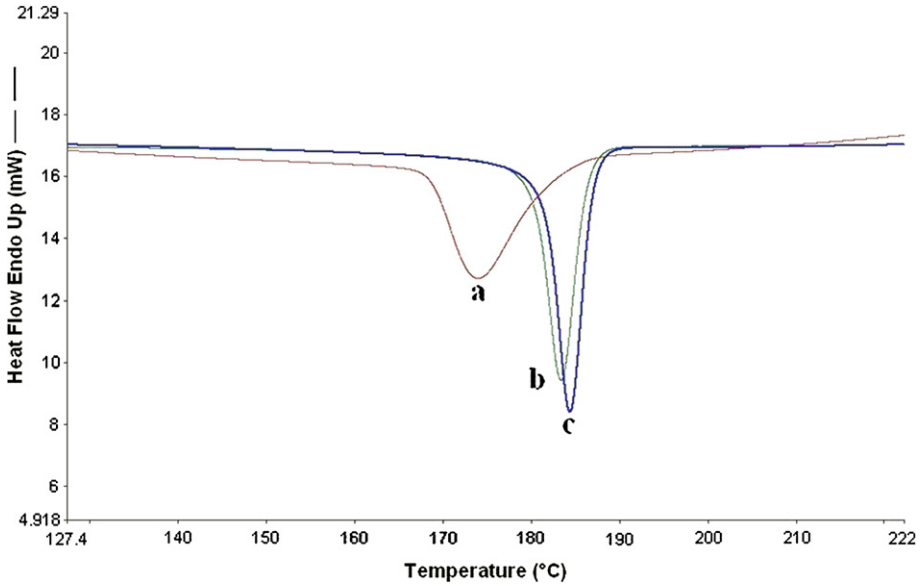

Fig. 7. DSC cooling scans (−5 °C/min) from the melts of (a) neat bulk N-6 (600,000), and the same N-6 coalesced from its (b) 1:1 and (c) 3:1 (n-s)-N-6-α-CD-ICs.

neat N-6, even after remaining in the melt for 5 min. Furthermore, the N-6 chains coalesced from the stoichiometric 1:1 and (n-s) α-CD-ICs crystallize at virtually the same temperature upon cooling from their melts. This is consistent with our view [10] of (n-s)-N-6-α-CD-ICs as high density polymer brushes [13,14], with highly extended and largely parallel chains that are unentangled, like those in Fig. 8.

Upon coalescence, the N-6 chain segments that emerge from the crystal surfaces of the 3:1 (n-s)-α-CD-IC are apparently as extended and unentangled as those that were threaded and covered completely by α-CDs in the stoichiometric 1:1 IC. Heating N-6 nucleated with coalesced N-6 for 1.5 h in the melt at 250 °C, did not produce a reduction of its melt-crystallization temperature to that of neat bulk N-6, a result that may at first appear surprising.

When guest polymers are coalesced from their CD-ICs by carefully removing the host CD lattices, they are observed to solidify with structures, morphologies, and even conformations that are distinct from bulk samples made from their solutions and melts [15]. Not only are the organizations and behaviors of bulk polymer samples significantly modified on coalescence from their CD-ICs, but both are also maintained for significant periods of time even when heated above their T_gs and T_ms, where their chains are mobile. While random-coiling of their initially coalesced, largely extended, separated, and unentangled chains may be relatively rapid, we recently concluded [16] that the subsequent establishment of homogeneous melts is extremely sluggish due to the hindered center-of-mass diffusion that must accompany full entanglement of their chains. Apparently, the process of entangling the largely separated and not fully interpenetrating randomly coiled chains initially coalesced from their CD-ICs is particularly slow, much slower in fact than the center-of mass diffusion of polymer chains in their fully entangled melts. We believe this to be a result of the absence of reptation tubes in bulk polymers coalesced from their CD-ICs, and their apparently very slow establishment upon heating.

Note in Fig. 9 that N-6 coalesced from the stoichiometric 1:1 and 3:1 (n-s)-N6-α-CD-ICs similarly nucleate the melt-crystallization of N-6, which mirrors the crystallization of their neat coalesced N-6 chains (See Fig. 7). On the other hand, as seen in Fig. 10, N-6 coalesced from its stoichiometric 1:1 α-CD-IC seems to nucleate a more homogeneous and finer grained morphology than the N-6 chains coalesced from the 3:1 (n-s)-α-CD-IC.

It should also be noted that N-6 films containing all of the nucleants discussed here were produced by solution-casting (dissolution of N-6 in 90% formic acid, suspension of the nucleant by addition with stirring, and removal of the formic acid by evaporation). This may appear surprising in the case of the coalesced N-6 nucleants, which are, after all, just N-6. However, it was observed that when coalesced N-6s were added to the N-6 solutions in 90% formic acid they did not immediately dissolve. Similar behavior has been noted previously for

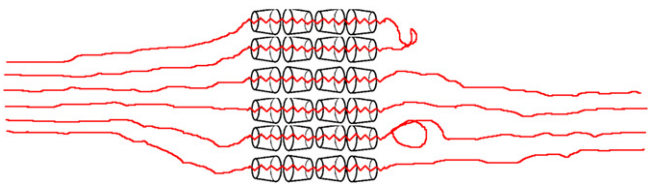

Fig. 8. Extended and highly oriented nature of un-included portions of polymer chains in their (n-s)-CD-ICs (Note that it is likely that both ends of the un-included portions are constrained by their inclusion in other CD-IC crystals not drawn here).

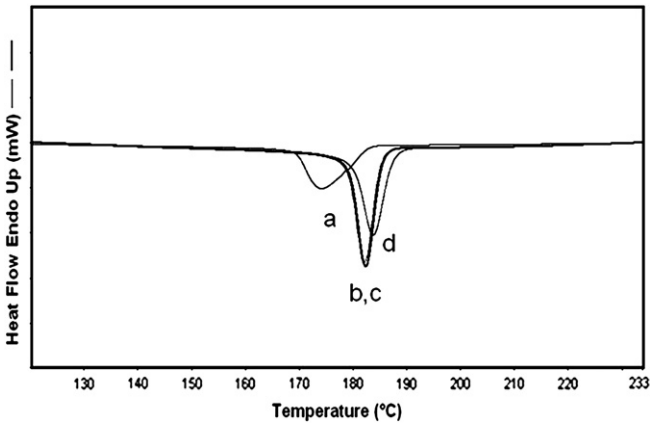

Fig. 9. DSC cooling scans for (a) neat N-6 sample (600,000 g/mol), with 2 wt% of (b) N-6 coalesced from 1:1 (n-s)-N6-α-CD IC, (c) N-6 coalesced from 3:1 (n-s)-N6-α-CD IC, and (d) N-6 with 2 wt% talc.

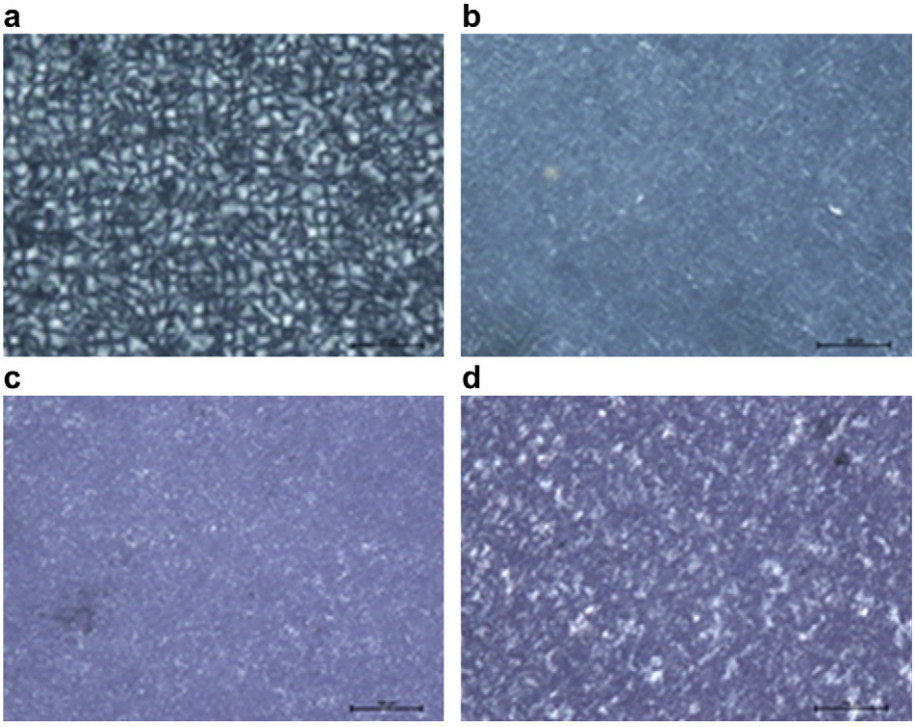

Fig. 10. Polarized micrographs of melt-crystallized films of (a) neat N-6, (b) N-6 with 2 wt% talc, (c) N-6 with 2 wt% N-6 coalesced from 1:1 N-6-α-CD-IC, and (d) N-6 with 2 wt% N-6 coalesced from 3:1 (n-s)-N6-α-CD-IC.

polymers coalesced from their CD-ICs [10,17]. Furthermore, though not presented here, the behaviors of nucleated N-6 films prepared by precipitation and melt-pressing were similar to those of the solution-cast nucleated N-6 films.

3.5. Properties of neat and nucleated N-6 films

Table 1 summarizes the nucleated melt-crystallization of N-6s with MW = 60,000 and 600,000 Da containing 2 wt% pure CDs, their stoichiometric (1:1) and [(n-s) = (2,3, or 6:1)] N-6-ICs, or the N-6s coalesced from them used as nucleants. All melt-nucleated N-6 samples, exhibit T_ms and X_cs very similar to those of the same neat bulk N-6. At the same time, however, all nucleated samples crystallize from the melt at higher temperatures (T_c) than the neat bulk N-6s, which explains their effectiveness as nucleants.

The densities and stress-strain responses of films melt-pressed from neat as-received, coalesced, and nucleated N-6 samples are presented and compared in Table 2 and Fig. 11, respectively. DSC observations were used to confirm that all films had very similar levels of crystallinity, which required annealing of the neat bulk N-6 films.

It is clear that coalesced N-6 has a higher density than as-received N-6, even though they possess closely similar crystallinities. Therefore, the non-crystalline regions in coalesced N-6 must have a higher density than those in as-received N-6. With the known [20] densities of crystalline (1.230 g/cm^3) and amorphous (1.084 g/cm^3) N-6, and using $X_C(\rho) = (\rho_c/\rho)[(\rho - \rho_a)/(\rho_c - \rho_a)]$, where $X_C(\rho)$, ρ, ρ_c, and ρ_a are the fractional crystallinity determined by density [assumed = X_C(DSC)] and the overall sample (1.1674), crystalline (1.230), and amorphous or non-crystalline densities, we estimate that the density of N-6 chains in the non-crystalline regions of the coalesced sample is 1.111 g/cm^3. This is ~3% greater the density of N-6 chains in the amorphous regions of the as-received sample (ρ_a = 1.084 g/cm^3), and is consistent with our view of the extended and largely unentangled organization of chains in polymer samples coalesced from their CD-ICs [15]. It should also be noted that $X_C(\rho)$ calculated for as-received N-6 is ~0.5 and agrees closely with X_C(DSC) = 0.53.

In Fig. 11 we can see that the N-6 film nucleated with 2 wt% of N-6 coalesced from its stoichiometric 1:1 α-CD-IC has a higher modulus and a greatly reduced elongation at break compared to the neat N-6 films, even after annealing to achieve a closely similar level of crystallinity as the nucleated N-6 film (See Table 2). We believe this to be a consequence of the more homogeneous and finer scale semi-crystalline morphology and possibly the increased packing density of unentangled and extended N-6 chains in some of the non-crystalline regions. Coalesced N-6 has been shown to crystallize predominantly in the most stable α-polymorph [12], with antiparallel chains that maximize interchain hydrogen-bonding. When this is considered in conjunction with the increased packing density of chains in the non-crystalline regions, the improved modulus (stiffness) of N-6 nucleated with N-6 coalesced from its stoichiometric α-CD-IC may be understood.

Though not presented here a N-6 film nucleated with 2 wt% of 3:1 (n-s)-N-6- α-CD-IC exhibited a modulus closely similar to the N-6 film nucleated with 2 wt% of N-6 coalesced from its stoichiometric 1:1 α-CD-IC, but an elongation at break that was midway between that of the annealed as-received and nucleated N-6 films. (See Fig. 11).

Table 2
Nylon-6 densities.

Material	X_c (DSC crystallinity)	Density (g/cm^3)
Nylon-6 pellets	0.53	1.1559
Nylon-6 (coalesced from 1:1 N-6-α-CD-IC)	0.51	1.1674
Density of non-crystalline regions in Nylon-6		1.084 g/cm^3
Density of non-crystalline regions in Coalesced Nylon-6		1.111 g/cm^3

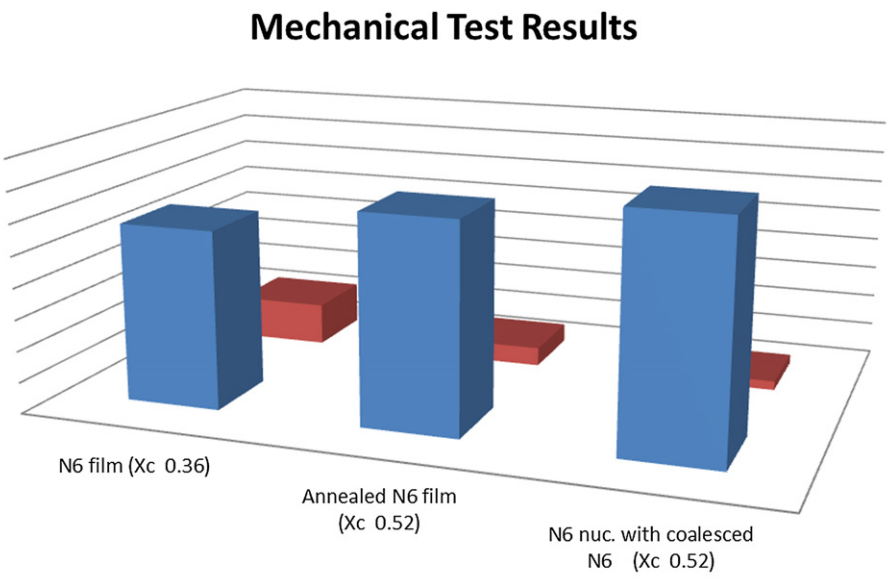

	N6 film (Xc 0.36)	Annealed N6 film (Xc 0.52)	N6 nuc. with coalesced N6 (Xc 0.52)
Modulus (MPa)	571.01	667.85	739.4
Elongation at break (mm)	136	59.7	28.7

Fig. 11. Stress-strain responses of thin melt-pressed neat bulk N-6 films (as-received and annealed), and N-6 film nucleated with N-6 coalesced from its 1:1 stoichiometric α-CD-IC.

Polymers coalesced from their CD-ICs and added in small quantities to the same bulk polymers would appear to be "ideal" nucleants for their melt-crystallization for the following reasons: i. chemical compatibility, ii. non-toxicity, and iii. "stealth" natures. Not only may they improve the mechanical properties of the polymer materials they nucleate, but they may be used in implantable medical applications as well.

3.6. Summary and conclusions

Non-covalently bonded crystalline inclusion compounds (ICs) have been formed by threading α- and γ-CDs onto guest N-6 chains. Non-stoichiometric (n-s)-N-6-CD-ICs, with partially uncovered and "dangling" N-6 chains are produced when an excess of the guest N-6 is employed, and they evidence shape-memory. When heated between the T_m of N-6 and the decomposition temperature of (n-s)-N-6-CD-ICs, they may be deformed into a new shape, which is retained following a rapid quench below T_m. When this newly-shaped sample is heated above the T_m of the un-included portions of N-6, it reverts back to its original shape in response to the constraining CD-IC crystals.

When added at low concentrations, the non-toxic (n-s)-N-6-CD-ICs serve as effective nucleating agents for the bulk crystallization of N-6 from the melt. This is a consequence of the ability of the N-6 chains protruding from their (n-s)-CD-ICs to crystallize more rapidly and at higher temperatures than bulk N-6 chains when their molten mixture is cooled, thereby providing finely dispersed crystalline nuclei for the subsequent crystallization of the bulk N-6 chains. Melt-crystallized N-6 samples nucleated with (n-s)-N-6-CD-ICs have finer grained more homogeneous morphologies than un-nucleated N-6 samples, and this is responsible for their improved mechanical properties and higher densities. Furthermore, N-6s coalesced from their CD-ICs by appropriate removal of the host CD are also found to be effective nucleating agents for the melt-crystallization of N-6, and are unaffected by long periods of annealing above the T_m of N-6. N-6 coalesced from stoichiometric CD-ICs, with full N-6 coverage, and from (n-s)-N-6-CD-ICs, with only partial N-6 coverage, show very similar crystallization behaviors and both are effective as nucleants, confirming our previous suggestion that the un-included portions of N-6 chains in (n-s)-N-6-CD-ICs form a dense brush anchored on both ends by inclusion into different CD-IC crystals and are characterized by high N-6 chain extension and orientation.

N-6 films nucleated with (n-s)-N-6-CD-ICs or the N-6 coalesced from them and from their stoichiometric 1:1 N-6-CD-ICs evidence more homogeneous finer grain semi-crystalline morphologies, with more densely packed chains in the non-crystalline sample regions that lead to improved mechanical properties.

References

[1] Harada A, Kamachi M. Macromolecules 1990;23:2821.
[2] He Y, Inoue Y. Biomacromolecules 1865;4:2003.
[3] Dong T, He Y, Zhu B, Shin K, Inoue Y. Macromolecules 2005;38:7736.
[4] Dong T, Shin K, Zhu B, Inoue Y. Macromolecules 2006;39:2427.
[5] Dong T, Kai W, Pan P, Cao A, Inoue Y. Macromolecules 2007;40:7244.
[6] Vogel R, Tandler B, Haussler L, Jehnichen D, Brunig H. Macromol Biosci 2006;6:730.
[7] Mori T, Dong T, Yazawa K, Inoue Y. Macromol Rapid Commun 2007;28:2095.
[8] Zhang S, Yu Z, Govender T, Luo H, Li B. Polymer 2008;49:3205.
[9] Luo HY, Liu Y, Yu ZJ, Zhang S, Li B. Biomacromolecules 2008;9:2573.
[10] Mohan A, Joyner X, Kotek R, Tonelli AE. Macromolecules 2009;42:8983.
[11] Shin DI, Huang L, Tonelli AE. Macromol Chem Symp Ed 1999;138:21.
[12] Wei M, Davis W, Urban B, Song Y, Porbeni FE, Wang X, et al. Macromolecules 2002;35:8039.
[13] Tsujii Y, Ohno K, Yamamoto S, Goto A, Fukada T. Adv Polym Sci 2006;197:1.
[14] He G-L, Merlitz H, Sommer J-U, Wu C-X. Euro Phys J E 2007;24:325.
[15] Tonelli AE. Adv Polym Sci 2009;222:115.
[16] Tonelli AE. J Polym Sci Part B Polym Phys 2009;47:1543.
[17] Rusa C, Tonelli AE. Macromolecules 2000;33:5321.
[18] Mandelkern L. In: Mark J, Ngai K, Graessley W, Mandelkern L, Samulski E, Koenig J, Wignall G, editors. Physical properties of polymers. 3rd ed. Cambridge, UK: Cambridge University Press; 2004 [Chap. 4].
[19] Gechele GB, Crescentini L. J Appl Polym Sci 1963;7:1349.
[20] Galanty PG, Jacob KI. In: Mark JE, editor. Polymer data handbook. 2nd ed. Oxford University Press; 2009. p. 255.

Polymer 52 (2011) 1063–1070

Contents lists available at ScienceDirect

Polymer

journal homepage: www.elsevier.com/locate/polymer

Shape memory polymer system of semi-interpenetrating network structure composed of crosslinked poly (methyl methacrylate) and poly (ethylene oxide)

Debdatta Ratna [a,*], J. Karger-Kocsis [b]

[a] Naval Materials Research Laboratory, Shil Badlapur Road, Addl. Ambernath, Maharastra 421506, India
[b] Department of Polymer Engineering, Faculty of Mechanical Engineering, Budapest University of Technology and Economics, H-1111 Budapest, Hungary

ARTICLE INFO

Article history:
Received 29 August 2010
Received in revised form
10 December 2010
Accepted 23 December 2010
Available online 7 January 2011

Keywords:
Shape memory polymers
Semi-interpenetrating polymer network
Creep

ABSTRACT

Shape memory semi-interpenetrating polymer networks (semi-IPNs) composed of crystalline poly (ethylene oxide) (PEO) and crosslinked poly (methyl methacrylate) (x-PMMA) have been investigated. The selected compositions show shape memory property with a reasonable fast recovery (recovery time ~1 min) and shape recovery ratio of 99%. Effects of composition (x-PMMA/PEO = 80/20…60/40) and crosslinker (triethyleneglycol dimethacrylate) concentration (up to 6 wt.%) on the creep property were also studied. The recovery time of the semi-IPNs increased and the creep compliance decreased with increasing crosslinker concentration. The network structure containing PEO crystal was characterized by scanning electron microscopy (SEM). Differential scanning calorimetry (DSC) indicated that the PEO, present confined in the semi-IPN, melts at a lower temperature compared to the pure PEO. Dynamic mechanical analysis (DMA) showed a decrease in the glass transition (T_g) of the semi-IPN due to the phase mixing of amorphous PEO and PMMA. Both the glassy and rubbery moduli (E_g and E_r, respectively) were lower for the semi-IPNs than for the x-PMMA network. On the other hand, the E_g/E_r ratio was markedly increased for the semi-IPNs supporting an easy shaping along with a good shape fixing.

1. Introduction

Materials are said to show shape memory effect [1–3] if they can be deformed and fixed into a temporary shape and recover their original permanent shape only on the exposure of external stimuli, like heat, light etc. Thermally induced shape memory effect is more common where the recovery takes place with respect to a certain critical temperature. The most widely used shape memory material is Ni–Ti alloy (Nitinol) [4]. Shape memory alloys (SMA) exhibit high recovery strength and have found wide technical applications [5–9]. However, they have obvious disadvantages such as high manufacturing cost, limited recoverable deformation, and toxicity issues [10,11].

Shape memory polymers (SMPs) offer deformation to a much higher degree and a wider scope of varying mechanical properties compared to SMAs, in addition to their inherent advantages of being cheap and easily processable (e.g. [12–15]). SMP can be designed by taking a polymer material, in which the polymer chains are able to fix a given deformation by cooling below a certain transition temperature (T_s) (e.g. [16,17]). The transition temperature (T_s) can be the glass transition (T_g) or melting point (T_m). Melting point is preferred over the glass transition as melting is comparatively sharper. Upon reheating to above T_s, the oriented chains in the network restore the random coil conformation resulting in a macroscopic recovery of the original shape [18–22].

Such polymer systems consist of two phases: one is the reversible or switching phase for maintaining a transient shape and the other is a fixed one for recovering the original shape [23,24]. In case of an amorphous system, at T_g the switching segment relaxes and allows the deformation. On cooling the switching segment "hardens" by entering in the glassy state and the shape is fixed. On further heating the shape is recovered due to softening of the switching segment [19–21]. In semicrystalline systems the crystals melt allowing the required deformation. On cooling, the shape is fixed due to crystallization and recovered on heating as a result of melting [25,26]. Physical or chemical crosslinking are responsible for the permanent shape (fixed phase).

The control of the fixed and the switching phases is most critical for the development of SMPs. A variety of polymer systems including polymer blends, block copolymers have been reported to show shape memory effect [27,28]. Among all, polyurethanes have been investigated most extensively [29,30], following the pioneering work carried out by Hayashi and coworkers [23,30]. The shape memory polyurethanes were first commercialized by Mitsubishi heavy industries, Japan.

* Corresponding author.
E-mail address: ratnad29@hotmail.com (D. Ratna).

0032-3861/$ – see front matter © 2010 Elsevier Ltd. All rights reserved.
doi:10.1016/j.polymer.2010.12.054

Full or semi-interpenetrating polymer networks (IPNs) often offer the possibility to broaden the range of properties [31,32]. However, there are only a limited number of reports on IPN-based SMPs [33–36] and detailed structure–property relationships for such systems have not been attempted. In an IPN system, the network properties are expected to play an important role in controlling the shape memory performance and need to be addressed for the successful development of IPN-based SMPs. The objective of the present investigation is to study the network properties (especially creep) and to establish the correlation with shape memory properties of IPN-based SMPs.

Poly (ethylene oxide) (PEO) has been widely used as a crystallizable switching component for SMP systems [37,38]. The fixed melting and crystallization temperature of a switching component often restricts the applications of the related SMPs. For example, biomedical application requires a switching temperature of 37 °C (body temperature). Hence use of a crystalline switching component with adjustable switching temperatures, will have broader scope of applications. Our recent investigation showed that the crystallization temperature of PEO can be widely varied and the switching temperature can be adjusted by a simple blending method using suitable polymers [39,40]. Accordingly, such blends will offer the possibility to develop SMP systems with adjustable T_s. That is why we have selected PEO as a switching component. The reported works have mostly used PEO of low molecular weight (<3000 g/mole) unlike to the present one (weight-average molecular weight = 20,000 g/mole).

In this work PEO/crosslinked PMMA (x-PMMA) based semi-IPNs have been investigated. Note that semi-IPNs are such systems in which one of the continuous phases is given by a thermoplastic, whereas the other by a thermoset (crosslinked) polymer. The selection of x-PMMA as a continuous phase is due to the fact that PEO forms compatible blend with PMMA in amorphous phase [33,34]. The combination of a crystalline phase and an amorphous crosslinked network is expected to produce SMPs with two transition temperatures; one corresponds to melting point of crystalline phase (PEO) and other due to the glass transition of the semi-IPN. The synthesis and characterization of semi-IPN systems and effect of crosslinking on the shape memory and creep properties of semi-IPNs will be discussed in the present paper. Use of PEO-based blends for the development of SMPs with adjustable switching temperature will be addressed in a later communication.

2. Experimental

2.1. Materials

PEO with weight-average molecular weight of 20,000 g/mole was purchased from Aldrich and used as received. Methyl methacrylate (MMA) (Fluka, 99%) was purified by washing twice with sodium hydroxide solution (5% w/v) to remove the inhibitors and then washed repeatedly with distilled water. It was then dried over anhydrous calcium chloride for 48 h. Benzoyl peroxide (Aldrich, 97%) and triethyleneglycol dimethacrylate (TEGDM) (Aldrich, 95%) were used as an initiator and a crosslinker, respectively, without any further purification.

2.2. Synthesis of x-PMMA PEO semi-IPN

About 20 ml of MMA was introduced in a circular aluminum mold (diameter10 cm) and heated to a temperature of 60 °C. Required amount of PEO was added and mixed with a glass rod. Once the PEO was completely dissolved in MMA, the required amount of crosslinker and initiator were mixed thoroughly and the mold was kept in an oven at 70 °C for 6 h. The sample was then placed in vacuum oven at 50 °C for 6 h to remove the unreacted monomer. An initiator concentration of 1 wt%(with respect to the weight of MMA) was used for all the samples. Different quantities of TEGDM (2, 4, 5, 6 wt%) were used to get the networks with various crosslink densities. Note that the concentration of TEGDM is calculated with respect to the quantity of monomer (MMA). The networks made with the crosslinker concentrations more than 6 wt % do not offer sufficient deformability to carry out the bend test for shape memory evaluation. That is why IPNs having crosslinker concentrations more than 6 wt% were not investigated.

2.3. Characterizations

Thermal behavior of PEO and the semi-IPN samples was studied with a differential scanning calorimeter (DSC) (Mettler–Toledo DSC821 Instrument, Greifensee, Switzerland). About 10 mg of sample was placed in an aluminium pan and heated from 25 to 150 °C at a heating rate of 5 °C min^{-1}.

Dynamic mechanical thermal analysis (DMTA) was carried out for all the specimens with dimensions of 20 mm × 8 mm × 2 mm (length × width × thickness) using a Q800 instrument (TA Instruments, New Castle, USA). The test specimens were analyzed from 30 to 150 °C with a heating rate of 3 °C/min. The experiments were carried out in a three-point bending mode using a fixed frequency of 1 Hz. Short-time flexural creep tests were also performed in the same DMTA machine using a three-point bending mode at the room temperature (RT). Each specimen was equilibrated for 5 min at RT (27 °C) and then the flexural creep was measured for 10 min. In a dynamic mechanical analysis, the viscoelastic properties are determined using the linear viscoelastic behavior. This linear behavior is realized up to a certain minimum strain depending on the nature of the material and beyond the optimum strain the behavior deviates from linearity. That is why it is necessary to use a load in such a way that the generated strain maintains the linear viscoelastic behaviour. In the present case, the tests were performed under a constant load of 0.9 MPa, which corresponds to the linear viscoelastic strain range. Test specimens of dimensions 60 × 15 × 2 mm^3 (length × width × thickness) were used for the creep tests.

The morphology of the semi-IPN samples was investigated by a Zeiss Supra 40 VP (Oberkochen, Germany) scanning electron microscope (SEM). For SEM analysis the samples were quenched in liquid nitrogen and cryogenically fractured to obtain cross sections, which were sputter coated with carbon to avoid charging prior to the SEM observation [31].

To demonstrate the shape memory property, a circular specimen was heated at 100 °C and folded to give a temporary bent shape and cooled to fix it. The diameter and thickness of the circular specimen were 7.5 cm and 3 mm, respectively. When the sample was heated it started recovering and the photographs at different time intervals were taken and presented in this paper. The shape memory properties were determined using a bend test method [33]. In this method a straight rectangular sample is bent to right angles (strain angle is 90°) at 100 °C. The temporary shape is fixed by cooling to room temperature (27 °C). The sample is then heated to a particular temperature (80, 90, 100, 110, 120 °C) and the time required for recovery is noted.

The strain recovery rate (R_r), which qualifies the ability of the material to memorize its permanent shape is determined from the following formula [3]:

$$R_r(\%) = \frac{\theta_1 - \theta_2}{\theta_1} \times 100 \quad (1)$$

The strain fixity rate (R_f), which describes the ability of the switching segment to fix the mechanical deformation is determined from the formula given below [3]:

$$R_f(\%) = \frac{\theta_3 - \theta_1}{\theta_1} \times 100 \quad (2)$$

where θ_3 is the deformed angle under loading, θ_1 is the fixed angle after load release, and θ_2 is the deformation angle after the recovery. Three specimens of each samples are tested and average values are reported. The heating, bending, cooling and recovery operations are repeated to study the effect number of cycles on the respective shape memory properties.

3. Results and discussions

PEO is miscible with MMA and TEGDM mixture at 70 °C. With the advancement of crosslinking reaction involving MMA and TEGDM, the combinatorial entropy of mixing tends to decrease. As a result the crystalline part of PEO undergoes phase separation leading to the formation of a two-phase microstructure and the amorphous part of PEO remains dissolved in the PMMA network. Thus PEO/x-PMMA semi-IPN systems consist of PEO crystals dispersed in the PMMA network. The SEM photographs of x-PMMA/PEO semi-IPNs (composition: 68/32) made using 2, 4, 5 and 6 wt% crosslinker concentrations are shown in Fig. 1. All the samples show uniformly dispersed PEO crystals in the x-linked PMMA network. The sizes of the PEO crystals are in the range of 0.1 to 0.2 μm. Similar sizes of PEO crystals were reported for PEO/phenolic blends [41,42]. However, it is clearly found that the best distribution PEO crystals are achieved at an optimum crosslinker concentration beyond which the uniformity is destroyed. We can see for the semi-IPN sample made using 6 wt% crosslinker (Fig. 1d), the fracture surface contains some area which does not seem to show the presence of PEO crystals. Initially, the PEO remains dissolved in the MMA/crosslinker mixture and with the progress of polymerization/crosslinking, the PEO crystals undergo phase separation leading to the formation of a two-phase microstructure. As mentioned above, this is attributed to the decrease in combinatorial entropy of mixing due to the polymerization/crosslinking reaction. At a very high crosslinker concentration, the crosslinking takes place very fast and the PEO crystalline phase cannot undergo phase separation uniformly. The amorphous PEO remains dissolved in the crosslinked PMMA matrix.

The PEO crystal is expected to serve the purpose of switching segment. It is well established that the concentration of switching segment plays an important role in determining the shape memory properties of SMP systems [3]. The best shape memory properties are observed at an optimum concentration of switching segment [2,10,13,16]. That is the reason why, the semi-IPNs with the varying concentrations of PEO were evaluated for their shape memory performance. Bending deformation is widely employed for evaluating shape memory properties of polymer materials because a large deflection is easily obtained in the range of small strain through bending. The shape fixity and recovery of various samples were determined at different cycles and presented in Table 1. The table compares the shape memory properties of semi-IPN samples with varying concentrations of PEO (switching component). It was observed that the semi-IPN sample having a composition (PMMA/PEO = 68/32) offers the best shape memory properties compared to the semi-IPNs having higher or lower concentration of

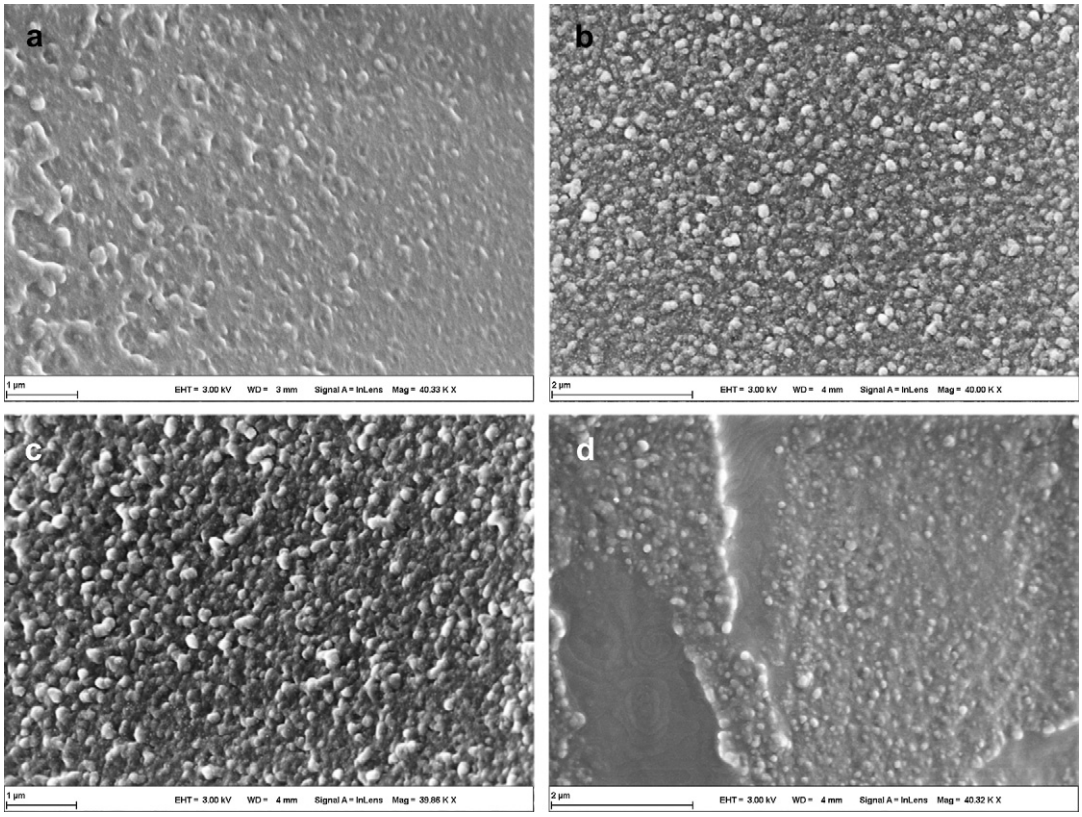

Fig. 1. a. SEM micrograph of the fracture surface of x-PMMA/PEO semi-IPN (x-PMMA/PEO = 68/32) prepared by using 2 wt.% of crosslinker. b. SEM micrograph of fracture surface of x-PMMA/PEO semi-IPN (x-PMMA/PEO = 68/32) prepared by using 4 wt.% of crosslinker. c. SEM micrograph of fracture surface of x-PMMA/PEO (x-PMMA/PEO = 68/32) semi-IPN prepared by using 5 wt.% of crosslinker. d. SEM micrograph of fracture surface of x-PMMA/PEO semi-IPN (x-PMMA/PEO = 68/32) prepared by using 6 wt.% of crosslinker.

Table 1
Shape memory properties of x-PMMA/PEO semi-IPNs measured at 100 °C.

Semi-IPN composition x-PMMA/PEO (wt/wt)	Crosslinker concentration %	Cycle number	Shape recovery (R_r) %	Shape fixity (R_f) %
78/22	2	1	80 ± 3	80 ± 4
59/41	2	1	90 ± 4	77 ± 3
68/32	2	1	98 ± 2	95 ± 2
68/32	2	2	92 ± 2	90 ± 3
68/32	2	3	90 ± 5	90 ± 4
68/32	4	1	99 ± 1	98 ± 1
68/32	4	2	92 ± 2	95 ± 3
68/32	4	3	89 ± 4	95 ± 2
68/32	5	1	83 ± 2	97 ± 2
68/32	5	2	77 ± 3	98 ± 1
68/32	5	3	75 ± 2	98 ± 2
68/32	6	1	80 ± 3	99 ± 1
68/32	6	2	75 ± 5	98 ± 2
68/32	6	3	74 ± 4	98 ± 2

PEO (e.g. x- PMMA/PEO: 59/41 and 78/32). Hence, this composition was used further for the optimization of crosslinker concentration. The increasing crosslinker concentration resulted in an improvement in the shape fixity.

At the same time, the increasing crosslinker concentration tends to decrease the deformability of the semi-IPN due to the formation of a tighter network resulting in a reduction in shape recovery performance. The optimum crosslinker concentration was found to be 4 wt%. The effect of number of cycles on the shape memory properties was also investigated. A decrease in shape recovery rate was observed with each successive cycle. However, the largest decrease occurred between cycles 1 and 2. This trend is commonly observed for SMPs and it is attributed to the fact that an extensive chain alignment in the originally cast sample takes place only during the first memory cycle [3,41].

In order to demonstrate the shape memory property, the recovery of a circular specimen was investigated. A circular specimen of semi-IPN (composition: x-PMMA/PEO = 68/32, crosslinker concentration = 4 wt%) was heated at 100 °C and given a temporary folded shape by bending and cooled to fix the shape. When the sample was heated, it started to recover the permanent shape which was photographed in different time intervals (see Fig. 2). Fig. 2 clearly demonstrates the shape memory behavior with almost a complete shape recovery.

The effects of crosslinker concentration and recovery temperature on the recovery time of the semi-IPNs are shown in Fig. 3. At a temperature below the melting point of PEO, the recovery is very

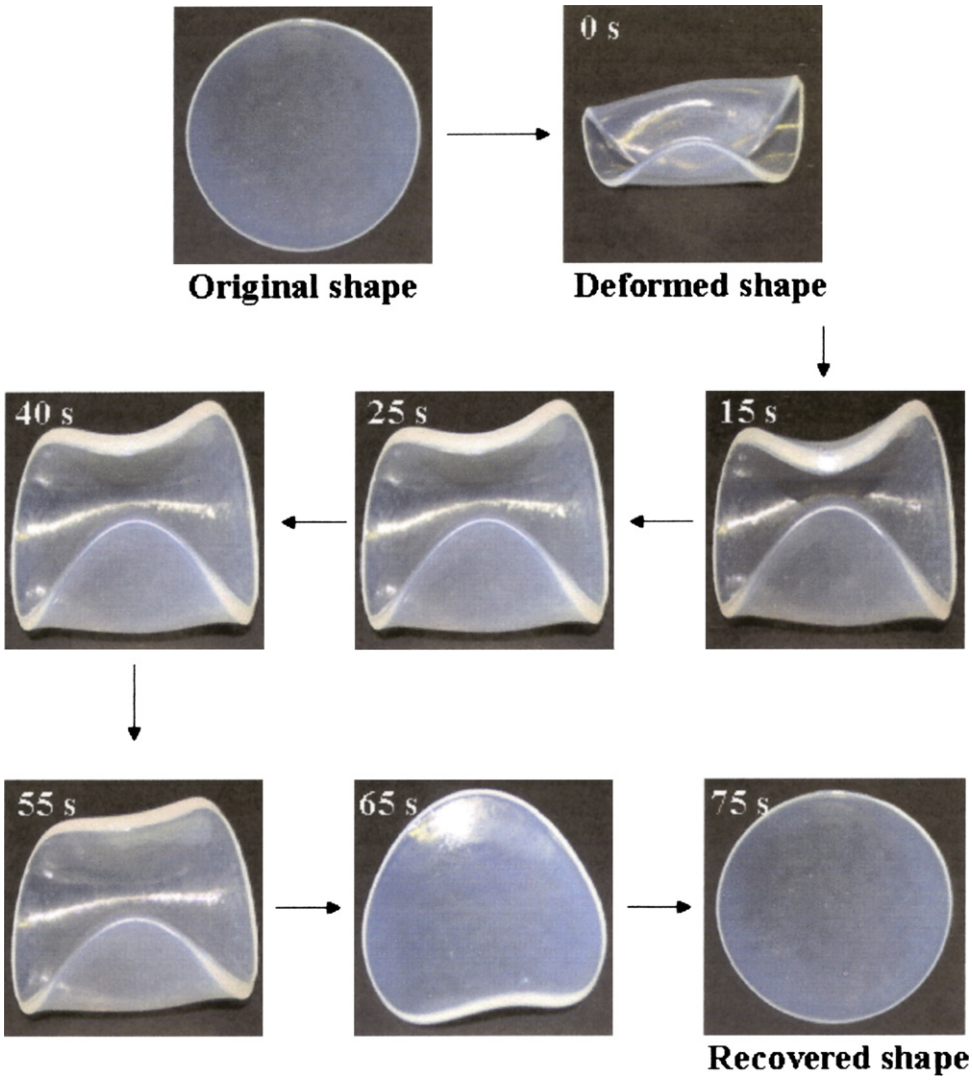

Fig. 2. Recovery of a disk shaped sample of x-PMMA/PEO semi-IPN (x-PMMA/PEO = 68/32, 4 wt% crosslinker) as a function of time at 100 °C.

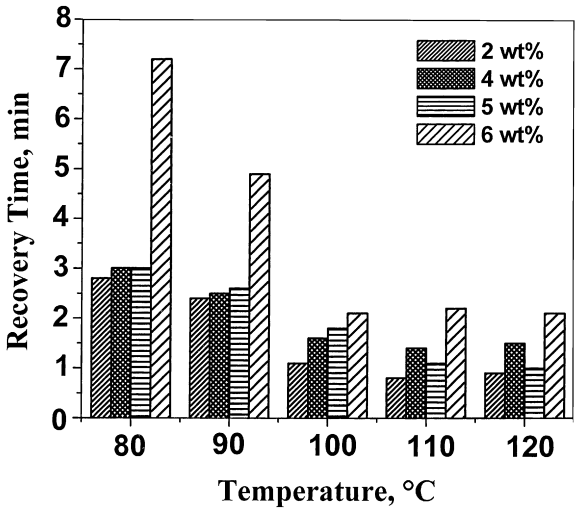

Fig. 3. Effect of crosslink density and temperature on the recovery time of x-PMMA/PEO based semi-IPN samples (x-PMMA/PEO = 68/32).

slow or not even visible. However, at a temperature higher than 70 °C, the semi-IPNs show a reasonably fast recovery. The recovery time decreases significantly up to 100 °C (Fig. 3), which is the T_g of the semi-IPN. Thus, the semi-IPNs show a shape memory function due to the melting of the switching phase (PEO) and the T_g of the x-PMMA-PEO network. It is noteworthy that the fixing mode in the semi-IPN has also a dual character: chemical (x-PMMA) and physical crosslinking (intermingling of the PEO and x-PMMA phases). The semi-IPN samples have different transition temperatures (DMA result – Fig. 7) ranging from 85 to 100 °C. The recovery behavior did not correlate exactly with the DMA results, probably due to the low thermal conductivity of the thick samples. However, it was observed that the difference between the values of recovery times at 90 °C and the same at 100 °C is the highest for a semi-IPN sample with the highest transition temperature i.e. the semi-IPN containing 6 wt% crosslinker. This supports the fact that the recovery was associated with both the melting of PEO crystals as well as the glass transition of the semi-IPN.

The recovery time is found to increase with increasing crosslinker concentration for all the recovery temperatures under investigation i.e. the networks with a lower crosslink density recovered faster. Hence to design a polymer system with a reasonably fast recovery (less recovery time), it is necessary to keep the crosslink density at a low value. However, the shape fixity tends to decrease with decreasing crosslink density, i.e. the network with a higher crosslink density shows a better fixity. This is well demonstrated by the related data in Table 1. Hence a shape memory polymer has to be designed with an optimum crosslink density considering the requirements: fast recovery and good shape fixity.

In this context it is essential to consider the creep properties of semi-IPN samples. Creep is the continuous deformation of a material at a constant load. It is desirable that the creep to be a minimum for an effective fixing of a shape memory polymer [3,41,42]. Interestingly, creep properties of shape memory polymers have not been explored extensively. We have studied the creep properties of the semi-IPNs using DMTA. The effects of composition and crosslinker concentration on their creep properties of semi-IPNs have been investigated and the results are shown in Figs. 4 and 5, respectively. It is clear that all the semi-IPNs show much higher creep compared to the x-PMMA. This is attributed to the presence of thermoplastic PEO. It is well known that a thermoplastic in general shows much higher creep compared to its thermoset counterpart due to the absence of chemical crosslinks in the former [43]. The creep did not change significantly with the compositional change in the studied range. The two semi-IPN samples made using 4 wt% crosslinker, however, having different compositions (namely x-PMMA/PEO = 68/32 and = 59/41)

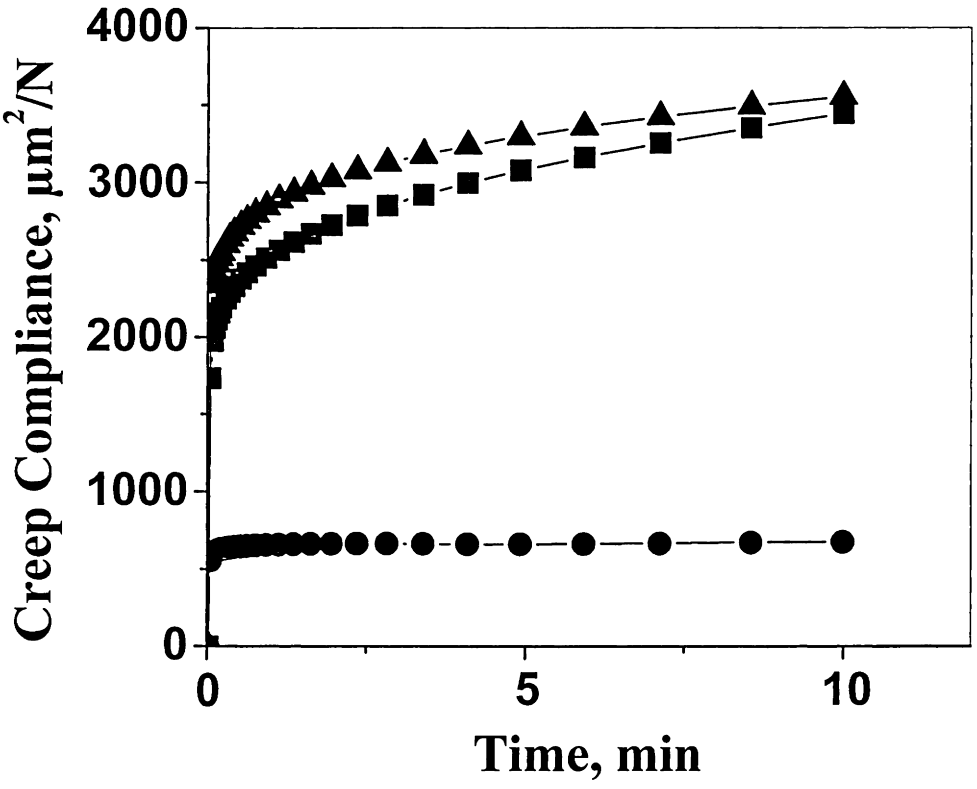

Fig. 4. Creep properties of semi-IPN samples with different compositions (x-PMMA/PEO ratio) using 4 wt.% of crosslinker : 100/0 (-●-●-) 68/32, (-◆-◆) 59/41 (-▲;-▲;-).

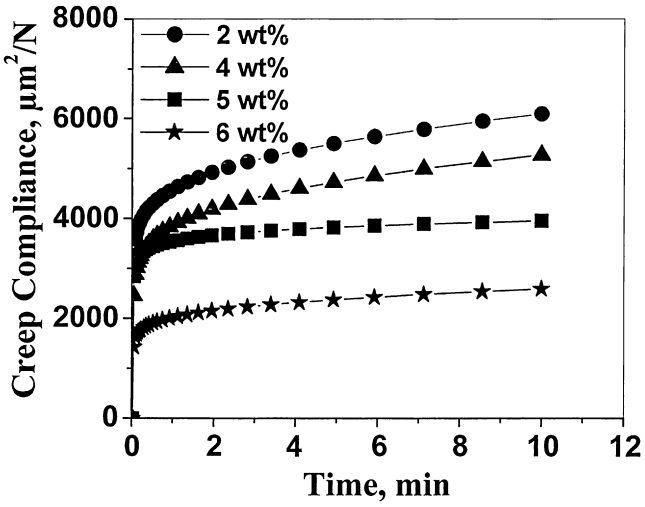

Fig. 5. Creep properties of x-PMMA/PEO semi-IPN (x-PMMA/PEO = 68/32) samples made using various concentrations of crosslinker.

display similar creep behavior. For a fixed semi-IPN composition (e.g. x-PMMA/PEO = 68/32), the creep compliance decreases with increasing crosslinker concentration for the obvious reason of the formation of a tighter network at a higher concentration of crosslinker.

However, at a very high crosslinker concentration the network loses its shape memory properties due to the lack of deformability as discussed above. For example the semi-IPN sample made using higher than 6 wt% crosslinker shows very low creep but does not show the expected shape memory properties. Thus, a semi-IPN (and probably also full IPN) should have an optimum crosslinker concentration to satisfy both the requirements of fast recovery and

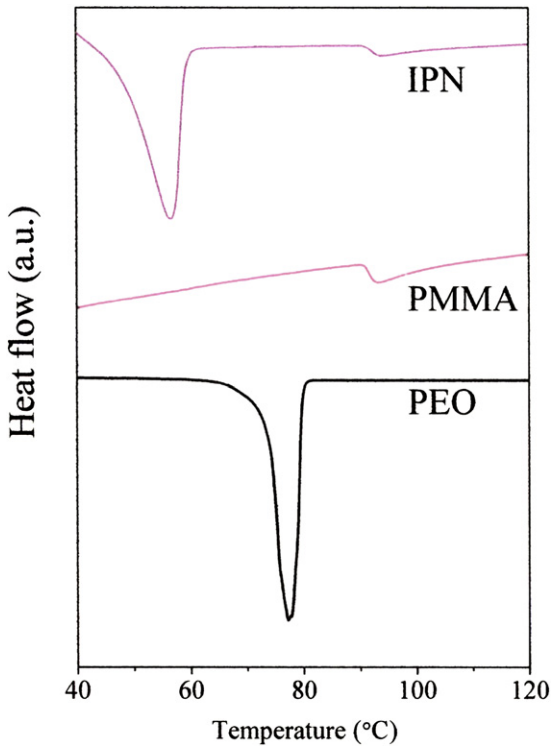

Fig. 6. DSC thermogram of PEO, PMMA and x-PMMA/PEO semi-IPN (x-PMMA/PEO = 68/32) made using 4 wt.% of crosslinker.

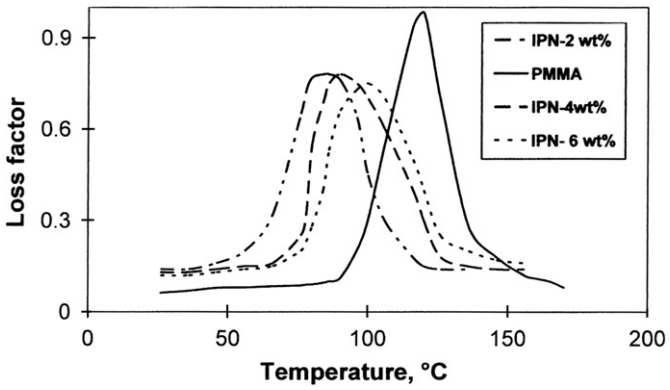

Fig. 7. Loss factor vs. temperature plots for x-PMMA/PEO semi-IPN prepared by using different concentrations of the crosslinker.

low creep (contributing to a better fixity). It may be noted that the above parameters again depend on for what application the material is going to be used. Apparently, the IPN with 4 wt% crosslinker shows optimum properties.

DSC thermograms of x-PMMA, PEO and the semi-IPN (x-PMMA/PEO = 68/32) are shown in Fig. 6. The appearance of the melting peak indicates the presence of PEO crystals in the semi-IPN system. The semi-IPN exhibits a melting peak at a lower temperature compared to the pure PEO. Melting point depression of a crystalline polymer observed in blends or interpenetrating polymer networks is the result of kinetic, morphological and thermodynamic factors [44,45]. The amorphous phase hinders the crystallization by exerting steric effect. The morphological effects are associated with the changes in crystal perfections or geometries with different thermal histories of the sample. Addition of amorphous component decreases the chemical potential and thereby reduces the T_m. The depression of melting point only due to the thermodynamic reason according to Flory-Huggins theory can be expressed as [46]:

$$\frac{1}{T_m} - \frac{1}{T_m^0} = \frac{RV_2}{\Delta H_0 V_1}\left[\frac{\ln\phi_2}{m_2} + \left(\frac{1}{m_2}\right)\phi_1 + \chi_{12}\phi_1^2\right] \quad (3)$$

The subscript 1 and 2 represent the x-PMMA and PEO, respectively, χ_{12} is the polymer–polymer interaction parameter, V is the molar volume of the polymer repeat unit at the equilibrium melting temperature, ϕ is the volume fraction, ΔH_0 is the heat of fusion of the crystalline polymer, m_2 is the degree of polymerization of PEO. Attempts have been made by various authors to determine the interaction parameter from the above equation but failed due to the

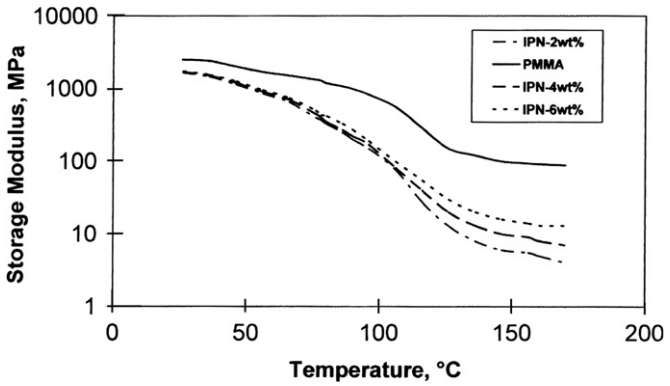

Fig. 8. Dynamic storage modulus vs. temperature plots for x-PMMA/PEO semi-IPN (x-PMMA/PEO = 68/32) made using different concentrations of crosslinker.

Table 2
DMTA properties of x-PMMA/PEO semi-IPNs.

Semi-IPN composition x-PMMA/PEO (wt/wt)	Crosslinker concentration wt %	Glassy modulus at 36 °C (E_g) GPa	Rubbery plateau modulus at 140 °C (E_r) MPa	T_g °C	Crosslink density mol m^{-3}
100/0	2	2.50 ± 0.05	91 ± 1.2	120	–
68/32	2	1.73 ± 0.03	5 ± 0.08	84	1389
68/32	4	1.70 ± 0.02	8 ± 0.10	90	2223
68/32	5	1.70 ± 0.04	11 ± 0.09	94	3056
68/32	6	1.66 ± 0.05	13 ± 0.13	100	3611

contributions of kinetic and morphological effects and composition dependence of the interaction parameter. That is why no attempt was made in this work to quantitatively determine the interaction parameter. The T_g value of the semi-IPN was also slightly reduced compared to the x-PMMA. This can be attributed to the mixing of amorphous PEO with the crosslinked PMMA.

Loss factor vs. temperature and storage modulus vs. temperature plots of x-PMMA and the semi-IPNs containing various concentrations of crosslinker are shown in Figs. 7 and 8, respectively. The broad loss peak indicates the formation of semi-IPN [25,26]. It is more interesting to see that the difference between the glassy (E_g) and rubbery moduli (E_r) is much higher in case of the semi-IPN compared to the pure x-PMMA. This is one of the criteria of SMPs as the shape memory effect is often described by the following mathematical model [47]:

$$\text{Shape fixity ratio } R_f = 1 - E_r/E_g \tag{4}$$

$$\text{Shape recovery ratio } R_r = 1 - f_{IR}/[(1 - E_r/E_g)f_\alpha] \tag{5}$$

where E_g is the glassy modulus, E_r is the rubbery modulus, f_{IR} is the viscous flow strain and f_α is the strain when $t >> t_r$. A high elasticity ratio (E_g/E_r) allows for an easy shaping at $T > T_S$ (shape memory temperature) and a great resistance to the deformation at $T < T_s$. Fig. 8 also demonstrates that the T_g and rubbery modulus (E_r) of the semi-IPN samples change significantly with increasing crosslinker concentration while the glassy modulus remains relatively constant. Similar observation was reported by Wornyo et al. [48] for a crosslinked acrylate based SMP network. The increase in the rubbery modulus is attributed to the increase in crosslink density. The rubbery modulus is often used to calculate and compare the crosslink density of similar types of networks. From the theory of rubber elasticity $E = 3RTv_e$ where R is universal gas constant, T is the temperature corresponding to the rubbery plateau modulus and v_e is the crosslink density. The apparent crosslink density calculated for the semi-IPNs made with different concentrations of the crosslinker used in this study are presented in Table 2. The crosslink density data obtained from the above equation can only be compared for similar systems, for example for semi-IPNs of same composition with different crosslink densities. The crosslink density of crosslinked PMMA cannot be compared with the semi-IPNs and hence the value of x-PMMA is not reported. It is obvious that the crosslink density of the semi-IPN samples increases with increasing crosslinker concentration.

4. Conclusion

Shape memory semi-interpenetrating polymer network (semi-IPN) systems, composed of crystalline poly (ethylene oxide) (PEO) and crosslinked poly (methyl methacrylate) (x-PMMA), have been prepared at various PMMA/PEO ratios using different amounts of crosslinker, and their shape memory properties were investigated. For the switching function the melting of the PEO and the glass transitions of the semi-IPN, whereas for the permanent shape fixing the x-PMMA and the semi-IPN structuring itself (representing a physical network structure) were made responsible. Based on the work done the following conclusions can be drawn:

- Shape memory polymers with two transition temperatures can be successfully developed by introducing a suitable crystalline component in an interpenetrating polymer network.
- Creep compliance of the semi-IPNs did not change significantly with the compositional change in the studied range. The same is significantly reduced with increasing degree of crosslinking of PMMA.
- Shape memory properties (shape recovery and shape fixity) of the semi-IPNs can be tailored upon the x-PMMA/PEO ratio and crosslinking degree of x-PMMA.

Acknowledgments

The first author (DR) is thankful to the Alexander von Humboldt (AVH) foundation for the grant of a post doctoral research fellowship at the Institute for Composite Materials (Kaiserslautern, Germany) and Defene Research & Development Organization, India for granting permission to avail the fellowship. The work was partly supported by the Hungarian Research Foundation OTKA. Authors are thankful to Dr. K. Banik for his help in carrying out the creep test.

References

[1] Huang WM, Ding Z, Wang CC, Wei J, Zhao Y, Purnawali H. Mater Today 2010;13:54.
[2] Lendlein A, Jiang H, Junger O, Langer R. Nature 2005;43:879.
[3] Ratna D, Karger-Kocsis J. J Mater Sci 2008;43:254.
[4] Buhler WJ, Gilfrich JW, Wiley RC. J Appl Phys 1963;34:1475.
[5] Wei ZG, Sandstrom R, Miyazaki S. J Mater Sci 1998;33:3743.
[6] Hornbogen E. J Mater Sci 2004;39:385.
[7] Feninat FE, Laroche G, Fiset M, Mantovani D. Adv Eng Mater 2002;4:91.
[8] Wataha JC, Hanks CT, Craig RG. J Biomed Mater Res 1991;25:1133.
[9] Humbeeck JV. Adv Eng Mater 2001;3:837.
[10] Uo M, Watari F, Yokoyama A, Matsumo H. Biomaterials 2001;22:677.
[11] Hornbogen E. Adv Eng Mater 2006;8:101.
[12] Huang WM, Lee CW, Teo HP. J Intell Mater Sys Struct 2006;17:753.
[13] Kim BS, Lee SH, Furukawa F. In: Fakirov S, editor. Handbook of condensation thermoplastic elastomers. Weinheim: Wiley-VCH; 2005. p. 521–66.
[14] Behl M, Lendlein A. Mater Today 2007;10:20.
[15] Schmidt AM. Macromol Rapid Commun 2006;27:1168.
[16] Kim BK, Lee SY, Xu M. Polymer 1996;37:5781.
[17] Lendlein A, Langer R. Science 2002;296:1673.
[18] Li Sun, Huang WM. Soft Matter 2010;6:4403.
[19] Alteheld A, Feng Y, Kelch S, Lendlein A. Angew Chem Int Ed 2005;44:1188.
[20] Feng Y, Xue Y, Guo J, Cheng Lei, Jiao Licai, Zhang Yu, et al. J Appl Polym Sci 2009;112:473.
[21] Feng Y, Behl M, Kelch S, Lendlein A. Macromol Biosci 2009;9:45.
[22] Zotzmann J, Behl M, Feng Y, Lendlein A. Adv Funct Mater 2010;20:3583.
[23] Tobushi H, Hoshimoto T, Ito N, Hayashi S, Yamada E. J Intell Mater Syst Struct 1998;9:127.
[24] Mondal S, Hu JL. J Elast Plast 2007;39:81.
[25] Kim H, Lee TJ, Huh JH, Lee DJ. J Appl Polym Sci 1999;73:345.
[26] Liu C, Qin H, Mather PT. J Mater Chem 2007;17:1543.
[27] Wang W, Ping P, Chen X, Jing X. Eur Polym J 2006;42:1240.
[28] Wang W, Ping P, Chen X, Jing X. J Appl Polym Sci 2007;104:4182.
[29] Baer G, Wilson TS, Mathews DL, Maitland DJ. J Appl Polym Sci 2007;103:3882.
[30] Hayashi S. Int. Prog. Urethanes 1993;60:90.

[31] Sperling LH, Mishra V. Polym Adv Technol 1995;7:197–208.
[32] Manoj NR, Ratna D, Dalvi V, Chandrasekhar L, Patri M, Chakraborty BC, et al. Polym Eng Sci 2002;42:1748–55.
[33] Zhang S, Feng Y, Zhang L, Sun J, Xu X, Xu Y. J Polym Sci A Polym Chem 2007;45:768.
[34] Liu G, Ding X, Cao Y, Zheng Z, Peng Y. Macromol Rapid Commun 2005;26:649.
[35] Feng Y., Zhang S., Zhang Li, Guo J., Xu Y. Polym Adv Technol, in press, doi:10.1002/Pat1780.
[36] Feng YK, Zhao HY, Guo JT. Macromol Symp (in press).
[37] Park, Lee JY, Chun BC, Chung YC, Cho JW, Cho BG. J Appl Polym Sci 2004; 94:308.
[38] Chun BC, Cha SH, Chung YC, Cho JW. J Appl Polym Sci 2002;83:27.
[39] Ratna D, Abraham T, Karger-Kocsis J. J Appl Polym Sci 2008;108(4):2156.
[40] Ratna D, Abraham T, Karger-Kocsis J. Macromol Chem Phys 2008;209:723.
[41] Lendlein A, Kelch S. Angew Chem Int Ed 2002;41:2034.
[42] Thorsten P. Polymers 2010;2:120.
[43] Ratna D. Handbook of thermoset resins. London: Smithers Rapra Technology; 2009.
[44] Cimmino S, Martuscelli E, Silvestre C, Canetti M, Delalla C, Seves A. J Polym Sci B Polym Phys 1989;27:1781.
[45] Paul DR, Burlow JW, Bernstein RE, Wahrmund DC. Polym Eng Sci 1978;18:1115.
[46] Nishi T, Wang TT. Macromolecules 1975;8:909.
[47] Abrahamson ER, Lake MS, Munshi NA, Gall K. J Intell Mater Sys Struct 2003; 14:623.
[48] Wornyo E, Gall K, Yang F, King W. Polymer 2007;48:3213.

Polymer 52 (2011) 1071–1083

Contents lists available at ScienceDirect

Polymer

journal homepage: www.elsevier.com/locate/polymer

Effect of tethering on the structure-property relationship of TPU-dual modified Laponite clay nanocomposites prepared by *ex-situ* and *in-situ* techniques

Ananta K. Mishra [a], Santanu Chattopadhyay [a,*], P.R. Rajamohanan [b], Golok B. Nando [a,**]

[a] Rubber Technology Center, Indian Institute of Technology Kharagpur, Kharagpur 721 302, India
[b] Central NMR Facility, National Chemical Laboratory, Pune 411008, India

ARTICLE INFO

Article history:
Received 7 June 2010
Received in revised form
27 September 2010
Accepted 7 October 2010
Available online 15 October 2010

Keywords:
Thermoplastic polyurethane
Nanocomposites
Dual modification

ABSTRACT

Novel Thermoplastic Polyurethane (TPU)-dual modified Laponite clay nanocomposites were prepared by *ex-situ* and *in-situ* techniques. Two types of modified clays used in this work differ from each other by the number of active functional groups (tethering). Modified nanoclays are characterized by FTIR, Solid State NMR, XRD and TGA. Structural differences in the modified clays lead to novel tubular, elliptical and spherically aggregated morphologies of clays together with the hard segments of TPU. Changes in such morphology result in the difference in segmental relaxation, mechanical and rheological properties of the nanocomposites. *In-situ* prepared nanocomposites register inferior properties as compared to their ex-situ counterparts. The percent improvement in tensile strength and elongation at break of the *ex-situ* prepared nanocomposites with the modified clay having lesser tethering are found to be 67% and 208%, respectively. Thermal stability is enhanced by 35 °C as compared to that of the neat TPU.

1. Introduction

Thermoplastic polyurethane (TPU) is a block copolymer of $(AB)_n$ type consisting of soft segments (B) and hard segments (A). The soft segment is prepared by the reaction of diisocyanate with the oligomeric polyol and the hard segment is formed by the reaction between the diisocyanate with the short chain diol or diamine. Due to the difference in polarity between the two segments and presence of higher degree of H-bonding in the hard segments, phase segregation occurs. This leads the hard domains to provide reinforcing effect to the soft segments [1–6]. When nanoclays are added into the TPU matrix, the mechanical and dynamic mechanical properties, thermal stability and barrier properties are improved significantly. Three different techniques are normally adopted to prepare TPU-clay nanocomposite (TPUCN), e.g., melt blending, *ex-situ* (solution mixing) and *in-situ* synthesis techniques. *Ex-situ* and *in-situ* preparation techniques are more favorable in the laboratory for the preparation of the nanocomposites [7,8]. In general, *in-situ* synthesis technique has been found to provide better improvement in property of the resulting nanocomposites as compared to the *ex-situ* prepared nanocomposites. This is because of the improved state of dispersion of the nanoclay that can be achieved by the former technique. At present, researchers are more focused towards using tethered clay as a pseudo chain extender [9–14]. Tethering of the clay (clay with modifiers containing active functional groups) is found to provide improved property spectrum as compared to the nontethered clay in nanocomposites prepared by both *ex-situ* and *in-situ* techniques [15].

It is observed that among the available nanoclays, modified montmorillonite (popularly known as Cloisite®) is most widely used and very well explored for the preparation of TPU-clay nanocomposite. However, literature is strikingly scanty [16–21] on TPU-Laponite clay nanocomposites, despite of several advantages associated with Laponite clay.

Laponite (synthetic hectorite nanoclay) possess well controlled dimensions, chemical purity and smaller diskette size (25–30 nm). The size scale of the individual diskettes matches well with the size of the hard domains in TPU. Laponite RD in the unmodified state remains aggregated in organic solvents like tetrahydrofuran (THF). Hence, it is mandatory to modify the surface of the clay by using either ionic [19,20,22] or covalent [23–27] modification techniques to improve its state of dispersion in polymers. Literature on the dual modification of Laponite [28–30] (combined ionic and covalent modification) is strikingly small in number. *In one of our recent communications, we have illustrated salient aspects of dual modified Laponite RD in commercial TPU matrix by solution mixing technique for the first time* [31].

This manuscript deals with the preparation of TPU-dual modified Laponite nanocomposite by both *ex-situ* and *in-situ* techniques. Ionic

* Corresponding author. Tel.: +91 3222 281758 (mob); fax: +91 3222 282292.
** Corresponding author. Tel.: +91 3222 283194 (mob); fax: +91 3222 282292.
E-mail addresses: santanuchat71@yahoo.com (S. Chattopadhyay), golokb@rtc.iitkgp.ernet.in (G.B. Nando).

0032-3861/$ – see front matter © 2010 Published by Elsevier Ltd.
doi:10.1016/j.polymer.2010.10.010

modification of Laponite RD has been carried out by using cetyltrimethyl ammonium bromide whereas, two types of alkoxy silanes (Octyl trimethoxy silane and 3-aminopropyl triethoxy silane, differing from each other by the number of active functional groups) have been used for the covalent modification of the −OH groups present on the surface of the clay. The resulting structures of the modified clays have been characterized by different spectroscopic techniques (FTIR and Solid State NMR, XRD) and thermogravimetric analysis. The developed supramolecular assemblies due to the addition of these dual modified nanoclays in TPU have been correlated with the mechanical, viscoelastic and thermal properties.

2. Experimental

2.1. Materials used

4,4′-Methylene bis(phenylisocyanate) (MDI), Polytetramethylene glycol (PTMG of $\overline{M}n = 1000$), 1,4-butanediol (BD), Dibutyltin dilaurate (DBTDL), Octyl trimethoxy silane (OS), 3-aminopropyl triethoxy silane (AP) and Cetryltrimethyl ammonium bromide (CTAB) were obtained from Sigma–Aldrich, USA. Laponite RD was purchased from Southern clay limited (Mumbai, India). Toluene and Tetrahydrofuran (THF) purchased from Merck, Germany were used as the solvents for the modification of nanoclays and for the preparation of nanocomposites, respectively. Toluene was dried over pressed sodium wire and kept for two days prior to use. THF was refluxed over pressed sodium metal and a pinch of benzophenone, until the appearance of deep blue colouration. Then the dried THF was collected by the process of distillation.

2.2. Clay modification

Laponite RD (*L*) was modified with CTAB by using the standard ion exchange process, as mentioned in one of our earlier publications[22]. The modified clay was purified by repeated washing with hot deionized water to remove the resulting sodium halide ion and the excess CTAB. It was then dried in a vacuum oven at 70 °C. The granules were grinded into powder and again dried to remove the physically adsorbed water. The equation for calculating the amount of surfactant required for the cation exchange is given below:

$$\text{Amount of Surfactant} = \frac{2.8 \times 1.2}{31 \times 100} \times W \times M \quad (1)$$

where, 2.8 is the percentage of Na_2O present in Laponite, 1.2 is the number of equivalents of surfactant taken, 31 is the equivalent weight of the replaceable sodium ion present, W is the amount of clay in grams to be modified and M is the molecular weight of the surfactant. Clay modified with 'c' is designated here onwards as '*cL*'.

2 gm of 'cL' (dried in vacuum oven at 70 °C) was dispersed in 50 ml of dry toluene in a two necked round bottomed flask (RB) under nitrogen atmosphere. Calculated amount of octyl trimethoxy silane (*OS*) was added to it and the resulting colloidal suspension was refluxed for 6 h with stirring. The solvent was dried and then the excess amount of silane (unreacted) was extracted with dry toluene by a soxhlet extractor for 12 h. The resulting modified clay was dried and ground into powder. The clay modified by this procedure is designated as '*cOSL*'. Similarly, 'cL' modified by 3-aminopropyl triethoxy silane (*AP*) is represented as, '*cAPL*'. Nomenclature for the modified clays is presented in Table 1. The extent of modification of the nanoclays are calculated from the weight loss in the temperature region from 130 to 600 °C and discussed in details in Section 4.1.4.

2.3. Preparation of TPU-clay nanocomposite by ex-situ technique

Calculated amount of PTMG (dried in a vacuum oven at 70 °C for 12 h) was weighed in a dry 3 necked round bottom flask under dry nitrogen atmosphere. 0.1% DBTDL catalyst with respect to the weight of PTMG taken, was added to it and stirred at 50 °C and 850 rpm speed by using an SCOTT magnetic stirrer (model SLR, SCHOTT Instruments GmbH, Germany). 3.5 equivalent of MDI with respect to the weight of PTMG premixed in THF was added drop wise for 1 h. After complete addition of MDI, the mixture was allowed to stir for additional 2hrs at 50 °C, to prepare the *prepolymer*.

2.35 equivalent of 1,4-butanediol was added to the prepolymer and further stirred at 50 °C and at 1000 rpm for a period of 2hrs to prepare the final TPU. The mixture was purified by precipitating in methanol followed by repeated washings. The precipitate was then dried in vacuum oven at 70 °C.

The TPU was dissolved in THF to prepare a 10% solution. It was then sonicated for 30 min and cast on a petridish. THF was evaporated at room temperature followed by vacuum drying at 70 °C and then molded into a sheet under pressure (at 170 °C and 5 MPa pressure). The samples were allowed to cool slowly under pressure by cold water circulation before further characterization. The TPU sheet so obtained is represented as "*PU*".

Calculated amount of clay was dispersed in THF and sonicated for 30 min. The colloidal dispersion of clay was added to the TPU solution (10 weight % in THF). It was stirred for 15 min followed by another round of sonication for 30 min and then cast on a petridish. THF was evaporated at room temperature followed by vacuum drying at 70 °C and then molded into sheets following the same process as described earlier. The resulting nanocomposites are represented as "*E*".

2.4. Preparation of polyurethane clay nanocomposite by in-situ technique

The prepolymer was prepared following the same procedure as described in Section 2.3. Calculated amount of clay dispersed in THF (sonicated for 30 min in a sealed container under N_2 atmosphere

Table 1
Nomenclature of modified clay along with percentage of modification and designation of TPUCN.

Designation	Details	Extent of modification (%)
cL	Laponite RD modified by cetyl trimethyl ammonium bromide	15.6
cOSL	Laponite RD modified by cetyl trimethyl ammonium bromide followed by octyl trimethoxy silane	21.9
cAPL	Laponite RD modified by cetyl trimethyl ammonium bromide followed by 3-aminopropyl triethoxy silane	29.3
PU	Neat TPU	
PUCN	Polyurethane clay nanocomposite	
E	Nanocomposites prepared by *ex-situ* technique	
I	Nanocomposites prepared by *in-situ* technique	

weight % of clay (1, 3%)

PUCN preparation technique ← Axy → types of clay (cOSL or cAPL)

Example:
PU = TPU with 0% clay; E1cOSL = TPU with 1% of cOSL prepared by *ex-situ* technique; I3cAPL = TPU with 3% of cAPL prepared by *in-situ* technique

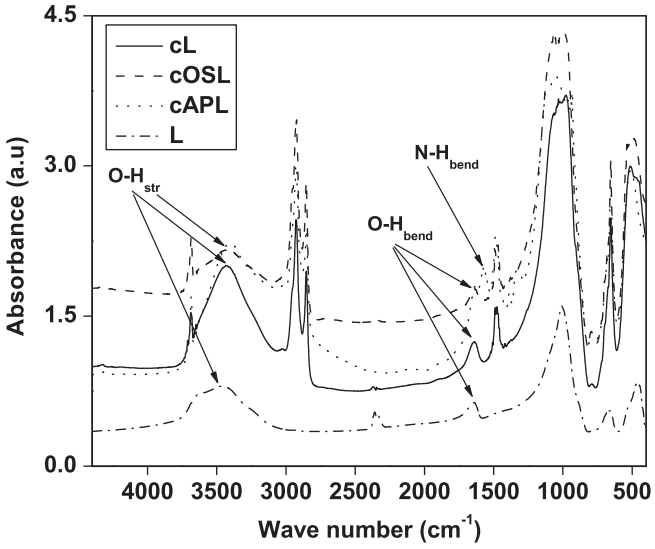

Fig. 1. FTIR spectra of the unmodified and modified clay.

prior to adding to the prepolymer solution) was added to the prepolymer at 50 °C. The mixture was stirred for 15 min and sonicated for another 30 min for homogeneous dispersion of the clay. 2.35 equivalent of 1,4-butanediol was added to the prepolymer-nanoclay composite and further stirred at 50 °C and at 1000 rpm speed for a period of 2hrs to prepare the final TPU-clay nanocomposite. The mixture was then purified by precipitating in methanol followed by repeated washing. The precipitate was then dried in a vacuum oven at 70 °C. The nanocomposite so prepared was molded into sheets under pressure at 170 °C and 5 MPa pressure followed by slow cooling. The resulting nanocomposites are represented as "*I*".

Nomenclature of the neat TPU and the resulting nanocomposites are given in Table 1.

3. Characterization

Fourier transform infrared (FTIR) spectroscopy studies were performed in a Perkin Elmer FTIR spectrophotometer at a resolution of 4 cm^{-1} in the range from 4000 to 400 cm^{-1}. The clay samples were ground with KBr salt (FTIR grade) and made in the form of a disk under pressure and used for the analysis. ^{13}C and ^{29}Si solid state Nuclear Magnetic Resonance Spectroscopy (NMR) was conducted on a Bruker instrument AV 300 spectrophotometer

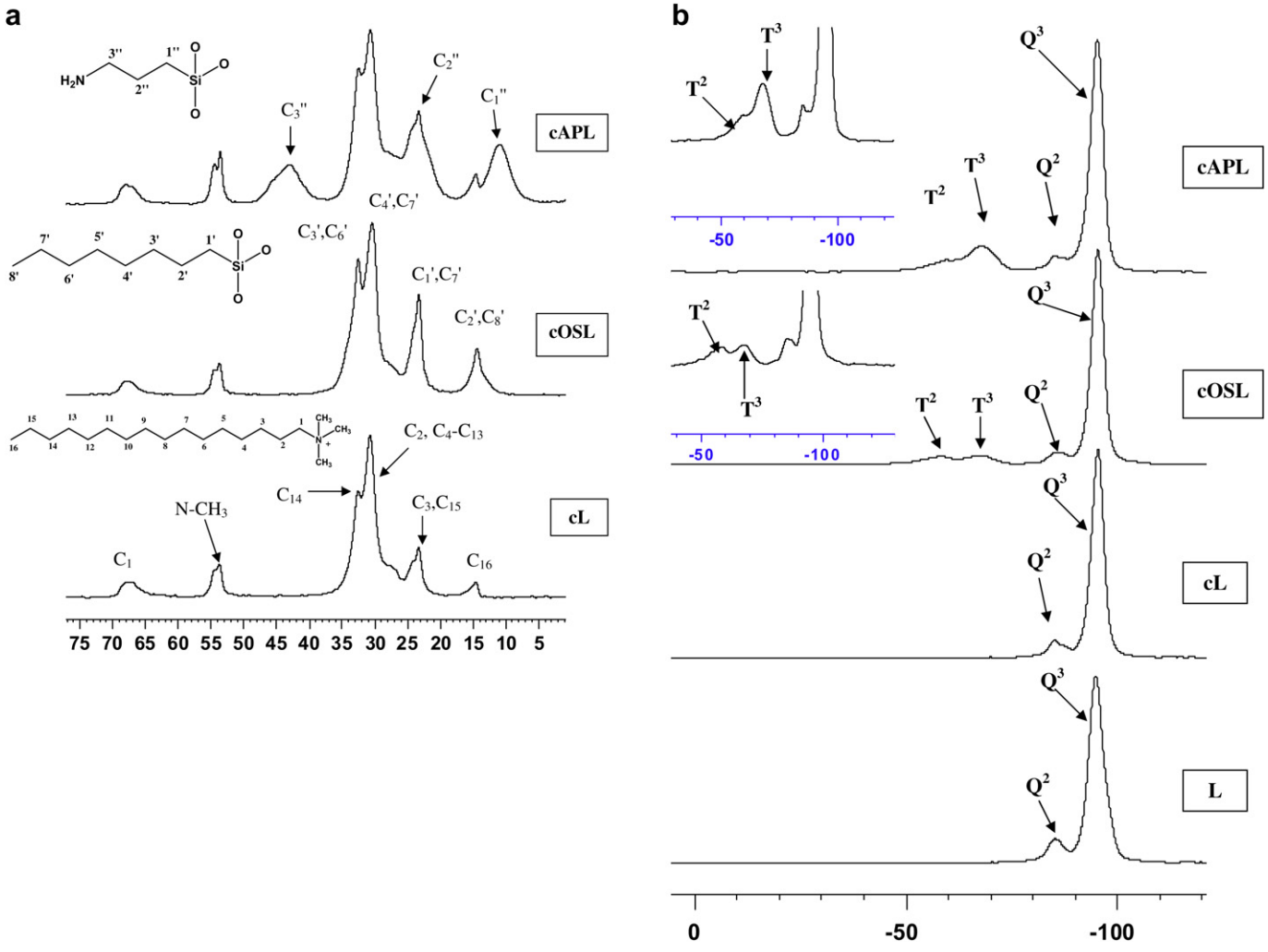

Fig. 2. a: ^{13}C NMR spectra of (i) cL (ii) cOSL and (iii)cAPL *b*: ^{29}Si NMR spectra of (i) L (ii) cL (iii) cOSL and (iv) cAPL.

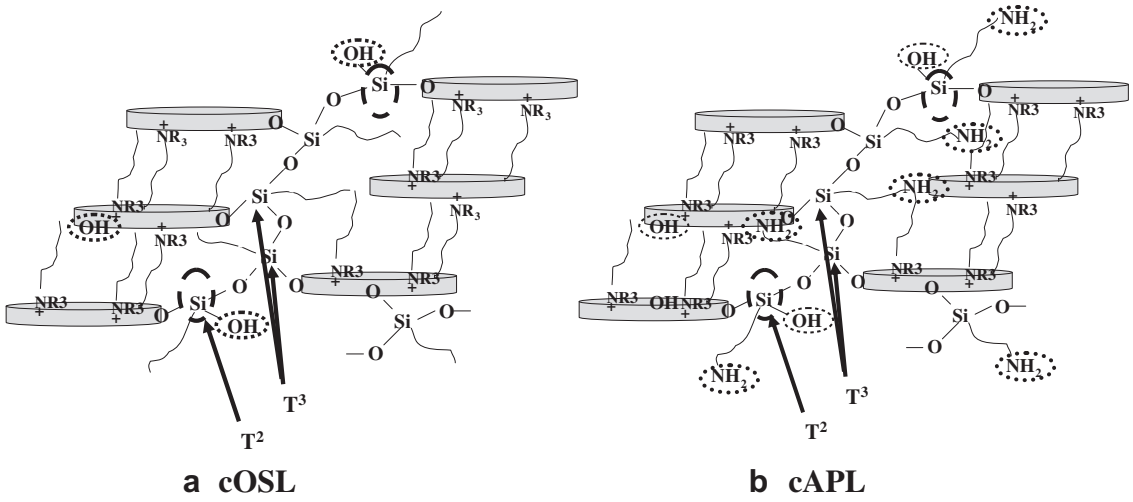

Scheme 1. Proposed structure of the dual modified clay platelets.

operating at 75.46 and 59.6 MHz, respectively using the CP/MAS technique. Wide angle XRD (WAXRD) in the lower angular range (2θ value 2 to 10°) and in the higher angular range (2θ value 10 to 50°) were performed using a Phillips Pan alytical X-ray diffractometer (model: Xpert Pro, the Netherlands) equipped with Cu target (Cu Kα) and Ni filter operating at a voltage of 40 kV and with a beam current of 30 mA.

Percentage crystallinity of the neat TPU and various nanocomposites has been calculated by using Hermans-Weidinger's method [32]. The crystallite sizes have been calculated by using Scherrer's equation corresponding to the most intense peak (peak at 19.4° 2θ) found in the X-ray diffractogram [33].

Transmission Electron Microscopy (TEM) was performed by using a high resolution TEM of JEOL JEM 2100 make, Japan, operating at a voltage of 200 kV after cutting thin sections from the samples (~50 nm section) using LEICA ULTRACUT UCT (Austria) cryomicrotome, equipped with a diamond knife. Thermal analysis was carried out using differential scanning calorimeter (model number DSC Q100 V8.1) and thermogravimetric analyzer (model number TGA Q50 V6.1) of TA instruments make, USA. DSC was performed under nitrogen atmosphere in the temperature range from 0 to 250 °C at a heating rate of 10 °C/min. TGA was performed in N_2 environment within the temperature range from ~50 to 600 °C, at a heating rate of 20 °C/min. Dynamic rheological behaviors of the samples were studied on a rubber process analyzer, RPA-2000 of Alpha Technologies, USA. Frequency sweep was carried out at 140 °C using 1% dynamic strain in the frequency range from 0.033 to 32 Hz. Temperature sweep experiment (dynamic) from high to low temperature was carried out within a temperature range of 180 to 40 °C at a constant frequency of 1 Hz and 1% strain by using RPA.

4. Results and discussion

4.1. Characterization of the modified nanoclay

4.1.1. Fourier transform infrared spectroscopy (FTIR)

Fig. 1 shows the FTIR spectra of unmodified and modified nanoclays. The presence of additional peaks corresponding to 2928 (C-$H_{assym\ str}$), 2852 (C-$H_{sym\ str}$), 1469 (C-H_{bend}) and 980 cm^{-1} (C-N_{bend}) in case of 'cL' as compared to that in the unmodified Laponite RD shows that the surface of Laponite RD is modified with cetyltrimethyl ammonium bromide by cation exchange process. Similarly, presence of the peaks at 3685 (N-H_{str}), 1042 (Si-O-Si_{str}), 796 (Si-C_{str}), 652 (Si-O_{bend}) and 518 cm^{-1} (Si-O-Si_{bend}) in case of 'cOSL' and 'cAPL', respectively, confirms the successful dual modification

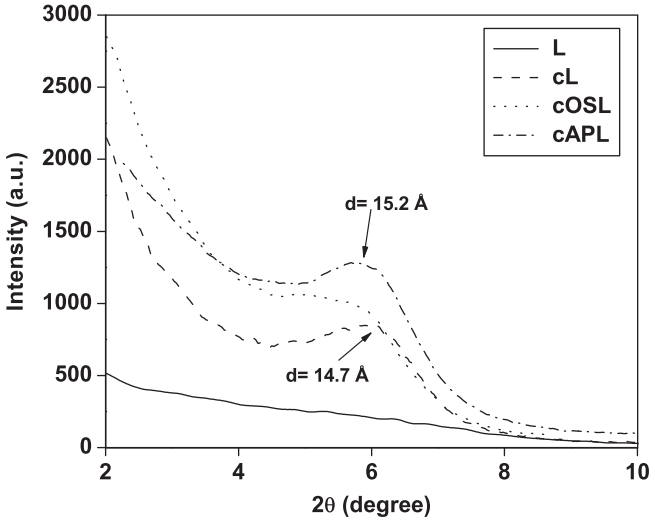

Fig. 3. WAXRD of unmodified and modified nanoclay at lower angular range.

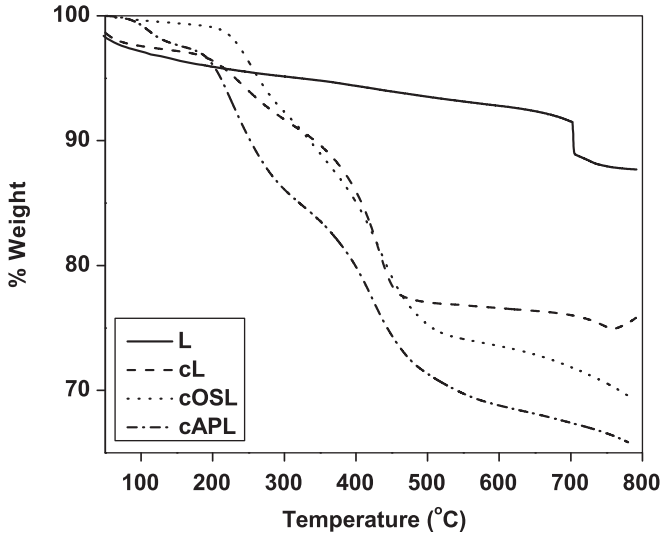

Fig. 4. TGA thermogram of the unmodified and modified Laponite clays.

of Laponite RD (with CTAB and silanes). Peaks corresponding to 3429 and 1636 cm^{-1} due to O-H_{str} and O-H_{def} confirm the presence of –OH group. 'cAPL' registers a new peak at 1568 cm^{-1} as compared to 'cL' and 'cOSL' due to N-H_{bend} [22,34].

4.1.2. Solid state nuclear magnetic resonance (NMR) spectroscopy

Fig. 2a and b display the ^{13}C and ^{29}Si NMR spectra of modified clays, respectively. ^{13}C NMR spectrum of unmodified Laponite confirms the absence of any carboneous species (not shown). ^{13}C NMR spectrum of 'cL' shows peaks at 14.6 ppm (C_{16}), 23.3 ppm (C_3 and C_{15}), 30.7 ppm (C_2 and C_4-C_{13}), 32.6 ppm (C_{14}), 53.8 ppm (N-CH_3) and 67.2 ppm (C_1) [35]. In case of the dual modified Laponites, several other peaks appear along with the signatures of 'cL' due to the additional covalent modification of 'cL' with 'OS' and 'AP', respectively, for 'cOSL' and 'cAPL'. In 'cOSL', NMR peaks for 'OS' are present at 14.2 ppm (C_8' and C_1'), 23.2 ppm (C_2' and C_7'), 29.9 ppm (C_4' and C_5') and 32.5 ppm (C_3' and C_6') [36] are embedded within the corresponding peaks present in 'cL'. This is reflected from the increase in the relative peak height of 'cOSL' in these regions as compared to that of 'cL'. Similarly, for 'cAPL', new peaks appear at 10.9 ppm (C_1'') and 43.0 ppm (C_3'') [37]. But the peak for C_2'' at 23.3 ppm, is not clearly discernable and it remains overlapped with the peak observed for 'cL'. The absence of –OMe (present in 'OS') peak at 50.0 ppm indicates the complete condensation of Si–OMe groups of 'OS' during silane modification [30]. Similarly, absence of –OEt (present in 'AP') peaks at 58.4 ppm and 18.4 ppm confirm the complete reaction of Si–OEt groups of 'AP' [38].

^{29}Si NMR spectrum of unmodified Laponite shows two peaks at –94.7 and –85.1 ppm due to Q^3 [$Si^*(OMg)(Osi)_3$] and Q^2 [$Si^*(OMg)(OSi)_2(OH)$] structures, respectively [30]. Both the peaks are retained in the same position with similar intensities in case of 'cL'. However, reduction in the relative intensity of the peak at –85.2 ppm and development of new peaks at –67.0 and –58.4 ppm due to T^3 [$Si^*(OSi)_3R$] and T^2 [$Si^*(OSi)_2(OR')R$] structures confirm the reaction of 'OS' with the Si-OH present only on the edge of the clay to produce 'cOSL' [27]. Similarly, in case of 'cAPL' two new peaks at –67.9 and –59.5 ppm due to T^3 and T^2 structures confirm the reaction of 'AP' with 'cL'. The absence of T^1 [$Si^*(OSi)(OR')_2R$] and appearance of T^2 and T^3 structure confirms the *oligomerization* of the respective silanes ('OS' and 'AP' in case of 'cOSL' and 'cAPL', respectively). Appearance of T^2 [$Si^*(OSi)_2(OR')R$] structure indicates the presence of either –OR (R = Me in OS and Et in AP) or –OH group on the surface of clay, after dual modification. However, absence of any peak corresponding to 50 ppm and 51 ppm in ^{13}C NMR spectrum of 'cOSL' and 'cAPL', respectively confirms the *presence of –OH group* on 'cOSL' as well as in 'cAPL'. Presence of –OH group is also indicated from the FTIR spectrum earlier. Based on these observations a scheme has been proposed to elucidate approximate structures of the dual modified clays (Scheme 1). The absence of T^0 [$Si^*(OR')_3R$] structure confirms the nonexistence of unreacted silanes.

4.1.3. Wide angle X-ray diffraction study

Fig. 3 shows the WAXRD at lower angular range (2–10° 2θ) of the unmodified and modified clays.

No distinct peak for unmodified Laponite RD is observed from the WAXRD pattern due to the disordered nature of clay diskettes [11,28]. However, the sharpness of the diffraction pattern increases upon modification and new peaks appear depending on the type of modifier. A peak centered at 6.0° 2θ (d value of 14.7 Å) is observed in case of 'cL'. Upon modification of 'cL' with octyl trimethoxy silane and aminopropyl triethoxy silane, the peak shifts towards a lower angle with a mean value of around 5.8° 2θ (d value of 15.2 Å) for both 'cOSL' and 'cAPL'. This further supports the fact that the Laponite is successfully modified by dual modification technique.

4.1.4. Thermogravimetric analysis

Fig. 4 represents the TGA thermogram of the unmodified and modified clays. Weight loss due to different types of associated water in clay has been reported by Burgentzlé et al. [39]. Weight loss from 130 to 600 °C corresponds mainly to the degradation of the alkyl groups (Fig. 4). The weight loss at higher temperature (600–700 °C) is probably due to the dehydroxylation of the magnesiosilicate (similar to that of aluminosilicate in case of MMT) [39]. It is observed that in the temperature range from 130 to 600 °C, unmodified Laponite RD suffers 4% loss in weight. Hence, the extent of grafting of the modifier can be calculated by deducting 4% weight loss from the corresponding weight loss of the modified clays. Thus the extent of modification is found to be 15.6, 22.0 and 29.3 weight % for 'cL', 'cOSL' and 'cAPL', respectively (Table 1). This further supports the success of dual modification of the clay surface.

4.2. Characterization of the nanocomposites

4.2.1. Wide angle X-ray diffraction study

4.2.1.1. WAXRD at lower angular range. Fig. 5a and b show the diffractograms of the TPUCN prepared by *ex-situ* and *in-situ* techniques, respectively. It is observed that neat TPU registers a peak at around 9–10° 2θ in the diffractogram (Fig. 5a and b)

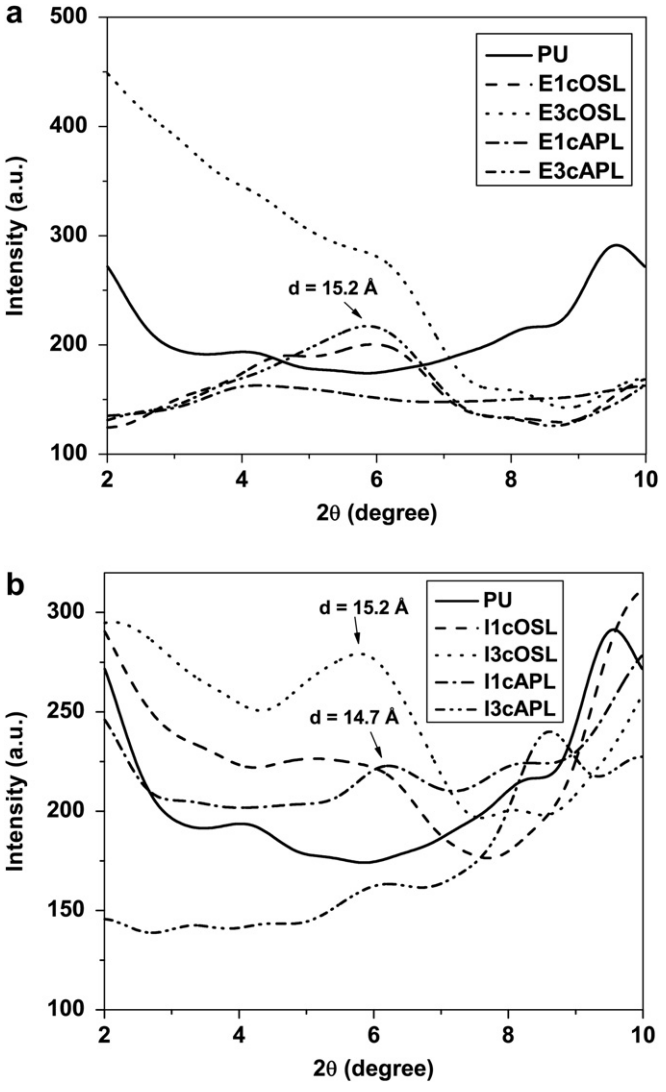

Fig. 5. a: WAXRD of PUCN prepared by *ex-situ* technique at lower angular range *b*: WAXRD of PUCN prepared by *in-situ* technique at lower angular range.

possibly due to an ordered hard domain. This peak almost diminishes upon incorporation of nanoclays. However, in I3cAPL an exception is noticed where, the signature remains rather at a lower angle.

In case of *ex-situ* prepared nanocomposites, addition of cOSL does not increase the d-spacing of the clay gallery and it remains at 5.8° 2θ (d value of 15.2 Å). But an increase in clay content increases the broadness of the peak. This reflects the presence of a broad distribution of the clay aggregates for cOSL based nanocomposites. However, E1cAPL does not exhibit any peak corresponding to the d-spacing in the clay gallery, whereas, E3cAPL shows a peak centered at 5.8° 2θ (d value of 15.2 Å) as a mark of the increased aggregation, which is not so apparent at lower clay content.

Similarly, in case of *in-situ* prepared nanocomposites, I1cOSL gives rise to a peak at 5.8° 2θ (d value of 15.2 Å). Although the peak position remains the same, but the intensity of the peak increases with I3cOSL. However, I1cAPL and I3cAPL show peak at 6.0° 2θ (d value of 14.7 Å) having similar peak intensities indicating the clay platelets to stay closer as compared to the parent modified clay, cAPL.

From these observations, it is apparent that the diskette spacing of the modified clay remains in the similar range except in case of cAPL based nanocomposites prepared by *in-situ* technique (where the clay diskettes approach closer). This can be ascribed to the formation of siloxane oligomers during covalent modification, which are attached to two closely spaced diskettes and do not allow the clay platelets to expand further. However, the interplatelet distance is slightly reduced in case of I1cAPL and I3cAPL. This is possibly due to the presence of greater number of active functional groups (like −OH and $-NH_2$ groups) in cAPL. This provides greater number of sites on the clay surface for the reaction with the −NCO group of the prepolymer (Scheme 2). Possibly this leads to an increased H-bonding within the vicinity of the clay platelets. The schemes depicting the intermolecular H-bonding in the polyurethane system is shown by Dai et al. [40].

4.2.1.2. WAXRD at higher angular range. WAXRD in the higher angular range (10–50° 2θ) for the *ex-situ* and *in-situ* prepared nanocomposites and the neat TPU are presented in Fig. 6a and 6b, respectively. It is observed that the neat TPU shows two broad

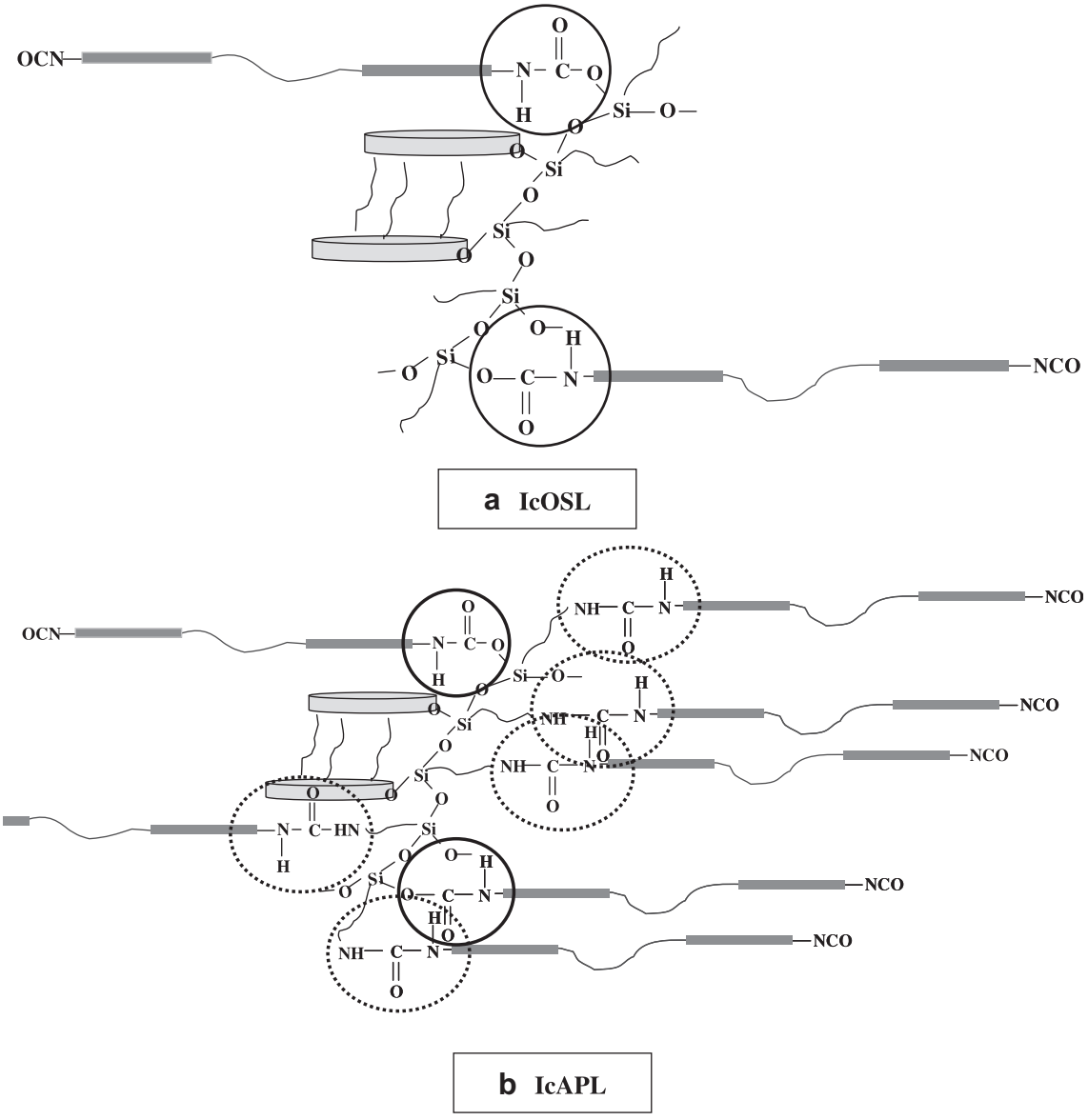

Scheme 2. Schematic representation of (a) IcOSL and (b) IcAPL. *Solid (○) and dotted (⁘) circles represent the urethane and urea linkages, respectively.

hallows starting from 12.6 to 33.2° 2θ and 34.5 to 50° 2θ, respectively. The broad hallows in the range from 12.6 to 33.2° 2θ contains a sharp peak at 19.4° 2θ along with two shoulders. The presence of sharp (semicrystalline) peaks in the neat TPU is due to the self organization of the hard domains present in TPU. The self organizations of the hard domains occur due to annealing and slow cooling process during molding. The sharp peak and shoulders remain in all the nanocomposites prepared by *ex-situ* technique with reduced intensity. Interestingly, these features completely disappear in case of the nanocomposite prepared by *in-situ* technique. Reduction in the peak intensities can be ascribed to the interference of the clay platelets with the ordering of the hard domain [19] (Scheme 3). However, absence of these features in case of *in-situ* prepared nanocomposites can be explained on the basis of reaction between the isocyanates (−NCO group) of the prepolymer with the −XH group (−X = −O in case of cOSL and −O and −NH in case of 'cAPL') of the modified clays. The extent of reaction is expected to be higher in case of 'cAPL' as compared to 'cOSL' (Scheme 2) due to the presence of greater number of active functional groups in cAPL (additional $-NH_2$ groups in each silane units for cAPL).

Relative crystallinity and crystallite size have been calculated from the WAXRD studies and are presented in Table 2. It is observed that the relative crystallinity of all the nanocomposites is lower than that of the neat TPU, but the crystallite size of the nanocomposites stands higher than that of the neat TPU. Relative crystallinity follows an increasing trend with the increase in amount of clay (in both 'cOSL' and 'cAPL'). Similar trend is observed in crystallite size with the addition of cOSL but interestingly, it follows a reverse trend upon

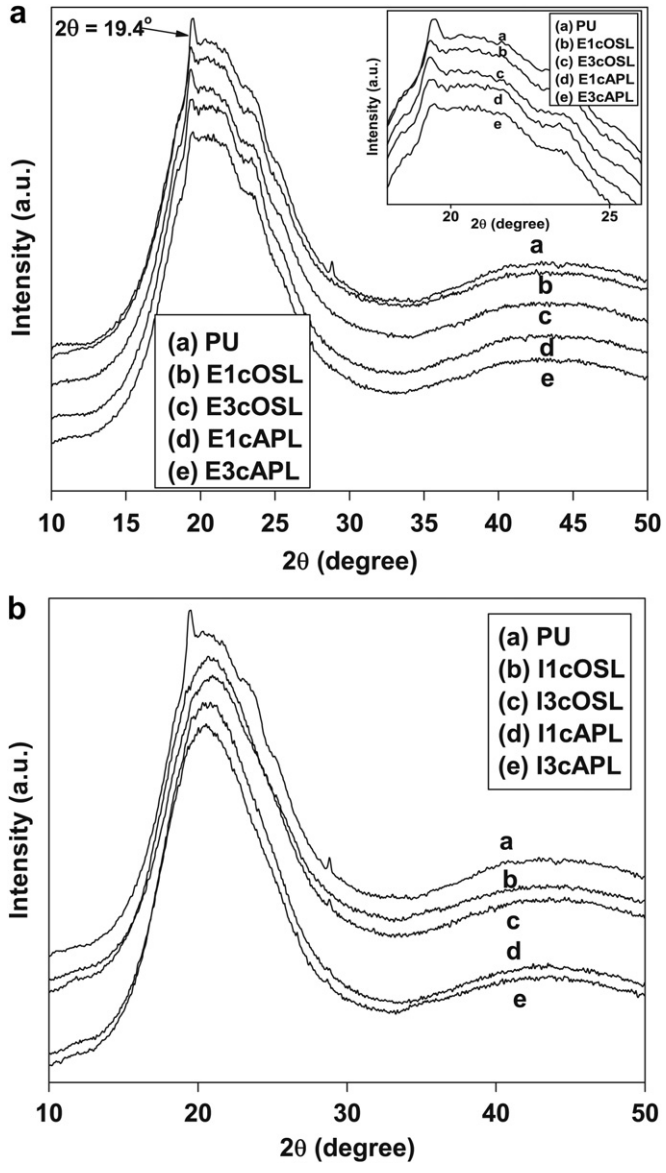

Fig. 6. a: WAXRD of PUCN prepared by *ex-situ* technique at higher angular range *b*: WAXRD of PUCN prepared by *in-situ* technique at higher angular range.

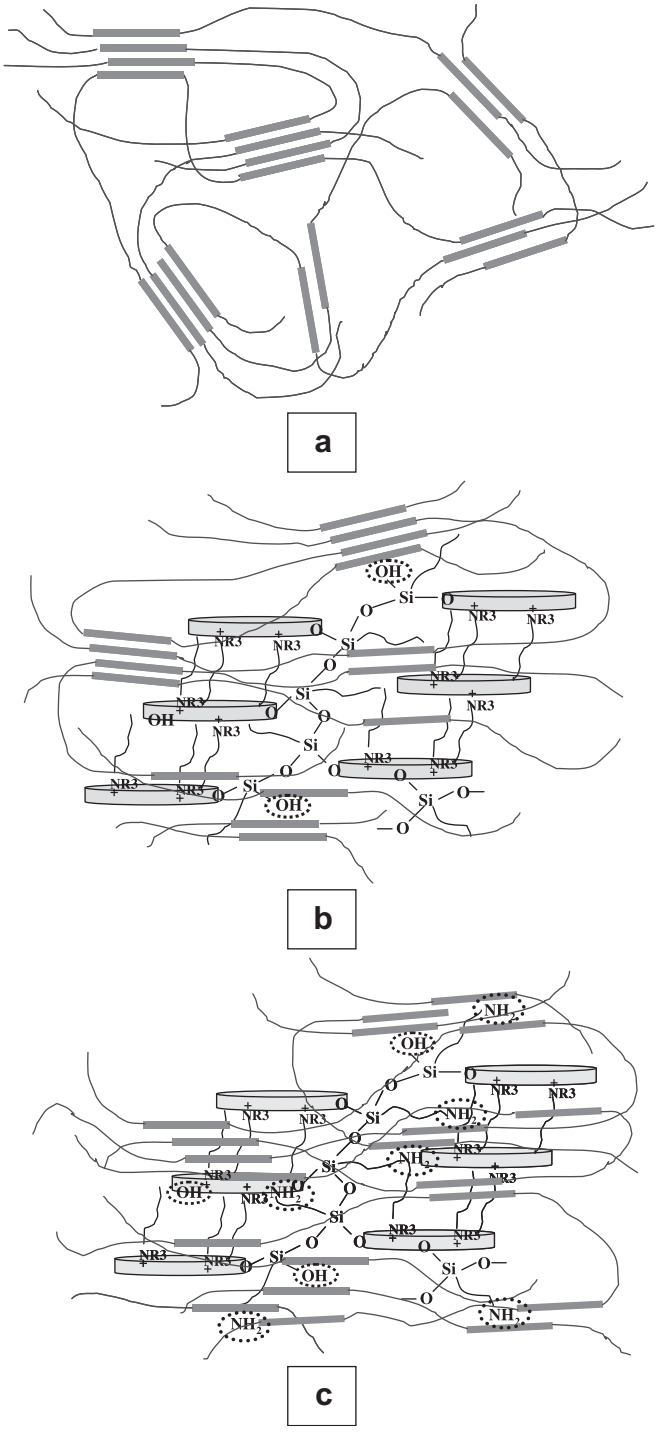

Scheme 3. Schematic representation of (a) PU (b) EcOSL and (c) EcAPL. *Encircled regions represent the presence of active functional groups in the modified clay.

Table 2
Percentage crystallinity and Crystallite size of the TPU and *ex-situ* prepared TPUCN.

Sample ID	Crystallinity* (%)	Crystallite Size (Å)
PU	33.9	19.8
E1cOSL	18.1	24.6
E3cOSL	18.9	25.5
E1cAPL	18.2	24.4
E3cAPL	22.0	21.6

* Crystallinity values calculated represent the relative values with respect to the neat TPU rather than the exact values for the peak at 19.4° 2θ.

addition of cAPL. The decreased relative crystallinity with the addition of clay is due to interference of clay in the hard domain ordering (Scheme 3). The increased crystallite size infers that the modified clays possess the capability to change the mode of organization of the hard domains due to the availability of the H-bonding sites (active functional groups) on its surface.

4.2.2. Differential scanning calorimetry (DSC)

DSC thermograms of the *ex-situ* and *in-situ* prepared nanocomposites are shown in Fig. 7a and b, respectively. Neat TPU shows two endotherms corresponding to the destruction of the short range (T_{m1}) and long range (T_{m2}) ordered hard domains (or

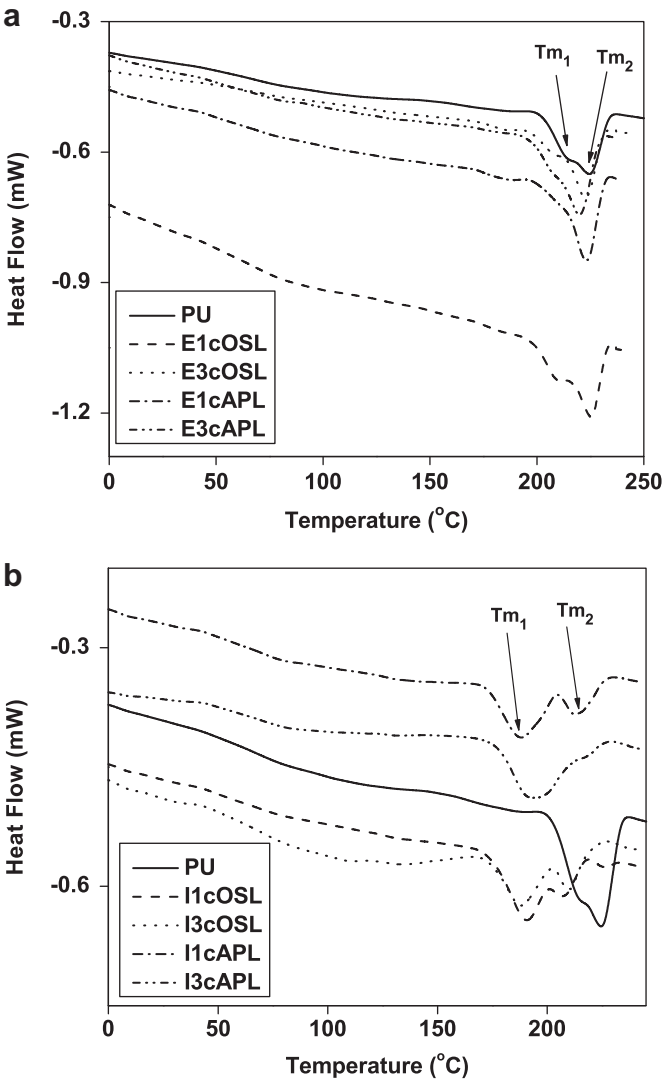

Fig. 7. a: DSC thermogram of the *ex-situ* prepared nanocomposites *b*: DSC thermogram of the *in-situ* prepared nanocomposites.

Table 3
Temperature corresponding to the melting of the hard domains of TPU and TPUCN as obtained from DSC thermograms (error = ±0.5%).

Sample ID	T_{m1} (°C)	T_{m2} (°C)
PU	214.2	224.7
E1cOSL	209.7	225.3
E3cOSL	208.4	222.7
E1cAPL	broad	223.4
E3cAPL	206.5	219.8
I1cOSL	190.4	206.8
I3cOSL	187.9	209.2
I1cAPL	188.2	213.3
I3cAPL	194.2	217.7

semicrystalline melting) resulting from enthalpy relaxation [20,41–44]. In case of neat TPU and nanocomposites prepared by *ex-situ* method, the relaxations due to short range ordering are very less prominent as compared to that of the long range ordering (Fig. 7a). Both the endothermic peaks T_{m1} and T_{m2} decrease with the addition of clay (Table 3). Increase in the amount of clay further decreases the corresponding values. This is possibly due to the interference of the clay platelets in the molecular arrangement of the hard domains (as reflected from WAXRD Section 4.2.1.2). Presence of more number of active functional groups on the surface of cAPL leads to further decrement in T_m values of the resulting nanocomposites as compared to their cOSL counterparts at a fixed clay content. This is possibly due to the change in molecular arrangement (Scheme 3).

However, a different kind of relaxation behavior is encountered with *in-situ* prepared nanocomposites. This is because of the difference in molecular arrangement and hard domain ordering in case of *in-situ* prepared nanocomposites (Scheme 2). Pattnaik and Jana [12] have already reported that a complete disappearance of the hard domain melting peak occurs, when tethered clay is used as a pseudo chain extender. Both the melting endotherms (T_{m1} and T_{m2}) are drastically reduced in case of *in-situ* prepared nanocomposites as compared to the neat TPU and their *ex-situ* based counterparts. T_{m2} of the *in-situ* prepared nanocomposites are very close to that of the T_{m1} of the *ex-situ* prepared nanocomposites. This is possibly due to the increased fraction of short range ordered hard domain in case of the *in-situ* based nanocomposites. However, the formation of new endotherm (T_{m1}) in case of *in-situ* based nanocomposite is possibly due to the presence of different type of molecular arrangement (as already mentioned).

4.2.3. Transmission electron microscopy

Fig. 8 shows the representative TEM photomicrographs of the neat TPU and TPUCN containing 3% clay prepared by *ex-situ* and *in-situ* technique. The grey regions indicate the hard domains, lighter regions indicate the soft domains and the dark regions reveal the clay platelets distributed in the hard domains. Fig. 8a shows the morphology of the phase separated self organized hard domains. In all the nanocomposites clay platelets are found not to be distributed in the soft domain regions. This is in agreement with our deductions presented earlier (Section 4.2.1.2).

The self organized hard domains in neat TPU forms a spherical pattern (Fig. 8a). Size of the individual spherical hard domains varies from 35 to 100 nm. Several such spherical hard domains join together, forming arrays of hard domains (with an average length of 200 nm and l/d ratio of 5). In case of E3cOSL, clay platelets along with the hard segment form a tubular type of morphology (with an average length of the aligned clay to be 780 nm and l/d ratio of nearly 6.4, Fig. 8b). Similarly, in case of E3cAPL elliptical type of morphology (with an average length of 400 nm with l/d ratio of 2.4, Fig. 8c) is formed. The tubular type of morphology can be ascribed

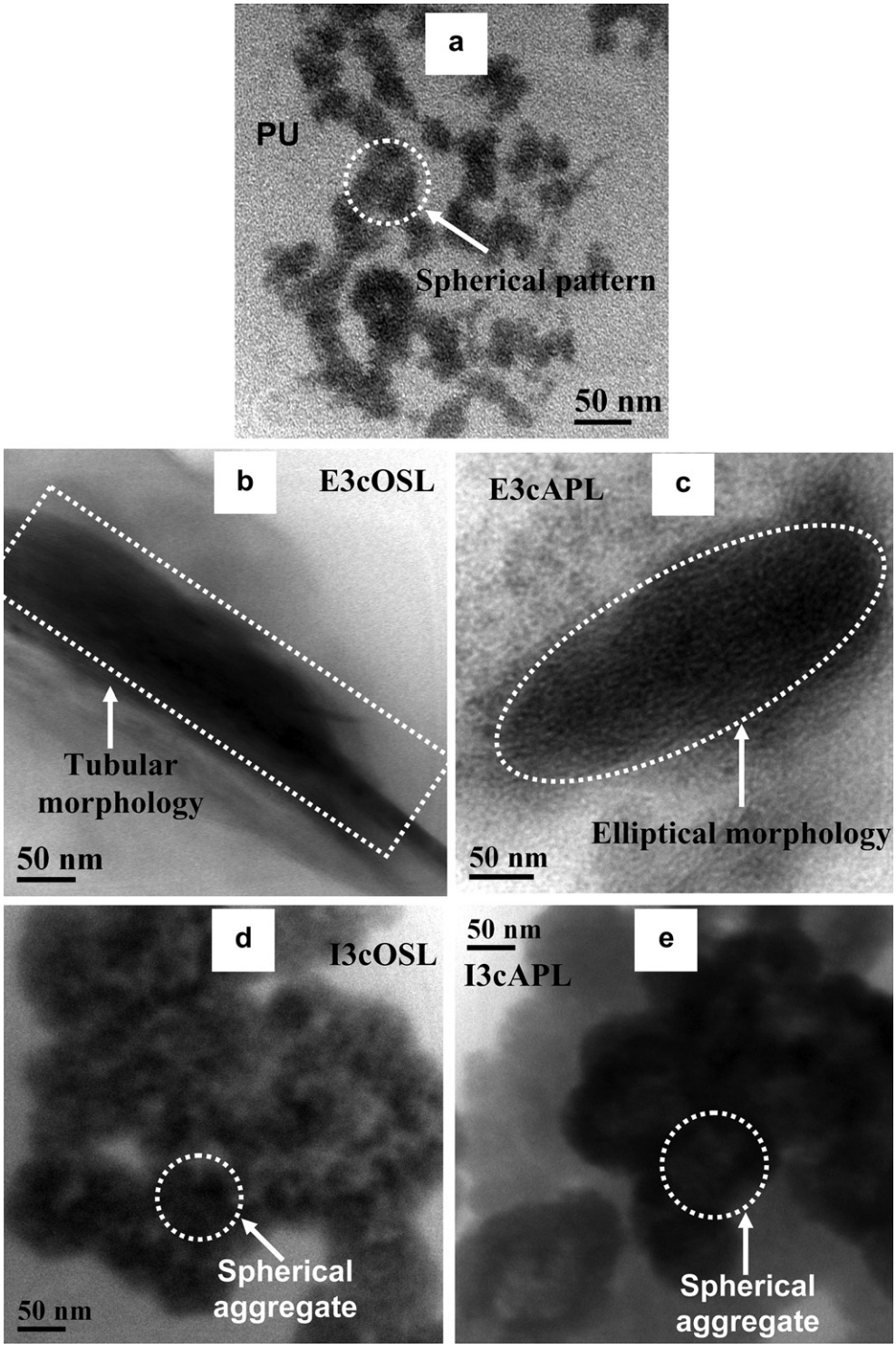

Fig. 8. TEM photomicrographs of neat TPU, *ex-situ* and *in-situ* prepared PUCN.

to the formation of arrays of H-bonding between the hard domain of TPU and the −OH groups of the siloxane oligomers (attached to the clay platelets) along with the hindrance offered by the cetyltrimethyl ammonium ions against the clay platelets to come closer. Presence of −OH group on the siloxane oligomers has been confirmed from FTIR and solid state NMR study earlier.

In case of *in-situ* prepared nanocomposites, (I3cOSL and I3cAPL) spherically aggregated morphology is obtained in both the cases (Fig. 8d and e). The size of the individual aggregate vary from 100 to 150 nm in case of I3cOSL, whereas, it is of the order of 100–320 nm in case of I3cAPL. However, several such small spherical units form long arrays of micro-aggregates with approximately 600 nm length (with average l/d ratio 4) in case of cOSL. For cAPL the average size of micro-aggregates is 800 nm (with average l/d ratio 4). Reaction between the −NCO group of prepolymer with the −XH group of the modified clay (X = −O for cOSL and −O and −NH for cAPL) leads to a different type of molecular arrangement of the hard domain leading to the spherical structures. The spherical aggregates are

relatively darker in case of I3cAPL as compared to that of I3cOSL. This may be due to the formation of a tight aggregate with I3cAPL due to the presence of more number of active functional groups.

Based on the spectroscopic analysis and the results obtained from WAXRD and TEM studies, a scheme has been proposed depicting the mechanisms of the formation of various types of morphologies (Scheme 4). The spherical pattern in case of neat TPU is due to the presence of H-bonding between the −C = O and −N-H groups (from the urethane linkage) present in the hard domain of TPU (Scheme 4a). Formation of the tubular morphology in case of E3cOSL can be explained on the basis of formation of an array of H-bonding between the urethane linkage of the hard domain and the −OH groups present on the modifier of the clay (Scheme 4b). However, the increased number of active functional groups (tethering) on the surface of cAPL possibly leads to elliptical type of morphology (to minimize the surface energy, Scheme 4c). The reaction between the −NCO group of the prepolymer with the surface −OH groups in case of I3cOSL and −OH and $-NH_2$ groups in case of I3cAPL escorts to a different type of molecular arrangement leading to the formation of spherically aggregated morphology (Scheme 4d and e).

Formation of these novel morphologies of the nanocomposites infers that the microphase separated morphology of the hard domain can be changed by changing the modifiers present in the dual modified Laponite.

4.2.4. Effect of frequency on complex viscosity at 140 °C

Fig. 9a and b display the complex viscosity (η^*) vs frequency plot of the nanocomposites at 140 °C, prepared by *ex-situ* and *in-situ* techniques, respectively. The corresponding values at selected frequencies are presented in Table 4.

Ex-situ prepared cOSL based nanocomposites show higher η^* values than their respective cAPL based counterparts, at a constant clay content. This can be ascribed to the tubular morphology of the nanocomposites with higher aspect ratio for cOSL as compared to that of the elliptical morphology present in cAPL. Increase in the clay content leads to an obvious increase in the η^* value in both the cases due to the increased reinforcement and hydrodynamic effects.

Similarly, *in-situ* prepared nanocomposites with cOSL possess higher η^* values as compared to cAPL based nanocomposites, at a constant clay content. However, an increase in the clay content leads to a decrease in η^* value in both varieties of clay (i.e., cOSL and

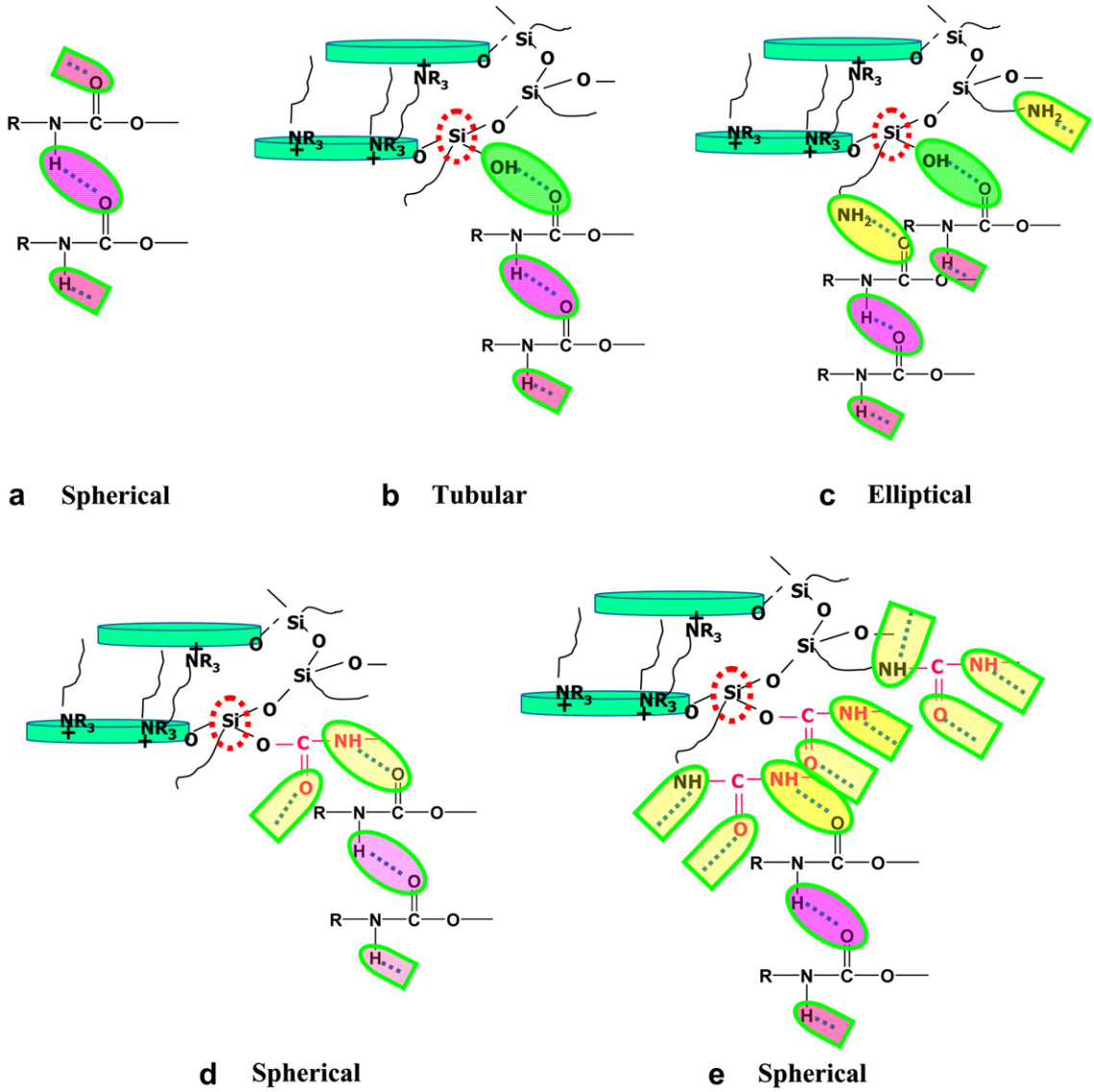

Scheme 4. Possible mechanism for the development of different types of structures.

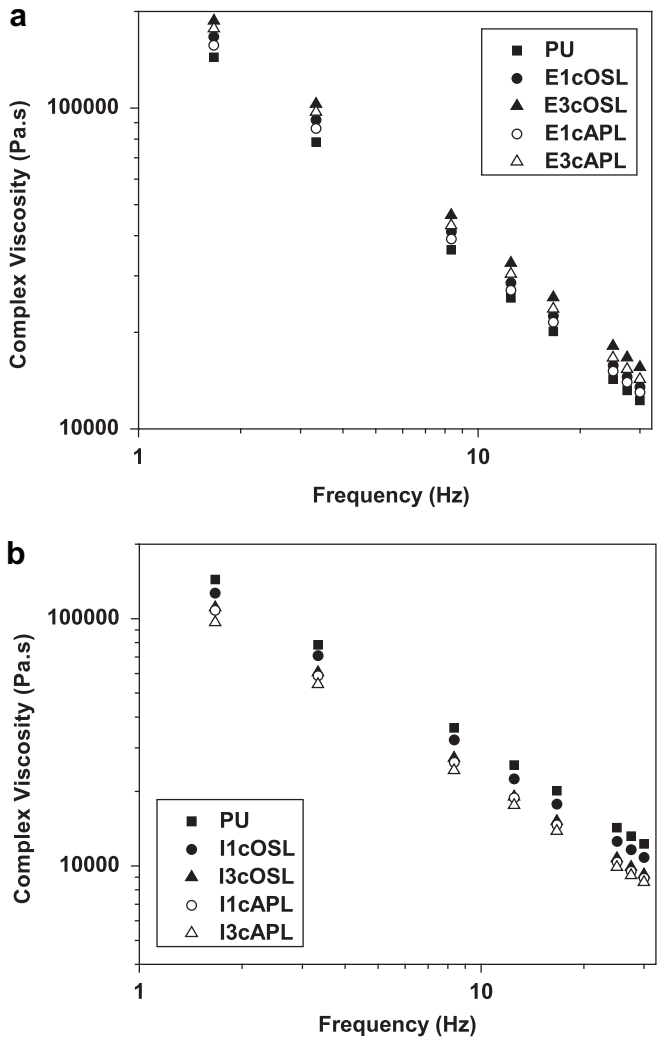

Fig. 9. a: Frequency sweep at 140 °C of *ex-situ* prepared nanocomposites *b*: Frequency sweep at 140 °C of *in-situ* prepared nanocomposites.

cAPL). The extent of decrement is however, greater with cAPL based nanocomposites. This is assumed to be due to increased active functional groups present on the modified clays providing increased reaction sites (for the −NCO group of the prepolymer). This causes hindrance to the growth of the main chain of TPU leading to change in the molecular arrangement and the segmental mobility.

η^* values of the neat TPU is always less than the nanocomposites in case of *ex-situ* prepared nanocomposites but the reverse is true for *in-situ* prepared nanocomposites. However, *ex-situ* prepared nanocomposite always possess higher η^* value as compared to their *in-situ* based counterpart. This is due to the difference in segmental mobility. This is also in accordance with our earlier observation in Section 4.2.2, where DSC results show a clear difference in segmental relaxation process between the *ex-situ* and *in-situ* prepared nanocomposites.

4.2.5. Effect of temperature on dynamic storage modulus

Temperature sweep experiment was carried out from a temperature very close to the softening of the ordered hard domains of TPU e.g., from 180 °C to 40 °C at a cooling rate of 3 °C/min by using RPA. This experiment was performed to observe the effect of crystallization or self organization of macromolecules during controlled cooling under a sinusoidal frequency of 1 Hz. The storage modulus values of the neat TPU and the nanocomposites at different temperatures are presented in Table 5.

In case of the *ex-situ* prepared nanocomposites it is observed that at a constant clay content cOSL based nanocomposites exhibit higher storage modulus values (G′) than their cAPL counterpart. This phenomenon is independent of the temperature range studied. Increase in clay content increases the storage modulus values (irrespective of the type of clay, cOSL or cAPL). These observations are in line with our earlier observations presented in Section 4.2.4 and the explanations are quite similar.

In-situ prepared cOSL based nanocomposites exhibits higher G′ value as compared to that of cAPL based nanocomposite at a constant clay content. However, contrary to the ex-situ based nanocomposites increase in clay content (of similar type), decreases the G′ value in both the varieties of clays (cOSL and cAPL).

The storage modulus values (G′) of the nanocomposites are always higher than that of the neat TPU irrespective of the technique of preparation of the nanocomposites and the type of clay used. The maximum improvement in G′ value is observed to be with E3cOSL irrespective of the temperature studied. The percent increase in G′ values are found to be 148 and 676% higher as compared to that of the neat TPU at 60 °C and 170 °C, respectively.

In-situ prepared nanocomposites show higher G′ value as compared to that of the neat TPU in reverse temperature sweep experiment, whereas, η^* values of the nanocomposites are lower than the neat TPU in case of the frequency sweep experiment. This is possibly because in case of the reverse temperature sweep, the initial thermal history and ordering is erased while heating upto 180 °C. In cooling cycle it is cooled at a relatively higher rate (3 °C/min). Hence, it can be presumed that the initial ordered hard domains has little chance to reform. This effect of loss in crystallinity can be significant in case of the neat TPU where the initial crystallinity is almost double as compared to the nanocomposites.

Table 4
Dynamic complex viscosity values of TPU and TPUCN at different frequencies as obtained from RPA (error = ±1.0%).

Sample ID	Complex viscosity at 140 °C (Pa-s) at			
	1.67 Hz	8.33 Hz	16.7 Hz	30 Hz
PU	144000	36170	20151	12264
E1cOSL	167000	41267	22505	13494
E3cOSL	187000	46348	25673	15578
E1cAPL	157000	39018	21488	13003
E3cAPL	177000	43063	23657	14281
I1cOSL	127000	32265	17763	10834
I3cOSL	111000	27308	15158	9220
I1cAPL	108000	26285	14640	8927
I3cAPL	96554	24336	13818	8590

Table 5
Dynamic storage modulus values of TPU and TPUCN at different temperatures as obtained from RPA (error = ±1.0%).

Sample ID	Dynamic Storage Modulus* (kPa) at			
	60 °C	90 °C	130 °C	170 °C
PU	4821.1	2533.8	947.6	172.1
E1cOSL	11802.0 (144.8)	7106.6 (180.5)	3179.1 (235.5)	969.4 (463.2)
E3cOSL	11970.0 (148.3)	7225.9 (185.1)	3574.5 (277.2)	1335.3 (675.9)
E1cAPL	9688.7 (100.9)	6016.2 (137.4)	2789.0 (194.3)	921.4 (435.4)
E3cAPL	11168.0 (131.6)	6754.8 (166.6)	3006.9 (217.3)	1054.3 (512.6)
I1cOSL	10562.0 (119.1)	6132.1 (142.0)	2814.5 (197.0)	798.5 (364.0)
I3cOSL	9602.1 (99.2)	5470.8 (115.9)	2495.2 (163.3)	685.3 (298.2)
I1cAPL	9197.9 (90.8)	5446.1 (114.9)	2640.0 (178.6)	786.4 (356.9)
I3cAPL	9188.3 (90.6)	5237.5 (106.7)	2480.1 (161.2)	642.8 (273.5)

* Values within the parenthesis indicate % improvement in dynamic storage modulus with respect to the neat TPU.

Thus, after the reverse temperature sweep, the reinforcement provided by the nanoclays is highly reflected in terms of higher G′ values for the nanocomposites.

4.2.6. Tensile properties

The tensile properties of the nanocomposites are given in Table 6.

Ex-situ prepared cOSL based nanocomposites possess higher tensile strength (TS) and elongation at break (EB) as compared to that of the cAPL based nanocomposites. Nearly 67% increase in TS, 208% increase in EB and 44% increase in modulus value are observed with E1cOSL as compared to the neat TPU. Increase in clay content reflects marginal change in TS for cOSL based nanocomposites but nearly 1 MPa increase in TS is observed when the amount of cAPL is increased from 1% to 3%. However, for both the types of nanocomposites (containing cSOL and cAPL), EB follows an increasing trend with the increase in clay content and the effect is more prominent in case of cOSL based nanocomposites. This is possibly due to the difference in morphology of the nanocomposites.

In-situ prepared cOSL based nanocomposites possess greater TS, EB and modulus at 50% strain as compared to their cAPL based counterpart. However, in these cases increase in clay content reduces all these properties (TS, EB and modulus at 50% strain) of the nanocomposites independent of the types of clay used (cOSL or cAPL). This is possibly due to the increase in the amount of active functional groups contributed from the modified clay leading to shorter length of the main chain of TPU so formed. A comparison between the ex-situ and in-situ prepared nanocomposites show that the former possess better tensile properties than the latter. This is mainly because in-situ prepared nanocomposites possess different morphology due to different molecular arrangement. These structures are evolved by the reaction of the active functional groups on the modified clays with the prepolymer. However, in ex-situ prepared nanocomposites the clay particles do not affect the original order of the neat TPU significantly (Scheme 3). This feature has been discussed in Section 4.2.1.2 from the WAXRD studies.

4.2.7. Thermogravimetric analysis

Table 7 shows the temperature corresponding to 5 and 10% degradation of the neat TPU and TPUCN, respectively. Thermal stability of all the nanocomposites is higher than that of the neat TPU.

In case of nanocomposites prepared by *ex-situ* technique, cOSL based nanocomposites exhibit higher thermal stability as compared to the cAPL based nanocomposites. The thermal stability (for 5% weight loss) of E3cOSL is found to be 34.6 °C higher than that of the neat TPU. Increase in clay content increases the overall thermal stability.

In case of nanocomposites prepared by *in-situ* technique, cOSL based nanocomposites possess greater thermal stability as compared to their cAPL based counterpart. The increase in clay content also increases the overall thermal stability. I3cSOL exhibits an improvement of 34.9 °C in thermal stability as compared to the neat TPU which is comparable with that of E3cOSL. However, the temperature corresponding to 10% degradation of E3cOSL is found to be the highest amongst all the nanocomposites studied here (40.7 °C higher than the neat TPU).

Surprisingly, the presence of additional H-bonding in case of cAPL does not reflect any observable influence on the initial degradation temperature of the nanocomposites. The enhancement in thermal stability at lower temperature is mostly due to the barrier effect of the nanoclay. But at the same time, at higher temperatures the active functional groups present on the surface of the clay possibly act as a nucleophile, thereby reducing the thermal stability.

Table 6
Tensile properties of the neat TPU and TPUCN.

Sample ID	TS (MPa) (error = ±1.0%)	EB (%) (error = ±3.0%)	Modulus at 50% strain (MPa) (error = ±0.5%)
PU	4.8	136	4.3
E1cOSL	8.0	275	6.2
E3cOSL	7.9	418	5.6
E1cAPL	5.9	165	5.8
E3cAPL	7.0	295	6.1
I1cOSL	6.8	246	5.3
I3cOSL	5.9	131	5.2
I1cAPL	5.5	111	5.2
I3cAPL	5.4	110	5.1

Table 7
Temperature corresponding to 5 and 10% degradation for neat TPU and TPUCN as obtained from TGA thermograms (error = ±2.0%).

Sample ID	T_5 (°C)	T_{10} (°C)
PU	256.1	267.3
E1cOSL	288.0 (31.9)*	302.1 (34.8)
E3cOSL	*290.7* (*34.6*)	*308.0* (*40.7*)
E1cAPL	278.3 (22.2)	296.1 (28.8)
E3cAPL	276.1 (20.0)	294.8 (27.5)
I1cOSL	285.1 (29.0)	298.0 (30.7)
I3cOSL	*291.0* (*34.9*)	305.3 (38.0)
I1cAPL	278.6 (22.5)	293.3 (26.0)
I3cAPL	279.7 (23.6)	295.7 (28.4)

* Values within the parenthesis indicate the numerical increase in thermal stability as compared to the neat TPU.

5. Conclusions

Dual modification of Laponite RD is carried out successfully to prepare two types of modified clays, viz., cOSL and cAPL which are characterized by FTIR, Solid State NMR (^{13}C and ^{29}Si), WAXRD and TGA experimental techniques. Among the two modified nanoclays obtained, cAPL contains greater number of active functional groups (−OH and $-NH_2$ groups) as against only −OH groups in cOSL. Significant changes in the morphology are observed between these two types of nanoclays in TPU matrix prepared by *ex-situ* and *in-situ* techniques. This is basically due to the change in number of active functional groups (tethering) on the dual modified Laponite surface. Among the two techniques of preparation of nanocomposites *ex-situ* prepared nanocomposites offer better property spectrum as compared to the *in-situ* prepared nanocomposites. In case of *ex-situ* prepared nanocomposites, increase in clay content increases the complex viscosity, dynamic storage modulus and tensile properties but the reverse trend is observed in case of *in-situ* prepared nanocomposites. cOSL (with lower degree of tethering) based nanocomposites exhibit better mechanical and rheological properties along with thermal stability as compared to its cAPL (with greater extent of tethering) counterpart. The dynamic storage modulus value of the nanocomposite containing 3% cOSL, is found to be enhanced by nearly 148 and 676% as compared to the neat TPU at 60 °C and 170 °C, respectively. Almost 67% increase in tensile strength, 208% increase in elongation at break and 44% increase in modulus value are observed for the *ex-situ* prepared nanocomposites containing cOSL. The onset of degradation of the cOSL based nanocomposite is found to be ~35 °C higher than that of the neat TPU.

In overall, it may be summarized that increase in H-bonding of the modifier and the supramolecular structure of the modifier within the clay platelet and the polymer chains play vital roles in the development of morphology, molecular relaxation, mechanical properties and rheological characteristics of the TPU based dual modified Laponite clay nanocomposite.

Acknowledgement

The authors thank Indian Space Research Organization (ISRO) and IIT Kharagpur for providing financial support to carry out this work. The authors are highly thankful to Dr N K Singha, Mr S Praveen and Prof A K Bhowmick for their help.

Appendix. Supplementary data

Supplementary data associated with this article can be found, in the online version, at doi:10.1016/j.polymer.2010.10.010.

References

[1] Harrell Jr LL. Macromolecules 1969;2:607–12.
[2] Wang CB, Cooper SL. Macromolecules 1983;16:775–86.
[3] Miller JA, Lin SB, Hwang KKS, Wu KS, Gibson PE, Cooper SL. Macromolecules 1985;18:32–44.
[4] Bonart RJ. Journal of Macromolecular Science, Part B: Physics 1968;2:115–38.
[5] Koberstein JT, Russel TP. Macromolecules 1986;19:714–20.
[6] Yeh F, Hsiao BS, Sauer BB, Michel S, Seisler HW. Macromolecules 2003;36:1940–54.
[7] Seo WJ, Sung YT, Han SJ, Kim YH, Ryu OH, Lee HS, et al. Journal of Applied Polymer Science 2006;101:2879–83.
[8] Cheng A, Wu S, Jiang D, Wu F, ShenColloid J. Polymer Science 2006;284:1057–61.
[9] Moon SY, Kim JK, Nah C, Lee YS. European Polymer Journal 2004;40:1615–21.
[10] Tien YI, Wei KH. Macromolecules 2001;34:9045–52.
[11] Ni P, Li J, Suo J, Li S. Journal of Applied Polymer Science 2004;94:534–41.
[12] Pattanayak A, Jana SC. Polymer 2005;46:3275–88.
[13] Pattanayak A, Jana SC. Polymer 2005;46:5183–93.
[14] Mallikarjuna SR, Sivaram S. Journal of Applied Polymer Science 2010;118:1774–86.
[15] Dan CH, Lee MH, Kim YD, Min BH, Kim JH. Polymer 2006;47:6718–30.
[16] Liff SM, Kumar N, McKinley GH. Nature Materials 2007;6:76–83.
[17] Korley LTJ, Liff SM, Kumar N, McKinley GH, Hammond PT. Macromolecules 2006;39:7030–6.
[18] Sormana JL, Chattopadhyay S, Meredith JC. article ID 869354 2008. Journal of Nanomaterials; 2008:9 [pages].
[19] Mishra AK, Nando GB, Chattopadhyay S. Journal of Polymer Science, Part B: Polymer Physics 2008;46:2341–54.
[20] Mishra AK, Chattopadhyay S, Nando GB. Journal of Applied Polymer Science 2010;115:558–69.
[21] Seydibeyoğlu MÖ, İşci S, Güngör N, Ece OI, Güner FS. Journal of Applied Polymer Science 2010;116:832–7.
[22] Mishra AK, Chattopadhyay S, Nando GB, Devadoss E. Designed Monomers Polymers 2008;11:395–407.
[23] Herrera NN, Putaux J-L, Bourgeat-Lami E. Progress in Solid State Chemistry 2006;34:121–37.
[24] Herrera NN, Letoffe J-M, Putaux J-L, David L, Bourgeat-Lami E. Langmuir 2004;20(5):1564–71.
[25] Herrera NN, Letoffe J–M, Reymond J-P, Bourgeat-Lami E. Journal of Materials Chemistry 2005;15:863–71.
[26] Park M, Shim I-K, Jung E-Y, Choy J-H. Journal of Physics and Chemistry of Solids 2004;65:499–501.
[27] Wheeler PA, Wang J, Baker J, Mathias LJ. Chemistry of Materials 2005;17:3012–8.
[28] Wheeler PA, Wang J, Mathias LJ. Chemistry of Materials 2006;18:3937–45.
[29] Borsacchi S, Geppi M, Ricci L, Ruggeri G, Veracini CA. Langmuir 2007;23:3953–60.
[30] Wang J, Wheeler PA, Jarrett WL, Mathias LJ. Journal of Applied Polymer Science 2007;106:1496–506.
[31] Mishra AK, Rajamohanan PR, Nando GB, Chattopadhyay S. Advanced Science Letters 2011;(4):65–73.
[32] Gusev GV. Polymer Sciences U.S.S.R 1978;20:1147–9.
[33] Basuli U, Chaki TK, Sabharwal S, Chattopahdyay S. Advanced Science Letters 2010;3:10–9.
[34] Socrates G. Wiley-Interscience Publication. In: Infrared characteristic group frequencies. New York: John Wiley & Sons; 1980.
[35] Venkataraman NV, Vasudevan S. Journal of Physical Chemistry B 2000;104:11179–85.
[36] Gadzała-Kopciuch R, Kluska M, Wełniak M, Buszewski B. Materials Chemistry and Physics 2005;89:228–37.
[37] Ferreira RB, da Silva CR, Pastore HO. Langmuir 2008;24:14215–21.
[38] Tonlé IK, Diaco T, Ngameni E, Detellier C. Chemistry of Materials 2007;19:6629–36.
[39] Burgentzlé D, Duchet J, Gérard JF, Jupin A, Fillon B. Journal of Colloid and Interface Science 2004;278:26–39.
[40] Dai X, Xu J, Guo X, Lu Y, Shen D, Zhao N, et al. Macromolecules 2004;37:5615–23.
[41] Chen TK, Shieh TS, Chui JY. Macromolecules 1998;31:1312–20.
[42] Tsen WC, Chuang FS. Journal of Applied Polymer Science 2006;101:4242–52.
[43] Seymour RW, Cooper SL. Macromolecules 1973;6:48–53.
[44] Shu YC, Lin MF, Tsen WC, Chuang FS. Journal of Applied Polymer Science 2001;81:3489–501.

Polymer 52 (2011) 1084–1091

Contents lists available at ScienceDirect

Polymer

journal homepage: www.elsevier.com/locate/polymer

Investigation of the complexation of proteins with neutral water soluble polymers through model analysis method

Zhiqiang Su [a], Liang Zhang [b], Jiaohong Zhao [a], Xiaonong Chen [a,b,*]

[a] Key Laboratory of Beijing City on Preparation and Processing of Novel Polymer Materials, Beijing University of Chemical Technology, Beijing 100029, China
[b] Key Laboratory of Carbon Fiber and Functional Polymers, Ministry of Education, Beijing University of Chemical Technology, Beijing 100029, China

ARTICLE INFO

Article history:
Received 13 October 2010
Received in revised form
30 December 2010
Accepted 7 January 2011
Available online 14 January 2011

Keywords:
Complexation
Protein
Polymer

ABSTRACT

In the current research, the complexation of bovine serum albumin (BSA) with poly(N-isopropylacrylamide) (PNIPAM) is studied in an aqueous system (pH 7) which contains NaCl as its supporting salt, and based on the electric charge conservation law a mathematical model used to quantitatively characterize the complexation between proteins and neutral polymers is established. This model, which is set up on the assumptions that there exists a dynamic equilibrium of absorption and desorption among free proteins, complexes and free polymers in the aqueous complex system and the complexation sizes of proteins with neutral water soluble polymers are not uniform, better reveals the actual state of complexation. By means of dynamic light scattering (DLS), fluorescence spectrophotometer and zeta potential analyzer, all necessary parameters of the mathematical model have been acquired accurately without destroying the dynamic equilibrium of the aqueous complex system. The calculated results demonstrate that, with the rise of mixing ratio (r_{mixing}, molar ratio of PNIPAM to BSA), both the average number of bound BSA per PNIPAM (n_b) and the diameters of complexes (R_h) decrease gradually, while the zeta potential (ζ) and the concentration of free PNIPAM ($[PNIPAM]_{free}$) increase. In addition, the average number of PNIPAM in the complexes (φ) and the molecular weight of the complexes (M_w) can also be calculated by this mathematical model. The changing pattern of M_w with r_{mixing} is in accordance with the results of static light scattering (SLS). This analysis method, which interprets the interaction between neutral polymers and proteins in an aqueous system, is a new way to calculate the complex parameters and study the complexation mechanism between proteins and polymers.

1. Introduction

The complexation of proteins with synthetic and natural polymers in aqueous system has great potential in the applications of protein separation [1–3], gene transfer [4–8], enzymes immobilization [9], and drug delivery [10], and consequently it is of great importance in the field of biochemistry and has received much attention over the last few decades. Since 1990, a number of studies have been conducted on the mechanism of complex formation of protein–water soluble polymers in aqueous salt free and salt containing systems under different pH conditions [11–28]. Among them, Dubin [5,13,16,21–26], de Kruif [6,19,20], Tribet [21,25,27,28] and Kokufuta [9,11,12,14,16,23]'s works are particularly comprehensive.

In general, electrostatic interactions dominate complex formation when polymer is polyelectrolyte [22]. However, when polymer is uncharged or complex solution has high salt concentration, the main driven forces which contribute to complex formation come from hydrogen bonds and hydrophobic effects [20,27]. Kaibara et al. [22] studied the complexation process of BSA with poly(diallyldimethyl-ammoniumchloride) (PDADMAC) and the subsequent coacervation by continuous measurements of turbidity and light scattering intensity. They identified that it is the electrostatic interactions between BSA and PDADMAC that eventually result in the separation of the coacervate phase which contains concentrated BSA. Two years later, a study conducted by Bohidar et al. [25] indicted that heterogeneities existed in the coacervate microstructures of BSA with PDADMAC, and hydrophobic interactions became stronger at higher salt concentration. Matsudo et al. [11,12] studied the intramolecular complex formation of PNIPAM with human serum albumin (HSA). They found that the increase of NaCl concentration and the rise of temperature brought about an increase in the number of bound proteins per polymer (n_b), which testified the hydrophobic-driven nature of PNIPAM and HSA

* Corresponding author. Key Laboratory of Beijing City on Preparation and Processing of Novel Polymer Materials, Beijing University of Chemical Technology, Beijing 100029, China.
E-mail address: chenxn@mail.buct.edu.cn (X. Chen).

0032-3861/$ – see front matter © 2011 Elsevier Ltd. All rights reserved.
doi:10.1016/j.polymer.2011.01.012

complexes. Kelarakis et al. [18] investigated the interaction between BSA and ethylene oxide/butylene oxide copolymers with various block lengths and varying molecular architectures. It has been found that the length of hydrophilic block of PEO has great influence on the complexation of protein–polymers.

At dilute or semi-dilute concentration, the binding of proteins with water soluble polymers usually forms liquid and reversibly complex. In most cases, quantitative characterization requires in situ complex information of samples, thus scattering techniques such as electrophoretic light scattering (ELS), DLS and SLS are the most widely used techniques in this field. However, problems still remain. First, it is difficult to measure the average molecular weight (M_w) of the complexes precisely by SLS due to the fact that the concentration of complexes and the value of the refractive index increment (dn/dc) cannot be quantitative measured in heterogeneous system as a result of scattering effects [26]. Second, as described by de Kruif et al. [6], since the complex of protein–neutral water soluble polymers is strongly hydrated and reversible, it is hard to isolate the intact complexes from aqueous system and to count the numbers of free proteins and free polymers accurately.

In view of these problems, previous literatures reported an empirical formula to calculate the value of dn/dc and further measure the Mw of the protein–polyelectrolyte complexes (PPCs) [13,26], which was later applied to the system of the protein–neutral water soluble polymer complexes with low protein concentration ([HSA] = 0.1 mg/ml) [11,12]. However, the calculated results obtained from this method failed to precisely describe the real complexation state of proteins with neutral water soluble polymers in aqueous system, for it is based on an assumption of uniform complexation state in which every soluble complex consists only one polymer chain and several bound proteins (i.e., "necklace" structure) [27]. Under most conditions, this ideal state doesn't exist for a complex may contain several polymer molecules. When the M_w value of proteins is close to that of the neutral water soluble polymers, the complexation is even more complicated [12].

A few other methods have also been developed to measure the average complex ability of proteins with neutral water soluble polymers in aqueous system, but they also have some limitations. For example, dialysis technique [11,12] is time-consuming, and it is possible to break the dynamic equilibrium of complex in dialysis process and therefore the measurement results may not be correspondent with practice. Other methods, such as potentiometric titration [29] and conductometric titration [30], are not suitable either, as for the complexation of protein with neutral polymer, potential and conductivity do not change obviously in the process of complexation.

In the present study, in order to characterize the complexation of proteins with neutral water soluble polymers in quantities and to understand their complex mechanism, a new model analysis method which combines analytical and experimental approaches has been established. This approach, established on an assumption that there exists a dynamic equilibrium of absorption and desorption among free proteins, complexes and free polymers in the aqueous complex system, better reflects the real complexation state of polymers with proteins. Furthermore, in the process of establishing the mathematic model, fluorescence spectroscopy has been adopted to measure the average number of bound proteins per polymer in the complex in order to avoid the experimental error produced in dialysis process. With the help of this mathematical model, both n_b and M_w of the complexes can be calculated accurately without destroying the dynamic equilibrium of aqueous complex system. Compared with traditional experimental techniques, this method has the advantages of simplicity, accuracy and extensive application, and can provide abundant information of complex system.

2. Experimental part

2.1. Materials

BSA was commercially obtained from Sigma Chem. Co. It is a single polypeptide chain consisting of about 583 amino acid residues and no carbohydrates. At pH 5–7 it contains 17 intrachain disulfide bridges and 1 sulfhydryl group, M_w = 66430 g/mol. Neutral water soluble polymer (PNIPAM) was prepared via controlled radical polymerization of N-isopropylacrylamide (NIPAM) monomer in our laboratory and was purified by dialysis method. It is a monodisperse one (PDI = 1.2) with the average molecular weight of 45,000 g/mol.

2.2. Complex formation

Water, used as solvent, was deionized and distilled. Aqueous tris–buffer (0.02 mol/L) solution was adjusted to pH 7 using HCl and NaCl (0.01 M) as medium. The solutions of BSA and PNIPAM with different concentrations were prepared in the tris–HCl buffer solution, respectively. Both the BSA and PNIPAM solutions were filtered through 0.22 μm syringe filters before complexation. The concentrations of BSA solutions were 5, 10 and 15 μmol/L and the concentrations of PNIPAM solutions were 3, 5.25, 13.5, 18, 27, 40.5, 52.5, 75 μmol/L. The complexation solutions were prepared via gently adding PNIPAM solutions with different concentrations into BSA solutions. Then the mixed solutions were standing for over 16 h before testing. The molar mixing ratio (r_{mixing}) is defined as:

$$r_{\mathrm{mixing}} = \frac{[\mathrm{PNIPAM}]_{\mathrm{total}}}{[\mathrm{BSA}]_{\mathrm{total}}} \quad (1)$$

where $[\mathrm{PNIPAM}]_{\mathrm{total}}$ and $[\mathrm{BSA}]_{\mathrm{total}}$ represent the total molar concentration of PNIPAM and BSA in the mixed solution, respectively.

2.3. Measurements

DLS measurements were performed on Zeta PLAS dynamic light scattering detector (Brookhaven Instrument, Holtsville, NY) which employed the technique of photon correlation spectroscopy of quasi-elastically scattered light. The particle sizes, distribution information and zeta potential of the complexes can be measured by this instrument. The scattered light was collected at a scattering angle of 90°. The wavelength of the laser light source was 658 nm and the power was 35 mW. All the measurements were carried out at 25 °C and the particle sizes were evaluated by light intensity. The results were obtained from Multimodal Size Distribution (MSD) option and Non-Negatively constrained Least Squares (NNLS) algorithm has been taken to fit the data.

Fluorescence spectra and fluorescence intensities were recorded on a Hitachi F-4500 fluorescence spectrophotometer. A high-quality quartz cuvette with 10 mm path length was employed for spectroscopic measurements. The excitation wavelength was set at 290 nm, and the emission was recorded from 310 to 450 nm. Before measurement, the cuvette was washed three times with blank solution (Tris–HCl buffer (0.02 mol/L), pH 7, NaCl (0.01 M)). All experiments were carried out at 25 °C.

3. Establishing mathematical model

In the aqueous complex system of PNIPAM and BSA, the neutral polymer (PNIPAM) interacts with the charged protein (BSA) and finally forms complex particles with different surface charge densities. During the whole complexation process, the total

electric charge value of the complex system keeps invariant. Therefore, according to the diffuse electric double layer model of Gouy–Chapman [31,32] and its modified version Stern model [33], the surface charge density on the diffuse layer of the complex particles can be described as follows:

$$\sigma_c = \frac{\varepsilon kTK}{2\pi Ze}\sinh\left(\frac{Ze\zeta}{2kT}\right) \tag{2}$$

$$K^2 = \frac{4\pi e^2}{\varepsilon kT}\sum_i n_{i0}Z_i^2 \tag{3}$$

$$n_{i0} = C_{i0} \times N_A/1000 \tag{4}$$

where ε denotes the dielectric constant, k expresses the Boltzmann constant, ζ represents the zeta potential of the complex particles, Z represents the absolute value of the ionic charge, T is the absolute temperature, e is the absolute value of electric charge of electron, n_{i0} represents the number of ions per volume and C_{i0} denotes the ionic concentration.

In the aqueous complex system, there exist free proteins, free polymers and complex particles of different sizes. The complexation includes not only the association of polymer chains with proteins, but the interaction among different complexes as well (shown in Fig. 1).

As has been proven by Dubin et al. [21], Debye lengths (k^{-1}) of proteins and polyelectrolytes extends at low ionic strength and suppresses at high salt concentrations. In the latter case, both electrostatic repulsion and attraction between the charged species are screened due to the salt addition, which leads to the coexistence of hydrophobic and electrostatic interactions. In our experiment, PNIPAM is a kind of uncharged polymer and the association between BSA and PNIPAM is induced by hydrogen bonding and hydrophobic interaction. A relatively high salt concentration would strongly reduce Debye length ($k^{-1} \approx 0.3/\sqrt{I}$) thus enhance the association among proteins [21]. Through the Monte Carlo simulation [34], it has been proved that the protein–protein association would promote protein–polymer complexation and facilitate clusters formation (i.e., complex particle consists of several polymers and several proteins).

The mathematical model proposed in this paper is based on the following assumptions:

1. The complexation of proteins with polymers is in a kind of dynamic equilibrium state of absorption and desorption and all the particles in the solution can move freely.
2. The shapes of both the complexes and the free proteins are considered to be spherical and the electric charge distributes evenly on the surface of the spherical. The polymers in the complex system are electroneutral.
3. The complexation state of proteins with neutral water soluble polymers is not uniform (i.e., not always the ideal state that one polymer molecule complex with several proteins, but possibly several polymer molecules may complex with several proteins)

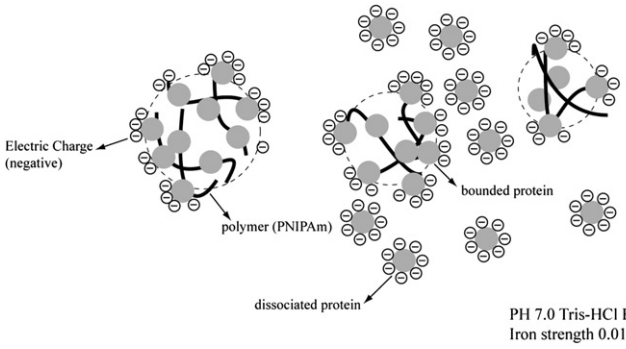

Fig. 1. The complexation state of PNIPAM and BSA in the aqueous solution.

Because of the relatively loose combination between polymers and proteins in the process of complexation, the surface charge density of the complex particles is lower than that of free proteins but higher than that of free polymers. Therefore, according to electric charge conservation law, a mathematical equation which is used to calculate the complexation between proteins and neutral polymers can be established.

According to our assumptions, the shapes of both the complexes and the free proteins in the aqueous complex system are spherical, so the surface area of a single protein or complex can be calculated as follows:

$$S_{pro} = 4\pi R_{pro}^2 \tag{5}$$

$$S_{com}^i = 4\pi R_i^2 \tag{6}$$

where S_{pro} and S_{com}^i donate the surface area of spherical protein and that of complex, respectively. R_{pro} and R_i represent the hydrodynamic radius of the protein and that of complex, respectively. Considering of the difference in the sizes of the complex particles, the superscript (i) in equation (6) represents the complexes with different hydrodynamic radius ($i = 1, 2, 3\ldots$).

The charge density on the stern layer of the complex can be described as the following:

$$\sigma_{com}^i = \frac{Q}{S_{com}^i} = \frac{n_b^i \times \sigma_{pro} \times S_{pro}}{4\pi R_i^2} \tag{7}$$

where σ_{com}^i and σ_{pro} represent the charge density of complexes and that of proteins, respectively. Q donates the electric charge of a single complex; n_b^i is the number of the bound proteins per polymer in a specific complex particle.

As mentioned above, in the aqueous complex system, the total electric charge value of all particles (including free proteins, free polymers and complexes) keeps invariant, namely the summation of the electric charge value of free proteins and that of complexes is equal to the average charge density of all particles multiply the total surface area of all particles (equation (8)).

$$\begin{aligned}&\sum_i\left(\sigma_{com}^i \times S_{com}^i \times c_i\right) + \sigma_{pro} \times S_{pro} \times \left(c_{pro} - \sum_i n_b^i \times c_i\right)\\ &\equiv \overline{\sigma} \times \left[S_{pro} \times \left(c_{pro} - \sum_i n_b^i \times c_i\right) + \sum_i\left(S_{com}^i \times c_i\right)\right]\end{aligned} \tag{8}$$

$$\sum_i n_b^i \times c_i = n_b \times c_{poly}^b \tag{9}$$

Combined with equations (7) and (9), equation (8) can be simplified as follows:

$$\begin{aligned}&\sigma_{pro} \times S_{pro} \times n_b \times c_{poly}^b + \sigma_{pro} \times S_{pro} \times \left(c_{pro} - n_b \times c_{poly}^b\right)\\ &\equiv \overline{\sigma} \times \left[S_{pro} \times \left(c_{pro} - n_b \times c_{poly}^b\right) + \sum_i\left(S_{com}^i \times c_i\right)\right]\end{aligned} \tag{10}$$

where c_{poly}^b represents the molar concentration of the bound polymers, c_{pro} denotes the molar concentration of protein and c_i represents the molar concentration of the complex with a specific

size. $\overline{\sigma}$ is the average charge density on the stern layer of the particles in the mixed solution, which can be calculated from equation (2). n_b is the average number of the bound protein per polymer in complexation.

According to equation (10), n_b can be calculated as follows:

$$n_b = \frac{S_{pro}\times c_{pro}\times(\overline{\sigma}-\sigma_{pro})+\overline{\sigma}\times\sum_i(S^i_{com}\times c_i)}{\overline{\sigma}\times S_{pro}\times c^b_{poly}} = \frac{S_{pro}\times(\overline{\sigma}-\sigma_{pro})+\overline{\sigma}\times\sum_i\left(S^i_{com}\times\frac{c_i}{c^b_{poly}}\right)\times\frac{c^b_{poly}}{c_{pro}}}{\overline{\sigma}\times S_{pro}\times\frac{c^b_{poly}}{c_{pro}}} = \frac{S_{pro}\times(\overline{\sigma}-\sigma_{pro})+r^b_{mixing}\times\overline{\sigma}\times\sum_i(S^i_{com}\times\theta_i)}{\overline{\sigma}\times S_{pro}\times r^b_{mixing}} \quad (11)$$

$$r^b_{mixing} = c^b_{poly}/c_{pro}, \quad \theta_i = c_i/c^b_{poly} \quad (12)$$

In equations (11) and (12), r^b_{mixing} represents the average number of bound polymer per protein molecule and θ_i represents molar ratio of the complexes with a specific size to the bound polymers. Particularly, the reciprocal of θ (φ) can be used to describe the average number of bound polymer in complexes (equation (13)).

$$\varphi = \frac{1}{\theta} = \frac{1}{\sum_i\frac{c_i}{c^b_{poly}}} = \frac{1}{\frac{c_{com}}{c^b_{poly}}} = \frac{c^b_{poly}}{c_{com}} \quad (13)$$

where c_{com} represents the total molar concentration of the complexes.

4. Results and discussion

In the above discussion, a mathematical model has been established based on the electric charge conservation law. In order to characterize the complexation between BSA and PNIPAM quantitatively, some important parameters (including r^b_{mixing}, n_b, R_h and σ values) in the mathematical model should be measured. In the following part, these parameters would be measured by dynamic light scattering, fluorescence spectrophotometer and zeta potential analyzer respectively, and we will further discuss the complexation mechanism.

4.1. Calculation of r^b_{mixing} and n_b value

It is well known that most proteins, including serum albumin, contain fluorescent residues such as tryptophan, which is a type of intrinsic fluorescence. According to our investigation [35], the addition of neutral polymer into protein solution leads to the appearance of fluorescent quenching of intrinsic tryptophan chromophores, and ultimately results in the decrease of fluorescence intensities at a given wavelength. Thus, the binding affinities can be reflected via the changes of fluorescence intensities [35,36]. In the experiments, the average number of bound proteins per polymer (n_b) in aqueous complex system is obtained by detecting the change of the fluorescence intensities of the complexes.

Fig. 2 shows the fluorescence spectra of the mixed solutions of BSA and PNIPAM with different molar mixing ratio. Apparently, the addition of PNIPAM into BSA solutions induces a decrease of the tryptophan fluorescence intensity. The decrease of the intensity of the tryptophan fluorescence can be quantified in terms of the ratio I_0/I (I_0 and I being the fluorescence intensities, registered at a given wavelength, in the absence and presence of the PNIPAM considered, respectively).

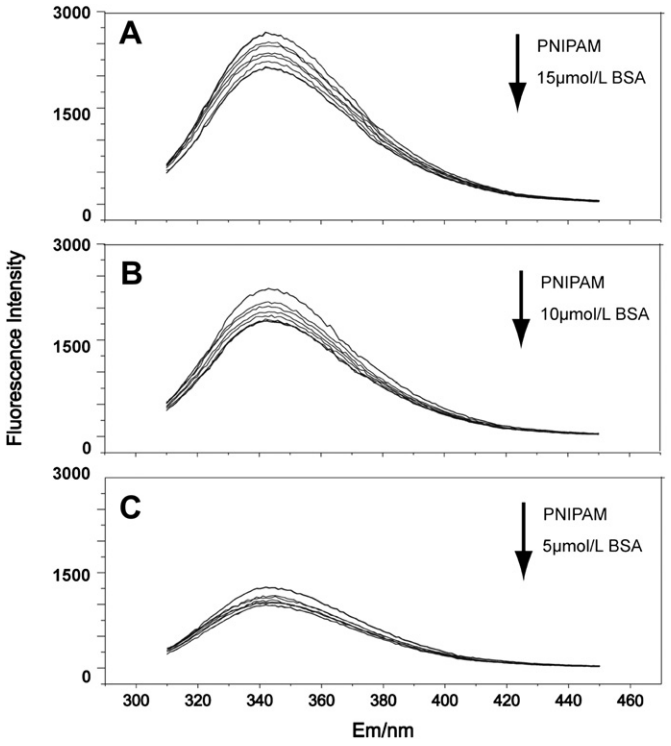

Fig. 2. The fluorescence spectra of the mixed solutions of BSA and PNIPAM with different molar mixing ratio. The concentrations of BSA were 5 μmol/L (A), 10 μmol/L (B) and 15 μmol/L (C); the concentrations of PNIPAM were 3, 5.25, 13.5, 18, 27, 40.5, 52.5, 75 μmol/L.

Fig. 3 shows the variation of I_0/I value as a function of PNIPAM concentration, obtained from the fluorescence spectra of Fig. 2. It can be observed that the rising trend of I_0/I value decrease gradually with the increase of PNIPAM concentration and finally reach a plateau (I_0/I_{min}). For the three groups of mixed solutions with different BSA concentrations (15, 10 and 5 μmol/L), the I_0/I_{min} values are 1.262, 1.265, 1.275 respectively. In the aqueous complex system, based on the mass conservation law, there exists a mass balance equation as follows:

$$[PNIPAM]_{total} = [PNIPAM]_{free} + r^b_{mixing}[BSA]_{total} \quad (14)$$

where $[PNIPAM]_{free}$ represents the molar concentration of free PNIPAM and r^b_{mixing} represents the average number of bound PNIPAM molecules per BSA molecule.

To quantify the amount of $[PNIPAM]_{free}$ and $[PNIPAM]_{complex}$ (the molar concentration of PNIPAM which are complexed with BSA), it is necessary to establish linear relationship between $[PNIPAM]_{total}$ and $[BSA]_{total}$. In Fig. 3, for an arbitrary I_0/I value, three sets of $[PNIPAM]_{total}$ and $[BSA]_{total}$ data can be obtained by drawing a horizontal line parallel to abscissa. With the help of these data sets, the linear relationship between $[PNIPAM]_{total}$ and $[BSA]_{total}$ can be established, as demonstrated in Fig. 4. According to equation (14), the intercepts of these lines in Fig. 4 correspond to $[PNIPAM]_{free}$ value, while the slopes of these lines present r^b_{mixing} value.

However, in the aqueous complex system the complexation state of proteins with neutral water soluble polymers is not uniform. Since r^b_{mixing} represents the average number of bound PNIPAM molecules per BSA molecule, including free BSA and complex BSA, it cannot reflect the real complex situations of aqueous complex system. To describe the complexation accurately,

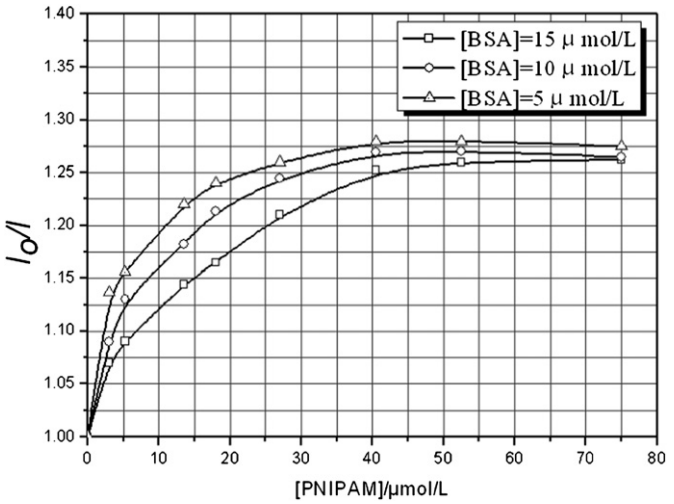

Fig. 3. The variation of I_0/I value, evaluated from the fluorescence spectra of Fig. 1, as a function of $[PNIPAM]_{total}$.

a more general parameter - the average number of bound proteins per polymer (n_b) - is defined as follows:

$$n_b = \frac{[BSA]_{total} - [BSA]_{free}}{[PNIPAM]_{total} - [PNIPAM]_{free}} \quad (15)$$

As mentioned above, the value of I_0/I increases with the increase of PNIPAM concentration and reaches a plateau (I_0/I_{min}) when PNIPAM concentration exceed a certain value. Fig. 5 is the schematic diagram of fluorescent quenching. As Fig. 5 shows, I_0/I_{min} represents the maximum fluorescent quenching ability of the complexation of PNIPAM and BSA. The value of $1 - I_{min}/I_0$ can be defined as the maximum fluorescent quenching ratio of complex, and the value of $1 - I/I_0$ as the fluorescent quenching ratio of complex at any a r_{mixing} value. The concentration of free BSA in the mixed solutions can be calculated according to equation (16):

$$\frac{[BSA]_{total} - [BSA]_{free}}{[BSA]_{total}} = \frac{1 - I/I_0}{1 - I_{min}/I_0} \quad (16)$$

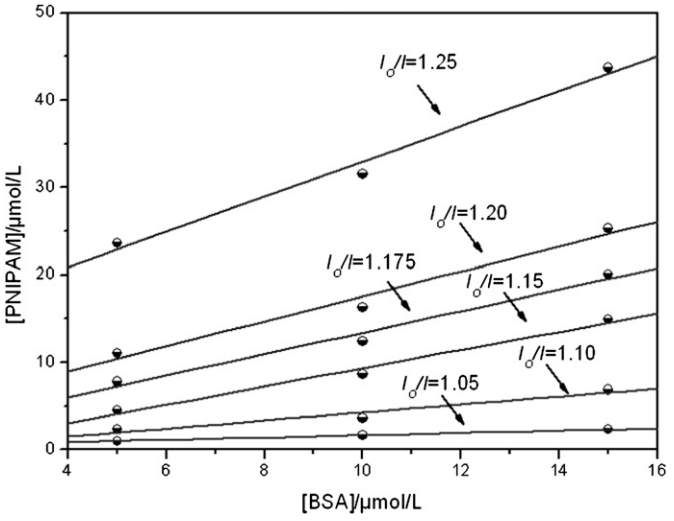

Fig. 4. The linear relationship between $[PNIPAM]_{total}$ and $[BSA]_{total}$ obtained from sets of data taken at different I_0/I values.

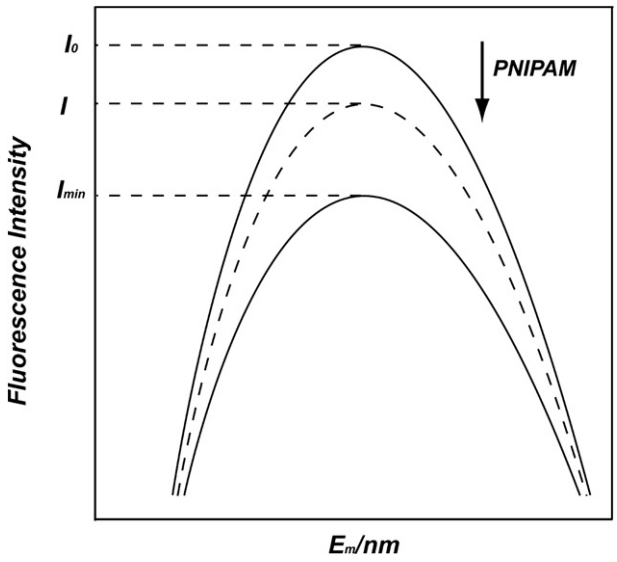

Fig. 5. The schematic diagram of fluorescent quenching.

Combined with equations (1), (15) and (16), n_b value can be calculated as follows:

$$n_b = \frac{[BSA]_{total} \times \frac{1 - I/I_0}{1 - I_{min}/I_0}}{r_{mixing} \times [BSA]_{total} - [PNIPAM]_{free}} \quad (17)$$

Here, the values of I/I_0, I_0/I_{min} and $[PNIPAM]_{free}$ can be obtained from Figs. 3 and 4, and the average number of bound proteins per polymer (n_b) in the complexation can be calculated accurately by equation (17). With the help of this formula, n_b can be calculated in all conditions, including its extreme value when PNIPAM concentration is rather low ($r_{mixing} < 0.01$). This extreme value can hardly be obtained by other methods [11,12].

Fig. 6 shows the changing patterns of n_b value with r_{mixing} under different BSA concentrations. As mentioned above, I_0/I_{min} values of the three groups of mixed solutions are different, hence, even with the same r_{mixing} value, their n_b values are still different. It is obvious that the n_b value of these three groups of mixed solutions all decrease with the increase of r_{mixing}. In addition to this, n_b value of the complex solution with lower BSA concentration is higher than that of the complex solution with higher BSA concentration. This changing pattern of n_b with r_{mixing} is similar to what has been reported in the previous literatures [11,12] which measured the n_b value with dialysis technique.

As it is known that, in the complex system of protein with neutral water soluble polymer, light scattering intensity of free neutral polymers is lower than that of proteins and complexes. Therefore, the free neutral polymers cannot be detected precisely by DLS [11,12]. Previous literatures have solved this problem by investigating the complexation of HSA–PNIPAM with ELS [11]. It was found that, using ELS method, the signal of free PNIPAM molecules can only be detected in the complex solutions when the PNIPAM concentration exceed a certain value. On the contrary, with the help of our method, both $[PNIPAM]_{free}$ and the transition point at which large amount of free PNIPAM appears can be calculated accurately. Fig. 7 shows the changing pattern of $[PNIPAM]_{free}$ with r_{mixing}. It can be observed that, with the rise of r_{mixing} value, $[PNIPAM]_{free}$ first increase slowly, but when $r_{mixing} > 1.2$, $[PNIPAM]_{free}$ value presents a rapid growth. This transition point is in accordance with the one measured by ELS. In this way, the accuracy of our method has been further proved.

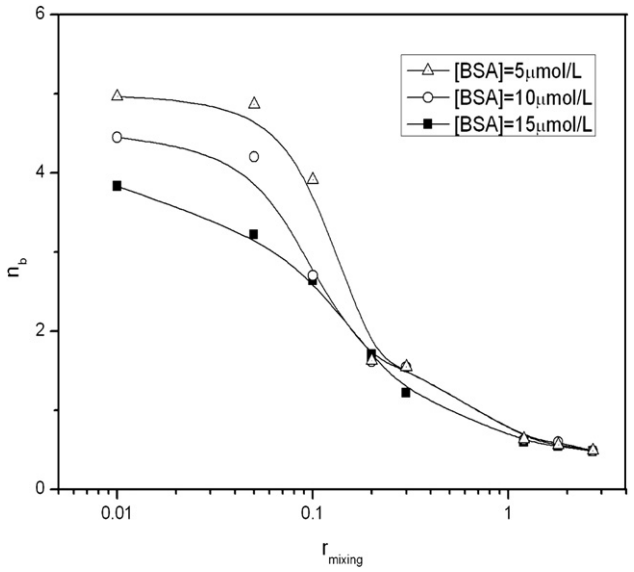

Fig. 6. The changing pattern of n_b value with r_{mixing} at different BSA concentrations.

It is also our interest to plot the number of polymers bounded with protein against free polymer concentration (shown in Fig. 8). The curve of Fig. 8 behaves like high-affinity polymers adsorption at interfaces [37]. Here, we would like to compare our results with the finding of Tribet [28] and Goddard [38], who have previously reported the interaction between BSA and hydrophobically modified poly(acrylic acid). They found that the association isotherm of low molecular weight poly(acrylic acid) (M_w around 5000) onto BSA (M_w around 67,000) is like protein–surfactant interaction [38], which is a cooperative-type association (S shape). Their result, combined with DLS data, encouraged them to presuppose a "hairy" structure of the complexes (i.e., proteins surrounded by many polymer chains). In our case, the molecular weight of PNIPAM (M_w around 45,000) is larger than that of poly(acrylic acid) used in Tribet's experiments, and the shape of association isotherm is a classic polymer adsorption isotherm. Though, lacking further evidence, we cannot jump to a conclusion of the space structure of the complexes, at least, we can say that BSA is saturated to its maximum loading capacity when r_{mixing} is larger than 1.2 in our experimental condition.

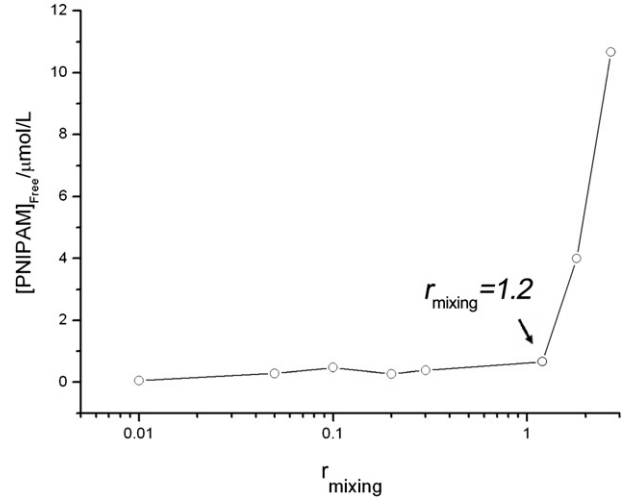

Fig. 7. The changing pattern of $[PNIPAM]_{free}$ with r_{mixing}.

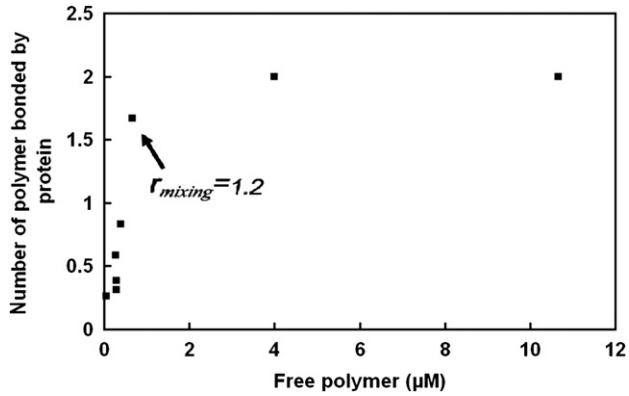

Fig. 8. The adsorption isotherm of the aqueous complex system of PNIPAM with BSA.

4.2. Measurement of R_h and ζ

In this work, the complexation between PNIPAM and BSA was studied as a function of r_{mixing} under a fixed solution condition: 25 °C, tris–HCl buffer (0.02 mol/L), NaCl (0.01 M), and pH 7.0. The particle diameters of PNIPAM/BSA complexes were measured by Zeta PLAS dynamic light scattering detector (Brookhaven Instrument, Holtsville, NY). Fig. 9 shows the typical examples of DLS results of PNIPAM/BSA mixture samples as a function of r_{mixing}.

In Fig. 9, two varieties of complex particles with different diameters can be observed in each PNIPAM/BSA mixture solution. According to Tribet and Matsudo's research results [11,12,27], the R_h value of small particles (~9 nm) is very close to that of BSA, and they assigned them to free proteins or free polymers. In addition, the large particles whose R_h ranges from 30 to 150 nm are assigned to PNIPAM/BSA complexes [11,12]. Thus, with the help of DLS, the changing pattern of R_h of PNIPAM/BSA complexes with the increasing r_{mixing} can be obtained (Fig. 10) and the sizes of PNIPAM/BSA complexes with different r_{mixing} can be measured (Table 1). It is obviously that all hydrodynamic diameters of PNIPAM/BSA complexes are larger than that of free polymers. The smallest one (34 nm, at $r_{mixing} = 1.8$) is about 2 times larger than that of free polymer coils under same solvent quantity, which strongly suggests the occurrence of *multipolymer* complexation in this complex system [38].

In our mathematical model, zeta potential (ζ) is another important parameter and the above-described Brookhaven system has been adopt to measure the zeta potentials of different complex

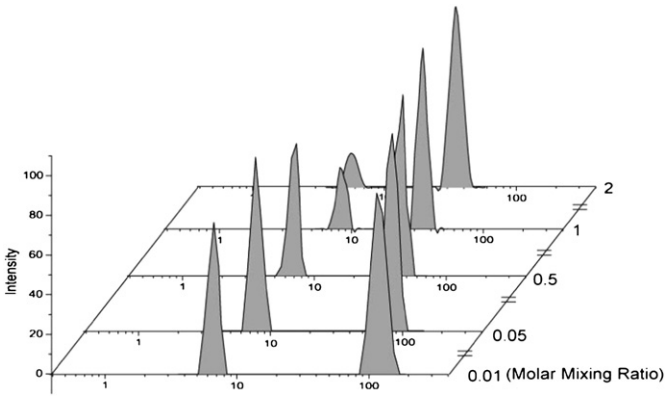

Fig. 9. The DLS results of PNIPAM/BSA mixture samples as a function of r_{mixing}. Complexation was studied at 25 °C, tris–HCl buffer (0.02 mol/L), NaCl (0.01 M), and pH 7.0. r_{mixing} = 0.01, 0.05, 0.5, 1, 2 respectively.

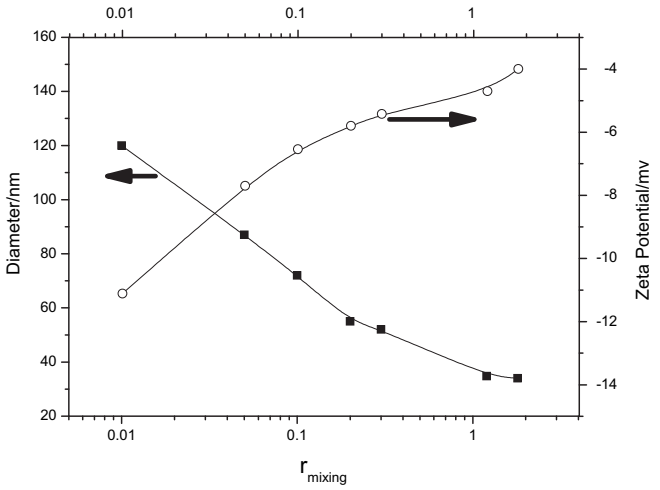

Fig. 10. The changing pattern of particle diameters and zeta potential of PNIPAM/BSA complexes as a function of r_{mixing}.

samples in this work. The zeta potential values of PNIPAM/BSA complex samples with different r_{mixing} are showed in Fig. 10. It is obviously that, with the rise of r_{mixing} value, the zeta potentials of PNIPAM/BSA complex samples increase gradually.

4.3. Calculation of φ and M_w values

In this work, with the help of DLS, zeta potential analyzer and fluorescence spectrophotometer, all necessary parameters of the mathematical model (such as the particle diameters, zeta potentials, r^b_{mixing} and n_b values of complexes) have been measured and the results are listed in Table 1. By virtue of the above parameters and equations (12) and (13), the average number of PNIPAM in the complexes (φ) can be calculated. Fig. 11 shows the changing pattern of the φ value of PNIPAM/BSA complex samples as a function of r_{mixing}.

In Fig. 11, it can be observed that the average number of PNIPAM in the complexes increases gradually with the rise of r_{mixing} value, indicating that the complexation state between BSA and PNIPAM depends mainly on r_{mixing}. It is the common knowledge that, in the complexation system, there exist both intramolecular interaction among segments within one polymer chain and intermolecular interaction among different polymer chains [11,12]. With the increase of r_{mixing}, the interaction among polymer molecular chains is enhanced, which made it even more difficult for proteins to overcome the strong intra- and inter-PNIPAM interactions [11] and finally results in the increase of the average number of PNIPAM in the complexes.

It is of great importance to obtain molecular weight of complexes with determinable species fraction because it reflects which kind of association happens (intra or intermolecular interaction) [27]. The most general method for calculating M_w is SLS

Table 1
The particle diameters, zeta potentials and n_b values of complexes under different r_{mixing}.

r_{mixing}	Particle diameter/nm	Zeta potential/mv	n_b
0.01	120.0	−0.0111	3.8
0.05	87.0	−0.0077	3.2
0.1	72.0	−0.0065	2.6
0.2	55.0	−0.0058	1.7
0.3	52.0	−0.0054	1.2
1.2	34.8	−0.0047	0.6
1.8	34.0	−0.0040	0.5

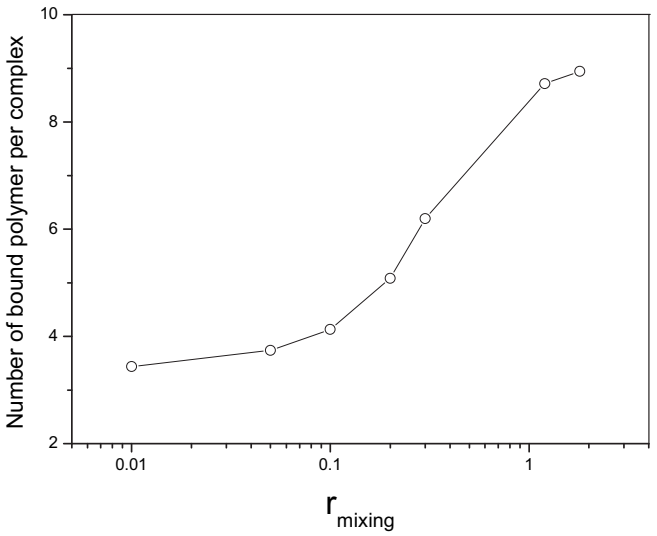

Fig. 11. The changing pattern of the φ value of PNIPAM/BSA complex samples as a function of r_{mixing}.

[11–13]. However, the calculated results obtained from this method cannot precisely describe the real complexation state of proteins with neutral water soluble polymers in aqueous system, for it is based on the assumption of uniform complexation state in which the soluble complex consist only one polymer chain and several bound proteins (i.e., "necklace" structure) [27]. Bearing these problems in mind, here we developed a new analytical approach to calculate species fraction in complexes particles, whose parameters are determined experimentally under various r_{mixing}. By means of model analysis method, M_w of the complex particles can also be calculated accurately.

$$M_w = \frac{1}{\theta} \times M_{PNIPAM} + \frac{n_b}{\theta} \times M_{BSA} = \varphi \times M_{PNIPAM} + \varphi \times n_b \times M_{BSA} \quad (18)$$

Equation (18) is the calculation formula of the molecular weight of the complex particles. With the help of equation (18), the molecular weights of the complexes can be obtained (Fig. 12). It is obviously that, with the rise of r_{mixing} value, the molecular weight

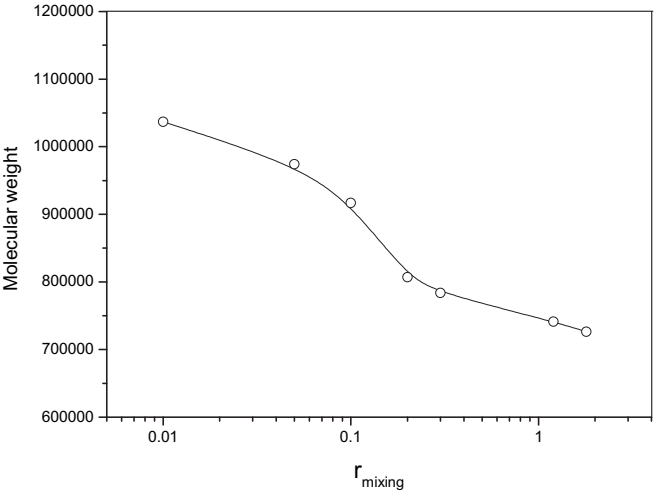

Fig. 12. The changing pattern of the molecular weight of the complexes as a function of r_{mixing}.

of the complex particles decreases gradually. As we known, the intermolecular interaction among polymer segments is strengthened by the increase of polymer concentration [11,12]. The protein binding needs to overcome both intramolecular and intermolecular interactions of polymers, so that the increase in r_{mixing} hinders the binding of BSA and results in the decrease of the molecular weight of the complexes.

5. Conclusions

The present study investigated the complexation of BSA with PNIPAM in an aqueous system by model analysis method. With the help DLS, fluorescence spectrophotometer and zeta potential analyzer, all necessary parameters (such as the particle diameters, zeta potentials, r^b_{mixing} and n_b values of complexes) have been measured without destroying the dynamic equilibrium of the aqueous complex system. These parameters have then been applied in the mathematical model to provide abundant information about the complexation state, including the average number of PNIPAM in the complexes (φ) and the molecular weight of the complexes. Furthermore, through comparing our results with previously literatures, the complexation mechanism of proteins with neutral water soluble polymers is further illuminated: the main driven forces of complexation come from hydrogen bonds and hydrophobic effects and there exist both intra and intermolecular interaction in the complex system, which results in the inhomogeneous complexation states (i.e., not always the ideal state that one polymer molecule complex with several proteins, but possibly several polymer molecules may complex with several proteins). This model analysis method, which quantitatively characterizes the interaction between neutral polymers and proteins in aqueous system, is a useful method to investigate the complexation between electroneutral polymers and proteins.

Acknowledgments

The financial support from National Natural Science Foundation of China (NSFC, grant No. 20874004 and No. 20974010), Beijing New-Star Program of Science and Technology (2009B10), Fundamental Research Funds for the Central Universities (project no. ZZ1007) and Program for Changjiang Scholars and Innovative Research Team in University (PCSIRT, grant No. IRT0807).

References

[1] Izumrudov VA, Galaev IY, Mattiasson B. Bioseparation 1998;7:207.
[2] Feng ZC, Shao ZZ, Yao JR, Huang YF, Chen X. Polymer 2009;50:1257.
[3] Valdebenito A, Espinoza P, Lissi EA, Encinas MV. Polymer 2010;51:2503.
[4] Liang E, Hughes J. Biochim Biophys Acta 1998;1369:39.
[5] Cooper CL, Dubin PL, Kayitmazer AB, Turksen S. Curr Opin Colloid Interface Sci 2005;10:52.
[6] de Kruif CG, Tuinier R, editors. Polysaccharide protein interactions. 2001 Elsevier Sci Ltd; 2001. p. 555–63.
[7] Rodriguez-Soca Y, Munteanu CR, Dorado J, Rabuñal J, Pazos A, González-Díaz H. Polymer 2010;51:264.
[8] Chen SF, Li LY, Zhao C, Zheng J. Polymer 2010;51:5283.
[9] Kokufuta E. Prog Polym Sci 1992;17:647.
[10] Martin TJ, Prochazka K, Munk P, Webber SE. Macromolecules 1996;29:6071.
[11] Matsudo T, Ogawa K, Kokufuta E. Biomacromolecules 2003;4:728.
[12] Matsudo T, Ogawa K, Kokufuta E. Biomacromolecules 2003;4:1974.
[13] Xia JL, Dubin PL, Dautzenberg H. Langmuir 1993;9:2015.
[14] Takahashi D, Kubota Y, Kokai K, Izumi T, Hirata M, Kokufuta E. Langmuir 2000;16:3133.
[15] Dilgimen AS, Mustafaeva Z, Demchenko M, Kaneko T, Osada Y, Mustafaev M. Biomaterials 2001;22:2383.
[16] Azegami S, Tsuboi A, Izumi T, Hirata M, Dubin PL, Wang BL, et al. Langmuir 1999;15:940.
[17] Edwards K, Chan RYS, Sawyer WH. Biochemistry 1994;33:13304.
[18] Kelarakis A, Castelletto V, Krysmann MJ, Havredaki V, Viras K, Hamley IW. Biomacromolecules 2008;9:1366.
[19] de Kruif CG, Tuinier R. Food Hydrocolloids 2001;15:555.
[20] de Kruif CG, Wenbreck F, de Vries R. Curr Opinion Colliod Interface Sci 2004;9:340.
[21] Seyrek E, Dubin PL, Tribet C, Gamble EA. Biomacromolecules 2003;4:273.
[22] Kaibara K, Okazaki T, Bohidar HB, Dubin PL. Biomacromolecules 2000;1:100.
[23] Xia J, Dubin PL, Kokufuta E. Macromolecules 1993;26:6688.
[24] Park JM, Muhoberac BB, Dubin PL, Xia J. Macromolecules 1992;25:290.
[25] Bohidar H, Dubin PL, Majhi PR, Tribet C, Jaeger W. Biomacromolecules 2005;6:1573.
[26] Tsuboi A, Izumi T, Hirata M, Xia JL, Dubin PL, Kokufuta E. Langmuir 1996;12:6295.
[27] Tribet C. Complexation between amphiphilic polyelectrolytes and proteins: from necklaces to gels. New York: Mercel Dekker Inc; 2001.
[28] Tribet C, Porcar I, Bonnefont PA, Audebert R. J Phys Chem B 1998;102(7):1327.
[29] Hiramatsu K, Yang JT. Biochim Biophys Acta 1983;743:106.
[30] Takeda K, Miura M, Takagi T. J Colloid Interface Sci 1981;82:38.
[31] Gouy G. ComtRend 1909;149:654.
[32] Chapman DL. Phil Mag 1913;6(25):475.
[33] Stern OZ. Electrochem 1924;30:508.
[34] Carlsson F, Malmsten M, Linse P. J Am Chem Soc 2003;125(10):3140.
[35] Zhang L, Wu BZ, Su ZQ, Chen XN. Polymer 2008;49:5622.
[36] Papadopoulou A, Green RJRA, Frazier J. Agric Food Chem 2005;53(1):158.
[37] Fleer G, Cohen Stuart M, Scheutjens J, Cosgrove T, Vincent B. Polymers at interfaces. Springer; 1993.
[38] Goddard E, Ananthapadmanabhan K. Interactions of surfactants with polymers and proteins. Boca Raton, FL: CRC Press; 1992.

Polymer 52 (2011) 1092–1101

Contents lists available at ScienceDirect

Polymer

journal homepage: www.elsevier.com/locate/polymer

Effect of N-substituents on the surface characteristics and hydrogen bonding network of polybenzoxazines

Huijie Dong, Zhong Xin*, Xin Lu, Yuhao Lv

State Key Laboratory of Chemical Engineering, East China University of Science and Technology, Shanghai 200237, China

ARTICLE INFO

Article history:
Received 14 September 2010
Received in revised form
11 December 2010
Accepted 6 January 2011
Available online 12 January 2011

Keywords:
Polybenzoxazine
Surface energy
Hydrogen bonding

ABSTRACT

In our study, the effect of N-substituents on the surface free energy and hydrogen bonding network structure of polybenzoxazine has been studied systematically. The contact angle measurement results show the surface energies of the polybenzoxazines decrease with the increase of alkyl chain length, and are not affected by the steric factor of the tert-butyl group. However, the FTIR curve fitting results show that both the chain length and bulkiness of alkyl group have an effect on the hydrogen bonding network of the polybenzoxazines, and facilitate the formation of intermolecular hydrogen bonding during the progress of cure. This indicates that both alkyl group and the fraction of intermolecular hydrogen bonding have an effect on the surface energy of the polybenzoxazines. Additionally, the transformation mechanism of the intermolecular and intramolecular hydrogen bonding during the progress of cure is proposed for the first time.

1. Introduction

A low surface energy behavior is important for many practical applications in coatings, selfcleaning, and biomaterials [1–6]. Recently, polybenzoxazine has been developed and reported as a novel class of nonfluorine, nonsilicon, low surface energy materials [6,7], having advantages of low cost and easy processability compared with conventional fluoropolymers or silicones [8–11]. It is expected to gain promising future due to their unique advantages, and having a wide range of applications such as super hydrophobic surfaces, in lithographic patterning, and as mold-release materials in nanoimprint technology [8–10].

As mentioned in the literature, polybenzoxazines have been reported to show both inter- and intramolecular hydrogen bonding network structure [12–14]. Wang et al. discovered that the lowest surface free energies of the two polybenzoxazines based on aniline and methylamine were 19.21 and 16.43 mJ/m^2 respectively, which were even lower than that of Teflon (21.0 mJ/m^2) [7]. They thought that this behavior is due to the presence of strong intramolecular hydrogen bonding matrix in the polybenzoxazines systems, and intramolecular hydrogen bonding leads to a decrease in the surface free energy, whereas increasing the fraction of intermolecular hydrogen bonding leads to opposite effect. Kuo prepared a low-surface-energy polymer material (16.8 mJ/m^2) by decreasing the fraction of intermolecular hydrogen bonds between the OH groups in poly(vinyl phenol)/polybenzoxazine blends [15]. Lin et al. discovered that poly(vinyl phenol) (PVPh) also possesses low surface energy (15.7 mJ/m^2) by decreasing the degree of intermolecular hydrogen bonding between its OH groups after a simple thermal treatment procedure. The manipulation of intermolecular hydrogen bonding interactions had shown a good prospect as a unique and simple approach toward preparing low-surface-energy materials without the need to employ fluoropolymers or silicones.

Although hydrogen bonding is important to control the surface properties in the polybenzoxazine system, the relationship between the surface free energy and the fraction of intermolecular or intramolecular hydrogen bonding remains poorly understood [15]. Up to now, the surface energy of only two polybenzoxazines based on aniline and methylamine were investigated, and a difference in hydrogen bonding network structure and surface energy was observed between methylamine based polybenzoxazines and aniline-based polybenzoxazines. Ishida et al. investigated the correlation between the –OH…N intramolecular hydrogen bonding interaction and amine functional groups in the asymmetric dimers by ^{1}H NMR spectra, and reported that the differences in the hydrogen-bonded structures of the model benzoxazine dimers is closely related to the amine groups [16]. They also studied that the compactness of a network structure is related to both the basicity and bulkiness of the functional amines [17]. The potential contribution of alkyl group of primary amine to the polymer hydrogen

* Corresponding author. Tel.: +86 021 64252972; fax: +86 021 64253159.
E-mail address: xzh@ecust.edu.cn (Z. Xin).

0032-3861/$ – see front matter © 2011 Elsevier Ltd. All rights reserved.
doi:10.1016/j.polymer.2011.01.009

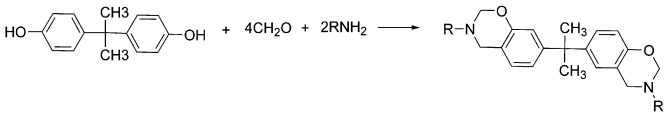

Scheme 1. Preparation of the benzoxazine monomers(R: methyl; ethyl; butyl; tert-butyl).

bonding network structure and surface free energy were not formally investigated.

In this study, four aliphatic primary amine based benzoxazine monomers were synthesized to explore the effect of N-substituents on the surface energy and hydrogen bonding structure of polybenzoxazine. The effect of aliphatic chain length and steric effect on the polybenzoxazines film-forming property is also probed. Additionally, the thermal stability of the polybenzoxazines was characterized through TGA.

2. Experimental

2.1. Materials

Bisphenol A and formaldehyde (37% in water), primary amine were supplied by the Sinopharm Chemical Reagent Co of China. All chemicals were used without further purification. In this paper, the benzoxazine monomers were synthesized according to the procedure presented in Scheme 1 [18], R in the structure denotes the substituent of the primary amine. Various primary amines including methylamine, ethylamine, butylamine, and tert-butylamine were used. The monomers will be referred to as B-m, B-e, B-b and B-t, respectively. The crude product was dissolved in ether and washed with aqueous NaOH for three times to remove phenolic oligomers, followed by distilled water, and then drying over sodium sulfate. Evaporating the ether resulted in white solid powder for B-m and B-t, and yellow viscous fluids for B-e and B-b respectively. All monomers were refrigerated until the time of use. Successful synthesis and purity were verified by ^{1}H NMR and FTIR spectroscopy.

2.2. Characterization

The benzoxazine monomer was diluted to 30 mg/ml or 200 mg/ml in THF respectively, and the solution was filtered through a 0.2 μm syringe filter (Celanese, America) before spin coating onto a glass slide ($100 \times 100 \times 1$ mm^3). The glass slides were cleaned by Piranha solution (7:3 mixtures (v/v) of 98% H_2SO_4 and 30% H_2O_2) at 120 °C for 30 min before use, and then rinsed by deionized water. The solution was spin-coated at 1500 rpm for 45 s and evaporated in a vacuum oven at 60 °C for 1 h, then cured in an oven at 180 °C or 210 °C. The cured polymers were referred to as B-m, B-e, B-b and B-t polybenzoxazine, respectively. The advancing contact angle measurement of the film was measured using the sessile drop (needle in) technique (OCA20, Data Physics Instruments, Germany) at room temperature. The contact angles of deionized water, ethylene glycol and diiodomethane were further adopted to estimate the surface free energy using van Oss-Good acid/base theory [19,20].

Infrared spectra were acquired with a Nicolet iS10 FTIR spectrophotometer. The sample was prepared by casting the solution directly onto a KBr plate and curing under conditions similar to those used in the film preparation.

Surface profiles of films were acquired with an optical microscope (BX41-P, Olympus). Thermogravimetric analysis (TGA) was conducted with SDT Q600 V5.0 Build 63 under a 40 ml/min flow of nitrogen gas at a scan rate of 10 °C/min over the temperature range from 30 to 800 °C.

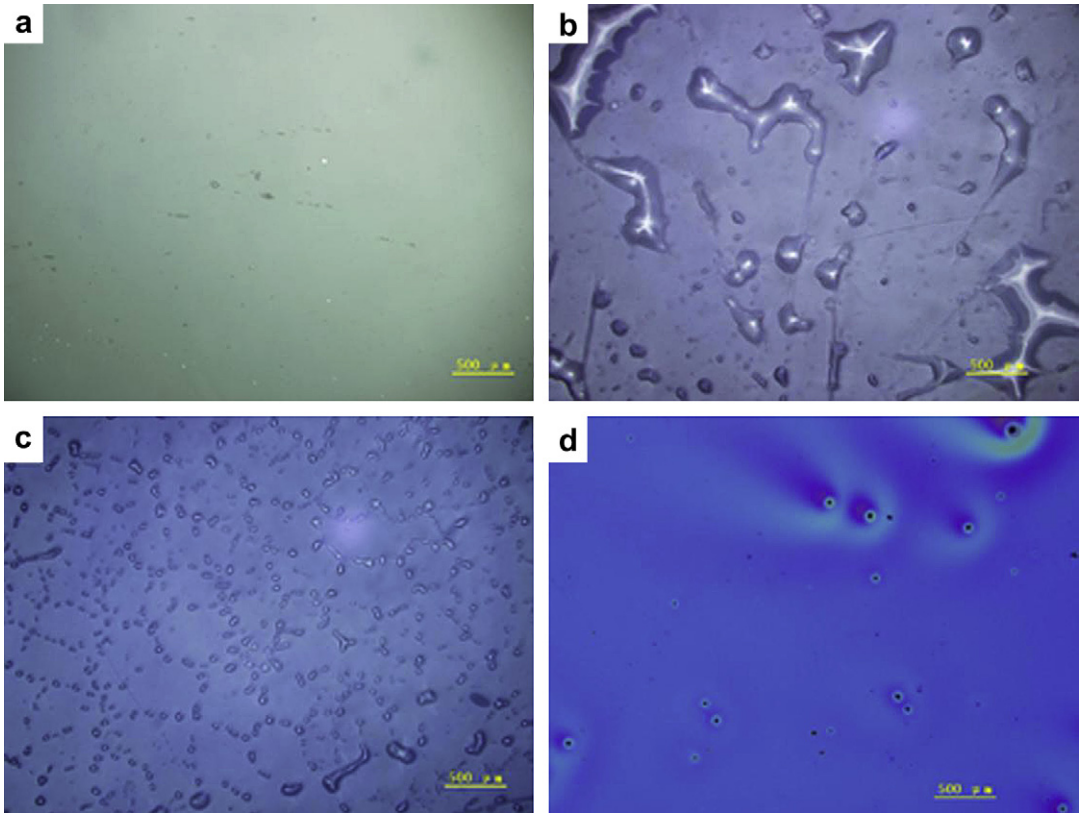

Fig. 1. Optical microscope of glass slides spin-coated with different benzoxazine monomers after drying at 60 °C for 1 h a) B-m; b) B-e; c) B-b; d) B-t.

3. Results and discussion

3.1. Film-forming characteristic of polybenzoxazines

We employed optical microscope to observe the surface morphology of the benzoxazines films. The solution was spin-coated at a concentration of 30 mg/ml. As shown in Fig. 1, B-m and B-t can form smooth and uniform films on the glass slides before and after cure. The B-m film thickness is 20 nm. Although B-e and B-b can form a film on the glass slides by spin coating initially, then the film dewets and beads up after dry at 60 °C for 1 h. We think that the thin films are not dynamically stable [21]. We know that the spreading coefficients, $S_{liquid/solid} = \gamma_{solid}-(\gamma_{liquid} + \gamma_{liquid/solid})$, should be positive for a liquid to spread on a solid surface [22]. As shown in Table 1, with the increase of alkyl chain length of primary amine, the surface tension (γ_{liquid}) of B-m, B-e and B-b are 55.03, 64.91, 54.99 mJ/m^2 respectively. So we think that the interfacial tension ($\gamma_{liquid/solid}$) between the solution and substrate probably increases very much because of the increase of alkyl group hydrophobic, which lead to the negative spreading coefficients [21].

Reiter [23] reported that film thickness has effect on the spreading and stability of liquid films on the substrate. Wang [9] suggested the observed surface free energy of the polybenzoxazine film is fairly independent of its film thickness, and the advancing contact angles vary insignificantly upon decreasing the thickness of the polybenzoxazine films as shown in the literature. Therefore, we improved the concentrations of the solution to 200 mg/ml and increase the thickness of the films. Upon this concentration, the films thickness is about 450 nm and all polybenzoxazines can form uniform and stable films before and after cure. As an example, B-m and B-e polybenzoxazine films cured at 180 °C for 1 h are listed in Fig. 2.

3.2. Surface free energy analysis of polybenzoxazines

The effect of alkyl functional group on the surface energies of the aliphatic primary amine based polybenzoxazine series was studied by the contact angle measurement. The surface free energies of the four polybenzoxazines films cured at 180 °C and 210 °C were measured respectively. The results cured at 180 °C were summarized in Table 1 as an example. As can be seen from the summarized data in Fig. 3 a), the surface free energies of the B-m, B-e and B-b polybenzoxazines decrease as a function of alkyl chain length, and all decrease initially and then remain almost constant upon increasing the curing time from 0.5 h to 18 h. The B-b polymer, butylamine-based benzoxazine, exhibits the lowest surface energy value of 15.72 mJ/m^2 after curing for 18 h, and that of the B-e polybenzoxazine is 20.61 mJ/m^2, which are all lower than that of the B-m polybenzoxazine (24.26 mJ/m^2). From the structural point of view, the B-b polybenzoxazine with a longer alkyl chain is expected to be more hydrophobic.

As shown in Table 1, the total surface surface energy of polybenzoxazine surfaces are dominated mainly by the apolar component (γ^{LW}). The γ^+ (lewis acid parameters), γ^- (lewis base parameters) and γ^{AB} (hydrogen bonding force) values of the four polybenzoxazines films follow a similar trend with that of surface free energy, and decrease initially and then remain almost in a close range (0–2 mJ/m^2) upon increasing the curing time from 0.5 h to 18 h. Ishida et al. have speculated that the –OH…N intramolecular hydrogen bond interaction results in helical conformations of the B-m polybenzoxazine. In such a structure, the hydrogen bonds are on the inner side of the helix, which induce the hydrophobic methyl groups to be located on the surface [12,14,24,25]. As we observed, with the increase of alkyl chain length, the surface energy of the polybenzoxazine decreases gradually. Therefore, we think

Table 1
Surface free energies and advancing contact angles for water, ethylene glycol (EG), and diiodomethane (DIM) on B-m, B-e, B-b and B-t polybenzoxazines films (cured at 180 °C).

T, °C	t,h	Contact angle, °			Surface free energy, mJ/m^2				
		H_2O	EG	DIM	γ^+	γ^-	γ^{AB}	γ^{LW}	γ
B-m polybenzoxazine									
60	1	76.3	60.4	16.8	0.88	11.58	6.38	48.65	55.03
180	0.5	98.7	62.3	42.5	0.05	0.03	0.07	38.33	38.41
	1	110.7	86.3	64.5	0.11	0.08	0.19	25.99	26.18
	2	109.1	85.8	62.4	0.19	0.21	0.40	27.19	27.59
	4	111.4	87.1	66.6	0.08	0.07	0.15	24.79	24.94
	8	111.3	86.2	66.2	0.06	0.04	0.10	25.02	25.11
	18	111.2	88.9	68.1	0.13	0.20	0.32	23.94	24.26
B-e polybenzoxazine									
60	1	72.2	74.0	20.0	4.01	25.23	20.12	47.78	67.91
180	0.5	106.6	80.2	53.6	0.17	0.08	0.24	32.25	32.49
	1	108.9	84.1	55.9	0.32	0.09	0.34	30.93	31.27
	2	109.8	84.9	59.7	0.20	0.07	0.24	28.75	28.98
	4	108.4	91.8	70.8	0.31	1.23	1.22	22.43	23.65
	8	107.2	90.1	74.9	0.08	1.44	0.66	20.18	20.84
	18	106.8	87.8	74.6	0.02	1.17	0.27	20.34	20.61
B-b polybenzoxazine									
60	1	94.3	82.4	23.0	3.45	4.82	8.15	46.84	54.99
180	0.5	110.2	85.9	59.1	0.29	0.07	0.30	29.09	29.39
	1	110.0	86.1	59.3	0.31	0.10	0.35	28.98	29.33
	2	110.3	85.1	63.7	0.08	0.06	0.14	26.45	26.59
	4	111.5	85.9	65.3	0.06	0.02	0.07	25.53	25.60
	8	109.0	95.2	75.1	0.36	1.75	1.59	20.07	21.66
	18	109.1	94.4	84.2	0.01	1.80	0.33	15.40	15.72
B-t polybenzoxazine									
60	1	82.1	70.0	4.8	2.33	9.91	9.61	50.62	60.23
180	0.5	110.6	83.3	56.1	0.20	0.00	0.01	30.82	30.83
	1	102.9	84.6	59.0	0.45	1.63	1.71	29.15	30.86
	2	109.5	89.8	61.4	0.59	0.49	1.07	27.77	28.84
	4	107.5	94.5	67.5	0.87	2.00	2.63	24.28	26.91
	8	108.6	93.9	78.1	0.14	1.73	1.00	18.48	19.48
	18	110.1	91.0	78.9	0.01	0.77	0.13	18.06	18.19

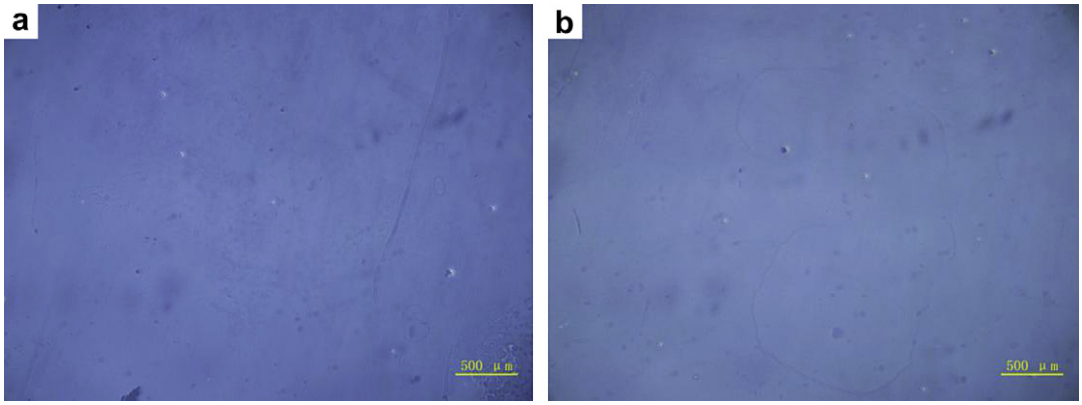

Fig. 2. Optical microscope of glass slides spin-coated with different polybenzoxazine after cured at 180 °C for 1 h a) B-m; b) B-e.

that the lowest surface energy of the B-b polybenzoxazine is due to the butyl group to be located on the surface. γ^{AB} values are far less than γ^{LW}, which is due to that the surfaces of the four polybenzoxazines are rich in the alkyl group. This results are consistent with the speculation that the hydrogen bonds are on the inner side of the helix which induce the hydrophobic groups to be located on the surface [12,14,24,25].

It is interesting that the surface energy of the B-t polybenzoxazine reaches 18.19 mJ/m^2 after curing for 8 h; it also exhibits the behavior of low surface energy, the low surface energy behavior is not affected by the steric factor of the bulkier tert-butyl group. Ishida et al. have reported that B-t dimer cannot form completely cross-linked polymer networks when cured at 155 °C due to the extensive degradation process, and the B-t polybenzoxazine is unexpectedly soluble in deuterated chloroform [16]. Whereas the B-t polybenzoxazine film we attained at 180 °C is unsoluble even after immersing in chloroform for 48 h, which indicates that the crosslinking degree of B-t polybenzoxazine cured at 180 °C is higher

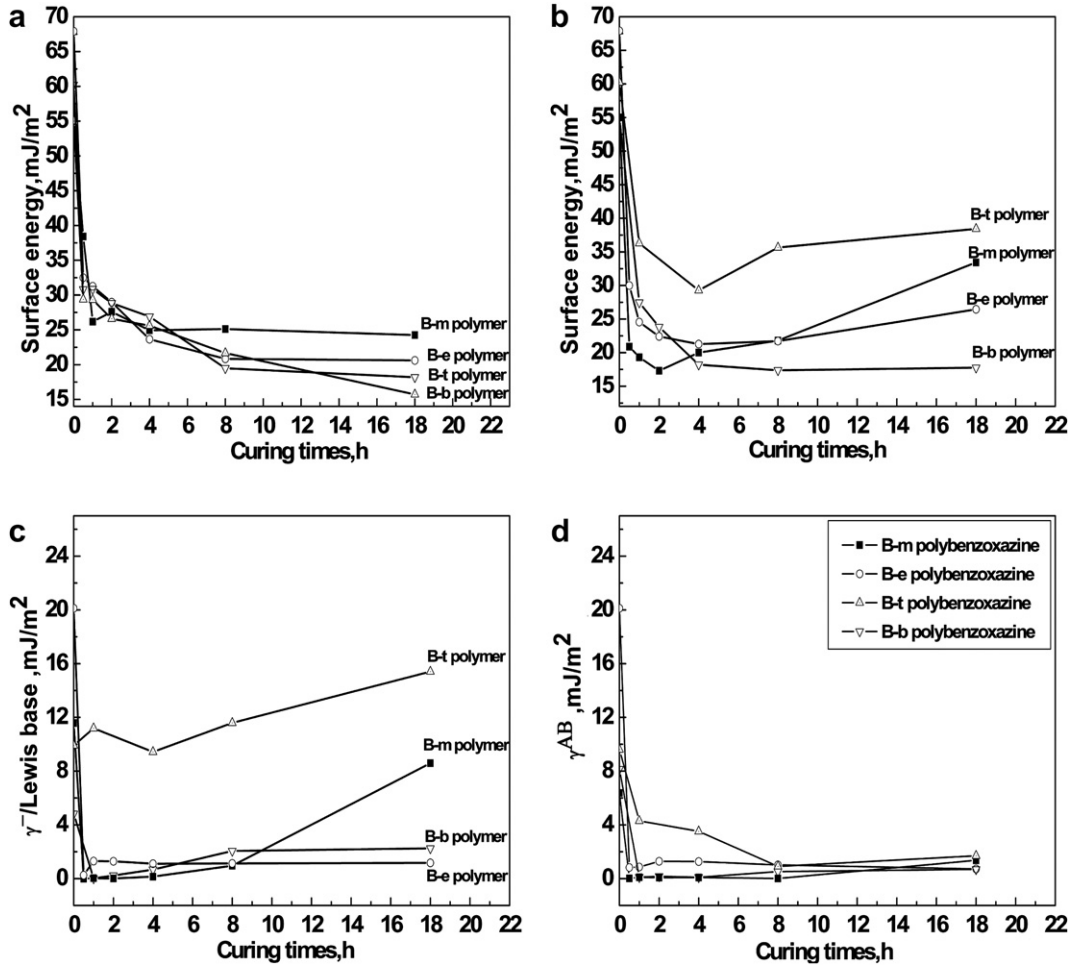

Fig. 3. Surface free energies (γ) the B-m, B-e, B-b and B-t polybenzoxazines films as a function of curing times. a) 180 °C; b) 210 °C and c) lewis base parameters (γ^-); d) hydrogen bonding force (γ^{AB}) of the four polybenzoxazines films as a function of curing times at 210 °C.

than that of polybenzoxazine cured at 155 °C, and the polymer network structure of the B-t polybenzoxazine is significantly different when cured at different temperatures. The effect of the alkyl group bulkiness on the surface energy is not noticeable.

Additionally, the surface energy results cured at 210 °C are listed in Fig. 3 b). The same trend can also be seen that the surface free energies of the polybenzoxazines decrease as a function of alkyl chain length. But it is quite noteworthy that the surface free energy of the polybenzoxazines as a function of curing time is different from each other. The B-m and B-e polybenzoxazine decreases initially and then increases steadily upon increasing the curing time from 0.5 h to 18 h, whereas that of the B-b polybenzoxazine decreases initially and then maintained almost constant up. Thus, it appears for these polymers that the surface energies are largely dependent of the alkyl chain length.

For B-m polybenzoxazine, the γ^- values decreases initially and then increases steadily upon increasing the curing time from 0.5 h to 18 h, and that of the B-e and B-b polybenzoxazine decreases initially and then maintained almost constant up (see Fig. 3c). Whereas the γ^{AB} values of the four polybenzoxazines remain almost in a close range (0–2 mJ/m^2) (see Fig. 3d), which indicates that the increase of surface energies of the B-m polybenzoxazine as a function of curing times can be attibuted to the increase of γ^- values and γ^{LW}. The smaller OH^- content of polybenzoxazine films leads to smaller γ^- values. This results show that hydroxyl groups (Lewis bases) on the film surface increase as a function of curing times for B-m polybenzoxazine.

Unexpectedly, the surface energy and γ^- value of the B-t polybenzoxazine is far higher than all the three other polybenzoxazines and increase straightly during the progress of cure. This indicated that the B-t polybenzoxazine doesn't possess the behavior of low surface energy when cured at 210 °C. Later results will show that the B-t polybenzoxazine have a somewhat lower thermal stability than the alkyl straight chain compounds, and thus it can be assumed that degradation rather than steric effect is responsible for the higher surface energy of the B-t polybenzoxazine.

3.3. Hydrogen bonding network analysis of polybenzoxazines

Wang et al. have reported that the hydrogen bonding interactions network structure of polybenzoxazine is a deciding factor of the surface energy of the polybenzoxazine [7]. Several kinds of H-bonded species has been identified in the polybenzoxazine system [13,14], such as $-OH\cdots O$ intermolecular hydrogen bonding at 3366 cm^{-1}, broad band between 2500 and 3300 cm^{-1} might be designated for $O^-\cdots H^+N$ intramolecular hydrogen bonding and/or $-OH\cdots N$ intramolecular hydrogen bonding at 3115 cm^{-1}. To investigate the effect of N-substituents on the hydrogen bonding network of the polybenzoxazines, FTIR spectra of the four polymers during the progress of cure were compared.

The spectra in the regions of hydroxyl stretching frequency were shown in Fig. 4. It can be seen clearly, the $O^-\cdots H^+N$ intramolecular hydrogen bonding around 2750 cm^{-1} of the B-m polymer appear to be stronger than that of the other three polybenzoxazines. Although methylamine, ethylamine and butylamine have similar structure, this unexpected strength difference in FTIR hydrogen bonding spectra for the longer chain length amine based polybenzoxazines implies that a size and structural factor may strongly affect the hydrogen-bonded network structure of the polymer.

We performed curve-resolving of FTIR spectra with respect to the corresponding frequencies of each hydrogen-bonded species. The results of curve-resolving of FTIR spectra of the B-m and B-b polybenzoxazines cured at 180 °C were shown in Fig. 5 as an example, and the variations of fraction of intermolecular hydrogen bonding with curing times were shown in Fig. 6.

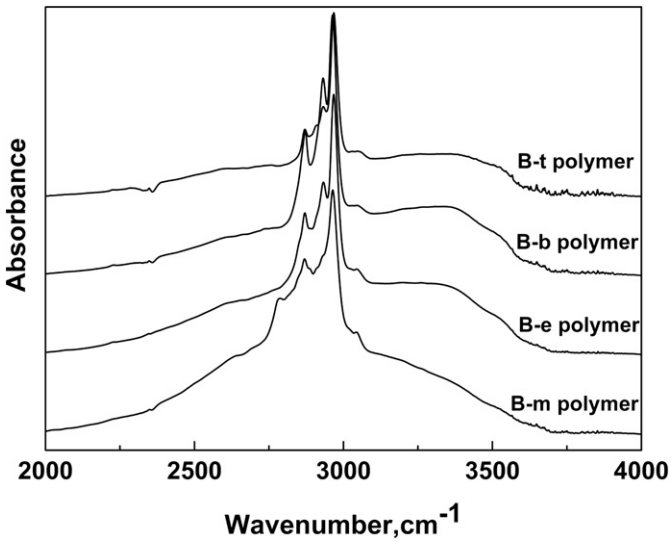

Fig. 4. FTIR spectra in the region of the hydroxyl stretching frequency for (a) B-m polymer, (b) B-e polymer, (c) B-b polymer, (d) B-t polymer cured at 180 °C for 8 h.

As shown in Fig. 5, for the B-m and B-b polybenzoxazines, the intensity of the signals corresponding to the intermolecular hydrogen bonding at 3356 cm^{-1} all increase upon increasing the curing time. However, the fraction of intermolecular hydrogen bonding in the B-b polybenzoxazine system is higher than that of the B-m polybenzoxazine.

From Fig. 6, it is apparent that the fraction of intermolecular hydrogen bonding increases as a function of curing times. This trend coincides with the conclusions reported by Wang et al. [7]. However, the fraction of intermolecular hydrogen bonding also increases as a function of alkyl chain length, which indicates that the distribution of hydrogen bond species is different for each of polybenzoxazines. As reported in the literature by Ishida [17], the intramolecular hydrogen bond length increases as the number of alkyl chain increases. Therefore, we think that both the chain length and bulkiness of alkyl group have an effect on the hydrogen bonding network of the polybenzoxazine, and facilitate the formation of intermolecular hydrogen bonding during the progress of cure.

As we discussed above, the surface free energies of the B-m, B-e and B-b polybenzoxazines decrease as a function of alkyl chain length. However, the γ^{AB} values of the four polybenzoxazines remain almost in a close range (0–2 mJ/m^2) and maintain constant up as a function of curing times. Therefore, the increase of the fraction of intermolecular hydrogen bonding as a function of curing times do not lead to the obvious increase of γ^{AB} value for each of polybenzoxazines, which indicates that surface energy of the polybenzoxazine is affected by both hydrogen bonding and alkyl group attached to the nitrogen atom. But for B-m polybenzoxazine, the γ^- values decrease initially and then increase upon increasing the curing time and that of the B-e and B-b polybenzoxazine maintained almost constant up. We think that the γ^- is a reflection of the reduced availability of the nonbonded electron pairs due to the masking effects of the long carbon chains.

3.4. Transformation mechanism of intramolecular and intermolecular hydrogen bonding

As discussed above, the surface energies of the B-m and B-e polybenzoxazine decreases initially and then increases steadily

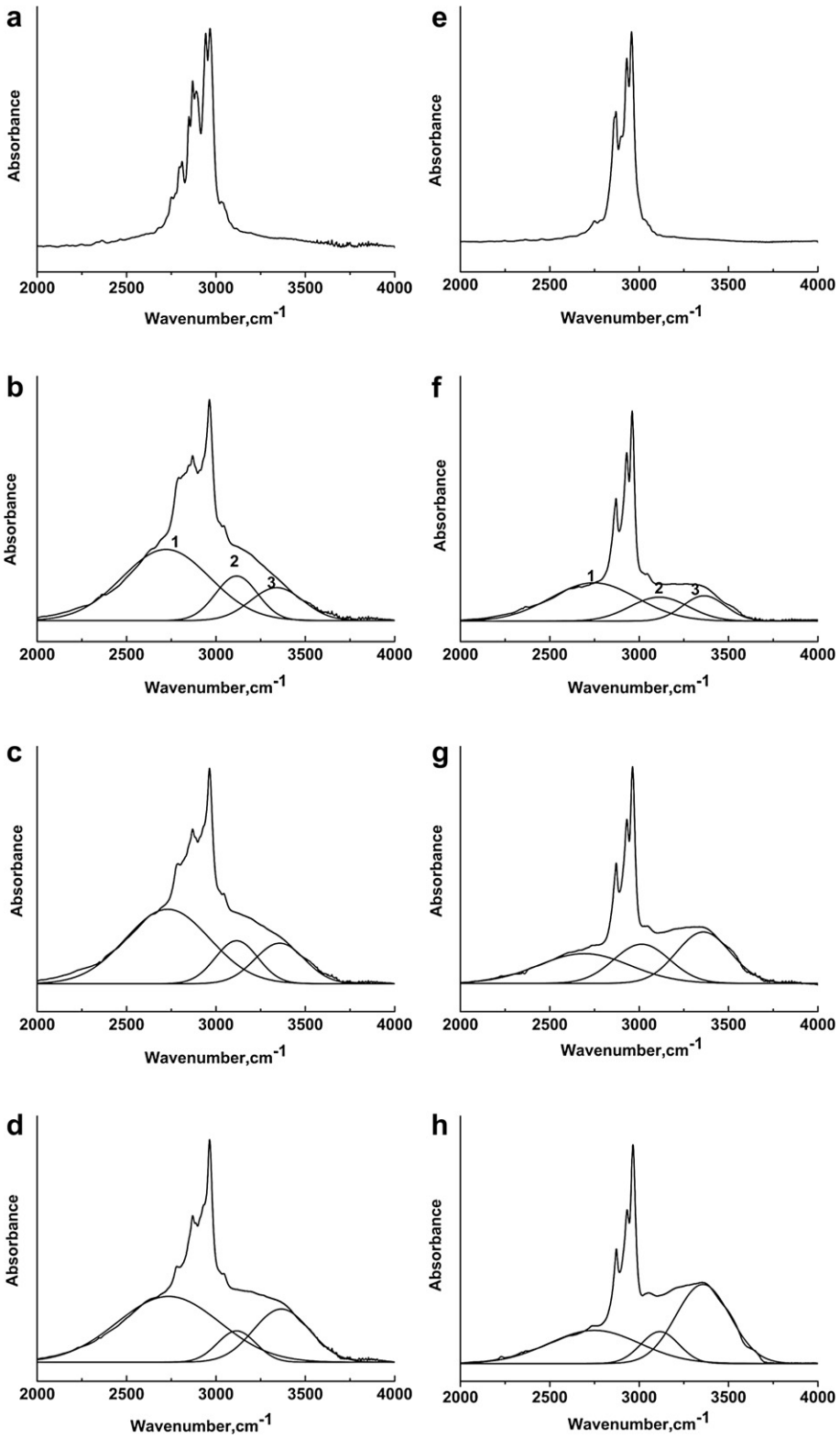

Fig. 5. Curve fitting for the FTIR spectra of the B-m polybenzoxazine cured at 180 °C for a) 0, b) 2, c) 8, and d) 18 h; and the B-b polybenzoxazine cured at 180 °C for e) 0, f) 2, g) 8, and h) 18 h. 1) $O^{-}\cdots H^{+}N$ intramolecular hydrogen bonding; 2) OH···N intramolecular hydrogen bonding; 3) OH···O intermolecular hydrogen bonding.

upon increasing the curing time from 0.5 h to 18 h when cured at 210 °C, whereas that of the B-b polybenzoxazine decreases initially and then maintained almost constant up. Wang et al. [7] proposed that enhanced intramolecular hydrogen bonding lead to a decrease in the surface free energy of the B-m polybenzoxazine, whereas increasing the fraction of intermolecular hydrogen bonding lead to the opposite effect. However, the intramolecular hydrogen-bonded structure of polybenzoxazine is very stable even as high of

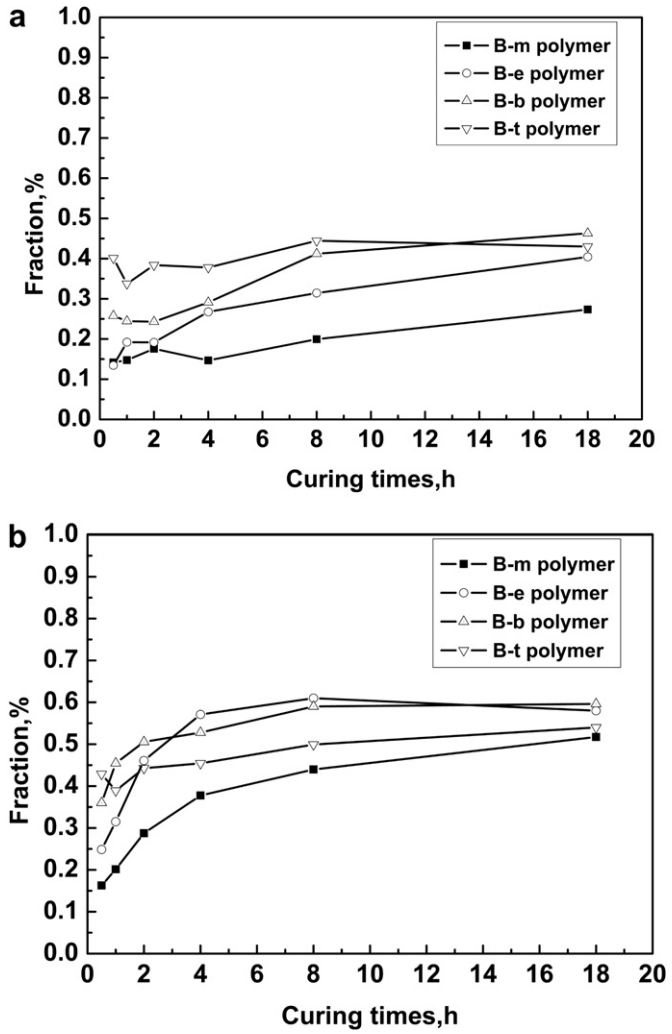

Fig. 6. Variations of the fraction of intermolecular hydrogen bonding of the four polybenzoxazines cured at: a) 180 °C; b) 210 °C.

a temperature as 300 °C [13,25–27]. Up to now, it is still unclear that how the fraction of intermolecular hydrogen bonding increases during the progress of cure. Therefore, the FTIR spectra between 600 and 2000 cm^{-1} of the polybenzoxazines as a function of curing times are compared and shown in Fig. 7.

In the B-m polybenzoxazine system cured at 180 °C, the characteristic absorptions of benzoxazine structure for B-m at 932 cm^{-1} and 1497 cm^{-1} (trisubstituted benzene ring of B-m) disappear when cured for 1 h. At the same time, one unexpected feature of a broad band at 1638 cm^{-1} appears when cured from 1 to 8 h, and the spectra of the B-b and B-t polybenzoxazines also show a similar broad band at 1635 and 1632 cm^{-1} respectively. As reported in the literature [28,29], these bands were assigned to a hydrogen-bonded Schiff base (C═N). The C═N stretching frequency is slightly lower for the B-b and B-t polybenzoxazines than that of the B-m polybenzoxazine, which is probably due to the inductive effect of increasing number of carbon atoms. In the B-b and B-t polybenzoxazines system, the Schiff base band is not as same strong as the B-m polybenzoxazine, indicating that the concentration of Schiff base may differ from one polybenzoxazine to another, depending on the substituent attached to the nitrogen.

Interestingly, for the B-m and B-b polybenzoxazines cured at 210 °C, it is shown that the concentration of the band at 1655 cm^{-1} and 1653 cm^{-1} increase as a function of the curing times, respectively. These band assignments of Schiff base have also been reported elsewhere, and were assigned to a free Schiff base (C═N) (non-hydrogen-bonded) [28,29]. We think that the free and hydrogen-bonded Schiff base could be the terminal groups in polybenzoxazines or defect structures after thermal degradation in polybenzoxazines when cured at 210 °C. At the same time, as shown in Fig. 8, a peak at 3650 cm^{-1} is detected in all of the polybenzoxazines spectra with the increase of the curing times, which indicates the appearance of free OH stretching. Combined with the results shown in Fig. 9, the onset thermal degradation temperature and char yield of the B-m polybenzoxazine increases with curing times; this indicates that thermal degradation partially of polybenzoxazines exists during the progress of cure. Therefore, we speculate that the increasing of the concentration of free Schiff base when cured at 210 °C is the results of thermal degradation partially of the B-m and B-b polybenzoxazines.

According to the thermal cleavage mechanism of the Mannich base proposed by Ishida [29], due to the energetically stable six-membered ring of intramolecular hydrogen bonding, a more likely cleavage point in this structure is the C-N bond that is not part of this six-membered ring. Based on our observations, the transformation progress of intramolecular and intermolecular hydrogen bonding in the polybenzoxazines system is proposed in Scheme 2. The increase of the fraction of intermolecular hydrogen bonding is not due to the disruption of intramolecular hydrogen-bonded, but the disruption of the C–C bond from the Mannich base.

Considering the electron donating effect of methyl group attached to the nitrogen atom in the B-m polybenzoxazine is weaker than butyl group in the B-b polybenzoxazine, the strength of the adjacent C-N bond of the former should be higher than the latter. Consequently, the B-b polybenzoxazine is easier to degrade to produce free Schiff base than the B-m polybenzoxazine during the progress of cure at 210 °C. Therefore the fraction of intermolecular hydrogen bonding increases with the alkyl chain length as we observed in Fig. 5. Although the fraction of intermolecular hydrogen bonding increases, the surface energy of the B-b polybenzoxazine can be maintained almost constant up at 210 °C. It may be contributed to the most hydrophobic of the butyl group.

3.5 Thermal stability of polybenzoxazines

TGA was studied to examine the effect of alkyl chain length and size on the thermal stability of the polybenzoxazines. Firstly, TGA of the B-m polybenzoxazine as a function of curing times was conducted. The results show that the onset and progression of weight loss is slower with the increase of curing times. The char yield B-m increased from 37.15%, to 45.94% and 49.86% as the curing times increase. Moreover, a two-stage weight loss process was observed for the B-m polybenzoxazine cured for 1 h, and a more rapid degradation (sharper slope) was observed between 260 and 320 °C for the B-m polybenzoxazine cured for 1 h when compared with 4 h and 8 h. It has been confirmed that the first step of degradation is due to Mannich base cleavage (the cleavage of the C-N bond), resulting in the release of Schiff base (C═N) in the literature. We think that the first step of degradation mainly happens when curing from 1 h to 4 h. This result suggests that the thermal degradation of the B-m polybenzoxazine exists in the progress of cure at 210 °C.

The four monomers were cured at 180 °C for 4 h respectively to prepare the TGA samples. Fig. 10 shows the TGA results of the four polybenzoxazines. For B-m, B-e and B-b polymers, it is obvious also that the onset temperature of weight loss decreased for the longer chain amine polybenzoxazines. The char yield decreased to 35.69%, 28.66% and 23.62% as the length of alkyl chain increases. For the B-t polybenzoxazine based on bulkier tert-butylamine, T_5 and T_{10} all

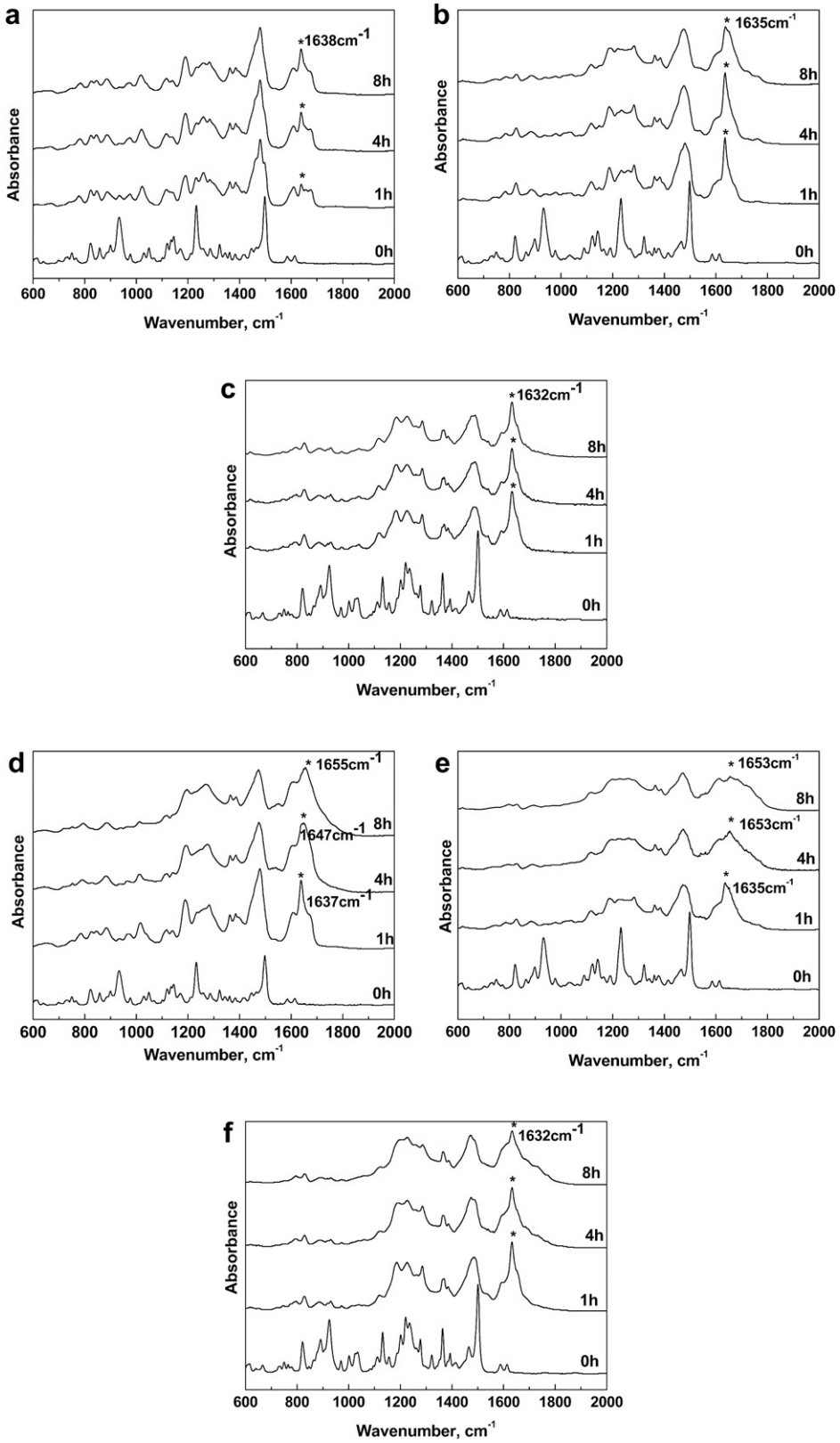

Fig. 7. FTIR spectra as a function of curing times. a, b, c) B-m, B-b, B-t polymers cured at 180 °C; d, e, f) B-m, B-b, B-t polymers cured at 210 °C.

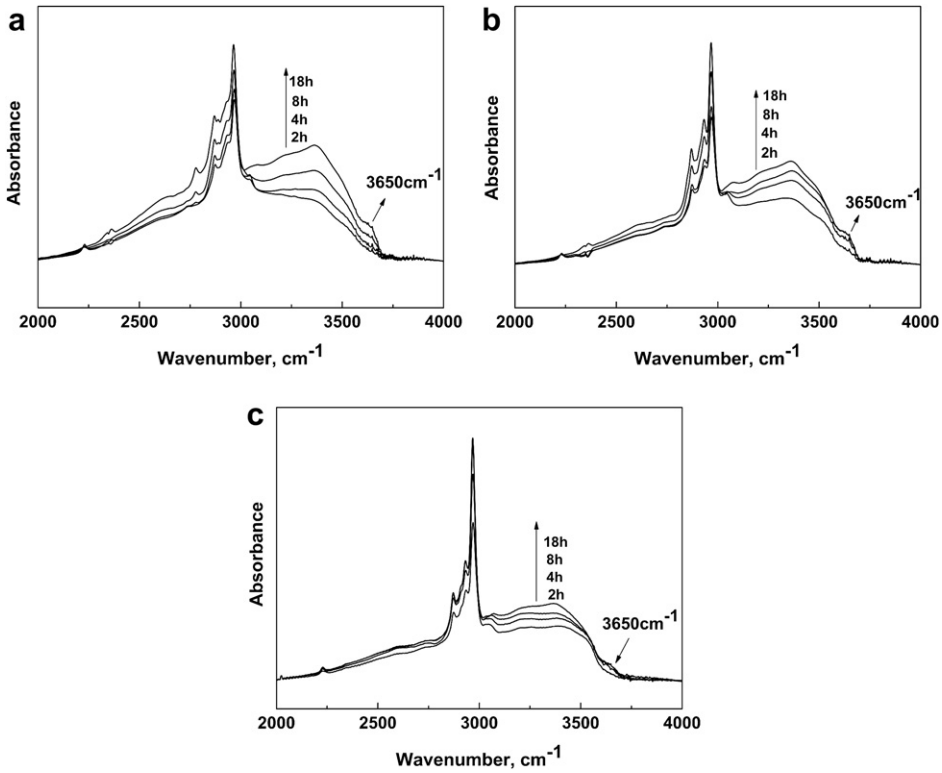

Fig. 8. FTIR spectra in the region of the hydroxyl stretching frequency for (a) B-m polymer, (b) B-b polymer, (c) B-t polymer cured at 210 °C.

are lower than the other three polybenzoxazines with straight alkyl chain, and the progression of weight loss is the fastest among the polybenzoxazines. This indicated that the thermal stability of the B-t polybenzoxazine is inferior to the polybenzoxazines with straight alkyl chain. We think that although the surface energy of the B-t polybenzoxazine after cured at 180 °C is even lower than the B-m and B-e polybenzoxazines, the polymer structure of the B-t polybenzoxazine is still unstable than the B-m, B-e and B-b polybenzoxazines at higher temperatures because of the steric factor of bulkier tert-butylamine, and the char yield of the B-t polybenzoxazine is 31.47%. As discussed in the literature [25,29], char is comprised of fused benzene rings, the decrease in char yield is mainly attributed to the longer aliphatic group has a higher weight contribution to the total weight of the polybenzoxazines. But the char yield of the B-t polybenzoxazine is not correlated with this trend, indicating that the decomposition process of the B-t polybenzoxazine is probably different from polybenzoxazines with straight alkyl chain.

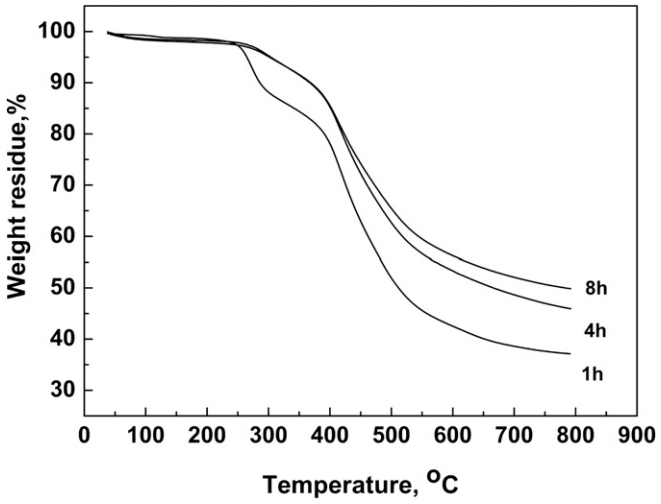

Fig. 9. TGA of the B-m polybenzoxazine as a function of curing times at 210 °C.

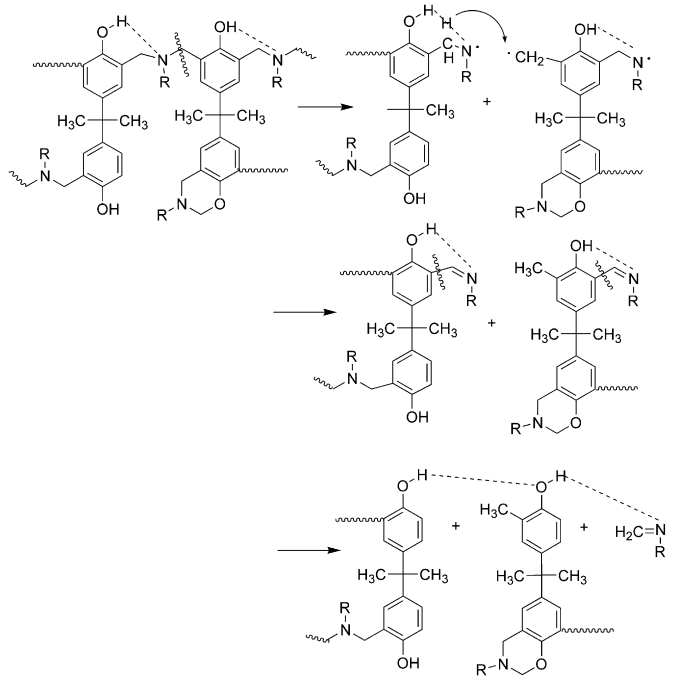

Scheme 2. Transformation mechanism of intramolecular into intermolecular hydrogen bonding in the polybenzoxazines system.

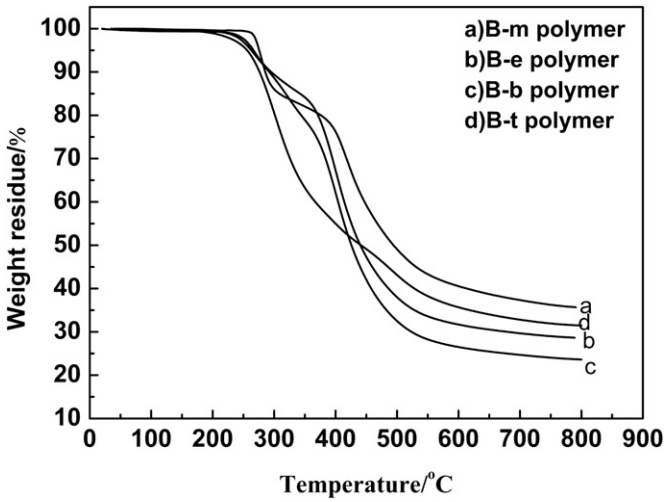

Fig. 10. TGA of the four polybenzoxazines cured at 180 °C for 4 h. (a) B-m polymer, (b) B-e polymer, and (c) B-b polymer. (d) B-t polymer.

4. Conclusions

Four benzoxazine monomers based on methylamine, ethylamine, butylamine and tert-butylamine were synthesized to study the effect of N-substituents on the surface energy and hydrogen bonding network structure of polybenzoxazines. The contact angle measurement results show the surface energies of the polybenzoxazines decrease with the increase of alkyl chain length, and are not affected by the steric factor of the tert-butyl group. The lowest value of surface energy of the B-b polybenzoxazine reaches 15.72 mJ/m^2 after curing at 180 °C for 18 h, which is lower than that of B-m polybenzoxazine (24.26 mJ/m^2). The FTIR curve fitting results indicate that both the chain length and bulkiness of alkyl group have an effect on the hydrogen bonding network of the polybenzoxazines, and facilitate the formation of intermolecular hydrogen bonding during the progress of cure. The increase of the fraction of intermolecular hydrogen bonding as a function of curing times do not lead to the obvious increase of γ^{AB} value for each of polybenzoxazines. We think that the surface energy of the polybenzoxazine is affected by both hydrogen bonding and alkyl group attached to the nitrogen atom.

FTIR spectra of the polybenzoxazine during the progress of cure were compared. The appearance of free OH stretching and the increasing bond strength of free Schiff base indicate that the thermal degradation exists during the cure. Combined with the thermal degradation progress of the polybenzoxazines, transformation mechanism of intramolecular and intermolecular hydrogen bonding during the cure is proposed for the first time.

Acknowledgments

This study was funded by the Nano-tech Foundation of Science and Technology Commission of Shanghai Municipality (Grant number: 0652nm001). The authors would like to thank Chih-Feng Wang of I-Shou University and professor Feng-Chih Chang of the Department of Applied Chemistry, National Chiao-Tung University in Taiwan, for their helpful discussion.

References

[1] Coulson SR, Woodward I, Badyal JPS, Brewer SA, Willis C. J Phys Chem B 2000;104:8836.
[2] Nakajima A, Fujishima A, Hashimoto K, Watanabe T. Adv Mater 1999;11:1365.
[3] Woodward I, Schofield WCE, Roucoules V, Badyal JPS. Langmuir 2003;19:3432.
[4] Tsibouklis J, Stone M, Thorpe AA, Graham P, Peters V, Heerlien R, et al. Biomaterials 1999;20:1229.
[5] Lindner E. Biofouling 1992;6:193.
[6] Lu CH, Su YC, Wang CF, Huang CF, Sheen YC, Chang FC. Polymer 2008;49:4852.
[7] Wang CF, Su YC, Kuo SW, Huang CF, Sheen YC, Chang FC. Angew Chem Int Ed 2006;45:2248.
[8] Liao CS, Wang CF, Lin HC, Chou HY, Chang FC. Langmuir 2009;25:3359.
[9] Wang CF, Chiou SF, Ko FH, Chen JK, Chou CT, Huang CF, et al. Langmuir 2007;23:5868.
[10] Wang CF, Wang YT, Tung PH, Kuo SW, Lin CH, Sheen YC, et al. Langmuir 2006;22:8289.
[11] Chernykh A, Agag T, Ishida H. Polymer 2009;50:3153.
[12] Kim HD, Ishida H. Macromol Symp 2003;195:123.
[13] Kim HD, Ishida H. J Phys Chem A 2002;106:3271.
[14] Goward GR, Sebastiani D, Schnell I, Spiess HW, Kim H-D, Ishida H. J Am Chem Soc 2003;125:5792.
[15] Kuo SW, Wu YC, Wang CF, Jeong KU. J Phys Chem C 2009;113:20666.
[16] Kim HD, Ishida H. Macromolecules 2003;36:8320.
[17] Ishida H, Low HY. Macromolecules 1997;30:1099.
[18] Ning X, Ishida H. J Polym Sci Part A: Polym Chem 1994;32:1121.
[19] Loeb GI, Schrader ME. Plenum New York. 1992.
[20] Van Oss CJ, Ju L, Chaudhury MK, Good RJ. J Colloid Interface Sci 1989;128:313.
[21] Cheng X, Guo LJ, Fu PF. Adv Mater 2005;17:1419.
[22] Yerushalmi-Rozen R, Klein J. Langmuir 1995;11:2806.
[23] Reiter G, Auroy P, Auvray L. Macromolecules 1996;29:2150.
[24] Dunkers J, Zarate EA, Ishida H. J Phys Chem 1996;100:13514.
[25] Schnell I, Brown SP, Low HY, Ishida H, Spiess HW. J Am Chem Soc 1998;120:11784.
[26] Freedman HH. J Am Chem Soc 1961;83:2900.
[27] Low HY, Ishida H. J Polym Sci Part B Polym Phys 1935;1998:36.
[28] Hemvichian K, Kim HD, Ishida H. Polym Degrad Stab 2005;87:213.
[29] Kim HJ, Brunovska Z, Ishida H. Polymer 1999;40:6565.

Polymer 52 (2011) 1102–1106

Contents lists available at ScienceDirect

Polymer

journal homepage: www.elsevier.com/locate/polymer

Nucleation effect on polymorphism of melt-crystallized syndiotactic polystyrene

Ming Lu [a], Xiang Zhao [b], Lan Chen [c], Xiaomin Xiong [c], Jingxiu Zhang [c], Kancheng Mai [b,*], Chuanbin Wu [a,**]

[a] School of Pharmaceutical Sciences, Sun Yat-sen University, Guangzhou 510006, China
[b] School of Chemistry and Chemical Engineering, Sun Yat-sen University, Guangzhou 510275, China
[c] School of Physics and Engineering, Sun Yat-sen University, Guangzhou 510275, China

ARTICLE INFO

Article history:
Received 4 September 2010
Received in revised form
14 November 2010
Accepted 27 November 2010
Available online 4 December 2010

Keywords:
Syndiotactic polystyrene
Nucleation barrier
Nucleating agent

ABSTRACT

The main purpose of this study is to examine the effect of nucleation on the formation of polymorphism in melt-crystallized syndiotactic polystyrene (sPS). By depressing the nucleation barrier (i.e., introducing nucleating agent), the tendency of forming, a metastable crystalline phase, α crystal, significantly increased. The metastability of crystalline phase was dependent upon the nucleation process in which the lower nucleation barrier led to the formation of metastable phase. Consistently, by crystallizing under shearing, the formation of α crystal dominated the crystalline polymorphism. Herein we suggest a practical method to control the polymorphism of melt-crystallized sPS.

1. Introduction

Polymorphism of syndiotactic polystyrene (sPS), generally including four crystal forms described as α, β, γ and δ, has been extensively studied in recent years [1–9]. As an excellent engineering material, polymorphous behavior of sPS during melt-crystallization obtained special attention. Two types of melt-crystallized crystal structures have been identified as α and β crystal, both containing a planar-zigzag conformation of backbone chains. β crystal form is characterized by orthorhombic chain packing, whereas α crystal form is characterized by trigonal chain packing. These two crystal forms have different physical properties, such as density [10,11], gas permeability [12–15], thermal stability [13,16,17], and solvent resistance [18] et al. Therefore, the control of crystalline polymorphism in melt-crystallized sPS is significantly important for its practical applications.

Many studies focused on the competition between α and β crystal forms during melt-crystallization. In general, the formation of melt-crystallized polymorphism is dependent upon thermal histories and crystallization conditions such as maximum annealing temperature (T_{max}), crystallization temperature (T_c), cooling rate, crystal form of starting material, and so on. Among these factors, T_{max} was considered as the most important one as many literatures reported. It is well known that lower T_{max} facilitates more α crystal, and there are two views about the origin of this phenomenon. Guerra [19] and De Rosa [20] found that only starting material in α, γ and δ crystal can produce α crystal (γ and δ crystal usually transformed into α crystal during the heating process), and then proposed that the T_{max} effect on the formation of polymorphism may be attributed to the memory effect of nucleus. The formation of α crystal is governed by α nuclei in sPS melts. However, Ho [16] did the similar experiment but obtained a contrary result that both α and β nuclei showed the possibilities to generate α crystal. Combining with the diagram of phase inversion, he interpreted the polymorphic behaviors of sPS at different T_{max} in terms of kinetic concept of nucleation barrier. By reducing the T_{max}, the size of remaining nucleus increases and thus the energy barrier for nucleation decreases. At low enough nucleation barrier, the formation rate of α crystal is faster than β crystal.

Obviously, nucleation is significantly important for ultimate crystalline structure of melt-crystallized sPS. Therefore, the primary objective of this paper was to investigate the nucleation effect on polymorphism of sPS during melt-crystallization. A similar experiment mentioned above was repeated to clarify the origin of favorable α crystal at low T_{max}. Two methods were employed to depress the nucleation energy barrier.

Nucleation can be classified as a homogeneous or heterogeneous process. Homogeneous nucleation starts at an arbitrary place within the volume of the mother phase. Heterogeneous nucleation occurs preferably on the surfaces of active centers, such as the residual nuclei in the melts, nucleating agent, impurities, or some

* Corresponding author. Tel.: +86 20 84115109; fax: +86 20 84115109.
** Corresponding author.
E-mail addresses: cesmkc@mail.sysu.edu.cn (K. Mai), cbwu2000@yahoo.com (C. Wu).

0032-3861/$ – see front matter © 2010 Elsevier Ltd. All rights reserved.
doi:10.1016/j.polymer.2010.11.053

structural defects et al. In macromolecular systems, nucleating agent was often used to promote heterogeneous nucleation, depressing nucleation energy barrier and increasing crystallization rate [21–26]. Aluminium salt of p-tert-butylbenzoate (PTBBA-Al) was reported as the nucleating agent in some early patents [27,28] to improve the mechanical properties of sPS composites. In this paper, PTBBA-Al was added into sPS system as nucleating agent to investigate the nucleation effect on the polymorphic behavior of melt-crystallized sPS.

Shear force was one of the common stresses during the practical polymer process. Shear-induced crystallization raises an increasing interest because the shear force can dramatically affect the nucleation process and the ultimate morphology of semi-crystal polymer. It has been well known that shear force imposed on polymer melts can result in molecular orientation and entropy loss [29,30], and these oriented precursors can act as nuclei to accelerate crystallization process and increase crystalline number [31–36]. In this study, Dynamic Mechanical Analysis (DMA) was used to apply oscillatory shear force on sPS samples to investigate the influence of shear force on the polymorphic behavior of sPS.

2. Experimental

2.1. Materials

Syndiotactic polystyrene (sPS) was provided by Dow Chemical Co. with Mw of 226,000 and Mw/Mn of 2.8, determined by GPC. Aluminium salt of p-tert-butylbenzoate (PTBBA-Al) was supplied by Royal Dutch Shell PLC.

2.2. Preparation of nucleated sPS samples

Dried sPS pellets were pre-mixed with PTBBA-Al powder. Then the mixture was melted and mixed in a HL-200 melt-mixer equipped with twin-screw (Jilin University, China). The temperature was kept at 280 °C and the screw speed was set at 50 rpm. The melt-mixed products were melted again on a hot-stage at 320 °C for 5 min and then pressed into thin film and quenched in ice cold water to obtain amorphous sPS/PTBBA-Al samples. The samples with 0.1%, 0.4% and 1% (w/w) of PTBBA-Al were named as 0.1 % PTBBA-Al-sPS、0.4 % PTBBA-Al-sPS and 1 % PTBBA-Al-sPS, respectively. Pure sPS was also processed under the same conditions for parallel comparison.

2.3. Differential scanning calorimetry (DSC) analysis

Non-isothermal melt-crystallization behaviors of sPS and sPS/PTBBA-Al samples were investigated on a Perkin–Elmer 7 differential scanning calorimeter. Temperature calibration was performed using an indium standard (T_m° = 156.6 °C and ΔH_f° = 28.5 J/g). The samples were heated to T_{max} and melted for 10 min to eliminate thermal history and then cooled to room temperature at a cooling rate of 10 °C/min. The crystallization curves were recorded for further analysis. All measurements were carried out in nitrogen atmosphere.

2.4. Polarized optical microcopy (POM) analysis

The morphology of sPS and sPS/PTBBA-Al samples was observed using an Orthoplan Pol Polarized optical microcopy (Leitz, Germany) with a Linkam-THMSE-600 automatic thermal control hot-stage (the controlling temperature precision of ±0.1 °C). The samples were heated to T_{max} annealing for 10 min and then quenched to crystallization temperature for crystallizing isothermally for 2 h. The morphology change during the whole process was recorded for further analysis.

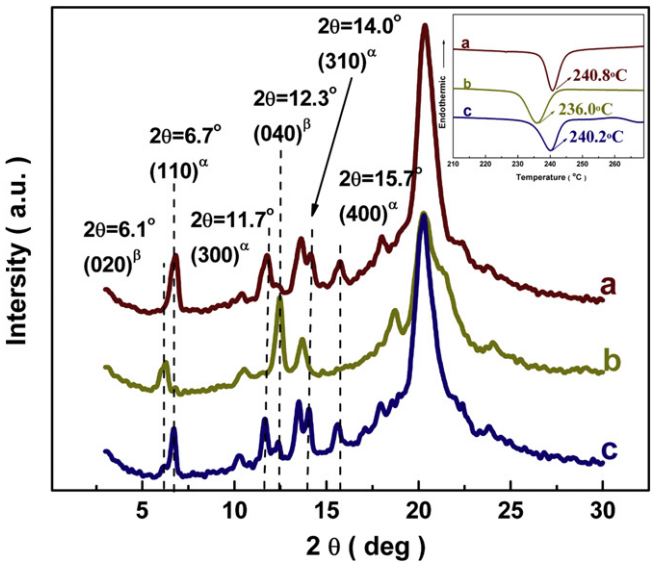

Fig. 1. WAXD patterns of sPS crystallized non-isothermally and the corresponding T_p^c shown on the DSC thermographs. (a) cooling from T_{max} = 276 °C; (b) after reheating to 320 °C; (c) after reheating again to 276 °C.

2.5. Wide angle X-ray diffraction (WAXD) analysis

The samples of pure sPS and sPS/PTBBA-Al for wide angle X-ray diffraction were prepared in DSC cell with the same thermal history as samples for DSC or POM experiment. The crystalline samples of sPS under oscillatory shear force were prepared in Dynamic Mechanical Analysis (DMA) cell. The samples were analyzed by using a Rigaku D/max 2200 vpc diffractometer (Cu Kα radiation, λ = 1.542 Å) with the step scanning rate of 2°/min. The X-ray source was operated at a voltage of 40 kV and a filament current of 30 mA.

2.6. Shear experiment

The influence of oscillatory shear on polymorphism of isothermally crystallized sPS was investigated in combination with DMA and WAXD. Mettler-Toledo DMA/SDTA861 which can provide precise measurements of shear rigidity ranging from 10 to 10^8 N/m was used. Firstly, sPS pellets were melted at 280 °C and then pressed into thin slices with 1 mm thickness under 4 MPa. The slices were tailored into round slices with diameter of 1 cm. Then two identical round slices of sPS samples were clamped symmetrically between two outer fixed parts and the central moving part which provided oscillatory force onto the samples. The samples were melted at 280 °C for 5 min and then cooled to 250 °C in a rate of 14 °C/min, followed by a 2 h-hold to complete the isothermal crystallization. Oscillatory shear forces with a fixed frequency of 8 Hz were imposed on the molten sPS during melting or isothermal crystallization process. The crystal samples were then characterized by WAXD. Time dependence of storage shear modulus, G'', and loss factor, tan δ, of sPS samples under oscillatory shear were recorded for further analysis.

3. Results and discussion

3.1. Lower nucleation energy barrier favors more α crystal

In non-isothermal crystallization, crystallization temperatures (T_c), including crystallization onset temperature (T_c^{on}) and

crystallization peak temperature (T_c^p), usually represented energy barrier of nucleation. Higher T_c means lower nucleation energy barrier. Our previous work [37] showed that sPS α crystal always generated with higher T_c and lower T_{max} compared with β crystal. This may be attributed to the self-seeding of α crystal. Lower T_{max} leads to some residual nuclei in the melts which may act as nucleation seeds in the consequential crystallization and increase the T_c. However, the equilibrium melting temperature of β form is higher than that of α form. Therefore, sPS melts at different T_{max} may possess various types of residual nuclei. Higher T_{max} intends to produce more β nuclei with smaller size. To clarify the effect of size and type of the residual nuclei on sPS polymorphism, sPS samples were cooled from different T_{max} with different starting states. The experiment results were shown in Fig. 1 and all of the cooling rates were fixed at 10 °C/min.

As shown in Fig. 1a, sPS sample which was cooled from the melts of T_{max} 276 °C produced large numbers of α crystal with high T_c^p of 240.8 °C. The obtained α crystal was then annealed at T_{max} of 320 °C and cooled to room temperature. Thus, pure β crystal was obtained with T_c^p of 236.0 °C as shown in Fig. 1b. This is because that the crystalline was completely melted at 320 °C and the nucleation mode transformed from heterogeneous nucleation to homogeneous nucleation which required higher supercooling. As the obtained pure β sPS sample was reheated to T_{max} of 276 °C, T_c^p was increased to 240.2 °C during the consequential crystallization indicating the residual β nuclei acted as nucleation seeds and induced sPS to crystallize at higher T_c. The final crystalline was composed of a large amount of α crystal and a little amount of β crystal shown in Fig. 1c. Thus, the results suggested that β nuclei also facilitated the formation of α crystal, which is in agreement with the report of Ho [16] but contrary to the results of Guerra [19] and De Rosa [20]. The formation of α crystal was really determined by the size of residual nuclei, not by the type of them. The residual nuclei determined just the nucleation barrier, but not the final crystalline structures. Larger nuclei at lower T_{max} meant lower nucleation barrier and always favored more α crystal regardless of α or β nuclei. The results also indicated that nucleation process is significantly important for the polymorphism of melt-crystallized sPS.

Based on the above experiment results, two methods were employed to depress the nucleation energy barrier to investigate the nucleation effect on the control of crystalline polymorphism of sPS melt-crystallization.

3.2. Introduce of nucleating agent

As mentioned above, attainment of sPS α crystal is favored as residual nuclei remains in the melt. Therefore, the addition of effective nucleating agent was expected to also facilitate the growth of α form because it could decrease the nucleation energy barrier.

Our early studies on non-isothermal crystallization behavior of sPS [37] reported that both the percentage of α crystal (P_α%) and the crystallization temperature gradually decreased with the increase of T_{max} due to the continuous melting of residual nuclei in the sPS melts. Above T_{max} of 296 °C, the crystallization temperature was nearly constant and pure β crystal was obtained as a result of complete melt of the residual nuclei. Therefore, a high annealing temperature of T_{max} = 320 °C was chosen in this study to avoid the influence of any residual nuclei, and thus, the sole effect of nucleating agent on the nucleation energy barrier and the polymorphism of sPS melt-crystallization can be investigated.

The DSC and WAXD results for PTBBA-Al-sPS samples crystallized non-isothermally after melted at 320 °C for 10 min were shown in Fig. 2. Obviously, with the addition of PTBBA-Al, crystallization temperature (both T_c^{on} and T_c^p) of sPS significantly increased as shown in Fig. 2a. And moreover, the more PTBBA-Al was added, the higher T_c^{on} and T_c^p were measured. This indicated that PTBBA-Al acted as the nucleation active sites and provided sPS chains with foreign surface to attach and fold, and thus, the nucleation energy barrier was decreased compared with the pure sPS with homogeneous nucleation.

Based on the WAXD data, P_α% in the crystallized sPS and PTBBA-Al-sPS samples was calculated using the following approximated relation [19]:

$$P_\alpha = \{[1.8A(11.7)/A(12.4)]/[1 + 1.8A(11.7)/A(12.4)]\} \times 100$$

in which A(11.7) and A(12.4) refer to the area of the peaks located at $2\theta = 11.7°$ and 12.2°, respectively. The results shown in Fig. 2b illustrated that more α crystal was generated with the addition of PTBBA-Al. Pure β crystal was obtained in neat sPS and 0.1%PTBBA-Al-sPS due to the higher T_{max} and insufficient nucleating agent. However, with addition of 0.4% PTBBA-Al, P_α% increased significantly to 73.4%. As the content of PTBBA-Al grew to 1%, α crystal became the dominant crystalline with P_α% of 83.9%. The results clearly proved the hypothesis that adding nucleating agent could facilitate the formation of α crystal even at high T_{max} of 320 °C due to the depression of nucleation barrier.

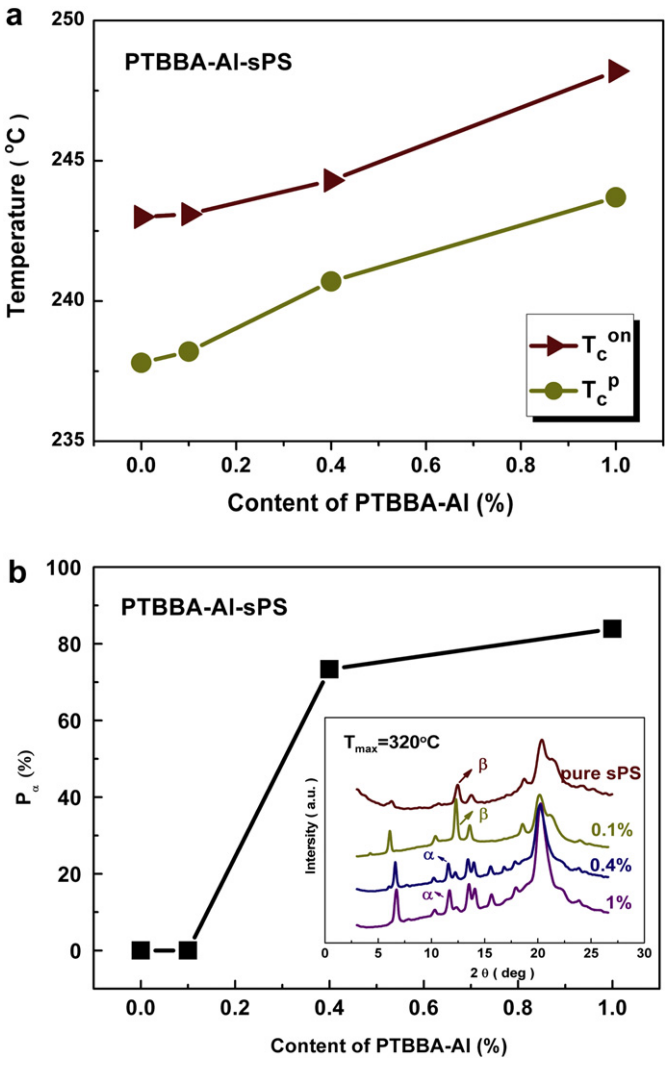

Fig. 2. The influence of PTBBA-Al on the non-isothermal crystallization behavior of sPS (T_{max} = 320 °C). (a) crystallization temperature including T^c_{on} and T^c_p; (b) percentage of α crystal P_α% and the corresponding WAXD patterns.

From POM micrographs as shown in Fig. 3, the difference in nucleation mode between pure sPS and nucleated sPS can be distinctly observed. As crystalline were completely melted at T_{max} of 320 °C, the typical slow growth mode of sPS β crystal [38,39] from homogeneous nucleation was illustrated in Fig. 3a. Obviously, β form became the optimum grow mode under this condition which was also affirmed by WAXD pattern in Fig. 4. For nucleated sPS system in Fig. 3b, typical fast growth mode of α crystal was observed [39,40] which was heterogeneous nucleation. Obviously, the addition of nucleation agent dramatically changed the nucleation mode, and 1% PTBBA-Al provided effective nucleating sites to depress the nucleation barrier. Under this condition, α crystal form became the preferential growth mode with its faster growth rate (see WAXD pattern in Fig. 4).

Based on these results, both unmelted α or β residual nuclei and foreign nucleating agents can promote the formation of α crystal due to the depression of nucleation barrier.

3.3. Imposition of oscillatory shear force on sPS melts

Polymorphism of sPS samples isothermally crystallized at quiescent and shear states were investigated by combination of DMA and WAXD. For all experiments, T_{max} and T_c were fixed at 280 °C and 250 °C, respectively. At quiescent condition, β crystal was found to dominate the crystalline as shown in Fig. 5a. However, as shear force was imposed on sPS samples during melting and crystallization, the content of α crystal dramatically increased as shown in Fig. 5b. These results indicated that shear force facilitated the formation of sPS α crystal. Then, shear force was applied at melting and isothermal crystallization separately to identify at which step shear force acted. The results shown in Fig. 5c and d displayed a mixture of α and β crystals. Therefore, the DMA experimental results demonstrated that shear force could promote the formation of more α crystal no matter at which step shear force was applied. This phenomenon may be explained in terms of metastability of crystalline phase [41], which is dependent upon nucleation process. Usually lower nucleation barrier leads to the formation of metastable phase. Shear force probably produced oriented molecular in the sPS melts which could act as nuclei to decrease the nucleation energy barrier. At low nucleation barrier, the formation rate of α crystal was faster than that of β crystal and the probability to grow α crystal thus increased owing to its faster growth rate. As a kinetic result of crystallization, the formation of α crystal was facilitated under shear force.

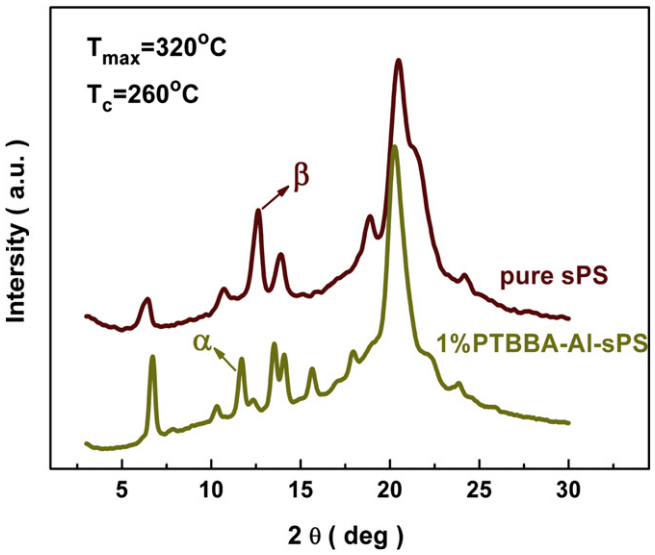

Fig. 4. WAXD patterns of neat sPS and 1%PTBBA-Al-sPS crystallized isothermally at 260 °C for 2 h after melted at 320 °C for 10 min.

The preferential growth of metastable phase in shear-induced crystallization for other polymer was also reported by some groups, such as isotactic polypropylene (iPP) [42–44] and poly(ethylene naphthalate) (PEN) [45] et al. For iPP, α form is thermodynamically more stable than β form and dominates the crystallization in quiescent state. However, the metastable β form became preferable crystal form in shear-induced crystallization. Wu [46] interpreted this phenomenon in PP by the concept of metastability [41] that the metastable phase possesses higher stability at its initial small size, grows at a faster rate in the sheared melts and finally dominates the crystallization. The origin of the metastable β form is accounted for

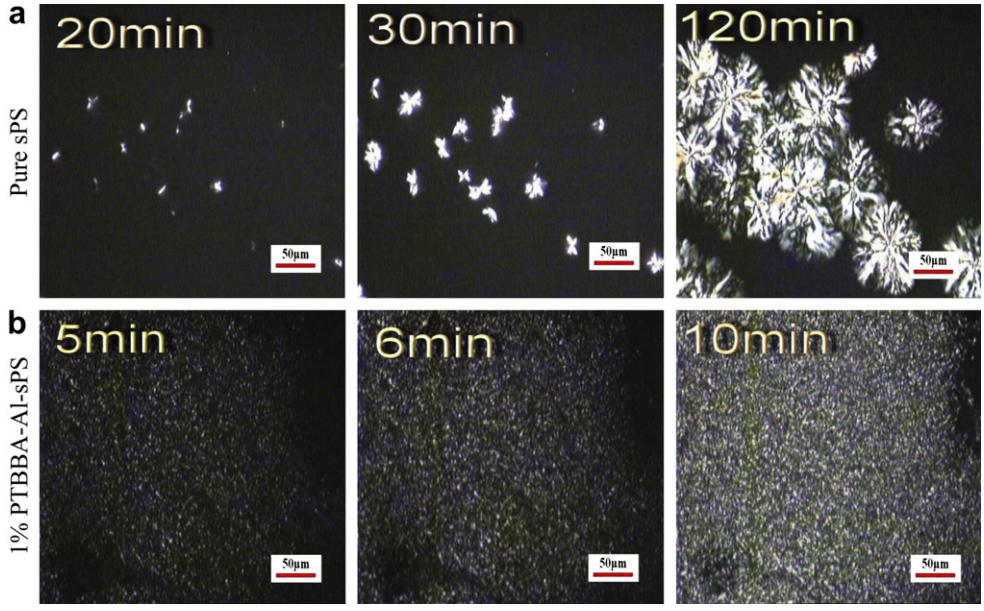

Fig. 3. POM micrographs of pure sPS and 1% PTBBA-Al-sPS crystallized isothermally at 260 °C after melted at 320 °C for 10 min.

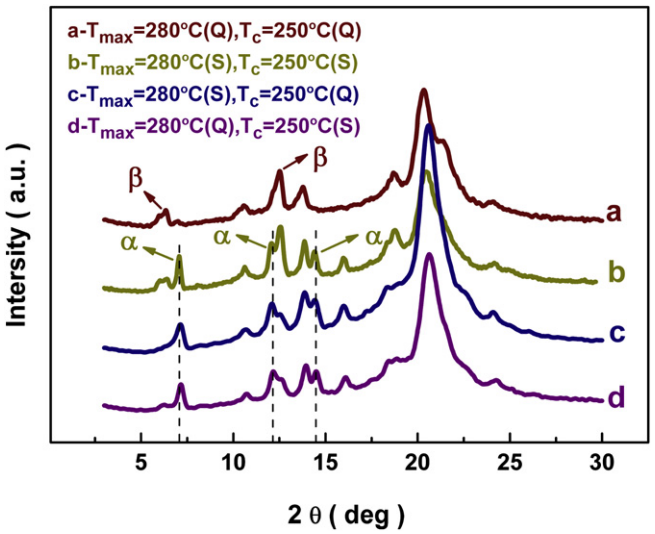

Fig. 5. WAXD patterns of sPS samples crystallized isothermally for 2 h under different conditions: (a) melted and crystallized under quiescent condition; (b) melted and crystallized under shear state; (c) melted under shear state and crystallized under quiescent condition; (d) melted under quiescent condition and crystallized under shear state. (Q-Quiescent condition; S-Shear state.)

kinetically controlled process through the smaller energy barrier involved in its formation.

The shear experiment result in this study afforded another model and method for the phase inversion of metastable phase in shear-induced crystallization. However, further investigations are needed.

4. Conclusions

As nucleation energy barrier was affirmed to be the primary factor to affect the polymorphism of melt-crystallized sPS, two methods were employed to change the nucleation environment to investigate the nucleation effect on polymorphism of sPS. Nucleating agent was induced to depress the nucleation energy barrier and accelerate the nucleation process. Consequently, the portion of metastable α crystal was significantly increased even at very high T_{max}. Shear force was applied on sPS melts by DMA to promote the orientation of molecular, and the content of α crystal was dramatically increased compared with crystallization under quiescent condition. It was concluded that the formation of α crystal is actually a kinetically controlled process, and lower nucleation barrier facilitates more α phase due to its rapid growth. Therefore, more α crystal was obtained by depressing the nucleation barrier, and this suggested a new method to control the polymorphism of melt-crystallized sPS during practical process.

References

[1] Woo EM, Sun YS, Yang CP. Progress in Polymer Science 2001;26:945–83.
[2] Fang J, Kiran E. Macromolecules 2008;41:7525–35.
[3] Wu H, Wang W, Huang Y, Wang C, So ZH. Macromolecules 2008;41:7755–8.
[4] Su CH, Jeng U, Chen SH, Lin SJ, Wu WR, Chuang WT, et al. Macromolecules 2009;42:6656–64.
[5] Milano G, Guerra G. Progress in Materials Science 2009;54:68–88.
[6] Wu H, Wang W, Huang Y, Su ZH. Macromolecular Rapid Communications 2009;30:194–8.
[7] Liu CK, Nguyen T, Yang TJ, Lee SB. Polymer 2009;50:499–509.
[8] Daniel C, Montefusco T, Rizzo R, Musto P, Guerra G. Polymer 2010;51:4599–605.
[9] Wang C, Huang CL, Chen YC, Hwang GL, Tsai SJ. Polymer 2008;49:5564–74.
[10] Greisa O, Xub Y, Asanob T, Petermann J. Polymer 1989;30:590–4.
[11] Suna Z, Morgana RJ, Lewis DN. Polymer 1992;33:660–1.
[12] Hodge K, Prodpran T, Shenogina NB, Nazarenko S. Journal of Polymer Science Part B: Polymer Physics 2001;39:2519–38.
[13] Prodpran T, Shenogin S, Nazarenko S. Polymer 2002;43:2295–309.
[14] Olson BG, Prodpran T, Jamieson AM, Nazarenko S. Polymer 2002;43:6775–84.
[15] Larobina D, Sanguigno L, Venditto V, Guerra G, Mensitieri G. Polymer 2004;45:429–36.
[16] Ho RM, Lin CP, Tsai HY, Woo EM. Macromolecules 2000;33:6517–26.
[17] Ho RM, Lin CP, Hseih PY, Chung TM, Tsai HY. Macromolecules 2001;34:6727–36.
[18] Rapacciuolo M, Derosa C, Guerra G, Mensitieri G, Apicella A, Delnobile MA. Journal of Materials Science Letters 1991;10:1084–7.
[19] Guerra G, Vitagliano VM, De Rosa C, Petraccone V, Corradini P. Macromolecules 1990;23:1539–44.
[20] De Rosa C, de Ballesteros OR, Di Gennaro M, Auriemma F. Polymer 2003;44:1861–70.
[21] Abraham F, Schmidt HW. Polymer 2010;51:913–21.
[22] Housmans JW, Gahleitner M, Peters GWM, Meijer HEH. Polymer 2009;50:2304–19.
[23] Wang K, Zhou CJ, Tang CY, Zhang Q, Du RN, Fu Q, et al. Polymer 2009;50:696–706.
[24] Yi QF, Wen XF, Dong JY, Han CC. Polymer 2008;49:5053–63.
[25] Zhang ZS, Wang CG, Yang ZG, Chen CY, Mai KC. Polymer 2008;49:5137–45.
[26] Zhao SC, Cai Z, Xin Z. Polymer 2008;49:2745–54.
[27] Osaka A. (JP) EP 587098. Idemitsu Kasan Co.; 1994.03.16.
[28] Osaka A, Sato N. (JP) US 5418275. Idemitsu Kasan Co.; 1995.05.23.
[29] Haas TW, Maxwell B. Polymer Engineering & Science 1969;9:225–41.
[30] Wolkowicz MD. Journal of Polymer Science: Polymer Symposia 1978;63:365–82.
[31] Somani RH, Hsiao BS, Nogales A, Srinivas S, Tsou AH, Sics I, et al. Macromolecules 2000;33:9385–94.
[32] Somani RH, Yang L, Sics I, Hsiao BS, Pogodina NV, Winter HH, et al. Macromolecular Symposia 2002;185:105–17.
[33] Kumaraswamy G, Kornfield JA, Yeh FJ, Hsiao BS. Macromolecules 2002;35:1762–9.
[34] Zhang RC, Xu Y, Lu A, Cheng KM, Huang YG, Li ZM. Polymer 2008;49:2604–13.
[35] Min M, Zhang RC, Lu A, Gao Y, Lu ZY. Iranian Polymer Journal 2008;17:199–207.
[36] Balzano LG, Rastogi S, Peters GWM. Macromolecules 2009;42:2088–92.
[37] Lu M, Zhou WH, Mai KC. Polymer 2006;47:1661–6.
[38] Wang C, Cheng YW, Hsu YC, Lin TL. Journal of Polymer Science Part B: Polymer Physics 2002;40:1626–36.
[39] Cai JL, Han Y. Journal of Applied Polymer Science 2007;103:1311–24.
[40] Wang C, Chen CC, Hung CH, Lin KS. Polymer 2004;45:6681–9.
[41] Keller A, Cheng SZD. Polymer 1998;39:4461–87.
[42] Varga J, Karger-Kocsis J. Journal of Polymer Science Part B: Polymer Physics 1996;34:657–70.
[43] Somani RH, Hsiao BS, Nogales A, Fruitwala H, Srinivas S, Tsou AH. Macromolecules 2001;34:5902–9.
[44] Ma CG, Chen L, Xiong XM, Zhang JX, Rong MZ, Zhang MQ. Macromolecules 2004;37:8829–31.
[45] Yoon WJ, Myung HS, Kim BC, Im SS. Polymer 2000;41:4933–42.
[46] Wu CM, Chen M, Karger-Kocsis J. Polymer 1999;40:4195–203.

Polymer 52 (2011) 1107–1115

Contents lists available at ScienceDirect

Polymer

journal homepage: www.elsevier.com/locate/polymer

Formation and reorganization of the mesophase of random copolymers of propylene and 1-butene

Daniela Mileva [a], René Androsch [a,*], Evgeny Zhuravlev [b], Christoph Schick [b], Bernhard Wunderlich [c]

[a] Martin-Luther-University Halle-Wittenberg, Center of Engineering Sciences, D-06099 Halle/Saale, Germany
[b] University of Rostock, Institute of Physics, D-18051 Rostock, Germany
[c] 200 Baltusrol Rd., Knoxville, TN 379234-37-7, USA

ARTICLE INFO

Article history:
Received 4 December 2010
Received in revised form
7 January 2011
Accepted 7 January 2011
Available online 15 January 2011

Keywords:
Poly(propylene–*ran*–1-butene)
Mesophase
Fast scanning chip calorimetry

ABSTRACT

Fast scanning chip calorimetry (FSC) has been employed to study the kinetics of formation of the mesophase of random copolymers of propylene and 1-butene from the glassy amorphous state and its reorganization on heating. The experiments performed consistently prove a distinct decrease of the rate of mesophase formation with increasing concentration of 1-butene chain defects. The time required for isothermal mesophase formation at 300 K is of the order of 0.1 s in case of the homopolymer, while it is prolonged by one order of magnitude to 1 s in the copolymer with 11 mol-% 1-butene. Similar, cold-ordering of amorphous structure on continuous heating at 1000 K s^{-1} is only completed in the homopolymer while it is almost completely suppressed in the random copolymer containing about 11 mol-% 1-butene. The perfection of the mesophase and/or its reorganization into crystals is faster in the homopolymer than in copolymers containing 1-butene. The critical heating rate for complete inhibition of perfection and reorganization is reduced from about 40,000 K s^{-1} in the homopolymer to about 10,000 K s^{-1} in copolymers. The reduced rate of mesophase formation in random copolymers of propylene and 1-butene is attributed to the decrease of the thermodynamic driving force for the phase transformation.

1. Introduction

Crystallization of the isotropic and quiescent melt of isotactic polypropylene (iPP) at low supercooling leads to direct formation of cross-hatched monoclinic lamellae which are arranged in a spherulitic superstructure [1–6]. Alternatively, the melt of iPP can be crystallized via intermediate formation of a metastable mesophase/conformationally disordered glass (CD glass) [7–9] at high supercooling, and its subsequent reorganization into crystals on heating [10–15]. The crystallization via the mesophase leads to a qualitatively different semicrystalline structure than the direct crystallization from the liquid state since the crystals obtained are of non-lamellar shape and not organized in a higher-order spherulitic superstructure [13–18]. As a consequence, ultimate properties of semicrystalline iPP crystallized along these different thermodynamic pathways are largely different [19–21]. Semicrystalline preparations of iPP containing cross-hatched lamellae and spherulites are opaque and rather non-ductile while iPP crystallized via the mesophase is highly transparent and rather ductile. The present study is related to the crystallization of iPP via the mesophase, which in the following is introduced in more detail.

The conditions for the formation of the mesophase and its transformation into crystals were quantitatively evaluated recently in the case of the iPP homopolymer. The mesophase forms at high supercooling of the melt at temperatures (T) between about 330 K and the glass transition temperature of the amorphous phase (T_g) at about 260 K [22–25]. In order to suppress the liquid – crystal phase transformation at low supercooling, the melt needs to be cooled rapidly at a rate faster than about 100 K s^{-1} [17,24–27]. If the cooling rate is lower, then spherulitic crystallization occurs at temperatures higher than 350 K and mesophase formation at low temperature gets increasingly reduced with decreasing cooling rate. Isothermal analysis of the kinetics of the liquid – mesophase transformation revealed a half-time of the ordering process of less than a second at ambient temperature [22,23]. Though the mesophase formation is fast, it can be suppressed by cooling the melt faster than 1000 K s^{-1} to $T < T_g$ [25]. Subsequent devitrification of the glass by heating then allows cold-ordering/mesophase formation between T_g and about 350 K if the heating rate is lower than 10,000 K s^{-1} [28]. The liquid – mesophase transition at high supercooling is incomplete even on long-term storage at ambient temperature, *i.e.*, quenched preparations of iPP are heterogeneous and contain about 25–50% [12,27,29]

* Corresponding author. Tel.: +49 3461 46 3762; fax: +49 3461 46 3891.
E-mail address: rene.androsch@iw.uni-halle.de (R. Androsch).

0032-3861/$ – see front matter © 2011 Elsevier Ltd. All rights reserved.
doi:10.1016/j.polymer.2011.01.021

isometric mesophase particles of size of 5–20 nm [14–18,30,31] and amorphous phase. The amorphous phase in semimesomorphic iPP is partially restrained and immobilized due to covalent coupling to the mesophase, *i.e.*, the amorphous phase contains mobile (MAF) and rigid amorphous fractions (RAF) with corresponding glass transition temperatures $T_{g,\,MAF}$ (270 K) and $T_{g,\,RAF}$ ($>T_{g,\,MAF}$), respectively [8]. The mesophase is of lower packing density than the monoclinic crystalline phase [27,32] and contains helix reversals as most important conformational defect [8]. At ambient temperature, the mesophase is below its own glass transition temperature ($T_{g,\,Mesophase}$), *i.e.*, the removal of helix reversals to achieve crystalline registry of molecular stems requires heating of the mesophase to $T > T_{g,\,Mesophase}$, with $T_{g,\,Mesophase} > T_{g,\,RAF}$. The mesophase – crystal phase transition has frequently been analyzed by temperature-resolved X-ray diffraction [10–12,15,33] and occurs in a wide temperature range starting at about 350 K, being related to the onset of helix mobility as detected by solid state NMR [34]. It has been suggested that the mesophase – crystal phase transition is a local process within the ordered domains, either proceeding by helix rewinding or by a chain translation mechanism [35–39]. The mesophase – crystal phase transition is a thermodynamically irreversible process toward equilibrium, obeys specific kinetics, and can be suppressed by heating at rates faster than about 20,000 K s^{-1} into the temperature range of the equilibrium liquid, *i.e.*, to temperatures higher than the equilibrium melting temperature [28]. In this case, complete disordering/isotropization of the mesophase occurs at about 350 K. An extensive review of the structure, stability and reorganization of the mesophase of iPP has been published recently [40].

In the present work, we focus on the evaluation of the change of the kinetics of mesophase formation in iPP as a result of random insertion of 1-butene co-units into the chain. Random isotactic copolymers of propylene and 1-butene (iPP-But) are commercially important polymeric materials, which were developed to broaden the range of application or the processability of the iPP homopolymer [1,41,42]. Significant research has been performed to describe structure formation of iPP-But copolymers from solution [43], or from the melt at low supercooling [44–52] while studies to gain information about the crystallization process via intermediate formation of a metastable mesophase at high supercooling are rare. The application-related potential of iPP-But copolymers crystallized along this specific thermodynamic pathway has been demonstrated [53,54], and initial investigations of the kinetics of both the liquid – mesophase and mesophase – crystal phase transitions have been performed [55–57]. In detail, it has been shown by non-isothermal fast scanning chip calorimetry (FSC) and by investigation of the structure of samples cooled at different rate that the critical cooling rate, required to suppress crystallization at low supercooling, slightly decreases with increasing concentration of 1-butene in the chain [57]. This result is in agreement with the earlier observation of a decreased maximum rate of crystallization at low supercooling [48]. Analysis of the fine structure of the mesophase of iPP-But copolymers revealed that the 1-butene chain defects are trapped in the mesophase, and the concentrations of co-units in the amorphous phase and the mesophase are probably identical [58]. Heating of the mesophase to $T > T_{g,\,Mesophase}$ allows its reorganization to crystals with the co-units, initially trapped in the mesophase, kept inside the crystals. The temperature of reorganization of the mesophase into crystals on slow heating decreases with increasing concentration of 1-butene chain defects, which has been attributed to a lowering of the glass transition temperature of the mesophase. Further information about the kinetics of formation and reorganization of the mesophase as a function of the copolymer composition are not available, which is therefore primary object of this work.

Summarizing the intention of the present work, we attempt to gain further quantitative information about the kinetics of mesophase formation and reorganization in iPP-But random copolymers. To the best of our knowledge, for random iPP-But copolymers, data about the kinetics of isothermal mesophase formation at ambient temperature, the kinetics of non-isothermal mesophase formation/cold-ordering on heating, and the kinetics of reorganization of mesophase into crystals are not available. We believe that these information are necessary to further complete the knowledge about the various pathways of crystallization of the important class of propylene-based polymers. In addition, and perhaps more importantly, the data observed may allow general conclusions about the effect of the variation of the molecular structure/introduction of chain irregularities on the crystallization behavior at conditions far from thermodynamic equilibrium, if quantified by the supercooling. The importance of such research from both polymer science and polymer engineering points of view has been recognized and resulted in organization of special seminars like the 9th Lähnwitz-Seminar on Calorimetry "Transitions far from Equilibrium – Super-heating; Super-cooling" in 2006 [59], and a workshop on "Polymer Crystallization under Conditions Relevant to Processing" in 2010 [60]. In order to achieve the goal of the present work, we employed the new experimental technique of fast scanning chip calorimetry (FSC). First instruments were developed in the 1990's to be used under quasi-adiabatic conditions for fast heating up to 10^7 K s^{-1} [61,62]. Further utilization of this technique for research of polymer crystallization at fast cooling required operation at non-adiabatic conditions, which has been achieved only less than 10 years ago [63,64]. The particular technique of non-adiabatic FSC needed to be used since mesophase formation at high supercooling, and cold-ordering and reorganization during heating occur at a time scale of few milliseconds (ms), being too fast to be monitored by standard differential scanning calorimetry (DSC). As such the present study is also performed to further establish and demonstrate the capabilities of the novel instrumental technique of FSC for analysis of phase transitions in polymeric materials.

2. Experimental section

For the present study we used an iPP homopolymer with a mass-average molar mass and polydispersity of 373 kDa and 6.2, respectively [65]. Isotactic poly(propylene–*ran*–1-butene) samples with a concentration of 6.0 and 10.9 mol-% 1-butene (iPP-But.6 and iPP-But.11) and a molar mass of 225 kDa and polydispersity of 3.1 were purchased from Sigma–Aldrich [66,67]. The as-received materials were compression-molded at 473 K to films of 100 μm thickness in a Collin press, using a rate of 10 K min^{-1} for cooling the films to ambient temperature. For subsequent FSC analyses, samples of 10–15 μm thickness and a lateral dimension of the order of 50 μm were prepared by microscope-aided cutting. The specimens were placed on a thin film chip sensor XI 395 (Xensor Integration, Netherlands), with the thermal contact between the sensor and the specimen improved by Apiezon® N grease. We used the recently developed dual-sensor instrument setup which allows recording of the electrical power difference between the sample and reference calorimeters according to the programmed temperature–time profile, and subsequent conversion into an apparent sample heat capacity [68,69]. The determination of an instrumental baseline, required to correct for temperature-dependent different losses of heat to the environment at the sample and reference sites, has been performed as recommended in the literature [68,69]. It included the measurement of the power difference as a function of temperature during heating and cooling at identical rates in presence of the sample of interest, and the construction of a baseline based on averaging heating- and

cooling-data at temperatures outside of phase transitions and interpolation in regions of phase transitions using 2nd or 3rd order polynomials. While calibration of the power signal was not required, the measurement of temperature considering the thermal lag as a function of heating/cooling rate was checked using the melting temperature of indium, with the indium placed on top of a sample, to consider the thermal resistance of the latter. In order to achieve high cooling rate, the encapsulated measuring system was inserted into liquid nitrogen, and the furnace was purged using cold, gaseous nitrogen. The mass m of the samples was estimated by comparing the measured total heat capacity C_p at temperatures higher than the melting temperature with specific heat capacity data c_p ($= C_p/m$) available in the ATHAS data base [70]. The sample mass was of the order of 10 ng.

The analysis of the kinetics of mesophase formation and reorganization as a function of the content of 1-butene co-units, from point-of-view of experiment organization, is illustrated in Fig. 1. The left part of Fig. 1 shows the temperature–time profile applied for preparation (P) of samples of different content of mesophase. Fully amorphous samples were obtained by heating to 473 K and cooling to 120 K at a rate of 10^4 K s^{-1}. Note that it is known from former research that the critical cooling rate to avoid both crystallization at low supercooling and mesophase formation at high supercooling is around 10^3 K s^{-1} [25,57]. Subsequently, the fully amorphous, glassy samples were heated to 300 K, and kept at this temperature for different period of time between 0 and 60 s. This treatment allowed preparation of semimesomorphic samples with different concentration of mesophase. The content of mesophase in the different preparations is then analyzed by evaluation of the heat of isotropization/disordering on heating at 2×10^4 K s^{-1}, illustrated in the right part of Fig. 1 with the heating segment H1. Heating of fully amorphous or semimesomorphic samples of iPP at 2×10^4 K s^{-1} suppresses cold-ordering of amorphous structure and reorganization of mesophase [28,71], and allows therefore an undisturbed evaluation of the heat of isotropization of mesophase initially formed during the isothermal segment in the preparation step (P). The kinetics of mesophase formation is then obtained by plotting the heat of isotropization obtained on fast heating (H1) as a function of the time of isothermal ordering during preparation (P). An identical sample preparation scheme was used for analysis of the effect of comonomer content on cold-ordering and reorganization. In this case, the samples were heated at a rate of 1×10^3 K s^{-1} (H2) which has been proven by preliminary experimentation to not only being sufficiently slow to allow cold-ordering and reorganization but also to identify different kinetics of these processes caused by the chemical composition of macromolecules.

An additional experiment has been performed for evaluation of a critical rate of heating which is required to completely suppress the reorganization of the mesophase into crystals. In a former work it has been shown that mesophase reorganization in case of the iPP homopolymer can only be avoided by heating faster than about 20,000 K s^{-1}, *i.e.*, by passing the temperature range from 300 to 400 K within 5 ms. It is now speculated that the removal/healing of conformational defects within the mesophase during heating, in order to obtain crystalline order, is affected by the presence of chain defects in both the mesophase and the surrounding amorphous phase. In order to prove this assumption, semimesomorphic samples were prepared by isothermal ordering at 300 K, and subsequently the extent of reorganization has been analyzed as a function of the rate of heating. The temperature–time profile of this particular experiment is shown in Fig. 2.

In case of FSC analysis, preparation of the samples of ng-size onto the surface of the sensor is the most time-consuming step of the experiment. Therefore, once a sample is prepared and properly placed on the sensor, all thermal treatments are performed with this particular specimen. In order to check for degradation, change of the nucleation mechanism/density, or instrumental drift during the course of the experiment, validation scans were performed between all consecutive measurements. Furthermore, selected annealing experiments were performed three times, for the sake of estimation the relative error on subsequent analysis of the heat and temperature of isotropization/melting. Typically, the relative error regarding the enthalpy of transitions is less than 1%, while the repeatability error of the onset temperature of transitions is less than 1 K.

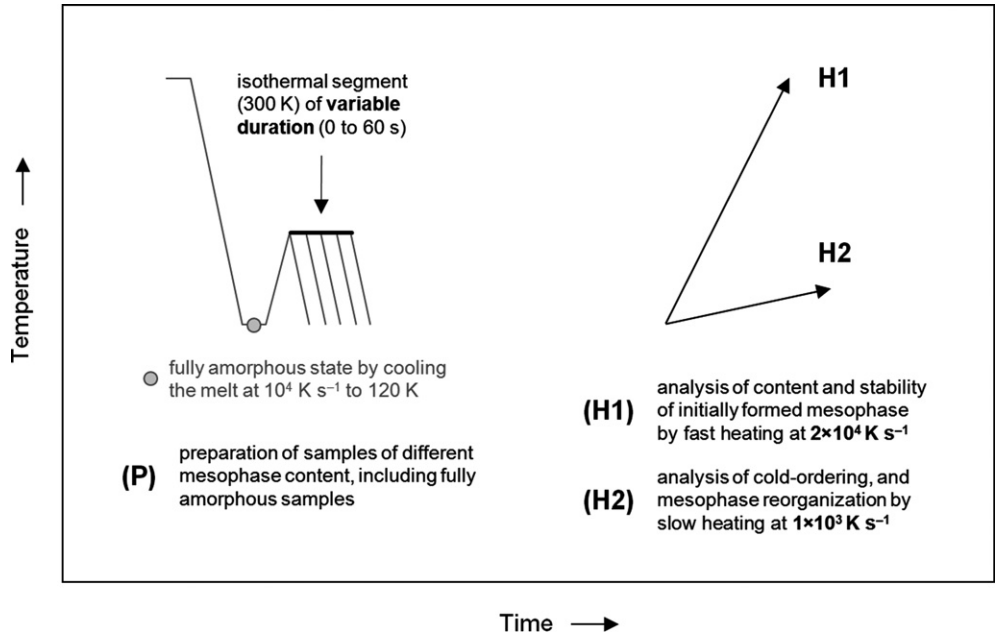

Fig. 1. FSC temperature – time profiles used for preparation of semimesomorphic specimens of iPP homopolymer and random iPP-But copolymers of different mesophase content (left), and for subsequent analysis of the mesophase content, cold-ordering of amorphous phase and mesophase reorganization on heating (right).

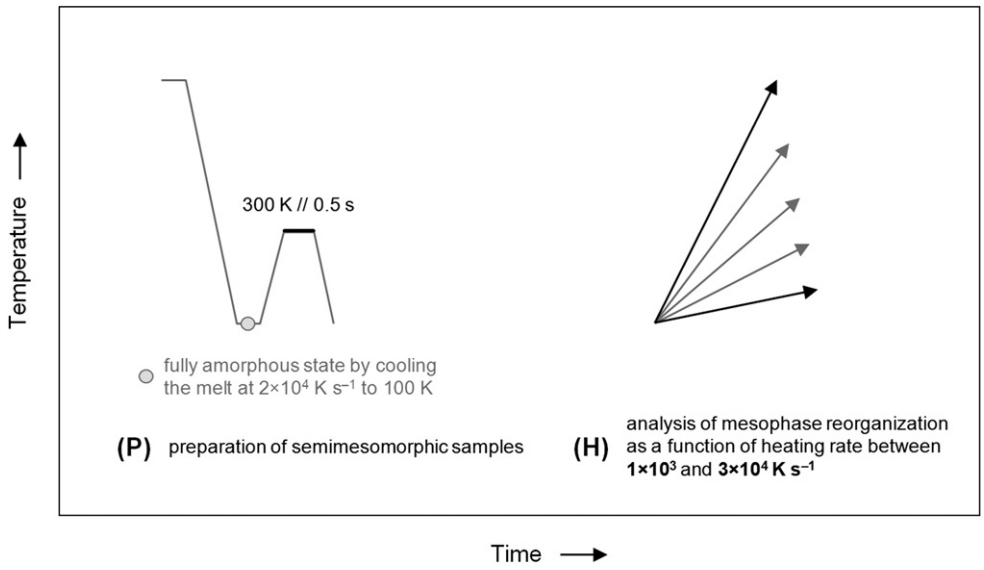

Fig. 2. FSC temperature–time profile used for determination of the critical rate of heating for complete suppression of reorganization of mesophase into crystals.

3. Results and discussion

3.1. Kinetics of isothermal mesophase formation

Fig. 3 shows FSC curves obtained on heating iPP (left plot), iPP-But.6 (center plot) and iPP-But.11 (right plot) at a rate of 20,000 K s^{-1}. The various curves in the individual plots represent samples which were cold-ordered at 300 K for different time between 0.1 ms (bottom curve) and 60 s (top curve), with the exact temperature–time profile shown in the left part of Fig. 1. The variation of the time of cold-ordering resulted in the formation of different amount of mesophase which effectively is analyzed by evaluation of the heat of disordering in the subsequently performed heating scans. It has been found in a former study that heating at 20,000 K s^{-1} suppresses both cold-ordering and reorganization, *i.e.*, any endothermic transition detected during heating is related to the structure before heating onset. Data shown in Fig. 3 reveal distinct differences of the kinetics of cold-ordering between the investigated samples of different 1-butene concentration. While in case of the iPP homopolymer a disordering peak is detected after cold-ordering for a period of time as low as 0.1 ms, in the random copolymers containing 6 and 11 mol-% 1-butene first traces of endothermic heat flow are only seen in preparations cold-ordered for 0.1 s or 0.2 s, respectively. Regarding the experiments performed on the iPP homopolymer, it is important to note the change of disordering temperature during the growth of the mesophase up to 0.1 s. In the early stage of the ordering process the mesophase seems of higher stability since the disordering temperature decreases, as has been discussed in detail in a separate study [71]. This is not observed in the copolymers, which suggests that the growth of small perfect mesophase domains in the initial stage of the ordering process is not permitted due to the random occurrence of 1-butene co-units.

The decrease of the rate of isothermal mesophase formation on addition of 1-butene co-units into the iPP chain is illustrated in Fig. 4 by a direct comparison of the FSC heating scans obtained on samples cold-ordered for 0.1 s, drawn in bold in Fig. 3. Cold-ordering of iPP for 0.1 s resulted in formation of about 21% mesophase which is calculated by normalizing the measured enthalpy of isotropization of 36 J g^{-1} with the bulk enthalpy of isotropization of 168 J g^{-1} [71]. The specific heat of isotropization of the iPP mesophase of 168 J g^{-1} is obtained by subtraction of the specific heat of

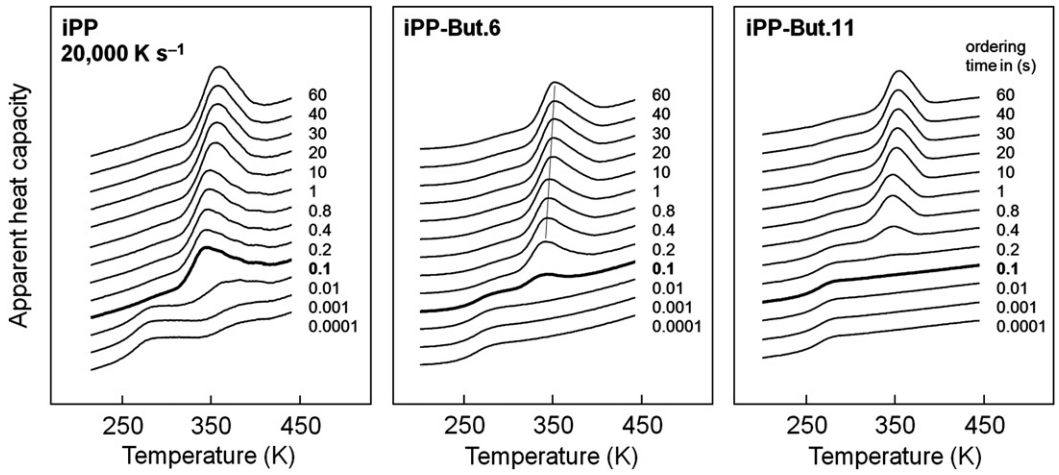

Fig. 3. Apparent heat capacity as a function of temperature obtained on heating iPP (left), iPP-But.6 (center), and iPP-But.11 (right) at a rate of 20,000 K s^{-1}. The different curves in the individual plots represent samples which were ordered at 300 K for different periods of time between 0.1 ms (bottom curve) and 60 s (top curve), according scheme P in Fig. 1.

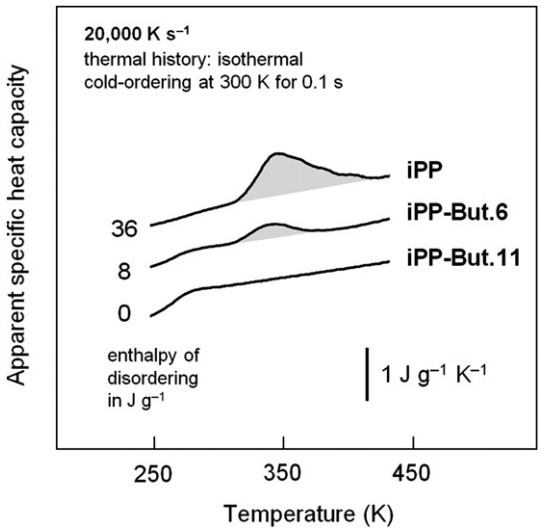

Fig. 4. Apparent heat capacity as a function of temperature on heating iPP (top curve), iPP-But.6 (center curve), and iPP-But.11 (bottom curve) at a rate of 20,000 K s^{-1}, after prior cold-ordering at 300 K for 0.1 s. The gray-shading of the endothermic disordering peak serves for illustration of decreasing amount of mesophase with increasing concentration of 1-butene co-units.

transition of mesophase into crystals of 14 J g^{-1} from the specific heat of melting of crystals of 182 J g^{-1}, valid at 350 K [8,70]. In contrast, in the copolymer with 6 mol-% 1-butene the enthalpy of isotropization after cold-ordering for 0.1 s is only 8 J g^{-1}, which is equivalent to a mesophase fraction of only 5%. Further increase of the 1-butene content to 11 mol-% delays the onset of mesophase formation to more than 0.1 s.

Further quantitative information about the kinetics of the cold-ordering process are summarized in Fig. 5. It is a plot of the enthalpy of isotropization of the mesophase of iPP, iPP-But.6 and iPP-But.11 as a function of the logarithm of the time of isothermal cold-ordering at 300 K, with the transition enthalpies calculated from the data shown in Fig. 3. The data sets in Fig. 5 for the various copolymers reveal that the process of isothermal mesophase formation, after the induction period, can be subdivided into two parts. First, there is a fast increase of the mesophase fraction, followed by a distinctly slower process. In Fig. 5, these two processes are indicated with the gray dotted arrows. It is assumed that the fast process is related to the primary formation of mesophase particles while the slow process may be related to their perfection. An indication for the slow perfection is the increase of the temperature of disordering by about 10 K during the time interval of the slow process, as seen in Fig. 3 with the line in the center graph, connecting the peaks. Note that there is not only an increase of the peak temperature but also of the onset temperature of the disordering transition. In other words, the peak shift is not instrumentally caused, due to the increase of the enthalpy of transition [72]; rather it is due to the increase of thermodynamic stability of the mesophase. A similar observation has been discussed in a preceding study about the isotropization, perfection and reorganization of the mesophase of isotactic polypropylene [71].

Beside the identification of two isothermal ordering processes of different kinetics/rate, the data of Fig. 5 confirm that mesophase formation essentially is complete after about 0.1 s in case of the iPP homopolymer, and after only about 0.5 and 1 s in the copolymers containing 6 and 11 mol-% 1-butene, respectively, referring to the times at the end of the fast process. The vertical arrows at the time axis of Fig. 5 indicate the approximate half-time of the cold-ordering of the various polymers of the present study which correspondingly are slightly lower than the time of completion of mesophase formation. For the homopolymer the half-time of cold-ordering is about 0.04 s while for iPP-But.6 and iPP-But.11, 0.2 and 0.7 s, respectively, have been observed. The half-time of ordering of the iPP homopolymer, however, is distinctly lower than has been observed earlier in an independent study [23]. Continuous recording of the FSC signal during the isothermal ordering process revealed a half-time of ordering of about 0.3 s (see Fig. 7 in [23]), and a completion of the process after close to 1 s (see Fig. 2 in [23]). We assume that the observed difference of the kinetics of mesophase formation is not only due to the use of different grades of polymers but also due to the different pathways of nucleation. In the present study the quiescent melt of iPP was cooled to 120 K, heated to 300 K and only then cold-ordered at constant temperature. In the earlier study, the ordering temperature was directly approached from the quiescent liquid state, *i.e.*, the thermal history and the pathway of nucleation were different. Obviously, the ordering process is accelerated on extension of the time of the sample in the glassy state. However, further experiments are needed to address the effect of using different grades, *i.e.*, molar mass, polydispersity, regio- and stereo-regularity *etc.* on the mesophase-formation kinetics.

3.2. Kinetics of non-isothermal mesophase formation and kinetics of reorganization

The kinetics of both non-isothermal mesophase formation and of mesophase reorganization were analyzed by heating samples at the low rate of 1000 K s^{-1} (path H2 in Fig. 1) after being isothermally ordered at 300 K for different periods of time (P in Fig. 1). In this analysis, identical preparations have been employed as discussed with Figs. 3 to 5. The reduction of the heating rate from 20,000 to 1000 K s^{-1} permits non-isothermal mesophase formation of initially completely amorphous samples during the slow heating experiments, and reorganization of either isothermally or non-isothermally formed mesophase into the more stable crystal phase.

Fig. 6 shows the apparent heat capacities of samples of iPP (left), iPP-But.6 (center), and iPP-But.11 (right), recorded on heating at 1000 K s^{-1}. The time of isothermal ordering at 300 K within the preceding preparation step, according scheme P of Fig. 1, is indicated at each curve. First, the data shown confirm the observation of retarded isothermal mesophase formation in case of the presence of

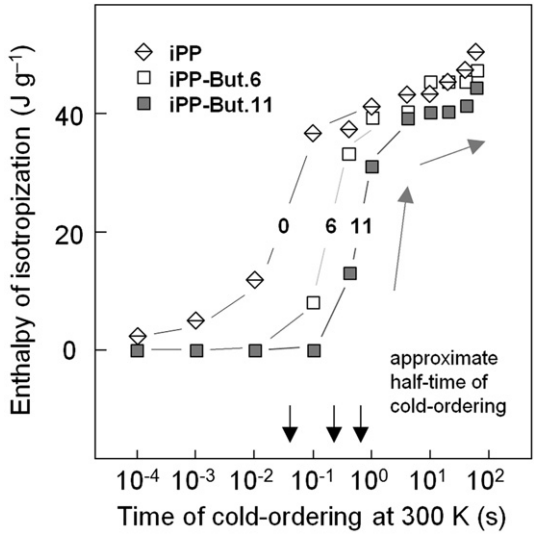

Fig. 5. Enthalpy of isotropization the mesophase of iPP, iPP-But.6, and iPP-But.11 as a function of the time of prior cold-ordering at 300 K. The vertical arrows mark the half-time of cold-ordering.

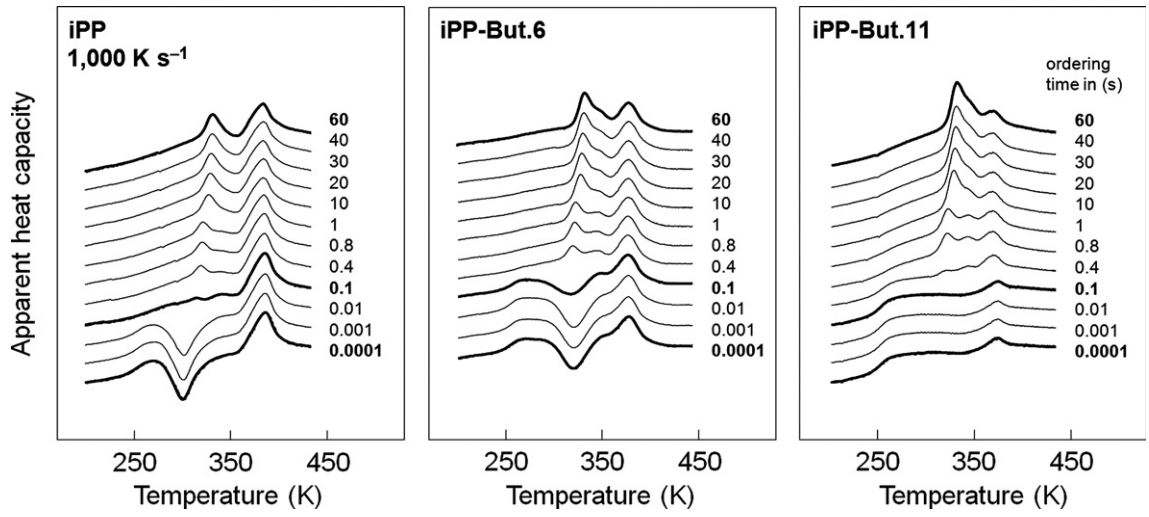

Fig. 6. Apparent heat capacity as a function of temperature obtained on heating iPP (left), iPP-But.6 (center), and iPP-But.11 (right) at a rate of 1000 K s^{-1}. The different curves in the plots represent samples which were ordered at 300 K for different periods of time between 0.1 ms (bottom curve) and 60 s (top curve), according preparation scheme P and analysis by path H2 in Fig. 1.

1-butene co-units, already discussed with Figs. 3 to 5. Inspection of the heating scans of the samples isothermally ordered at 300 K for a period of 0.1 s (bold drawn) reveals presence of mesophase only for the iPP homopolymer. The mesophase formation seems negligible in case of the random iPP-But copolymers since the exothermic and endothermic peaks approximately have the same area.

Furthermore, the data of Fig. 6 provide new information about the kinetics of non-isothermal mesophase formation on heating. Irrespective of the concentration of 1-butene co-units, samples isothermally ordered at 300 K for a period of 0.1 ms are completely amorphous before heating onset . However, the concentration of 1-butene in the various samples distinctly affects the process of cold-ordering during heating at 1000 K s^{-1}. Note that the choice of the heating rate is crucial for identification of differences of the cold-ordering behavior. If the heating rate is too high then cold-ordering may completely be suppressed in all samples, as was demonstrated with the experiment of Fig. 3. In contrast, if the heating rate is too low, then cold-ordering may complete in all samples of different co-unit content — preventing an efficient identification of different kinetics of cold-ordering in the various copolymers. As such, heating at 1000 K s^{-1} seems optimum for evaluation of the different cold-ordering kinetics of the copolymers of the present study. In Fig. 7, the bottom curves in the individual plots of Fig. 6, representing fully amorphous specimens of different comonomer concentration, were re-drawn for direct comparison of the cold-ordering during heating. The data show that cold-ordering gets increasingly suppressed with increasing concentration of 1-butene co-units. The enthalpy of cold-ordering is about 38 J g^{-1} in case of the iPP homopolymer, while it is reduced to 34 and 7 J g^{-1} in the copolymers containing 6 and 11 mol-% 1-butene, respectively. The values of 38, 34 and 7 J g^{-1} correspond to mesophase fractions of 23, 20, and 4%, respectively. A further indication of deceleration of the rate of mesophase formation on addition of 1-butene co-units is the shift of the exothermic cold-ordering peak to higher temperature. Finally, the data of Fig. 7 show that the composition of the copolymers affects the temperature of isotropization of mesophase or melting of crystals, formed by reorganization of mesophase. The temperature of the endothermic peak succeeding the exothermic cold-ordering on heating decreases with increasing amount of 1-butene co-units in the copolymers which likely is due increasing suppression of perfection and/or reorganization of mesophase during heating. As such, the addition of 1-butene co-units not only slows down the formation of mesophase from the liquid structure, but also decreases the rate of mesophase perfection and reorganization. In addition, the decrease of the temperature of disordering or melting may be due to the inclusion of 1-butene co-units into the mesophase which has recently been evidenced by X-ray scattering [58].

The tendency for a reduction of the rate of mesophase perfection and reorganization on increasing the concentration of 1-butene can also be recognized on inspection of the heating scans of semimesomorphic preparations. The top curves in the individual graphs of Fig. 6 were obtained on specimens that have isothermally been cold-ordered at 300 K for a period of 60 s, and were re-drawn in Fig. 8 for direct comparison. It has been shown with the experiments of Figs. 3 and 5 that the cold-ordering process at 300 K has been completed after 60 s. Heating of these semimesomorphic preparations of iPP homo- and copolymers, in general leads to isotropization of the mesophase, which, however, can only be completed if perfection and reorganization into the crystal phase

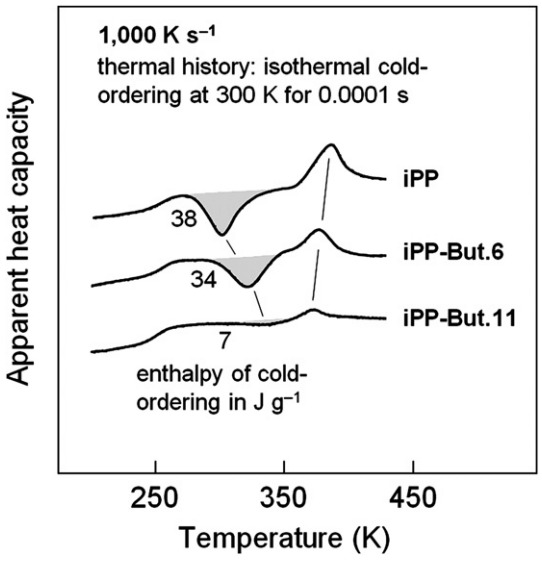

Fig. 7. Apparent heat capacity as a function of temperature on heating fully amorphous iPP (top curve), iPP-But.6 (center curve), and iPP-But.11 (bottom curve) at a rate of 1000 K s^{-1}. The gray-shaded areas indicate exothermic cold-ordering.

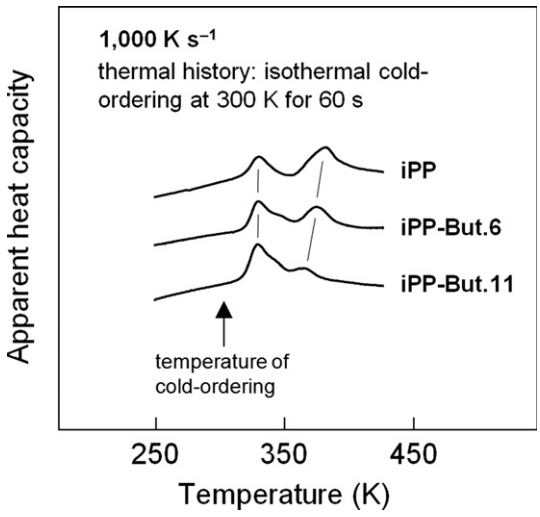

Fig. 8. Apparent heat capacity as a function of temperature on heating semimesomorphic iPP (top curve), iPP-But.6 (center curve), and iPP-But.11 (bottom curve) at a rate of 1000 K s^{-1}.

get suppressed. For the iPP homopolymer, the critical heating rate for complete suppression of perfection and reorganization is 20,000 K s^{-1}. If the heating rate is lower, then completion of the disordering process, *i.e.*, of the mesophase – liquid phase transition is incomplete due to simultaneous onset of perfection and reorganization, inducing disordering/melting of perfected/reorganized mesophase at higher temperature. The data of Fig. 8 clearly show that the rate of perfection and reorganization of the mesophase during heating at 1000 K s^{-1} decrease with increasing concentration of 1-butene co-units since both the enthalpy of isotropization/fusion and the temperature of the high-temperature transition decrease. Simultaneously, and as expected, the enthalpy of isotropization of the low-temperature peak increases. The temperature of the low-temperature peak represents the initial thermodynamic stability of the mesophase formed and perfected at constant temperature of 300 K (see Fig. 5), and, apparently, is identical for all samples of the present study.

3.3. Critical rate of heating for complete suppression of mesophase reorganization

In general, the kinetics of reorganization of semimesomorphic or semicrystalline structures can advantageously be evaluated by variation of the heating rate. While slow heating allows reorganization of ordered structures, it gets increasingly suppressed on increasing the heating rate. With respect to the mesophase of the iPP homopolymer it has been found that reorganization into crystals can only be suppressed by heating at a rate faster than 20–40,000 K s^{-1}. The degree of mesophase perfection and transformation into crystals depends on the temperature of the initial growth of the mesophase and the heating rate used for analysis. For the iPP-But copolymers of the present study, the dependence of mesophase reorganization on the heating rate has not been analyzed yet, and was therefore studied with the experiments of Fig. 2. Semimesomorphic samples were prepared by isothermal cold-ordering at 300 K, and the reorganization has been followed on heating at rates between 1000 and 30,000 K s^{-1}. The corresponding FSC heating curves are shown in Fig. 9. The data confirm the expectation of a lower rate of mesophase reorganization in case of presence of 1-butene co-units in the iPP chain, surmised already from the experiments of Fig. 8. The low-temperature peak in the curves of Fig. 9 represents onset of isotropization of the mesophase, and is only slightly higher than the temperature of prior cold-ordering. With increasing heating rate, this peak shifts slightly toward higher temperature which may be related to the glass transition of the mesophase [28,73]. However, more important in the context of the discussion of mesophase reorganization is the observation of an increase of the enthalpy of disordering of the low-temperature peak with increasing heating rate. The low-temperature isotropization of the mesophase is incomplete on slow heating due to simultaneous onset of mesophase perfection and reorganization into crystals, with the reorganized structure melting at higher temperature. With increasing heating rate, the ratio of enthalpies of the low- and high-temperature transition increases, which is a quantitative measure of the reorganization, and its change with heating rate [74].

The data of Fig. 9 show that mesophase reorganization in random copolymers of propylene with 6 and 11 mol-% 1-butene is fully inhibited at distinctly lower rate than in case of the iPP homopolymer. While the high-temperature melting peak of reorganized mesophase in iPP seems completely absent on heating at 20,000 K s^{-1}, in iPP-But copolymers with 6 and 11 mol-% 1-butene the critical heating rate for complete suppression of mesophase reorganization is reduced to 10,000 and 5000 K s^{-1}, respectively.

Heating at rates faster than the reported critical heating rates results in direct transformation of the initially at 300 K formed mesophase into liquid structure. Though not expected, the temperature of the mesophase – liquid phase transformation seems independent on the concentration of 1-butene and is

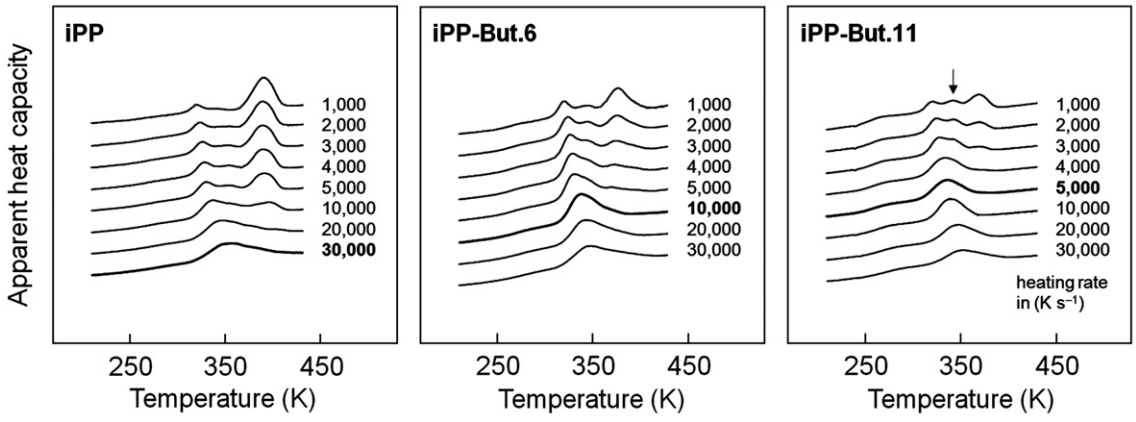

Fig. 9. Apparent heat capacity as a function of temperature obtained on heating semimesomorphic iPP (left), iPP-But.6 (center), and iPP-But.11 (right) at different rate between 1000 (top curves) and 30,000 K s^{-1} (bottom curves).

approximately 350 K on heating at 30,000 K s^{-1}. Initially we expected a decrease not only of the critical rate of heating for complete suppression of reorganization but also of the temperature of the mesophase – liquid phase transformation, based on the knowledge of incorporation of 1-butene co-units into the mesophase, [58] decreasing their thermodynamic stability. However, assessing the thermodynamic stability of the mesophase as a function of comonomer concentration, as defined by intersection of the free-enthalpy – temperature curves, would require analysis of the equilibrium transition temperature. In the present study, the mesophase in all samples of different co-unit concentration was formed at identical temperature of 300 K, though different respective supercooling below the equilibrium melting temperature. As such it is not surprising that the disordering temperature in all copolymers is unchanged.

Finally, careful viewing of the data of Fig. 9 suggests annealing/perfection of mesophase, as is indicated by detection of a small endothermic peak on heating at low rate, following the low-temperature isotropization peak of initially formed mesophase (see arrow in the right plot). On fast heating, the annealing/perfection of mesophase apparently is reduced, and is then only recognized as a shoulder. The observation of a discrete annealing peak on continuous heating may display the maximum degree of perfection of the mesophase, or may be due to interruption of the annealing by the shallow mesophase – crystal transition exotherm, preceding the final melting peak.

4. Conclusions

In the present study, the effect of presence of 1-butene co-units in the iPP macromolecule on the kinetics of structure formation at high supercooling and the kinetics of temperature-triggered reorganization has been evaluated. It has been shown that mesophase formation at high supercooling is distinctly slower in random iPP-But copolymers than in the iPP homopolymer, with the decrease of the rate of both isothermal and non-isothermal mesophase formation being dependent on the concentration of 1-butene chain defects (see Figs. 4, 5 and 7). The finding of a decreased rate of ordering at high supercooling is in line with independent observation of a lowered rate of crystallization at low supercooling. The decrease of both the rate of crystallization at low supercooling and the rate of mesophase formation at high supercooling, however, cannot primarily be attributed to the selection of molecule segments free of constitutional defects at the growth front of the ordered phase. X-ray analyses revealed incorporation of 1-butene co-units into the crystalline phase and into the mesophase, apparently without partitioning between ordered and amorphous phases [58]. It is therefore suggested that the decrease of the (gross) rate of crystallization and rate of mesophase formation in iPP-But copolymers, compared to the iPP homopolymer, is mainly due to the decrease of the thermodynamic driving force, *i.e.*, the difference of the bulk free enthalpies of parent and daughter phases of the ordering process. In random copolymers, the free enthalpy of the liquid phase is lower than that of the homopolymer at identical temperature (otherwise, there would be phase separation), which reduces the free-enthalpy difference between liquid and ordered phases and the equilibrium melting temperature [75]. For iPP-based random copolymers, the decrease of the equilibrium melting temperature has been discussed and seems experimentally proven [55,76–78], and the link between the rate of phase transformation and the free-enthalpy difference between parent and daughter phases is well documented with the Turnbull–Fisher equation [79]. The advance of the present work, however, seems the proof that heterogeneous nucleation evident on crystallization at low supercooling, and homogeneous nucleation, assumed to be the dominant nucleation mechanism on mesophase formation at high supercooling, obviously obey identical rules regarding the relationship between the thermodynamic driving force and the rate of phase transformation. Despite this result is expected from the classical nucleation and crystallization theory [80,81], experimental evidence is rare since homogenous nucleation in bulk samples barely can be assessed regarding its kinetics with standard analytics. With the present work, the experimental tool of fast scanning chip calorimetry has been proven to be outstanding beneficial for quantitative analysis of the kinetics of homogeneous nucleation/crystallization at high supercooling of iPP-based materials, finally providing valuable data for further establishment of correlations between the chemical architecture of macromolecules and structure formation from the quiescent liquid state.

Acknowledgments

The authors gratefully acknowledge financial support by the Deutsche Forschungsgemeinschaft (DFG). EZ acknowledges financial support by a European Union funded Marie Curie EST fellowship.

References

[1] Pasquini N. Polypropylene handbook. Munich: Carl Hanser Verlag; 2005.
[2] Natta G, Corradini P. Structure and properties of isotactic polypropylene. Nuovo Cimento Suppl 1960;15:40–51.
[3] Hock CW. Morphology of polypropylene crystallized from the melt. J Polym Sci Part A 1966;4:227–42.
[4] Binsbergen FL, De Lange BGM. Morphology of polypropylene crystallized from the melt. Polymer 1968;9:23–40.
[5] Norton DR, Keller A. The spherulitic and lamellar morphology of melt-crystallized isotactic polypropylene. Polymer 1985;26:704–16.
[6] Olley RH, Bassett DC. On the development of polypropylene spherulites. Polymer 1989;30:399–409.
[7] Wunderlich B, Grebowicz J. Thermotropic mesophases and mesophase transitions of linear, flexible macromolecules. Adv Polym Sci 1984;60:1–59.
[8] Grebowicz J, Lau SF, Wunderlich B. The thermal properties of polypropylene. J Polym Sci Symp 1984;71:19–37.
[9] Wu ZQ, Dann VL, Cheng SZD, Wunderlich B. Fast DSC applied to the crystallization of polypropylene. J Therm Anal 1988;34:105–14.
[10] Zannetti R, Celotti G, Fichera A, Francesconi R. The structural effects of annealing time and temperature on the paracrystal–crystal transition in isotactic polypropylene. Makromol Chem 1969;128:137–42.
[11] O'Kane WJ, Young RJ, Ryan AJ, Bras W, Derbyshire GE, Mant GR. Simultaneous SAXS/WAXS and d.s.c. analysis of the melting and recrystallization behaviour of quenched polypropylene. Polymer 1994;35:1352–8.
[12] Konishi T, Nishida K, Kanaya T. Crystallization of isotactic polypropylene from prequenched mesomorphic phase. Macromolecules 2006;39:8035–40.
[13] Grubb DT, Yoon DY. Morphology of quenched and annelaed isotatic polypropylene. Polym Commun 1986;27:84–8.
[14] Hsu CC, Geil PH, Miyaji H, Asai K. Structure and properties of polypropylene crystallized from the glassy state. J Polym Sci Polym Phys 1986;24:2379–401.
[15] Wang ZG, Hsiao BS, Srinivas S, Brown GM, Tsou AH, Cheng SZD, et al. Phase transformation in quenched mesomorphic isotactic polypropylene. Polymer 2001;42:7561–6.
[16] Ogawa T, Miyaji H, Asai K. Nodular structure of polypropylene. J Phys Soc Jpn Lett 1985;54:3668–70.
[17] Zia Q, Androsch R, Radusch HJ, Piccarolo S. Morphology, reorganization, and stability of mesomorphic nanocrystals in isotactic polypropylene. Polymer 2006;47:8163–72.
[18] Zia Q, Radusch HJ, Androsch R. Direct analysis of nodular crystals in isotactic polypropylene by atomic force microscopy, and its correlation with calorimetric data. Polymer 2007;48:3504–11.
[19] Gezovich DM, Geil PH. Deformation and aging of quenched polypropylene. Polym Eng Sci 1968;8:210–5.
[20] Zia Q, Androsch R, Radusch HJ. Effect of structure at the micrometer and nanometer length scales on the light transmission of isotactic polypropylene. J Appl Polym Sci 2010;117:1013–20.
[21] Zia Q, Radusch HJ, Androsch R. Deformation behavior of isotactic polypropylene crystallized via a mesophase. Polym Bull 2009;63:755–71.
[22] Silvestre C, Cimmino S, Duraccio D, Schick C. Isothermal crystallization of isotactic poly(propylene) studied by superfast calorimetry. Macromol Rap Comm 2007;28:875–81.
[23] De Santis F, Adamovsky S, Titomanlio G, Schick C. Isothermal nanocalorimetry of isotactic polypropylene. Macromolecules 2007;40:9026–31.

[24] Gradys A, Sajkiewicz P, Minakov AA, Adamovsky S, Schick C, Hashimoto T, et al. Crystallization of polypropylene at various cooling rates. Mat Sci Eng 2005;A413–A414:442–6.
[25] De Santis F, Adamovsky S, Titomanlio G, Schick C. Scanning nanocalorimetry at high cooling rate of isotactic polypropylene. Macromolecules 2006;39:2562–7.
[26] Piccarolo S. Morphological changes in isotactic polypropylene as a function of cooling rate. J Macromol Sci Phys 1992;B31:501–11.
[27] Piccarolo S, Alessi S, Brucato V, Titomanlio G. Crystallization behaviour at high cooling rates of two polypropylenes. In: Dosier M, editor. Crystallization of polymers. Dordrecht: Kluwer; 1993. p. 475–80.
[28] Mileva D, Androsch R, Zhuravlev E, Schick C. The temperature of melting of the mesophase of isotactic polypropylene. Macromolecules 2009;42:7275–8.
[29] Farrow GJ. Measurement of the smectic content in undrawn polypropylene filaments. J Appl Polym Sci 1965;9:1227–32.
[30] Zia Q, Androsch R, Radusch HJ, Ingolic E. Crystal morphology of rapidly cooled isotactic polypropylene: a comparative study by TEM and AFM. Polym Bull 2008;60:791–8.
[31] Zia Q, Androsch R. Effect of atomic force microscope tip geometry on the evaluation of the crystal size of semicrystalline polymers. Meas Sci Technol 2009;20. 097003. p. 4.
[32] Natta G. Progress in stereospecific polymerization. Makromol Chem 1960;35:94–131.
[33] Androsch R, Wunderlich B. Reversible crystallization and melting at the lateral surface of isotactic polypropylene crystals. Macromolecules 2001;34:5950–60.
[34] Schaefer D, Spiess HW, Suter UW, Fleming WW. Two-dimensional solid-state NMR studies of ultraslow chain motion: glass transition in atactic poly (propylene) versus helical jumps in isotactic poly(propylene). Macromolecules 1990;23:3431–9.
[35] De Rosa C. Temperature dependence of intramolecular disorder in the high-temperature phase of poly(tetrafluoroethylene) (phase I). Macromolecules 1988;21:1174–6.
[36] Watanabe J, Okamoto S, Satoh K, Sakajiri K, Furuya H, Abe A. Reversible helix-helix transition of poly(β-phenylpropyl L-aspartate) involving a screw-sense inversion in the solid state. Macromolecules 1996;29:7084–8.
[37] Lotz B, Mathieu C, Thierry A, Lovinger AJ, Rosa C, De Ruiz de Ballesteros O, et al. Chirality constraints in crystal–crystal transformations: isotactic poly(1-butene) versus syndiotactic polypropylene. Macromolecules 1998;31:9253–7.
[38] Wang C, Hsieh TC, Cheng YW. Solution-electrospun isotactic polypropylene fibers: processing and microstructure development during stepwise annealing. Macromolecules 2010;43:9022–9.
[39] Androsch R. In situ atomic force microscopy of the mesomorphic-monoclinic phase transition in isotactic polypropylene. Macromolecules 2008;41:533–5.
[40] Androsch R, Di Lorenzo ML, Schick C, Wunderlich B. Mesophases in polyethylene, polypropylene and poly(1-butene). Polymer 2010;51:4639–62.
[41] De Rosa C, Auriemma F, Ruiz de Ballesteros O, Resconi L, Camurati I. Tailoring the physical properties of isotactic polypropylene through incorporation of comonomers and the precise control of stereo and regioregularity by metallocene catalysts. Chem Mater 2007;19:5122–30.
[42] Maier C, Calafut T. Polypropylene: the definite user's guide and data book. Norwich: Plastics design library by William Andrew; 1998.
[43] Cavallo C, Martuscelli E, Pracella M. Properties of solution grown crystals of isotactic propylene/butene-1 copolymers. Polymer 1977;18:42–8.
[44] Turner-Jones A. Cocrystallization in copolymers of α-olefins II—Butene-1 copolymers and polybutene type II/I crystal phase transition. Polymer 1966;7:23–59.
[45] Gou Q, Li H, Yu Z, Chen E, Zhang Y, Yan S. Crystallization behavior of a propylene-1-butene random copolymer in its α and γ modifications. Colloid Polym Sci 2007;285:1149–55.
[46] Marega C, Marigo A, Saini R, Ferrari P. The influence of thermal treatment and processing on the structure and morphology of poly(propylene-*ran*-1-butene) copolymers. Polym Int 2001;50:442–8.
[47] De Rosa C, Auriemma F, Ruiz de Ballesteros O, Resconi L, Camurati I. Crystallization behavior of isotactic propylene–ethylene and propylene–butene copolymers: effect of comonomers *versus* stereodefects on crystallization properties of isotactic polypropylene. Macromolecules 2007;40:6600–16.
[48] Jeon K, Palza H, Quijada R, Alamo RG. Effect of comonomer type on the crystallization kinetics and crystalline structure of random isotactic propylene 1-alkene copolymers. Polymer 2009;50:832–44.
[49] Hosier IL, Alamo RG, Lin JS. Lamellar morphology of random metallocene propylene copolymers studied by atomic force microscopy. Polymer 2004;45:3441–55.
[50] Hosier IL, Alamo RG, Esteso P, Isasi JR, Mandelkern L. Formation of the α and γ polymorphs in random metallocene–propylene copolymers. Effect of concentration and type of comonomer. Macromolecules 2003;36:5623–36.
[51] Hosoda S, Hori H, Yada K, Nakahara S, Tsuji M. Degree of comonomer inclusion into lamella crystal for propylene/olefin copolymers. Polymer 2002;43:7451–60.
[52] Abiru T, Mizuno A, Weigand F. Microstructural characterization of propylene-butene-1 copolymer using temperature rising elution fractionation. J Appl Polym Sci 1998;68:1493–501.
[53] Mileva D, Androsch R, Radusch HJ. Effect of structure on light transmission in isotactic polypropylene and random propylene-1-butene copolymers. Polym Bull 2009;62:561–71.
[54] Mileva D, Zia Q, Androsch R. Tensile properties of random copolymers of propylene with ethylene and 1-butene: effect of crystallinity and crystal habit. Polym Bull 2010;65:623–34.
[55] Mileva D, Androsch R, Radusch HJ. Effect of cooling rate on melt-crystallization of random propylene-ethylene and propylene-1-butene copolymers. Polym Bull 2008;61:643–54.
[56] Mileva D, Zia Q, Androsch R, Radusch HJ, Piccarolo S. Mesophase formation in poly(propylene-ran-1-butene) by rapid cooling. Polymer 2009;50:5482–9.
[57] Mileva D, Androsch R, Zhuravlev E, Schick C. Critical rate of cooling for complete suppression of crystallization of random copolymers of propylene with ethylene and 1-butene. Thermochim Acta 2009;492:67–72.
[58] Mileva D, Androsch R, Funari SS, Wunderlich B. X-ray study of crystallization of random copolymers of propylene and 1-butene via a mesophase. Polymer 2010;51:5212–20.
[59] 9th Lähnwitz seminar on calorimetry "Transitions far from Equilibrium – Super-heating; Super-cooling", May 29 – June 1, 2006, Rostock, Germany (organized by Schick C.) see also Thermochim Acta; 2009, 492 (1–2).
[60] Workshop on "Polymer Crystallization under Conditions Relevant to Processing", May 27–28, 2010, Genova, Italy (organized by Alfonso GC, Peters GWM).
[61] Efremov MY, Olson EA, Zhang M, Schiettekatte F, Zhang ZS, Allen LH. Ultrasensitive, fast, thin-film differential scanning calorimeter. Rev Sci Inst 2004;75:179–91.
[62] Allen LH, Ramanath G, Lai SL, Ma Z, Lee S, Allman DDJ, et al. 1,000,000 C/s thin film electrical heater: in situ resistivity measurements of Al and Ti/Si thin films during ultra rapid thermal annealing. Appl Phys Lett 1994;64:417–9.
[63] Adamovsky SA, Minakov AA, Schick C. Scanning microcalorimetry at high cooling rate. Thermochim Acta 2003;403:55–63.
[64] Minakov AA, Schick C. Ultrafast thermal processing and nanocalorimetry at heating and cooling rates up to 1 MK/s. Rev Sci Inst 2007;78:073902–10.
[65] Private communication, Basell Bayreuth Chemie GmbH, 2001.
[66] Sigma Aldrich, product information.
[67] Private communication, Linz, Borealis, 2008.
[68] Zhuravlev E, Schick C. Fast scanning power compensated differential scanning nano-calorimeter: 1. The device. Thermochim Acta 2010;505:11–3.
[69] Zhuravlev E, Schick C. Fast scanning power compensated differential scanning nano-calorimeter: 2. Heat capacity analysis. Thermochim Acta 2010;505:14–21.
[70] Advanced thermal analysis system ATHAS, with its data bank available in the internet at http://athas.prz.rzeszow.pl.
[71] Mileva D, Androsch R, Zhuravlev E, Schick C, Wunderlich B. Isotropization, perfection and reorganization of the mesophase of isotactic polypropylene. Thermochim Acta; 2010, in press.
[72] Hemminger WF, Cammenga HK. Methoden der Thermischen Analyse. Berlin: Springer; 1989.
[73] Minakov AA, Wurm A, Schick C. Superheating in linear polymers studied by ultrafast nanocalorimetry. Eur Phys J E 2007;23:43–53.
[74] Minakov AA, Mordvintsev DA, Schick C. Melting and reorganization of poly (ethylene terephthalate) on fast heating (1,000 K/s). Polymer 2004;45:3755–63.
[75] Flory PJ. Theory of crystallization in copolymers. Trans Faraday Soc 1955;51:848–57.
[76] Mezghani K, Phillips PJ. γ-phase in propylene copolymers at atmospheric pressure. Polymer 1995;36:2407–11.
[77] Alamo RG, Ghosal A, Chatterjee J, Thompson KL. Linear growth rates of random propylene ethylene copolymers. The changeover from γ dominated growth to mixed (α + γ) polymorphic growth. Polymer 2005;46:8774–89.
[78] Jeon K, Chiari YL, Alamo RG. Maximum rate of crystallization and morphology of random propylene ethylene copolymers as a function of comonomer content up to 21 mol%. Macromolecules 2008;41:95–108.
[79] Turnbull D, Fisher JC. Rate of nucleation in condensed systems. J Chem Phys 1949;17:71–3.
[80] Hoffmann JD, Davis GT, Lauritzen JI. The rate of crystallization of linear polymers with chain folding. In: Hannay HB, editor. Crystalline and non-crystalline solids. Treatise on solid state chemistry, vol. 3. New York: Plenum Press; 1976.
[81] Wunderlich B. Macromolecular physics. In: Crystal nucleation, growth, annealing, vol 2. New York: Academic Press; 1976.

Polymer 52 (2011) 1116–1123

Contents lists available at ScienceDirect

Polymer

journal homepage: www.elsevier.com/locate/polymer

Morphology of syndiotactic polypropylene/alumina nanocomposites

Le Thuy Truong [a,b], Åge Larsen [a,*], Børge Holme [a], Finn Knut Hansen [b], Jaan Roots [b]

[a] SINTEF Materials and Chemistry, P.O. Box 124 Blindern, NO-0314 Oslo, Norway
[b] University of Oslo, Department of Chemistry, P.O. Box 1033 Blindern, NO-0315 Oslo, Norway

ARTICLE INFO

Article history:
Received 23 September 2010
Received in revised form
10 November 2010
Accepted 6 January 2011
Available online 14 January 2011

Keywords:
Syndiotactic polypropylene/alumina nanocomposites
Al_2O_3 nanoparticles
Morphology

ABSTRACT

The effect of the addition of 50 nm spherical alumina nanoparticles with hydrophilic or hydrophobic surfaces on the morphology of syndiotactic polypropylene (sPP) was investigated. The filler content in the nanocomposites was 3 wt%. Polarized Optical Microscopy and Small Angle Light Scattering (SALS) studies showed that sPP and the nanocomposites form hedrites. The addition of alumina nanoparticles significantly increased the number of hedrites. A higher number of nucleation sites in the nanocomposites promote a higher crystallization rate, and thus hedritic growth was stopped at the early stage of crystallization. Quantitative evaluations by SALS analysis show that the object size is decreased by not only the crystallization conditions but also the presence of Al_2O_3 nanoparticles. A small amount of Al_2O_3 nanoparticles did not noticeably affect the crystallinity of sPP, but increased the melting point. Transmission Electron Microscopy images showed that the lamellar thickness did not change significantly with the incorporation of nanoparticles. The lamella thickness, however, depends on cooling rates. X-ray diffraction characterization indicated that the sPP and the nanocomposites were crystallized in disordered "form I". The incorporation of alumina nanoparticles had a small effect on the crystal structure of syndiotactic polypropylene.

1. Introduction

There have been many studies on syndiotactic polypropylene (sPP) over recent years on account of its remarkable physical and mechanical properties. Recent studies showed that sPP exhibits excellent properties that overcome weaknesses, such as poor flexibility and low electrical breakdown strength, known for isotactic polypropylene (iPP) [1]. This makes sPP very attractive for power cable and innovative applications [1–3]. Many researches have focused on the polymorphism, morphology and crystallization kinetics of syndiotactic polypropylene under various processing conditions [4]. In comparison with iPP, sPP shows a more fine grained morphology [5] which contributes to better electrical characteristics. The continuous development of sPP-based materials aims at achieving improved properties. Modification of polypropylene performance by inorganic nanoparticles incorporation is a promising way of broadening the use of this material.

Many studies on inorganic/polypropylene composites based on iPP have been reported so far [6–9]. Considerable improvement of polypropylene's mechanical properties, crystallization behavior, electrical conductivity, and thermal stability can be expected for this polymer. Very little, however, has been known about nanocomposites based on syndiotactic polypropylene. The effect of layered silicates on chain conformational transformations of sPP during mechanical elongation and thermal treatment was recently reported [10]. Both organic layered silicates and silver nanoparticles significantly increased the crystallization rate of sPP due to their heterogeneous nucleation effect [11,12]. Although alumina has recently received large interest thanks to its excellent dielectric properties, good thermal conductivity, high strength, and resistance to strong acids and bases even at elevated temperatures [13], its use as filler in polymers is limited up to the present. Zhao and Li [14] reported improved tensile and impact properties of iPP from addition of alumina nanoparticles. They also found that incorporation of alumina nanoparticles significantly reduces the iPP spherulitic size. Most studies, however, have focused on the effect of alumina nanoparticles in polar polymers such as poly(ethylene terephthalate), polyamides, polyurethane and epoxy resins [15–20]. Thus, additional studies on sPP/alumina nanocomposites are needed for future development.

In a previous paper [21] we investigated the selection of silane coupling agents possessing a good compatibility with PP. We achieved a good dispersion of hydrophobic functionalized alumina nanoparticles by melt mixing. The purpose of this work was to study the effect of alumina nanoparticles on the morphology of syndiotactic polypropylene using Differential Scanning Calorimetry

* Corresponding author.
E-mail address: age.larsen@sintef.no (Å. Larsen).

0032-3861/$ – see front matter © 2011 Elsevier Ltd. All rights reserved.
doi:10.1016/j.polymer.2011.01.014

(DSC), Polarized Optical Microscopy (POM), Small Angle Light Scattering (SALS), Transmission Electron Microscopy (TEM), and X-ray analysis (XRD).

2. Experimental

2.1. Materials

Commercial syndiotactic polypropylene used in this work was supplied by Total Fina with the following parameters: a melt flow index of 4 g/10 min, density 0.88 g/cm^3, a melting point of 130 °C (DSC), tensile strength 15 MPa (ASTM D638), tensile modulus 480 MPa (ASTM D638), elongation at break 10% (ASTM D790), and flexural modulus 340 MPa (ASTM D638). Spherical γ-phase alumina (Al_2O_3) nanoparticles with nominal size 50 nm, were purchased from Aldrich. (3-chloropropyl)triethoxysilane (95%), and anhydrous toluene (99.8%) were also from Aldrich and used as supplied.

2.2. Sample preparation

The silane modification of the alumina was adapted from the procedures as described elsewhere [21]. The Al_2O_3 NP surface was modified with a silane coupling agent, (3-chloropropyl)triethoxysilane, in anhydrous toluene. The mixture was refluxed for 23 h at 135 °C to create hydrocarbon groups for dispersibility improvements of alumina nanoparticles in an sPP matrix [21]. The sPP and alumina were manually premixed, and the mixture was melt blended in a co-rotating twin batch screw extruder (DSM Midi 2000) at 70 rpm and 200 °C for 5 min. All the nanocomposites contained an equal amount of 3 wt% alumina. The extruded samples were then molded in a hot press at 200 °C for 5 min, and crystallized at two different cooling rates by using air or water cooling to obtain 1 mm thick films. Average cooling rates for air and water cooling are 0.25 and 25 K/min, respectively.

2.3. Characterization

A Perkin–Elmer Pyris 8500 Differential Scanning Calorimeter (DSC) was applied to record melting endotherms for these resins. Calibration for the temperature and heat flow was carried out using both an indium standard (T_m = 156.6 °C and ΔH = 28.5 J/g) and a zinc standard (T_m = 419.47 °C and ΔH = 108.37 J/g). Standard aluminum pans (Perkin–Elmer 0219-0041) were used to minimize thermal lag between the polymer sample and the DSC furnace. Typical sample sizes were 2–4 mg and 1–1.5 mg for slow and fast heating, respectively. All measurements were carried out under nitrogen atmosphere.

A Polarizing Optical Microscope (POM) (Olympus BX51, Japan) was used to observe the morphology of the neat sPP and the composites. The thin sample pieces ca. 10 μm thick cut from the hot-pressed plates were sandwiched between optical glass plates.

Small Angle Light Scattering (SALS) experiments were performed on a home-built light scattering set-up composed of a He–Ne laser source (wavelength 632.8 nm), optical devices to define the scattering volume and angle, and a QImaging Retiga CCD camera (with effective pixel dimension 12.9 × 12.9 μm^2). The sample (sandwiched between optical glass plates) was placed

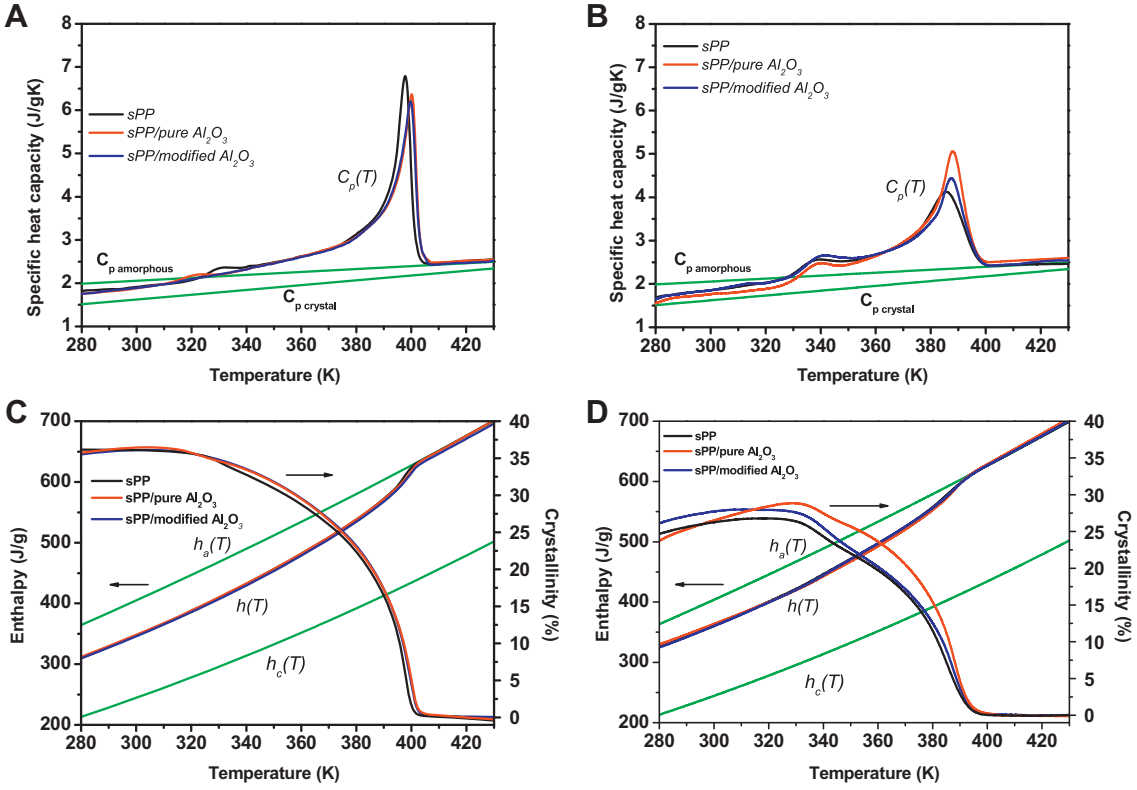

Fig. 1. (A) and (B) Specific heat capacity of neat sPP, 3 wt% pure Al_2O_3/sPP, and 3 wt% modified-Al_2O_3/sPP nanocomposites at heating rates 30 K/min and 150 K/min, respectively. The samples were non-isothermally melt-crystallized at 0.25 K/min, and 25 K/min, respectively, in a hot press. The straight lines ($C_{p\ \text{amorphous}}$ and $C_{p\ \text{crystal}}$) are the specific heat capacity for amorphous and crystalline polypropylene from the ATHAS data bank. (C) and (D) Temperature dependences of the enthalpy and the degree of crystallinity using data from melting exotherms (A) and (B), respectively. The curves $h_a(T)$ and $h_c(T)$ are the enthalpy for amorphous and crystalline PP integrated from $C_{p\ \text{amorphous}}$ and $C_{p\ \text{crystal}}$.

between crossed polarizers (depolarized light) to investigate the concentration fluctuations or the anisotropy fluctuations. The Fraunhofer diffraction pattern from a 25 μm pinhole was employed for the calibration of the scattering angle. The scattering patterns were analyzed using the "Fit2D" software [22].

The lamella structures of the sPP and nanocomposites were observed by a JEOL 2000FX Transmission Electron Microscope (TEM) operated at 120 kV. The samples were stained by mixing 0.15 g $RuCl_3 \cdot 3H_2O$ and 5 ml sodium hypochlorite, and leaving the sample in an air-tight container for 1.5 days. RuO_4 diffuses only into the amorphous components, leaving the crystals unaffected. Ultra-thin samples of 70 nm thickness were prepared at −100 °C by using a Reichert Ultracut S ultramicrotome equipped with a diamond knife. A large number of images (approximately 6 micrographs per sample) made at various positions in the samples were analyzed using the "ImageJ" software to obtain the lamella thickness distribution histograms [23].

X-ray diffraction (XRD) characterization of the samples was performed at room temperature using a Siemens D-5000 with a $Cu_{K\alpha 1}$ radiation and wavelength 0.154 nm. The signal was obtained in step mode with a step size of 0.02°, and the collection time was 1 s.

3. Results and discussion

Fig. 1(A and B) presents the experimental heat capacity of neat sPP, 3 wt% pure Al_2O_3/sPP, and 3 wt% modified-Al_2O_3/sPP nanocomposites at heating rates 30 K/min and 150 K/min, respectively, and the C_p reference curves for amorphous and crystalline polypropylene. The samples were non-isothermally melt-crystallized at 0.25 K/min and 25 K/min in a hot press, respectively. In the melt part, $C_p(T)$ and $C_{p\ \mathrm{amorphous}}(T)$ coincide, except for a slightly higher curve for sPP/pure alumina in Fig. 1(B), but which is still within the 2–3% uncertainty in the DSC method. The coincidence is an indicator of the quality of the measurement. This is very important for C_p characterization. Fig. 1(A) shows that the melting temperature for the neat sPP is 124.0 °C, and shifts to higher temperature, 126.4 °C, when the Al_2O_3 nanoparticles are incorporated into the sPP matrix. The same trend can be seen for the samples crystallized at a faster cooling rate, 25 K/min, shown in Fig. 1(B) where the

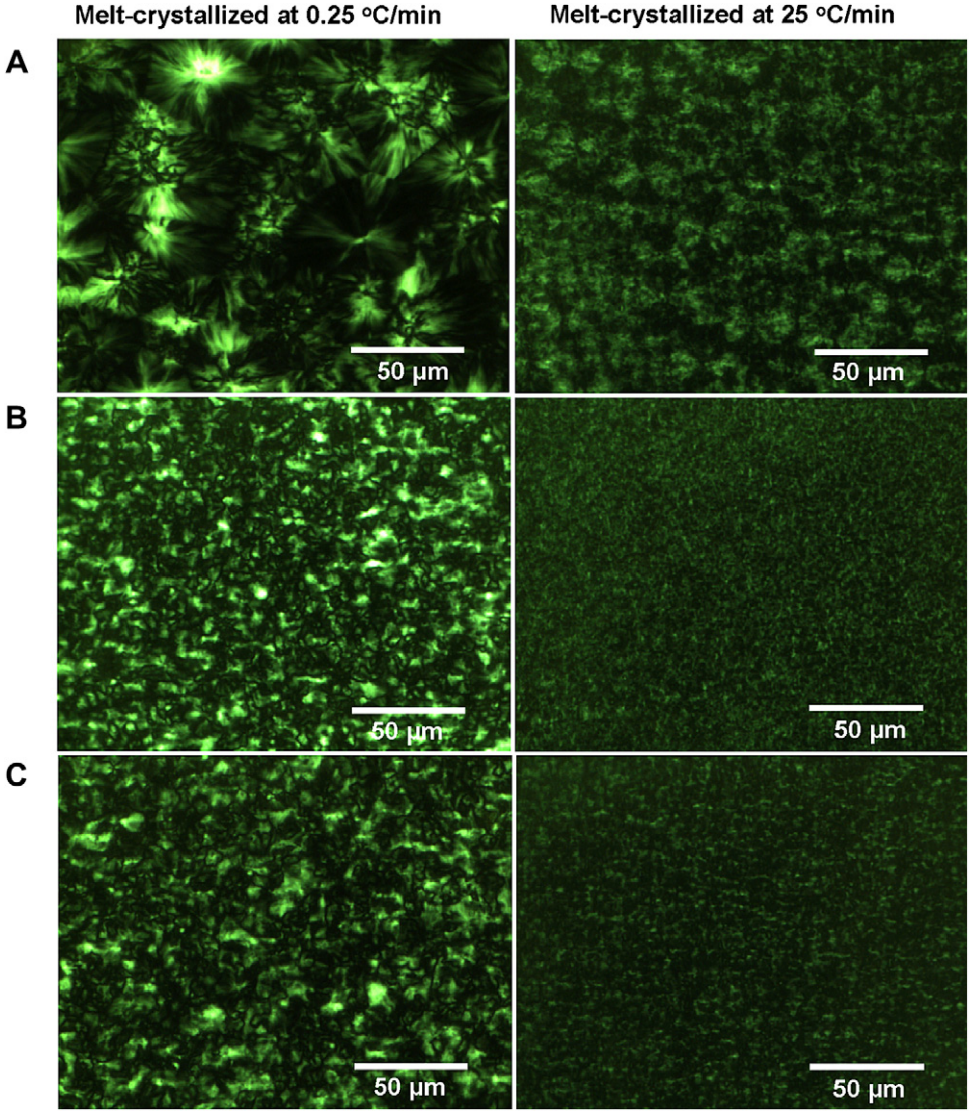

Fig. 2. Polarized optical micrographs of the neat sPP (A), 3 wt% pure Al_2O_3/sPP (B), and 3 wt% modified-Al_2O_3/sPP nanocomposites (C) non-isothermally melt-crystallized at 0.25 K/min (left-hand side) 25 K/min (right-hand side) in a hot press.

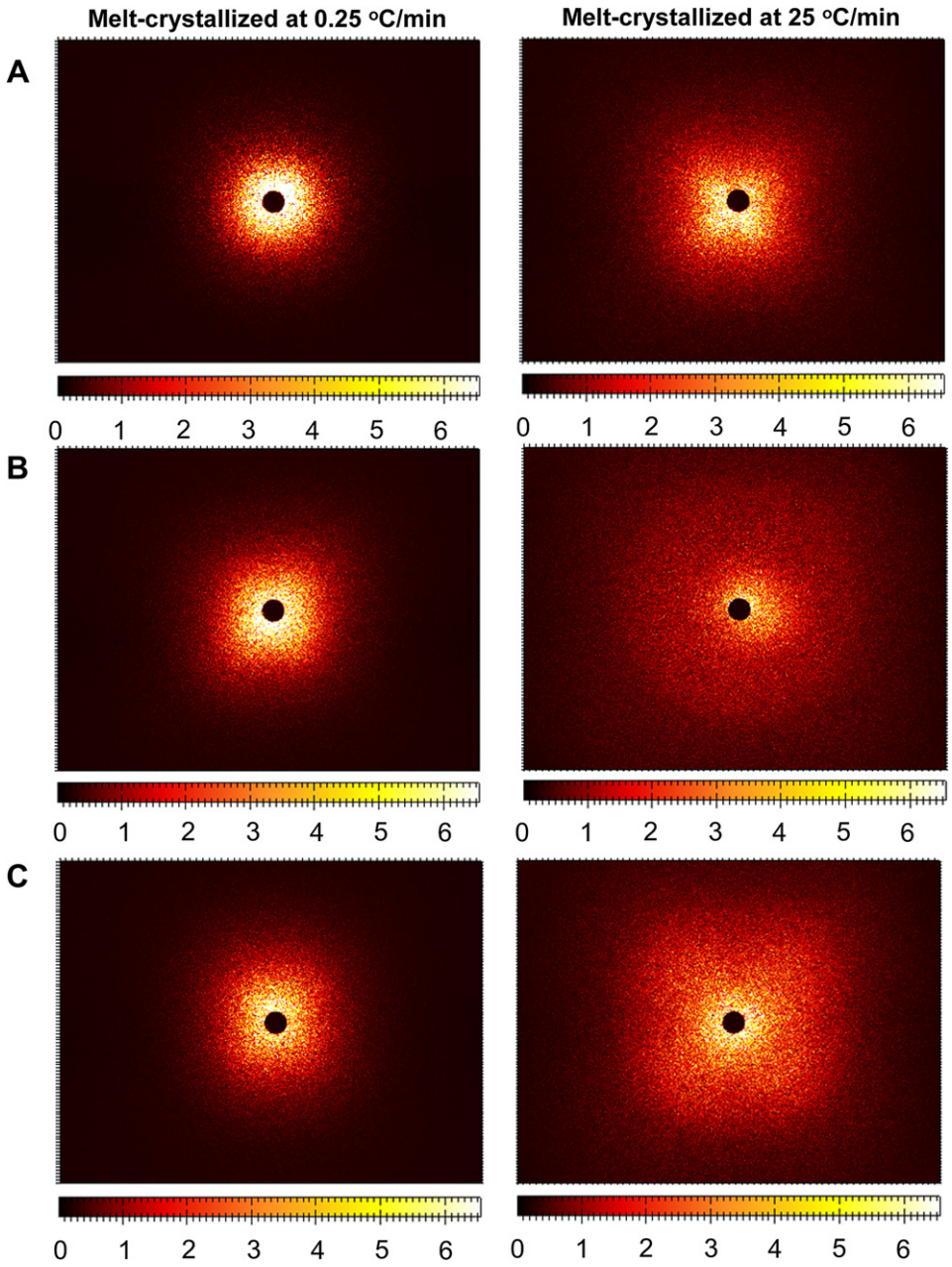

Fig. 3. SALS patterns of the neat sPP (A), 3 wt% pure Al_2O_3/sPP (B), and 3 wt% modified-Al_2O_3/sPP nanocomposites (C) non-isothermally melt-crystallized at 0.25 K/min (left-hand side) 25 K/min (right-hand side) in a hot press.

melting temperature for the sPP and the composites are 113.3 °C and 114.8 °C, respectively. The melting point shift to higher temperature indicates that the crystallites in the polymeric matrix are more stable due to the presence of the nanoparticles.

Fig. 1(C and D) shows the experimental enthalpy, $h(T)$, and reference functions $h_a(T)$ and $h_c(T)$, integrated from $C_p(T)$, $C_{p\ \text{amorphous}}(T)$ and $C_{p\ \text{crystal}}(T)$ in Fig. 1(A and B), respectively, together with the heat of melting at the equilibrium melting temperature, $\Delta h(T_m^0)$. From the data of Fig. 1(A and B), the degree of crystallinity as a function of temperature was obtained in Fig. 1(C and D). The calculation of crystallinity has been described by Schick [24] and Mathot [25]. Assuming a simple two phase model consisting of a crystalline phase and an amorphous phase is valid for sPP. This means the amorphous phase is always in the liquid state above its glass transition temperature, around 3 °C for syndiotactic polypropylene. The enthalpy of the samples, $h(T)$ is the integration of the specific heat of the crystalline part. The degree of crystallinity, $w_c(T)$ can be obtained from [26]:

$$w_c(T) = \frac{h_a(T) - h(T)}{h_a(T) - h_c(T)} \tag{1}$$

Fig. 1(C) shows that the degree of crystallinity for the samples non-isothermally crystallized at 0.25 K/min was constant, about 0.35, between 10 °C and 50 °C. The differences between the samples were insignificant. The addition of alumina nanoparticles and surface treatment of the particles did not affect the overall degree of crystallinity.

Similarly, Fig. 1(D) presents the degree of crystallinity for the samples non-isothermally crystallized at 25 K/min. The crystallinity

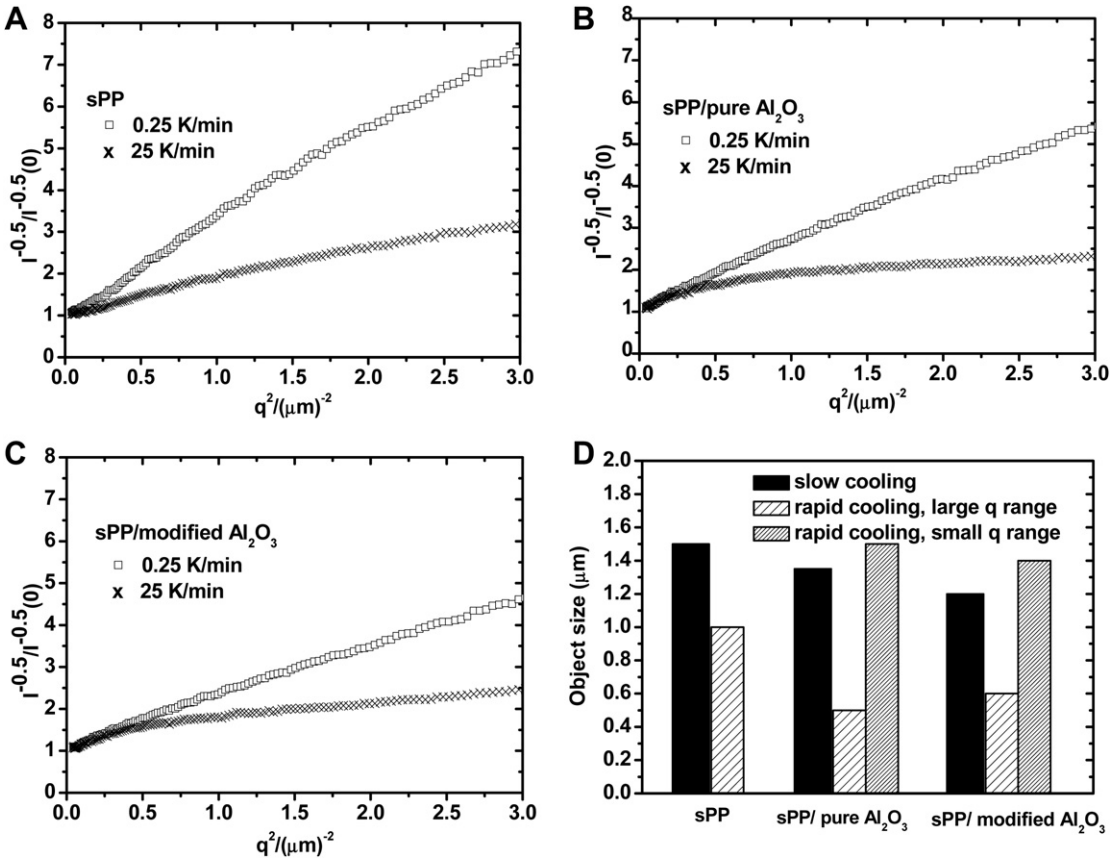

Fig. 4. sPP and sPP/alumina nanocomposites non-isothermally melt-crystallized at 0.25 K/min and 25 K/min in a hot press. Intensities $I(q)$ of polarized-scattering according to the Debye–Bueche function (A), (B) and (C). Size of the final objects given by the correlation lengths (D).

for sPP with alumina nanoparticles was 0.27, which is 0.02 higher than that for pristine sPP between 30 °C and 40 °C. Degree of crystallinity for all samples increases with increasing temperature from 10 to 50 °C. We carried out DSC crystallization and subsequent melting runs (not shown here) at various cooling rates ranging from 1 to 100 K/min and a standard heating rate 10 K/min, and found that recrystallization for these samples occurs in this temperature region. In principle, melting may give recrystallization during heating. Recrystallization is a very rapid process, within milliseconds for poly(ethylene terephthalate) for example [27]. For slowly cooled samples in Fig. 1(A and C), recrystallization may take place at 10–50 °C. This crystal perfection created more stable crystals but did not increase crystallinity. In contrast, crystallization of the rapidly cooled samples shown in Fig. 1(B and D) not only created more stable crystals but also increased the degree of crystallinity since new lamellae grew between the primary crystallization.

Fig. 2 presents the POM images of the pristine sPP (A), 3 wt% pure Al_2O_3/sPP (B), and 3 wt% modified-Al_2O_3/sPP nanocomposites (C) non-isothermally melt-crystallized at 0.25 K/min (left-hand side) and 25 K/min (right-hand side) in the hot press. Fig. 2(A) shows the crystal aggregates seen in slowly cooled pristine sPP with clearly defined objects of size around 50 μm. The size of the aggregates decreases with addition of nanoparticles and increased cooling rate, Fig. 2(B and C), but typical length scales are difficult to identify. The general knowledge is that sPP forms hedrites and not spherulites [28]. We come back to this in the discussion on the SALS results. We investigated crystallization kinetics to be reported in a following article and found that the crystallization of the nanocomposites takes place at higher temperatures and with a sharper crystallization peak, indicating that the nanoparticles induce heterogeneous nucleation and result in faster crystallization. Therefore, Fig. 2(B and C) shows an effect of the nanoparticles on the nucleation of the sPP. The crystal growth of sPP with the two nanocomposites ends by the impingement of crystals at an early stage of growth.

Since POM does not reveal the complete picture of the structure of crystal aggregates, we carried out SALS experiments. Fig. 3 shows SALS patterns of the samples from Fig. 2. The scattering patterns show a uniform azimuthal angular distribution for the neat sPP cooled at 0.25 K/min and a slight azimuthal anisotropy for the other samples. Also, the scattering intensity decreases monotonically from $q = 0$. This confirms that sPP forms hedrites [28]. The anisotropic scattering intensity distribution indicates that the individual objects possess their anisometric shape [29]. Especially for our rapidly cooled samples in Fig. 2, there is a tendency of changing hedrites into structures with a higher symmetry.

For quantitative evaluations of an object size, the Debye–Bueche function (equation (2)) was reported as a direct approach being applicable for hedrites with a uniform chain orientation [28,29]

$$I(q) = \frac{I_0}{\left(1 + l^2 q^2\right)^2} \tag{2}$$

Here $I(q)$ is the radially integrated scattering intensity and I_0 is the scattering intensity in the forward direction, l is a correlation length characterizing the object's size, and q is the magnitude of the scattering vector given by: $q = (4\pi/\lambda)\sin(\theta/2)$, λ is the wavelength of light, θ is the scattering angle between the incident and scattered

ray. The Debye–Bueche plot ($I(q)^{-1/2}$ vs q^2) should show a linear dependence and the correlation length is determined as a square root of the slope-to-intercept ratio.

For slow cooling, the Debye–Bueche plots in Fig. 4(A–C) shows an approximately linear dependence over a large q range, indicating that one correlation length can be determined. For rapid cooling, an approximately straight line can also be seen for the neat syndiotactic polypropylene. However, for the two nanocomposites, the Debye–Bueche plot shows a marked deviation from linearity at small q. This nonlinear behavior over a large q range is indicative of that a single correlation length is not appropriate [30–33]. A modified version of the Debye–Bueche function [30], to include two correlation lengths, l_1 and l_2, has been applied in the analysis of the intensity distribution

$$I(q) = \frac{A_1}{\left(1 + l_1^2 q^2\right)^2} + A_2 \exp\left(-\frac{l_2^2 q^2}{4}\right) \quad (3)$$

where $I_0(q) = A_1 + A_2$.

Fig. 4(D) shows a comparison of the scattering objects' size for the neat sPP and the nanocomposites at two different crystallization conditions, determined according to equation (2) or equation (3). The incorporation of alumina nanoparticles decreases the object size of sPP for the slowly cooled samples. Rapid cooling also decreases the object size, but with the nanocomposites a fraction of larger objects is also present. This quantitative evaluation shows that the object size is significantly influenced by not only crystallization condition but also the presence of Al_2O_3 nanoparticles.

The lamellar structure was examined by TEM. Fig. 5 shows TEM images of the neat sPP non-isothermally melt-crystallized in the hot press at 0.25 K/min (A) and 25 K/min (B), and 3 wt% Al_2O_3/sPP nanocomposites (B) non-isothermally melt-crystallized at 0.25 K/min in the hot press. The crystalline lamellae are randomly distributed in the model sPP system. The bright ribbons correspond to the crystalline lamellae, while the dark regions represent the amorphous phase. The width of the linear patterns represents the lamellar thickness. Similarly, in Fig. 5(C), the TEM image of the Al_2O_3/sPP also exhibits a lamella structure in addition to the dark spheres corresponding to the alumina nanoparticles. Based on many such TEM images, it can be concluded that the lamellar thickness did not change significantly with the addition of nanoparticles, but was significantly influenced by crystallization rate.

A comparison of the lamella thickness distributions was carried out to quantify the thickness differences between the sPP samples prepared by slow or rapid cooling. This gave a more accurate evaluation of the effect of non-isothermal cooling rates on the lamella thickness of syndiotactic polypropylene. Fig. 6 shows lamella thickness histograms of slowly and rapidly cooled sPP based on more than hundred lamellae. The lamella thickness varies in the range 4–15 and 4–10 nm for slowly (A) and rapidly (B) cooled sPP. The most common thickness is 10 nm, and 8 nm for the slowly and rapidly cooled samples. Representative TEM micrographs can be found in Fig. 5, where a wide distribution of lamellar thicknesses is present in both slowly and rapidly cooled samples. The thickness differences between the two crystallization conditions are in a good agreement with the differences in melting points from the DSC in Fig. 1.

X-ray diffraction (XRD) was performed for pure sPP and the nanocomposites non-isothermally melt-crystallized at 0.25 and 25 K/min (Fig. 7). All XRD profiles exhibited four peaks at the scattering angle, $2\theta = 12.36^\circ, 16.05^\circ, 20.74^\circ, 24.75^\circ$, corresponding to the reflecting planes of sPP at (200), (010), (111), (400), respectively. The data indicates that both sPP and sPP composites were crystallized in modifications close to "form I" of sPP as proposed by Lotz and Lovinger [34–37]. "Form I" is characterized by chains in s(1/2)2 helical conformation packed in the orthorhombic unit cell with axes $a = 1.45$ nm, $b = 1.12$ nm, $c = 0.74$ nm [4,34–37]. The total absence of the (211) reflection at $2\theta \approx 18.8^\circ$ shows the presence of structural disorder, a random substitution of right and left-handed chains in each site of the lattice. The structural disorder due to defects in the alternation of enantiomorphous helices along the

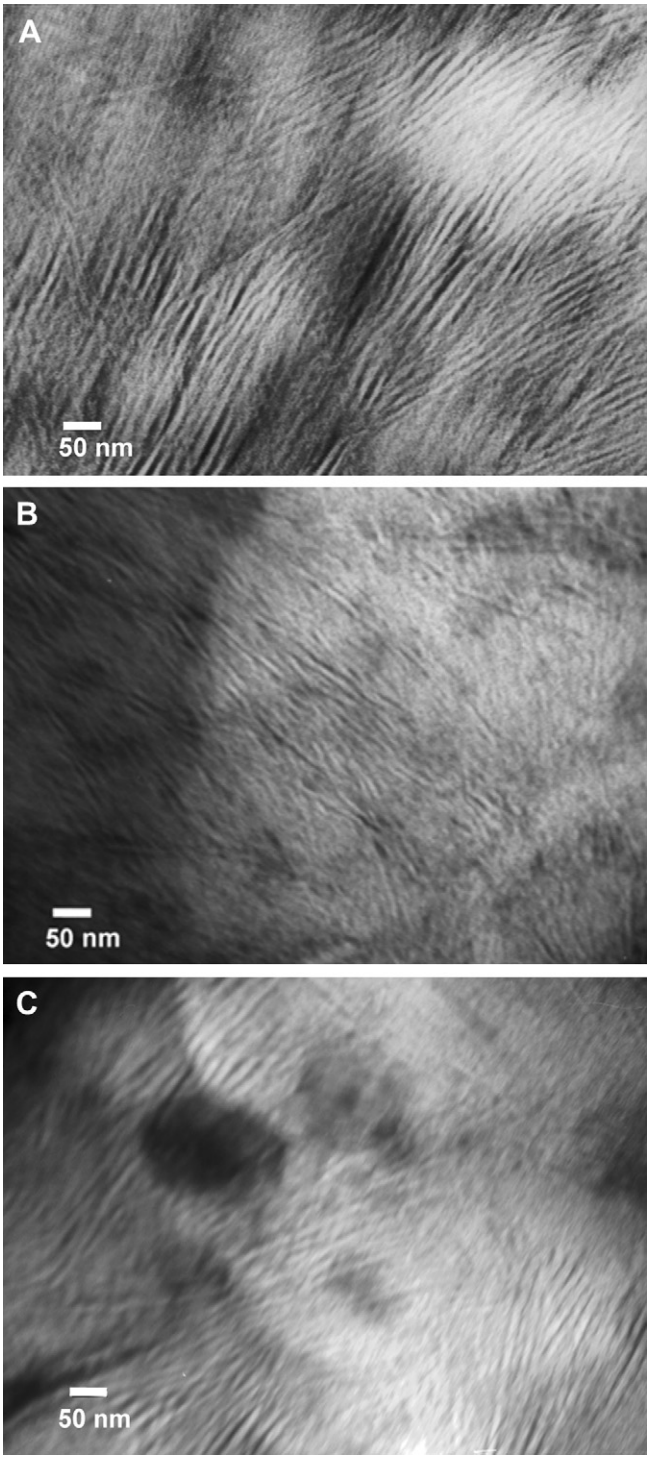

Fig. 5. TEM images of the neat sPP non-isothermally melt-crystallized in the hot press at 0.25 K/min (A) and 25 K/min (B), and 3 wt% Al_2O_3/sPP nanocomposites (C) non-isothermally melt-crystallized at 0.25 K/min in a hot press.

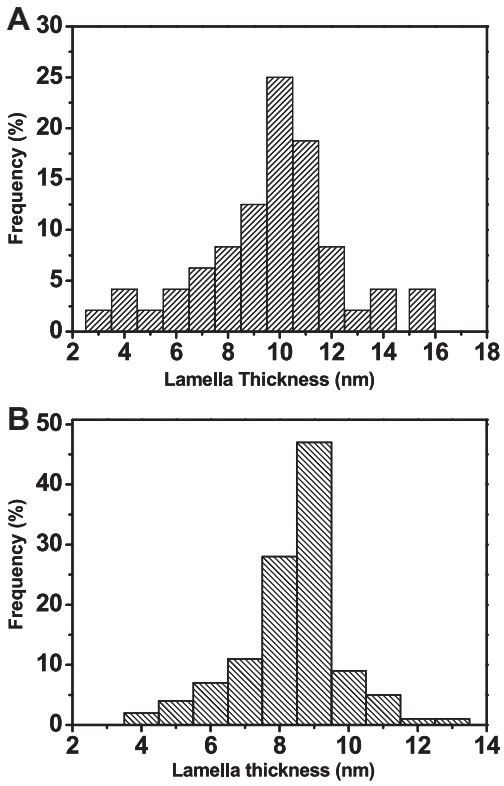

Fig. 6. Lamella thickness distribution of the neat sPP non-isothermally melt-crystallized at 0.25 K/min (A) 25 K/min (B) in a hot press.

a and *b* axes [4] is usually present in either low stereoregular sPP or rapidly crystallized samples. No formation of additional peaks in the nanoparticle/sPP interface can be seen. However, the peaks at 16.05° are not symmetric, showing a shoulder at 17°. This is typical of the trans-planar mesomorphic form [4,38]. Previous studies showed that a maximum of trans-planar mesophase can be formed by rapid cooling to 0 °C and keeping the sample for a long time at this temperature [4,39]. The present data shows that a small fraction of this modification can also be formed during rapid, non-isothermal cooling. This is in good agreement with the DSC curves in Fig. 1(D), where a small peak can be seen around 50 °C. The peak can be attributed to the transition of the mesomorphic form to

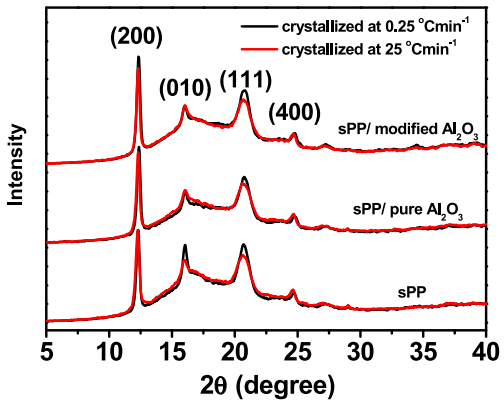

Fig. 7. X-ray diffraction profiles of the neat sPP, 3 wt% pure Al_2O_3/sPP, and 3 wt% modified-Al_2O_3/sPP nanocomposites non-isothermally melt-crystallized at 0.25 K/min (black curves) 25 K/min (red curves) in a hot press.

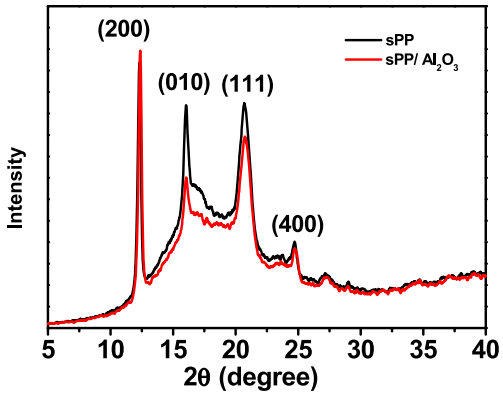

Fig. 8. X-ray diffraction patterns of the neat sPP, 3 wt% pure Al_2O_3/sPP nanocomposites non-isothermally melt-crystallized at 0.25 K/min in a hot press.

"form I" [38] or the melting of the small crystals observed by TEM. The shoulder at $2\theta \approx 17°$ may also represent the (110) reflection of "form II" [4]. The disordered "form II" is characterized by defects in the stacking of ordered *bc* layers of chains along the *a* axis due to shifts *b*/4 between successive layers [4,37,40]. Comparing the diffractograms of Fig. 7, the sharper peaks of the slowly cooled samples indicate larger and more perfect crystals. This is very consistent with the DSC in Fig. 1.

Fig. 8 shows a comparison between the sPP and the sPP/alumina nanocomposites at the same crystallization condition, cooling rate 0.25 K/min. The intensity of the shoulder at $2\theta \approx 17°$ for the pristine sPP is higher than that of the nanocomposite. This suggests that the dispersed nanoparticles reduce the amount of the trans-planar mesomorphic form (or disordered "form II"). For iPP/alumina nanocomposites, the Al_2O_3 NPs can act as β-PP inducing nucleating agents and thus a small amount of β crystals can be formed in iPP [41].

4. Conclusion

The effect of Al_2O_3 nanoparticles with a nominal size 50 nm on crystal morphology of syndiotactic polypropylene was studied. The main points can be summarized as follows:

1. The alumina nanoparticles (3 wt%) do not considerably affect the crystallinity, but increase the melting point of sPP.
2. Syndiotactic polypropylene forms hedrites rather than spherulites for both slowly and rapidly cooled samples. The addition of the nanoparticles yields more hedrites with much smaller size due to the higher density of nucleation sites in the nanocomposites. Quantitative evaluations by SALS analysis show that the object size is significantly influenced by not only crystallization condition but also the presence of Al_2O_3 nanoparticles.
3. Based on the TEM results, it can be concluded that the lamellar structure did not change significantly with the addition of nanoparticles. The lamella thickness depends on the cooling rate. A most common thickness found is around 10 nm, and 8 nm for the samples cooled at 0.25 and 25 K/min, respectively.
4. X-ray diffraction profiles show that both the sPP and the nanocomposites were crystallized in disordered "form I". Small amount of disordered "form II" or trans-planar mesomorphic form was observed for all the samples. Less trans-planar mesomorphic form (or disordered "form II") was found in sPP/alumina nanocomposites than in sPP. This indicates that the incorporation of alumina nanoparticles had a small effect on the microstructure of syndiotactic polypropylene.

Acknowledgements

This work is part of the Petromaks project "Electrical Insulation Materials and Insulation Systems for Subsea High Voltage Power Equipment" funded by the Research Council of Norway and the industrial partners Deutsch, Nexans Norway AS, Statoil ASA, Total E&P Norge AS and Vetco Gray-Ge Oil and Gas. Support from SINTEF Materials and Chemistry is also gratefully acknowledged.

Thanks are due to Kjell Windsland for DSC contributions, Erik Andreassen and Britt Sommer for the XRD experiments and discussions.

References

[1] Yoshino K, Demura T, Kawahigashi M, Miyashita Y, Kurahashi K, Matsuda Y. Electrical Engineering in Japan 2004;146:18–26.
[2] Yoshino K, Ueda A, Demura T, Miyashita Y, Kurahashi K, Matsuda Y. In: Proceedings of the 7th international conference on properties and applications of dielectric materials, Nagoya, 2003; pp. 175–8.
[3] Kurahashi K, Matsuda Y, Miyashita Y, Demura T, Ueda A, Yoshino K. Electrical Engineering in Japan 2006;155:1–8.
[4] Rosa CD, Auriemma F. Progress in Polymer Science 2006;31:145–237.
[5] Kim DW, Yoshino K. Journal of Physics D: Applied Physics 2000;33:464–71.
[6] Chen CH, Mao CF, Tsai MS, Yen FS, Lin JM, Tseng CH, et al. Journal of Applied Polymer Science 2008;110:237–43.
[7] Galgalia G, Agarwalb S, Lelea A. Polymer 2004;45:6059–69.
[8] Manias E, Touny A, Wu L, Strawhecker K, Lu B, Chung TC. Chemistry of Materials 2001;13:3516–23.
[9] Avella M, Cosco S, Di Lorenzo ML, Di Pace E, Errico ME, Gentile G. European Polymer Journal 2006;42:1548–57.
[10] Gregoriou VG, Kandilioti G, Bollas ST. Polymer 2005;46:11340.
[11] Pucciariello R, Villani V, Guadagno L, Vittoria V. Polymer Engineering and Science 2006;46:1433.
[12] Chae DW, Shim KB, Kim BC. Journal of Applied Polymer Science 2008;109:2942.
[13] Morrell R. Handbook of properties of technical and engineering ceramics, part 1: an introduction for the engineer and designer. England: Her Majesty's Stationary Office; 1985.
[14] Zhao H, Li RKY. Journal of Polymer Science: Part B: Polymer Physics 2005;43:3652–64.
[15] Tee DI, Mariatti M, Azizan A, See CH, Chong KF. Composites Science and Technology 2007;67:2584–91.
[16] Laachachi A, Cochez M, Leroy E, Gaudon P, Ferriol M, Lopez Cuesta JM. Polymers for Advanced Technologies 2006;17:327–34.
[17] Vassileva E, Friedrich K. Journal of Applied Polymer Science 2006;101:4410–7.
[18] Shi H, Liu F, Yang L, Han E. Progress in Organic Coatings 2008;62:359–68.
[19] Zheng J, Ozisik R, Siegel RW. Polymer 2006;47:7786–94.
[20] Bhimaraj P, Yang H, Siegel RW, Schadler LS. Journal of Applied Polymer Science 2007;106:4233–40.
[21] Truong LT, Larsen Å, Holme B, Diplas S, Hansen FK, Roots J, et al. Surface and Interface Analysis 2010;42:1046–9.
[22] http://www.esrf.eu/computing/scientific/FIT2D/.
[23] http://rsbweb.nih.gov/ij/.
[24] Schick C. Analytical and Bioanalytical Chemistry. 2009;395:1589–611.
[25] Mathot VBF. Thermochimica Acta 2000;355:1–13.
[26] Mathot VBF. Polymer 1984;25:579.
[27] Minakov AA, Mordvintsex DA, Schick C. Polymer 2004;45:3755.
[28] Kawai T, Strobl G. Macromolecules 2004;37:2249–55.
[29] Hoffmann A, Strobl G. Polymer 2003;44:5803–9.
[30] Debye P, Anderson HR, Brumberger Jr H. Journal of Applied Physics 1957;28:679–83.
[31] Cheung YW, Stein RS, Wignall GD, Yang HE. Macromolecules 1993;26:5365–71.
[32] Marr DWM. Macromolecules 1995;28:8470–6.
[33] Marr DWM, Wartenberg M, Schwartz KB, Agamalian MM, Wignall GD. Macromolecules 1997;30:2120–4.
[34] Lotz B, Lovinger AJ, Cais RE. Macromolecules 1988;21:2375.
[35] Lovinger AJ, Lotz B, Davis DD. Polymer 1990;31:2253.
[36] Lovinger AJ, Davis DD, Lotz B. Macromolecules 1991;24:552.
[37] Lovinger AJ, Lotz B, Davis DD, Padden FJ. Macromolecules 1993;26:3494–503.
[38] Vittoria V, Guadagno L, Comotti A, Simonutti R, Auriemma F, Rosa CD. Macromolecules 2000;33:6200.
[39] Rosa CD, Ballesteros ORD, Santero M, Auriemma F. Polymer 2003;44:6267–72.
[40] Lovinger AJ, Lotz B, Davis DD, Schumacher M. Macromolecules 1994;27:6603–11.
[41] Reddy KR, Tashiro K, Sakurai T, Yamaguchi N. Macromolecules 2009;42:1672–8.

Polymer 52 (2011) 1124–1132

Contents lists available at ScienceDirect

Polymer

journal homepage: www.elsevier.com/locate/polymer

Structure–property relationships on uniaxially oriented carbon nanotube/polyethylene composites

Giuliana Gorrasi [a,*], Roberta Di Lieto [a], Giovanni Patimo [b], Salvatore De Pasquale [b], Andrea Sorrentino [a,*]

[a] Department of Chemical and Food Engineering, University of Salerno, via Ponte don Melillo, 84084 Fisciano, Salerno, Italy
[b] Department of Physics E.R. Caianiello, University of Salerno, via Ponte don Melillo, 84084 Fisciano, Salerno, Italy

ARTICLE INFO

Article history:
Received 22 November 2010
Received in revised form
1 January 2011
Accepted 5 January 2011
Available online 11 January 2011

Keywords:
Carbon nanotube/polyethylene composites
High energy ball milling
Highly oriented polymeric films

ABSTRACT

Multi walled carbon nanotubes have been incorporated into a linear low density polyethylene matrix through high energy ball milling technique at room temperature, without any chemical modification or physical treatment of the nanotubes. Highly oriented samples, with different draw ratios, were obtained by drawing at 80 °C the composite films. SEM and FTIR results on the drawn PE films demonstrate that the molecular chains in both crystalline and amorphous phases are well oriented along the drawing direction. The effect of different weight percent loadings of nanotubes and draw ratio on the morphology, thermal, mechanical and electrical properties of the composite fibers have been investigated.

1. Introduction

The technological significance of the highly oriented polymer materials derives from their properties that may exceed those of the isotropic species by orders of magnitude. For example, the stiffness and strength of highly oriented crystalline polymers [1,2] can increase to a factor of 100 compared with their non-oriented counterparts. For flexible regular chain polymers, macromolecules tend to fold upon crystallization and different routes have been developed to transform chain-folded crystals into extended structures [3,4].

Carbon nanotubes (CNT) have attracted interest as reinforcing fillers because of their excellent mechanical and thermal properties [5,6], but they are also regarded as the ultimate fillers for several advanced applications [7,8]. Carbon nanotubes possess an extremely high elastic modulus ≈1 TPa, comparable to that of diamond (1.2 TPa) and report strengths of 10–100 times that of the strongest steel [7,8]. In addition, they exhibit electrical conductivity as high as 10^5–10^7 S/m [9] and can transform an insulating polymer into a conducting composite at very low loading because of their extremely high aspect ratio [10]. The introduction of nanofillers like CNTs in polymer fibers can lead to multifunctional high-performance materials that combine high strength with electrical conductivity [11]. The keys to achieve maximum performances from nanocomposite are to obtain a uniform distribution of nanoparticles within the polymer matrix, and to have the best nanoparticle–polymer adhesion, which is critical for load transfer from the matrix to the particle. Nanotubes can be dispersed in the polymer matrices using different techniques such as melt mixing, solution processing, or in situ polymerization. An alternative and innovative strategy relies on solid-state mixing at near room temperature, which ought to involve an efficient mixing of two or more species by mechanical milling, avoiding high temperatures and solvents. High Energy Ball Milling (HEBM) is an effective unconventional technique currently used in material synthesis and processing [12]. It consists of repeated events of energy transfer, promoted by the milling device, from the milling tools (generally balls) to the milled powder. Recently it has been proved that HEBM on polymeric materials can help obtaining materials with new characteristics, which can be barely achieved through other conventional processes [13–15].

Uniaxial alignment of CNT using magnetic [16], shear fields [17], casting-drawing and gel spun processes [18,19] has been the focus of several recent studies. Linear Low Density Polyethylene (LLDPE) is a commodity polymer, cheap, versatile, with well-known applications and commercial uses in a variety of forms, including fibers. Thus, enhancing of LLDPE properties through the dispersal and alignment of CNT should be of significant interest in order to expand its application fields. Very few papers report the preparation and characterization of Polyethylene/Carbon Nanotubes fibers. In particular, only few papers present a detailed

* Corresponding authors. Fax: +39 089 964057.
E-mail addresses: ggorrasi@unisa.it (G. Gorrasi), asorrent@unisa.it (A. Sorrentino).

0032-3861/$ – see front matter © 2011 Elsevier Ltd. All rights reserved.
doi:10.1016/j.polymer.2011.01.008

investigation about the arrangement of both the PE chains and the carbon nanotube in melt drawn oriented composite films [9–11,17].

In the present work we performed Multi walled Carbon Nanotubes dispersion an LLDPE matrix through HEBM at room temperature in the dry state with no chemical or physical treatment of the nanotubes. Fibers with different draw ratios were obtained by drawing at 80 °C the composite films. The effect of different weight percentage of nanotubes and draw ratio was analyzed as function of the morphology, thermal, mechanical and electrical properties.

2. Experimental

2.1. Materials

Multi walled carbon nanotubes (CNT) were purchased by Nanocyl (Belgium) (NC 3100). They were synthesized by catalytic carbon vapor deposition (ccvd) process. By thermogravimetric analysis (TGA) the carbon purity was found higher than 95% whereas the metal oxide impurity was less than 5%. The specific surface area determined with the BET method was around 250–300 m^2/g.

Linear Low Density Polyethylene (Flexirene® CM50) was supplied from Polimeri Europa (Italy) in ultrafine powder, form with a melt flow index MFI = 4.1 g/10 min (at 190 °C, 2.16 kg).

2.2. Composite preparation (HEBM process)

CNT powders and Polyethylene, as received, were milled in the solid state in a Retsch (Germany) centrifugal ball mill (model PM100). The milling process was carried out in a cylindrical steel jar of 50 cm^3 with 5 steel balls of 10 mm of diameter. The rotation speed used was 650 r.p.m. and the milling time was fixed to 60 min. HEBM of powders constituted by organic polymers and fillers has been proved to be an alternative and efficient technique to produce novel composites with high performances [13–15]. During the milling the carbon nanotube bundles crack, and "intimate mixing" are promoted [15].

In these experimental conditions, five series of composites LLDPE/CNT with 1, 2, 3, 5, 10 wt/wt% of carbon nanotubes were prepared. An additional LLDPE sample to be taken as a reference was also milled in absence of filler.

2.3. Samples preparation

The LLDPE/CNT mixtures and the pure milled LLDPE were molded in a hot press (Carver Inc.) at 170 °C forming 250 ± 50 μm thick films, which were rapidly quenched in a water–ice bath (0 °C). From the obtained films were obtained strips large 1 cm. The strips were put between the clamps of an Instron Dynamometer (Mod 4301), equipped with a temperature chamber. The temperature was fixed to 80 °C. As soon as the temperature was stabilized, the upper traverse of the dynamometric apparatus was moved at a speed rate of drawing of 10 mm/min. Films were drawn at different draw ratios $\lambda = l/lo$, where l is the final length and lo the initial length. The selected values of the draw ratios (followed by a display) for all the composites were $\lambda = 6; 8; 10$.

In the following, the resulting samples will be coded as follows: PEXλY where $X = 1, 2, 3, 5, 10$ is the weight percent of CNT and Y is the draw ratio of the samples.

2.4. Methods of investigation

Scanning electron microscopy (SEM) analysis was performed with a LEO 1525 microscope. The etching mixture was prepared by stirring 1.0 g of potassium permanganate in a solution of 95 mL of sulfuric acid (95–97 vol%) and 48 mL of orthophosphoric acid (85 vol%). Subsequent to the etching treatment, a first washing was done using a cold mixture of 2 parts by volume of concentrated sulfuric acid and 7 parts of distilled water. A second washing was performed with 30 vol % aqueous hydrogen peroxide to remove any manganese dioxide and, finally, a 3 times washing using distilled water. Before the SEM analysis the sample was kept under vacuum for 2 days at ambient temperature. The samples were finally covered with a 250 Å thick gold film using a sputter coater (Agar mod. 108 A) and observed with SEM.

IR spectra were collected by means of an FTIR Spectrometer M2000 FTIR (by *Midac Co.*). For each sample, the average of 32 scans was used, working at a resolution of 2 cm^{-1}. The scan wave-number range of the collected spectrum was 4000–400 cm^{-1}.

In order to evaluate the molecular orientation of the samples, the IR beam was polarized with the polarization axis parallel and orthogonal to draw direction [20]. Polarization of the beam was done by a zinc selenide wire grid polarizer. The average Hermans orientation factor f_{av} can be determined by measuring the dichroic ratio $D = (Ap/Ao)$ where Ap is the absorbance for the plane parallel to the draw direction and Ao the absorbance for the polarization plane orthogonal to the draw direction. The Hermans factor, assuming uniaxial orientation, is related to dichroic ratio at wave-number ν by [21]:

$$f_i = K_\nu \left(\frac{D-1}{D+2}\right)_\nu \tag{1}$$

where K_ν is an auxiliary variable that in our case was assumed to be 1. The absorption bands at 730 and 719 cm^{-1} were employed to evaluate the orientations of the crystal a-axis and b-axis, respectively [20]. The IR technique gives f_a and f_b, from which f_c can be evaluated by means of equation (2):

$$f_a + f_b + f_c = 0 \tag{2}$$

Differential scanning calorimetry (DSC) analysis was carried out on samples with a mass ranging between 5 and 7 mg. The tests were carried out by means of a DTA Mettler Toledo (DSC 30) under nitrogen atmosphere. The samples were heated from 25 °C to 200 °C at 10 °C/min. To ensure reliability of the data obtained, heat flow and temperature were calibrated with standard materials, indium, and zinc. The percent crystallinity was calculated by taking the specific heat of fusion of perfectly crystalline PE to be 290 J/g [22].

Thermogravimetric analysis (TGA) was carried out with a Mettler TC-10 thermobalance. Polymer composites samples were heated from 25 to 800 °C at 10 °C/min heating rate under air flow. The weight loss was recorded as function of temperature.

The elastic moduli were evaluated using an Instron Dynamometer (Mod 4301), and derived from the initial part of the stress–strain curves, giving to the sample a deformation of 0.1%. The experiments were conducted at room temperature with the deformation rate of 2 mm/min. The initial length of the samples was 10 mm. The data were averaged on five samples.

The electrical conductivity was measured with a Keithley 6517A source measurement unit in a two-probe resistance measurement configuration. The sample thicknesses were carefully measured by a micrometer, whereas the length and the width were 3 and 50 mm, respectively. The electrical conductivity was measured in the voltage range −10 + 10 V. All the samples showed a linear behavior of the current (I) versus the applied voltage (V). The electrical conductivity was calculated by using the equation (3):

$$\sigma = \frac{L}{\tau W}\frac{1}{R} = \frac{L}{\tau W}\frac{I_{\text{measured}}}{V_{\text{applied}}} \tag{3}$$

where R, τ, W, L are the resistance, the thickness, the width and the length of the specimens respectively.

3. Results and discussion

3.1. Morphological analysis

Fig. 1 reports the SEM images of some etched samples. The undeformed sample (Fig. 1a) shows the classical spherulitic morphology. A uniform morphology with structure aligned randomly along the sample surface can be observed. Under high uniaxial drawing in the solid state, the original morphology is transformed into highly oriented microfibril morphology (Fig. 1b). The arrow in the picture represents the drawing direction of the film during stretching.

The deformation processes produce the shear of the stressed spherulitic lamellae into crystal blocks via chain slip. These blocks rotate and decrease in width until microfibrils of alternating crystal and amorphous regions are formed. Ward [21,23] proposed a morphological model, which considers that the drawn morphology consists of stacks of short lamellar-type crystallites linked by intercrystalline bridges. Since the crystalline phase is essentially continuous in the draw direction, the modulus of the drawn materials is expected to be quite high, whereas the degree of crystallinity is expected to increase with draw ratio.

The presence of CNTs in the polymer matrix seems to enhance this deformation process (Fig. 1c). In fact, the oriented composite samples show a clear fibrillar morphology with numerous microcrazes. The CNTs are confined between the fibril and clearly show a high degree of alignment in the drawing direction. Such morphology has a strong influence on the thermal, mechanical and electrical properties of the resulting samples.

3.2. Detection of molecular orientation

The orientation of the structural units in a solid polymer, as a result of various forming processes such as drawing and extrusion, may have a profound influence on the macroscopic physical properties of the material. Several experimental methods have been employed to characterize the orientation of crystalline and semicrystalline polymers. Birefringence, Nuclear Magnetic Resonance, X-ray diffraction, Polarized Raman spectroscopy and Infrared dichroism are among the most popular methods used to characterize different aspects of molecular order [21]. Each of these techniques has inherent advantages and disadvantages when compared with one another.

Infrared spectroscopy (FTIR) and birefringence measurements often cannot be used for thick polymer specimens. In contrast, Raman spectroscopy provides an effective means for the study of samples that do not efficiently transmit radiation, provided care is taken to minimize polarization scrambling by the sample [24]. A second advantage of Raman spectroscopy is the ability to determine both the second and fourth coefficients of the orientation distribution function, whereas infrared dichroism and birefringence measurements are sensitive only to the second moment of the expansion [25,26]. Unfortunately, Raman spectroscopy is more complex from both an experimental and theoretical point of view when compared to infrared dichroism and birefringence. Not surprisingly, in spite of the usefulness of the method, its practical applications have been limited to a few specific materials, for which the molecular structures are relatively simple and which polarizability tensors were already known [27]. Due to the presence of not well characterized interactions of the carbon nanotubes with the scattering nature of Raman spectroscopy, in this paper, only the FTIR technique was employed to determine the molecular orientation of samples.

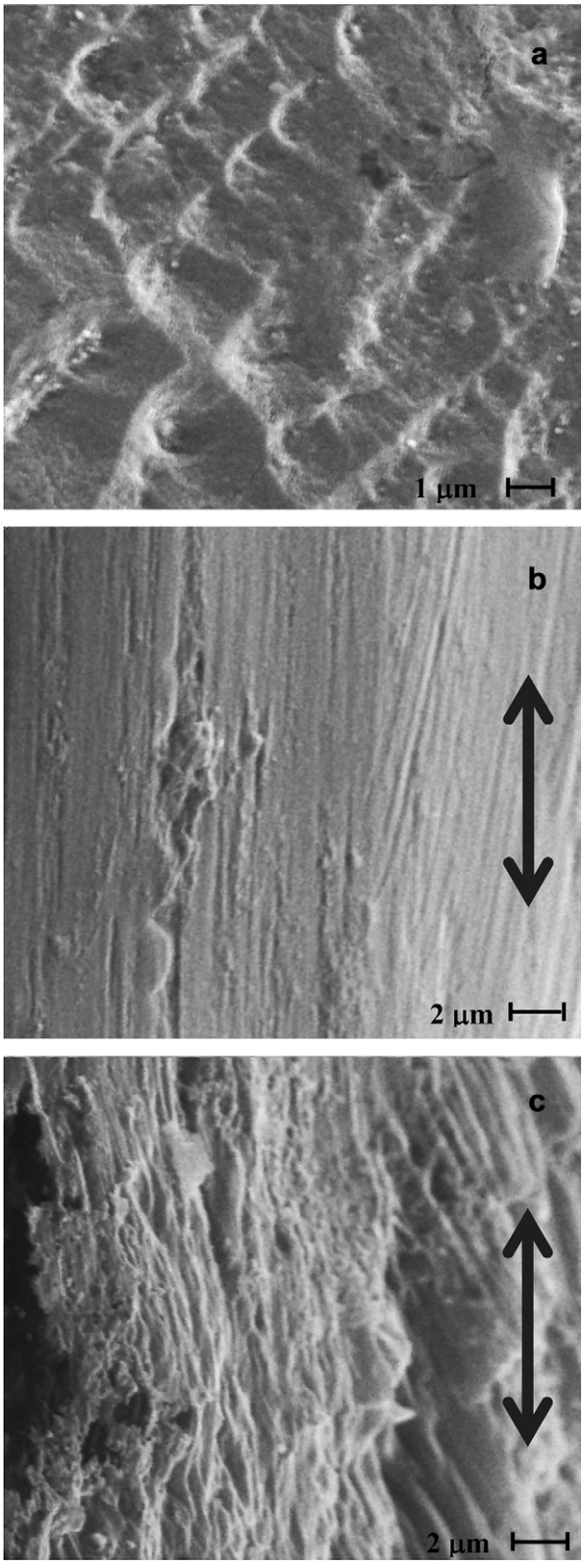

Fig. 1. SEM microphotographs showing the microstructure of the samples: (a) PE0λ0; (b) PE0λ8; (c) PE3λ8. The arrows show the draw direction.

Detailed analyses are available in literature on PE regarding the band assignments, using FTIR spectroscopy combined with

polarized infrared beam [20,28,29]. In particular, the band doublet observed in the spectrum of polyethylene in the range 710–740 cm^{-1} has been analyzed in order to characterize the orientation of the crystal unit cell as a function of the deformation [29]. This band doublet has been assigned to in- and out-of-phase CH_2-rocking vibrations, respectively, of the crystal phase with the 730 cm^{-1} band polarized along the crystallographic *a*-axis and the 719 cm^{-1} band polarized along the *b*-axis [30].

Fig. 2 shows the Hermans factor obtained with equation (1)–(2) as function of the CNT content for the LLDPE composites analyzed in this study. The undeformed samples were also reported as reference in the same Fig. 2. By changing the CNT content, the spectra corresponding to the undeformed samples exhibit a similar dicroic ratio because they have random molecular orientation. As strain was applied to the sample and the strain increased up to $\lambda = 6$ the changes in the orientation function indicate that there is an appreciable modification in the mean orientation of the crystalline phase.

In Fig. 2 the relative molecular orientation is evidenced to increase with increasing CNT content for all the composites. This result indicates that the orientation of the crystallites changes with the extension ratio and the CNT content. In the range 5–10% of CNT all the curves of f_c level off, reaching values close to unity. This behavior reflects a typical transformation from spherulitic to fibrous structure during elongation.

The transitions in the orientation function curves may arise from yielding and perhaps other morphological changes occurring during straining [31]. It is well known that during the stretching of LLDPE between the glass transition and melting temperature (which is the case here) the amorphous phase will orient itself as the crystalline regions rotate and orient themselves in the direction of stretching, as a result of this process the macromolecules can be oriented by a rotation of lamellae or by unfolding [21].

3.3. DSC analysis

The DSC curves obtained for some selected samples are shown in Fig. 3. The unoriented samples display a single broad peak. It is clearly the results of two endothermic events of different intensity. Multiple melting features are characteristic of commercial LLDPEs, due to the presence of a broad distribution of crystal sizes [32] that extends over a broad range of temperatures. Upon stretching, the sample shows (Fig. 3a) a narrower melting peak and at higher temperature compared to that of the isotropic undeformed samples. This phenomenon is associated with the molecular orientation of the structure into the straining direction. For the sample with the higher draw ratio ($\lambda = 10$), the melting feature tends to move toward lower temperature and the maximum of melting shifts to lower temperature. This behavior can be attributed to a decrease in crystals size, or to an improvement in their perfection drawing inducted, or to the existence of a polymorphic transition occurring during heating [33]. This structural effect is not visible for lower draw ratio, probably because it is overridden by the molecular orientation effect and the disruption of the crystalline phase. Similar behavior in the melting process was observed also in presence of CNTs (Fig. 3b): an increase in draw ratio produces an increase in the melting peak temperature, followed by a decrease at higher draw ratio. However, this second stage seems to be anticipated with respect to the pure polymer. At constant draw ratio, also the CNT content shows a significant effect on the melting behavior of LLDPE. Fig. 3c shows that for the lower CNT content there is an increase in melting temperature with increasing draw ratio, but for higher CNT content the melting temperatures decrease slightly.

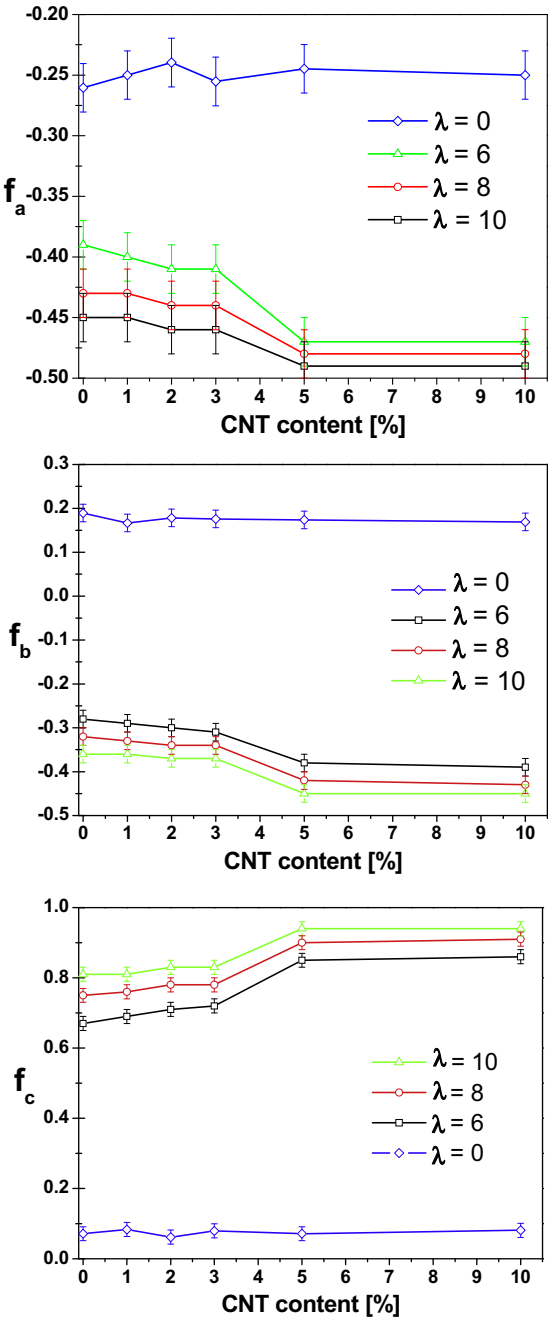

Fig. 2. Orientation function as function of CNT content and draw ratio, obtained with IR analysis of all investigated samples.

It is worth noting that solid-state drawing at 80 °C for LLDPE is a condition for additional crystallization. The heats of fusion of unoriented and oriented samples are reported in Table 1. They are higher for the oriented samples and increase with increasing draw ratio. At relative small elongations, the crystallinity was increased due to strain induced crystallization. As the draw ratio increases, the crystallinity decreases as consequence of the fragmentation of crystalline lamellae, increasing the draw ratio the crystallinity is expected to increase again [34]. This behavior could be associated to partial melting of smallest or less perfect crystallites followed by recrystallization. Upon addition of CNT, the heats of fusion decrease slightly probably due to the hindering phenomena from carbon nanotubes.

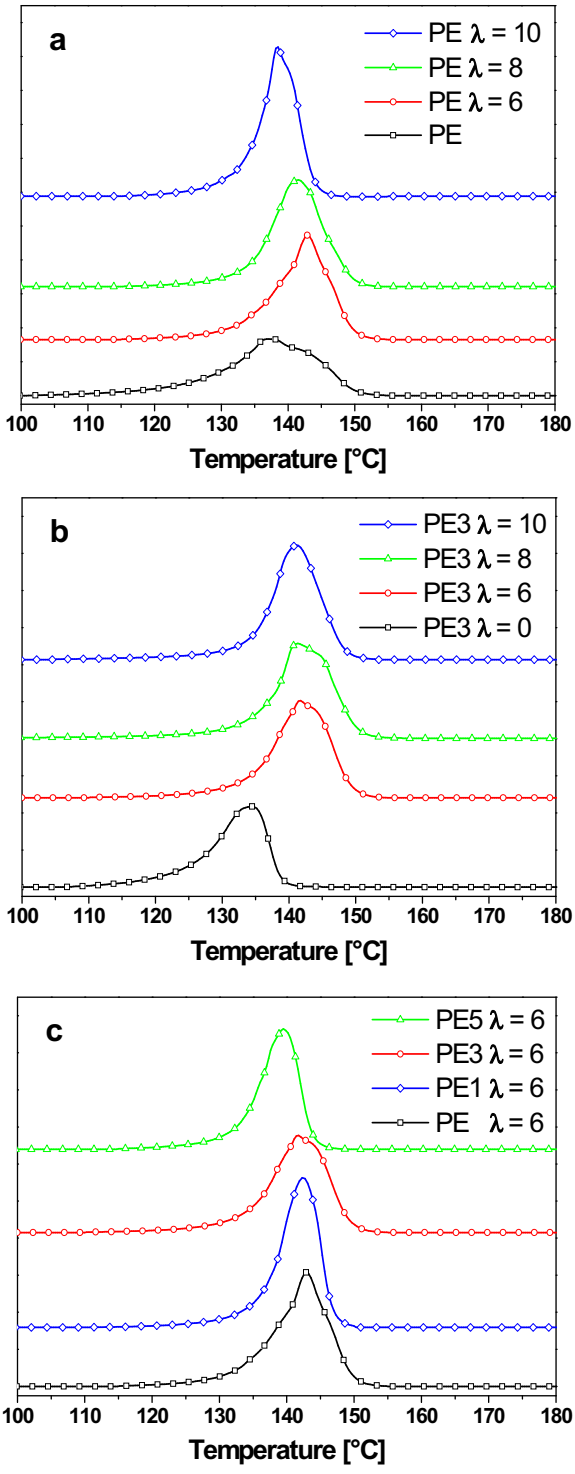

Fig. 3. DSC melting endotherms of the reported samples.

3.4. Thermogravimetric analysis

Fig. 4 reports the thermogravimetric curves, evaluated in air flow, for all the samples in the range 200 °C–600 °C. Pure polyethylene shows an initial degradation temperature at about 320 °C. Above this temperature free radicals are generated leading to sequential degradation and break-down of the main chain due to the thermal decomposition of the covalent C–C bond [35]. The two main stages of PE oxidation, centered at 405 °C and 454 °C respectively, are to be ascribed to a two steps process of which one controlled by oxygen diffusion. In terms of solid-state oxidation of PE, the oxygen-controlled step may be related to the oxidation of the bulk, while the first stage to the oxidation of the polymer surface and the less to the ordered phase degradation. The last residue (~8%) oxidizes in a last step extended up to 550 °C. The thermal stability of the composite fibers results greatly improved compared to the undeformed PE.

Table 2 reports the maximum degradation temperature, Td^{max} (°C), corresponding to about 50% of weight loss. Either the incorporation of carbon nanotubes into the polymer matrix or the drawing process greatly improves the thermal stability of all the samples, such improvement increases with nanotube increasing and draw ratio. The improvement in thermal stability can be attributed to several synergistic factors. During the thermal degradation, the carbon nanotubes form a shielding layer. This layer reduces the heat transmitted to the core of the sample, prevent the recombination the polymer peroxyl radicals, and form a barrier to the oxygen diffusion [36,37].

Table 1
Melting peak temperature and heat of fusion of all the analyzed samples.

Sample	T_m [°C]	Δ_h [J/g]	Xc
PE	136.2 (±0.2)	168 (±3.0)	58%
PEλ6	141.2 (±0.2)	179 (±3.0)	62%
PEλ8	140.3 (±0.2)	188 (±3.0)	65%
PEλ10	137.6 (±0.2)	190 (±3.0)	66%
PE1	136.0 (±0.2)	162 (±3.0)	56%
PE1λ6	140.7 (±0.2)	177 (±3.0)	61%
PE1λ8	140.3 (±0.2)	180 (±3.0)	62%
PE1λ10	135.8 (±0.2)	183 (±3.0)	63%
PE3	131.5 (±0.2)	141 (±3.0)	48%
PE3λ6	140.6 (±0.2)	174 (±3.0)	60%
PE3λ8	140.7 (±0.2)	178 (±3.0)	61%
PE3λ10	139.8 (±0.2)	179 (±3.0)	62%
PE5	130.0 (±0.2)	179 (±3.0)	49%
PE5λ6	137.9 (±0.2)	157 (±3.0)	54%
PE5λ8	139.2 (±0.2)	179 (±3.0)	56%
PE5λ10	136.7 (±0.2)	179 (±3.0)	57%
PE10	132.1 (±0.2)	179 (±3.0)	45%
PE10λ6	137.6 (±0.2)	147 (±3.0)	51%
PE10λ8	138.4 (±0.2)	147 (±3.0)	53%
PE10λ10	133.4 (±0.2)	147 (±3.0)	55%

3.5. Mechanical properties

The enhancement of the mechanical properties of composites requires a high degree of load transfer between the matrix and the nanotubes. If the interfacial adhesion between the phases is weak, the nanotubes behave as holes or nanostructured flaws, introducing local stress concentrations, and the benefits of the CNT properties are lost [38]. The nanotubes must be well dispersed. In case of poor dispersion, they will fail by separation of the bundle rather than by failure of the nanotube itself, resulting in significantly reduced strength [8,9]. On the other hand, solid-state drawing of nanocomposites is largely dominated by regions of lower nanotube volume fraction and this could certainly alter both distribution and orientation of CNTs along the length of the fiber. Strength in composites is a complex issue involving load transfer, stress concentrations and defect distribution, especially in the case of fibers. Fig. 5 shows the elastic moduli, as function of CNT percentages, for all the samples at different draw ratios. The drawing process already increased the elastic modulus of pure PE with increasing the draw ratio. The elastic modulus evaluated for the undeformed PE was about 450 MPa, it results about three times increased after drawing at $\lambda = 6$, about five times increased at $\lambda = 8$, and about seven times increased after drawing at $\lambda = 10$. The

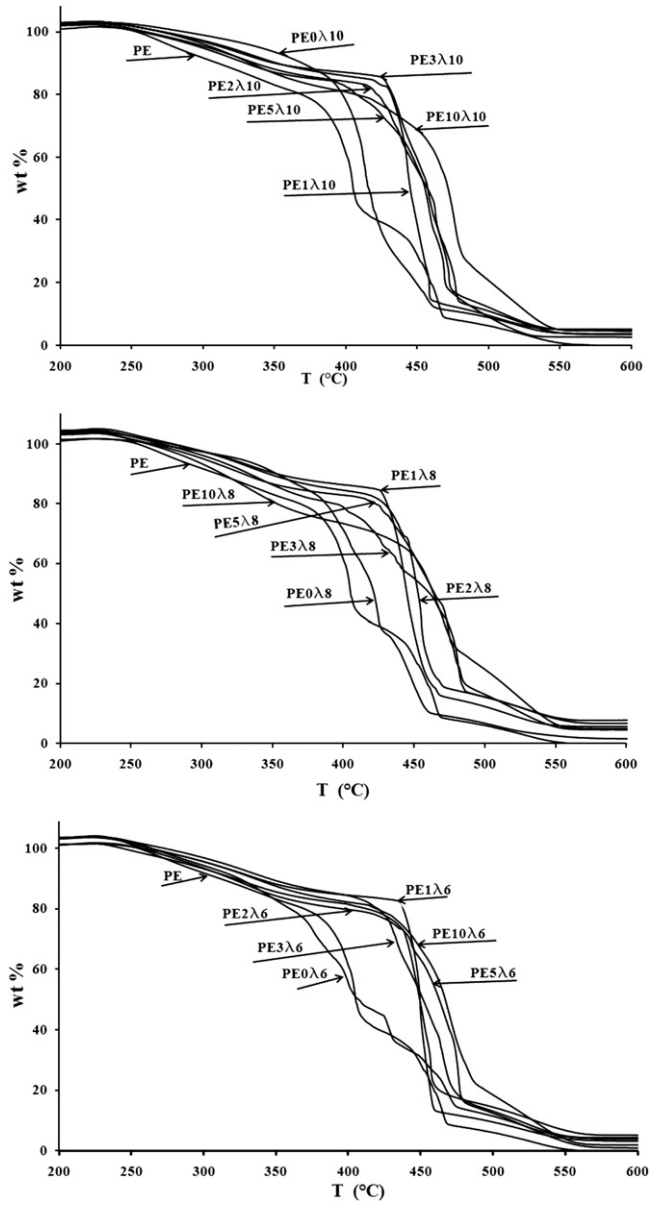

Fig. 4. Thermogravimetric analysis (TGA) for all the samples in the range 200°C–600 °C.

composite fibers show significantly increased strength with increasing the draw ratio, in all the investigated composition range. The enhancement is more pronounced at low nanotubes loading (i.e. 1–3% wt/wt), a further increasing in modulus is observed for 5% wt/wt CNT (more evident for samples drawn at $\lambda = 6$ and $\lambda = 8$) and a plateau value for 10% wt/wt of filler. The data suggest that the

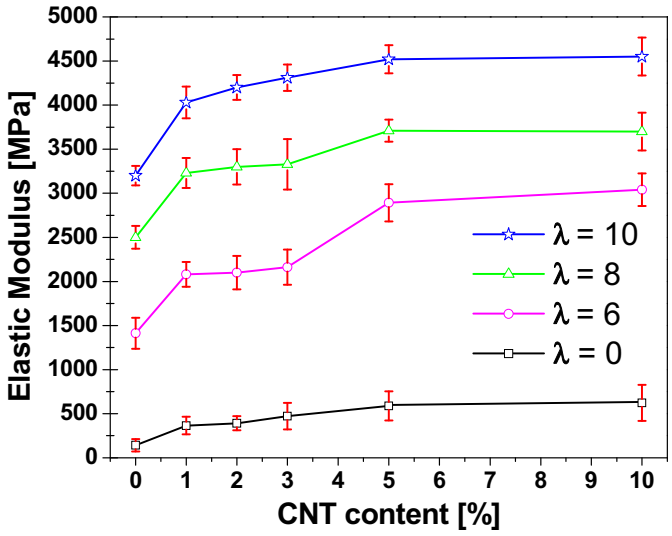

Fig. 5. Elastic moduli, E (MPa), as function of CNT content.

significant property enhancement, at low CNT percentages (wt/wt), could be attributed to highly dispersed and well aligned nanotubes and/or good adhesion between nanotubes and polymer matrix.

Fig. 6 shows the elastic moduli as function of the samples draw ratios. The higher the draw ratio the lower is the improvement in the strength due to the CNT addition. It seems to suggest that the high orientation of the polymer chains enforce high alignment of the nanotubes also at low concentrations.

3.6. Electrical properties

Fig. 7 reports the conductivity values, σ (S/m), of the fibers, as function of CNT percentages. Percolation theory deals with the effect of varying, in a random system, the number of interconnections present. In this case the interconnections are the highly conductive nanotubes. In literature [39] was proposed an analytical model, based on the Fermi-Dirac distribution, which describes the critical insulator to conductor transition:

$$\log\left(\frac{\sigma_c}{\sigma_n}\right) = \frac{\log\left(\frac{\sigma_p}{\sigma_n}\right)}{(1+\exp(t(X-X_c)))} \quad (4)$$

where σ_c, σ_n and σ_p are the composite, filler, and polymer conductivities, respectively, X is the CNT mass fraction, and t is an empirical parameter that leads to the change in conductivity at the percolation threshold X_c.

By assuming a constant value for σ_n and σ_p, from equation (4) were obtained the best fitted values of X_c and t for the four sets of samples. The data are reported in Table 3.

The percolation threshold decreases from the undeformed samples to the fibers, going from 2 to 4 with increasing the draw

Table 2
Maximum degradation temperature, Td^{max} (°C), of undeformed and drawn polyethylene and all the composite fibers, evaluated by TGA.

Sample	Td^{max} (°C)	Sample	Td^{max} (°C)	Sample	Td^{max} (°C)
Undeformed PE	405 °C (±3 °C)	Undeformed PE	405 °C (±3 °C)	Undeformed PE	405 °C (±3 °C)
PE0λ6	424 °C (±3 °C)	PE0λ8	422 °C (±3 °C)	PE0λ10	417 °C (±3 °C)
PE1λ6	450 °C (±3 °C)	PE1λ8	445 °C (±3 °C)	PE1λ10	446 °C (±3 °C)
PE2λ6	450 °C (±3 °C)	PE2λ8	454 °C (±3 °C)	PE2λ10	457 °C (±3 °C)
PE3λ6	453 °C (±3 °C)	PE3λ8	467 °C (±3 °C)	PE3λ10	456 °C (±3 °C)
PE5λ6	463 °C (±3 °C)	PE5λ8	468 °C (±3 °C)	PE5λ10	457 °C (±3 °C)
PE10λ6	467 °C (±3 °C)	PE10λ8	468 °C (±3 °C)	PE10λ10	473 °C (±3 °C)

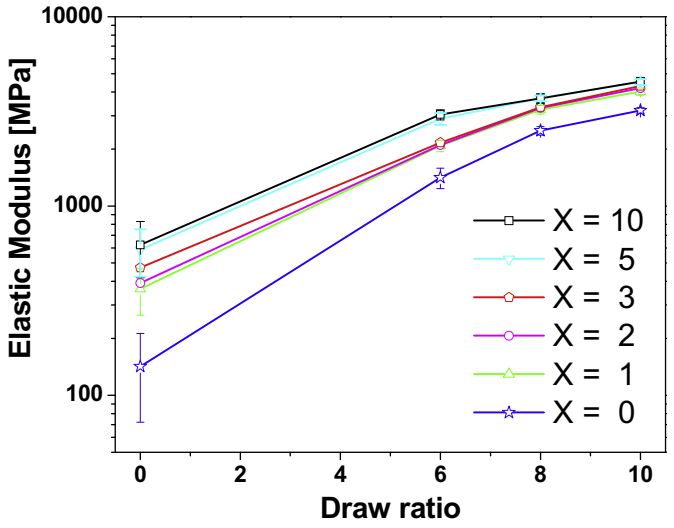

Fig. 6. Elastic moduli, E (MPa), as function of samples draw ratio.

ratio from 0 to 10. Such a phenomenon, already found for nanocomposites based on oriented thermoplastic polymers-carbon nanofillers [40–42], could be justified as a break-down of the conductive network, inducted by the solid-state drawing. The drawing process of LLDPE/CNT composites decreases the number of conduction pathways present above the percolation threshold with a resulting decrease in conductivity. However, we point out that the electrical conductivity of LLDPE, soon after percolation, results increased of about nine orders of magnitude at low nanotube loadings at all draw ratios.

Fig. 8 illustrates the samples conductivity as function of the draw ratio. At high draw ratio the platelets are aligned parallel each other along the stretching direction and only at higher loading they form a conductive path. At higher loadings, where there are more tube–tube connections, greater anisotropy is required to break the contacts and disrupt percolation.

4. Discussion

The initial stages of deformation involved a displacement of the spherulitic lamellae within the sample with a non-homogeneous sliding or shear of the folded molecules. The intermolecular interactions (i.e. van der Waals forces) existing between polymer chains contribute to the sample morphology [43,44]. Based on the SEM experiments, it was proposed that the microstructure of LLDPE is an interconnected network of anisotropically shaped particles, connected by array of fibrils. Considering the FTIR data presented in Fig. 2 and the proposed mechanisms of deformations, the transition at $6<\lambda<8$ can be attributed to the process prior to which two events seem to happen: initially, at a tensile load, only those displacements of crystallites occur that result in an increase in the orientation function values; and upon further stretching, rotation of striation or folded molecules may occur.

It should be mentioned that the transition point may depend upon the thermal and mechanical history of the polymer.

The above scenario is schematically depicted in Scheme 1a that represents the semicrystalline material in the undeformed state. Scheme 1b illustrates how tension produces a macroscopic expansion of the sample in the draw directions. The sample deformation produces a rotation with a simultaneous alignment of the crystalline regions. The CNT network present in the undeformed sample loses partially its dimensionality. As result, the electrical percolation threshold tends to slightly increase with increasing the draw ratio. Upon further elongation, Scheme 1c, the alignment of the crystalline regions became complete. At this level of molecular orientation the CNT network present two-dimensions. Additional elongation of the LLDPE/CNT samples decreases the number of conduction pathways present with a resulting decrease in conductivity.

As evidenced by the SEM and FTIR analysis, the presence of CNT in the polymeric matrix induces an additional draw oriented structure. These oriented structures are known to increase the strain hardening in draw direction, increasing the capability of interparticle ligaments to transfer load and deformation in the

Table 3
Percolation threshold, X_c (wt%), electrical conductivity of filler, σ_n (S/m), electrical conductivity of matrix, σ_p (S/m), and t parameters as evaluated from Equation (1), as function of draw ratio (λ).

λ	X_c (wt%)	σ_n (S/m)	σ_p (S/m)	t
0	2.0	1.00E-01	2.24E-11	2.0
6	3.0	1.00E-01	2.24E-11	1.6
8	3.5	1.00E-01	2.24E-11	1.6
10	4.0	1.00E-01	2.24E-11	1.6

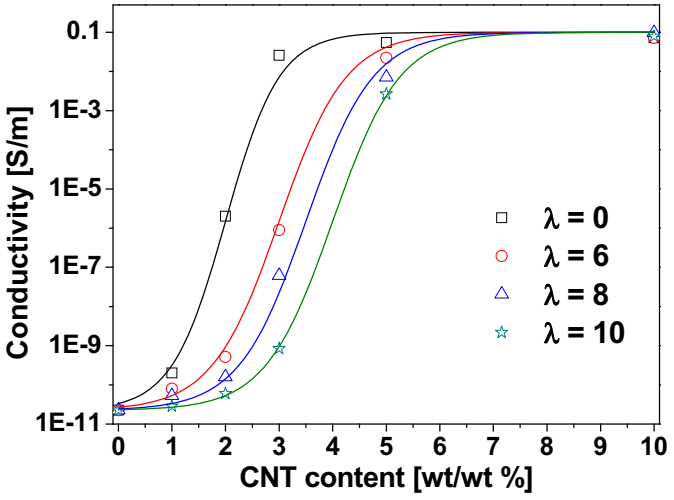

Fig. 7. Electrical conductivity (S/m) as function of CNT content (wt/wt%)

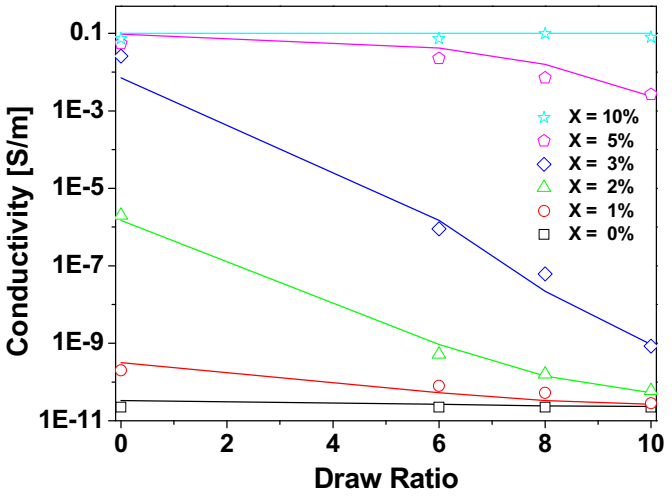

Fig. 8. Electrical Conductivity (S/m) as function of draw ratio.

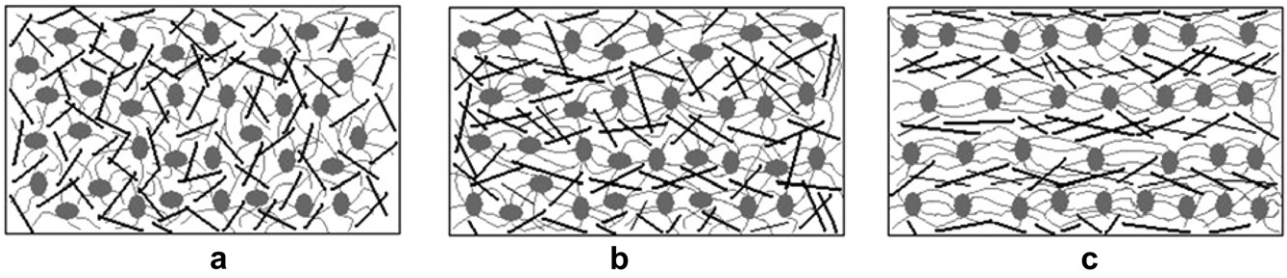

Scheme 1. Model illustrating the structural changes during tensile deformation.

direction of loading. In that case, the effect of the CNT seems to be less important with respect to this improvement produced by the lamellae orientation.

5. Conclusions

Multi walled carbon nanotubes dispersion was achieved into a linear low density polyethylene matrix through high energy ball milling technique using 1%; 2%; 3%; 5% and 10% (wt/wt) of CNT loadings.

Films from composite powders were obtained on a laboratory scale and drawn at 80 °C at different draw ratios $\lambda = 6$; 8; 10.

- Morphological analysis showed that under high uniaxial drawing in the solid state, the original morphology is transformed into highly oriented microfibril morphology.
- FTIR demonstrated that molecular orientation increases with increasing draw ratio and CNT content for all the composites. This behavior reflects a typical transformation from spherulitic to fibrous structure during elongation.
- DSC analysis showed that for the lower CNT content there is an increase in melting temperature with the increasing draw ratio, but for higher CNT content the melting temperatures decrease slightly.
- The analysis of thermal degradation in air flow showed a high improvement of thermal stability for the composite fibers, proportionally to CNT content and draw ratio.
- Mechanical properties showed a significantly increased strength with increasing the draw ratio, in all the investigated composition range. The enhancement resulted more pronounced at low nanotubes loading (i.e. 1–3% wt/wt) and a plateau value was reached for 10% wt/wt of filler.
- Electrical properties showed that the electrical conductivity of insulating LLDPE matrix, results increased of about nine orders of magnitude, with quite low nanotube loadings at all draw ratios, and the percolation threshold tends to decrease with increasing the draw ratio for a break-down of the conductive network, inducted by the solid state drawing.

References

[1] Peijs T, Jacobs MJN, Lemstra PJ. High performance polyethylene fibres. In: Chou TW, Kelly A, Zweben C, editors. Comprehensive composites, vol. 1. Oxford: Elsevier Science Publishers Ltd.; 2000. p. 263–302.
[2] Nakamae K, Nishino T, Ohkubo H. Elastic modulus of crystalline regions of polyethylene with different microstructures: experimental proof of homogeneous stress distribution. J Macromol Sci Phys 1991;B30(1–2):1–23.
[3] Smith P, Lemstra PJ. Ultra-high-strength polyethylene filaments by solution spinning/drawing. J Mater Sci 1980;15(2):505–14.
[4] Smith P, Lemstra PJ, Pijpers JPL, Kiel AM. Ultra-drawing of high molecular weight polyethylene cast from solution III. Morphology and structure. Colloid Polym Sci 1981;259(11):1070–80.
[5] Yu MF, Files BS, Arepalli S, Ruoff RS. Tensile loading of ropes of single wall carbon nanotubes and their mechanical properties. Phys Rev Lett 2000;84:5552–5.
[6] Thostenson ET, Chou TW. On the elastic properties of carbon nanotube-based composites: modeling and characterization. J Phys D Appl Phys 2003;36:573–82.
[7] Robertson J. Realistic applications of CNTs. Mater Today 2004;7:46–52.
[8] Guadagno L, Vertuccio L, Sorrentino A, Raimondo M, Naddeo C, Vittoria V, et al. Mechanical and barrier properties of epoxy resin filled with multi-walled carbon nanotubes. Carbon 2009;47:2419–30.
[9] Thostenson ET, Ren Z, Chou TW. Advances in the science and technology of carbon nanotubes and their composites: a review. Compos Sci Technol 2001;61:1899–912.
[10] Sandler JKW, Kirk JE, Kinloch IA, Shaffer MSP, Windle AH. Ultra-low electrical percolation threshold in carbon-nanotube-epoxy composites. Polymer 2003;44:5893–9.
[11] Bauhofer W, Kovacs JZ. A review and analysis of electrical percolation in carbon nanotube polymer composites. Compos Sci Technol 2009;69:1486–98.
[12] Suryanarayana C. Mechanical alloying and milling. Prog Mater Sci 2001;46:1–184.
[13] Shaw WJD. Current understanding of mechanically alloyed polymers. Mater Sci Forum 1998;269:19–29.
[14] Sorrentino A, Gorrasi G, Tortora M, Vittoria V, Costantino U, Marmottini F, et al. Incorporation of Mg–Al hydrotalcite into a biodegradable Poly (ε-caprolactone) by high energy ball milling. Polymer 2005;46:1601–8.
[15] Gorrasi G, Sarno M, Di Bartolomeo A, Sannino D, Ciambelli P, Vittoria V. Incorporation of carbon nanotubes into polyethylene by high energy ball milling: morphology and physical properties. J Polym Sci Part B Polym Phys 2007;45:597–606.
[16] Kuriger RJ, Alam MK, Anderson DP, Jacobsen RL. Processing and characterization of aligned vapor grown carbon fiber reinforced polypropylene. Compos Part A: Appl Sci Manufacturing 2002;33:53–62.
[17] Haggenmueller R, Gommans H, Rinzler AG, Fischer JE, Winey KI. Aligned single-wall carbon nanotubes in composites by melt processing methods. Chem Phys Lett 2000;330:219–25.
[18] Bin Y, Kitanaka M, Zhu D, Matsuo M. Development of highly oriented polyethylene filled with aligned carbon nanotubes by gelation/crystallization from solutions. Macromolecules 2003;36:6213–9.
[19] Ruan S, Gao P, Yu TX. Ultra strong gel spun ultra-high molecular weight polyethylene fiber reinforced using multiwalled carbon nanotubes. Polymer 2006;47:1604–11.
[20] Read BE, Stein RS. Macromolecules 1968;1(2):116.
[21] Ward IM, Coates PD, Dumoulin MM, editors. Characterization of orientation in solid phase processing of polymers. Munich: Carl Hanser Verlag; 2000.
[22] Lagaron JM, Lopez-Quintana S, Rodriguez-Cabello JC, Merino JC, Pastor JM. Comparative study of the crystalline morphology present in isotropic and uniaxially stretched “conventional” and metallocene polyethylenes. Polymer 2000;41:2999–3010.
[23] Clements J, Jakeways R, Ward IM. Polymer 1978;639:19.
[24] Voyiatzis GA, Andrikopoulos KS. Fast monitoring of the molecular orientation in drawn polymers using Micro-Raman spectroscopy. Appl Spectrosc 2002;56:528–35.
[25] Everall N, Chalmers J, Mills P. Use of polarized resonance Raman spectroscopy of a polyene probe, and FT-IR dichroism, to probe amorphous-phase orientation in uniaxially drawn poly(ethylene). Appl Spectrosc 1996;50:1229–34.
[26] Balabin RM. Conformational equilibrium in glycine: experimental jet-cooled Raman spectrum. J Phys Chem Lett 2010;1:20–3. doi:10.1021/jz900068n.
[27] Tanaka M, Young RJ. Polarised Raman spectroscopy for the study of molecular orientation distributions in polymers. J Mater Sci 2006;41:963–91.
[28] Nielsen JR, Woollett AH. Vibrational spectra of polyethylenes and related substances. J Chem Phys 1957;26(6):1391–400.
[29] Kissin YV. J Polym Sci Polym Phys Ed 1992;30:1165.
[30] Agosti E, Zerbi G, Ward IM. Structure of the skin and core of ultra-drawn polyethylene films by vibrational spectroscopy. Polymer 1992;33(20):4219–29.
[31] Bhattacharyya AR, Sreekumar TV, Liu T, Kumar S, Ericson LM, Hauge RH, et al. Crystallization and orientation studies in polypropylene/single wall carbon nanotube composite. Polymer 2003;44:2373–7.
[32] Wunderlich B. Macromolecular Physics, vol. 3. Academic Press; 1980.

[33] Pennings AJ, Zwijnenburg AJ. J Polym Sci Polym Phys Ed 1979;17:1011.
[34] Bowden PB, Young RJ. J Mater Sci 1974;9:2034.
[35] Jana RN, Mukunda PG, Nando GB. Thermogravimetric analysis of compatibilized blends of low density polyethylene and poly(dimethyl siloxane) rubber. Polym Degrad Stab 2003;80:75–82.
[36] Kashiwagi T, Grulke E, Hilding J, Groth K, Harris R, Butler K, et al. Thermal and flammability properties of polypropylene/carbon nanotube nanocomposites. Polymer 2004;45:4227–39.
[37] Watts PCP, Fearon PK, Hsu WK, Billingham NC, Kroto HW, Walton DRM. Influence of MWCNT morphology on dispersion and thermal properties of polyethylene nanocomposites. J Mater Chem 2003;13:491–5.
[38] Schadler LS, Giannaris SC, Ajayan PM. Load transfer in carbon nanotube epoxy composites. Appl Phys Lett 1998;73:3842–4.
[39] Munson-Mcgee SH. Estimation of the critical concentration in an anisotropic percolation network. Phys Rev B 1991;43(4):3331–6.
[40] Ciselli P, Zhang R, Wang Z, Reynolds CT, Baxendale M, Peijs T. Oriented UHMW-PE/CNT composite tapes by a solution casting-drawing process using mixed-solvents. Eur Polym J 2009;45:2741–8.
[41] Deng H, Skipa T, Zhang R, Lellinger D, Bilotti E, Alig I, et al. Effect of melting and crystallization on the conductive network in conductive polymer composites. Polymer 2009;50(15):3747–54.
[42] Deng H, Zhang R, Bilotti E, Peijs T. A novel concept for highly oriented carbon nanotubes composite tapes or fibres with high strength and electrical conductivity. Macromol Mater Eng 2009;12:749–55.
[43] Balabin RM. Intermolecular dispersion interactions of normal alkanes with rare gas atoms: van der Waals complexes of n-pentane with helium, neon, and argon. Chem Phys 2008;352:267–75. doi:10.1016/j.chemphys.2008.06.015.
[44] Tasi G, Nagy B. Comment on Enthalpy difference between conformations of normal alkanes: Raman spectroscopy study of n-pentane and n-Butane. J Phys Chem A 2010;114(24):6728–9. doi:10.1021/jp103549e.

Polymer 52 (2011) 1133–1140

Contents lists available at ScienceDirect

Polymer

journal homepage: www.elsevier.com/locate/polymer

Crystal growth pattern changes in low molecular weight poly(ethylene oxide) ultrathin films

Guoliang Zhang [a], Yan Cao [b], Liuxin Jin [a], Ping Zheng [a], Ryan M. Van Horn [b], Bernard Lotz [c,**], Stephen Z.D. Cheng [b,*], Wei Wang [a,**]

[a] The Key Laboratory of Functional Polymer Materials of Ministry of Education and Institute of Polymer Chemistry, College of Chemistry, Nankai University, Tianjin 300071, China
[b] Department of Polymer Science, College of Polymer Science and Polymer Engineering, The University of Akron, Akron, OH 44325-3909, USA
[c] Institut Charles Sadron, 23 Rue du Loess, BP 84047, Strasbourg 67034, France

ARTICLE INFO

Article history:
Received 18 November 2010
Accepted 3 January 2011
Available online 9 January 2011

Keywords:
Ultrathin film
PEO
Crystal pattern

ABSTRACT

A low molecular weight (MW) poly(ethylene oxide) (PEO) crystallized in ultrathin films displays various crystal growth patterns in a crystallization temperature (T_x) range from 20.0 °C to 50.0 °C. In succession, the following patterns are found: nearly one-dimensional (1D) dendrite-like crystal patterns at $T_x \leq 38.0$ °C, two-dimensional (2D) seaweed-like patterns between 39.0 °C $\leq T_x \leq$ 42.0 °C and again, nearly 1D dendrite-like patterns at $T_x \geq 43.0$ °C. These transitions result from a complex interplay of varying growth rates along different growth directions and preservation of growth planes. Structural analysis carried out via electron diffraction indicates that the dendrite-like crystals formed at the low and high T_x values differ by their fast growth directions: along the {120} normal at the low T_x values and along the (100) and (010) normal at the high T_x values. In the later case however, the major growth faces are still the {120}, this time tilted at 45° and indicating the a^* and b axes growth tips. In the intermediate T_x range (39.0 °C–42.0 °C), three growth directions coexist giving rise to the seaweed morphology. The crystal growth rates at the low and high T_x values are constant versus time. For the seaweed, a square-root dependence is obtained. These differences are probably due to 1D and 2D growth in the ultrathin films and are associated with different growth patterns of the dendrites and the seaweed, respectively.

1. Introduction

Crystallization of polymers is one of the most intriguing topics in macromolecular physics [1,2]. Due to their long-chain nature, polymer chains kinetically prefer to fold back and forth to form metastable folded-chain lamellar crystals under supercooled conditions [1–4]. The shape of single crystals may change with crystallization conditions (solution, bulk, crystallization temperature (T_x), and others) due to the different dependencies of the growth rates of different crystallographic planes. For example, single crystals of polyethylene (PE) show a lozenge or truncated lozenge shape in good solvent and even a lenticular habit in poor solvent at high T_x [2,5–8]. Toda observed that PE single crystals grown in the bulk change from truncated lozenge to lenticular shape with increasing T_x [9,10]. Kovacs et al. and Cheng et al. found that the shape of poly(ethylene oxide) (PEO) single crystals change from a faceted habit to rounded and back to faceted in a T_x range near the equilibrium melting temperature [11–14].

Recently, polymer crystallization in thin and ultrathin films has attracted increasing attention for both practical and scientific reasons [15–36]. Crystallization in ultrathin films is very different from bulk crystallization. Monolayer 2D lamellar crystals are formed in ultrathin films as opposed to three-dimensional (3D) spherulites in the bulk. Furthermore, different types of crystal shapes (*e.g.* labyrinthine, dendrite, seaweed, compact and faceted single crystals) have been observed in polymer ultrathin films [16–18,22,23,25,31,32,34,35]. A transition from dendrite to seaweed in PEO ultrathin films has also been observed [16,25,28], although the crystallographic relationship and the underlying reason of the transition are still obscure [36–51]. It is accepted that the differences in growth anisotropy are the origin of the different pattern formations [38,41]. A gradual change in the growth anisotropy may result in a progressive pattern evolution from dendrite to seaweed or from one to another dendrite [25,37,39–45,49,52]. Although theoretical studies have illustrated the pattern selection principle in some aspects of growth kinetics [44,45], the limited set

* Corresponding author. Tel.: +1 330 972 7539; fax: +1 330 972 6581.
** Corresponding authors.
E-mail addresses: guoliang2008@mail.nankai.edu.cn (G. Zhang), yc41@uakron.edu (Y. Cao), jlx115@mail.nankai.edu.cn (L. Jin), zhengping@nankai.edu.cn (P. Zheng), rmv4@uakron.edu (R.M. Van Horn), bernard.lotz@ics-cnrs.unistra.fr (B. Lotz), scheng@uakron.edu (S.Z.D. Cheng), weiwang@nankai.edu.cn (W. Wang).

0032-3861/$ – see front matter © 2011 Elsevier Ltd. All rights reserved.
doi:10.1016/j.polymer.2011.01.002

of experimental data is still insufficient to obtain a universal morphological diagram based on an in-depth understanding of the origin of pattern selections [17,25,31,32,37,39–42,49,52].

In this work, we describe and analyze a dendrite-seaweed-dendrite crystal evolution in ultrathin films of a low molecular weight (MW) PEO in the 20.0–50.0 °C T_x range. Atomic force microscopy (AFM) was used to observe crystal morphologies. Transmission electron microscopy (TEM), and more specifically electron diffraction (ED) patterns helped to determine the crystal growth directions and growth planes. Crystal growth rates were measured at different T_x in order to analyze the formation mechanisms of the dendrite and seaweed crystals. The possible origin of crystal growth pattern evolution is discussed.

2. Experimental section

A PEO fraction with weight-average molecular weight ($\overline{M}_w$) 7.2×10^3 g/mol and polydispersity index (PDI) 1.01 was purchased from Polymer Source. The two end groups are a methyl group and a hydroxyl group. Its equilibrium melting temperature is $T_m^0 = 64.1$ °C [53]. A toluene solution of PEO ($c = 0.01\%$ w/v) was prepared for film deposition.

Square 0.8 × 0.8 cm^2 silicon wafers were treated in Piranha solution of H_2SO_4 (98%): $H_2O_2 = 3{:}1$ at 120 °C for 30 min to provide a layer of –OH groups on the silicon surface. These substrates were then cleaned in an ultrasonic water bath. The contact angle, θ, of water on treated silicon wafer was $\theta = 8°$. Silicon monoxide substrates supported by copper grids were purchased from Ted Pella Inc for TEM experiments.

Ultrathin PEO films were prepared by drop-casting the solution onto the silicon wafer or the copper grid supported silicon monoxide. The samples were dried at ambient condition and then treated in vacuum for 12 h. The as-prepared samples were heated to 80.0 °C for 10 min to form a uniform molten layer of 3–4.5 nm thick (measured by AFM). They were then cooled to a preset T_x for isothermal crystallization for 12 h. The samples were then cooled to room temperature for AFM and TEM examination.

Crystal growth patterns were imaged with a hot-stage multimode AFM (Digital Instrumental Nanoscope IV). The tapping mode was used to obtain height and amplitude images. The cantilever force was adjusted to a set-point value of 1.3–1.5 V to limit damage to the sample. The scanning rate was 1.0–1.2 Hz for low-magnification images at a resolution of 512 × 512 pixels/image. Taking advantage of in-situ and real-time observations on polymer crystallization using AFM [54–58], kinetic growth experiments were performed in a T_x range of 34.0 °C ≤ T_x ≤ 50.0 °C. When T_x < 34.0 °C, the growth is difficult to track because the AFM tip induces many nuclei around the growing tips. For fast crystal growth kinetics, resolutions of 128 × 128 pixels or 256 × 256 pixels/image and a scanning rate of 1.5 Hz were used.

Crystals were also observed using TEM (Philips Tecnai) at an accelerating voltage of 120 kV. Selected area electron diffraction (SAED) experiments were carried out to determine crystal growth directions and growth planes. The *d*-spacings were calibrated using a TlCl standard. Molecular modeling and analysis of the diffraction patterns were performed using the Cerius^2 package of Accelrys.

3. Results and discussion

3.1. Evolution of crystal patterns with crystallization temperatures

Fig. 1a–f shows six AFM amplitude images of the PEO crystals at T_x's ranging from 20.0 °C to 49.0 °C. Ribbon-like branches are indicative of the preferred growth directions. Fig. 1a represents a typical dendrite-like crystal formed at $T_x = 20.0$ °C with primary, secondary, and sometimes even tertiary branches. These branches possess narrow backbones along the center line (denoted as B-branches). The angles between the primary and secondary branches or between secondary and tertiary branches are all 90°. The crystals formed at $T_x = 37.0$ °C (Fig. 1b) are almost identical to those in Fig. 1a. Yet, some of the branches do not display their recognized backbones along the central line (denoted as NB-branches). The angles between the B- and NB-branches are at 45°. On average, the 90° angle between primary and secondary B-branches is dominant. When crystallization takes place at $T_x = 40.0$ °C (Fig. 1c), numerous B- and NB-branches grow alternately and thus, lead to a seaweed-like crystal. Again, the angles between the B- and NB-branches are 45°. At $T_x = 44.0$ °C (Fig. 1d), the NB-primary branches become the major population with NB-secondary branches. The branching angles between NB-branches are always 90°. B-branches at a 45° angle to the NB-secondary branches exist only in tertiary branches. When increasing T_x to 46.0 °C (Fig. 1e), a new type of dendrite-like crystal appears. It is only composed of NB-branches with a 90° branching angle. At $T_x = 49.0$ °C (Fig. 1f), crystals have a typical dendrite-like shape with four branches and approximately a four-fold symmetric structure.

These AFM images illustrate a transition from one type of dendrite crystal to another dendrite type with a seaweed crystal as an intermediate stage with increasing T_x. The angles between branches of the same kinds (either within the B- or NB-type) are 90°, while those between B- and NB-branches are 45°. Furthermore as shown in Fig. 2, the backbone width in the B-braches is T_x dependent. At $T_x = 20.0$ °C, the width is ~50 nm, and it increases to ~320 nm at 45.0 °C. Fig. 3 shows the thickness H_c of the backbone and the periphery in the B-branches and, the thickness of NB-branches. Backbone thickness increases from 7.2 nm at $T_x = 20.0$ °C to 9 nm at $T_x = 30.0$ °C. The 9 nm value corresponds to a quadruple-folded-chain crystal. The thickness then suddenly increases to 11 nm at $T_x = 36.0$ °C and further to 15 nm at 43.0 °C, which suggests that the chains fold three and two times, respectively [59]. It should be noted however that the thickness of the backbone in B-branches is generally 1 nm thicker than the periphery until $T_x = 45.0$ °C. Specifically, these two thickness values are in the non-integral folding stage at lower T_x and increase in a quantized fashion based on integral folding at higher T_x. Beyond 46.0 °C, the B-branches disappear, and the dendrites are only composed of NB-branches. The NB-branch thickness reaches 15 nm (twice-folded integral chains). Further increase to $T_x = 50.0$ °C leads to a substantial increase of the thickness, indicating that the number of folds decreases, although the H_c value does not yet reach the expected extended chain length.

Upon analysis of the crystal growth patterns of dendrites and seaweeds and the determination of backbone and lamellae thickness, it appears that we are dealing with a complex growth pattern. The crystal growth kinetics in ultrathin films depend on diffusion of crystallizable molecules as well as on the tendency of PEO chains to crystallize in integrally quantized stem lengths that are two, three and four times smaller than the chain length. Only for fast growth rates, especially for $T_x < 30.0$ °C, are the PEO chains in the crystal non-integrally folded [59,60].

3.2. Crystal growth directions

The PEO crystal structure and chain conformation are well known (Fig. 4a): four distorted 7_2 helical molecules are packed in a monoclinic unit cell, $a = 0.805$ nm, $b = 1.304$ nm, $c = 1.948$ nm and $\beta = 125.4°$ [61]. It turns out that $a \times \sin\beta = 0.656$ nm is only nearly half of the *b* dimension in the *c* axis projection. In most (but not all) growth processes, therefore, the PEO crystal lies on an apparent tetragonal projection. Prominent crystallographic planes are thus 90° apart, *e.g.* (120) and $(1\bar{2}0)$, or (100) and (010). This explains the nearly square

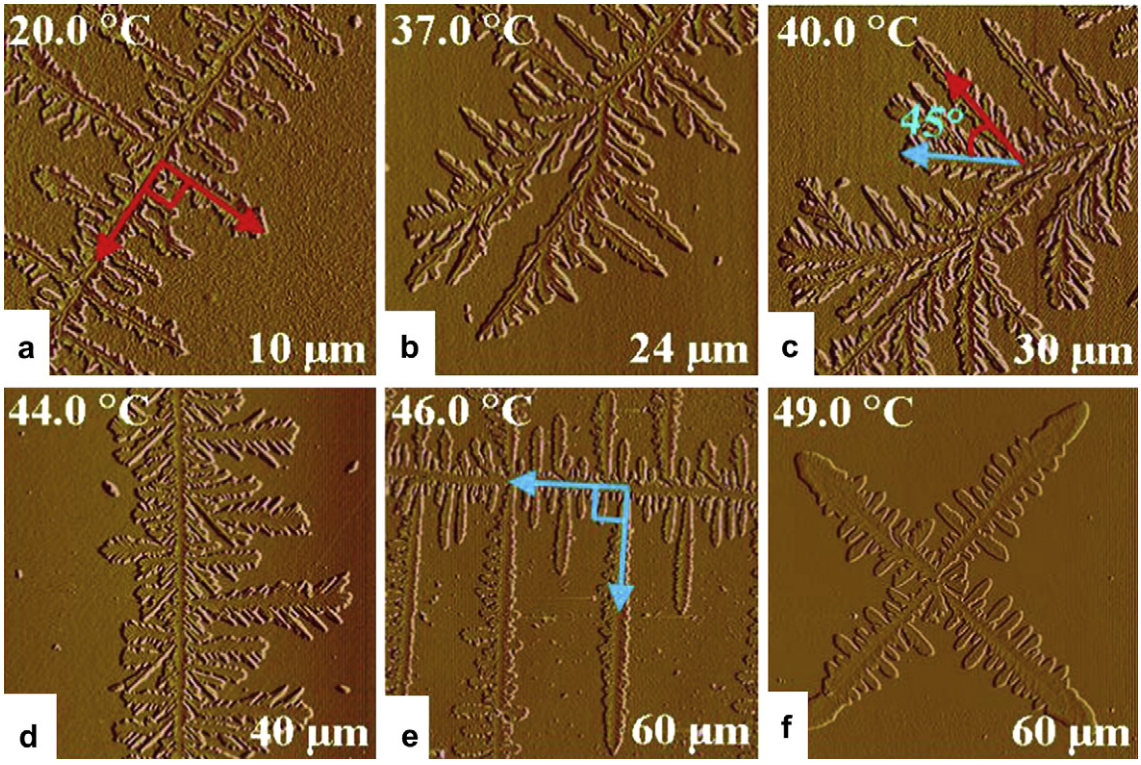

Fig. 1. A set of AFM amplitude images showing crystal growth pattern evolution as a function of T_x. Red and blue arrows represent B-branches and NB-branches respectively, and the angles between them are 90° or 45°. (For interpretation of the references to colour in this figure legend, the reader is referred to the web version of this article).

shape of solution grown crystals, and the existence of branches at 90° in dendrite growth. Because of this apparent high symmetry, it is not possible to determine the crystallographic axes in the dendrite on morphological outline alone. Such a determination requires, in this case, SAED. Fig. 4b shows the calculated (hk0) diffraction pattern of PEO from the Cerius[2] model. The four strongest diffractions correspond to densely packed (120) planes. The six weaker spots close to the center help to determine a^* and b axes. We expect that the observed angle selections between branches should be related to the growth directions along the <120>, the a^* and b axes [28,62,63].

The SAED patterns in correct orientation to the dendrite and seaweed crystals are shown in Fig. 5a. Analysis of the figures reveals the essential difference between the dendrites grown at the low and the high T_x values, in spite of their similar morphologies. In the low T_x dendrites, the branches are parallel to the <120>, whereas for high T_x, the branches are extended along the a^* and b axes (compare the dendrites at $T_x = 26.0$ °C and 46.0 °C). In other words, the major growth directions are 45° away for the low and high T_x dendrites. Dendrites composed of B-branches are denoted $DB_{(120)}$, while dendrites composed of NB-branches are denoted $DNB_{(100)/(010)}$. At intermediate T_x, between 38.0 °C and 43.0 °C, three growth directions coexist. They give rise to more ill defined morphologies, with curved growth faces, characteristic of the seaweed patterns, although they yield clear single crystal ED patterns. Note however that a^* and b axes can be differentiated only via SAED experiments.

To summarize the morphological transition of the PEO crystals, three T_x regions are obtained as follows (Fig. 5b): At $T_x \leq 38.0$ °C, $DB_{(120)}$ dendrites with a backbone in preferential growth directions

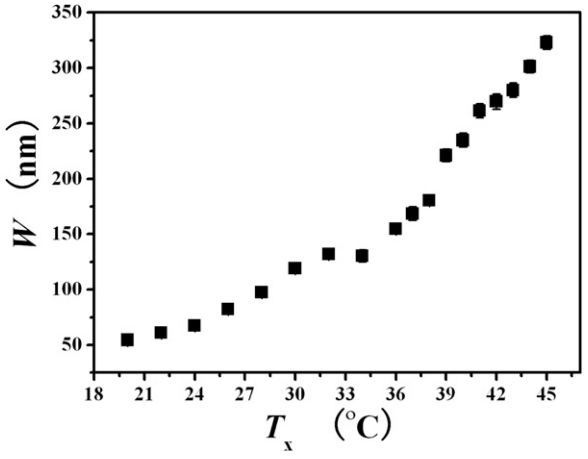

Fig. 2. Width (W) of the backbone in B-branches as a function of T_x.

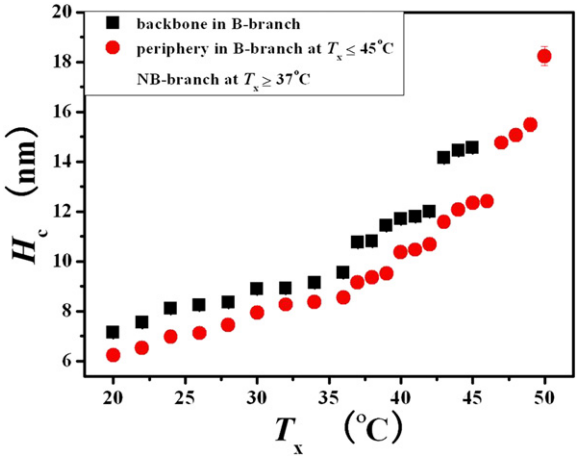

Fig. 3. Thickness (H_c) of crystal as a function of T_x. ■ represents the thickness of backbone in B-branch. ● represents the thickness of the periphery in the B-branch at $T_x \leq 45.0$ °C and the thickness of the NB-branch at $T_x \geq 37.0$ °C. In the region 37.0 °C $\leq T_x \leq$ 45.0 °C, the thickness of the periphery in the B-branch is equal to the thickness of the NB-branch.

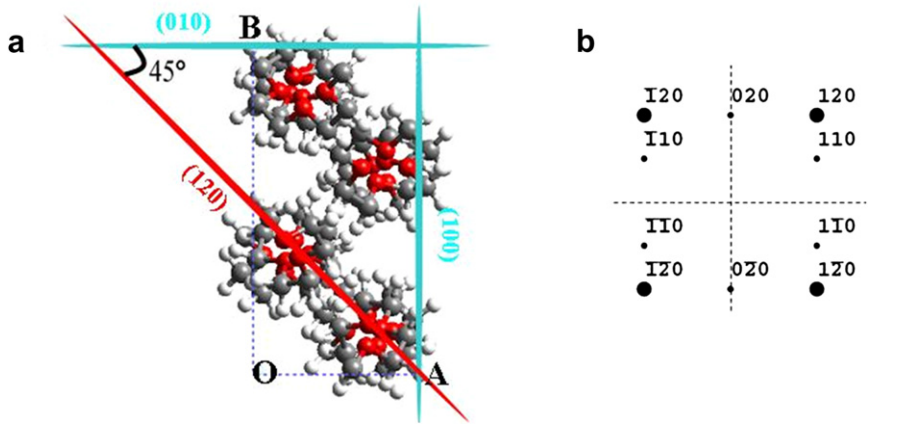

Fig. 4. (a) Unit cell of PEO crystal in the direction of *c* axis. The angle between the {120} and the (100) or (010) planes is 45°. (b) Calculated [001] zone ED pattern.

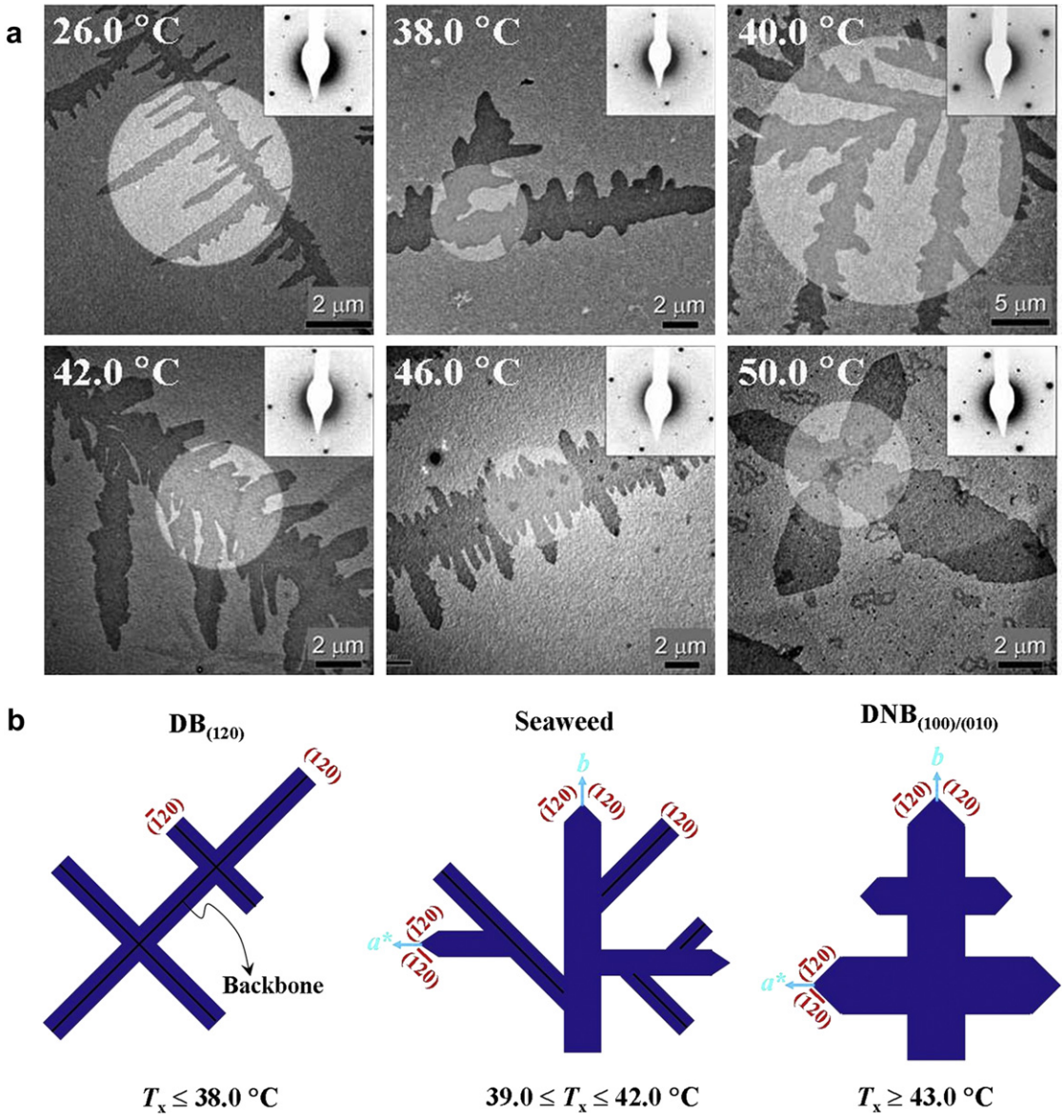

Fig. 5. (a) TEM images and SAED patterns at different T_x. (b) Schematics showing crystal growth direction changing from the <120> to *a** and *b* axes with increasing T_x.

along the <120> and a 90° branching angle; at 39.0 °C ≤ T_x ≤ 42.0 °C, seaweed with growth direction along the <120> and the a^* and b axes and a 45° branching angle; at T_x ≥ 43.0 °C, $DB_{(100)/(010)}$ dendrites with preferential growth direction along the a^* and b axes and a 90° branching angle.

3.3. Crystal growth rate and mechanisms

In-situ experiments were performed using AFM to determine the crystal growth rates. AFM is useful in the high T_x range since homogeneous nucleation is difficult in this T_x region, while the AFM tip can induce the crystal nucleation. The results indicate a significant difference between the growth rate time dependencies of both the low and high T_x dendrites on one side and seaweed on the other.

For the dendrites in both temperature regions of $T_x \leq 38.0$ °C and $T_x \geq 43.0$ °C, the length of the primary branches, R, along the <120> and the a^* and b axes are linearly proportional to time (t) as shown in Figs. 6 and 7. This means that dendrite growth rate, G, is a constant

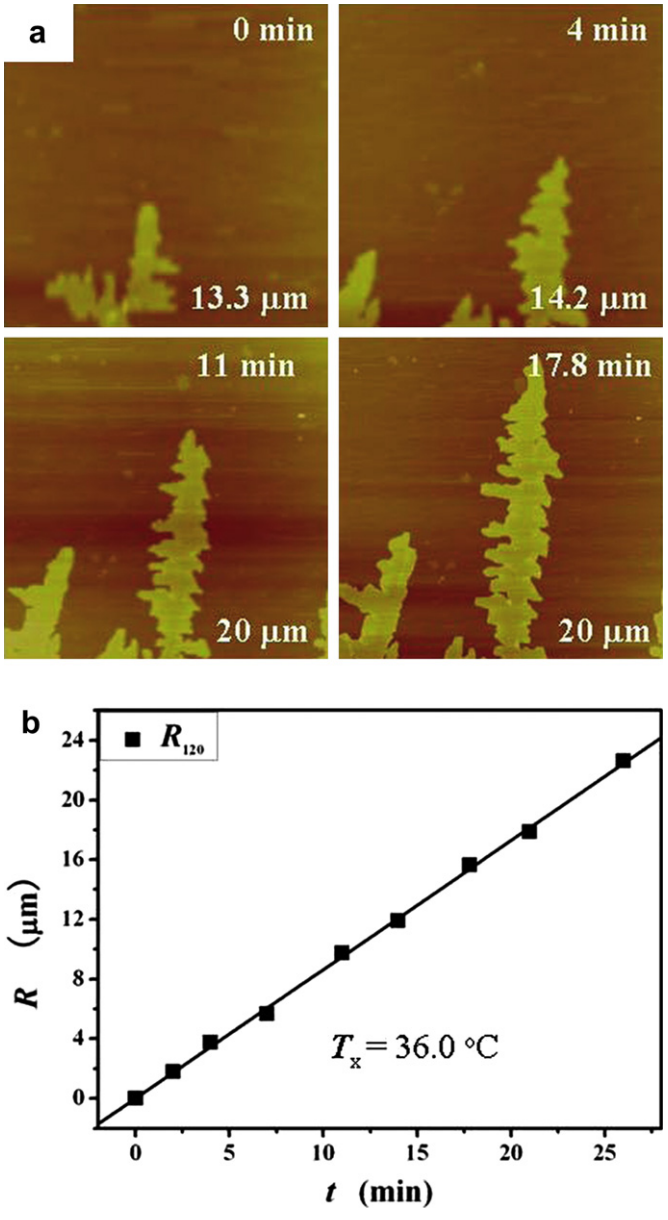

Fig. 6. (a) AFM height images present crystal growth as a function of t at T_x = 36.0 °C. (b) Plot of R versus t. R_{120} represents the length of the B-branch along <120>.

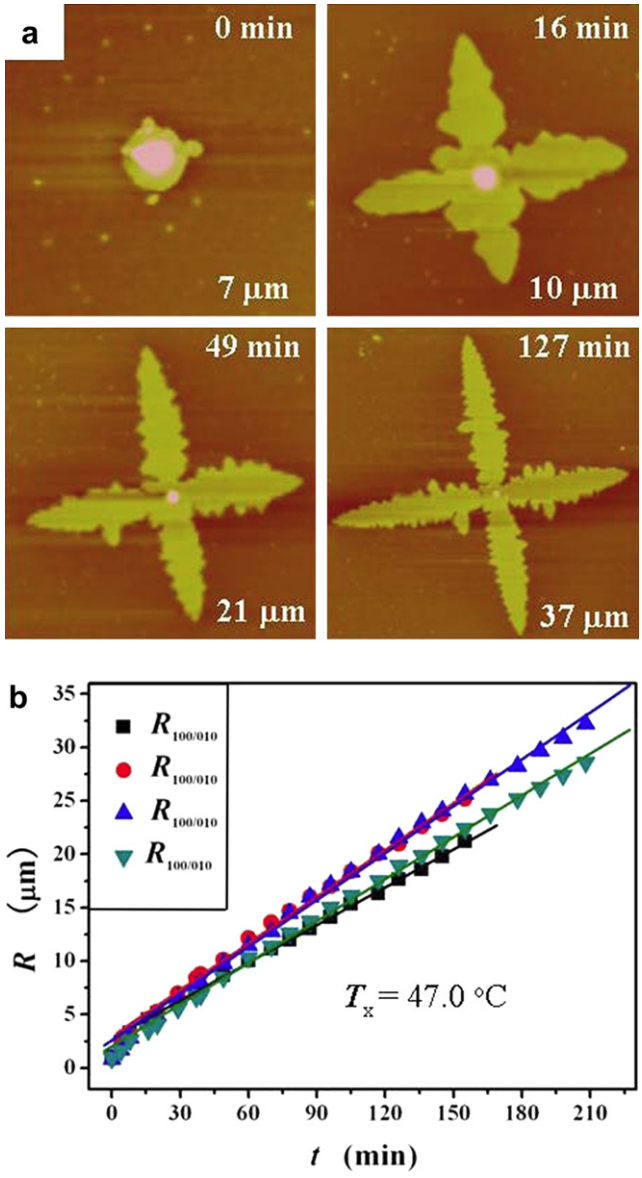

Fig. 7. (a) AFM height images present crystal growth as a function of t at T_x = 47.0 °C. (b) Plots of R versus t. $R_{100/010}$ represents the length of the NB-branch along a^* and b axes.

with respect to t. Fig. 8 shows the growth rate obtained for both the low and high T_x dendrites. The figure illustrates the expected rapid decrease of G with increasing T_x in the low T_x range. In 43.0 °C ≤ T_x ≤ 47.0 °C region however, G remains nearly a constant before decreasing again rapidly when $T_x \geq 48.0$ °C. The overall curve of G versus T_x is strongly reminiscent of plots obtained for similar MW PEO isothermal crystallization from the bulk. In the transition region from integral fold number n to a longer stem length corresponding to n-1 folds, similar growth rate variations have indeed been observed [13,14]. However, the growth mechanism is diffusion-limited in our case versus nucleation-limited in the bulk.

For the seaweeds in the range 39.0 °C ≤ T_x ≤ 42.0 °C missing in Fig. 8, G is not constant for these entities. Fig. 9 illustrates the growth of the seaweeds and the crystal size R plotted as a function of t and $t^{1/2}$. The slope of the R versus t curve decreases with increasing t, which indicates that G continuously decreases with respect to t. On the other hand, R is linearly proportional to $t^{1/2}$.

It is known that the formations of both the dendrite and seaweed crystals are controlled by a diffusion-limited mechanism.

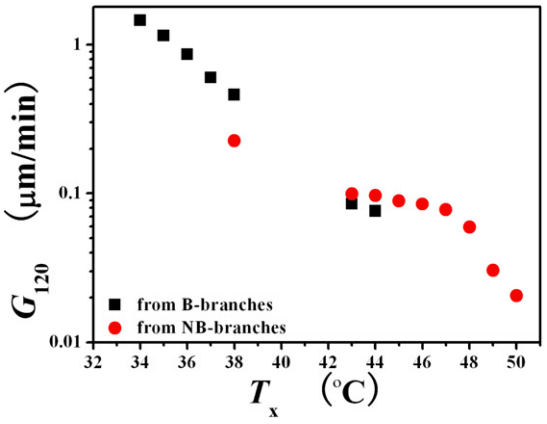

Fig. 8. Plots of G_{120} versus T_x. ■ represents the G_{120} directly measured from B-branches along <120>. ● represents the G_{120} derived from the growth rate of NB-branches along a^* and b axes, $G_{100/010}$, where $G_{120}=(\sqrt{2}/2)G_{100/010}$. In the seaweed-like crystal region of $T_x = 39.0\ ^\circ C–42.0\ ^\circ C$, the growth rate is not plotted as it is not constant versus t.

Why then should we observe a linear growth versus t in the dendrites and a linear growth versus $t^{1/2}$ in the seaweeds? Let us first point out that our observation of linear growth versus t is consistent with earlier observations on other dendrite systems [20,64–67], but no clear explanation has been proposed so far. In the following, we attempt to provide a possible explanation.

The linear growth may be explained by the following reasoning and schematic illustrations in Fig. 10. The primary branch in the dendrite is actually a quasi-1D object. Each individual growth tip is surrounded by a local supercooled PEO diffusion field. The growth of a dendrite branch generates a quasi-1D depletion zone parallel to the growth direction of the primary branch. The material transformation from supercooled melt to crystal implies $dm_c = -dm_a$, where m_c and m_a represent the masses of crystal and supercooled melt, respectively. According to Fick's first law and diffusion controlled growth in quasi-1D case,

$$\frac{\partial(\rho_c W_c H_c R)}{\partial t} = W_a \times D\frac{\partial \phi_a}{\partial x} \quad (1)$$

where ρ_c is the density of the crystal; W_c is the width of the quasi-1D crystal; H_c is the height of the crystal; R is the length of the crystal; W_a is the width of the depletion zone; φ_a represents the mass of the supercooled melt per unit area; and x is the distance from the crystal tip to a specific site ahead of the tip. Because ρ_c, W_c, H_c, and W_a are all constants at a specific T_x, we have

$$\rho_c W_c H_c \frac{\partial R}{\partial t} = D W_a \frac{\partial \phi_a}{\partial x} \quad (2)$$

then,

$$\frac{\partial R}{\partial t} = (D W_a / \rho_c W_c H_c)\frac{\partial \phi_a}{\partial x} \quad (3)$$

where $\frac{\partial \phi_a}{\partial x}$ represents the supercooled melt gradient ahead of the crystal tip. At steady state, $\frac{\partial \phi_a}{\partial x}$ is constant, and therefore, R is linearly proportional to t. This may explain why we observe the linear growth versus t even though the growth is diffusion-limited. This analysis may also provide a possible interpretation for similar observations reported in earlier works [20,64–67].

For the seaweeds, simultaneous growths of B- and NB-branches generate a 2D entity. This leads to the observation that their growths are linearly proportional to $t^{1/2}$. The mathematic analysis for this type of 2D growth was made in Ref. [29]. Therefore, the time-dependent change of growth rate from the dendrite to the seaweed is due to growth dimension change, rather than change of the growth mechanism.

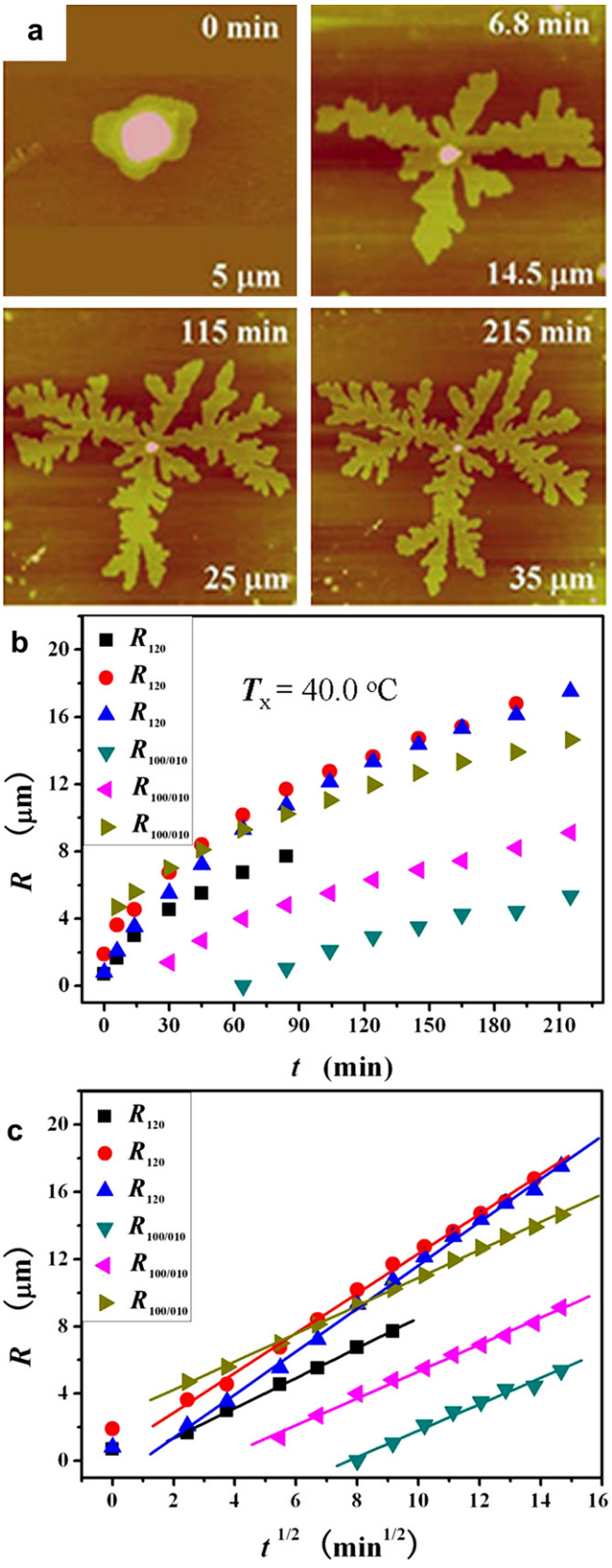

Fig. 9. (a) AFM height images present crystal growth as a function of t at $T_x = 40.0\ ^\circ C$. (b) Plots of R versus t. (c) Plots of R versus $t^{1/2}$. R_{120} represents the length of the B-branch along <120>, and $R_{100/010}$ represents the length of the NB-branch along a^* and b axes.

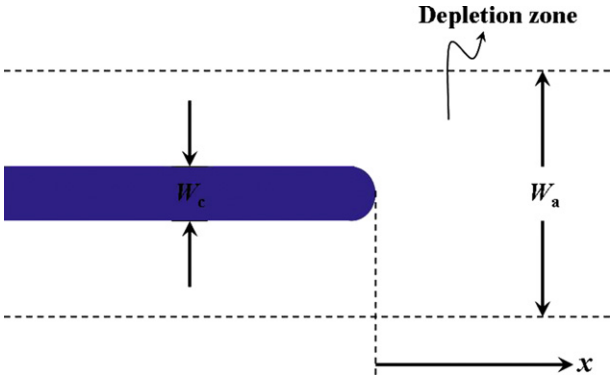

Fig. 10. Schematic illustration of 1D dendrite growth (top view).

3.4. Origin of the crystal pattern change

As illustrated in Fig. 5, the preferential crystal growth direction is along the <120> at $T_x \leq 38.0$ °C and along the a^* and b axes at $T_x \geq 43.0$ °C. Why does the fastest crystal growth direction change in these two T_x regions? Note that in the seaweed-like crystals grown at 39.0 °C $\leq T_x \leq$ 42.0 °C, three growth directions prevail. Let us analyze the growth tips of the B-branch at $T_x \leq 38.0$ °C and NB-branch at $T_x \geq 43.0$ °C. For the B-branches in $DB_{(120)}$ (Fig. 11a), the tips are flat, and correspond to the {120} planes as indicated by the SAED pattern. For the NB-branch in $DNB_{(100)/(010)}$, although the angle between two {120} planes is smaller than 90° as shown in Fig. 11b (see below for reason), the primary NB-branch grows along the merged corner of the two {120} planes. Therefore, the crystal growth planes remain the same in the entire T_x region, although the fastest growth directions are different.

In the high T_x region above 43.0 °C, the crystal growth mechanism is diffusion-limited [29]. For the diffusion coefficient, D, of PEO chains in ultrathin films, Bi et al. reported $D = 0.6 \times 10^{-14}$ m^2/s for a PEO with MW = 5.0×10^3 g/mol in the depleted zone on the surface of −OH decorated glass (that is similar to the surface of −OH decorated silicon wafer in our experiments) at 45.0 °C [68]. Based on the molecular weight dependence [69], the D value for the present PEO is 4.16 × 10^{-15} m^2/s, or 0.25 μm^2/min. The PEO growth rate, G, in the high T_x region is around 0.1–0.01 μm/min. Since G and D are comparable, a materials gradient is expected at the growth front. In turn, this speeds up the growth of the crystal tip (the a^* and b axes), although the growth planes remain the {120} planes. This leads to an angle between two {120} planes smaller than 90° (Fig. 11b). As a result, the $DNB_{(100)/(010)}$ dendrites form in this T_x region.

Next, what is the origin of the $DB_{(120)}$ dendrites formed in the region $T_x \leq 38.0$ °C? We speculate that it is because of the preferential fast growth along the <120> direction with a narrow backbone width at the {120} growth face. In this T_x region, G is much larger than D, so the crystal growth is close to the case of diffusion-limited aggregation [64]. This type of dendrite growth may rely on the fact that the primary nuclei developed in the PEO with a very small size are bounded by {120} planes. The Hoffman–Lauritzen theory predicts that when the crystal growth substrate length is smaller than a critical value that has been responsible for one nucleus and a few hundred nanometers, the growth rate along the substrate normal is faster than the growth rate after the substrate width exceeds this critical value [2,70]. One recent experimental observation has shown that the lateral spread extent increases with T_x on a length scale between 30 nm and 60 nm in single crystals of a specific polymer [71]. As shown in Fig. 2, the width of the backbone in B-branch increases with T_x, while their absolute values range from ~50 nm at $T_x = 20.0$ °C to ~320 nm at $T_x = 45.0$ °C. These width values are expected to be close to but smaller than the upper-limit of the critical substrate width at each T_x for the PEO crystal. The narrow backbone width at the growth front leads to a fast growth along the <120> directions, which results in the $DB_{(120)}$ dendrites in the region $T_x \leq 38.0$ °C.

The final question is: what are the origins of forming the B- and NB-branches? It is noted that although both growth planes are the {120} planes, the B-branches can form only when the <120> is the fastest growth direction for constructing the frames of the $DB_{(120)}$ dendrite, while the NB-branches possess a favorable growth direction along the a^* and b axes forming the $DNB_{(100)/(010)}$ dendrite. Above $T_x = 30.0$ °C, the backbones in the B-branch are more or less integrally folded-chain crystals. This indicates that the backbones are formed first with certain rearrangements resulting in integral chain crystals. Only below $T_x = 30.0$ °C can non-integral folded crystals be stabilized. It is worth mentioning that backbones in the B-branches are about 1 nm thicker than the periphery (Fig. 3). During the formation process (Fig. 6a), the thicker backbones always form ahead of the periphery, which is similar to the observation on a similar MW PEO at high T_x values [11,12]. Other parts of the crystals epitaxially grow on the backbones in the later stages with about a 1 nm thickness decrease. The thinner part may not be able to further reorganize since there is an exhausting of PEO molecules. Any thickening process would generate holes in the crystals and thus, increase the free energy and destabilize the crystals [72]. On the other hand, the NB-branches are developed from a PEO single crystal and grow along the a^* and b axes, whose tips are composed of two {120} planes. Therefore, the thickness of these two sectors of one single crystal is identical.

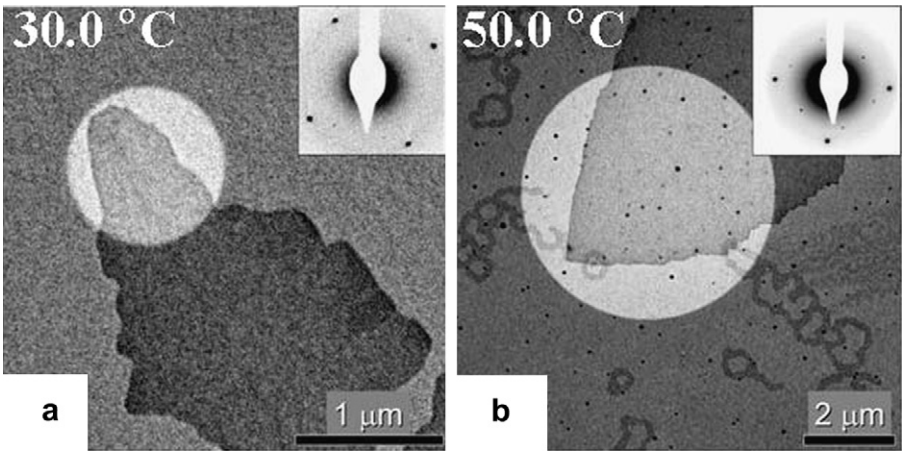

Fig. 11. (a) TEM image and SAED pattern of a B-branch tip at 30.0 °C. (b) TEM image and SAED pattern of an NB-branch tip at $T_x = 50.0$ °C.

Before concluding, it is useful to compare the present results with earlier reports on similar transitions between dendrite and seaweed type crystals. First, it must be noted that no SAED experiments were performed and therefore the crystal growth directions could not be identified [16,25,28]. As a rule, the PEO film thickness was larger or significantly larger than the crystal thickness. Also, the branching angles in seaweed crystals did not have a fixed value. Therefore, the origin of crystal growth transition was not clearly identified. In this work, the PEO film thickness is smaller than the crystal thickness. The crystal growth patterns are therefore strongly dependent on molecular diffusion. The combination of SAED analyses and crystal growth kinetics reveal that the crystal growth transitions between dendrites and seaweed result from a complex interplay of crystallographic aspects and growth mechanisms.

4. Conclusion

We have observed and analyzed T_x-dependent crystal growth patterns in a low MW PEO in ultrathin films. SAED results indicate that when $T_x \leq 38.0\,^{\circ}C$, dendritic crystals are formed with branches elongated along the <120> directions. Above $T_x = 43.0\,^{\circ}C$, dendritic crystals are also formed, but the growth directions are along the a^* or b axes. In the intermediate T_x range, $39.0\,^{\circ}C \leq T_x \leq 42.0\,^{\circ}C$, seaweed crystals are observed, in which three growth directions coexist (a^*, b and <120>). We consider that the crystal growth mechanism in the entire T_x region is a diffusion-limited process, although the crystal growth rates differ for dendrites and seaweeds because of their different growth geometries. Linear crystal growth rates are observed when $T_x \leq 38.0\,^{\circ}C$ and $T_x \geq 43.0\,^{\circ}C$ due to the 1D growth geometry of the dendrites. In the intermediate T_x region where the seaweed crystals are formed, the crystal growth is linearly proportional to $t^{1/2}$ due to the 2D growth geometry. The origin of dendrite crystals in both low and high T_x regions is also discussed. It is suggested that at $T_x \leq 38.0\,^{\circ}C$, the growth is close to diffusion-limited aggregation, and the 1D growth may be due to the fact that the substrate width of the growth front is smaller than the critical value of the nucleation event. On the other hand, in the $T_x \geq 43.0\,^{\circ}C$ region, the material gradient near the growth front generates an increase of crystal tip growth leading to the formation of dendrites with branches elongated in the a^* and b axes directions.

Acknowledgments

The Nankai group greatly appreciates the National Science Foundation of China for a grant (NSFC20474033 and 20874053) and the China Scholarship Council (CSC). Part of the work carried out at the University of Akron was supported by the National Science Foundation (DMR-0906898).

References

[1] Wunderlich B. Macromolecular physics. New York: Academic; 1973. 1976, 1980.
[2] Cheng SZD. Phase transitions in polymers: the role of metastable States. Elsevier Science; 2008.
[3] Keller A, Cheng SZD. Polymer 1998;39:4461.
[4] Cheng SZD, Keller A. Annu Rev Mater Sci 1998;28:533.
[5] Khoury F. Faraday Discuss Chem Soc 1979;68:404.
[6] Khoury F, Bolz L. Proceedings-Annual Meet Electron Microsc Soc America 1980;38:242.
[7] Khoury F, Bolz L. Bull Am Phys Soc 1985;30:493.
[8] Organ SJ, Keller A. J Mater Sci 1985;20:1571;
J Mater Sci 1985;20:1586;
J Mater Sci 1985;20:1602.
[9] Toda A. Faraday Discuss 1993;95:129.
[10] Toda A, Keller A. Colloid Polym Sci 1993;271:328.
[11] Kovacs AJ, Gonthier A, Straupe C. J Polym Sci Polym Symp 1975;50:283.
[12] Kovacs AJ, Straupe C. Faraday Discuss Chem Soc 1979;68:225.
[13] Kovacs AJ, Straupe C. J Cryst Growth 1980;48:210.
[14] Cheng SZD, Chen JH. J Polym Sci Part B Polym Phys 1991;29:311.
[15] Miller A, Mohwald H. J Chem Phys 1987;86:4258.
[16] Reiter G, Sommer JU. Phys Rev Lett 1998;80:3771;
J Chem Phys 2000;122:4376.
[17] Taguchi K, Miyaji H, Izumi K, Hoshino A, Miyamoto Y, Kokawa R. Polymer 2001;42:7443.
[18] Zhang F, Liu J, Huang H, Du B, He T. Eur Phys J E 2002;8:289.
[19] Ferreiro V, Douglas JF, Warren JA, Karim A. Phys Rev E 2002;65:042802.
[20] Ferreiro V, Douglas JF, Warren J, Karim A. Phys Rev E 2002;65:051606.
[21] Schönherr H, Frank CW. Macromolecules 2003;36:1188;
Macromolecules 2003;36:1199.
[22] Wang MT, Braun HG, Meyer E. Macromolecules 2004;37:437.
[23] Zhai XM, Wang W, Ma ZP, Wen XJ, Yuan F, Tang XF, et al. Macromolecules 2005;38:1717.
[24] Meyer E, Braun H-G. J Phys: Condensed Matter 2005;17:S623.
[25] Zhai XM, Wang W, Zhang GL, He BL. Macromolecules 2006;39:324.
[26] Flores A, Corvera-Poire E, Garza C, Castillo R. J Phys Chem B 2006;110:4824.
[27] Li BB, Esker AR. Langmuir 2007;23:2546.
[28] Okerberg BC, Marand H. J Mater Sci 2007;42:4521.
[29] Zhu DS, Liu YX, Chen EQ, Li M, Chen C, Sun YH, et al. Macromolecules 2007;40:1570.
[30] Okerberg BC, Soles CL, Douglas JF, Ro HW, Karim A. Macromolecules 2007;40:2968.
[31] Ma ZP, Zhang GL, Zhai XM, Jin LX, Tang XF, Zheng P, et al. Polymer 2008;49:1629.
[32] Zhang GL, Jin LX, Ma ZP, Zhai XM, Yang M, Zheng P, et al. J Chem Phys 2008;129:224708.
[33] Liu Y-X, Li J-F, Zhu D-S, Chen E-Q, Zhang H-D. Macromolecules 2009;42:2886.
[34] Jin LX, Zhang GL, Zhai XM, Ma ZP, Zheng P, Wang W. Polymer 2009;50:6157.
[35] Zhang GL, Jin LX, Zheng P, Shi AC, Wang W. Polymer 2010;51:554.
[36] Chen R, Li L, Zhao J. Langmuir 2010;26:5951.
[37] Chan SK, Reimer HH, Kahlweit M. J Crys Growth 1976;32:303.
[38] Langer JS. Rev Mod Phys 1980;52:1.
[39] Ben-Jacob E, Godbey R, Goldenfeld NG, Koplik J, Levine H, Mueller T, et al. Phys Rev Lett 1985;55:1315.
[40] Honjo H, Ohta S, Matsushita M. Phys Rev A 1987;36:4555.
[41] Ben-Jacob E, Garik P, Muller T, Grier D. Phys Rev A 1988;38:1370.
[42] Ben-Jacob E, Garik P. Nature (London) 1990;343:523.
[43] Ohta S, Honjo H. Phys Rev A 1991;44:8425.
[44] Brener E, Müller-Krumbhaar H, Temkin D. Europhys Lett 1992;17:535.
[45] Shochet O, Eshel BJ. Phys Rew E 1993;48:4168.
[46] Kassner K. Pattern formation in diffusion-limited crystal growth. Singapore: World Scientific; 1996.
[47] Saito Y. Statistical physics of crystal growth. Singapore: World Scientific; 1996.
[48] Meakin P. Fractals, scaling and growth far from equilibrium. Cambridge: Cambridge University Press; 1997.
[49] Bogoyavlenskiy VA, Chernova NA. Phys Rev E 2000;61:1629.
[50] Utter B, Ragnarsson R, Bodenschatz E. Phys Rev Lett 2001;86:4604.
[51] Libbrecht KG. Rep Prog Phys 2005;68:855.
[52] Haxhimali T, Karma A, Gonzales F, Rappaz M. Nat Mater 2006;5:660.
[53] Cheng SZD, Chen J, Janimak JJ. Polymer 1990;31:1018.
[54] Hobbs JK, Miles MJ. Macromolecules 2001;34:353.
[55] Organ SJ, Hobbs JK, Miles MJ. Macromolecules 2004;37:4562.
[56] Hobbs JK. Polymer 2006;47:5566.
[57] Kailas L, Vasilev C, Audinot J-N, Migeon H-N, Hobbs JK. Macromolecules 2007;40:7223.
[58] Hobbs JK, Farrance OE, Kailas L. Polymer 2009;50:4281.
[59] Cheng SZD, Chen J, Barley JS, Zhang A, Habenschuss A, Zschack PR, et al. Macromolecules 1992;25:1453.
[60] Cheng SZD, Wu SS, Chen J, Zhuo Q, Quirk RP, von Meerwall ED, et al. Macromolecules 1993;26:5101.
[61] Takahashi Y, Tadakoro H. Macromolecules 1973;6:672.
[62] Point JJ, Damman P, Janimak JJ. Polymer 1993;34:3771.
[63] Marentette JM, Brown GR. Polymer 1998;39:1405.
[64] Witten TA, Sander LM. Phys Rev Lett 1981;47:1400;
Phys Rev B 1983;27:5686.
[65] Saito Y, Ueta T. Phys Rev A 1989;40:3408.
[66] Lereah Y, Deutscher G, Grunbaum E. Phys Rev A 1991;44:8316.
[67] Couder Y, Maurer J, Gonzalez-Cinca R, Hernandez-Machado A. Phys Rev E 2005;71:031602.
[68] Bi W, Teguh JS, Yeow EKL. Phys Rev Lett 2009;102:048302.
[69] Cheng SZD, Barley JS, Von Meerwall ED. J Polym Sci Part B Polym Phys 1991;29:515.
[70] Point JJ, Colet MC, Dosière M. J Polym Sci Polym Phys Ed 1986;24:357.
[71] Alcazar D, Thierry A, Schultz P, Kawaguchi A, Cheng SZD, Lotz B. Macromolecules 2006;39:9120.
[72] Zhu DS, Liu YX, Shi AC, Chen EQ. Polymer 2006;47:5239.

Polymer 52 (2011) 1141–1154

Contents lists available at ScienceDirect

Polymer

journal homepage: www.elsevier.com/locate/polymer

Effect of organoclay on the morphology, phase stability and mechanical properties of polypropylene/polystyrene blends

Rajkiran R. Tiwari, D.R. Paul*

Department of Chemical Engineering and Texas Materials Institute, The University of Texas at Austin, Austin, Texas 78712, USA

ARTICLE INFO

Article history:
Received 3 November 2010
Received in revised form
4 January 2011
Accepted 8 January 2011
Available online 15 January 2011

Keywords:
Polypropylene
Polystyrene
Phase stability

ABSTRACT

The effect of organically modified clay on the morphology, phase stability and mechanical properties of polypropylene (PP) and polystyrene (PS) blends was studied using three molecular weight grades of PP. Maleated polypropylene was used, at a PP-g-MA/organoclay ratio of 1, to preferentially promote dispersion of the organoclay in the PP matrix. The MMT content was fixed at 3 wt% based on the PP/PP-g-MA/MMT phase and the PS content was varied from 0–100 wt% in the blend. All blends were processed using a twin screw extruder. The organoclay resides in the PP phase and at the PP/PS interface. The dispersed PS particle size is significantly reduced by the presence of MMT, with maximum decrease observed for the low viscosity PP compared to its blend without MMT. The blends with MMT did not show any change in onset of co-continuity, though MMT shifts the phase inversion composition toward lower PS contents. The phase stability of the blend was significantly improved by the presence of MMT; for blends annealed at 210 °C for 2 h the dispersed phase particle size increased by as much as 10x without MMT with little change was noted with MMT present in the blend. The tensile modulus of blends improved with the addition of MMT at low PS contents. Blends based on the highest molecular weight grade PP showed increase in the tensile yield stress up to 40 wt% PS in the absence of MMT. The tensile strength at break for blend increased slightly with MMT while elongation at break and impact strength decreased in the presence of MMT. Surface energy analysis model was used to predict the orientation and equilibrium position of the clay platelet at the interface based on the surface energies.

1. Introduction

Blends of two different polymers potentially offer materials with an attractive combination or balance of properties; however, most polymer pairs are immiscible and many have weak interfacial interactions that lead to an unstable morphology and poor mechanical performance, i.e., they are incompatible. In such cases, compatibilization can be achieved by block (or graft) copolymers located at the domain interface that produce a fine and stable morphology and improved mechanical properties [1–7]. Polypropylene (PP) and polystyrene (PS) form such incompatible blends, and several reports describe the use of commercial triblock copolymers such as SBS and SEBS as compatibilizers to achieve a finer morphology and improved performance [8–10].

Recently, organoclays have been suggested as compatibilizers for polymer blends [11–47]. Addition of organoclay to polymer blends has been shown to have dramatic effects on blend morphology, typically a much finer dispersion is found; however, there remain many unanswered questions including how useful this strategy can be for improving mechanical properties. A well dispersed organoclay in the continuous phase clearly leads to an increase in viscosity which can affect morphology; in addition, there is evidence that the clay platelets can act as a barrier toward coalescence of the dispersed phase polymer particles thereby reducing their size [17,19,27,29,35]. A change in the viscosity ratio between the continuous and dispersed phases can significantly influence the deformability and breakup of droplets and could affect phase continuity [28,35]. The presence of organoclay in the dispersed phase has also been reported to increase dispersed domain size thereby promoting "co-continuity" in HDPE/PA6 system [37,38]. On the contrary, Zhu et al. proposed that organoclay platelets acts like a "knife" thereby reducing dispersed PS domain size due to shear stress generated during mixing [39]. Wang et al. proposed that the decreased domain size of PS in PP/PS blends caused by addition of organoclay results from the two immiscible polymer chains existing together between intercalated clay platelets causing them to locate at the interface like a block graft copolymer [42]. There has been recent discussion concerning the

* Corresponding author. Tel.: +1 512 471 5392; fax: +1 512 471 0542.
E-mail address: drp@che.utexas.edu (D.R. Paul).

0032-3861/$ – see front matter © 2011 Elsevier Ltd. All rights reserved.
doi:10.1016/j.polymer.2011.01.019

relative roles of the barrier to coalescence mechanism versus the viscosity effect on the decrease in dispersed phase particle size caused by organoclay [43]. The state of the literature in this area points to the need for systematic studies to better understand the effect of the organoclay on the morphology and mechanical properties of polymer blends.

This paper explores blends of PP and PS with and without an organoclay (plus a maleated polypropylene, PP-g-MA, to promote dispersion of the organoclay in the PP phase) where the melt viscosity of the PP has been varied by use of different molecular weight grades. This blend system was chosen because of some recent commercial interest in these materials for automobile applications. A partnership between Putsch Kunststoffe GmBH and Süd-chemie AG has described PP/PS with PS morphology modified with organoclay and advertised these blends for automotive application. However, it is necessary to understand the possibilities and limitations to this approach and provide the scientific base for determining when this concept can be reliably utilized. Recently our laboratory has reported the effect of PP-g-MA/organoclay ratio on the extent of organoclay dispersion, thermal expansion behavior and mechanical properties of PP nanocomposites. [48] This work showed that a ratio of PP-g-MA/organoclay = 1 gave optimum improvement in performance of PP nanocomposites; thus, the same ratio is used in the present study. The effects of PP viscosity and the presence of organoclay on the morphology stabilization of dispersed phase particle size, phase inversion behavior and the co-continuity region were explored and supported by various characterization techniques. An issue of paramount importance is where the organoclay particles locate in such blends. To add some fundamental understanding of this issue, surface energy models for particles in polymer blends are reviewed and extended to particles with plate-like structure. The effects of organoclay on tensile and impact properties of the blend are also reported.

2. Background and theory of emulsion stabilization by solid fillers

The role of colloidal particles in stabilization of low viscosity emulsions was considered more than a century ago by Ramsden [49] and Pickering [50]. The presence of colloidal particles around droplets acts as a barrier against coalescence forming particle stabilized emulsions; these are called “Pickering emulsions” due to the original work by Pickering [50]. There has been a renewed interest in the stabilization of emulsions by solid particles in the last decade [51–59]. Tambe and Sharma [51] observed an increase in stability of decane-water emulsions with $CaCO_3$ content. Similar effects of nano-silica, laponite and smectites on the stabilization of liquid emulsions has been extensively described [52–59]. Aveyard et al. [54] reported that addition of 6 wt% of silica particles leads to an 8 fold decrease in particle size for a polydimethylsiloxane PDMS/water mixture. The advantage of using relatively high concentrations of silica particles is that the excess silica causes gelation of the continuous phase thereby, retarding or completely preventing creaming of oil drops or sedimentation of water drops which lead to long self-life of the product. Several mechanisms have been suggested for particle stabilized emulsions including (a) steric stabilization of droplets by particles and particle bridging between the droplets, (b) surface rheological effects and (c) flocculation in the bulk.

It is natural then to ask whether solid fillers also provide stabilization in immiscible polymer blends. The use of compatibilizers to improve morphology and interfacial adhesion in immiscible blends has been widely used for various reasons discussed previously. Recently, several authors have shown the effect of particle stabilization in immiscible polymer blends. Vermant et al. [60] observed that fumed silica suppresses coalescence in a polydimethylsiloxane (PDMS)/polyisobutylene (PIB) (70/30) blend. These authors found that the effect of shear rate on storage modulus became insignificant with increased particle concentration in the blend. The mixing protocol did not appear to affect the rheology or morphology of the blend. In contrast to results by Vermant et al. [60], Thareja and Velankar [61] later studied the same system and found gel-like behavior at low viscosities as particle concentration increased and differences in storage modulus with blending sequence. The differences in these two studies were due to the different rheological characteristics of the materials and the rheological measurements [62]. Elias et al. [63] studied the effect of nano-silica polarity on dispersion of PS in immiscible PP/PS blends and concluded that hydrophilic silica in the PS dispersed phase stabilizes morphology due to reduction in interfacial tension whereas hydrophobic silica in PP matrix, stabilizes the morphology by reducing coalescence of dispersed PS particles. A common theme has been to interpret rheological data in terms of the Palierne model to infer information about the nature of the interface including the interfacial energy.

Various surface energy analyses have been used to aid the understanding of the morphology of multiphase polymer blend systems [64–69]. Hobbs et al. [64] first suggested the use of spreading coefficients λ_{ij}, defined in terms of interfacial tensions, γ_{mn}, via a form of Harkins' equation;

$$\lambda_{31} = \gamma_{12} - \gamma_{32} - \gamma_{13} \tag{1}$$

to predict the morphology of ternary blends. Here 1 and 3 are two dissimilar phases dispersed in matrix 2. In the above equation if $\lambda_{31} > 0$, component 3 will encapsulate component 1 and eliminate its contact with component 2. If λ_{31} and λ_{13} are negative, 1 and 3 will tend to disperse separately in phase 2. Cheng et al. [66] used an analogous interfacial energy analysis to predict where small spherical polymer particles would locate in an immiscible blend of polymer 1 and 2. Such surface free energy analyses agree well with experiments in some cases; however, kinetic effects during processing can also be a factor. In the following, we compare the predictions of such analyses for the cases of spherical or low aspect ratio particles, with that of circular high aspect ratio platelets since this gives some insights about how organoclays may affect blend morphology.

2.1. Case of spherical particles

We consider a spherical filler particle p interrupted at the interface 1–2 created by phase 1 and 2 as shown in Fig. 1. The surface free energy of this system is given by:

$$G = A_{1p}\gamma_{1p} + A_{2p}\gamma_{2p} - A_{12}\gamma_{12} \tag{2}$$

where A_{1p}, A_{2p} are the surface areas of particle p in contact with phases 1 and 2, respectively and A_{12} is the loss in contact area of 1–2 due to particle p; the mathematical relationships for these cases are well known from geometry [66]. The corresponding interfacial surface energies are designated by γ_{1p}, γ_{2p} and γ_{12}. Fig. 1 shows the plots of the surface free energy, G, as a function of the location of the particle along the x-axis. The particle p will reside completely in either phase 1 or 2 when $\gamma_{12} \leq |\gamma_{1p} - \gamma_{2p}|$ provided surface energy effects are dominant. However, for the situation where $\gamma_{1p} > \gamma_{2p}$ and $\gamma_{12} > \gamma_{1p} - \gamma_{2p}$, a minimum occurs in the plot of G versus x at

$$\frac{x}{R} = \frac{\gamma_{1p} - \gamma_{2p}}{\gamma_{12}} \tag{3}$$

Thus, the equilibrium location of the particle in this case is to be trapped at the interface rather than locating in polymer 2. Such

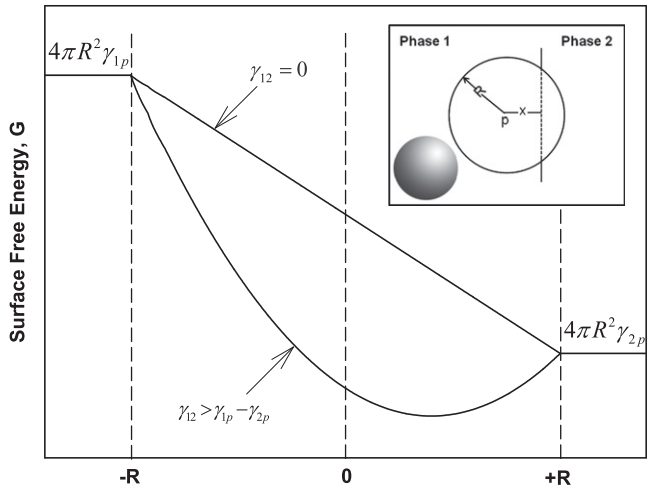

Fig. 1. Surface free energy for a spherical filler versus location relative to the interface for the case where $\gamma_{1P} > \gamma_{2P}$.

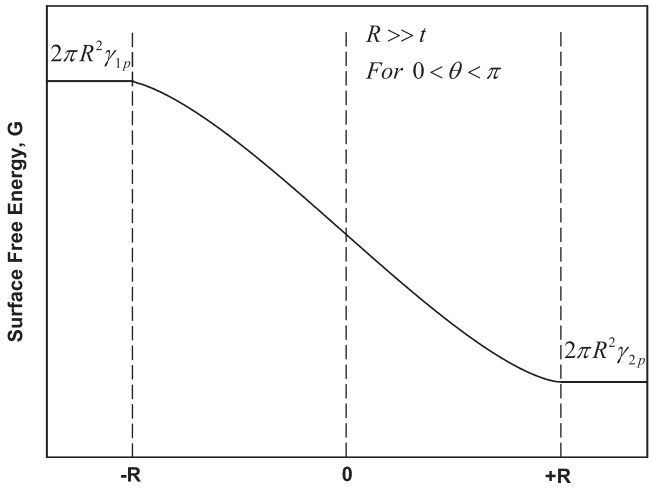

Fig. 3. Surface free energy for a clay platelet versus location relative to the interface for the special case where $\gamma_{1P} > \gamma_{2P}$ when $\theta \neq 0$ or π.

situations arise when having the particle *p* in contact with 1 and 2 is more favorable than having 1 and 2 in contact with each other. Such cases have been observed [65,66], but kinetic contributions during processing may preclude achieving this equilibrium state [65].

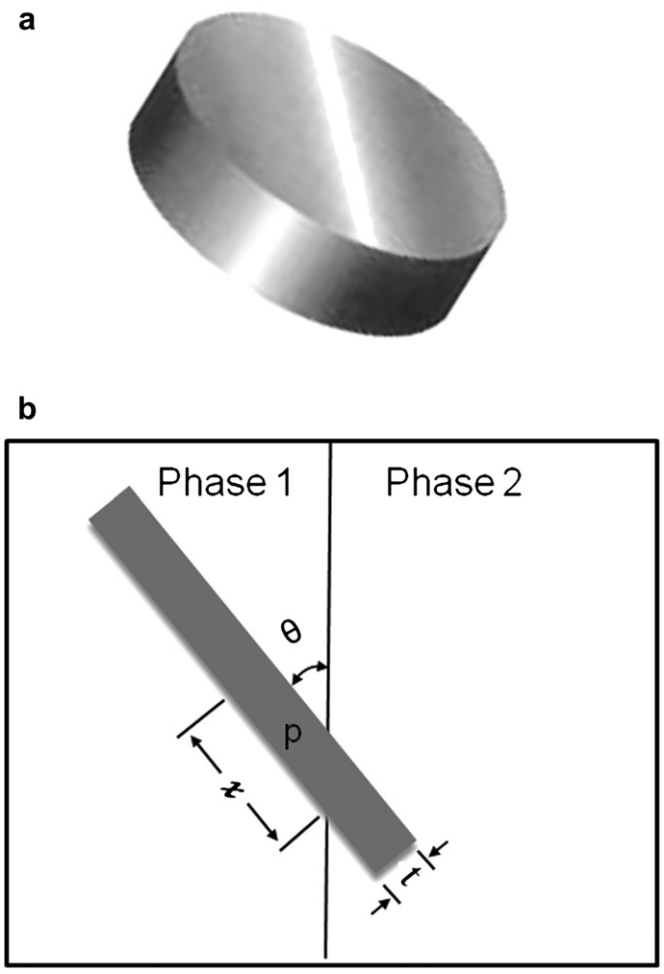

Fig. 2. Schematic of the clay particle (a) single clay platelet; (b) clay platelet oriented at the interface.

2.2. Case of circular platelets

We might think of clay particles as circular platelets or a disk as suggested in Fig. 2(a). This case differs from that of a sphere in at least two important ways, i.e. there is an angular orientation relative to the interface and the relative areas of the edge of the disk compared to its faces or the aspect ratio. For simplicity, we assume here that the surface energies for the edge and faces of the disk are the same. Fig. 2(b) shows a disk of radius *R* and thickness *t* located at an angle $0 < \theta < \pi$ relative to the interface with the center of the disk at a distance *x* from the interface. From known geometrical relationships for the partial areas of a disk [70], the surface free energy $G = f(x,\theta)$ for $0 < \theta < \pi$ of equation (2) takes the form:

$$G/A = \left(A_{1top} + A_{1bottom} + 2Rt\cos^{-1}\left(\frac{x}{R}\right)\right)\gamma_{1p} + \left(A_{2top} + A_{2bottom} + 2\pi Rt - 2Rt\cos^{-1}\left(\frac{x}{R}\right)\right)\gamma_{2p} - \left(2\sqrt{R^2-x^2}t\right)\gamma_{12} \quad (4)$$

where A_{1top} and $A_{1bottom}$ are the surface areas of the top and bottom parts of the disc in contact with polymer 1. It is interesting to consider the case of disk with very high aspect ratios, i.e. $R >> t$ This leads to considerable simplification of equation (4), i.e.,

$$G = \left(\pi R^2 - 2\left(x\sqrt{R^2-x^2} + R^2\sin^{-1}\left(\frac{x}{R}\right)\right) + 2Rt\cos^{-1}\left(\frac{x}{R}\right)\right)\gamma_{1p} + \left(\pi R^2 + 2\left(x\sqrt{R^2-x^2} + R^2\sin^{-1}\left(\frac{x}{R}\right)\right) + 2\pi Rt - 2Rt\cos^{-1}\left(\frac{x}{R}\right)\right)\gamma_{2p} - \left(2\sqrt{R^2-x^2}t\right)\gamma_{12} \quad (5)$$

For $R >> t$, *G* is independent of θ so long as θ is not identical to 0 or π Fig. 3 shows a plot of *G* versus *x* for the situation where $\gamma_{1p} > \gamma_{2p}$

Table 1
Details of the materials used in this study.

Grade	Supplier	MFI g/10 min at 230 °C and 2.16 kg	Designation[a]
Pro-fax PH020	LyondellBasell	37.0	L-PP
Pro-fax 6301	LyondellBasell	12.0	M-PP
Pro-fax 6523	LyondellBasell	4.0	H-PP
Styron 685D	Dow	1.5	PS
Polybond 3200	Chemtura	115	PP-g-MA

[a] The L-PP, M-PP and H-PP designate the low, medium and high molecular weight PP grade, respectively.

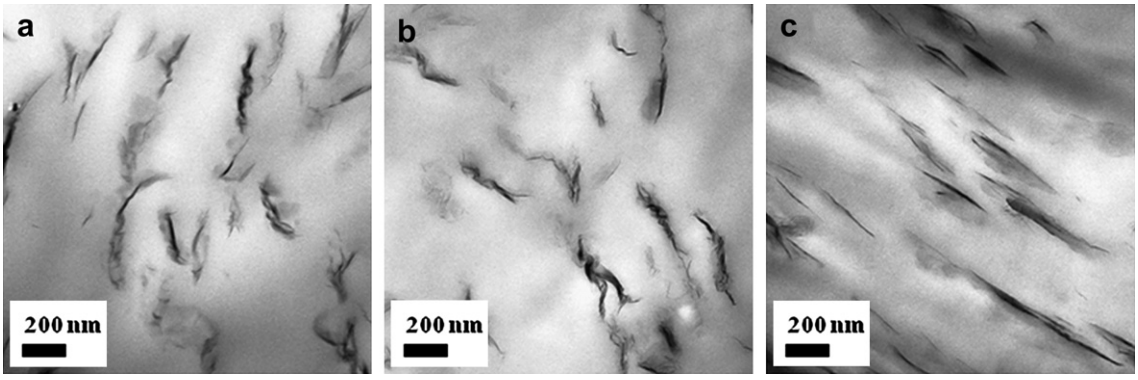

Fig. 4. TEM images of PP/PP-g-MA/MMT nanocomposites prepared from various PP grades: (a) L-PP; (b) M-PP and (c) H-PP. The MMT content is 3 wt% in all nanocomposites. Images were taken from the core and viewed perpendicular to the flow direction (FD).

and the terms in equation (5) involving t are negligible. Interestingly, G goes monotonically between the two limits of the disk being entirely in phase 1 or phase 2. This means that if the disk enters the interface from phase 1, there will be a force $\partial G/\partial x$ that moves it right through the interface into phase 2. Thus, unlike the sphere (see Fig. 1) there is no possibility of a free energy minimum that would trap the disk in the interface. This is so because there is no finite 1–2 contact that is interrupted by the disk in the limit that $R>>t$ The same would be true for a rod, like a high aspect ratio carbon nanotube.

However, the situation is very different when the disk approaches the interface with $\theta = 0$ or π. For this case, equation (2) becomes

$$G = \pi R^2\left[\gamma_{1p} + \gamma_{2p} - \gamma_{12}\right] \tag{6}$$

When $\gamma_{12} > \gamma_{1p} + \gamma_{2p}$, the surface free energy is negative indicating that the equilibrium position of a disk with $R>>t$ is to be trapped at the interface. It is likely that many disks entering the interface would rotate into this orientation and become trapped at the interface. For disks with finite aspect ratios, it turns out that a minimum in G and even $G<0$ become possible for disk orientations other than $\theta = 0$ or π. These minima become possible because of a finite extent of interruption of the 1–2 contact.

3. Experimental

3.1. Materials

Three different commercial grades of polypropylene PP having low, medium and high molecular weight were supplied by LyondellBasell and a commercial grade polystyrene PS was obtained from Dow Chemical. The commercial organoclay Cloisite®20A having dimethyl bis(hydrogenated tallow) quaternary ammonium as the organic modifier was supplied by Southern Clay Products, Gonzales, TX. The organic loading is 95 mequiv/100 g of clay and weight% of organic content determined from loss on ignition test (LOI) is 39.6 wt %. The polypropylene-grafted maleic anhydride (PP-g-MA, MA content = 1.0 wt%) was supplied by Chemtura Corporation. Further details about these materials and designations are provided in Table 1.

3.2. Blend preparation

All materials were dried in a vacuum oven at 80 °C for 12 h prior to extrusion. All blends with and without MMT were prepared using a Haake co-rotating twin screw extruder (diameter = 30.5 mm, L/D = 10). The barrel and die temperatures were set at 210 °C and 215 °C respectively. The melt mixing was carried out at a screw speed of 280 rpm and feed rate of 1 kg/h. The melt extrudate was passed through a cold water bath and pelletized into uniform pellet size.

Blends without MMT contain PP/PP-g-MA/PS while blends with MMT contain PP/PP-g-MA/MMT/PS. The PS composition was varied from 0–100 wt% in the blends with and without MMT. All blends with MMT have 3 wt% MMT based on the PP/PP-g-MA/MMT phase unless mentioned separately. The PP-g-MA to organoclay ratio of 1.0 was fixed in all blends with MMT. When no MMT was present, the polypropylene phase included the same amount of PP-g-MA as when MMT was present so that appropriate comparison of properties could be made. Initially, a single and a two step mixing methods were used to prepare blends with and without MMT, at a fixed PS composition of 30 wt% to explore the effect of mixing protocols on blend properties. In the single step method, all materials were fed simultaneously to the extruder at a feed rate of 1 kg/h. In the two step method either PP/PP-g-MA/MMT or PP/PP-g-MA were first prepared using processing conditions reported elsewhere [48,71] and then further extruded with PS to prepare blends with and without MMT, respectively.

The blends without MMT did not show any difference in morphology and mechanical properties irrespective of mixing protocols; hence, the single step method was used to prepare these blends for all PS compositions. However, for blends containing MMT, the two step method showed higher mechanical properties and better control of dispersed PS particle size compared to those obtained from the single step method. Hence, the two step method was used to prepare blends with MMT for all PS compositions.

Extruded blend samples (with and without MMT) were dried at 80 °C for 8 h in a vacuum oven and then injection molded into standard tensile bars (ASTM D638, Type I) and Izod bars (ASTM D256) in an Arburg Allrounder 305-210-700 injection molding

Table 2
MMT particle analysis results for PP/PP-g-MA/MMT nanocomposites at a fixed MMT content of 3 wt% and PP-g-MA/organoclay ratio of 1.0. (viewed perpendicular to FD).

Matrix	Total Number of particles	Number average particle length $\bar{l}_n$ (nm)	Weight average particle length $\bar{l}_w$ (nm)	Number average particle thickness $\bar{t}_n$ (nm)	Weight average particle thickness $\bar{t}_w$ (nm)	Aspect ratio $\bar{l}_n/\bar{t}_n$	Aspect ratio $\bar{l}_w/\bar{t}_w$	Number average aspect ratio $< l/t >_n$	Weight average aspect ratio $< l/t >_w$
L-PP	211	185	255	7	12	26	21	30	62
M-PP	244	197	289	6	12	33	24	32	75
H-PP	221	218	301	6	10	36	30	48	88

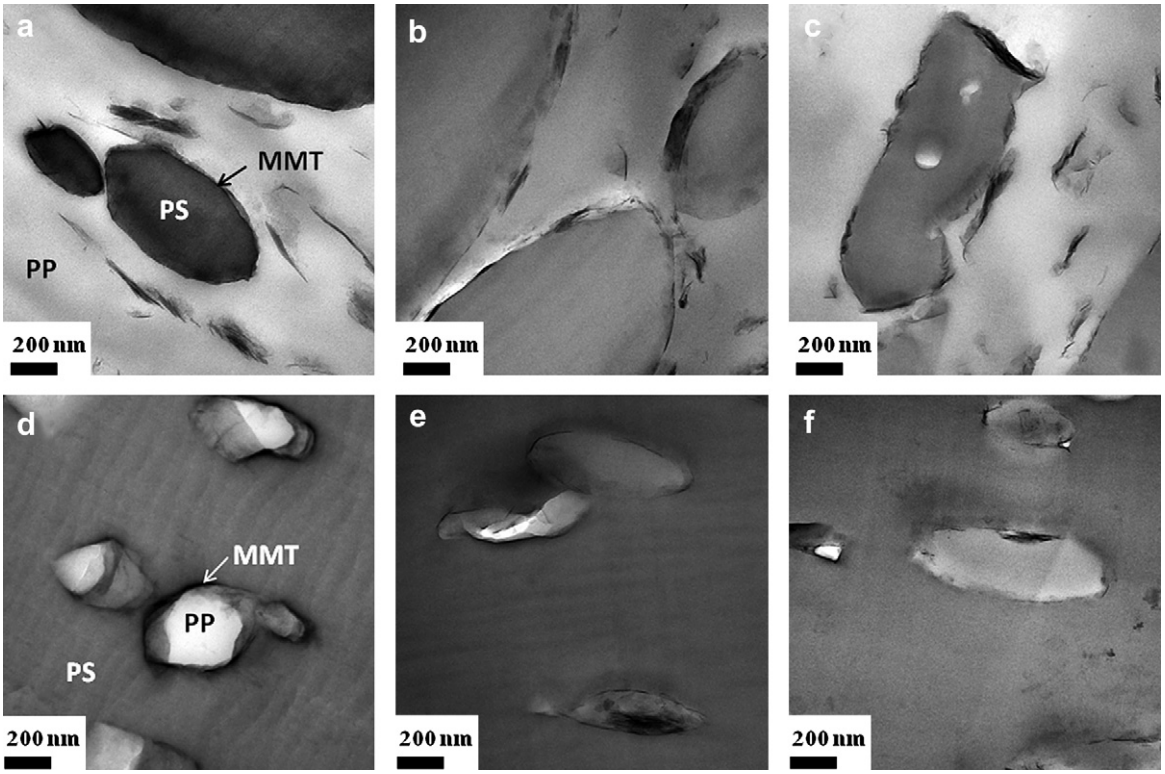

Fig. 5. TEM micrographs showing location of the MMT particles in PP/PP-g-MA/MMT/PS blend having 30 wt% PS (top row) and 90 wt% PS (bottom row). The blends were prepared with different PP grades: L-PP (a and d); M-PP (b and e) and H-PP (c and f). Images were taken from the core and viewed perpendicular to the flow direction (FD).

machine using a barrel temperature of 220 °C (feed) to 230 °C (die) and a mold temperature of 40 °C. The injection pressure was varied from 35 to 55 bar based on the PS composition in the blend, the holding pressure was maintained at 35 bar.

3.3. Characterization

Ultra-thin sections ~50–60 nm were cut cryogenically from the central core region of an Izod bar using an RMC PowerTome XL ultramicrotome. The sections were cut perpendicular to the flow direction (FD), i.e., in the FD-ND plane; at ~3 cm away from the far end of an Izod bar. The knife and sample temperatures were adjusted based on the PS composition to get uniform thin sections. Sections were collected on 300 mesh copper grids and subsequently dried on filter paper. The PS phase in the blend was preferentially vapor stained by 2 wt% solution of osmium tetroxide for 8 h at room temperature in a closed glass chamber. Low and high magnification TEM images were obtained using a JEOL 2010F field emission TEM operating at an accelerating voltage of 120 kV.

The phase morphology of the blends with and without MMT was also observed using a Leo 1530 SEM at an accelerating voltage of 10 kV. Samples for SEM were also taken from the core of injection molded bars and cut perpendicular to the flow direction (FD) at ~3 cm away from the far end of an Izod bar. The sample was cryo-polished using a glass knife to obtain a smooth surface. The PS phase was preferentially extracted using toluene at 40 °C for 8 h.

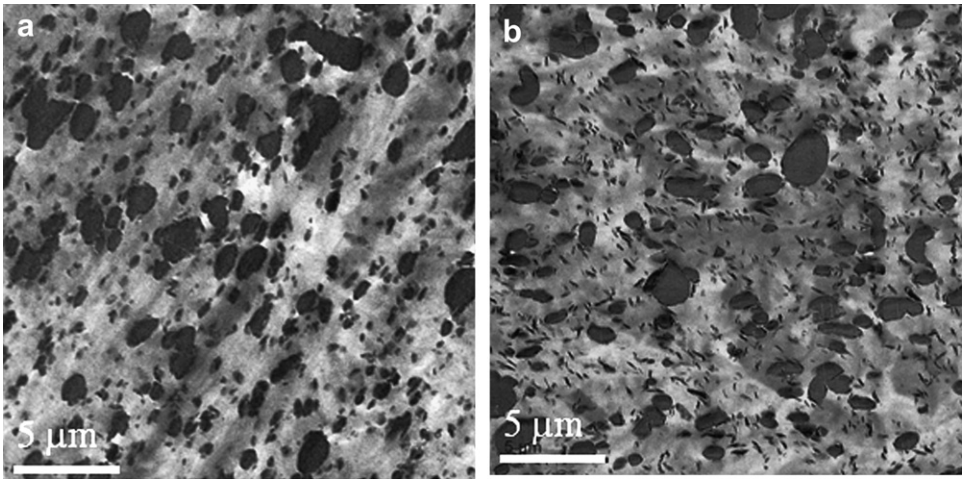

Fig. 6. TEM images of extruded (a) H-PP/PP-g-MA/PS and (b) H-PP/PP-g-MA/MMT/PS blend at 30 wt% PS. Images were taken from the core and viewed perpendicular to the flow direction (FD).

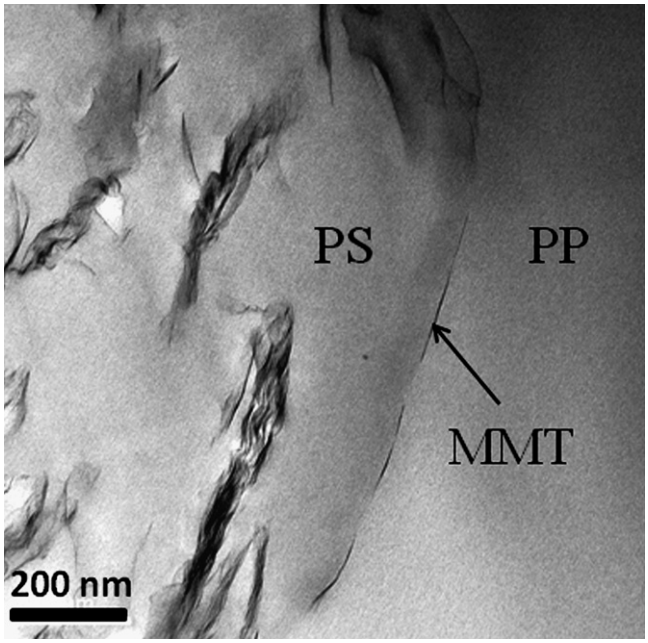

Fig. 7. TEM image of L-PP/PS/MMT blend having 30 wt% PS in blend. Images were taken from the core and viewed perpendicular to the flow direction (FD).

The etched samples were further vacuum dried at room temperature for ~8 h to remove any traces of solvent prior to silver or gold-palladium (50:50) coating. Samples were imaged perpendicular to the flow direction similar to TEM. A semi-automatic digital image analysis software Image J (NIH Image software v1.43°) was used to determine the area of the extracted PS phase. The apparent particle diameter was then evaluated from the area as follows

$$d = \left(\frac{4A}{\pi}\right)^{1/2} \tag{7}$$

The effective number average, $\overline{d}_n$, and weight average, $\overline{d}_w$; particle diameters were then calculated from the statistical data obtained from image analysis based on TEM or SEM photomicrographs.

The rheological parameters for PP/PP-g-MA, PP/PP-g-MA/MMT and PS were determined on a TA AR2000*ex* rheometer using 25 mm EHP parallel plate geometry and a sample gap of 1 mm. Samples with a diameter of 25 mm and a thickness of ~1.5 mm were compression molded at 200 °C for 5 min. All rheological measurements were

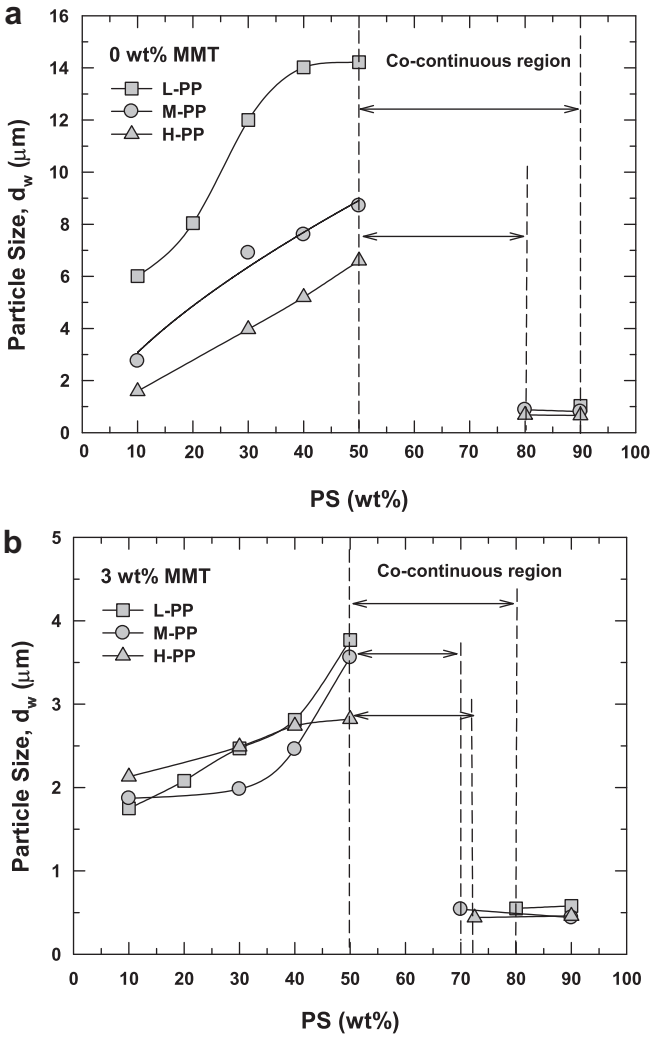

Fig. 8. Effect of PS content and PP melt viscosity on the dispersed phase particle size for (a) blends without MMT and (b) blends with MMT. PS is the dispersed phase when the PS content is below 50 wt% while the matrix is PP/PP-g-MA or PP/PP-g-MA/MMT. The wt% MMT is based on the MMT content in PP/PP-g-MA/MMT. The dashed line represents the co-continuous region as observed from TEM images for blends prepared with various grades of PP.

Table 3
Quantitative particle analysis results for dispersed phase particle size in blends prepared with and without MMT using different grades of PP. The particle size has units of μm.

PS (wt%)	Blend without MMT[a]						Blend with MMT[b]					
	L-PP		M-PP		H-PP		L-PP		M-PP		H-PP	
	$\overline{d}_n$	$\overline{d}_w$	$\overline{d}_n$	$\overline{d}_w$	$\overline{d}_n$	$\overline{d}_w$	$\overline{d}_n$	$\overline{d}_w$	$\overline{d}_n$	$\overline{d}_w$	$\overline{d}_n$	$\overline{d}_w$
10	4.21	6.01	1.87	2.75	1.22	1.59	1.48	1.75	1.08	1.87	1.67	2.13
20	6.25	8.04	–[c]	–	–	–	1.62	2.08	–	–	–	–
30	7.7	12.00	3.35	6.90	2.32	3.82	1.77	2.47	1.56	1.98	1.63	2.49
40	9.04	14.02	3.58	7.60	2.25	5.20	2.1	2.81	2.08	2.46	2.14	2.74
50	9.83	14.22	4.21	8.71	2.84	6.60	3.02	3.77	2.49	3.56	2.45	2.82
60	Co-continuous region[d]						Co-continuous region[d]					
70									0.37	0.54		
72.5									–	–	0.32	0.44
80			–	–	–	–	0.44	0.55	–	–	–	–
90	0.68	1.03	0.48	0.81	0.41	0.66	0.43	0.58	0.34	0.44	0.37	0.46

[a] The dispersed phase for blends without MMT is PS (above co-continuous region) and PP/PP-g-MA (below co-continuous region) based on the PP grade.
[b] The dispersed phase for blends with MMT is PS (above co-continuous region) and PP/PP-g-MA/MMT (below co-continuous region) based on PP grade. The MMT content is 3 wt% based on PP/PP-g-MA/MMT and the PP-g-MA/organoclay ratio is 1.0.
[c] The dash indicates that these blends were not prepared.
[d] The shaded region represents the co-continuous morphology observed for blends prepared with and without MMT.

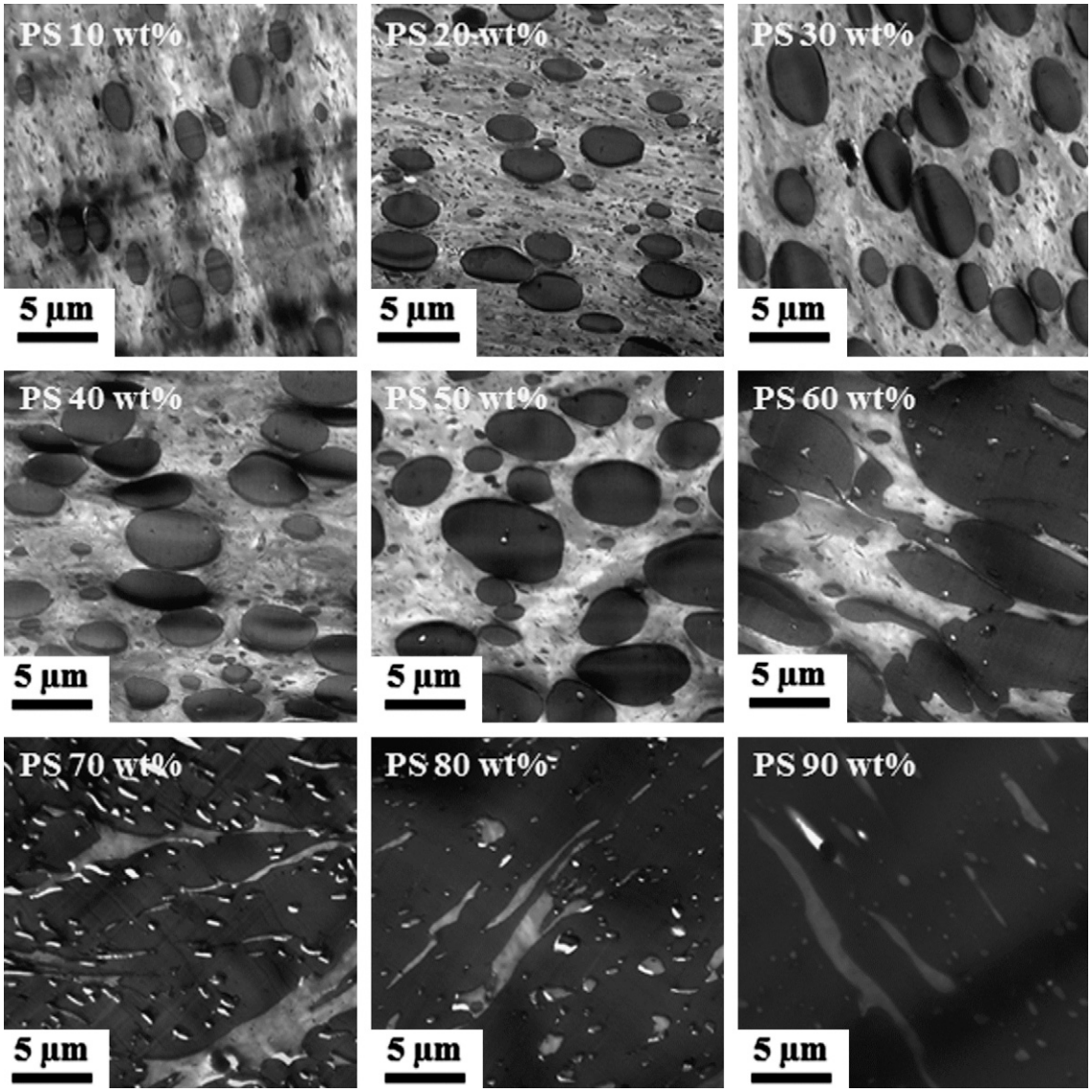

Fig. 9. Low magnification TEM images showing various morphologies of L-PP/PP-g-MA/MMT/PS blends as a function of increasing PS content. The blend shows co-continuity at 60 wt% PS and phase inversion occurs at 80 wt% PS.

carried out at a fixed temperature of 205 °C under UHP dry nitrogen at flow rate of 4 l/min. Strain sweep tests were carried out for each sample to ensure the strain used was within the linear viscoelastic range. Frequency sweep tests were then performed from 0.04 to 300 rad/s.

4. Results and discussion

4.1. TEM analysis of MMT particles in PP/PP-g-MA/MMT nanocomposites

As discussed in the experimental section, PP/PP-g-MA/MMT nanocomposites were prepared from various grades of PP prior to blending with PS. TEM was performed on PP/PP-g-MA/MMT nanocomposites to determine the extent of MMT dispersion in the PP matrix. All views were taken perpendicular to the flow direction (FD), i.e., in the FD-ND plane. Fig. 4 shows representative TEM images for PP/PP-g-MA/MMT nanocomposites prepared from the three different PP materials. The TEM micrograph for L-PP/PP-g-MA/MMT shows randomly distributed intercalated MMT particles along with a few skewed and bent stacks. The low shear stress exerted by L-PP on the MMT particles results in the formation of skewed stacks which is also observed for M-PP/PP-g-MA/MMT nanocomposites. In H-PP/PP-g-MA/MMT nanocomposite, the MMT particles exhibits a mixed morphology of intercalated tactoids as well as more exfoliated particles. The MMT particles in the H-PP nanocomposite are longer than those in the L-PP or M-PP nanocomposites. The increased shear stress resulting from the high matrix viscosity facilitates the dispersion and orientation of the MMT particles in the H-PP/PP-g-MA/MMT system.

To quantify the dispersion of MMT particles in the PP matrix, particle analyses were performed on at least 200–300 MMT particles with the results summarized in Table 2. The MMT particle length increases while the thickness decreases with increasing PP viscosity for reasons mentioned above. The various aspect ratios computed from the MMT particle analyses for PP nanocomposites $\bar{l}_n/\bar{t}_n$, $\bar{l}_w/\bar{t}_w$ and $< l/t >_w$ show a gradual increase with the increase in PP viscosity; however, $< l/t >_n$ shows a more dramatic increase for the H-PP/PP-g-MA/MMT nanocomposite. The average aspect ratios $< l/t >_n$ and $< l/t >_w$ are higher than those calculated from

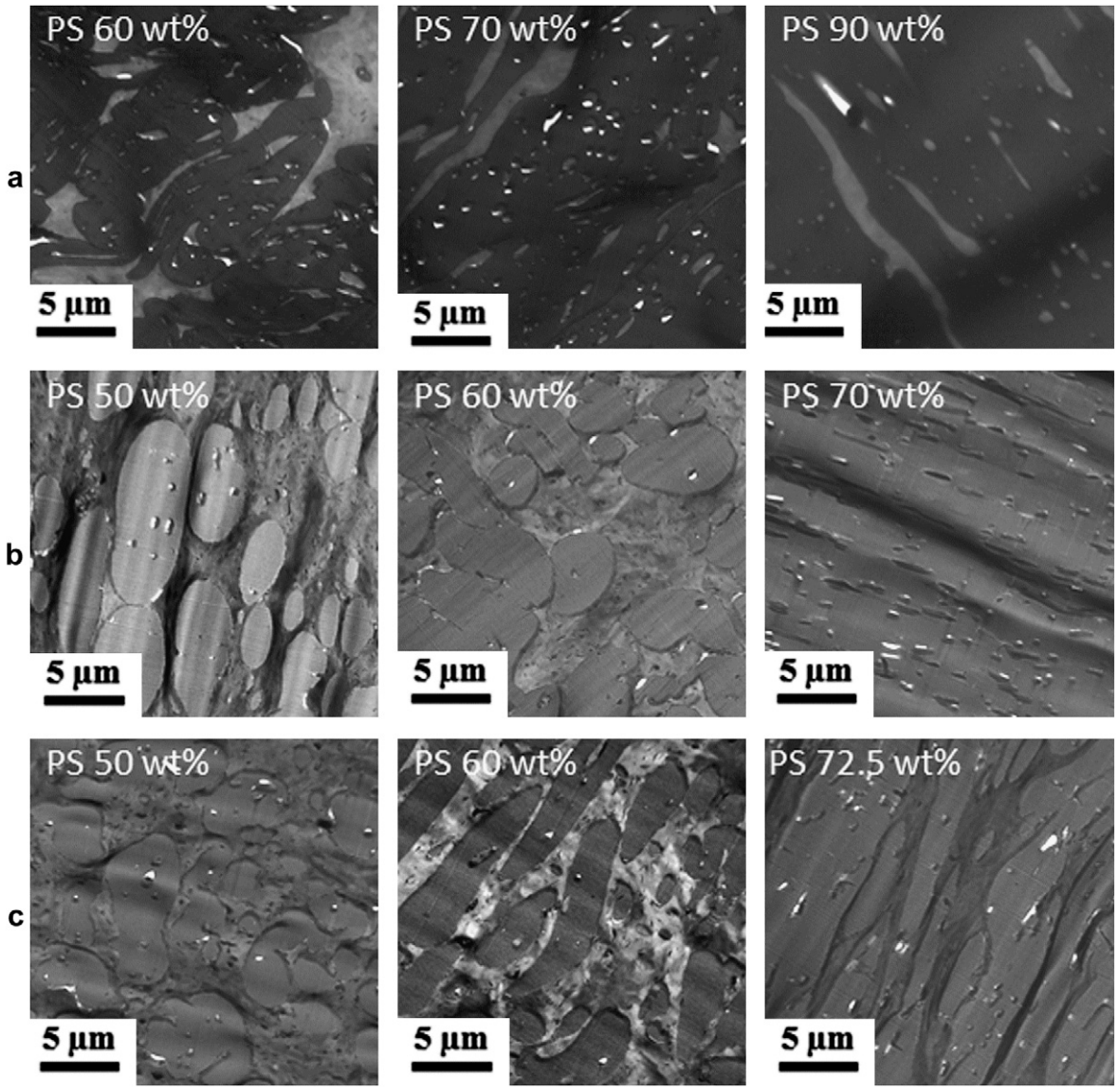

Fig. 10. Low magnification TEM images showing co-continuous and phase inversion behavior for blends with MMT prepared from PP materials with different melt viscosities: (a) L-PP/PP-g-MA/MMT/PS; (b) M-PP/PP-g-MA/MMT/PS and (c) H-PP/PP-g-MA/MMT/PS. All views were taken perpendicular to the flow direction (FD).

the ratio of the corresponding average values of length and thickness, $\bar{l}_n/\bar{t}_n$ and $\bar{l}_w/\bar{t}_w$, respectively. Also, the ratio of number average particle length and thickness, $\bar{l}_n/\bar{t}_n$, is larger than the ratio of weight average particle length and thickness, $\bar{l}_w/\bar{t}_w$, while the weight average aspect ratio obtained by averaging values of each particle, $< l/t >_w$, is always larger than the corresponding number average ratio, $< l/t >_n$ for all PP nanocomposites. Similar trends have been observed previously [48].

4.2. Location of MMT particles in blends

Fig. 5 shows high magnification TEM images for blends with MMT, prepared from three different PP materials at two different PS compositions, where PS forms either the dispersed or continuous phase. Fig. 5(a)–(c) shows dispersed PS particles in the different PP matrices for 30 wt% PS. The MMT particles are located in the PP matrix as well at the PP/PS interface thereby acting as compatibilizers. The fraction of MMT particles located around the PS particles appears to decrease as the PP viscosity increases. The PS particles are elongated in the H-PP/PP-g-MA/MMT/PS blend due to the high shear stress exerted by the H-PP on the dispersed phase during injection molding. This has also been observed for H-PP/PP-g-MA/PS blends at 30 wt% PS composition. Fig. 5(d)–(f) shows dispersed PP/PP-g-MA/MMT particles in a PS matrix for blends containing 90 wt% PS. The PP particles are dispersed in the PS matrix and MMT particles are located in the PP phase as well at the interface.

To show that injection molding tends to elongate the PS particles in the H-PP based blends (with and without MMT) having 30 wt% PS, the morphology of extruded samples were also investigated for comparison. Fig. 6 shows TEM images for extruded blends, with and without MMT, viewed perpendicular to FD. The PS particles in extruded blends, with and without MMT tend to have a more globular shape as opposed to the elongated morphology seen for injection molded specimens. This confirms that the PS particle shape is due to processing effects in H-PP based blends with and without MMT.

The location of MMT particles at the interface is governed in part by the affinity between the polymers and the organoclay arising from interfacial energies. In PP/PS blends without PP-g-MA, all

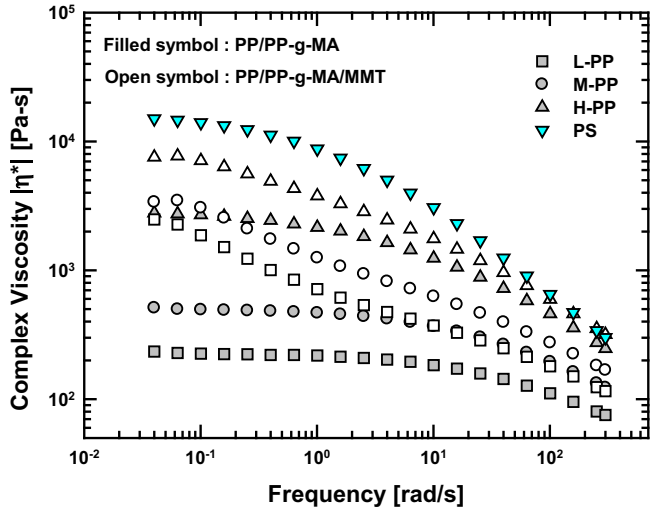

Fig. 11. Complex viscosities of PS, PP and PP nanocomposites prepared using different PP grades. Filled symbols represent PP/PP-g-MA, corresponding open symbols represent PP/PP-g-MA/MMT for same grade PP. The MMT content is fixed at 3 wt% in PP nanocomposites.

MMT particles reside in the PS phase or at the PP/PS interface (as seen in Fig. 7) since $\gamma_{PS-MMT} < \gamma_{PP-MMT}$ and γ_{PP-PS} is high. Addition of PP-g-MA to the PP matrix reduces interfacial energy such that $\gamma_{PP/PP-g-MA-MMT} < \gamma_{PP-MMT}$; however γ_{PP-PS} is still high owing to the strong immiscible behavior of PP and PS. In the absence of kinetic factors, the location of MMT particles can be predicted from the wetting parameter

$$\omega = \frac{\gamma_{PP/PP-g-MA-MMT} - \gamma_{PS-MMT}}{\gamma_{PP/PP-g-MA/PS}} \quad (8)$$

where γ represents interfacial tension between polymer–polymer and polymer-filler. The filler is expected to locate at the interface when ω is between -1 and 1. The unavailability of interfacial energy data for PP/PP-g-MA makes this reasoning qualitative; evaluation of these interfacial energies is beyond the scope of this work.

4.3. Effect of MMT on dispersed phase particle size

Quantitative particle size analyses were performed on blends with and without MMT to see the effect of PP viscosity, MMT content, and PP/PS ratio on the dispersed phase particle size. For best statistical validity, quantitative analyses were done on 200-1100 particles for various systems. Table 3 summarizes the number average, $\bar{d}_n$ and weight average, $\bar{d}_w$, diameters of the dispersed polymer phase for blends prepared with and without MMT. For blends prepared without MMT, the dispersed phase is PS (above co-continuous region) and PP/PP-g-MA (below co-continuous region). Similarly, for blends prepared with MMT, PS and PP/PP-g-MA/MMT forms the dispersed phase above and below the co-continuous region, respectively.

Fig. 8 shows weight average particle sizes for the dispersed polymer phase versus PS composition for blends with and without MMT. As seen from Fig. 8(a), at any fixed PS composition, the PS particle size decreases with increased PP viscosity in a range where PP forms the continuous phase. A higher PP viscosity increases the breakup of PS particles due to high shear stress and reduces the dispersed phase particle size. The final morphology in the blend reflects the competing effects of breakup and coalescence during blending. At higher PS composition where PP forms the dispersed phase, the PP viscosity has negligible effect on dispersed PP particle size.

Fig. 8(b) shows the dispersed phase particle size versus PS compositions in the blends with MMT. In nearly all cases, the presence of MMT leads to a lower particle size; an exception is for H-PP/PP-g-MA/MMT/PS at 10 wt% PS. The M-PP/PP-g-MA/MMT/PS shows lower PS particle size compare to all blends with MMT until 40 wt% PS. The effect of PP viscosity on PS particle size is more apparent at 50 wt% PS. At higher PS compositions, when PP/PP-g-MA/MMT forms the dispersed phase, the PP viscosity has no effect on the particle size similar to what is observed for blends without MMT.

Fig. 8 also shows the effect of PS composition on the dispersed phase particle size, location of the co-continuous region and the phase inversion composition for blends with and without MMT. The dispersed PS particle size increases with increased PS content in blends without MMT resulting from a higher rate of coalescence during mixing [72–74]. The rate of coalescence increases with the increase in PS content, resulting in the formation of co-continuous structure followed by phase inversion. For blends with MMT, the increase in PS particle size with PS content is much less than for blends without MMT; this seems to be due to reduced rate of coalescence caused by the presence of the MMT. Fig. 9 illustrates the morphology of L-PP/PP-g-MA/MMT/PS blend at different PS compositions with TEM images. The blend shows dispersed PS particles at lower PS compositions; co-continuity is observed at 60 wt% PS followed by phase inversion at 80 wt% PS.

All blends show the onset of co-continuity beyond 50 wt% PS, irrespective of PP viscosity and MMT. The L-PP/PP-g-MA/PS blend shows phase inversion at 90% PS, whereas for M-PP/PP-g-MA/PS and H-PP/PP-g-MA/PS blends, phase inversion occurs at 80 wt% PS.

Table 4
Viscosity of PP/PP-g-MA, PP/PP-g-MA/MMT and PS at a shear rate of 250 s^{-1}.

Polymer	Viscosity η (Pa s)[a]		η_d/η_c[c]	
	0 wt% MMT	3 wt% MMT	0 wt% MMT	3 wt% MMT
L-PP[b]	80.3	124	4.25	2.75
M-PP[b]	133	182	2.56	1.87
H-PP[b]	274	353	1.24	0.97
PS	341	–	–	–

[a] The melt viscosities were determined at shear rate of 250 s^{-1} assuming Cox-Merz rule to be valid.
[b] The various PP represents viscosities for PP/PP-g-MA (0 wt% MMT) and PP/PP-g-MA/MMT (3 wt% MMT).
[c] η_d is viscosity of dispersed phase PS; η_c is the viscosity of continuous phase PP/PP-g-MA (0 wt% MMT) and PP/PP-g-MA/MMT (3 wt% MMT). The viscosity ratio for two phase is assumed for blends where PS forms the dispersed phase.

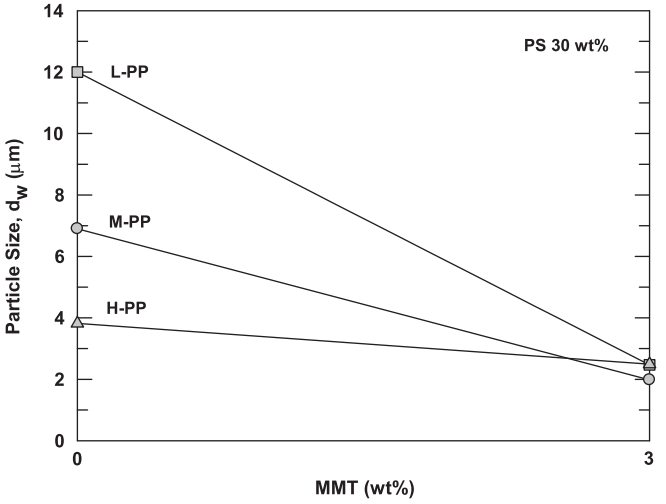

Fig. 12. Effect of MMT content on dispersed PS particle size in a blend prepared with various grades of PP. The PS content in the blend is 30 wt% and the MMT content is 3 wt% based on PP/PP-g-MA/MMT.

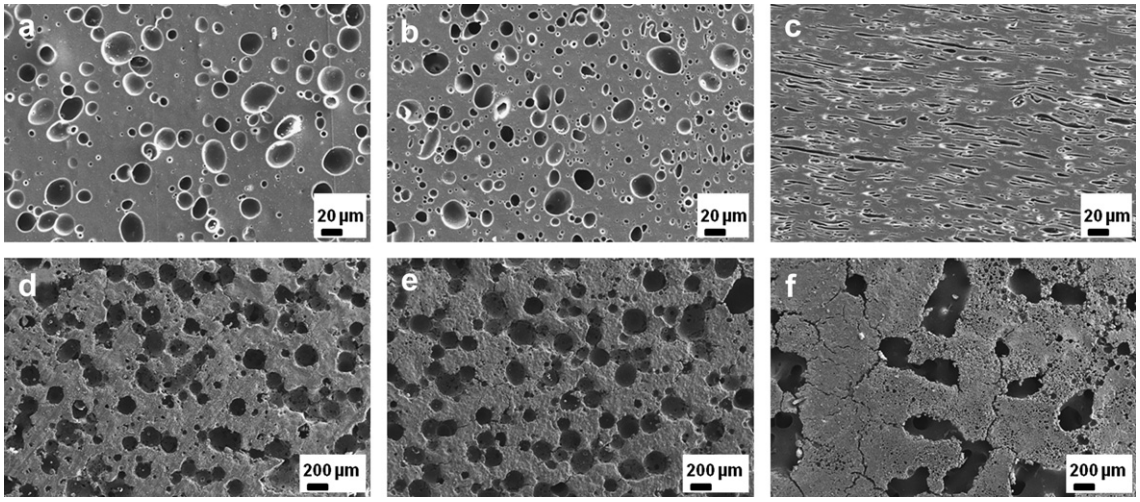

Fig. 13. SEM images of blends without MMT containing 30 wt% PS. Top row shows images for as-molded samples while the bottom row shows images for annealed samples at 210 °C for 2 h. The blends were prepared with different PP grades: L-PP (a and d); M-PP (b and e) and H-PP (c and f).

However, the PP viscosity has a clear effect on the phase inversion composition as does the presence of MMT. Fig. 10 shows TEM images representing the co-continuous regions and phase inversion compositions observed for blends with MMT prepared from the different grades of PP. The blends with MMT show phase inversion at lower PS content than blends without MMT. The phase inversion shifts toward lower PS compositions with increased PP viscosity. The L-PP/PP-g-MA/MMT/PS shows phase inversion at 80 wt% PS followed by phase inversion at 70 wt% and 72.5 wt% PS for M-PP/PP-g-MA/MMT/PS and H-PP/PP-g-MA/MMT/PS blends respectively. The possible explanation for decrease in phase inversion composition is due to increase in the PP viscosity in the presence of MMT; however, viscosity may not be the only factor in reducing the phase inversion composition. However, at this time it is difficult to predict the exact reason for the decrease in phase conversion composition.

4.4. Role of PP melt viscosity on dispersed phase particle size

Fig. 11 shows the complex melt viscosity results for PP/PP-g-MA, PP/PP-g-MA/MMT and PS. The viscosity for PP/PP-g-MA/MMT is higher than PP/PP-g-MA due to the presence of organoclay. The relative increase in viscosity of PP in the presence of organoclay is more pronounced for L-PP/PP-g-MA/MMT and M-PP/PP-g-MA/MMT than for the H-PP/PP-g-MA/MMT nanocomposite. The differences in viscosity are more discernible in the low frequency region. The high shear stress exerted by the extruder during melt mixing is best judged by the viscosity in the high frequency region. During extrusion, the molten polymer experiences a range of stresses with some being very high as it passes through the kneading and mixing zones. The average shear rate experienced by the melt depends on screw design and operating parameters [75], we estimate an average shear rate of $\sim$250 s^{-1} in the twin screw used here owing to its high shear elements. Table 4 shows the absolute viscosities for PP/PP-g-MA, PP/PP-g-MA/MMT and PS at a shear rate of 250 s^{-1} assuming validity of Cox-Merz rule; as it was not possible to carry out high steady shear experiments with the rheometer used.

To elucidate the effect of MMT content and PP viscosity on PS particle size, it is useful to compare blends prepared with the different PP at fixed PS content. Fig. 12 shows the effect of MMT content on PS particle size for blends containing 30 wt% PS. The addition of MMT reduces the PS particle size in all cases with the maximum decrease in PS particle size observed for blends based on L-PP. The PS particle size for blends containing MMT is nearly the same for all these PP materials; whereas without MMT, they are very different. The effect of PP viscosity on dispersed PS particle size is clearly seen for blends without MMT resulting in lower PS particle size with increasing PP viscosity. The effect of PP viscosity is not significant in the presence of MMT, with similar PS particle sizes observed for blends having different PP viscosities. This is also seen for blends prepared from matrices with similar viscosities, i.e., M-PP/PP-g-MA and L-PP/PP-g-MA/MMT where the PS particle size in the L-PP based blend with MMT is 2.47 μm compared to 6.9 μm observed for M-PP based blends without MMT at 30 wt% PS. Similarly, in H-PP based blend, although the ratio of two phases does not change with MMT, the PS particle size reduces from 3.82 μm to 2.49 μm in the presence of MMT. This suggests that although rheology is a factor in decreasing particle size of dispersed phase, MMT acts as a barrier to the coalescence of the dispersed particles thereby reducing PS particle size to a much greater extent than in blend without MMT for matrices having similar viscosities. However, the presence of MMT is much more beneficial in controlling dispersed phase particle size in blends where it leads to much higher increase in the matrix viscosity as seen for L-PP nanocomposite.

4.5. Stability of phase morphology in blends with and without MMT

Often blends are subjected to further processing steps to prepare molded parts or they may experience a number of temperature/shear histories. In uncompatibilized blends, some low shear processing steps can lead to the coalescence of the dispersed

Table 5
Number average $\bar{d}_n$ and weight average $\bar{d}_w$ PS particle size in blends with and without MMT. The PS composition in blend is 30 wt%. The particle size has unit of μm.

Matrix	MMT wt% in Matrix[a]	As-molded		After 2 h in melt at 210 °C	
		$\bar{d}_n$	$\bar{d}_w$	$\bar{d}_n$	$\bar{d}_w$
L-PP	0	7.7	12.0	24.5	60.5
	3	1.77	2.47	1.79	2.66
M-PP	0	3.35	6.9	27.5	72.3
	3	1.56	1.98	1.49	2.38
H-PP	0	2.32	3.82	22.0	44.5
	3	1.63	2.49	1.13	2.71

[a] The PP/PP-g-MA or PP/PP-g-MA/MMT was used as a matrix to prepare blends at 30 wt% PS. The MMT wt% is based on MMT content in PP/PP-g-MA/MMT. The PP-g-MA/organoclay ratio is 1.0.

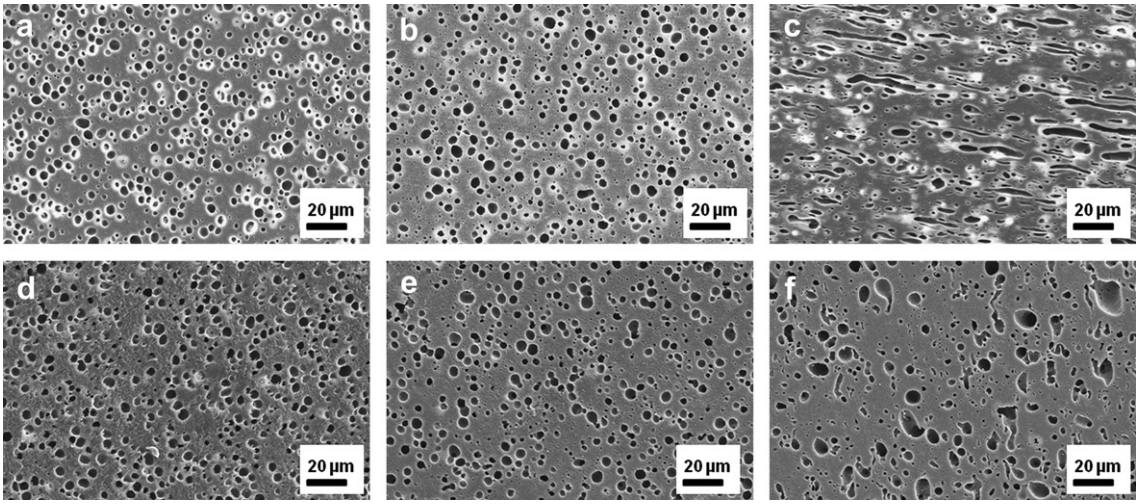

Fig. 14. SEM images of blends with MMT having 30 wt% PS. Top row shows images for as-molded samples while bottom row shows images for annealed samples at 210 °C for 2 h. The blends were prepared with different PP grades: L-PP (a and d); M-PP (b and e) and H-PP (c and f).

phase particles and reduce their performance. An increase in phase stability in the melt state extends the possibility of commercial applications for blends. Addition of an organoclay can significantly reduce the dispersed phase particle size as demonstrated above. To evaluate the effect of organoclay on the morphology stability, blends with and without MMT having 30 wt% PS were held at 210 °C for 2 h in a quiescent state. Fig. 13 compares the SEM images for blend samples before and after annealing in the melt. The number average $\bar{d}_n$ and weight average $\bar{d}_w$ PS particle diameter for as-molded and annealed blends with and without MMT are tabulated in Table 5. The PS particle size in the blend increased by factors of as much as an order of magnitude when no MMT is present. Interestingly, the change is greatest for H-PP/PP-g-MA/PS; the highly elongated PS particles in this blend undergo retraction followed by significant coalescence. However, for blends containing MMT (Fig. 14), the change in PS particle size after annealing is very slight for all these PP materials. The presence of MMT significantly improves the phase stability of the blends, especially for the H-PP blend where the PS particle size increased by ~10x on annealing in the absence of MMT. The location of the MMT in the blend appears to have an important role in stabilizing the phase morphology stability as shown by a few recent reports [17,47]. Khatua et al. [17] showed that the presence of MMT in a nylon 6/EPR (80/20) blend led to good phase stability in the melt; the MMT resides in the nylon 6 phase for this blend. These authors also reported poor phase stability in the melt for a PP/PS (70/30) blend where the MMT is in the dispersed PS phase and at the interface. Moghbelli et al. [47] observed a 30% increase in dispersed SAN particle size in nylon 6/SAN (80/20) nanocomposites after annealing at 260 °C for 10 min; the organoclay is located in the nylon 6 phase in this system. The presence of MMT at the interface and in the matrix has significant impact on the phase morphology stability as observed for the current PP/PP-g-MA/MMT/PS system. The presence of clay at the interface effectively acts as a compatibilizer; suppression of coalescence leading to smaller dispersed phase particles and morphology stability in the quiescent melt state.

4.6. Mechanical properties of blends with and without MMT

The mechanical properties of blends are important factors for performance in most applications. Fig. 15 shows the effect of PS composition on the tensile modulus for blends with and without MMT. The addition of PS to PP/PP-g-MA or PP/PP-g-MA/MMT substantially increases the modulus. The PP grade has little effect on blend modulus. The addition of MMT increases blend modulus

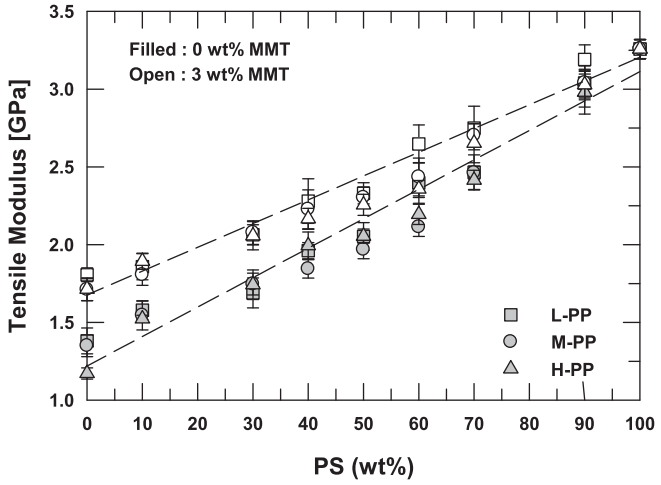

Fig. 15. Tensile modulus for blends without and with MMT at various PS compositions. The blends were prepared with different grades of PP. The symbols represents PP phase which is either PP/PP-g-MA (0 wt% MMT) or PP/PP-g-MA/MMT (3 wt% MMT).

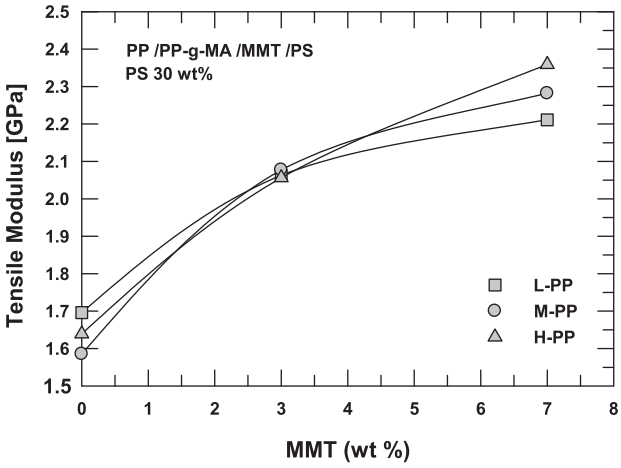

Fig. 16. Effect of MMT content on tensile modulus of blends prepared with different grades of PP. The PS composition in the blend is 30 wt%. The MMT wt% is based on the PP/PP-g-MA/MMT phase in blend.

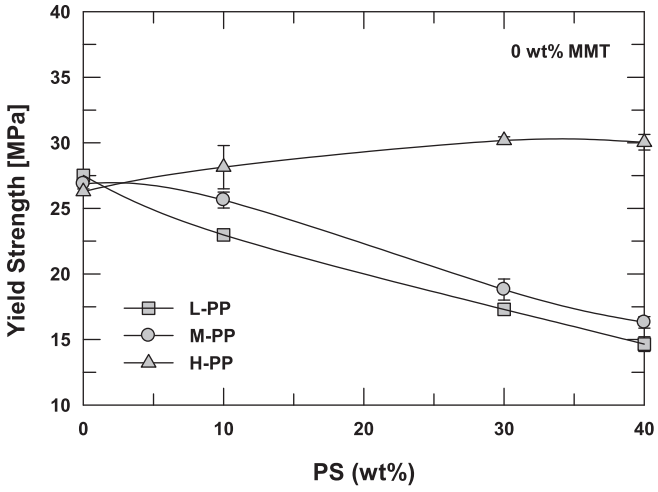

Fig. 17. Effect of PS content on yield stress of blend without MMT. The blends with MMT did not yield except for the H-PP based blend containing 10 wt% PS.

with the greatest increase observed at low PS contents. The contribution of MMT on blend modulus decreases as the PS content increases due to increasing PS contribution to the blend modulus. The increase in blend modulus is due to the reinforcement effect of MMT in the PP matrix. Fig. 16 shows the effect of MMT content in the PP/PP-g-MA/MMT phase on the tensile modulus of blends containing 30 wt% PS. The blend modulus increases with the increase in MMT content due to increase in the stiffness of the PP matrix. As seen from Fig. 16, the effect of PP molecular weight on tensile modulus becomes more significant at 7 wt% MMT.

Fig. 17 shows the tensile yield strength for blends without MMT as a function of PS content. The tensile yield strength for PP/PP-g-MA without PS is nearly the same irrespective of PP grade. The H-PP blend shows a small increase in yield strength with increased PS content whereas the L-PP and M-PP based blends show a decrease in yield strength. All blends break before yielding at PS contents beyond 40 wt%. Blends with MMT did not yield except for H-PP/PP-g-MA/MMT/PS containing 10 wt% PS. Fig. 18 shows the variation in tensile strength at break for blends with and without MMT over the entire PS composition range for all these PP materials. As seen from Fig. 18(a), the L-PP and M-PP based blends show a minimum at ~50 wt% PS; the H-PP based blend shows higher break stress than the L-PP and M-PP based blends. The break stress for H-PP based blends does not change much with PS composition up to 90 wt%. The blend with MMT (Fig. 18(b)) shows similar trends as the blends without MMT but with slightly higher values due to the presence of the MMT.

Fig. 19 shows the elongation at break for blends with and without MMT for different PS compositions and various PP

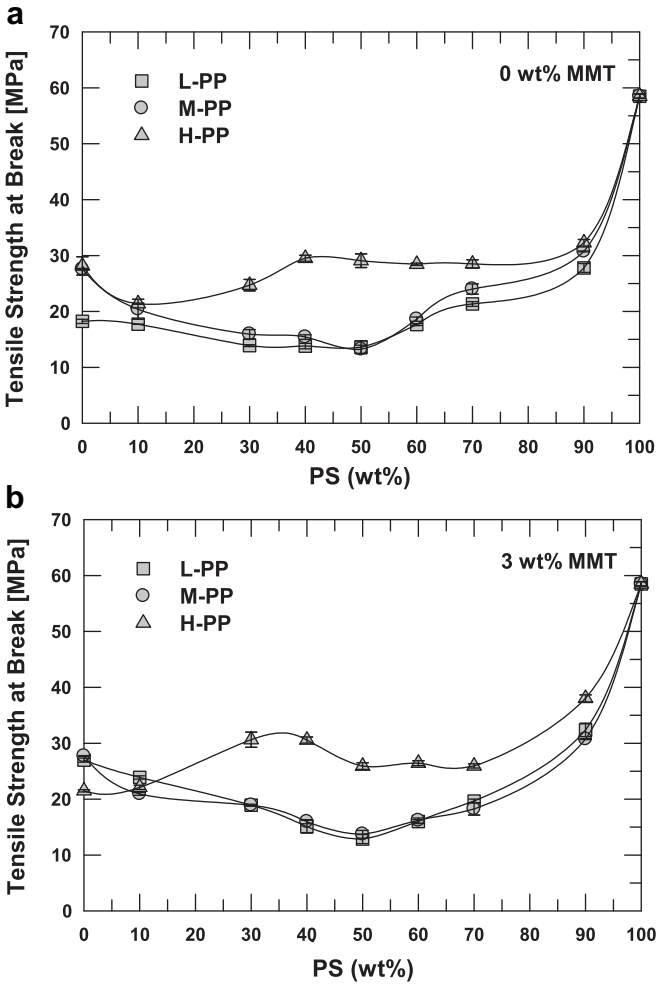

Fig. 18. Effect of PS content on tensile strength at break for blends without MMT (a) and with MMT (b). The blends were prepared from different grades of PP. The symbols represents PP phase which is either PP/PP-g-MA (0 wt% MMT) or PP/PP-g-MA/MMT (3 wt% MMT).

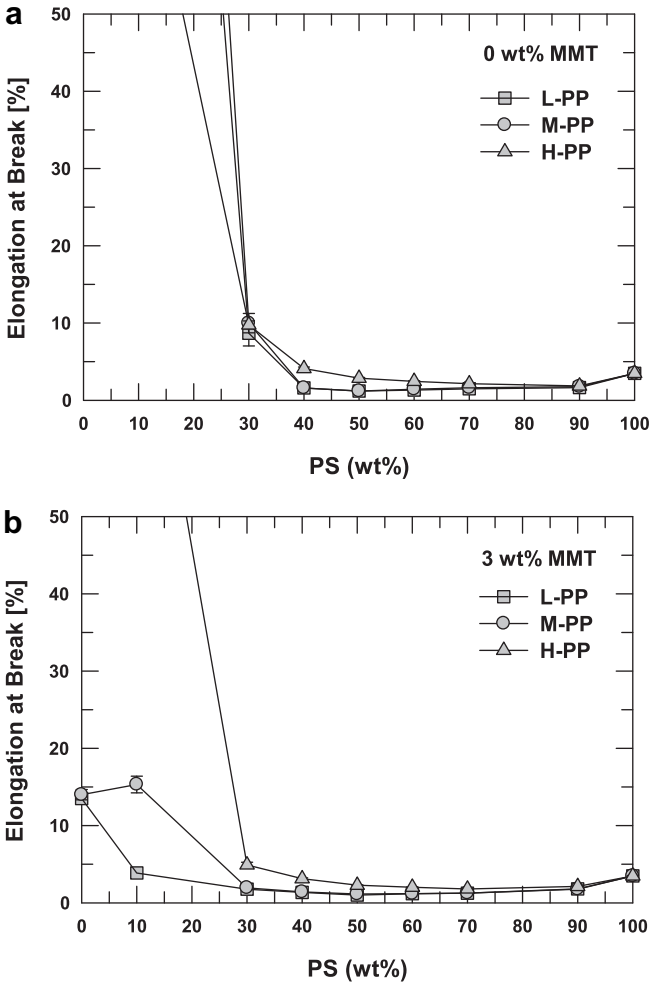

Fig. 19. Effect of PS content on elongation at break (%) for blends without MMT (a) and with MMT (b). The blends were prepared with different grades of PP. The symbols represents PP phase which is either PP/PP-g-MA (0 wt% MMT) or PP/PP-g-MA/MMT (3 wt% MMT).

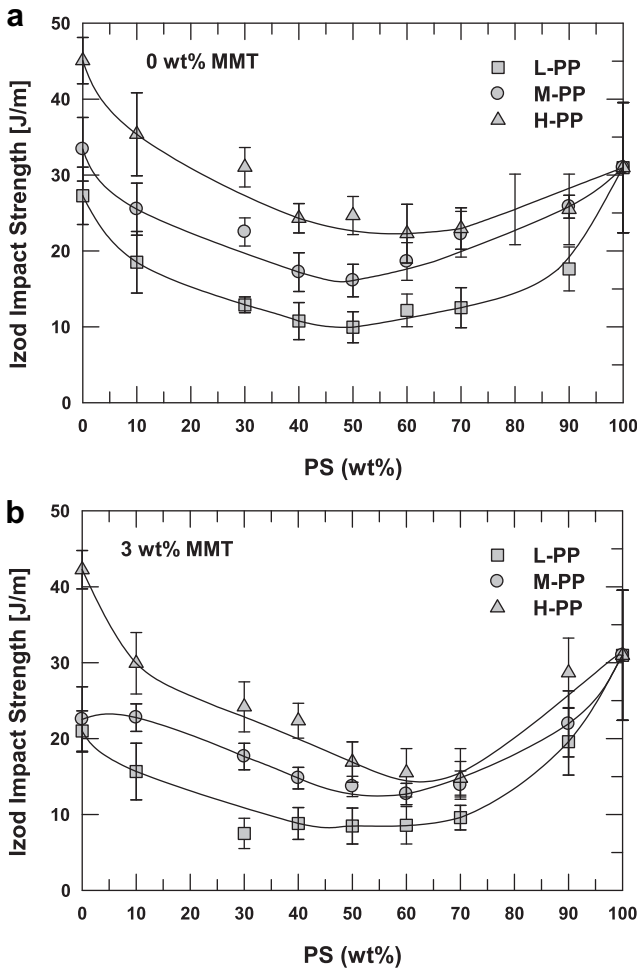

Fig. 20. Effect of PS content on notched Izod impact strength for blends without MMT (a) and with MMT (b). The blends were prepared with different grades of PP. The symbols represents PP phase which is either PP/PP-g-MA (0 wt% MMT) or PP/PP-g-MA/MMT (3 wt% MMT).

viscosities. As seen in Fig. 19(a), blends without MMT have elongations at break $>$ 50% up to 20 wt% PS irrespective of the PP molecular weight. Above 20 wt% PS, the elongation at break drops below 10% for all PS compositions with no significant difference among blends from different PP grades. For blends with MMT (Fig. 19(b)), elongation reduces to $<$ 20 wt% for L-PP and M-PP based blends at just 10 wt% PS and it reduced further with increased PS content. The H-PP/PP-g-MA/MMT/PS blend shows elongations $>$ 50% up to 20 wt% PS and then $<$ 10% beyond 30 wt% PS with no discernible difference among blends from different PP grades. The presence of MMT embrittles PP thereby reducing the elongation at break. Fig. 20 shows the effect of MMT and PS content on notched Izod impact strength of blends with and without MMT. The impact strength of PP is greater the greater its molecular weight and this translates into the blends with and without MMT. In every case there is a minimum in impact strength versus PS content. The impact strength of all the blends are reduced by the addition of MMT with the maximum decrease observed in the co-continuous region.

5. Conclusions

PP/PS blends with and without MMT were prepared from various molecular weight PP grades through melt blending in a twin screw extruder. In all cases PP-g-MA was added to the polypropylene so that the organoclay located primarily in the PP phase and to some extent at the PP/PS interface thereby acting as a compatibilizer for the blend. Surface energy analysis for high aspect ratio platelet predicted the possibility of clay platelet to be trapped at the interface which is confirmed experimentally. The presence of the organoclay significantly reduced the dispersed PS particle size when PP formed the matrix. The maximum decrease in particle size was observed for L-PP followed by M-PP and H-PP based blends with MMT. The decrease in the dispersed PS particle size caused by the organoclay was greatest for the lower viscosity PP materials. In this work, we have recognized that the presence of MMT in the matrix and at the interface is more effective in reducing dispersed phase particle size. The organoclay shifts the phase inversion toward lower PS compositions in blends with MMT than blends without MMT. The presence of MMT at the interface suppresses coalescence of dispersed PS particles in the quiescent melt condition with nearly no change compared to up to 10x increase in PS particle size observed for blend without MMT. The tensile modulus for blends with MMT is higher than blends without MMT due to increase in stiffness of PP phase. The maximum improvement in tensile modulus was observed at lower PS content. The presence of MMT slightly improves the tensile break strength whereas elongation at break reduced significantly. The blend showed increase in impact strength with PP molecular weight owing to inherent ductility of PP whereas impact strength for blends with MMT were slightly lower than that for blends without MMT.

Acknowledgments

This work was supported in part by a grant from General Motors Global Research and Development; the authors would like to thank William R. Rodgers for his continued interest and help. The authors sincerely thank D. L. Hunter of Southern Clay Products, Inc. for providing organoclay materials and many helpful discussions. The authors would like to acknowledge the utilization of excellent characterization facilities at Texas Materials Institute. The generous supply of PP-g-MA from Chemtura Corp. is highly appreciated.

References

[1] Paul DR, Bucknall CB. Polymer blends. New York: Wiley Interscience; 2000.
[2] Wu S. Polymer interface and adhesion. New York: Marcel Dekker; 1982.
[3] Wu S. Polymer 1985;26:1855–63.
[4] Utracki LA. In: Polymer alloys and blends. Munich: Hanser Publishers; 1989.
[5] Folkes MJ, Hope PS. Polymer blends and Alloys. 1st edn. London: Blackie Academic and Professional An imprint of Chapman & Hall; 1993.
[6] Brown HR. Macromolecules 1989;22:2859–60.
[7] Ho R-M, Chiang Y-W, Lin C-C, Bai SJ. Macromolecules 2002;35:1299–306.
[8] Radonjič G, Musil V, Šmit I. Journal of Applied Polymer Science 1998;69:2625–39.
[9] Hlavatá D, Horák Z, Hromádková J, Lednický F, Pleska A. Journal of Polymer Science, Part B: Polymer Physics 1999;37:1647–56.
[10] Raghu P, Nere CK, Jagtap RN. Journal of Applied Polymer Science 2003;88:266–77.
[11] Xiucuo L, Park H-M, Lee J-O, Ha C-S. Polymer Engineering and Science 2002;42:2156–64.
[12] Gelfer MY, Song HH, Liu L, Hsiao BS, Chu B, Rafailovich M, et al. Journal of Polymer Science, Part B: Polymer Physics 2003;41:44–54.
[13] Mehta S, Mirabella FM, Rufener K, Bafna A. Journal of Applied Polymer Science 2004;92:928–36.
[14] Zhang Q, Yang H, Fu Q. Polymer 2004;45:1913–22.
[15] Lee S-S, Kim J. Journal of Polymer Science, Part B: Polymer Physics 2004; 42:246–52.
[16] Ray SS, Pouliot S, Bousmina M, Utracki LA. Polymer 2004;45:8403–13.
[17] Khatua BB, Lee DJ, Kim HY, Kim JK. Macromolecules 2004;37:2454–9.
[18] Chow WS, Ishak ZAM, Ishiaku US, Karger-Kocsis J, Apostolov AA. Journal of Applied Polymer Science 2004;91:175–89.
[19] Li Y, Shimizu H. Polymer 2004;45:7381–8.
[20] Doshev P, Lach R, Lohse G, Heuvelsland A, Grellmann W, Radusch H-J. Polymer 2005;46:9411–22.
[21] Mishra JK, Hwang K-J, Ha C-S. Polymer 2005;46:1995–2002.
[22] Chow WS, Bakar AA, Ishak ZAM, Karger-Kocsis J, Ishiaku US. European Polymer Journal 2005;41:687–96.

[23] González I, Eguiazábal JI, Nazábal J. Journal of Polymer Science, Part B: Polymer Physics 2005;43:3611–20.
[24] Yuan Q, Misra RDK. Polymer 2006;47:4421–33.
[25] González I, Eguiazábal JI, Nazábal J. European Polymer Journal 2006; 42:2905–13.
[26] Si M, Araki T, Ade H, Kilcoyne ALD, Fisher R, Sokolov JC, Rafailovich MH. Macromolecules 2006;39:4793–801.
[27] Lee MH, Dan CH, Kim JH, Cha J, Kim S, Hwang Y, Lee CH. Polymer 2006;47:4359–69.
[28] Hong JS, Namkung H, Ahn KH, Lee SJ, Kim C. Polymer 2006;47:3967–75.
[29] Zou H, Zhang Q, Tan H, Wang K, Du R, Fu Q. Polymer 2006;47:6–11.
[30] Xu Y, Brittain WJ, Vaia RA, Price G. Polymer 2006;47:4564–70.
[31] Wu D, Zhou C, Zhang M. Journal of Applied Polymer Science 2006; 102:3628–33.
[32] González I, Eguiazábal JI, Nazábal J. Composites Science and Technology 2006;66:1833–43.
[33] Lai S-M, Li H-C, Liao Y-C. European Polymer Journal 2007;43:1660–71.
[34] Wang K, Wang C, Li J, Su J, Zhang Q, Du R, Fu Q. Polymer 2007;48:2144–54.
[35] Kontopoulou M, Liu Y, Austin JR, Parent JS. Polymer 2007;48:4520–8.
[36] Kelnar I, Khunová V, Kotek J, Kaprálková L. Polymer 2007;48:5332–9.
[37] Filippone G, Dintcheva NT, Acierno D, Mantia FPL. Polymer 2008;49:1312–22.
[38] Filippone G, Dintcheva NT, Mantia FPL, Acierno D. Polymer 2010;51:3956–65.
[39] Zhu Y, Ma HY, Tong L, Fang Z. Journal of Zhejiang University-Science A 2008;9:1614–20.
[40] Rosales C, Contreras V, Matos M, Perera R, Villarreal N, Garcia-Lopez D, Pastor JM. Journal of Nanoscience and Nanotechnology 2008;8:1762–74.
[41] Martins CG, Larocca NM, Paul DR, Pessan LA. Polymer 2009;50:1743–54.
[42] Wang Y, Zhang Q, Fu Q. Macromolecular Rapid Communications 2003; 24:231–5.
[43] Vo LT, Giannelis EP. Macromolecules 2007;40:8271–6.
[44] Kelnar I, Rotrekl J, Kotek J, Kaprálková L, Hromádková J. European Polymer Journal 2009;45:2760–6.
[45] Yang Q-Q, Guo Z-X, Yu J. Journal of Applied Polymer Science 2010; 115:3697–704.
[46] Filippone G, Dintcheva NT, Mantia FPL, Acierno D. Journal of Polymer Science, Part B: Polymer Physics 2010;48:600–9.
[47] Moghbelli E, Sue H-J, Jain S. Polymer 2010;51:4231–7.
[48] Kim DH, Fasulo PD, Rodgers WR, Paul DR. Polymer 2007;48:5308–23.
[49] Ramsden W. Separation of solids in the surface-layers of solutions and suspensions. Proceedings of the Royal Society A Mathematical, Physical and Engineering Sciences 1903;72:156–64. London.
[50] Pickering SU. Journal of Chemical Society 1907;91:2001–21.
[51] Tambe DE, Sharma MM. Advances in Colloid and Interface Science 1994;52:1–63.
[52] Binks BP, Lumsdon SO. Physical Chemistry Chemical Physics 1999;1:3007–16.
[53] Binks BP, Kirkland M. Physical Chemistry Chemical Physics 2002;4:3727–33.
[54] Aveyard R, Binks BP, Clint JH. Advances in Colloid and Interface Science 2003;100:503–46.
[55] Binks BP, Philip J, Rodrigues JA. Langmuir 2005;21:3296–302.
[56] Yan N, Masliyah JH. Colloids and Surfaces A: Physicochemical and Engineering Aspects 1995;96:229–42.
[57] Binks BP, Lumsdon SO. Langmuir 2000;16:8622–31.
[58] Midmore BR. Colloids and Surfaces A: Physicochemical and Engineering Aspects 1998;132:257–65.
[59] Lagaly G, Reese M, Abend S. Applied Clay Science 1999;14:83–103.
[60] Vermant J, Cioccolo G, Nair KG, Moldenaers P. Rheologica Acta 2004;43: 529–38.
[61] Thareja P, Velankar S. Rheologica Acta 2007;46:405–12.
[62] Vermant J, Vandebril S, Dewitte C, Moldenaers P. Rheologica Acta 2008;47: 835–9.
[63] Elias L, Fenouillot F, Majeste JC, Cassagnau P. Polymer 2007;48:6029–40.
[64] Hobbs SY, Dekkers MEJ, Watkins VH. Journal of Materials Science 1988;23: 1219–24.
[65] Fowler ME, Keskkula H, Paul DR. Journal of Applied Polymer Science 1989;37:225–32.
[66] Cheng TW, Keskkula H, Paul DR. Polymer 1992;33:1606–19.
[67] Guo HF, Packirisamy S, Gvozdic NV, Meier DJ. Polymer 1997;38:785–94.
[68] Virgilio N, Marc-Aurele C, Favis BD. Macromolecules 2009;42:3405–16.
[69] Virgilio N, Desjardins P, L'Espérance G, Favis BD. Polymer 2010;51:1472–84.
[70] Bronshteĭn IN. Handbook of Mathematics. 4th edn. Berlin: Springer-Verlag; 2004.
[71] Lee H-s, Fasulo PD, Rodgers WR, Paul DR. Polymer 2005;46:11673–89.
[72] Sundararaj U, Macosko CW. Macromolecules 1995;28:2647–57.
[73] Fortelný I, Zivný A. Polymer 1995;36:4113–8.
[74] Wildes G, Keskkula H, Paul DR. Polymer 1999;40:5609–21.
[75] Mohamed IO, Ofoli RY, Morgan RG. Journal of Food Process Engineering 1990;12:227–46.

Polymer 52 (2011) 1155–1162

Contents lists available at ScienceDirect

Polymer

journal homepage: www.elsevier.com/locate/polymer

Wear resistant UHMWPE with high toughness by high temperature melting and subsequent radiation cross-linking

Jun Fu [a,b], Bassem W. Ghali [a], Andrew J. Lozynsky [a], Ebru Oral [a,b,*], Orhun K. Muratoglu [a,b]

[a] Harris Orthopaedic Laboratory, Massachusetts General Hospital, 55 Fruit Street, Boston, MA 02114, USA
[b] Department of Orthopedic Surgery, Harvard Medical School, Boston, MA, USA

ARTICLE INFO

Article history:
Received 16 November 2010
Received in revised form
7 January 2011
Accepted 8 January 2011
Available online 14 January 2011

Keywords:
High temperature melting
Radiation cross-linking
Low wear

ABSTRACT

The goal of this study was to create wear resistant ultra high molecular weight polyethylene (UHMWPE) with improved strength and toughness. It was previously demonstrated that high temperature melting (HTM) of UHMWPE at 280–320 °C improved its toughness without detrimentally affecting its wear resistance. We hypothesized that radiation cross-linking after high temperature melting could further improve the wear resistance of UHMWPE, and the loss in toughness by radiation cross-linking could be compensated by the improved toughness achieved by the high temperature melting prior to irradiation. In this work, we demonstrated that irradiation after HTM generated UHMWPE with improved toughness compared to the irradiated UHMWPEs without HTM, partly due to the low cross-link density of irradiated HTM UHMWPE. At a given cross-link density, irradiated HTM UHMWPEs showed higher wear resistance than irradiated UHMWPE. Therefore, successive HTM and radiation cross-linking strategy is promising to create UHMWPE materials with low wear and improved mechanical properties for total joint implants.

1. Introduction

Implants fabricated from ultra high molecular weight polyethylene (UHMWPE) have been highly successful in general with implant survival rates over 80% at 15 years [1]. Nevertheless, the longevity of the implants presents a challenge since the overall number of total joint replacements is increasing and the average age of patients undergoing total joint arthroplasty is decreasing steadily [2]. It is desirable to improve the performance of implants such that the number of revision operations is decreased.

The leading cause of implant failure is wear debris-induced osteolysis and implant loosening mainly due to the wear of UHMWPE [3]. Radiation cross-linking effectively reduces the wear at the articulating surface of the implants [4], but also decreases the mechanical strength [5]. In addition, post-irradiation melting used to eliminate oxidation-prone radiation-induced free radicals also leads to further reduction in the mechanical and fatigue strength of UHMWPE [6]. An alternate method of obtaining oxidative stability in radiation cross-linked UHMWPE is stabilizing these free radicals by an antioxidant such as vitamin E [7–9]. Using this method, post-irradiation melting can be avoided and the mechanical properties can be maintained. Nevertheless, the mechanical properties of the material are already somewhat sacrificed by radiation cross-linking to increase wear resistance. Thus, it is desirable to improve the strength of highly cross-linked UHMWPEs, especially for younger patients with higher activity and also for the expansion of the use of joint implants in diverse implant geometries, where the mechanical properties remain as a bottleneck for the survivorship of the implants.

Manufacturing of all UHMWPE implants starts with the consolidation of UHMWPE resin powder into solid form. Inevitably, fusion defects [10] are present in these materials, essentially due to the incomplete fusion of the high molecular weight polymer granules under the consolidation conditions. According to the reptation theory [11,12], a single polymer chain relaxes in a tube along its axis defined by the neighboring chains (entanglements). At 180 °C, the relaxation time for a UHMWPE chain to reptate through this tube is about 15 h [13], much longer than a typical consolidation cycle. The polymer chains cannot adequately diffuse through the granule boundaries to achieve complete fusion, leaving numerous granule boundaries with weak mechanical properties in comparison to those in bulk. Such weak boundaries have been widely observed by scanning electron microscopy of freeze-fractured surfaces of UHMWPE [14–16]. These boundaries usually have reduced toughness [17] in comparison to the bulk and may serve as fatigue crack

* Corresponding author. Harris Orthopaedic Laboratory, Massachusetts General Hospital, 55 Fruit Street, Boston, MA 02114, USA. Tel.: +1 617 7260657; fax: +1 617 6432521.
E-mail address: eoral@partners.org (E. Oral).

0032-3861/$ – see front matter © 2011 Published by Elsevier Ltd.
doi:10.1016/j.polymer.2011.01.017

initiation sites under cyclic loading, which may also contribute to fatigue-induced wear [15,18].

We demonstrated that melting consolidated UHMWPE at very high temperatures above the melting point (circa 300 °C) markedly increased its toughness without detrimentally affecting wear, presumably due in part to the elimination of fusion defects. At high temperatures, two major effects, i.e., chain scissioning and accelerated inter-granular diffusion, were responsible for the increases in plasticity and toughness, as we found a marked increase in the elongation-at-break up to 1100%, work-to-failure up to 6600 kJ/m^2, and double notched IZOD impact strength up to 175 kJ/m^2 [19].

For applications in total joint implants, however, it is necessary to further improve the wear resistance by high dose radiation cross-linking after high temperature melting (HTM). Inevitably, high dose radiation cross-linking will decrease the strength and toughness of UHMWPE. We hypothesized that the improved toughness by the HTM before irradiation could compensate for some of the loss in mechanical properties induced by radiation cross-linking, thus leading to new UHMWPE materials with low wear and improved toughness in comparison to radiation cross-linked UHMWPE.

2. Experimental

2.1. High temperature melting (HTM) of consolidated UHMWPE

Compression molded GUR 1050 UHMWPE (Orthoplastics, Bacup Lancashire, UK) with approximate dimensions of 250 × 60 × 45 mm^3 (length × width × height) were melted by using a programmable convection oven with inert gas flow (LLD1-16N-3, Despatch Industries, Minneapolis, MN). The oven was pre-heated to a preset temperature with nitrogen purge (flow rate ~ 2 m^3/min). Then, the UHMWPE was placed in the oven and was held at the temperature for different durations. The temperatures used were 280, 300, and 320 °C [19]. At each temperature, the UHMWPE was held for 2, 5, or 12 h and then cooled down to 40 °C within 2 h (at an average cooling rate of 2.5 °C/min) and held at 40 °C for 20 min in the oven before retrieval. These melted UHMWPEs were denoted as UH *T*–*t*, where *T* is temperature, and *t* is time. For example, UH 280-2 denotes a UHMWPE melted at 280 °C for 2 h. Compression molded UHMWPE without HTM was used as control and denoted as such.

2.2. Radiation cross-linking

High temperature melted UHMWPEs (HTM-PE) were vacuum packed and cross-linked by using a 10 MeV electron beam at room temperature at Iotron Inc. (Vancouver, BC) at a dose rate of 50 kGy/pass. The total doses were 50, 100, and 150 kGy. Radiation cross-linked UHMWPEs without HTM was used as irradiated controls, and were denoted as 'irradiated PEs' or PE-50, PE-100, and PE-150 for doses of 50, 100, and 150 kGy, respectively.

The irradiated HTM-PEs were denoted as UHI *T*-*t*-*D*, where *T* is temperature, *t* is time, and *D* is radiation dose. For example, UHI 280-2-50 denotes a UHMWPE melted at 280 °C for 2 h and then e beam cross-linked with a dose of 50 kGy.

2.3. Pin-on-disc (POD) wear test

Bi-directional POD wear test was performed on an MTS machine (Eden Prairie, MN) in bovine serum. Pins of 13-mm long and 9-mm diameter (n = 3 for each material) were machined and tested under bi-directional motion on implant-grade polished CoCr discs (R_a = 0.03–0.05) at 2 Hz as previously described [20]. Wear was determined gravimetrically at every 0.15 million-cycles (MC) until a total of 1.2 MC. The wear rate was a linear regression of the weight loss as a function of number of cycles from 0.5 to 1.2 MC.

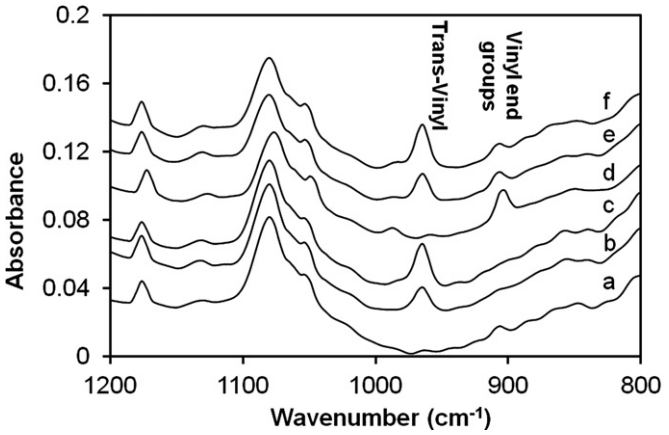

Fig. 1. FTIR spectra of (a) control PE; (b) PE-50; (c) PE-100; (d) UH 320-5; (e) UHI 320-5-50; and (f) UHI 320-5-100.

2.4. Tensile testing

Thin sections (3.2 mm thickness) of the above-mentioned UHMWPE materials were machined and dog-bone-shaped specimens (Type V, n = 5 each) were stamped from these thin sections according to ASTM D638. Uni-axial tensile testing was conducted by using an MTS machine (Eden Prairie, MN) at a crosshead speed of 10 mm/min. The axial displacement and force were sampled at a rate of 100 Hz. The extension of a specific gauge on the specimen was measured by a laser extensometer, which was used to determine the elongation-at-break (EAB).

The ultimate tensile strength (UTS), yield strength (YS), and elastic modulus (E) were calculated according to ASTM D-638. The work-to-failure was calculated by integrating the area below the engineering stress-strain curve.

2.5. Double-notched IZOD impact strength measurements

Notching and double-notched IZOD impact strength measurements were conducted at Orthoplastics Inc. (Lancashire, UK). The specimens (n = 5 for each material) were machined to 63.5 × 12.7 × 6.35 mm^3 bars and double notched to a depth of 4.57 ± 0.08 mm according to ASTM F648. The specimens were conditioned after notching for not less than 16 h at 23 ± 2 °C and tested in accordance with ASTM F648. The energy absorbed by the specimens was recorded for the calculation of the impact strength in kJ/m^2. The average values of five specimens, together with the standard deviations, are reported.

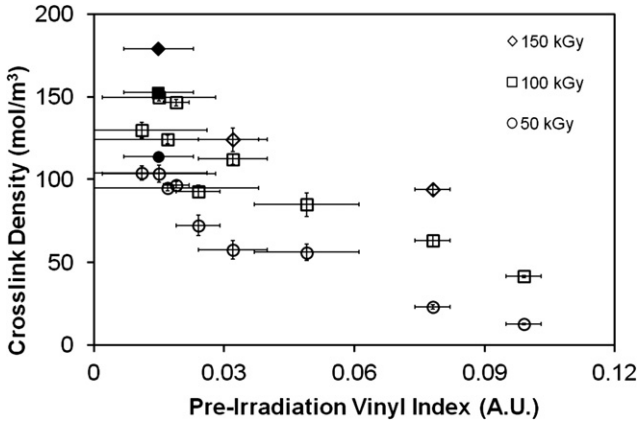

Fig. 2. The effect of the initial vinyl content on the cross-link density of irradiated HTM-PEs. The solid symbols represent the irradiated control PEs.

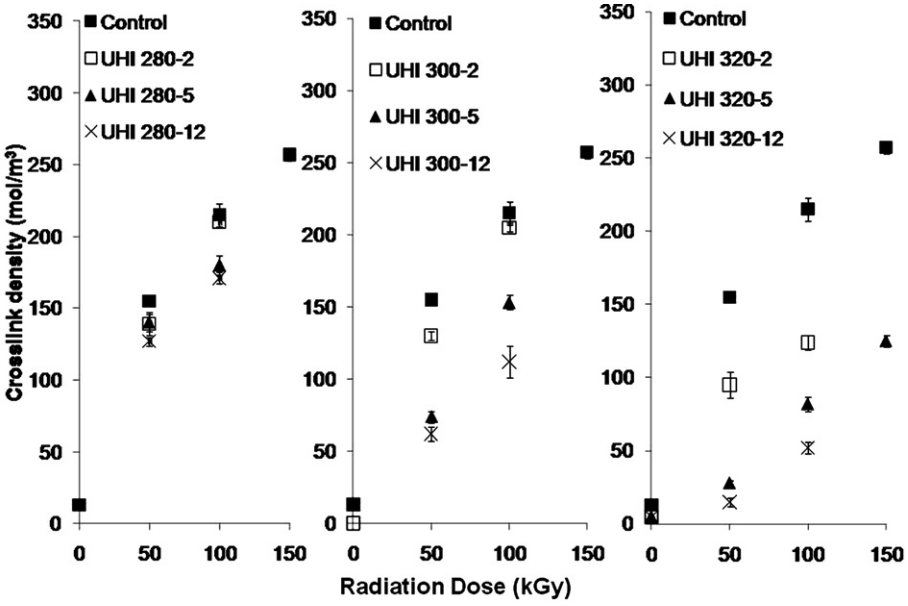

Fig. 3. The effect of melting temperature and time on the cross-link density of irradiated HTM-PEs. The solid symbols represent the irradiated control PEs.

2.6. Determination of peak melting points and percentage crystallinity

The peak melting points (T_m) and percentage crystallinity (X_c) were determined by using a Q-1000 Differential Scanning Calorimeter (TA Instruments, Newark, DE) that had been calibrated with an indium standard. Three specimens of each material were weighed with a Sartorius CP 225D balance to a resolution of 0.01 mg and placed in standard aluminum pans. With a nitrogen flow at 50 ml/min, the cell temperature was ramped from −20 °C to 180 °C at 10 °C/min, then from 180 °C to 20 °C at −10 °C/min, and finally from −20 °C to 180 °C at 10 °C/min again. Before each cycle, the cell temperature was held at each start temperature for 2 min. Thus, three traces were recorded as heat flow versus temperature. The cycles are referred to as 1st heat, 1st cool, and 2nd heat, respectively.

The percentage crystallinity of each sample was calculated by integrating the enthalpy peak from 20 to 160 °C and normalizing it with the fusion enthalpy of 100% crystalline polyethylene (291 J/g). The percentage crystallinity was calculated by averaging the values of three specimens of each material.

2.7. Vinyl end group measurement by fourier transform infrared Spectroscopy (FTIR)

Thin slices (thickness ~ 150 μm) were microtomed by using an LKB Sledge Microtome (Sweden). FTIR absorption spectra of these thin slices were collected by using a UMA-500 infrared microscope (Bio-Rad Laboratories, Natick, MA) scanning from 400 to 4000 cm^{-1} (resolution 8 cm^{-1}) in transmission mode. A vinyl index was calculated based on the area under the absorbance at 909 cm^{-1}

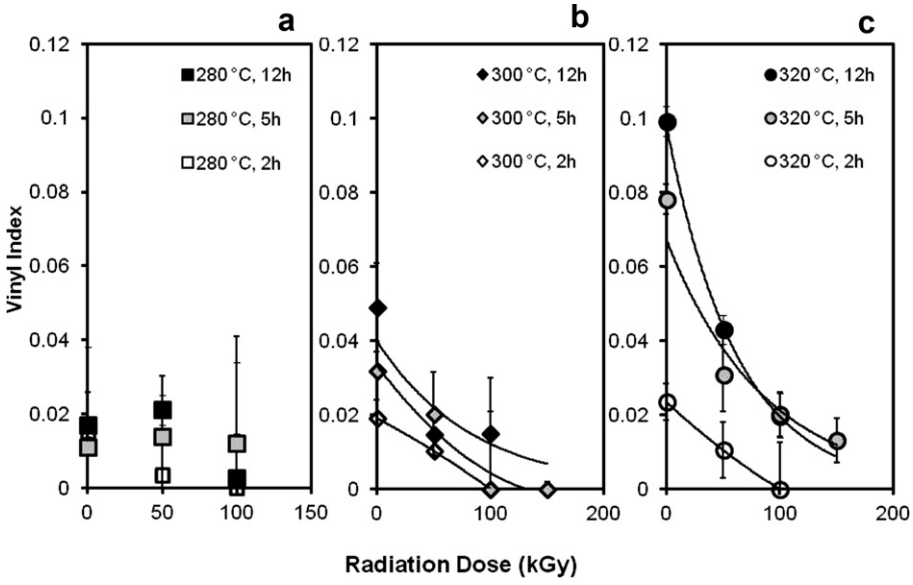

Fig. 4. Effect of radiation dose on the vinyl index for radiation cross-linked UHMWPE with pre-irradiation HTM for 5 h at (a) 280 °C; (b) 300 °C and (c) 320 °C.

Table 1
Thermal, mechanical properties, and wear rate of control PEs, irradiated PEs, HTM-PEs, and irradiated HTM-PEs.

Samples	Description	T_m (°C)	X_c (%)	WF (kJ/m^2)	EAB (%)	I (kJ/m^2)	POD wear rate (mg/MC)
Control PE	CM GUR 1050	135.1 ± 0.1	52 ± 2.9	3242 ± 444	401 ± 15	127 ± 7	10.2 ± 0.9
PE-50	50 kGy	138.1 ± 0.5	62 ± 0.5	3240 ± 224	389 ± 29	–	6.8 ± 1.1
PE-100	100 kGy	139.4 ± 0.6	60 ± 0.6	2006 ± 301	303 ± 12	77 ± 3	2.7 ± 0.8
PE-150	150 kGy	139.6 ± 1.1	61 ± 0.5	1559 ± 132	266 ± 19	62 ± 3	1.8 ± 1.1
UH 280-2	280 °C, 2h	133.7 ± 0.2	55 ± 1.3	3314 ± 167	444 ± 0.7	109 ± 4	7.4 ± 2.4
UHI 280-2-50	280 °C, 2h + 50 kGy	136.1 ± 0.4	54 ± 2.7	2739 ± 436	400 ± 19	–	7.0 ± 0.8
UHI 280-2-100	280 °C, 2h + 100 kGy	138.1 ± 0.4	54 ± 0.8	2093 ± 203	324 ± 13	74 ± 1	3.5 ± 2.0
UH 280-5	280 °C 5h	134.2 ± 0.03	52 ± 0.8	3120 ± 637	473 ± 36	123 ± 3	10.7 ± 1.1
UHI 280-5-50	280 °C 5h + 50 kGy	135.8 ± 0.4	56 ± 0.4	3121 ± 490	422 ± 41	–	7.5 ± 1.7
UHI 280-5-100	280 °C 5h + 100 kGy	137.3 ± 0.1	56 ± 0.5	2114 ± 105	339 ± 4.5	76 ± 2	3.2 ± 1.1
UH 280-12	280 °C, 12h	133.5 ± 0.2	57 ± 0.9	3673 ± 550	513 ± 16	175 ± 9	11.2 ± 0.3
UHI 280-12-50	280 °C, 12h + 50 kGy	136.8 ± 0.3	51 ± 3.1	3096 ± 311	431 ± 12	–	8.1 ± 2.5
UHI 280-12-100	280 °C, 12h + 100 kGy	137.9 ± 0.2	57 ± 0.6	2028 ± 230	334 ± 28	80 ± 4	5.7 ± 3.3
UH 300-2	300 °C, 2h	133.6 ± 0.1	57 ± 1.7	3266 ± 379	457 ± 20	123 ± 6	11.2 ± 2.3
UHI 300-2-50	300 °C, 2h + 50 kGy	135.1 ± 0.5	59 ± 0.6	2582 ± 411	412 ± 18	–	6.0 ± 1.1
UHI 300-2-100	300 °C, 2h + 100 kGy	137.0 ± 0.1	56 ± 1.3	2066 ± 120	321 ± 19	75 ± 2	2.8 ± 1.5
UH 300-5	300 °C 5h	134.3 ± 0.1	56 ± 0.6	4691 ± 653	546 ± 37	140 ± 4	11.3 ± 0.7
UHI 300-5-50	300 °C 5h + 50 kGy	135.4 ± 0.2	61 ± 0.9	3817 ± 298	484 ± 8	114 ± 6	7.0 ± 2.9
UHI 300-5-100	300 °C 5h + 100 kGy	136.3 ± 0.7	59 ± 0.3	2270 ± 277	371 ± 12	87 ± 2	3.2 ± 0.1
UHI 300-5-150	300 °C 5h + 150 kGy	137.3 ± 0.3	67 ± 1.0	1959 ± 203	318 ± 23	83 ± 2	1.4 ± 0.3
UH 300-12	300 °C, 12h	133.7 ± 0.1	62 ± 1.4	6646 ± 991	752 ± 23	111 ± 5	12.1 ± 2.9
UHI 300-12-50	300 °C, 12h + 50 kGy	135.1 ± 0.2	61 ± 0.9	3766 ± 671	516 ± 45	–	7.4 ± 1.5
UHI 300-12-100	300 °C, 12h + 100 kGy	136.5 ± 0.4	61 ± 1.7	2882 ± 405	434 ± 28	94 ± 3	4.0 ± 2.7
UH 320-2	320 °C, 2h	133.9 ± 0.3	61 ± 0.3	4638 ± 1133	521 ± 24	139 ± 2	9.7 ± 2.7
UHI 320-2-50	320 °C, 2h + 50 kGy	135.7 ± 0.3	58 ± 0.4	2907 ± 363	425 ± 38	–	5.9 ± 1.9
UHI 320-2-100	320 °C, 2h + 100 kGy	136.8 ± 0.2	64 ± 1.2	2530 ± 179	382 ± 31	78 ± 7	6.0 ± 1.0
UH 320-5	320 °C, 5h	134.1 ± 0.2	62 ± 2.1	6651 ± 263	974 ± 46	94 ± 4	11.6 ± 1.7
UHI 320-5-50	320 °C, 5h + 50 kGy	134.7 ± 0.2	66 ± 0.3	5190 ± 398	740 ± 39	–	7.4 ± 1.5
UHI 320-5-100	320 °C, 5h + 100 kGy	136.1 ± 0.3	67 ± 0.7	3361 ± 394	519 ± 27	101 ± 4	4.8 ± 1.6
UHI 320-5-150	320 °C, 5h + 150 kGy	138.6 ± 0.1	62 ± 0.9	2331 ± 141	372 ± 17	83 ± 4	1.9 ± 0.3
UH 320-12	320 °C, 12h	133.7 ± 0.2	64 ± 2.6	5726 ± 505	1061 ± 71	66 ± 5	15.6 ± 2.5
UHI 320-12-50	320 °C, 12h + 50 kGy	135.5 ± 0.6	69 ± 1.1	5376 ± 369	831 ± 53	93 ± 3	10.9 ± 1.0
UHI 320-12-100	320 °C, 12h + 100 kGy	134.9 ± 0.8	65 ± 0.8	3362 ± 398	566 ± 61	96 ± 3	4.8 ± 2.4

normalized to the area under the polyethylene skeletal absorbance at 1895 cm^{-1} [19].

2.8. Cross-link density measurements

Small sections were cut by razor blade (approximately 3 × 3 × 3 mm^3). These small pieces were swollen for 2 h in xylene (25 mL), which was pre-heated to 130 °C. The gravimetric swelling ratio was converted to a volumetric swelling ratio using the density of the dry polymer as 0.94 g/cm^3 and the density of xylene at 130 °C as 0.75 g/cm^3. The cross-link density of the samples (n = 3 each) was calculated using the following equations:

$$d_x = \frac{\ln\left(1 - q_{eq}^{-1}\right) + q_{eq}^{-1} + Xq_{eq}^{-2}}{V_1\left(q_{eq}^{-1/3} - q_{eq}^{-2}\right)} \quad (1)$$

$$X = 0.33 + \frac{0.55}{q_{eq}} \quad (2)$$

where the specific volume of xylene, V_1, was 136 cm^3/mol.

Statistical analysis was performed by using a Student's t-test for two-tailed distributions with unequal variance where applicable.

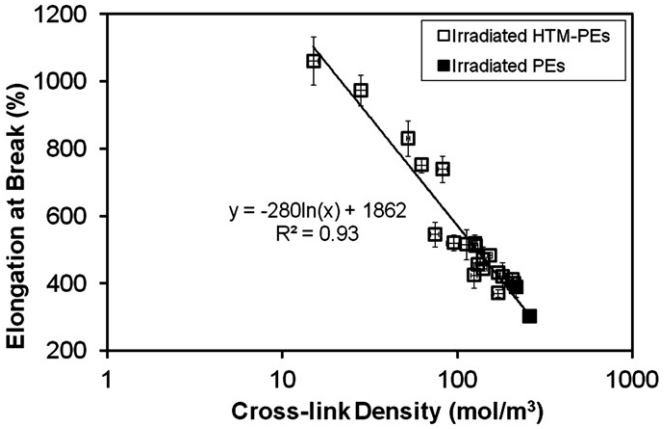

Fig. 5. The cross-link density dependence of elongation-at-break (EAB) for irradiated PEs and irradiated HTM-PEs.

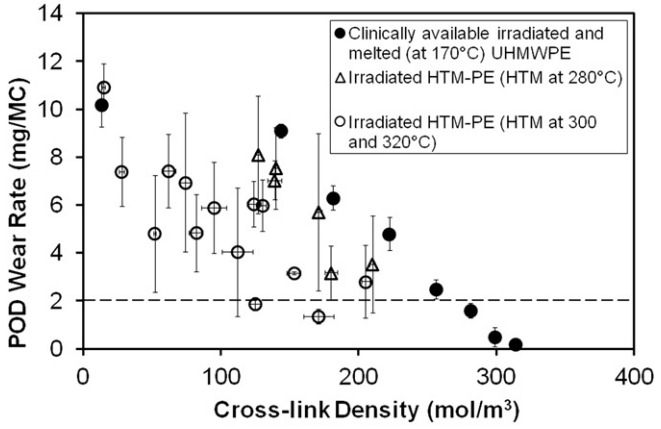

Fig. 6. The cross-link density dependence of the wear rate of irradiated HTM-PEs compared to clinically available UHMWPE.

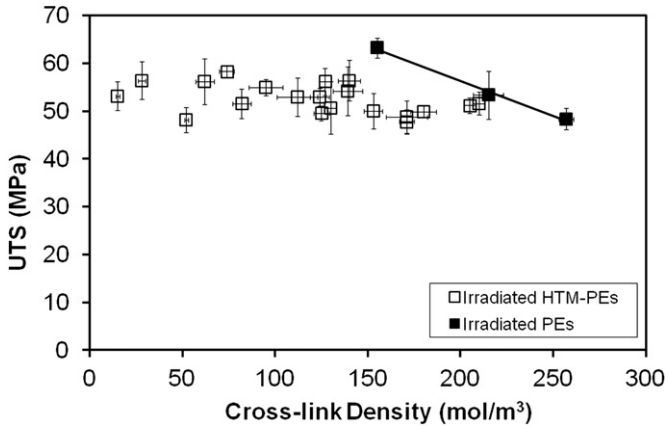

Fig. 7. The cross-link density dependence of the ultimate tensile strength (UTS) of irradiated PEs and irradiated HTM-PEs.

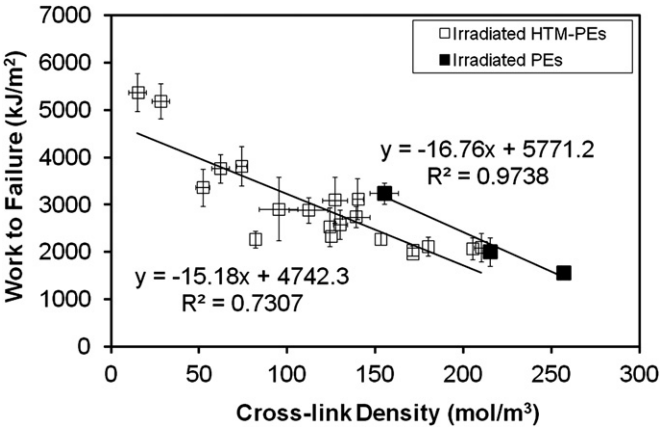

Fig. 9. The cross-link density dependence of the tensile work-to-failure (WF) of irradiated PEs and irradiated HTM-PEs.

3. Results

Radiation cross-linking of HTM-PEs consumed the vinyl end groups formed at high temperatures [19] and generated trans-vinyl groups (Fig. 1). The higher vinyl index prior to irradiation resulted in lower cross-link density after irradiation (Fig. 2), and thus radiation cross-linked HTM-PEs (UHI) had lower cross-link density in comparison to the irradiated PEs at given radiation doses (Fig. 3). The cross-link density of these UHI materials decreased with increased HTM time and temperature prior to irradiation. For example, with 100-kGy irradiation, the cross-link density decreased from 215 mol/m^3 for PE-100–153 mol/m^3 for UHI 300-5-100 and further to 112 mol/m^3 for UHI 300-12-100 (Fig. 3). After irradiation, the vinyl index decreased with increasing radiation dose (Fig. 4).

Radiation cross-linking significantly decreased the elongation-at-break (EAB) with increasing dose both for PEs and HTM-PEs (Table 1). Meanwhile, the EAB for all irradiated HTM-PEs was higher than that of the irradiated PEs at the same radiation dose (Table 1). The EAB of UHI 300-12-100, UHI 320-2-100, and UHI 320-5-150, were comparable to that of control PE without HTM or irradiation (Table 1).

The EAB of all irradiated PEs and HTM-PEs showed a similar logarithmic dependence on the cross-link density (Fig. 5). The low cross-link density range (10–150 mol/m^3) was dominated by the irradiated HTM-PEs since even at the lowest radiation dose of 50 kGy, the cross-link density of irradiated PEs was higher than 150 mol/m^3.

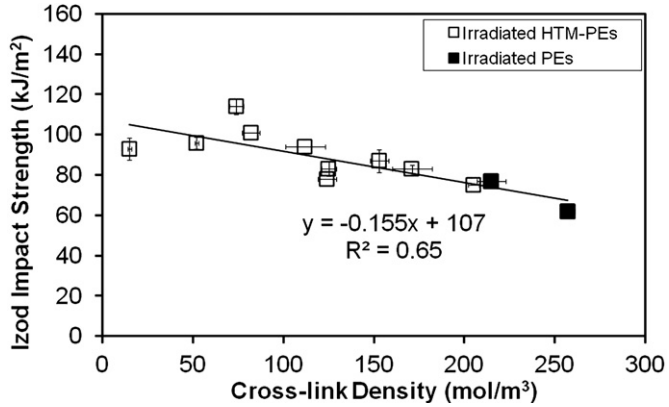

Fig. 8. The cross-link density dependence of the double-notched Izod impact strength of irradiated PEs and irradiated HTM-PEs.

Radiation cross-linking significantly decreased the wear rate of the HTM-PEs and control PE with increasing radiation dose (Table 1). When compared to previously published wear data as a function of cross-link density for clinically available irradiated and subsequently melted UHMWPE [4], irradiated HTM-PEs with similar cross-link density showed significantly lower wear rates (Fig. 6). The wear rate of UHI decreased as the HTM temperature and time increased prior to irradiation.

Except for the UH 320-12 (or UHMWPE melted at 320 °C for 12 h), for which the UTS (43 MPa before irradiation) was increased

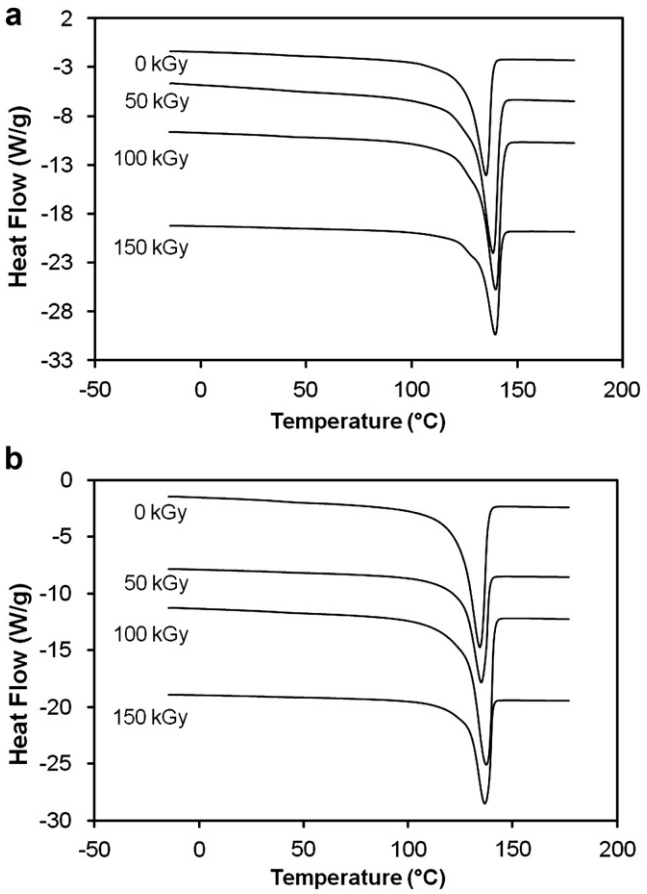

Fig. 10. The 1st heat thermograms of (a) irradiated PEs and (b) irradiated HTM-PE (300 °C 5 h).

to 53 MPa ($p = 0.0004$) and 48 MPa ($p = 0.009$) after 50- and 100-kGy irradiation respectively (Table 1), the UTS showed little dependence on the cross-link density for HTM-PEs, in contrast to the decrease of UTS with increasing cross-link density for irradiated PEs (Fig. 7).

The double-notched IZOD impact strength (I) decreased with increasing radiation dose for both PEs and HTM-PEs (Table 1). The impact strength of irradiated HTM-PEs was higher than those for irradiated PEs at a given radiation dose (Table 1). For example, the impact strength of UHI 320-5-100 was 101 kJ/m^2 compared to 77 kJ/m^2 for PE-100, namely a 30% improvement. The IZOD impact strength for all irradiated samples showed a gradual decrease with cross-link density; however, irradiated HTM-PEs represented higher impact strength at lower values of cross-link density (Fig. 8).

The tensile work-to-failure (WF) of irradiated HTM-PEs decreased with increasing cross-link density, similar to that of irradiated PEs (Fig. 9). However, the WF of irradiated PEs was higher than those of the irradiated HTM-PEs with cross-link density values higher than 150 mol/m^3.

Radiation cross-linking after high temperature melting increased the peak melting point (T_m) of the polyethylene crystals but did not appreciably change the crystallinity compared to the HTM-PEs (Table 1). Irradiation of the control PE with 50, 100, and 150 kGy increased the T_m significantly ($p < 0.05$) up to 139.6 °C, and generated a shoulder at around 126 °C in the first heat thermogram (Fig. 10a). In contrast, no obvious shoulders were observed for the irradiated HTM-PEs while the T_m was similarly increased significantly ($p < 0.05$) up to 137.3 °C for UHI 300-5-150 (Fig. 10b).

The crystallization behavior of irradiated HTM-PEs during cooling was different from that of irradiated PEs: the irradiated PEs' crystallization peak was broadened with a shoulder at higher than 118 °C (e.g., 123 °C for 150 kGy, Fig. 11a), while there were no shoulders for the irradiated HTM-PEs (Fig. 11b). The thermograms of the second heating cycle showed broadened melting peaks with high doses for irradiated PEs (Fig. 12a) but this was not the case for the irradiated HTM-PEs (Fig. 12b).

4. Discussion

Radiation cross-linking of high temperature melted UHMWPE resulted in materials with low wear rate and improved impact strength in comparison to the highly cross-linked UHMWPE without pre-irradiation HTM, corroborating our hypothesis.

Despite the expected cross-link density increase with increasing radiation dose for HTM-PEs, the presence of vinyl end groups (Fig. 1) resulted in lower cross-link density for irradiated HTM-PEs (Fig. 2) than those of the irradiated PEs that received the same radiation dose (Fig. 3). We would hypothesize that an increase in the vinyl end groups in the structure before irradiation would increase the formation of Y cross-links, that is, the cross-links between a macroalkyl free radical and the vinyl end groups. The fact that the consumption of vinyl end groups with irradiation (Fig. 4) did not increase cross-link density to the same level as non-HTM UHMWPEs suggested that a significantly different cross-linked structure resulted. One explanation is the increased probability of the reaction of vinyl end groups with themselves, effectively increasing the molecular weight between cross-links. Another contribution is the formation of short chain branches instead of cross-links due to the extensive chain scissioning during the pre-irradiation high temperature melting process.

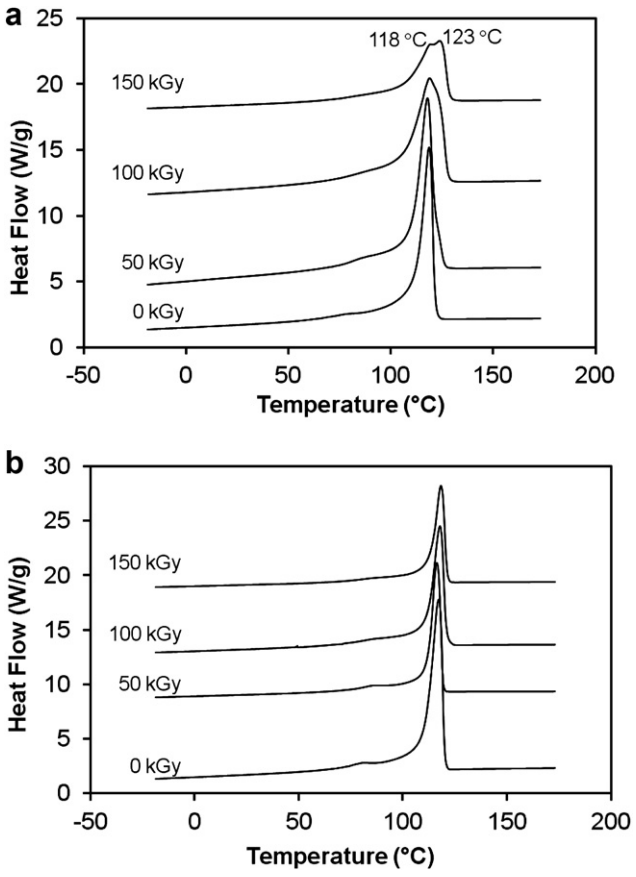

Fig. 11. The 1st cooling thermograms of (a) irradiated PE and (b) irradiated HTM-PE (300 °C 5 h) at 50 kGy/pass with different doses.

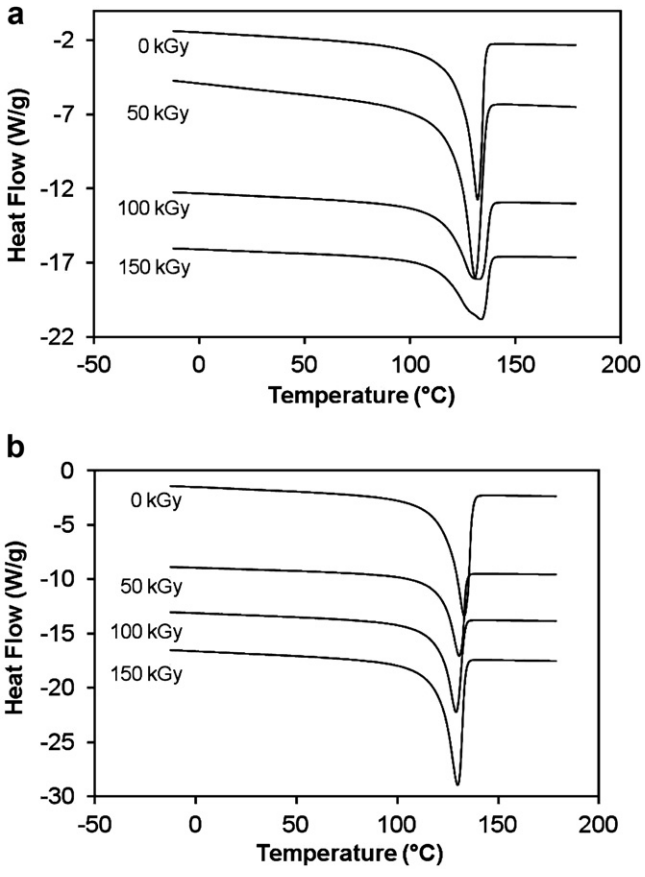

Fig. 12. The 2nd heating thermograms of (a) irradiated PEs and (b) irradiated HTM-PE (300 °C 5 h) at 50 kGy/pass with different doses.

Table 2
Comparison of the mechanical properties of irradiated PE and irradiated HTM-PEs (melted at 300 °C or 320 °C for 5 h) with wear rates less than 2 mg/MC.

Sample	Description	UTS (MPa)	WF (kJ/m^2)	EAB (%)	I (kJ/m^2)	d_{XL} (mol/m^3)	POD wear rate (mg/MC)
PE-150	150 kGy	48 ± 2.3	1559 ± 132	266 ± 19	62 ± 3	257 ± 4	1.8 ± 1.1
UHI 300-5-150	300 °C 5h + 150 kGy	49 ± 3.4	1959 ± 203	318 ± 23	83 ± 2	171 ± 11	1.4 ± 0.3
UHI 320-5-150	320 °C, 5h + 150 kGy	50 ± 1.5	2331 ± 141	372 ± 17	83 ± 4	125 ± 4	1.9 ± 0.3

Our current understanding of wear resistance in UHMWPE total joint implants is that radiation cross-linking leads to a decrease in wear by decreasing the plasticity of the polymer. Adhesive/abrasive wear occurs in UHMWPE when the polymer is plastically deformed along the principal direction of motion to such an extent that its strength in the transverse direction is reduced. When the material is subjected to stresses in directions other than the principal direction of motion, particles break from the surface, causing macroscopic wear. This explanation is corroborated by a plasticity induced damage layer preceding wear damage on implant surfaces [21]. Thus, radiation cross-linked UHMWPEs with decreasing plasticity, as measured by the tensile elongation-at-break (EAB), have increased wear resistance [4].

Interestingly, high temperature melting increased the EAB of unirradiated UHMWPE to previously unprecedented levels, up to 1100% without significantly changing its wear properties [19]. As we hypothesized, despite irradiation after HTM decreasing EAB as a function of increasing radiation dose (Table 1), the resulting EAB values were higher than those of irradiated PEs without previous HTM. More interestingly, despite having high plasticity due to increased EAB (Fig. 5) and decreased cross-link density (Fig. 3), the irradiated HTM-PEs showed remarkably low wear rates compared to the irradiated PEs without HTM (Fig. 6). We attribute this to the modified cross-link structure of the irradiated HTM-PEs, as mentioned above, and to the increased integrity of the semi-crystalline polymer network due to the inter-granular diffusion of the polymer chains during HTM. Both of these may contribute to providing restraints to the local plastic deformation and presumably also contribute to the UTS of irradiated HTM-PEs not being affected by changes in cross-link density (Fig. 7).

Further information can be gained on the cross-linked structure by observing the effects of the cross-links on crystallization. In the first heat thermogram, the irradiated HTM-PEs did not show any shoulders (Fig. 10b) that are usually observed for high dose irradiated UHMWPEs (Fig. 10a), indicating that the irradiation of HTM-PEs did not generate additional thin crystalline lamellae. Further, the single crystallization peak of irradiated HTM-PEs in contrast to the double peaks observed in irradiated PEs (Fig. 11a and b) implies that the cross-links are distributed homogeneously in irradiated HTM-PE and do not influence the crystallization thermodynamics and kinetics as significantly. This was also supported by the thermal behavior during the second heat where irradiated PEs showed broadened melting peak with increasing dose with a shoulder at the low temperature side (Fig. 12a). In contrast, the irradiated HTM-PEs did not show broadening behavior and the melting peak shifted slightly to the low temperature side with increasing dose (Fig. 12b), indicating that the chains folded into thinner lamellae during cooling from the melt. It is likely that both the enhanced inter-granular chain entanglements by HTM [19] and the cross-links work together to constrain the chains from forming thick lamellae.

The toughness of irradiated HTM-PEs, as measured by IZOD impact strength testing (Fig. 8) and tensile work-to-failure (Fig. 9), showed a strong dependence on cross-link density. The low cross-link density of irradiated HTM-PEs (Fig. 3) was presumably a strong factor in their improved toughness. Interestingly, at the same cross-link density, the WF of irradiated HTM-PEs was lower than that of irradiated PEs without HTM (Fig. 9). This may be due to the crystallinity of the irradiated HTM-PEs with equivalent cross-link density being lower than those of irradiated PEs without HTM (54–57% compared to 60–62%, respectively; Fig. 3 and Table 1).

If we compare the irradiated HTM-PEs to the irradiated PEs from the perspective of their potential as joint implant bearing surfaces, wear resistance is perhaps the most important property. The POD wear rate for 100-kGy irradiated and melted UHMWPE, which is the most wear resistant clinically available UHMWPE is 1.6 mg/MC tested in the same setup [4]. For the UHMWPEs in this study showing wear rates less than 2 mg/MC (Table 2), the WF of the irradiated HTM-PEs were improved up to 50%, the impact strength was improved 34% and the EAB was improved up to 28% without detrimental changes to the UTS compared to 150-kGy irradiated PE without HTM.

One limitation of this wear resistant UHMWPE with improved toughness is that it is not stable against oxidation. Radiation-induced free radicals that are trapped in the crystalline regions of the polymer [22] can cause oxidation in the long-term [23]. Two methods, i.e., post-irradiation melting [5,24] and incorporation of antioxidants [7,25,26], can be used to stabilize these residual free radicals to produce oxidatively stable UHMWPE for clinical applications. Our current efforts are toward stabilizing radiation cross-linked HTM-PE against oxidation.

5. Conclusion

Radiation cross-linking of UHMWPE with pre-irradiation high temperature melting at around 300 °C resulted in improved toughness without sacrificing wear resistance. Chain scission and enhanced inter-granular entanglements by high temperature melting improved the toughness of UHMWPE prior to irradiation, which in turn compensated for some of the loss in toughness after irradiation. As a result, irradiated HTM-PE achieved a POD wear rate of 2 mg/MC with approximately 30% increase in toughness compared to irradiated UHMWPE without HTM.

Acknowledgment

This research was supported by a laboratory funds.

References

[1] Vessely MB, Whaley AL, Harmsen WS, Schleck CD, Berry DJ. Clinical Orthopaedics and Related Research 2006;452:28–34.
[2] Kurtz SM, Ong K, Lau E, Mowat F, Halpern M. Journal Bone Joint Surgery British 2007;89:780–5.
[3] Bozic KJ, Kurtz SM, Lau E, Ong K, Vail TP, Berry DJ. Journal of Bone and Joint Surgery-American Volume 2009;91A(1):128–33.
[4] Muratoglu OK, Bragdon CR, O'Connor DO, Jasty M, Harris WH, Gul R, et al. Biomaterials 1999;20(16):1463–70.
[5] Muratoglu OK, Bragdon CR, O'Connor DO, Jasty M, Harris WH. Journal of Arthroplasty 2001;16(2):149–60.
[6] Oral E, Malhi A, Muratoglu O. Biomaterials 2006;27:917–25.
[7] Oral E, Wannomae KK, Hawkins NE, Harris WH, Muratoglu OK. Biomaterials 2004;25(24):5515–22.
[8] Oral E, Rowell SL, Muratoglu OK. Biomaterials 2006;27:5580–7.
[9] Costa L, Carpentieri I, Bracco P. Polymer Degradation and Stability 2009; 94(9):1542–7.
[10] Wu JJ, Buckley CP, O'Connor JJ. Biomaterials 2002;23:3773–83.
[11] Doi M, Edwards SF. The theory of polymer dynamics. Oxford: Clarendon; 1986.
[12] de Gennes P-G. Scaling concepts in polymer physics. 4 ed. Ithaca: Cornell University Press; 1979.

[13] Rastogi S, Lippits DR, Peters GWM, Graf R, Yao Y, Spiess HW. Nature Materials 2005;4:635.
[14] Buckley CP, Wu J, Haughie DW. Biomaterials 2006;28:3178–86.
[15] Gul RM, McGarry FJ, Bragdon CR, Muratoglu OK, Harris WH. Biomaterials 2003;24:3193–9.
[16] Gul RM, McGarry FJ. Polymer Engineering and Science 2004;44:1848–57.
[17] Haughie DW, Buckley CP, Wu J. Biomaterials 2006;28:3875–81.
[18] Bragdon CR, Jasty M, Elder J, Lowenstein J, Harris WH. Types of fusion defects in UHMWPE polyethylene and their role in wear in vivo. Atlanta: Orthopaedic Research Society; 1996. 42nd Annualing Meeting.
[19] Fu J, Ghali B, Lozynsky AJ, Oral E, Muratoglu OK. Polymer 2010;51(12):2721–31.
[20] Bragdon CR, O'Connor DO, Lowenstein JD, Jasty M, Biggs SA, Harris WH. Journal of Arthroplasty 2001;16(5):658–65.
[21] Edidin AA, Pruitt L, Jewett CW, Crane DJ, Roberts D, Kurtz SM. Journal of Arthroplasty 1999;14(5):616–27.
[22] Bhateja S, Duerst R, Aus E, Andrews E. Journal of Macromolecular Science-Physics 1995;B34(3):263–72.
[23] Jahan M, MCKinny K. Nuclear Instruments and Methods in Physics Research B 1999;151:207–12.
[24] Shen FW, McKellop H, Salovey R. Crosslinking of polyethylene for low wear using readiation and thermal treatments. United States: The Orthopedic Hospital and University of Southern California; 2001.
[25] Oral E, Godleski Beckos C, Malhi AS, Muratoglu OK. Biomaterials 2008; 29(26):3557–60.
[26] Wolf C, Maninger J, Lederer K, Fruhwirth-Smounig H, Gamse T, Marr R. Journal of Materials Science: Materials in Medicine 2006;17:1323–31.

Polymer 52 (2011) 1163–1171

Contents lists available at ScienceDirect

Polymer

journal homepage: www.elsevier.com/locate/polymer

Structure and dynamic mechanical properties of highly oriented PS/clay nanolaminates over the entire composition range

Erik Dunkerley [a], Hilmar Koerner [b,c], Richard A. Vaia [b], Daniel Schmidt [a,*]

[a] Department of Plastics Engineering/Nanomanufacturing Center, University of Massachusetts Lowell, Lowell, MA 01854, USA
[b] Nanostructured and Biological Materials Branch, United States Air Force Research Laboratory, WPAFB, OH, USA
[c] UES Inc., Dayton, OH, USA

ARTICLE INFO

Article history:
Received 24 November 2010
Received in revised form
21 December 2010
Accepted 1 January 2011
Available online 9 January 2011

Keywords:
Nanocomposite
Nanolaminate
Dynamic mechanical analysis

ABSTRACT

A series of highly oriented model polymer/clay nanocomposites (nanolaminates) are prepared via a newly developed solvent deposition process with compositions ranging from neat polymer to neat organoclay. Morphology is analyzed via scanning electron microscopy (SEM) and wide-angle X-ray diffraction (WAXD) while thermogravimetric analysis (TGA) is used to confirm composition and solvent removal. Dynamic mechanical analysis (DMA) is used to examine the trends in stiffness and damping properties as the composition is shifted from polymer-rich to polymer-starved. The role of the organoclay modifier in determining the structure and properties of these nanolaminates is also reported. Experimental moduli are compared to relevant micromechanical models including Tandon–Weng and Halpin–Tsai. These comparisons allow for the identification of deviations from the behavior expected of conventional blends and composites, highlighting the effects of nanostructuration and the presence of the organic modifier on materials behavior.

1. Introduction

Polymer/platelet nanolaminates possessing a highly ordered bricks-and-mortar nanostructure promise a number of property improvements not usually seen together, including flame resistance [1], excellent barrier properties [2] and significant optical clarity [3]. Nanolaminates are created when a sufficiently high organoclay concentration induces intercalated organoclay tactoids to form a well-ordered layered structure without large organoclay-free domains. Due to the high aspect ratio and low percolation threshold of the platelets, the transition from nanocomposite to nanolaminate begins to occur at organoclay concentrations as low as 5 vol%, where geometric limitations preclude organoclay from existing in a randomly exfoliated state [4]. This work examines how platelet orientation and mechanical properties evolve as the organoclay content is increased and the structure approaches the critical concentration where just enough polymer is present to intercalate all platelet galleries.

Mechanical energy dissipation in organoclay nanocomposites originates from three interrelated sources: the chemical nature of the macromolecule/inorganic interface; molecular-level viscoelastic dissipation within the macromolecular phase; and kinematic deformation of the hierarchical morphology. These properties are all the more significant versus traditional composites due to the high internal interfacial area (>500 m^2/g) and refined spatial dimensions inherent to nanofillers. In addition to giving optical transparency, this refinement implies that the thickness of the constituent layers is comparable to the critical length-scales controlling viscoelastic dissipation processes in the polymer phase (e.g. distance between entanglements, size of secondary structure), causing fundamental changes in behavior [5,6]. The same three factors have also been implicated in the deformation behavior and toughness observed in lightweight, high performance natural systems [7] (sea urchin spines, bone [8], tooth enamel and nacre [9–11]). The presence of strong secondary inter- and intra-molecular interactions (hydrogen bonding, electrostatics) rather than covalent bonds also contributes to their incredible resilience, leading to a rich array of potential secondary and tertiary structures [12] and allowing energy dissipation via molecular hidden length and sacrificial bonds [13,14]. Examples of natural systems demonstrating hidden length and sacrificial bonds include silkworm and spider silk [15], the muscle protein titin [16] and elastin [17]. This hierarchy of structure and interactions (Van der Waals, electrostatic and covalent) enables a combination of reversible deformation and mechanical dissipation over a broad frequency range, enabling bond reformation and self-healing behavior.

Mimicking natural structures on the nanoscale has shown promise with respect to barrier [2] and mechanical properties

* Corresponding author. Tel.: +1 (978) 934 3451.
E-mail address: daniel_schmidt@uml.edu (D. Schmidt).

0032-3861/$ – see front matter © 2011 Elsevier Ltd. All rights reserved.
doi:10.1016/j.polymer.2011.01.006

[3,18], but creating scalable, high-rate nanomanufacturing processes that preserve those properties is challenging, and the degree of exploration and exploitation of interfacial interactions and dynamics has been very limited. Much of the work along these lines has focused on the use of high aspect ratio organoclays. In particular, organically modified montmorillonite has been found to be very convenient to work with. Montmorillonite (MMT) is a high aspect ratio 2:1 phyllosilicate that is part of the smectite family. It consists of stacks of crystalline platelets, with each platelet being composed of two sublayers of tetrahedral silica sandwiching a sublayer of aluminium magnesium hydroxide [19]. The untreated (sodium) organoclay is highly hydrophilic and can be dispersed in water based systems as-is. For compatibility with organic systems, however, the platelet surfaces must be modified, typically with quaternary ammonium salts [20]. The high aspect ratio and modulus (commonly assumed to be similar to the 160 GPa estimated for isostructural phyllosilicate layers [21]) MMT makes it an ideal reinforcing agent for polymer nanocomposites.

As it is one of the most well studied polymers available, polystyrene (PS) was chosen for this work. It was paired with dimethylditallowammonium-modified montmorillonite (DMDT-MMT), also readily available and with known compatibility with non-polar solvents [22–24] as well as a large number of polymers including polystyrene [25–35]. While work has been done on intercalated PS/DMDT-MMT nanocomposites, it has generally focused on melt blending [26], in situ polymerization [25,31] or emulsion polymerization [27,33] as a means of preparing materials with much lower organoclay contents than some of those described here. The aforementioned work, however, does provide useful context for our lower organoclay content samples.

Here, a series of materials are prepared, ranging from neat polymer to neat organoclay and possessing a well-organized nanostructure. The changes in morphology as organoclay content is increased to the extreme are characterized via wide-angle X-ray diffraction (WAXD) and scanning electron microscopy (SEM), and related to the thermomechanical properties via comparisons with the results of dynamic mechanical analysis (DMA). Alpha transition behavior over a wide range of organoclay contents is examined and used to demonstrate the existence of multiple phases within the nanolaminates. In addition to identifying the material as a semi-miscible blend, the transition data can be used to identify the phases present. With respect to mechanical properties, based on the morphology of these materials the Tandon–Weng and Halpin–Tsai are chosen as the most relevant models describing composite stiffness. While these models fail to account for several factors, including particle–particle interactions, non-linear elasticity, platelet orientation and non-uniformity, etc, their application nevertheless provides useful information regarding the extent to which the behaviors of these materials are captured by classical micromechanical modeling. In order to enhance the value of this comparison, platelet orientation is accounted for by calculating a weighted average of each model's upper and lower bounds based on the Hermans orientation parameter, as obtained from WAXD experiments.

The results of these investigations have important ramifications for organoclay nanocomposite systems in general. Recent work concerning the role of tactoid size in predicting the mechanical properties of a nanocomposite has shown that the number of layers within a tactoid can affect nanocomposite properties [36]. Accurately measuring the properties of the tactoids themselves, however, is difficult due to their size. Nanolaminates are analogous in both composition and structure to the intercalated tactoids found in the vast majority of organoclay nanocomposites, and allow for a direct assessment of the properties of these important substructures.

2. Experimental

2.1. Sample preparation

Cloisite 20A, a dimethylditallowammonium-modified montmorillonite (DMDT-MMT) from Southern Clay Products (powder), and polystyrene #845 (PS, $M_w = 190{,}000$ g/mol, pellets) from Scientific Polymer served as the basis for the materials described here, the characteristics of the latter being typical of commercial polystyrene resins. All mixtures consisted of 1 part total solids per 25 parts solvent (by mass) in toluene. The concentrations of clay and polymer as a function of total solids were expressed in volume percent, and varied in 10 vol% increments from 0 to 100 vol% DMDT-MMT. In a typical preparation, DMDT-MMT was added to toluene and the mixture was stirred for at least 24 h by magnetic stirrer to ensure complete dispersion. After the mixture was examined to confirm the expected level of clarity and lack of visible particulate matter, the polymer was added and stirring continued until dissolution was complete.

Films were formed by spraying the resultant mixture onto a polymeric substrate. Fluorinated ethylene propylene (FEP) film was chosen as the substrate material due to its excellent solvent resistance and release characteristics. A standard air powered spray gun (Husky HDS550) with a 1.8 mm (0.071 in) nozzle ID was used to atomize the solution and apply it to the film, which was mounted on a rotating drum. For the film to have enough strength to be demolded in one piece, multiple coats were applied to build up the film thickness to between 50 and 200 μm. Following completion of all coating cycles, samples were dried at 125 °C for 4 h in a convection oven to remove residual solvent and relieve any residual stresses trapped during film formation. Thermogravimetric analysis was then immediately performed to ensure all solvent was removed and to confirm the film composition. Finally, samples were conditioned at 50% humidity for at least 48 h prior to testing to ensure equilibrium moisture content and repeatability of the results.

2.2. Scanning electron microscopy (SEM)

Cross-sectional scanning electron micrographs were taken to ascertain film thickness and composite morphology. Films were fractured to expose their cross-sections and subsequently mounted vertically, fractured cross-section up, in a custom-built SEM holder. The film cross-sections were observed in a high-resolution field emission scanning electron microscope (JEOL JSM-7401F). All samples were coated with gold–palladium using a desktop gold sputter coater and imaged with an accelerating voltage of 2.0–5.0 kV.

2.3. Wide-angle X-ray diffraction (WAXD)

Wide-angle X-ray diffraction (WAXD) measurements were performed using a Statton box camera and Cu K_α radiation generated with a Rigaku ultraX18 system. The sample to detector distance was set to 193 mm for all samples unless otherwise noted. The detector consisted of a reusable X-ray sensitive image plate that was scanned to create a two-dimensional digital image of the X-ray diffraction pattern. All samples were mounted edge-on, with the beam parallel to the plane of the film, and analyzed under vacuum to minimize scattering due to air. The 2D diffraction patterns were analyzed using FIT2D v12.077 for Windows to produce radial 2 theta and azimuthal integration plots in order to quantify interlayer spacing and degree of orientation utilizing Bragg's law and the Hermans orientation parameter, respectively. Interlayer spacings were calculated from the first order diffraction peaks observed. Hermans orientation parameters were calculated based on azimuthal scans of the second order diffraction peak [37]. To correct for slight experimental

variations, all radial integration data was normalized to the minimum observed intensity prior to the first peak before peak area and full width at half maximum was calculated.

2.4. Thermogravimetric analysis (TGA)

Thermogravimetric analysis was conducted on each batch of material using a TA Instruments Q50 thermogravimetric analyzer (TGA). For all tests a platinum pan was used, and samples were heated at 20 °C/min to a maximum temperature of 850 °C. The non-volatile content was compared to the theoretical inorganic clay content for each sample, accounting for dehydroxylation of the clay during analysis, to assess deviations from the desired composition.

2.5. Dynamic mechanical analysis (DMA)

Dynamic mechanical analysis was performed on each composition using a TA Instruments Q800 dynamic mechanical analyzer (DMA). All tests used a standard tension fixture for films. All samples were cut to a width of approximately 4 mm with thicknesses ranging from 50 to 200 μm and clamped at a length of approximately 8 mm. All films were cut so that the strain axis was in the film plane. A preload stress of 250 kPa was applied to each sample during the testing. The samples were conditioned at −100 °C for 12 min, then heated to 120 °C at a rate of 3 °C/min while testing in multi-frequency, controlled strain mode using an amplitude of 10 μm and a frequency of 1.0 Hz. The thermal transition temperatures of the polymer and modifier were determined via deconvolution of the strongest loss modulus and storage modulus derivative peaks (derivative taken with respect to temperature) using a Gaussian model. In the case of the loss modulus peaks in particular, Gaussian and asymmetric double sigmoidal fits were used for samples containing less than 40 vol% organoclay due to the asymmetric shape of the loss modulus peak associated with the neat polymer. Along the same lines, an asymmetric double sigmoidal fit was also used for analysis of the storage modulus derivative peak observed for the pure polymer film [38].

3. Results and discussion

Following film formation, TGA was performed to confirm the compositions of the hybrids. Overall the experimental compositions were found to vary by at most 1% from the theoretical values. While subsequent discussions will reference the DMDT-MMT content in vol% as a means of identifying the samples, volume fraction of inorganic material is the relevant composition variable as far as mechanical modeling is concerned. This can be calculated as shown in Eqs. (1a) and (1b), where V denotes volume fraction, M denotes mass fraction, and ρ denotes density. The subscripts i, oc and p refer to inorganic, organoclay and polymer fractions or densities, respectively, while the superscripts oc and c refer to fractions in the organoclay and composite, respectively. The overall expressions are as follows, with Eq. (1a) being useful for predicting inorganic content based on organoclay content and Eq. (1b) being useful for calculating inorganic content based on inorganic residue measured via TGA:

$$V_i^c = V_{oc}^c V_i^{oc} = \left(\frac{\frac{M_{oc}^c}{\rho_{oc}}}{\frac{M_{oc}^c}{\rho_{oc}} + \frac{M_p^c}{\rho_p}}\right)\left(\frac{M_i^{oc}\rho_{oc}}{\rho_i}\right) \quad (1a)$$

$$V_i^c = \left(\frac{\frac{M_i^c}{\rho_i}}{\frac{M_{oc}^c}{\rho_{oc}} + \frac{M_p^c}{\rho_p}}\right) \quad (1b)$$

In this work we take ρ_{oc}, ρ_p and ρ_i to be 1.77 g/cm^3, 1.05 g/cm^3, and 2.86 g/cm^3, based on manufacturer data for the densities of DMDT-MMT, polystyrene and unmodified MMT (Southern Clay Products Cloisite Na$^+$), respectively.

Having confirmed their compositions, identifying the morphology of these materials represents the next critical step in understanding how the observed thermomechanical properties come to be. To that end, the samples were characterized using WAXD by performing both radial and azimuthal integrations of the two-dimensional wide-angle diffraction patterns obtained, as shown in Fig. 1.

The first observation is that with the addition of just 10 vol% of polystyrene, the interlayer spacing increases from an unintercalated $d_{neat} = 24.2$ Å to about 30.8 Å as shown in Fig. 2. As the amount of polystyrene increases, the shift in the first order diffraction peak increases from 30.8 Å at 90 vol% DMDT-MMT to a plateau value of $d_{composite} = 33.7 \pm 0.1$ Å over the rest of the composition range. This matches well with previous studies of PS/DMDT-MMT composites reporting interlayer spacings of between 32 and 34 Å depending on concentration and processing method [26]. Knowledge of the interlayer spacing at complete intercalation

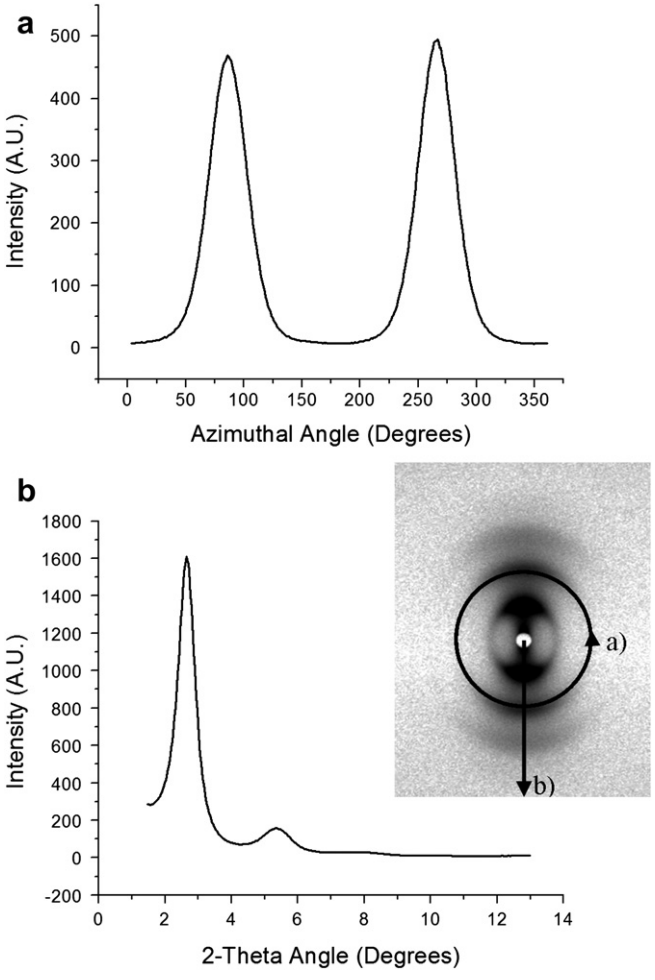

Fig. 1. (a) Sample azimuthal and (b) radial integrations of 2D WAXD data (inset) for a nanolaminate containing 60 vol% organoclay.

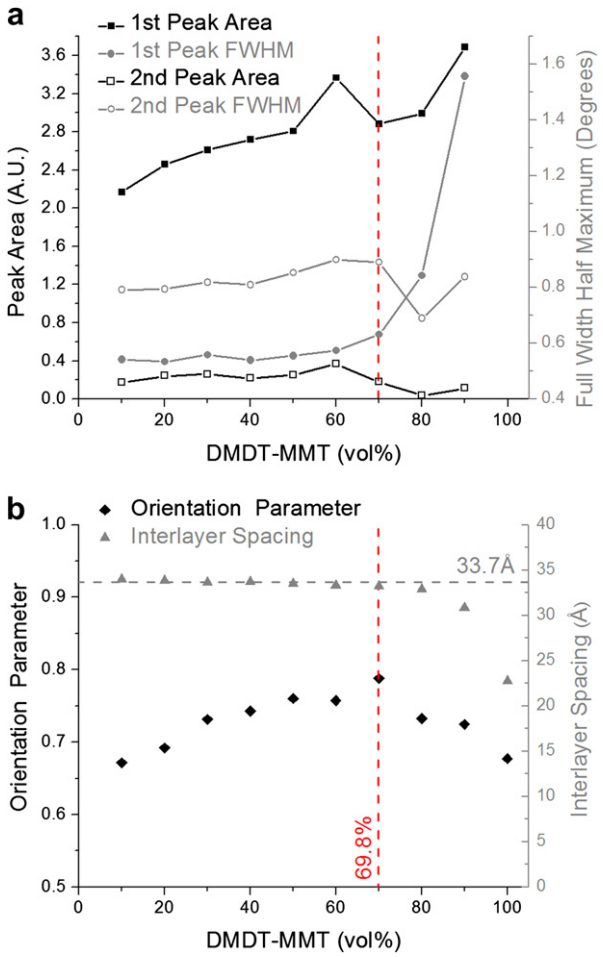

Fig. 2. (a) Variations in the Hermans orientation parameter and interlayer spacing (via WAXD) as well as (b) peak area and full width at half maximum (FWHM) versus nanolaminate composition. The composition corresponding to complete intercalation of all silicate layers with no excess polymer outside of the interlayer galleries is marked in red. (For interpretation of the references to colour in this figure legend, the reader is referred to the web version of this article).

allows the polymer concentration required to fill all of the organoclay galleries to be estimated via Eq. (2), yielding a critical volume concentration (CVC) of 30.2 ± 0.2 vol% PS (69.8 vol% DMDT-MMT).

In parallel with these changes in interlayer spacing, the areas of the first and second order diffraction peaks gradually increase with increasing organoclay content until an organoclay content of 60 vol % is reached. Beyond this point, while the shape of the curves remains similar, the trends diverge to some extent. First order peak area continues to grow overall, consistent with an increase in the concentration of diffracting clay domains. At the same time, second order peak area shows an overall decreasing trend, consistent with an increase in the level of disorder associated with the aforementioned clay domains. This demonstrates that (second order) peak area and orientation track with each other to a certain extent, as would be expected given the geometry of the diffraction experiment. This maximum in peak area also corresponds closely to the critical concentration of polymer required for full intercalation, as shown in Fig. 2 and is consistent with the morphological changes expected in these systems when deviating substantially from this concentration. At organoclay concentrations significantly above the CVC, a mixture of two types of diffracting domains (intercalated vs. non-intercalated) will tend to reduce the average correlation length and also increase the full width at half maximum as shown in Fig. 2, FWHM, as compared to the fully intercalated case and as observed in the FWHM data. At organoclay concentrations significantly below the CVC, on the other hand, the reduced organoclay content alone will reduce the number of diffracting domains, with further reductions in peak area, but not necessarily in FWHM, expected due to the increasing freedom of tactoids to misorient.

$$\mathrm{CVC} = 100\left(\frac{d_{\mathrm{composite}} - d_{\mathrm{neat}}}{d_{\mathrm{composite}}}\right) \tag{2}$$

Looking at Hermans orientation parameter [39] as a function of composition (Fig. 2) it is observed that the orientation of the platelets is highest at the CVC (69.8 vol% designated by vertical line) and decreases at both higher and lower organoclay contents. This is a logical result given that the platelets have an increasing tendency to organize in a parallel fashion when their concentration increases, but will become less well-organized (due to local variations in interlayer spacing) if the organoclay content exceeds the point where complete intercalation is possible. When the organoclay content is low, however, polymer chains screen inter-platelet interactions and the layers with sufficient room to form less well-oriented structures as shown in Fig. 3.

Moving from WAXD to SEM, while the images shown in Fig. 4 probe different length-scales than the WAXD results, they nevertheless support the conclusion that disorder increases when departing from the CVC. In particular, the most well-ordered samples appear to be those in Fig. 4b and c (80 vol% and 60 vol%, respectively). In contrast, the 100 vol% sample (Fig. 4a) displays significant undulations in platelet orientation and the 10 vol% sample (Fig. 4d) shows further disorientation. In spite of these observations, the overall layered structure and a significant level of orientation are maintained in all nanolaminates.

3.1. Mechanical properties – dynamic mechanical analysis

Considering storage modulus first, a gradual increase is observed with increasing organoclay concentration at all temperatures (Fig. 5a). Above 50 vol% organoclay the data becomes more variable, with 90 vol% organoclay giving the maximum storage modulus value observed. This indicates that even a small amount of polymer present in an intercalated state greatly improves stiffness. We propose that, while higher inorganic content enhances modulus, a minimum amount of polymer is necessary for effective stress inter-platelet transfer, leading to this result.

Considering the loss modulus data, the disappearance of the bulk PS E'' peak is noteworthy. This begins at 10 vol% organoclay (as indicated by the slight shoulder on the PS alpha transition shown in

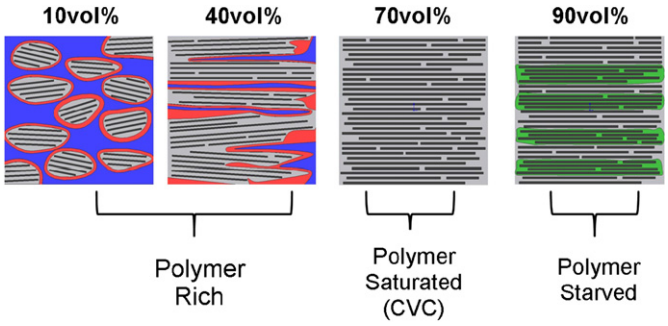

Fig. 3. Schematic of structures with PS/DMDT-MMT composites; blue designates "bulk" polystyrene, red designates polystyrene in close proximity to the organoclay tactoids, grey designates the interphase and green designates the unintercalated organoclay phase. (For interpretation of the references to colour in this figure legend, the reader is referred to the web version of this article).

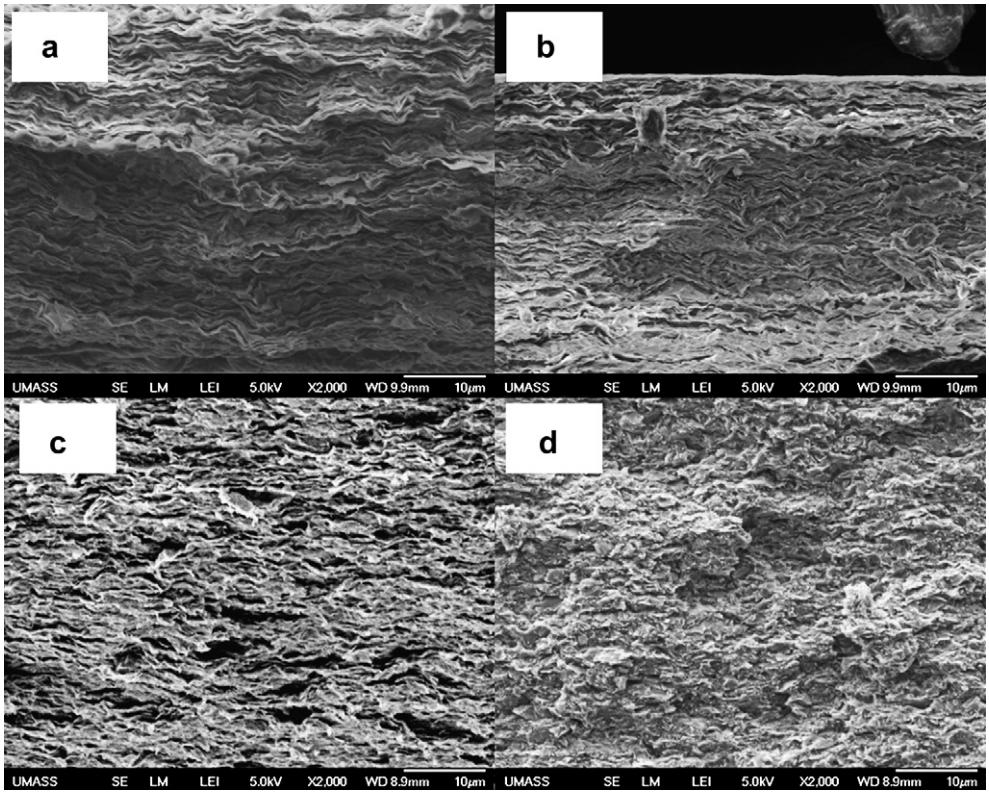

Fig. 4. SEM images of fractured edges of nanolaminate films containing (a) 100 vol% organoclay; (b) 80 vol% organoclay (c) 60 vol% organoclay and (d) 10 vol% organoclay.

Fig. 5b) and is ostensibly complete by 50 vol% organoclay, leaving only the modifier and intercalated PS peak(s). As organoclay content increases in this range, the PS alpha transition becomes weaker and weaker and the aforementioned shoulder develops into a second peak (assigned to the organoclay modifier) which becomes stronger and stronger. This peak shift is likely related to chain confinement and mixing of the polymer and modifier chains. This is consistent with our proposed schematic of these systems (Fig. 3). In a polymer-rich system, some polymer is far enough from the organoclay layers to present bulk-like behavior. Increases in organoclay concentration increase the fraction of polymer at or near an interface with the organoclay, with material behavior and properties evolving towards those of the fully intercalated system. In parallel, increases in layer content and orientation cause the storage modulus to increase beyond that of the pure polymer. The simultaneous increase in loss modulus at higher organoclay contents may be explained by an increase in the number of mechanically lossy polymer/clay interfaces present in the system, given the weak interactions present. At 60 vol% organoclay, domains of unintercalated polymer are no longer a significant part of the sample, and beyond this point the modifier/intercalated polymer peak continues to grow and shift towards the transition observed in the neat organoclay. This peak also narrows until a maximum loss modulus is reached at 70 vol% organoclay. This is likely because further increases in organoclay content actually reduce the number of polymer/organoclay interfaces present, thus decreasing mechanical loss.

The next feature to discuss is a loss modulus peak that occurs at approximately −25 °C. This peak is non-existent in the pure polymer and pure organoclay, but appears most noticeably between 40 and 70 vol% organoclay and displays a maximum amplitude at 70 vol% organoclay. One explanation for this peak would be a shifted beta or gamma transition. The reported values for the beta and gamma transitions of PS are 27 °C and −135 °C, respectively [40]. Therefore, for this explanation to be accepted, the chain dynamics must have been significantly affected by intercalation-induced confinement and/or interactions between the polymer and the organoclay surface. For the beta transition this would imply local density variations giving excess free volume in the vicinity of the styrene rings, enhancing their mobility. For the gamma transition, this would imply strong polymer/organoclay interactions and/or local increases in density, resulting in reductions in molecular mobility. Other possible explanations include water/organoclay, modifier/polymer or modifier/solvent interactions. This last possibility is unlikely, however, since TGA confirms the removal of all trace solvents prior to DMA testing. More work is needed to positively identify the origin of this transition.

The final feature of note is the increase in loss modulus at −100 °C for organoclay concentrations above 50 vol%. This appears to be the start of another low temperature transition, but one that cannot be associated with the polymer given its observation in the 100% organoclay sample. One possible explanation is that this transition is caused by trace amounts of confined water undergoing a depressed thermal transition [41].

3.2. Thermal transitions

The observations concerning the loss modulus peaks associated with intercalated polymer and organoclay modifier may be explained by interactions between the two. The thermal transition of the DMDT-MMT in particular has been observed before via DSC [42], while other studies have demonstrated that similar organic modifiers on silicate surfaces can undergo thermal transitions from an ordered/solid-like state to a disordered/liquid-like state, as measured via DSC, FTIR and WAXD measurements [43,44]. Although the appearance of a detectable thermal transition will

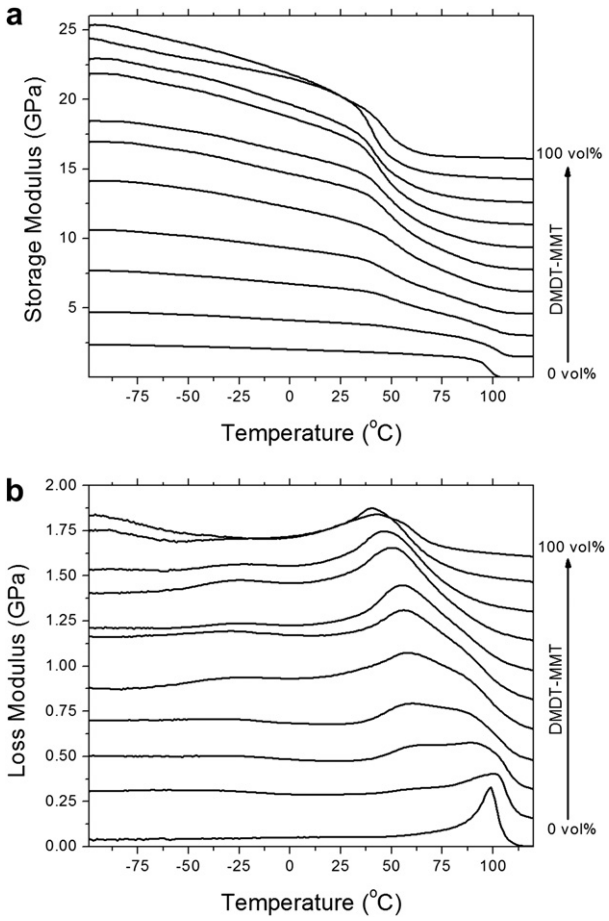

Fig. 5. DMDT-MMT/PS nanolaminate DMA (a) storage modulus and (b) loss modulus data as a function of temperature and composition.

depend on modifier chemistry, structure and grafting density [45], as well as the physical basis for the measurement being performed, the effects of such transitions on mechanical properties cannot be ignored. While such shifts are often system- and interaction-dependent and make defining general rules difficult, previous work has shown T_g shifts to higher values with the addition of unmodified organoclay [19,27,46] while depressed T_g values have been observed in some systems based on modified organoclays [47–49]. Cases of upward shifts in T_g are often ascribed to confinement effects on the polymer chains resulting in higher energy being required to induce rotation of the polymer molecules, while cases of depressed T_g values are often attributed to plasticization by the modifiers, with both effects potentially explained by local density variations as well.

The shoulders observed in the loss modulus peaks at lower clay contents, however, suggest a more complex explanation, namely the presence of multiple phases within our materials. We propose that this system can be described by considering four main phases over the entire composition range, as shown in Fig. 3. Below the CVC of 69.8 vol% the material should consist of unintercalated ("bulk") PS that is well-separated from and unaffected by the modifier chains, unintercalated PS that is in close proximity to the organoclay tactoids and affected by the modifier chains, and interphase material consisting of a mixture of modifier and PS in the organoclay galleries. Above the CVC the bulk PS phase cannot exist and the material instead consists of a combination of interphase material and an unintercalated organoclay phase. The WAXS analysis has demonstrated the unintercalated and intercalated interlayer spacings to be fixed quantities, implying that the composition of the interphase is constant. In particular, based on the unintercalated and intercalated interlayer spacings in this system, the composition of the interphase can be estimated to be approximately 60 vol% DMDT, 40 vol% PS, and should produce a relatively invariant thermal transition temperature due to the unavoidable mixing of modifier chains and polymer molecules. Similarly, the bulk PS and unintercalated organoclay phases should also display relatively invariant thermal transition temperatures. In contrast, the unintercalated PS fraction in close proximity to the organoclay tactoids should display a composition-dependent transition temperature. As the organoclay content is increased, the size of the unintercalated PS domains decreases, and a greater and greater fraction of the unintercalated PS will be brought into close contact with the modifier chains present on the exterior of the intercalated organoclay tactoids, causing additional mixing and a shift in the thermal transition of this material towards that of the interphase.

In support of these arguments, analysis of the full range of DMDT-MMT/PS compositions reported here are consistent with a multiphase structure, with clear trends observed in the most prominent storage and loss transitions with increasing organoclay content (Fig. 5). Deconvolution of the main loss modulus peaks via model fits found to work well with DMA results [38] yields a best fit with two separate peaks for each of the nanolaminate samples (Fig. 6a). Based on the transition temperatures observed at low and

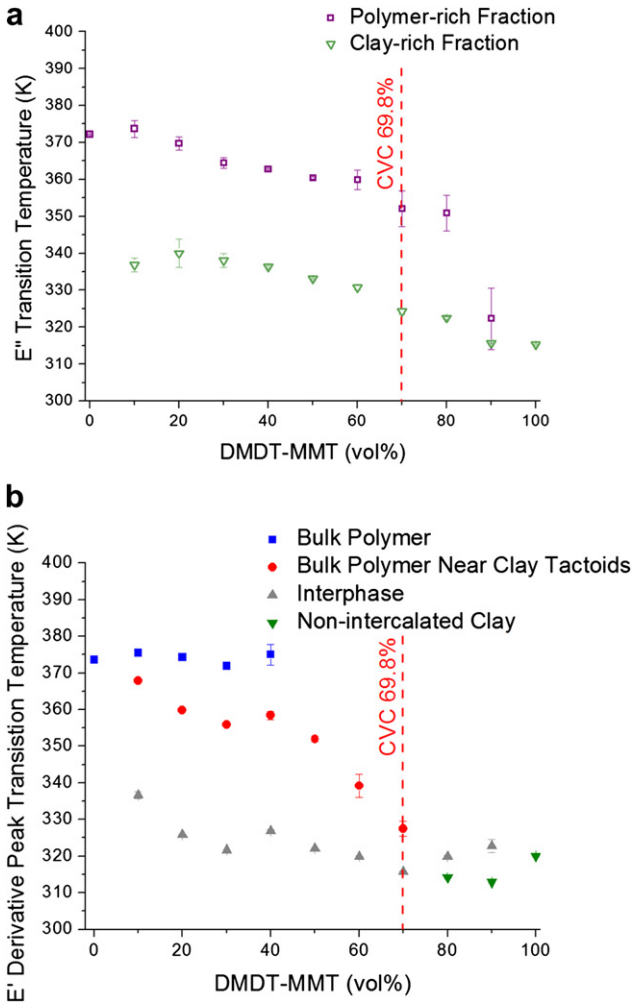

Fig. 6. Transition temperatures in the DMDT-MMT/PS system assessed via dynamics mechanical analysis (DMA) according to the (a) deconvoluted E″ peaks and (b) deconvoluted E′ derivative peaks.

high organoclay contents, these peaks can be assigned to the transition temperatures of the polystyrene-rich and modifier-rich fractions. The peak corresponding to the PS-rich fraction in this case represents not only bulk PS but also unintercalated PS in close proximity to the organoclay, explaining the gradual shift in the transition temperature of the PS-rich phase with composition, up to the point where the CVC is reached. Over the same range of compositions, the transition temperature of the modifier-rich phase is higher than what was observed for neat DMDT-MMT but remains relatively constant with increasing organoclay content until the CVC is reached, consistent with the idea of an interphase with an invariant transition temperature. Above the CVC, the system becomes polymer-starved and the modifier peak is influenced by both intercalated and unintercalated regions, shifting from the interphase transition temperature to that of the neat DMDT-MMT as a result. Consistent with this picture, the peak associated with the PS-rich fraction shows a significant shift above the CVC to the interphase transition temperature as all of the PS present becomes intercalated material.

This picture of nanolaminate behavior was further confirmed via analysis of the first derivative of the storage modulus, which was found to be more sensitive to the presence of minority phases than the loss modulus data. In particular, the storage modulus derivative peaks, as shown in Fig. 6b were found to deconvolute into up to three separate peaks, corresponding to the bulk polystyrene, the polystyrene in close proximity to the clay, and the modifier-rich phase. In the case of the bulk polystyrene peak, no shift was observed with composition until an organoclay concentration of 50 vol% was reached, at which point the peak disappeared entirely, consistent with the disappearance of bulk polystyrene from the system. In contrast, the peak assigned to polystyrene in close proximity with the organoclay was found to shift in a similar manner to what was observed for the PS-rich phase in the loss modulus data, approaching the thermal transition temperature of the organoclay modifier up until the CVC was exceeded, where this peak disappeared as well and the system transitioned to a polymer-starved state. Similar observations were made by Manias et al. in their DSC study of PS/DMDT-MMT composites [50]. Above the CVC, only two peaks were found to be present, representing the interphase and the unintercalated organoclay phase. In both cases the peak transition temperatures were found to remain relatively constant as would be expected given the constant compositions of these phases. The presence of the observed peaks and trends supports the proposed structure for this type of nanocomposite system.

3.3. Mechanical modeling

Storage moduli at 25 °C were compared to predictions of the Voigt, Reuss, Halpin–Tsai and Tandon–Weng models. The temperature of 25 °C was chosen both as a typical environmental temperature and because it is below all of the transition temperatures assigned to the various phases present based on the aforementioned DMA analysis. For comparison purposes, trends in storage moduli were also assessed at temperatures well below (−25 °C, −75 °C) and well above (120 °C) all measured thermal transitions. Model calculations were performed using the storage modulus measured for the neat polystyrene (0 vol% organoclay) sample prepared here, while the modulus of a single montmorillonite layer was assumed to be 160 GPa, the value reported for an isostructural montmorillonite layer [21]. At 25 °C and below, the actual storage modulus values for these materials consistently fell between the upper and lower limits of the Halpin–Tsai and Tandon–Weng models, as shown in Fig. 7, with the highest organoclay concentrations producing moduli approaching the lower limits of the Halpin–Tsai model. In contrast, at 120 °C the experimental storage moduli observed substantially exceed the upper limits of both the Halpin–Tsai and Tandon–Weng models for all but the lowest organoclay concentrations.

While the Halpin–Tsai and Tandon–Weng models are appropriate for conventional composites, the deviations from the model predictions observed in these organoclay composites may be

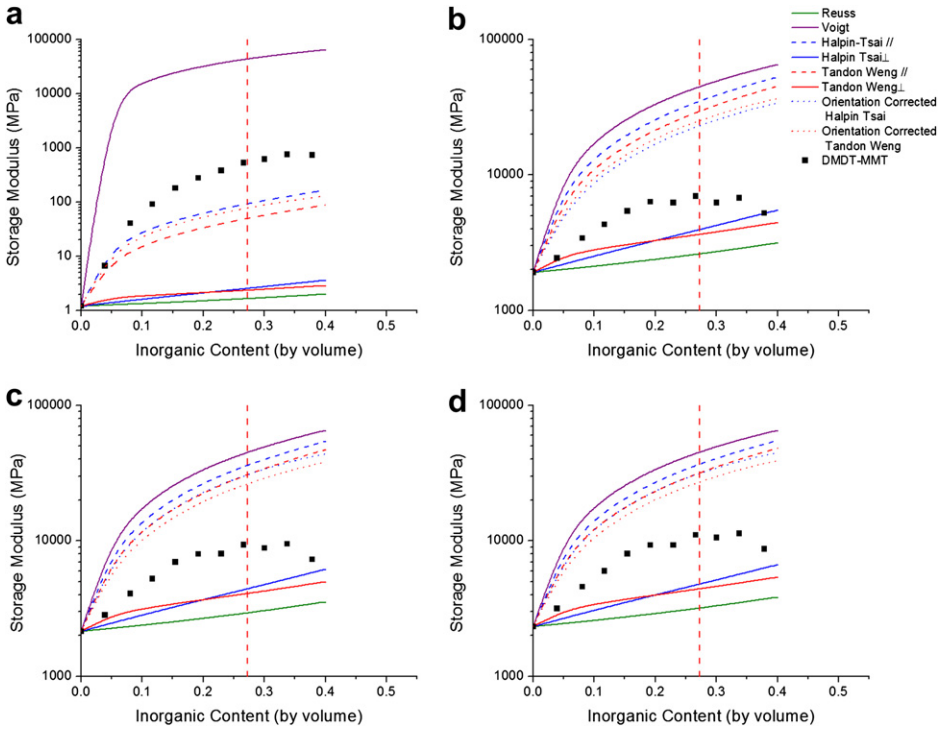

Fig. 7. Comparison of experimental storage modulus data to mechanical models for DMDT-MMT/PS nanolaminates at (a) 120 °C; (b) 25 °C; (c) −25 °C; and (d) −75 °C.

explained in several ways including deviations from the idealized composite morphology assumed in these models and the effects of variations in component properties as a function of hybrid structure and composition. The Halpin–Tsai and Tandon–Weng models both assume that the filler and matrix are isotropic, perfectly bonded, linearly elastic, and that the filler particles are perfectly aligned, anisotropic, uniform in size and shape, with particle–particle interactions neglected [51]. Many of these assumptions are inappropriate for the materials reported here. For instance, while the models assume uniform particles, the natural processes that create montmorillonite platelets produce a distribution of sizes and shapes, the numbers used for modeling being an average derived from that distribution. Likewise, the individual organoclay layers are anisotropic not only morphologically but compositionally as well making it unlikely that layer modulus is the same in all directions. Furthermore, the Hermans orientation parameter determined from X-ray diffraction indicates that while these nanolaminates are highly aligned, a degree of disorder is still present.

One means to account for the disorder is to use the Hermans orientation parameter, S, as a weighting factor and calculate a simple weighted average of the Halpin–Tsai or Tandon–Weng results for the storage modulus, E', as calculated when stress is applied parallel ($E_{\parallel}'$) or perpendicular ($E_{\perp}'$) to the plane of layer alignment, as indicated in Eq. (3) (where S is used to indicate the Hermans orientation parameter). The results of these estimates are shown in Fig. 7 as well (HS with orientation and TW with orientation). While weighted average moves closer to the data at 25 °C and below, the high orientation of the nanolaminate causes the parallel modulus estimates to dominate resulting in an overall prediction close to the upper bounds associated with each model. While incorporating the measured orientation parameters into such modeling efforts represents a clear and logical improvement over predictions assuming perfect alignment, it is equally apparent that the aforementioned assumptions associated with these models do not hold, and none of the aforementioned factors would seem to be able to account for the results observed at 120 °C. This comparison highlights the effects of details not captured by conventional models. It is important to note, however, that the deviations in modeled and observed moduli are fairly consistent as a function of organoclay content. This implies that mechanical behavior is dominated by a factor that does not substantially depend on transition temperature. One possible explanation for this at least at 25 °C and below would be screening of polymer/organoclay stress transfer by the bulky head-groups of the organoclay modifier, coupled with dilution of the polymer in the interlayer galleries by modifier tails, thus reducing the number of macromolecules available for stress transfer.

$$E' = \left(\frac{2}{3}\right)\left(S+\frac{1}{2}\right)E_{\parallel}' + \left(\frac{2}{3}\right)(1-S)E_{\perp}' \tag{3}$$

As the above discussion implies, another critical assumption that is clearly violated in these systems is that the particles are perfectly bonded. As the loss moduli observed in the nanolaminates are consistently higher than in either the polymer or the organoclay alone, it is clear that the interfaces in these materials are mechanically lossy. While this enhances the damping capacity of these materials, it certainly depresses the storage moduli, and is likely a major explanation of the differences between the experimental data and the model predictions at 25 °C and below. As further evidence that this is the case, we note that when a film is prepared using only unmodified (sodium) MMT, the storage modulus of this film is approximately 14.8 GPa, roughly an order of magnitude less than the reported modulus of a single mica sheet [52], due to the weak adhesion and poor stress transfer between adjacent MMT platelets.

Finally, while not typically stated, the aforementioned models make an additional major assumption, namely that two homogeneous materials are present – a polymer matrix and a high aspect ratio reinforcing phase – with well-defined properties. In contrast, our DMA analysis clearly shows that these materials consist of multiple distinct phases whose compositions and relaxation behavior vary considerably and whose properties are not always well-defined. The filler and organoclay modifier phases experience significant mixing, in addition to confinement effects (conformational restrictions, local density variations, changes in entanglement concentration) that alter the properties of the intercalated polystyrene chains vs. bulk polystyrene and give rise to the observed DMA data. In a film that includes no polystyrene matrix, that surfactant makes up approximately 62% of the volume of the material. The bulk of the modifier consists of long alkyl substituents and is therefore likely to have a storage modulus similar to that of paraffin wax, reducing the overall stiffness of the material. Likewise, since these alkyl substituents are always localized at interfaces where matrix to filler load transfer occurs, their effects on mechanical bonding are expected to be substantial. On the other hand, previous reports [34,53] on the broadening of the glass transitions in intercalated polystyrene may nevertheless provide a mechanism for the greatly enhanced moduli observed at 120 °C. Such broadening implies the coexistence of intercalated polystyrene chains with a distribution of thermal transitions, including some whose transition temperatures exceed the value for bulk polystyrene. It may be that the presence of small numbers of these less mobile chains at 120 °C results in an increase in modulus above and beyond what would otherwise be expected under these circumstances.

4. Conclusions

Experiments on nanolaminates demonstrate that even a rigid, poorly damping polymer such as polystyrene can be used in combination with modified organoclays to create stiff but highly damping materials. The storage and loss moduli increase with increasing organoclay content until the critical volume concentration of 69.8% is reached, at which point further increases are minimal. We also report DMA data showing variations in the alpha transition associated with the organoclay modifier, consistent with previous reports of a thermal transition observed in modified organoclays via DSC [42,54]. A more in-depth analysis of this data involving deconvolution of the loss modulus and storage modulus derivative peaks demonstrates that multiple phases exist within these materials that can be assigned to bulk polymer, polymer influenced by the organoclay, polymer that has been fully intercalated, and unintercalated organoclay, depending on whether the material in question is polymer-rich or polymer-starved. Comparing DMA storage modulus values with a range of mechanical models reveals that these materials fall short of the upper bonds of the Halpin–Tsai and Tandon–Weng predictions as well as orientation-corrected results from these approaches at 25 °C or lower, consistent with the proposition that these nanolaminates achieved their damping properties through the presence of many mechanically lossy interfaces. On the other hand, at elevated temperature (120 °C), the measured storage moduli substantially exceed the upper bounds of both of these models, again implying that significant factors exist that are not accounted for via traditional micromechanical treatments. As the properties of these nanolaminates reflect those of intercalated organoclay tactoids, these results have implications for polymer/organoclay nanocomposites in general.

Acknowledgments

We thank Gary Price and Scott Fillery at the United States Air Force Research Laboratory (WPAFB, OH) for assistance with XRD and SEM analysis and editing, as well as AFRL/RXBN for general support, assistance, and facilities access. We thank the NSF-sponsored Center for High-Rate Nanomanufacturing at UML for access to the thermal analysis equipment, the UML Baseball Research Laboratory for sample conditioning facilities, and the Department of Plastics Engineering for general support. Finally, we would like to thank the United States Air Force Laboratory and the Universal Technology Corporation for providing the financial support that made this work possible.

Appendix A. Supplementary data

Supplementary data associated with this article can be found, in the online version, at doi:10.1016/j.polymer.2011.01.006.

References

[1] Pavlidou S, Papaspyrides C. Prog Polym Sci 2008;33(12):1119.
[2] Jang W, Rawson I, Grunlan JC. Thin Solid Films 2008;516(15):4819.
[3] Podsiadlo P, Kaushik AK, Arruda Ellen M, Waas AM, Shim BS, Xu J, et al. Science 2007;318:80.
[4] Hbaieb K, Wang Q, Chia Y, Cotterell B. Polymer 2007;48(3):901.
[5] Winey KI, Vaia RA. MRS Bull 2007;32(4):314.
[6] Vaia RA, Wagner HD. Mater Today 2004;7(11):32.
[7] Smith BL, Schäffer TE, Viani M, Thompson JB, Frederick NA, Kindt J, et al. Nature 1999;399:761.
[8] Thompson JB, Kindt JH, Drake B, Hansma HG, Morse DE, Hansma PK. Nature 2001;414:773.
[9] Sarikaya M, Aksay IA. Results Probl Cell Differ 1992;19:1.
[10] Mayer G. Science 2005;310:1144.
[11] Katti KS, Katti DR. Mater Sci Eng C 2006;26(8):1317.
[12] Roder H. Proc Natl Acad Sci U S A 2004;101(7):1793.
[13] Fantner GE, Oroudjev E, Schitter G, Golde LS, Thurner P, Finch MM, et al. Biophys J 2006;90(4):1411.
[14] Fantner GE, Hassenkam T, Kindt JH, Weaver JC, Birkedal H, Pechenik L, et al. Nat Mater 2005;4(8):612.
[15] Shulha H, Po Foo CW, Kaplan DL, Tsukruk VV. Polymer 2006;47(16):5821.
[16] Vazina A, Lanina N, Alexeev D, Bras W, Dolbnya I. J Struct Biol 2006; 155(2):251.
[17] Lillie MA, Gosline JM. Int J Biol Macromol 2002;30(2):119.
[18] Tang Z, Kotov NA, Magonov S, Ozturk B. Nat Mater 2003;2(6):413.
[19] Vaia RA, Sauer BB, Tse OK, Giannelis EP. J Polym Sci B: Polym Phys 1997; 35(1):59.
[20] Jones TR. Clay Miner 1983;18:399.
[21] Zartman GD, Liu H, Akdim B, Pachter R, Heinz H. J Phys Chem C 2010;114: 1763.
[22] Vaia RA, Liu W, Koerner H. J Polym Sci B: Polym Phys 2003;41(24):3214.
[23] Ho DL, Briber RM, Glinka CJ. Chem Mater 2001;13:1923.
[24] Ho DL, Glinka CJ. Chem Mater 2003;15:1309.
[25] Fu X, Qutubuddin S. Mater Lett 2000;42(1–2):12.
[26] Yilmazer U, Ozden G. Polym Compos 2006;27(3):249.
[27] Noh MW, Lee DC. Polymer Bull 1999;42:619.
[28] Doh JG, Cho I. Polymer Bull 1998;41:511.
[29] Zhong Y, Zhu Z, Wang S. Polymer 2005;46(9):3006.
[30] Salahuddin N, Akelah A. Polym Adv Technol 2002;13(5):339.
[31] Uthirakumar P, Hahn YB, Nahm KS, Lee Y. Eur Polym J 2005;41(7):1582.
[32] Hoffmann B, Dietrich C, Thomann R, Friedrich C, Mulhaupt R. Macromol Rapid Commun 2000;21(1):57.
[33] Ding C, Guo B, He H, Jia D, Hong H. Eur Polym J 2005;41(8):1781.
[34] Zax DB, Yang D, Santos RA, Hegemann H, Giannelis EP, Manias E. J Chem Phys 2000;112(6):2945.
[35] Vaia RA, Jandt KD, Kramer EJ, Giannelis EP. Macromolecules 1995;28:8080.
[36] Sheng N, Boyce MC, Parks DM, Rutledge GC, Abes JI, Cohen RE. Polymer 2004;45(2):487.
[37] Koerner H, Luo Y, Li X, Cohen C, Hedden RC, Ober CK. Macromolecules 2003;36(6):1975.
[38] Arrighi V, McEwen I, Qian H, Prieto MS. Polymer 2003;44:6259.
[39] Yoonessi M, Toghiani H, Pittman CU. J Appl Polym Sci 2006;102(3):2743.
[40] Brandrup J, Immergut EH, Grulke EA. The Polymer Handbook. 4th ed. New York: John Wiley & Sons; 1999.
[41] Dunkerley E, Schmidt D. PMSE Prepr 2010;103. PMSE-336.
[42] Jacobs JD, Koerner H, Heinz H, Farmer BL, Mirau P, Garrett PH, et al. J Phys Chem B 2006;110:20143.
[43] Osman MA, Seyfang G, Suter UW. J Phys Chem B 2000;104:4433.
[44] He H, Ding Z, Zhu J, Yuan P, Xi Y, Yang D, et al. Clays Clay Miner 2005;53 (3):287.
[45] Heinz H, Vaia RA, Farmer BL. Langmuir 2008;24:3727.
[46] Ou C, Hsu M. J Polymer Res 2007;14(5):373.
[47] Xie W, Hwu JM, Jiang GJ, Buthelezi TM, Pan W. Polym Eng Sci 2003;43 (1):214.
[48] Xiong J, Liu Y, Yang X, Wang X. Polym Degrad Stab 2004;86(3):549.
[49] Kalgaonkar RA, Jog JP. J Polym Sci: B 2003;41:3102.
[50] Manias E, Kuppa V, Yang D, Zax D. Colloids Surf A: Physicochem Eng Aspects 2001;187:509.
[51] Yung KC, Wang J, Yue TM. J Reinf Plast Compos 2006;25(8):847.
[52] Chen B, Evans JR. Scr Mater 2006;54:1581.
[53] Vaia RA, Giannelis EP. MRS Bull 2001;26:394.
[54] Dunkerley E, Schmidt D. Proc. SPE ANTEC 2009;67:92.

Polymer 52 (2011) 1172–1179

Contents lists available at ScienceDirect

Polymer

journal homepage: www.elsevier.com/locate/polymer

Structural and property changes during uniaxial drawing of ethylene–tetrafluoroethylene copolymer films as analyzed by *in-situ* X-ray measurements

Yasunori Ono [a], Masaki Kakiage [a,1], Takeshi Yamanobe [a], Yasumasa Yukawa [b], Yoshiaki Higuchi [b], Hiroki Kamiya [b], Kiyotaka Arai [c], Hiroki Uehara [a,*]

[a] Department of Chemistry and Chemical Biology, Gunma University, Kiryu, Gunma 376-8515, Japan
[b] R & D Division, Asahi Glass Co., Ltd., Ichihara, Chiba 290-8566, Japan
[c] Central Laboratory, Asahi Glass Co., Ltd., Yokohama, Kanagawa 221-8755, Japan

ARTICLE INFO

Article history:
Received 21 September 2010
Received in revised form
14 December 2010
Accepted 19 December 2010
Available online 24 December 2010

Keywords:
Ethylene–tetrafluoroethylene copolymer (ETFE)
Drawing
In-situ WAXD

ABSTRACT

The structure–property relationship during uniaxial drawing of high-molecular-weight ethylene–tetrafluoroethylene copolymer (ETFE) film was analyzed based on a combination of *in-situ* wide-angle X-ray diffraction (WAXD) and stress measurements. *In-situ* WAXD patterns indicated that the hexagonal (100) reflection transformed from the initial un-oriented ring into equatorial spots via split arcs at temperatures both below and above T_g, but that the critical strain when such transition occurred was delayed above T_g. Drawing above T_g produced an equatorial concentration of the spot reflections; thus, the extended chain crystal was enhanced as a result of elongation of the strain-hardening region. In contrast, the draw below T_g remained less oriented even just before breaking. However, the high orientation component also appeared beyond the critical strain; it could be assigned to the so-called "tie molecules" that bind the deformed lamellae. Changes in resultant tensile strength could be interpreted by these extended chain crystals and characteristic tie molecule components.

1. Introduction

Ethylene–tetrafluoroethylene copolymer (ETFE) has the superior characteristics of both polyethylene (PE) and poly(tetrafluoroethylene) (PTFE); specifically, it has the excellent processability of PE and the chemical resistance or heat resistance of PTFE. Thus, ETFE is industrially adopted as sheets or films for agricultural housing and dome stadium roofs. Because such applications require a thinning process to enhance light transmission and reduce weight, improvement in mechanical properties is a key for wider industrial usage of ETFE. Various drawing technologies have been applied to improve mechanical properties of PE or PTFE; however, ETFE has been examined less because of its limited supply due to the sophisticated control required in its synthesis. For PE [1–9] and PTFE [10–12] we have found that ultra-drawings are possible when processing accompanies their phase transitions, giving the remarkable development of the mechanical properties and transparency of the resultant film. Ultra-drawing techniques that utilize phase transitions enable the property development of ETFE films because ETFE can be regarded as a diagonal of PE and PTFE.

Several polymorphisms of ETFE and their phase transitions during heating have been investigated [13–15]. Tanigami et al. [16] compared the wide-angle X-ray diffraction (WAXD) patterns obtained for ETFE films drawn below and above glass transition temperature (T_g). Changes in WAXD patterns during heating of these drawn ETFE films also indicate that their phase transition mechanism depends on drawing conditions for sample preparation. Recently, Funaki et al. [17] reported that the content of the third monomer component also affects the phase transition during heating of ETFE. However, these data were obtained under static conditions, not under deformation; thus, the *in-situ* observation of phase transition during drawing gives us valuable information for optimizing drawing conditions for developing the resultant mechanical properties of ETFE films.

Our previous *in-situ* WAXD measurement during drawing of PE [5–7,9] and PTFE [12] using a synchrotron radiation source revealed that disentanglement-induced crystallization with chain orientation

* Corresponding author. Tel.: +81 277 30 1332; fax: +81 277 30 1333.
E-mail address: uehara@chem-bio.gunma-u.ac.jp (H. Uehara).
[1] Present address: Department of Applied Chemistry, Saitama University, Sakura-Ku, Saitama 338-8570, Japan.

0032-3861/$ – see front matter © 2011 Elsevier Ltd. All rights reserved.
doi:10.1016/j.polymer.2010.12.040

occurs even above the sample melting temperature (T_m). These highly crystalline polymers are crystallizable during drawing above T_m; thus, resultant property development is achievable even from the melt. In contrast, the ultra-drawing for less-crystallizable polymers is enabled from the solid amorphous phase, not melt. Therefore, these polymers are often ultra-drawable just above T_g. Kawakami et al. [18–20] examined *in-situ* WAXD analyses during drawing of poly (ethylene terephtalate) (PET) film above T_g. They reported that stacking of the phenyl group perpendicular to the drawing axis is induced with fibrillar crystallization with chains extended during drawing. Ohkoshi et al. [21] also reported that fibrilar crystals appear just after necking during drawing of PET monofilament. The origin of such phase transition from un-oriented amorphous state into the oriented crystalline state can be assigned to the combination of rigid phenyl groups and flexible ethylene units, which is coincident with rigid TFE and flexible E units for ETFE.

Another issue in this study is the ultra-drawing of high-molecular-weight materials. Indeed, the chain ends act as defects on drawing. Therefore, reduction of such defects, which is enabled by increase of molecular weight, promises ultra-drawability of PE [22]. Such strategy has been also applied for ultra-drawing of the other crystalline polymers, including polypropylene (PP) [23], poly(lactic acid) [24], poly(acrylonitrile) [25] and poly(1-butene) [26].

This study analyzed the phase transition during drawing of high-molecular-weight ETFE by *in-situ* WAXD measurement. Higher molecular weight material was selected for property development of the resultant drawn films. Here, we focus on deformation near T_g because ETFE yields lower crystallinity, similar to PET. The relationship between the molecular deformation mechanism and achievable mechanical properties of the drawn films was also analyzed.

2. Experimental section

2.1. Materials

The ETFE powder material used in this study was supplied by Asahi Glass Company. The melt-flow index measured at 297 °C under an applied pressure of 300 MPa was 0.63 mm^3/s. This value was significantly lower than that of commercial ETFE Fluon AX55 (77 mm^3/s), which was used in previous studies by Tanigami et al [13,14,16]. This means that ETFE used in this study has the higher molecular weight than above commercial grade. Since ETFE exhibits the excellent chemical resistance and is insoluble in any solvent, the conventional gel permeation chromatography (GPC) used for molecular weight (MW) measurement is ineffective. Therefore, the MW of ETFE cannot be determined accurately. The T_m of this ETFE powder was 257 °C, which was 2 °C higher than that for Fluon AX55 (255 °C).

2.2. Film preparation

The as-received ETFE powder material was sandwiched between commercial polyimide films (Ube, UPILEX-125S) and was compression-molded into the film. A press machine equipped with a vacuum chamber (Boldwin, Japan) was used. The above assembly was kept in the molten state at 310 °C for 5 min, compression-molded at 2.2 MPa, and subsequently cooled to room temperature. The prepared film was 0.3 mm thick.

2.3. Measurement

A Perkin–Elmer Pyris 1 DSC was used for differential scanning calorimetry (DSC) measurement. DSC heating scans were performed from 30 to 300 °C at a rate of 10 °C/min under a nitrogen gas flow. The sample weight was 5 mg. The sample T_m was evaluated as the peak temperature of the melting endotherm. The temperature and fusion heat were calibrated using indium and lead standards.

Dynamic mechanical analysis (DMA) was performed using a Mellter Toledo DMA861e. The heating scan was from 30 to 140 °C at a rate of 2 °C/min under a nitrogen gas flow. The measurement specimen was cut from the compression-molded film into ribbons, that were 4 mm wide and 20 mm long, and contained a strained region that was 10.5 mm long.

The drawing specimens were cut from the prepared film in dumbbell shapes, with a 4 mm-wide, 12.5 mm-long straight region. These dumbbell specimens were set in a custom-made high-temperature extension device [27,28] and tensile-drawn at various temperatures from 80 to 280 °C. The cross-head speed (CHS) of drawing was 24 mm/min. The sample specimen was isothermally held at drawing temperature (T_d) for 5 min before starting the draw to equilibrate the temperature. The drawing stress was recorded using a load cell (Kyowa Electronic Instruments Co., Ltd., LUR-A-50NSA1) installed in the extension device.

In-situ WAXD measurement during drawing was carried out using a synchrotron radiation source at the BL40B2 beamline of SPring-8 (Japan Synchrotron Radiation Research Institute, Hyogo, Japan). An extension device (described above) was installed in the beamline BL40B2, and WAXD images were continuously recorded during drawing on a cooling CCD camera (Hamamatsu Photonics K.K., C4880). A 0.3 mm-diameter beam was radiated at the center of the dumbbell sample, where the measurement temperature was detected by thermocouples placed less than 1 mm from the sample surface. The wavelength of the synchrotron beam was 1.00 Å. The exposure time for each pattern was 1.0 s, with a time interval of 6.0 s for data storage.

In contrast, *ex-situ* WAXD measurement for drawn samples was carried out using Ni-filtered Cu-Kα radiation generated by a Rigaku RU-200B rotating anode X-ray generator at 40 kV and 120 mA. The WAXD image was recorded on a Fuji Film imaging plate BAS-SR at room temperature. The wavelength of the radiation beam was 1.54 Å. An X-ray beam was collimated in 0.3 mm diameter and radiated at the center of the drawn film. The recorded WAXD pattern was monitored by a Rigaku R-AXIS DS3 data reader.

The resultant tensile properties of the drawn films were measured using a universal tensile tester (Orientec RTC-1325A) at room temperature and at a strain rate of 0.5 min^{-1}. The tensile strength of each drawn film was calculated from the maximum stress just before breaking of the sample.

3. Results and discussion

In order to determine the sample T_g and T_m, DSC measurement was conducted for the initial compression-molded ETFE film prepared in this study. Fig. 1a depicts the thermograms recorded during heating at a rate of 10 °C/min. The single melting endotherm is recognized at 256 °C. It has been known the characteristic double melting endotherms are often recorded for the ETFE having defective unit propagation of ethylene (E) and tetrafluoroethylene (TFE) [15]. However, the single endotherm was observed for the film prepared in this study. Additionally, the inset in Fig. 1b, an enlarged temperature region from 35 to 135 °C, exhibits slope changes at 50 °C and 100 °C. However, it was difficult to determine whether they were “peak” for crystal transition and melting, or “jump” for glass transition.

Therefore, DMA measurements were performed for this initial ETFE film to accurately assign these critical temperatures on the DSC thermograms. Fig. 2 compares the changes in storage modulus and tan δ recorded during heating from room temperature to 140 °C at measurement frequencies of 1, 5, 10 and 100 Hz. The storage

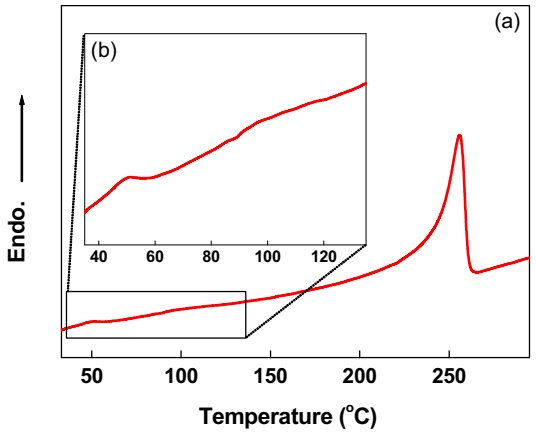

Fig. 1. DSC thermogram of heating from 30 °C to 300 °C for ETFE film prepared in this work. The low-temperature region of the whole profile (a) was enlarged in (b).

modulus significantly decreases in temperatures from 70 to 120 °C. In contrast, the tan δ curve exhibits a shoulder at 50 °C and a peak at 100 °C. The shoulder does not seem frequency dependent. Thus, the transition at 50 °C is attributed to the crystalline phases. Indeed, Tanigami et al. [13] assigned it to the crystal–crystal transition from orthorhombic to hexagonal form of ETFE. In contrast, the peak position at 100 °C clearly depends on measurement frequency, as is characteristic of the amorphous component. Therefore, the T_g of the ETFE film prepared in this study is determined to be 100 °C.

Based on the above information from thermal analyses, T_d's were selected from temperatures of 80 °C below T_g to 280 °C above T_m. Fig. 3 compares the stress/strain curves recorded during drawing at various temperatures. The sample film was isothermally kept at a given temperature for 5 min before starting the draw. The drawing stress gradually decreased with increasing T_d, indicating that the deformation of ETFE film prepared in this study exhibits remarkable temperature dependence. In particular, yielding is apparent for drawing at 80 °C below T_g, whereas only a gentle slope is recognized above 150 °C. The achievable draw ratio (*DR*) gradually increases with T_d to a maximum at 150 °C. However, the achievable *DR* gradually decreases with increasing T_d beyond 200 °C. At 280 °C, effective drawing is impossible, due to the complete melting of the sample film well above T_m. It has been reported that PE and PTFE with high MW can be drawn even from the molten state [2–9,12]; however, the melt viscosity of ETFE used in this study is too low to transmit the applied stress during melt-drawing although its MW is much higher than that of the commercial ETFE described above.

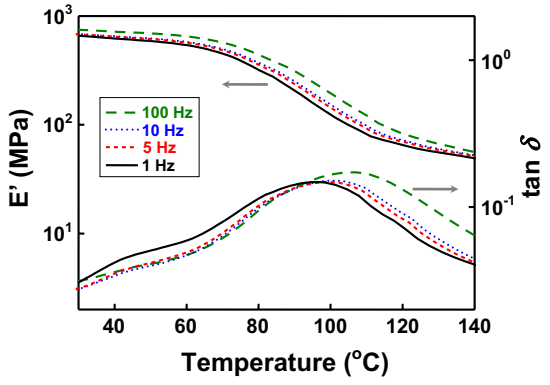

Fig. 2. Dynamic viscoelastic properties of ETFE films prepared in this work. Storage modulus (E′) and tan δ are plotted as a function of temperature.

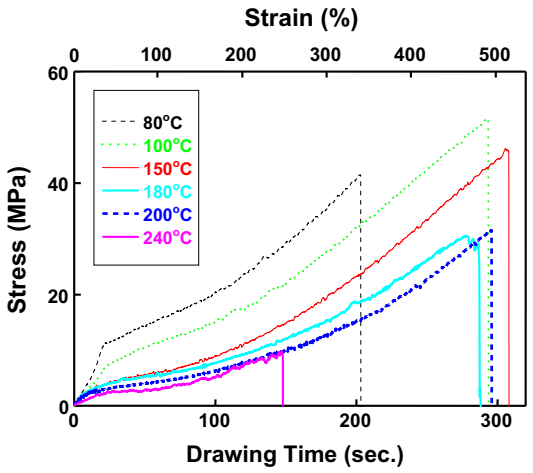

Fig. 3. Stress profiles recorded at 80–240 °C during drawing of ETFE films prepared in this work.

These results reveal that the drawing behavior dramatically differs at T_g; thus, typical T_d's below (80 °C) and above T_g (150 °C) were selected. Structural change during such drawing was analyzed by *in-situ* measurement. Fig. 4 depicts a series of WAXD patterns recorded during drawing at 80 °C with corresponding stress profiles. Drawing stress rapidly increases with the start of the draw. It yields at 10 MPa, but again increases linearly up to sample breaking. The WAXD image recorded before drawing exhibits ring-shaped crystalline reflections, indicating random chain orientation. Tanigami et al. [13] observed the hexagonal (100) reflection for the undrawn film in this temperature range. However, the X-ray wavelength in our study differ from that in their study; thus, the scattering vectors of these reflection peaks were calculated from corresponding 2θ positions using Eq. (1).

$$q = \frac{4\pi \sin\theta}{\lambda} \tag{1}$$

The resultant q values were 1.35 Å^{-1} for undrawn film for our case and theirs; thus, the ring obtained before drawing in Fig. 4 could be ascribed to this hexagonal (100) reflection. The position

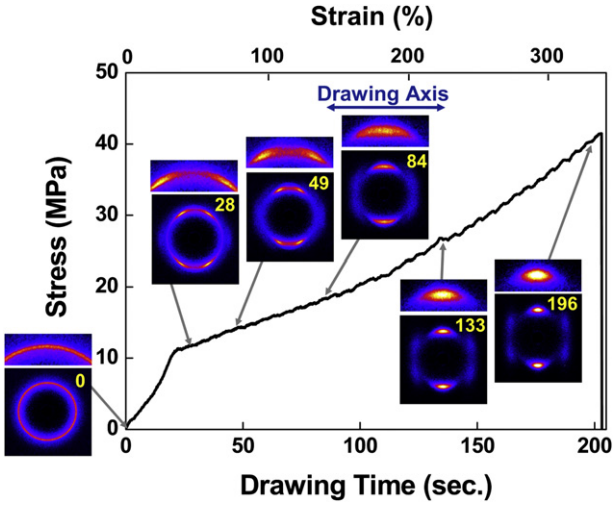

Fig. 4. Stress profiles recorded at 80 °C with the corresponding change of *in-situ* WAXD patterns. The draw direction on WAXD patterns is horizontal. Enlarged images of the crystalline reflection regions are presented in the upper portion. The drawing time in seconds is denoted in each pattern.

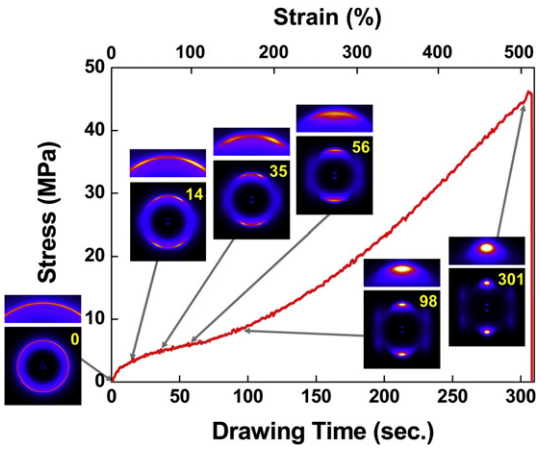

Fig. 5. Stress profile recorded at 150 °C with the corresponding change of *in-situ* WAXD patterns. The draw direction on WAXD patterns is horizontal. Enlarged images of the crystalline reflection regions are presented in the upper portion. The drawing time in seconds is denoted in each pattern.

of this reflection was unchanged even with the start of the drawing and during drawing.

This ring-shaped reflection was split into two arcs beyond the yielding point, which are clearly visible in the enlarged image in Fig. 4. This indicates the molecular inclination to the drawing direction. Tanigami et al. [16] reported a similar split of the (100) reflection ring for a drawn sample of commercial ETFE film. With an increase in strain, these reflections are further concentrated on the equator (longitudinal direction in Fig. 4). This result indicates that the crystalline molecules are gradually oriented along the drawing direction. The stress/strain curve recorded around T_g of 100 °C was similar to that at 80 °C, thus, the above deformation mechanism is also expected at 100 °C.

In contrast, drawing at 150 °C above T_g (Fig. 5) produced a lower yielding stress of 5 MPa, which was half of that for the 80 °C drawing. However, the stress profile observed at the later stage of draw became steeper. Changes in WAXD patterns for both T_d's were similar up to stress yielding, where the initial reflection ring was split and transformed into an arc shape; however, further drawing produced characteristic spot-shaped reflections for 150 °C drawing, corresponding to the rapid stress increase described above. Such higher molecular orientation indicates that extended chain crystals are formed in the later drawing stage.

Changes in molecular orientation were compared for these different drawings. Hexagonal (100) reflection intensities located at $q = 1.34–1.40$ Å^{-1} were extracted along the azimuthal angle, and the obtained profiles were stacked as a function of drawing time. This q range covers the crystalline reflection region, but does not include the amorphous scattering region [13]. Fig. 6 compares the changes in such azimuthal profiles for 80 °C and 150 °C drawings. The plotted region of azimuthal angle was 90° to 270°, where 0° was the equator (longitudinal axis in Figs. 4 and 5). Reflection intensity is represented by color gradation from blue (low intensity) to red (high intensity). These orientation analyses clearly demonstrate that deformation mechanisms below and above T_g are quite different from each other. In drawing at 80 °C, none of the peak maxima appear with the early stage of draw, indicating the random orientation of crystalline molecules. At the drawing time of 20 s, corresponding to the yielding point on the stress/strain curve in Fig. 4, split maxima were observed at 150° and 210°. However, separation between these two maxima gradually narrowed. This result suggests that the crystalline molecules initially inclined to the drawing direction, exhibiting a parallel chain arrangement with increasing strain. Such double peak maxima were transformed into a single maximum at the critical drawing time of 75 s, corresponding to the slope change on the stress profile in Fig. 4. Beyond this slope change, reflection intensity further increases with strain, but its increase is moderated.

In contrast, 150 °C drawing produces the apparent split of crystalline reflection at the early stage of drawing. The lamellar inclination, giving two initial reflection maxima, gradually transformed into a parallel chain arrangement, with the single peak maximum at 55 s. Such accelerated transition for drawing above T_g indicates easier deformation, compared to that below T_g, as also suggested by the lower drawing stress depicted in Fig. 5. Reflection intensity rapidly increases with increasing strain beyond this critical strain.

Corresponding small-angle X-ray scattering (SAXS) change during drawing is suitable for complete understanding the lamellar deformation mechanism. However, the given operation time at SPring-8 was limited, thus we concentrated on the crystalline deformation detected by WAXD change. Now, we are planning the

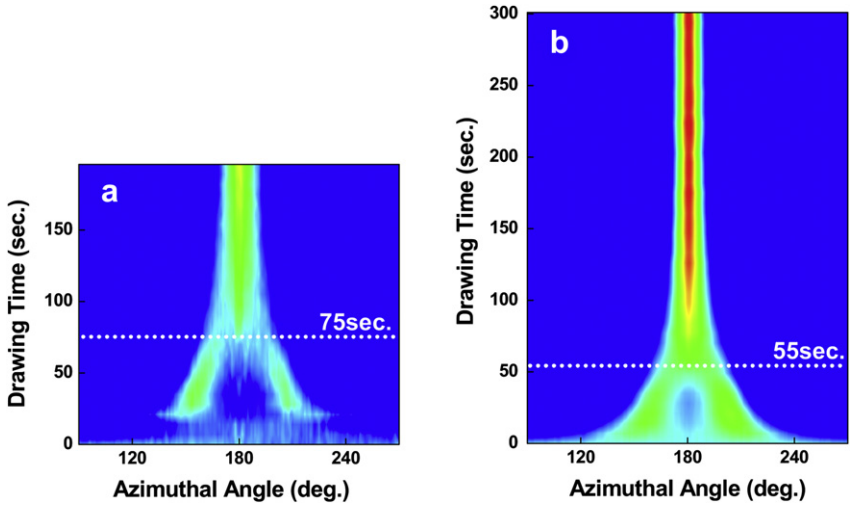

Fig. 6. Stacked line profiles of azimuthal scans extracted from *in-situ* WAXD patterns recorded during drawing at (a) 80 °C and (b) 150 °C. Intensity is denoted by color gradation from red (high intensity) to blue (low intensity). The dotted lines denote the critical drawing time where split peaks merge into a single peak.

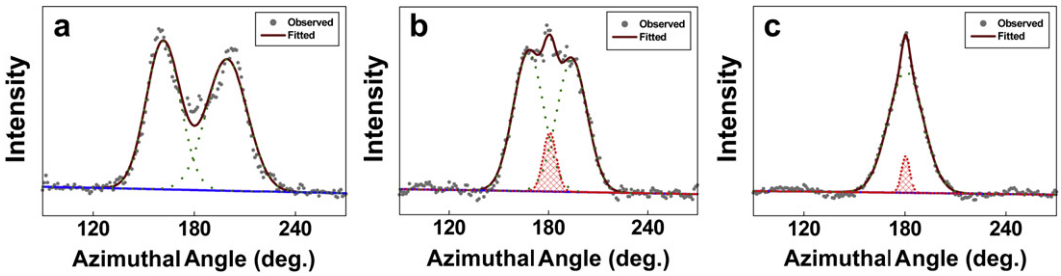

Fig. 7. Comparison of line profiles extracted along the azimuthals of *in-situ* WAXD patterns recorded at different times during drawing at 80 °C. These data were obtained at the drawing times of (a) 50 s, (b) 75 s, and (c) 150 s. Observed and resultant fitted data are denoted by gray dots and red solid lines. The green and red dotted lines indicate the peak resolution results. The red shaded peak corresponds to the highly oriented component. (For interpretation of the references to colour in this figure legend, the reader is referred to the web version of this article).

future SAXS analyses during drawing for concrete structure analysis at different strain.

As discussed above, the double peak maximums were transformed into a single maximum for drawings both below and above T_g; however, their critical strains where such phase transition occurred were quite different, due to corresponding deformation mechanisms. Therefore, detailed changes in the azimuthal profiles were compared before and after such critical strain for both T_d's. Figs. 7 and 8 depict a set of azimuthal profiles extracted along the azimuthals of *in-situ* WAXD patterns recorded at different times during drawing at 80 °C and 150 °C. The peaks decomposed into components with initial lamellar inclination and having higher molecular orientation are denoted by green and red dotted lines. For this peak decomposition, the conventional Gaussian function was adopted for reproducing the reflection of each component. Fig. 7a depicts former two-peak maxima corresponding to the initial lamellae inclined toward the drawing direction. In contrast, the profile obtained at the critical drawing time (Fig. 7b) contains the latter new peak on the equator center, as well as the former two-maximum peaks ascribed to the initially inclined lamellae. The reflection intensity of the latter center peak is lower, but its width is much narrower, than those of the former two-maximum peaks, indicating higher molecular orientation. Beyond the critical drawing time (Fig. 7c), the former two-maximum peaks transform into a single maximum, reflecting the parallel arrangement of the crystalline chains along the drawing direction. However, the latter highly oriented component still survives beyond this critical strain.

Changes in azimuthal profiles were also compared for drawing at 150 °C. Two-maximum peaks ascribed to the inclined lamellar structure, similar to the 80 °C drawing, were initially observed (Fig. 8a). At the critical drawing time (Fig. 8b), a single peak was obtained on the equatorial center, but it was significantly broader than that for the highly oriented component for 80 °C drawing. Beyond the critical drawing time (Fig. 8c), this single peak narrowed, indicating improved molecular orientation at higher T_d.

This *in-situ* WAXD pattern was quite different from the conventional *ex-situ* one obtained for the static sample. Fig. 9 compares the *in-situ* pattern obtained during drawing at 80 °C at a drawing time of 115 s (left) and an *ex-situ* pattern obtained for the film drawn at a *DR* of 3.0 at 80 °C. The achievable strains for the former drawing time and for the latter *DR* were almost the same. Here, the latter *ex-situ* WAXD measurement was made at room temperature with no tension applied. The bottom profiles are the hexagonal (100) reflection scans extracted along the azimuthal angle, as indicated by the white dotted line in each reflection pattern. For the *in-situ* pattern in Fig. 9a, the split two-maximum peaks attributed to the inclined lamellae and the central narrower peak with high molecular orientation coexist. In contrast, no latter central peak was observed for the *ex-situ* patterns in Fig. 9b, indicating that a component with high molecular orientation is transient during drawing, but disappears once the draw is stopped. In contrast, there is no transient reflection both for *in-situ* and *ex-situ* results recorded at 150 °C.

Comparison of a series of azimuthal profiles in Figs. 7 and 8 clearly reveals differences in orientation behavior during drawing below and beyond T_g. Therefore, quantitative analyses of the chain orientation were conducted by using the following equation.

$$\text{Degree of Chain Orientation} = \frac{180^\circ - \text{Integral Width}(^\circ)}{180^\circ} \quad (2)$$

Here, the integral width was estimated by peak resolution of the azimuthal profile into the two-maximum or central peaks using the Gaussian function. In the two-maximum peaks, the total of integral widths of each peak was used to calculate molecular orientation. Indeed, Lorentz fitting was also applied, but the asymmetric peak deconvolution with different width was achieved for such two-maximum peaks, thus symmetric Gauss fitting was adopted in this study. Fig. 10 depicts the changes in degree of chain orientation during drawing at 150 °C. In the early stage of draw before the critical drawing time in Fig. 6b, the value change exhibits a gentle slope. Considering that the two-maximum peak transformed into a single peak in this drawing time range, the molecular chains in folded chain crystals (FCCs) of lamellae were gradually arranged

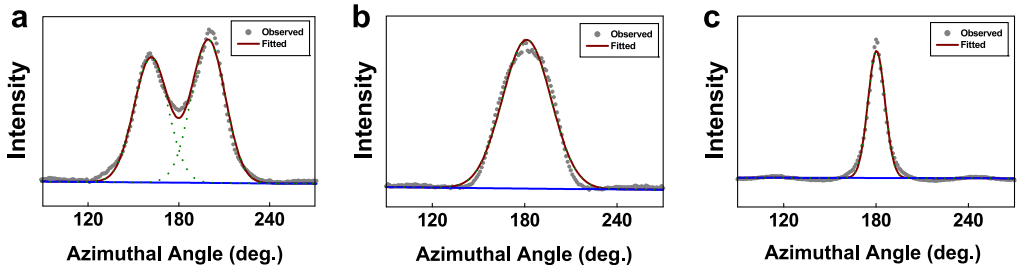

Fig. 8. Comparison of line profiles extracted along the azimuthals of *in-situ* WAXD patterns recorded during drawing at 150 °C. These data were obtained at the drawing times of (a) 30 s, (b) 55 s, and (c) 150 s.

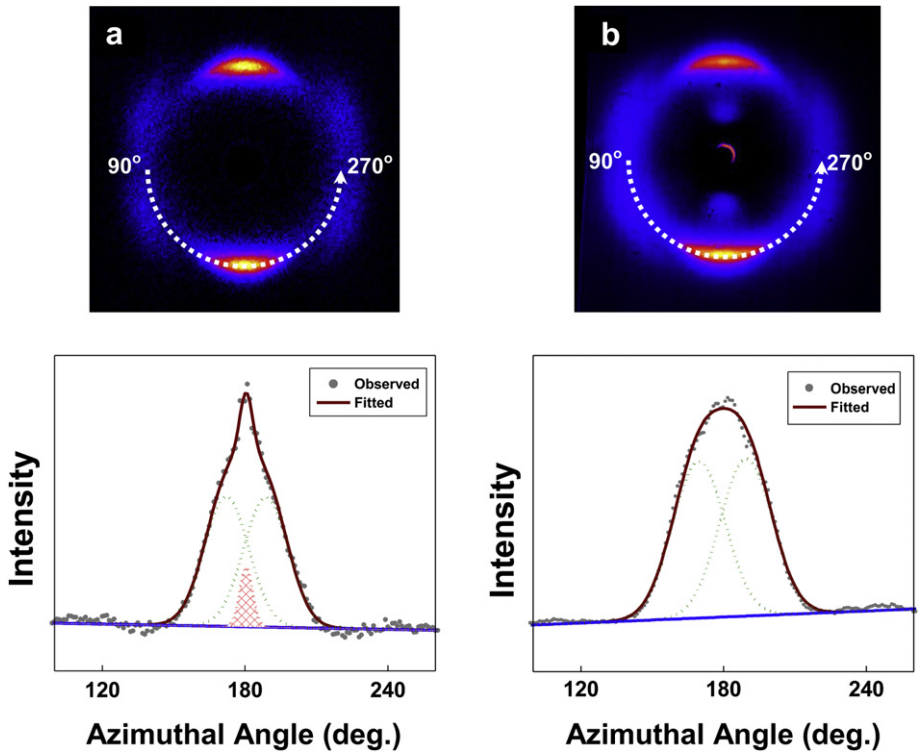

Fig. 9. Comparison of (a) *in-situ* and (b) *ex-situ* WAXD patterns (top) and corresponding plots of line profiles (bottom) extracted along the azimuthals of the series of crystalline diffraction region for drawing at 80 °C. These data were obtained at (a) the drawing time of 115 s and (b) a corresponding *DR* of 3.0. The white dotted circles in the top patterns represent analyzed azimuthal scans. The gray dotted lines in the bottom profiles are decomposed into reflection peaks ascribed to a pair of the tilted lamellar components (green dots) and a well-oriented component (red shade).

along the drawing direction. The change in degree of chain orientation becomes steep beyond the critical drawing time of 55 s, which is coincident with Fig. 6b. However, the value change is gradually depressed and finally saturated at a constant value beyond 200 s. This result indicates that for drawing above T_g, extended chain crystals (ECCs) were formed in a later stage of draw. The region between the former critical time of 55 s and the latter critical time of 200 s exhibits a transitional structure from FCC to ECC. A similar deformation from FCC to ECC has been reported for deformation of PP above its T_g [29].

Also, changes in the degree of chain orientation during drawing at 80 °C are compared in Fig. 11. As with the 150 °C drawing discussed above, a break of degree of chain orientation is recognized at the critical drawing time estimated from Fig. 6a. However, the value is not saturated even in the later stage of draw, indicating that the sample is broken at structural defects produced before ECC

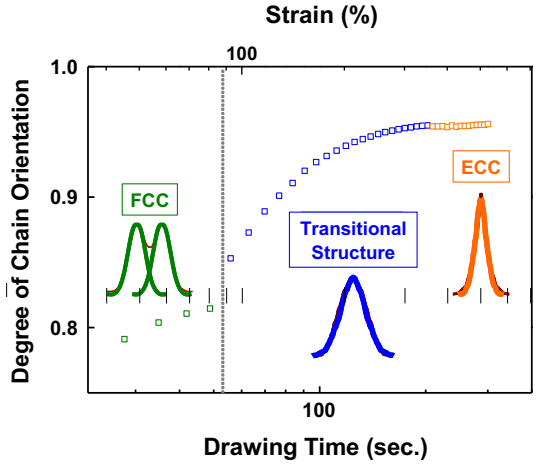

Fig. 10. Changes in degree of chain orientation during drawing at 150 °C as a function of drawing time. Degrees of chain orientation were calculated from the integral width of azimuthal scans, which were resolved in the components attributed to lamellar (folded chain crystals (FCC)), transitional structure, and extended chain crystals (ECC) as represented in the illustrations in the figure. The dotted line indicates the critical drawing time in Fig. 6b.

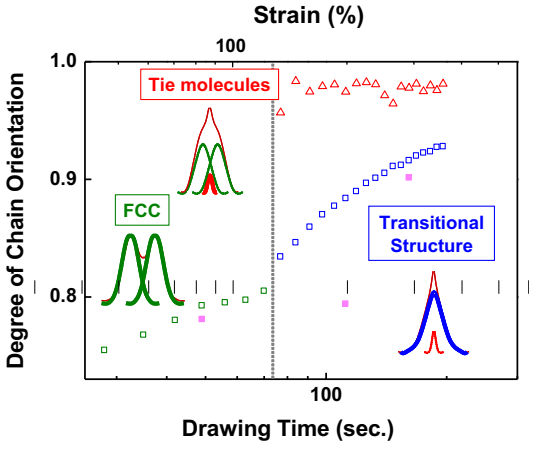

Fig. 11. Changes in degree of chain orientation during drawing at 80 °C as a function of drawing time (open symbols). Triangles represent the values for the highly oriented components correspond to transient "tie molecules". For comparison, the values estimated from *ex-situ* WAXD patterns are also plotted at the corresponding drawing time (filled squares). The dotted line indicates the critical drawing time in Fig. 6a. (For interpretation of the references to colour in this figure legend, the reader is referred to the web version of this article).

formation. This phenomenon is coincident with the void formation induced by drawing below T_g, as reported by Tanigami et al. [16].

Another characteristic of 80 °C drawing is the appearance of a highly oriented component beyond the critical drawing time of 75 s (Fig. 7). Its degree of chain orientation is even higher than that for ECC in Fig. 10. Considering that this component appears during deformation from FCC to the transitional structure, it is assigned to "tie molecules" that transmit drawing stress between FCCs. Comparison of the values of orientation degree obtained for *ex-situ* and *in-situ* patterns indicates that the *ex-situ* value at a *DR* of 3.0 is lower than that of the *in-situ* one. Namely, transient extension of tie molecules bound between FCCs contributes to the resultant oriented crystallization with chain relaxation after drawing. This is coincident with the fact that the tie molecular reflection peak on *in-situ* measurements disappeared for dead samples with no tension under the *ex-situ* static condition.

Several methods have been proposed for detection of tie molecules. Wunderlich and coworkers [30] have estimated rigid-amorphous fraction attributed to tie molecules from sophisticated thermal analyses of polyesters. In contrast, Tshmel et al. [31,32] have observed Raman spectroscopy for PE, and reported the length of straight chains, which tie FCC layers with passing though the amorphous region. In the present study, we discussed tie molecule based on *in-situ* WAXD measurements, but collaborative comparisons of the results obtained from these different methods will be effective for complete understanding a role of tie molecules on deformation in future study.

Such tie molecules must exist above T_g. However, it can immediately transform into ECC above T_g, thus its existence is not evidenced by chain orientation analyses in Fig. 8. As a result, an ease of crystalline phase change from FCC to ECC is accelerated by increasing temperature above T_g in Fig. 10. This is a reason why an orientation characteristic of tie molecule is emphasized for drawing below T_g in Fig. 11.

In order to determine the relationship between such oriented structure and resultant properties, tensile tests were conducted at room temperature for a series of ETFE films drawn at 80 °C and 150 °C. Fig. 12 depicts the resultant tensile strength as a function of *DR*. With increasing *DR*, the tensile strength increases, independent of T_d. However, higher values are obtained for the films drawn at 80 °C in the *DR* region of 2.5–4.0. This *DR* region is coincident with the strain region where the highly oriented component appears in Fig. 11. This result indicates that tie molecules with high orientation appear during tensile tests, similar to drawing below T_g. In contrast, 150 °C drawing exhibited higher tensile strength in the higher *DR* region beyond 4.0, reflecting the effect of the ECC formation induced by drawing at 150 °C. The maximum achievable tensile strength approached 400 MPa for films drawn at 150 °C up to a *DR* of 5.0, which is eight times higher than that of commercial undrawn ETFE film.

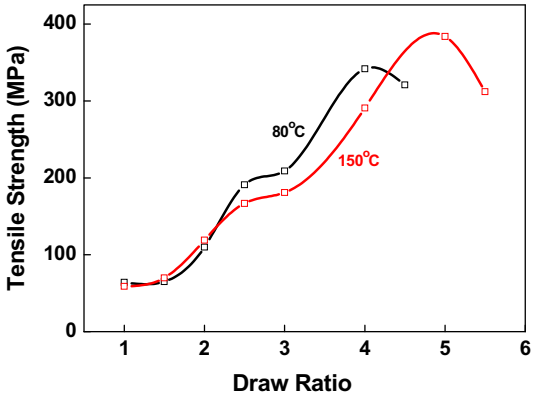

Fig. 12. Comparison of the resultant tensile strength of films drawn at 80 °C and 150 °C. Tensile tests were conducted at room temperature.

In summary, the uniaxial deformation mechanism of ETFE film having high MW is clearly divided at the T_g, and tie molecules formed during drawing dominate the tensile properties of the resultant ETFE films. *In-situ* X-ray measurement enabled us to detect the transient appearance of tie molecules observed in this study. This result confirms that the effective availability of high luminescent synchrotron radiation contributes to detection of the real-time deformation during drawing, which is often different from usual prediction using the conventional *ex-situ* measurement for dead samples in the static state.

4. Conclusions

Structural development during uniaxial drawing of ETFE film having high MW could be successfully analyzed by *in-situ* X-ray measurement using a synchrotron radiation source. The orientation change of crystalline molecules enabled quantitative comparison between lamellar deformation characteristics observed below and above T_g. The crystalline molecules are first inclined to the drawing direction, giving split arc reflections with yielding, followed by gradual change to spot reflections with increasing strain, indicating parallel orientation of crystalline molecules along the drawing direction. The critical time where the split arcs transformed into single spots shifted to the larger strain side for drawing below T_g. Another notable characteristic of drawing below T_g was the recognizable transient component with the highest molecular orientation. Considering that this component was not observed for later *ex-situ* measurement for dead samples, it can be assigned to latent tie molecules that bind oriented crystals with load applied. When the resultant tensile strength measured at room temperature was compared at the same strain, larger values were obtained for the sample drawn below T_g, which is especially significant above the critical strain where the transient component was developed. This result indicates that such tie molecules effectively transmit the applied stress on the tensile tests, which plays a similar role for tensile drawing. In contrast, the maximum achievable tensile strength was obtained for films drawn above T_g into the higher strain, corresponding to the ultra-drawing region. Such strength was ascribed to the extended chain crystals formed during drawing.

Acknowledgments

In-situ measurement using synchrotron radiation was performed at the BL40B2 in the SPring-8, Japan. We appreciate the kind cooperation of Drs. Hiroyasu Masunaga and Sono Sasaki at the Japan Synchrotron Radiation Research Institute. This work was supported in part by the Industrial Technology Research Grant Program from the New Energy and Industrial Technology Development Organization (NEDO) of Japan.

References

[1] Uehara H, Kanamoto T, Kawaguchi A, Murakami S. Macromolecules 1996;29:1540.
[2] Uehara H, Nakae M, Kanamoto T, Zachariades AE, Porter RS. Macromolecules 1999;32:2761.
[3] Nakae M, Uehara H, Kanamoto T, Ohama T, Porter RS. J Polym Sci Polym Phys Ed 1999;37:1921.
[4] Nakae M, Uehara H, Kanamoto T, Zachariades AE, Porter RS. Macromolecules 2000;33:2632.
[5] Uehara H, Kakiage M, Yamanobe T, Komoto T, Murakami S. Macromol Rapid Commun 2006;27:966.

[6] Kakiage M, Yamanobe T, Komoto T, Murakami S, Uehara H. J Polym Sci Polym Phys Ed 2006;44:2455.
[7] Kakiage M, Yamanobe T, Komoto T, Murakami S, Uehara H. Polymer 2006;47:8053.
[8] Uehara H, Yoshida R, Kakiage M, Yamanobe T, Komoto T. Ind Eng Chem Res 2006;45:7801.
[9] Kakiage M, Sekiya M, Yamanobe T, Komoto T, Sasaki S, Murakami S, et al. Polymer 2007;48:7385.
[10] Uehara H, Jounai K, Endo R, Okuyama H, Kanamoto T, Porter RS. Polym J 1997;29:198.
[11] Endo R, Jounai K, Uehara H, Kanamoto T, Porter RS. J Polym Sci Polym Phys Ed 1998;36:2551.
[12] Morioka T, Kakiage M, Yamanobe T, Komoto T, Kamiya H, Higuchi Y, et al. Macromolecules 2007;40:9413.
[13] Tanigami T, Yamaura K, Matsuzawa S, Ishikawa M, Mizoguchi K, Miyasaka K. Polymer 1986;27:1521.
[14] Tanigami T, Yamaura K, Matsuzawa S, Ishikawa M, Mizoguchi K, Miyasaka K. Polymer 1986;27:999.
[15] Pucciariello R. J Appl Polym Sci 1996;59:1227.
[16] Tanigami T, Yamaura K, Matsuzawa S, Ishikawa M, Miyasaka K. Polym Eng Sci 1986;26:1323.
[17] Funaki A, Arai K, Aida S, Phongtamrug S, Tashiro K. Polymer 2008;49:5497.
[18] Kawakami D, Ran S, Burger C, Fu B, Sics I, Chu B, et al. Macromolecules 2003;36:9275.
[19] Kawakami D, Ran S, Burger C, Avila-Orta C, Sics I, Chu B, et al. Macromolecules 2006;39:2909.
[20] Kawakami D, Burger C, Ran S, Avila-Orta C, Sics I, Chu B, et al. Macromolecules 2008;41:2859.
[21] Yamaguchi T, Kim K, Murata T, Koide M, Hitooka S, Urakawa H, et al. J Polym Sci Polym Phys Ed 2008;46:2126.
[22] Sawai D, Nagai K, Kubota M, Ohama T, Kanamoto T. J Polym Sci Polym Phys Ed 2006;44:153.
[23] Uehara H, Hirao T, Yamanobe T, Komoto T, Yamamoto Y. Polymer 2006;47:7145.
[24] Sawai D, Yokoyama T, Kanamoto T, Sungil M, Hyon SY, Myasnikova LP. Macromol Symp 2006;242:93.
[25] Sawai D, Fujii Y, Kanamoto T. Polymer 2006;47:4445.
[26] Sawai D, Anyashiki T, Nakamura K, Hisada N, Ono T, Kanamoto T. Polymer 2007;48:363.
[27] Murakami S, Tanno K, Tsuji M, Kohjiya S. Bull. Inst. Chem. Res., vol. 72. Kyoto Univ.; 1995. 418.
[28] Murakami S. Nippon Kagaku Kaishi 2000;2:141.
[29] Uehara H, Yamazaki Y, Kanamoto T. Polymer 1996;37:57.
[30] Androscha R, Wunderlich B. Polymer 2005;46:12556.
[31] Tsobkallo T, Vasilieva V, Kakiage M, Uehara H, Tshmel AJ. Macromol Sci Phys 2006;45:407.
[32] Galitsyn V, Gribanov S, Kakiage M, Uehara H, Khizhnyak S, Pakhomov P, et al. Int J Polym Anal Charact 2007;12:221.

Polymer 52 (2011) 1180–1190

Contents lists available at ScienceDirect

Polymer

journal homepage: www.elsevier.com/locate/polymer

Film instability induced evolution of hierarchical structures in annealed ultrathin films of an asymmetric block copolymer on polar substrates

Ya-Sen Sun [a,*], Shih-Wei Chien [a], Jiun-You Liou [a], Chiu Hun Su [b], Kuei-Fen Liao [b]

[a] Department of Chemical and Materials Engineering, National Central University, Taoyuan 32001, Taiwan
[b] National Synchrotron Radiation Research Center, Hsinchu 30077, Taiwan

ARTICLE INFO

Article history:
Received 12 August 2010
Received in revised form
16 December 2010
Accepted 19 December 2010
Available online 25 December 2010

Keywords:
Copolymer
Dewetting
Hierarchical structure

ABSTRACT

With an atomic-force microscope and a grazing-incidence small-angle X-ray scattering we studied *ex situ* the evolution of hierarchical structures in isothermally annealed ultrathin films of asymmetric polystyrene-*block*-poly(methyl methacrylate) P(S-*b*-MMA) that dewetted on polar substrates via a mechanism involving nucleation and growth. Film instability causes the surface to acquire an undulating thickness through incommensurability, producing not only the relief structures on a micrometer scale but also mesophase-separated domains on a nanometer scale. The dewetted morphologies strongly influence the ordering behavior of the nanoscale domains. The noncylindrical nanostructures become stable at the curved edges of the relief microstructures in the destabilized P(S-*b*-MMA) films, for which a preferential wetting of the PS block with the free surface is prohibited. Additionally, the shape of relief structures as result of film instability correlates with the formation of mesophase-separated nanodomains. At early stages of film instability, the formation of parallel-oriented PMMA cylindrical nanodomains increases the deformation energy and it further persists to force the shape of relief structures between irregular holes to have a facet-wedge shape. However, those relief structures are expected to be not at equilibrium. At high temperatures, the relief structures between irregular holes progressively developed to form hemispherical-cap drops accompanied by a transformation of cylindrical into noncylindrical nanodomains at curved surfaces.

1. Introduction

Because of the repulsion between chemically connected incompatible blocks, block copolymers can self-assemble into various ordered structures, such as lamellae, cylinders, spheres and other complicated structures on length scales ranging from 10 to 100 nm [1]. The morphology of block copolymers in the bulk state is controllable on varying the compositions (volume fraction, f) of constituents, interactions between blocks (Flory–Huggins interactions, χ) and molecular weights (the degree of polymerization, N) [1]. Much effort has been devoted to mesophase-separated morphologies in thin films of block copolymers as two additional effects – film thickness and interactions at the interfaces between air and polymer or substrate and polymer – enrich the mesophase-separated morphologies [2–15]. For instance, an asymmetric block copolymer that has in the bulk a single morphology comprising hexagonally packed nanocylinders (constituted by the minor component) embedded within a matrix (constituted by the major component) reveals in thin films a series of distinct morphologies such as perforated layers and spheres [5–11].

Dewetting of thin films commonly produces terraced structures (such as holes or drops) if the thickness is incommensurate with the intrinsic spacing of ordered nanodomains [12–14]. Upon annealing at high temperatures or exposure to solvents, the film surface acquires an undulating thickness so that the film stature becomes quantized in integer (symmetric wetting) or 1.5 integer (asymmetric wetting) units of the nanodomain spacing. Such typical features are well known for symmetric block copolymers [3,4,12–14]. For an asymmetric block copolymer, the morphology of a thin film is more complicated than for a symmetric block copolymer: not only variations in spatial orientation of nanostructures but also surface-induced phase transitions evolve during dewetting [10,11,16]. Although theoretical results confirm that surface-induced versatile morphologies remain stable in thin films [6,7], the morphological transformations typically occur in destabilized films [10,11]; particularly at the relief edges with a curved surface appear spherical nanodomains or perforated layers [5].

On the other hand, dewetting of block copolymer thin films on a solid typically reveals hierarchical structures in comparison with

* Corresponding author. Tel.: +886 3422 7151x34205; fax: +886 3425 2296.
E-mail address: yssun@cc.ncu.edu.tw (Y.-S. Sun).

0032-3861/$ – see front matter © 2010 Elsevier Ltd. All rights reserved.
doi:10.1016/j.polymer.2010.12.039

that of homopolymer thin films [17–19]. In other words, in addition to various morphologies at micrometer length scales resulting from dewetting [20,21], mesophase-separated nanodomains buried within the dewetting relief microstructures in thin films of block copolymers are also obtained. Since in most investigations characterization of the surface morphologies of polymeric thin films on a substrate mainly relies on measurements of atomic-force microscope (AFM), scanning electron microscopy (SEM), optical microscope (OM) and such real space observation techniques, the structural study is thus limited to the morphological observation at the polymer–air interface [17], making probing internal nanostructures unlikely unless chemically etching protocols are additionally imposed on thin films of block copolymers to remove surface materials with air affinity [22]. Nevertheless, characterization of gazing-incidence small-angle X-ray scattering (GISAXS) on thin films has received recent attention, as it offers useful insights in not only interfacial structures at air but also buried internal nanostructures [23]. Particularly, GISAXS is a nondestructive tool of surface characterization, which the characterizing length scales in the film configuration cover a wide range from a few nanometers to submicrometers [18,19,24,25]. Furthermore, upon combination with external controls over experimental environments, for instance temperature control in a hot stage, the GISAXS measuring technique can be utilized to in situ characterize the evolution dynamics of hierarchical structures during thermal annealing [26].

The objective of our work was to study the evolution of mesophase-separated nanostructures and relief microstructures in asymmetric P(S-*b*-MMA) thin films that dewetted on polar substrates (SiO_x/Si and PMMA–SiO_x/Si) upon isothermal annealing at various temperatures. We observed dewetting morphologies in four stages to be driven by a mechanism involving nucleation and growth [20,21], and variations in the PMMA nanodomains (micelle–cylinder or cylinder–sphere transformations) were present in the destabilized films. The effect of the curved surface at the edge of a relief microstructure on the cylinder–sphere transformation is discussed in this report. Finally, experimental gazing-incidence small-angle X-ray scattering (GISAXS) characterizations and analytical GISAXS modeling were implemented to gain more understanding about the evolution of relief structures as a result of film instability.

2. Modeling of GISAXS by using IsGISAXS

Typically, complicated GISAXS scattering patterns or profiles result from multiple scattering in terms of a combination of reflection and refraction. Detail analyses of GISAXS data have been reviewed in the comprehensive article [27]. According to the distorted-wave Born approximation (DWBA), the total amplitude can be expressed as a coherent sum of four scattered amplitudes [27]. The four scattered amplitudes originate from a different scattering path each.

As shown in the early work, we demonstrated that diffuse scattering streaks at an angle with respect to the $q_\perp$ axis can be taken as indication of the formation of relief structures with a facet-like wedge edge [28]. In continuing the previous work, we also aimed to examine how distinct shapes of relief structures may be related to the diffuse scattering streaks in GISAXS. Our previous study indicated that on polar substrates (SiO_x/Si and PMMA–SiO_x/Si) the areas between irregular holes in destabilized P(S-*b*-MMA) films comprise one layer of PMMA nanocylinders with parallel orientation embedded in the PS matrix [28]. Here, we noted that at the final dewetting stage to form P(S-*b*-MMA) droplets, the spherical relief microstructures might not have an observable in-plane correlation length; in other words, for destabilized ultrathin films the droplets with a long inter-droplet distance install in the plane of the substrate [24]. As a result, the correlation length for the droplets due to dewetting in ultrathin films might not be detectable in the GISAXS configuration. Therefore, we assumed that the positions of the relief structures are completely random and independent without a positional correlation. For simplification, we also implicitly neglected simulation of the scattering associated with mesophase-separated cylindrical nanostructures within relief structures in the model simulation of the GISAXS data. Therefore, the simulated diffuse GISAXS scattering is mainly contributed from the form factor of relief structures on a micrometer length scale [28]. Fig. 1(a) and (b) shows diagrammatic representation of the two types of relief structures – (a) islands on a thin layer over a substrate; (b) holes in a layer on top of a substrate – for the models of simulating GISAXS data. For the model simulation of the GISAXS data, we used the IsGISAXS software [29]. In the modeling of GISAXS data, the two simple types of the island (or hole) shape – cone and hemisphere (*cf.* Fig. 1(c) and (d)) – were used to describe a variety of dewetting morphologies. The form-factor formulism of the two shapes was described in detail in Refs. [27] and [29]. The formation of the relief structures will be discussed in the following.

3. Experiments

3.1. Materials, film preparation and annealing

Polystyrene-*block*-poly(methyl methacrylate) (P(S-*b*-MMA), $M_n = 82$ kg/mol, $f_{ps} = 72\%$ and $f_{PMMA} = 28\%$, $I_p = 1.07$, Polymer Source, Inc.) was used as received. Bare silicon wafers (SiO_x/Si) were cleaned in a piranha solution (3:7 v/v 30% H_2O_2:H_2SO_4) for 40 min, rinsed with deionized water, and dried under flowing N_2. PMMA–SiO_x/Si substrates were achieved by spin coating (4000 rpm, 1 min) a PMMA–OH solution (1 mass% in toluene) on silicon wafers. The irreversibly grafted layers resulted from annealing (160 °C for 2 days) spin-coated films on hydroxylated silicon wafers under vacuum. Non-grafted materials were removed by sonication in toluene, followed by drying the substrates under flowing N_2. P(S-*b*-MMA) films (thickness 34.2 or 36.4 nm) were prepared via spin coating at 5000 rpm for 30 s from P(S-*b*-MMA) solutions (1.4 and 1.5 mass%) in toluene. Isothermally annealing the samples at 170, 190, 210, 230 and 245 °C in a closed hot stage (HCS402 Instec) purged with gaseous N_2 caused dewetting of the P(S-*b*-MMA) films on SiO_x/Si and PMMA–SiO_x/Si substrates. After thermal annealing (12 h), the thermally induced morphologies of the thin films were frozen by quenching into liquid N_2.

3.2. Topographies of thin films from use of an atomic-force microscope (AFM)

To determine the nanodomains and dewetted morphologies, we investigated the surface of thin films with an atomic-force microscope (SPA400 Seiko) in the tapping mode. AFM images were recorded with scan ranges between 2 μm × 2 μm, 5 μm × 5 μm and 25 μm × 25 μm. We used aluminum-coated silicon cantilevers of length 125 μm, width 30 μm and thickness 4 μm. The force coefficient was approximately 42 N/m and the resonance frequency used was 330 kHz.

3.3. Small-angle X-ray scattering (SAXS) and grazing-incidence small-angle X-ray scattering (GISAXS)

Before use of SAXS and GISAXS to characterize the mesophase-separated domains of the P(S-*b*-MMA) thin films, we imposed the same thermal annealing procedure described previously on all P(S-*b*-MMA) thin films. The SAXS and GISAXS experiments were

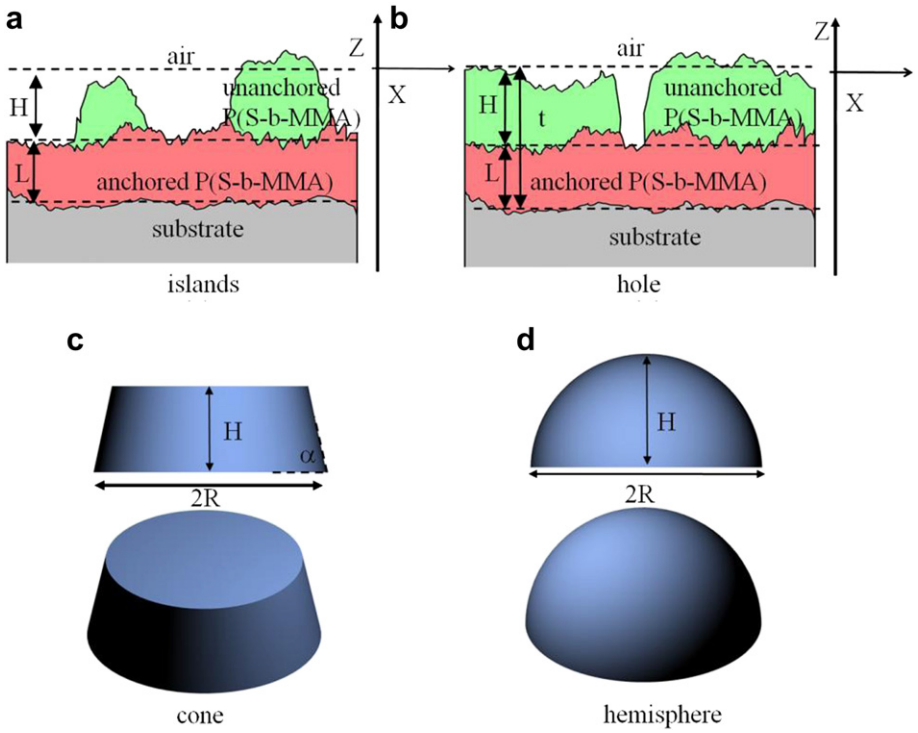

Fig. 1. Schematic illustration showing the two types of relief structural morphologies: (a) islands on a thin layer over a substrate; (b) holes in a layer on top of a substrate. The two simple types of the island (or hole) shapes – (c) cone and (d) hemisphere [27,29] – are shown to illustrate islands or holes as a result of film instability.

performed at beamline BL23A in the National Synchrotron Radiation Research Center (NSRRC), Hsinchu. The configuration of the GISAXS at BL23A was detailed elsewhere [30]. A monochromatized X-ray radiation source of photon energy 8 keV (wavelength $\lambda = 1.55$ Å) was used to collect the GISAXS patterns and a SAXS pattern with a MAR CCD detector. The distances from sample to detector were 2613.5 mm for GISAXS and 2268.1 mm for SAXS. The scattering vector, q ($q = 4\pi/\lambda \sin\theta$, with scattering angle θ) in these patterns was calibrated using silver behenate. The films for GISAXS measurements were mounted on a z-axis goniometer. The angle of incidence of each X-ray beam was $\alpha_i = 0.1875°$, which is between the critical angles of the P(S-*b*-MMA) film and of the silicon substrate ($\alpha_{c,f}$ and $\alpha_{c,s}$). Scattering angles were calibrated with the positions of X-ray beams reflected from the silicon substrate interface with varied incidence angle α_i.

4. Results and discussion

4.1. Cylindrical nanodomains in bulk

Fig. 2 shows the SAXS pattern for bulk P(S-*b*-MMA), as cast, measured at 30 °C, featuring diffraction signals located at $q = 0.0192$ and 0.0335 Å^{-1}. These features with q^* ratio = 1:$3^{1/2}$ are characteristic for the diffraction of cylindrical nanodomains, ordered with a hexagonally packed lattice. The position of the principal signal indicates a long period 37.79 nm of mesophase-separated cylinders according to an expression $D = (4/3)^{1/2} \times (2\pi/q^*)$ [28]. Scattering as an additional broad hump at $q = 0.0528$ Å^{-1} reflects the first-order form-factor scattering of an individual cylindrical domain. The radius of the PMMA cylindrical nanodomains was estimated to be 9.43 nm. We thus obtained a P(S-*b*-MMA) bulk comprising PMMA cylinders of mean radius 9.45 nm embedded within a PS matrix with an intra-cylinder distance 37.79 nm [28].

4.2. Dewetted morphologies and mesophase-separated nanodomains in thin films

The AFM topographies in Fig. 3 show the dewetted morphologies of isothermally annealed films. Upon annealing at temperatures 170, 190, 210, 230 and 245 °C for 12 h, the P(S-*b*-MMA) films

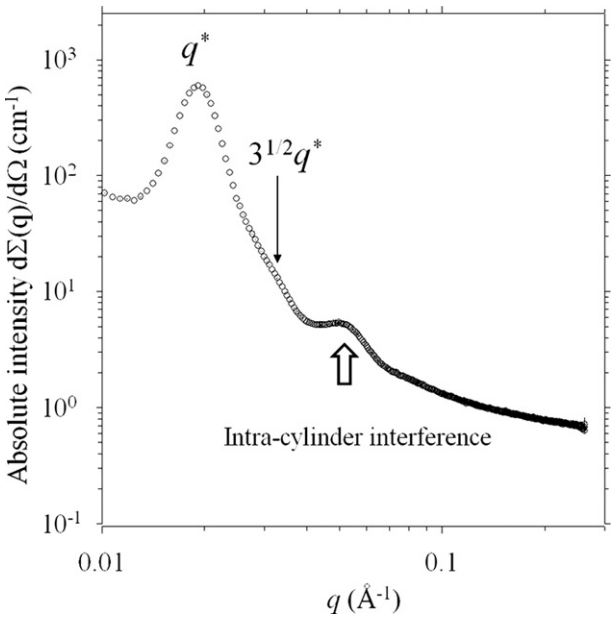

Fig. 2. SAXS datum for bulk P(S-*b*-MMA) as cast from the toluene solution (5 mass%), followed by isothermal annealing at 170 °C for 12 h. The depressed intensity observed for the second- and third-order diffraction features is due to a destructive interference between the form-factor scattering and the diffractions of the structure factor in the q range 0.02–0.04 Å^{-1}.

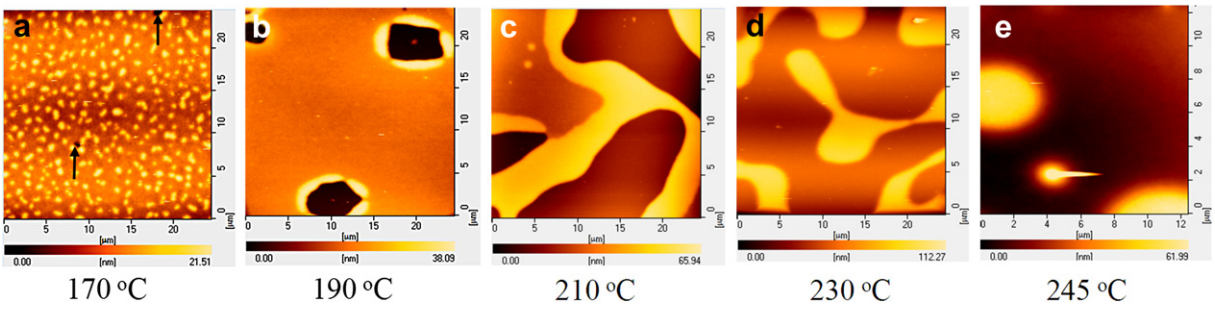

Fig. 3. AFM topographies of P(S-*b*-MMA) films on SiO_x/Si (initial thickness: 36.4 nm) after isothermal annealing for 12 h at temperatures (a) 170, (b) 190, (c) 210, (d) 230 and (e) 245 °C.

(initial thickness 36.4 nm) dewetted on SiO_x/Si according to a mechanism of nucleation and growth, causing the film surface to acquire an undulating thickness. The series of AFM images display a dewetting process that involves in the four stages – (i) rupture of the film (Fig. 3(a)), (ii) formation of holes with uneven wavy rims (Fig. 3(b) and (c)), (iii) progressive growth of the rims until impinging together to form a polygonal network (Fig. 3(c) and (d)), and (iv) final breaking of the polygonal network into micro-drops or micro-slabs (Fig. 3(e)). Although the observation of the dewetting evolution by optical microscopy was reported previously [28], the AFM characterization provides additional structural information at tens of nanometers, which is unable to be feasible by OM. For instance, close scrutiny of the AFM image (Fig. 3(a)) indicates that the irregular tiny granules are due to excess PS blocks that are unable to fully cover over a homogenous layer underneath. Besides, the underneath continuous layer reveals a few small holes, indicated by arrows.

The instability of the film thickness upon heating reflects an incommensurability of the film thickness, t, with the spacing, D, of nanodomains. For P(S-*b*-MMA) films on SiO_x/Si, the PMMA blocks preferentially segregate on the hydrophilic surface of the Si substrate, whereas the PS block with a smaller surface energy resides at the free surface. This preferential wetting with the substrate and free surfaces by each of the two blocks constitutes an asymmetric wetting [3,4]. The films thus remain stable only when the thickness of the film as spun matches a natural thickness given approximately by [31]

$$t = nD + \beta$$

in which n is an integer and β represents the thickness of a layer of P(S-*b*-MMA) brush autophobically anchored on the silicon substrate, with the PMMA block anchoring at the substrate surface and the PS block facing outward [12,13].

As thin films spin-coated from a solution in toluene, the P(S-*b*-MMA) samples without thermal annealing reveal disordered micelles in AFM topography (not shown for brevity). Toluene is known to be a selective solvent – an effective solvent for PS but poor for PMMA [32]. We suggest that those micelles appear when the concentration of the solution increases on solvent evaporation to attain a critical point at which micelles are initiated. The micelles are thus a kinetically trapped morphology as a result of rapid evaporation of solvent during spin coating, and are therefore metastable [33]. Upon annealing, we expect a morphological transformation from disordered micelles into cylinders. The AFM stature and corresponding phase images of the annealed P(S-*b*-MMA) films are shown in Figs. 4 and 5, which reveal the revolution of cylindrical domains on nanometer scales. At 170 °C, the film presents a remarkable dual presentation of PS and PMMA at the free surface (Figs. 4(a),(f) and 5(a),(f)). A large density of defects is also observable, revealing a pattern with a much smaller correlation length. Such a pattern is due to the pinning effect of a strong affinity between the PMMA block and the hydrophilic surface of SiO_x/Si [34]. As a result, the P(S-*b*-MMA) films have small polymer chain mobility in the plane of SiO_x/Si so that cylindrical nanodomains evolve slowly from disordered micelles at 170 °C. Beside, because of the PS block having a low surface energy, excess PS materials preferentially migrated onto the free surface displaying as featureless granules.

Upon annealing at 190 °C for 12 h, the P(S-*b*-MMA) film shows large grains of PMMA cylinders embedded within a PS matrix, as shown in the AFM phase and topography images (Figs. 4(b),(g) and 5(b),(g)). The large cylindrical grains resulted from removal of the defects on annealing [35]. In particular, upon annealing the PMMA cylinders with a parallel orientation grow at the expense of the grains of disordered micelles. Scrutiny of the AFM images (Fig. 4(b) and (g)) indicates discrete regions present as nano-size spotted or striped morphologies protruding slightly in height relative to the continuous PS matrix. The spot- or strip-like nanodomains hence appear white while the matrix appears dark in the topographic images.

The corresponding AFM phase image shown in Fig. 5(b) and (g) reveals that the protruding regions have a large phase shift. We thus attribute the discrete regions to PMMA domains of large modulus because the T_g (the glass-transition temperature) of PMMA is greater than that for PS. The difference between the heights of the discrete nanodomains and the continuous matrix shown in the AFM images is attributed to the two blocks having different surface energies [36]. In contrast, a distinct morphology is present at the areas near the edges of the holes with wavy uneven rims, at which occurs preferential wetting with the free surface by PS chains. We speculate that, for the P(S-*b*-MMA) thin film annealed at 190 °C, a mixed morphology of spot-like and stripe-like nanodomains shown in the AFM image is due to a mixture of PMMA spherical and parallel cylindrical nanostructures coexisting in the destabilized film. This mixed morphology is similar to those reported by Naik *et al.* for Pluronic F127 (PEO_{106}-PPO_{70}-PEO_{106}) templated films [37] and by Tate *et al.* for Pluronic P123 (PEO_{20}-PPO_{70}-PEO_{20}) mesoporous silica thin films [38].

Furthermore, as the spin-coated film thickness was incommensurate with the natural spacing of the cylindrical nanodomains, during the course of annealing the films began to dewet on the SiO_x/Si according to a mechanism of nucleation and growth, in which the PS block crawled slowly along the free surface forming irregular wavy rims. Consistent with conservation of mass, the PS block advancing onto the free surface as a result of a strong attraction with the free surface is accompanied by a depletion of the volume fraction of the PS block in local areas of the film. According to this argument, the AFM measurements in a tapping mode demonstrate that the PMMA cylindrical nanodomains at the free

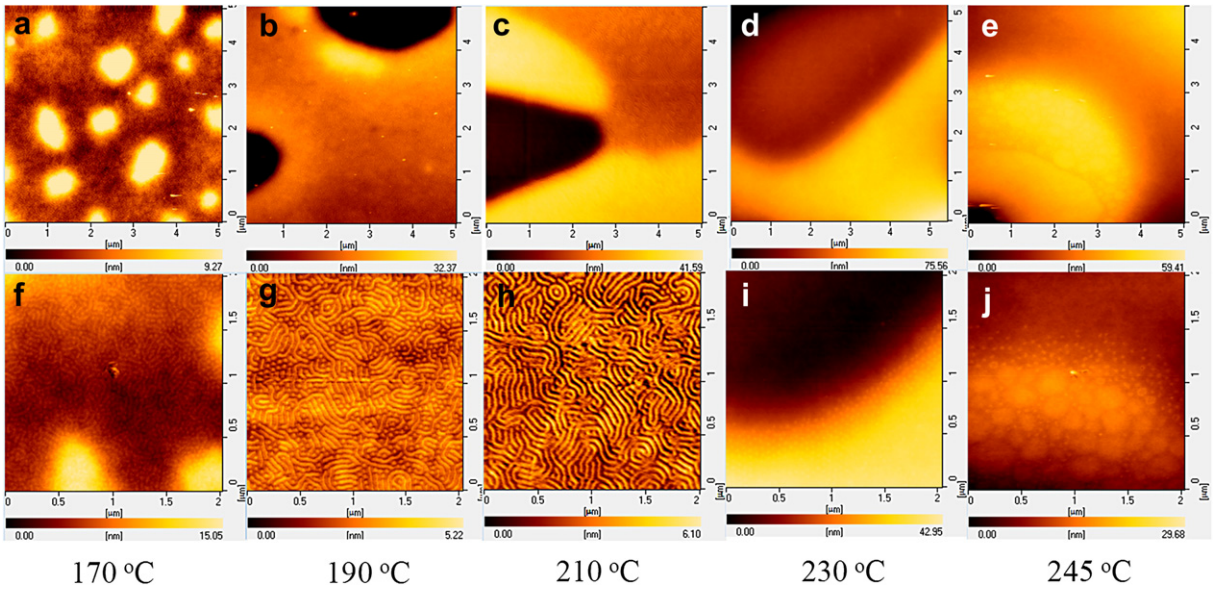

Fig. 4. AFM height images 5 μm × 5 μm (top images) and 2 μm × 2 μm (bottom images) for P(S-*b*-MMA) films of initial thickness 36.4 nm on SiO_x/Si after isothermal annealing for 12 h at various temperatures (a) and (f) 170, (b) and (g) 190, (c) and (h) 210, (d) and (i) 230, and (e) and (j) 245 °C. AFM topographies (g) and (h) were obtained by zoom-in scanning the PS-uncovered areas in images b and c, respectively.

surface without PS covering were enhanced reliefs of height ~3–6 nm. On the other hand, since the affinity of the PMMA block with the substrate surface first led to the formation of a ca. 21-nm monolayer of anchored P(S-*b*-MMA), the dewetting represents that the top layer of unanchored P(S-*b*-MMA) dewetted from the bottom brush layer with an entropic penalty (i.e. an autophobic behavior) [12–14,28].

Upon annealing at 210 °C for 12 h, the holes expand through continued growth of the rims; the P(S-*b*-MMA) film then shows two regions. As Figs. 4(c) and 5(c) show, one region at the rim front reveals the presence of PS chains preferentially wetting on the free surface. Between the rims is the PS-uncovered region that clearly displays the presence of both PS and PMMA domains, in which the major portions of PMMA are long cylinders oriented parallel with the substrate surface (Figs. 4(h) and 5(h)). The mean intra-cylinder distance of the annealed thin films is ca. 53 nm, larger than the value 37.78 nm calculated from the SAXS pattern for P(S-*b*-MMA) bulk. This result indicates that the annealed P(S-*b*-MMA) film has parallel PMMA nanocylinders arranging in one row, which represents an expansion in the lateral direction [37].

Through this advancing growth the rims impinge together, resulting in a polygonal network microstructure composed of long ridges and valleys (as shown in Figs. 4(d),(i) and 5(d),(i)). At that stage, rim coalescence and continued growth of holes result in a slight corrugation with a depression particularly within some junctions of the long ridges. Upon annealing at 245 °C (Figs. 4(e),(j) and 5(e),(j)), in some regions the polygonal network progressively breaks into microscale slabs or drops. At the edges of drops appears a nanospot-like pattern, which might correspond to spherical nanodomains as a result of a cylinder-sphere transformation [5]. At

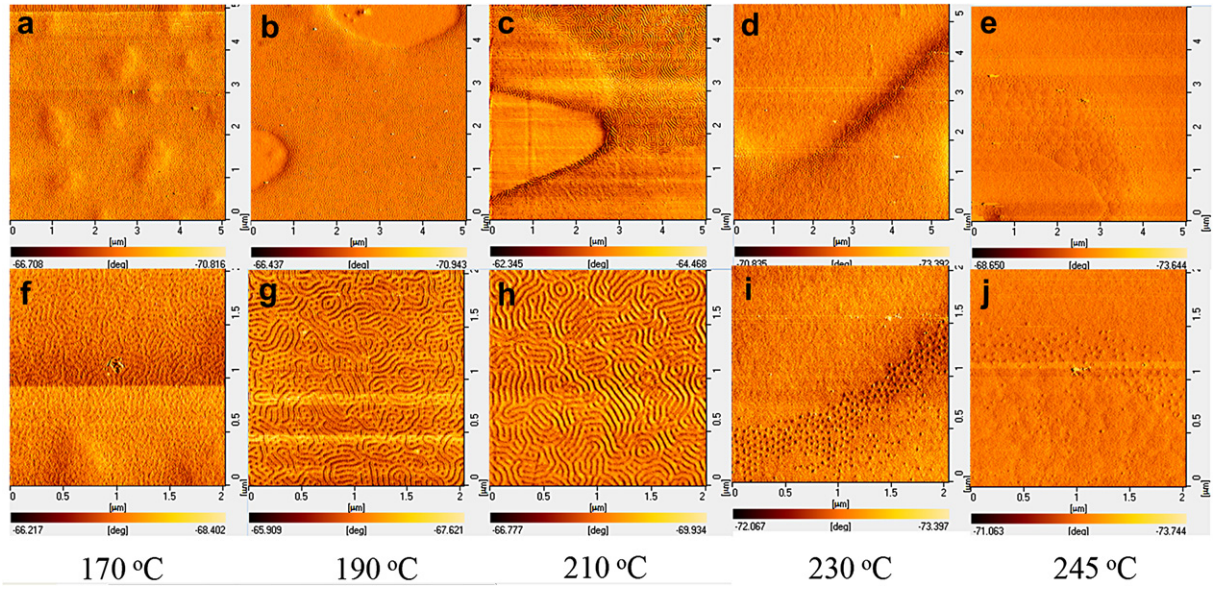

Fig. 5. Corresponding AFM phase images 5 μm × 5 μm (top images) and 2 μm × 2 μm (bottom images) for the same annealed samples shown in Fig. 4.

the curved edges of slabs or drops the preferential wetting of the free surface by the PS block is hindered, because the energy barrier for the formation of a wetting layer of PS is large at a curved surface.

Now we examine the morphologies of the P(S-*b*-MMA) films on top of PMMA-SiO_x/Si. For the P(S-*b*-MMA) thin films of initial thickness 34.2 nm on PMMA-SiO_x/Si, isothermal annealing at various temperatures causes film stability proceeding via a nucleation and growth mechanism (Fig. 6). In comparison, the P(S-*b*-MMA) films dewetted more quickly on PMMA–SiO_x/Si than on SiO_x/Si except for 170 °C, at which temperature the films on both SiO_x/Si and PMMA–SiO_x/Si reveal a morphology displaying featureless granules on a homogeneously continuous layer (Fig. 6 (a) and (f)). As mentioned, the irregular tiny granules are due to incomplete covering of the PS block over an underneath continuous layer. Upon annealing at 190 °C, the film spread on top of PMMA–SiO_x/Si reveals that holes with uneven rims have grown with time to form a network (Fig. 6(b) and (g)). At 210, 230 and 245 °C, a part of the network structure on PMMA–SiO_x/Si has broken to form slabs or drops (Fig. 6(c)–(e) and (h)–(j)). By contrast, in the temperature region the P(S-*b*-MMA) films on SiO_x/Si reveal a network of relief structures. On the other hand, Fig. 6(k)–(o) reveal the similar nanostructural revolution in the destabilized films on PMMA–SiO_x/Si as compared with that on SiO_x/Si. We also noted that the nanostructures on curved edges of relief structures on PMMA–SiO_x/Si reveal nanospheres (Fig. 6(o)).

4.3. Characterizations of hierarchical structures by GISAXS

To characterize the mesophase-separated nanostructures of the P(S-*b*-MMA) films that dewetted on SiO_x/Si after annealing at the designed temperatures, we performed GISAXS measurements. The 2D GISAXS patterns for destabilized films are shown in Fig. 7, which reveals rod-like or spot-like scattering typical for strongly fiber-textured films. The rod-like scattering is due to the elongation of the Bragg diffraction spots (sharp along $q_{\|}$ and slightly diffuse along $q_{\perp}$) ascribed to the small thickness of the film. For the P(S-*b*-MMA) film annealed at 170 °C, the GISAXS pattern reveals spots in two sets symmetrically on either side of the beam stop, with each set at the same $q_{\|}$ having a series of spots along $q_{\perp}$. As can be seen in Fig. 7, two brightly striped lines appear parallel to the $q_{\|}$ direction; these striped lines of intense scattering result from a standing-wave phenomenon and from total reflection occurring at the interface between the film and the substrate [39,40]. Intersection of the striped lines with the diffractions of the ordered nanodomains produces the intense spots. For the P(S-*b*-MMA) films annealed at 190 °C, the spots have increased intensity, accompanied by broadening of the signals of the spots along the thickness direction ($q_{\perp}$). In addition, a series of Kiessig fringes along the $q_{\perp}$ direction emerge for the film annealed at 190 °C. The amplitude of the Kiessig fringes became enhanced at 210 and 230 °C. At 245 °C, the amplitude of the fringes, however, became depressed. The presence of the Kiessig fringes associated with resonant diffuse scattering indicates the presence of a correlated rough layer [41,42]. In order to clearly discern the fringes, one-dimensional scan cuts along the film direction at $q_{\|} = 0\ \text{Å}^{-1}$ were imposed on the 2D GISAXS patterns to show 1D detector-scan GISAXS profiles. As shown in Fig. 8, the detector-scan-cut 1D profiles for the films at annealed 170 °C reveal no fringes, indicative of the absence of the monolayer of anchored P(S-*b*-MMA) brushes. For the films annealed at 190, 210 and 230 °C, the detector-scan-cut 1D profiles reveal a series of fringes with enhanced amplitude, whose frequency corresponds to the correlated thickness of the anchored

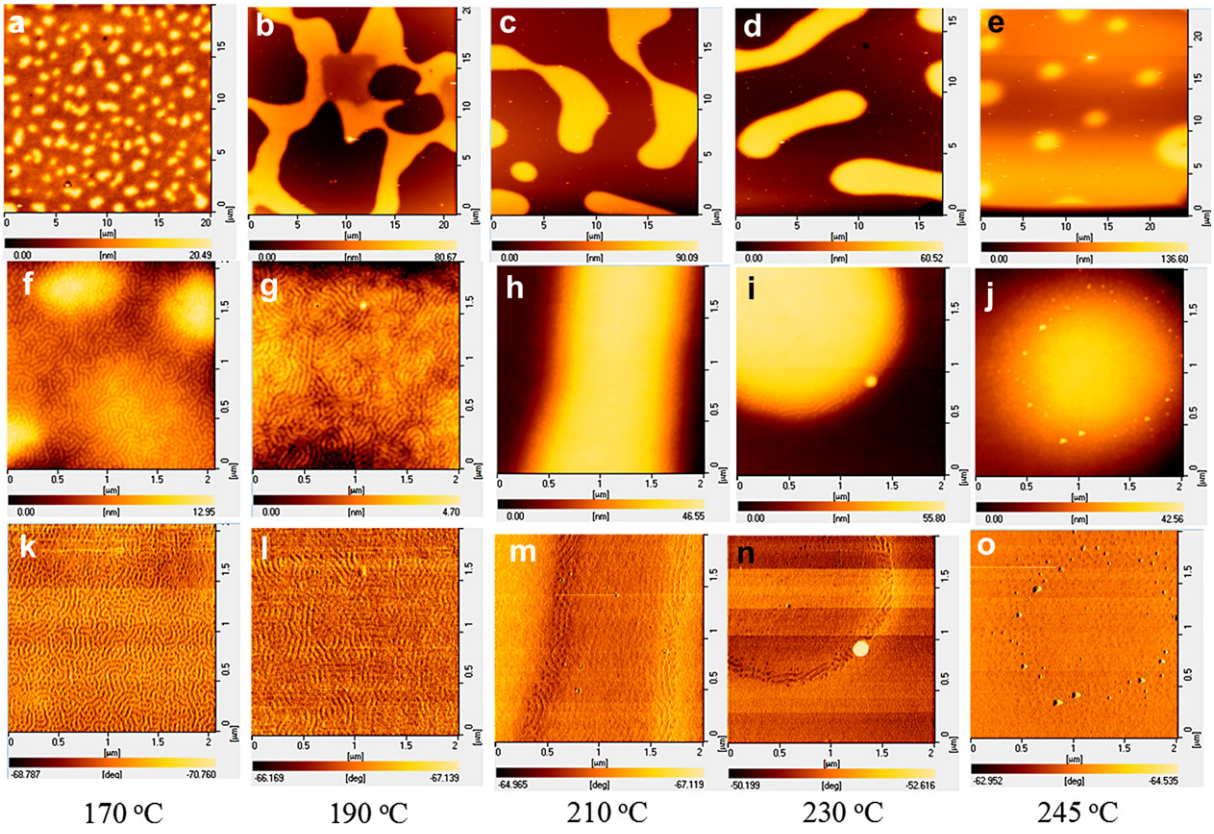

Fig. 6. AFM topographies (the top and middle rows of images) and phase images (the bottom row of images) of P(S-*b*-MMA) films of initial thickness 34.2 nm on PMMA-SiO_x/Si after isothermal annealing for 12 h at various temperatures 170, 190, 210, 230 and 245 °C. The middle and bottom rows of images are the corresponding 2 μm × 2 μm AFM height ((f)–(j)) and phase ((k)–(o)) images for the same annealed samples. AFM images (g) and (l) were obtained by zoom-in scanning the PS-uncovered areas in image (b).

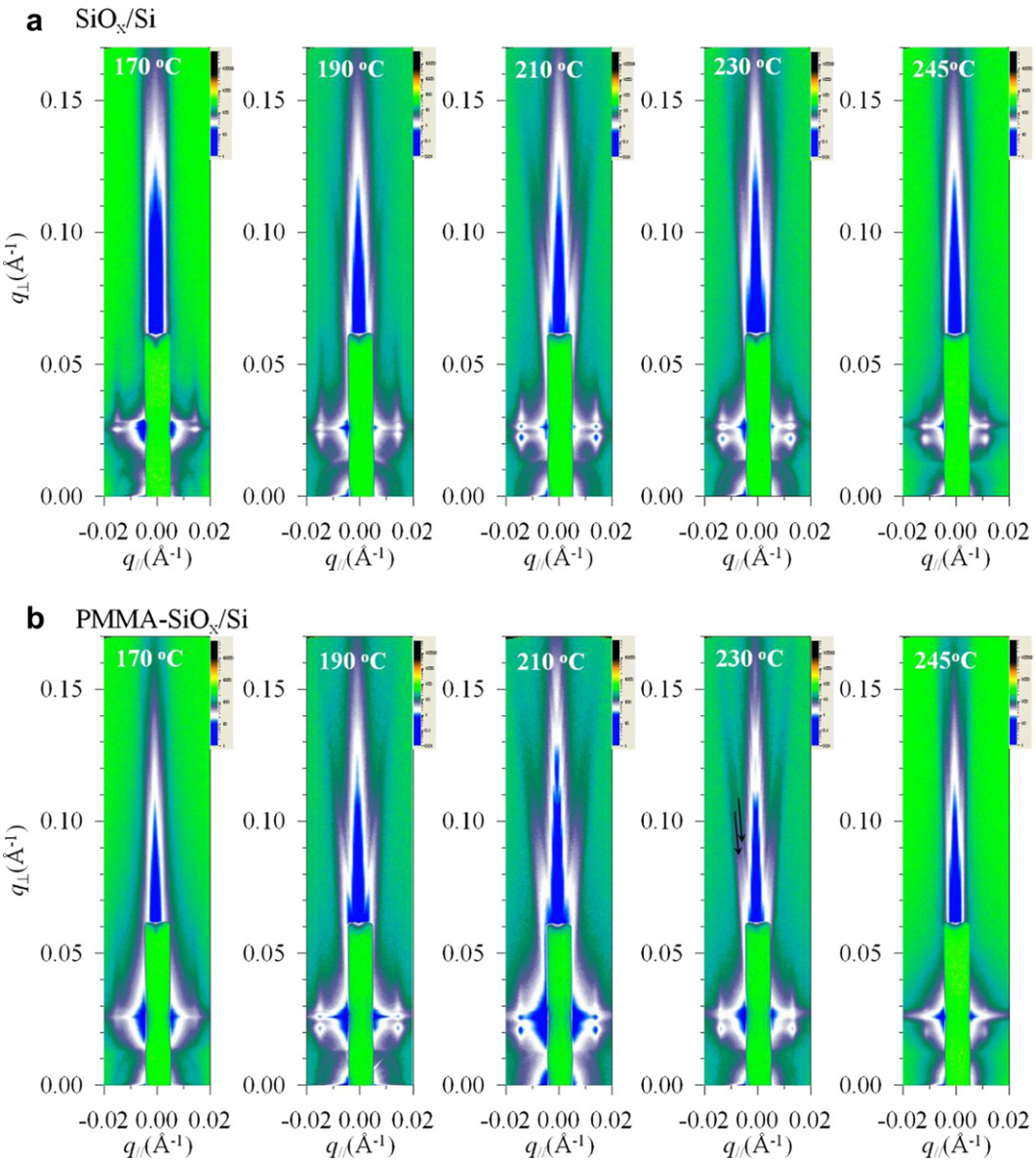

Fig. 7. 2D GISAXS patterns measured at $\alpha_i = 0.1875°$ of grazing incidence for P(S-*b*-MMA) thin films spread on (a) SiO_x/Si (the top row of patterns) and (b) PMMA–SiO_x/Si (the bottom row of patterns) after isothermal annealing at various temperatures: 170, 190, 210, 230 and 245 °C for 12 h.

P(S-*b*-MMA) brushes with a roughness correlation [28,41,42]. For the film annealed at 245 °C, the presence of the depressed fringes indicates that the roughness correlation of the monolayer of anchored P(S-*b*-MMA) brushes decays significantly. Nevertheless, the depressed fringes with weak amplitude are still discernible, indicative of a certain extent of partially interfacial roughness correlation of the P(S-*b*-MMA) wetting monolayer retaining at equilibrium.

In addition to the Bragg rods/spots and Kiessig fringes, the GISAXS patterns display additional diffuse scattering streaks (indicated by arrows) emerged at angles with respect to the $q_\perp$ direction for the thin films annealed at 190 °C. However, for the films annealed at 170 and 245 °C, the GISAXS patterns do not reveal the diffuse scattering streaks. In the temperature region between 190 and 245 °C, the scattering streaks reveal variations in intensity. A comparison of the results shown in the AFM images indicates that the emergence of scattering streaks seems accordingly to be accompanied with the formation of film instability induced relief structures within P(S-*b*-MMA) films having ordered nanostructures. In particular, the streaks (indicated by arrows) for the film containing isolated relief slabs were found to be double in comparison with those for the films having irregular holes within a continuous layer. Variations in intensity of diffuse scattering streaks with various extent of dewetting may indicate that the intensity of diffuse scattering streaks and the intensity in areas between the two streaks strongly correlate with the shape of relief structures.

In order to clearly discern the 1D profile of the streaks, one-dimensional scan cuts along the film direction at various $q_\parallel (q_\parallel \neq 0$ off-detector-scan cuts) were imposed on the 2D GISAXS patterns. Fig. 9 shows the 1D off-detector-scan scattering profiles, which were extracted from the vertical scan cuts along the $q_\perp$ direction at $q_\parallel = 0.004$, 0.008, 0.012 and 0.016 $Å^{-1}$. At the lowest annealing temperature of 170 °C, the 1D off-detector-scan profiles only reveal standing-wave features in the low $q_\perp$ region ($q_\perp < 0.05$ $Å^{-1}$). For the destabilized P(S-*b*-MMA) films with annealing at temperatures above 190 °C, a hump indicated by arrows emerged and became enhanced in the 1D off-detector-scan profiles obtained via vertical

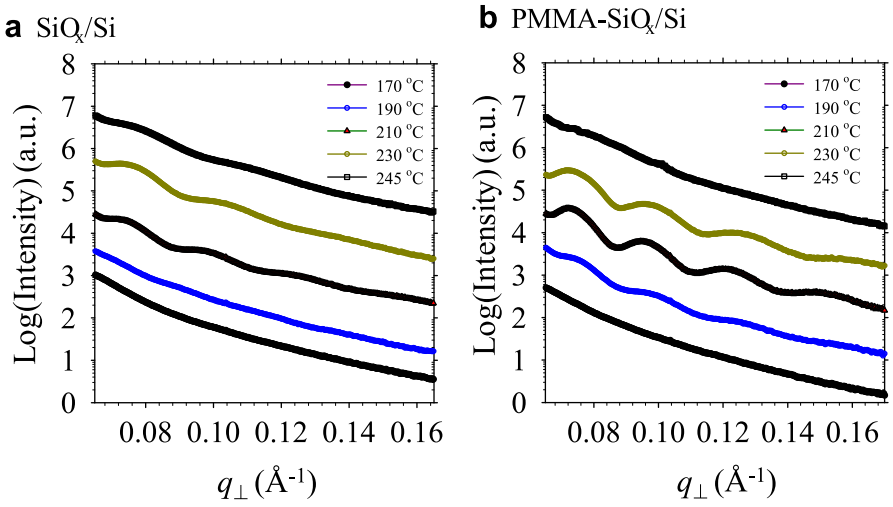

Fig. 8. 1D detector-scan GISAXS profiles with intensity as a function of $q_\perp$ obtained with vertical cuts at $q_\parallel = 0$ Å^{-1} corresponding to Fig. 7 for P(S-*b*-MMA) thin films spread on (a) SiO_x/Si and (b) PMMA−SiO_x/Si after isothermal annealing at various temperatures: 170, 190, 210, 230 and 245 °C for 12 h. The curves were shifted for clarity along the *y* axis.

cuts at various $q_\parallel$. At the highest temperature of 245 °C, there is no hump associated with the diffuse streaks displaying in the 1D GISAXS profiles.

To quantitatively understand how the distinct shapes of relief structures correlate with variations in intensity of diffuse scattering streaks, we thus performed the simulation modeling of GISAXS. Taking into account information obtained from the qualitative AFM microscopy, we attempted to analyze quantitatively the measured GISAXS data. For simplification, we neglected all possible scattering of the scattered intensity from the mesophase-separated nano-domains, but only examined all possible scattering models (cone, and hemisphere) of the scattered intensity from the relief microstructure as a result of film instability. The cone and hemi-sphere shapes were used to describe facetted drops, holes, and spherical-cap shaped granules or rounded-shape drops.

As shown in Fig. 10(a), the simulated GISAXS pattern reveals no diffuse scattering streaks for the hemisphere shape of 12 nm in height and 1000 nm in radius acting as the shape of tiny granules covering over a continuous layer of 34 nm. The absence of diffuse scattering streaks for the spherical shape is well consistent with the corresponding the GISAXS pattern of the P(S-*b*-MMA) thin films containing tiny granules covering over a continuous layer. In contrast, as shown in Fig. 10(b) and (c), the diffuse streaks can be well reproduced for the shapes of cone acting as holes or islands

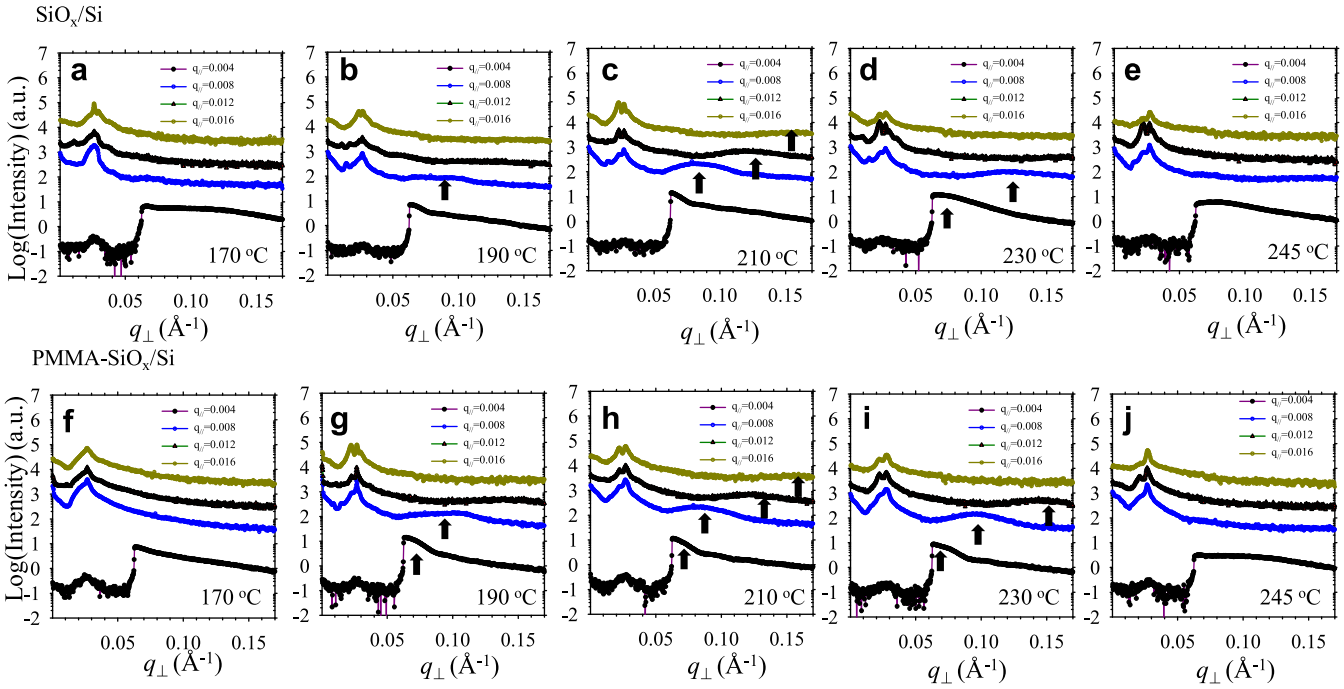

Fig. 9. 1D off-detector-scan GISAXS profiles with intensity as a function of $q_\perp$ obtained with vertical cuts at $q_\parallel = 0.004$, 0.008, 0.012 and 0.016 Å^{-1} corresponding to Fig. 7 for P(S-*b*-MMA) thin films spread on SiO_x/Si (the top row of figures) and PMMA−SiO_x/Si (the bottom row of figures) after isothermal annealing at various temperatures: ((a) and (f))170, ((b) and (g))190, ((c) and (h)) 210, ((d) and (i)) 230, and ((e) and (j)) 245 °C for 12 h. The curves were shifted for clarity along the *y* axis. The depressed intensity in the low $q_\perp$ region of the 1D off-detector-scan GISAXS profiles obtained with a vertical cut at $q_\parallel = 0.004$ Å^{-1} is due to the blocked area from X-ray by the rod-shaped beam stop.

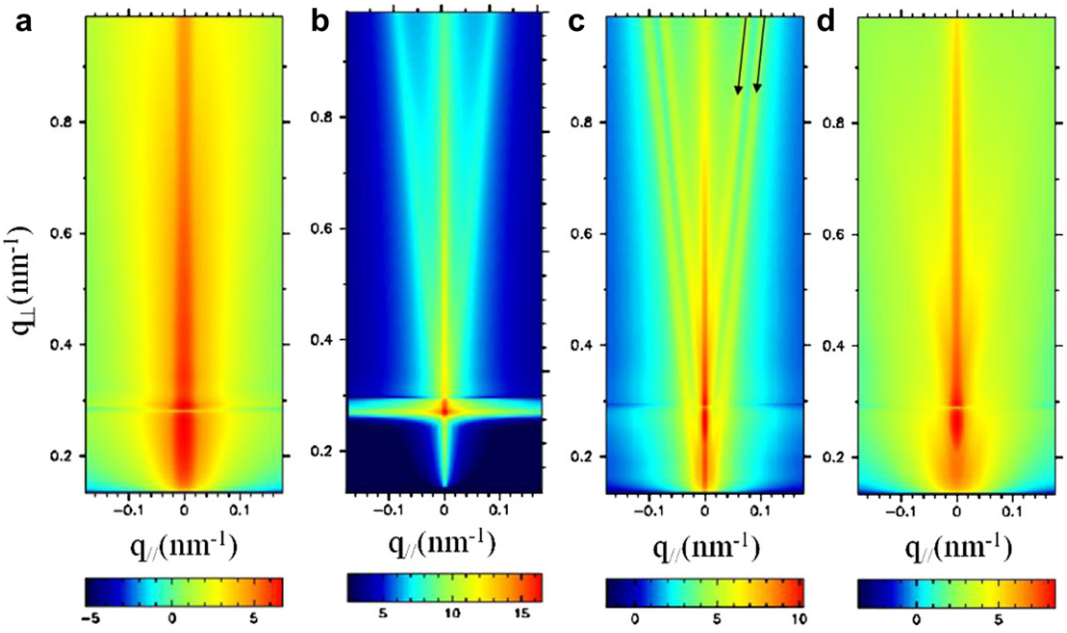

Fig. 10. Simulated GISAXS patterns of various types of relief structural morphologies: (a) a hemisphere-shape granule of $R = 1000$ nm and $H = 12$ nm over on a layer of thickness $L = 34$ nm; (b) cone-shape holes of $R = 1000$ nm and $H = 38$ nm within a film of thickness $t = 59$ nm; (c) cone-shape, and (d) hemisphere-shape drops of $R = 1000$ nm and $H = 38$ nm over a layer of thickness $L = 21$ nm. The radius and height of the relief structures have a distribution $\sigma_R = 0.5$ and $\sigma_H = 0.5$, respectively. The base angle α for the cone shape was set as 6°.

within a destabilized film. For holes of depth 38 nm in a layer of thickness 59 nm on top of a substrate, their simulated GISAXS patterns display a set of two diffuse scattering streaks, which symmetrically appears at the both sides with respect to the $q_\perp$ axis (Fig. 10(b)). In addition, the patterns also clearly display the striped lines parallel to the $q_\parallel$ axis. These lines are associated with the effects of standing waves [39,40]. By contrast, for facetted islands of height 38 nm covering a layer of thickness 21 nm on top of a substrate, the simulated GISAXS patterns display two sets of narrow streaks, in which each set has two scattering diffuse streaks appearing at the both sides with respect to the $q_\perp$ axis (see Fig. 10 (c)). The double diffuse scattering streaks are due to an effect of superposition of the refraction and reflection beams (indicated by the arrows) [27]. In contrast, the diffuse scattering streaks shown in Fig. 10(d) seem much broader in width and much weaker in intensity for the shape of a hemispherical cap acting as rounded-shape islands of 38 nm over on a 21-nm wetting monolayer of P(S-*b*-MMA) brushes. The GISAXS simulation for the hemisphere shape indicates that the full width at half maximum (FWHM) of diffuse scattering streaks and the angle between the streaks and the $q_\perp$ axis strongly depend on the size and size distribution of the hemisphere shape (for brevity, the data are not shown). Although the simulated GISAXS patterns for the hemisphere shape displays very weak diffuse scattering streaks, the weak diffuse scattering streaks, however, are not discernible in the experimental GISAXS patterns for the samples annealed at 245 °C. The reason is that the density of drops on top of the wetting layer is low so that the diffuse scattering streaks with very weak intensity may not be easily observed in practice. Also, it has been shown that the intensity of diffuse scattering streaks decays as q^{-4} for a rounded-shape object with a curved surface [43]. Therefore, the intensity for such a round shape decays quickly at high q so that the streaks in the high q region are the weakest. All these reasons may make the diffuse scattering streaks uneasily observable for the curved-surface drops with a low density of population.

In order to compare with the experimentally measured off-detector-scan 1D GISAXS profiles, vertical scan cuts along the $q_\perp$ direction at $q_\parallel = 0.004$, 0.008, 0.012 and 0.016 Å^{-1} were imposed on the simulated GISAXS patterns. Fig. 11 shows the simulated off-detector-scan GISAXS profiles with intensity as a function of $q_\perp$. Apparently, only for facetted relief structures describing by a cone shape with a base angle 6°, the simulated 1D off-detector-scan

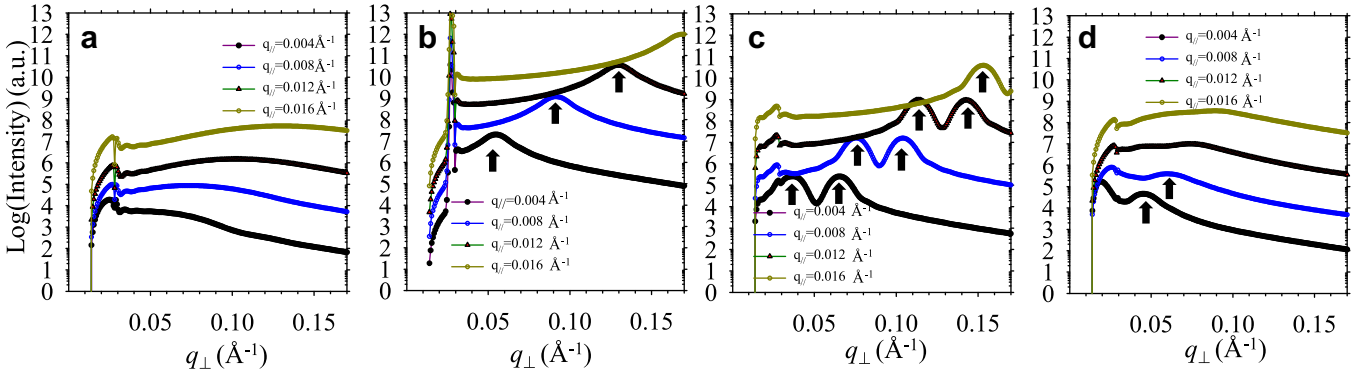

Fig. 11. 1D off-detector-scan GISAXS profiles with intensity as a function of $q_\perp$ obtained with vertical cuts at $q_\parallel = 0.004$, 0.008, 0.012 and 0.016 Å^{-1} corresponding to Fig. 10.

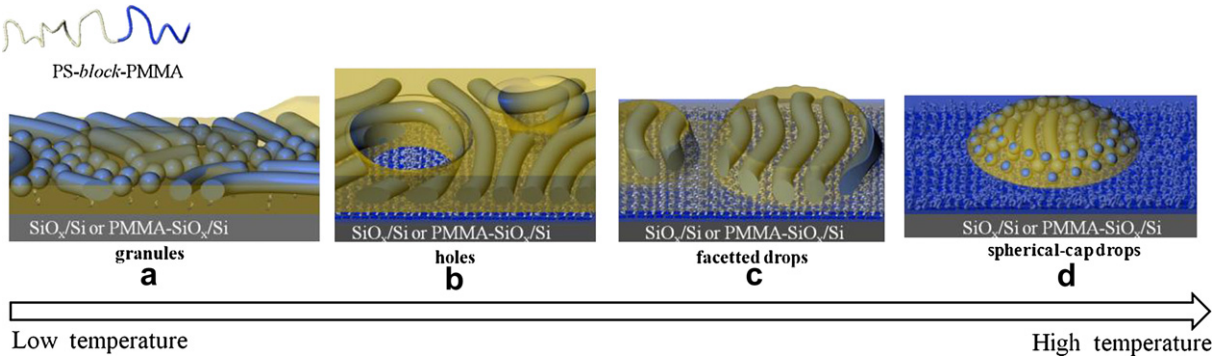

Fig. 12. Schematic illustration showing the four types of relief structural morphologies: (a) granules, (b) areas between irregular holes, (c) facetted drops and (d) spherical-cap drops.

GISAXS patterns clearly reveal one (cone-shaped hole, Fig. 11(b)) or two humps (cone-shaped island, Fig. 11(c)). On the other hand, the position of the hump indicated by arrows was found to vary with different cuts at various $q_{\|}$ values. The hump for facetted relief structures are still clearly discerned when vertical scan cuts were carried out at $q_{\|} = 0.012$ and $0.016\ \text{Å}^{-1}$. In contrast, the hump for spherical-cap shaped relief structures (hemisphere-shaped granules and drops, Fig. 11(a) and (d)) depresses significantly in intensity so as to become much diffuse when vertical scan cuts were carried out at $q_{\|} = 0.012$ and $0.016\ \text{Å}^{-1}$. In comparison with the GISAXS experimental profiles of the destabilized films, the simulated GISAXS profiles for a destabilized film with various types of shape of relief structures are in good agreement with the measured scattering profiles. From the trends and evidences of the measured and simulated GISAXS profiles, it can be proposed that diffuse scattering streaks at angles with respect to the $q_{\perp}$ direction are associated to the relief structures with a facet-like edge, while no diffuse scattering streaks yield for a low-density population of relief structures with a curved spherical shape.

The relationship between the shape of relief microstructures and ordered mesophase-separated nanodomians, however, requires further interpretation. Based on the AFM observations and a comparison between the measured GISAXS and simulated GISAXS patterns, we proposed a possible scenario of film instability induced the evolution of hierarchical structures in annealed P(S-*b*-MMA) films on a polar substrate. Before thermal annealing, the intact film consists of disordered PMMA micelles embedded within the PS matrix. Thermal treatment imposed on the spin-coated P(S-*b*-MMA) film lead to not only a structural change on a nanometer scale but also film instability on a micrometer scale. Isothermal annealing at 170 °C gave rise to tiny featureless granules. The featureless granules are due to the PS block incompletely covering over a continuous layer that consists of disordered micelles and shorts cylinders (*cf.* Fig. 12(a)). We speculated that at the lowest temperature of 170 °C the anchoring density of the P(S-*b*-MMA) chains absorbed on the polar surface of the substrate was too low to form a complete brush layer at the substrate interface. Due to lacking an autophobic effect driven by an entropic penalty, large-scale undulations in thickness by dewetting could not be able to be triggered off. Only the PS chains segregating onto the free surface was allowable to reach the film commensurability instead, giving rise to the featureless granules displaying in the AFM images. On the other hand, at the lowest annealing temperature of 170 °C, the mobility of polymer chains should be slow at the attractive surface of a solid even although the annealing temperature is above the glass-transition temperatures of the two blocks in bulk state [44]. Therefore, only a very few of small holes forming at a low rate could be achieved by film rupture. At 190 °C, large-scale film instability occurred. The large-scale film instability is due to an autophobic effect that unanchored P(S-*b*-MMA) chains dewetted on a monolayer of anchored P(S-*b*-MMA) brushes since the density of anchoring with the polar surface of the substrate is high enough to form a brush layer. At the early stage of film instability that the film ruptures to form large holes with uneven wavy rims, disorder micelles gradually transformed into nanocylinders via a large-scale undulation in film thickness (Fig. 12(b)). With annealing at high temperatures (210 and 230 °C) to increase film instability to an extent of progressive growth of the PS constituted rims until impinging together to form a polygonal network, the ordering of mesophase-separated cylindrical nanodomains became improved. In some areas that film instability advanced quickly, the polygonal network broke to form drops and slabs. As a result, the formation of parallel-oriented PMMA cylindrical nanodomains increases the deformation energy, and it will persist to force the shape of relief structures to be a facet-wedge shape (Fig. 12(c)). However, those relief structures are expected to be not at equilibrium. Upon annealing at the highest temperature (245 °C), curved drops causes a transformation of cylinders to noncylindrical nanodomains since the discrete, noncylindrical nanodomains experiences less structural frustration with the curvature of a spherical cap than the cylinder nanodomains with a parallel orientation (Fig. 12(d)) [45]. The noncylindrical nanodomains at the edge of spherical-cap shaped drops have been observed in polystyrene-*block*-polyethylene oxide, (PS-*b*-PEO) diblock copolymer thin films with exposure to solvent vapor by Kim *et al.* [45,46]. They attributed the formation of the spherical nanodomains to the two factors: selective swelling of the major block by a solvent and the packing frustration of cylindrical nanodomains in a spherical cap [45,46]. In our study, the latter factor solely dominates the formation of the cylinder-to-sphere transformation at the edge of isolated relief structures since only thermal annealing was imposed on the P(S-*b*-MMA) thin films to induce the film instability.

5. Conclusion

In destabilized thin films of P(S-*b*-MMA) induced by thermal annealing, the mesophase-separated nanodomains are found to be strongly correlated with the formation of relief microstructures as a result of the four stages of dewetting. In the first stage, the P(S-*b*-MMA) film ruptures, forming holes without rims; the nanodomains within the destabilized film are mainly disordered micelles. In the second stage, uneven wavy rims initiate from the rupture, as a result of the preferential wetting of the PS block by air, whereby the PS block slowly crawls onto the free surface; the cylindrical PMMA nanodomains that orient parallel with the substrate surface concurrently grow at the expense of the grains of disordered micelles. At the third stage of dewetting, a slight

corrugation with a depression occurs in some areas within the interconnected network structure when the rims gradually grow and eventually contact each other to form an interconnected network structure. At the stages of film instability, the formation of internal parallel-oriented PMMA nanodomains buried within the relief structures gives rise to an increase in deformation energy so that the edge shape of relief structures has a facet-like wedge. The network structure finally breaks, forming drops or slabs; at the stage, due to affinities between the PMMA block and the polar surface of a substrate and between the PS block and the free surface the depletion of the blocks into the polymer–substrate or polymer–air interfaces causes a nanostructural transformation from PMMA cylinders to spheres. The spherical PMMA nanodomains are stable and persist at the edges of spherical-cap drops.

Acknowledgements

National Science Council provided support (NSC 97-2218-E-008-011-MY2). We thank Dr. U-Ser Jeng and Dr. Chun-Jen Su for assistance in the GISAXS experiments at beamline BL23A in NSRRC, and also gratefully acknowledge discussions with Dr. Rémi Lazzari of Institut des NanoSciences de Paris for the IsGISAXS software.

References

[1] Bates FS, Fredrickson GH. Annu Rev Phys Chem 1990;41:525–57.
[2] Hamley IW. Prog Polym Sci 2009;34:1161–210.
[3] Coulon G, Russell TP, Deline VR, Green PF. Macromolecules 1989;22:2581–9.
[4] Anastasiadis SH, Russell TP, Satija SK, Majkrzak CF. Phys Rev Lett 1989;62:1852–5.
[5] Harrison C, Park M, Chaikin P, Register RA, Adamson DH, Yao N. Macromolecules 1998;31:2185–9.
[6] Huinink HP, Brokken-Zijp JCM, van Dijk MA, Sevink GJA. J Chem Phys 2000;112:2452–62.
[7] Huinink HP, van Dijk MA, Brokken-Zijp JCM, Sevink GJA. Macromolecules 2001;34:5325–30.
[8] Knoll A, Horvat A, Lyakhova KS, Krausch G, Sevink GJA, Zvelindovsky AV, et al. Phys Rev Lett 2002;89:035501-1–035501-4.
[9] Horvat A, Lyakhova KS, Sevink GJA, Zvelindovsky AV, Magerle R. J Chem Phys 2004;120:1117–26.
[10] Tsarkova L, Knoll A, Krausch G, Magerle R. Macromolecules 2006;39:3608–15.
[11] Park I, Park S, Park HW, Chang T, Yang HC, Ryu CY. Macromolecules 2006;39:315–8.
[12] Limary R, Green PF. Langmuir 1999;15:5617–22.
[13] Limary R, Green PF. Macromolecules 1999;32:8167–72.
[14] Masson JL, Limary R, Green PF. J Chem Phys 2001;114:10963–7.
[15] Henkee CS, Thomas EL, Fetters LJ. J Mater Sci 1988;23:1685–94.
[16] Epps III TH, Delongchamp DM, Fasolka MJ, Fischer D, Jablonski EL. Langmuir 2007;23:3355–62.
[17] Geoghegan M, Krausch G. Prog Polym Sci 2003;28:261–302.
[18] Müller-Buschbaum P. J Phys Condens Matter 2003;15:R1549–82.
[19] Müller-Buschbaum P, Bauer E, Wunniche O, Stamm M. J Phys Condens Matter 2005;17:S363–86.
[20] Reiter G. Langmuir 1993;9:1344–51.
[21] Sharma A, Reiter G. J Colloid Interface Sci 1996;178:383–99.
[22] Jung YS, Ross CA. Nano Lett 2007;7:2046–50.
[23] (a) Lee B, Park Y-H, Hwang Y-T, Oh W, Yoon J, Ree M. Nat Mater 2005;4:147–50;
(b) Lee B, Oh W, Yoon J, Hwang Y, Kim J, Landes BG, et al. Macromolecules 2005;38:8991–5;
(c) Yoon J, Yang SY, Heo K, Lee K, Joo W, Kim JK, et al. J Appl Crystallogr 2007;40:305–12;
(d) Yoon J, Jin KS, Kim HC, Kim G, Heo K, Jin S, et al. J Appl Crystallogr 2007;40:476–88;
(e) Jin S, Yoon J, Heo K, Park H-W, Shin TJ, Chang T, et al. J Appl Crystallogr 2007;40:950–8;
(f) Heo K, Yoon J, Jin S, Kim J, Kim K-W, Shin TJ, et al. J Appl Crystallogr 2008;41:281–91;
(g) Yang SY, Park J, Yoon J, Ree M, Jang SK, Kim JK. Adv Funct Mater 2008;18:1371–7.
[24] Müller-Buschbaum P. Anal Bioanal Chem 2003;376:3–10.
[25] (a) Müller-Buschbaum P, Gutmann JS, Cubitt R, Petry W. Physica B 2004;350:207–10;
(b) Müller-Buschbaum P, Gutmann JS, Stamm M. Phys Chem Chem Phys 1999;1:3857–63;
(c) Müller-Buschbaum P, Hermsdorf N, Roth SV, Wiedersich J, Cunis S, Gehrke R. Spectrochim Acta Part B At Spectrosc 2004;59:1789–97.
[26] (a) Lee B, Yoon J, Oh W, Hwang Y, Heo K, Jin KS, et al. Macromolecules 2005;38:3395–405;
(b) Heo K, Jin KS, Yoon J, Jin S, Oh W, Ree M. J Phys Chem B 2006;110:15887–95;
(c) Yoon J, Jung SY, Ahn B, Heo K, Jin S, Iyoda T, et al. J Phys Chem B 2008;112:8486–95;
(d) Yoon J, Jin S, Ahn B, Rho Y, Hirai T, Maeda R, et al. Macromolecules 2008;41:8778–84.
[27] Renaud G, Lazzari R, Leroy F. Surf Sci Rep 2009;64:255–380.
[28] (a) Sun YS, Chien SW, Wu PJ. Macromolecules 2010;43:5016–23;
(b) Sun YS, Chien SW, Liu JY. Macromolecules 2010;43:7250–60.
[29] Lazzari R. J Appl Crystallogr 2002;35:406–21.
[30] Jeng US, Su CH, Su CJ, Liao KF, Chuang WT, Lai YH, et al. J Appl Crystallogr 2010;43:110–21.
[31] Hammond MR, Cochran E, Fredrickson GH, Kramer EJ. Macromolecules 2005;38:6575–85.
[32] Peng J, Kim DH, Knoll W, Xuan Y, Li B, Han Y. J Chem Phys 2006;125:064702-1–064702-8.
[33] Xuan Y, Peng J, Cui L, Wang H, Li B, Han Y. Macromolecules 2004;37:7301–7.
[34] Harrison C, Chaikin PM, Huse DA, Register RA, Adamson DH, Daniel A, et al. Macromolecules 2000;33:857–65.
[35] Horvat A, Sevink GJA, Zvelindovsky AV, Krekhov A, Tsarkova L. ACS Nano 2008;2:1143–52.
[36] Peng J, Xuan Y, Wang H, Yang Y, Li B, Han Y. J Chem Phys 2004;120:11163–70.
[37] Naik SP, Yamakita S, Sasaki Y, Ogura M, Okubo T. Chem Lett 2004;33:1078–9.
[38] Tate MP, Eggiman BW, Kowalski JD, Hillhouse HW. Langmuir 2005;21:10112–8.
[39] Lee B, Park I, Yoon J, Park S, Kim J, Kim KW, et al. Macromolecules 2005;38:4311–23.
[40] Narayanan S, Lee DR, Guico RS, Sinha SK, Wang J. Phys Rev Lett 2005;94:145504-1–145504-4.
[41] Müller-Buschbaum P, Stamm M. Macromolecules 1998;31:3686–92.
[42] Müller-Buschbaum P, Gutmann JS, Wolkenhauer M, Kraus J, Stamm M, Smilgies D, et al. Macromolecules 2001;34:1369–75.
[43] Roe RJ. Methods of X-ray and neutron scattering in polymer science. New York: Oxford University Press; 2000 [chapter 5].
[44] Wang J, Tolan M, Seeck OH, Sinha SK, Bahr O, Rafailovich MH, et al. Phys Rev Lett 1999;83:564–7.
[45] Kim TH, Hwang J, Hwang WS, Huh J, Kim HC, Kim SH, et al. Adv Mater 2008;20:522–7.
[46] Kim TH, Huh J, Park C. Macromolecules 2010;43:5352–7.

Polymer 52 (2011) 1191–1196

Contents lists available at ScienceDirect

Polymer

journal homepage: www.elsevier.com/locate/polymer

Hierarchical self-assembly of fluorine-containing diblock copolymer: From onion-like nanospheres to superstructured microspheres

Shan Qin, Hong Li, Wangzhang Yuan, Yongming Zhang*

School of Chemistry and Chemical Technology, Shanghai Jiao Tong University, Shanghai 200240, People's Republic of China

ARTICLE INFO

Article history:
Received 25 September 2010
Received in revised form
30 December 2010
Accepted 10 January 2011
Available online 15 January 2011

Keywords:
Block copolymers
Fluorine-containing
Self-assembly

ABSTRACT

Superstructured microspheres were prepared via a two-tier hierarchical assembly of a fluorine-containing diblock copolymer, poly(tert-butyl acrylate)-*b*-poly(2-[(perfluorononenyl)oxy]ethyl methacrylate) (PtBA-*b*-PFNEMA) with well controlled block lengths. At tier 1, water induced self-assembly of the diblock copolymer produced nanospheres of low dispersity with onion-like multilayer inside structures, which were the consequence of the gradual aggregation of the fluorinated segments by accessing the super-strong segregation regime. And both the size and inner structure could be tuned by changing the water addition rate. At tier 2, nanospheres with different sizes were chosen as the building blocks for the formation of closely packed superstructural microspheres through an evaporation assisted process. The packing rules were governed by the volatility distinction between THF and water, the dispersity of nanospheres, and other various forces, such as the capillary force.

1. Introduction

Hierarchical assembly with specific molecular ordering and superstructure at multilength scales is universal in nature and has shown extraordinary multifunctions as physical properties are directly associated with specific structures at diverse scales [1–4]. The "Lotus effect" gives us a perfect example of the hierarchical assembly on plant surface [5]. The unique nano- and microstructures bring not only the water repellency, but also transpiration barrier, signaling, and recognition [6]. This strategy is also utilized to enhance adhesion of gecko feet via assembly of nanohairs, reduce friction and turbulence near shark skin by arrangement of scales and microgrooves [7–9]. Inspired by nature, several attempts have been contributed to the generation of hierarchical structures. Semiconductor nanoparticles were utilized as building blocks for the hierarchical assembly to binary superlattices [10]. Self-Assembly of Janus cylinders was introduced in selective solvents to prepare hierarchical superstructures [11]. The re-assembly of spherical micelles of the polystyrene-b-poly(acrylic acid) diblock copolymer could form necklace-like aggregates in water through solvent evaporation [12]. Large mono-layered films with a well-ordered hexagonal packing of spherical micelles were prepared by controlled organization of the rod-coil block copolymer micelles [13]. Spherical "superaggregates" with different surface morphologies were formed via Pickering effect and the fusion of adsorbed block copolymer micelles [14]. While superstructures building from different blocks can be diverse, various methods are also developed for specific systems. However they are not well understood to warrant the prediction of the shape and size of superstructures that can be prepared.

Onion-like polymer particles are a kind of particles with complex morphology comprising alternating polymer layers, which could find diverse applications in three-dimensional optical memory storage, cavity quantum electrodynamics, and new photonic devises [15–17]. Up to now, such multilayered particles could be prepared by sequential seeded polymerization, temperature-modulated precipitation polymerization, and solvent evaporation methods [18–21]. From the viewpoint of applications, it is of substantial importance to find a facile approach to control microphase structures, layer thickness, and number of interfaces [20]. Besides, only by knowing and being able to control the aggregation patterns of subdivided particles, we will be capable of transferring their unique properties into future applications.

Block copolymers have attracted increasing attentions in self-assembly, preparation of periodic patterns, and templating for nanoparticles synthesis due to their special physical and chemical properties [22–27]. It has been indicated that the introduction of fluorine-containing segments into block copolymers could facilitate their phase behavior as a result of the inherently immiscible of fluorine-containing blocks with other polymers induced by their high cohesive energies [28,29]. In this article, we report the formation of superstructured microspheres via a two-tier hierarchical assembly of a fluorine-containing diblock copolymer. At tier

* Corresponding author. Tel.: +86 21 34202613; fax: +86 21 54742567.
E-mail address: ymzsjtu@yahoo.com.cn (Y. Zhang).

0032-3861/$ – see front matter © 2011 Elsevier Ltd. All rights reserved.
doi:10.1016/j.polymer.2011.01.022

1, onion-like nanospheres were facilely prepared by water induced self-assembly of the diblock copolymer. At tier 2, nanospheres with different sizes were packed together to built the superstructured microspheres through an evaporation assisted process. The utilizing of onion-like polymer particles as the building block for the secondary assembly is fundamentally different from usual self-assembly studies because the final superstructured microspheres were hierarchical assemblies of the diblock copolymer at different length scales.

2. Experiment part

2.1. Materials

Tert-Butyl acrylate (tBA) (BASF) and N, N-dimethylformamide (DMF) (AR, Sinopharm Chemical Reagent Company) were vacuum distilled before use. 2-[(Perfluorononenyl)oxy]ethyl methacrylate (FNEMA) was synthesized by the reaction of hexafluoropropylene trimer with 2-hydroxyethyl methacrylate. CuBr (CP, Sinopharm Chemical Reagent Company) was purified before use. N, N, N′, N″, N″-Pentamethyldiethylenetriamine (PMDETA) (TCI), Ethyl-2-bromoisobutyrate (Alfa Aesar), chloroform (AR, Sinopharm Chemical Reagent Company), and tetrahydrofuran (THF,AR, Sinopharm Chemical Reagent Company) were used as received.

2.2. Synthesis of PtBA-Br macroinitiator

A dry round-bottomed flask with a magnetic stir bar was charged with CuBr (0.1076 g, 7.5×10^{-4} mol), tBA (19.23 g, 0.15 mol), PMDETA (0.1300 g, 7.5×10^{-4} mol), and ethyl-2-bromoisobutyrate (0.2926 g, 1.5×10^{-3} mol). The flask was sealed and the mixtures were bubbled with nitrogen for 15 min. The flask was then placed in an oil bath heated to 60 °C for designed time. The homopolymer (PtBA-Br) was precipitated in methanol/H_2O (1:1 by volume) after passing through an alumina column to remove the copper complexes, and dried under vacuum at 60 °C. The molecular weight was determined by GPC.

2.3. Synthesis of $PtBA_{90}$-b-$PFNEMA_{12}$

$PtBA_{90}$-*b*-$PFNEMA_{12}$ was synthesized via ATRP according to literature methods [30]. A dry round-bottomed flask with a magnetic stir bar was charged with CuBr (0.2152 g, 1.5×10^{-3} mol), PtBA-Br (3×10^{-4} mol), PMDETA (0.3132 g, 1.5×10^{-3} mol), DMF (25.0 ml), and FNEMA (11.76 g, 2.1×10^{-2} mol). The flask was sealed and the mixtures were bubbled with nitrogen for 15 min. The flask was then placed in an oil bath heated to 100 °C for designed time. The diblock copolymer was precipitated in methanol/H_2O (1:1 by volume) and dried under vacuum at 60 °C. Then the copolymer was dissolved in THF for passing through an alumina column and dried under vacuum at 60 °C. As the diblock copolymer formed associate in THF even at very low concentrations, we used ^{1}H NMR to determine the molecular weight. Two resonances at 2.15–2.35 and 3.8–4.43 ppm, which correspond to the –CH– proton of the PtBA backbone and $-CH_2CH_2-$ protons of ester groups in FNEMA units, were observed. $M_{n,NMR}$ was calculated on the basis of the area ratio of above two peaks and the molar mass of PtBA-Br.

2.4. Preparation of nanospheres solutions

$PtBA_{90}$-*b*-$PFNEMA_{12}$ was dissolved in THF to give a polymer solution of 2.0 mg/ml. After the polymer was completely dissolved, the solution was filtered through a 0.45 μm PVDF membrane. Then 0.50 ml of water was added into 1.00 ml of solution utilizing a syringe pump at the rates of 1.25, 0.25, and 0.05 ml/min under stirring, respectively.

2.5. Preparation of microspheres

One drop of the nanospheres solution was placed on a silicon wafer or carbon-coated copper grid. After the solvents were evaporated under normal atmosphere, microspheres were formed.

2.6. Characterization

Gel Permeation Chromatography (GPC) was performed on a GPC system consisting of a multi-angle laser light scattering instrument (MALLS) (DAWN EOS, Wyatt Technology, USA), THF was used as eluent at 30 °C with a flow rate of 1.0 ml/min. All ^{1}H NMR spectra were recorded on a MERCURY plus 400 NMR spectrometer (Varian, USA) using TMS as inner reference and $CDCl_3$ as solvent. Dynamic light scattering (DLS) test was performed at a scattering angle $\theta = 90°$ with a high-performance particle sizer (Nano-ZS90, Malvern Instruments, UK) equipped with a He–Ne laser ($\lambda = 633$ nm). Apparent mean hydrodynamic diameters D_h (according to volume distribution) of micelles or aggregates were calculated according to Stokes–Einstein equation, $D_h = kT/3\pi\eta D_{app}$, with D_{app} and η being the apparent diffusion coefficient and viscosity of the solution, respectively. The melting behavior of the nanospheres was measured with a TA Instruments Q2000 differential scanning calorimeter (DSC) under nitrogen (N_2) atmosphere. The sample was heated from 0 to 100 °C at a heating rate of 10 °C/min. The melting temperature (T_m) was taken as the temperature of the maximum of endothermic peak. Scanning electron microscope (SEM) images of microspheres on the silicon wafers were recorded using a JSM-7401F SEM. Transmission Electron Microscopy (TEM) images of microspheres were observed on a JEM-2100 TEM operating at an acceleration voltage of 120 kV.

3. Results and discussion

3.1. Synthesis of $PtBA_{90}$-b-$PFNEMA_{12}$

The fluorine-containing diblock copolymer $PtBA_{90}$-*b*-$PFNEMA_{12}$ was synthesized via ATRP according to literature methods [30]. In

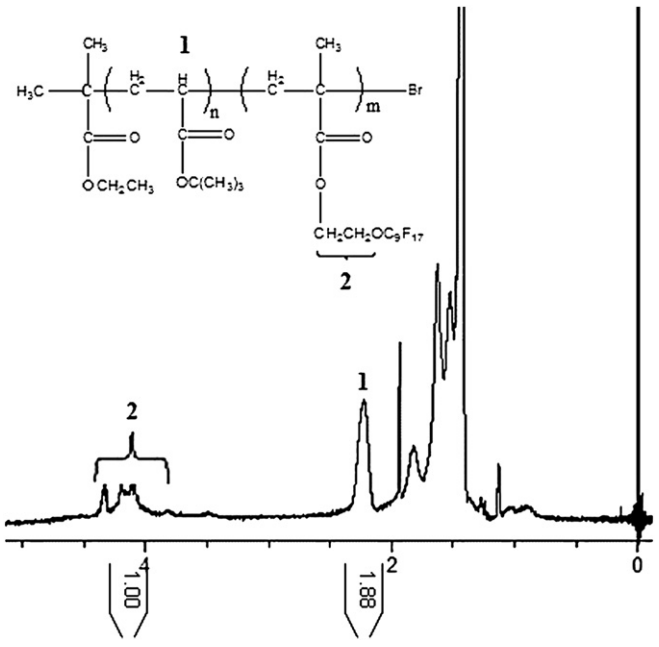

Fig. 1. ^{1}H NMR spectrum of $PtBA_{90}$-*b*-$PFNEMA_{12}$ diblock copolymer in $CDCl_3$.

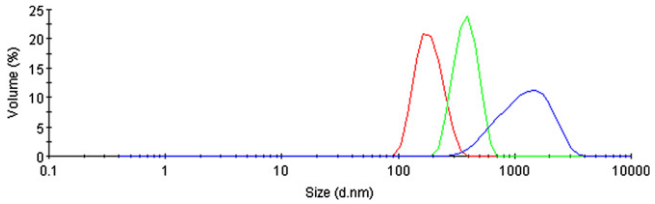

Fig. 2. Particle size distributions of the nanospheres of NS1 (red), NS2 (green), and NS3 (blue) studied by DLS (For interpretation of the references to colour in this figure legend, the reader is referred to the web version of this article.)

order to prepare diblock copolymer with long enough fluorine-containing segments, chain extension of the fluorinated monomer was carried out in DMF at 100 °C for prolonged time. The resulting fluorine-containing diblock copolymer $PtBA_{90}$-*b*-$PFNEMA_{12}$ coordinates closely with our two-tier assembly strategy. The long fluorinated segments at the side chains exhibit solvophobic interactions and immiscibility with other polymer chains, which could facilitate the assembling behavior of the block copolymer induced by water addition [31,32]. And the water insoluble PtBA block would contribute to the aggregation during selective evaporation process at tier 2.

The molecular weight (M_n) and polydispersity index of the homopolymer (PtBA-Br) were determined by GPC analysis, which suggests $PtBA_{90}$-Br with $M_n = 1.16 \times 10^4$ g•mol^{-1} and $M_w/M_n = 1.10$ was obtained. The diblock copolymer formed associate in THF even at very low concentrations, which hampered its meaningful molecular weight analysis by GPC, thus we used ^{1}H NMR to determine its molecular weight[31]. The ^{1}H NMR spectrum of $PtBA_{90}$-*b*-$PFNEMA_{12}$ is shown in Fig. 1. Two resonances at 2.15–2.35 and 3.8–4.43 ppm, which correspond to the −CH− proton (H_1) of the PtBA backbone and $-CH_2CH_2-$ protons (H_2) of ester groups in FNEMA units, are observed. $M_{n,NMR}$ of the fluorine-containing diblock copolymer was calculated to be 1.83×10^4 g•mol^{-1} on the basis of the area ratio of such two peaks and M_n of PtBA.

3.2. Water induced self-assembly of fluorine-containing diblock copolymer into nanospheres

Nanospheres solutions were prepared by adding water to the solutions of block copolymer $PtBA_{90}$-b-$PFNEMA_{12}$ in THF at three addition rates. The obtained nanospheres were named as NS1, NS2, and NS3 for the water addition rates of 0.05, 0.25, and 1.25 ml/min, respectively. After the addition of water, the solutions became turbid and appeared bluish which suggested the formation of nanoparticles. Fig. 2 shows the DLS results of $PtBA_{90}$-*b*-$PFNEMA_{12}$ nanospheres in THF/water (50 vol %). The mean hydrodynamic diameters (D_h) of NS1, NS2, and NS3 are 190 nm, 362 nm, and 807 nm, with polydispersity indexes of 0.02, 0.03, and 0.22, respectively. The measured average particle sizes are too large to correspond to the hydrodynamic diameters of normal spherical micelles, as the contour length of the fully stretched polymer chain of $PtBA_{90}$-b-$PFNEMA_{12}$ is merely 13 nm. Therefore, nanospheres with higher inner structures might be formed.

In our case, the water addition rate has a great effect on the sizes of nanospheres. Water is a non-solvent for both blocks, among

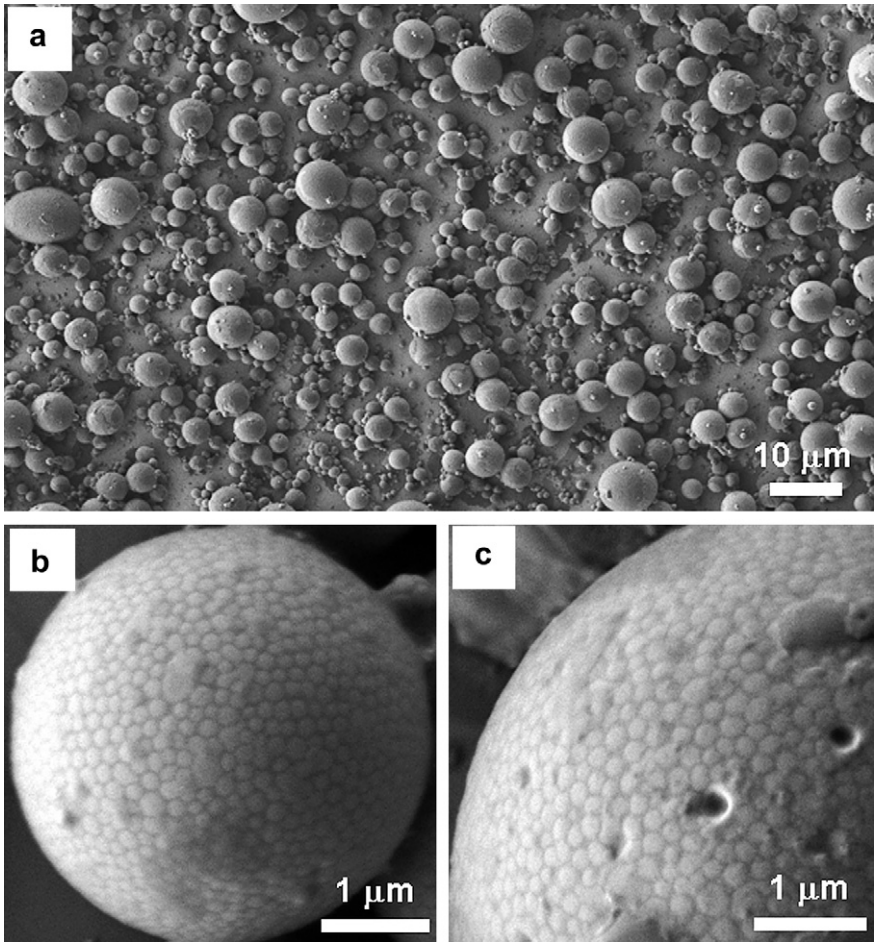

Fig. 3. SEM image of the microspheres assembled from (a, b) NS1 (MS1) and (c) NS2 (MS2).

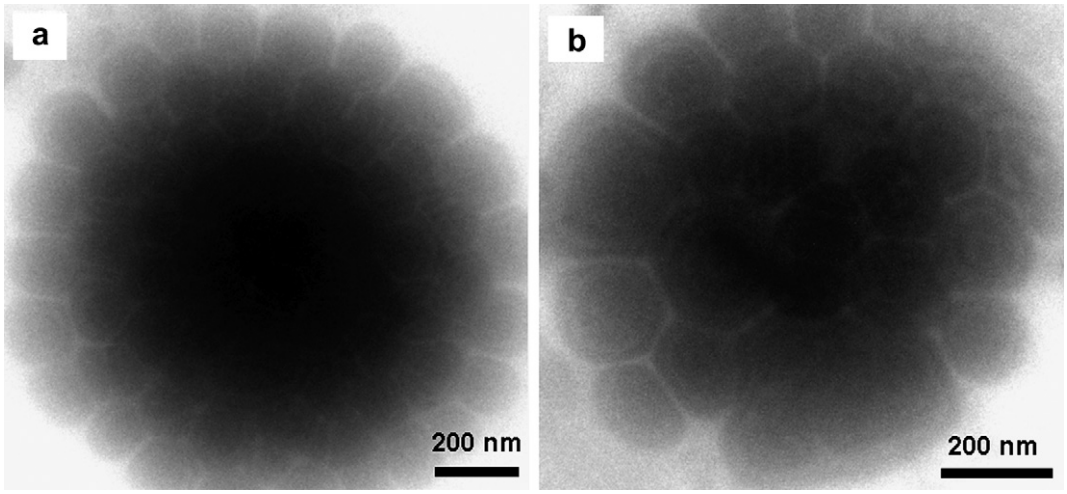

Fig. 4. TEM images of the microspheres assembled from NS1 (MS1).

which the fluorine-containing block is apparently more hydrophobic. As the interactions between the solvent and blocks were changed by the addition of water, the fluorine-containing block tended to aggregate first, starting the formation of the nanospheres. And the introduction of water affects not only the thermodynamic equilibrium but also the kinetic pathway of the diblock copolymer self-assembly, so the sizes of nanospheres could be facilely tuned by the water addition rate.

3.3. Evaporation assisted assembly of nanospheres to microspheres

3.3.1. The surface morphologies of the microspheres

The polydispersity indexes of NS1 and NS2 are very small, such rather uniform sizes of the nanospheres makes it possible for the assembly of nanospheres to higher superstructures. Drops of nanospheres solution were placed on silicon wafer or carbon-coated copper grid under atmosphere for the following selective evaporation process. As THF is more volatile than water, it evaporates preferentially from NS1 solution, inducing the PtBA block becomes less swollen and the trend of aggregation of NS1. When the solvents are totally evaporated, superstructured microspheres are formed through self-assembly of the nanospheres.

The surface morphology of microspheres was firstly studied by SEM. As shown in Fig. 3a, the original individual NS1 have assembled together. The diameters of microspheres assembled from NS1 (MS1) could get to more than 10 μm as they are consisted of hundreds of NS1. A few effects have contributed to the secondary assembly of polymeric nanoparticles, however, unfortunately, the packing rule for such kind of particles is not well understood [33–35]. But it is still reasonable to assume that simple polymeric nanospheres tend to adopt a close-packed structure to get the maximum packing density, as the arrangement of the NS1 is obviously close and somehow regular, as shown in Fig. 3b.

Considering their size tunability, nanospheres with different sizes were used as the building blocks for the secondary assembly. Fig. 3c shows the SEM image of the aggregates assembled from NS2, similar to MS1, nanoparticles are densely packed to form regular micropheres (MS2).

3.3.2. The inside structures of the microspheres

Besides the surface morphology, the inside structures could provide more information about the hierarchical assembly. TEM allows imaging the aggregates directly, moreover segregated fluorocarbon nano-domains can be visualized, as fluorocarbons are

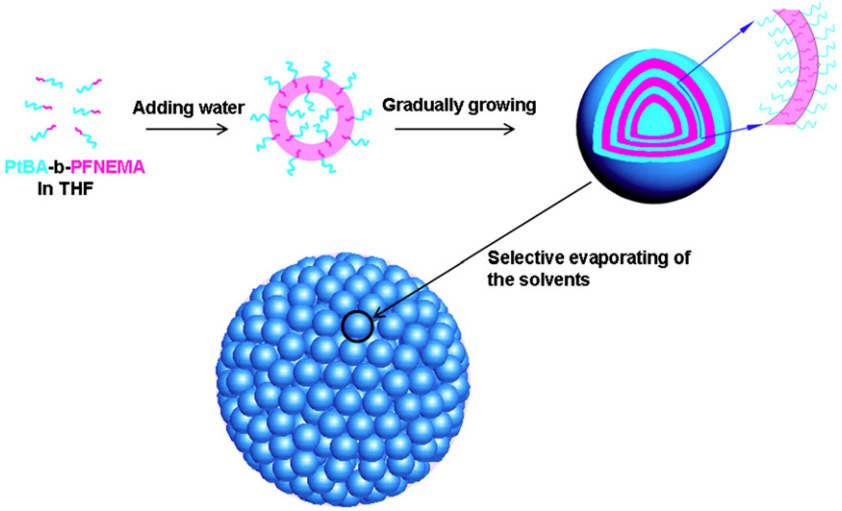

Fig. 5. Schematic representation of the hierarchical self-assembly of fluorine-containing diblock copolymer: from onion-like nanospheres to superstructured microspheres.

known to have high contrast in TEM [36]. So it is expected that TEM observations could give us more detailed structure information and hints to understand the assembly mechanism. Fig. 4 shows the TEM image of MS1. It is clear that NS1 arrange layer by layer from the core to the edge, forming a superstructured ball. And the diameters of the individual NS1 measured from the TEM images are about 160 nm, which are similar to the DLS result.

The shapely spherical morphology of MS1, the orderly layered packing of NS1, and the evaporation assisted procedure suggested the assembly mechanism. Fig. 5 schematically illustrates the hierarchical self-assembly of fluorine-containing diblock copolymer: as THF is more volatile than water and thus evaporates preferentially from NS solution, the PtBA block become less swollen which means the trend of aggregation of NS. The gradually evaporation process also provides a dynamic pathway to pack the NS regularly. The capillary force between NS may also play a great role at the end of the evaporation which contributes to a closer packing. At the same time nearly mono dispersed NS make it easier to achieve the maximum packing density which determines the final spherical shape [37].

Another interesting finding is that the inside structure of the nanospheres is also unique and complex. As shown in Fig. 4b (high magnification image of another MS1), there are more than two dark stripes in nanospheres in MS1. The light–dark alternating stripes suggest the onion-like structural feature of NS1. Since fluorocarbons are known to have high contrast in TEM, the dark stripes should be formed by the segregation of the fluorinated segments. Hence, these onion-like inside structures of nanospheres are consisted of several layers of bright PtBA and dark PFNEMA segments one after another. And the widths of the PFNAMA layers are about 10–20 nm.

This unique inside structure of nanospheres indicates that the self-assembly behavior of the diblock copolymer with fluorinated segments is different from the formation of core-shell micelles. The layered structures of the fluorinated domains might be the consequence of accessing the super-strong segregation regime (SSSR) [38]. According to Semenov's theory, the interfacial free energy per chain of the vesicle is the most favorable since there is no edge effect for the vesicle[39]. In our situation, the onion-like multilayered nanospheres could be treated as the superposition of several layers of vesicles. The layered structures also imply a growing assembly process. So the sizes of NS could be tuned by the water addition rate through different kinetic pathways. Therefore, it is reasonable to assume that the sizes are tuned by the water addition rates through influence on their growing rates.

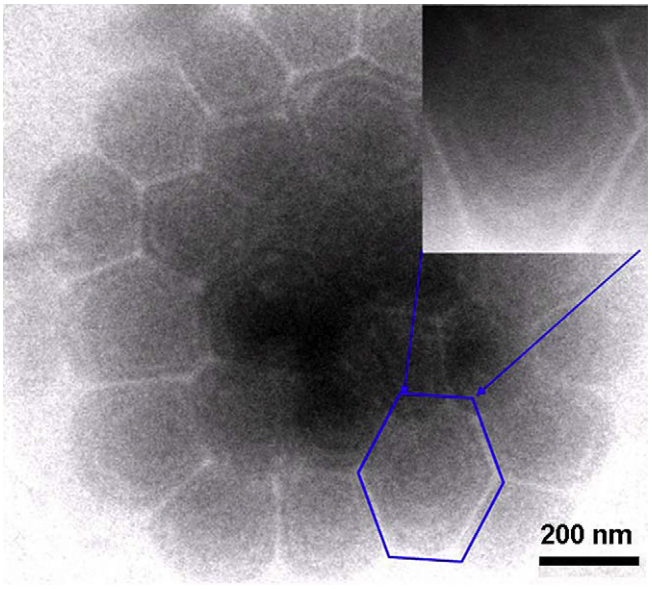

Fig. 6. TEM image of the microspheres assembled from NS2 (MS2). The inserted image shows the magnification of the selected area.

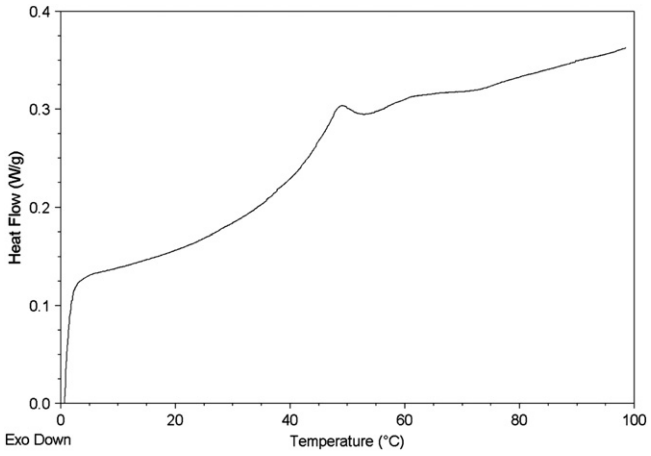

Fig. 7. DSC trace of nanospheres (NS2) under nitrogen at a heating rate of 10 °C/min.

Fig. 6 shows the TEM image of the microspheres assembled from NS2 (MS2). Since NS2 are larger than NS1, the PFNEMA layers seem much clearer in MS2. Meanwhile, the distinct polygon morphology and sharp edges of the PFNEMA layers indicate the fluorinated domains may undergo crystalline ordering (as shown in the inserted image) [31,32]. So we performed DSC measurement for NS2. From Fig. 7, a broad peak at about 49 °C was observed, which might be attributed to the melting of the PFNEMA microphase. And the glass transition of PtBA at about 38 °C was not obvious, as the interaction between polymer blocks may affect the segment movement of corresponding polymers [40]. The widths of the PFNEMA layers are about 20 nm, which are just close to twice of the length for PFNAMA block. This finding also supports the chain-packing motif of the onion-like inside structure shown in Fig. 5.

4. Conclusions

In summary, we have demonstrated the hierarchical assembly of a fluorine-containing block polymer $PtBA_{90}$-*b*-$PFNEMA_{12}$ into nanospheres through water induced aggregation, and then to microspheres by evaporation assisted packing. The sizes of the nanospheres could be tuned by water addition rates through a gradually growing process. And the inside onion-like structures consist of several polygon stripes illustrated that the super-strong segregation of the fluorinated segments and preferential lamellar packing of the crystallized fluorocarbon side chains might play significant roles in the morphology determination. An elementary mechanism was also proposed to explain the packing rule of the nanospheres. This two-tier hierarchical assembly of block copolymer not only shows the unique self-assembly behavior of the fluorine-containing diblock copolymer, but also provides a novel method to prepare superstructures. Though the generality of this phenomenon remains to be discovered and the roles of various parameters still need to be investigated and demonstrated, it is promising to generate well controlled superstructures at different levels.

References

[1] Watson GS, Cribb BW, Watson JA. ACS Nano 2010;4(1):129–36.
[2] Lin W, Zhang J, Wan X, Liang D, Zhou Q. Macromolecules 2009;42(12):4090–8.

[3] Zhao Y, Wei M, Lu J, Wang ZL, Duan X. ACS Nano 2009;3(12):4009–16.
[4] Lee SJ, Hupp JT, Nguyen ST. Journal of the American Chemical Society 2008;130(30):9632–3.
[5] Nun E, Oles M, Schleich B. Macromolecular Symposia 2002;187:677.
[6] Koch K, Bhushan B, Barthlott W. Progress in Materials Science 2009;54:137.
[7] Autumn K, Sitti M, Liang YA, Peattie AM, Hansen WR, Sponberg S, et al. Proceedings of the National Academy of Sciences of the United States of America 2002;99:12252.
[8] Baumgartner W, Saxe F, Weth A, Hajas D, Sigumonrong D, Emmerlich J, et al. Journal of Bionic Engineering 2007;4:1.
[9] Gao X, Yan X, Yao X, Xu L, Zhang K, Zhang J, et al. Advanced Materials 2007;19:2213.
[10] Shevchenko EV, Talapin DV, Kotov NA, O'Brien S, Murray CB. Nature 2006; 439:55–9.
[11] Walther A, Drechsler M, Rosenfeldt S, Harnau L, Ballauff M, Abetz V, Müller AHE. Journal of the American Chemical Society 2009;131(13):4720–8.
[12] Zhang Y, Xiao X, Zhou J-J, Wang L, Li Z-B, Li L, et al. Polymer 2009;50(25): 6166–71.
[13] Tu Y, Graham MJ, Van Horn RM, Chen E, Fan X, Chen X, et al. Polymer 2009;50(22):5170–4.
[14] Hu J, Liu G, Nijkang G. Journal of the American Chemical Society 2008;130: 3236–7.
[15] Pham HH, Gourevich I, Oh JK, Jonkman JEN, Kumacheva E. Advanced Materials 2004;16:516–20.
[16] Petukhova A, Paton AS, Wei Z, Gourevich I, Nair SV, Ruda HE, et al. Advanced Functional Materials 2008;18:1961–8.
[17] Zhang K, Gao L, Chen Y, Yang Z. Chemistry of Materials 2008;20(1):23–5.
[18] Gourevich I, Field LM, Wei Z, Paquet C, Petukhova A, Alteheld A, et al. Macromolecules 2006;39:1449–54.
[19] Takekoh R, Li W-H, Burke NAD, Stover HDH. Journal of the American Chemical Society 2005;128(1):240–4.
[20] Saito N, Okubo M. Macromolecules 2009;42(19):7423–9.
[21] Kitayama Y, Yorizane M, Kagawa Y, Minami H, Zetterlund PB, Okubo M. Polymer 2009;50(14):3182–7.
[22] Datta H, Bhowmick AK, Singha NK. Polymer 2009;50(14):3259–68.
[23] Yang X, Chen Y, Yuan R, Chen G, Blanco E, Gao J, et al. Polymer 2008;49 (16):3477–85.
[24] Akcora P, Briber RM, Kofinas P. Polymer 2009;50(5):1223–7.
[25] Liu J, Sue H-J, Thompson ZJ, Bates FS, Dettloff M, Jacob G, et al. Polymer 2009;50(19):4683–9.
[26] Meristoudi A, Pispas S. Polymer 2009;50(13):2743–51.
[27] Stepek M, Uchman M, Prochka K. Polymer 2009;50(15):3638–44.
[28] Edmonds WF, Li Z, Hillmyer MA, Lodge TP. Macromolecules 2006;39(13): 4526–30.
[29] Valtola L, Koponen A, Karesoja M, Hietala S, Laukkanen A, Tenhu H, et al. Polymer 2009;50(14):3103–10.
[30] Li H, Zhang ZB, Hu CP, Ying SK, Wu SS, Xu XD. Reactive and Functional Polymers 2003;56(3):189–97.
[31] Skrabania K, Berlepsch HV, Böttcher C, Laschewsky A. Macromolecules 2010; 43(1):271–81.
[32] Skrabania K, Laschewsky A, Berlepsch HV, Böttcher C. Langmuir 2009;25 (13):7594–601.
[33] Zhang W, Shi L, An Y, Shen X, Guo Y, Gao L, et al. Langmuir 2003;19(15): 6026–31.
[34] Yan X, Liu G, Hu J, Willson CG. Macromolecules 2006;39(5):1906–12.
[35] Cui H, Chen Z, Zhong S, Wooley KL, Pochan DJ. Science 2007;317:647–50.
[36] Li Z, Kesselman E, Talmon Y, Hillmyer MA, Lodge TP. Science 2004;306: 98–101.
[37] Talapin DV. ACS Nano 2008;2(6):1097–100.
[38] Lodge TP, Hillmyer MA, Zhou Z, Talmon Y. Macromolecules 2004;37(18): 6680–2.
[39] Semenov AN, Nyrkova IA, Khokhlov AR. Macromolecules 1995;28(22): 7491–500.
[40] Lin W, Fu Q, Zhang Y, Huang J. Macromolecules 2008;41(12):4127–35.

Polymer 52 (2011) 1197–1205

Contents lists available at ScienceDirect

Polymer

journal homepage: www.elsevier.com/locate/polymer

Structure of polyamide 6 and poly (*p*-benzamide) in their rod-coil-rod triblock copolymers investigated with in situ wide angle X-ray diffraction

Lu Xu [a], Junjun Li [a], Daoliang Wang [a], Youju Huang [a], Mingming Chen [b], Liangbin Li [a,b,*], Guoqiang Pan [a]

[a] National Synchrotron Radiation Laboratory and College of Nuclear Science and Technology, University of Science and Technology of China, Hefei, China
[b] Department of Polymer Science and Engineering, CAS Key Lab of Soft Matter Chemistry, University of Science and Technology of China, Hefei, China

ARTICLE INFO

Article history:
Received 14 July 2010
Received in revised form
19 December 2010
Accepted 26 December 2010
Available online 9 January 2011

Keywords:
Triblock copolymer
Wide angle X-ray diffraction
Crystallinity

ABSTRACT

A series of rod-coil-rod triblock copolymers containing polycaprolactam (PA6) as the coil block and poly (*p*-benzamide) (PBA) as the rod block were synthesized by a two-step polycondensation reaction. Proton nuclear magnetic resonance (^{1}H NMR), UV–vis spectrophotometry (UVS) and differential scanning calorimetry (DSC) were performed to determine the fundamental molecular structure and thermal property of copolymers. UV–vis spectrophotometry results revealed that the content of PBA homopolymer increased with the block length (number of monomer) of PBA and reached a plateau value ranging from 22 to 40 monomers of PBA. The wide angle X-ray diffraction (WAXD) measurements indicated that the crystallization of PA6 blocks was strongly suppressed due to the stretching from rods after annealed at temperature above the melting point of PA6. Only a few imperfect crystals of PA6 existed in the samples with low volume fraction of PBA. Moreover, the variation of PA6 block length hardly affected the crystallinity of PBA, which was dominantly controlled by the block length of PBA as diffusion was the control step for PBA crystallization at the annealing temperature.

1. Introduction

Rod-coil block copolymers covalently connecting rigid and flexible blocks possess some intrinsic phase behaviours like liquid crystal ordering, microphase separation and outstanding properties [1–8], which have attracted extensive interests in both academia and industry [9,10]. The phase behaviours of rod-coil block copolymers are more complicated than that of generic coil–coil block copolymers due to the remarkable steric interaction among the rods and geometric mismatch between straight rod and flexible coil [2,11]. The organization of the coils can be easily influenced by the stretching effect and geometric confinement from rod blocks [12–14]. Conversely, the packing of rods can also be disturbed by the coils through entropic stretch, although this passive action is relatively weak. Nevertheless, if the stretching is not only entropic but also enthalpic origin, the coil can still impose strong confinement on the rod. The phase behaviour of double crystalline block copolymers is a good example where crystallization leads parallel packing of coil blocks and sometimes generates strong confinement on the rod with an enthalpic origin [15–17].

In material application, the combination of specific rod and coil blocks in copolymers leads to excellent mechanical properties. The rods contribute more to the integrity and modulus of materials while the coils sustain major strain or deformation. Some novel polyurethanes which can suffer large elastic deformation and own shape memory properties are good examples in industry [18–20], while spider fiber is a perfect demo from nature [21,22]. In recent years, learning from natural silk, there has been a new trend of creating high performance polymer materials through optimizing the contributions of rods and coils, including varying the block length and sequence [23,24]. Moreover, adding the homopolymers into the rod-coil block copolymers is also an attractive approach to controlling the size of domains and modifying the morphology without additional synthesis. Coil–coil block copolymers blended with homopolymers have been studied extensively both theoretically and experimentally [25–28]. Nevertheless, due to the complicated behaviours of the rods, the blending of rod-coil-rod triblock copolymer and homopolymers has been rarely studied [29–32].

Recently, we carried out some studies on this complicated system. Polycaprolactam (PA6) [2] was used to initiate the polymerization of *p*-Aminobenzoic acid (PABA) via the method frequently used in industrial synthesis [33] and rod-coil-rod triblock copolymer containing poly (*p*-benzamide) (PBA) as rod and polycaprolactam (PA6) as coil was obtained. As PBA homopolymers were generated inevitably during synthesis and difficult to be

* Corresponding author. National Synchrotron Radiation Laboratory and College of Nuclear Science and Technology, University of Science and Technology of China, Hefei, China. Tel.: +86 551 3602081.
E-mail address: lbli@ustc.edu.cn (L. Li).

0032-3861/$ – see front matter © 2011 Elsevier Ltd. All rights reserved.
doi:10.1016/j.polymer.2010.12.058

removed in the following treatment, triblock copolymers obtained by this method contained a certain content of PBA homopolymers. After annealed at 180 °C, the morphology of this blending system has been studied. Due to the stretching between rod and coil, a quasi-γ mesomorphic order has been found for PA6 blocks in the transition-region nearby the PBA domain. The quasi-γ mesomorphic order was more favoured with the increase of volume fraction of PBA (φ_{PBA}). With low volume fraction of PBA, the Brill transition, a common thermal behaviour in PA6 homopolymers, has been observed. This transition vanished with the increase of volume fraction of PBA. On the other hand, the crystallization of PBA blocks was also disturbed by PA6 blocks when volume fraction of PBA reached approximately 45% [2].

In this work, for the purpose of further studying these blending systems, the range of rod/coil ratio was extended based on three different molecular weight PA6s. The molecular structure, thermal property and morphology of copolymers were characterized by UV–vis spectrophotometry (UVS), proton nuclear magnetic resonance (^{1}H NMR), differential scanning calorimetry (DSC) and wide angle X-ray diffraction (WAXD). On the basis of these results, three issues have been discussed: (i) Can PA6 blocks crystallize after annealed at the temperature of 230 °C? (ii) Will the variation of length of PA6 block affect the crystallization of PBA? (iii) What is the role of the PBA homopolymers in this blending system?

2. Experimental section

2.1. Materials

Lithium chloride (LiCl) was dried at 300 °C for 5 h prior to use. Hexane diacid and ε-caprolactam were dried at 50 °C under vacuum for 24 h before use. 1-Methyl-2-pyrrolidone (NMP) and pyridine (Py) were refluxed over calcium hydride for 4 h, then distilled and stored over 4 Å molecular sieves. *p*-Aminobenzoic acid (PABA) was purchased from Aladdin and purified using the method mentioned in the Ref. [34]. Triphenyl phosphate (TPP), ethanol, acetone and formic acid (88%) were used as received without any further purification. All the reagents except PABA were purchased from Sinopharm Chemical Reagent Co., Ltd. (Shanghai, China).

2.2. Synthesis procedure

A series of triblock copolymers containing polycaprolactam (PA6) as the coil block and poly (*p*-benzamide) (PBA) as the rod block were synthesized by two-step method as shown in Scheme 1. For convenience of describing the data in the following sections, the triblock copolymers in which the designed molecular weights of PA6 block is 1000, 2000 and 3000 g/mol are denoted as T1, T2 and T3, respectively.

2.2.1. Synthesis of PA6

Following the procedure in the previous paper [2], PA6 with three different number-average molecule weights was synthesized by varying the mass ratio of hexane diacid/ε-caprolactam (1/25 for T3, 3/50 for T2 and 3/25 for T1).

2.2.2. Synthesis of triblock copolymers

2.50 g of LiCl, 2.51 g of PA6 and 30 mL of NMP were added into a three-neck reaction flask equipped with a constant-pressure dropping funnel and magnetic stirrer under the nitrogen atmosphere. After all solid dissolved at 115 °C, TPP and 10 mL of Py were added dropwise into the solution via dropping funnel. Heating and stirring was continued for 30 min then a solution of PABA in NMP was added dropwise via dropping funnel within 8 h [35]. The system was kept for another 3 h to make the reaction complete, then

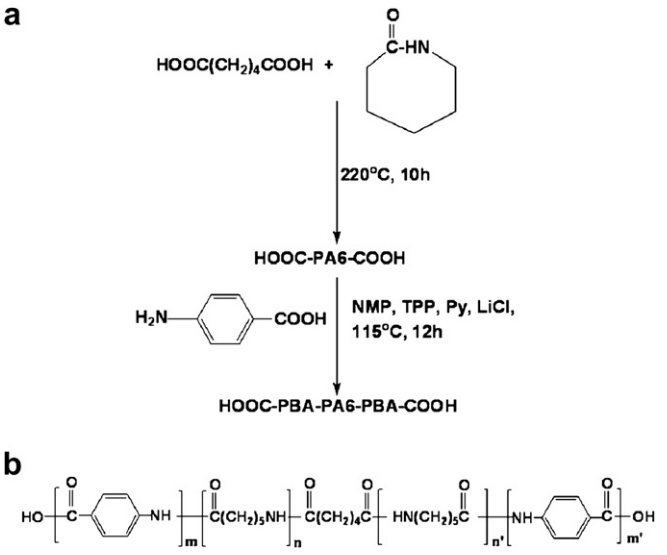

Scheme 1. Synthesis procedure (a) and molecular structure formula (b) of PBA-PA6-PBA triblock copolymer.

precipitated into ethanol (500 mL). The precipitate was further washed by acetone for three times. The obtained light yellow product was subsequently extracted by ethanol in Soxhlet apparatus for 24 h. The final product was dried at 60 °C in a vacuum oven. A series of triblock copolymers were synthesized via regulating the charge amount of PABA and TPP as shown in the Table 1.

2.3. Measurement

The carboxyl end groups determination was carried out to determine the molecular weight of PA6. This was accomplished by titration as follows: The sample (0.0300, 0.0600 and 0.0900 g for T1, T2 and T3, respectively) was dissolved in 30 mL of benzyl alcohol at 120 °C. Then the solution was cooled freely to room temperature, and 10 mL of methanol/water (2:1, v:v) and 3 drops of phenolphthalein were added subsequently. The conductometric titration of this solution was performed with a 0.0260 N KOH methanol/water (2:1, v:v) solution.

UV–vis spectrophotometry (UV-2802PC, UNICO Instruments) was employed to determine the content of homo-PBA through determining the content of amino groups (all amino groups are connected to homo-PBA, both ends of triblock copolymers are carboxyl groups) using the method mentioned in Ref. [36].

Proton nuclear magnetic resonance (^{1}H NMR) spectra of each copolymer sample were recorded in D_2SO_4 solution using a 400 MHz Super Conducting NMR Spectrometer (Bruker Advance AV 400).

Prior to WAXD and DSC measurement, all samples were annealed at 230 °C for 2 h and then cooled freely to room temperature under vacuum condition.

Table 1
The charge amount of PABA and TPP (g) for each ratio of triblock copolymer.

Molar ratio of rod/coil unit		0.4	0.6	0.8	1.0	1.2	1.4	1.6
T1	PABA	1.21	1.82	2.43	3.03	3.64	4.24	4.85
	TPP	4.85	6.90	9.00	11.04	13.09	15.15	17.21
T2	PABA	1.21	1.82	2.43	3.03	3.64	4.24	4.85
	TPP	5.35	7.40	9.50	11.54	13.60	15.65	17.70
T3	PABA	1.21	1.82	2.43	3.03	3.64	4.24	4.85
	TPP	5.85	7.90	10.00	12.04	14.10	16.15	17.70

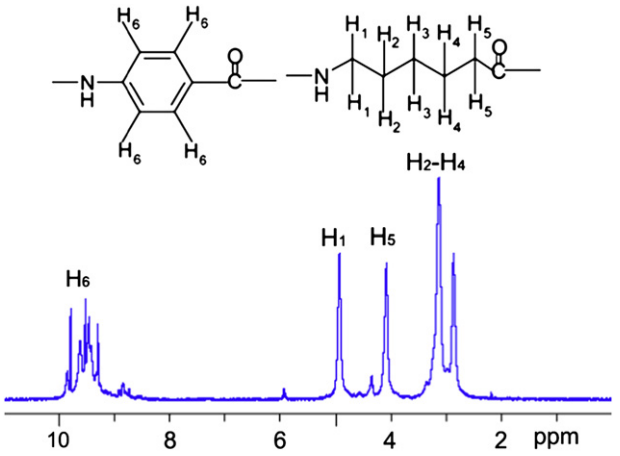

Fig. 1. ^{1}H NMR spectra and the peak assignments of PA6 and PBA in the copolymers.

Table 2
The volume fraction (φ_{PBA}) (%) and the number of monomer of PBA in each sample calculated from ^{1}H NMR spectra.

Molar ratio of rod/coil unit		0.4	0.6	0.8	1.0	1.2	1.4	1.6
T1	φ_{PBA}	37.5	46.3	50.3	53.1	57.6	59.7	62.2
	Number of monomer	8.2	11.8	13.9	15.6	18.6	20.4	22.6
T2	φ_{PBA}	35.3	44.8	49.3	51.5	55.8	58.9	62.2
	Number of monomer	11.2	16.7	20.0	21.8	25.9	29.4	33.8
T3	φ_{PBA}	34.1	43.4	48.0	50.5	53.9	57.5	61.4
	Number of monomer	18.0	26.6	32.0	35.4	40.5	46.8	55.2

Differential scanning calorimetry (DSC) measurements were performed with a Differential Scanning Calorimetry (DSCQ2000) using a heating rate of 20 °C/min.

Wide angle X-ray diffraction (WAXD) measurements were carried out at X-ray Diffraction and Scattering Beamline (U7B), National Synchrotron Radiation Laboratory (NSRL) in Hefei, China. The wavelength used was 0.154 nm. All WAXD experiments were performed with a stepwise temperature shift (60 °C–300 °C–60 °C, a step of 30 °C, 10 min for every point).

3. Results

3.1. Molecular mass

The number-average molecular weights of PA6 were measured by carboxyl end groups determination. The experimental results of molecular weights of PA6 were 1247 g/mol for T1, 1868 g/mol for T2 and 3150 g/mol for T3, respectively.

By analyzing the relative signal intensities of different protons in ^{1}H NMR spectra (protons in PBA: δ range 8–10 ppm, protons in the PA6: δ range 2–5 ppm) as shown in Fig. 1, the compositions of copolymers were determined [37]. The corresponding results including the volume fraction (φ_{PBA}) and number of monomers of PBA are shown in Table 2.

3.2. UVS

The contents of PBA homopolymers in all samples were analyzed with UV–vis spectrophotometry as presented in Fig. 2. As shown in Fig. 2a, the content of homo-PBA in T1 increases with the increase of the molar ratio of rod/coil in the whole range we synthesized. This simple trend does not hold in either T2 or T3 series. In T2 series, a relative constant content about 19% (molar ratio of homo-PBA/triblock copolymer) of homo-PBA exists when the molar ratio of rod/coil units exceeds 1.3. This behaviour can also be observed in T3 within rod/coil molar ratio from 0.9 to 1.5. Fig. 2b plots the content of homo-PBA vs the average block length (number of monomer) of PBA. Irrespective of the block length of PA6, the variation of homo-PBA content in all samples falls into one line, which can be divided into three zones and denoted as zone I, II and III in Fig. 2b. In both zone I and III the content of homo-PBA increases with the increase of PBA monomers, while zone II is a plateau region with a constant value about 19%.

3.3. DSC

Fig. 3 shows the DSC traces (first heating) of some representative samples in the melting region of the PA6 with a heating rate 20 °C/min from 0 to 300 °C. Only sample T2-0.4 shows a very broad endothermic peak which indicates the imperfect PA6 crystals. It shows that the crystallization of PA6 was suppressed dramatically by PBA block after annealed at 230 °C.

3.4. WAXD

The WAXD diagrams of T1-0.4, T2-0.4 and T3-0.4 (the samples with the lowest PBA content) during step heating and cooling process are shown in Fig. 4. Two diffraction peaks at 2θ of 20.3° and 23.4° can be assigned to (110) and (200) planes of PBA crystal and denoted as peaks I and II, respectively. Nevertheless, the α form of PA6 has two main diffraction peaks around 20.2° and 23.7° at 60 °C, which are close to peak I and II in Fig. 4. Due to the broadness of peaks I and II, without detailed analysis it is not possible to completely exclude the contribution of α crystal of PA6. On the other hand, the formation of PA6 γ phase is demonstrated to be absent as no diffraction peak at $2\theta = 22.2°$ [2,38,39] in all triblock copolymers. The absence of γ phase is also confirmed by that no obvious change around the diffraction peak position of γ phase in WAXD diagrams during heating and cooling process.

The temperature dependencies of the crystallinity and d-spacings of all samples obtained through Gaussian multi peak fitting on

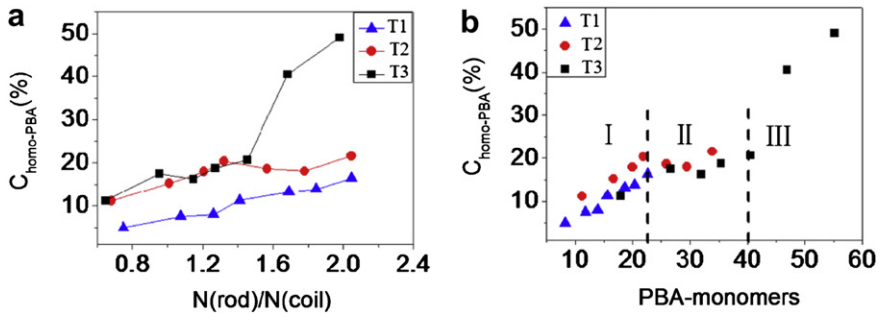

Fig. 2. Content of homo-PBA as a functions of N (rod)/N (coil) (a) and PBA monomers (b).

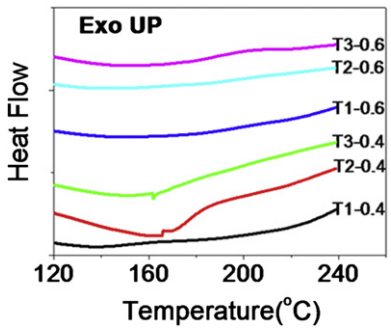

Fig. 3. DSC traces of copolymers in the melting region of the PA6 (heating rate: 20 °C/min).

the curves in Fig. 4 are further analyzed and plotted in Fig. 5. With the increase of temperature, all samples show reductions of crystallinity ranging from 1% to 8%. Only T2-0.4 shows a gradual transition, which indicates the melting of PA6 α crystal. Other samples (including T2 series with higher content of PBA and all T1/T3 series) show no obvious transition although the increase of amorphous halo at 2θ of about 19° and the decrease of crystallinity are observed during heating process without exception (WAXD data of other samples are not shown here). If 172 °C [2] is taken as the final melting temperature of PA6 blocks, the total reduction of crystallinity from 60 to 180 °C is about 1–4%.

In our previous work [2], the Brill transition [40–42] has been observed in the sample contained the same length of PA6 block and content of PBA block as sample T3-0.4 after annealed at 180 °C. The sign of Brill transition is that the positions of peak I and II run closer along with the increase of temperature, which is not observed in Fig. 5. The absence of Brill transition further confirms the suppressing effect on PA6 block in these samples as a result of higher perfection of PBA crystal at a higher annealing temperature of 230 °C. The changes of *d*-spacings of these three samples are almost completely reversible throughout the stepwise temperature shift. From 60 to 210 °C in which the influence of PA6 has been taken into consideration, the *d*-spacing changes of peak I and II are less than 1.0% and 1.6% respectively, which can be mainly attributed to the thermal expansion of PBA crystal. The thermal expansion rates along a, b and c axis of PBA crystal between 60 and 210 °C are 1.1%, 0.6% and −0.1%, respectively [43].

The idea discussed above is supported by the WAXD results of PBA homopolymer as shown in Fig. 6. This homo-PBA was prepared in our laboratory, and annealed at 230 °C for 1 h before measurement.

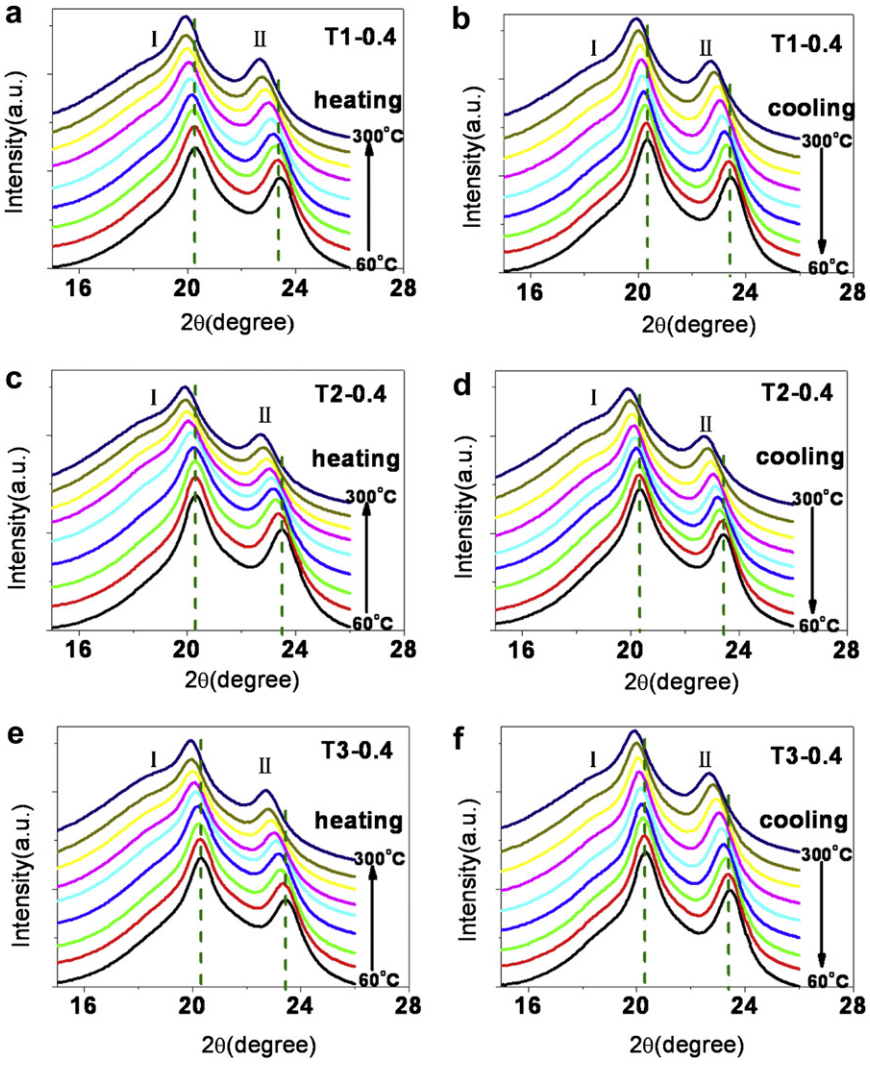

Fig. 4. WAXD diagrams of T1-0.4, T2-0.4 and T3-0.4 during heating (a, c, e) and cooling (b, d, f) process.

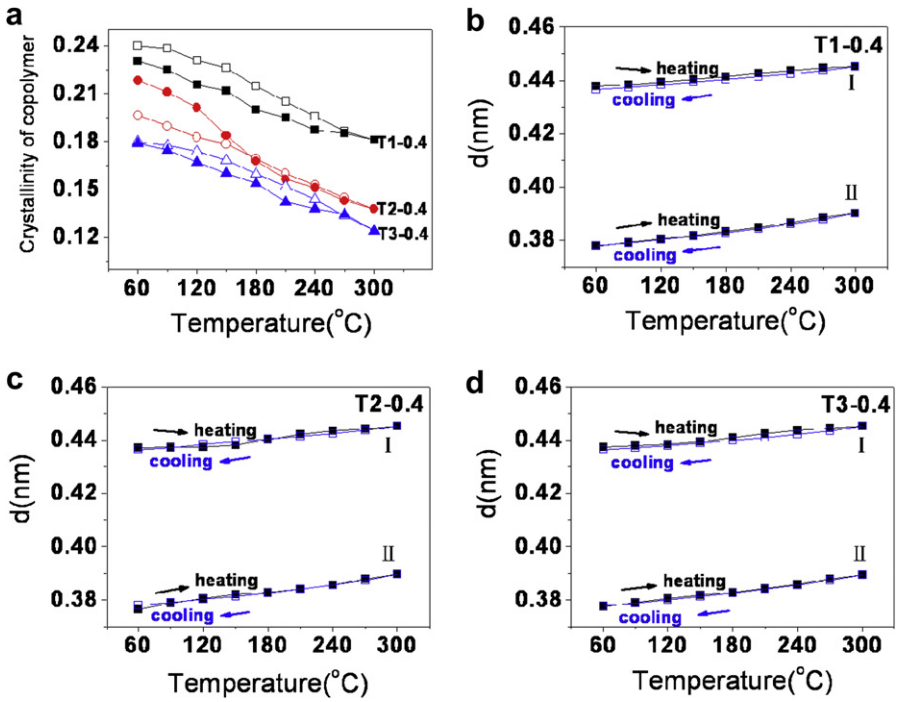

Fig. 5. Crystallinity of copolymers (a) and *d*-spacings (b, c and d) of sample T1-0.4, T2-0.4 and T3-0.4 as a function of temperature (60 °C–300 °C–60 °C). The heating and cooling process are denoted as solid and hollow symbols, respectively.

Fig. 6c shows that the crystallinity of PBA homopolymer decreases by 22% during the entire heating process, and 10% from 60 to 180 °C. The *d*-spacings of peak I and II increase by 1.1% and 1.4% from 60 to 210 °C as shown in Fig. 6d. The crystallinity of PBA homopolymer increases by 0.8% after cooling process while the changes of *d*-spacings are almost reversible throughout the temperature shift.

Furthermore, a comparison has been made among samples T2-0.4, T2-0.6 and T2-0.8. WXAD diagrams of T2-0.6 and T2-0.8 during heating and cooling process are presented in Fig. 7. The corresponding crystallinity and *d*-spacings of these samples are plotted vs temperature in Fig. 8. Comparing with Fig. 4c, d, both diffraction peaks at 60 °C are kept at the same position in spite of the increase of PBA content (φ_{PBA}), while the amorphous halo becomes weak in WAXD diagrams of T2-0.6 and almost disappears in T2-0.8. The crystallinity of T2-0.4 decreases by 2.2% after heating and cooling process due to the irreversible melting of imperfect

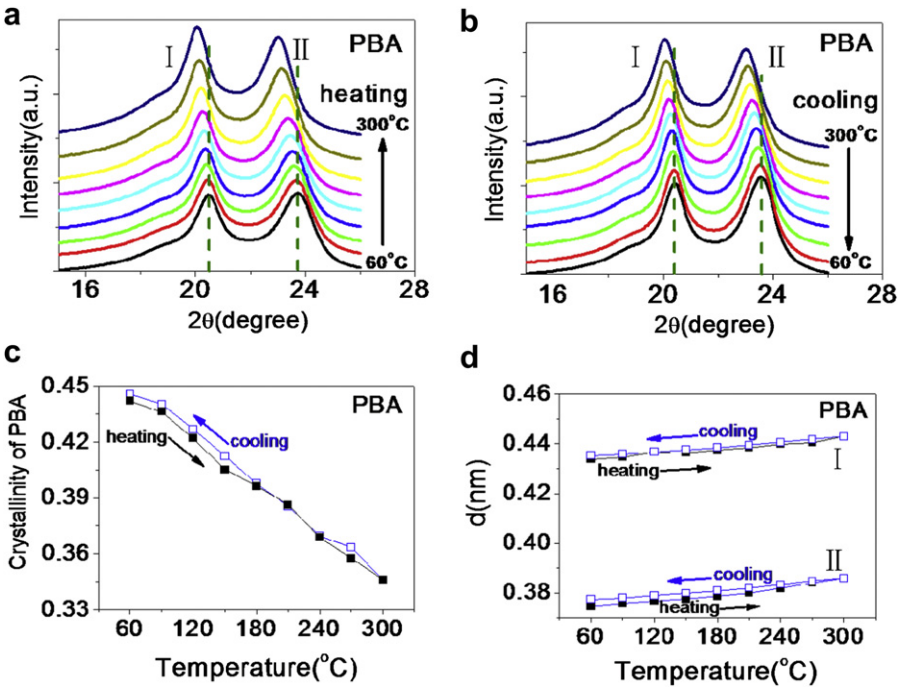

Fig. 6. WAXD diagrams (a, b), crystallinity (c) and *d*-spacings (d) of PBA homopolymer as a function of temperature (60 °C–300 °C–60 °C). The heating and cooling process are denoted as solid and hollow symbols, respectively.

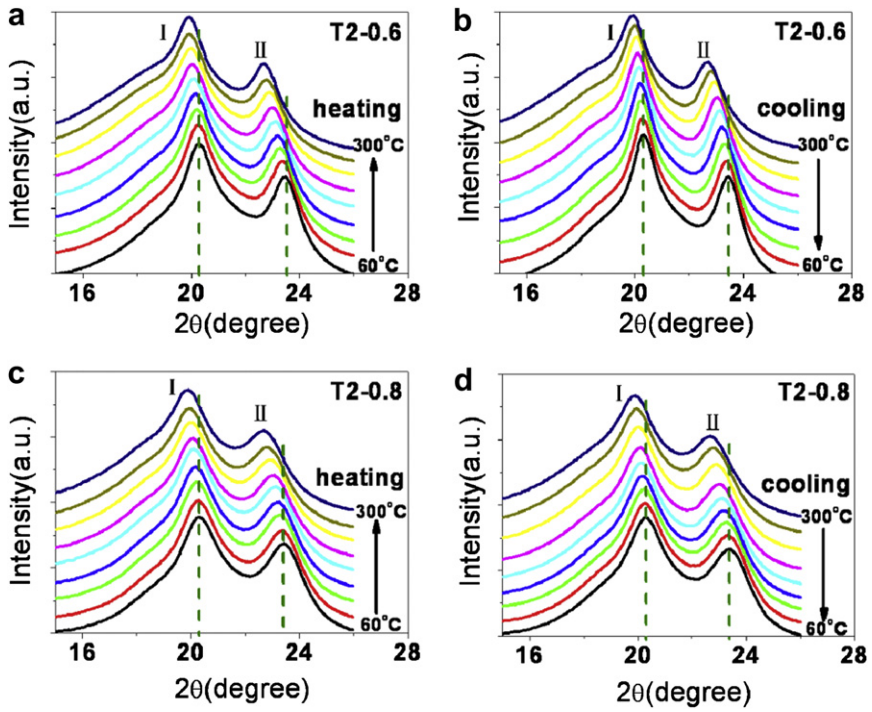

Fig. 7. WAXD curves of T2-0.6 and T2-0.8 during heating (a, c) and cooling (b, d) process.

crystal of PA6, but the crystallinities of T2-0.6 and T2-0.8 increase by 1.4% and 0.4%, respectively, which can be attributed to the perfection of PBA crystals as shown in Fig. 6c. Fig. 8c and d show that the changes of *d*-spacings in samples with high content of PBA are also reversible.

At 300 °C, PA6 blocks are completely melted while PBA are still in crystalline state, therefore the WAXD diagrams of all samples at 300 °C (Fig. 9) can give a direct comparison on the crystallinity of PBA block. As presented in Fig. 9, the amorphous halo ($2\theta = 19°$) decreases with the reduction of PA6 content.

The changes of crystallinity of PBA blocks at 300 °C are plotted vs φ_{PBA} and the average block length (number of monomers) of PBA in Fig. 10. To eliminate the effect caused by difference of φ_{PBA}, the total crystallinity of PBA (as presented in Figs. 5 and 8) is

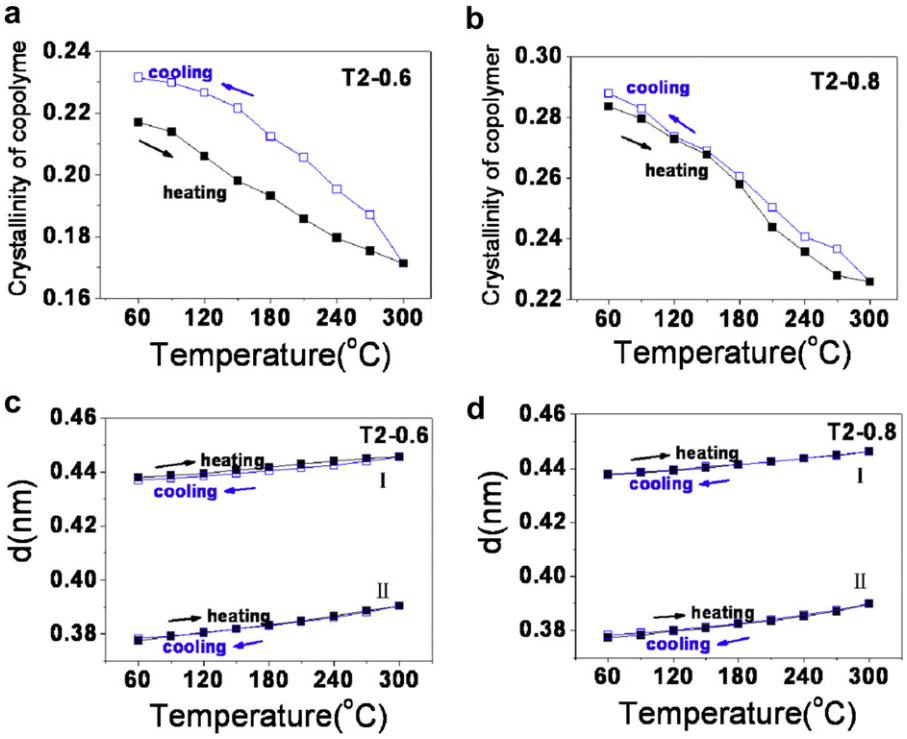

Fig. 8. Crystallinity of copolymers (a, b) and *d*-spacings (c, d) of sample T2-0.6 and T2-0.8 as a function of temperature (60 °C–300 °C–60 °C). The heating and cooling process are denoted as solid and hollow symbols, respectively.

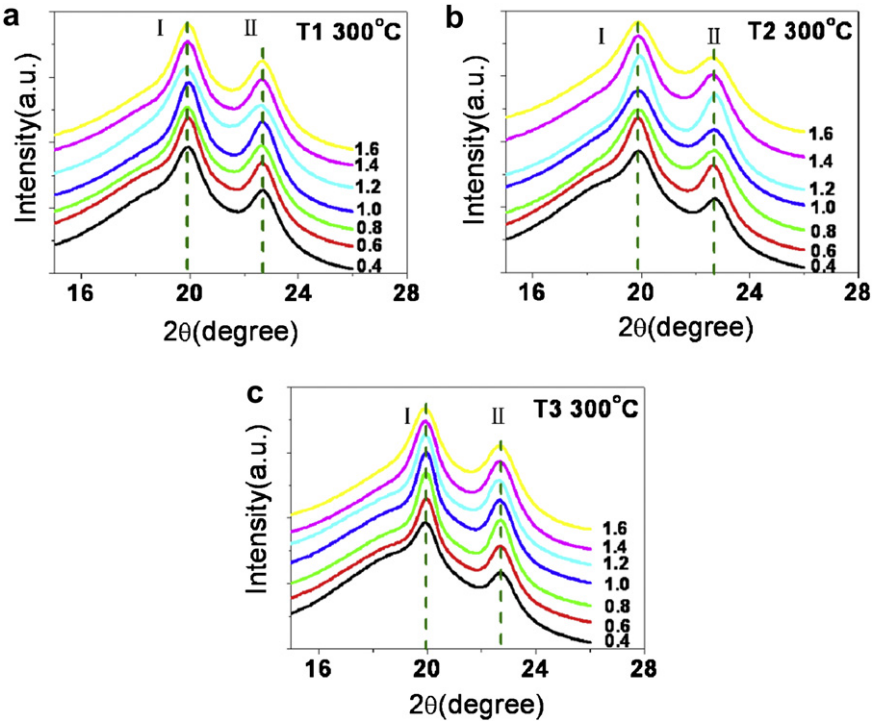

Fig. 9. WAXD diagrams of sample T1 (a), T2 (b) and T3 (c) at 300 °C.

normalized via divided by the content of PBA. As shown in Fig. 10a, the global trend is that the crystallinity of PBA blocks decreases with the increase of φ_{PBA} in all samples. An exception is that an up-turn appears in two samples in T3 series with the contents of PBA above 54%. Fig. 10b gives a clearer trend in terms of the average block length of PBA that all three series fall into almost the same line although T2 series have slightly higher crystallinity. With a block length with monomer number of 8, the crystallinity of PBA domains reaches 44%, while increasing the block length to 40 monomers the crystallinity reduces to 34%. It is evident that the crystallinity of PBA blocks is determined by the block length rather than the volume fraction. In another word, the length of PA6 coil has little effect on the crystallization of PBA rod block when annealed at 230 °C. When the number of PBA monomers exceeds 40, the crystallinity of PBA domains in T3 shows a slight increase, which may be due to the level-off of homo-PBA content (see Fig. 2b).

4. Discussion

4.1. Content of PBA homopolymers

Based on the UV–vis spectrophotometry, the variation of PBA homopolymer in all samples can be divided into three zones as shown in Fig. 2b. In zone I, as the concentration of reaction points in system was low at the beginning, the PABA (PBA monomer) added cannot be consumed promptly by triblock copolymers. Therefore, partial of PABA were prone to react with each other to generate homopolymers, and consequently leaded to the increase of content of homo-PBA. In zone II, with the increase of homo-PBA, the concentration of reaction points in the system increased to an equilibrium and the PABA added afterwards can be consumed promptly by both triblock copolymers and PBA homopolymers. As a result, the content of homo-PBA was kept constant while the molecular weights of triblock copolymers and PBA homopolymers

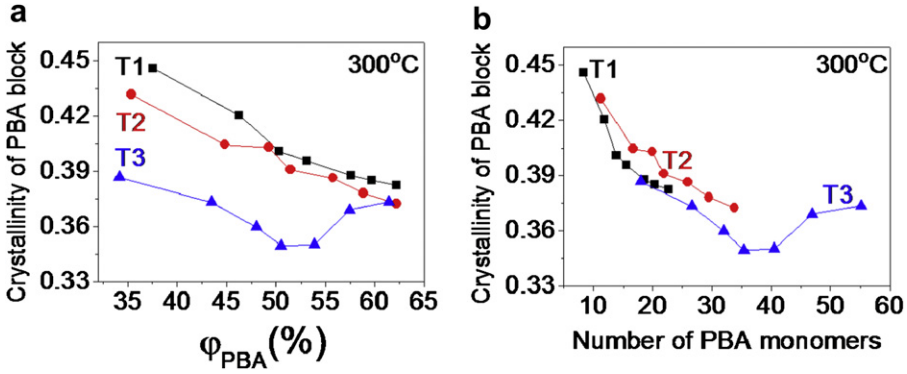

Fig. 10. Crystallinity of PBA domains as functions of volume fraction of PBA (a) and number of PBA monomers (b) at 300 °C.

increased. This broad plateau is useful in material synthesis as one can regulate the molecular weight of triblock copolymers while the content of rod homopolymers can be kept at a relatively steady level. In zone III, as the viscosity of reaction system climbed to a certain level due to the increase of molecular weight of triblock copolymer, the reactivity of reaction points decreased. The result is that the PABA was more apt to react with each other to generate new PBA homopolymers and the content of homo-PBA increased again in this region.

4.2. Morphology of copolymers

In our previous work [2], the samples with low content of PBA annealed at 180 °C and then cooled freely generated high content of PA6 crystal and even showed a clear Brill transition during heating process. Nevertheless, with the same content of PBA and PA6 block length, the samples annealed at a higher temperature (230 °C) in this work held only a trace amount of PA6 crystal and the Brill transition was not observable as confirmed by DSC and WAXD data. It should be noticed here that the actually melting temperature of PA6 block in triblock copolymers is 172 °C, which is also lower than our early annealing temperature (180 °C), so the crystallization of PA6 blocks can only occur during slow cooling process. When annealed at 230 °C or 180 °C, PBA blocks are always in crystalline state while PA6 blocks are always in molten state and the crystallization capability of PA6 blocks is controlled by the crystal perfection of PBA blocks. Higher annealing temperature allows PBA blocks to develop more perfect packing, which consequently imposes stronger stretching on PA6 blocks. Following this idea, one can easily understands more restriction on crystallization of PA6 blocks after annealed at 230 °C as the stretching or locking effect is enhanced due to the increase of crystal perfection of PBA blocks.

In rod-coil system, the coils undergo the stretching effect from the rods while the rod blocks sustain an equal counterforce from the coil blocks [14,44]. In our samples, the interactions between the rods like hydrogen bonding and π–π interaction are much stronger than that between the coil blocks with hydrogen bonding and van de Waals force. When annealed at 230 °C, which is above the melting temperature of PA6 blocks but below that of PBA blocks, PA6 blocks are free to move locally but cannot crystallize. The main role of PA6 is to assist the crystallization of PBA blocks on diffusion. On the other hand, the crystallization of PBA has to face the counter stretching from PA6 coil blocks due to entropy effect, as the parallel packing of PBA blocks forces PA6 coil to be stretched. Consequently PA6 coils suffer an entropic penalty although this effect is very weak as compared with the enthalpic gain caused by parallel packing of PBA blocks. If the entropic penalty is significant, some changes of crystallinity can be expected among T1, T2 and T3 at the same length of PBA block as these three series have different PA6 length. Nevertheless, this has not been observed as shown in Fig. 10b, irrespective of the PA6 block length. That is to say, the crystallinity of PBA is dominantly controlled by the length of PBA blocks. This seems logical as diffusion is the control step for the crystallization of PBA blocks at 230 °C. Longer block length corresponds to a lower diffusivity, leading to a lower crystallinity.

In addition, the influence of PBA homopolymers has been taken into consideration in current work. In our samples, PBA exist in two forms: PBA blocks in the triblock copolymers and PBA homopolymers. If PBA homopolymers enter the PBA domains of the triblock copolymers, the interfacial area between PBA and PA6 domains increases [15,16]. As a result, the stretching force on the coils is reduced, which will provide more freedom for both blocks to reach higher crystallinity. Moreover, when the content exceeds 40%, the homo-PBA can also crystallize independently which will make some contribution to the crystallinity of PBA domains. Therefore, the crystallinity of PBA in the sample T3-1.4 and −1.6 (Fig. 10) has a slight increase when the content of homo-PBA in these two samples exceeds 40% (Fig. 2).

5. Conclusion

Based on PA6 with three different number-average molecular weights, a series of triblock copolymers containing PBA as the rod blocks and PA6 as the coil blocks were prepared by two-step polycondensation method with different block ratio. The content of homo-PBA was studied by UVS. The results from DSC and WAXD revealed that: in all samples, the crystallization of PA6 was strongly suppressed due to the stretching effect between the rods and the coils after annealed at high temperature (230 °C). Only a trace amount of imperfect crystal of PA6 block was observed in the sample with lowest volume fraction of PBA (T2-0.4). Due to the strong interaction between the rods, the crystallization of PBA was not significantly disturbed by the counterforce from the coils and the variation of PA6 block length had little effect on the crystallization of PBA. As the mobility of PBA blocks decreased with the increase of the length of the rod blocks, the crystallinity of PBA domains decreased with the increase of volume fraction and the length (number of monomer) of PBA. Furthermore, the homo-PBA can also make contribution to the crystallinity of PBA domains.

Acknowledgement

This research was supported by the National Natural Science Foundation of China (NNSFC, 20774091), Fund for the one hundred talent scientist, 973 program of MOST (2010CB934504) and the experimental fund of National Synchrotron Radiation Laboratory (NSRL).

References

[1] Kim JH, Rahman MS, Lee JS, Park JW. Macromolecules 2008;41:3181–9.
[2] Li JJ, Huang YJ, Cong YH, Xu L, Wang DL, Hong ZF, et al. Polymer 2010; 51:232–9.
[3] Minicha EA, Nowakb AP, Demingb TJ, Pochan DJ. Polymer 2004;5:1951–7.
[4] Olsen BD, Segalman RA. Mater Sci Eng R 2008;62:37–66.
[5] Lee M, Jang DW, Kang YS, Zin WC. Adv Mater 1999;11:1018–20.
[6] Rahman MS, Samal S, Lee JS. Macromolecules 2006;39:5009–14.
[7] Rabani G, Luftmann H, Kraft A. Polymer 2006;47(12):4251–60.
[8] Li LB, Lambreva D, de Jeu WH. J Macromol Sci Phys 2005;43(1):59–70.
[9] Minich EA, Nowak AP, Deming TJ, Pochan D. J Polym 2004;45:1951.
[10] Tu Y, Wan X, Zhang H, Fan X, Chen X, Zhou QF, et al. Macromolecules 2003; 36:6565.
[11] Matsena MW, Barrett CJ. Chem Phys 1998;109:4108–18.
[12] Lee M, Cho BK, Zin WC. Chem Rev 2001;101(12):3869–92.
[13] Muthukumar M, Ober CK, Thomas EL. Science 1997;277:1225–32.
[14] Liu XB, Zhao YF, Chen EQ, Ye C, Shen ZH, Fan XH, et al. Macromolecules 2008; 41(14):5223–9.
[15] Sary N, Rubatat L, Brochon C, Hadziioannou G, Ruokolainen J, Mezzenga R. Macromolecules 2007;40:6990–7.
[16] Castillo RV, Müller AJ, Raquez JM, Dubois P. Macromolecules 2010;43:4149–60.
[17] Castillo RV, Müller AJ. Prog Polym Sci 2009;34:516–60.
[18] Lee BS, Chun BC, Chung YC, Sul KI, Cho JW. Macromolecules 2001;34:6431–7.
[19] Miller JA, Lin SB, Hwang KKS, Wu KS, Gibson PE, Cooper SL. Macromolecules 1985;18:32–44.
[20] Christenson EM, Anderson JM, Hiltner A, Eric Baer E. Polymer 2005;46: 11744–54.
[21] Agnarsson I, Boutry C, Wong SC, Baji A, Dhinojwala A, Sensenig AT, et al. Zoology 2009;112:325–31.
[22] Askarieh G, Hedhammar M, Nordling K, Saenz A, Casals C, Rising A, et al. Nature 2010;465:236–8.
[23] König HM, Kilbinger AFM. Angew Chem Int Ed 2007;46:8334–40.
[24] Marsden HR, Kros A. Macromol Biosci 2009;9:939–51.
[25] Ptaszynski B, Terrisse J, Skoulios A. Makromol Chem 1975;176:3483.
[26] Hashimoto T, Tanaka H, Hasegawa H. Macromolecules 1989;22:965.
[27] Muthukumar M, Ho JS. Macromolecules 1989;22:965.
[28] Schull KR, Winey K. Macromolecules 1992;25:2637.
[29] Gao LC, Yao J, Shen ZH, Wu YX, Chen XF, Fan XH, et al. Macromolecules 2009; 42:1047–50.
[30] Tao YF, Olsen BD, Ganesan V, Segalman RA. Macromolecules 2007;40:3320–7.

[31] Matsen MW. Macromolecules 1995;28:5765–73.
[32] Winey K, Thomas EL, Fetters LJ. Macromolecules 1991;24:6182.
[33] Higashi F, Goto M, Kakinoki H. J Polym Sci: Polym Chem Ed 1980;18:1711.
[34] Armarego WLF, Chai CLL. Purification of laboratory chemicals. Oxford: Butterworth-Heinemann; 2003. pp. 104.
[35] Russo S, Mariani A, Ignatov VN, Ponomarev II. Macromolecules 1993;26:4984–5.
[36] Schaefgen JR, Foldi VS, Logullo FM, Good VH, Gulrich LW, Killian FL. Polym Prepr 1976;17:69–74.
[37] De Ruijter C, Jager WF, Groenewold J, Picken SJ. Macromolecules 2006;39 (11):3824–9.
[38] Takahashi Y, Ozaki Y, Takase M, Krigbaum WR. J Polym Sci Part B Polym Phys 1992;31(9):1135–43.
[39] Bao H, Rybnikar F, Saha P, Yang J, Geil PH. J Macromol Sci Phys 2001;B40 (5):869–911.
[40] Murthy NS, Curran SA, Aharoni SM, Minor H. Macromolecules 1991;24:3215–20.
[41] Ramesh C, Gowd EB. Macromolecules 2001;34:3308–13.
[42] Murthy NS. J Polym Sci Part B Polym Phys 2006;44(13):1763–82.
[43] Daniel J, Lackst DJ, Rutledge Gregory C. Macromolecules 1994;27:7197–204.
[44] Cavalleri P, Ciferri A, Dell'Erba C, Novi M, Purevsuren B. Macromolecules 1997;30(12):3513–8.

Polymer 52 (2011) 1206–1216

Contents lists available at ScienceDirect

Polymer

journal homepage: www.elsevier.com/locate/polymer

Theoretical study of molecular interactions of TNT, acrylic acid, and ethylene glycol dimethacrylate – Elements of molecularly imprinted polymer modeling process

Julia Saloni [a], Pawel Lipkowski [b], Samuel S.R. Dasary [a], Yerramilli Anjaneyulu [a], Hongtao Yu [a], Glake Hill Jr. [a,*]

[a] Department of Chemistry and Biochemistry, Jackson State University, Jackson, MS 3921, USA
[b] Department of Chemistry, Wroclaw University of Technology, Wroclaw, Poland

ARTICLE INFO

Article history:
Received 31 August 2010
Received in revised form
28 October 2010
Accepted 29 November 2010
Available online 7 December 2010

Keywords:
Molecularly imprinted polymers
Monomer selection
MIP model

ABSTRACT

This study aims to provide simple but reliable theoretical model for monomer selection for molecular imprinting towards detection of nitroaromatic compounds. Presented data show that molecular imprinted polymer/non-imprinted polymer (MIP/NIP) system can be characterized sufficiently by use of very simple model. This model provides detailed description (qualitative and quantitative) regarding hydrogen bonding between the template and polymeric matrix hence can become good theoretical tool for monomer selection. *Ab initio* DFT (Density Functional Theory) method has been applied for structural, solvent, and vibrational frequency calculations. Binding energy and IR spectra have been carefully evaluated. Additionally, experimental FT-IR spectroscopy has been conducted to validate the formation of hydrogen bonding between studied species.

1. Introduction

Molecular imprinting is a method to prepare polymers with highly specific binding sites for small molecules. Molecularly imprinted polymers (MIPs) have been synthesized for a variety of applications, such as catalysis [1] and sensor technology [2,3]. As presented in Fig. 1. the following stages of molecular imprinting can be recognized: functional monomer self-assembly, polymerization, template solvent extraction and template rebinding. During self-assembly stage functional monomers (acrylic acid, AA) recognize and bind through intermolecular forces to the template (2,4,6-TNT) active sites. Then polymerization occurs, where functional monomers and cross linking molecules (ethylene glycol dimethacrylate, EGDMA) form polymer matrix around template preserving monomer-template binding sites. Template molecule can be removed from the formed cavity by solvent extraction and then be rebounded to the empty one. Cavities can be visualized as "locks" - complementary with size and shape and functional group orientation to the template, the "key", as in the "lock-key" system.

A great amount of experimental and theoretical work has been devoted to molecular imprinting for detection of different compounds including warfare agents and explosive compounds. An overview on synthesis and characterization of MIPs has been reported by Cormack and Elorza [4]. This summary includes discussion on the nature of possible templates and functional monomers, the role of cross-linker (s) and initiators, as well as the role solvent plays.

Detection techniques of gas phase nitroaromatic explosive using colorimetry or fluorimetry, as well as their dependence on applied functional monomers have been studied experimentally by Toal and Trogler [5]. Electronic and structural interactions between the sensing material and the analyte have been reported to be a base for the detection process. Pawel et al. [6] reported molecular dynamics simulations for different monomeric systems to predict interaction energies, binding distances and active site groups between molecular systems and different chemical warfare agents. Accordingly, the electrostatic interactions play the most significant role in the formation of MIP material, and the functional groups of monomers interacting with a template tend to be either $-COOH$ or $-CH-CH_2$.

Dong et al. [7] performed computational and experimental investigations on the interaction between the template and functional monomer used in MIPs. Binding energy criteria has been chosen for monomer selection, where monomer of higher binding energy is suitable for MIP preparation. They have chosen theophylline, THO, as a template and methacrylic acid, MAA, as one of the functional monomers. Theoretical investigations have been performed applying DFT level of theory and 6-31 + G**and 3-21G basis

* Corresponding author.
E-mail address: glakeh@icnanotox.org (G. Hill).

0032-3861/$ – see front matter © 2010 Elsevier Ltd. All rights reserved.
doi:10.1016/j.polymer.2010.11.057

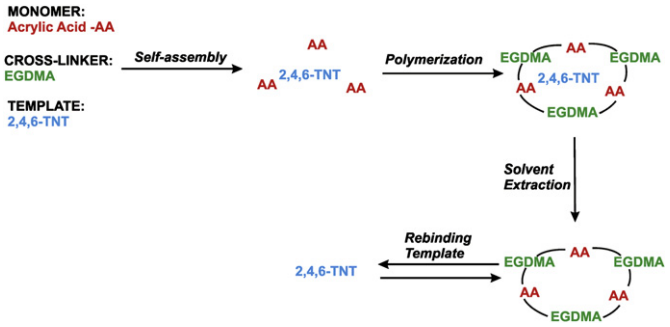

Fig. 1. Scheme for molecular imprinting process of 2,4,6-TNT in acrylic acid and EGDMA.

sets. Experimentally, the adsorption of THO on the MIPs was studied using ^{1}H NMR spectroscopy to find out the hydrogen bonding interactions in the complex. FT-IR study confirmed existence of C═O and O–H bonds in MIP binding to THO.

The purpose of this work is to provide an insight into the nature of intermolecular interactions between polymer and template towards implementation of computational chemistry as a tool for monomer selection for molecular imprinting synthesis. Applying proposed theoretical approach one can evaluate variety of interacting monomer-template systems without laborious synthesis. Saving time and money and limiting environmentally hazardous wastes, computational chemists can work hand-in-hand with experimentalists to design new materials with better strategies for syntheses. We have shown that a theoretical model, as simple as a 1:1 complex to mimic the monomer-template interactions, is sufficient for monomer and solvent selections. Theoretical predictions of monomer-template MIP/NIP complex formation has been verified by experimental FT-IR spectra. In our previous research [8], we found that calculated IR spectra resemble remarkably well with experimental results, giving us a confidence to use theoretical studies to aid monomer selections. Additionally, computational chemistry provides data on structural arrangement of species involved in bonding and detailed characterization of existing interactions including interaction energies, bonding distances and charge transfer information. Theoretically calculated IR spectrum includes assignments of vibrational frequencies of different functional groups as well as potential energy distribution (PED) of normal modes. Ab initio calculations also provide insights into solvent impact on bonding in monomer-template complexes.

From the large pool of functional monomers which can non-covalently bind to the TNT template during molecular imprinting process, we selected acrylic acid (AA) as the monomer and ethylene glycol dimethacrylate (EGDMA) as the cross-linker. The croslinking molecule links polymer chains and causes change in physical state of polymer. However, no interactions between EGDMA and template have been observed. Acrylic acid as a monomer and 2,4,6-TNT as a template have been used to build model of cavity as well as other simple models for interaction energy and solvent effects analyses, such as model for MIP active site and simple monomer-template system. Lock-key interactions through hydrogen bonding between active site and the template has been presented on theoretical results and confirmed by experimental IR spectra for the MIP and NIP. Detailed theoretical vibrational frequency analysis including PED assignment is presented for AA, 2,4,6-TNT, and their complex in the simplest 1:1 complex model.

2. Applied methods

2.1. Computations

Ground state geometry of the complex was obtained by the DFT [9] approach utilizing Becke's three parameter functional [10] with the Vosko et al. [11] local and Lee et al. [12] non-local correlation, abbreviated as B3LYP. No symmetry constraints were imposed during the optimization process. The location of its true minimum was confirmed by vibrational analysis performed at the DFT level of theory. Calculations were performed using standard Pople's 6-31G (d, p) basis set [13] including *d* polarization [14] functions for carbon, nitrogen and oxygen and *p* polarization functions for hydrogen atoms.

The thermodynamic properties including IR spectra of AA and TNT were calculated applying ideal gas, rigid rotor, and harmonic oscillator approximations [15]. The electron distribution was studied using natural bond orbital (NBO) [16] electronic population analysis approach. The effect of solvent was modeled by the CPCM SCRF [17] method, where acetone and methanol have been used as solvents. Basis set superposition error (BSSE) [18,19] has been included in the total interaction energy calculations [20]:

$$\Delta E_{\mathrm{MP2}} = E_{\mathrm{AB}} - E_{\mathrm{A}} - E_{\mathrm{B}} \tag{2.1}$$

where ΔE_{MP2} is further partitioned into Hartree-Fock (ΔE_{HF}) and correlation ($\epsilon_{\mathrm{MP}}^{(2)}$) components according to the equation

$$\Delta E_{\mathrm{MP2}} = \Delta E_{\mathrm{HF}} + \epsilon_{\mathrm{MP}}^{(2)} \tag{2.2}$$

The HF interaction energy decomposition scheme [21] was performed within the variational-perturbational scheme corrected for basis set superposition error (BSSE). In this scheme, ΔE_{HF} is

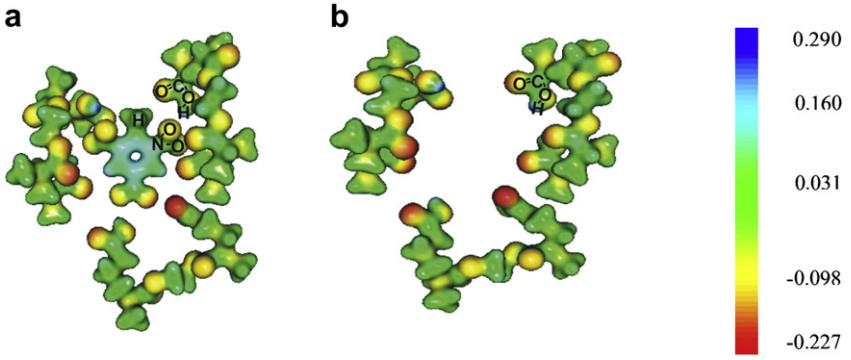

Fig. 2. Map of electrostatic potential of a) 2,4,6-trinitrotoluene encapsulated in a cave consisting of acrylic acid- ethylene glycol dimethacrylate matrix; b) empty cave; and c) electrostatic potential scaling bar.

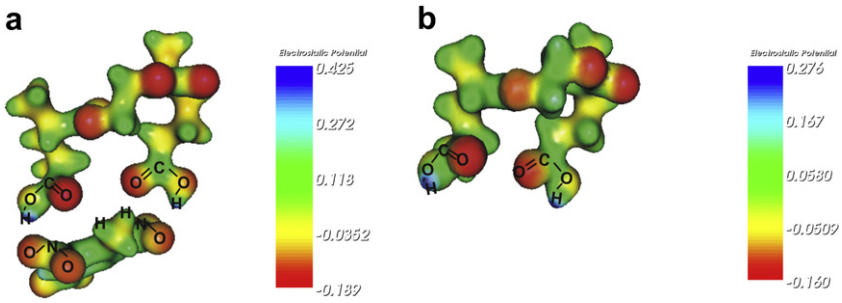

Fig. 3. Map of electrostatic potential of models: a) MIP and b) NIP.

partitioned into electrostatic ($\epsilon_{el}^{(10)}$) and Heitler-London exchange (ϵ_{ex}^{HL}) first-order components and higher order delocalization (ΔE_{del}^{HF}) terms. The delocalization energy represents charge transfer, induction, and other higher order Hartree-Fock terms [22]. The ($\epsilon_{MP}^{(2)}$) correlation correction includes the intermolecular dispersion contribution term ($\epsilon_{disp}^{(20)}$) and the higher order correlation energy components [23]. Calculation of monomer energy was performed in the dimer basis set according to the "full" correction scheme proposed by Boys and Bernardi [19]. Molecular Electrostatic Potential (MEP) was generated using the Molekel 5.3 visualization program [24]. The computations were carried out using the Gaussian 03 suite of programs [25]. The interaction energy decomposition was performed applying the modified version [26] of the Gamess code [27].

2.2. Experiment

EGDMA, AA and **c**hloroform were from Sigma Aldrich and used without further purification. TNT was provided by the United States Army Engineering Research and Development Center, ERDC (Vicksburg, MS). A 1:2:1 volume ratio of 1 mM TNT, 1 mM of AA and 1 mM EGDMA was mixed in chloroform. The as prepared complex was used for FT-IR analysis after 24 h. Individual spectrum for TNT, AA or EGDMA was obtained by mixing 1 mM each of these

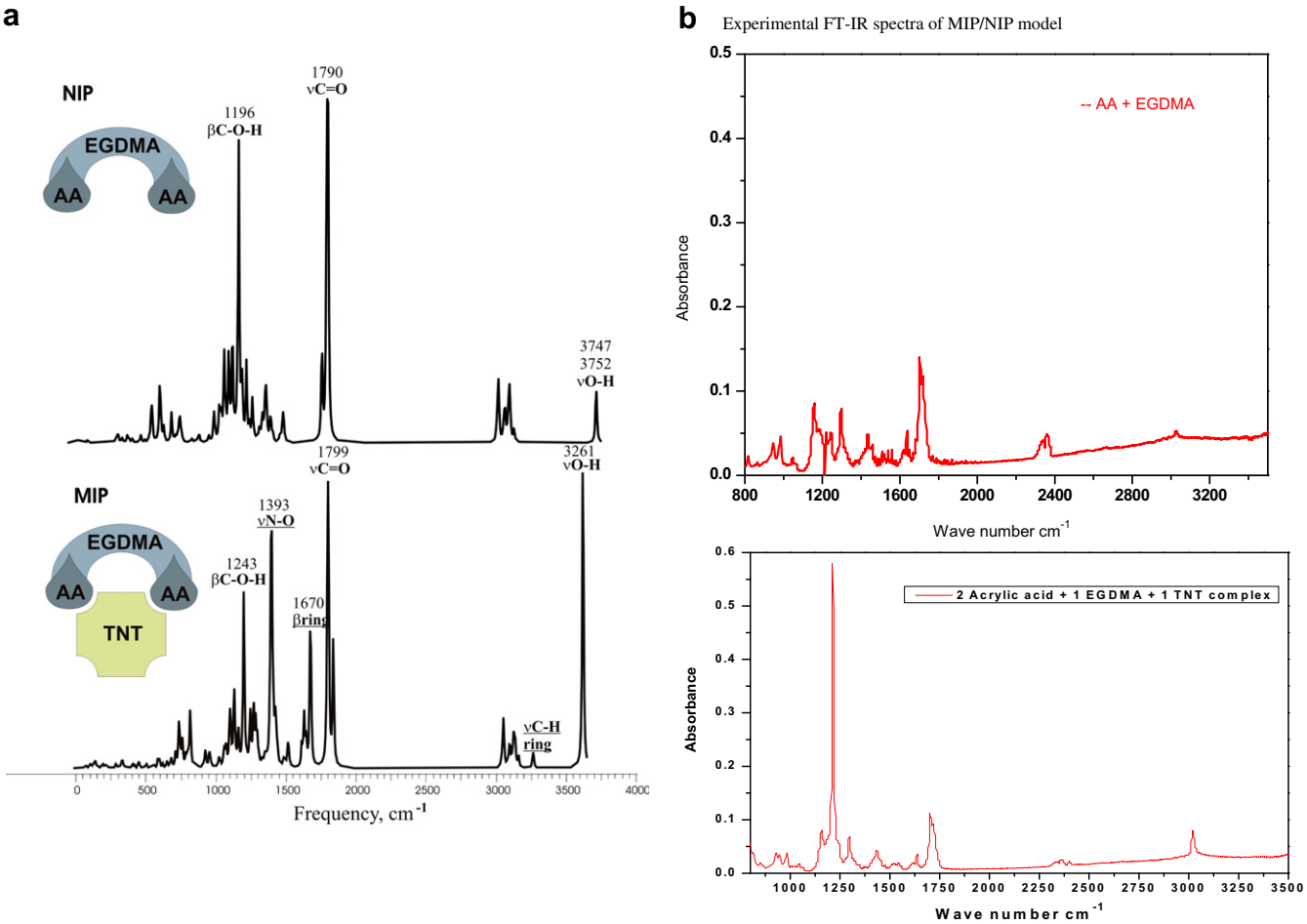

Fig. 4. a) Theoretical IR spectra for NIP (non-imprinted polymer) and MIP (imprinted polymer with TNT as a template) calculated at B3LYP/6-31G(d,p) level of theory. Abbreviations: AA- acrylic acid, EGDMA- ethylene glycol dimethacrylate, TNT- 2,4,6-trinitrotoluene; b) Experimental FT-IR spectra of MIP/NIP model.

Table 1
The assignment of computed vibrational frequencies (ν, cm^{-1}), with PED (%) and intensities (*A*, $km*mol^{-1}$) of acrylic acid obtained at B3LYP/6-31G (d,p) level.[a]

	ν	ν_{scaled}	ν^{29}_{exp}	A	Assignment and PED
1	116.3	111.8	95	0.1	τC_4C_5(78), $\gamma(CC_2)_4$(16),
2	282.2	271.2		0.9	$\beta(CC_2)_4$(51), $\beta(CO_2)_5$(30), $\beta(CO_2)_5$(16),
3	482.6	463.8	480	9.7	$\gamma(CO_2)_5$(43), $\gamma(CC_2)_4$(27), τC_1C_4(22), τC_5O_7(7),
4	533.1	512.3	525	8.1	$\beta(CO_2)_5$(57), $\beta(CC_2)_4$(15), νC_4C_5(15),
5	584.1	561.3	574	42.2	$\beta(CO_2)_5$(63), $\beta(CC_2)_4$(17), $\beta C_5O_7H_8$(10), $\beta(CH_2)_1$(6),
6	614.2	590.2		95.7	τC_5O_7(88), $\gamma(CC_2)_4$(7),
7	826.6	794.4	816	40.8	$\gamma(CO_2)_5$(63), $\gamma(CC_2)_4$(21), τC_1C_4(13),
8	842.4	809.5	828	7.2	νC_4C_5(46), νC_5O_7(25), $\beta(CH_2)_1$(15),
9	998.2	959.3	974	26.2	$\gamma(CH_2)_1$(95),
10	1035.7	995.3	989	19.0	τC_1C_4(64), $\gamma(CC_2)_4$(32),
11	1040.6	1000.0	1021	74.8	$\beta(CH_2)_1$(48), νC_5O_7(25), $\beta(CC_2)_4$(17),
12	1215.9	1168.5	1191	172.9	$\beta C_5O_7H_8$(53), νC_5O_7(19), νC_4C_5(9), $\beta(CH_2)_1$(5),
13	1314.3	1263.4		1.4	$\beta(CC_2)_4$(62), $\beta(CH_2)_1$(16), νC_1C_4(11),
14	1381.6	1327.7	1334	56.1	νC_5O_7(24), $\beta C_5O_7H_8$(19), $\beta(CO_2)_5$(14), $\beta(CH_2)_1$(13), νC_4C_5(12), $\beta(CC_2)_4$(7),
15	1458.7	1401.8	1411	33.4	$\beta(CH_2)_1$(64), νC_4C_5(11), $\beta(CC_2)_4$(6),
16	1703.0	1636.6	1625	10.9	νC_1C_4(67), $\beta(CH_2)_1$(17), $\beta(CC_2)_4$(6), νC_5O_6(5),
17	1827.2	1755.9	1752	301.9	νC_5O_6(72), νC_4C_5(7), $\beta(CO_2)_5$(6),
18	3170.3	3046.6		4.1	νC_1H_3(58), νC_1H_2(40),
19	3212.6	3087.3		2.2	νC_4H_9(95),
20	3264.1	3136.8		4.2	νC_1H_2(56), νC_1H_3(42),
21	3765.1	3618.3	3552	62.7	νO_7H_8(100),

[a] *Abbreviations*: ν stretching; β in-plane bending; γ out-of-plane bending; τ torsional vibration. ν_{scaled} represents the scaled frequencies (NIST, CCCBDB scaling factor 0.961) and ν_{exp} represents the experimental frequencies obtained from Charles et al. [30].

compounds in the same volume ratio used in the complex with a Nicolet Nexus 670 Fourier Transform Infrared spectrometer. The IR spectra were recorded between 3500 and 750 cm^{-1} by averaging 32 scans for each spectrum with a Smart Multi Bounce ZnSe ATR. In order to compress the sample against the crystal, a pressure plate and clamp were provided. The background spectrum was obtained using 10 μL of chloroform on ZnSe ATR surface. The FT-IR spectra of TNT, AA, EGDMA or complexes were recorded using 10 μL of the solution on ZnSe ATR surface by subtracting the solvent background. Spectral manipulation such as baseline adjustment, smoothing and normalization were performed using the OMNIC software package (Thermo Scientific, USA).

3. Theoretical modeling for TNT imprinting

3.1. Cavity

The model for MIP has been created from six AA molecules, three EGDMA molecules, and one TNT molecule as the template. Electrostatic potential for TNT has recently been published by Politzer et al. [28]. It has also been reported [6] that electrostatic interactions predominate in the cavity for template binding. TNT binding to the polymer is proposed to be formed through interactions with carboxyl and nitro groups. To locate and verify actual interactions, the molecular electrostatic potential, has been calculated and mapped over DFT optimized structure of the MIP model and is presented in Fig. 2, where three nitro groups of TNT are available for binding with the AA's carboxyl group. MEP analysis shows that bonding occurs mostly between O–H of AA and O–N of TNT; whereas C=O …H–C interaction seems to be much weaker. No EGDMA carbonyl group is involved in bonding to the template. MEP analysis provides useful information about electrostatic interactions between cavity and the template; however, it is necessary to have quantitative answer about bonding for monomer selection. In order to avoid time consuming calculations, smaller MIP/NIP model has been proposed.

3.2. MIP/NIP model

The MIP/NIP model possesses the cavity characteristics and consists of all species involved in imprinting process, including two monomers, one cross linking agent and one template. Preferred position of AA with respect to TNT has been theoretically established as an *ortho* position to the TNT methyl group. Energies of the *ortho-meta*, and *ortho-para* isomers differ from the ground state by 0.7 and 0.8 kcal/mol, respectively. In the proposed MIP model, two AA molecules interact with TNT's C2 and C6 nitro groups (*ortho–ortho* position to the methyl group). AA molecules are connected to each other through EGDMA bridge as shown in Fig. 3a. Due to steric effects, EGDMA does not interact with the TNT molecule. The NIP complex is formed above the TNT molecular plane allowing the template freely enter or leave an active site. The presence of a cross-linker during polymerization process stabilizes the cave formed from AA matrix around the template molecule. It has been observed that the size of the cavity, as shown for the NIP model in Fig. 3b, expands slightly from 3.893 Å to 4.404 Å after template removal (distance between oxygen from opposite AA carbonyl groups). However, no other structural changes have been observed.

Interaction energy between a template and proposed MIP/NIP model of active site has been calculated according to formula:

$$\Delta E = E_{MIP} - E_{NIP} - E_{template} \quad (3.2)$$

where ΔE is a template to active site binding energy, E_{MIP} is the energy of MIP model, E_{NIP} is NIP model energy and finally $E_{template}$ is the calculated energy of TNT. Single O–H … O–N binding energy for MIP/NIP model calculated at the DFT level of theory amounts to −7.0 kcal/mol.

3.3. MIP/NIP-IR spectra

MIP and NIP Models have been proposed as a truncated version of MIP, which includes all species involved in molecular imprinting. IR spectra for molecularly imprinted and non-imprinted TNT has been calculated and presented in Fig. 4a. Fig. 4b includes complementary experimental FT-IR spectra for studied complexes. IR spectra for imprinted and non-imprinted 2,4-dinitrophenol in acrylamide and EGDMA matrix have been reported by Zakaria et al. [29]. In their study, experimental spectra of NIP and MIP show only very subtle differences in values representing N–H, O–H as well as C–N and C–O vibrations. The small red shift of C–H and C=O NIP vibrations has also been reported. In the present work, theoretically and experimentally obtained IR spectra for TNT imprinted with AA and EGDMA matrix show similar trends. However, calculated vibrations are more intense and distinctive than the experimental data. This is due to the nature of calculation where NIP and MIP models are treated as isolated systems which automatically exclude any noises/interferences that the experimental spectra usually have.

Table 2
The assignment of computed vibrational frequencies (ν, cm^{-1}), with PED (%) and intensities (*A*, km*mol^{-1}) of 2,4,6-trinitrotoluene obtained at B3LYP/6-31G(d,p) level.[a]

	ν	ν_{scaled}	ν^{30}_{exp}	A	Assignment and PED
1	50.9	48.9		0.1	$\tau C_2N_{14}(22)$, $\tau C_4N_{13}(22)$, $\tau C_6N_{15}(19)$, $\tau C_3C_9(16)$, $\tau_2$ring(8),
2	53.2	51.1		0.1	$\tau C_2N_{14}(29)$, $\tau C_4N_{13}(29)$, $\tau C_6N_{15}(23)$, $\tau C_3C_9(11)$,
3	57.5	55.3		0.6	$\tau C_4N_{13}(31)$, $\tau C_2N_{14}(31)$, $\tau_3$ring(22), $\tau_2$ring(7),
4	95.9	92.2		5.6	$\gamma C_4N_{13}(11)$, $\gamma C_2N_{14}(11)$, $\beta C_4N_{13}(10)$, $\beta C_2N_{14}(10)$, $\tau C_2N_{14}(9)$, $\tau C_4N_{13}(9)$, $\tau_3$ring(7), $\gamma C_6N_{15}(6)$, $\tau_1$ring(6),
5	122.0	117.2		4.8	$\gamma C_6N_{15}(21)$, $\tau_3$ring(12), $\gamma C_4N_{13}(11)$, $\gamma C_2N_{14}(11)$, $\gamma C_5H_8(5)$, $\gamma C_1H_7(5)$,
6	150.5	144.6		2.8	$\beta C_6N_{15}(40)$, $\beta C_2N_{14}(15)$, $\beta C_4N_{13}(15)$, $\tau C_3C_9(14)$,
7	177.7	170.8		0.3	$\tau C_3C_9(66)$, $\beta C_3C_9(19)$,
8	188.9	181.5		0.2	$\tau_2$ring(21), $\gamma C_2N_{14}(16)$, $\gamma C_4N_{13}(16)$, $\tau_3$ring(7), $\tau C_6N_{15}(5)$,
9	197.0	189.3		5.1	$\beta C_4N_{13}(37)$, $\beta C_2N_{14}(-37)$,
10	296.1	284.5		2.2	$\gamma C_3C_9(27)$, $\gamma C_6N_{15}(21)$, $\gamma C_4N_{13}(12)$, $\gamma C_2N_{14}(12)$, $\tau_1$ring(8),
11	324.7	312.0		0.2	$\nu C_4N_{13}(24)$, $\nu C_2N_{14}(24)$, $\beta_1$ring(11), $\beta_3$ring(8), $\nu C_6N_{15}(6)$,
12	329.1	316.3		0.0	$\beta C_2N_{14}(16)$, $\beta C_4N_{13}(16)$, rock$(NO_2)_{15}(15)$, rock$(NO_2)_{14}(11)$, rock$(NO_2)_{13}(11)$, $\beta C_6N_{15}(-11)$,
13	353.6	339.8		2.9	$\beta_3$ring(35), $\nu C_6N_{15}(27)$, $\beta_2$ring(12),
14	368.5	354.1		1.3	$\beta_2$ring(21), rock$(NO_2)_{15}(14)$, $\nu C_2N_{14}(12)$, $\nu C_4N_{13}(12)$, $\tau_2$ring(8), $\beta_3$ring(7),
15	388.6	372.4		1.4	$\beta C_3C_9(29)$, $\tau_2$ring(23), $\tau_3$ring(8), rock$(NO_2)_{14}(7)$, rock$(NO_2)_{13}(7)$, $\gamma C_2N_{14}(6)$, $\gamma C_4N_{13}(6)$,
16	468.6	450.3	465	1.9	$\gamma C_3C_9(23)$, rock$(NO_2)_{13}(20)$, rock$(NO_2)_{14}(20)$, $\tau_3$ring(12),
17	479.2	460.5	467	0.0	$\tau_2$ring(26), $\beta C_3C_9(20)$, $\gamma C_2N_{14}(13)$, $\gamma C_4N_{13}(13)$, $\tau_3$ring(9),
18	536.3	515.4	565	1.2	$\gamma C_6N_{15}(25)$, $\tau_3$ring(25), $\tau_1$ring(16), $\tau_2$ring(8), $\gamma C_3C_9(7)$,
19	547.2	525.8	579	2.2	rock$(NO_2)_{15}(47)$, $\beta_2$ring(11), $\beta C_6N_{15}(9)$,
20	656.0	630.4	639	8.2	$\tau_1$ring(46), $\gamma C_3C_9(9)$, wag$(NO_2)_{14}(6)$, wag$(NO_2)_{13}(6)$,
21	665.1	639.2	664	0.1	rock$(NO_2)_{14}(11)$, rock$(NO_2)_{13}(11)$, $\beta C_4N_{13}(11)$, $\beta C_2N_{14}(11)$, $\beta C_3C_9(10)$, $\gamma C_2N_{14}(7)$, $\gamma C_4N_{13}(7)$, $\beta C_6N_{15}(7)$, $\tau_2$ring(6),
22	710.5	682.8	704	23.6	$\tau_1$ring(37), $\gamma C_3C_9(10)$, sciss$(NO_2)_{15}(7)$, $\gamma C_2N_{14}(7)$, $\gamma C_4N_{13}(7)$,
23	736.3	707.6	720	56.1	$\beta_2$ring(26), sciss$(NO_2)_{14}(22)$, sciss$(NO_2)_{13}(22)$, $\beta_3$ring(9),
24	741.4	712.5	735	30.6	wag$(NO_2)_{15}(47)$, $\gamma C_6N_{15}(14)$, $\tau_1$ring(12),
25	780.0	749.6		0.3	wag$(NO_2)_{13}(31)$, wag$(NO_2)_{14}(31)$, $\gamma C_4N_{13}(9)$, $\gamma C_2N_{14}(9)$,
26	781.8	751.3		4.3	wag$(NO_2)_{14}(13)$, wag$(NO_2)_{13}(13)$, wag$(NO_2)_{15}(13)$, $\tau_1$ring(10), $\gamma C_2N_{14}(10)$, $\gamma C_4N_{13}(10)$, $\gamma C_3C_9(5)$, $\tau_3$ring(5),
27	801.8	770.5		16.9	$\nu C_3C_9(18)$, sciss$(NO_2)_{15}(14)$, $\beta_1$ring(11), $\beta_3$ring(10), wag$(NO_2)_{14}(5)$, wag$(NO_2)_{13}(5)$,
28	835.5	802.9	793	1.8	sciss$(NO_2)_{15}(28)$, sciss$(NO_2)_{14}(24)$, sciss$(NO_2)_{13}(24)$, $\beta_1$ring(7),
29	917.4	881.6		38.8	$\nu C_2N_{14}(16)$, $\nu C_4N_{13}(16)$, sciss$(NO_2)_{14}(16)$, sciss$(NO_2)_{13}(16)$, $\beta_2$ring(5), $\beta CH_3(5)$,
30	948.9	911.9	909	36.4	$\nu C_6N_{15}(18)$, $\gamma C_5H_8(13)$, $\gamma C_1H_7(13)$, sciss$(NO_2)_{15}(9)$, $\tau_1$ring(8), $\beta_3$ring(6),

Table 2 (*continued*)

	ν	ν_{scaled}	ν_{exp}^{30}	A	Assignment and PED
31	956.8	919.5	940	10.8	$\gamma C_1H_7(27)$, $\gamma C_5H_8(27)$, $\tau_1$ring(17),
32	959.5	922.1		2.3	$\gamma C_5H_8(42)$, $\gamma C_1H_7(42)$, $\tau_2$ring(6),
33	1049.7	1008.8		4.2	$\beta CH_3(55)$, $\nu C_4N_{13}(7)$, $\nu C_2N_{14}(7)$, $\beta CH_3(5)$,
34	1053.5	1012.4	1026	1.7	$\beta CH_3(67)$, $\gamma C_3C_9(11)$, $\beta CH_3(6)$, $\tau_1$ring(5),
35	1099.6	1056.7		52.6	$\beta C_5H_8(18)$, $\beta C_1H_7(18)$, $\beta_1$ring(17), $\nu C_1C_6(12)$, $\nu C_5C_6(12)$,
36	1186.8	1140.5	1086	10.9	$\beta_1$ring(41), $\nu C_6N_{15}(10)$, $\nu C_3C_9(9)$, $\nu C_2N_{14}(8)$, $\nu C_4N_{13}(8)$,
37	1215.6	1168.2	1171	15.9	$\beta C_1H_7(30)$, $\beta C_5H_8(30)$, $\beta C_3C_9(9)$, $\beta CH_3(9)$,
38	1222.6	1174.9	1208	0.5	$\nu C_3C_9(31)$, $\nu C_4C_5(13)$, $\nu C_1C_2(13)$, $\nu C_3C_4(7)$, $\nu C_2C_3(7)$,
39	1359.7	1306.7		5.5	$\nu C_3C_4(21)$, $\nu C_2C_3(21)$, $\nu C_1C_6(11)$, $\nu C_5C_6(11)$, $\nu C_1C_2(9)$, $\nu C_4C_5(9)$,
40	1394.0	1339.6		339.8	$\nu N_{15}O_{21}(22)$, $\nu N_{15}O_{20}(22)$, $\nu C_6N_{15}(11)$, sciss$(NO_2)_{15}(11)$, $\nu N_{14}O_{19}(6)$, $\nu N_{13}O_{16}(6)$,
41	1396.8	1342.3		329.0	$\nu N_{13}O_{17}(16)$, $\nu N_{14}O_{18}(16)$, $\nu N_{13}O_{16}(16)$, $\nu N_{14}O_{19}(16)$, $\nu C_4N_{13}(8)$, $\nu C_2N_{14}(8)$, sciss$(NO_2)_{13}(8)$, sciss$(NO_2)_{14}(8)$,
42	1406.9	1352.0	1356	9.7	$\nu N_{13}O_{17}(11)$, $\nu N_{14}O_{18}(11)$, $\nu N_{15}O_{21}(11)$, $\nu N_{15}O_{20}(11)$, $\nu N_{13}O_{16}(10)$, $\nu N_{14}O_{19}(10)$, $\nu C_4N_{13}(6)$, $\nu C_2N_{14}(6)$, sciss$(NO_2)_{15}(5)$, sciss$(NO_2)_{13}(5)$, sciss$(NO_2)_{14}(5)$,
43	1427.8	1372.1	1356	8.6	$\beta CH_3(71)$, $\beta CH_3(15)$, $\nu C_3C_9(5)$, $\beta CH_3(5)$,
44	1429.1	1373.4	1356	3.9	$\nu C_1C_2(25)$, $\nu C_4C_5(25)$, $\beta C_5H_8(10)$, $\beta C_1H_7(10)$, $\beta CH_3(7)$, $\beta C_3C_9(6)$,
45	1480.4	1422.7	1406	1.9	$\nu C_2C_3(13)$, $\nu C_3C_4(13)$, $\beta C_1H_7(9)$, $\beta C_5H_8(9)$, $\beta CH_3(8)$, $\nu C_5C_6(7)$, $\nu C_1C_6(7)$, $\beta CH_3(5)$,
46	1485.4	1427.5	1437	12.7	$\beta CH_3(53)$, $\beta CH_3(18)$, $\beta CH_3(14)$,
47	1502.8	1444.2	1466	11.6	$\beta CH_3(41)$, $\beta CH_3(16)$, $\beta CH_3(14)$, $\beta CH_3(6)$,
48	1615.3	1552.3	1541	63.7	$\nu C_1C_6(18)$, $\nu C_5C_6(18)$, $\nu N_{15}O_{21}(13)$, $\nu N_{15}O_{20}(13)$, $\nu C_3C_4(8)$, $\nu C_2C_3(8)$, $\beta_2$ring(5),
49	1633.6	1569.9	1541	127.5	$\nu C_4C_5(12)$, $\nu C_1C_2(12)$, $\nu N_{13}O_{17}(12)$, $\nu N_{14}O_{18}(12)$, $\nu N_{13}O_{16}(10)$, $\nu N_{14}O_{19}(10)$, $\nu C_5C_6(5)$, $\nu C_1C_6(5)$,
50	1648.3	1584.0	1541	6.9	$\nu N_{14}O_{18}(19)$, $\nu N_{13}O_{17}(19)$, $\nu N_{14}O_{19}(19)$, $\nu N_{13}O_{16}(19)$, $\nu N_{15}O_{20}(6)$, $\nu N_{15}O_{21}(6)$,
51	1677.0	1611.6	1603	245.4	$\nu N_{14}O_{19}(11)$, $\nu N_{13}O_{16}(11)$, $\nu N_{14}O_{18}(11)$, $\nu N_{13}O_{17}(11)$, $\nu C_4C_5(9)$, $\nu C_1C_2(9)$,
52	1678.0	1612.6	1619	189.8	$\nu N_{15}O_{20}(26)$, $\nu N_{15}O_{21}(26)$, rock$(NO_2)_{15}(9)$, $\nu C_1C_6(8)$, $\nu C_5C_6(8)$, $\beta C_6N_{15}(7)$,
53	3085.3	2965.0	2955	0.6	$\nu C_9H_{10}(62)$, $\nu C_9H_{12}(19)$, $\nu C_9H_{11}(19)$,
54	3156.2	3033.1	3015	4.9	$\nu C_9H_{10}(38)$, $\nu C_9H_{12}(31)$, $\nu C_9H_{11}(31)$,
55	3189.5	3065.1	3057	3.7	$\nu C_9H_{11}(50)$, $\nu C_9H_{12}(50)$,
56	3264.5	3137.2	3087	13.3	$\nu C_5H_8(50)$, $\nu C_1H_7(50)$,
57	3264.6	3137.3	3096	33.4	$\nu C_1H_7(50)$, $\nu C_5H_8(50)$,

[a] *Abbreviations*: ν, stretching; β, bending or ring deformation; γ, bending (change of dihedral angle); wag, wagging; tw, twisting; sciss, scissoring; τ, torsional vibration or ring deformation. Contributions of less than 5% are not included. ν_{scaled} represents the scaled frequencies (NIST, CCCBDB scaling factor 0.961) and ν_{exp} represents the experimental frequencies obtained from Stewart et al. [31].

Analysis of NIP and MIP theoretical spectra (Fig. 4a) reveals the following regions which represents the template (TNT) binding to the AA matrix: 1) νOH high intensity, red shifted frequency of 3747–3752 cm^{-1} for NIP and 3261 cm^{-1} for MIP, represents hydrogen bonding between AA and TNT; 2) Stretching of C═O is slightly blue shifted, and bending mode of C–O–H red shifted. Decreasing intensities for C═O and C–O–H vibrations for MIP systems are observed; 3) N–O stretching at frequency of 1393 cm^{-1} and benzene ring deformation at 1670 cm^{-1} are observed for template in MIP spectrum. Both nodes possess decreased intensity when compared to IR spectra of unbounded TNT. As shown in Fig. 4b, the following regions are recognizable on the experimental NIP spectrum: β COH at ~1150 cm^{-1}, νC═O at ~1750 cm^{-1}, and νOH at ~3000 cm^{-1}. Additionally νNO at 1200 cm^{-1}, and νCH_{ring} at ~2400 cm^{-1} from 2,4,6-TNT in MIP spectrum are also present. No blue or red shift is observed in the experimental spectra; however, both experimental and calculated spectra show significant resemblance. As in the theoretical spectrum, experimental data show

Table 3
The assignment of computed vibrational frequencies (ν, cm^{-1}), with PED (%) and intensities (*A*, $km*mol^{-1}$) of acrylic acid − 2,4,6-trinitrotoluene complex obtained at B3LYP/6-31G(d,p) level.[a]

	ν	ν_{scaled}	A	Assignment and PED
1	15.3	14.7	0.0	$\tau O_{18}H_{24}(47)$, $\tau O_{22}H_{24}(40)$, $\tau C_2N_{14}(5)$,
2	23.5	22.6	0.9	$\tau O_{22}H_{24}(53)$, $\tau O_{18}H_{24}(27)$, $\tau N_{14}O_{18}(11)$,
3	41.5	39.9	0.6	$\tau O_{22}H_{24}(32)$, $\tau C_4N_{13}(20)$, $\tau_3$ring(19), $\tau C_2N_{14}(5)$,
4	53.3	51.2	0.1	$\tau C_6N_{15}(57)$, $\tau O_{18}H_{24}(15)$, $\tau_2$ring(13), $\tau O_{22}H_{24}(8)$,
5	61.2	58.8	1.5	$\tau C_4N_{13}(53)$, $\tau C_3C_9(11)$, $\tau C_2N_{14}(11)$,
6	63.0	64.0	0.6	$\tau O_{18}H_{24}(59)$, $\tau O_{22}H_{24}(23)$,
7	65.4	62.8	0.5	$\tau N_{14}O_{18}(26)$, $\tau C_2N_{14}(16)$, $\tau O_{22}H_{24}(14)$, $\beta O_{18}H_{24}O_{22}(11)$, $\tau O_{18}H_{24}(9)$, $\beta N_{14}O_{18}H_{24}(6)$, $\tau_3$ring(6),
8	90.3	86.8	2.5	$\tau O_{18}H_{24}(20)$, $\nu O_{18}H_{24}(11)$, $\beta N_{14}O_{18}H_{24}(10)$, $\gamma C_2N_{14}(8)$, $\tau C_2N_{14}(6)$, $\gamma C_4N_{13}(5)$,
9	99.5	95.6	8.4	$\beta O_{18}H_{24}O_{22}(30)$, $\nu O_{18}H_{24}(18)$, $\beta N_{14}O_{18}H_{24}(15)$, $\beta C_{23}O_{22}H_{24}(6)$,
10	124.7	119.8	0.8	$\tau O_{22}H_{24}(35)$, $\tau O_{18}H_{24}(32)$, $\tau C_{23}C_{25}(9)$,
11	125.0	120.1	3.0	$\tau O_{22}H_{24}(39)$, $\tau O_{18}H_{24}(31)$, $\tau C_{23}C_{25}(8)$,
12	139.1	133.7	3.6	$\tau O_{22}H_{24}(37)$, $\tau O_{18}H_{24}(-18)$, $\nu O_{18}H_{24}(11)$, $\tau C_2N_{14}(8)$,
13	154.1	148.1	1.9	$\beta C_6N_{15}(40)$, $\beta C_4N_{13}(14)$, $\beta C_2N_{14}(10)$, $\tau N_{14}O_{18}(6)$,
14	190.3	182.9	0.8	$\tau_2$ring(16), $\tau C_3C_9(16)$, $\gamma C_4N_{13}(11)$, $\gamma C_2N_{14}(10)$,
15	200.3	192.5	7.6	$\tau N_{14}O_{18}(25)$, $\beta C_2N_{14}(16)$, $\beta C_4N_{13}(15)$, $\tau O_{18}H_{24}(8)$,
16	215.3	206.9	2.0	$\tau C_3C_9(66)$, $\beta C_3C_9(15)$,
17	296.6	285.0	2.2	$\gamma C_3C_9(26)$, $\gamma C_6N_{15}(19)$, $\gamma C_2N_{14}(13)$, $\gamma C_4N_{13}(12)$, $\tau_1$ring(8),
18	298.7	286.9	10.3	$\beta(CC_2)_{25}(41)$, $\beta(CO_2)_{23}(23)$, $\beta(CO_2)_{23}(8)$, $\nu O_{18}H_{24}(7)$, $\beta O_{18}H_{24}O_{22}(6)$,
19	328.2	315.4	0.7	$\nu C_4N_{13}(11)$, $\beta C_2N_{14}(9)$, $\beta C_4N_{13}(8)$, $rock(NO_2)_{14}(7)$, $rock(NO_2)_{15}(7)$, $\nu C_2N_{14}(7)$, $rock(NO_2)_{13}(6)$, $\beta C_6N_{15}(6)$,
20	330.4	317.5	2.7	$\nu C_4N_{13}(12)$, $rock(NO_2)_{15}(10)$, $\beta C_2N_{14}(8)$, $\beta C_4N_{13}(8)$, $\nu C_2N_{14}(7)$, $\beta C_6N_{15}(5)$,
21	353.8	340.0	2.4	$\beta_3$ring(34), $\nu C_6N_{15}(27)$, $\beta_2$ring(12),
22	371.3	356.8	5.1	$\beta_2$ring(21), $\nu C_2N_{14}(13)$, $rock(NO_2)_{15}(12)$, $\nu C_4N_{13}(9)$, $\beta_3$ring(9), $\tau_2$ring(5),
23	388.2	373.1	1.0	$\tau_2$ring(23), $\beta C_3C_9(23)$, $\tau_3$ring(9), $\gamma C_2N_{14}(8)$, $rock(NO_2)_{13}(7)$, $rock(NO_2)_{14}(7)$, $\gamma C_4N_{13}(6)$,
24	470.5	452.1	4.0	$\gamma C_3C_9(25)$, $rock(NO_2)_{14}(18)$, $rock(NO_2)_{13}(18)$, $\tau_3$ring(14),
25	480.6	461.9	0.1	$\tau_2$ring(25), $\beta C_3C_9(20)$, $\gamma C_2N_{14}(13)$, $\gamma C_4N_{13}(13)$, $\tau_3$ring(7),
26	497.8	478.4	0.7	$\tau O_{18}H_{24}(24)$, $\gamma(CO_2)_{23}(23)$, $\tau O_{22}H_{24}(19)$, $\gamma(CC_2)_{25}(18)$, $\tau C_{25}C_{27}(14)$,
27	536.2	515.3	11.0	$\beta(CO_2)_{23}(42)$, $\beta(CC_2)_{25}(11)$, $\nu C_{23}C_{25}(10)$, $\gamma C_6N_{15}(7)$, $\tau_3$ring(6),
28	537.2	516.2	3.2	$\tau_3$ring(23), $\gamma C_6N_{15}(23)$, $\tau_1$ring(16), $\tau_2$ring(7), $\gamma C_3C_9(6)$,
29	546.7	525.4	2.2	$rock(NO_2)_{15}(46)$, $\beta_2$ring(11), $\beta C_6N_{15}(9)$,
30	613.1	589.2	20.7	$\beta(CO_2)_{23}(49)$, $\beta O_{18}H_{24}O_{22}(19)$, $\beta(CC_2)_{25}(12)$, $\beta(CH_2)_{27}(6)$,

Table 3 (*continued*)

	ν	ν_{scaled}	A	Assignment and PED
31	655.4	629.8	15.2	$\tau_1$ring(38), γC_3C_9(8), $\tau O_{18}H_{24}$(7), $\tau O_{22}H_{24}$(6), wag$(NO_2)_{14}$(6), wag$(NO_2)_{13}$(5),
32	666.4	640.4	0.3	rock$(NO_2)_{14}$(11), rock$(NO_2)_{13}$(11), βC_2N_{14}(10), βC_4N_{13}(10), βC_3C_9(9), γC_2N_{14}(9), γC_4N_{13}(7), βC_6N_{15}(7), $\tau_2$ring(6),
33	710.9	683.2	37.8	$\tau_1$ring(28), $\tau O_{22}H_{24}$(15), $\tau O_{18}H_{24}$(11), γC_3C_9(8), γC_2N_{14}(6),
34	724.0	695.8	36.2	$\tau O_{22}H_{24}$(49), $\tau O_{18}H_{24}$(41),
35	741.6	712.7	30.8	wag$(NO_2)_{15}$(47), γC_6N_{15}(14), $\tau_1$ring(11), wag$(NO_2)_{14}$(5),
36	752.5	723.1	53.3	$\tau O_{22}H_{24}$(48), $\tau O_{18}H_{24}$(42),
37	780.2	749.8	3.4	wag$(NO_2)_{14}$(34), γC_2N_{14}(17), wag$(NO_2)_{15}$(7), $\tau_1$ring(6), $\tau_3$ring(5),
38	781.3	750.8	0.8	wag$(NO_2)_{13}$(37), γC_4N_{13}(16), $\tau O_{22}H_{24}$(7), wag$(NO_2)_{15}$(5),
39	803.2	771.9	16.1	νC_3C_9(15), sciss$(NO_2)_{15}$(14), $\beta_1$ring(10), $\beta_3$ring(9), $\tau O_{22}H_{24}$(8), $\tau O_{18}H_{24}$(7), wag$(NO_2)_{14}$(5),
40	829.5	797.1	23.3	$\tau O_{22}H_{24}$(30), $\gamma(CO_2)_{23}$(26), $\tau O_{18}H_{24}$(18), $\gamma(CC_2)_{25}$(8),
41	842.2	809.3	18.3	$\tau O_{22}H_{24}$(33), $\tau O_{18}H_{24}$(26), sciss$(NO_2)_{13}$(8), sciss$(NO_2)_{15}$(8), sciss$(NO_2)_{14}$(7),
42	860.3	826.7	8.2	$\nu C_{23}C_{25}$(26), $\tau O_{22}H_{24}$(21), $\tau O_{18}H_{24}$(16), $\nu C_{23}O_{22}$(14), $\beta(CH_2)_{27}$(9),
43	923.6	887.6	40.0	νC_4N_{13}(15), sciss$(NO_2)_{13}$(12), sciss$(NO_2)_{14}$(12), νC_2N_{14}(11), $\tau O_{22}H_{24}$(10), $\tau O_{18}H_{24}$(10),
44	949.8	912.8	33.8	γC_1H_7(31), $\tau_1$ring(14), γC_5H_8(12), νC_6N_{15}(9),
45	955.9	918.6	8.0	γC_1H_7(47), νC_6N_{15}(9), $\tau_1$ring(7),
46	959.2	921.8	5.0	γC_5H_8(68), $\tau_1$ring(6),
47	998.5	959.6	24.3	$\gamma(CH_2)_{27}$(95),
48	1034.6	994.2	17.4	$\tau C_{25}C_{27}$(65), $\gamma(CC_2)_{25}$(32),
49	1052.8	1011.7	44.3	$\beta(CH_2)_{27}$(46), $\nu C_{23}O_{22}$(21), $\beta(CC_2)_{25}$(18), $\beta C_{23}O_{22}H_{24}$(6),
50	1058.2	1016.9	4.8	βCH_3(43), βCH_3(14), νC_2N_{14}(7),
51	1063.5	1022.0	1.5	βCH_3(54), βCH_3(11), γC_3C_9(10), βCH_3(6),
52	1099.5	1056.6	53.6	βC_1H_7(19), βC_5H_8(19), $\beta_1$ring(16), νC_1C_6(12), νC_5C_6(12),
53	1187.5	1141.2	13.7	$\beta_1$ring(41), νC_3C_9(10), νC_6N_{15}(10), νC_2N_{14}(8), νC_4N_{13}(8),
54	1215.9	1168.5	14.6	βC_5H_8(32), βC_1H_7(27), βCH_3(9), βC_3C_9(9), νC_4C_5(6),
55	1222.6	1174.9	0.3	νC_3C_9(30), νC_1C_2(14), νC_4C_5(12), νC_2C_3(8), νC_3C_4(6), βC_1H_7(6),
56	1273.3	1223.6	176.2	$\beta C_{23}O_{22}H_{24}$(33), $\beta O_{18}H_{24}O_{22}$(16), $\tau O_{22}H_{24}$(13), $\nu C_{23}O_{22}$(12), $\tau O_{18}H_{24}$(11), $\nu C_{23}C_{25}$(5),
57	1313.2	1262.0	6.5	$\beta(CC_2)_{25}$(59), $\beta(CH_2)_{27}$(17), $\nu C_{25}C_{27}$(10),
58	1359.1	1306.1	6.9	νC_3C_4(21), νC_2C_3(21), νC_5C_6(11), νC_1C_6(11), νC_1C_2(9), νC_4C_5(9),
59	1394.3	1339.9	424.8	$\nu N_{15}O_{20}$(24), $\nu N_{15}O_{21}$(23), νC_6N_{15}(12), sciss$(NO_2)_{15}$(12),
60	1396.8	1342.3	327.6	$\nu N_{14}O_{18}$(14), $\nu N_{13}O_{17}$(14), $\nu N_{13}O_{16}$(14), $\nu N_{14}O_{19}$(6), sciss$(NO_2)_{13}$(6), νC_4N_{13}(6), νC_2N_{14}(5),
61	1406.4	1351.5	18.0	$\nu N_{13}O_{17}$(12), $\nu N_{13}O_{16}$(11), $\nu N_{15}O_{21}$(8), $\nu N_{15}O_{20}$(7), νC_4N_{13}(6), sciss$(NO_2)_{13}$(6), $\beta(CH_2)_{27}$(6), $\beta C_{23}O_{22}H_{24}$(6),
62	1417.2	1361.9	43.0	$\nu N_{14}O_{18}$(17), $\beta(CH_2)_{27}$(15), $\nu N_{14}O_{19}$(9), $\beta C_{23}O_{22}H_{24}$(9), sciss$(NO_2)_{14}$(7), νC_2N_{14}(6), $\nu C_{23}O_{22}$(5), $\beta O_{18}H_{24}O_{22}$(5),
63	1429.0	1373.2	13.2	νC_4C_5(24), νC_1C_2(24), βC_1H_7(11), βC_5H_8(9), βCH_3(6), βC_3C_9(6),
64	1434.0	1378.1	9.1	βCH_3(72), βCH_3(12), βCH_3(7), νC_3C_9(5),
65	1466.4	1409.2	53.8	$\beta(CH_2)_{27}$(39), $\nu C_{23}C_{25}$(12), $\nu C_{23}O_{22}$(10), $\beta C_{23}O_{22}H_{24}$(8), $\beta O_{18}H_{24}O_{22}$(6),
66	1482.1	1424.3	6.9	νC_2C_3(15), νC_3C_4(14), βC_1H_7(11), βC_5H_8(10), νC_5C_6(9), νC_1C_6(7), βC_2N_{14}(5), βC_4N_{13}(5),
67	1491.1	1432.9	6.2	βCH_3(58), βCH_3(15), βCH_3(10),

(*continued on next page*)

Table 3 (*continued*)

	ν	ν_{scaled}	A	Assignment and PED
68	1516.2	1457.1	7.1	$\beta CH_3(58)$, $\beta CH_3(-16)$, $\beta CH_3(7)$, $\beta CH_3(6)$,
69	1614.6	1551.6	60.5	$\nu C_5C_6(19)$, $\nu C_1C_6(17)$, $\nu N_{15}O_{20}(13)$, $\nu N_{15}O_{21}(13)$, $\nu C_2C_3(8)$, $\nu C_3C_4(8)$, $\beta_2$ring(6),
70	1628.9	1565.4	133.6	$\nu N_{14}O_{19}(23)$, $\nu N_{14}O_{18}(19)$, $\nu C_4C_5(10)$, $\nu C_1C_2(9)$, $\nu C_1C_6(6)$,
71	1645.2	1581.0	13.1	$\nu N_{13}O_{17}(24)$, $\nu N_{13}O_{16}(22)$, $\nu N_{14}O_{19}(16)$, $\nu N_{14}O_{18}(11)$,
72	1673.7	1608.4	222.6	$\nu N_{13}O_{16}(10)$, $\nu N_{14}O_{19}(10)$, $\nu N_{13}O_{17}(9)$, $\nu C_1C_2(9)$, $\nu C_4C_5(9)$, $\nu N_{14}O_{18}(7)$, $\nu C_5C_6(6)$, $\nu N_{15}O_{21}(5)$,
73	1677.5	1612.1	210.8	$\nu N_{15}O_{20}(23)$, $\nu N_{15}O_{21}(23)$, $\nu C_1C_6(9)$, rock$(NO_2)_{15}(8)$, $\nu N_{13}O_{17}(6)$, $\beta C_6N_{15}(6)$, $\nu N_{13}O_{16}(5)$,
74	1700.0	1633.7	20.9	$\nu C_{25}C_{27}(65)$, $\beta(CH_2)_{27}(17)$, $\nu C_{23}O_{26}(8)$, $\beta(CC_2)_{25}(5)$,
75	1796.6	1726.5	406.5	$\nu C_{23}O_{26}(62)$, $\beta C_{23}O_{22}H_{24}(8)$, $\nu C_{23}C_{25}(7)$, $\beta(CO_2)_{23}(6)$,
76	3075.8	2955.8	12.7	$\nu C_9H_{10}(58)$, $\nu C_9H_{12}(26)$, $\nu C_9H_{11}(15)$,
77	3148.8	3026.0	11.7	$\nu C_9H_{12}(45)$, $\nu C_9H_{10}(41)$, $\nu C_9H_{11}(14)$,
78	3170.1	3046.5	5.3	$\nu C_{27}H_{30}(58)$, $\nu C_{27}H2_9(39)$,
79	3184.8	3060.6	10.1	$\nu C_9H_{11}(70)$, $\nu C_9H_{12}(29)$,
80	3211.1	3085.9	3.0	$\nu C_{25}H_{28}(95)$,
81	3262.5	3135.3	18.9	$\nu C_1H_7(97)$,
82	3263.1	3135.8	27.3	$\nu C_5H_8(97)$,
83	3264.7	3137.4	5.0	$\nu C_{27}H2_9(56)$, $\nu C_{27}H_{30}(41)$,
84	3601.7	3461.2	719.9	$\nu O_{22}H_{24}(92)$, $\beta C_{23}O_{22}H_{24}(5)$,

[a] *Abbreviations*: ν, stretching; β, bending or ring deformation; γ, bending (change of dihedral angle); wag, wagging; tw, twisting; sciss, scissoring; τ, torsional vibration or ring deformation. Contributions of less than 5% are not included. ν_{scaled} represents the scaled frequencies (NIST, CCCBDB scaling factor 0.961).

increasing OH stretching and a slight decrease in C═O stretching and COH bending due to hydrogen bond formation between polymer and template.

According to MIP/NIP model the role of croslinking agent is limited to structural one and has no implications in the cavity–template interactions. Due to that reason our model may be reduced to simple 1:1 monomer-template interaction without compromising/jeopardizing the quality of the calculations. Using theoretical 1:1 model one can obtain fast and reliable predictions on monomer-template interactions, IR spectra and solvent influence.

3.4. 1:1 Model

TNT can interact with single AA molecule forming three possible isomers where AA can be located in *ortho*, *meta*, and *para* positions to the methyl group of TNT. Search for the lowest energy complex has been performed and energetically preferred TNT-AA complex has been verified to have AA molecule in *ortho* position. Higher energy isomers differ from the ground state by 0.4 and 1.7 kcal/mol for *meta* and *para* complexes, respectively. The ground state energy isomer of TNT-AA alone has been chosen for study of the 1:1 complex. The interaction energy for this system has been obtained from the formula:

$$\Delta E_{\text{model 1:1}} = E_{\text{model 1:1}} - E_{\text{template}} - E_{\text{monomer}} \quad (3.4)$$

where $\Delta E_{\text{model 1:1}}$ represents interaction energy for 1:1 complex; $E_{\text{model 1:1}}$ is the energy of TNT-AA complex; E_{template} is the calculated energy of TNT, and E_{monomer} is the theoretical energy for *trans* AA. Total interaction energy for the 1:1 complex obtained from the DFT calculations equals −8.9 kcal/mol. Significant discrepancy exists in bond distances between two h-bonds. Bond distances of 2.359 for CH…OC and 1.937 Å for NO…HO indicate that the hydrogen bonding in TNT-AA complex is in indeed dominated by the NO…HO interactions, while the CH…OC interaction plays a minor role in stabilizing the complex.

Additional calculations of interaction energy have been performed where basis set superposition error, BSSE, has been taken into consideration. Counterpoise corrected energy for 1:1 model was found to be 3.0 kcal/mol higher than the uncorrected. The nature of this interaction has been performed through electron density calculations and interaction energy decomposition analyses. NBO charge distribution shows minor charge transfer between studied species, charge transfer from HO to NO amounts only 0.010 electrons. More detailed study of the interaction energy decomposition analysis indicates that the binding energy is dominated by the electrostatic interactions ($\epsilon_{el}^{(10)}$), of −15.5 kcal/mol. However they are significantly reduced by repulsive exchange energy (ϵ_{ex}^{HL}),contribution which amounts to 13.5 kcal/mol. Delocalization (ΔE_{del}^{HF}), and correlation contribution ($\epsilon_{MP}^{(2)}$), terms amount −3.9 and −1.3 kcal/mol respectively, and they do not have significant influence on binding in studied system.

In addition, study on solvent influence on TNT-AA interaction energy has been performed due to its importance for solvent selection for the polymerization process. Acetone and methanol are the two most commonly used solvents for template extraction. It has been found that the presence of solvent molecules significantly lowers the TNT-AA binding energy with a value of −1.8 kcal/mol, whereas binding energy between TNT and acetone or TNT and methanol has been calculated to be −4.4 and −5.2 kcal/mol, respectively.

3.5. IR spectra for TNT-AA 1:1 complex, AA, and TNT

Calculated vibrational frequencies of AA, TNT and their 1:1 complex on the B3LYP/6-31G(d,p) level, their assignments and the percent potential energy distribution (%PED) of normal modes are shown in Tables 1–3. They are compared with experimental data

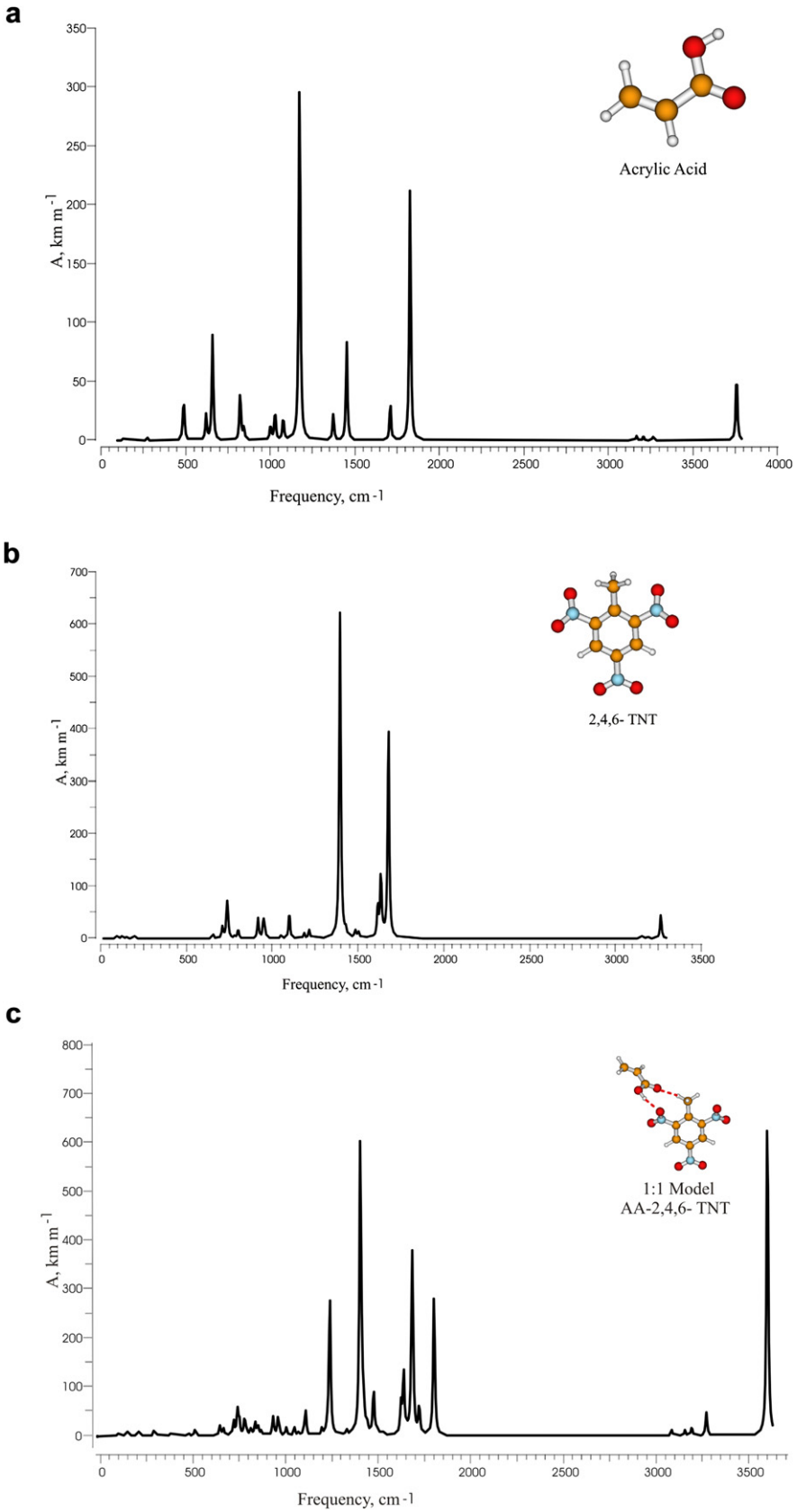

Fig. 5. Theoretically obtained IR spectra for a) acrylic acid, b) 2,4,6-trinitrotoluene and c) 1:1 model (acrylic acid – TNT complex).

obtained by Charles et al. [30] and Stewart et al. [31] for AA and TNT. Additionally, calculated frequencies have been scaled applying NIST CCCBDB scaling factor. Computational IR spectra had been presented in Fig. 5a for AA, Fig. 5b for TNT, and Fig. 5c for the 1:1 complex. AA assigned modes are in good agreement with that assigned by Charles et al. Thus, the OH stretching vibrational mode is observed at 3552 cm^{-1} experimentally, and the corresponding theoretical value is at 3618.3 cm^{-1} (scaled value). Experimental value of CO stretching is localized at 1752 cm^{-1} while the theoretical value is at 1756 cm^{-1}. In plane COH bending vibrational mode has values of 1191 cm^{-1} and 1168.5 cm^{-1} from experiment and theory, respectively. Nitro group stretching mode for TNT is at 1356 cm^{-1} experimentally, which corresponds to theoretical value at 1339.6–1352.0 cm^{-1}. TNT's benzene ring deformation experimental vibrational frequency mode of 1541 cm^{-1} agrees very well with theoretical one of 1552.3 cm^{-1}. The 1:1 complex of AA and TNT has been proposed to verify if TNT imprints into the structure composed from AA molecules. Thus, complex spectra analysis shows the following: OH stretching mode is blue shifted from 3618.3 cm^{-1} (AA) to 3461.2 cm^{-1} (1:1 complex) and possess much higher intensity. CO mode is localized at 1752 cm^{-1} for monomer and also blue shifted to 1633.7 cm^{-1} for the complex. Moreover, COH bending vibrational mode changes from experimental value of 1191 cm^{-1} to red shifted 1223.6 cm^{-1} for the complex, and its intensity decreases significantly. NO vibrational mode for TNT shifts from 1339.6–1352.0 cm^{-1} to 1551.6–1677.5 cm^{-1} for the complex. Also, the TNT's benzene ring vibrational mode decreases with intensity and slightly shifts from 1541 cm^{-1} to 1551.6 cm^{-1}.

4. Conclusions

A model for the cavity formed during molecular imprinting of TNT in AA and EGDMA matrix has successfully been created and electrostatic interactions operated during the imprinting process between cavity and a template have been visualized. It has been verified that three nitro groups of TNT are available for hydrogen bonding with O–H from AA carboxyl group. EGDMA molecule is found to preserve structural shape of the polymeric cavity. MIP/NIP model gave more detailed insight into the bonding within matrix-template system. Based on that model, theoretical IR spectra of MIP and NIP have successfully been calculated at the DFT level and compared with experimental FT-IR data of TNT-AA-EGDMA and AA-EGDMA. Analysis of the bonding, solvent studies and theoretical IR spectra performed on the simplest 1:1 complex shows that applied approximation is sufficient as a tool for monomer selection for molecular imprinting process, as was the main interest of the study. It has been established that molecular imprinting leads to the formation of stable "lock-key" system between polymeric species and a template. Theoretical IR spectra for imprinted and non-imprinted TNT has been compared, where TNT-AA complex formation is shown by OH stretching at wavelength ~3600 cm^{-1}, and intensity ~650 km/mol, which indicates that the "key-lock" complex formation in a gas phase occurs due to hydrogen bonding between OH group of acrylic acid and *ortho* nitro group of TNT.

Acknowledgements

This work has been supported by the Department of Defense through the U.S. Army Engineer Research and Development Center (ERDC, Vicksburg, MS), Contract #W912HZ-06-C-0057; we also thank the Mississippi Center for Supercomputing Research and Wroclaw Centre for Networking and Supercomputing.

References

[1] Binet C, Ferrere S, Lattes A, Laurent E, Marty JD, Mauzac M, et al. Anal Chim Acta 2007;591(1):1–6.
[2] Bunte G, Hurttlen J, Pontius H, Hartlieb K, Krause H. Anal Chim Acta 2007;591(1):49–56.
[3] Alizadeh T, Zare M, Ganjali MR, Norouzi P, Tavana B. Biosens Bioelectron 2010;25(5):1166–72.
[4] Cormack PAG, Elorza AZ. J Chromatogr B 2004;804(1):173–82.
[5] Toal SJ, Trogler WC. J Mater Chem 2006;16:2871–83.
[6] Pawel D, Lagowski J, Lepage CJ. Polymer 2006;47:8389–99.
[7] Dong W, Yan M, Zhang M, Liu Z, Li Y. Anal Chim Acta 2005;542:186–92.
[8] Saloni J, Dasary SSR, Yerramilli A, Yu H, Hill Jr G. Struct Chem 2010;21(6):1171–84.
[9] Parr RG, Yang W. Density-functional theory of atoms and molecules. New York: Oxford University Press; 1994.
[10] Becke D. J Chem Phys 1993;98:5648.
[11] Vosko SH, Wilk L, Nusiar M. Can J Phys 1980;58:1200.
[12] Lee C, Yang W, Parr RG. Phys Rev B 1988;37:785.
[13] Ditchfield R, Hehre WJ, Pople JA. J Chem Phys 1971;54:724.
[14] Clark T, Chandrasekhar J, Spitznagel GW, Schleyer PvR. J Comp Chem 1983;4:294.
[15] Frisch MJ, Pople JA, Binkley JS. J Chem Phys 1984;80:3265.
[16] Davidson N. Statistical mechanics. New York: McGraw-Hill; 1962.
[17] Reed AE, Weinstock RB, Weinhold F. J Chem Phys 1985;83:735.
[18] Simon S, Duran M, Dannenberg JJ. J Chem Phys 1996;105:11024.
[19] Boys SF, Bernardi F. Mol Phys 1970;19:553.
[20] Barone V, Cossi M. J Phys Chem A 1998;102:1995–2001.
[21] Sokalski WA, Roszak S, Pecul K. Chem Phys Lett 1988;153:153.
[22] Jeziorski B, van Hemert MC. Mol Phys 1976;31:713.
[23] Chalasinski G, Szczesniak MM. Mol Phys 1988;63:205.
[24] Varetto U. MOLEKEL version 5.3: Swiss National Supercomputing Centre. Manno, Switzerland.
[25] Frisch MJ, Trucks GW, Schlegel HB, Scuseria GE, Robb MA, Cheeseman JR, et al. Gaussian 03, revision C 02. Pittsburgh, PA; 2004.
[26] Góra RW. EDS v2.1.2 package, Wrocław, Poland. MS, USA: Jackson; 1998–2003.
[27] Schmidt MW, Baldridge KK, Boatz JA, Elbert ST, Gordon MS, Jensen J, et al. J Comput Chem 1993;14:1347.
[28] Politzer P, Murray JS, Koppes WM, Concha MC, Lane P. Cent Europ J Energet Mat 2009;6:165–80.
[29] Zakaria ND, Yusof NA, Haron J, Abdullah AH. Int J Mol Sci 2009;10:354–65.
[30] Charles SW, Cullen FC, Owen NL, Williams GA. J Mol Struct 1987;157:17–29.
[31] Stewart JJP, Bosco SR, Carper WR. Spectrochim Acta 1986;42(1):13–21.